

Springer Series in Materials Science 190

Xiaodong Wang
Zhiming M. Wang *Editors*

High- Efficiency Solar Cells

Physics, Materials, and Devices



Springer

Springer Series in Materials Science

Volume 190

Series Editors

Robert Hull, Charlottesville, VA, USA

Chennupati Jagadish, Canberra, ACT, Australia

Richard M. Osgood, New York, NY, USA

Jürgen Parisi, Oldenburg, Germany

Zhiming M. Wang, Chengdu, P.R. China

For further volumes:

<http://www.springer.com/series/856>

The Springer Series in Materials Science covers the complete spectrum of materials physics, including fundamental principles, physical properties, materials theory and design. Recognizing the increasing importance of materials science in future device technologies, the book titles in this series reflect the state-of-the-art in understanding and controlling the structure and properties of all important classes of materials.

Xiaodong Wang • Zhiming M. Wang
Editors

High-Efficiency Solar Cells

Physics, Materials, and Devices

 Springer

Editors

Xiaodong Wang
Engineering Research Center
for Semiconductor Integrated
Technology
Chinese Academy of Sciences
Beijing, China, People's Republic

Zhiming M. Wang
Engineering Research Center
for Semiconductor Integrated
Technology
Chinese Academy of Sciences
Beijing, China, People's Republic

ISSN 0933-033X

ISBN 978-3-319-01987-1

DOI 10.1007/978-3-319-01988-8

Springer Cham Heidelberg New York Dordrecht London

ISSN 2196-2812 (electronic)

ISBN 978-3-319-01988-8 (eBook)

Library of Congress Control Number: 2013949411

© Springer International Publishing Switzerland 2014

This work is subject to copyright. All rights are reserved by the Publisher, whether the whole or part of the material is concerned, specifically the rights of translation, reprinting, reuse of illustrations, recitation, broadcasting, reproduction on microfilms or in any other physical way, and transmission or information storage and retrieval, electronic adaptation, computer software, or by similar or dissimilar methodology now known or hereafter developed. Exempted from this legal reservation are brief excerpts in connection with reviews or scholarly analysis or material supplied specifically for the purpose of being entered and executed on a computer system, for exclusive use by the purchaser of the work. Duplication of this publication or parts thereof is permitted only under the provisions of the Copyright Law of the Publisher's location, in its current version, and permission for use must always be obtained from Springer. Permissions for use may be obtained through RightsLink at the Copyright Clearance Center. Violations are liable to prosecution under the respective Copyright Law.

The use of general descriptive names, registered names, trademarks, service marks, etc. in this publication does not imply, even in the absence of a specific statement, that such names are exempt from the relevant protective laws and regulations and therefore free for general use.

While the advice and information in this book are believed to be true and accurate at the date of publication, neither the authors nor the editors nor the publisher can accept any legal responsibility for any errors or omissions that may be made. The publisher makes no warranty, express or implied, with respect to the material contained herein.

Printed on acid-free paper

Springer is part of Springer Science+Business Media (www.springer.com)

Preface

As a renewable energy source, solar energy can be harvested and will be increasingly important in the inevitable transition from our current level of dependence on fossil fuels. One of the biggest challenges in photovoltaic technology is how to increase the photocurrent conversion efficiency. Since solar cells were developed several decades ago, consistent efforts have been made in exploring variables that influence optimal efficiency. In recent years, research into high-efficiency solar cells has accelerated with the rapid emergence of new materials and devices showing promising performance characteristics. To achieve further increases in the photocurrent conversion efficiency, it is necessary to choose a suitable material, fabricate a device with proper structure, and to understand the physics behind the materials and devices as a basis for developing new approaches to optimize the materials and device characteristics.

This book addresses these issues comprehensively. It covers the physics needed to understand the performance of a high-efficiency solar cell, presents a variety of novel materials that have emerged in recent years, and describes device optimization approaches such as light-trapping structures and surface plasmons. Chapter 1 is a general introduction to many aspects of high-efficiency Si solar cells developed over the last 20 years. Some representative examples of high-efficiency Si solar cells with excellent performance are presented. Chapter 2 describes the dominant mechanism of radiative recombination in c-Si and the dependence of the intensity of the edge luminescence on the intensity of its excitation. Chapter 3 analyzes the balance between generation, recombination, and transport, and its effect on the photocurrent and open circuit voltage of solar cells for overcoming the Shockley-Queisser limit. Chapters 4 and 5 focus on nanostructures for use in solar cells, including nanowires and quantum wells and dots. High band gap silicon nanocrystal solar cells are discussed in Chap. 6.

In Chap. 7, thiophene-based copolymers synthesized by electropolymerization and used as a hole transport layer in organic photovoltaic cells are presented. Chapter 8 focuses on molecular engineering of efficient dyes for p-type semiconductor sensitization. Chapter 9 describes the production and characterization of Luminescent Solar Concentrator devices based on the dye Lumogen Red

305 dispersed in a matrix (polysiloxane). Chapter 10 introduces the manipulation of energy and electron transfer processes in a light-harvesting assembly in engineered FRET-based solar cells, and efficient near-infrared absorption donor materials for dye-sensitized and organic solar cells. Chlorophyll-derived-, cyclic-Tetrapyrrole-based Purpurins are described in Chap. 11. Chapter 12 highlights the materials, interfaces, and devices of hybrid solar cells. Chapter 13 studies porous TiO_2 nanoparticles applied in PEDOT: PSS photovoltaic devices.

Chapters 14–21 cover device issues of high-efficiency solar cells. Chapter 14 studies the textured microstructures and the photonic nanostructures for light-trapping structures, aiming to suppress the surface reflection. Anti-reflective silicon oxide p-layer for thin-film silicon solar cells is introduced in Chap. 15. Chapters 16 and 17 cover plasmonic silicon solar cells and plasmon-enhanced excitonic solar cells. Finally, Chaps. 18–21 discuss some key aspects of III–V solar cells, including the interfaces (Chap. 18), the anti-reflective coating (Chap. 19), radiation effects (Chap. 20), and the epitaxial lift-off technology used in III–V solar cells (Chap. 21).

The editors would like to express their great appreciation to all of the authors for their excellent chapters. Their enthusiasm and care as seen in every word makes us believe that this book will be an indispensable reference for students, scientists, and engineers in exploring high-efficiency solar cells. We hope it will be seen in retrospect as a milestone volume in this rapidly developing research area. We also thank Mr. Yanpeng Shi for helpful editorial assistance. All of the postgraduate students in our laboratory, especially those working on high-efficiency solar cells, provided much help and a stimulating environment for research. Our appreciation also goes to Springer staff for their support. Finally, the editors acknowledge the support of the National Natural Science Foundation of China under Grant No. 61274066.

Beijing, China, People's Republic

Xiaodong Wang
Zhiming M. Wang

Contents

1	Status and Progress of High-efficiency Silicon Solar Cells	1
	Shaoqing Xiao and Shuyan Xu	
2	Luminescent Study of Recombination Processes in the Single-Crystal Silicon and Silicon Structures Fabricated Using High-Efficiency Solar Cell Technology	59
	A.M. Emel'yanov	
3	Emerging PV Nanomaterials: Capabilities Versus Recombination Losses	85
	Kimberly A. Sablon and Andrei Sergeev	
4	Chalcopyrite Quantum Wells and Dots in Solar-Cell Applications	115
	Esa Räsänen, Sascha Sadewasser, Sebastian Lehmann, and David Fuertes Marrón	
5	Nanostructured Silicon-Based Photovoltaic Cells	131
	Mohamed M. Hilali and S.V. Sreenivasan	
6	High-Bandgap Silicon Nanocrystal Solar Cells: Device Fabrication, Characterization, and Modeling	165
	Philipp Löper, Mariaconcetta Canino, Manuel Schnabel, Caterina Summonte, Stefan Janz, and Margit Zacharias	
7	Thiophene-Based Copolymers Synthesized by Electropolymerization for Application as Hole Transport Layer in Organic Photovoltaics Cells	195
	Spyridon Soulis and Despina Triantou	

8	Molecular Engineering of Efficient Dyes for p-Type Semiconductor Sensitization	215
	Fabrice Odobel, Yann Pellegrin, Frédéric B. Anne, and Denis Jacquemin	
9	Dye-Doped Polysiloxane Rubbers for Luminescent Solar Concentrator Systems	247
	Marta Buffa and Michael G. Debije	
10	Engineering FRET-Based Solar Cells: Manipulation of Energy and Electron Transfer Processes in a Light Harvesting Assembly	267
	Soumik Sarkar, Samim Sardar, Abhinandan Makhal, Joydeep Dutta, and Samir Kumar Pal	
11	Chlorophyll-Derived, Cyclic Tetrapyrrole-Based Purpurins as Efficient Near-Infrared-Absorption Donor Materials for Dye-Sensitized and Organic Solar Cells	319
	Taojun Zhuang, Yuwei Wang, and Xiao-Feng Wang	
12	Hybrid Solar Cells: Materials, Interfaces, and Devices	357
	Giacomo Mariani, Yue Wang, Richard B. Kaner, and Diana L. Huffaker	
13	Implication of Porous TiO₂ Nanoparticles in PEDOT:PSS Photovoltaic Devices	389
	Yahia Djaoued, Jacques Robichaud, Srinivasan Priya, Balaji Subramanian, E. Gondek, M. Pokladko-Kowar, P. Karasinski, and I.V. Kityk	
14	Light Trapping for Solar Cells	449
	Hsin-Hung Cheng, Shih-Wen Chen, Jen-You Chu, Ding-Zheng Lin, Tsung-Dar Cheng, Yi-Ping Chen, Ying-Yu Chang, Hung-Ying Yang, Yung-Ming Yeh, Yu-Sheng Wang, and Jia-Han Li	
15	Anti-reflective Silicon Oxide p-Layer for Thin-Film Silicon Solar Cells	475
	Konrad Schwanitz and Stefan Klein	
16	Design Guidelines for High Efficiency Plasmonics Silicon Solar Cells	497
	Pushpa Raj Pudasaini and Arturo A. Ayon	
17	Plasmon-Enhanced Excitonic Solar Cells	515
	Shuai Chang, Lawrence Tien Lin Lee, and Tao Chen	

18 Interfaces in III–V High Efficiency Solar Cells 545
Alexander S. Gudovskikh, Nikolay A. Kalyuzhnyy,
Sergey A. Mintairov, and Vladimir M. Lantratov

**19 Broadband and Omnidirectional Anti-reflection
Coating for III/V Multi-junction Solar Cells 571**
Silke L. Diedenhofen, Gabriele Vecchi, Gerard Bauhuis,
and Jaime Gómez Rivas

20 Radiation Effects of Space Solar Cells 597
Xin Gao, Sheng-sheng Yang, and Zhan-zu Feng

21 Thin-Film III–V Solar Cells Using Epitaxial Lift-Off 623
G.J. Bauhuis, P. Mulder, and J.J. Schermer

Index 645

Contributors

Frédéric B. Anne CEISAM, CNRS, UMR 6230, Université de Nantes, Nantes cedex 3, France

Arturo A. Ayon MEMS Research Laboratory, Department of Physics and Astronomy, University of Texas at San Antonio, San Antonio, TX, USA

Gerard Bauhuis Applied Materials Science, Institute for Molecules and Materials, Radboud University Nijmegen, Nijmegen, The Netherlands

Marta Buffa Dipartimento di Ingegneria dei Materiali e Tecnologie Industriali, Università di Trento, Povo, Trento, Italy

Mariaconcetta Canino CNR-IMM, Bologna, Italy

Ying-Yu Chang Department of Engineering Science and Ocean Engineering, National Taiwan University, Taipei, Taiwan

Shuai Chang Department of Physics, The Chinese University of Hong Kong, Shatin, N.T., Hong Kong, China

Shih-Wen Chen Department of Engineering Science and Ocean Engineering, National Taiwan University, Taipei, Taiwan

Yi-Ping Chen Material and Chemical Research Laboratories, Industrial Technology Research Institute, Hsinchu, Taiwan

Tao Chen Department of Physics, The Chinese University of Hong Kong, Shatin, N.T., Hong Kong, China

Hsin-Hung Cheng Department of Engineering Science and Ocean Engineering, National Taiwan University, Taipei, Taiwan

Tsung-Dar Cheng Material and Chemical Research Laboratories, Industrial Technology Research Institute, Hsinchu, Taiwan

Jen-You Chu Material and Chemical Research Laboratories, Industrial Technology Research Institute, Hsinchu, Taiwan

Michael G. Debije Chemical Engineering & Chemistry, Eindhoven University of Technology, Eindhoven, The Netherlands

Silke L. Diedenhofen ICFO—The Institute of Photonic Sciences, Castelldefels, Barcelona, Spain

Yahia Djaoued Laboratoire de recherche en matériaux et Micro-spectroscopies Raman et FTIR, Université de Moncton, Shippagan, NB, Canada

Joydeep Dutta Water Research Center, Sultan Qaboos University, Muscat, Sultanate of Oman

A.M. Emel'yanov Ioffe Physical-Technical Institute of the Russian Academy of Sciences, St. Petersburg, Russia

Zhan-zu Feng Science and Technology on Material Performance Evaluating in Space Environment Laboratory, Lanzhou institute of physics, China Academy of Space Technology, Lanzhou, China

Xin Gao Science and Technology on Vacuum & Cryogenics Technology and Physics Laboratory, Lanzhou institute of physics, China Academy of Space Technology, Lanzhou, China

E. Gonddek Institute of Physics, Krakow Technical University, Krakow, Poland

Alexander S. Gudovskikh Renewable Energy laboratory, Nanotechnology Research and Education Centre of the Russian Academy of Sciences, St. Petersburg Academic University, St. Petersburg, Russia

Mohamed M. Hilali Microelectronics Research Center, The University of Texas at Austin, Austin, TX, USA

Diana L. Huffaker Department of Electrical Engineering, University of California, Los Angeles, CA, USA

Denis Jacquemin CEISAM, CNRS, UMR 6230, Université de Nantes, Nantes cedex 3, France

Stefan Janz Fraunhofer ISE, Freiburg, Germany

Nikolay A. Kalyuzhnyy Photovoltaics Lab, IOFFE Physical-Technical Institute, St. Petersburg, Russia

Richard B. Kaner Department of Chemistry and Biochemistry, University of California, Los Angeles, Los Angeles, CA, USA

P. Karasinski Institute of Optoelectronics, Silesian Technical university, Gliwice, Poland

I.V. Kityk Electrical Engineering Department, Czestochowa University of Technology, Czestochowa, Poland

Stefan Klein Thin Film Solar Cells, Solar Business Group, Applied Materials GmbH & Co. KG, Alzenau, Germany

Vladimir M. Lantratov Photovoltaics Lab, IOFFE Physical-Technical Institute, St. Petersburg, Russia

Sebastian Lehmann Solid State Physics, Lund University, Lund, Sweden

Lin Lee Department of Physics, The Chinese University of Hong Kong, Shatin, N.T., Hong Kong, China

Jia-Han Li Department of Engineering Science and Ocean Engineering, National Taiwan University, Taipei, Taiwan

Ding-Zheng Lin Material and Chemical Research Laboratories, Industrial Technology Research Institute, Hsinchu, Taiwan

Philipp Löper Fraunhofer ISE, Freiburg, Germany

Abhinandan Makhil Department of Chemical, Biological and Macromolecular Sciences, S. N. Bose National Centre for Basic Sciences, Salt Lake, Kolkata, India

Giacomo Mariani Department of Electrical Engineering, University of California, Los Angeles, Los Angeles, CA, USA

David Fuertes Marrón Instituto de Energía Solar, ETSIT, Universidad Politécnica de Madrid, Ciudad Universitaria, Madrid, Spain

Sergey A. Mintairov Photovoltaics Lab, IOFFE Physical-Technical Institute, St. Petersburg, Russia

P. Mulder Institute for Molecules and Materials, Radboud University Nijmegen, Nijmegen, The Netherlands

Fabrice Odobel CEISAM, CNRS, UMR 6230, Université de Nantes, Nantes cedex 3, France

Samir Kumar Pal Department of Chemical, Biological and Macromolecular Sciences, S. N. Bose National Centre for Basic Sciences, Salt Lake, Kolkata, India

Yann Pellegrin CEISAM, CNRS, UMR 6230, Université de Nantes, Nantes cedex 3, France

M. Pokladko-Kowar Institute of Physics, Krakow Technical University, Krakow, Poland

Srinivasan Priya Laboratoire de recherche en matériaux et Micro-spectroscopies Raman et FTIR, Université de Moncton, Shippagan, NB, Canada

Pushpa Raj Pudasaini MEMS Research Laboratory, Department of Physics and Astronomy, University of Texas at San Antonio, San Antonio, TX, USA

Esa Räsänen Department of Physics, Tampere University of Technology, Tampere, Finland

Jaime Gómez Rivas FOM Institute AMOLF, c/o Philips Research, Eindhoven, The Netherlands

Applied Physics, Photonics and Semiconductor Nanophysics, Eindhoven University of Technology, Eindhoven, The Netherlands

Jacques Robichaud Laboratoire de recherche en matériaux et Microspectroscopies Raman et FTIR, Université de Moncton, Shippagan, NB, Canada

Kimberly A. Sablon Sensors and Electron Devices, U.S. Army Research Laboratory, Adelphi, MD, USA

Sascha Sadewasser International Iberian Nanotechnology Laboratory (INL), Braga, Portugal

Samim Sardar Department of Chemical, Biological and Macromolecular Sciences, S. N. Bose National Centre for Basic Sciences, Salt Lake, Kolkata, India

Soumik Sarkar Department of Chemical, Biological and Macromolecular Sciences, S. N. Bose National Centre for Basic Sciences, Salt Lake, Kolkata, India

J.J. Schermer Institute for Molecules and Materials, Radboud University Nijmegen, Nijmegen, The Netherlands

Manuel Schnabel Fraunhofer ISE, Freiburg, Germany

Konrad Schwanitz Sensor Development, Electronic Pressure Measurement, WIKA Alexander Wiegand SE & Co. KG, Klingenberg, Germany

Andrei Sergeev Department of Electrical Engineering, State University of New York, Buffalo, Buffalo, NY, USA

Yan-Peng Shi Engineering Research Center for Semiconductor Integrated Technology, Institute of Semiconductors, Chinese Academy of Sciences, Beijing, China

Spyridon Soulis Laboratory Unit “Composite and Advanced Materials, Department III “Materials Science and Engineering”, School of Chemical Engineering, National Technical University of Athens, Athens, Greece

S.V. Sreenivasan Department of Mechanical Engineering, The University of Texas at Austin, Austin, TX, USA

Balaji Subramanian Laboratoire de recherche en matériaux et Microspectroscopies Raman et FTIR, Université de Moncton, Shippagan, NB, Canada

Caterina Summonte CNR-IMM, Bologna, Italy

Lawrence Tien Department of Physics, The Chinese University of Hong Kong, Shatin, N.T., Hong Kong, China

Despina Triantou Laboratory Unit “Composite and Advanced Materials”, Department III “Materials Science and Engineering”, School of Chemical Engineering, National Technical University of Athens, Athens, Greece

Gabriele Vecchi FOM Institute AMOLF, c/o Philips Research Laboratories, Eindhoven, The Netherlands

Yue Wang Department of Chemistry and Biochemistry, University of California, Los Angeles, Los Angeles, CA, USA

Xiao-Feng Wang Research Center for Organic Electronics (ROEL), Graduate School of Engineering, Yamagata University, Yamagata, Japan

Yuwei Wang Department of Chemistry, Renmin University of China, Beijing, People’s Republic of China

Yu-Sheng Wang Department of Engineering Science and Ocean Engineering, National Taiwan University, Taipei, Taiwan

Shaoqing Xiao Plasma Sources and Applications Centre, NIE, Nanyang Technological University, Singapore, Singapore

Institute of Advanced Studies, Nanyang Technological University, Singapore, Singapore

Shuyan Xu Plasma Sources and Applications Centre, NIE, Nanyang Technological University, Singapore, Singapore

Institute of Advanced Studies, Nanyang Technological University, Singapore, Singapore

Hung-Ying Yang Department of Engineering Science and Ocean Engineering, National Taiwan University, Taipei, Taiwan

Sheng-sheng Yang Science and Technology on Vacuum & Cryogenics Technology and Physics Laboratory, Lanzhou institute of physics, China Academy of Space Technology, Lanzhou, China

Yung-Ming Yeh Department of Engineering Science and Ocean Engineering, National Taiwan University, Taipei, Taiwan

Margit Zacharias IMTEK, University Freiburg, Freiburg, Germany

Taojun Zhuang Research Center for Organic Electronics (ROEL), Graduate School of Engineering, Yamagata University, Yamagata, Japan

Chapter 1

Status and Progress of High-efficiency Silicon Solar Cells

Shaoqing Xiao and Shuyan Xu

Abstract High-efficiency Si solar cells have attracted more and more attention from researchers, scientists, engineers of photovoltaic (PV) industry for the past few decades. Many high-quality researchers and engineers in both academia and industry seek solutions to improve the cell efficiency and reduce the cost. This desire has stimulated a growing number of major research and research infrastructure programmes, and a rapidly increasing number of publications in this field. This chapter reviews materials, devices and physics of high-efficiency Si solar cells developed over the last 20 years. In this chapter there is a fair number of topics, not only from the material viewpoint, introducing various materials that are required for high-efficiency Si solar cells, such as base materials (FZ-Si, CZ-Si, MCZ-Si and multi-Si), emitter materials (diffused emitter and deposited emitter), passivation materials (Al-back surface field, high–low junction, SiO₂, SiO_x, SiN_x, Al₂O₃ and a-Si:H), and other functional materials (antireflective layer, TCO and metal electrode), but also from the device and physics point of view, elaborating on physics, cell concept, development and status of all kinds of high-efficiency Si solar cells, such as passivated emitter and rear contact (PERC), passivated emitter and rear locally diffused (PERL), passivated emitter and rear totally diffused (PERT), Pluto, interdigitated back-contacted (IBC), emitter-wrap-through (EWT), metallization-wrap-through (MWT), Heterojunction with intrinsic thin-layer (HIT) and so

S. Xiao (✉)

Plasma Sources and Applications Centre, NIE, and Institute of Advanced Studies,
Nanyang Technological University, 1 Nanyang Walk, Singapore 637616

Key Laboratory of Advanced Process Control for Light Industry (Ministry of Education),
Department of Electronic Engineering, Jiangnan University, Wuxi 214122, China
e-mail: larring0078@hotmail.com

S. Xu

Plasma Sources and Applications Centre, NIE, and Institute of Advanced Studies,
Nanyang Technological University, 1 Nanyang Walk, Singapore 637616
e-mail: shuyan.xu@nie.edu.sg

on. Some representative examples of high-efficiency Si solar cell materials and devices with excellent performance and competitive advantages are presented.

1 Introduction

Among various kinds of renewable energies that have been developed, solar power can be said to be the champion of clean energy since there is no other one being as abundant as our sun. The amount of solar energy reaching our earth within 1 h equals to the total annual energy need of all of mankind, taking into account both heat and electricity. In contrast to fossil fuels, solar energy is starting to be used as the panacea for solving climate change or global warming problems since solar energy sources can provide electricity without giving rise to carbon dioxide and other greenhouse gas emissions. Moreover, it is expected that energy resources on Earth will be almost exhausted and solar energy will have to serve as the main energy source for humans in the next century and beyond.

Silicon-based solar cell invented in 1954 [1], as an important means of the universe space development and competition between American and Soviet in 1960s, has gone through its childhood regardless of the cost. In the 1990s, Si-based solar cell has been industrially commercialized in large scale and the installation of solar cells in personal housing or public facilities has been boosted significantly. For the latest 10 years, Si-based solar cell has reached its mature period because the photovoltaic (PV) market (Si-based solar cell covers 90 % of the PV market) is growing rapidly at an annual rate of 35–40 %, with PV installation around 25 GW in 2012 [2]. A cross-sectional scheme of a typical Si-based solar cell (namely, industrial standard screen-printed p-type Si solar cell) is shown in Fig. 1.1. In general, the light is absorbed in a region more or less close to the surface due to the absorption properties of the material. When incident light is absorbed, electron hole pairs are generated and if their recombination is prevented they can reach the junction where they are separated by the built-in electric field. Even for weakly

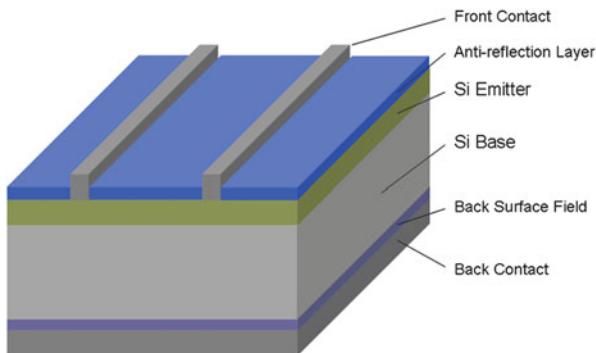


Fig. 1.1 A cross-sectional scheme of a typical Si-based solar cell

absorbing semiconductors like silicon most carriers are generated near the surface. This leads to the typical solar cell structure of Fig. 1.1: the p–n junction separating the emitter and base layer is very close to the surface in order to have a high collection probability for free carriers. The thin emitter layer above the junction has a relatively high conductance which requires a well designed contact grid also shown in the figure. The physics mechanism have been described in many publications [3, 4], and will not be addressed further here.

In the past decade, the cost of Si-based solar cell has been reduced greatly due to the fact that the conversion efficiency increases drastically with the introduction and application of more sophisticated technologies. However, the production cost of Si-based solar cell is still high when compared with conventional fossil-fuel based technologies. Therefore, a large number of research groups all over the world have been devoting to high-efficiency technologies and low-cost technologies. Low-cost technologies are often related to the cost reduction of original material (Si) production, manufacturing facilities, energy consumption and manpower. They are out of scope of this chapter and are not discussed. High-efficiency technologies usually involves novel design of solar cell devices, optimization of light absorption, effective collection of photo-generated carriers, suppression of recombination loss of photo-generated carriers, reduction of electrode area and so on. These technologies result in a variety of high-efficiency Si-base solar cell devices, such as passivated emitter and rear cell (PERC) devices, passivated emitter and rear locally diffused (PERL) cells, passivated emitter and rear totally diffused (PERT) cells, Pluto-cells, interdigitated back-contacted (IBC) solar cells, emitter-wrap-through (EWT) solar cells, metallization-wrap-through (MWT) solar cells and Heterojunction with intrinsic thin-layer (HIT) solar cells.

A high-efficiency silicon-based solar cell not only requires a high-quality p–n junction, whether which is a homojunction or heterojunction, but also requires other functional materials that can enhance the light absorption, provide front and back surface passivation, provide back-surface-field (BSF), act as electrodes to collect currents and so on. For high-efficiency Si-based solar cells, the base material refers to silicon wafer including mono-crystalline (mono-Si) and multi-crystalline (multi-Si) silicon, while the emitter material can be the same kind as the base material for homojunction or amorphous silicon (a-Si) for heterojunction. The functional materials used in high-efficiency silicon-based solar cells usually include silicon nitride (SiN_x), silicon oxide (SiO_2 and SiO_x), aluminium oxide (Al_2O_3), hydrogenated amorphous silicon (a-Si:H), aluminium–silicon alloy, zinc oxide (ZnO), indium tin oxide (ITO), aluminium (Al), silver (Ag), titanium (Ti), etc. These materials have been extensively studied and reported anywhere, from journal literatures to proceeding of symposium.

We feel pleased to write this chapter since high-efficiency Si solar cells substantially step a bright new field with superior importance. The main objective of this work is to create a platform for knowledge sharing and dissemination on latest advances in the areas of high-efficiency solar cells and to provide a comprehensive overview of recent achievements. In this chapter, we explain the most important properties of every material that serve as indispensable part of Si-based solar cell to

contribute to high efficiency, and shed a light on some of the most important points and subjects raised in individual contributions, and also give a brief survey of relevant research efforts in a broader context. The device design and physics mechanism of all kinds of high-efficiency Si solar cells are carefully discussed. In addition, the most significant milestones achieved in each high efficiency Si-based solar cell device are pinpointed and the corresponding opportunities and challenges for large-scale commercialization are also identified. Finally, the long list of relevant references will save time and effort for those producing literature surveys for whatever purpose.

This chapter is organized as follows. Since Si wafer is the core of high-efficiency Si-based solar cells, we first introduce Si material including mono-Si and multi-Si. In this section, the growth mechanisms and characteristics of Czochralski silicon (CZ-Si), float-zone silicon (FZ-Si), magnetically grown Czochralski silicon (MCZ-Si) and multi-Si materials are elaborated. Then we briefly discuss the emitter materials including diffused emitter and deposited emitter. The former induces a homojunction, while the latter usually creates an amorphous–crystalline heterojunction. Next, we present the development and status of most common passivation materials, such as back surface field (BSF) including aluminium–silicon alloy and $p-p^+$ or $n-n^+$ high–low junction, silicon oxide (thermally grown SiO_2 and deposited SiO_x), silicon nitride (SiN_x), aluminium oxide (Al_2O_3) and hydrogenated amorphous silicon (a-Si:H), due to extensive and profound researches in this area. The growth method, passivation performance, processing parameters and their relations of every passivation material are systematically discussed. Also, whether the chemical passivation or field-effect passivation is dominant (or coefficient) in every material is pinpointed. Fourth, other functional materials including antireflective materials, transparent conductive materials and metal electrode materials are briefly presented. In the fifth section, the development and status of a variety of high-efficiency solar cell devices such as PERC, PERL, PERT, Pluto-PERC, Pluto-PERL, IBC, EWT, MWT and HIT are carefully reviewed. The design concept, unique feature and competitive advantage of every high-efficiency Si solar cell device are highlighted. The cell efficiency evolution of every high-efficiency Si solar cell device is also briefly reviewed. This chapter ends with a short summary in the last section.

2 Materials

2.1 Base Material: Mono-Si and Multi-Si

Silicon-based solar cell technology benefits greatly from the high standard of silicon technology developed originally for transistors and later for semiconductor industry. This applies as well to the quality and availability of single crystal silicon of high perfection. In semiconductor industry, more than 85 % of monocrystalline Si (mono-Si) material is grown based on Czochralski (Cz) method [5–7]. Therefore,

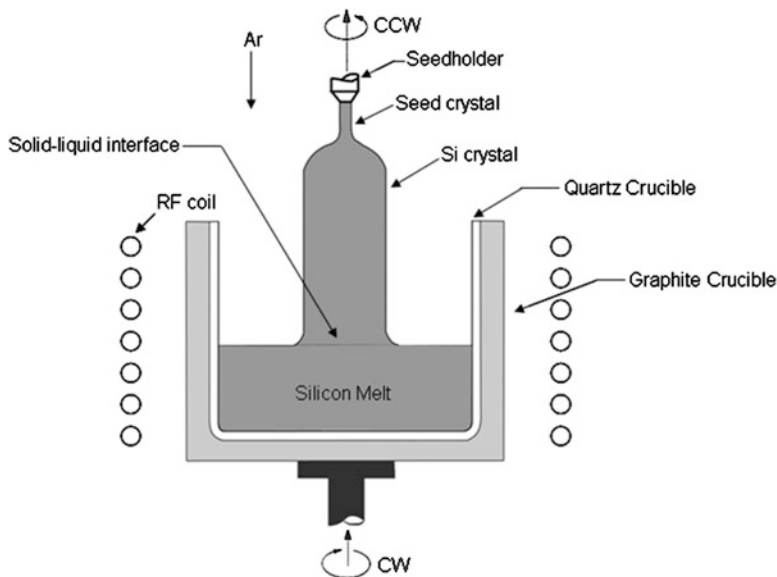
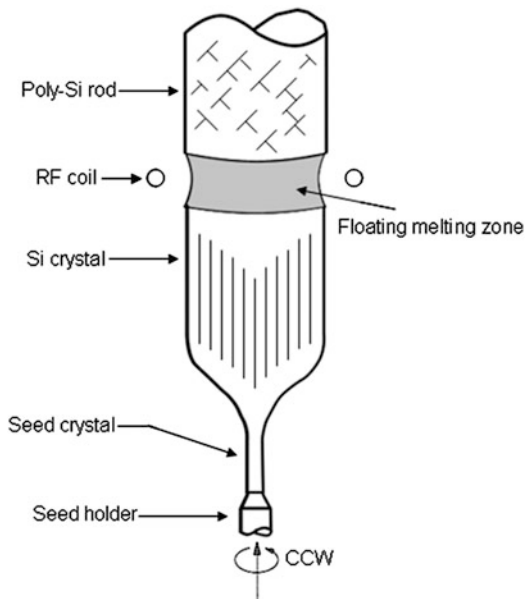


Fig. 1.2 A scheme of Czochralski method for mono-Si growth (CW clock-wise, CCW counter clock-wise)

in the first years only Cz grown mono-Si were used for solar cells. The growth principle of this method is shown in Fig. 1.2. Polycrystalline Si material in the form of fragments is placed in a quartz crucible located in a graphite crucible and melted under inert gases by induction heating [8]. A seed crystal with a certain orientation (like $\langle 111 \rangle$) placed in seedholder is immersed into the melted liquid. Although the seed crystal will be partially melted, the tip of other unmelted part will contact the melt surface. Then as the seed crystal is slowly withdrawn under rotation, a huge single crystal will be formed at the solid–liquid interface as a result of gradual cooling. A standard growth velocity of Cz-grown mono-Si is several millimetres per minute. The silicon melt reacts with every material to a large extent. Only silica can be used as a crucible material, because its product of reaction, i.e. silicon monoxide, evaporates easily from the melt. Even so, approximately 1 % of the oxygen from the crucible goes into the mono-Si ingot [9, 10] and thus Cz grown mono-Si materials contain 10^{17} – 10^{18} cm³ of mainly interstitial oxygen. Mono-Si material grown by Cz method is free of dislocation but still contains point defects. The type of point defect and their concentration are controlled by (1) the V/G ratio, where V is the growth rate and G is the temperature gradient; (2) the cooling rate, $V \times G$; and (3) the oxygen level [11].

An alternative crystal growth technique is the float zone technique (Fig. 1.3), which can grow Si crystals with lower impurities (mainly interstitial oxygen) than that prepared by Czochralski method. A rod of solid and highly purified but polycrystalline silicon with a seed crystal at the bottom is kept in perpendicular

Fig. 1.3 Principle of the float zone (Fz) technique for mono-Si growth (CCW counter clock-wise)



direction and rotated. This rod is sealed in a quartz pipe filled with inert gas (Ar). During the growing process, a small area of the polycrystalline silicon rod is melted by induction heating using rf coil. The rf heater sweeps over the entire polycrystalline silicon rod from the bottom seed crystal to the upper, thus the floating molten zone sweeps as well over the entire polycrystalline silicon rod. The silicon melt is supported by the surface tension between the melting silicon and the growing solid silicon. As the floating melting zone moves up, a highly purified single crystal is formed at the recrystallization zone according to the extended direction of seed crystal. This material is of exceptional purity because no crucible is needed but is more costly than Cz material. In particular, it has a very low oxygen contamination which cannot be avoided with the Cz-material because of the quartz crucible. Float zone (Fz) Si material is frequently used in lab research work and record efficiency for Si solar cells has often been manufactured with Fz Si material. However, it is too expensive for regular solar cell production, where cost is of overriding importance.

Recently, interesting results have been obtained with an advanced technique, magnetically grown Czochralski (Mcz) silicon by Shin-Etsu Handotai in Japan. The principle has been described earlier in [12]. The magnetic field interacts with the free electrons of the silicon and retards convective melt flows. The transport of oxygen from the crucible walls is minimized. Furthermore the distribution of impurities is more uniform.

For solar cells, as well as for all other devices the crystal rods are separated into wafers of 0.2–0.5 mm thickness by multiwire sawing. A wire of several kilometres in length is moved across the crystal in an abrasive suspension, whilst being wound

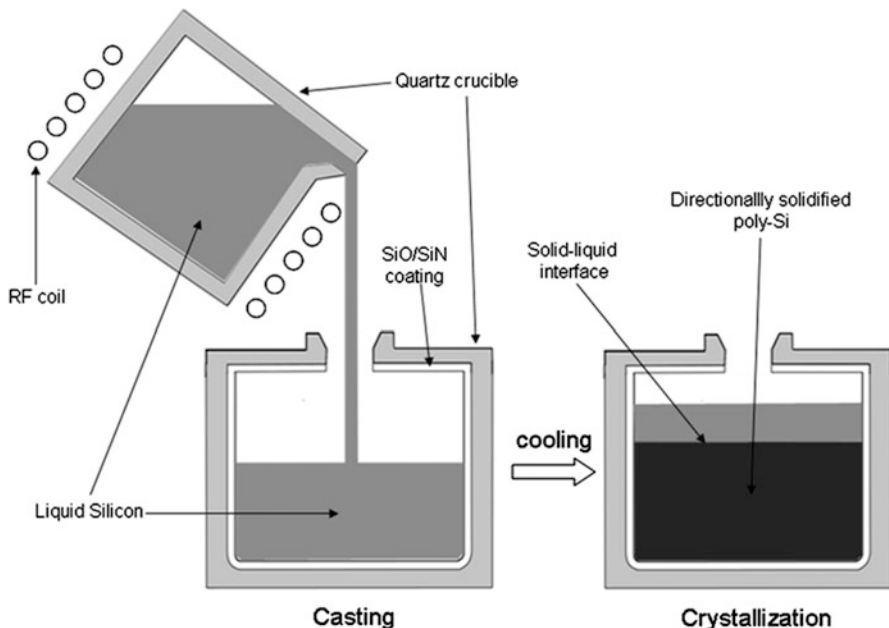


Fig. 1.4 A scheme of block casting for poly-Si

from one coil to another. In this manner, thinner wafers can be produced and sawing losses are reduced by about 30 %.

Since the cost of silicon material is the highest proportion of the cost of a silicon-based solar cell, great efforts have been made to reduce these costs. The dominant technology is block casting [13] which avoids the costly pulling process in comparison with Cz method. Silicon is melted in a square quartz crucible and then poured into a square SiO/SiN-coated quartz crucible (Fig. 1.4). The SiO/SiN coating is used to prevent poly-Si ingot from breaking during the cooling and crystal growth processes since the thermal expansivity of Si is so much larger than quartz that a buffer layer (SiO/SiN coating) is needed. Controlled cooling produces a polycrystalline silicon (poly-Si, also called multicrystalline silicon: multi-Si) block with a large crystal grain structure [14]. The grain size is some millimetre to centimetre and the silicon blocks are also sawn into wafers by multiwire sawing. Poly-Si is only used for solar cells and not for other semiconductor devices. The crystal structure of poly-Si ingot obtained by casting based on a unidirectional growth technique is markedly different from that of mono-Si, as illustrated by the formation of grain boundaries and the distribution of crystallographic orientations, which prevent the realization of high-efficiency solar cells. However, it is much cheaper than mono-Si material. Another advantage of poly-Si is that the blocks can be manufactured easily into square solar cells in contrast to pulled mono-Si rods which are always round. It is much easier to assemble poly-Si wafers into modules with

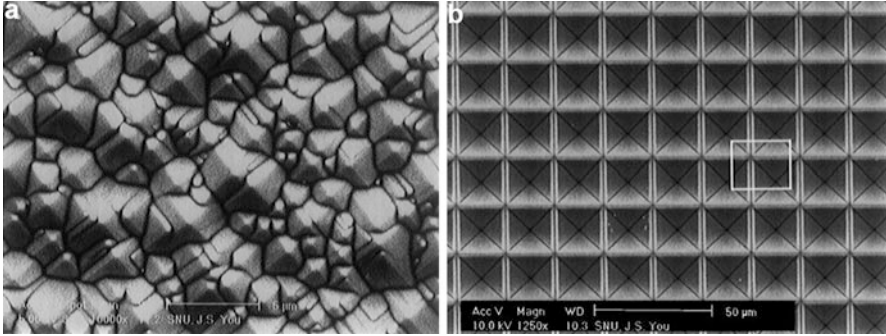


Fig. 1.5 SEM images of mono-Si surface showing random distributed pyramids (a) and uniform inverted pyramids (b) (reproducible from [29])

nearly complete utilization of the module area. Thus, the lower efficiency of poly-Si material tends to disappear at the module level.

In the present-day PV market, mono-Si (Cz) and poly-Si solar cells cover almost 90 % of the total solar cell production, with an average efficiency of 18.5 % and 16.5 %, respectively. Due to the advantages of poly-Si as described above, the proportion of poly-Si solar cells is increasing year by year [15]. In order to obtain high-quality poly-Si material, various new methods such as dendritic casting [16–18], seeded casting [19–21] and other methods [22–24] have been presented by controlling macro- and microstructures of poly-Si ingots in recent years. The crystal growth phenomena during melt growth processes including the morphological transformation of crystal–melt interfaces, grain boundary formation, parallel-twin formation and faceted dendrite growth have also been carefully studied [25]. These contexts are out of scope of this chapter and will not be discussed (please see Refs. [15–25] if the readers are interested) since high-efficiency Si-based solar cells are always fabricated based on mono-Si material (including Cz, Fz and MCz Si material). Advanced solar cells with high efficiency require single crystals of very high perfection other than poly-Si with various types of defect, such as grain boundaries, dislocations, sub-grain boundaries and metallic impurities.

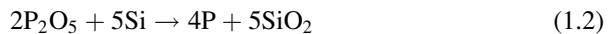
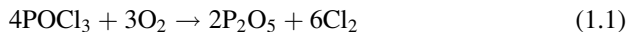
For fabricating high-efficiency Si-based solar cells, an indispensable step after the preparation of silicon wafers is surface texturization. As the refractive index of Si is very high, reflection at the surface of solar cells has to be minimized. Surface texturing not only reduces reflection but also provides oblique coupling of light into the cell. In this manner, the radiation paths are increased and the absorption of infrared radiation is therefore enhanced. Wet chemical treatment is still state of the art to texturize the surface of mono-Si. In general, randomly distributed pyramids (see Fig. 1.5a) are obtained on the surface of mono-Si (100) by a standard anisotropic etching treatment in alkaline solution [26–29]. By using an etching mask (pattern), the pyramids are etched down into the silicon surface rather than etched pointing upwards from the surface, so uniform inverted pyramids (see Fig. 1.5b)

can be produced on the surface [29]. Such texturing is not suitable to apply on poly-Si substrate due to its anisotropic nature. Presently, technique such as acid etch [30, 31] and reactive ion etching [32, 33] have been developed to texturize the surface of poly-Si. Acid texturing, performed with solutions containing hydrofluoric acid (HF) and nitric acid (HNO₃) that tend to isotropically etch poly-Si, can result in features with rounded (pit) surfaces, as opposed to flat-sided features which arise from alkaline etches.

2.2 Emitter Materials

2.2.1 Diffused Emitter

The emitter layer is a requisite to form the p–n junction for (high-efficiency) Si-based solar cells. Nowadays, most Si solar cell manufacturing companies in the world use p-type silicon wafer as the base material. Therefore, phosphorus precursors such as gaseous POCl₃, solid paste P₂O₅ are utilized to realize the phosphorus diffusion and thus the n-type doping [34]. The n-type base is only used in lab for high-efficiency Si-based solar cell. In order to fabricate a p–n junction on the n-type Si wafers, gaseous BBr₃ is employed as the precursor to realize the boron diffusion. Here, we just briefly describe the diffusion process of phosphorus, which is the mainstream in industrial process for Si-based solar cells [35–37]. The diffusion process mainly consists of two processes: i.e. pre-deposition and drive-in. The Si wafers in quartz boat are loaded into the furnace and then heated to 800–900 °C. Nitrogen is bubbled through the temperature-controlled POCl₃ liquid source to deliver dopant in vapour form to the furnace. POCl₃ vapour is mixed with oxygen and then led into the furnace and reacts with the Si surface in high temperature. This pre-deposition process creates a thin and solid doping silicon oxide layer (P₂O₅-SiO₂) with high concentration on the Si surface. The chemical reactions are shown below:



Then these wafers are heated to 850–950 °C for drive-in process by simultaneously stopping supplies of dopant source. At such high temperature, the phosphorus in the silicon oxide layer can diffuse rapidly into Si wafer. Consequently, the emitter profile depends on the processing temperature and time. During the diffusion process, the phosphorous silicate glass (PSG) can also be formed through the reaction between O₂, POCl₃ and Si. The PSG layer (20–40 nm) is usually removed by acid etch in industry.

2.2.2 Deposited Emitter: p-(n-) a-Si:H

Apart from the above diffusion process for the formation of an emitter layer, there is another deposition process that can also fabricate a p-n junction on Si surface. Thin films of p-type (or n-type) hydrogenated amorphous silicon (a-Si:H) are usually deposited on n-type (or p-type) Si surface to fabricate a p-n junction. These thin films are commonly synthesized using SiH_4 , H_2 and B_2H_6 (or PH_3) precursors by a variety of deposition methods, such as plasma enhanced chemical vapour deposition (PECVD) [38–42], hot-wire chemical vapour deposition (HWCVD) [43–45] and inductively coupled plasma chemical vapour deposition (ICPCVD) [46, 47]. Different from the diffusion process where a homojunction is produced (both base and emitter are mono-Si or poly-Si materials), the deposition process typically creates a heterojunction since the base is crystalline while the emitter is amorphous. Amorphous–crystalline silicon heterojunction solar cells have attracted increased attention since it was demonstrated that high efficiencies (21 %) can be achieved on Cz silicon using a simple structure and only low temperature processes [48].

Such emitter is formed by a low temperature deposition process and not by the conventional high-temperature diffusion process above 900 °C. The deposition process has the advantage of not only being a low temperature process, but is also a process in which the doping, band gap, and thickness of the deposited layers can be controlled and profiled accurately, which offers new opportunities for optimizing the device performance. Because of the low temperature process, cheaper lower-quality Si substrates (which would normally degrade in a high-temperature process) can be used. Back surface fields (BSFs) and passivating layers can also be made by deposition and the details will be discussed in the flowing context.

2.3 Passivation Materials

Since the PV solar cells generate solar power by converting the incident illumination into electron-hole pairs and separating the electron-hole pairs to flow out, high-efficiency Si solar cells can be obtained only when both the loss of photo-generated carriers and the loss of sunlight entering into solar cells are reduced [49]. In other words, to produce high-efficiency Si solar cells, the effective minority carrier lifetime (τ_{eff}) should be lengthened and the surface-reflection loss of sunlight should be reduced. To enhance the effective minority carrier lifetime, the surface recombination of photo-generated carriers has to be minimized by using a passivation layer (A reduction in surface recombination is called surface passivation). To reduce the optical loss due to the reflection at the air-c-Si interface, the use of an anti-reflective layer is preferred. We first discuss the surface passivation scheme for high-efficiency Si-based solar cells because the minimization of electronic losses at

the crystal silicon surface is a more delicate challenge compared with the optical management by conventional methods like using an antireflection layer.

Physically, the surface passivation is achieved by two effects: the direct saturation of defects (also called chemical passivation) and the field effect passivation. The chemical passivation aims to reduce the surface defects by saturating the remaining silicon dangling bonds. Technologically, this strategy is much more sensitive to the presence of defects at the surface than the field effect passivation and usually related to a passivating layer deposited or grown over the c-Si surface. In this sense, the cleaning steps before deposition or growth of the passivating film are of paramount importance to reduce the surface defect density. In the last step of RCA [50] or other chemical cleaning methods the wafer is dipped into diluted HF solution in order to eliminate the native oxide at the c-Si surface. Furthermore, this immersion may also achieve a perfect coverage of the c-Si surface dangling bonds by atomic hydrogen (leading to very low surface recombination velocity values [51]). Other approaches to wafer cleaning that are economically less expensive than RCA and therefore easier to transfer to solar cell mass production are dry cleaning methods. They normally consist of subjecting the wafer to plasma with an etching gas [52–54]. The method is also helpful to roughen the surface, thus providing a light trapping scheme. Last but not the least, some passivation techniques are based on dangling bond saturation by atomic hydrogen. For instance, it is common to add molecular hydrogen (H_2) into the precursor gases when a passivating layer of amorphous hydrogenated silicon-based compound like a-Si:H, amorphous hydrogenated silicon nitride ($a-SiN_x$), amorphous hydrogenated silicon carbide ($a-SiC_x:H$), amorphous hydrogenated silicon oxide ($a-SiO_x:H$) is deposited [55]. The same idea is exploited in annealing the samples within a N_2/H_2 atmosphere (Forming Gas).

The field effect passivation consists of producing a band bending at the silicon surface, thus creating an electric field. This electric field will make one type of carriers hard to reach the surface defect centre. Therefore, the recombination rate is strongly reduced since two types of carriers, namely, electrons and holes, are needed to complete the recombination process at the surface defect centre. Technically, the electric field can be produced in several ways, by depositing a charged film or by creating a heavily doped region. Dielectric films storing a high charge density, like amorphous silicon nitride (SiN_x), have already been successfully applied in solar cell industry for both mono- and poly-crystalline silicon solar cells. Recently, another dielectric film, namely, Al_2O_3 with a high negative fixed charge density, which is different from the positive fixed charge density of SiN_x , has attracted much attention as a passivation scheme for high-efficiency Si solar cells. It may also be possible to deposit or grow dielectric layers with a relatively low charge density, like thermally silicon dioxide (SiO_2), and apply an external voltage or an electrostatic charge at the surface by a corona charging instrument to provide the field effect. In the case of heavily doped regions, they can be either high–low junctions with the same type of impurities ($p^+–p$ or $n^+–n$) or $p–n$ junction with opposite doping types. The $p^+–p$ combination is commonly employed at rear side of industrial p -type silicon solar cells using silicon–aluminium alloy and aluminium,

contacting the base and achieving at the same time what is called as back surface field (BSF). On the contrary, the p–n junctions consisting of Si base and emitter are usually contacted and located at the front side of the solar cell, though they can also be not contacted (in the case they are called floating junctions).

In principle, most dielectric layers such as SiN_x , Al_2O_3 and SiO_x provide not only chemical passivation but also field effect passivation. However, a-Si:H can only provide chemical passivation, which is mainly used for high-efficiency silicon heterojunction solar cells. The ability of a passivation layer to perform c-Si surface passivation can be evaluated by the effective minority carrier lifetime (τ_{eff}) of the double-sided passivated c-Si wafer. The effective minority carrier lifetime is currently measured by using the quasi-steady state photoconductance decay (QSSPCD) technique, which was invented by Sinton and Cuevas in 1996 [56]. The effective surface recombination velocity S_{eff} is correlated with the effective minority carrier lifetime τ_{eff} through the following equation:

$$\frac{1}{\tau_{\text{eff}}} = \frac{1}{\tau_{\text{bulk}}} + \frac{2S_{\text{eff}}}{d} \quad (1.3)$$

Where τ_{bulk} is the bulk lifetime of silicon and d is the substrate's thickness. By neglecting the bulk lifetime ($\tau_{\text{bulk}} \rightarrow \infty$), we can obtain the upper limit of S_{eff} .

2.3.1 Back Surface Field (BSF)

Back surface field (BSF) consists of creating a high–low junction, i.e. p–p⁺ or n–n⁺ at the rear side of the solar cell (depending on the doping type of the substrate) that builds a field effect passivation. For industrial standard screen-printed p-type Si solar cells, the state-of-the-art rear side passivation is realized by the p–p⁺ junction using aluminium BSF. Aluminium paste is a standard electrode material for the rear side contacting. Aluminium–silicon alloy can be produced after a firing at a relatively low temperature of 577 °C (the eutectic temperature), with aluminium acting as a p⁺ acceptor. This property is used to create an already contacted p–p⁺ high–low junction. The aluminium BSF is optimal for industrial solar cells since it provides good contact, field effect passivation and reflection at the rear side in a very simple step. However, the maximum open circuit voltage provided by this structure is around 630 mV (corresponding to rear surface recombination velocities ranging from 200 to 600 cm/s [57, 58]), which is insufficient for high-efficiency Si solar cells. For high-efficiency Si solar cells, the Al BSF is partially used such as the implementation of a passivated rear with local Al BSF (PERC-type solar cell).

For high-efficiency HIT solar cells, the rear side passivation is controlled by both the chemical passivation of intrinsic a-Si:H films and the field-effect passivation of the high–low junction, i.e. p–p⁺ or n–n⁺. Thin films of intrinsic and p⁺ (or n⁺) a-Si:H are deposited on the rear side of p-type (or n-type) Si wafers to induce these passivation effects. The chemical passivation of intrinsic a-Si:H films will be discussed in Sect. 2.3.5.

2.3.2 SiO₂ and SiO_x

Thermally grown silicon dioxide (SiO₂) is one of the pioneer passivation schemes for high-efficiency silicon-based solar cells due to the high-quality interface between SiO₂ and c-Si. The formation of SiO₂ is often accomplished by exposing the Si substrate to an oxidizing environment at elevated temperature. Thermal oxidation can be carried out in tube furnaces or in rapid thermal anneal furnaces in O₂ ($T \sim 950\text{--}1,000\text{ }^\circ\text{C}$) or H₂O-vapour ($T \sim 850\text{--}900\text{ }^\circ\text{C}$) atmosphere [59–61]. The corresponding chemical reactions involved are expressed by:



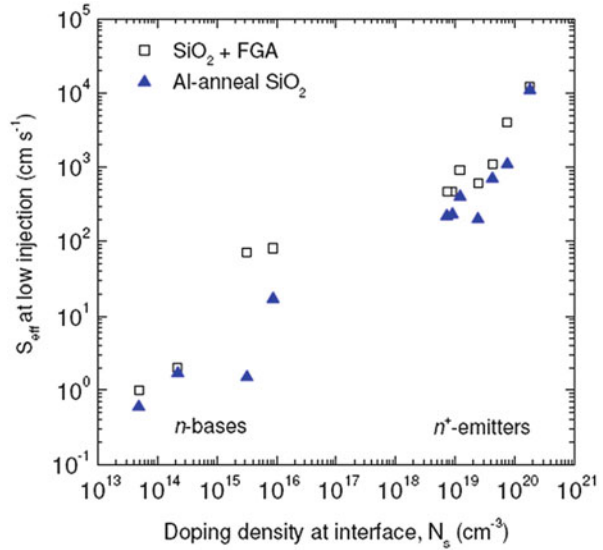
According to the model predicted by Deal and Grove [62] the thickness of SiO₂ depends on the root square of the processing time, the process temperature, the orientation of crystalline surface, and the atmosphere type. In dry atmosphere the growing rates are very low. For instance, to grow a 110 nm thick layer (adequate for antireflective layers on Si) the wafer needs to undergo dry thermal oxidation for 70 min at 1,100 °C. With the H₂O molecule being smaller than the O₂ molecule its diffusion through the already existing oxide layer to the Si–SiO₂ interface is much faster [63] and consequently the growing rate is significantly higher in wet atmosphere [64–66]. However, the quality of the Si–SiO₂ interface is poorer than that obtained by dry oxidation. Therefore, in order to achieve thick SiO₂ layers with good interface quality in a reasonable time it is common to combine dry and wet thermal oxidation.

From the viewpoint of surface passivation, silicon dioxide works mainly by reducing the density of states at the interface. Analysis of the charge density reveals that there is a positive fixed charge density (Q_f) within the dielectric layer with a value in the range of $10^{10}\text{--}10^{11}\text{ cm}^{-2}$ [67, 68]. However, this value level is not high enough to activate the field-effect passivation, which is usually accompanied by a fixed charge density of $>10^{12}\text{ cm}^{-2}$ [69]. Hence, an important benefit of thermal SiO₂ is the high level of chemical passivation that can be achieved for both n- and p-type Si surfaces over a wide range of relevant doping levels.

To further improve passivation effect, forming gas anneal treatment and Al-anneal treatment [60, 61, 70–72] are often used after oxidation. The former is achieved by exposing the passivated wafer to the forming gas at 400 °C for a certain time. The latter is realized by evaporating a sacrificial aluminium layer over the SiO₂ followed by an annealing at 400 °C in H₂O atmosphere. During this anneal, atomic hydrogen is created from the oxidation of the aluminium by H₂O. For both processes, the hydrogen that is introduced during the annealing process diffuses easily towards the interface and saturates most of the remaining dangling bonds, thus leading to a reduction of the interface state density [70, 73].

Up to now, the best results of thermally grown SiO₂ surface passivation after forming gas annealing or Al-annealing allow S_{eff} values below 3 cm/s for both n- and p-type Fz c-Si wafers with a representative resistivity of 1–10 Ω cm [72].

Fig. 1.6 Surface recombination velocity of phosphorus doped bases and emitters as a function of the doping density at the interface provided by thermally grown silicon dioxide. (Reproducible from [77])



For Cz c-Si wafers with high resistivity ($>100 \Omega \text{ cm}$), the lowest S_{eff} values is below 10 cm/s [74, 75]. For lower resistive Cz c-Si wafers this excellent surface passivation is still providing very good results (on p-type silicon $S_{\text{eff}} < 20 \text{ cm/s}$ for $14 \Omega \text{ cm}$ [68] and $S_{\text{eff}} = 41 \text{ cm/s}$ for $0.7 \Omega \text{ cm}$ [76] are achieved). The surface recombination velocity of n-type bases and emitter as a function of the doping density at the interface for silicon dioxide with FGA and Al-anneal treatments is shown in Fig. 1.6 [77]. The trend shown in Fig. 1.6 is actually a general trend for all surface passivation strategies, i.e. the surface recombination velocity increases with doping density due to a higher presence of defects introduced at the interface.

Owing to the excellent passivation properties in combination with good optical properties provided by thermally grown SiO_2 , many research groups have devoted to high-efficiency Si solar cell devices using thermally grown SiO_2 and its stack with other functional materials like silicon nitride or aluminium oxide as the passivation and/or antireflection scheme. Particularly, Zhao et al. at the University of New South Wales achieved a world-record efficiency of 24.0% [78] at a standard test conditions (AM 1.5, 25 °C) with the concept of PERL cell based on Fz Si materials and SiO_2 passivation scheme. With the same concept of cell the efficiency was later improved up to 24.7% [79], which is the present efficiency record of c-Si solar cells working at 1 sun illumination.

Although thermally grown SiO_2 provides excellent passivation properties and thus is quite suitable for high-efficiency Si solar cells, it cannot yet be applied in conventional Si solar industry since it still suffers from inherent disadvantages such as extremely high process temperature and low deposition rate, which are not desirable from not only the throughput but the process compatibility viewpoint. Therefore, various other methods have been explored for developing SiO_x surface passivation films at low temperatures, such as PECVD [80, 81], ICPCVD [82] and

expanding thermal plasma (ETP) technique [83]. These low-temperature processes can be technologically interesting as they open up the possibility for using materials that are less thermally stable and avoids the risk of bulk lifetime degradation. For ICPCVD developed by our group, the minority carrier lifetime in the $\text{SiO}_x\text{:H}$ -passivated p-type Cz Si substrate is up to 428 μs and the corresponding surface recombination velocity is as low as 70 cm/s [82]. Hoex et al. [83] also developed SiO_2 films deposited by means of ETP technique at high deposition rates in the range of 0.4–1.4 $\mu\text{m}/\text{min}$ using an argon/oxygen/octamethylcyclotetra-siloxane (OMCTS) gas mixture. These plasma-deposited SiO_2 films yield effective surface recombination velocities as low as 54 cm/s on 1.3 $\Omega\text{ cm}$ n-type silicon after a 15 min forming gas anneal at 600 $^\circ\text{C}$. Sai et al. studied the fixed charge density values for different growing conditions [68], measuring low values for dry oxidation ($2\text{--}10 \times 10^{10}\text{ cm}^{-2}$), higher values for wet oxidation ($2\text{--}4 \times 10^{11}\text{ cm}^{-2}$), and significantly higher values for CVD ($>10^{12}\text{ cm}^{-2}$). However, higher Q_f values are not beneficial to the surface passivation since it has been deduced that the value of the fixed charge density (Q_f) is approximately proportional to the density of states at midgap position ($D_{\text{it, midgap}}$). On the contrary, surface passivation gets worse as Q_f increases due to the increment of $D_{\text{it, midgap}}$. This is the reason why the lowest S_{eff} values are always obtained for dry thermal oxidation.

2.3.3 Amorphous Silicon Nitride (SiN_x)

The present state of the art in surface passivation and antireflection of industrial silicon wafer solar cells including mono-Si and poly-Si is amorphous hydrogenated silicon nitride (a- $\text{SiN}_x\text{:H}$ or SiN_x for brevity) synthesized by PECVD or microwave plasma PECVD [72, 84–88]. SiN_x is usually made from a gas mixture of SiH_4 and NH_3 . Silane acts as silicon and hydrogen sources. The ammonia, in addition to being a source of nitrogen, has a tendency to deposit SiN with a high ratio of incorporated hydrogen [89]. In SiH_4/NH_3 discharge, electron collisions with SiH_4 and NH_3 produce H and all of the SiH_n and NH_m : SiH_3 , SiH_2 , SiH , Si, NH_2 , NH, N. The reactions between nitrogen-, silicon- and hydrogen-species in the plasma results in an amorphous solid deposit commonly denoted a- $\text{SiN}_x\text{:H}$.

The expansion of this low temperature plasma technology is attributed to a substantial improvement in solar cell efficiency resulting from the deposition of SiN_x in conjunction with fire-through techniques for the metallization step. This enhancement can be ascribed to three driving forces. First, a large amount of hydrogen originating from the plasma gas dissociation and incorporated in the SiN_x film can be driven into the solar cell during the metallization step, leading to an excellent bulk passivation for c-Si or poly-Si solar cells [90, 91]. This effect is particularly significant for poly-Si solar cells [88, 91, 92] since poly-Si contains various types of defects in the bulk as described in Sect. 2.1. The second driving force is the antireflective (ARC) properties of the nitride layer which reduce significantly the light reflection. Indeed, the optical properties of the material can be varied in a wide range by changing the composition. A representative plot

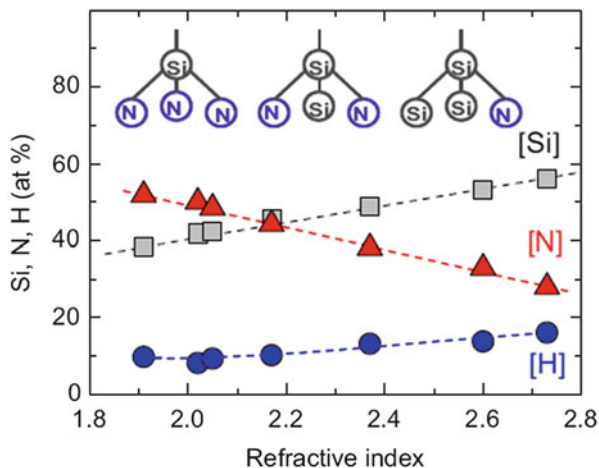


Fig. 1.7 Composition of a-SiN_x:H films in terms of H, Si and N density plotted over the resulting refractive index. The films were deposited in a Roth and Rau MW-PECVD reactor. The atomic densities were obtained by Rutherford backscattering spectroscopy and elastic recoil detection. The inset shows some possible bonding configurations of Si (with dangling bonds) where N₃≡Si- represents the amphoteric K-centre, which is typically positively charged for a-SiN_x:H films on Si substrates (reproducible from [93])

(see Fig. 1.7) presents the material composition in terms of the atomic H, Si and N density as a function of the refractive index [93]. Films with comparatively high nitrogen content (N-rich SiN_x) exhibit refractive indexes of approximately 2, which results in optimal antireflection properties when applied on the front side of a solar cell. In contrast, films with low nitrogen content (Si-rich SiN_x) show higher refractive indexes and therefore higher extinction coefficients, leading to some absorption of light within the film that degrades the antireflection effect. The films also contain a relatively large amount of hydrogen of ~10–15 %, which plays as the first driving force. The third driving force is the surface passivation effect, which is achieved by chemical passivation or/and field-effect passivation.

Whether the chemical passivation or field-effect passivation is dominant in the surface passivation of the a-SiN_x:H films strongly depends on the nitrogen content. When the nitrogen content is relatively low, the Si-rich films exhibit amorphous Si-like properties. In this case, the high level of passivation is mainly governed by chemical passivation. On the other hand, for high nitrogen content, the N-rich films induce a significant amount of field-effect passivation with fixed positive charge densities of the order of 10¹² cm⁻². This is related to the so-called K-centre (a Si atom backbone with three N atoms) that can be charged positively [see Fig. 1.7 (inset)] [94–97]. In general, Capacitance–Voltage (C–V) measurements of metal-oxide-semiconductor (MIS) structures are used to determine the fixed charge density (Q_f) in the film. A very high fixed charge density $Q_f = 3 \times 10^{12}$ cm⁻² was measured by Elmiger and Kunst [98] in their SiN_x films prepared by PECVD. In our previous work [99], we also obtained a high fixed charge density of

$2 \times 10^{12} \text{ cm}^{-2}$ in $\text{SiN}_{0.81}:\text{H}$ films with a refractive index of 2 synthesized by ICP using SiH_4 , N_2 and H_2 precursors. Obviously, this field effect passivation is more beneficial for n-type substrates or emitters than p-type Si surfaces due to the positive polarity of charge density at the interface.

In silicon nitride passivation schemes the comparison between chemical passivation and field-effect passivation has been extensively studied. In a recent work [100], the authors systematically investigate the passivation properties of $\text{SiN}_x:\text{H}$ films prepared by PECVD as a function of the ratio of Si/N. They obtained the best results (n-type Si: $S_{\text{eff}} = 4 \text{ cm/s}$; p-type Si: $S_{\text{eff}} = 14 \text{ cm/s}$) for the Si-rich $\text{SiN}_{0.35}:\text{H}$ films. However, for the N-rich $\text{SiN}_{0.78}:\text{H}$ films the lowest surface recombination velocity (S_{eff}) is 33 cm/s for n-type Si and 68 cm/s for p-type Si, respectively. Note that in the Si-rich films the chemical passivation is dominant while it is contrary in the case of N-rich films. Consequently, it can be deduced that the dominant chemical passivation provides better passivation performances than the dominant field-effect passivation. Nevertheless, the N-rich $\text{SiN}_x:\text{H}$ films provide an appropriate refractive index around 2 for optimal antireflection and thus are generally adopted as the front passivation and antireflection layer for industrial and high-efficiency Si solar cells. In addition, a firing step is performed after the deposition of silicon nitride in industrial processes as well as in the fabrication processes of some high-efficiency Si solar cells, so it is desirable that the films applied keep or enhance their properties after the firing process. Schmidt et al. [101] showed that films with a refractive index of 2.1 (N-rich SiN_x) enhanced the wafer effective lifetime after a short treatment at 900 °C, while when the index was slightly higher ($n = 2.4$) and therefore the films was a bit more rich in silicon, the tendency was inverted. The reason is closely associated with the denser and thermally more stable properties of N-rich $\text{SiN}_x:\text{H}$ films in comparison with Si-rich $\text{SiN}_x:\text{H}$ films. When subjected to a high-temperature treatment, such a layer is believed to induce the release of hydrogen in its atomic form, which consequently leads to an efficient passivation of surface and bulk defects of the Si substrate. This further explains why N-rich SiN_x films with appropriate refractive index of around 2 are generally used in industrial and high-efficiency silicon solar cells.

From the viewpoint of passivation performances, silicon nitride films exhibit a lower level of passivation than silicon dioxide and aluminium oxide. Therefore, N-rich SiN_x films are often incorporated into stacked films such as $\text{SiN}_x/\text{SiO}_2$ and $\text{SiN}_x/\text{Al}_2\text{O}_3$ as a capping layer for high-efficiency Si solar cells due to their dense and thermally stable properties.

2.3.4 Aluminium Oxide (Al_2O_3)

Aluminium oxide (Al_2O_3) has recently emerged as an outstanding passivation scheme for p-type or n-type c-Si wafers or emitters. The field-effect passivation associated with the negative fixed charges near the Al_2O_3 -c-Si interface [102–104], proved to be especially beneficial for the passivation of highly doped p-type wafers or emitters. For achieving high-efficiency p-type c-Si wafer solar cells, the conventional Al-back-surface-field (Al-BSF) has to be replaced by a dielectrically

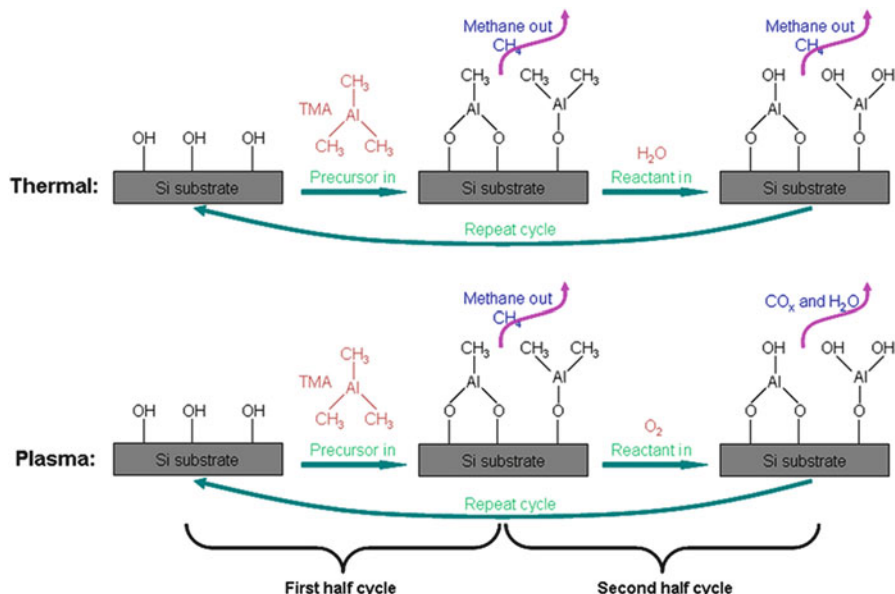


Fig. 1.8 Schematic of one cycle of a thermal and a plasma-assisted ALD process. Each cycle consists of two half-cycles: first, the trimethyl aluminium (TMA) molecules attach to the hydroxyl groups bound to the silicon surface; second, the molecules are oxidized by H_2O (thermal ALD) or an O_2 plasma (plasma ALD)

passivated rear in order to realize better surface passivation and internal reflection as well as reduce wafer bow for thin wafers. Due to the positive polarity of charge density at the SiN_x -Si interface, a-Si N_x :H is not a suitable candidate for the p-type Si rear. As described in Sect. 2.3.1, thermally grown SiO_2 can provide an excellent level of passivation for both p- and n-type Si wafers, and thus has been utilized as the rear passivation scheme for high-efficiency Si wafer solar cells [78, 79]. However, the cost, complexity and a possible adverse impact of high temperatures on the bulk quality make it not appropriate as a first choice. This is why the studies of Al_2O_3 as a passivation scheme for high-efficiency silicon solar cells are becoming a hot and active research area in recent years. Moreover, for high-efficiency n-type Si solar cells a suitable passivation solution of the p^+ emitter is required. The negative charges of Al_2O_3 are an ideal match for the passivation of such emitters in comparison with SiN_x and thermally grown SiO_2 . To date, the application of Al_2O_3 on p^+ emitter and on the p-type Si rear has resulted in enhanced solar cell efficiencies up to 23.9 % [105, 106].

In general, Al_2O_3 films with an outstanding surface passivation quality are usually deposited by plasma-assisted as well as thermal atomic layer deposition (ALD) in lab with a very low deposition rate of < 2 nm/min [107–110]. In the plasma (or thermal) ALD process, one monolayer of Al_2O_3 is grown per cycle, with each cycle consisting of two half-cycles, as depicted in Fig. 1.8. In the first half-cycle, the trimethyl aluminium (TMA) molecules react with hydroxyl (OH) groups

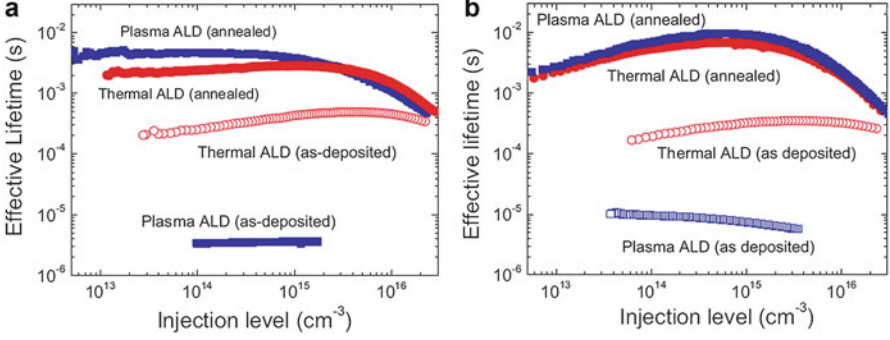
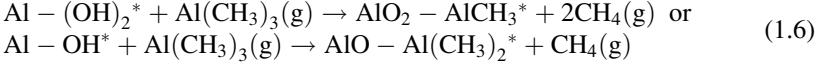
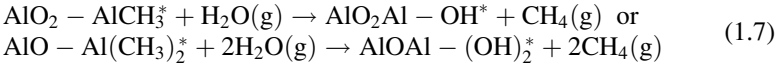


Fig. 1.9 The effective lifetime as a function of the excess carrier density for plasma and thermal ALD- Al_2O_3 before and after annealing (N_2 , 400°C , 10 min) on (a) $\sim 2\ \Omega\ \text{cm}$ p-type c-Si and (b) $\sim 3.5\ \Omega\ \text{cm}$ n-type c-Si (Reproducible from Refs. [114, 116]). The wafers underwent a dip in diluted HF prior to being loaded into the deposition chamber. Films with a thickness of $\sim 30\ \text{nm}$ were deposited at a substrate temperature of $\sim 200^\circ\text{C}$

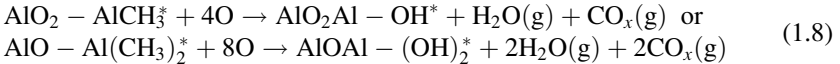
under formation of methane and O–Al bonds. This reaction is very efficient due to the formation of the strong O–Al bond [107]. The surface chemical reaction during the first half-cycle is similar for plasma and thermal ALD, and can be described by



During the second half-cycle step, the surface changes from methyl-terminated to hydroxyl-terminated. For thermal ALD, the surface chemistry can be summarized by



For plasma ALD, H_2O and CO_x are produced during the second half-cycle,



It is noteworthy that the formation of the H_2O by-product during the plasma step can lead to a secondary reaction pathway [111].

Both thermal and plasma ALD deposited Al_2O_3 films can provide an excellent level of passivation effect with very low surface recombination velocities $S_{\text{eff}} < 5\ \text{cm/s}$ on low-resistivity p-type and n-type Si (typically, $1\text{--}4\ \Omega\ \text{cm}$) after annealing at moderate temperatures [102, 103, 112–115]. Figure 1.9 shows the comparison of passivation performances between plasma and thermal ALD deposited Al_2O_3 by

presenting the injection-level-dependent effective lifetime for Al_2O_3 film deposited on p-type and n-type Si [114, 116]. In the as-deposited state, thermal ALD provides a reasonable level of surface passivation with $S_{\text{eff}} \lesssim 30$ cm/s (at an injection level of 10^{15} cm^{-3}) in striking contrast with plasma ALD Al_2O_3 ($S_{\text{eff}} \sim 10^3$ cm/s). After annealing at ~ 400 °C, very high levels of surface passivation with $S_{\text{eff}} < 5$ cm/s (p-type Si) and $S_{\text{eff}} < 2$ cm/s (n-type Si) were obtained for both ALD methods. In contrast to the as-deposited state, the plasma ALD process afforded a lightly higher level of passivation than the thermal ALD process in the annealing state. These intriguing behaviours can be related to small differences in the level of chemical and field-effect passivation obtained by both methods. For thermal ALD Al_2O_3 , the key effect of annealing is the increase of Q_f , whereas for plasma ALD Al_2O_3 the chemical passivation improves dramatically [116–119]. Dingermans et al. [116] reported a relatively low interface defect density (D_{it}) value of $\sim 3 \times 10^{11}$ $\text{eV}^{-1} \text{cm}^{-2}$ for the as-deposited thermal ALD Al_2O_3 , which is consistent with the moderate level of surface passivation obtained prior to annealing. The boost of surface passivation performance for thermal ALD Al_2O_3 after annealing corresponds to the increase in Q_f at Al_2O_3 –Si interface from low values of the order of 10^{11} cm^{-2} to high values of the order of 10^{12} cm^{-2} [116, 119]. However, it has been reported that high Q_f value of 10^{12} cm^{-2} was measured at Al_2O_3 –Si interface for plasma ALD in the as-deposited state whereas this method provided a low level of passivation as shown in Fig. 1.9. This low passivation performance is highly related to the high D_{it} values, which may be due to the exposure of the deposited Al_2O_3 surface to vacuum UV radiation that is present in the plasma [116, 120]. After annealing, the interface defect density (D_{it}) can be reduced to a low value of $\leq 1 \times 10^{11}$ $\text{eV}^{-1} \text{cm}^{-2}$, which is responsible for the dramatically improved chemical passivation and therefore the high level of surface passivation. For both ALD methods, the Al_2O_3 –Si interface after annealing at moderate temperatures features low $D_{\text{it}} \leq 1 \times 10^{11}$ $\text{eV}^{-1} \text{cm}^{-2}$ and high Q_f values in the range of $(2\text{--}13) \times 10^{12}$ cm^{-2} [104, 113, 116–120], both of which contribute to efficient surface passivation and thus result in very low surface recombination velocities.

Due to the negative polarity of Q_f at Al_2O_3 –Si interface, Al_2O_3 is particularly suitable as a passivation scheme for boron-doped emitters. For example, the ALD synthesized Al_2O_3 films can limit the emitter saturation current density to -10 and -30 fA/cm^2 , respectively, for boron doped p^+ emitters with sheet resistances of >100 and 54 Ω/sq [121]. These low saturation current densities imply that a maximum open-circuit voltage (V_{oc}) of up to 700 mV can be obtained for these emitters passivated by Al_2O_3 [112, 122]. One can see from the previous studies [104, 121] that the level of passivation achieved by Al_2O_3 for p^+ surfaces was higher than that obtained by thermal SiO_2 and a-Si:H and significantly higher than that by SiN_x . This can be easily understood due to the differences in strength and polarity of the fixed charges present in the passivation schemes. For n^+ emitters, however, it is expected that the negative Q_f of Al_2O_3 will not contribute to optimal passivation properties when compared to SiN_x containing positive charges. Nevertheless, a recent study [123] shows that implied V_{oc} between 640 and 680 mV can

still be achieved for n^+ emitters with sheet resistances between 20 and 100 Ω/sq using plasma ALD Al_2O_3 . The low interface defect density induced by Al_2O_3 as described above may be primarily responsible for this moderate passivation level.

The chemical passivation of Al_2O_3 has been experimentally associated with the hydrogenation of the Al_2O_3 -Si interface during annealing [124, 125]. In addition to the interface hydrogenation, the chemical passivation may also be influenced by film relaxation, Si-O bond rearrangements, and some additional interfacial oxide growth during annealing [93]. In the meanwhile, simulations and experiments have provided evidence that the negative charge at Si- Al_2O_3 interface may be related to Al vacancies and interstitial O defects [126–130]. Charge injection phenomenon across the interface may play a role in the formation of the negative charge associated with these defects [130–134]. It is worth stressing that also other mechanisms can contribute to negative charges, and that more research is needed to draw final conclusions.

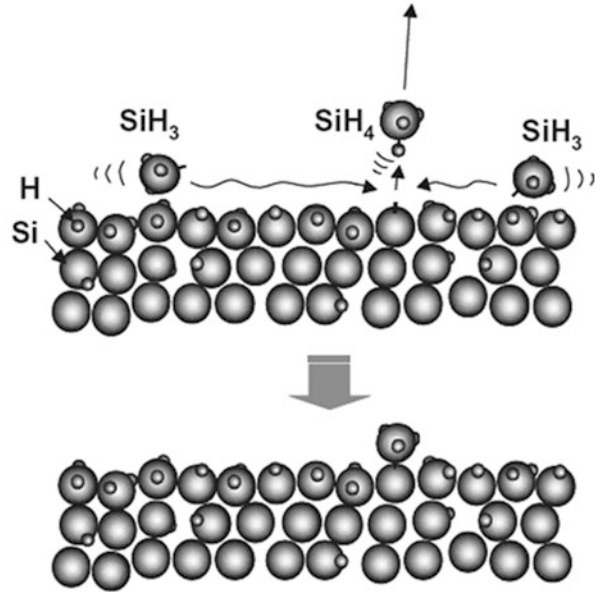
In order to increase the deposition rate of Al_2O_3 for industrial PV applications, a high-rate ALD concept, namely, spatial ALD equipment has recently been developed [135–138]. It is quite remarkable that the high-rate (typically 14 nm/min) spatial ALD produces exactly the same excellent level of surface passivation as the slow-rate conventional thermal or plasma ALD [119, 139–141]. In addition, two other techniques have recently been demonstrated to be suitable for depositing surface-passivating Al_2O_3 layers. PECVD [113, 142, 143] has been shown to provide S_{eff} of only 10 cm/s on 1 Ω cm p-type Fz-Si, whereas reactive sputtering [144] on comparable material has resulted in S_{eff} down to 55 cm/s. However, these two techniques cannot be applied in high-efficiency Si solar cells due to their relatively lower passivation performances in comparison with ALD.

2.3.5 Amorphous Silicon (a-Si:H)

Hydrogenated amorphous silicon (a-Si:H) is a semiconductor material, in contrast to the above passivation materials that are all dielectric materials. Therefore, in addition to being a passivation scheme, a-Si:H has also been used as the base and emitter materials for Si thin-film solar cells. Here we will not elaborate on Si thin-film solar cells because they are out of the subject of high efficiency due to their lower efficiencies ($\sim 10\%$) in comparison with c-Si wafer solar cells, although a record efficiency of 13.1% has been achieved based on a “micromorph” tandem Si thin-film solar cell consisting of a top a-Si:H cell and a bottom microcrystalline Si ($\mu\text{c-Si:H}$) cell [145]. Furthermore, the a-Si:H films can be n or p-type doped by introducing phosphine (PH_3) or diborane (B_2H_6) as precursor gases together with the silane (SiH_4). As discussed in Sect. 2.2.2, these doped films can be deposited on c-Si wafers as the emitter layers to fabricate Si heterojunction solar cells.

The growth mechanism of a-Si:H has been thoroughly studied and a surface-diffusion scheme has been proposed based on experimental results [146]. It has been demonstrated that SiH_3 radical is dominant chemical species of $\text{SiH}_4 + \text{H}_2$ plasma for the growth of a-Si:H [147]. For a-Si:H growth, SiH_3 radical reaching the

Fig. 1.10 A surface-diffusion scheme for the growth of a-Si:H (reproducible from [147])



film-growing surface starts to diffuse on the surface. During surface diffusion, SiH_3 abstracts surface-covering bonded hydrogen, forming SiH_4 and leaving dangling bond on the surface (growth-site formation). Toward the dangling-bond site on the surface, another SiH_3 diffuses to find the site and to make Si-Si bond (film growth) as schematically shown in Fig. 1.10. In general, besides the adsorbed SiH_3 , remaining part of unity-flux density of SiH_3 is reflected by the growing surface. The adsorbed SiH_3 changes its form as follows: (1) SiH_3 abstracts surface-covering bonded H forming SiH_4 or two SiH_3 radicals are encountered on the surface forming Si_2H_6 , and (2) surface-diffusing SiH_3 sticks to the dangling-bond site forming Si-Si bond. Once the building unit SiH_3 has stuck to the dangling-bond site forming Si-Si network, further integration becomes ultimately controlled by the self-organization processes on the nanoscale [148]. It is imperative that, depending on the surface-diffusion scheme, the development of a-Si:H thin films be able to proceed through the layer-by-layer growth scenarios [149].

This a-Si:H has been mainly used as a passivation scheme for high-efficiency Si heterojunction solar cells in recent years [150–153]. In order to improve the performance of heterojunction solar cells a thin intrinsic amorphous silicon (i-a-Si:H) is sometimes inserted between the p layer (or n layer) and the n-type (or p-type) crystalline silicon (the so-called HIT solar cell: heterojunction with intrinsic thin film) [154, 155]. Some other studies [156] have also reported high-efficiency c-Si solar cells using a-Si:H or its stack as the c-Si surface passivation scheme. The passivation principle of amorphous silicon is dominantly based on hydrogen-related chemical passivation. To provide low interface state density at the c-Si-a-Si:H interface good hydrogenation of the interface is critical. Amorphous hydrogenated

silicon (a-Si:H) usually deposited by conventional PECVD at a low temperature of around 225 °C contains a large hydrogen content of >10 % [157], which is responsible for the hydrogenation of the c-Si/a-Si:H interface. Therefore, effective surface recombination velocities of around 2–5 cm/s, which are close to the passivation level of thermally grown oxide, are typically reported in literatures for p-type and n-type wafers with a resistivity of $\sim 1.5 \Omega \text{ cm}$ [156, 158–163]. In particular, surface recombination values as low as 3 cm/s were achieved in $1.5 \Omega \text{ cm}$ wafers by a-Si:H grown by conventional PECVD at 225 °C, which were then applied at the rear side to manufacture a 20.1 % efficient crystalline silicon solar cell [156]. Amorphous silicon can be also deposited by HWCVD and ICP CVD. For example, Muñoz et al. reported implied open circuit voltage near 700 mV after surface passivation of p-type $0.8 \Omega \text{ cm}$ wafers, with S_{eff} around 15 cm/s [164]. In our published work [47, 165], we used a remote ICP system to deposit a-Si:H films and obtained S_{eff} of 30 cm/s after surface passivation of p-type 1–2 $\Omega \text{ cm}$ Cz-Si wafers. Recently, we have also developed a novel capacitive-coupled electrode-less plasma (CCEP) system based on ICP for the deposition of a-Si:H films and obtained S_{eff} as low as 5 cm/s [166].

The excellent passivation properties of a-Si:H deposited at low temperature advance the development of HIT solar cells and a record high efficiency of 23.0 % on HIT solar cells has been achieved by SANYO LTD [167, 168]. However, for industrial c-Si wafer solar cells, there are some limitations of the application of a-Si:H surface passivation films, such as parasitic absorption effect and the lack of thermal stability during high-temperature processes (such as contact firing). The former is related to the strong absorption of a-Si:H for photon energies above the bandgap $E_g = 1.7 \text{ eV}$ [169]. This problem can be solved by tuning the thickness of a-Si:H films to achieve the optimum of transmission and passivation [170]. The latter is associated with the structural properties of a-Si:H. At a high temperature of >450 °C, high hydrogen effusion from the a-Si:H film may occur due to the high mobility of this atom or molecule, leaving remaining dangling bonds at the interface and therefore diminishing the surface passivation quality [171]. Introducing a cap layer (like SiN_x) on the a-Si:H surface (namely, using passivation layer stacks) could lead to more stable films under post annealing effects [158, 159, 171]. The cap layer acts as a diffusion barrier for hydrogen and thus avoid the effusion of hydrogen out of a-Si:H films. In addition, if the cap layer is transparent then it could be applied as an antireflective layer (like SiN_x) at the front side of the solar cell. In this case, the thickness of a-Si:H film can be optimized so that parasitic absorption will be minimized consequently.

2.4 Other Functional Materials

Other functional materials for high-efficiency silicon solar cells include antireflective materials, metal electrode materials, and transparent conductive materials. For high-efficiency c-Si wafer solar cells, SiN_x is the dominant material

as the antireflective layer whether it being a whole passivation scheme simultaneously or being a part of passivation stacks because SiN_x is transparent to sun light and provides a good passivation performance with a tunable refractive index in the range of 1.9 ~ 2.8 [93]. In some other cases, thermally grown SiO_2 can also be used as the antireflection and passivation scheme for high-efficiency Si wafer solar cells since it is transparent to sun light and has an excellent passivation performance with an appropriate refractive index of 1.46. The metal electrode materials generally refer to screen-printed aluminium or silver pastes, ion-beam evaporation deposited aluminium or silver layers, superlattices such as Ti/Pd/Ag and so on. The transparent conductive materials are only used in high-efficiency HIT solar cells. For HIT solar cells, the lateral conductivity of the thin dope a-Si:H layers (emitters) is rather poor, so transparent conductive oxide (TCO) layers are deposited on the a-Si:H films. Ideally, these TCO layers simultaneously guarantee lateral charge transport to the external metal contacts, low contact resistance to the underlying doped a-Si:H layers, and maximal optical transmission into the active absorber, i.e. the c-Si wafer. Indium tin oxide (ITO) and zinc oxide (ZnO) are often the choice of TCO materials in HIT solar cell devices and are usually deposited by reactive magnetron sputtering.

3 High-Efficiency Solar Cell Devices

3.1 *Passivated Emitter and Rear Cell (PERC)*

In this section, we elaborate on high-efficiency PERC devices, which are a developed and improved design of industrial standard screen-printed p-type Si solar cells. As described above, the full-area Al BSF exhibits only a moderate passivation quality for industrial standard screen-printed p-type Si solar cells. In addition, only about 70 % of the infrared light reaching the aluminium rear contact is reflected back into the silicon wafer [172]. These electrical and optical losses can be reduced by applying the passivated emitter and rear cell (PERC) solar cell design [71], as shown in Fig. 1.11. At the cell rear, a significantly improved surface passivation and optical reflectivity are achieved by dielectric layers compared with the full-area Al-BSF. The adaptation from the standard Al-BSF cell to a PERC cell requires local contact formation by, for example, laser processing [173, 174]. Among all dielectric layers discussed above, ALD-deposited Al_2O_3 and thermally grown SiO_2 are most outstanding for the rear side passivation of PERC cells in consideration of the base polarity (p-type). In general, passivation layer stacks such as $\text{Al}_2\text{O}_3/\text{SiN}_x$ or $\text{SiO}_2/\text{SiN}_x$ are applied as the rear side passivation scheme for high-efficiency PERC cells. We will discuss the role of SiN_x capping layer in the following context.

The detailed fabrication process of PERC cells is slightly different from that of industrial standard Al-BSF cells. Before texturing and phosphorus diffusion, a dielectric protection layer such as SiN_x is deposited on the rear side of the solar

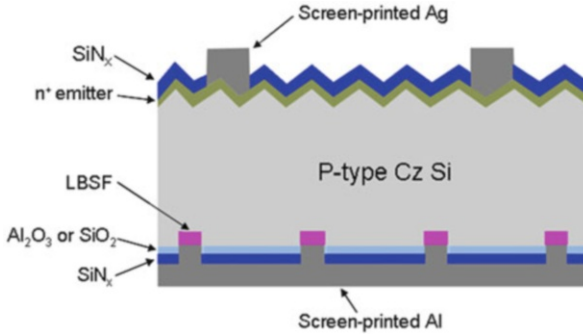


Fig. 1.11 A scheme of the PERC solar cells with screen-printed front and rear contacts with $\text{Al}_2\text{O}_3/\text{SiN}_x$ or $\text{SiO}_2/\text{SiN}_x$ rear passivation stacks. LBSF represents local back surface field

cell. The dielectric layer plays as a barrier against the alkaline texturing process and the phosphorus diffusion. Therefore, only the front side of the solar cell is textured and phosphorus doped, whereas the rear side remains planar and boron doped. The HF etch after the diffusion step is slightly adjusted in order to remove the dielectric layer at the rear in addition to the phosphorus silicate glass (PSG) at the front. Afterwards, a 10-nm ALD-deposited Al_2O_3 layer is deposited or a dry thermal oxidation is carried out resulting in a 10-nm-thick SiO_2 layer on both the rear surface and the front surface. This SiO_2 layer capped by a following deposited SiN_x layer on the front surface can provide a better passivation performance than the single SiN_x layer. Subsequently, a PECVD- SiN_x with a refractive index of $n = 2.05$ and a thickness of about 200 nm is deposited at the rear. The SiN_x capping layer at the rear serves in several roles: (1) it decreases the surface recombination velocity after the firing process of the rear passivation layer for both Al_2O_3 [115] as well as SiO_2 [175]; (2) it protects the 10-nm thin rear surface passivation layer from being etched by the Al paste during the firing process; and (3) it improves the internal optical reflectance of the rear side [176]. The front side is then coated with a 80-nm-thick SiN_x layer. However, for the SiO_2 -passivated PERC cell, the SiN_x thickness is slightly reduced in order to compensate the 10-nm thin SiO_2 at the front and achieve good antireflection properties. Then, the dielectric passivation layer stacks at the rear side are locally ablated by laser contact opening using a pulsed laser to form local line openings. Finally, a screen-printing process on both the front side and rear side followed by a firing step promotes the formation of local Al-BSF and thus finalizes the PERC cell.

In a recent study on high-efficiency PERC cells (p-type Cz Si) [176], Dullweber et al. compared the reflectance and internal quantum efficiency (IQE) between PERC and Al-BSF solar cells, as shown in Fig. 1.12. In the long wavelength region $\lambda > 900$ nm, the dielectric rear surface passivation strongly improves the reflectivity and the IQE. In the inserted table, the $S_{\text{eff, rear}}$ and the internal reflectance R_{rear} are also shown, extracted from the data in the long wavelength region using the software LASSIE [177]. The obtained $S_{\text{eff, rear}}$ values of 70 ± 30 cm/s and

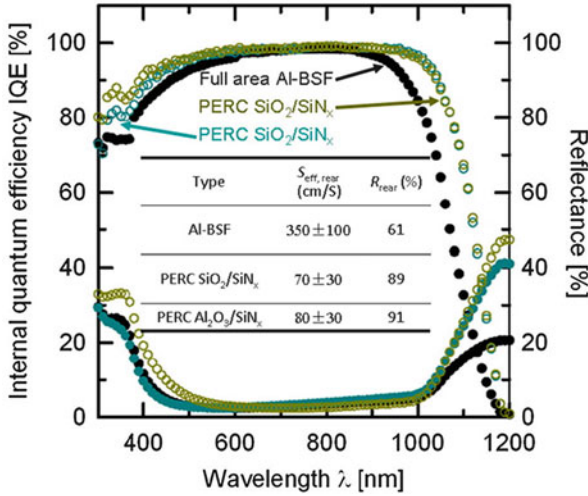
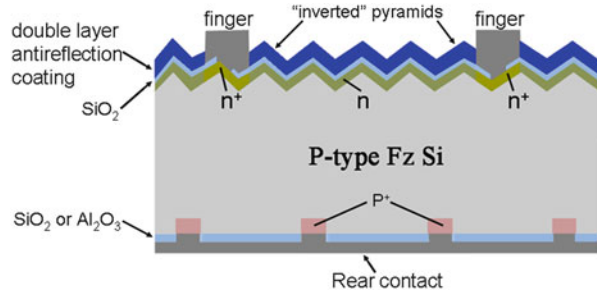


Fig. 1.12 Comparison of internal quantum efficiency (IQE) and reflectance between PERC solar cells with $\text{SiO}_2/\text{SiN}_x$ and $\text{Al}_2\text{O}_3/\text{SiN}_x$ passivation stacks at the rear and a full-area Al BSF reference cell. The *inset table* shows the rear surface recombination velocity $S_{\text{eff, rear}}$ and internal reflectance R_{rear} of the Al-BSF cell and the PERC cells with dielectric passivation stacks at the rear. (Reproducible from [176])

80 ± 30 cm/s for SiO_2 -passivated and Al_2O_3 -passivated PERC cells, respectively, are obviously far smaller than that (350 ± 100 cm/s) for Al-BSF solar cells, indicating a much stronger passivation effect of the dielectric layers than that of Al-BSF. Both the IQE and reflectance results suggest that the dielectric rear surface passivation can provide a higher reflectance especially in the long wavelength region. In particular, they have achieved a high efficiency of 19.0 % and an enhanced efficiency up to 19.4 % for the PERC cell with $\text{Al}_2\text{O}_3/\text{SiN}_x$ passivation stacks and the one with $\text{SiO}_2/\text{SiN}_x$ passivation stacks, respectively.

In the very early time of 1989, a record efficiency of 22.8 % was obtained by Blakers et al. [71] for small-area PERC solar cells based on p-type Fz Si substrates. This strong gain in efficiency can be ascribed to the higher bulk lifetime of Fz Si substrates in comparison with that of Cz Si substrates. In other reports [178–180], high conversion efficiencies up to 19.6 % has been achieved for large-area screen-printed PERC solar cells based on p-type Cz Si substrates. Recently, a novel print-on-print (PoP) process has been considered as a technological improvement that should enable conversion efficiencies of up to 20 % for PERC silicon solar cells (p-type Cz Si substrates) in the near future [176]. For the PoP process, the Ag front contact is deposited in two consecutive screen-printing steps using a DEK PVP1200 printer. In this case, the number of fingers has been increased from 50 for standard single print to 60 for PoP in order to minimize resistive losses due to the significantly smaller finger width. Also the shadowing loss can be reduced, resulting in a higher short-circuit current density. Another technology is the use of Physical Vapour Deposition (PVD) for the metallization of PERC cells instead of the

Fig. 1.13 A schematic structure of the Passivated emitter, rear locally diffused (PERL) cells



standard screen printing of metal pastes for establishing either the complete metalization or a seed layer for subsequent electroplating. Less shadowing and a lower contact resistance are compared to screen printed contacts the two major advantages of sputtered contacts. Using this in-line sputtering technology, the Fraunhofer Institute for Solar Energy Systems (Germany) manufactured large scale ($125 \times 125 \text{ mm}^2$) PERC0020cells based on Fz Si substrates with a high efficiency of 21.1 % [181]. Efficiencies of small-area p-type multi-Si solar cells exceeding 18 % with Al BSF [182] or silicon nitride [183] have been reported, but a much better result of 19.8 % has been achieved by PERC concepts with “honeycomb” textured front surface and thermally grown SiO₂ passivation scheme [184]. However, the high-temperature oxidation (more than 1,000 °C) [185, 186] leads to the significant reduction of minority-carrier lifetime in multi-Si, and thus degrades the efficiency. This thermal degradation can be prevented by lowering the process temperature to 800 °C during wet oxidation of the rear surface. Using this process, Schultz et al. [187] demonstrated conversion efficiencies of 20.3 % for multi-Si and 21.2 % for FZ-Si PERC silicon solar cells on small device areas (1 cm^2).

3.2 *Passivated Emitter, Rear Locally Diffused (PERL) and Passivated Emitter, Rear Totally Diffused (PERT) Cells*

The passivated emitter cell series, particularly the PERL (passivated emitter, rear locally diffused) cells, developed at the University of New South Wales, have made major contributions to the development of high-efficiency silicon solar cells [78, 79, 188–192]. Figure 1.13 shows the schematic structure of PERL cells. In pursuit of the highest cell efficiencies, high carrier lifetime p-type Fz silicon wafers of $1.0 \Omega \text{ cm}$ resistivity and $450 \mu\text{m}$ thickness were often used as the base material for these PERL cells [188–190, 193]. Both the front and rear surface can be passivated and almost completely enshrouded by thermally grown SiO₂, while the rear surface (p⁺) also can be passivated by ALD-deposited Al₂O₃. This oxide reduces recombination along cell surfaces, improving both the collection probability for carriers generated near the surface and the open-circuit voltage. Metal contact to the cell rear is made through small holes in this oxide by laser opening to keep the contact

area as small as possible due to the inferior recombination properties of the contact region. Immediately beneath these rear contact areas, the silicon is heavily doped (with boron) to further suppress contact recombination by providing a field-effect passivation effect and suppressing minority carrier concentrations. Such local $p-p^+$ high–low junction provides a better passivation performance than the local Al-BSF as used in PERC cells. A high lifetime BBr_3 boron diffusion was specially developed for such cell processing [78, 79, 193]. The top surface contact was made via a contact stripe through the oxide to further reduce the recombination loss at this contact. The front contact areas were also further passivated by a heavily phosphorus diffused area. The distribution of emitter layer consisting of heavily doped region (n^+) beneath the contact area and routinely doped region (n) at the non-metallized area is the so-called selective emitter (SE) design [194], which is high on the roadmap list towards high-efficiency Si solar cells.

Apart from the above features that induce almost complete surface passivation and the formation of SE, the incorporation of an efficient rear surface mirror formed by the rear aluminium layer displaced from the silicon surface by the intervening oxide gives a high internal surface reflectance for all internal angles of incidence of light onto this stack. Furthermore, the “inverted pyramid” texture on the front surface by anisotropic etching of the originally (100) orientated surface not only reduces the external surface reflection by giving the incident light two chances to enter, but also gives a high internal reflection for the light reflected from the rear surface. In this way, weakly absorbed light can be trapped in the cell for an average path length enhancement of about 40 times for the present devices [195]. The antireflection coating can be simply single layer such as SiN_x or double layers consisting of two SiN_x layers with different refractive indexes as well as MgF_2/ZnS stacks.

In particular, Zhao et al. at the University of New South Wales fabricated PERL cells based on both multi-Si and Fz-Si materials using thermally grown SiO_2 as the whole passivation scheme and MgF_2/ZnS double layer as the antireflection coating [189]. The “inverted-pyramid” surface texturing of Fz mono-Si substrates is not applicable to multi-Si substrates since it relies on anisotropic etching of the originally (100) orientated surface. Therefore, the authors used a masking oxide with uniformly distributed holes to fabricate honeycomb texture surfaces on multi-Si substrates by isotropic etching through these holes. The insert table in Fig. 1.14 compares the independently confirmed performance of the honeycomb multi-Si PERL cell to both an untextured multi-Si PERL cell and a high-performance Fz mono-Si PERL cell. The latter demonstrates an ultrahigh performance of 24.4 % with extremely high open-circuit voltage of 696 mV, short-circuit current of 42 mA/cm² and fill factor of 83.6 %. The textured multi-Si PERL cell also moves into high-efficiency Si solar cell class since it exhibits a high efficiency of 19.8 % in comparison with the untextured multi-Si PERL cell.

As the wavelength dependent reflection and external quantum efficiency (EQE) of the three cells show (see Fig. 1.14), honeycomb texturing results in reflection generally intermediate between that of untextured cell and the inverted-pyramid cell. At the longest wavelengths, silicon becomes transparent and reflection from all three devices increases. The lower reflection from the textured sample results from

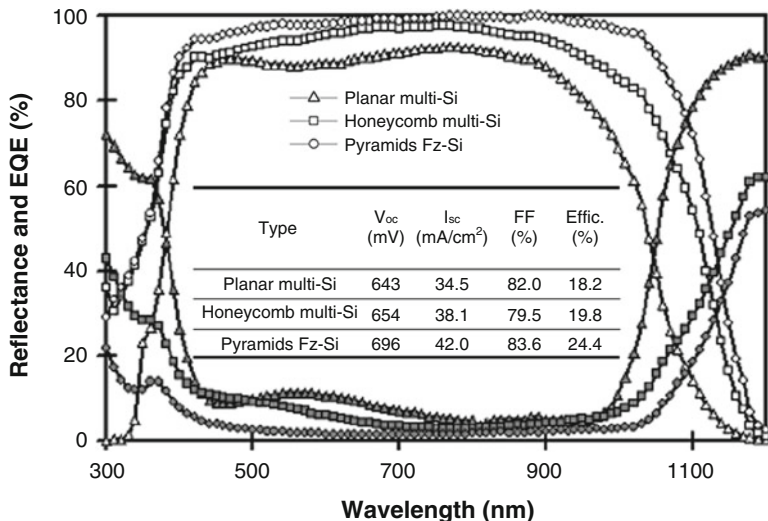
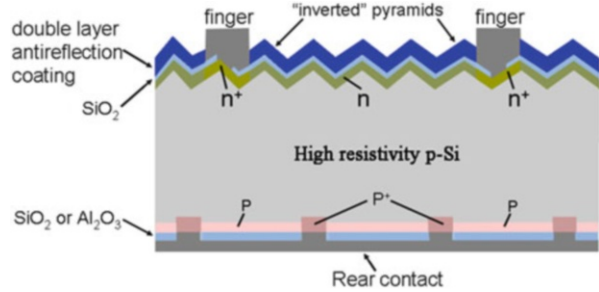


Fig. 1.14 Reflection (*lower curves*) and external quantum efficiency (*upper curves*) as a function of wavelength for the three cells: planar multi-Si PERL cell, honeycomb multi-Si PERL cell and pyramids Fz-Si PERL cell. The *inset table* presents the performances including open-circuit voltage, short-circuit current, fill factor and efficiency of the three PERL cells. Cell area is 1 cm^2 for multi-Si cells and 4 cm^2 for Fz mono-Si device, respectively. Measurements are carried out under standard test conditions (Global AM1.5 spectrum, $100 \text{ mW}/\text{cm}^2$ intensity, $25 \text{ }^\circ\text{C}$ cell temperature). (Reproducible from [189])

increased absorption in this rear reflector due to multiple light passes across the cell. The results suggest light trapping in the honeycomb textured cell is comparably effective to that in inverted-pyramid cells. From overall prospective, the planar cell suffers considerably in reflection and EQE due to poor light trapping. The difference at shorted wavelengths between the textured cells are primarily due to marginally superior optical performance of the inverted-pyramid scheme augmented by the better quality of the Fz monocrystalline material, which ensures that essentially every photogenerated carrier is collected.

In fact, the record efficiencies of small area (4 cm^2) PERL cells on Fz ($1 \text{ } \Omega \text{ cm}$) and MCZ ($\sim 5 \text{ } \Omega \text{ cm}$) Si substrates have been updated to 24.7 % and 23.5 % [190], respectively. The slightly lower efficiency of MCZ Si PERL cells may be related to the fact that many of these MCZ substrates have higher resistivities than those of Fz wafers, and hence giving relatively lower fill factors on such high resistivity wafers due to the current crowding effect at the low coverage small rear contact areas [196]. To reduce this current crowding effect and to improve the cell fill factors, a PERT (passivated emitter, rear totally diffused) cell structure was designed [79, 190–192]. As shown in Fig. 1.15, the PERT cell has added one more processing step to diffuse a light boron layer along the entire rear surface of the cell, while all the other features of the PERL cells remain. The conducting p-type layer totally diffused along the rear surface is expected to supply a low resistance path whereby the photo-generated holes move vertically towards this layer, and then move

Fig. 1.15 Passivated emitter, rear totally diffused (PERT) cell structure



through this diffused layer laterally towards the rear contact windows with minimum resistance loss. This total rear diffusion had also to be compromised between high conductivity and low rear surface recombination velocities. Hence, it was made with a lower boron doping level than the local boron diffusion regions, which were required for passivation of the high recombination rear metal contact.

The PERT structure was firstly reported to improve the fill factors for very-high-resistivity substrates of 100 Ω cm in the early stages of the PERL cell development in early 1991 [197]. In two representative reports [190, 192], for MCZ substrates with a high resistivity of ~ 5 Ω cm, the small area (4 cm²) PERL cells exhibit a relatively lower fill factor of 81.1 % and a lower efficiency of 23.5 % than the corresponding small area (4 cm²) PERT cells with a fill factor of 83.5 % and a high efficiency of 24.5 %, although their open-circuit voltages and short-circuit currents are almost the same. The remarkable 24.5 % efficiency is the highest ever reported efficiency for a silicon cell made on MCZ Si substrate. However, for small area PERL and PERT cells on p-type Cz Si substrates, the maximum efficiency can only reach about 21 % [191, 192].

Apart from p-type substrates, PERL and PERT cells can also be fabricated on n-type substrates. An Al₂O₃/SiN_x stack was used on the front boron-diffused emitter while the back side is still passivated by thermally grown SiO₂ [106]. For n-type Fz Si PERL cells, Benick et al. in Fraunhofer ISE reported record efficiencies of, at that time, 23.2 % ($V_{oc} = 703$ mV, $J_{sc} = 41.2$ mA/cm², FF = 80.2 %) [106]. In a subsequent work, the efficiency was even improved further to 23.9 % ($V_{oc} = 705$ mV, $J_{sc} = 41.1$ mA/cm², FF = 82.5 %) [105]. Internal quantum efficiencies of approximately 100 % were obtained for the front side, in combination with V_{oc} values >700 mV. The n-type PERL cell, featuring local n⁺ BSFs fabricated using photolithography processes, presents a complex cell concept involving many different process steps. To simplify the formation of the n⁺ BSF, a novel process was developed at Fraunhofer ISE where a phosphorous containing passivation layer (called PassDop) is locally opened by a laser under the simultaneous diffusion of P atoms into Si. Using this process, promising efficiencies of 22.4 % have already been demonstrated on Fz n-type Si PERL cells [198]. In recent studies [199], Glunz et al. fabricated small area (4 cm²) n-type PERT cells using Al₂O₃/SiN_x stacks as the front passivation scheme and full metallization of n⁺ diffused rear side, and obtained efficiencies of 20.8 % and 19.4 % for 1 Ω cm Fz and Cz substrates, respectively.

3.3 *Pluto-PERC and Pluto-PERL Cells (Full-Scale Commercialization)*

Among the emerging high-efficiency cell designs, the concept of the SE appears to be the most eagerly pursued approach for commercial application in recent times [200]. Various innovative SE technologies such as doped Si inks [201, 202], oxide mask process [203], ion implantation process [204], etch-back process [205] and laser doping [206–210] have been developed which have demonstrated an average efficiency of 18.5 % in pilot or full-scale Cz mono-Si cell production. Also employing the SE concept is the Pluto cell technology developed by Suntech Power in collaboration with the University of New South Wales [211] based on the world-record holding PERL cell structure [188, 190, 212]. Pluto achieves an average cell efficiency of ~19 % in a 0.5 GW production, with highest efficiency of 19.6 % independently confirmed [213, 214]. This result translates to a 5–10 % boost in efficiency, when directly compared with standard screen-printed cells. However, device loss analysis has indicated that the full Al-BSF at the rear surface accounts for over 50 % of the total dark saturation current of the Pluto cell [215, 216]. This finding clearly reveals that changes and improvements to the rear surface design by incorporating further attributes of PERC or PERL cells may further enhance the cell efficiency. Earlier in 2011, a new record of 19.7 % [214] was independently confirmed by Solar Energy Research Institute for a Pluto cell using the Pluto-PERC cell structure and the same commercial p-type Cz mono-Si wafers. More recently, an efficiency of 20.3 % has again been independently confirmed by SERIS on similar commercial-grade Cz mono-Si wafers, this time using the Pluto-PERL structure [217].

In comparison with PERL cells developed by the University of New South Wales, the Pluto-PERL cells used solar grade p-type Cz wafers instead of high-quality Fz wafers. Also the double-layer antireflection coating is replaced by single layer antireflection coating, namely, SiN_x . The inverted pyramids texture developed by photolithographic texturing is also replaced by upright pyramid texture fabricated by anisotropic etching. Reflection from this surface is below that of the inverted pyramids texture due to the elimination of the flats between adjacent inverted pyramids. This cancels out the loss resulting from the use of a single layer antireflection coating. The effective surface recombination velocity however of the upright pyramids when diffused and passivated with SiN_x is not quite as good as for the photolithographically defined inverted pyramids leading to the loss of several mV in open circuit voltage when the V_{oc} is exceeding 700 mV, but leading to negligible loss when used in conjunction with Cz wafers where the V_{oc} is only in the vicinity of 660 mV. Innovative patterning techniques for the silicon nitride have alleviated the need for both high-temperature thermal oxidations and photolithographic/mask aligning processes. The complicated and expensive metallization scheme consisting of evaporated Ti/Pd/Ag metal contacts have been replaced by a simple, low-cost, high-throughput self-aligned metallization technique. When used in conjunction with the above silicon nitride patterning techniques, metal

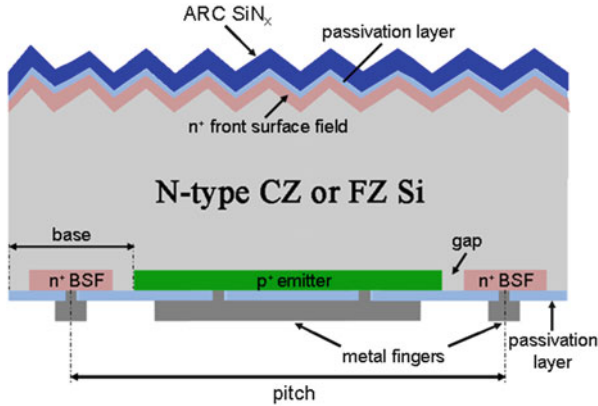


Fig. 1.16 Schematic of an IBC cell, indicating the n^+ -Front Surface Field (FSF), n^+ -BSF, p^+ -emitter, contacts and passivation layers. The definition of pitch, base and gap are also included (The pitch size is the sum of the emitter size and the base size). All contacts are located at the rear

lines comparable in width and conductivity with the photolithographically defined Ti/Pd/Ag metal contacts have been achieved and implemented into large scale production with full size commercial substrates. This important transition was achieved with no performance loss compared to the PERL cells. A 5 % power loss for the Pluto-PERL cells resulted from scaling the typical size ($2 \times 2 \text{ cm}^2$) to that ($12.5 \times 12.5 \text{ cm}^2$) used commercially. This was contributed to by a 2 % loss in short circuit current resulting from the increased metal shading loss and a 3.4 % loss in fill factor [213]. The combined efficiency losses associated with all of the above correspond to a performance loss of 17.3 % for the large area Cz Pluto-PERL cell compared to the small area laboratory type Fz PERL cell. This translates to a reduction in efficiency from approximately 25 % to about 20.5 % [213].

3.4 Interdigitated Back-Contact (IBC) Cells

Interdigitated back-contact (IBC) silicon solar cells become more and more attractive for the industry mass production because of its high-efficiency potential and simple cell interconnection in modules [218]. The main structure differences are the location of the emitter and its contact, which is on the rear for the IBC cell instead of the front for the industrial standard p-type silicon solar cells. For the IBC cell, the emitter and the BSF dopings are both located in an interdigitated structure on the back side of the solar cell, as shown in Fig. 1.16. Thus, both metallization grids are also located at the rear side of the cell. The IBC solar cell has many advantages. The most prominent one is the adoption of all rear contacts, which eliminates optical shading losses at the front side. Therefore, this cell type has an increased absorption and short circuit current density. One more advantage is the

possibility of wide emitter and base metallization fingers at the rear side of the cell to reduce the series resistance of the metal contacts. In general, these IBC cells are mainly fabricated on n-type Si wafers with boron-diffused emitters since n-type Si material has been proved to be more suitable for IBC solar cells due to its larger tolerance to most common impurities compared to p-type Si [219]. Moreover, n-type CZ Si is free of light-induced degradation related to boron–oxygen complexes, which is often seen in p-type CZ Si material.

The fabrication process of IBC cell usually involves the following sequences. First, to enable an optimal light trapping, the front surface of n-type CZ (or FZ) silicon wafers is textured with random pyramids while the rear surface is polished. Second, the front surface field (FSF) and BSF are formed separately by POCl_3 diffusion. Subsequently, the rear emitter pattern is defined by lithography and formed by locally etching the BSF region. This is followed by rear boron diffusion to create p^+ -emitter or screen-printing and firing of aluminium paste to create Al-alloyed p^+ -emitter. Then, a front surface passivation layer followed by an antireflection coating layer (usually single SiN_x layer or $\text{SiO}_2/\text{SiN}_x$ stack) is deposited at the front. Meanwhile, a passivation layer (usually single SiO_2 layer or $\text{SiO}_2/\text{SiN}_x$ stack) is also deposited on the rear. Later on, all the rear contact holes are opened by lithography, and metal contacts are applied by screen-printing or e-beam evaporation.

For IBC cells, the FSF acts as an electrical field that repels the minority carriers at the front surface and thus reduces the front surface recombination [220]. Furthermore, the FSF strongly improves the stability of the passivation quality under UV-light exposure [221]. Finally, solar cells with FSF show a linear current response under low-illumination conditions [222]. In a recent study published by Gong et al. [223], the authors investigated the performance dependence of IBC cells on three different FSF-doping profiles and came to a conclusion that the optimum short-circuit current density (J_{sc}) is expected for the shallowest profile with a low surface concentration.

Many experimental and simulated results [218, 221, 223–231] have shown that the IBC cell performance significantly depends on the pitch size and the emitter fraction (namely, the ratio of the emitter size to the pitch size). Higher J_{sc} values were found for larger emitter fractions and thus a larger current collecting area [223, 228, 229]. In a recent simulation study based on 150- μm -thick n-type FZ wafers with a resistivity of 1 or 8 $\Omega\text{ cm}$ [224], Kluska et al. in Fraunhofer Institute for Solar Energy Systems (ISE) mainly attributed the loss of cell efficiency to both the electrical shading effects on the short circuit current density for small emitter coverage and series resistance losses for large emitter coverage, as shown in Fig. 1.17 (reproducible from [224]). Therefore, the maximum cell efficiencies for the typical IBC cell designs have an emitter fraction between 70 and 80 %, which determines the optimum balance between these two losses. Furthermore, the graphs show the positive influence of an increasing base resistivity on the electrical shading losses as well as its negative effect on the series resistance losses. The positive influence of a rising base resistivity can be seen in the decreasing slope of the cell efficiencies that are limited by electrical shading losses. On the other hand

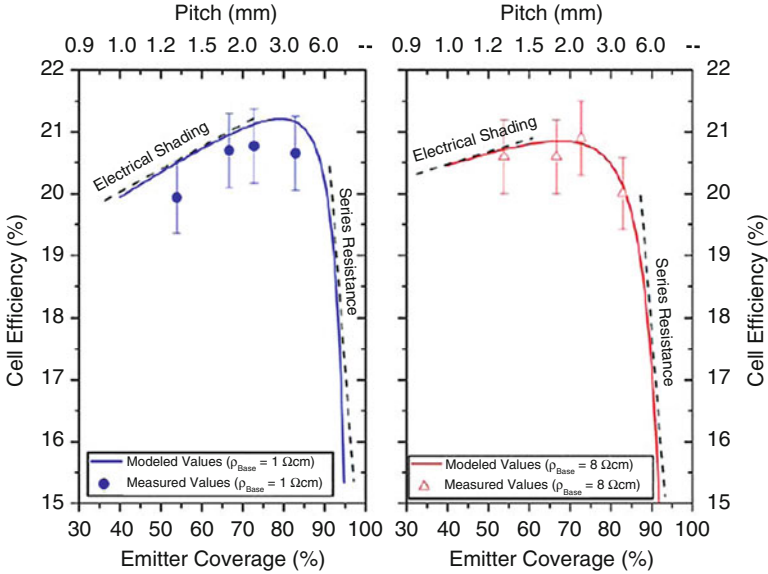


Fig. 1.17 Modeled and measured cell efficiencies for a varying emitter coverage and a constant base width of $600\ \mu\text{m}$. The maximum cell efficiency is a balance between the limiting electrical shading losses and series resistance losses. The error bars are caused by measurement errors. Note that the upper scale of the pitch is not linear. (Reproducible from [224])

the rising base resistivity leads to more series resistance losses, which cause an early decrease of the maximum cell efficiency for large emitter fractions. The same group in Fraunhofer ISE [228, 229] also experimentally demonstrated maximum efficiencies of 21.3 % and 20.7 % on $1\ \Omega\ \text{cm}$ and $8\ \Omega\ \text{cm}$ FZ wafers, respectively for those IBC cells with a pitch of $1,800\ \mu\text{m}$ and an emitter fraction of 67 %. In another experimental investigation based on $2\text{--}3\ \Omega\ \text{cm}$ $300\text{-}\mu\text{m}$ -thick n-type FZ and $2\ \Omega\ \text{cm}$ $200\text{-}\mu\text{m}$ -thick n-type CZ Si wafers [223], the best cells with an efficiency of 19.1 % were those with smallest pitch ($1,600\ \mu\text{m}$) and largest emitter fraction (85.7 %).

Several dielectric layers or stacks such as SiN_x , SiO_2 , Al_2O_3 and their stacks have been tested for their passivation on both the front and rear surface of the IBC cells [218, 220, 223, 226, 229, 232–234]. In a recent paper, Sunpower Corp. has demonstrated a record efficiency of 24.2 % based on large area ($155.1\ \text{cm}^2$) IBC cell designs using n-type FZ wafers and thermally grown- SiO_2 passivation scheme [232]. To date Sunpower Corp. worldwide have successfully implemented their proprietary fabrication approach and industrial feasible patterning techniques in large scale CZ Si IBC cell manufacturing with an average efficiency above 22 % [218]. By applying ALD- Al_2O_3 and PECVD- SiO_x films to the small-area ($4\ \text{cm}^2$) IBC cells based on $1\ \Omega\ \text{cm}$ $200\text{-}\mu\text{m}$ -thick n-type FZ Si wafers, Reichel et al. [234] in Fraunhofer ISE have achieved an efficiency of 22.7 % ($V_{\text{oc}} = 706\ \text{mV}$, $J_{\text{sc}} = 41.0\ \text{mA}/\text{cm}^2$, $\text{FF} = 78.5\ \%$). Other groups also investigated low-cost approaches using currently well-established manufacturing process technologies, such as

wet-processing, tube furnace diffusion, PECVD and screen printing for metallization and patterning, as well as screen-printed Al-alloyed p^+ emitter. Since 2009, Siliken has been building a pilot production line to explore both mainstream and alternative cost-effective processing approaches that can be scaled to production while reaching stabilized efficiencies beyond the 20 % benchmark for CZ Si IBC cells [226]. In a recent study, Bock et al. [233] developed IBC cells using screen-printed Al-alloyed p^+ emitter and Al_2O_3 as the rear passivation scheme and achieved an efficiency of 19.0 % on 1.8 Ω cm 150- μ m-thick n-type FZ wafers. In addition to the n-type Si wafers, IBC cells can also be fabricated on p-type FZ Si wafers. In 2007, Engelhart et al. [220] fabricated the Rear Interdigitated contact scheme through a Single Evaporation (RISE) process and demonstrated an independently confirmed efficiency of 22.0 % for IBC cells on 1.5 Ω cm 300- μ m-thick p-type FZ wafers.

3.5 *Emitter-Wrap-Through (EWT) and Metallization-Wrap-Through (MWT) Cells*

The concept of Emitter-Wrap-Through (EWT) solar cell was first introduced by Gee et al. [235, 236] and then demonstrated by Glunz et al. [237] reporting a cell efficiency of 21.4 % on an area 4 cm² on high-quality material (FZ Si) using PVD for metallization and photolithography as masking technology. As shown in Fig. 1.18, the EWT cell has an emitter at both the front and rear side, but the metal contacts are restricted to the rear, so the front emitter should be connected by a large number of laser-drilled and emitter-diffused via-holes with the rear side emitter. As in the case of IBC cells, the rear side emitter covers a significant fraction of the rear side commonly with interdigitated doping and metallization structure. The advantages of the EWT solar cell are comparable to the ones of IBC cells: (1) complete elimination of optical shading losses at the front side; and (2) the possibility of the coplanar interconnection of metal contacts. However there exists one major advantage of the EWT cells over IBC cells. Due to the presence of emitter on both the front and rear sides, some of the photo-generated minority carriers in the base diffuse to the front emitter, where they become majority carriers and drift through the EWT via-holes to the rear emitter. The other minority carriers diffuse directly to the rear emitter. In this situation, the average distance of the photo-generated minority carriers to the emitter is significantly reduced. This results in the much lower required minority carrier lifetime in the base than in the case of IBC cells. Therefore high current densities can be collected and thus high efficiency can be achieved in this cell structure with medium quality base silicon in comparison with IBC cell structures.

The fabrication process of EWT solar cells usually involves several delicate technologies, such as physical vapour deposition (PVD) for metallization, photolithography as masking technology and laser technology for drilling holes and local

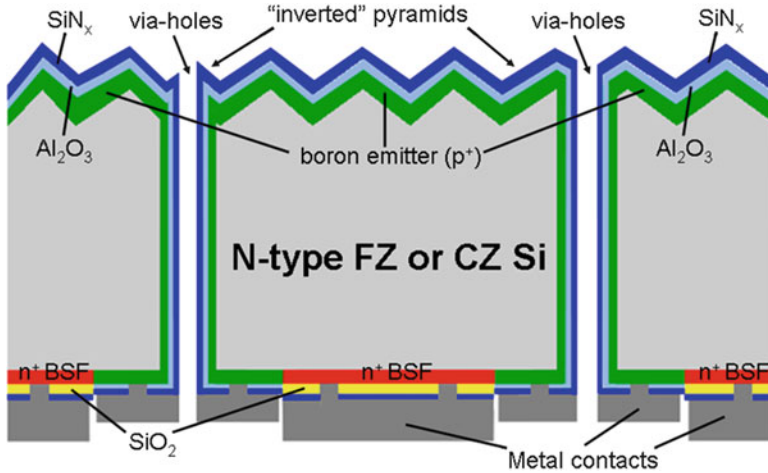
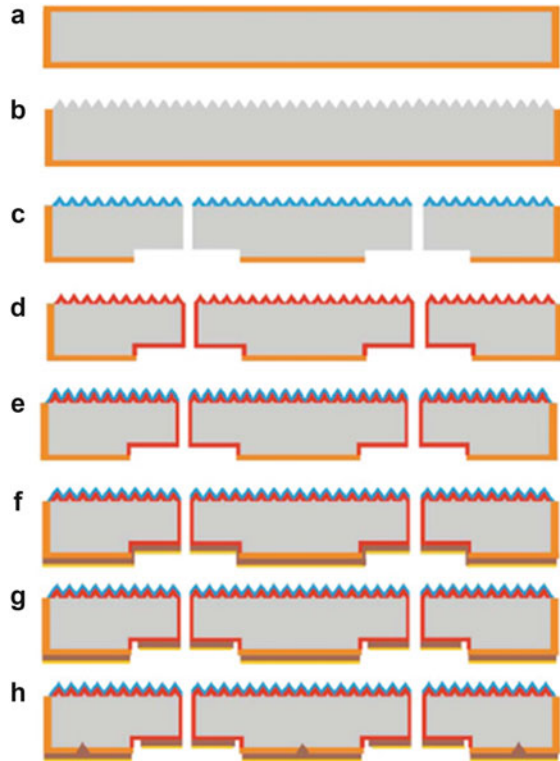


Fig. 1.18 A representative cross-sectional scheme of the n-type FZ or CZ Si EWT solar cells with passivation schemes covering all the Si surfaces: the front side, the rear side and the via-holes. In general, the passivation schemes usually cover only the front and rear surfaces for most Si EWT solar cells

contact openings. Figure 1.19 is a representative processing sequence of p-type CZ-Si EWT solar cells (reproducible from [238]). A detailed description of the process sequence can also be found in [239–241].

- (a) After a standard cleaning step, a wet thermal oxidation at 1,000 °C is performed.
- (b) The SiO₂ is chemically removed from the intended front side to permit texturing using random pyramids.
- (c) After the alkaline texturing, a SiN_x protection layer is deposited onto the textured front side by means of PECVD. Laser technology is then used to locally ablate the SiO₂ layer on the rear side in an interdigitated pattern with photolithography defining the rear side emitter regions. In the meantime, via-holes are also drilled through the wafer using laser technology. The laser-induced damage caused by both processes is subsequently removed by means of a wet-chemical etching step in a KOH solution. During the damage etch, the remaining SiO₂ layer on the rear side acts as an etch barrier leading to the two-level rear side structure of the cell as shown in Fig. 1.19.
- (d) The front side is protected by the SiN_x-coating, which is removed from the wafer after etching. Following that, in a conventional POCl₃ diffusion step at 880 °C, the phosphorus-emitter is formed in the inner wall of the via-holes, on the full textured front side area and at the laser structured and damage etched rear side areas. On the elevated areas of the rear surface the SiO₂ layer acts as a diffusion barrier and thus defines the base structure of the cell.
- (e) Anti-reflection properties and an excellent front surface passivation are achieved by depositing a PECVD-SiN_x.

Fig. 1.19 A representative fabrication sequence of the p-type CZ-Si EWT solar cells. (Reproducible from [238])



- (f) At the rear, a $10\ \mu\text{m}$ thick Al layer is evaporated, followed by a $300\ \text{nm}$ thin layer of SiO_x , which acts as an etching barrier.
- (g) The flanks between emitter and base are selectively etched off [242] because they are less protected by the SiO_x layer, due to its columnar growth. This separates the emitter from the base regions.
- (h) Finally, local base contacts are formed by laser firing.

According to the above discussion, the EWT cells usually exhibit a better performance on medium-quality Si substrates than IBC cells. In early 2003, Kray et al. [243] from Fraunhofer ISE had proved it by comparing the cell performance between EWT cells and IBC cells on degraded silicon substrates. An EWT efficiency of 18.7 % on degraded $1.4\ \Omega\ \text{cm}$ p-type CZ silicon substrates with bulk lifetime of $35\ \mu\text{s}$ and thickness of $250\ \mu\text{m}$ outperforms clearly the IBC (14.9 %) and even the PERC (18.1 %) cell [243]. The superiority comes mainly from the very high J_{sc} of the EWT cell of more than $41\ \text{mA}/\text{cm}^2$ on FZ as well as degraded CZ-Si substrates. This striking difference becomes manifest in very different external and internal quantum efficiencies for EWT and IBC cells, as shown in Fig. 1.20 (reproducible from [243]). From around 400–850 nm, the EQE/IQE of the EWT cell is more than 25 % absolute higher than that of the IBC. This underlines the excellent carrier collection efficiency of the EWT cell compared to the IBC that

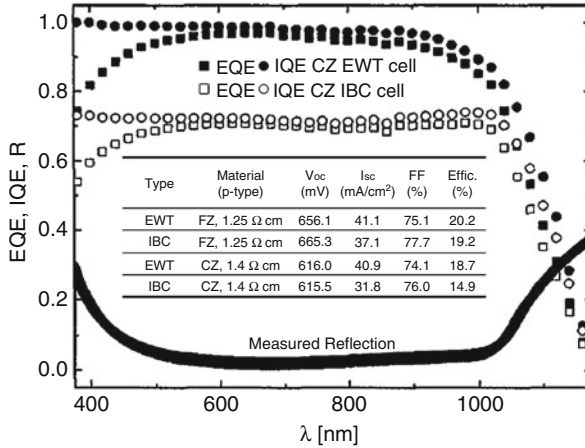
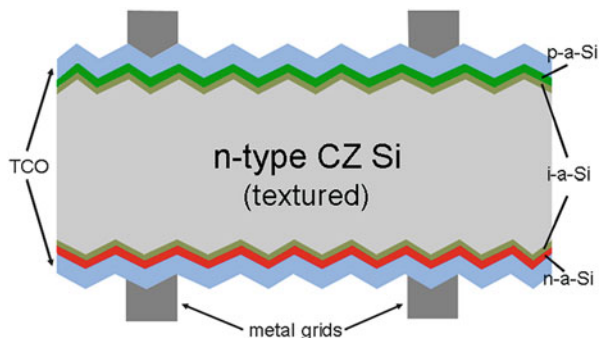


Fig. 1.20 Measurement of external and internal quantum efficiencies as well as reflection of EWT and IBC cells on degraded 1.4 Ω cm CZ-Si substrates. The *inset table* presents EWT and IBC cell results on 1.25 Ω cm FZ-Si and degraded 1.4 Ω cm CZ-Si substrates. (Reproducible from [243])

cannot cope with medium-quality silicon substrates. As for high-quality Si substrates, a maximum efficiency of 21.4 % on p-type FZ Si substrates with 91.9 cm^2 aperture area has been reported by Engelhart et al. [240, 244] using laser processing and PVD-metallization. The highest efficiency on industrial p-type monocrystalline material quality (1.4 Ω cm CZ-Si) is 20.3 % achieved by Lim et al. using laser-processing and PVD-metallization with a comparatively simple process (“RISE-EWT”) [245]. The abbreviation “RISE” means a Rear side Interdigitated contact pattern and mask-free metallization by a Single vacuum Evaporation step. This process involves only one phosphorus diffusion and one thermal oxidation process step and thus is considered suitable for large-scale industrial production. In a recent study published by Mingirulli et al. [246], designated area (16.7 cm^2) conversion efficiencies of up to 18.8 % on FZ materials have been obtained by applying the single step side SE fabrication unique and conventional screen-printing for metallization instead of PVD-metallization. Apart from the mainstream studies on p-type Si EWT cells, Kiefer et al. [247] from the Institute for Solar Energy Research Hamelin (ISFH), Germany, have developed high-efficiency EWT cells for n-type silicon wafers. By passivating the front and rear boron-diffused p-type emitter by a stack of aluminium oxide and silicon nitride (Al_2O_3 - SiN_x) and using a POCl_3 -diffusion process that forms a BSF as shown in Fig. 1.18, they have demonstrated a record efficiency of 21.6 % ($V_{oc} = 661$ mV, $J_{sc} = 40.4$ mA/cm^2 , FF = 80.8 %) on small area (4 cm^2) 1.5 Ω cm CZ-Si substrates [247].

Despite these high performances, EWT cells have not yet performed as well as expected, because their efficiency levels are usually reduced by small fill factors (FFs) [237, 239, 240, 243, 244]. Recently, Ulzhöfer et al. [238, 248] have demonstrated that a recombination enhancement caused by lateral current flows is

Fig. 1.21 The schematic structure of the n-type CZ-Si HIT cell developed by Sanyo



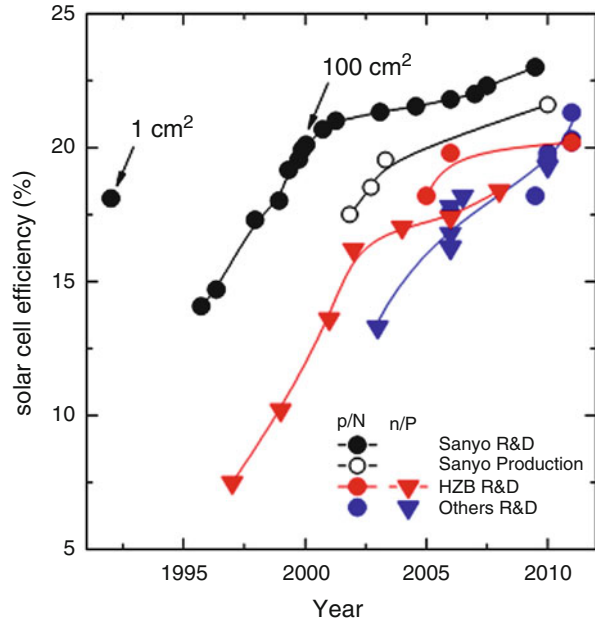
responsible for reducing the FF and efficiency, particularly for relatively high wafer resistivities higher than $3 \Omega \text{ cm}$. It is shown [238] that the critical parameter for optimizing FF is the base resistivity, which strongly determines the injection-dependent excess carrier density and the recombination mechanisms in the base. For this reason, silicon wafers with low resistivities are often used as silicon substrates for high-efficiency EWT cells.

3.6 HIT Solar Cells

Heterojunction with intrinsic thin-layer (HIT) solar cell is an improved version of silicon heterojunction (SHJ) solar cell, which was first proposed by Fuhs et al. [249]. SHJ solar cells composed of a-Si/c-Si use only doped hydrogenated amorphous silicon (p-type or n-type a-Si:H) as the emitter and contact layers on c-Si substrates, so the resultant efficiencies are usually low due to the unpassivated c-Si surfaces. In order to achieve high-efficiency devices, Sanyo Co. Ltd [250, 251] developed a new a-Si/c-Si heterojunction structure called HIT, which features a very thin intrinsic a-Si layer inserted between the doped a-Si layer and the c-Si substrate. This simple yet novel structure has been attracting a growing amount of attention year by year. This is because: (1) it simultaneously enables an excellent surface passivation and p-n junction, resulting in high efficiency; (2) its low-temperature processes ($<200 \text{ }^\circ\text{C}$) can prevent any degradation of bulk quality that happen with high-temperature cycling processes in low-quality silicon materials such as solar grade CZ Si; and (3) compared with conventional diffused cells, a much better temperature coefficient can be obtained with high- V_{oc} cells [38, 40, 252] (Fig. 1.21).

A typical scheme of the n-type Si HIT solar cell developed by Sanyo is shown in Fig. 1.22. The n-type 250- μm -thick CZ Si substrate is first cleaned and textured for double sides. The p-n junction is usually created by the deposition of intrinsic a-Si and p-type a-Si layers on the n-type textured c-Si substrate with the PECVD method. On the rear side, the BSF structure is achieved by depositing intrinsic

Fig. 1.22 Conversion efficiencies development of HIT solar cells in Sanyo, Helmholtz Zentrum Berlin (HZB) and other research institutes. HZB group achieved maximum efficiencies of 19.8 % and 17.8 % on n-type and p-type c-Si, respectively. (Reproducible from [257])



a-Si and n-type a-Si layer stacks. On both deposited surfaces, TCO layers and metal electrodes are formed with the sputtering and screen-printing method, respectively. All processes (including metallization process) are performed at temperatures of below 200 °C. As Sect. 2.4 describes, the TCO layer on the front surface also works as a transparent and anti-reflection (AR) layer through the optimization of its thickness. In general, the finger electrode on the AR layer is narrower than that of conventional p–n diffused solar cells, to compensate for the poor sheet resistance of the TCO layer. As for the electrode on the back, the researchers in Sanyo Co. Ltd [38, 40, 252] also use a finger electrode to make the HIT cell symmetrical between front and rear so that the thermal and mechanical stresses in the device can be reduced. Therefore, this solar cell is suitable for various applications, such as the bifacial modules. This symmetrical structure and the low temperature processes further offer the advantage of decreasing the thickness of the cell and reducing the production cost.

The most striking feature of the HIT cell is the very high efficiency (>20 %) realized with a simple fabrication process. This high efficiency is highly associated with the high open-circuit voltage (V_{oc}) (>700 mV) due to the effective carrier trapping within the generation region (c-Si) of the symmetrical heterostructure. In comparison, for a simple p-a-Si/n-c-Si SHJ structure, only a V_{oc} of less than 600 mV can be obtained [40]. In the p/n heterojunction, the interface state density caused by the doping materials, which attach to the c-Si surface during the deposition process, seems to deteriorate the junction properties significantly. By inserting an intrinsic layer into the p-a-Si/n-c-Si heterojunction, these defects caused by the doping materials can be avoided and thus the junction properties could be improved

drastically [253]. Furthermore, as Sect. 2.3.5 discusses, the intrinsic a-Si:H layer can play as an excellent passivation scheme on c-Si wafers and help reduce the recombination at the heterointerface.

The evolution of HIT cell efficiency can be traced back to 1994, when an efficiency of 20 % has been achieved for an aperture area of 1 cm² by Sanyo [251]. After that, Sanyo devoted to creating a better heterointerface by cleaning the c-Si wafer as much as possible and using a low-damage plasma deposition processes for high-quality a-Si:H films [38, 40, 252]. Therefore, in 2004, an even higher conversion efficiency of 21.5 % ($V_{oc} = 712$ mV, $I_{sc} = 3.837$ A, FF = 78.7 %) with a size of 100.3 cm² has been achieved in their laboratory [40]. By further optimizing the viscosity and rheology of the silver paste and the process parameters in the screen printing, the grid electrode with lower resistance and finer lines (without a spreading area) can be achieved. Therefore, the cell efficiency can be further enhanced by about 1.6 % [150]. By developing high-quality wide-gap alloys such as a-SiC:H and high-quality TCO with high carrier mobility, the optical losses can be further reduced and thus a higher I_{sc} can be obtained [150]. As a result of these progressive studies, Sanyo have achieved a higher efficiency of 22.3 % ($V_{oc} = 725$ mV, $I_{sc} = 3.909$ A, FF = 79.1 %) with a total size of 100.5 cm² in 2007 [150, 254]. Later in 2009, the conversion efficiency of the standard HIT solar cell developed by Sanyo has reached a record level of 23.0 % for a 100.4 cm² practical size n-type c-Si substrate ($V_{oc} = 729$ mV, $J_{sc} = 39.52$ mA/cm², FF = 80.0 %) [255]. Furthermore, Sanyo has customized these high-efficiency technologies to develop thinner-substrate (98 μ m) HIT solar cells. By developing new technologies consisting of a new device design, an improved junction formation process and an enhanced optical confinement, they have obtained a conversion efficiency of 22.8 % ($V_{oc} = 743$ mV, $J_{sc} = 38.84$ mA/cm², FF = 79.1 %) for a 98- μ m-thick practical size cell [255, 256]. Figure 1.22 presents the history of conversion efficiency for HIT solar cells developed by Sanyo both in R&D and mass production (reproducible from [257]). During the last few years, they have accelerated the improvement of the conversion efficiency. Surprisingly, the efficiency of 22.8 % for thinner-substrate (98 μ m) is comparable to the best efficiency of 23.0 % for standard substrate (250 μ m). Reducing the thickness of the substrates by more than 50 % and maintaining its efficiency at the same time provides the possibility of further reducing the cost production of HIT solar cells.

While Sanyo has focused on n-type CZ-Si substrates, European and US groups have concentrated on developing the HIT solar cell on both n-type and p-type Si substrates [258–263], as summarized in Fig. 1.22. In 2010, Roth and Rau obtained a conversion efficiency of 21.0 % [258] on 4 cm² area and 19.3 % [259] on 148 cm² area for FZ n-type Si substrates with a resistivity of 3 Ω cm. At Institute of Microengineering (IMT) in Neuchâtel, Switzerland, Descocudres et al. [260] have achieved a conversion efficiency of 20.3 % on 4 cm² area for 300- μ m-thick 4 Ω cm FZ n-type Si substrates, and then improved the efficiency to 21.0 % [261] by using H₂ plasma treatment to enhance the surface passivation. In contrast, p-type Si HIT solar cells usually exhibit inferior performances as compared with those HIT

cells fabricated on n-type Si substrates. For example, Wang et al. [262] at National Renewable Energy Laboratory (NERL) have achieved remarkable efficiencies of 19.3 % ($V_{oc} = 678$ mV, $J_{sc} = 36.20$ mA/cm², FF = 78.61 %, area = 0.9 cm²) and 18.8 % ($V_{oc} = 670.1$ mV, $J_{sc} = 36.71$ mA/cm², FF = 76.56 %, area = 0.81 cm²) on 220–330- μ m-thick 1–4 Ω cm p-type FZ-Si and CZ-Si textured substrates, respectively, while Damon-Lacoste et al. [263] at LPICM-Ecole Polytechnique Paris have achieved a low efficiency of 17.1 % ($V_{oc} = 664$ mV, $J_{sc} = 33$ mA/cm², FF = 77.8 %, area = 0.81 cm²) on 330- μ m-thick 1–4 Ω cm p-type CZ-Si flat substrates. The lower efficiency may be attributed to the lower J_{sc} value obtained with non-textured wafers. The roadmap of the conversion efficiency of the HIT solar cells based on p-type Si substrates has also been summarized in Fig. 1.22. It is obvious that the inferior cell performance of HIT solar cells fabricated on p-type substrates is highly related to the lower value of V_{oc} as compared to the corresponding HIT solar cells fabricated on n-type substrates. In particular, for n-type HIT solar cells developed by Sanyo, the maximum V_{oc} can easily exceed 700 mV, whereas that for p-type HIT solar cells is usually in a range between 660 and 690 mV.

In order to explain the different cell performance between n-type HIT solar cells and p-type HIT solar cells, the band diagrams of n-type and p-type bifacial heterojunction devices are depicted in Fig. 1.23a, b, respectively. In the case of n-type wafers (a), the minority carriers of hole are collected in the front side electrode, and the majority carrier of electrons are collected in the back side electrode. The large valence band offset at the front junction results in such a potential well where hole could be trapped, preventing efficient photogenerated carrier transport. However, the trapped carrier holes may be able to pass through the thin (i)a-Si:H layer into the (p)a-Si:H emitter by the aid of the tunneling and hopping. On the back side, the large valence band offset provides a field effect passivation as demonstrated in Sect. 2.3.1, minimizing the surface recombination on the back side. The small conduction band offset allows efficient electron collection at the back side contact. Thus the (i/n)a-Si:H stack at the back side provides an excellent back contact with adequate majority carrier electron transport and excellent passivation repelling minority carrier holes from the back contact. In such case, an extraordinarily high open-circuit voltage of >700 mV can be achieved for n-type HIT solar cells.

By contrast, in the case of p-type wafers as shown in Fig. 1.23b, the minority carrier electrons are collected on the front side electrodes, and the majority carrier holes are collected on the back side electrode. The minority transport is easier than in N-type c-Si case because of the smaller band offset in the entire path. However, lower open-circuit voltages are expected since the built-in potential (from the vacuum level bending) at the front junction is comparable to a homojunction, much less than that on n-type wafers. On the back side, the small conduction offset provides a much less effective mirror for the minority carrier electrons. Worse, the larger offset in the valence band edges would present a large barrier for majority

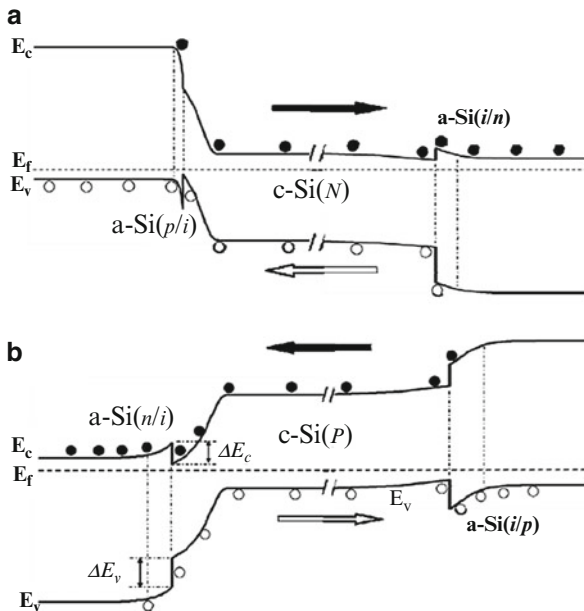


Fig. 1.23 The band diagrams of the bifacial junction HIT solar cells based on the n-type (a) and p-type (b) c-Si wafers. The transport direction of the hole (open circles) and electron (solid circles) is schematically marked by the hollow and solid arrows, respectively

carrier holes to be collected at the back side contact. Though thinner or i-layer suppression can favour tunneling transport, the passivation quality would be partially reduced in such case. Therefore, the open-circuit voltage cannot exceed 700 mV for p-type HIT solar cells and thus the efficiency is limited to below 20 % consequently.

Since the fabrication of HIT solar cells involves a large number of processing variables, such as the doping concentration of the amorphous emitter, the thickness of the intrinsic and doped a-Si:H layer, the deposition of TCO films and metal electrodes, the band alignment of a-Si/c-Si heterojunction, etc., it is a formidable task to scrutinize the effect of each variable on the cell performance experimentally. Numerical simulation using AMPS or AFORS-HET software is often adopted as a convenient way to accurately evaluate the role of various parameters [264–268]. In a recent simulation [267], modeling indicates that the defect on the front surface of c-Si reduce the open-circuit voltage and fill factor, while those on the rear surface degrade mainly the short-circuit current density and fill factor. It has also been found by simulation [268] that not only the transparency and conductivity but also the work function of TCO films can affect the cell performance obviously.

4 Summary

The interest and quest for high-efficiency Si solar cells has attracted more and more attention from researchers, scientists and engineers in both academia and industry for the past several decades. Of all the materials that are discussed in this review, Si material is the core material for Si solar cells while passivation material is the critical material for high-efficiency Si solar cells. Thermally grown SiO₂ has seldom been adopted as the passivation scheme for high-efficiency Si solar cells in recent years since its deposition processes are not desirable from not only the throughput but also the process compatibility viewpoint due to extremely high-temperature process and low deposition rate. In comparison, a-Si:H, SiO_x, SiN_x and Al₂O₃ layers deposited by plasma processes as well as their layer stacks such as SiO_x/SiN_x, Al₂O₃/SiN_x and a-Si:H/SiN_x have been given a lot of importance owing to their excellent passivation qualities and relatively easier deposition conditions, particularly in the fabrication of high-efficiency PERC, PERL, IBC, EWT and HIT solar cells. Among all the high-efficiency devices that are reviewed in this chapter, PERC, PERL and HIT solar cells are most promising for mass production in industrial scale due to the minimization of the use of high-temperature processes and photolithography techniques. Indeed, Pluto-PERC and Pluto-PERL cells as well as HIT cells have been produced in elementary industrial scale by Suntech and Sanyo, respectively. Applying these delicate and advanced cell designs and concepts to industrial Si wafer-based solar cells without increasing production cost still remains a challenge and needs further research.

References

1. Chapin, D.M., Fuller, C.S., Pearson, G.L.: *J. Appl. Phys.* **25**, 676 (1954)
2. http://www.pv-magazine.com/news/details/beitrag/mid-year-pv-review_100007695/#axzz2-KCHj6DvK
3. Goetzberger, A., Knobloch, J., Voss, B.: *Crystalline Silicon Solar Cells*. Wiley, New York (1998)
4. Green, M.A.: *Silicon Solar Cells: Advanced Principles and Practice*. Bridge Printery, Sydney (1995)
5. CZochralski, J.: Ein Neues Verfahren zur Messung der Kristallisations geschwindigkeit der Metalle. *Z. Phys. Chem.* **92**, 219 (1918)
6. Teal, G.K., Little, J.B.: Growth of germanium single crystals. *Phys. Rev.* **78**, 219 (1959)
7. Teal, G.K., Bühler, E.: Growth of silicon single crystals and single crystal pn junctions. *Phys. Rev.* **87**, 190 (1952)
8. Anttila, O.: In: Lindroos, V., Tilli, M., Lehto, A., Motooka, T. (eds.) *Handbook of Silicon Based MEMS Materials and Technologies*. William Andrew (2010) ISBN: 978-0-8155-1594-4
9. Ming Liaw, H.: Crystal growth of silicon. In: Mara, W.C.O. (ed.) *Handbook of Semiconductor Silicon Technology*. William Andrew (1990) ISBN: 978-0-8155-1237-0
10. Zulehner, W.: CZochralski growth of silicon. *J. Cryst. Growth* **65**, 189 (1983)
11. Voronkov, V.V., Falster, R.: Vacancy-type microdefect formation in CZochralski silicon. *J. Cryst. Growth* **194**, 76–88 (1998)

12. Zulehner, W.: Status and future of silicon crystal growth. *Mater. Sci. Eng. B* **4**, 1–10 (1989)
13. Dieltl, J., Helmreich, D., Sirtl, E.: *Crystals: Growth, Properties and Application*, vol. 5, p. 57. Springer, Berlin (1981)
14. Goetzberger, A., Hebling, C., Schock, H.W.: Photovoltaic materials, history, status and outlook. *Mater. Sci. Eng. R* **40**, 1–46 (2003)
15. Arnberg, L., Sabatino, M.D., Ovrelid, E.J.: State-of-the-art growth of silicon for PV applications. *J. Cryst. Growth* **360**, 56 (2012)
16. Fujiwara, K., Pan, W., Usami, N., et al.: Growth of structure-controlled polycrystalline silicon ingots for solar cells by casting. *Acta Mater.* **54**, 3191–3197 (2006)
17. Fujiwara, K., Pan, W., Sawada, K., et al.: Directional growth method to obtain high quality polycrystalline silicon from its melt. *J. Cryst. Growth* **292**, 282–285 (2006)
18. Nakajima, K., Kutsukake, K., Fujiwara, K., Morishita, K., Ono, S.: Arrangement of dendrite crystals grown along the bottom of Si ingots using the dendritic casting method by controlling conductivity under crucibles. *J. Cryst. Growth* **319**, 13–18 (2011)
19. Stoddard, N., Wu, B., Witting, I., et al.: Casting single crystal silicon: novel defect profiles from BP solar's mono2 wafers. *Diffus. Defect Data B* **131–133**, 1–8 (2008)
20. Wu, B., Clark, R.: Influence of inclusion on nucleation of silicon casting for photovoltaic (PV) application. *J. Cryst. Growth* **318**, 200–207 (2011)
21. Zhang, H., Zheng, L., Ma, X., Zhao, B., Wang, C., Xu, F.: Nucleation and bulk growth control for high efficiency silicon ingot casting. *J. Cryst. Growth* **318**, 283–287 (2011)
22. Wang, T.Y., Hsu, S.L., Fei, C.C., Yei, K.M., Hsu, W.C., Lan, C.W.: Grain control using spot cooling in multi-crystalline silicon crystal growth. *J. Cryst. Growth* **311**, 263–267 (2009)
23. Nose, Y., Takahashi, I., Pan, W., Usami, N., Fujiwara, K., Nakajima, K.: Floating cast method to realize high-quality Si bulk multicrystals for solar cells. *J. Cryst. Growth* **311**, 228–231 (2009)
24. Yeh, K.M., Hseih, C.K., Hsu, W.C., Lan, C.W.: High-quality multi-crystalline silicon growth for solar cells by grain-controlled directional solidification. *Prog. Photovolt. Res. Appl.* **18**, 265–271 (2010)
25. Fujiwara, K.: Crystal growth behaviors of silicon during melt growth processes. *Int. J. Photoenergy*. Article Id: 169829 (2012)
26. Zubel, I.: The influence of atomic configuration of (h k l) planes on adsorption processes associated with anisotropic etching of silicon. *Sens. Actuators A* **94**, 76 (2001)
27. Dziuban, J. A.: *Proc. Eurosensors XIII Conf.* 18B4, 671 (1999)
28. Wang, T., Surve, S., Hesketh, P.J.: Anisotropic etching of silicon in rubidium hydroxide. *J. Electrochem. Soc.* **141**, 2493 (1994)
29. You, J.S., Kim, D., Huh, J.Y., Park, H.J., Pak, J.J., Kang, C.S.: Experiments on anisotropic etching of Si in TMAH. *Sol. Energy Mater. Sol. Cells* **66**, 37–44 (2001)
30. Cheng, Y.T., Ho, J.J., Tsai, S.Y., Ye, Z.Z., Lee, W., Hwang, D.S., Chang, S.H., Chang, C.C., Wang, K.L.: Efficiency improved by acid texturization for multi-crystalline silicon solar cells. *Sol. Energy* **85**, 87–94 (2011)
31. De Wolf, S., Einhaus, R., De Clercq, K., Szlufcik, J.: In: *Proceedings of the 16th European PV Solar Energy Conference*, Glasgow, p. 1521 (2000)
32. Burgers, A.R., Bultman, J.H., Beneking, C., Nositchka, W.A., Voigt, O., Kurz, H.: In: *Proceedings of the 16th European PV Solar Energy Conference*, Glasgow, p. 1427 (2000)
33. Ruby, D.S., Zaidi, S.H., Narayanan, S.: In: *Proceedings of the 28th IEEE Photovoltaic Specialists Conference*, Anchorage, Alaska, USA, p. 75 (2000)
34. Kwon, T.Y., Yang, D.H., Ju, M.K., Jung, W.W., Kim, S.Y., Lee, Y.W., Gong, D.Y., Yi, J.: Screen printed phosphorus diffusion for low-cost and simplified industrial mono-crystalline silicon solar cells. *Sol. Energy Mater. Sol. Cells* **95**, 14–17 (2011)
35. Chaoui, R., Messaoud, A., Zitouni, M.L., Charif, M.R.: Development of an emitter for industrial silicon solar cells using the doped oxide solid source diffusion technique. *Renew. Energy* **23**, 417–428 (2001)

36. Nakaya, H., Nishida, M., Takeda, Y., Moriuchi, S., Tongegawa, T., Machida, T., Nunoi, T.: Polycrystalline silicon solar cells with V-grooved surface. *Sol. Energy Mater. Sol. Cells* **34**, 219–225 (1994)
37. Rohatgi, A., Chen, Z., Sana, P., Crotty, J., Salami, J.: High efficiency multi-crystalline silicon solar cells. *Sol. Energy Mater. Sol. Cells* **34**, 227–236 (1994)
38. Taguchi, M., Kawamoto, K., Tsuge, S., Baba, T., Sakata, H., Morizane, M., Uchihashi, K., Nakamura, N., Kiyama, S., Oota, O.: HITM cells—high-efficiency crystalline Si cells with novel structure. *Prog. Photovolt. Res. Appl.* **8**, 503–513 (2000)
39. Neitzert, H.C., Spinillo, P., Bellone, S., Licciardi, G.D., Tucci, M., Roca, F., Gialanella, L., Romano, M.: Investigation of the damage as induced by 1.7 MeV protons in an amorphous/crystalline silicon heterojunction solar cells. *Sol. Energy Mater. Sol. Cells* **83**, 435–446 (2004)
40. Taguchi, M., Terakawa, A., Maruyaman, E., Tanaka, M.: Obtaining a higher V_{oc} in HIT cells. *Prog. Photovolt. Res. Appl.* **13**, 481–488 (2005)
41. Fujiwara, H., Kondo, M.: Impact of epitaxial growth at the heterointerface of a-Si:H/c-Si solar cells. *Appl. Phys. Lett.* **90**, 013503 (2007)
42. De wolf, S., Kondo, M.: Boron-doped a-Si:H/c-Si interface passivation: degradation mechanism. *Appl. Phys. Lett.* **91**, 112109 (2007)
43. Wang, Q., Page, M.R., Xu, Y., Iwaniczko, E., Williams, E., Wang, T.H.: Development of a hot-wire chemical vapor deposition n-type emitter on p-type crystalline Si-based solar cells. *Thin Solid Films* **430**, 208–211 (2003)
44. Martin, I., Munoz, D., Voz, C., Vetter, M., Alcubilla, R., Damon-Lacoste, J., Roca i Cabarrocas, P., Villar, F., Bertomeu, J., Andreu, J.: Comparison of (n+) a-Si:H/(p) c-Si heterojunction emitters using a-Si:H films deposited by PECVD or HWCVD. Conference record of the 2006 I.E. 4th World Conference on Photovoltaic Energy Conversion, vols. 1 and 2, pp. 1091–1094 (2006)
45. Hernandez-Como, N., Morlaes-Acevedo, A., Matsumoto, Y.: I-V characteristics of a-Si-c-Si hetero-junction diodes made by hot wire CVD. *Sol. Energy Mater. Sol. Cells* **95**, 1996–2000 (2011)
46. Pysch, D., Meinhardt, C., Ritzau, K.-U., Bivour, M., Zimmermann, K., Schetter, C., Hermle, M., Glunz, S.W.: Comparison of intrinsic amorphous silicon buffer layers for silicon heterojunction solar cells deposited with different PECVD technologies. 35th IEEE Photovoltaic Specialists Conference, pp. 3570–3576 (2010)
47. Xiao, S.Q., Xu, S., Zhou, H.P., Wei, D.Y., Huang, S.Y., Xu, L.X., Sern, C.C., Guo, Y.N., Khan, S.: Amorphous/crystalline silicon heterojunction solar cells via remote inductively coupled plasma processing. *Appl. Phys. Lett.* **100**, 233902 (2012)
48. Sawada, T., Terada, N., Tsuge, S., Baba, T., Takahama, T., Wakisaka, K., Tsuda, S., Nakano, S.: In: Proceedings of IEEE 1st World Conference on Photovoltaic Energy Conversion, Hawaii, 1994. IEEE, New York (1994)
49. Goetzberger, A., Knobloch, J., Vob, B.: *Crystalline Silicon Solar Cells*, pp. 87–131. Wiley, New York (1998)
50. Kern, W., Puotinen, D.A.: Cleaning solutions based on hydrogen peroxide for use in silicon semiconductor technology. *RCA Rev.* **31**, 187 (1970)
51. Yablonovitch, E., Allara, D.L., Chang, C.C., Gmitter, T., Bright, T.B.: Unusually low surface recombination velocity on silicon germanium surfaces. *Phys. Rev. Lett.* **57**, 249 (1986)
52. Macdonald, D.H., Cuevas, A., Kerr, M.J., Samundsett, C., Ruby, D., Winderbaum, S., Leo, A.: Texturing industrial multicrystalline silicon solar cells. *Sol. Energy* **76**, 277 (2004)
53. Schnell, M., Ludemann, R., Schaefer, S.: Plasma surface texturing for multicrystalline silicon solar cells. Proc. Photovoltaic Specialists Conference, 2000, Conference Record of the Twenty-Eighth IEEE, Anchorage, AK, USA, p. 367. IEEE (2000)
54. Anthony, B., Hsu, T., Breaux, L., Qian, R., Banerjee, S., Tasch, A.: Very low defect remote hydrogen plasma clean of Si (100) for homoepitaxy. *J. Electron. Mater.* **19**, 1027 (1990)

55. Martin, I., Vetter, M., Orpella, A., Voz, C., Puigdollers, J., Alcubilla, R., Kharchenko, A.V., Roca i Cabarrocas, P.: Improvement of crystalline silicon surface passivation by hydrogen plasma treatment. *Appl. Phys. Lett.* **84**, 1474 (2004)
56. Sinton, R.A., Cuevas, A.: Contactless determination of current-voltage characteristics and minority-carrier lifetime in semiconductors from quasi-steady-state photoconductance data. *Appl. Phys. Lett.* **69**, 2510 (1996)
57. Narasimha, S., Rohatgi, A.: Optimized aluminum back surface field techniques for silicon solar cells. Proceedings of the 26th IEEE Photovoltaic Specialists Conference, Anaheim, USA, pp. 63–66 (1997)
58. Peters, S.: Rapid thermal processing of crystalline silicon materials and solar cells. Ph.D. thesis, University of Konstanz, p. 62 (2004)
59. Schultz, O., Mette, A., Hermle, M., Glunz, S.W.: Thermal oxidation for crystalline silicon solar cells exceeding 19 % efficiency applying industrially feasible process technology. *Prog. Photovolt. Res. Appl.* **16**, 317 (2008)
60. Benick, J., ZXimmermann, K., Spiegelman, J., Hermle, M., Glunz, S.W.: Rear side passivation of PERC-type solar cells by wet oxides grown from purified steam. *Prog. Photovolt. Res. Appl.* **19**, 361 (2011)
61. Mack, S., Wolf, A., Walczak, A., Thaidigsmann, B., Allan Wotke, E., Spiegelman, J.J., Preu, R., Biro, D.: Properties of purified direct steam grown silicon thermal oxides. *Sol. Energy Mater. Sol. Cells* **95**, 2570 (2011)
62. Deal, B.E., Grove, A.S.: General relationship for the thermal oxidation of silicon. *J. Appl. Phys.* **36**, 3770 (1965)
63. Deal, B.E.: Thermal oxidation kinetics of silicon in pyrogenic H₂O and 5% HCl/H₂O mixtures. *J. Electrochem. Soc.* **125**, 576–579 (1978)
64. Stocks, M., Cuevas, A.: Surface recombination velocity of thermally oxidized multicrystalline silicon. In: Proceedings of the 2nd World Conference on Photovoltaic Energy Conversion, Vienna, Austria, pp. 1623–1626 (1998)
65. Schultz, O., Glunz, S.W., Willeke, G.P.: Multicrystalline silicon solar cells exceeding 20% efficiency. *Prog. Photovolt. Res. Appl.* **12**, 5530558 (2004)
66. Schmiga, C., Nagel, H., Steckemetz, S., Hezel, R.: 17% efficient multicrystalline silicon solar cells with rear thermal oxide passivation. In: Proceedings of the 19th European Photovoltaic Solar Energy Conference, Paris, France, pp. 1060–1063 (2004)
67. Glunz, S.W., Biro, D., Rein, S., Warta, W.: Field-effect passivation of the SiO₂-Si interface. *J. Appl. Phys.* **86**, 683 (1999)
68. Sai, H., Imai, R., Yamamoto, N., Ishiwata, T., Arafune, K., Ohshita, Y., Yamaguchi, M.: Surface recombination at Si/SiO₂ interface with various interface state densities and oxide charges. Proc. 21st European Photovoltaic Solar Energy Conference, p. 915, Dresden, Germany, 3–6 Sept 2006. WIP-Renewable Energies, Munich, Germany (2006)
69. Jana, T., Mukhopadhyay, S., Ray, S.: Low temperature silicon oxide and nitride for surface passivation of silicon solar cells. *Sol. Energy Mater. Sol. Cells* **71**, 197 (2002)
70. Reed, M.L., Plummer, J.D.: Chemistry of Si-SiO₂ interface trap annealing. *J. Appl. Phys.* **63**, 5776 (1988)
71. Blakers, A.W., Wang, A., Milne, A.M., Zhao, J., Green, M.A.: 22.8% efficient silicon solar cell. *Appl. Phys. Lett.* **55**, 1363 (1989)
72. Kerr, M.J., Cuevas, A.: Very low bulk and surface recombination in oxidized silicon wafers. *Semicond. Sci. Technol.* **17**, 35 (2002)
73. Eages, W.D., Swanson, R.M.: Calculation of surface generation and recombination velocities at the Si-SiO₂ interface. *J. Appl. Phys.* **58**, 4267 (1985)
74. Gruenbaum, P.E., Gan, J.Y., King, R.R., Swanson, R.M.: Stable passivation for high-efficiency silicon solar cells. In: Proc. 21st IEEE Photovoltaic Specialist Conference, Orlando, p. 317 (1990)

75. Stephens, A.W., Aberle, A.G., Green, M.A.: Surface recombination velocity measurements at the silicon-silicon dioxide interface by microwave-detected photoconductance decay. *J. Appl. Phys.* **76**, 363 (1994)
76. King, R.R., Sinton, R.A., Swanson, R. M.: Low surface recombination velocities on doped silicon and their applications for point contact solar cells. Proc. 19th IEEE Photovoltaic Specialist Conference, New Orleans, p. 1168 (1987)
77. i Tomàs, R.F.: Surface passivation of crystalline silicon by amorphous silicon carbide films for photovoltaic applications. Ph.D. Thesis, Polytechnic University of Catalonia (2008)
78. Zhao, J., Wang, A., Altermatt, P., Green, M.A.: Twenty-four percent efficient silicon solar cells with double layer antireflection coatings and reduced resistance loss. *Appl. Phys. Lett.* **66**, 3636 (1995)
79. Zhao, J., Wang, A., Green, M.A.: High-efficiency PERL and PERT silicon solar cells on Fz and MCZ substrates. *Sol. Energy Mater. Sol. Cells* **65**, 429 (2001)
80. Hofmann, M., Janz, S., Schmidt, C., Kambor, S., Suwito, D., Kohn, N., Rentsch, J., Preu, R., Glunz, S.W.: Recent developments in rear-surface passivation at Fraunhofer ISE. *Sol. Energy Mater. Sol. Cells* **93**, 1074 (2009)
81. Dingemans, G., van de Sanden, M.C.M., Kessels, W.M.M.: Excellent Si surface passivation by low temperature SiO₂ using an ultrathin Al₂O₃ capping film. *Phys. Status Solidi (RRL)* **5**, 22 (2011)
82. Zhou, H.P., Wei, D.Y., Xu, S., Xiao, S.Q., Xu, L.X., Huang, S.Y., Guo, Y.N., Khan, S., Xu, M.: Si surface passivation by SiO_x:H films deposited by a low-frequency ICP for solar cell applications. *J. Phys. D Appl. Phys.* **45**, 395401 (2012)
83. Hoex, B., Peeters, F.J.J., Creatore, M., Blauw, M.A., Kessels, W.M.M., van de Sanden, M.C. M.: High-rate plasma-deposited SiO₂ films for surface passivation of crystalline silicon. *J. Vac. Sci. Technol. A* **24**, 1823 (2006)
84. Leguijt, C., et al.: Low-temperature surface passivation for silicon solar cells. *Sol. Energy Mater. Sol. Cells* **40**, 297 (1996)
85. Schmidt, J., Cuevas, A.: Carrier recombination at silicon-silicon nitride interfaces fabricated by plasma-enhanced chemical vapor deposition. *J. Appl. Phys.* **85**, 3626 (1999)
86. de Wolf, S., Agostinelli, G., Beaucarne, G., Vitanov, P.: Influence of stoichiometry of direct plasma-enhanced chemical vapor deposited SiNx films and silicon substrate surface roughness on surface passivation. *J. Appl. Phys.* **97**, 063303 (2005)
87. Hoex, B., Van Erven, A.J.M., Bosch, R.C.M., Stals, W.T.M., Bijker, M.D., Van den Oever, P. J., Kessels, W.M.M., Van de Sanden, M.C.M.: Industrial high-rate (similar to 5 nm/s) deposited silicon nitride yielding high-quality bulk and surface passivation under optimum anti-reflection coating conditions. *Prog. Photovolt. Res. Appl.* **13**, 705 (2005)
88. Hong, J., Kessesl, W.M.M., Soppe, W.J., Weeber, W.W., Amoldbik, W.M., Van de Sanden, M.C.M.: Influence of the high-temperature “firing” step on high-rate plasma deposited silicon nitride films used as bulk passivating antireflection coatings on silicon solar cells. *J. Vac. Sci. Technol. B* **21**, 2123 (2003)
89. Pierson, H.O.: Processing of refractory carbides and nitrides (coatings), Chapter 15. In: Pierson, H.O. (ed.) *Handbook of Refractory Carbides and Nitrides*, p. 290. Noyes, Westwood, NJ (1996)
90. Soppe, W.J., Duijvelaar, B.G., Schiermeier, S.E.A.: Proc. of 16th European PVSEC, Glasgow, UK, pp. 1420–1423 (2000)
91. Duerinckx, F., Szlufcik, J.: Defect passivation of industrial multicrystalline solar cells based on PECVD silicon nitride. *Sol. Energy Mater. Sol. Cells* **72**, 231 (2002)
92. Bertoni, M.I., et al.: Influence of defect type on hydrogen passivation efficacy in multicrystalline silicon solar cells. *Prog. Photovolt. Res. Appl.* **19**, 187 (2010)
93. Dingemans, G., Kessels, W.M.M.: Status and prospects of Al₂O₃-based surface passivation schemes for silicon solar cells. *J. Vac. Sci. Technol. A* **30**, 040802 (2012)

94. Warren, W.L., Kanicki, J., Robertson, J., Poindexter, E.H., McWhorter, P.J.: Electron-paramagnetic-resonance investigation of charge trapping centers in amorphous-silicon nitride films. *J. Appl. Phys.* **74**, 4034 (1993)
95. Curry, S.E., Lenahan, P.M., Krick, D.T., Kanicki, J., Kirk, C.T.: Evidence for a negative electron-electron correlation-energy in the dominant deep trapping center in silicon-nitride films. *Appl. Phys. Lett.* **56**, 1359 (1990)
96. Mäckel, H., Lüdemann, R.: Detailed study of the composition of hydrogenated SiN(x) layers for high-quality silicon surface passivation. *J. Appl. Phys.* **92**, 2602 (2002)
97. Dauwe, S., Mittelstädt, L., Metz, A., Hezel, R.: Experimental evidence of parasitic shunting in silicon nitride rear surface passivated solar cells. *Prog. Photovolt. Res. Appl.* **10**, 271 (2002)
98. Elmiger, J.R., Kunst, M.: Investigating of charge carrier injection in silicon nitride/silicon junctions. *Appl. Phys. Lett.* **69**, 517 (1996)
99. Zhou, H.P., Wei, D.Y., Xu, L.X., Guo, Y.N., Xiao, S.Q., Huang, S.Y., Xu, S.: Low temperature SiN_x:H films deposited by inductively coupled plasma for solar cell applications. *Appl. Surf. Sci.* **11**, 111 (2012)
100. Lelièvre, J.-F., Fourmond, E., Kaminski, A., Palais, O., Ballutaud, D., Lemiti, M.: Study of the composition of hydrogenated silicon nitride SiNx:H for efficient surface and bulk passivation of silicon. *Sol. Energy Mater. Sol. Cells* **93**, 1281 (2009)
101. Schmidt, J., Moschner, J.D., Henze, J., Dauwe, S., Hezel, R.: Recent progress in the surface passivation of silicon solar cells using silicon nitride. Proc. 19th European Photovoltaic Solar Energy Conference, Paris, France, 7–11 June 2004, p. 391. WIP-Renewable Energies, Munich, Germany (2004)
102. Hoex, B., Heil, S.B.S., Langereis, E., Van de Sanden, M.C.M., Kessels, W.M.M.: Ultralow surface recombination of c-Si substrates passivated by plasma-assisted atomic layer deposited Al₂O₃. *Appl. Phys. Lett.* **89**, 042112 (2006)
103. Agostinelli, G., Delabie, A., Vitanov, P., Alexieva, Z., Dekkers, H.F.W., De Wolf, S., Beaucame, G.: Very low surface recombination velocities on p-type silicon wafers passivated with a dielectric with fixed negative charge. *Sol. Energy Mater. Sol. Cells* **90**, 3438 (2006)
104. Hoex, B., Schmidt, J., Pohl, P., Van de Sanden, M.C.M., Kessels, W.M.M.: Silicon surface passivation by atomic layer deposited Al₂O₃. *J. Appl. Phys.* **104**, 044903 (2008)
105. Glunz, S.W., Benick, J., Biro, D., Bivour, M., Hermle, M., Pysch, D., Rauer, M., Reichel, C., Richter, A., Rüdiger, M., Schmiga, C., Suwito, D., Wolf, A., Preu, R.: n-type silicon-enabling efficiencies >20% in industrial production. Proceedings of the 35th IEEE Photovoltaic Specialists Conference, Honolulu, Hawaii, USA, pp. 50–56 (2010)
106. Benick, J., Hoex, B., van de Sanden, M.C.M., Kessels, W.M.M., Schultz, O., Glunz, S.W.: High efficiency n-type Si solar cells on Al(2)O(3)-passivated boron emitters. *Appl. Phys. Lett.* **92**, 253504 (2008)
107. George, S.M.: Atomic layer deposition: an overview. *Chem. Rev.* **110**, 111 (2010)
108. Puurunen, R.L.: Surface chemistry of atomic layer deposition: A case study for the trimethylaluminum/water process. *J. Appl. Phys.* **97**, 121301 (2005)
109. Goldstein, D.N., McCormick, J.A., George, S.M.: Al(2)O(3) atomic layer deposition with trimethylaluminum and ozone studied by in situ transmission FTIR spectroscopy and quadrupole mass spectrometry. *J. Phys. Chem. C* **112**, 19530 (2008)
110. Elliott, S.D., Greer, J.C.: Simulating the atomic layer deposition of alumina from first principles. *J. Mater. Chem.* **14**, 3246 (2004)
111. Heil, S.B.S., Van Hemmen, J.L., Van de Sanden, M.C.M., Kessels, W.M.M.: Reaction mechanisms during plasma-assisted atomic layer deposition of metal oxides: A case study for Al(2)O(3). *J. Appl. Phys.* **103**, 103302 (2008)
112. Benick, J., Richter, A., Hermle, M., Glunz, S.W.: Thermal stability of the Al₂O₃ passivation on p-type silicon surfaces for solar cell applications. *Phys. Status Solidi (RRL)* **3**, 233 (2009)

113. Dingemans, G., Van de Sanden, M.C.M., Kessels, W.M.M.: Influence of the deposition temperature on the c-Si surface passivation by Al_2O_3 films synthesized by ALD and PECVD. *Electrochem. Solid State Lett.* **13**, H76 (2010)
114. Dingemans, G., Seguin, R., Engelhart, P., Van de Sanden, M.C.M., Kessels, W.M.M.: Silicon surface passivation by ultrathin Al_2O_3 films synthesized by thermal and plasma atomic layer deposition. *Phys. Status Solidi (RRL)* **4**, 10 (2010)
115. Schmidt, J., Veith, B., Brendel, R.: Effective surface passivation of crystalline silicon using ultrathin Al_2O_3 films and $\text{Al}_2\text{O}_3/\text{SiN}_x$ stacks. *Phys. Status Solidi (RRL)* **3**, 287 (2009)
116. Dingemans, G., Terlinden, N.M., Pierreux, D., Profijt, H.B., Van de Sanden, M.C.M., Kessels, W.M.M.: Influence of the oxidant on the chemical and field-effect passivation of Si by ALD Al_2O_3 . *Electrochem. Solid State Lett.* **14**, H1 (2011)
117. Benick, J., Richter, A., Li, T.-T.A.A., Grant, N.E., Mc Intosh, K.R., Ren, Y., Weber, K.J., Hermle, M., Glunz, S.W.: Proceedings of the 35th IEEE Photovoltaic Specialists Conference, Honolulu, HI, 20–25 June 2010. IEEE, New York (2010)
118. Werner, F., Veith, B., Zielke, D., Kuhnemund, L., Tegenkamp, C., Seibt, M., Brendel, R., Schmidt, J.: Electronic and chemical properties of the c-Si/ Al_2O_3 interface. *J. Appl. Phys.* **109**, 113701 (2011)
119. Werner, F., Veith, B., Tiba, V., Poodt, P., Roozeboom, F., Brendel, R., Schmidt, J.: Very low surface recombination velocities on p- and n-type c-Si by ultrafast spatial atomic layer deposition of aluminum oxide. *Appl. Phys. Lett.* **97**, 162103 (2010)
120. Profijt, H.B., Kudlacek, P., Van de Sanden, M.C.M., Kessels, W.M.M.: Ion and photon surface interaction during remote plasma ALD of metal oxides. *J. Electrochem. Soc.* **158**, G88 (2011)
121. Hoex, B., Schmidt, J., Bock, R., Altermatt, P.P., Van de Sanden, M.C.M.: Excellent passivation of highly doped p-type Si surfaces by the negative-charge-dielectric Al_2O_3 . *Appl. Phys. Lett.* **91**, 112107 (2007)
122. Richter, A., Benick, J., Hermle, M., Glunz, S.W.: Excellent silicon surface passivation with 5 angstrom thin ALD Al_2O_3 layers: influence of different thermal post-deposition treatments. *Phys. Status Solidi (RRL)* **5**, 202 (2011)
123. Hoex, B., Van de Sanden, M.C.M., Schmidt, J., Brendel, R., Kessels, W.M.M.: Surface passivation of phosphorus-diffused n(+)-type emitters by plasma-assisted atomic-layer deposited Al_2O_3 . *Phys. Status Solidi (RRL)* **6**, 4 (2012)
124. Dingemans, G., Beyer, W., Van de Sanden, M.C.M., Kessels, W.M.M.: Hydrogen induced passivation of Si interfaces by Al_2O_3 films and $\text{SiO}_2/\text{Al}_2\text{O}_3$ stacks. *Appl. Phys. Lett.* **97**, 152106 (2010)
125. Dingemans, G., Einsele, F., Beyer, W., Van de Sanden, M.C.M., Kessels, W.M.M.: Influence of annealing and Al_2O_3 properties on the hydrogen-induced passivation of the Si/ SiO_2 interface. *J. Appl. Phys.* **111**, 093713 (2012)
126. Matsunaga, K., Tanaka, T., Yamamoto, T., Ikuhara, Y.: First-principles calculations of intrinsic defects in Al_2O_3 . *Phys. Rev. B* **68**, 085110 (2003)
127. Weber, J.R., Janotti, A., van de Walle, C.G.: Native defects in Al_2O_3 and their impact on III-V/ Al_2O_3 metal-oxide-semiconductor-based devices. *J. Appl. Phys.* **109**, 033715 (2011)
128. Shin, B., Weber, J.R., Long, R.D., Hurley, P.K., van de Walle, C.G., McIntyre, P.C.: Origin and passivation of fixed charge in atomic layer deposited aluminum oxide gate insulators on chemically treated InGaAs substrates. *Appl. Phys. Lett.* **96**, 152908 (2010)
129. Afanas'ev, V.V., Stesmans, A., Mrstik, B.J., Zhao, C.: Impact of annealing-induced compaction on electronic properties of atomic-layer-deposited Al_2O_3 . *Appl. Phys. Lett.* **81**, 1678 (2002)
130. Gielis, J.J.H., Hoex, B., Van de Sanden, M.C.M., Kessels, W.M.M.: Negative charge and charging dynamics in Al_2O_3 films on Si characterized by second-harmonic generation. *J. Appl. Phys.* **104**, 073701 (2008)

131. Mack, S., Wolf, A., Brosinsky, C., Schmeisser, S., Kimmerle, A., Saint-Cast, P., Hofmann, M., Biro, D.: Silicon surface passivation by thin thermal oxide/PECVD layer stack systems. *IEEE J. Photovoltaics* **1**, 135 (2011)
132. Dingemans, G., Terlinden, N.M., Verheijen, M.A., Van de Sanden, M.C.M., Kessels, W.M. M.: Controlling the fixed charge and passivation properties of Si(100)/Al₂O₃ interfaces using ultrathin SiO₂ interlayers synthesized by atomic layer deposition. *J. Appl. Phys.* **110**, 093715 (2011)
133. Guha, S., Narayanan, V.: Oxygen vacancies in high dielectric constant oxide-semiconductor films. *Phys. Rev. Lett.* **98**, 196101 (2007)
134. Foster, A.S., Lopez Gejo, F., Shluger, A.L., Nieminen, R.M.: Vacancy and interstitial defects in hafnia. *Phys. Rev. B* **65**, 174117 (2002)
135. Poodt, P., et al.: High-speed spatial atomic-layer deposition of aluminum oxide layers for solar cell passivation. *Adv. Mater.* **22**, 3564 (2010)
136. Poodt, P., Cameron, D.C., Dickey, E., George, S.M., Kuznetsov, V., Parsons, G.N., Roozeboom, F., Sundaram, G., Vermeer, A.: Spatial atomic layer deposition: A route towards further industrialization of atomic layer deposition. *J. Vac. Sci. Technol. A* **30**, 010802 (2012)
137. Suntola, T., Antson, J.: Method for producing compound thin films. US Patent 4058430, 15 Nov 1977
138. Levy, D.H., Freeman, D., Nelson, S.F., Cowdery-Corvan, P.J., Irving, L.M.: Stable ZnO thin film transistors by fast open air atomic layer deposition. *Appl. Phys. Lett.* **92**, 192101 (2008)
139. Dingemans, G., Kessels, W.M.M.: Proceedings of the 25th European Photovoltaic Energy Conference, Valencia, Spain, 6–10 Sept 2010
140. Vermang, B., Rothschild, A., Racz, A., John, J., Poortmans, J., Mertens, R., Poodt, P., Tiba, V., Roozeboom, F.: Spatially separated atomic layer deposition of Al₂O₃, a new option for high-throughput Si solar cell passivation. *Prog. Photovolt. Res. Appl.* **19**, 733 (2011)
141. Werner, F., Stals, W., Görtzen, R., Veith, B., Brendel, R., Schmidt, J.: High-rate atomic layer deposition of Al(2)O(3) for the surface passivation of Si solar cells. *Energy Procedia* **8**, 301 (2011)
142. Miyajima, S., Irikawa, I., Yamada, A., Konagai, M.: High quality aluminum oxide passivation layer for crystalline silicon solar cells deposited by parallel-plate plasma-enhanced chemical vapor deposition. *Appl. Phys. Express* **3**, 012301 (2010)
143. Saint-Cast, P., Kania, D., Hofmann, M., Benick, J., Rentsch, J., Preu, R.: Very low surface recombination velocity on p-type c-Si by high-rate plasma-deposited aluminum oxide. *Appl. Phys. Lett.* **95**, 151502 (2009)
144. Li, T.T., Cuevas, A.: Effective surface passivation of crystalline silicon by rf sputtered aluminum oxide. *Phys. Status Solidi (RRL)* **3**, 160 (2009)
145. Yamamoto, K., Nakajima, A., Yoshimi, M., et al.: A thin-film silicon solar cell and module. *Prog. Photovolt. Res. Appl.* **13**, 489 (2005)
146. Matsuda, A., Nomoto, K., Takeuchi, Y., et al.: Temperature-dependence of the sticking and loss probabilities of silyl radicals on hydrogenated amorphous-silicon. *Surf. Sci.* **227**, 50 (1990)
147. Matsuda, A.: Microcrystalline silicon. Growth and device application. *J. Non-Cryst. Solids* **338–340**, 1–12 (2004)
148. Stangl, J., Holy, V., Bauer, G.: Structural properties of self-organized semiconductor nanostructures. *Rev. Mod. Phys.* **76**, 725 (2004)
149. Shchukin, V., Ledentsov, N.N., Bimberg, D.: *Epitaxy of Nanostructures*. Springer, Berlin/Heidelberg (2003)
150. Tsunomura, Y., Yoshimine, T., Taguchi, M., Baba, T., Kinoshita, T., Kanno, H., Sakata, H., Maruyama, E., Tanaka, M.: Twenty-two percent efficiency HIT solar cell. *Sol. Energy Mater. Sol. Cells* **93**, 670 (2009)
151. Mingirulli, N., et al.: Efficient interdigitated back-contacted silicon heterojunction solar cells. *Status Solidi (RRL)* **5**, 159 (2011)

152. Martín de Nicolás, S., Muñoz, D., Ozanne, A.S., Nguyen, N., Ribeyron, P.J.: Optimisation of doped amorphous silicon layers applied to heterojunction solar cells. *Energy Procedia* **8**, 226 (2011)
153. Bätzner, D.L., et al.: Properties of high efficiency silicon heterojunction cells. *Energy Procedia* **8**, 153 (2011)
154. Keppner, H., Torres, P., Flueckiger, R., Meier, J., Shah, A., Fortmann, C., Fath, P., Happle, K., Kiess, H.: Passivation properties of amorphous and microcrystalline silicon layers deposited by VHF-GD for crystalline silicon solar-cells. *Sol. Energy Mater. Sol. Cells* **34**, 201 (1994)
155. Tanaka, M., Taguchi, M., Matsuyama, T., Sawada, T., Tsuda, S., Nakano, S., Hanafusa, H., Kuwano, Y.: Development of new a-Si c-Si heterojunction solar-cells—ACJ-HIT (Artificially constructed junction-heterojunction with intrinsic thin-layer). *Jpn. J. Appl. Phys.* **31**(Pt 1), 3518 (1992)
156. Schaper, M., Schmidt, J., Plagwitz, H., Brendel, R.: 20.1%-efficient crystalline silicon solar cell with amorphous silicon rear-surface passivation. *Prog. Photovolt. Res. Appl.* **13**, 381 (2005)
157. Stannowski, B., Schropp, R.E., Wehrspohn, R.B., Powell, M.J.: Amorphous-silicon thin-film transistors deposited by VHF-PECVD and hot-wire CVD. *J. Non-Cryst. Solids* **299–302**, 1340 (2002)
158. Gatz, S., Plagwitz, H., Altermatt, P.P., Terheiden, B., Brendel, R.: Thermal stability of amorphous silicon/silicon nitride stacks for passivating crystalline silicon solar cells. *Appl. Phys. Lett.* **93**, 173502 (2008)
159. Plagwitz, H., Takahashi, Y., Terheiden, B., Brendel, R.: In: Poortmans, J., Ossenbrink, H., Dunlop, E., Helm, P. (eds.) *Proceedings of the 21st European Photovoltaic Solar Energy Conf.*, p. 688 WIP-Renewable Energies, Munich (2006)
160. Dauwe, S., Schmidt, J., Hezel, R.: In: *Proceedings of the 29th IEEE Photovoltaic Specialists Conference*, p. 1246. IEEE, New Orleans (2002)
161. Leendertz, C., Mingirulli, N., Schulze, T.F., Kleider, J.P., Rech, B., Korte, L.: Discerning passivation mechanisms at a-Si:H/c-Si interfaces by means of photoconductance measurements. *Appl. Phys. Lett.* **98**, 202108 (2011)
162. Schulze, T.F., Beaushausen, H.N., Leendertz, C., Dobrich, A., Rech, B., Korte, L.: Interplay of amorphous silicon disorder and hydrogen content with interface defects in amorphous/crystalline silicon heterojunctions. *Appl. Phys. Lett.* **96**, 25102 (2010)
163. De Wolf, S., Demareux, B., Descoedres, A., Ballif, C.: Very fast light-induced degradation of a-Si:H/c-Si(100) interfaces. *Phys. Rev. B* **83**, 233301 (2011)
164. Muñoz, D., Voz, C., Martin, I., Orpella, A., Puigdollers, J., Alcubilla, R., Villar, F., Bertomeu, J., Andreu, J., Damon-Lacoste, J., Roca i Cabarrocas, P.: Progress in a-Si:H/c-Si heterojunction emitters obtained by Hot-Wire CVD at 200°C. *Thin Solid Films* **516**, 761 (2008)
165. Zhou, H.P., Wei, D.Y., Xu, S., Xiao, S.Q., Xu, L.X., Huang, S.Y., Guo, Y.N., Khan, S., Xu, M.: Crystalline silicon surface passivation by intrinsic silicon thin films deposited by low-frequency inductively coupled plasma. *J. Appl. Phys.* **112**, 013708 (2012)
166. Xiao, S.Q., Xu, S., Xu, L.X., Huang, S.Y., Zhou, H.P., Wei, D.Y., Guo, Y.N.: A novel capacitive-coupled electrode-less plasma (CCEP) for deposition of passivating layer a-Si:H (unpublished)
167. Taguchi, M., Tsunomura, Y., Inoue, H., Taira, S., Nakashima, T., Baba, T., Sakata, H., Maruyama, E.: High-efficiency HIT solar cell on thin (<100 μm) silicon wafer. In: *Proceedings of the 24th European Photovoltaic Solar Energy Conference*, pp. 1690–1693 (2009)
168. Green, M.A., Emery, K., Hishikawa, Y., Warta, W.: Solar cell efficiency tables (Version 34). *Prog. Photovolt. Res. Appl.* **17**, 320–326 (2009)

169. Ulyashin, A., Wright, D.N., Bentzen, A., Suphellen, A., Marstein, E., Holt, A.: In: Willeke, G., Ossenbrink, H., Helm, P. (eds.) *Proceedings of the 22nd European Photovoltaic Solar Energy Conference*, p. 1690. WIP-Renewable Energies, Munich (2007)
170. Plagwitz, H.: Ph.D. thesis, Institut für Solarenergieforschung Hameln (2007)
171. Bentzen, A., Ulyashin, A., Suphellen, A., Sauar, E., Grambole, D., Wright, D.N., Marstein, E. S., Svensson, B.G., Holt, A.: In: *Proceedings of the 15th International Photovoltaic Science and Engineering Conference*, p. 316. China Solar Energy Society, Shanghai (2005)
172. Lorenz, A., John, J., Vermang, B., Poortmans, J.: Influence of surface conditioning and passivation schemes on the internal rear reflectance of bulk silicon solar cells. *Proceedings of the 25th European Photovoltaic Solar Energy Conference*, Valencia, Spain, pp. 2059–2061 (2010)
173. Schneiderlöchner, E., Preu, R., Lüdemann, R., Glunz, S.W.: Laser-fired rear contacts for crystalline silicon solar cells. *Prog. Photovolt. Res. Appl.* **10**, 29 (2002)
174. Engelhart, P., Hermann, S., Neubert, T., Plagwitz, H., Grischke, R., Meyer, R., Schoonderbeek, A., Stute, U., Brendel, R.: Laser ablation of SiO₂ for locally concated Si solar cells with ultra-short pulses. *Prog. Photovolt. Res. Appl.* **15**, 521 (2007)
175. Lauinger, T., Schmidt, J., Aberle, A.G., Hezel, R.: Surface passivation properties of silicon/silicon oxide/silicon nitride structures for solar cells. *Proceedings of the 13th European Photovoltaic Solar Energy Conference*, Nice, France, pp. 1291–1294 (1995)
176. Dullweber, T., Gatz, S., Hannebauer, H., Falcon, T., Hesse, R., Schmidt, J., Brendel, R.: Towards 20% efficient large-area screen-printed rear-passivated silicon solar cells. *Prog. Photovolt. Res. Appl.* **20**, 630–638 (2012)
177. Fischer, B.: PV-Tools, Hameln, Germany (2011)
178. Münzer, K.A., Schöne, J., Teppe, A., Schlosser, R.E., Hein, M., Hammer, D., Hüls, S., Hanke, M., Keller, S., Fath, P.: Advanced rear side technology for industrial high efficiency solar cells. *Proceedings of the 25th European Photovoltaic Solar Energy Conference*, Valencia, Spain, pp. 2314–2318 (2010)
179. Böске, T., Hellriegel, R., Wütherich, T., Bornschein, L., Helbig, A., Carl, R., Dupke, M., Stichtenoth, D., Aichele, T., Jesswein, R., Roth, T., Schöllhorn, C., Geppert, T., Grohe, A., Lossen, J., Krokoszinski, H.-J.: Fully screen-printed PERC cells with laser-fired contacts—an industrial cell concept with 19.5% efficiency. *Proceedings of the 37th IEEE Photovoltaic Specialists Conference*, Seattle, USA, pp. 3663–3666 (2011)
180. Lai, J.-H., Upadhyaya, A., Ramanathan, R., Das, A., Tate, K., Upadhyaya, V., Kapoor, A., Chai-Chen, C.-W., Rohatgi, A.: Large area 19.4% efficient rear passivated silicon solar cells with local Al BSF and screen-printed contacts. *Proceedings of the 37th IEEE Photovoltaic Specialists Conference*, Seattle, USA, p. 1929 (2011)
181. Reinwand, D., Specht, J., Stüwe, D., Seitz, S., Nekarda, J.-F., Biro, D., Preu, R., Trassl, R.: 21.1% efficient PERC silicon solar cells on large scale by using in-line sputtering for metallization. *Proceedings of the 35th IEEE Photovoltaic Specialists Conference*, Honolulu, USA, pp. 3582–3586 (2010)
182. Rohatgi, A., Narasimha, S.: Design, fabrication, and analysis of greater than 18% efficient multicrystalline silicon solar cell. *Proceedings of the 9th International Photovoltaic Science and Engineering Conference*, pp. 187–197 (1996)
183. Mittelstädt, L., Dauwe, S., Metz, A., Hezel, R., Häbler, C.: Front and rear silicon-nitride-passivated multicrystalline silicon solar cells with an efficiency of 18.1%. *Prog. Photovolt. Res. Appl.* **10**, 35–39 (2002)
184. Zhao, J., Wang, A., Green, M.A.: 19.8% efficient multicrystalline silicon solar cells with ‘honeycomb’ textured front surface. *Proceedings of the 2nd World Conference on Photovoltaic Energy Conversion*, pp. 1681–1684 (1998)
185. Macdonald, D., Cuevas, A.: The trade-off between phosphorus gettering and thermal degradation in multicrystalline silicon. *Proceedings of the 16th European Photovoltaic Solar Energy Conference*, pp. 1707–1710 (2000)

186. Schultz, O., Riepe, S., Glunz, S.W.: Influence of high-temperature processes on multicrystalline silicon. *Solid State Phenom* **95–96**, 235–240 (2004)
187. Schultz, O., Glunz, S.W., Willeke, G.P.: Multicrystalline silicon solar cells exceeding 20% efficiency. *Prog. Photovolt. Res. Appl.* **12**, 553–558 (2004)
188. Zhao, J., Wang, A., Altermatt, P., Wenham, S.R., Green, M.A.: 24% Efficient PERL silicon solar cell: recent improvements in high efficiency silicon cell research. *Sol. Energy Mater. Sol. Cells* **41–42**, 87–99 (1996)
189. Zhao, J., Wang, A., Green, M.A., Ferrazza, F.: 19.8% efficient “honeycomb” textured multicrystalline and 24.4% monocrystalline silicon solar cells. *Appl. Phys. Lett.* **73**, 1991 (1998)
190. Zhao, J., Wang, A., Green, M.A.: 4.5% Efficiency silicon PERT cells on MCZ substrates and 24.7% efficiency PERL cells on Fz substrates. *Prog. Photovolt. Res Appl.* **7**, 471–474 (1999)
191. Zhao, J., Wang, A., Green, M.A.: Performance degradation in Cz(B) cells and improved stability high efficiency PERT and PERL silicon cells on a variety of SHE MCZ(B), Fz (B) and Cz(Ga) substrates. *Prog. Photovolt. Res. Appl.* **8**, 549–558 (2000)
192. Zhao, J., Wang, A., Green, M.A.: 24.5% efficiency PERT silicon solar cells on SHE MCZ substrates and cell performance on other SHE Cz and Fz substrates. *Sol. Energy Mater. Sol. Cells* **66**, 27–36 (2001)
193. Green, M.A., Zhao, J., Wang, A.: 23% PV module and other silicon solar cell advances. *Proc. 2nd World Conference and Exhibition on Photovoltaic Solar Energy Conversion*, pp. 1187–1192 (1998)
194. Hahn, G.: Status of selective emitter technology. *Proceedings of the 25th EU PVSEC/WCPEC, Valencia, Spain* (2010)
195. Campbell, P., Green, M.A.: Light trapping properties of pyramidally textured surfaces. *J. Appl. Phys.* **62**, 243 (1987)
196. Zhao, J., Wang, A., Green, M.A.: Series resistance caused by the localized rear contact in high-efficiency silicon solar-cells. *Sol. Energy Mater. Sol. Cells* **32**, 89 (1994)
197. Wang, A.: Ph.D. Thesis, University of New South Wales, p. 111 (1992)
198. Suwito, D., Jäger, U., Benick, J., Janz, S., Hermle, M., Glunz, S.W.: Industrially feasible rear passivation and contacting scheme for high-efficiency n-type solar cells yielding a V_{oc} of 700 mV. *IEEE Trans. Electron Devices* **57**, 2032 (2010)
199. Richter, A., Hörteis, M., Benick, J., Henneck, S., Hermle, M., Glunz, S.W.: *Proceedings of the 35th IEEE Photovoltaic Specialists Conference, Honolulu, HI, 20–25 June 2010. IEEE, New York* (2010)
200. Colville, F.: Laser-assisted selective emitters and the role of laser doping. *Technical papers in Photovoltaic International Magazine, 5th edn.*, pp. 1–6 (2010)
201. Antoniadis, H.: Silicon ink high efficiency solar cells. *Proceedings of the 34th IEEE Photovoltaics Specialists Conference, Philadelphia* (2009)
202. Antoniadis, H., Jiang, F., Shan, W., Liu, Y.: All screen printed mass production silicon ink selective emitter solar cells. *Proceedings of the 35th IEEE Photovoltaic Specialists Conference, Honolulu* (2010)
203. Esturo-Breton, A., Binaie, F., Breselge, M., Friess, T., Geiger, M., Holbig, E., Isenberg, J., Keller, S., Kuehn, T., Maier, J., Muenzer, A., Schlosser, R., Schmid, A., Voyer, C., Winter, P., Bayer, K., Kruemberg, J., Henze, S., Melnyk, I., Schmidt, M., Klingbeil, S., Walter, F., Kopecek, R., Peter, K.: Crystalline silicon solar cells with selective emitter for industrial mass production. *Proceedings of the 24th European Photovoltaic Solar Energy Conference and Exhibition, Hamburg*, pp. 1068–1071 (2009)
204. Low, R.J., Gupta, A., Baterman, N.P., Ramappa, D., Sullivan, P., Skinner, W., Mullin, J., Peters, S., Weiss-Wallrath, H.: High efficiency selective emitter cells enabled through patterned ion implantation. *Proceedings of the 35th IEEE Photovoltaic Specialists Conference, Honolulu* (2010)

205. Haverkamp, H., Dastgheib-Shirazi, A., Raabe, B., Book, F., Hahn, G.: Minimizing the electrical losses on the front side: development of a selective emitter process from a single diffusion. Proceedings of the 33rd IEEE Photovoltaic Specialists Conference, Diego (2008)
206. Eisele, S.J., Röder, T.C., Köhler, J.R., Werner, J.H.: 18.9% efficient full area laser doped silicon solar cell. *Appl. Phys. Lett.* **95**, 133501 (2009)
207. Röder, T.C., Eisele, S.J., Grabitz, P., Wagner, C., Kulushich, G., Köhler, J.R., Werner, J.H.: Add-on laser tailored selective emitter solar cells. *Prog. Photovolt. Res. Appl.* **18**, 505–510 (2010)
208. Kray, D., Bay, N., Cimiotti, G., Kleinschmidt, S., Kösterke, N., Lösel, A., Sailer, M., Träger, A., Kühnlein, H., Nussbaumer, H., Fleischmann, C., Granek, F.: Industrial LCP industrial emitter solar cells with plated contacts. Proceedings of the 35th IEEE Photovoltaic Specialists Conference, Honolulu, (2010)
209. Tjahjono, B.S., Wu, V., Anditsch, H.T., Cheng, J., Ting, J., Yang, M.J., Szpitalak, T., Beilby, B., Hsu, K.C.: Optimizing selective emitter technology in one year of full scale production. Proceedings of the 26th European Photovoltaic Solar Energy Conference and Exhibition, Hamburg, pp. 901–905 (2011)
210. Tjahjono, B.S., Yang, M.J., Lan, C.Y., Ting, J., Sugianto, A., Ho, H., Kuepper, N., Beilby, B., Szpitalak, T., Wenham, S.R.: 18.9% efficient laser doped selective emitter solar cell on industrial grade p-type czochralski wafer. Proceedings of the 25th European Photovoltaic Solar Energy Conference and Exhibition, Valencia, pp. 1396–1400 (2010)
211. Shi, Z., Wenham, S., Ji, J.: Mass production of the innovative Pluto solar cell technology. Proceedings of the 34th IEEE Photovoltaics Specialists Conference, Philadelphia (2010)
212. Green, M.A., Zhao, J., Wang, A., Wenham, S.R.: Progress and outlook for high efficiency crystalline silicon solar cells. *Sol. Energy Mater. Sol. Cells* **65**, 9–16 (2001)
213. Shi, Z., Wenham, S., Ji, J., Partlin, S., Sugianto, A.: Suntech whitepaper: mass production of the innovative Pluto solar cell technology. http://am.suntech-power.com/images/stories/pdf/other/whitepaper_final_081511.pdf. Retrieved 16 Oct 2011
214. Wenham, S.: Multi-gigawatt manufacturing in China. Invited Plenary session Paper presented at the 37th IEEE Photovoltaics Specialists Conference, Seattle (2011)
215. Wenham, S.: Bouried-contact silicon solar cells. *Prog. Photovolt. Res. Appl.* **1**, 3–10 (1993)
216. Hameiri, Z.: Laser-doped selective emitter and local back surface field solar cells with rear passivation. Ph.D. Thesis, The University of New South Wales, Sydney (2010)
217. Wang, Z., Han, P., Lu, H., Qian, H., Chen, L., Meng, Q., Tang, N., Gao, F., Jiang, Y., Wu, J., Wu, W., Zhu, H., Ji, J., Shi, Z., Sugianto, A., Mai, L., Hallam, B., Wenham, S.: Advanced PERC and PERL production cells with 20.3% record efficiency for standard commercial p-type silicon wafers. *Prog. Photovolt. Res. Appl.* **20**, 260–268 (2012)
218. De Ceuster, D., Cousins, P., Rose, D., Vicente, D., Tipones, P., Mulligan, W.: Low cost, high volume production of >22% efficiency silicon solar cells. Proceedings of the 22nd European Photovoltaic Solar Energy Conference and Exhibition, Milan, Italy, pp. 816–819 (2007)
219. Macdonald, D., Geerligs, L.J.: Recombination activity of interstitial iron and other transition metal point defects in p- and n-type crystalline silicon. *Appl. Phys. Lett.* **85**, 4061 (2004)
220. Engelhart, P., Harder, N.-P., Grischke, R., Merkle, A., Meyer, R., Brendel, R.: Laser structuring for back junction silicon solar cells. *Prog. Photovolt. Res. Appl.* **15**, 237 (2007)
221. Granek, F., Hermle, M., Reichel, C., Schultz-Wittmann, O., Glunz, S.W.: High-efficiency back-contact back-junction silicon solar cell research at Fraunhofer ISE. Proceedings of the 23rd European Photovoltaic Solar Energy Conference and Exhibition, Valencia, Spain, pp. 991–995 (2008)
222. Guo, J.-H., Tjahjono, B.S., Cotter, J.E.: 19.2% efficiency n-type laser-grooved silicon solar cells. Proceedings of the 31st IEEE Photovoltaic Specialist Conference, Orlando, FL, pp. 983–986 (2005)
223. Gong, C., Van Kerschaver, E., Robbelein, J., Janssens, T., Posthuma, N., Poortmans, J., Mertens, R.: Screen-printed aluminum-alloyed p⁺ emitter on high-efficiency n-type interdigitated back-contact silicon solar cells. *IEEE Electron Devices Lett.* **31**, 576 (2010)

224. Kluska, S., Granek, F., Rüdiger, M., Hermle, M., Glunz, S.W.: Modeling and optimization study of industrial n-type high-efficiency back-contact back-junction silicon solar cells. *Sol. Energy Mater. Sol. Cells* **94**, 568 (2010)
225. Verlinden, P.J., Aleman, M., Posthuma, N., Fernandez, J., Pawlak, B., Robbelein, J., Debucquoy, M., Van Wichelen, K., Poortmans, J.: Simple power-loss analysis method for high-efficiency interdigitated back contact (IBC) silicon solar cells. *Sol. Energy Mater. Sol. Cells* **106**, 37 (2012)
226. Castano, F.J., Morecroft, D., Cascant, M., Yuste, H., Lamers, M.W.P.E., Mewe, A.A., Romijn, I.G., Bende, E.E., Komatsu, Y., Weeber, A.W., Cesar, I.: Industrially feasible >19% efficiency IBC cells for pilot line processing. *Proceedings of the 36th IEEE-PVSEC*, Seattle, USA, pp. 1038–1042 (2011)
227. Reichel, C., Granek, F., Hermle, M., Glunz, S.W.: Investigation of electrical shading effects in back-contacted back-junction silicon solar cells using the two-dimensional charge collection probability and the reciprocity theorem. *J. Appl. Phys.* **109**, 024507 (2011)
228. Granek, F., Hermle, M., Huljic, D.M., Schultz-Wittmann, O., Glunz, S.W.: Enhanced lateral current transport via the front n^+ diffused layer of n-type high-efficiency back-junction back-contact silicon solar cells. *Prog. Photovolt. Res. Appl.* **17**, 47 (2009)
229. Granek, F.: High-efficiency back-contact back-junction silicon solar cells. Ph.D. thesis, Fraunhofer ISE (2009)
230. Harder, N.-P., Mertens, V., Brendel, R.: Buried emitter solar cell structures: decoupling of metallization geometry and carrier collection geometry of back contacted solar cells. *Phys Status Solidi (RRL)* **2**, 148 (2008)
231. Reichel, C., Granek, F., Hermle, M., Glunz, S.W.: Enhanced current collection in back-contacted back-junction Si solar cells by overcompensating a boron emitter with a phosphorus base-type doping. *Phys. Status Solidi A* **207**, 1978 (2010)
232. Cousins, P.J., Smith, D.D., Luan, H.C., Manning, J., Dennis, T.D., Waldhauer, A., Wilson, K. E., Harley, G., Mulligan, G.P.: Gen III: improved performance at lower cost. *Proceedings of the 35th IEEE Photovoltaic Specialists Conference*, pp. 823–826 (2010)
233. Bock, R., Mau, S., Schmidt, J., Brendel, R.: Back-junction back-contact n-type silicon solar cells with screen-printed aluminum-alloyed emitter. *Appl. Phys. Lett.* **96**, 263507 (2010)
234. Reichel, C., Reusch, M., Granek, F., Hermle, M., Glunz, S.W.: Decoupling charge carrier collection and metallization geometry of back-contacted back-junction silicon solar cells by using insulating thin films. *Proceedings of the 35th IEEE Photovoltaic Specialists Conference*, Honolulu, Hawaii, USA, pp. 1034–1038 (2010)
235. Gee, J.M., Schuber, W.K., Basore, P.A.: Emitter wrap-through solar cell. In: *Proceedings of the 23rd IEEE Photovoltaic Specialists Conference*, Louisville, Kentucky, USA, pp. 265–270 (1993)
236. Gee, J.M., Buck, M.E., Schuber, W.K., Basore, P.A.: Progress on the emitter wrap-through silicon solar cell. In: *Proceedings of the 12th European Photovoltaic Solar Energy Conference*, Amsterdam, The Netherlands, pp. 743–746 (1994)
237. Glunz, S.W., Dicker, J., Kray, D., Lee, J.Y., Preu, R., Rein, S., Schneiderlöchner, E., Sölter, J., Warta, W., Willeke, G.: High-efficiency cell structures for medium-quality silicon. In: *Proceedings of the 17th European Photovoltaic Solar Energy Conference*, Munich, Germany, pp. 1287–1292 (2001)
238. Ulzhöfer, C., Altermatt, P.P., Harder, N.-P., Brendel, R.: Loss analysis of emitter-wrap-through silicon solar cells by means of experiment and three-dimensional device modeling. *J. Appl. Phys.* **107**, 104509 (2010)
239. Engelhart, P., Teppe, A., Merkle, A., Grischke, R., Meyer, R., Harder, N.-P., Brendel, R.: The RISE-EWT solar cell—a new approach towards simple high efficiency silicon solar cells. In: *Proceedings of the 17th Photovoltaic Solar Energy Conference*, Shanghai, China, pp. 802–803 (2005)
240. Engelhart, P.: Ph.D. Thesis, University of Hannover (2007)

241. Hermann, S., Merkle, A., Ulzhöfer, C., Dorn, S., Feihaber, I., Berger, M., Friedrich, T., Brendemühl, T., Harder, N.-P., Ehlers, L., Weise, K., Meyer, R., Brendel, R.: Progress in emitter wrap-through solar cell fabrication on boron doped Czochralski-grown silicon. *Sol. Energy Mater. Sol. Cells* **95**, 1069 (2011)
242. Sinton, R.A., Verlinden, P., Kane, D.E., Swanson, R.M.: Development efforts in silicon backside-contact solar cells. Proceedings of the 8th European Photovoltaic Solar Energy Conference, Florence, Italy, pp. 1472–1476 (1988)
243. Kray, D., Dicker, J., Osswald, D., Leimenstoll, A., Glunz, S.W., Zimmermann, W., Tentscher, K.-H., Strobl, G.: Progress in high-efficiency emitter-wrap-through cells on medium quality substrates. In: Proceedings of the 3rd World Conference on Photovoltaic Energy Conversion, Osaka, Japan, pp. 1340–1343 (2003)
244. Hermann, S., Engelhart, P., Merkle, A., Neubert, T., Brendemühl, T., Meyer, M., Harder, N.-P., Brendel, R.: 21.4%-efficient emitter wrap-through RISE solar cell on large area and picosecond laser processing of local contact openings. In: Proceedings of the 22nd European Photovoltaic Solar Energy Conference, Milan, Italy, pp. 970–975 (2007)
245. Lim, B., Hermann, S., Bothe, K., Schmidt, J., Brendel, R.: Solar cells on low-resistivity boron-doped Czochralski-grown silicon with stabilized efficiencies of 20%. *Appl. Phys. Lett.* **93**, 162102 (2008)
246. Mingirulli, N., Stüwe, D., Specht, J., Fallisch, A., Biro, D.: Screen-printed emitter-wrap-through solar cells with single step side selective emitter with 18.8% efficiency. *Prog. Photovolt. Res. Appl.* **19**, 366 (2011)
247. Kiefer, F., Ulzhöfer, C., Brendemühl, T., Harder, N.-P., Brendel, R., Mertens, V., Bordihn, S., Peters, C., Müller, J.W.: High efficiency n-type Emitter-Wrap-Through silicon solar cells. *IEEE J. Photovoltaics* **1**, 49 (2011)
248. Ulzhöfer, C., Hermann, S., Harder, N.-P., Altermatt, P.P., Brendel, R.: The origin of reduced fill factors of emitter-wrap-through-solar cells. *Phys Status Solidi (RRL)* **2**, 251 (2008)
249. Fuhs, W., Niemann, K., Stuke, J.: Heterojunctions of amorphous silicon and silicon single-crystals. *Bull. Am. Phys. Soc.* **19**, 394 (1974)
250. Takahama, T., Taguchi, M., Kuroda, S., Matsuyama, T., Tanaka, M., Tsuda, S., Nakano, S., Kuwano, Y.: High efficiency single- and poly-crystalline silicon solar cells using ACJ-HIT structure. Proceedings of the 11th EC PVSEC, Montreux, Switzerland, pp. 1057–1060 (1992)
251. Sawada, T., Terada, N., Tsuge, S., Baba, T., Takahama, T., Wakisaka, K., Tsuda, S., Nakano, S.: High efficiency a-Si/c-Si heterojunction solar cell. Conference Record of the 1st WCPEC, Hawaii, USA, pp. 1219–1226 (1994)
252. Tanaka, M., Okamoto, S., Tsuge, S., Kiyama, S.: Development of HIT solar cells with more than 21% conversion efficiency and commercialization of highest performance HIT modules. Proceedings of the 3rd WCPEC, Osaka, Japan, pp. 955–958 (2003)
253. Taguchi, M., Tanaka, M., Matsuyama, T., Matsuoka, T., Tsuda, S., Nakano, S., Kishi, Y., Kuwano, Y.: Improvement of the conversion efficiency of polycrystalline silicon thin film solar cell. Technical Digest of the International PVSEC-5, Kyoto, Japan, pp. 689–692 (1990)
254. Kanno, H., Ide, D., Tsunomura, Y., Taira, S., Baba, T., Yoshimine, Y., Taguchi, M., Kinoshita, T., Sakata, H., Maruyama, E.: Over 20% efficient HIT solar cell. In: Proceedings of the 23rd European Photovoltaic Solar Energy Conference, pp. 1136–1139 (2008)
255. Mishima, T., Taguchi, M., Sakata, H., Maruyama, E.: Development status of high-efficiency HIT solar cells. *Sol. Energy Mater. Sol. Cells* **95**, 18 (2011)
256. Taguchi, M., Tsunomura, Y., Inoue, H., Taira, S., Nakashima, T., Baba, T., Sakata, H., Maruyama, E.: High-efficiency HIT solar cell on thin (<100 μm) silicon wafer. In: Proceedings of the 24th European Photovoltaic Solar Energy Conference, pp. 1690–1693 (2009)
257. Schulze, T.F.: Structural, electronic and transport properties of amorphous/crystalline silicon heterojunctions. PhD thesis, HZB (2011)

258. Lachenal, D., Andraut, Y., Bätzner, D., Guérin, C., Kobas, M., Mendes, B., Strahm, B., Tesfai, M., Wahli, G., Buechel, A., Descoedres, A., Choong, G., Bartlome, R., Barraud, L., Zicarelli, F., Bôle, P., Fesquet, L., Damon-Lacoste, J., De Wolf, D., Ballif, C.: High efficiency silicon heterojunction solar cell activities in Neuchatel, Switzerland. Proceedings of the 25th European Photovoltaic Solar Energy Conference and Exhibition and the 5th World Conference on Photovoltaic Energy Conversion, Valencia, Spain, pp. 1272–1275 (2010)
259. Strahm, B., Andraut, Y., Baetzner, D., Guérin, C., Holmes, N., Kobas, M., Lachenal, D., Mendes, B., Tesfai, M., Wahli, G., Wuensch, F., Buechel, A., Mai, J., Schulze, T., Vogt, M.: Progress in silicon hetero-junction solar cell development and scaling for large scale mass production use. Proceedings of the 25th European Photovoltaic Solar Energy Conference and Exhibition and the 5th World Conference on Photovoltaic Energy Conversion, Valencia, Spain, pp. 1286–1289 (2010)
260. Descoedres, A., Barraud, L., Bartlome, R., Choong, G., De Wolf, S., Zicarelli, F., Ballif, C.: The silane depletion fraction as an indicator for the amorphous/crystalline silicon interface passivation quality. *Appl. Phys. Lett.* **97**, 183505 (2010)
261. Descoedres, A., Barraud, L., De Wolf, S., Strahm, B., Lachenal, D., Guérin, C., Holman, Z. C., Zicarelli, F., Demaurex, B., Seif, J., Holovsky, J., Ballif, C.: Improved amorphous/crystalline silicon interface passivation by hydrogen plasma treatment. *Appl. Phys. Lett.* **99**, 123506 (2011)
262. Wang, Q., Page, M.R., Iwaniczko, E., Xu, Y., Roybal, L., Bauer, R., To, B., Yuan, H.-C., Duda, A., Hasoon, F., Yan, Y.F., Levi, D., Meier, D., Branz, H.M., Wang, T.H.: Efficient heterojunction solar cells on p-type crystal silicon wafers. *Appl. Phys. Lett.* **96**, 013507 (2010)
263. Damon-Lacoste, J.: Ph.D. thesis, Ecole Polytechnique Paris (2007)
264. Froitzheim, A., Stangl, R., Elstner, L., Schmidt, M., Fuhs, W.: Interface recombination in amorphous/crystalline silicon solar cell, a simulation study. In: Conference Record of the 29th IEEE Photovoltaic Specialists Conference, New Orleans, USA, pp. 1238–1241 (2002)
265. Hu, Z.H., Liao, X.B., Zeng, X.B., Xu, Y.Y., Zhang, S.B., Diao, H.W., Kong, G.L.: Computer simulation of a-Si:H/c-Si heterojunction solar cells. *Acta Phys. Sin.* **52**, 217 (2003)
266. Emanuele, C., Daniele, I.: Role of front contact work function on amorphous silicon/crystalline silicon heterojunction solar cell performance. *IEEE Electron Devices Lett.* **24**, 177 (2003)
267. Datta, A., Damon-Lacoste, J., Roca i Cabarrocas, P., Chatterjee, P.: Defect states on the surfaces of a p-type c-Si wafer and how they control the performance of a double heterojunction solar cell. *Sol. Energy Mater. Sol. Cells* **92**, 1500 (2008)
268. Zhao, L., Zhou, C.L., Li, H.L., Diao, H.W., Wang, W.J.: Design optimization of bifacial HIT solar cells on p-type silicon substrates by simulation. *Sol. Energy Mater. Sol. Cells* **92**, 673 (2008)

Chapter 2

Luminescent Study of Recombination Processes in the Single-Crystal Silicon and Silicon Structures Fabricated Using High-Efficiency Solar Cell Technology

A.M. Emel'yanov

Abstract Some results of the author's researches in the last decade of the luminescence in the region of the fundamental absorption edge (edge luminescence) of the single-crystal silicon (c-Si), including structures which were made using high-efficiency solar cell technology, are summarized and systematized. This chapter presents experimental evidences and justifications of the dominant mechanism of radiative recombination in c-Si and of the dependence of the intensity of the edge luminescence on the intensity of its excitation. Considerable consideration is given to the study of recombination parameters at high excitation intensities of the edge luminescence in the structures fabricated using high-efficiency solar cell technology.

1 Introduction

Single-crystal silicon (c-Si) is a nondirect-gap semiconductor and, therefore, has been regarded as an inefficient source of luminescence during many decades. But relatively recently it was experimentally demonstrated that in c-Si it is possible to achieve the edge luminescence external quantum efficiencies (η_{ext}) which are very high in magnitude for the class of indirect-gap semiconductors (by edge luminescence it is meant luminescence in the region of the fundamental absorption edge). As far as we know, the present-day record parameter at room temperature is $\eta_{\text{ext}} = 6\%$ for photoluminescence (PL) of c-Si with no p–n junction [1]. A value $\eta_{\text{ext}} = 0.6\%$ [2] for electroluminescence (EL) of Si-based light-emitting diodes (LEDs) at room temperature for the first time was achieved in [2]. In the case of EL, such value of η_{ext} was obtained for p–n junctions in c-Si structures fabricated by the

A.M. Emel'yanov (✉)
Ioffe Physical-Technical Institute of the Russian Academy of Sciences,
Politekhnicheskaya 26, St. Petersburg 194021, Russia
e-mail: Emelyanov@mail.ioffe.ru; Emelyanov.49@inbox.ru

high-efficiency solar cell technology. The large values of η_{ext} make it possible to use the edge luminescence of c-Si in Si-based optoelectronic devices. The author of this work some years ago achieved high values of the integrated edge EL power and the emissive power per unit surface area for LEDs, fabricated using high-efficiency solar cell technology. This defines one of the reasons of interest in the investigations described below.

The efficiency of the edge luminescence of c-Si depends on the effective lifetime of minority charge carriers (τ) and their diffusion length (L_D) (i.e., the parameters defining the characteristics of many semiconductor devices including solar cells). Therefore, in the last few years, a large number of studies, in which the parameters of edge luminescence of c-Si were used to determine the lifetime τ or the diffusion length L_D , the distribution of τ or L_D over the area of semiconductor wafers at different stages of device fabrication, and the dependence of τ or L_D on the concentration of minority charge carriers, have been published (see, e.g., [3–12]). The PL measurements present contactless techniques, and, according to [3], PL and EL techniques are most sensitive for determining the effective lifetimes. In addition, the authors of [3, 4] state that, in contrast to the photoconductivity measurements widely used to determine lifetimes, the quasi-steady-state luminescence technique is practically insensitive to the space charge region (SCR) in the single crystal and, in the cases of practical importance, to the capture of minority charge carriers by trapping centers. According to the description of products of the world-famous firm Hamamatsu, “detection of luminescence signals from wafer, solar cells and solar panels have become major techniques for characterization and quality inspection.” Hamamatsu offers a complete “luminescence analysis system” as well as individual cameras for luminescence imaging.

In a basis of luminescent methods for determining τ and L_D lies the dependence of the radiative recombination rate in a unit volume of semiconductor (R) on the free carrier concentration. In general, this dependence is determined by the mechanism of radiative recombination. But earlier in opinion of the author there were no convincing experimental proofs of the mechanism of radiative recombination in c-Si at room temperature. Such views were based on theoretical estimates. In accordance with them at room temperature dominate or the radiative recombination of free charge carriers (see for example [13]), or approximately equal the contributions of the radiative recombination of free charge carriers and free excitons (see for example the review of the literature in [15]). Usually the dependence of the radiative recombination rate R on the concentrations of free electrons (n) and holes (p) is described by the formula

$$R = Bnp, \quad (2.1)$$

where B —radiative recombination coefficient. At a relatively small n and p , B not depend on n and p (see for example [13]). But with the growth of n and/or p , according to the calculations of some researchers, it may vary. This change at the various mechanisms of the radiative recombination can be due to various reasons and therefore be described by various dependences. For example, the authors of work [13] associated decrease of B with screening of Coulomb interaction among

the free carriers. At the exciton mechanism of radiative recombination the value R is determined by the formula

$$R = n_{\text{ex}}/\tau_{\text{ex}}, \quad (2.2)$$

where τ_{ex} —radiative lifetime of excitons and n_{ex} —concentration of free excitons. According to the results of [14], n_{ex} may depend on the concentration of free charge carriers due to screening of Coulomb interaction among charge carriers in excitons. This effect can also influence the value of B . Proved by the author of the present work in recent years the representations of the dominant mechanism of radiative recombination via free excitons in c-Si in a wide range of temperatures (including room temperatures) are the second reason of interest in the investigations presented below.

The distinguishing features of present work from similar works of other researchers are using a significantly higher intensity of luminescence excitation, especially manufacturing structures and in some cases combined impact on the structure of the two sources of luminescence excitation. For example it was shown that the linear or close-to-linear portions of the dependences of the edge luminescence intensity of c-Si on the luminescence excitation intensity under high injection levels are caused by the existence of linear or close-to-linear portions of the dependences of the free exciton concentration on the free carrier concentration at sufficiently high free carrier concentrations. Under these conditions the value of R cannot be described by formula (2.1). This is the third major reason of interest to the research results shown below.

In this work the results of the works first published in [15–22, 34] by publisher «Pleiades Publishing, Inc.» <http://www.maikonline.com>, <http://www.maik.ru> are summarized and combined.

2 Experimental Details

For the measurement of the EL and PL spectra, the light emitted from a surface of sample was focused by a system of lenses onto the entrance slit of a monochromator and detected at the exit with an uncooled InGaAs diode. The spectra were corrected for the spectral characteristic of the photodetector and the entire optical tract. The EL and PL kinetics was measured using a Ge or a Si photodetector operating at room temperature, which provided a time constant of $\sim 1 \mu\text{s}$ in response to a rectangular pulse of light. The EL was excited by voltage pulses with a repetition frequency about 30 Hz applied to the c-Si diode. The pulses had a rectangular shape with a width of 0.1–5 ms and the pulse rise and fall times shorter than $1 \mu\text{s}$. The maximum pumping forward current pulse amplitude was 18 A. At the PL measuring the input window of the detector was covered with a Si filter to protect it from laser radiation. To excite the PL signal in the pulse mode of experiments, we used mainly a laser emitting at the wavelength $\lambda = 658 \text{ nm}$ (with the exception of some

special experiments). In some cases, we used a semiconductor laser emitting at the wavelength $\lambda = 0.98 \mu\text{m}$. Laser radiation was focused on the center of the sample to form a spot of diameter $d = 1\text{--}1.5 \text{ mm}$. The laser pulses were rectangular in shape, the duration of the pulses was $0.6\text{--}1 \text{ ms}$, the rise time and decay time were shorter than $1 \mu\text{s}$, and the repetition interval was 50 ms . The pulse duration chosen for the experiments practically provided the conditions for quasi-steady-state PL at the end of the pulse.

For determined η_{ext} at EL the LED radiation power was measured using a Ge photodiode (Hamamatsu B5170-50) with the known area S_{ph} and sensitivity K in the spectral range under consideration. The photodetector was situated at a distance of $L_{\text{ph}} = 25 \text{ cm}$ from the emitting surface and oriented perpendicular to this surface. The photodiode current Y_{ph} was measured, and the output radiation power was calculated using the formula

$$W = 2\pi L_{\text{ph}}^2 Y_{\text{ph}} / K S_{\text{ph}} M. \quad (2.3)$$

We introduced the empirical coefficient $M = 1.7$, which took into account the nonisotropic distribution of emission from a textured crystal surface within a hemisphere at a given distance L_{ph} from the LED. This coefficient was empirically determined from the results of measurements of Y_{ph} as a function of the angle between the normal to the sample surface and the direction to the sensitive area of the Ge photodetector [18].

The value η_{ext} was calculated as the ratio of the number of quanta (N_{w}) emitted by the LED per unit time ($N_{\text{w}} = W/h\nu_{\text{m}}$, where $h\nu_{\text{m}}$ is the quantum energy at the maximum of their energy distribution) to the number (N_{inj}) of minority carriers injected into the LED base per unit time ($N_{\text{inj}} = Y/q$, where Y is the forward current and q is the elementary charge). To determine the values of η_{ext} at PL we used the procedure described above, with the only difference being that the number of PL photons emitting per unit time was normalized to the number of photons of laser radiation (N_{ing}) incident on the sample surface per unit time ($N_{\text{ing}} = P/h\nu_{\text{L}}$), where P is the quasi-steady-state laser radiation power and $h\nu_{\text{L}}$ is the photon energy of laser radiation).

During measurements of the emission intensity distribution over the LED area, the samples were placed in the field of view of a microscope. The diameter of the microscope field of view on the emitting surface was about 0.5 mm . The germanium photodiode was placed in front of the eyepiece of the microscope.

When measuring the laser-induced free carrier absorption, the sample was illuminated from the front side by an incandescent lamp. On the opposite side of laser beam incidence, a germanium photodiode was placed, whose photodetecting area was covered by a thin ($\sim 0.5 \text{ mm}$) polished wafer of single-crystal germanium. Thus, the laser-induced free carrier absorption at wavelengths of the fundamental absorption edge of Ge was experimentally studied. The free carrier absorbance was determined by changes in the photodiode current during the laser irradiation pulses.

Analysis of the literature has shown that the c-Si LED with the highest efficiency and power was earlier described in [2]. This diode had a large emitting area of

$\sim 4 \text{ cm}^2$ (in fact, a forward-biased high-efficiency solar cell was used). At the highest currents studied in [2] ($\sim 0.2 \text{ A}$), the diode provided, according to our estimates, up to $\sim 1.8 \text{ mW}$ of power (W) emitted by the entire surface area of the diode and, accordingly, up to $\sim 0.45 \text{ mW/cm}^2$ of average emitted power per unit area (P_0). In the present study, c-Si LEDs fabricated using the technology described in [2] were examined, but measurements were performed up to currents at which the decrease in the minority carrier lifetime, caused by Auger recombination, becomes important. Making the area of the structures smaller by cutting a larger area solar cell enabled a significant increase in P_0 and brought the emitting area closer to that typical of commercial LEDs of other types, whose emission can be readily focused (in contrast to that of large solar cells) on an illuminated object of a comparatively small-size photodetector area. Because of the increase in the working current, W could be substantially raised. In the present study the LEDs were produced from a silicon solar cell of dimensions $3.5 \times 6 \text{ cm}^2$ fabricated on a single-crystal p-Si ($\sim 1 \Omega \text{ cm}$) wafer. Its design and fabrication technology, described in [2], provided a combination of a low density of nonradiative recombination centers, low areas of n^+ and p^+ contacts, and special surface texturing for a considerable increase in the ratio between the external and internal quantum efficiencies of EL and PL [2]. In addition to the texturing and an antireflection coating, the face surface of the Si wafer contained thin heavily doped n^+ strips formed with a step of about 1 mm in parallel to the smaller side of the solar cell. From above, these bands were metallized and interconnected by a metallic busbar at the wafer edge. The Si LEDs studied were fabricated by cutting a solar cell. Most of the measurements were performed on three rectangular structures with faces parallel or perpendicular to the long sides of metallized n^+ -layers. The structure with area $S_1 = 0.9 \times 0.95 = 0.85 \text{ cm}^2$ (sample S_1) contained nine 9-mm-long metallized strips of n^+ -p junctions which were not interconnected by a metallic busbar, in contrast to the structure described in [2]. The structure with area $S_2 = 0.4 \times 0.25 = 0.1 \text{ cm}^2$ (sample S_2) corresponded in design to that shown in Fig. 2.1 of [2] and contained two metallized strips of n^+ -p junctions connected by a metallic busbar. The area of the emitting (unmetallized) surface of this LED was $s = 0.055 \text{ cm}^2$. We also have studied an LED structure of rectangular shape with an area of $S_3 = 12 \text{ cm}^2$ (sample S_3) and the edges parallel and perpendicular to the long sides of metallized (3 cm long) n^+ -p junctions not connected by a metal busbar. The use of such a long n^+ -p junction allowed us to minimize the influence of nonradiative recombination centers formed along the cuts. In order to exclude the effect of such centers present near the lines of cutting parallel to the metallized n^+ -bands, the measurement was performed on the n^+ -p junctions spaced more than 1.5 cm from these lines.

PL together with free carrier absorption was studied using a non-textured n-Si wafer 0.35 mm thick thermally oxidized in dry oxygen ($20 \Omega \text{ cm}$), oriented in the (100) plane. Thermal oxidation passivated the silicon surface to prevent significant surface recombination.

In a number of experiments for studies of the edge luminescence laws industrial c-Si diodes in which the part of the case has been removed for a lead-out of radiation from edge area of diode have been used.

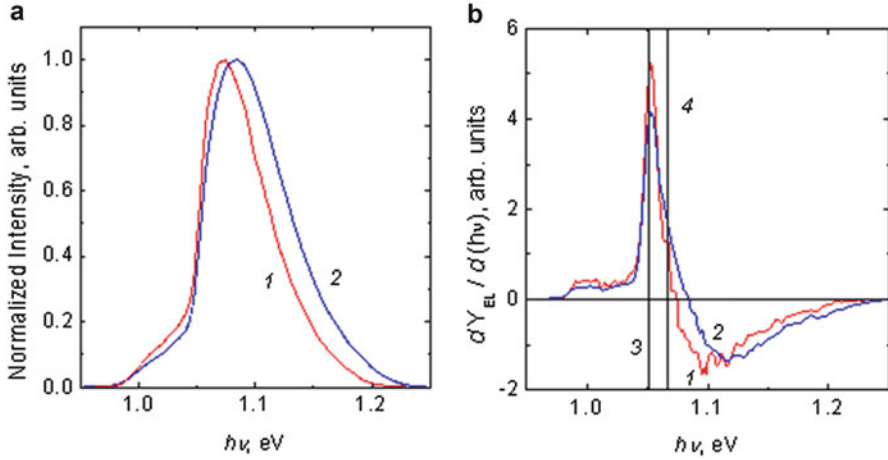


Fig. 2.1 Normalized spectra of the edge luminescence (a) and spectra for their derivatives (b) of c-Si at room temperature (294 K) for the diodes with surface texturing (curve 1) and without it (curve 2). The vertical straight lines 3 and 4 indicate the photon energies which correspond to the absorption edge at 294 K involving single-TO phonons and with free exciton generation (3) and absorption edge involving single-TO phonons and with free carrier generation (4)

3 The Spectrum and Basic Laws of the Edge Luminescence in the Single-Crystal Silicon

Measured at relatively small currents (not causing heating of diodes) the normalized spectra of the edge luminescence of c-Si at room temperature (294 K) for the diodes with surface texturing by technology [2] (curve 1) and without surface texturing (curve 2) are submitted in Fig. 2.1a. A distinction of the curve 1 and the curve 2 is connected to various conditions of radiation exit. The basic edge luminescence peak of c-Si is commonly interpreted as being due to radiative recombination with emission of solitary transverse optical (TO) phonons. In addition, it is believed that a relatively minor contribution to the spectrum is made by radiative transitions with absorption of phonons, participation of two or larger number of TO phonons in recombination events, and participation of other phonons. In this work, we use the results of [23] as reference data. In [23] the band gap c-Si ($E_g = 1.1242$ eV at 300 K) as well as the temperature dependence of E_g were determined from the experimental absorption spectra of c-Si. The TO phonon energy emitted in the recombination event ($E_{ph} = 57.3$ meV for the basic peak) and the binding energy of free excitons ($E_{ex} = 14.7$ meV) were taken from [23] too.

In the work [17] the differential method of the analysis of spectra of the edge luminescence of semiconductors has been offered. It has allowed to show most evidently that the prevailing mechanism of edge radiative recombination in Si single crystals in a wide temperature region, including room temperature, is

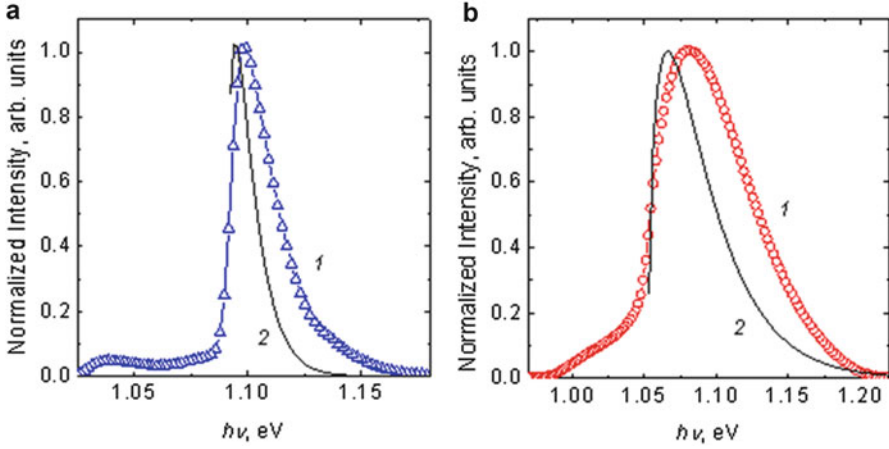


Fig. 2.2 The experimental edge EL spectra of c-Si (1) and the Maxwell distributions (2) with peaks at the absorption edges corresponding to the formation of free excitons and solitary TO phonons at $T = 80$ K (a) and $T = 300$ K (b) [17]

annihilation of free excitons. For the first time this conclusion has been made by the author of the present work in [15] and then confirmed by the experiments published in [16]. Figure 2.1b shows the spectra for the derivatives of the curves 1 and 2 from Fig. 2.1a. The vertical straight lines 3 and 4 indicate the photon energies which, according to the fundamental absorption measurements for c-Si [23], correspond to the absorption edge at 294 K involving single-TO phonons and with free exciton generation (2.3) and absorption edge involving single-TO phonons and with free carrier generation (2.4). According to the technique for analyzing the derivatives of the edge luminescence spectra, described below, the main spectral maxima observed are caused by the radiative recombination of free excitons in silicon involving TO phonons. Note that the dominant role of the radiative recombination in c-Si via free excitons near the temperature of liquid nitrogen is well known and needs no proof.

If edge radiative recombination is due to the annihilation of free excitons, the shape of the spectral curve is bound to be defined by the Maxwell distribution of the number of excitons n_{ex} with the kinetic energy E :

$$n_{\text{ex}}(E) = AE^{0.5}\exp(-E/kT). \quad (2.4)$$

Here, A is a coefficient independent of E , T is temperature, and k is the Boltzmann constant. The expression of the derivative dn_{ex}/dE , where n_{ex} is determined by (2.4), has a maximum at $E = 0$ (the derivative tends to infinity). Consequently, if the spectrum is described by formula (2.4), we can determine the photon energy corresponding to $E = 0$ from the position of the maximum of the derivative in (2.4). The experimental edge luminescence spectra of c-Si cannot be described by formula (2.4), at least at $T = 80\text{--}300$ K (see Fig. 2.2).

This may be caused by several factors, specifically (1) the self-absorption of emission in the short-wavelength region and (2) the superposition of some other peaks. In addition, as can be seen from (2.2), this can be attributed to the dependence of the radiative lifetime of excitons (τ_{ex}) on their kinetic energy. From (2.2), it is evident that the function $R(E)$ is similar to $n_{\text{ex}}(E)$ only if $\tau_{\text{ex}} = \text{const}$. However, the last mentioned condition seems to be rather improbable, since for the radiative recombination event to occur in indirect-gap semiconductors in certain conditions, it is necessary that the exciton should interact with a phonon (or an impurity atom, as in the case of the SiGe alloy). However, the probability of satisfying these conditions is bound to depend on the exciton kinetic energy. To date, the dependence $\tau_{\text{ex}}(E)$ practically has not been studied. Therefore, whether or not the position of the maximum of the derivative of the $R(E) = n_{\text{ex}}(E)/\tau_{\text{ex}}(E)$ spectral curve coincides with the photon energy corresponding to $E = 0$ can be judged only from comparison of the experimental position of this maximum with the experimentally determined absorption edge for free excitons. This is what is done in this study. In accordance with (2.2), the derivative dR/dE is described by the expression

$$dR/dE = (dn_{\text{ex}}/dE)/\tau_{\text{ex}} - n_{\text{ex}}(d\tau_{\text{ex}}/dE)/\tau_{\text{ex}}^2. \quad (2.5)$$

As follows from the analysis of formula (2.5), the position of the maximum of dR/dE can be inconsistent with $E = 0$ if $\tau_{\text{ex}}(E = 0)$ is infinitely large. Infinitely large $\tau_{\text{ex}}(E = 0)$ would mean that the radiative annihilation of excitons with $E = 0$ is practically impossible. To date, this effect has not been theoretically understood. It can lead to shift of the maximum of the derivative in the direction of high photon's energy. The absence of such significant shift under different conditions of the emission output of the samples (Fig. 2.1b) indicates that at using of the differential method of analysis of the luminescence spectra this effect can usually be ignored. Such coincidence of the positions of the maximums of the derivative with the absorption edge defined by free excitons and the lack of pronounced maximums near the intersections of curves 1 and 2 with straight lines 4 on Fig. 2.1b support the conclusion [15] that the prevailing mechanism of radiative recombination in c-Si at room temperature is the phonon-assisted radiative annihilation of free excitons. The above model notions require that τ_{ex} would be smaller by more than two orders of magnitude than the radiative lifetime of free charge carriers (τ_f). Such a considerable difference between τ_{ex} and τ_f can be related to the fact that the average distance between free carriers in the experiments was more than Bohr radius of exciton ($r_B = 4.2$ nm). In addition, radiative recombination in c-Si requires a certain correlation in the mutual arrangement of electron, hole, and phonon, which is most probably realized in the case of recombination via excitons.

The authors of [24–26] drew a similar conclusion for the prevailing mechanism of edge radiative recombination in SiGe alloys. Previously, the conclusion that the prevailing mechanism of edge luminescence at room temperature is annihilation of free excitons was drawn in a study of the luminescence spectra of another semiconductor, GaP [27]. In [28], it was proved that, at room temperature, radiative recombination in the region of the fundamental absorption edge of silicon carbide

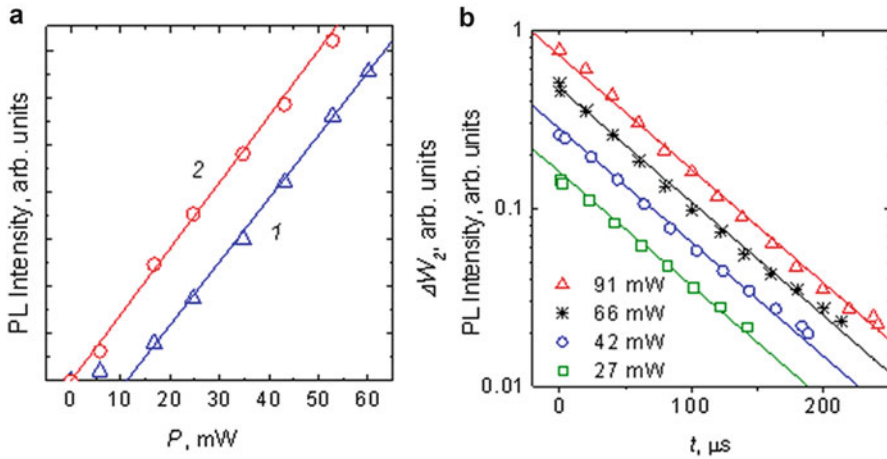


Fig. 2.3 (a) Dependences of the total intensity of the edge PL (I) and radiation absorption in the sample by free carriers ΔW_2 on the laser radiation power P incident on the sample (2) [21]. (b) Measured at different P the kinetics of the PL intensity decay in the linear region of the dependence of the PL intensity on P

occurs via annihilation of free excitons. All semiconductors explored in the abovementioned studies are indirect-gap materials with binding energies of free excitons ~ 6 meV and higher. From the aforesaid studies, we can infer that, in the region of the fundamental absorption edge of all indirect-gap semiconductors with no defect-related luminescence, radiative recombination via the annihilation of free excitons prevails in a wide temperature range, including room temperature (in spite of the relatively low concentration of excitons, as compared to the concentration of free charge carriers at room temperature).

In the work [21] the edge PL intensity and the change of absorption by free charge carriers, depending on the power (P) of the laser radiation causing these effects, were measured in the same place of the thermally oxidized c-Si. Figure 2.3a (data 1) shows the dependence of the structure's edge PL intensity on the laser radiation power incident on the sample. We can see the almost linear dependence of the edge PL intensity on P but only after the initial superlinear region. The kinetics of the order of magnitude decay of the PL in the linear region of the dependence of the PL intensity on P was approximated by an exponential function with a time constant, which was almost independent of P (Fig. 2.3b).

In [21] the dependences of the number of laser-induced free minority carriers on P were studied. To this end, the absorbance of infrared radiation from the silicon conduction band by free carriers was measured. The data of such measurements were processed using the theory published in [29] and improved by the author, taking into account features of the present experiments. The radiation power W_0 incident on the sample from the region of the fundamental absorption edge of germanium is related to the power W_1 passed through the wafer as

$$W_1 = W_0(1 - R_1)(1 - R_2)\exp(-kL) [1 + R_2^2\exp(-2kL)], \quad (2.6)$$

where R_1 is the reflectance from the outer sample surface, R_2 is the reflectance of radiation incident on the silicon surface from the inside, L is the silicon wafer thickness, and k is the effective absorbing coefficient by free carriers. Expanding the exponential functions in expression (2.2) in series, taking into account the smallness of kL (<0.005 according to estimations), we obtain

$$\begin{aligned} W_0 - W_1 &= W_0[1 - (1 - R_1)(1 - R_2)(1 - kL)][1 + R_2^2 - kL2R_2^2] \\ &= \Delta W_1 + \Delta W_2(kL) = \Delta W_1 + W_0(1 - R_1)(1 - R_2)(1 + 3R_2^2)kL. \end{aligned} \quad (2.7)$$

According to the above conditions for measuring the free carrier absorbance, the quantity ΔW_2 caused by free carrier generation is proportional to the Ge photodiode photocurrent pulse amplitude measured using an oscilloscope under pulsed laser exposure. As can be seen from (2.7), the quantity ΔW_2 is also proportional to kL . The results of experimental studies are shown in Fig. 2.3a (dependence 2). The quantity ΔW_2 caused by free carrier generation almost linearly depended on P in the whole studied P range. The theoretical expression for kL considering the nonuniform distribution of free carriers over the silicon wafer thickness is given by [29]

$$kL = \int_0^L \alpha(x) dx, \quad (2.8)$$

where α is the absorbing coefficient of free carriers and x is the distance from the irradiated Si surface. The value of α is determined by the formula [29]

$$\alpha(x) = \sigma_{n+p} \Delta p(x), \quad (2.9)$$

where $\Delta p(x)$ is the change in the hole concentration due to laser irradiation, σ_{n+p} is the total cross section of electron and hole absorption at the probe light wavelength, and $\sigma_{n+p} = 2 \times 10^{-17} \text{ cm}^2$ for the spectral composition of the light (1.8–2.5 μm) used in [28], which is close to that in the Ge fundamental absorption edge region used in this study. The kinetic measurements of the carrier lifetime in the sample under study allowed us to determine the carrier diffusion length (L_p) which was approximately equal to the silicon wafer thickness. In view of this fact and the circumstance that the penetration depth of a major fraction of the used laser beam radiation into silicon did not exceed 1 % of this value, we calculated $\Delta p(x)$ using the formula [30] describing the carrier distribution over the thickness of the thin diode base with a blocking contact to the base:

$$\Delta p(x) = \Delta p_1 \cosh[(x - L)/L_p] / \cosh(L/L_p), \quad (2.10)$$

where Δp_1 is the concentration of free holes (generated by the laser beam in this study) near the silicon surface, where $x = 0$. Substituting (2.10) and (2.9) by (2.8), we obtain

$$kL = \sigma_{n+p} \Delta p_1 L_p \tanh(L/L_p). \quad (2.11)$$

According to [30], Δp_1 can be determined by the formula

$$\Delta p_1 = \beta PL_p/D_p, \quad (2.12)$$

where β is the coefficient independent of L_p and D_p is the hole diffusion coefficient. Then, substituting (2.12) by (2.11), taking into account $L_p = (\tau_p D_p)^{0.5}$, we obtain

$$kL = \sigma_{n+p} \beta P \tau_p \tanh\left[L/(D_p \tau_p)^{0.5}\right]. \quad (2.13)$$

Thus, if ΔW_2 (and, according to (2.7), kL) depends linearly on P , the linear behavior of recombination follows from (2.13), at which the hole lifetime τ_p is independent of P . The linear behavior of recombination is also independently confirmed by measurements of the PL decay kinetics in the linear portion of curve *I* in Fig. 2.3a. Since the time of reaching the equilibrium exciton concentration is significantly smaller than τ_p , the independence of the order of magnitude decay time constant for the PL intensity of P means also the τ_p independence of P . In the case of the linear behavior of recombination, it follows from (2.10), (2.12), and

$$P = \gamma \int_0^L \Delta p(x) dx / \tau_p \quad (2.14)$$

(where γ is a factor) that $\Delta p(x)$ are proportional to P . At the same time, it follows from the above that $n_{\text{ex}}(x)$ are also proportional to P . Indeed, at the same n_{ex} , the edge PL power entering the photodetecting area from the unit volume depends on the distance between the emitting volume and the sample surface. This is due to edge PL self-absorption in silicon. The unchanged shape of the normalized PL spectrum as P varies in the linear portion of curve means that a change in the distribution function of free excitons with P is reduced to only a proportional change in $n_{\text{ex}}(x)$ for all distances from the sample surface. Accordingly, $n_{\text{ex}}(x)$ are proportional to $\Delta p(x)$. Figure 2.4 shows the results of studies at room temperature the edge EL of the industrial diode with area of $\sim 3 \text{ mm}^2$ and a donor impurity concentration in the base $\sim 10^{14} \text{ cm}^{-2}$. We can see the almost linear dependence of the edge EL intensity on current after the initial superlinear region. According to Fig. 2.4b on the linear portion of the dependence the lifetime of the charge carriers is independent of the intensity of the luminescence excitation (current value). At sufficiently high currents after the linear region sublinear region, in which

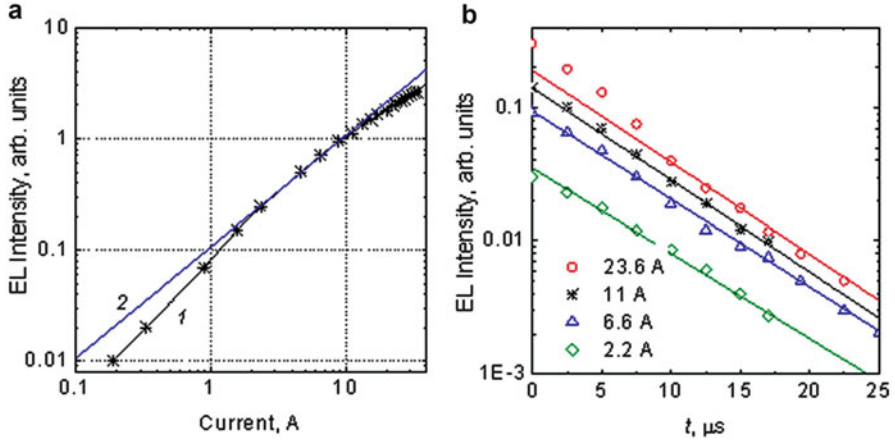


Fig. 2.4 The dependences of EL intensity of the c-Si LED on the forward current (a) and at different currents on the time after the current was cut off (b). *Straight line 2* in (a)—approximation of section of the experimental curve *1* by linear fit

there is a more rapid initial intensity decay kinetics of EL, is observed. This may be due to the fact that at such currents in addition to Shockley–Read–Hall recombination Auger recombination begins to have a significant influence.

It is well known that for low injection levels, when the concentration of minority carriers injected from the p–n junction or generated by radiation is significantly lower than the dopant concentration, explanation of the linear regions within the existing theoretical concepts does not present difficulties. But according to the author's estimations, the close-to-linear dependence of the PL intensity on P and EL intensity on current (accordingly, n_{ex} on $\Delta p(x)$) in the samples under study began at average hole concentrations of $\sim(1-2) \times 10^{16} \text{ cm}^{-3}$. Because the specific resistance of thermally oxidized n-Si wafer was $20 \Omega \text{ cm}$ and donor impurity concentration in the LED's base $\sim 10^{14} \text{ cm}^{-2}$, at such concentrations conditions of high injection levels (when the concentration of minority carriers is significantly higher than the dopant concentration) took place. The above results showed that the linear or the close-to-linear portions of the dependences of the edge luminescence intensity of c-Si on the luminescence excitation intensity under conditions of high injection levels are caused by radiative recombination predominantly via free excitons and by the existence of linear or close-to-linear portions of the dependences of the free exciton concentration on free carrier concentration at the sufficiently high free carrier concentrations. The results presented show that at sufficiently high concentrations of free charge carriers (for example, greater than $\sim(1-2) \times 10^{16} \text{ cm}^{-3}$), (2.1) cannot be used to describe the rate of radiative recombination in c-Si. According to the experiments in this case the dependence of the rate of radiative recombination on the concentration of free electrons or holes should be described by a linear function and does not depend on the concentration of free charge carriers of opposite sign. Note also that as calculated in [13]

dependence of B on the concentration of free charge carriers does not explain the linear sections of the dependences of the EL and PL intensity on the excitation intensity, as it is not sufficiently strong. Similarly, the effect of screening taking into account that in [14] is not sufficiently strong to explain the experimental results. The presented results of researches allow to expand opportunities of luminescent methods of definition of c-Si parameters (for example, τ and L_D) on the area of high levels of injection and high intensities of the luminescence excitation. Earlier it was impossible due to the lack of the adequate description of the dependence of the radiative recombination rate R on the concentrations of free charge carriers for considered area of free charge carrier concentrations.

4 Near-Band-Edge Electroluminescence in Silicon Light-Emitting Structures Fabricated Using High-Efficiency Solar Cell Technology

Figure 2.5 shows EL spectrums of the diode S_2 , measured at room temperature (a) and 80 K (b), at different forward currents and normalized to the maximum intensity. At room temperature up to currents ~ 6.5 A, changes in the spectrum upon an increase in the current are insignificant. An analysis of the long-wavelength part of the EL spectrum at the currents not more than 6.5 A demonstrated the predominance of the TO phonon-assisted radiative recombination of free excitons. The distortion of the spectrum at the current of 10 A is possibly due to heating of the sample by the flowing current. In addition, the mechanism of radiative recombination can change at sufficiently high free carrier concentrations: the radiative recombination of an electron-hole plasma may become important.

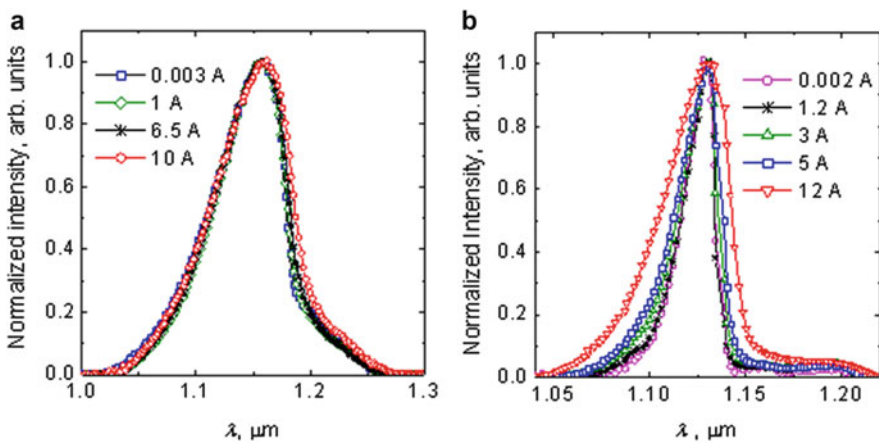


Fig. 2.5 EL spectrums of the diode with area S_2 , measured at different forward currents at room temperature [18] (a) and 80 K [22] (b)

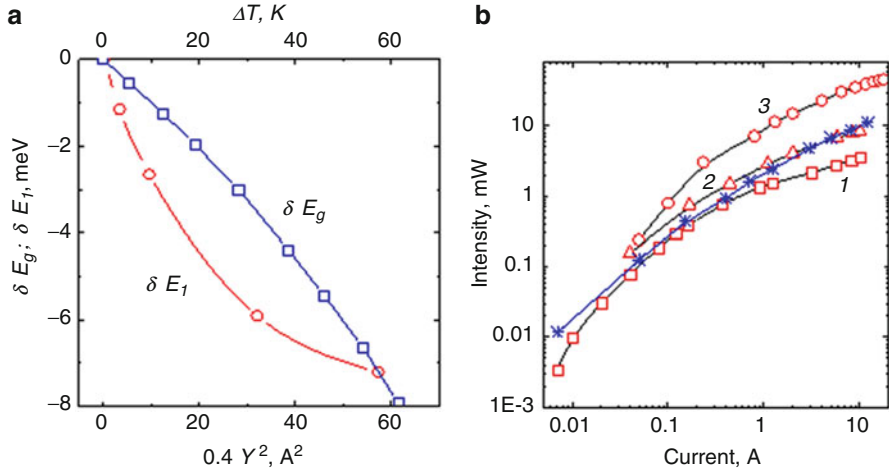


Fig. 2.6 (a) Difference (δE_1) between the photon energy corresponding to half the maximum of the normalized EL intensity on the long-wavelength side of the peak and the value of this photon energy at a current of 0.002 A as a function of the square of current (Y^2) and the dependence of the change (δE_g) in the band gap width of c-Si on the increase (ΔT) in temperature relative to 80 K (data from [23]). (b) Current dependence of the integrated LED edge EL power measured at 300 K (1–3) and 80 K (4). 1,4—to sample S_2 , 2—to sample S_1 , 3—to sample S_3 (data from [18, 19, 22])

At 80 K the position of the maximum of the wavelength distribution (λ_{\max}) is almost the same over the entire range of currents studied. The half-width of the spectra also remains almost unchanged for currents $Y \leq 1.2$ A. At currents exceeding 1.2 A, the spectra are significantly broadened and, accordingly, the area under the spectral curves (S_{sp}) increases. At a current of 12 A, the area under the spectral curve in Fig. 2.5b is approximately twofold greater than that at currents smaller than 1.2 A. The wavelength $\lambda_{\max} = 1.13 \mu\text{m}$ and the spectral half-width 0.018–0.020 μm (at currents smaller than 1.2 A) coincide (to within experimental error) with the respective quantities measured earlier for Si LEDs without a surface texture. Such EL peaks are usually interpreted as being due to radiative recombination of free excitons in c-Si with the formation of a single-TO phonon. In addition, the EL spectrum contains relatively small contributions from radiative transitions of excitons with absorption of a phonon and with involvement of two or more TO phonons and other phonons. At currents exceeding 1.2 A, the EL spectra are observed to broaden to both longer and shorter wavelengths and the broadening increases with current. Figure 2.6a shows the difference (δE_1) between the photon energy corresponding to half the maximum of the normalized EL intensity on the long-wavelength side of the peak and the value of this photon energy at a current of 0.002 A as a function of the square of current (Y^2). The difference δE_1 increases with the square of current following a sublinear law. The reason why the quantity δE_1 is plotted as a function of the square of current will become apparent later on. We have shown that the broadening of the EL spectra of the high-efficiency c-Si

LED studied is caused by the change of the EL mechanism rather than by the heating effect of the current passing through the LED. Indeed, the contribution of heating to the spectrum broadening can be revealed by analyzing the c-Si EL spectra at different temperatures (see, e.g., [2]). As the temperature of c-Si LEDs increases above 80 K, the EL spectra are usually broadened to both shorter and longer wavelengths. The broadening to longer wavelengths is usually due to a decrease in the band gap width (E_g) of silicon. According to [22], the change in E_g (Fig. 2.6a) and the change in the photon energy corresponding to half the maximum of the normalized EL intensity on the long-wavelength side of the peak (at least in the range 80–200 K) exhibit a superlinear dependence on the increase in temperature relative to 80 K (Fig. 2.6a). However, according to theoretical estimates [31], the current dependence of the difference between the temperature of an LED attached to a cold finger and the temperature of the cold finger follows a square law. Therefore, the sublinear dependence of δE_1 on the square of current and, hence, on temperature (Fig. 2.6a) is inconsistent with the assumption that the broadening of the EL spectra is due to the heating effect of the current passing through the LED. This assumption is also inconsistent with the small duration of current pulses, the large pulse period-to-pulse duration ratio, and good heat-removing conditions.

It was shown in [22] that the mechanism of radiative recombination can change at sufficiently high free carrier and exciton concentrations: the radiative recombination of an electron–hole plasma may become important. Figure 2.6b shows the integrated radiation power (over the entire spectral range studied) emitted by an LED at 300 and 80 K into a hemisphere as a function of current. The initial small nonlinear segments are seen to be followed by an almost linear dependence, which, in turn, is followed by long sublinear segments. At 80 K and a maximum current of 12 A, the LED radiation power $W = 11$ mW. This value corresponds to a record area-averaged radiation power per unit surface area $P_0 = 0.2$ W/cm² for c-Si LEDs (edge luminescence and other types of luminescence), which is more than threefold greater than the value of P_0 obtained for the same LED at 300 K at a pulsed current of 10 A [2]. At the same current (10 A), the value of P_0 at 80 K is also almost threefold greater than that at 300 K. Pumped by a pulsed current of 18 A, the LED S_3 (see graph 4 in Fig. 2.6b) showed a record high power of the near-band-edge electroluminescence at room temperature (~46 mW).

The current dependences of the external EL quantum efficiency that measured the samples at 80 and 300 K are presented in Fig. 2.7a. These curves are seen to exhibit a maximum. The reasons why the efficiency η_{ext} decreases with increasing current at 300 K were analyzed in [18]. It was shown in [18] that the decrease in η_{ext} with an increase in current is mainly due to the occurrence of Auger recombination, which is added to nonradiative recombination by the Shockley–Read–Hall mechanism operating at smaller currents as well. This assumption is confirmed by data on the kinetics of EL decay at various currents, which are presented in Figs. 2.7b and 2.8. For the maximum η_{ext} the EL intensity decay by an order of magnitude is well described by an exponent with a characteristic decay time (τ_d) (maximum of 380 μ s for sample S_3 , Fig. 2.8b, curve). On the descending parts of the η_{ext} curves, the EL

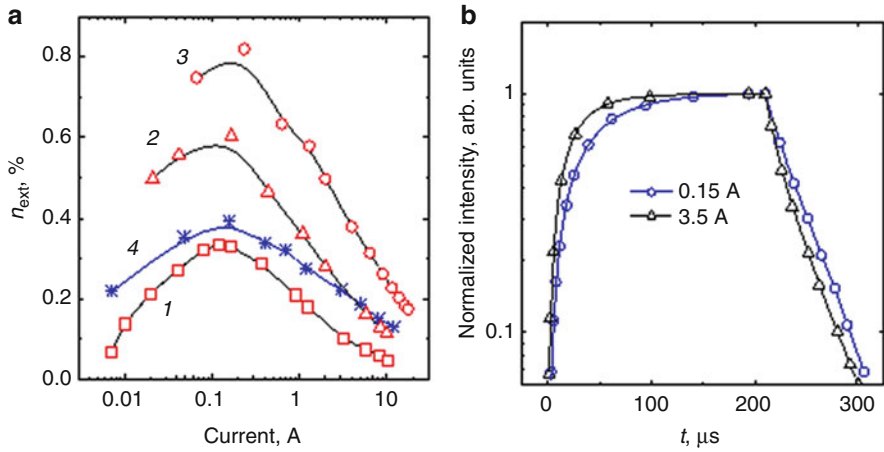


Fig. 2.7 (a) Current dependences of the LED external quantum efficiency measured at 300 K (1–3) and 80 K (4). 1,4—to sample S_2 , 2—to sample S_1 , 3—to sample S_3 . (b) LED EL kinetics at 80 K for two different values of the current (to sample S_2) [22]

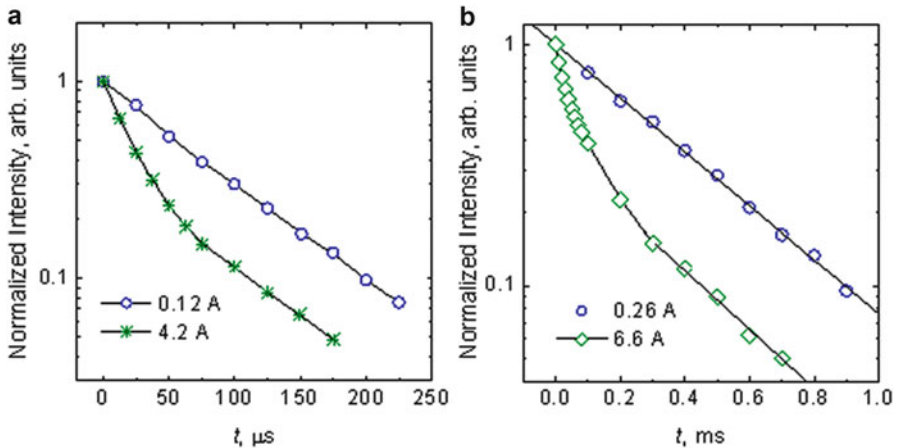


Fig. 2.8 LED EL kinetics at 300 K for two different values of the current: (a) to sample S_1 [18], (b) to sample S_3 [19]

intensity decay kinetics is described by an exponent with the same τ_d only after the initial, more rapid decay (Figs. 2.7b and 2.8, curves 2), that is, after a decrease in the carrier density to a level where the Auger recombination becomes insignificant. Another reason (apart from Auger recombination) for the observed behavior of η_{ext} with increasing current at 80 K is the significant broadening of the EL spectra, as seen from Fig. 2.5b. As can be seen from Figs. 2.6b and 2.7a, the area of the sample by means of its cutting decreases significantly radiating power and the external EL quantum efficiency of the LEDs. This may be connected with formation of the

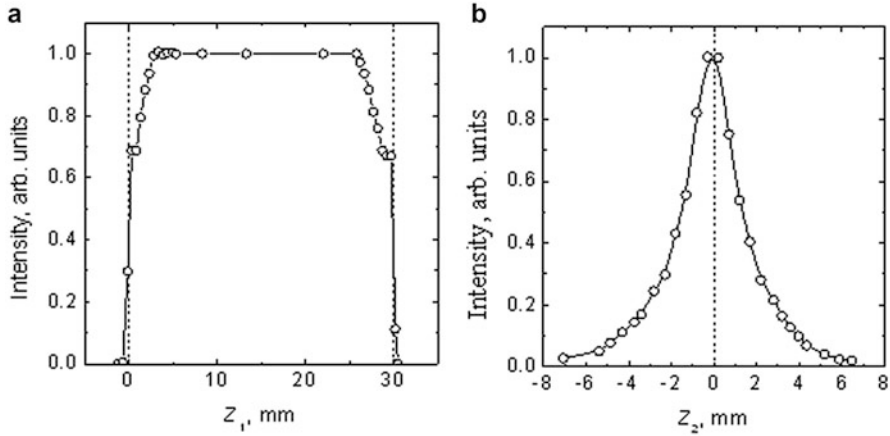


Fig. 2.9 Normalized distribution of the near-band-edge EL relative to the axis along (a) and perpendicular (in the *center*) (b) to the long side of the $n^+ - p$ junction [19]

centers of nonradiative recombination near the lines of cutting. The influence of the nonradiative recombination near the lines of cutting appears in EL intensity decay near the lines of cutting (see Fig. 2.9a). EL intensity decay perpendicular to p-n junction in Fig. 2.9b is determined by diffusion length of minority charge carriers and by lateral extension of radiation in the sample.

5 The Edge Photoluminescence and Nonradiative Recombination in Single-Crystal Silicon with a p-n Junction: Structures Produced by High-Efficiency Solar Cell Technology

The studies of the edge PL were made at room temperature for the structure of the design which corresponded to that shown in Fig. 2.1 in [2]. The nonmetallized surface area of the structure was $S_4 = 0.3 \times 0.4 = 0.12 \text{ cm}^2$. Laser radiation was focused on the center of the sample to form a spot of diameter $d = 1 \text{ mm}$. Figure 2.10a illustrates the kinetics of the edge PL at different laser radiation powers P at the laser wavelength $\lambda = 658 \text{ nm}$. The experimental points corresponding to the rise in the PL intensity with time (t) well fit the dependence

$$Y_{\text{PL}} = Y_{\text{PL max}}[1 - \exp(-t/\tau_r)], \quad (2.15)$$

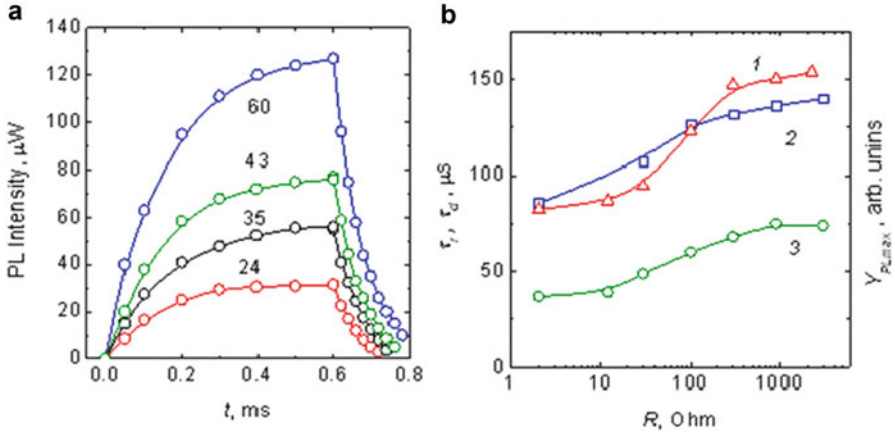


Fig. 2.10 (a) The kinetics of PL at zero external voltage and at different laser radiation powers (expressed in mW and indicated near curves). (b) Dependences of the quasi-steady-state PL intensity $Y_{\text{PL,max}}$ and the PL rise and decay time constants τ_r and τ_d on the bypass resistance R ($P = 60$ mW) [20]

where τ_r is the rise time constant and $Y_{\text{PL,max}}$ is the quasi-steady-state PL intensity. The portions of experimental curves corresponding to the PL decay can be described by the expression

$$Y_{\text{PL}} = Y_{\text{PL,max}} \exp(-t/\tau_d), \quad (2.16)$$

where τ_d is the decay time constant. In Fig. 2.10a, the quantities τ_r and τ_d differ widely in magnitude. The value of τ_r is practically independent of P and corresponds to ~ 140 μs . In the range of laser radiation powers used in the study, the value of τ_d increases with P from ~ 60 to ~ 75 μs . According to formula (2.15), the value of τ_r corresponds to the time ($\tau_{0.63}$), in which the increasing PL intensity reaches approximately a 0.63 fraction of the maximum intensity [32]. A considerable excess $\tau_{0.63}$ of over τ_d has been already observed in the previous studies of edge EL in Si-based LEDs [33]. However, in [33], this difference was attributed mainly to the time delay of establishment of the quasi-steady-state current. Such an interpretation is inapplicable to the results of this study, since the quasi-steady-state laser radiation intensity is achieved here in a time shorter than 3 μs . In order to gain an insight into the causes of the large difference between τ_r and τ_d , we carried out experiments in which forward and back DC voltages were applied across the structure simultaneously exposed to pulsed laser radiation. Modulation of the quasi-steady-state edge PL intensity in such a structure under variations in the voltage across the p-n junction was first demonstrated elsewhere [34]. Upon application of voltages, the p-n junction of the structure is bypassed to a certain extent by the internal resistance of the voltage source. For this reason, we initially studied the effect of the bypassing resistance (R) on the parameters of PL of the structure.

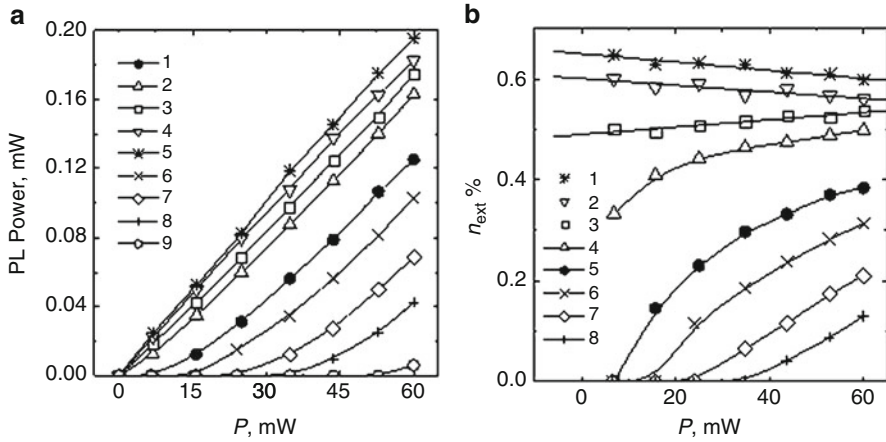


Fig. 2.11 (a) Plots of PL pulse power versus exciting laser radiation power P at $\lambda = 658$ nm for various direct currents: 0 (1), 6 (2), 9.3 (3), 16 (4), and 22.6 mA (5) and reverse-bias voltages: 0 (1), 4.2 (6), 9.3 (7), 12.8 (8), and 17.6 V (9) [34]. (b) Plots of the external quantum efficiency η_{ext} versus exciting laser radiation power P for various direct currents: 22.6 (1), 16 (2), 9.3 (3), 6 (4), and 0 mA (5) and reverse-bias voltages: 0 (5), 4.2 (6), 9.3 (7), and 12.8 V (8) [34]

Figure 2.10b shows the dependences of the PL intensity and the quantities τ_r and τ_d on R at $P = 60$ mW. From Fig. 2.10b, it can be seen that, as R is decreased to values smaller than 1 k Ω , the PL intensity $Y_{\text{PL max}}$ and the time constants τ_r and τ_d drastically decrease. Therefore, in all of the experiments described below, the internal resistance of the voltage source was chosen in the range 1.2–1.4 k Ω . Connection of such resistance only negligibly changed the PL intensity.

Figure 2.11a (curve 1) shows the dependence of the quasi-steady-state edge PL peak intensity on P at zero external voltage and $\lambda = 658$ nm. In these conditions, the quasi-steady-state PL external quantum efficiency steadily increases with P , starting from some threshold value of P and tending to saturate at $\eta_{\text{ext}} = 0.4$ % (the dependences $\eta_{\text{ext}}(P)$ at different forward currents and back voltages are shown in Fig. 2.11b). In curve 1 in Fig. 2.11a, we can distinguish three portions. In the first portion, no PL signal was detected at the achieved sensitivity level of the recording system. Starting from some threshold value of P , the PL intensity $Y_{\text{PL max}}$ first increases superlinearly with P and then approaches a practically linear dependence. Estimations show that, for the structure and the experimental system used here, the quasi-steady-state PL technique in the mode of measuring described in publications cannot be applied to the determination of the effective lifetimes at laser radiation densities lower than ~ 1 W cm 2 primarily because of the lack of the PL signal. Figure 2.11a shows also the dependences of the PL intensity on the laser radiation power P at four forward currents (curves 2–5). With increasing forward current, the threshold power P at which the PL signal becomes evident decreases and the dependences $Y_{\text{PL max}}(P)$ become more and more closer to linear functions. Correspondingly, the quantum efficiency η_{ext} increases (see Fig. 2.1b). At the current

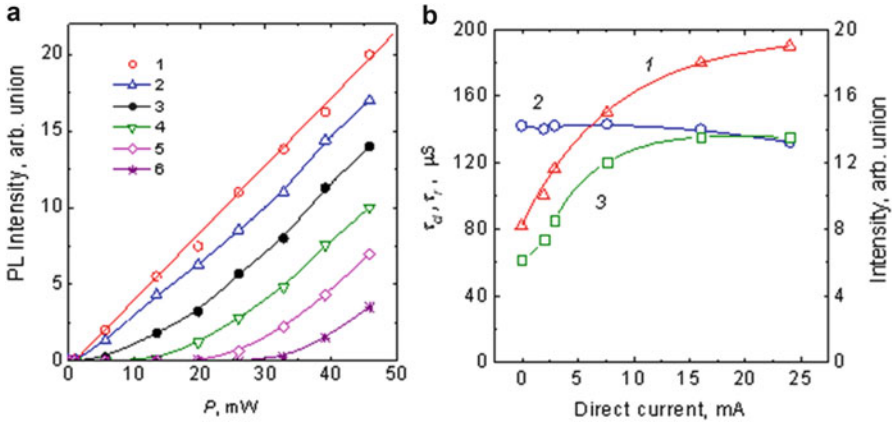


Fig. 2.12 (a) Dependences of the quasi-steady-state PL intensity on the laser radiation power at $\lambda = 0.98 \mu\text{m}$. Curves 1–6 refer to the dependences at (3) zero external voltage, (1, 2) the forward currents (2) 7.5 and (1) 24 mA, and (4, 5, 6) the reverse voltages (4) 7.5, (5) 14.5, and (6) 20 V [20]. (b) Dependences of the quasi-steady-state PL intensity (1) and the PL rise (2) and decay (3) time constants on the forward current for sample S_4 [20]

23 mA, η_{ext} is almost independent of P and corresponds to $\sim 0.6\%$. A DC reverse voltage applied to the sample decreases the PL intensity (see curves 6–9 in Fig. 2.11b) and, correspondingly, the quantum efficiency η_{ext} . In this case, the threshold power P behaves inversely: it increases, and the increase is more noticeable at higher reverse voltages. As the reverse DC voltage is increased, we observe a decrease in the PL decay time constant. Based on the results of studies of edge EL in c-Si [35], the author of [34] suggested that one of the possible causes of the effect of modulation of the edge PL, when excited by laser radiation at the wavelength $\lambda = 658 \text{ nm}$, under variations in the voltage across the p–n junction was a change in the width of the SCR. It was noted that this effect could be due to the fact that the excitation radiation intensity became e times lower in intensity at a small depth (about $2.5 \mu\text{m}$) comparable to the SCR penetration depth. To verify this assumption, we studied the effect of modulation of the edge PL power in c-Si by varying the voltage across the p–n junction on excitation of PL by laser radiation at $\lambda = 0.98 \mu\text{m}$. In c-Si, radiation at this wavelength is attenuated by a factor of e at a much larger depth (about $100 \mu\text{m}$). The results are shown in Fig. 2.12a. The results are qualitatively similar to those shown in Fig. 2.11a. Consequently, the penetration depth of laser radiation in the samples is of no principal significance for observation of the effect of modulation of edge PL.

Figure 2.12b shows the dependences of the quasi-steady-state PL intensity and the PL rise and decay time constants on the forward current for the sample exposed to laser radiation pulses ($P = 35 \text{ mW}$). From the results shown in Fig. 2.12b, it follows that the increase in the PL intensity correlates with the increase in the decay time constant τ_d . The time constant τ_d is larger at lower recombination rates of nonequilibrium charge carriers generated by laser radiation. Consequently, from

the results, it follows that the forward current slows down the recombination processes in the structure when responding to laser radiation pulses and, thus, increases the amplitude of PL pulses. It should be noted that, as the forward current is increased, the time constant τ_r changes only slightly; at rather large currents, the values of τ_d and τ_r practically coincide.

The effects observed at different forward currents can be understood in the first approximation, if it is assumed that there are two recombination channels in the structure. Moreover, it must be assumed that one of the channels is much less efficient than the other and the nonradiative recombination rate in the second, more efficient channel ceases to depend on the concentration of nonequilibrium charge carrier at sufficiently high concentrations. If these assumptions are accepted and the radiative recombination rate is negligible compared to the nonradiative recombination rate (because of the relatively low quantum efficiency of radiative recombination), the rate of changes in a number of nonequilibrium minority charge carriers generated by laser radiation (N) can be described in the first approximation by the expression

$$dN/dt = G - N/\tau - F. \quad (2.17)$$

Here, G is the rate of generation of minority charge carriers by laser radiation, N/τ is the rate of nonradiative recombination via the first mechanism (Shockley–Read–Hall mechanism), and F is the rate of nonradiative recombination of nonequilibrium charge carriers via the second mechanism. In the subthreshold conditions, the quantities G and N are small (because of the fast recombination of charge carriers mainly through the second channel), and, hence, the PL intensity is low. If the quantity G is sufficiently large and, therefore, the quantity F rapidly becomes practically constant, from formula (2.3) it follows that the time variations in N are described by the expression

$$N = N_{\max}[1 - \exp(-t/\tau)], \quad (2.18)$$

where N_{\max} is a maximum number of minority charge carriers at a specified generation rate G . If laser radiation is turned off ($G = 0$) and there is no forward current, there is no source of minority charge carriers to provide saturation of recombination via the second mechanism; then the rate F can depend on t , as can be seen from (2.17), and the decay time constant for the quantity N can be smaller than τ . However, if a rather large forward DC current passes through the sample, the second recombination channel for optically generated charge carriers is turned off by nonequilibrium charge carriers generated by the current passing through the p–n junction. In this case, from (2.3) it follows that the decay kinetics of minority charge carrier number generated by laser radiation is described by the expression

$$N = N_{\max}\exp(-t/\tau). \quad (2.19)$$

It should be noted that, in this case, the rise and decay time constants for N are practically identical and equal to τ , since the quantity F for optically generated charge carriers in formula (2.17) must be assumed to be zero also for the rise of the PL intensity. Upon application of a reverse voltage, the external field separates charge carriers, resulting in an acceleration of the kinetics of PL and in a decrease in the PL intensity. In the foregoing, we considered the kinetics of changes in the concentration of optically generated free minority charge carriers in the structure under study. However, as reported previously, radiative recombination in c-Si at room temperature occurs basically through the formation of free excitons and, correspondingly, the PL intensity depends on the concentration of excitons (N_{ex}) in accordance with the formula

$$Y_{\text{PL}} = C_1 N_{\text{ex}} / \tau_{\text{ex}}. \quad (2.20)$$

Here, C_1 is a constant. The problem of interconnection between the kinetics of free excitons and that of free charge carriers was discussed elsewhere [36]. It was shown that the description of the kinetics of annihilation of excitons led to a nonlinear second-order differential equation that has not yet been solved in the general case. On the assumptions accepted in [36], it was found that, in the case of radiative recombination via free excitons, the quantity τ_{d} was half the quantity τ . For the qualitative consideration presented here, it is important that the faster (or slower) the kinetics of N , the faster (or slower) the kinetics of N_{ex} . This conclusion can be drawn on the basis of the results of [36] as well as from the value of the time of binding of free charge carriers into excitons. The last-mentioned time is several orders of magnitude shorter than τ_{d} and τ_{r} . Therefore, at a qualitative level, the above analysis of the kinetics of N can be used to interpret the systematic features of the kinetics of N_{ex} and, hence, the kinetics of PL in different experimental conditions.

It was of importance here to understand to what extent these effects are inherent in high-efficiency Si solar cells described in [2]. The answer to this question can be obtained from comparison of the data presented above with the data reported in [37]. In [37], the quantum efficiency of a solar cell similar to that considered here reached the slightly varying level at EL excitation intensities of about 0.1 mW cm^{-2} . These intensities are several orders of magnitude lower than the PL excitation intensities observed for the structure studied here. Thus, the above-described effects as such and their manifestation in high-efficiency solar cells may be a consequence of specific features of the solar cell technology, variations in the manufacturing process, and cutting of elements to form separate parts; the last-mentioned procedure brings about the formation of new recombination centers. It is important to note that the basic objective laws of the second channel of nonradiative recombination of the edge PL described above are qualitatively similar to those obtained in studies of edge PL in sample S_3 at least 1 cm away from the cut line. This means that the described effect of the second channel of nonradiative recombination is not associated with edge effects arising from the cutting of the solar cells only. This chapter was written on the basis of published works. But it should be noted that very

important information relating to this chapter is contained in the article [38], which is being prepared for publication in 2014. It was shown in [38] that at sufficiently high concentrations of free electrons and holes the impact ionization of excitons dominates over their thermal ionization. At such concentrations and the high level of injection the effect causes practically linear sites of dependences the concentration of excitons on the concentration of free charge carriers and of dependences the near-band-edge luminescence intensity in c-Si on the intensity of its excitation.

The work has been partly technically maintained by the Ministry of Education and Sciences of the Russian Federation (State contract 16.526.12.6017). This work was written only thanks to the help to the author in the vital situation, which gave him M.A. Green, E.S. Nevirovich, E.V. Ershov, M.S. Moso'yan, A.A. Mar'in. The author expresses them sincere gratitude.

References

1. Ttrupke, T., Zhao, J., Wong, A., Corkish, R., Green, M.A.: Very efficient light emission from bulk crystalline silicon. *Appl. Phys. Lett.* **82**, 2996–2998 (2003)
2. Green, M.A., Zhao, J., Wang, A., Reece, P.J., Gal, M.: Efficient silicon light-emitting diodes. *Nature* **412**, 805–808 (2001)
3. Trupke, T., Bardos, R.A., Schibert, M.C., Warta, W.: Photoluminescence imaging of silicon wafers. *Appl. Phys. Lett.* **89**, 044107-1–044107-3 (2006)
4. Bardos, R.A., Trupke, T., Schubert, M.C., Roth, T.: Trapping artifacts in quasi-steady photoluminescence and photoconductance lifetime measurements on silicon wafers. *Appl. Phys. Lett.* **88**, 053504-1–053504-3 (2006)
5. Fuyuki, T., Kondo, H., Kaji, Y., Ogane, A., Takahashi, Y.: Analytic findings in the electroluminescence characterization of crystalline silicon solar cells. *J. Appl. Phys.* **101**, 023711-1–023711-5 (2007)
6. Abbott, M.D., Cotter, J.E., Chen, F.W., Trupke, T., Bardos, R.A., Fisher, K.C.: Application of photoluminescence characterization to the development and manufacturing of high-efficiency silicon solar cells. *J. Appl. Phys.* **100**, 114514-1–114514-10 (2006)
7. Killani, D., Micard, G., Raabe, B., Herguth, A., Hahn, G.: Minority charge carrier lifetime mapping of crystalline silicon wafers by time-resolved photoluminescence imaging. *J. Appl. Phys.* **110**, 054508-1–054508-7 (2011)
8. Gundel, P., Heinz, F., Schubert, M.C., Giesecke, J.A., Warta, W.: Quantitative carrier lifetime measurement with micron resolution. *J. Appl. Phys.* **108**, 033705-1–033705-7 (2010)
9. Mitchell, B., Trupke, T., Weber, J.W., Nyhus, J.: Bulk minority carrier lifetimes and doping of silicon bricks from photoluminescence intensity ratios. *J. Appl. Phys.* **109**, 083111-1–083111-12 (2011)
10. Green, M.A.: Analytical expressions for spectral composition of band photoluminescence from silicon wafers and bricks. *Appl. Phys. Lett.* **99**, 131112-1–131112-3 (2011)
11. Mitchell, B., Weber, J.W., Walter, D., Macdonald, D., Trupke, T.: On the method of photoluminescence spectral intensity ratio imaging of silicon bricks: advances and limitations. *J. Appl. Phys.* **112**, 063116-1–063116-13 (2012)
12. Nærland, T.U., Andelskår, H., Kirkengen, M., Søndena, R., Marstein, E.S.: The role of excess minority carriers in light induced degradation examined by photoluminescence imaging. *J. Appl. Phys.* **112**, 033703-1–033703-8 (2012)

13. Altermatt, P.P., Geelhaar, F., Trupke, T., Dai, X., Neisser, A., Daub, E.: Injection dependence of spontaneous radiative recombination in crystalline silicon: experimental verification and theoretical analysis. *Appl. Phys. Lett.* **88**, 261901-1–261901-3 (2006)
14. Kane, D.E., Swanson, R.M.: The effect of excitons on apparent band gap narrowing and transport in semiconductors. *J. Appl. Phys.* **73**, 1193–1197 (1993)
15. Emel'yanov, A.M.: The mechanism of radiative recombination in the region of interband transitions in single crystal silicon. *Tech. Phys. Lett.* **30**(11), 964–966 (2004) (Original Russian text published in *Pis'ma Zh. Tekh. Fiz.* **30**(22), 75–81 (2004))
16. Emel'yanov, A.M.: Determination of bandgap variations in nondirect-band semiconductors from their edge luminescence spectra. *Tech. Phys. Lett.* **35**(3), 253–255 (2009) (Original Russian text published in *Pis'ma Zh. Tekh. Fiz.* **35**(6), 9–16 (2009))
17. Emel'yanov, A.M.: Differential method of analysis of luminescence spectra of semiconductors. *Semiconductors* **44**, 1134–1139 (2010) (Original Russian text published in *Fiz. Tekh. Poluprovodn.* **44**, 1170–1175 (2011))
18. Emel'yanov, A.M., Sobolev, N.A.: Silicon light-emitting diodes with strong near-band-edge luminescence. *Semiconductors* **42**, 329–333 (2008) (Original Russian text published in *Fiz. Tekh. Poluprovodn.* **42**, 336–340 (2008))
19. Emel'yanov, A.M., Sobolev, N.A.: High-power silicon LEDs with near-band-edge luminescence. *Tech. Phys. Lett.* **34**(2), 166–168 (2008) (Original Russian text published in *Pis'ma Zh. Tekh. Fiz.* **34**(4), 64–70 (2008))
20. Emel'yanov, A.M.: Edge photoluminescence of single-crystal silicon with a p–n junction: structures produced by high-efficiency solar cell technology. *Semiconductors* **45**, 805–810 (2011) (Original Russian text published in *Fiz. Tekh. Poluprovodn.* **45**, 823–828 (2011))
21. Emel'yanov, A.M.: Edge electroluminescence of heavily doped by boron p⁺-n silicon diodes with small area: analysis of modeling representations. *Semiconductors* **47**, 110–115 (2013) (Original Russian text will be published in *Fiz. Tekh. Poluprovodn.* **47**, 112–117 (2013))
22. Emel'yanov, A.M.: Edge electroluminescence of single-crystal silicon at 80 K: structures based on high-efficiency solar cell. *Phys. Solid State* **51**, 244–249 (2009) (Original Russian text will be published in *Fiz. Tverd. Tela* **51**, 231–236 (2009))
23. Bludau, W., Onton, A., Heinke, W.: Temperature dependence of the band gap of silicon. *J. Appl. Phys.* **45**, 1846–1848 (1974)
24. Emel'yanov, A.M., Sobolev, N.A., Mel'nikova, T.M., Abrosimov, N.V.: Mechanism of radiative recombination in the region of interband transitions in Si-Ge solid solutions. *Fiz. Tekh. Poluprovodn* **39**, 1170–1172 (2005). *Semiconductors* **39**, 1128–1130 (2005)
25. Emel'yanov, A.M., Sobolev, N.A., Mel'nikova, T.M., Abrosimov, N.V.: SiGe light-emitting diodes and their characteristics in the region of band-to-band transitions. *Solid State Phenom.* **108–109**, 761–766 (2005)
26. Sobolev, N.A., Emel'yanov, A.N., Shek, E.I., Abrosimov, N.V., Yakimenko, A.N.: Efficient SiGe LED on wavelength ~1.3 μm, made by ion implantation. In *Proceedings of the 16th International Workshop on Radiation Physics of Solid State*, Sevastopol, 3–8 July, 2006, pp. 490–496.
27. Bachrach, R.Z., Lorimor, O.G.: Recombination processes responsible for the room-temperature near-band-gap radiation from GaP. *Phys. Rev. B* **7**, 700–712 (1973)
28. Altaiskii, Y.M., Avramenko, S.F., Guseva, O.A., Kiselev, V.S.: Electroluminescence of p–n junctions in cubic silicon carbide. *Fiz. Tekh. Poluprovodn.* **13**, 1978–1983 (1979) [*Sov. Phys. Semicond.* **13**, 1152–1157 (1979)]
29. Blinov, L.M., Bobrov, E., Vavilov, V.S., Galkin, G.N.: On the recombination of nonequilibrium carriers in silicon at high photoexcitation. *Sov. Phys. Solid State* **9**, 2537–2541 (1967)
30. Nosov, Y.R.: *Physical Principles of Semiconductor Diode Operation in Pulse Regimes*. Nauka, Moscow (1968) [in Russian]
31. Ryabtsev, N.G.: *Materials for Quantum Electronics*. Sovetskoe Radio, Moscow (1972) [in Russian]
32. Emel'yanov, A.M., Sobolev, N.A., Shek, E.I.: Silicon LEDs emitting in the band-to-band transition region: effect of temperature and current strength. *Fiz. Tverd. Tela* **46**, 44–48 (2004) [*Phys. Solid State.* **46**, 40–44 (2004)]

33. Emel'yanov, A.M., Nikolaev, Y.A., Sobolev, N.A., Mel'nikova, T.M.: Kinetics of electroluminescence in an efficient silicon light-emitting diode with thermally stable spectral characteristics. *Fiz. Tekh. Poluprovodn.* **38**, 634–638 (2004) [*Semiconductors.* **38**, 610–614 (2004)]
34. Emel'yanov, A.M.: Edge luminescence of single-crystal silicon modulated by voltage variation on the p–n junction. *Pis'ma Zh. Tekh. Fiz.* **35**(18), 80–86 (2009) [*Tech. Phys. Lett.* **35**, 873–875 (2009)]
35. Michaelis, W., Pilkuhn, M.H.: Radiative recombination in silicon p–n junction. *Phys. Stat. Sol.* **36**, 311–319 (1969)
36. Nolle, E.L.: Kinetics of recombination via exciton states in semiconductors. *Fiz. Tekh. Poluprovodn.* **2**, 1679–1682 (1968) [*Sov. Phys. Semicond.* **2**, 1397–1399 (1968)]
37. Zhao, J., Wang, A., Trupke, T., Green, M.A.: High efficiency bulk crystalline silicon light emitting diodes. *Mat. Res. Soc. Symp. Proc.* **744**, M4.7.1 (2003)
38. Emel'yanov, A.M.: Impact ionization of excitons in single-crystal silicon and its influence on concentration of excitons and luminescence in the field of fundamental absorption edge. *Fiz. Tekh. Poluprovodn.* **48**(2), (2014) (in press). *Semiconductors* **48**(2), (2014) (in press)

Chapter 3

Emerging PV Nanomaterials: Capabilities Versus Recombination Losses

Kimberly A. Sablon and Andrei Sergeev

Abstract Suppressing recombination processes and improving the minority carrier lifetime are critical for enhancing the performance of solar cells. Analysis of the balance between generation, recombination, and transport and its effect on the photocurrent and open circuit voltage of solar cells as well as a review of modern approaches employed to overcome the Shockley–Queisser limit are presented.

1 Introduction

Our energy needs have been forecast to at least double within the next 50 years. Therefore, unless renewable energy can cover the large deficit that fossil fuels can no longer furnish, the stage is set for a major energy shortage. One promising solution is the conversion of solar energy into usable electric power. However, in conventional single-junction solar cells, the maximum efficiency for the conversion of unconcentrated solar radiation is 31 % [1], because a significant part (20.3 %) of solar energy is lost due to thermalization of photocarriers, and another part is lost due to poor or no absorption of below-bandgap photons (33.3 %). To minimize thermalization losses and to increase the conversion efficiency, the electron energy levels should be adjusted to the incoming photons. To reach effective harvesting of solar radiation in a broad spectral range, the absorption processes should include various electron transitions [2–5], in particular IR transitions (Fig. 3.1).

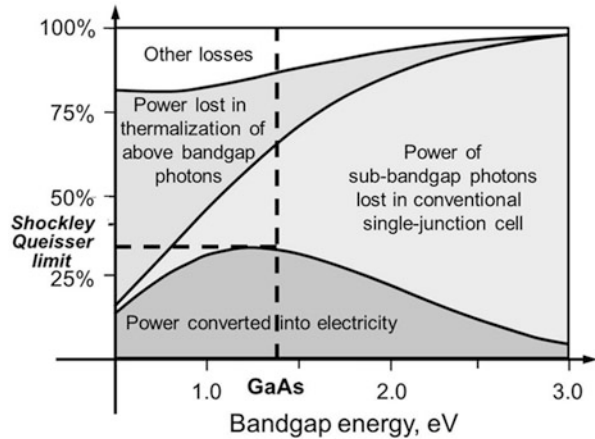
K.A. Sablon (✉)

Sensors and Electron Devices Directorate, U.S. Army Research Laboratory, 2800 Powder Mill Road BLDG 207 (RDRL-SEE-1), Adelphi, MD 20783, USA
e-mail: kimberly.a.sablonramsey.civ@mail.mil

A. Sergeev

Department of Electrical Engineering, State University of New York, Buffalo, Buffalo, NY 14260, USA

Fig. 3.1 Usable power, thermalization losses, and losses of sub-bandgap photons as a function of the bandgap in a single-junction solar cell



A number of practical technologies were proposed to extend the harvesting edge into the infrared range and reduce thermalization losses enough to increase the efficiency.

Summarizing scientific ideas and technical approaches aimed at overcoming the Shockley–Queisser (SQ) limit [1], recent advances in the development of nanomaterials with a tunable band structure, enhanced carrier multiplication in specific nanoblocks, and recent achievements in nano-plasmonics hold significant promise for achieving substantial improvements in the efficiency of solar cells. However, while nanotechnology provides numerous possibilities [2–7] to engineer electronic levels as well as to manipulate photon dynamics, nanostructured materials have one significant drawback: nanostructuring enhances recombination processes and decreases the *photocarrier lifetime*. More than 10 years ago, during critical discussions of perspectives of nanostructured materials for PV applications, in his paper “Photovoltaic conversion at reduced dimensions” [8], Hans Queisser highlighted: “Carrier lifetime is the most sensitive measure of crystalline perfection. Any deviation from an ideal single crystal reduces the lifetime, and thus lowers conversion efficiency. Indeed, single-crystal materials, especially Si and GaAs, provide cells with highest efficiencies. Any nanocrystalline material is, therefore, in principle an inappropriate choice for a cell material.”

This chapter focuses on high-efficiency approaches proposed for reaching or exceeding the SQ thermodynamic limit of solar energy conversion. The chapter begins with a brief description of the physics required to approach or exceed the SQ limit with emphasis on the role of carrier lifetime and recombination processes on the photocurrent and operating voltage of a solar cell. Fundamental limitations of solar energy conversion are then described, followed by an overview of high-efficiency concepts with specifics on approaches geared towards minimizing recombination processes via electronic levels for enhancing photocarrier lifetime in nanostructured materials.

2 The Physics of High-Efficiency Solar Cells

For a given solar cell, the power output is determined by its current–voltage product, $P = I \cdot V$. In general, the current is the most forthright parameter to evaluate as it depends on the rate at which incident photons are absorbed, the generation of carriers, and the extraction probability of generated carriers via an external circuit. Therefore, several key material and device parameters such as absorption coefficient, electric field (drift), minority carrier lifetime, and diffusion length or carrier mobility play a role in the optimization of the current and hence output power. To the contrary, optimizing the output voltage is rather delicate as it not only depends on how effectively the cell luminesces but also on the dark current: Is it diffusion or generation–recombination (g–r) limited?

2.1 Light Absorption, Lifetime, and Extraction

Once photons with an energy greater than or equal to the bandgap of the cell are efficiently absorbed, electron–hole pairs (EHPs) are generated within the absorber layer. The p–n junction creates the built-in field that sweeps out photogenerated carriers, thereby producing current in an external circuit. However, the effectiveness of this process depends upon the balance between carrier generation, recombination, and transport. The carrier generation rate depends on the wavelength and intensity of incident light as well as on the type of semiconductor. Since EHPs are created by photogeneration, the carrier concentration exceeds the thermodynamic equilibrium. Every system wants to be at its lowest potential. Therefore, to reach equilibrium, recombination of charge carriers comes into play. The recombination rate is described by

$$\left(\frac{d\Delta n}{dt}\right)_{\text{rec}} = -\frac{\Delta n}{\tau}, \quad (3.1)$$

where τ is the carrier lifetime which characterizes the level of recombination in the system. Since a solar cell is a transport device, i.e., the ultimate collection efficiency depends on the carrier lifetime and diffusion, carrier lifetime mechanisms in solar cells should be closely examined.

Minority carrier lifetime is determined by several recombination mechanisms [9–18]. Specifically, radiative, Auger, and Shockley–Read–Hall (SRH) processes are important recombination mechanisms. The first two, radiative and Auger mechanisms, are fundamental to the material, while the last is primarily due to the presence of defects within the semiconductor. The radiative process [13] is the dominant recombination mechanism in lightly doped ($5 \times 10^{17} \text{ cm}^{-3}$) and direct bandgap semiconductors such as GaAs. In this mechanism, the recombination of EHPs occurs directly between the conduction and valence bands, and the emitted

photon has energy similar to the bandgap and is therefore only weakly absorbed. Radiative recombination lifetime has been described in terms of [13]

$$\tau_r = \frac{1}{B(n_0 + p_0)}, \quad (3.2)$$

where n_0 and p_0 are the electron and hole densities in equilibrium, given by n_i^2/N_a and N_d , respectively. B is a coefficient, which is carrier density independent, given by

$$B = 5.8 \times 10^{-13} \varepsilon^{\frac{1}{2}} \left(\frac{m_0}{m_e^* + m_h^*} \right) \left(1 + \frac{m_0}{m_e^*} + \frac{m_0}{m_h^*} \right) \left(\frac{300}{T} \right)^{\frac{3}{2}} \left(E_g^2 + 3kTE_g + 3.75k^2T^2 \right). \quad (3.3)$$

The coefficient B has been found to be $\sim 2 \times 10^{-10} \text{ cm}^{-3} \text{ S}^{-1}$ for GaAs [14]. On the other hand, Auger recombination involves a three-particle Coulomb interaction, where an excited electron in the conduction band recombines with a hole in the valence band, transferring energy to another charge carrier. While Auger recombination does not dominate at or below room temperature in lightly doped GaAs solar cells, it can limit the performance of cells made from narrow-gap semiconductors. For example, in multijunction solar cells where the bottom cell is either InGaAs or Ge, at high carrier concentration (10^{16} – 10^{18} cm^{-3}), Auger-1 and -S processes are expected to dominate in the n-type and p-type materials, respectively. The carrier lifetime for Auger-1 limited recombination has been described in terms of [15]

$$\tau_{A1} = \frac{2n_i^2 \tau_{A1}}{(n_0 + p_0)(n_0 + \xi p_0)}, \quad (3.4)$$

where n_i is the intrinsic carrier concentration, n_0 and p_0 are equilibrium electron and hole concentration, τ_{A1} is the Auger lifetime for an intrinsic low-bandgap material, and ξ is the hole–hole collision term.

Assuming a single-recombination-level E_t below the conduction band edge and low injection levels, Shockley–Read lifetime may be presented as [16, 17]

$$\tau_{SR} = \left(\frac{\tau_{p0}(n_0 + n_1)}{n_0 + p_0} \right) + \left(\frac{\tau_{n0}(p_0 + p_1)}{n_0 + p_0} \right), \quad (3.5)$$

where τ_{n0} and τ_{p0} denote shortest time constant values for electron and hole capture at the level, respectively, n_1 is $n_0 \exp [(E_t - E_F)/kT]$, p_1 is $p_0 \exp [(E_F - E_t)/kT]$, and E_F is the Fermi energy (Fig. 3.2).

When the lifetime is not dominated by a single process, it is necessary to calculate the lifetime accordingly. Thus if all three recombination mechanisms are important, the overall effective lifetime τ is then calculated from

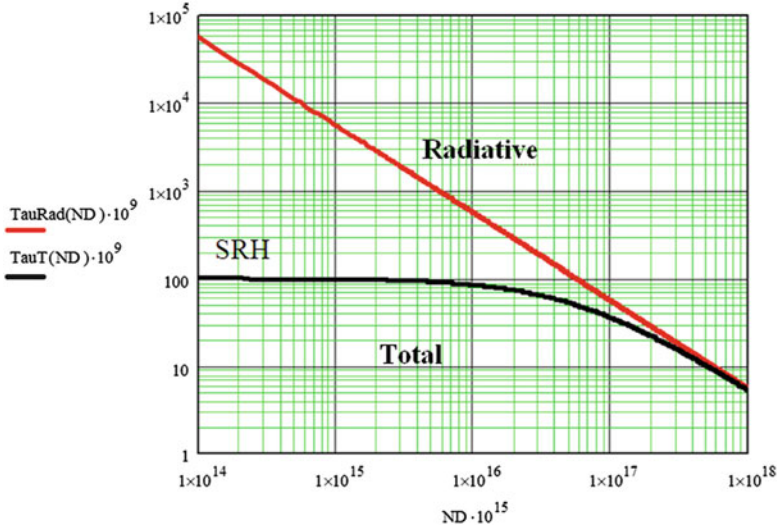


Fig. 3.2 Dependence of minority carrier lifetime on doping concentration. The plot shows the relationship between SRH and radiative recombination processes as a function of electron density. Auger contributions are not displayed since it has very little influence on lightly doped GaAs

$$\frac{1}{\tau} = \frac{1}{\tau_A} + \frac{1}{\tau_R} + \frac{1}{\tau_{SR}}, \quad (3.6)$$

where τ_A , τ_R , and τ_{SR} are the Auger, radiative, and SRH lifetimes, respectively.

As mentioned earlier, carrier transport is crucial in determining the extraction or the collection efficiency. Therefore, in addition to carrier lifetime, carrier mobility and diffusion lengths are very important. For instance, if we assume full collection of all photogenerated free electrons and holes, the external photocurrent becomes saturated implying that both the mean electron and hole drift lengths $\gamma_{e(h)} = \mu_{e(h)}\tau_{e(h)}E$ are equal to or longer than the absorber thickness, d , ($\mu_{e(h)}$ is the carrier mobility of electrons (holes), $\tau_{e(h)}$ is the carrier lifetime, and E is the electric field). Of course, in this case, no recombination occurs, and the photocurrent density (J_{ph}) is given by $J_{ph} = qGL$, where G is the generation rate, q is the electric charge, and L is the diffusion length. However, in practice, 100 % carrier extraction is extremely difficult to achieve. A necessary, but not sufficient, requirement for improving carrier extraction is to design the solar cell so that the depletion width is much smaller than the diffusion length for the ideal diode assumption to be valid. Si and Ge p–n diodes almost always satisfy this requirement, while GaAs p–n diodes rarely do because of the short carrier lifetime and diffusion length. Si makes a good solar cell, but its performance is strongly limited by Auger recombination. This prevents Si from reaching the S–Q limit. Therefore, since III–V materials such as GaAs are better candidates for reaching or exceeding the S–Q limit, methods of improving extraction should be explored.

Recently, Mills and Yablonoitch [18] proposed an approach for optimizing photon rather than carrier extraction in III–V solar cells. The main idea is to enhance the external emission of photons from the front surface of the cell. This theory stems from the S–Q thermodynamic limit which requires the incoming light to be balanced with 100 % external fluorescence at open circuit.

2.2 Open-Circuit Voltage

Maximizing the open-circuit voltage (V_{OC}) is key towards achieving high conversion efficiencies. One way to increase the V_{OC} is to reduce the dark current, i.e., the corresponding generation–recombination processes. One parameter that has been shown to reduce the dark current is the minority carrier lifetime. This is because the open-circuit voltage depends strongly on the reverse saturation current density J_0 , and J_0 is sensitive to both doping levels and minority carrier lifetimes:

$$V_{OC} = \frac{kT}{q} \left(\frac{J_{SC}}{J_0} + 1 \right), \quad (3.7)$$

where J_{SC} is the short circuit current density.

The current J_0 is given by the following expression [13]:

$$J_0 = q \frac{D_n}{L_n} n_{p0} \frac{\sinh\left(\frac{W_B}{L_n}\right) + \eta_n \cosh\left(\frac{W_B}{L_n}\right)}{\cosh\left(\frac{W_B}{L_n}\right) + \eta_n \sinh\left(\frac{W_B}{L_n}\right)} + q \frac{D_n}{L_n} p_{n0} \frac{\sinh\left(\frac{W_E}{L_p}\right) + \eta_n \cosh\left(\frac{W_E}{L_p}\right)}{\cosh\left(\frac{W_E}{L_p}\right) + \eta_n \sinh\left(\frac{W_E}{L_p}\right)}, \quad (3.8)$$

where the first term contributes to a p-type base (thickness W_B) and the second term signifies the contribution of an n-type emitter (thickness W_E). L_n and L_p are diffusion lengths of minority carrier lifetimes in p- and n-type material, respectively.

In addition to minority carrier lifetime, the geometry of the solar cell can also govern the type of dark currents that impact performance. As mentioned above, in an ideal design, the absorber layer thickness, d , is less than the diffusion length of the minority carriers. In this case, the dark diffusion current dominates and can be expressed as follows [19]:

$$I_{Diff} = I_{0Diff} \left[\exp\left(\frac{qV}{nkT}\right) - 1 \right], \quad (3.9)$$

where k is Boltzmann's constant, T is absolute temperature, n is the ideality factor, V is the bias voltage across the diode, and J_{0Diff} is the saturation diffusion current

density. The diffusion current contributes to the reverse saturation current $J_{0\text{Diff}}$ and consists of components from both p- and n-sides of the junction, as expressed here in current density superposition form:

$$J_{0\text{diff}} = qn_i^2 \left[\frac{L_p}{N_d \tau_p} + \frac{L_n}{N_a \tau_n} \right], \quad (3.10)$$

where $J_{0\text{diff}}$ denotes diffusion current density, $L_{p,n}$ and $\tau_{p,n}$ denote minority diffusion lengths and lifetimes on respective n- and p-sides of the junction, and $N_{a,d}$ denote donor and acceptor concentration levels on the n- and p-sides of the junction. For the case of p-on-n double heterostructures, where the p-side has a wider bandgap and high doping N_a , the second term in $J_{0\text{diff}}$ is negligible compared with the first and $J_{0\text{diff}}$ reduces to

$$J_{0\text{diff}} = \frac{qn_i^2 L_p}{N_d \tau_p}. \quad (3.11)$$

When the n-type absorber layer thickness d is smaller than the diffusion length L_p , dimension d effectively replaces L_p to give

$$J_{0\text{diff}} = \frac{qn_i^2 d}{N_d \tau_p}. \quad (3.12)$$

The other important current mechanism is the g-r current density which arises due to imperfections in the space charge region. Early treatments developed the seminal formulation for generation-recombination phenomena in semiconductor junctions [20, 21]. EHPs generated thermally in the depletion region give rise to a current that is recombination dominated under forward bias and generation dominating under reverse bias. Derivations for the g-r current take the form

$$J_{g-r} = \frac{qn_i W}{\sqrt{\tau_{n0} \tau_{p0}}} \frac{\sinh\left(\frac{qV}{2kT}\right)}{q \left[\frac{(V_{bi}-V)}{2kT} \right]} f(b), \quad (3.13)$$

where

$$f(b) = \int_0^{\infty} \frac{du}{u^2 + 2bu + 1}, \quad b = e \frac{-qV}{2kT} \cosh \left[\frac{E_t - E_i}{kT} + \frac{1}{2} \ln \left(\frac{\tau_{p0}}{\tau_{n0}} \right) \right]. \quad (3.14)$$

Trap levels due to defects are most effective when they exist close to the intrinsic Fermi level, i.e., when $E_t = E_i$. For bias conditions where $V = 0$, along with assumptions that $E_t = E_i$ and $\tau_{p0} = \tau_{n0} = \tau_0$, it follows that $b = 1$ and $f(b) = 1$. Under these conditions, J_{g-r} reduces to

$$J_{g-r} = \frac{qn_i W}{\tau_0} \frac{2kT}{q(V_{bi} - V)} \sinh\left(\frac{qV}{2kT}\right). \quad (3.15)$$

The current J_{g-r} is seen to be proportional to n_i . As such, J_{g-r} currents will tend to dominate over diffusion J_{diff} current at low voltages.

From above, the g-r current arises due to imperfections in the space charge region and takes the form

$$I_{g-r} = I_{0g-r} \sqrt{V_{bi} - V} \left[\exp\left(\frac{qV}{nkT}\right) - 1 \right], \quad (3.16)$$

where I_{0g-r} is the g-r saturation current (which is a fitting parameter) and n is the ideality factor equal to 2.

In the case of narrow-gap devices, tunneling currents can often dominate at low temperatures, where thermally generated currents are low, and this becomes the dominant current mechanism under reverse biases. This is particularly important for solar cells used in space applications. Tunneling currents come in two forms, namely, (1) band-to-band (BTB) and (2) trap-assisted tunneling (TAT), where forbidden gap energy states promote and participate in a two-step process. BTB tunneling currents result in electrons tunneling directly from the valance band to the conduction band and are given by [11, 22]

$$I_{BTB} = \frac{Aq^3 EV}{4\pi^2 \hbar^2} \sqrt{\frac{2m^*}{E_g}} \left[\exp\left(-\frac{4\sqrt{2m^* E_g^{1.5}}}{3qE\hbar}\right) \right] \left[1 - \exp\left(\frac{qV}{kT}\right) \right], \quad (3.17)$$

where A is the junction area, E is the electric field, \hbar is the reduced Planck constant, m^* is the tunneling effective mass, and E_g is the bandgap. These currents are due to direct tunneling of carriers under relatively high reverse biases and are fairly independent of temperature. On the other hand, TAT current (I_{TAT}) arises from tunneling to the conduction band following electron transition from the valance band to a trap level within the forbidden gap. The current density is given by

$$I_{TAT} = \frac{A\pi^2 q^2 m^* EM^2 N_t W}{\hbar^3 (E_g - E_t)} \sqrt{\frac{2m^*}{E_g}} \left[\exp\left(-\frac{F(a)\sqrt{m^*}/2E_g^{1.5}}{2qE\hbar}\right) \right] \left[1 - \exp\left(\frac{qV}{kT}\right) \right], \quad (3.18)$$

where M is the transition matrix element, N_t is the trap density in cm^{-3} , E_t is the trap energy, and $F(a)$ is function of E_t/E_g .

Finally, the shunt current (I_{SH}) across the diode is defined as

$$I_{SH} = \frac{V}{R_{SH}}, \quad (3.19)$$

where R_{SH} is the shunt resistance. Usually, surface leakage currents and shunt currents are due to the intersection of dislocation, defects, etc. By combining the

abovementioned considerations relative to diffusion, g-r, BTB, TAT, and shunt currents, the overall dark current of a solar cell is given by

$$I_{\text{Total}} = I_{\text{Diff}} + I_{\text{g-r}} + I_{\text{BTB}} + I_{\text{TAT}} + I_{\text{SH}}. \quad (3.20)$$

Note that J_{diff} depends on the ratio of the intrinsic carrier concentration and doping concentration (see (3.12)). In GaAs, since the intrinsic carrier concentration (10^6 cm^{-3}) \ll doping concentration (10^{17} cm^{-3}), we cannot expect to achieve diffusion-limited currents by simply improving the material quality. In fact, this is the main reason why g-r currents tend to dominate in GaAs solar cells. Therefore, in order to further reduce the g-r contribution to the dark current, other techniques such as photon recycling (PR) should be considered. This can potentially lead to minority carrier lifetimes that exceed the radiative recombination limit, thereby improving the J_0 and hence V_{OC} .

2.3 Radiative Recombination and Photon Recycling

The S-Q limit is often referred to as the “radiative recombination limit.”

However, radiative recombination requires all EHPs to bear the same chemical potential μ . This chemical potential is the product of the voltage, V , at the cell’s terminal and elementary charge, $q(\mu = e_{\text{FC}} - e_{\text{FV}} = qV)$. In practice, to approach or exceed the radiative recombination limit, PR schemes may be useful. By introducing PR, a balance between the absorption and emission may be shifted to increase the PV efficiency. To understand how this affects the lifetime and diffusion current, the interaction between external light radiation and the radiation re-emitted in a solar cell should be examined. As mentioned in Sect. 2.1, when light photons are absorbed, EHPs are created but after sometime will recombine. This recombination process can either generate heat (non-radiative recombination) where it is irreparable or emit a photon (radiative recombination). Keep in mind that the emitted photon can move in any direction through the cell. It is either emitted through the surface of the cell or reabsorbed along its path within the cell. In the latter case, there is interplay between absorption, generation, and emission. This multi-pass absorption and emission of photons are referred to as PR.

The reabsorption and reemission processes effectively decrease the loss of carriers caused by radiative recombination. Note that only the carriers which radiatively recombine near the surface are lost while those within the bulk material are recycled and therefore not lost at all. Consequently, the internal generation caused by photon recycling increases the minority carrier lifetime and hence improves the efficiency of the cell, reducing the dark current and increasing the open-circuit voltage. Again, the most crucial parameter governing recombination is the minority carrier lifetime. This lifetime consists of two components—radiative, τ_r , and non-radiative, τ_{nr} . Ultimately, the photon emission rate, P_r , depends on the radiative lifetime. Therefore, τ_r can be defined as corresponding to P_r as [23]

$$P_r = \frac{n}{\tau_r}, \quad (3.21)$$

where n is the carrier concentration.

Theoretical work by Asbeck [24] provides a numerical expression for a modified radiative lifetime that includes reabsorption of photons where he calculated the PR factor, φ , as a function of thickness, d . Taking the PR effect into consideration, the simplified radiative lifetime (3.2) can be written in terms of the PR factor as

$$\tau_r = \frac{\varphi d}{B(n_0 + p_0)}. \quad (3.22)$$

Taking the non-radiative contribution into account, the bulk minority carrier lifetime can be computed as

$$\frac{1}{\tau_b} = \frac{1}{\tau_{nr}} + \frac{1}{\varphi\tau_r}. \quad (3.23)$$

τ_b is the bulk minority carrier lifetime, and τ_{nr} is the non-radiative lifetime which includes both Auger and SRH.

Since PR results in additional generation of EHPs, the internal generation rate should be taken into account to accurately determine the effect of PR on the performance of the cell. In 1997, Badescu and Landsberg [25] demonstrated the influence of PR on the performance of solar cells by formulating a mathematical expression that accounts for the internal generation rate. Similarly, in 2008 Mattheis et al. [26] presented a sophisticated mathematical treatment where they combined the diffusion equation with a detailed balance approach to better quantify the PR effect on solar cell efficiency with emphasis on carrier transport in the radiative efficiency limit. Both theoretical treatments extended the diffusion equation to include the internal generation rate caused by the radiative interaction within the semiconductor. The internal generation rate due to radiative recombination is given by [26]

$$G_{\text{int}}(x_g) = \int_{x_r=0}^{x_r=d} \delta G_{\text{int}}(x_g, x_r), \quad (3.24)$$

where

$$\delta G_{\text{int}}(x_g, x_r) = \frac{4\pi\bar{n}^2}{h^3 c^2} \int_0^\infty dE \delta x_r \alpha^2(E) E^2 \exp\left(\frac{-E}{k_B T}\right) f_r(x_g, x_r) \frac{n x_r}{n_0} \quad (3.25)$$

is the generation rate at $x = x_g$ caused by radiatively recombined carriers in x_r . \bar{n} is the refractive index, h is Planck's constant, c is the speed of light, E is the photon

energy, and $\alpha(E)$ is the absorption coefficient. Therefore, the minority carrier diffusion equation for a solar cell designed to maximize PR becomes [26]

$$D_n \frac{d^2 n}{dx^2} + G_{\text{int}}(x) - \frac{n}{\tau_r} - \frac{n - n_0}{\tau_{\text{nr}}} = -G_{\text{sun}}(x) - G_{\text{bb}}(x), \quad (3.26)$$

where G_{sun} is the non-equilibrium solar generation rate and G_{bb} is the equilibrium black body generation rate.

As mentioned earlier, a solar cell is essentially a transport device, and transport is a diffusive process with a diffusion constant D_n that is related to carrier mobility μ_n via $D_n = (k_B T/q)\mu_n$. While the carrier mobility limits the photocurrent (diffusion length is the product of mobility and lifetime), it has no influence on the V_{OC} . The most crucial factor for enhancing the V_{OC} is the minority carrier lifetime. Therefore, the radiative recombination lifetime should be substantially smaller than the non-radiative component in order to achieve high radiative efficiency. Often, the conversion efficiency is discussed in terms of the radiative efficiency, η_{rad} , and is given by [27]

$$\eta_{\text{rad}} = \frac{\tau_{\text{nr}}}{\tau_r + \tau_{\text{nr}}}. \quad (3.27)$$

Note that the maximum performance is reached when cells are 100 % radiatively efficient. To further optimize the PR effect in solar cells and hence enhance the radiative efficiency, the substrate is removed and a highly reflective mirror is deposited to the back of the cell. In this cell design, photons emitted during radiative recombination are more likely to reflect back into the active region where they can be reabsorbed. As discussed earlier, the emitted photon can move in any direction through the cell. Therefore, by depositing a highly reflective mirror ($>>90$ % reflectivity) at the back of the cell, the photon can be efficiently extracted from the front surface of the cell (see [28]).

3 Fundamental Limitations of Solar Energy Conversion

The fundamental limits on conversion of solar energy have been the subject of numerous works. Some of them considered general constraints based on reversible or irreversible thermodynamics, and others provided detailed analysis of specific solar cell devices. Here, the review is limited to general considerations. Therefore, limiting efficiencies discussed in this section may be treated as an upper bound for PV conversion. The most general limit on PV efficiency is the Carnot limit. According to the second law of thermodynamics, the limit for the conversion of an engine which receives photon energy from the sun at $T_s = 6,000$ K, and exhausts its waste at a terrestrial temperature T_0 , is given by

$$\eta = 1 - \frac{T_0}{T_s} = 95\%. \quad (3.28)$$

This limit is essentially based on thermodynamics of reversible processes and assumes no entropy generation during the conversion. Even conceptually, it is rather difficult to design this type of photovoltaic engine. It is well understood that light absorption inevitably leads to entropy generation, unless for each mode, this absorption is accompanied by the emission of light with the same intensity. Thus, the reversible thermodynamics requires reciprocity of absorption and emission processes. However, in this case, no light energy is transformed into usable electric power. To take into account the entropy production in the absorption process, (3.28) should be modified as

$$\eta = 1 - \frac{T_0}{T_s} - \frac{T_0 S_G}{E_s}, \quad (3.29)$$

where E_s is the energy of light photons and S_G is the entropy generated in absorption and conversion processes. The entropy term in the last equation is always negative and depending on solar cell design may substantially decrease the PV efficiency.

Therefore, Landsberg took into account the entropy production related to the absorption process and reemission of the solar radiation in the PV converter. Under these assumptions, the PV efficiency may be presented as

$$\eta = \left(1 - \frac{T_0 S_R}{E_s}\right) - \frac{T_0 S_R}{E_s} - \frac{E_R}{E_s} \left(1 - \frac{T_0 S_R}{E_R}\right). \quad (3.30)$$

Here, the first term in (3.30) is the Carnot-like term, the second term is the correction to the entropy generation as in (3.29), and the third term describes the power lost in the PV converter due to re-emitted radiation with energy E_R and entropy S_R at temperature T_R . Landsberg associated the input and re-emitted energy and entropy with fluxes of black body radiation, for which

$S = (4/3) E/T$. Then (3.30) takes the form

$$\eta = \left(1 - \frac{4T_0}{3T_s}\right) - \frac{T_0 S_G}{E_s} - \left(\frac{T_R}{T_s}\right)^4 \left(1 - \frac{4T_0}{3T_R}\right). \quad (3.31)$$

Obviously, if entropy generation is absent ($S_G = 0$) and the radiation is re-emitted at the temperature T_0 , this expression will have a maximum. In this case, the maximal efficiency is given by

$$\eta = \left(1 - \frac{4T_0}{3T_s}\right) + \frac{1}{3} \left(\frac{T_0}{T_s}\right)^4. \quad (3.32)$$

The Landsberg limit calculated with (3.32) leads to 93.3 % power conversion efficiency. It is highly questionable whether such an efficiency may be realized in practice, because zero entropy production requires a reversible absorption of radiation with the temperature T_S by a black body with a temperature T_0 . Therefore, the Landsberg limit in (3.32) gives an upper bound on the efficiency of any kind of PV converter.

In 1960, Shockley and Queisser published their famous paper [1] on the thermodynamic limit of PV efficiency in a semiconductor single-junction solar cell. As shown in the derivation of the Carnot and Landsberg limits, Shockley and Queisser also showed that the maximal efficiency of semiconductor cell corresponds to the minimal unavoidable entropy production. In this case the maximum efficiency is reached when only photon reemission from the cell, or the so-called radiative recombination, is accounted for in the detailed balance of generation–recombination processes. Ironically, their paper was rejected because it was deemed “trivial” during the initial submission [8]. During the APS March Meeting in 1960, the scientists participating in the discussion agreed that the SQ theory may be applicable to at least GaAs with relatively weak non-radiative recombination processes [29].

In the SQ approach, the electric current produced by photon generation–recombination processes is given by

$$I = q(\dot{N}_g - \dot{N}_r), \quad (3.33)$$

where $\dot{N}_g(\varepsilon)$ and $\dot{N}_r(\varepsilon)$ are the photon fluxes absorbed and re-emitted by the semiconductor cell, respectively.

The next important assumption is that the emitted photons are in equilibrium with the non-equilibrium EHPs created by the radiation. The incoming radiation increases the number of electrons and holes, which reach thermal equilibrium with the lattice due to electron–phonon relaxation. Therefore, the non-equilibrium distribution functions of electrons and holes are described by the non-equilibrium chemical potentials (Fermi energies), ε_{FC} and ε_{FV} correspondingly, and by the lattice temperature of the semiconductor cell. Thus, the re-emitted radiation obtained in recombination of EHPs is described by the chemical potential $\mu = \varepsilon_{FC} - \varepsilon_{FV} = qV$, where V is the voltage on the cell. Then, the re-emitted photon flux may be calculated as [30]

$$\begin{aligned} \dot{N}_r &= \dot{N}(T, qV, \varepsilon_g, \infty) = f_r \frac{2\pi}{h^3 c^2} \int_{\varepsilon_g}^{\infty} \varepsilon^2 \exp\left(\frac{qV - \varepsilon}{k_B T}\right) d\varepsilon \\ &= f_r \frac{2\pi k_B T}{h^3 c^2} \left(\varepsilon_g^2 + 2\varepsilon_g k_B T + 2(k_B T)^2 \right) \exp\left(\frac{qV - \varepsilon_g}{k_B T}\right), \end{aligned} \quad (3.34)$$

where $f_r = (\sin \theta_r)^2$, where θ_r is the semi-angle of the reemission cone.

The absorbed flux, i.e., the sun flux, may be considered as the flux of photons with the temperature T_S and zero chemical potential, $\dot{N}_g = f_s \dot{N}(T_S, 0, \varepsilon_g, \infty)$, where for nonconcentrating light $f_s = (\sin \theta_s)^2 = 2.164 \times 10^{-5}$ ($\theta = 0.267$) is the sun's semi-angle as viewed from the Earth, for the optimally concentrated light $f_s = 1$. Then, the generation-induced electric current, i.e., the short circuit current, is given by

$$I = q\dot{N}_g = f_s \frac{2\pi k_B T_S}{h^3 c^2} \left(\varepsilon_g^2 + 2\varepsilon_g k_B T_S + 2(k_B T_S)^2 \right) \exp\left(-\frac{\varepsilon_g}{k_B T_S}\right). \quad (3.35)$$

Finally, the efficiency is calculated as the difference between the absorbed and re-emitted radiation energy divided by the total energy flux:

$$\eta(V) = \frac{qV(\dot{N}_g - \dot{N}_r)}{\sigma_S T_S^4}. \quad (3.36)$$

To find the efficiency limit, the function $\eta(V)$ should be optimized over V (the re-emitted flux depends on the voltage). As found by Shockley and Queisser, for $T_s = 6,000$ K and $T = 300$ K, the peak efficiency reaches 31 % at $\varepsilon_g = 1.3$ eV. For the concentrator solar cell ($f_s = 1$) the maximal efficiency 40.8 % is obtained at $\varepsilon_g = 1.1$ eV.

It is important to note that the SQ approach does not consider any particular properties of the p–n junction. As highlighted above, it is mainly based on a quasi-thermodynamic postulate where the re-emitted photons are in equilibrium with an electron–hole system as described by the non-equilibrium chemical potentials that are created by the absorbed light. The SQ approach for the analysis of PV conversion was a significant conceptual achievement and a valuable tool for analysis of other PV devices, such as cells based on photochemical and photosynthesis processes.

Another general approach used for the analysis of photovoltaic limitations is based on thermodynamics of irreversible processes and Onsager relations. The irreversible thermodynamics is well formulated for transport coefficients that describe the linear response of the system to the shift in temperature, chemical potential, etc. To extend the linear irreversible thermodynamics to a nonlinear regime of photovoltaic conversion, Markwart and Lansberg [31] proposed to replace the shift of the chemical potential $\Delta\mu/T$ by the exponential function $k_B[\exp(\Delta\mu/k_B T) - 1]$ and the change of the temperature $\Delta T/T^2$ by the function $(k_B/h\nu)\exp[(h\nu/k_B T)(T^{-1} - T_S^{-1}) - 1]$. They demonstrated that such replacement is consistent with the general Onsager reciprocity relations and leads to well-known equations for carrier kinetic and transport in a PV device. Thus, the SQ approach is consistent with the irreversible thermodynamics.

The SQ consideration was based on a simple band structure consisting of only conduction and valence bands. Additional intermediate bands allow for better adjustment of the solar spectrum to the electron transitions which can potentially

improve the efficiency. Moreover, any multiband solar cell can be represented by an equivalent circuit diagram of conventional cells, for which the SQ approach is fully applicable. For example, the three-band cell may be represented as a combination of three traditional cells operating at the transitions from the valence to the conducting band, from the valence to the intermediate band, and from the intermediate to the conducting band. The efficiency of this type of cell is limited to 63.2 %. The addition of the fourth band increases the efficiency limit up to 71.7 % [32]. Various attempts to create the intermediate bands from the impurity, quantum well, or quantum dot electron levels are discussed in Sect. 4.2.

4 High-Efficiency Concepts

To overcome the SQ limit, the following general approaches can be employed:

1. Adjustment of electron levels to the energy of incoming photons, for example impurity solar cells and intermediate band solar cells
2. Optimization of photocarrier kinetics, such as photocarrier multiplication (impact ionization), multi-exciton generation, and other ways to use energy of hot electrons
3. Adjustment of photons to the electron levels in the photovoltaic material, for example photon up-conversion, photon down-conversion, and light management to redirect solar light at the angle corresponding to the disk of the sun

This section reviews the technical approaches aimed at overcoming the SQ limit with discussion on how these approaches work in current and emerging photovoltaic technologies, such as multijunction PV devices, up- and down-conversion of solar radiation, impurity band solar cell, intermediate band cell, and hot electron conversion. Prior to discussing recent ideas based on numerous possibilities provided by achievements in nanotechnology, note that the only technology that results in an efficiency that exceeds the SQ limit is multijunction solar cells.

This system was designed to target the issue of thermalization losses while converting broadband radiation. It employs a set of junctions, each designed for effective harvesting and conversion of a specific spectral range near the material bandgap [33, 34]. A two-junction cell can reach 42 % efficiency, and three-junction cells can achieve 49 % efficiency [34]. In devices with five or more junctions the ultimate efficiency may even reach ~70 %. However, current technology enables only triple-junction cells. This is mainly due to limitations and high cost of multijunction devices as determined by the need for lattice match, thermal expansion match, and current match in a cascade of p–n (n–p) junctions [35, 36]. Nonetheless, multijunction cells demonstrate record high power conversion efficiencies (~42 %) under concentration.

4.1 *Photon Management*

In this section, the possibilities for photon management are briefly discussed. According to Sect. 3, modification of both input and output photons allows for increasing the PV conversion. Here, traditional methods aimed at modification of the incoming photons as well as discussion of control of re-emitted photons are explored.

Significant recent efforts have been devoted to the increase of light absorption. Enhanced absorption enables the reduction of the solar cell width and hence suppresses the recombination losses. It is well understood that plasmonic structures provide numerous possibilities to enhance electron interaction with incoming photons. First, micro- or nano-patterned metallic structures at the front or the rear surface of a cell lead to effective subwavelength scattering and light trapping in the cell. For example, it is experimentally demonstrated that Ag nanoparticles placed at the surface of the solar cell can increase the power conversion efficiency by $\sim 1\%$ [37]. Second, metallic nanoblocks placed inside of the absorber material act as subwavelength antennas and can be used to concentrate the electromagnetic field enough to enhance photo-generated electron transitions. Finally, light scattering from the back interface of a PV device coated with a corrugated metal film leads to the generation of the surface plasmon-polariton modes at the metal–semiconductor interface as well as guided modes in a semiconductor PV material, where these modes decay into EHPs [7, 38, 39]. For the purpose of this review, note that the strong potential of plasmonics for PV applications is limited by the efficient light absorption of metallic structures, in particular by metallic nanoparticles. In fact, the use of heavily doped semiconductor nanoblocks such as quantum dots provides more flexibility and opportunities to the solar cell design, especially if the quantum dots are used as light scatterers and converters of IR subband photons simultaneously (see Sect. 5).

One of the possibilities to match the photon energy to electron transitions in a conventional single-junction solar cell is to convert the frequency of high-energy photons down or to convert the frequency of low-energy photons up towards the semiconductor bandgap. For a solar cell with optimized down-conversion, the efficiency limit is 40 %, and for up-conversion this limit is 48 %. Up- and down-conversion do not require modification of a solar cell design. The corresponding down- or up-conversion layers may be added to the front (down-conversion) or the rear (up-conversion) surfaces of a conventional solar cell to match the incident light to the bandgap energy. Up-conversion is substantially less effective than down-conversion, which for many years has attracted significant attention within the photovoltaic community [40, 41]. Dyes and rare-earth materials were intensively studied. However, a fluorescent material with efficient conversion that is required for photovoltaic applications has not been developed yet. Recently, quantum dots gained traction due to high tunability of electron levels and compatibility with PV technologies. For example, in [42] the effect of inkjet printing of Si quantum dots at

the surface of a multicrystalline Si solar cell was associated with down-conversion in quantum dots. The improvement in the absolute efficiency was limited to 0.3 %.

Another interesting and very nontrivial idea to manage the photon system for high-energy conversion aims at controlling re-emitting photons by restriction of the reemission angle. As discussed in Sect. 3, the photon reemission from a solar cell is an important part of the photovoltaic conversion. Conventional solar cells without concentrating systems absorb solar energy in a narrow angle ($\theta_s = 0.267^\circ$) but re-emits it isotropically. This light transformation results in the entropy generation and decreases the photovoltaic efficiency. Therefore, the restriction in the angle of photon reemission θ_r should increase the efficiency. The reduction of the reemission angle does not decrease the short circuit current if the reemission angle is still larger than θ_r . Marti et al. [43] calculated the effect of the reemission angle restriction and found that without photon recycling the angle restriction design provides practically negligible improvement. However, the effect becomes very significant in a system with PR. For example, for the case of total angular restriction ($\theta_r = \theta_s$), the limiting efficiency increases to 38.7 %. In this limiting case, the efficiency is independent of the light concentration. Thus, according to [43], the cell with the reemission angle restriction design under 1 sun radiation will have the same efficiency as the conventional solar cell under 46,000 suns. This example shows significant potential of the management of re-emitting photons. However, according to detailed modeling [43], this design requires again very pure materials which strongly suppress non-radiative recombination. The effect disappears if the non-radiative recombination rate exceeds just 10 % of the radiative recombination.

4.2 Adjustment of Electron Levels

The oldest concept related to the adjustment of electron levels to the solar spectrum was the impurity band solar cell. Impurity band solar cells have been studied for many years. In the early sixties, Wolf proposed the use of impurity levels to collect the long-wavelength radiation [44] while minimizing the cost and complexity associated with multijunction solar cells. Cells with a variety of impurities within the bandgap of the host semiconductor are expected to have a maximum efficiency of 77 %. In response, Shockley and Queisser [1] argued that additional impurity levels can drastically enhance recombination processes (SRH recombination) and consequently deteriorate the device performance. Trade-off between IR energy harvesting and recombination losses due to impurity electron levels is a long-term problem studied without noticeable success in a number of theoretical and experimental investigations. To date, no laboratory cell that improves efficiency due to light harvesting via impurity levels has been demonstrated.

Analogous to the impurity band solar cell concept, the intermediate band solar cells have been intensively investigated during the last decade. In this device, the intermediate band is formed from discrete quantum dot (QD) levels due to strong tunneling coupling between QDs [4, 45]. Theoretical calculations predict that the

intermediate band solar cell can provide a maximum efficiency of ~65 % under full concentration. However, intensive experimental efforts to improve the intermediate band solar cell show that an increase in the photovoltaic efficiency has not exceeded a few percent [46–48]. This is due to the fact that QDs enhance recombination via intermediate electronic levels, and in the best case, the QD-enhanced IR harvesting just slightly exceeds the QD-related recombination losses. One of the technological limitations for the intermediate band solar cell originates from stress accumulation which results when QD layers are placed close to each other to provide the level of electron coupling needed to form the intermediate band. Stress drastically increases recombination processes.

4.3 Optimization of Photocarrier Kinetics

The electron, photon, and phonon distribution functions strongly depend on the hierarchy of the characteristic relaxation rates. As discussed in Sect. 3, the SQ analysis assumes that the interaction of electrons and holes with phonons is the strongest interaction in the system. In this case, the distribution functions of electrons and holes under solar radiation are described by the non-equilibrium chemical potentials, and the difference between these chemical potentials is equal to the open-circuit voltage. Now let us presume the opposite situation where the interaction in the electron–hole subsystem is the strongest interaction. Such interaction establishes the distribution functions with zero chemical potential and the temperature shift in the electron temperature T_e , which can be found from the energy balance equation, which in the linear regime has a form

$$\frac{C_e}{\tau_{e-ph}}(T_e - T) = P, \quad (3.37)$$

where C_e is the heat capacity of electrons and holes, τ_{e-ph} is the inelastic electron–phonon relaxation time, and P is the power of the radiation absorbed by the solar cell. Thus, in accordance with (3.37), the shift of the electron temperature is determined by the electron–phonon interaction. The energy balance equation may be generalized to the nonlinear regime via the so-called energy control function. When the electron temperature is found, the SQ approach can be extended and applied to the case of electron heating. Assuming that re-emitting photons are in equilibrium with the electron subsystem, the limiting efficiency may be directly calculated from the equation which is analogous to (3.36). Obviously, the efficiency limit strongly depends on the electron temperature. For example, for an electron temperature of 2,500 K and for $f_s = f_r$, the limiting efficiency can be as high as 85 %. Unfortunately, in every known material, the electron–phonon interaction is strong and does not allow overheating of the electron–hole subsystem with respect to the lattice. Moreover, it is well understood that such strong overheating under solar radiation is practically impossible in any material. In fact, electron

overheating up to several thousand degrees would lead to large carrier densities. The electron–phonon interaction itself at high densities is determined by the deformation potential, which strongly increases if the carrier density increases. Therefore, in any material with high densities of free carriers, the electron–phonon interaction is enhanced and provides effective cooling of the electron subsystem.

The above examples of the hot electron solar cell [49–51] show that the electron–electron interaction does not change the energy of the electron subsystem and, therefore, leads to the photocarrier kinetics favorable for photovoltaic conversion. At the same time, to suppress energy losses in the solar cell, the electron–phonon processes should be suppressed.

Another example of management of the photocarrier kinetics for effective conversion is a solar cell with carrier multiplication via impact ionization, i.e., the inverse Auger-type process [5, 6, 52]. Carrier multiplication increases the number of photocarriers and improves efficiency. It is realized via electron–electron interaction and requires relatively high carrier concentration. These conditions may be realized in confined nanoblocks, such as nanocrystals and QDs. In this case, the high-energy exciton created by a photon in a nanocrystal decays into several low-energy excitons. As a result, several excitons are formed by one absorbed photon [5, 6, 52]. This effect is strong in nanomaterials with low bandgap values and is intensively studied in colloidal solar cells [53, 54].

5 Conversion with Charged Quantum Dots

In this section, the technology based on IR harvesting and conversion by negatively charged QDs [55–57] is reviewed. The dot charging is realized by selective doping of the QD medium. Charged quantum dots may be randomly distributed in QD layers without correlation between QD layers or their positions may be correlated in the current direction in the range of several QD layers. Charged QDs may form correlated clusters, which include 3–7 QDs. The quantum dot with built-in charge (Q-BIC) approach does not require any interdot coupling which relaxes the limitations imposed by interdot coupling on design and fabrication of the intermediate band solar cell. Moreover, for broadband conversion, the QD photovoltaic devices should employ a wide range of electron transitions, which may be controlled by a corresponding broad-range distribution of QD sizes.

5.1 Enhanced IR Harvesting by Charged QDs

It is well understood that quantum dots provide strong and tunable IR absorption, which creates EHPs localized in the dots [58]. We proposed to enhance extraction of trapped photocarriers by n-charging of QDs [55–57]. Note that the effective extraction from n-charged QDs is realized due to the strong asymmetry of electron

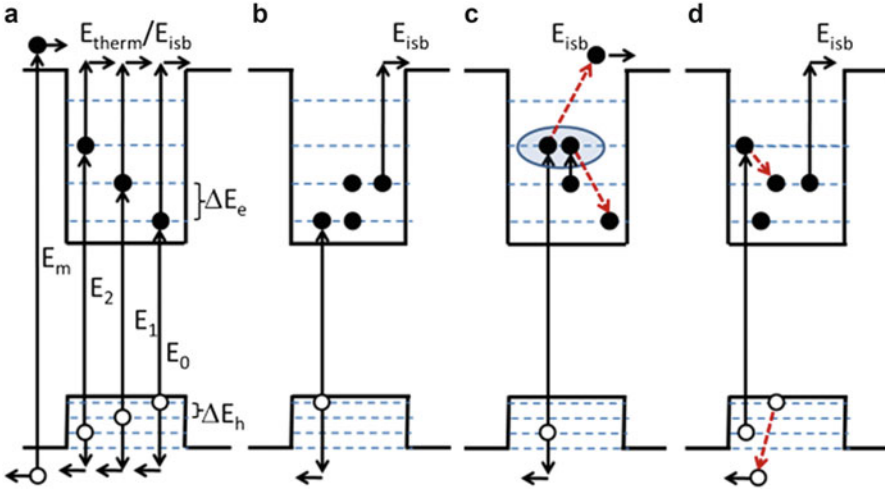


Fig. 3.3 IR-assisted photogeneration of electron–hole pairs in undoped QD structures (a) and n-doped QD structures (b–d). Processes (c) and (d) are realized via E–e and E–h interaction

and hole levels in QDs. The level structure in InAs/GaAs quantum dots has been investigated in numerous photoluminescence measurements [59, 60] which show practically equidistant level positions of electrons and holes. The total level spacing, $\Delta E = \Delta E_c + \Delta E_h$, is found to be 60–80 meV [61]. The ratio, $\Delta E_c/\Delta E_h$, is evaluated indirectly and changes from 2 to 8 from one work to another [62–64]. It is quite possible that the specific equidistant positions of energy levels may be associated with the quasi-parabolic form of the confinement potential in InAs/GaAs QDs. In this model, the spacing ratio, $\Delta E_c/\Delta E_h$, is given by $(m_h/m_e)^{1/2}4$, which is in agreement with the scope of experimental results. Using this model, $\Delta E_c = 55$ meV and $\Delta E_h = 14$ meV are achieved. Therefore, the electron transitions in QDs significantly exceed the thermal energy and cannot be induced by thermal phonons, while the hole transitions are easily induced by acoustic thermal phonons. The processes of light harvesting via QDs are shown in Fig. 3.3. Without dot charging the absorption of sub-bandgap photons can be realized exclusively via multistep absorption, as it is shown in Fig. 3.3a. As discussed above, QDs act as shallow traps for holes and deep traps for electrons. Therefore, to stimulate electron transitions by IR radiation for photovoltaic applications, additional electrons should be placed in QDs. Corresponding processes in n-doped QD structures are presented in Fig. 3.3b–d. Figure 3.3b describes a process where the electron trapped in a QD is excited by IR radiation from the localized to the conducting state. Figure 3.3c, d shows other n-doping-induced processes that involve inter-electron interaction in QDs. In Fig. 3.3c, the radiation promotes an electron to a QD excited state; a second electron, thermally lifted into a second excited state, is promoted to a higher excited state by long-wavelength radiation; and then due to strong electron–electron interaction, one of these electrons transfers to the conducting state and the other transfers

to a low-energy state. In Fig. 3.3d the relaxation of an electron to a low-energy state leads to the escape of a hole from the QD. Because of the small hole level spacing, the hole escape from QDs can be easily generated by electrons (see below). Thus, doping should stimulate the radiation-induced electron escape from QDs. Therefore, contrary to lasing applications of QDs, which are strongly enhanced by p-doping, the photovoltaic applications require n-doping.

5.2 *Optical Enhancement of Electron Extraction from Charged QDs via Electron Heating*

As mentioned above, absorption of high-energy photons creates hot electrons with energy significantly higher than the thermal energy of the lattice, and thermalization to the conduction band edge via interaction of hot electrons with the electrons localized in QDs will result in extraction of electrons from QDs (see Fig. 3.4). As discussed above, QDs are shallow traps for holes, and, therefore, holes photogenerated in QDs may be extracted from dots by thermal phonons. Therefore, the extraction of electrons from QDs via interaction with hot electrons will create charge transfer and enhance the photovoltaic conversion due to reduction of thermalization losses.

Thus, the n-charging of QDs strongly enhances the probability of electron escape via interaction with corresponding IR photons or with hot electrons, obtained in thermalization processes. Therefore, strong light-absorbing and spectrally tunable QDs provide photogenerated electrons and holes moving along a p–n-junction electrochemical potential to corresponding contacts.

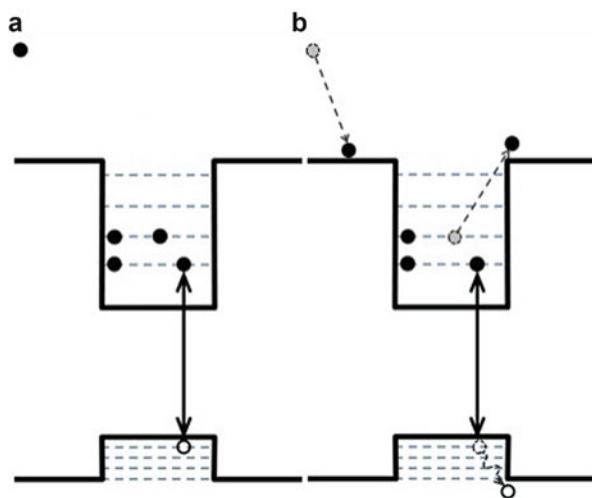


Fig. 3.4 Electron extraction from QD by hot electron

5.3 *Suppressed Photoelectron Capture and Recombination via QDs*

It is also well understood that the QDs are effective centers of recombination. Therefore, electrons and holes moving in the QD media have a high probability of being captured in QDs and recombined. The capture processes of electrons and holes are substantially different because the QDs are deep traps for photoelectrons but shallow traps for holes. As confirmed by numerous photoluminescence measurements, in the undoped QD media, the capture of electrons is significantly faster than the capture of holes. Again, the n-charging of QDs allows management of the 3D nanoscale potential profile as well as suppression of fast capture of photoelectrons. Operation of semiconductor devices is essentially based on manageable potential barriers for electrons and holes. In most modern devices, the potential profile changes only in one direction. Charged quantum dots provide unique possibilities for creating specific 3D potential profiles favorable for photovoltaics and sensing. Potential barriers around QDs are always created when electrons from dopants outside of the QDs are transferred inside. In the simplest case, uniformly distributed charged quantum dots create local potential barriers. Charged quantum dots with correlated positions, such as QD clusters, planes, and rows, may be used for creating higher collective potential barriers, which separate the groups of QDs from conducting channels (see Fig. 3.5).

In general, the photoelectron capture to the n-charged QD is strongly suppressed by the repulsive Coulomb interaction between the electron and QD. In general, the photoelectron capture to the n-charged QD is strongly suppressed by the repulsive Coulomb interaction between the electron and QD. In general, the capture may be realized via tunneling through the barrier or the thermal excitation above the barrier.

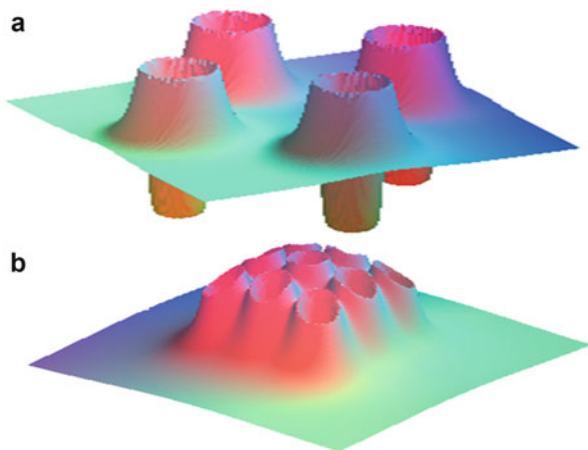


Fig. 3.5 Potential barriers created by charged spherical quantum dots and dopants outside dots: (a) the barriers around single dots; (b) the collective barriers around a dot cluster

Tunneling processes strongly dominate in photoelectron capture by n-charged impurities. However, for QDs with a radius larger than 5–10 nm, the thermoexcitation processes dominate over tunneling and the capture rate exponentially decreases with increasing the negative built-in dot charge [55–57]:

$$\frac{1}{\tau_{\text{capt}}^e} = \pi N_d R^3 \tau_e^{-1} \exp\left(-\frac{Ne^2}{k_B T \kappa R}\right), \quad (3.38)$$

where N is the number of electrons in the dot, N_d is the dot concentration, R is the quantum dot radius, τ_e is the electron–phonon inelastic scattering time which corresponds to transitions with characteristic electron-level spacing in QD, and κ is the permittivity.

It can be expected that the Coulomb attraction may increase the capture rate for holes, as it is widely observed for the capture on negatively charged impurities. In fact, for QDs the effect of charging is small because of the relatively large size of QDs. In a simple model with spherical dots, the hole capture rate is given by [57]

$$\frac{1}{\tau_{\text{capt}}^h} = \frac{4}{3} \pi N_d (R^*)^3 \tau_h^{-1}, \quad (3.39)$$

where τ_h is the hole cascade relaxation time ($\tau_h = \tau_0(3k_B T/\Delta E_h)$) and τ_0 is the relaxation time between adjacent hole levels; R^* is the dot radius, R , or the Thomson’s radius, $R_{\text{Th}} = e^2 N/(\kappa k_B T)$, depending on which of these parameters is the largest one. Simple evaluations show that the Thomson’s radius is smaller than the typical base of the pyramidal QDs. Therefore, according to (3.38) and (3.39), the n -charging of QDs exponentially suppresses the electron capture processes but does not practically affect the hole capture.

5.4 Optimization of Microscale Potential Profile by Charged QDs and Selective Doping

Under sunlight, the electron and hole capture rates are equated by changing the QD charge. In “underdoped” structures, QDs will be filled by photoelectrons, while in the “overdoped” structures, electrons will leave the QDs. Therefore, to optimize the potential profile in a QD solar cell, one should choose the optimal doping that provides equal electron and hole capture rates, i.e., $\tau_{\text{capt}}^e(N) = \tau_{\text{capt}}^h(N)$, where the filling of QDs, N , should correspond to the number of dopants per dot. Note that charge redistribution that includes QD population may drastically change the potential profile, especially the profile near the p–n junction, and strongly deteriorate the device performance. Therefore, for the most effective PV conversion, doping and position of the QD media as well as selective doping of the pre-junction area should be optimized simultaneously.

5.5 Q-BIC Technology: Efficiency Improvement Due to Conversion of IR Radiation

Data obtained with Q-BIC solar cells are summarized in Table 3.1, where N is the electron dot population, FF is the fill factor, and η is the efficiency of the solar cell. As seen, an increase in the built-in-dot charge results in a 13.23 % increase in the short circuit current, J_{SC} , going from 22.3 to 25.7 mA/cm² in the case where the device is doped to provide three electrons per dot, practically without substantial degradation of the open-circuit voltage, V_{OC} . In fact, the open-circuit voltage for the doped sample improved by 3.5 % relative to the undoped QD cell. Note that these devices do not contain an optimized antireflective (AR) coating.

The experimental I - V characteristics of the Q-BIC devices are shown in Fig. 3.6.

As seen from Fig. 3.6 and Table 3.1, the power conversion efficiency increases with the increase of the built-in-dot charge. At the n-doping level which provides three electrons per dot, the conversion efficiency increased by 16 % relative to the undoped sample. Thus, in the Q-BIC test devices, it is clear that the harvesting and conversion of the IR part of the solar spectrum contribute substantially to the photovoltaic efficiency. This effect of optical enhancement of IR conversion is expected to be especially strong in concentrator solar cells.

Table 3.1 Measured Q-BIC solar cell parameters as a function of dot charge

N	J_{SC} (mA/cm ²)	V_{OC} (V)	FF (%)	η (%)
Ref. cell (no dots)	22.5	0.93	79.3	16.8
0	22.3	0.82	76.2	14.3
3	25.7	0.85	78.9	17.1

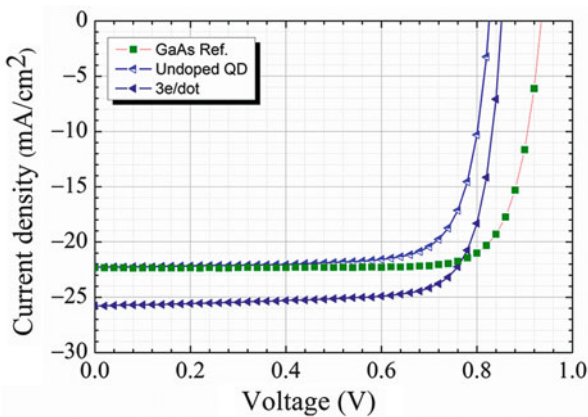


Fig. 3.6 The I - V characteristics obtained under 1 sun (AM 1.5G) illumination for a GaAs reference cell, an undoped QD cell and a Q-BIC cell doped to provide ~ 3 elec/dot

5.6 Future Possibilities

5.6.1 IR Radiation Trapping Employing Plasmonic Oscillations in Layers of Charged QDs

Under radiation, charged QDs behave like oscillating dipoles intensively scattering long-wavelength radiation. Light scattering on layers of charged QDs and, especially, on blocks of layers with vertically correlated positions of QDs will form waves that are substantially localized in the PV device. This will strongly increase the harvesting of solar energy. Note that the positive effects of light scattering on the power conversion efficiency by metallic nanoparticle arrays were intensively studied and confirmed by a number of experiments using conventional solar cells [37, 38]. In the case of utilizing semiconductor doped nanoparticles, efficient light trapping would require minimal parasitic absorption in the nanoparticles. This would create some challenging technological requirements. In the Q-BIC approach, absorption can be enhanced in the barriers as well as in the quantum dots. Therefore, the light trapping by charged QDs seems like a very attractive idea for improving the Q-BIC technology.

5.6.2 QD Media with Vertically Correlated Positions of QDs

Here, blocks of closely placed QD layers alternate with relatively thick barriers to suppress stress accumulation (see Fig. 3.7) [65, 66]. In this case, clusters of vertically correlated dots with built-in charge can create collective potential barriers

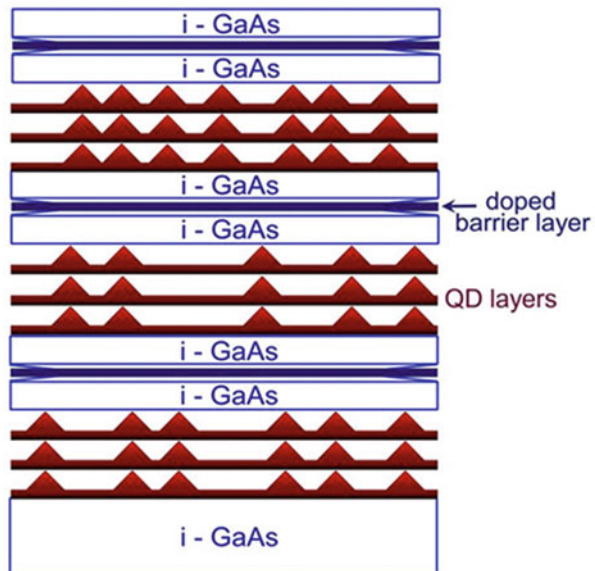


Fig. 3.7 QD medium with vertically correlated positions of QDs enhances the effect of potential barriers

around the clusters. These barriers will serve to separate the clusters from the high-mobility (no electron scattering from dots) conducting channels to provide effective transfer of photocarriers to the external circuit. In other words, by using vertically correlated clusters, we can potentially enhance the effect of Coulomb repulsion between photoelectrons and n-charged quantum dots.

6 Conclusion

In summary, the interplay between generation and recombination processes as well as the fundamental limitations of solar cell efficiency were highlighted, and modern technologies developed specifically to achieve effective conversion of solar energy were discussed. Achievements in nanotechnology provide numerous possibilities for researchers to tune electron energy levels, to modify photon modes in a PV device, and also to manage photocarrier kinetics. At the same time, integrating nanocrystalline materials into PV materials results in stress and defects at boundaries and interfaces of nanoblocks. Such defects enhance the recombination processes and increase the recombination losses. The best way to overcome this drawback of modern nanomaterials is to separate the conducting channels from the nanoblocks so that the photocarriers excited from nanoblocks can move along these high-mobility channels free from stress and defects. We proposed and analyzed the original solar cell design, where such channels are formed by quantum dots charged by selective doping. This approach allows for enhanced harvesting of IR radiation by dots and effective control of photoelectron processes by the nanoscale potential created by charged dots and offers a wide range of possibilities to manage photon modes due to scattering on charged dots. It does not require electron interdot coupling that leads to substantial technological limitations on fabrication of the intermediate band solar cell. Note that in the very recent paper [67], A. Martí et al. proposed the use of quantum dot solar cells without formation of the intermediate band. This is essentially the same as the design reviewed in Sect. 5 (see also [55–57]).

Acknowledgement Special thanks to P. Wijewarnasuriya, J. Little, V. Mitin, and N. Vagidov for valuable discussions. The work described herein was supported by the ARO, AFOSR, and the National Science Foundation.

References

1. Shockley, W., Queisser, H.J.: Detailed balance limit of efficiency of p-n junction solar cells. *J. Appl. Phys.* **32**, 510 (1961)
2. Luque, A., Hegedus, S. (eds.): *Handbook of Photovoltaic Science and Engineering*. John Wiley & Sons, New York (2003)
3. Würfel, P.: *Physics of Solar Cells: From Basic Principles to Advanced Concepts*. Wiley-VCH, Weinheim, Germany (2005)

4. Luque, A., Martz, A.: Increasing the efficiency of ideal solar cells by photon induced transition at intermediate levels. *Phys. Rev. Lett.* **78**, 5014 (1997)
5. Nozik, A.J.: Nanoscience and nanostructures for photovoltaics and solar fuels. *Nano Lett.* **10**, 2735 (2010)
6. Semonin, O.E., Luther, J.M., Choi, S., Chen, H.Y., Gao, J., Nozik, A.J., Beard, M.C.: Peak external photocurrent quantum efficiency exceeding 100% via MEG in a quantum dot solar cell. *Science* **334**, 1530 (2011)
7. Atwater, H.A., Polman, A.: Plasmonics for improved photovoltaic devices. *Nat. Mater.* **9**, 205 (2010)
8. Queisser, H.: Photovoltaic conversion at reduced dimensions. *Phys. E* **14**, 1 (2002)
9. Bonch-Bruевич, V.L., Landsberg, E.G.: Recombination mechanisms. *Phys. Stat. Sol. (b)* **29**, 1 (1968)
10. Sze, S.M.: *Physics of Semiconductor Devices*, 2nd edn. John Wiley & Sons Inc., New York (1981)
11. Rogalski, A., Adamec, K., Rutkowski, J.: *Narrow-Gap Semiconductor Photodiodes*. SPIE Press, Bellingham (2000)
12. Schroder, D.K.: *Semiconductor Material and Device Characterization*, 2nd edn. John Wiley & Sons Inc., New York (1998)
13. Dumke, W.P.: Spontaneous radiative recombination in semiconductors. *Phys. Rev.* **105**, 139–144 (1957)
14. 't Hooft, G.W.: The radiative recombination coefficient of GaAs from laser delay measurements and effective nonradiative carrier lifetimes. *Appl. Phys. Lett.* **39**, 389 (1981)
15. Landsberg, P.T.: *Recombination in Semiconductors*. Cambridge University Press, Cambridge (1991)
16. Shockley, W.: *Electrons and Holes in Semiconductors*. D. Van Nostrand, Princeton, NJ (1950)
17. Shockley, W., Read, W.T.: Statistics of the recombinations of holes and electrons. *Phys. Rev.* **87**, 835–842 (1952)
18. Mills, O.D., Yablonovitch, E., Kurtz, S.R.: Strong internal and external luminescence as solar cells approach the Shockley-Queisser limit. *IEEE J. Photovolt.* **2**, 3 (2012)
19. Streetman, B.G.: *Solid State Electronic Devices*, p. 07632. Prentice-Hall, Inc, Englewood Cliffs, NJ (1980)
20. Sah, C.-T.T., Noyce, R.N., Shockley, W.: Carrier generation and recombination in pn junctions and p-n junction characteristics. *Proc. IRE* **45**, 9 (1957)
21. Colinge, J.-P., Colinge, C.A.: *Physics of Semiconductor Devices*, 2nd edn. Kluwer Academic Publishers, Boston (2002)
22. Palankovski, V., Quay, R.D.: *Analysis and Simulation of Heterostructure Devices*. Springer, New York (2004)
23. Badescu, V., Landsberg, P.T.: Theory of some effects of photon recycling in semiconductors. *Semicond. Sci. Technol.* **3**, 1267–1276 (1993)
24. Asbeck, P.: Self-absorption effects on the radiative lifetime in GaAs-GaAlAs double heterostructures. *J. Appl. Phys.* **48**, 820 (1977)
25. Badescu, V., Landsberg, P.T.: Influence of photon recycling on solar cell efficiencies. *Semicond. Sci. Technol.* **12**, 1491 (1997)
26. Mattheis, J., Werner, J.H., Rau, U.: Finite mobility effects on the radiative efficiency limit of pn junction solar cells. *Phys. Rev. B* **77**, 085203 (2008)
27. Parrott, J.E.: Radiative recombination and photon recycling in photo-voltaic solar cells. *Sol. Energy Mater. Sol. Cells* **30**, 221–231 (1993)
28. Wang, J.-B., Zhang, Y.-H.: Increased power conversion efficiency through photon recycling in quantum well lasers. *Phys. Stat. Sol. (c)* **4**, 5 (2007)
29. Addison, C.: "Oral history of Hans Queisser," Computer History Museum (2006). (<http://archive.computerhistory.org/resources/access/text/2012/07/10265805-05-01-acc.pdf>)
30. Green, M.A.: *Third Generation Photovoltaics*. Springer, Berlin (2003)

31. Markwart, T., Lansberg, P.T.: Thermodynamics and reciprocity of solar energy conversion. *Phys. E* **14**, 71 (2002)
32. Brown, A.S., Green, M.A., Corkish, R.P.: Limiting efficiency for a multi-band solar cell containing three and four bands. *Physica E* **14**, 121 (2002)
33. Matthews, I., O'Mahony, D., Corbett, B., Morrison, A.P.: Theoretical performance of multijunction solar cells combining III-V and Si materials. *Opt. Express* **20**, 5 (2012)
34. Kurtz, S., Meyers, D., McMahon, W.E., Geisz, J., Steiner, M.: A comparison of theoretical efficiencies of multijunction concentrator solar cells. *Prog. Photovolt. Res. Appl.* **16**, 6 (2008)
35. King, R., et al.: 40% efficient metamorphic GaInP/GaInAs/Ge multijunction solar cells. *Appl. Phys. Lett.* **90**, 183516 (2007)
36. Tobias, I., Luque, A.: Ideal efficiency of monolithic, series-connected multijunction solar cells. *Prog. Photovolt. Res. Appl.* **10**, 323–329 (2002)
37. Kim, S.-S., Na, S.-I., Jo, J., Kim, D.-Y., Nah, Y.-C.: Plasmon enhanced performance of organic solar cells using electrodeposited Ag nanoparticles. *Appl. Phys. Lett.* **93**, 073307 (2008)
38. Ferry, V.E., Sweatlock, L.A., Pacifici, D., Atwater, H.A.: Plasmonic nanostructure design for efficient light coupling into solar cells. *Nano Lett.* **8**, 4391 (2008)
39. Polman, A.: Plasmonics applied. *Science* **322**, 868 (2008)
40. Shalav, A., Richards, B.S., Green, M.A.: Luminescent layers for enhanced silicon solar cell performance: up-conversion. *Sol. Energy Mater. Sol. Cells* **91**, 829 (2007)
41. Richards, B.S.: Luminescent layers for enhanced silicon solar cell performance: down-conversion. *Sol. Energy Mater. Sol. Cells* **90**, 1189 (2006)
42. Pi, X.D., Zhang, L., Yang, D.: Enhancing the efficiency of multicrystalline silicon solar cells by the inkjet printing of silicon-quantum-dot ink. *J. Phys. Chem. C* **116**, 21240 (2012)
43. Marti, A., Balenzategui, J.L., Reyna, R.R.: Phonon recycling and Shockley's diode equation. *J. Appl. Phys.* **82**, 4067 (1997)
44. Wolf, M.: Limitations and possibilities for improvement of photovoltaic solar energy converters. *Proc. IRE* **48**, 1246 (1960)
45. Luque, A., Marti, A.: The intermediate band solar cell: progress toward the realization of an attractive concept. *Adv. Mater.* **22**, 160 (2010)
46. Zhou, D., Vullum, P.E., Sharma, G., Thomassen, S.F., Holmestad, R., Reenaas, T.W., Fimland, B.O.: Positioning effects on quantum dot solar cells grown by molecular beam epitaxy. *Appl. Phys. Lett.* **96**, 083108 (2010)
47. Hubbard, S.M., Cress, C.D., Bailey, C.G., Raffaele, R.P., Bailey, S.G., Wilt, D.M.: Effect of strain compensation on quantum dot enhanced GaAs solar cells. *Appl. Phys. Lett.* **92**, 123512 (2008)
48. Oshima, R., Takata, A., Okada, Y.: Strain-compensated InAs/GaNAs quantum dots for use in high-efficiency solar cells. *Appl. Phys. Lett.* **93**, 083111 (2008)
49. Ross, R.T., Nozik, A.J.: Efficiency of hot-carrier solar energy converters. *J. Appl. Phys.* **53**, 3813 (1982)
50. Würfel, P.: Solar energy conversion with hot electrons from impact *ionization*. *Sol. Energy Mater. Sol. Cells* **46**, 43 (1997)
51. Kempa, K., Naughton, M.J., Ren, Z.F., Herczynski, A., Kirkpatrick, T., Rybczynski, J., Gao, Y.: Hot electron effect in nanoscopically thin photovoltaic junctions. *Appl. Phys. Lett.* **95**, 233121 (2009)
52. Schaller, R., Klimov, V.: High efficiency carrier multiplication in PbSe nanocrystals: implications for solar energy conversion. *Phys. Rev. Lett.* **92**, 186601 (2004)
53. Semonin, O.E., Luther, J.M., Beard, M.C.: Quantum dots for next generation photovoltaics. *Mater. Today* **15**, 508 (2012)
54. Nair, G., Chang, L.Y., Geyer, S.M., Bawendi, M.G.: Perspective on the prospects of a carrier multiplication nanocrystal solar cell. *Nano Lett.* **11**, 5 (2011)
55. Sablon, K.A., Little, J.W., Mitin, V., Sergeev, A., Vagidov, N., Reinhardt, K.: Strong enhancement of solar cell efficiency due to quantum dots with built-in charge. *Nano Lett.* **11**, 2311–2317 (2011)

56. Sablon, K., Sergeev, A., Vagidov, N., Antipov, A., Little, J., Mitin, V.: Effective harvesting, detection, and conversion of IR radiation due to quantum dots with built-in charge. *Nanoscale Res. Lett.* **6**, 584-1–584-13 (2011)
57. Sablon, K.A., Sergeev, A., Vagidov, N., Little, J.W., Mitin, V.: Effects of quantum dot charging on photoelectron processes and solar cell characteristics. *Sol. Energy Mater. Sol. Cells*; published on line: <http://dx.doi.org/10.1016/j.solmat.2012.10.002>.
58. Konstantatos, G., Badioli, M., Gaudreau, L., Osmond, J., Bernechea, M., Garcia de Arquer, F. P., Gatti, F., Koppens, F.H.L.: Hybrid graphene–quantum dot phototransistors with ultrahigh gain. *Nat. Nanotechnol.* **7**, 363 (2012)
59. Siegert, J., Marcinkevicius, S., Zhao, Q.X.: Carrier relaxation and electronic structure in InAs self-assembled quantum dots. *Phys. Rev. B* **72**, 085316-1–085316-7 (2005)
60. Adler, F., Geiger, M., Bauknecht, A., Scholz, F., Schweizer, H., Pilkuhn, M.H., Ohnesorge, B., Forchel, A.: Optical transitions and carrier relaxation in self assembled InAs/GaAs quantum dots. *J. Appl. Phys.* **80**, 4019–4026 (1996)
61. Schmidt, K.H., Medeiros-Ribeiro, G., Oestreich, M., Petroff, P.M., Döhler, G.H.: Carrier relaxation and electronic structure in InAs self-assembled quantum dots. *Phys. Rev. B* **54**, 11346 (1996)
62. Steer, M.J., Mowbray, D.J., Tribe, W.R., Skolnick, M.S., Sturge, M.D., Hopkinson, M., Cullis, A.G., Whitehouse, C.R., Murray, R.: Electronic energy levels and energy relaxation mechanisms in self-organized InAs/GaAs quantum dots. *Phys. Rev. B* **54**, 17738 (1996)
63. Chang, W.-H., Hsu, T.M., Huang, C.C., Hsu, S.L., Lai, C.Y., Yeh, N.T., Nee, T.E., Chyi, J.-I.: Photocurrent studies of the carrier escape process from InAs self-assembled quantum dots. *Phys. Rev. B* **62**, 6959 (2000)
64. Itskevitch, I.E., Skolnick, M.S., Mowbray, D.J., Trojan, I.A., Lyapin, S.G., Wilson, L.R., Steer, M.J., Hopkinson, M., Eaves, L., Main, P.C.: Excited states and selection rules in self-assembled InAs/GaAs quantum dots. *Phys. Rev. B* **54**, R2185–R2188 (1999)
65. Sergeev, A., Mitin, V., Strasser, G.: Nanostructures for long photoelectron lifetime. SPIE Newsroom, March 2010, <http://spie.org/x39405.xml>.
66. Chien, L.-H., Sergeev, A., Mitin, V., Oktyabrsky, S.: Quantum dot photodetectors based on structures with collective potential barriers. *Proc. SPIE* **7608**, 760826 (2010)
67. Martí, A., Antolín, E., García Linares, P., Ramiro, I., Artach, I., López, E., Hernández, E., Mendes, M.J. Mellor, A., Tobías, I., Fuertes Marrón, D., Tablero, C., Cristóbal, A.B., Bailey, C.G., Gonzalez, M., Yakes, M., Lumb, M.P., Walters, R., Luque, A.: Six not so easy pieces in intermediate band solar cell research. *Proc. SPIE* **8620**, Physics, Simulation, and Photonic Engineering of Photovoltaic Devices II, 86200J, 25 Mar 2013.

Chapter 4

Chalcopyrite Quantum Wells and Dots in Solar-Cell Applications

Esa Räsänen, Sascha Sadewasser, Sebastian Lehmann,
and David Fuertes Marrón

Abstract Chalcopyrite structures are promising candidates for efficient advanced solar cells in thin-film technology. Here we discuss the nanostructuring approach to thin-film photovoltaics and introduce the benefits and challenges of chalcopyrite materials for that purpose. We focus on chalcopyrite quantum wells and quantum dots by describing in detail the growth procedure as well as the theoretical modeling of the obtained structures. We demonstrate that both quantum wells and dots have, in principle, desirable characteristics for applications in photovoltaics.

1 Introduction

1.1 Chalcopyrite Structures in Thin-Film Photovoltaics

The trade-off between production costs and energy conversion efficiency determines the acceptance of photovoltaic (PV) technologies in the market. Chalcopyrite-based solar cells belong to thin-film (TF) approaches to PV.

E. Räsänen (✉)

Department of Physics, Tampere University of Technology, FI-33101 Tampere, Finland
e-mail: esa.rasanen@tut.fi

S. Sadewasser

International Iberian Nanotechnology Laboratory (INL), Avenida Mestre José Veiga,
4715-330 Braga, Portugal
e-mail: sascha.sadewasser@inl.int

S. Lehmann

Solid State Physics, Lund University, Box 118, S-22100 Lund, Sweden
e-mail: Sebastian.Lehmann@ftf.lth.se

D. Fuertes Marrón

Instituto de Energía Solar, ETSIT, Universidad Politécnica de Madrid,
Ciudad Universitaria, 28040 Madrid, Spain
e-mail: dfuertes@ies-def.upm.es

As such, and in contrast to wafer-based PV, the technological strategy has been to minimize the fabrication costs, largely associated to material requirements, while maintaining a reasonable efficiency record from the corresponding devices. The recent history of PV has shown the success of TF approaches, specifically that based on CdTe, with regard to positioning itself as a major player in the industrial sector [1].

Among TF technologies, however, CdTe is neither the most efficient type of device nor the one with the largest potential for improving its performance. Comparing the best small-area devices, those based on chalcopyrites are currently ahead of their CdTe counterparts by two percentage points. Furthermore, the best small-area chalcopyrite device is only one decimal point behind the best wafer-based polycrystalline Si solar cell [2]. Efficiency appears as a robust and objective indicator of the quality and the chances a given technology is capable of in terms of market acceptance. Considering efficiency as an indicator alone, it might then be tempting to imagine a scenario where chalcopyrite-based PV is a direct competitor of crystalline Si. However, such a comparison is unfair, and the market acceptance is nowadays largely set by the price of Si-based Watt-peak (Wp) as reference, currently as low as \$0.5/Wp [3]. Like for any other commercial product, the financial analysis of production costs is normally subject to market-driven fluctuations and biases of different nature affecting, for instance, the price of raw materials, the global economic scenario, and large-scale dumping strategies of significant playmakers. All of them are largely unpredictable in the long term. Whether the price of Si-based Wp will remain low or not is not predictable with certainty, although the history generally says that the price of technology is essentially a monotonically decreasing function of time.

Any alternative PV technology able at most to approximately level off poly-Si in terms of cost and efficiency is therefore not expected to have a significant impact on the market acceptance. It is necessary to go beyond that, either in cost, in efficiency or in both. As material scientists, we will just focus here on the efficiency issue. What can be done in this respect? On the road to higher efficiencies there are two main issues to be addressed by TF technologies:

- (1) for a technological process of choice, the upscaling from small up to large module areas;
- (2) a breakthrough of a new device concept demonstrating improved efficiencies superior to those of Si solar cells.

The former is a specific problem of all TF technologies related to a large extent to monolithic integration of cells into modules in a single processing step. No such problem affects wafer-based PV, where module assembly follows after individual cell sorting. In addition, to ensure homogeneity as required in the fabrication over large areas of films comprised within the device structure as thin as a few tens of nm is not trivial. As a matter of fact, the large gap between highest performances of chalcopyrite-based modules (15 %) and small cells (over 20 %) is to a large extent related to losses associated with monolithic interconnection and inhomogeneity. One may consider upscaling merely as a technological issue: independently of the

inner structure of the device and its performance, it is basically an engineering task to find the way to grow homogeneous layers and to reduce resistive losses. Something different applies to a new device concept.

In this respect, nanotechnology appears as the key to unlock many of the barriers imposed on conventional device architectures that limit their performance. Most of the device concepts belonging to the so-called third-generation PV [4] include nanotechnology in one way or another: quantum wells and quantum dots, multi-color absorbers and intermediate bands, multi-exciton generation and hot carriers, plasmonic enhancement, and light trapping; all of these are examples in which nanodimensional structures are foreseen as ingredients of novel solar cells. A general consensus seems to exist stating that it is through the incorporation of nanostructures how solar cells can surpass the limiting efficiencies imposed by the Shockley–Queisser limit [5].

Before entering the discussion in the next sections on how nanostructures can in principle boost efficiencies, it is also worth mentioning that nanotechnology is expected to play an important role not only in efficiency lift-off but also in reducing processing costs of functional cells. Non-vacuum deposition processes represent a significant advantage in terms of reduced processing costs in comparison to conventional evaporation or sputtering processes. Non-vacuum fabrication is normally based on rapid thermal processing of precursors that utilize inks consisting of emulsions formed by colloidal nanocrystals of the active absorber material in a dispersing medium [6–8]. In addition, this type of material can be used in either organic/inorganic composites [9, 10] or in fully inorganic structures, like porous $\text{TiO}_2/\text{Cu}(\text{In,Ga})\text{S}_2$ -nanocrystal injection cells [11, 12]. These type of processes are currently under development, and they still have to demonstrate whether a sufficient level of device performance, at least comparable to vacuum-based devices, is attainable.

1.2 Nanostructuring Approach: Techniques and Challenges

There has been an increasing number of contributions related to the growth and characterisation of chalcopyrite nanocrystals in recent years (see [13] and references therein). By far, the most of the literature on the topic has considered approaches based on wet chemistry and solvothermal methods, whereby colloidal suspensions and inks are produced for non-vacuum growth processes of conventional devices. Such “wet” processes have resulted in a variety of nanoshapes, including cubes, rods, whiskers, spheres, polyhedra, and beads, also provided with various coatings in subsequent chemical processes.

On the other hand, novel device architectures including nanostructured materials will require the incorporation of nanostructures into solid-state matrices—a difficult task with scarce related literature [9, 10, 13–18].

In principle, conventional deposition methods like molecular beam epitaxy (MBE) or metal-organic vapor phase epitaxy (MOVPE) can be employed for the

growth of chalcopyrite materials and nanostructures, in a similar fashion as used for III–V and II–VI compounds. Such methods allow fine control on the deposition parameters and growth of single crystals in the form of epitaxial layers, when substrates are appropriately selected. Heteroepitaxy is the method of choice for the growth of quantum wells. It can also be used for the growth of three-dimensional nanocrystals acting as quantum dots and permits control between Volmer–Weber and Stranski–Krastanov growth modes. The heteroepitaxy approach will be discussed in the next sections for the cases of quantum dots and wells.

Borrowing methods from wafer-based technologies, however, adds little value by itself to the main advantage of chalcopyrites for PV applications. When speaking of TF-PV one is implicitly speaking of microcrystalline (even amorphous) materials as active layers. The tolerance of such materials to the presence of numerous defects in the crystal lattice must be significant if operative devices can be constructed from them. Such tolerance is well known from devices made of chalcopyrites and CdTe in the form of microcrystalline TFs, devices which do not count with single-crystalline counterparts outperforming them like in the case of III–V, II–VI, or group-IV-based solar cells. It is also of interest to explore ways of incorporating nanostructured material without losing the inherent flexibility of processing materials not too demanding in terms of crystallinity and perfection.

In fact, the nature of chalcopyrite compounds makes them relatively easy to incorporate as nanostructures into certain binary or multinary semiconductors with which they share atomic species, even in the form of microcrystalline layers. Such an approach has been demonstrated before [17, 18], and appears particularly suitable as it can be implemented with standard deposition methods like those employed in industrial scale production. The method profits from the well-known band gap anomaly of ternary (and higher order alloy) compounds of the type I–III–VI₂ with respect to their related II–VI binaries [19]. The anomaly refers to a significant reduction in the value of the band gap observed when comparing I–III–VI₂ compounds with their II–VI relatives, e.g. CuGaS₂ vs. ZnS, or even with III₂VI₃ compounds like Ga₂S₃. If the two elements contained in the binary compound (to act as barrier, with a large gap) are all included in the ternary compound (to act, e.g., as quantum dot with a lower gap), pulsed provision of the third species in the ternary may serve as a switch for the deposition of dot and barrier materials, alternatively. Furthermore, use can be made of metallic precursors, like copper, in order to separate “nanostructuring” from “embedding” mechanisms. The size and distribution of nanoscopic precursors on the surface acting as substrate (not necessarily monocrystalline) will determine the dimensions and distribution of the semiconducting nanostructure when processed chemically, whereas the deposition method (chemical deposition, physical evaporation or thermal annealing) will control the simultaneous formation of the ternary compound and the embedding of the nanostructure into the selected matrix compound. Furthermore, the process can be optimized as to yield bare nanostructures instead of buried ones, as to grow selectively on patterned surfaces and to scale the process from nano-, to meso- up to macroscopic dimensions [17, 18].

Regardless of the methods in use for the growth of active material and geometries foreseen, little impact would be expected from nanostructured chalcopyrites if evidences of quantum confinement could not be demonstrated. Experimental evidence of size-dependent light emission in chalcopyrite nanocrystals in the form of colloidal suspensions has been reported though [20–23], opening the door to the incorporation of electronic confining effects into chalcopyrite-based devices. It is worth mentioning at this point that optical response of nanostructures is a necessary property for any type of operative photovoltaic device based on the action of such nanostructures as light absorbers—not only in terms of light absorption but, perhaps most importantly, in terms of light emission as result of carrier recombination mechanisms. As a matter of fact, luminescence is the key factor determining ultimately whether such a device would operate in the radiative limit and thus if maximum efficiencies can be expected from it.

In the following sections we will focus on two particular aspects of chalcopyrite-based nanostructures with regard to new device architectures and possible ways to improve their performance over that of current record holders. We will describe the growth and properties of quantum wells and quantum dots, highlighting the main properties and issues raising up from quantum confinement effects in one and three dimensions and discussing ways to exploit such effects in operating devices.

2 Chalcopyrite Quantum Wells

2.1 Growth Procedure

Quantum-well structures are typically grown using MBE or MOVPE. Both methods allow for a high level of compositional and spatial control of the deposited layers. While quantum-well structures are frequently realized using III–V or II–VI material systems, reports of chalcopyrite-based quantum wells are very limited [24, 25]. Chalcopyrite-based quantum-well superlattices can result in improved excitonic absorption compared to bare films, leading to a potential enhancement in efficiency figures. For these studies, several different CuInSe₂ and CuGaSe₂ quantum well samples have been grown in a commercial MOVPE system (AIXTRON AIX200SC). Various metal-organic compounds were used as precursors for copper, gallium, indium, and selenium, namely: cyclopentadienyl-coppertriethylphosphine (Cp-CuTEP), triethylgallium (TEGa), trimethylindium (TMIn), and ditert-butylselenide (DTBSe). Epiready GaAs:Zn (100) wafers (EpiChem) were used as substrates.

Prior to growth, the substrates were annealed in hydrogen atmosphere at a temperature of 650 °C before setting the growth temperatures to $T_{\text{sub}} = 500$ °C for CuInSe₂ and $T_{\text{sub}} = 570$ °C for CuGaSe₂, respectively. Samples were grown with a ratio of $[\text{Cu}]/[\text{Ga}] \approx 0.9$ for the nominal value of the incoming precursor fluxes which corresponds to slightly Cu-poor conditions. The validity of this

procedure is based on the rather forgiving chemistry of the considered chalcopyrite materials for Cu-poor off-stoichiometries. Further, it assures the suppression of parasitic Cu_{1-x}Se phase formation [26, 27]. Details of the growth conditions and its optimization can be found elsewhere [28, 29].

For this exploratory study of the possibility to grow chalcopyrite quantum wells, several samples were prepared. For comparative purposes, single CuInSe_2 or CuGaSe_2 layers were grown on the $\text{GaAs}(100)$ substrate as references using identical growth conditions as used for multilayer structures. The final layer thickness of these single layer samples was about 350 nm. Those samples served as references in order to compare material properties of thick layers with the thin ones as prepared in the multilayer stack samples. A multilayer stack sample was grown consisting of 50 nm layers with the following sequence $\text{GaAs}/\text{CuGaSe}_2/\text{CuInSe}_2/\text{CuGaSe}_2$. This stack provides a CuInSe_2 well surrounded by CuGaSe_2 barriers. For this sample, the top CuGaSe_2 layer was grown at $T_{\text{sub}} = 500$ °C instead of the usual 570 °C, in order to avoid exposure of the CuInSe_2 quantum well to a temperature higher than its growth temperature. However, for photoluminescence experiments, this stack sequence is not optimal, as the light emitted from the CuGaSe_2 bottom barrier can be reabsorbed by the CuInSe_2 well. Therefore, an additional multilayer sample was fabricated with a sequence of $\text{GaAs}/\text{CuInSe}_2/\text{CuGaSe}_2/\text{CuInSe}_2$.

One important difference between chalcopyrite semiconductors and widely used III–V semiconductors is the process of doping. While for III–V semiconductors, active extrinsic doping is necessary and typically applied during the growth, the Cu-chalcopyrites are not extrinsically doped. For most of the investigated growth processes including MBE and MOVPE chalcopyrites normally show p-type conductivity. This behavior is mainly explained by the spontaneous formation of intrinsic defects during preparation. It leads to a net excess of Cu vacancies and thus to the commonly reported conductivity behavior [30].

The multilayer structure was analyzed using energy dispersive X-ray spectroscopy (EDX) in a transmission electron microscope (TEM), to study interdiffusion phenomena of In and Ga between the quantum well and the barrier layers. Figure 4.1 shows the elemental distribution (intensity of the L-emission) of Cu, Ga, In, Se, and As through the layer stack. The interface between the GaAs substrate and the chalcopyrite layer stack is clearly resolved. While Cu and Se appear homogeneously distributed throughout the entire layer stack, In and Ga exhibit an inhomogeneous distribution. Both elements, In and Ga, are observed in all three layers of the stack, despite the nominal growth of a $\text{CuGaSe}_2/\text{CuInSe}_2/\text{CuGaSe}_2$ sequence. This indicates a significant diffusion of In and Ga on the cation sublattice at the growth temperatures. Nevertheless, the In concentration in the center of the layer stack is higher compared to the surrounding layers. In contrast, the Ga concentration is higher in the embedding layers compared to the centered one. This can be more clearly seen in the extracted line profiles of the elemental distribution along the growth direction of the layer stack as displayed in Fig. 4.1g. This elemental distribution was also independently confirmed by secondary ion mass spectrometry (SIMS) measurements [25]. In addition to the

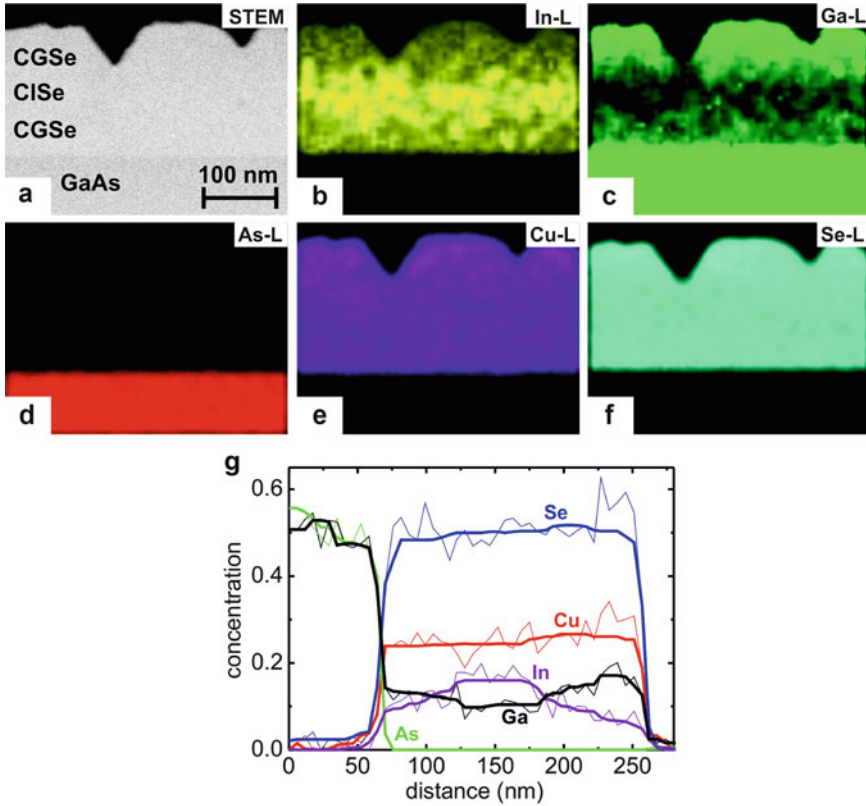


Fig. 4.1 (a) Scanning TEM image of a GaAs/CuGaSe₂/CuInSe₂/CuGaSe₂ multilayer stack. EDX mappings showing the intensity of the L-emission lines of the elements (b) In, (c) Ga, (d) As, (e) Cu, and (f) Se. The relative elemental concentration is proportional to the intensity. (g) Line profiles of the elemental distribution along the growth direction obtained from the EDX maps. Despite a strong interdiffusion of In and Ga throughout the three chalcopyrite layers, the center CuInSe₂ layer shows a significantly higher In concentration than the surrounding CuGaSe₂ layers. Figures adapted from [24, 25]

variation of In and Ga along the growth direction of the multilayer stack, an inhomogeneous distribution in the lateral direction can also be observed. Spots of about 10–30 nm size with an increased In content can clearly be observed from Fig. 4.1b.

2.2 Modeling of the Multilayer Sample

In order to assess quantum confinement in the CuInSe₂ layer, the multilayer stack has to be modeled. In particular, the band diagram of the stack is needed. The depth profile of the Cu(In,Ga)Se₂ material composition can be extracted from the EDX

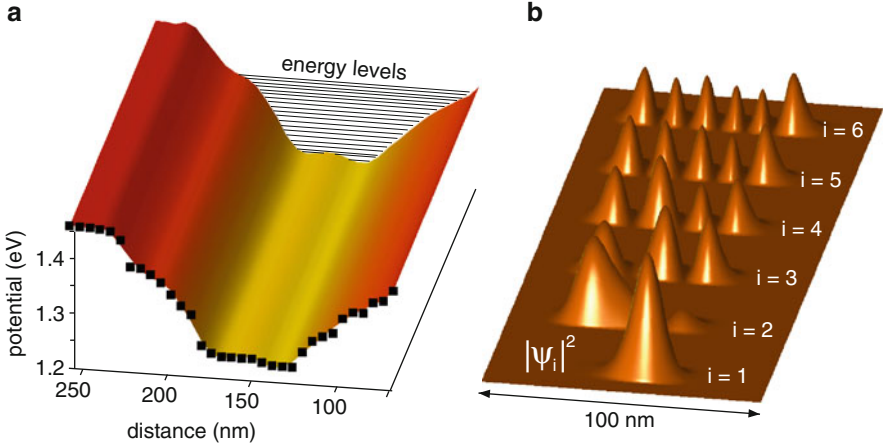


Fig. 4.2 (a) Quantum-well potential obtained through polynomial fitting to the measured profile (squares) and the first quantized energy levels (lines). (b) Squares of the first six eigenstates confined in the potential. Figures adapted from [25]

results shown in Fig. 4.1g. The band gap E_g of $\text{CuIn}_{1-x}\text{Ga}_x\text{Se}_2$ depends on the composition x as

$$E_g(x) = (1 - x)E_g(\text{CuInSe}_2) + xE_g(\text{CuGaSe}_2) - bx(1 - x), \quad (4.1)$$

where $b = 0.21$ is the bowing factor [31]. The band offset between CuGaSe_2 and CuInSe_2 is expected to evolve only in the conduction band. Hence, a CuInSe_2 well is formed for electrons between CuGaSe_2 barriers. Here we neglect the small valence band offset between CuGaSe_2 and CuInSe_2 . Now, the composition profile x for the In/Ga ratio can be obtained as a function of position. Further, using (4.1) we can obtain the band gap as function of position, see the square points in Fig. 4.2a. This result can now be applied as a model potential in order to calculate the quantized energy levels.

2.3 Quantum Confinement

The measured profile in Fig. 4.2a (square points) is modeled by fitting a one-dimensional polynomial in the 17th order. The result of the fit is taken as an external confining potential for the electronic states in the quantum well. The energy levels of the quantized states are then obtained by solving the (one-dimensional) single-particle Schrödinger equation. The effective-mass approximation [32] with material parameters $m^* = 0.1m_e$ and $\epsilon = 5\epsilon_0$ was used.

As shown in Fig. 4.2a (solid lines), several (~ 20) confined states were obtained. Within a two- or three-dimensional model the number of confined states would be

even larger due to additional symmetry leading to degenerate states. Figure 4.2b shows the squares of the first six eigenstates confined in the quantum-well model. The first state clearly localizes at the global minimum of the potential, whereas the second state localizes in the neighboring local minimum. The higher states then form a rather regular nodal structure and a pattern of Gaussian-shaped peaks.

In conclusion of this part, distinctive quantum wells can be grown of chalcopyrite materials with the MOVPE technique. Considerable interdiffusion between In and Ga at the interfaces leads to a smooth conduction band profile between the well and the barriers. Theoretical modeling gives clear signatures of quantum confinement in the CuInSe₂ well. In the future, more efforts are needed to fabricate smaller CuInSe₂ wells as well as multilayer stacks that include several quantum wells. Experimental evidence of electronic confinement for this structure was in fact reported based on modulation spectroscopy results [24].

3 Chalcopyrite Quantum Dots

3.1 Growth Procedure

For the growth of chalcopyrite quantum dots, a variety of different approaches have been reported. Solution-based methods result in colloidal particles, while dry deposition methods have been used to grow nanodots on substrate surfaces, or embedded into a matrix material. Colloidal nanoparticles have been fabricated from solution resulting in different chalcopyrite compounds including CuInSe₂, CuGaSe₂, and CuInS₂ [33–35]. One application for such nanoparticles is their deposition onto a Mo/glass substrate and subsequent sintering of this nanoparticle layer into a thin film [36, 37]. This approach aims at the fabrication of regular thin film devices by a rather cost-effective method. Since this approach does not lead to a high-efficiency solar cell exploiting the quantum effects of the nanoparticles, it is not considered further in this chapter. In other applications of such colloidal nanoparticles the aim is to provide the nanoparticle for an effective absorption of light, possibly covering various parts of the solar spectrum and transfer the excited charge carriers into an electron acceptor material, e.g. TiO₂ [12]. The function of the nanoparticle in this approach is similar to that of dye molecules and such solar cells are called nanoparticle-sensitized solar cells [38]. While the quantum effect can possibly be exploited in these approaches, prototype solar cells have typically low efficiencies and stability is a critical issue also.

The growth of chalcopyrite quantum dots has also been realized following the standard dry deposition methods applied for the growth of III–V quantum dots, namely MBE and MOVPE. MBE growth has been realized for CuGaSe₂ on Si(111) substrates. The single elements were evaporated from effusion cells onto the substrate at a temperature of $T_{\text{sub}} = 600$ °C and the growth time was set to 10 min. Figure 4.3b shows an overview scanning electron microscopy (SEM)

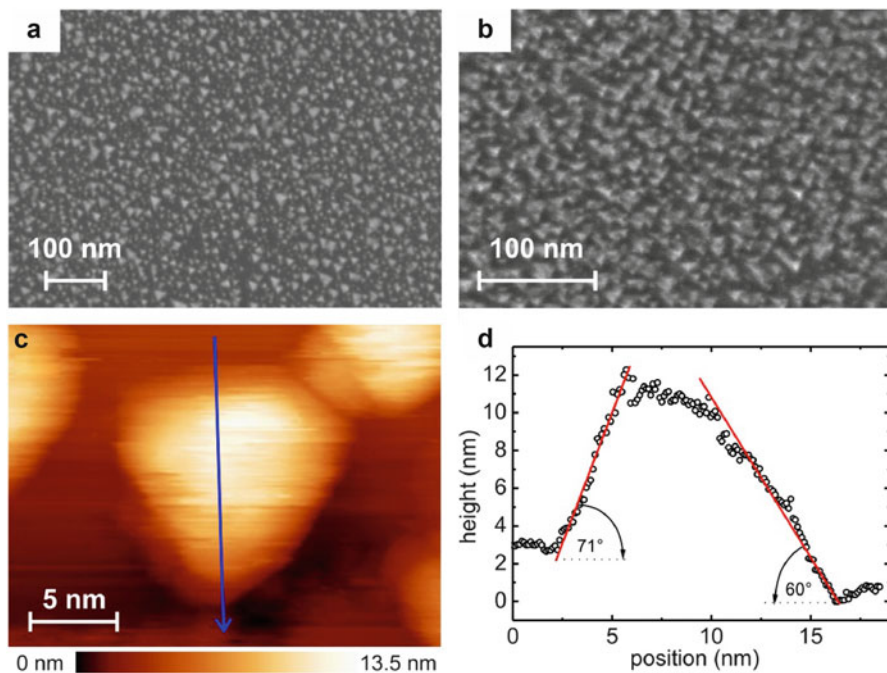


Fig. 4.3 (a) SEM *top view* image of CuInSe₂ nanodots grown by MOVPE on a Si(111) substrate. (b) SEM *top view* image of CuGaSe₂ nanodots grown by molecular beam epitaxy on a Si(111) substrate. (c) STM image of one individual CuGaSe₂ nanodot. (d) Height profile of the CuGaSe₂ nanodot showing the relevant angles of the side and the facets, as determined from the topography. Figure reproduced with permission from Applied Physics Letters [44]

image of a representative sample after deposition and Fig. 4.3c a scanning tunneling microscopy (STM) image of a single quantum dot. The geometry of the resulting quantum dots was analyzed from an average of numerous STM height profiles, as displayed in Fig. 4.3d. The shape was found to be close to that of a tetrahedron and independently confirmed by transmission electron microscopy. MOVPE has also been successfully used for the preparation of CuInSe₂ and CuGaSe₂ quantum dots. Figure 4.3a shows an overview image for the growth of a 5 min CuInSe₂ deposition onto a Si(111) substrate at $T_{\text{sub}} = 500$ °C. This growth was performed in an Aixtron AIX200SC MOVPE using the metal-organic compounds cyclopentadienyiltrisethylphosphinecopper (CPTPC), trimethylindium (TMIn), triethylgallium (TEGa), and ditertiarybutylselenide (DTBSe). Nanodot growth has been realized over a broad temperature range from 500 to 620 °C for both CuInSe₂ and CuGaSe₂ materials.

A different growth approach without the requirement of an epitaxial substrate is based on decoupling the nanostructuring step from the reaction step forming the chalcopyrite compound [17, 18]. In a first step, Cu precursors are deposited in a nanostructured way, for example by self-assembly or masks onto an

arbitrary substrate. In the second step, a reactive atmosphere containing i.e. In and Se is supplied to transform the Cu-dots into CuInSe_2 dots. As a function of the reaction conditions, the growth can be tuned to deposit a binary matrix material simultaneously to the chemical reaction of converting the Cu precursor dots into chalcopyrite material.

Yet another approach [24] is to embed quantum dots into a wider band gap absorber material, with a growth process as similar as possible to conventional chalcopyrite TF growth. The device structure was designed to lead to a conceptual intermediate band absorber with CuInS_2 quantum dots embedded in an In_2S_3 matrix material. This material combination could in principle result in quantum dots entirely surrounded by a higher band gap ($E_g = 2.0$ eV) matrix material. The samples were grown as polycrystalline layers on Mo-coated, Na-free glass (Corning 7059) using physical vapor deposition and a substrate temperature of $T_{\text{sub}} = 200$ °C. A metal precursor sequence of In (55 nm)/Cu(1 nm)/In(60 nm)/Cu(1 nm)/In(65 nm)/Cu(1 nm)/In(70 nm) was used during constant supply of sulfur, leading to an overall $[\text{Cu}]/([\text{Cu}] + [\text{In}])$ ratio of 2–3 at.%. Reference indium sulfide samples without Cu addition were also grown.

3.2 Modeling of Tetrahedral Quantum Dots

Next we turn our attention into theoretical modeling of tetrahedral chalcopyrite quantum dots shown in Fig. 4.3. It is noteworthy that here we do not resort to atomistic ab initio calculations but apply the effective mass approximation [32] and solve the electronic states in a model potential. Recent discussion about the challenges of first-principles calculations on chalcopyrite materials can be found, e.g., in [39, 40] and in references therein. These atomistic approaches to *confined* chalcopyrite nanostructures (such as quantum dots) are particularly challenging as the systems cannot be handled computationally using periodic cells.

As in Sect. 2.3 we apply the effective-mass approximation by assuming that the electrons are near the band minimum, where the band can be approximated as parabolic. In general, the effective mass approximation has a few drawbacks. For example, the space dependence of the effective mass and the dielectric constant in heterostructures can lead to non-parabolicity of the energy bands near $k = 0$ [41]. In practice, however, the effective mass approximation has been successfully used in various electronic-structure calculations on semiconductor (such as GaAs and InAs) quantum dots [42]. Here we use the electron effective mass in the CuInSe_2 QD $m^* = 0.09m_0$. As another assumption, the electronic wave functions are not expected to penetrate deep into the matrix material. Hence, we may use the same dielectric constant throughout both the quantum dot and the matrix material, i.e., $\epsilon = 15.1$ [43].

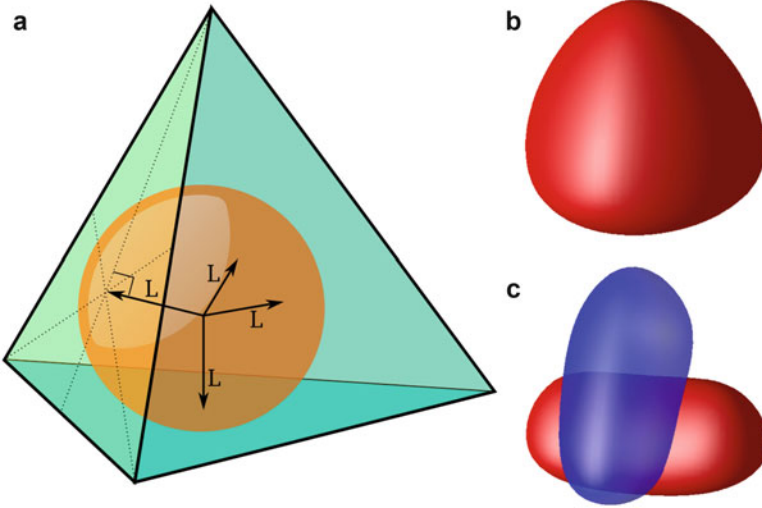


Fig. 4.4 (a) Tetrahedral model potential used in the calculations. The distance $L = 4.42$ nm is the radius of the sphere fitting inside the tetrahedron. (b, c) Eigenfunctions of the lowest and second lowest bound states, respectively, in the system. The *red* and *blue* surfaces correspond to constant values 41 and -41 nm $^{-3/2}$, respectively. The viewing angle is the same as for the external model potential in (a)

Based on the SEM image and the height profile of the quantum dot (Fig. 4.3) we construct a model potential for the electronic confinement in the quantum dot. The external model potential, that essentially accounts for the surroundings of the conduction-band electrons, is given by

$$V_{\text{ext}}(\mathbf{r}) = -V_0 \exp\left[\frac{-(\mathbf{r} \cdot \mathbf{n}_i)^2}{2L^2}\right], \quad (4.2)$$

where \mathbf{n}_i are the normal vectors of the faces of the tetrahedron and L is the radius of the quantum dot, or, more explicitly, it is the radius of the sphere fitting inside the tetrahedron as visualized in Fig. 4.4a.

The radius of the typical grown dot in Fig. 4.3 is approximately $L_{\text{exp}} = 3, \dots, 4$ nm. The depth of the potential $V_0 = 1.18$ eV is set to be equal to the conduction band offset between the dot and the matrix materials [44]. The Gaussian tail in V_{ext} models the slowly varying confinement at the smooth interface between the quantum dot and matrix regions. On the other hand, the Gaussian form is approximately harmonic close to the dot center; this is a reasonable approximation in view of previous quantum dot studies (for recent combined works of experiment and theory verifying the validity of a harmonic model potential, see, e.g., [42, 45, 46]).

OCTOPUS code package [47] was used in solving the static single-particle Schrödinger equation with the external potential in (4.2). OCTOPUS is a versatile tool for dealing with both static and time-dependent electronic-structure

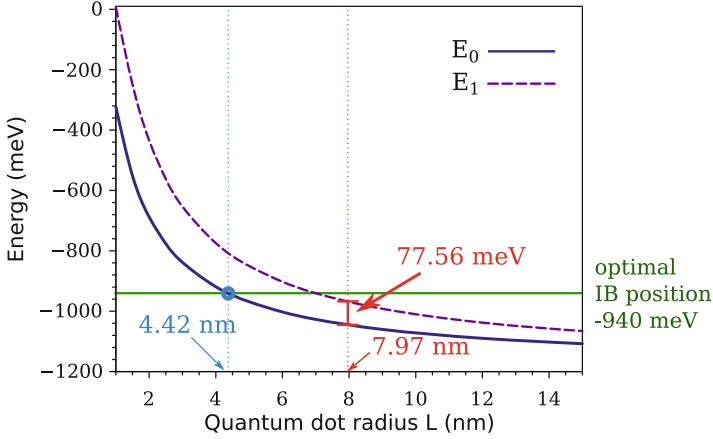


Fig. 4.5 Energies of the first and second electronic states of a CuInSe₂ dot in a CuGaS₂ matrix as a function of the quantum dot size L [see Fig. 4.4a]. The *solid horizontal line* marks the optimal intermediate-band position corresponding to the radius of 4.42 nm (*left dotted line*). The *right dotted line* marks the maximum size of the quantum dot to satisfy the thermal constraint (see text). The bound-state constraint corresponds the left border of the figure (~ 1 nm). Figure reproduced with permission from Applied Physics Letters [44]

calculations—especially within the density-functional theory framework—in real space and real time. It is a free software published under the GPL license. Here the grid spacing was $L/70$, leading to about 1,400,000 grid points altogether.

The eigenfunctions of the two lowest bound states are shown in Fig. 4.4b and c, respectively. The lowest state resembles an atomic 1s orbital with a slight tetrahedral deviation, whereas the second lowest state has a planar node across the tetrahedron. The two lowest energy levels as a function of the quantum dot size L are shown in Fig. 4.5 (higher levels omitted in the figure). The energies are compared to the optimal intermediate-band position at -940 meV that can be obtained from the procedure introduced by Luque and Martí [48]. In principle, the optimal position yields maximum efficiency of 61.1 % in concentrated sunlight. This is close to the *overall* maximum of an intermediate-band solar cell that is as high as 63.2 %. In fact, significant recent advances have been achieved in Sn-doped chalcopyrites that show wide-spectrum solar response [49]. Here, the crossing point between the optimal position and the ground-state energy is found at $L_{\text{opt}} = 4.42$ nm. This can be regarded as the optimal size of the quantum dot, which qualitatively agrees very well with the sizes of the grown samples (Fig. 4.3).

Finally, we can verify that the optimal quantum dot size satisfies two important physical constraints. First, the *minimum* dot diameter, ensuring the existence of at least one bound state, is given by [50]

$$D_{\min} = \frac{\pi\hbar}{\sqrt{2m^*\Delta E_b}}, \quad (4.3)$$

and ΔE_b is the energy barrier between the dot and the matrix, i.e., the conduction band offset (electrons) or the valence band offset (holes). For our system this condition yields $L_{\min} = 0.94$ nm, which corresponds to the left boundary in Fig. 4.5. On the other hand, the *maximum* quantum-dot size can be estimated from the requirement that the thermal population of the excited states remains small [51]. If we require less than 5 % occupation at room temperature 300 K, the level separation needs to be

$$kT \leq \frac{1}{3} |E_1 - E_0|, \quad (4.4)$$

where E_0 and E_1 are the first two energy levels of the dot. This condition yields $L_{\max} = 7.97$ nm marked in Fig. 4.5.

In conclusion of this section, we have constructed a realistic model for the single chalcopyrite quantum dot and have shown that the dot size that yields the optimal efficiency is in qualitative agreement with the grown experimental samples. In addition, the important condition for the existence of a bound state, as well as the thermal condition for the level population, are satisfied. However, application of chalcopyrite quantum dots in an intermediate-band solar cell requires controlled growth of periodic tetrahedral nanodots regarding their size, shape, and structuring.

Acknowledgements This work was supported by the Academy of Finland, the Fortum Foundation, and the European Community's FP7 through the CRONOS project, grant agreement no. 280879.

References

1. Jäger-Waldau, A.: PV-Status Report 2012, p. 28. European Union (2012). Available at <http://re.jrc.ec.europa.eu/>
2. Green, M.A., Emery, K., Hishikawa, Y., Warta, W., Dunlop, E.: Prog. Photovolt.: Res. Appl. **21**, 1 (2013)
3. Photon International, January 2013, p. 63
4. Green, M.A.: Third Generation Photovoltaics, Advanced Solar Energy Conversion. Springer, New York (2006)
5. Shockley, W., Queisser, H.J.: J. Appl. Phys. **32**, 510 (1961)
6. Guo, Q., Kim, S.J., Kar, M., Shafarman, W.N., Birkmire, R.W., Stach, E.A., Agrawal, R., Hillhouse, H.W.: Nano Lett. **8**, 2982 (2008)
7. Guo, Q., Ford, M., Hillhouse, H.W., Agrawal, R.: Nano Lett. **9**, 3060 (2009)
8. Panthani, M.G., Akhavan, V., Goodfellow, B., Schmidtke, J.P., Dunn, L., Dodabalapur, A., Barbara, P.F., Korgel, B.A.: J. Am. Chem. Soc. **130**, 16770 (2008)
9. Arici, E., Sariciftci, N.S., Meissner, D.: Adv. Funct. Mater. **13**, 165 (2003)
10. Kruszynska, M., Knipper, M., Kolny-Olesiak, J., Borchert, H., Parisi, J.: Thin Solid Films **519**, 7374 (2011)
11. Nanu, M., Schoonman, J., Goossens, A.: Nano Lett. **5**, 1716 (2005)
12. Santra, P.K., Nair, P.V., Thomas, K.G., Kamat, P.V.: J. Phys. Chem. Lett. **4**, 722 (2013)

13. Fuertes Marrón, D.: Thin film technology in intermediate band solar cells: advanced concepts for chalcopyrite solar cells. In: Cristóbal, A.B., Martí, A., Luque, A. (eds.) *Next Generation of Photovoltaics*, p. 277. Springer, Berlin (2012)
14. Bodnar, I.V., Gurin, V.S., Molochko, A.P., Solovei, N.P., Prokoshin, P.V., Yumashev, K.V.: *Semiconductors* **36**, 298 (2002)
15. Bodnar, I.V., Gurin, V.S., Molochko, A.P., Solovei, N.P.: *Inorg. Mater.* **40**, 797 (2004)
16. Arici, E., Meissner, D., Schäffler, F., Sariciftci, N.S.: *Int. J. Photoenergy* **5**, 199 (2003)
17. Fuertes Marrón, D., Lehmann, S., Kosk, J., Sadewasser, S., Lux-Steiner, M.Ch.: *Mater. Res. Soc. Symp. Proc.* **1012**, Y02-07 (2007)
18. Fuertes Marrón, D., Lehmann, S., Lux-Steiner, M.Ch.: *Phys. Rev. B* **77**, 085315 (2008)
19. Jaffe, J.E., Zunger, A.: *Phys. Rev. B* **27**, 5176 (1983)
20. Kuo, K.T., Chen, S.Y., Cheng, B.M., Lin, C.C.: *Thin Solid Films* **517**, 1257 (2008)
21. Li, D., Zou, Y., Yang, D.: *J. Lumin.* **132**, 313 (2012)
22. Allen, P.M., Bawendi, M.G.: *J. Am. Chem. Soc.* **130**, 9240 (2008)
23. Hamanaka, Y., Ogawa, T., Tsuzuki, M., Kuzuya, T.: *J. Phys. Chem. C* **115**, 1786 (2011)
24. Fuertes Marrón, D., Cánovas, E., Levy, M.Y., Martí, A., Luque, A., Afshar, M., Albert, J., Lehmann, S., Abou-Ras, D., Sadewasser, S., Barreau, N.: *Sol. Energy Mater. Sol. Cells* **94**, 1912 (2010)
25. Afshar, M., Sadewasser, S., Albert, J., Lehmann, S., Abou-Ras, D., Fuertes Marrón, D., Rockett, A.A., Räsänen, E., Lux-Steiner, M.Ch.: *Adv. Energy Mater.* **1**, 1109 (2011)
26. Mikkelsen, J.C.J.: Ternary phase relations of the chalcopyrite compound CuGaSe₂. *J. Electron. Mater.* **10**, 541–558 (1981)
27. Goedecke, T., Haalboom, T., Ernst, F.: Phase equilibria of Cu–In–Se I–III. *Z. Metallkd.* **91**, 622–662 (2000)
28. Bauknecht, A., Siebentritt, S., Albert, J., Lux-Steiner, M.Ch.: *J. Appl. Phys.* **89**, 4391 (2001)
29. Rega, N., Siebentritt, S., Albert, J., Nishiwaki, S., Zajogin, A., Lux-Steiner, M.Ch., Kniese, R., Romero, M.: *Thin Solid Films* **480–481**, 286 (2005)
30. Siebentritt, S., Igalson, M., Persson C., Lany, S.: *Prog. Photovolt.: Res. Appl.* **18**, 390 (2010)
31. Wei, S.-H., Zunger, A.: *J. Appl. Phys.* **78**, 3846 (1995)
32. See, e.g., Ullrich, C.: In: Marques, M.A.L., Ullrich, C.A., Nogueira, F., Rubio, A., Burke, K., Gross, E.K.U. (eds.) *Time-Dependent Density Functional Theory. Lecture Notes in Physics*, pp. 271–285. Springer, Berlin (2006)
33. Zhong, H., Li, Y., Ye, M., Zhu, Z., Zhou, Y., Yang, C., Li, Y.: *Nanotechnology* **18**, 025602 (2007)
34. Peng, S., Liang, Y., Cheng, F., Liang, J.: *Sci. China Chem.* **55**, 1236–1241 (2012)
35. Panthani, M.G., Akhavan, V., Goodfellow, B., Schmidtke, J.P., Dunn, L., Dodabalapur, A., Barbara, P.F., Korgel, B.A.: *J. Am. Chem. Soc.* **130**, 16770–16777 (2008)
36. Guo, Q., Kim, S.J., Kar, M., Shafarman, W.N., Birkmire, R.W., Stach, E.A., Agrawal, R., Hillhouse, H.W.: *Nano Lett.* **8**, 2982 (2008)
37. Guo, Q., Ford, G.M., Hillhouse, H.W., Agrawal, R.: *Nano Lett.* **9**, 3060 (2009)
38. O'Regan, B., Grätzel, M.: *Nature* **353**, 737–740 (1991)
39. Vidal, J., Botti, S., Olsson, P., Guillemoles, J.-F., Reining, L.: *Phys. Rev. Lett.* **104**, 056401 (2010)
40. Oikkonen, L.E., Ganchenkova, M.G., Seitsonen, A.P., Nieminen, R.M.: *Phys. Rev. B* **86**, 165115 (2012)
41. Burt, M.G.: *J. Phys. Condens. Matter* **4**, 6651 (1992)
42. For a review, see Reimann, S.M., Manninen, M.: *Rev. Mod. Phys.* **74**, 1283 (2002)
43. Syrbu, N.N., Bogdanas, M., Tezlevan, V.E., Mushcutariu, I.: *Physica B* **229**, 199 (1997)
44. Ojajarvi, J., Räsänen, E., Sadewasser, S., Lehmann, S., Wagner, Ph., Lux-Steiner, M.Ch.: *Appl. Phys. Lett.* **99**, 111907 (2011)
45. Räsänen, E., Saarikoski, H., Harju, A., Ciorga, M., Sachrajda, A.S.: *Phys. Rev. B* **77**, 041302 (R) (2008)
46. Rogge, M.C., Räsänen, E., Haug, R.J.: *Phys. Rev. Lett.* **105**, 046802 (2010)

47. Castro, A., Appel, H., Oliveira, M., Rozzi, C.A., Andrade, X., Lorenzen, F., Marques, M.A.L., Gross, E.K.U., Rubio, A.: *Phys. Status Solidi (b)* **243**, 2465 (2006)
48. Luque, A., Martí, A.: *Phys. Rev. Lett.* **78**, 5014 (1997)
49. Yang, C., Qin, M., Wang, Y., Wan, D., Huang, F., Lin, J.: *Sci. Rep.* **3**, 1286 (2013)
50. Bimberg, D., Grundmann, M., Ledentsov, N.N.: *Quantum Dot Heterostructures*. Wiley, Chichester (1998)
51. Fuertes Marrón, D., Martí, A., Luque, A.: *Phys. Status Solidi A* **206**, 1021 (2009)

Chapter 5

Nanostructured Silicon-Based Photovoltaic Cells

Mohamed M. Hilali and S.V. Sreenivasan

Abstract In recent years significant research has been conducted on the materials, design, and device physics of nanostructured solar cells to obtain enhanced performance. While there are several promising results, practical deployment of these nanostructured cells is quite limited due to the need for (1) cost-effective, scalable fabrication techniques; (2) readily available raw materials; and (3) cells that can reliably perform as installed with minimal performance degradation. This book chapter focuses on nanostructured silicon solar cells. Silicon has been chosen in this chapter as it is an abundantly available raw material; silicon cells are well understood due to broad deployment of conventional monocrystalline, multi-crystalline, and amorphous silicon solar cells; and silicon cells also are by far the dominant one in terms of production scale in the photovoltaic industry.

The book chapter is divided into five sections and mainly focuses on nanostructured silicon-based solar cells to evaluate their potential for enhanced performance beyond conventional, commercial silicon cells. Section 1 discusses the value of nanoscale patterning in wafer-based crystalline silicon (c-Si) solar cells (e.g., mono- and multi-crystalline silicon). In Sect. 2 of the book chapter nanostructured designs that relate mainly to the electronic performance of the solar device are reviewed. In this category, nanostructured thin-film solar cells for enhanced carrier collection or enhanced internal quantum efficiency (such as nano-wire array solar cells) are illustrated. In Sect. 3 nanostructured hybrid silicon-organic solar cells are illustrated. Section 4 discusses nanostructured thin-film amorphous silicon cells for

M.M. Hilali

Microelectronics Research Center, The University of Texas at Austin, Austin, TX 78758, USA
e-mail: mhilali76@yahoo.com

S.V. Sreenivasan (✉)

Microelectronics Research Center, The University of Texas at Austin, Austin, TX 78758, USA

Department of Mechanical Engineering, The University of Texas at Austin,
Austin, TX 78712, USA

e-mail: sv.sreeni@mail.utexas.edu

photocurrent enhancement. These designs include those that enhance the optical path length for similar or less absorber thickness as that of conventional non-structured solar cells. Nanostructured solar cells that exhibit plasmonic effects for enhanced optical absorption at wavelength ranges of interest are also discussed in some detail. Finally, nanostructured silicon quantum dot-based materials for tandem solar cells as well as nanostructured inorganic third-generation solar cells that exhibit phenomena like multiple-exciton generation, which can potentially make use of silicon-based materials, are briefly discussed. A broad background literature review of the value of nanostructuring in the major kinds of solar cell materials including silicon, III–V materials, and organic solar cells is often referenced in this book chapter and briefly discussed for the various technologies presented.

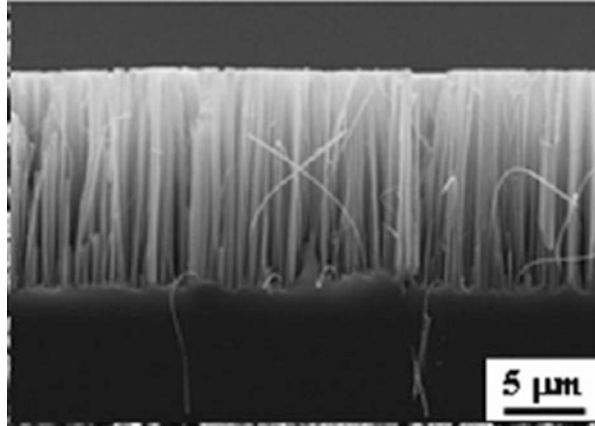
In general, an attempt is made to explain the physics of the various nanostructures as well as to illustrate the processes and process conditions that were employed for the solar cell fabrication with reference to various materials and concepts used for each technology. Industrial feasibility of some of these technologies and the related challenges are also briefly discussed.

1 Nanostructured Si Wafer Crystalline Solar Cells for Optical Absorption Enhancement

The potential of nanostructured photovoltaics is demonstrated by the absorption enhancement limit as derived by Yu et al. for nanostructures in the wave-optics regime [1]. This limit is significantly higher than the ray-optics Yablonovitch limit of $4n^2$, where n is the refractive index of the material [2]. Nano-patterned wafer-based Si solar cells have been recently investigated for broadband antireflection and optical absorption enhancement. For example, one technique to achieve this involved the use of nano-sphere lithography (this technique involves the use of a self-assembled monolayer of nano-spheres to act as a mask for the surface to be etched or nano-patterned) to pattern a P-type Si wafer for optical absorption enhancement [3]. In this work it was reported that the surface reflection can be lowered due to the enhanced absorption in a broad spectral range (400–1,000 nm) by forming sub-wavelength nano-patterned Si structures. Heterojunction crystalline Si solar cells were made by depositing n-type amorphous Si on top of the silicon nanostructures. Less than 5 % average-weighted reflection was demonstrated after 12-min etching [3], and the absorption was significantly enhanced to over 90 % (compared to 60 % for a flat Si wafer solar cell) in the useful spectral range of Si solar cells.

Recently, the development of nanostructures involving vertically aligned silicon nano-wire (SiNW) array has shown significant absorption enhancement potential that exceeds the Yablonovitch limit [4, 5]. This structure is typically fabricated on Si wafers using etching techniques. Excellent light-trapping with high path length enhancement factors has been demonstrated for vertically aligned SiNW [6]. Understanding the physical absorption enhancement mechanism(s) is complex as there

Fig. 5.1 Cross-sectional SEM image of vertically aligned silicon nanowires (after [11])



are multiple effects that take place that ultimately result in lower surface reflectance and enhanced photo-absorption. These effects are wavelength dependent, and they include photon propagation along the nanowires, diffraction by the periodic nanowire array, as well as Fabry–Perot resonances caused by reflections off the top and bottom surfaces [7]. A recent study showed that the main optical absorption enhancement of these nanowires is due to some optical modes that exhibit strong Fabry–Perot resonances [7].

Nanowires have been explored recently for minimizing the front-surface reflectance of conventional wafer-based silicon solar cells to create the so-called “black silicon” surface. While nanowire/nanopillar array solar cells show lower conversion efficiencies compared with conventional silicon solar cells, wafer-based silicon solar cells with nanostructured “black silicon” have shown >18 % (18.2 % maximum) conversion efficiency very recently [8]. These solar cells do not need the single-layer antireflection coating that is typically deposited on random pyramid textured conventional industrial silicon solar cells that reach about 18.6 % conversion efficiency on average in production. Nanowires have been created via an aqueous etch in order to form “black silicon” on the front surface of Si solar cells. These nanowires can act as a substitute for traditional antireflective coatings like titanium dioxide, silicon nitride, or indium-tin-oxide (ITO). The “black silicon” solar cells are nanostructured by using a wet-chemical etching process that makes use of HF and AgNO₃ that is heated at ~50 °C [9, 10]. The silver residue is removed at the end of the etching process. These nanowires forming “black silicon” offer a very low broadband front-surface reflectance of about 1.5–3 % in the 300–800 nm wavelength range [11]. This is lower than the 10–12 % average-weighted reflectance (AWR) for silicon random pyramid texture wafers with no antireflective coating. Figure 5.1 shows a micrograph image of such “black silicon”-etched nanowires.

Low doping was used to minimize the Auger recombination, and a silicon dioxide passivating layer was then grown to passivate the nanostructured surfaces in order to minimize the surface recombination. In the work by Oh et al. [8]

Auger recombination has been reported to be the dominant effect and not surface recombination; however, one should note that in optimizing the emitter to be lowly doped to reduce Auger recombination, the surface recombination is also decreased due to the decrease in the surface defects and traps with less doping. This surface-recombination velocity (SRV) dependence on the surface doping concentration can be illustrated by the equation below for passivated emitter surfaces [12]:

$$SRV = \alpha N_s^\beta + \kappa N_s^\nu \quad (5.1)$$

where α , β , κ , and ν are empirical coefficients that depend on the passivating layer material, silicon crystal orientation, dopant element, and doping type. It is shown from (5.1) that the SRV increases with increasing dopant surface concentration. Hence, the solar cell performance enhancement will be due to the effect of both the decrease in surface recombination as well as decrease in Auger recombination for the high sheet-resistance emitter (i.e., lowly doped emitters).

One should note that these nanostructured wafer-based Si solar cells recently developed were fabricated using photolithography techniques and not using industrially compatible screen-printing method, which accounts for the overwhelming majority of contact metallization used for crystalline Si solar cells. Developing high-throughput screen-printed thick-film contacts (the main technique used for industrial Si solar cells) for this type of structure may be challenging and may require significant development work particularly for high sheet-resistance emitters (123 Ω /sq. used in the reported 18.2 % solar cell) that also have a shallow junction depth. Without an antireflective coating to buffer the contact fire-through paste etching reaction the shallow junction may be etched or degraded by the fired screen-printed contact [13]. Hence, for manufacturability, seed layer metal evaporation/sputtering and electroplating can be employed, or alternatively such a nanostructured solar cell may be more easily metallized using ink-jet printing of a low-temperature curable silver ink.

2 Micro- and Nanowire Si Solar Cells

In addition to their excellent optical absorption enhancement properties, nanowire/micro-wire solar cells have been proposed as a means to decouple the optical path length from the carrier diffusion length by providing a collection path separate from the photon absorption thickness. Hence, they create a possibility for thinner layers and less absorber materials (e.g., Si) to be used for making the solar cell. This could be particularly useful for poor-quality silicon material with short charge-carrier diffusion length. There has been recent progress on III–V nanowire (NW) solar cells. For example recently 180-nm diameter InP NWs were grown epitaxially achieving 13.8 % conversion efficiency for an n-i-p device structure passivated with silicon dioxide and having transparent conductive oxide (TCO) contacts [14]. There has been other work and solar cell designs involving III–V NWs on Si solar cells in

tandem [15]. Results showed that >30 % absolute efficiency can be achieved in theory based on detailed balance simulations. These devices require that the number of photons absorbed in the nanowires does not exceed that absorbed in the bottom Si solar cell in order to achieve high solar cell performance (for NW materials with bandgaps less than the 1.7 eV optimum) for this type of solar cell structure. The main focus of this subsection will be on Si nano- and micro-wire solar cells, since Si remains the dominant material in the PV industry.

Nanowire solar cells with a radial junction can be modeled by a simple collection probability model of the photogenerated charge carriers as described by the following cylindrical geometry continuity equation [16]:

$$\frac{\partial^2 \Delta}{\partial r^2} + \frac{1}{r} \frac{\partial \Delta}{\partial r} + \frac{\partial^2 \Delta}{\partial z^2} - \frac{\Delta}{L} = -\frac{G}{D} \quad (5.2)$$

where G is the photogeneration rate, Δ represents the excess minority carriers, L is the minority-carrier diffusion length, and D is the minority-carrier diffusion coefficient. Based on this model it was found that for poor-carrier-lifetime Si (e.g., upgraded metallurgical grade Si) nanowires with radii less than the material diffusion length a rapid decline in performance takes place the smaller the radii of the nanowires. This shows the electronic disadvantage of nanowires or micro-wires as the saturation current density continues to increase for smaller Si wire sizes as the surface area-to-volume ratio increases. This is a general problem with nanowire solar cells. Nevertheless, with different and novel designs such as lower doped outer shell nanowire region (i.e., the heavier doped junction is around the center of the nanowire rather than at the circumference) for example, this problem may be circumvented. In such a case the SRV effect could be mitigated. However, this concept could be practically quite challenging to fabricate into a working solar cell. On the other hand, micro-wire solar cells may not exhibit the electronic disadvantage mentioned above since the wires can have a wide enough diameter to allow for optimum emitter diffusion for enhanced surface passivation for the whole length of the semiconductor micro-wire. Moreover, the surface-to-volume ratio is decreased as compared to the nanowire solar cell case. To demonstrate the benefit of micro-wire or micro-pillar arrays highly doped crystalline silicon solar cells were patterned and deep RIE etched to create 25 μm deep pillars [17]. The radial n^+p^+ junction was formed by POCl_3 diffusion after removing the oxide. It was found that the short-circuit current (J_{sc}) is highest for micro-wire diameters that are less than the minority-carrier diffusion length (L_n). However, for micro-wire diameters d that are about three times the diffusion length the J_{sc} was almost decreased by half the former case (where $d < L_n$). Increasing the filling ratio (FR) of the micro-pillars from 0.2 to 0.5 monotonically decreased the total spectral reflectance, which did not increase with higher filling ratios. 8 μm diameter micro-pillars that are spaced 3 μm apart (FR = 0.5) gave 8.7 % conversion efficiency on crystalline Si with 10 μm diffusion length. Deeper etching to create deeper (i.e., taller) micro-pillars improves the J_{sc} up till process limits or constraints permit.

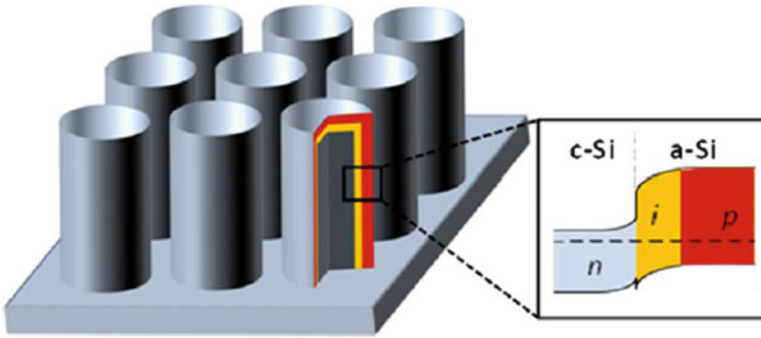


Fig. 5.2 Schematic and energy band diagram of a c-Si/a-Si heterojunction micro-wire solar cell (after [18])

To improve the surface passivation of micro-wires, amorphous Si heterojunction solar cell design was employed [18]. These nanostructured cells with radial heterojunction micro-wire geometry covering 50 % of the area gave a 2 % absolute efficiency enhancement over planar solar cells on the same upgraded metallurgical grade Si material with low (1 μ s) minority-carrier lifetime. The best solar cell conversion efficiency achieved for this type of NW structure was 12.2 %. A schematic of the heterojunction Si micro-wire solar cell along with the representative energy band diagram is shown in Fig. 5.2 above.

Nanowire/micro-wire solar cells have been generally fabricated by CVD growth techniques or by masking and etching techniques (wet-chemical or deep RIE etching). The CVD methods generally involve wire growth by a vapor–liquid–solid (VLS) mechanism, where a catalyst metal forms a eutectic mixture with Si to result in the decomposition of gas precursors, which promotes one-dimensional growth that is typically in the $\langle 111 \rangle$ direction [19]. However, recently a novel micro-wire layer-transfer technique has been proposed where micro-wires were CVD grown by making use of a patterned oxide and an electrodeposited catalyst to promote the CVD silicon wire growth [20]. After the growth process, the micro-wires were embedded in a polydimethylsiloxane (PDMS) polymer and a curing agent and subsequently cured to solidify the polymer forming a Si wire–polymer matrix. The Si wire–polymer matrix was then layer transferred or removed from a “parent” Si wafer; this removal was mechanically induced. After the Si wire removal, anisotropic alkali (e.g., KOH) etching of the Si parent wafer is performed to allow for subsequent reuse of the parent wafer and repeated CVD growth for the next layer of Si wire array. The exfoliated solar cell micro-wire film was then made into a final solar cell by forming the metal contact electrodes. Light-scattering elements could be embedded in between these micro-wires to enhance the optical reflection and photo-absorption in the micro-wires [21]. These solar cells yielded 16.6 mA/cm² short-circuit current and 5.64 % conversion efficiency.

For industrial feasibility of these micro-wire solar cells presented in this section one should also consider the fact that about half the silicon is lost or wasted in

the process to create these micro-wires. It should also be noted that it becomes very challenging to fabricate these nanostructured solar cells from tightly packed nano- or micro-wires. For tall and/or tightly packed vertically aligned nano- or micro-wires conformity of deposited layers such as antireflective coatings or deposited heterojunctions becomes quite challenging; this is an important factor to consider in the process design and selection for these types of wire solar cell structures.

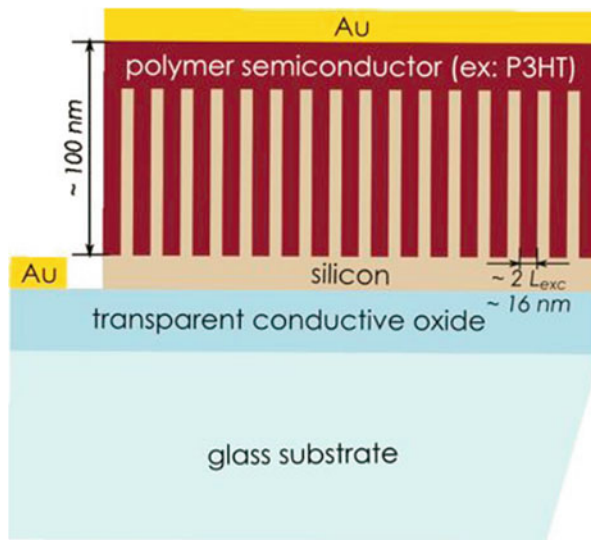
3 Nanostructured Hybrid Organic Si Solar Cells

Another solar cell structure that makes use of nanostructuring to offer a performance improvement for both low-grade Si and polymer semiconductors is the hybrid nanostructured organic Si solar cell. Organic-based photovoltaic cells are not yet competitive because of low conversion efficiency and short lifetime. The main reason why organic solar cells have a poorer performance compared to inorganic ones is because in organic solar cells bound electron–hole pairs or excitons are created under photoexcitation. These electron–hole pairs cannot be easily separated by thermal excitation due to the larger excitonic binding energy. Hence, electron–hole dissociation at the interface between two materials with different electron affinities becomes the only known practically feasible way to dissociate these electron–hole pairs [22]. The electron then goes to the material with higher electron affinity, i.e., the acceptor material, while the hole goes to the material with the lower electron affinity, i.e., the donor. The main issue is the short lifetime and short diffusion length of the excitons, which recombine after a few nanometers only from their creation. Hence, they must be separated to create a photo-generation current before they recombine. And thus, one main criterion for organic and hybrid organic–inorganic solar cells is to have any point of the absorber organic material within the excitonic diffusion length (L_{exc}) of the separator interface material that has large enough difference in electron affinity. The efficiency of polymer solar cells greatly depends on the proximity of mixed donors and acceptors used in these solar cell devices to create charges that are collected through unimpeded percolative pathways to be collected at their respective contacts [23].

One organic solar cell design approach has been to make blends, where an electron acceptor and a donor are in nanometer-scale domains of proximity such that excitons can be collected efficiently. Traditionally fullerene-based derivatives were used as acceptors [24]. Alternatively, blends have been fabricated using inorganic nanocrystals (e.g., II–VI semiconductors such as CdSe) as the electron acceptors [25]. The advantage of this is that the shapes/morphology of these nanocrystals can be tuned to engineer their bandgap to optimize the absorption spectrum to the incident light.

The second design or approach, which is the main one of interest in this section, is the hybrid nanostructured layer solar cell. The nanostructured device approach of interest here is one having a semiconductor material, namely, silicon in this case,

Fig. 5.3 Polymer–silicon hybrid solar cell (after [30])



filled with an organic semiconductor material. This type of hybrid device is derived from the dye-synthesized solar cell (DSSC) concept which is based on a nanostructured metal oxide (e.g., ZnO or TiO₂) that is surrounded by the absorber material, i.e., the dye, and an electrolyte [26]. P3HT, which is probably the most commonly investigated organic material for solar cells, has been used as the donor material infiltrating into TiO₂ nanowires to form a hybrid polymer–metal oxide solar cell [26, 27]. This type of structure has been recently incorporated with silicon semiconductor materials to be used as the donor instead of the metal oxides for hybrid polymer–semiconductor solar cells. The advantage of this structure is that in addition to the organic/inorganic interface acting as the electron–hole pair separator, it also provides a direct current path for the charge collection. Moreover, this heterojunction structure also allows for a fixed region for excitonic diffusion, which is defined by the inorganic nanostructure as shown in Fig. 5.3 above. Recently, P-type polymer/silicon nanowire hybrid solar cells have been investigated. For example, such nanostructured solar cells have been recently fabricated using n-type-doped Si wafers and PEDOT:PSS polymer [28]. The effect of the length of the silicon nanowires on the performance was also investigated by Syu et al. [29]. Nanowire lengths were varied from 0.73 to 5.15 μm. Electrical results showed that the shortest nanowire gave the highest short-circuit current (J_{sc}) of 21.7 mA/cm² and highest power conversion enhancement (PCE) of 7.02 %. On the other hand, the hybrid solar cell devices with the longest nanowires gave lower J_{sc} of ~13 mA/cm² and a lower PCE of 3.8 % [29]. The most likely reason for this result is the poor coverage of the nanowire surfaces (for long nanowires) by the PEDOT:PSS—with deeper nanowires it becomes harder to cover all the surfaces to form the Si/polymer heterojunction. With longer wires more surface area is exposed and the total surface recombination is increased and, consequently, the degradation

in open-circuit voltages (V_{oc}) with deeper nanowires. Nevertheless, all Si nanowire/PEDOT:PSS solar cells had a higher J_{sc} and PCE compared with the planar PEDOT:PSS/silicon solar cell. This result indicates the benefit of the nanowire design. There are two possible reasons for this performance enhancement. One reason could be the lower surface reflectance due to the nanowire structures and/or due to the enhanced carrier collection by increasing the interface region where carriers can be generated and collected.

This hybrid nanostructured solar cell structure was investigated not only for bulk wafer-based crystalline silicon material but also for thin-film silicon materials like microcrystalline and amorphous silicon deposited by plasma-enhanced chemical vapor deposition (PECVD). Microcrystalline and amorphous thin-film silicon have a much lower mobility than that of bulk crystalline silicon. Higher photovoltage was achieved for hybrid nanostructured solar cells with hydrogenated a-Si (a-Si:H). A thin interfacial intrinsic a-Si:H in between the polymer and n-type a-Si:H film was needed to enhance the open-circuit voltage of the solar cell. Conversion efficiencies up to 1.6 % were achieved for this hybrid nanostructured a-Si and P3HT semiconductor polymer solar cell. Both materials contributed to the photocurrent in this case. Handling such organic polymers needs to be done in a glove box as these materials are quite sensitive to oxygen and water; hence, all solar cell processing after incorporation of such polymers needs to be done in a controlled atmosphere.

The hybrid solar cells discussed in this section are quite promising for low-cost industrial applications. Improved nanofabrication techniques and better understanding of the device physics can lead to better solar cell designs with improved performance for these hybrid nanostructured Si-organic solar cells.

4 Nanostructured Thin-Film Si Solar Cells

Thin-film solar cells (TFSCs) have well-established advantages that allow them to significantly contribute to electricity generation and to ultimately compete with traditional energy sources for powering the grid. These advantages include the lower manufacturing cost as well as the versatility in the types of applications [31]. However, further reduction in the \$/Watt-peak is needed to achieve grid-parity. An attractive approach to achieve this in TFSCs is by increasing the cell conversion efficiency via enhanced optical absorption without significantly adding to the manufacturing cost. Amorphous Si is a technologically mature thin-film photovoltaic (PV) material, and Si is more abundant in nature than elements such as tellurium or indium that make up other photovoltaic materials such as CdTe and CIGS [32, 33]. However, the a-Si thin-film absorber layer would need to be thick enough to absorb as much of the solar radiation as possible while still being thin enough to lessen the Staebler–Wronski effect (SWE) that results in a degradation of the solar cell conversion efficiency due to increased defects of the hydrogenated amorphous Si i-layer with the light exposure [34]. Thus, thin-film a-Si solar cells

absorb fewer photons than conventional wafer-based Si solar cells and, hence, are less efficient. Light trapping photonic structures can be useful in keeping the absorber layer adequately thin to mitigate light-induced degradation while at the same time attaining good optical absorption and high photocurrent [35]. Since thin-film photovoltaic a-Si cells have an absorber layer thickness that is on the order of or less than the wavelengths of interest, the geometric Lambertian scattering approach for light-trapping, which increases absorption by randomizing light based on statistical ray optics [36], would not be effective in this case. Also, the typical surface texturing structures [37, 38] such as pyramidal structures used to enhance light absorption in wafer-based silicon solar cells due to the wide-angle light scattering and the surface double bounce are not suitable for use for thin-film solar cells because of their large-scale geometries. In this section we investigate structures where the optical absorption volume is significantly increased while the carriers still have a small distance to travel to the collecting junction. In other words, the electrical performance is decoupled from the optical performance of the solar cell. For this concept mainly, 3D-wrapped nanoscale structures for enhancing the optical absorption of thin-film single junction (TFSJ) a-Si solar cells as well as plasmonic nanostructures are evaluated.

4.1 *Nano-Patterned 3D-Wrapped Amorphous Silicon Nanostructures*

Several 3D nanostructures have been investigated recently for amorphous silicon solar cells for enhanced photo-absorption. Such solar cell devices have been simulated, characterized, and fabricated to show that for a thin-film amorphous silicon solar cell the photocurrent can be significantly enhanced demonstrating that these 3D nanostructures have substantial merit for thin-film solar cells. In the past few years nano-coaxial amorphous Si nano-pillar solar cells have been proposed and investigated for their enhanced optical absorption [39–41]. Figure 5.4 shows a

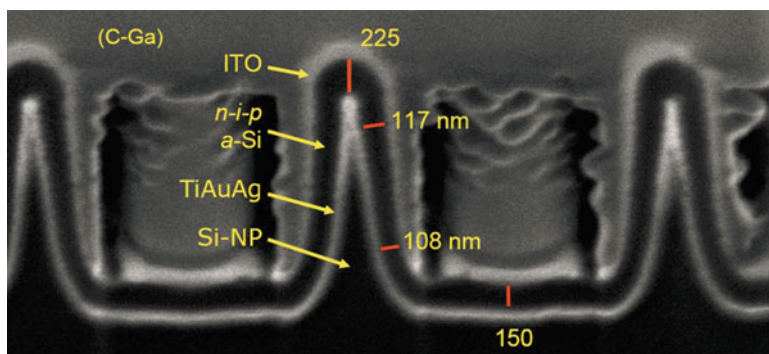


Fig. 5.4 Cross-sectional SEM image of nano-coaxial a-Si solar cells (after [40])

Fig. 5.5 SEM image of a 3D-wrapped nano-pyramid a-Si solar cell structure (after [42])

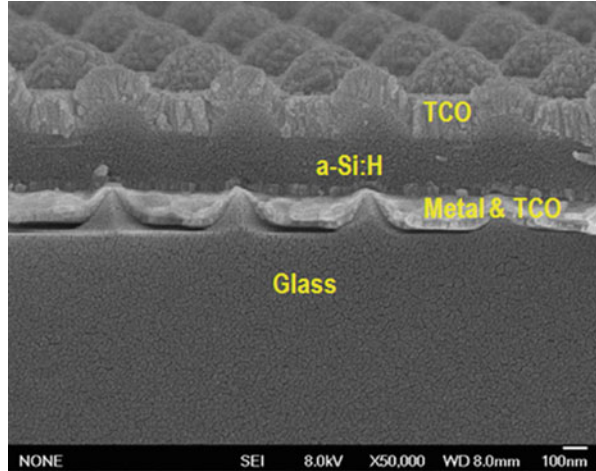
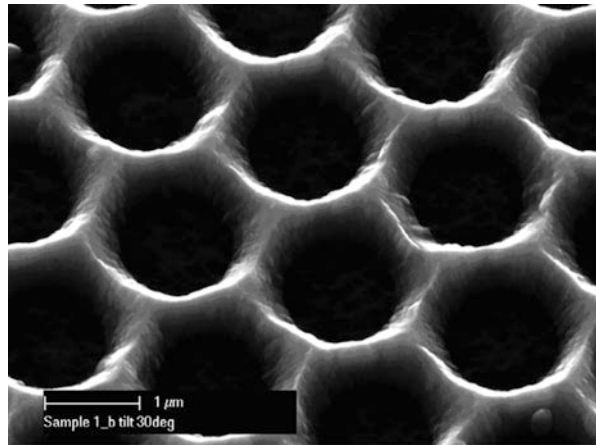


Fig. 5.6 SEM image of the “Swiss cheese” nano-pattern for light trapping in thin film a-Si solar cells (after [43])



cross-sectional SEM image of these nano-pillar/nano-coax a-Si solar cells. Also, in recent research work, 3D nano-pyramidal structures (shown in Fig. 5.5) that can enable both good conformability and good light trapping have been proposed for thin-film amorphous silicon solar cells [42]. Nano-hole or micro-hole design structure that was dry-etched into the ZnO front contact layer to create a “Swiss cheese” pattern has been recently reported for enhanced optical absorption in thin-film amorphous silicon solar cells [43]. Figure 5.6 shows an SEM micrograph of this “Swiss cheese” 3D nano-pattern. An enhancement of 40 % in short-circuit current was achieved for this nano-patterned solar cell with an excellent open-circuit voltage of 1.41 V. Shir et al. fabricated cylindrical nanostructures of monocrystalline Si solar micro-cells of $\sim 6 \mu\text{m}$ thickness using imprint lithography and showed substantial improvement in optical absorption over bare Si layer as well

as a Si layer coated with an antireflective coating [44]. Also, recently, silicon nanostructures such as nano-cone and Si nano-pillar or nanowire array structures have suggested a potential for excellent antireflection and light trapping ability based on simulation [45] and optical characterization [46]. Incorporating these nano-features could provide a potential for thin-film Si-based solar cells to have enhanced light absorption by increasing the optical path length.

Optical modeling can help guide the design and optimization for the experimental work involving the fabrication of these 3D nanostructured a-Si TFSCs. However, simulating or predicting the behavior of nanostructured thin-film a-Si PV cells becomes a nontrivial problem that requires the solution of Maxwell's equations for electromagnetic waves in order to obtain accurate and representative results. For such simulations the reflected and transmitted light waves need to be calculated from the incident field for these scattering problems. Finite-difference time domain (FDTD) method [47] is typically used to simulate the optical absorption of thin-film a-Si solar cells having any type of structures, whether random or periodic. However, for patterned structures that are purely periodic with horizontally periodic boundary conditions a rigorous coupled wave analysis (RCWA) algorithm [48] can be used. In this algorithm a periodic permittivity function is represented using Fourier harmonics, where each harmonic is related to a coupled wave. The RCWA technique has been previously used to model sub-wavelength metallic gratings [49], and it has been more recently used to model optical absorption in nanostructured solar cells [42]. This analysis technique enables full vectorial Maxwell's equations to be efficiently solved in the Fourier domain and the spatial field distribution to be derived from the Fourier harmonics. An otherwise direct solution of the Maxwell's equations with boundary conditions would be a computationally challenging task. Using the periodicity property of the simulated structures the incident field in a periodic layer according to Bloch's theorem [50] could be expressed as follows for incident plane waves:

$$\mathbf{E}(x, y) = \hat{z} E_{\Lambda}(x, y) e^{-i(k_{x,0}x + k_{y,0}y)} \quad (5.3)$$

where the electric field $\mathbf{E}(x, y)$ is expanded as a periodic function with period Λ_x in the x -direction and a propagation constant $k_{x,0}$ and with period Λ_y in the y -direction and a propagation constant $k_{y,0}$. $E_{\Lambda}(x, y)$ is the periodic electric field that propagates in the xy -plane only and can be expressed as a double-Fourier series expansion in x and y with coefficients $a_{p,q}$ representing the dependence on the z -direction:

$$E_{\Lambda}(x, y) = \sum_p \sum_q a_{p,q} e^{-i\left(\frac{2\pi p}{\Lambda_x}x + \frac{2\pi q}{\Lambda_y}y\right)} \quad (5.4)$$

Similarly, the magnetic field can be expressed as

$$\mathbf{H}(x, y) = \hat{z} H_{\Lambda}(x, y) e^{-i(k_{x,0}x + k_{y,0}y)} \quad (5.5)$$

where the periodic magnetic field $H_{\Lambda}(x,y)$ can be expanded in a double-Fourier series with coefficients $b_{p,q}$:

$$H_{\Lambda}(x,y) = \sum_p \sum_q b_{p,q} e^{-i\left(\frac{2\pi}{\Lambda_x}px + \frac{2\pi}{\Lambda_y}qy\right)} \quad (5.6)$$

Using the above formulation in the transverse form of Maxwell's wave equations with the time harmonic factored out yields an eigenvalue problem formulation. Modal transmission line theory and methods are used to solve the boundary-value problem [51].

The number of electron-hole pairs generated at a certain wavelength and collected at the junction electrodes can be given by

$$n_{\text{ph}}(\lambda) = \frac{\lambda}{hc} \sum_i \eta_c S(\lambda) \alpha_i(\lambda) \quad (5.7)$$

where h is the Planck constant, c is the speed of light, λ is the wavelength, $S(\lambda)$ is the incident spectrum (for the simulations performed in this work the AM1.5G spectrum is used), and α_i is the absorption spectrum in layer i . If no recombination or shunting issues are taken into account and if only optical phenomena are considered η_c the carrier collection efficiency can be assumed to be equal to 1 or 100 %. The total number of electron-hole pairs collected can be expressed as the following:

$$N_{\text{ph}} = \int n_{\text{ph}}(\lambda) d\lambda \quad (5.8)$$

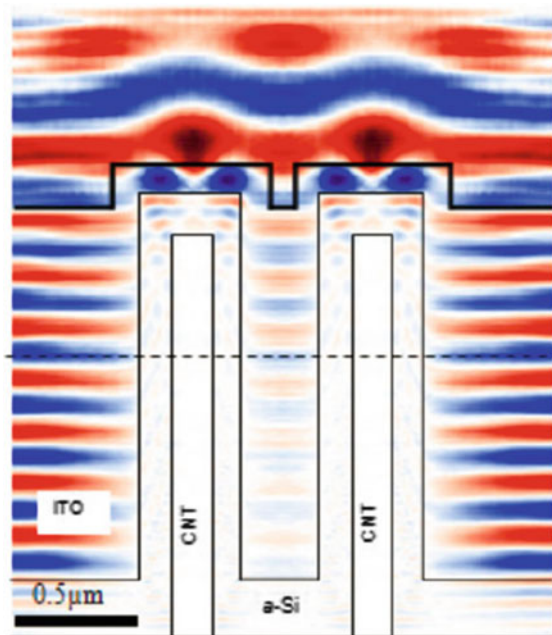
And the photocurrent can then be computed as

$$J_{\text{ph}} = eN_{\text{ph}} \quad (5.9)$$

where e is the electron charge density.

The optical simulations based on the theory illustrated above showed that high-aspect-ratio nano-pillar structures are superior to other 3D structures in photocurrent enhancement. However, it is very difficult to obtain good conformal deposition of a-Si and electrode films on such pillar structures. For instance, the a-Si layer tends to be much thicker on the pillar top and thinner on the bottom and on the sides. The larger the aspect ratio of the pillars and higher the density of the pillars, the more severe this problem is. High-aspect-ratio pyramids can come close to achieving the photocurrent enhancement of nano-pillar structures and are more suited for scalable fabrication. For such a global optimization of the 3D nanostructures a genetic algorithm was used [42]. Such an algorithm ranks a population of designs or "children" to search through the parameter space until an optimal design is found after a repetitive process [52]. This algorithm gives a probabilistic estimate of a global optimum. The algorithm also gives a list of solutions with a best solution or

Fig. 5.7 FDTD simulations showing the electromagnetic field absorption by the a-Si nano-coaxial solar cell (after [41])



an optimal solution that has a certain high probability as well as alternative suboptimal solutions to the optimization problem. The algorithm is used to find a global maximum of the absorption in the a-Si absorber layer as the objective is to find an optimum design that will yield the highest photocurrent and conversion efficiency. This type of algorithm is useful for a large number of variables with a complex parameter space. In this case a six-parameter optimization was performed or six independent variables are optimized. These are as follows: the thickness of the a-Si absorber layer, the thickness of the ITO layer, the thickness of the bottom contact AZO layer, the height of the features, the period or the pitch of the features, and the base width or diameter (in case of a nano-pillar) of the feature. The optimization results showed that the optimum design converges towards taller nanostructures whether the nanostructure design is a nano-cylinder or a nano-pyramid, and ultimately taller pillars (several microns) should in theory give the best performance. A smaller nanostructure pitch, within certain minimum limits, generally gives better results for the same set of feature parameters. The parameters obtained for a best solution of a constrained optimization of the nano-pyramid structure were as follows: a base width of 535 nm, a height of 3.8 μm, a pitch of ~2.38 μm, an ITO thickness of ~125 nm, AZO thickness of ~42 nm, and an amorphous Si thickness of ~436 nm. Even though they are closer to enhanced optical absorption optimal designs, these types of tall nano-pillar structures are harder to fabricate using manufacturable/scalable techniques. This type of solar cell nanostructure design is similar to that of the nano-coax a-Si solar cell reported in [39–41]. The simulated E-field shown in Fig. 5.7 demonstrates the effectiveness of such a structure for photo-absorption enhancement, as the field is dampened as it

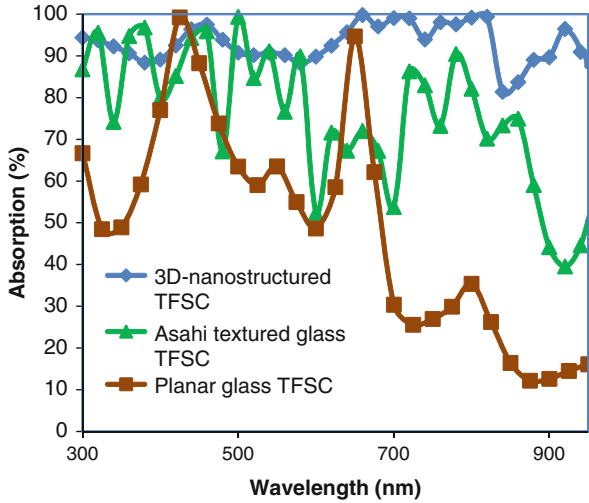


Fig. 5.8 Simulated absorption plots of 3D pyramidal nanostructured thin-film a-Si solar cell compared with planar and textured Asahi glass a-Si solar cells (after [42])

goes through the 3D nano-coaxial amorphous silicon indicating enhanced optical absorption in the nano-patterned TFSC.

Monte Carlo optical simulations showed that a conversion efficiency of over 12 % is possible for the “Swiss cheese” nano-patterned amorphous silicon P-I-N solar cells [43]. For the micromorph cells, using these simulations an efficiency of over 15 % was shown to be possible with the thickness of the amorphous silicon layer less than 200 nm and a microcrystalline silicon thickness of ~500 nm [43].

Spectral optical absorption simulation results of the 3D-patterned nano-pyramidal structures showed significant enhancement over both a typical planar a-Si cell as well as over a typical Asahi textured glass a-Si cell. As shown by the absorption simulations in Fig. 5.8 this enhancement is broadband. Hence, simulation results for 3D nano-patterned pyramidal structures yielded a higher photocurrent compared with the Asahi textured glass a-Si solar cell. These results are in good agreement with the recent findings in [3] mentioned in Sect. 1 of this book chapter. From the simulated absorption results, it can be concluded that the merit of the 3D nanostructures is mainly in enhancing the optical absorption in the 590–750 nm wavelength range, which is the critical part of the spectrum for improving thin-film a-Si solar cell performance. As illustrated by the simulated absorption plots shown in Fig. 5.8 and the experimental absorption plots in Fig. 5.9 the 3D pyramid a-Si TFSC nanostructure yielded an 88 % average-weighted absorption (AWA) compared with the Asahi textured glass a-Si TFSC with an AWA of about 78 %. Both experimental and simulated results showed good agreement in the short wavelength and visible part of the spectrum. This result also translated to a higher simulated and experimental external quantum efficiency (EQE) for the 3D nano-pyramid a-Si TFSC (after [42]).

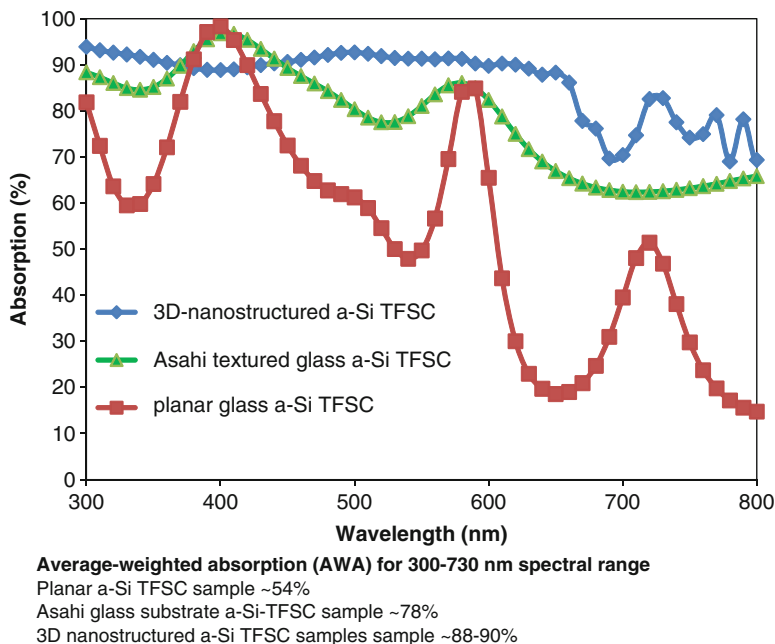


Fig. 5.9 Experimentally measured optical absorption plots for 3D pyramidal nanostructured, planar, and Asahi glass thin-film a-Si solar cells (after [42])

Current–voltage measurements showed a clear advantage of the 3D pyramid nanostructured a-Si TFSC over the Asahi textured glass a-Si TFSC and a significant enhancement over the planar or the flat glass a-Si TFSC. Substantial stable short-circuit current enhancement of ~80 % was achieved for the 3D-wrapped nano-pyramid a-Si TFSC (typically from to ~13 mA/cm² with the highest measured J_{sc} of 13.8 mA/cm² for the nano-pyramid-wrapped a-Si TFSC over the flat a-Si TFSC). This photocurrent enhancement is similar to that recently obtained in the literature [40, 41] for nano-coax-based solar cells for a similar a-Si thickness deposited on the sides of the nano-pyramids. However, in addition to the scalable manufacturability of the fabrication process used for the nano-pyramids, they only have about 380 nm feature height compared with 1–2 μm for the nano-pillars/nano-coax solar cells reported in [40, 41]. The very thin a-Si of ~140 nm deposited on the nano-pyramids has a much thinner thickness than the typical 500 nm thickness used for planar a-Si solar cells, which should mitigate the SWE that degrades the a-Si TFSC performance. Conversion efficiencies approaching 6 % were achieved for these nano-pyramid-wrapped a-Si solar cells, which is also comparable to the result reported in [41], and which also shows a ~50 % enhancement in relative conversion efficiency compared with their planar a-Si solar cell counterparts. Further process improvements are needed particularly for the a-Si and TCO deposition parameters and conditions to improve the solar cell performance.

With regard to fabrication of such nanostructured TFSCs, it has been recently found that the morphology of the textured TCO (LP CVD ZnO) on glass substrates strongly affects the microcrystalline Si absorber material quality and the solar cell performance [53]. V-shaped morphologies were found to strongly enhance light trapping but at the same time degrade the absorber film growth and quality by helping induce micro-cracks. Thus, the V-shaped morphologies were smoothed to a more U-shaped form by optimizing a plasma treatment process and time. In our work amorphous Si is used, and hence micro-cracking should be less of an issue. Nevertheless, we optimized the nano-pyramid surface morphology in order to avoid or mitigate the degradation of the amorphous Si P-I-N and N-I-P solar cell devices. This type of morphology performance degradation mainly shows up in the open-circuit voltage (V_{oc}) and fill factor (FF) of the device and not in the absorbed photocurrent. As reported in [42] photocurrent improvement was generally observed for an N-I-P a-Si cell design (N-layer deposited first) on a substrate configuration where the P-type a-Si layer is facing the incident light. This significant photocurrent enhancement was not observed for a P-I-N superstrate configuration where the P-layer is deposited first, on the TCO on the glass superstrate light facing side. This is probably due to stresses and delamination that can take place in the ITO layer when deposited directly on these pyramidal structures. This may not be the case for the substrate configuration as the metal back reflector is deposited first, which is probably less prone to the disadvantageous stresses and CTE mismatch effects that may take place during the amorphous silicon deposition on these nano-patterned structures.

4.2 Plasmonic Si-Based Solar Cells

There is a real need for optical absorption enhancement in thin-film and third-generation solar cells. For these device structures one needs to manipulate light at scales below the diffraction limit, this can be achieved by making use of plasmonics. The advantage of plasmonic light trapping is that it has the potential to allow thin-film solar cells (particularly thin-film Si solar cells) to achieve spectral quantum efficiencies that approach those of wafer-based Si solar cells. There are two types of surface plasmons (SPs): there is the surface plasmon polariton (SPP), which is an electromagnetic wave that is coupled to the electron plasma of a metal that propagates along the metal dielectric or metal semiconductor interface [54]. SPPs that are excited at the metal–semiconductor interface can trap and guide light in the semiconductor absorber layer of a solar cell.

The second type is the localized surface plasmon (LSP), which is an excitation of conduction-band electrons that are coupled to an external electromagnetic field. LSPs can result in resonant light scattering. Both LSP and SPP enhance near-field electromagnetic radiation, and so both have generated a lot of interest recently in the photovoltaics community particularly for thin-film solar cells. There are several plasmonic structures and techniques, which can allow for reduction in the

semiconductor absorber layer thickness while maintaining the same optical thickness. These techniques and the associated physics and device structures are discussed in the following subsections.

4.2.1 Light Scattering by Plasmonic Particles

Metallic nanoparticles can be employed for sub-wavelength scattering of the sunlight to trap and couple sunlight plane waves into the absorbing semiconductor for enhanced photo-generation.

For particles with diameters much smaller than the impinging wavelength of light ($d < \lambda$), the absorption and scattering of light can be described by a point-dipole moment, which can be respectively expressed as [55]

$$C_{\text{abs}} = \frac{d^3 \pi^2}{\lambda} \text{Im} \left[\frac{\epsilon_p - \epsilon_{\text{em}}}{\epsilon_p + 2\epsilon_{\text{em}}} \right] \quad (5.10)$$

$$C_{\text{scat}} = \frac{2d^6 \pi^5}{3\lambda^4} \left| \frac{\epsilon_p - \epsilon_{\text{em}}}{\epsilon_p + 2\epsilon_{\text{em}}} \right|^2 \quad (5.11)$$

where ϵ_p and ϵ_{em} are the dielectric functions of the particle and embedding medium, respectively. When $\epsilon_p = -2\epsilon_{\text{em}}$ the particle polarizability is maximized. This is the surface plasmon resonance condition. At this condition the scattering cross section (as well as the absorption cross section) can be much larger than the geometric cross section of the particle [56]. For light-trapping in a solar cell it is desirable that the scattering dominates over the absorption of the particle; hence, the ratio $C_{\text{scat}}/C_{\text{abs}}$ would need to be maximized. As illustrated by the d^6 dependence in (5.11), the scattering cross section is highly dependent on the size of the particle (assuming $d < \lambda$). For example, for a silver nanoparticle of 100 nm diameter the scattering cross section can be as high as ten times that of the geometric cross-sectional area at the plasmon resonance frequency [56–58]. Using silver nanocrystals on the top surface of solar cells a seven-fold optical absorption enhancement at a wavelength of 1,200 nm for wafer-based Si solar cells has been reported as well as a 16-fold enhancement at a wavelength of 1,050 nm for a silicon-on-insulator 1.25 μm thick TFSC [59]. As reported by Catchpole and Polman, the shape and size of the metal plasmonic nanoparticles is an important factor in determining the light coupling enhancement in the solar cell [58, 60]. This is illustrated in Fig. 5.10a, b. Some of these nanostructured plasmonic metals may be fabricated on a solar cell surface, for example, via thin-film deposition and nanoimprint lithography patterning. An interesting application of surface plasmons is illustrated in Fig. 5.11 where metal nanoparticles can provide wavelength-dependent light trapping for tandem solar cells, where shorter wavelength is coupled into the top layer of the tandem solar cell using smaller nanoparticles for absorption of higher energy photons, and larger nanoparticles can be used for coupling longer wavelength light for the bottom layers of the tandem cell.

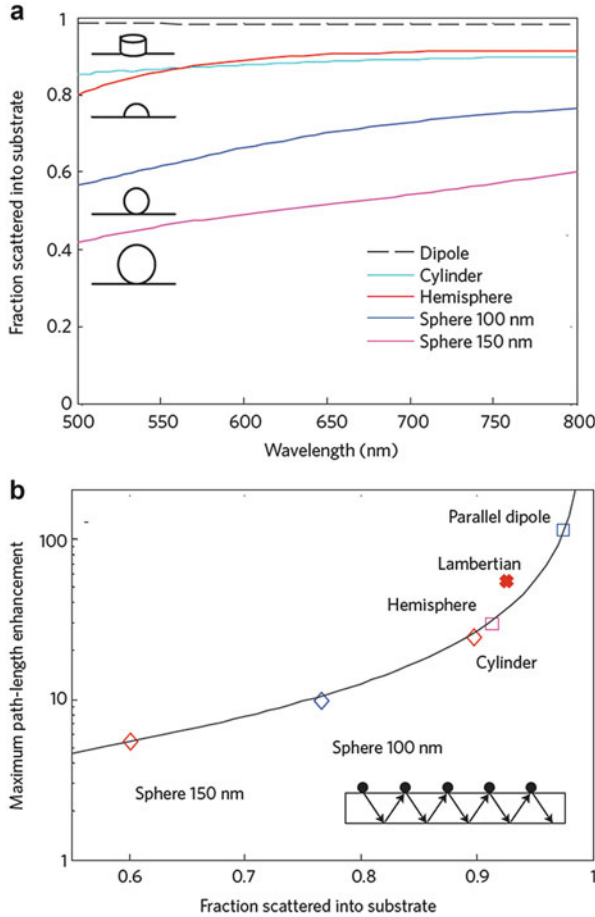
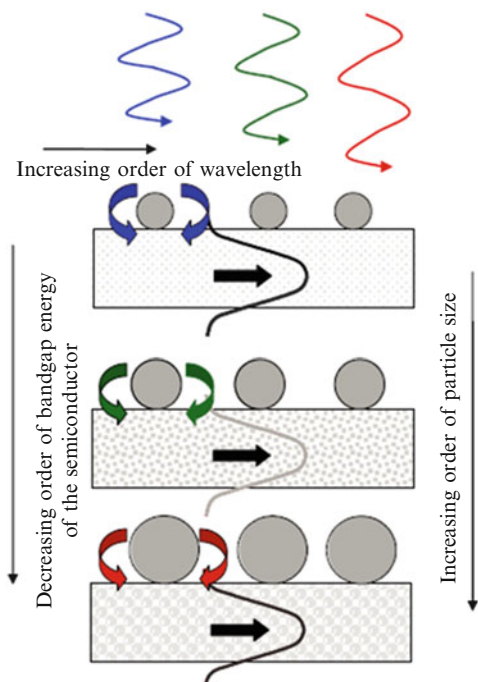


Fig. 5.10 (a) Fraction of light scattered into a silicon substrate, divided by total scattered intensity, for different sizes and shapes of Ag nanoparticles on silicon. The *dashed line* shows the fraction of light scattered into the silicon for a parallel electric dipole that is 10 nm from a Si substrate, (b) maximum path-length enhancement for the nanoparticle geometries shown in (a) for a wavelength of 800 nm (absorption within the particles is neglected in the model calculations, and an ideal rear reflector is assumed) (after [61] with modification)

4.2.2 Optical Antennas: Light Concentration Using Plasmonic Particles

An alternative use of resonant plasmon excitation in TFSCs is to take advantage of the strong local field enhancement around the metal nanoparticles to increase absorption in a surrounding semiconductor material. Metallic nanoparticles can be used as sub-wavelength antennas in which the plasmonic near-field is coupled to the semiconductor, increasing its effective absorption cross section.

Fig. 5.11 A schematic showing wavelength-dependent light trapping for a tandem quantum dot solar cell structure that makes use of plasmonic metal nanoparticles with tailored size for each energy level (after [57])



The nanoparticles then act as an “optical antenna” for the incident sunlight that stores the incident energy in a localized surface plasmon mode. This works particularly well for small (few nanometers to ~ 20 nm diameter) particles for which the scattering efficiency is low. These antennas are particularly useful in materials where the carrier diffusion lengths are short, and photogenerated carriers must therefore be generated close to the collecting junction region. For these optical-antenna energy conversion effects to take place efficiently, the absorption rate in the semiconductor must be larger than the reciprocal of the plasmon lifetime, which is typically $\sim 10\text{--}50$ fs [61]; otherwise, the absorbed energy is dissipated as ohmic damping in the metal nanoparticle. Several examples of this concept have recently appeared in the literature demonstrating photocurrent enhancements due to this plasmonic light concentration effect. In one case it was concluded that near-field effects of plasmonic metal nanoparticles embedded in crystalline Si can excite electron–hole pairs without phonon assistance (necessary for indirect bandgap bulk semiconductors) [62]. In this case the momentum is transferred to the nanoparticle. Surface recombination can be an issue; however, for metal nanoparticles embedded in Si, it would need to be minimized.

For modeling the optical properties of surface plasmons and for describing the dielectric function of a material the generalized Drude theory model can be employed. This model describes the response of damped free electrons (representing the conduction electrons in the Drude model) to an applied electromagnetic field

with angular frequency ω [63]. Starting with the equation of motion of free electrons with time dependence t and displacement \vec{r}

$$m^* \left(\frac{\partial^2 \vec{r}}{\partial t^2} \right) + m^* \gamma \left(\frac{\partial \vec{r}}{\partial t} \right) = e E_0 e^{-i\omega t} \quad (5.12)$$

where m^* is the effective mass of an electron, e is the electronic charge, and E_0 is the amplitude of the electromagnetic field. The total damping rate $\gamma = 1/\tau$, where τ is the mean relaxation time of the conduction electrons, which, based on classical mechanics theory, is dependent on lattice defects and/or grain boundaries, electron–phonon scattering, electron–electron scattering, and the size of the plasmonic particle. Solving the above differential equation for \vec{r} yields the complex dielectric function shown below:

$$\hat{\epsilon}_D(\omega) = \epsilon'_D(\omega) + i\epsilon''_D(\omega) = \epsilon_{\text{InT}} - \frac{\omega_p^2}{\omega^2 + i\gamma\omega} \quad (5.13)$$

where $\epsilon'_D(\omega)$ and $\epsilon''_D(\omega)$ are the real and imaginary parts of the permittivity, respectively. For negligible interband absorption (e.g., for perfectly free-electron gas or for metals with very low interband absorption) ϵ_{InT} , the permittivity contribution due to interband transitions becomes unity. The permittivity of the material can then be expressed as

$$\hat{\epsilon}_D(\omega) = 1 - \frac{\omega_p^2}{\omega^2 + i\gamma\omega} \quad (5.14)$$

ω_p is the bulk plasmon frequency given by

$$\omega_p = \sqrt{\frac{Ne^2}{m^* \epsilon_0}} \quad (5.15)$$

where N is the density of free electrons, and ϵ_0 is the free-space dielectric constant. The surface plasmon resonance frequency for a spherical particle in free space can be given by $\omega_{\text{sp}} = \sqrt{3}\omega_p$, which depends on the density of free electrons in the particle [60]. This density is highest in metals like aluminum and silver giving surface plasmon resonance in the ultraviolet part of the light spectrum, and it is lowest in metals like gold and copper giving surface plasmon resonances in the visible part of the spectrum [60]. Nevertheless, the resonance can be tailored by adjusting the dielectric of the embedding medium [64]. For a metal particle in a dielectric medium the surface plasmon resonance frequency can be expressed as [65]

$$\omega_{\text{sp}} = \frac{\omega_{\text{p}}}{\sqrt{\epsilon_{\text{dm}} + 1}} \quad (5.16)$$

A higher dielectric constant would shift the resonance frequency towards the infrared part of the spectrum [66].

Recent results have shown an enhancement in the short-circuit current of a hexagonal nano-cylinder array-patterned thin-film amorphous Si solar cell [67] fabricated using nano-sphere lithography. The photocurrent enhancement in that case was only $\sim 2 \text{ mA/cm}^2$, and the nano-cylinders had a depth of only 65 nm, which is much smaller than the features used in the nano-coaxial a-Si solar cell work [40, 41] and also smaller than those used in the wrapped nano-pyramid a-Si solar cells [42] discussed in the previous subsection. The enhancement in light absorption in that case was attributed to enhanced light trapping mainly due to the localized surface plasmon effect [68].

4.2.3 Surface-Plasmon Polaritons for Light Trapping

In this light-trapping mechanism light is converted into SPPs or electromagnetic waves that travel along the metal–semiconductor interface at the back of the solar cell. A corrugated metallic film (e.g., a grating structure) on the back surface of a thin photovoltaic absorber layer can couple sunlight into SPP modes at the metal/semiconductor interface as well as guided modes into the semiconductor absorber to enhance the carrier photo-generation.

Based on the wave equation derived from Maxwell's equations for a p-polarized electromagnetic wave incident on an interface between two materials with dielectric functions ϵ_1 and ϵ_2 , the localized surface charge oscillations, or surface plasmons coupled to the EM wave, have to obey the dispersion relation shown below [69]:

$$k_x^2 = \frac{\epsilon_1 \epsilon_2}{\epsilon_1 + \epsilon_2} \frac{\omega}{c} \quad (5.17)$$

where k_x is the propagation wave-vector parallel to the interface, and c is the speed of propagation of light. Note that an electromagnetic wave in vacuum impinging on a flat surface (i.e., metal surface) does not excite surface plasmons, and hence, the corrugations or specifically gratings are useful to allow for the surface plasmon coupling. For a bound solution where the electromagnetic field decays away from the interface, the condition $\epsilon_1 + \epsilon_2 < 0$ must be satisfied. For wave propagation along the surface, k_x must be positive and real; thus, $\epsilon_1 \epsilon_2 < 0$ also must be satisfied. For ϵ_2 real and positive (e.g., for a semiconductor or for a dielectric) ϵ_1 must be negative and larger in absolute value. These conditions are satisfied by many metals in the visible range of the spectrum. Typically, silver and gold

are the most commonly utilized metals for this application. The SPP propagation wavelength and distance can be expressed as a function of the incident wavelength and dielectric functions of the materials at the interface. For metals the imaginary part of the dielectric function is much smaller than the absolute value of the real part (for a meta dielectric function $\epsilon_m(\omega) = \epsilon'_m(\omega) + i\epsilon''_m(\omega)$, $|\epsilon''_m(\omega)| \ll |\epsilon'_m(\omega)|$). For such a case the dispersion relation of an SPP on a flat semi-infinite metal surface can be expressed as [69]

$$k'_x = \frac{\omega}{c} \sqrt{\frac{\epsilon'_m(\omega)\epsilon_d}{\epsilon'_m(\omega) + \epsilon_d}} \quad (5.18)$$

and

$$k''_x = \frac{1}{2} \frac{\omega}{c} \frac{\epsilon''_m(\omega)}{(\epsilon'_m(\omega))^2} \left(\frac{\epsilon'_m(\omega)\epsilon_d}{\epsilon'_m(\omega) + \epsilon_d} \right)^{3/2} \quad (5.19)$$

where k'_x and k''_x are the real and imaginary parts of the propagation wave-vector parallel to the interface surface, respectively, and the dielectric constant $\epsilon_d = n^2$ of the dielectric material with refractive index n . The SPP wavelength is then given by

$$\lambda_{\text{SPP}} = \frac{2\pi}{k'_x} = \lambda \sqrt{\frac{\epsilon'_m(\omega)\epsilon_d}{\epsilon'_m(\omega) + \epsilon_d}} \quad (5.20)$$

for an incidence wavelength λ . Also, the $1/e$ propagation length can be given by $1/k''_x$. For SPPs increasing the plasmon propagation length typically comes at the expense of lower optical confinement; hence, optimum solar cell design must take this into consideration.

Diffraction effects are one way to excite the SPP as they can allow for wave-vector/momentum conservation for the SPP excitation. This can be done through corrugated plasmonic structures such as plasmonic metal gratings. In this case, near the plasmon resonance frequency, the evanescent electromagnetic SPP fields are confined near the interface at dimensions much smaller than the wave-length. SPPs excited at the metal/dielectric or metal/semiconductor interface can efficiently guide and confine the light in the semiconductor layer. For such a case the effect is that the incident solar irradiance is more or less rotated by 90° and light is absorbed along the lateral direction of the solar cell as shown in the schematic of Fig. 5.12 below. This leads to an optical propagation path that is much larger than the optical absorption length. Since metal contacts are a standard part of the solar cell structure, such a plasmonic coupling geometry can be integrated in a simple way in the solar cell, e.g., as part of the solar cell back reflector. Nanofabrication of these structures could be implemented in a straightforward way using soft-imprint patterning and etching techniques. The component of the diffracted light that coincides with the SPP wave-vector (k_{SPP}) will be

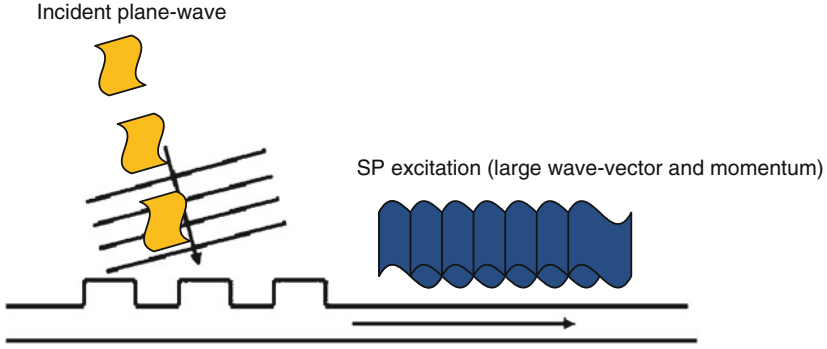


Fig. 5.12 SP excitation at a corrugated or a grating structure interface (e.g., metal/dielectric interface). See (5.20) for surface plasmon dispersion (SP wavelength will be smaller than wavelength in incidence medium)

coupled to the surface polaritons, in this case the photon can gain or lose momentum in multiples of the reciprocal lattice vectors [69, 70]:

$$k_{\text{SPP}} = \frac{\omega}{c} n_m u_{xy} P_p \sin \theta \pm m \frac{2\pi}{\Lambda} u_x \pm l \frac{2\pi}{\Lambda} u_y \quad (5.21)$$

where Λ is the period of the grating (in this case assumed to be identical in the x - and y -directions), n_m is the refractive index of the medium through which the plasmonic structure is illuminated, θ is the angle of incidence with respect to the surface normal, u_{xy} is the unit vector of the in-plane of the incident light wave-vector, u_x and u_y are the unit lattice vectors of a periodic structure, and m and l are integer numbers that correspond to the different propagation directions of the SPPs defining the particular order of the Bloch modes. P_p is equal to 1 for p-polarized light (with respect to the surface plane) and 0 for s-polarized light; s-polarized light cannot excite SPPs. For a one-dimensional periodic grating structure, for phase-matching (momentum conservation condition) the SPP wave-vector can be given as [70]

$$k'_x = k_0 \sin \theta + \frac{2m\pi}{\Lambda} \quad (5.22)$$

k_0 is the vacuum or free-space wave-vector. For normal incidence ($\theta = 90^\circ$), and substituting (5.22) by (5.20), the SPP wavelength for the 1-D periodic grating structure is given as

$$\lambda_{\text{SPPG1}} = \frac{\Lambda}{2\pi m} \sqrt{\frac{\epsilon'_m(\omega)\epsilon_d}{\epsilon'_m(\omega) + \epsilon_d}} \quad (5.23)$$

For a two-dimensional square array of dielectric embedded in a metal grating with periodicity Λ , the SPP wavelength can be expressed as

$$\lambda_{\text{SPPG2}} = \frac{\Lambda}{\sqrt{m^2 + l^2}} \sqrt{\frac{\epsilon'_m(\omega)\epsilon_d}{\epsilon'_m(\omega) + \epsilon_d}} \quad (5.24)$$

Examples of such plasmonic square arrays are illustrated in [61, 71].

Several research groups have recently demonstrated the benefit of surface plasmon back reflectors for ultrathin amorphous Si solar cells [72, 73]. These types of nanostructured back reflectors allow for light trapping beyond those of randomly textured solar cells.

In general, for solar cell photo-generated current enhancement it is useful to employ SPP design in TFSCs when the absorption of the SPP in the semiconductor is more than that of the metal. Typically the SPP has a narrowband spectrum that depends on the feature size/dimensions, material, and periodicity of the corrugated structure. However, broadband optical absorption may be made possible with aperiodic plasmonic nanostructures [74].

5 Nanostructured Third-Generation Silicon Solar Cells

5.1 Tandem Quantum Dot Si Solar Cells

Third-generation solar cells have been proposed to achieve high solar cell efficiencies while using abundant materials, ultimately to achieve lower \$/Watt for the solar cells and modules. Silicon quantum dots (QDs) have been suggested as a method to tune or engineer the effective bandgap of a top cell of a tandem stack “all-silicon” solar cell [75–77]. Silicon QDs embedded in a dielectric matrix can tune the bandgap by making use of quantum confinement to allow for the optimization of tandem Si solar cell structures for enhanced absorption and photo-generation. Si QDs of 2 nm diameter will have a bandgap of ~1.8 eV, which can be used for this purpose, for example for a tandem thin-film crystalline Si bottom cell and a tandem superlattice QD top cell solar cell as shown in the band diagram in Fig. 5.13(a). To form such a structure it has been proposed that thin layers of Si-rich oxide can be sputtered in between a stoichiometric oxide as shown in Fig. 5.13(b) below. Upon annealing these Si QDs could potentially crystallize to form nanocrystals of uniform size [77]. Fabrication of this structure has been demonstrated, and by incorporating dopants (e.g., phosphorus) of the Si QDs a rectifying junction with an open-circuit voltage of ~490 mV has been achieved [78]. Phosphorus doping of the Si QDs was found to significantly decrease the resistivity of the tandem cell, and it also shifted the recombination mechanism in

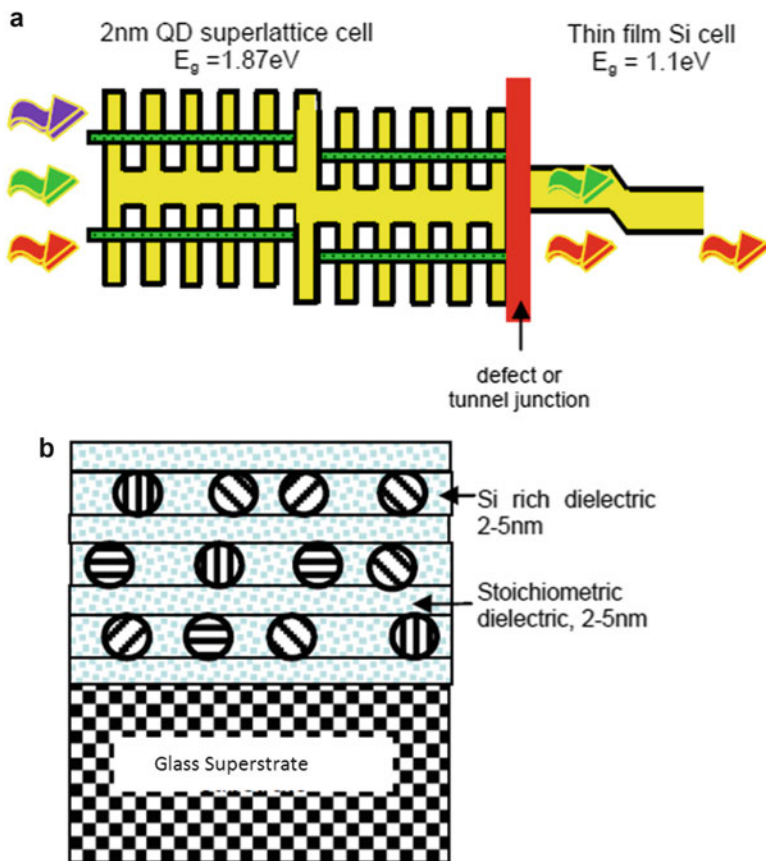


Fig. 5.13 (a) Silicon nanostructure/silicon tandem cell energy band diagram. (b) Multilayer deposition of alternating Si-rich dielectric and stoichiometric dielectric in layers of a few nanometers (after [77] with modification)

the solar cell towards radiative recombination [79]. However, more work needs to be done to resolve process issues and to improve the fundamental understanding of such structures particularly with QD doping in order to achieve solar cells with higher short-circuit current and better conversion efficiencies.

One can also imagine using plasmonic nanostructures or nanoparticles in tandem such as shown in Fig. 5.11 in the previous section in conjunction with the tandem QD structure shown in Fig. 5.13(b) or, in general, for any tandem QD structure used for bandgap engineering to optimize optical absorption for each energy layer. In such a case one can see the advantage of using these plasmonic structures or nanoparticles to couple light into the optical modes of each Si QD layer as it may be possible to integrate them in the same thin-film QD layer.

5.2 Multiple Exciton Generation in Silicon Solar Cells

Multiple exciton generation (MEG) takes place when a single-photon impinging on the solar cell yields more than one electron–hole pair. This takes place via impact ionization process when the energy of the photon is much greater than the bandgap of the semiconductor (ideally $E > 2E_g$) [80, 81]. This behavior does not typically take place in bulk semiconductors as the excess energy is lost as heat in the semiconductor before it can be used to create other electron–hole pairs. However, for quantum dots of semiconducting materials, this excess energy dissipation rate is greatly reduced (carrier thermalization is greatly reduced or negligible) as the charge carriers are confined to a very small space which increases the probability of their interaction (wave-function interaction), which in turn increases the probability of the MEG process to take place. For quantum confinement to take place the material needs to be of a size smaller than its Bohr excitonic radius. This is about 4 nm for silicon. Quantum dots with the optimum bandgap can, in theory, yield approximately double the maximum conversion efficiency given by a single-junction solar cell resulting in an absolute efficiency of 65 % without concentration.

The thermodynamic upper conversion efficiency limits can be derived mathematically for the MEG effect [82, 83]. For maximizing the photo-generation current it is assumed that every single photon of energy $E_{ph} = h\nu$ generates the following quantum yield (QY) for a material of bandgap E_g :

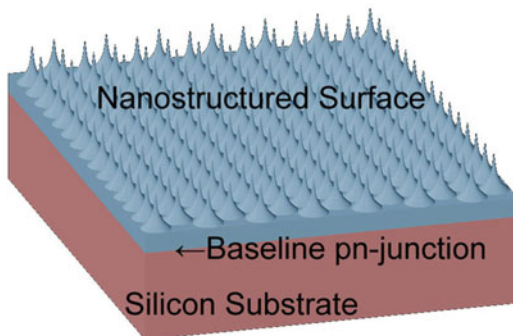
$$\text{QY}(E_{ph}) = \left\{ \begin{array}{ll} 0 & 0 < E_{ph} < E_g \\ m & mE_g < E_{ph} < (m+1)E_g \\ m_{\max} & E_{ph} \geq m_{\max}E_g \end{array} \quad m = 1, 2, 3, \dots, m_{\max} - 1 \right\} \quad (5.25)$$

With these carrier multiplicities the photo-generation current can be obtained as follows:

$$J_{ph} = \sum_{m=1}^{m_{\max}-1} me \int_{mE_g}^{(m+1)E_g} n_{ph}(E_{ph}) dE_{ph} + m_{\max} e \int_{m_{\max}E_g}^{\infty} n_{ph}(E_{ph}) dE_{ph} \quad (5.26)$$

where e is the electron charge and n_{ph} is the photon flux per energy interval and time interval under a certain optical concentration. The existence of a concentrator allows the solar cell to receive radiation from a solid angle larger than that subtended by the sun. The photon flux per energy interval can be described by Planck's law of radiation for a black body, as the sun's spectrum can be almost described by a black body at a temperature equal to $\sim 5,760$ K. The conversion efficiency can then be obtained from $J(V)/\Phi_1$, where Φ_1 is the incident energy flux, $J(V)$ is the current density of the photovoltaic cell ($J(V) = J_{ph} - J_o(V)$), where $J_o(V)$ is the saturation current density of the solar cell), and V is the bias voltage of the solar cell under operation.

Fig. 5.14 A nano-tip Si solar cell structure (after [87])



For larger material bandgap the MEG effect becomes less significant since for multiplicities $m > 2$ the number of photons in the solar spectrum for these large energies is greatly reduced. Hence, it is preferred that materials with smaller bandgaps be used for greater enhancement of the solar cell performance due to the MEG effect, particularly when the solar cell is under high optical concentration. An almost ideal material for this is PbSe which has a direct bandgap of 0.27 eV. Both PbSe and PbS have been used to demonstrate the MEG effect [84]. Solar cells employing these semiconducting QDs typically have a zinc oxide (as an inversion layer) or thin ZnO/ITO anode and metal cathode (e.g., Au back contact) [85]. The ZnO electrode can be structured into nanowires that penetrate deep into the QDs, thus increasing the effective collecting junction depth [86]. However, these quantum dots suffer resistive losses due to low mobility between QDs and all the way to the contact electrodes, which lowers the fill factor and overall performance of the solar cell. A different solar cell design with MEG potential that also offers more straightforward carrier collection with minimal resistive and contact losses compared with the PbSe or PbS QD solar cells has been proposed [87]. This solar cell is based on Si material, and it can be nanostructured to produce the MEG effect in the nano-pillar structures or at least at the peaks of these nano-pillars. Figure 5.14 shows the simple structure of such a solar cell device. By adjusting the nano-pillar size and peak diameter the bandgap of the Si in these regions can be tuned to allow for the MEG condition and effect to take place. Even though Si has a larger bandgap than PbSe (Si has a larger bandgap than the optimum bandgap for high multiplicity factors), nevertheless, there is still a significant number of photons in the solar spectrum at energies that are more than double the bandgap of silicon. Based on theoretical detailed balance calculations there is a maximum potential of almost 8 % absolute efficiency enhancement for Si nanostructured solar cells with no optical concentration, assuming only radiative recombination losses in the solar cell (note that these quantum confined nanoscale material structures will have a direct bandgap). In practice photon energies greater than the ideal energy of $2E_g$ with ultrafast carrier multiplication rates (<200 fs) may be required in order to give a greater than unity quantum yield [88]. Moreover, a QY of 3 or larger may be challenging to achieve due to the higher degree of freedom for such nano-tip

structures with one degree of freedom as opposed to a QD nanocrystal with zero degree of freedom; instead, quantum yields of 2 may be more realistic for such structures based on observations made by Htoon et al. [89]. In practice, there may be other challenges which include possible surface recombination at unpassivated interface defect sites of the nano-tips.

Such nano-tip structures may be formed by making use of a metal nanocrystal salicidation process on the Si surface as illustrated in [90] followed by reactive-ion etching. This kind of process may result in a few nanometer scale nano-tips or nano-pillars. Alternatively, nano-imprinting could be used to form such structures; however, it may be challenging to obtain a template with only few nanometer features needed for the c-Si MEG solar cell using this technique. Hence, nano-imprinting may be more suitable to use for materials that have less stringent feature size requirements for quantum confinement.

6 Summary and Conclusions

In this book chapter several technologies and physical concepts associated with solar cell design and operation have been presented. An attempt has been made to concisely explain the underlying physics of some of the involved phenomena presented such as the physics of nanowire Si solar cells, light trapping, plasmonics, and the MEG effect.

Even though nanowire Si solar cells have generated a lot of interest lately, nevertheless, they have some technical as well as processing challenges to compete with conventional wafer-based Si solar cells both on a performance and a cost basis. Micro-wire solar cells may have some benefit for low-cost poor-quality UMG Si material or for some poor-carrier-lifetime Si ribbon materials without the need to resort to high-temperature gettering methods.

Hybrid silicon–polymer solar cells have also been presented—these solar cells offer an alternative path to the implementation of low-cost solar cells using low-temperature processes, with potential performance that could be competitive with those of thin-film Si solar cells. However, more work needs to be done to better understand the interface properties and to enhance the organic material incorporation into the nanostructures in order to achieve higher conversion efficiencies.

We have presented various nanostructures investigated for thin-film a-Si solar cells in this book chapter; these nanostructures have been mostly investigated for amorphous Si absorber material. One should note that CdTe or CIGS are deposited to form significantly thicker absorber layers than a-Si and, hence, do not gain as much as a-Si from nanostructured light trapping schemes. However, this may change for thinner CdTe or CIGS layers that may be employed in the future to save cost or save on the usage of rare materials such as tellurium or indium. Based on the simulation and experimental results reported in the literature, it can be concluded that 3D-wrapped nanostructured a-Si solar cells yield a better

enhancement in photocurrent compared with plasmonic nanostructures for a-Si TFSCs. Single-pitch-design plasmonic nanostructures give more narrowband improvements, and they typically show a photocurrent enhancement that is similar to that of the Asahi U-type textured glass a-Si TFSC. However, novel plasmonic aperiodic nanostructures may yield broader band improvements that may result in more significant photocurrent enhancements for these thin-film Si solar cells. In general, plasmonic nanostructures for TFSCs, either as SPP back reflectors or for light scattering and coupling, for example, from the top surface of the solar cell can also have a significant impact in the solar cell field.

Third-generation solar cells utilizing concepts such as MEG or “hot-electron” collection are of great interest to the photovoltaics community, and it is expected that they could play a bigger role in the future to break the current efficiency barriers for industrial solar cells. However, this would require better understanding of the underlying physics and material behavior at the nanoscale. Moreover, new concepts of integration using scalable processing techniques would need to be investigated and developed. Integration of plasmonics with third-generation solar cell designs to target certain absorption spectra, for example for tandem quantum dot solar cells or for MEG solar cells, could have a big impact in the photovoltaics field. Novel nanofabrication techniques such as nano-imprinting, which offer a much more cost-effective approach for nano-fabrication and better control over pattern shape and size, can offer a robust fabrication technology for nanostructured solar cells as opposed to the more expensive advanced photolithography or research nanofabrication approaches such as e-beam lithography techniques.

Acknowledgements This work was partially funded by the National Science Foundation Scalable Nanomanufacturing Program (NSF Contract No. ECCS-1120823), the DARPA Tip-Based Nanofabrication Program (DARPA Contract No. N66001-08-C-2040), and the Texas Emerging Technology Funds Program and by a research grant from Molecular Imprints, Inc.

References

1. Yu, Z., Raman, A., Fan, S.: Fundamental limit of light trapping in grating structures. *Opt. Express* **18**, 366–380 (2010)
2. Yablonovitch, E., Cody, G.D.: Intensity enhancement in textured optical sheets for solar cells. *IEEE Trans. Electron. Dev.* **29**, 300–305 (1982)
3. Liu, Y., Sun, S.H., Xu, J., Zhao, L., Sun, H.C., Li, J., Mu, W.W., Xu, L., Chen, K.J.: Broadband antireflection and absorption enhancement by forming nano-patterned silicon structures for solar cells. *Opt. Express* **19**(S5), A1051–A1056 (2011)
4. Peng, K., Xu, Y., Wu, Y., Yan, Y.: Aligned single-crystalline Si nanowire arrays for photovoltaic applications. *Small* **1**, 1062–1067 (2005)
5. Lin, C., Povinelli, M.L.: Optical absorption enhancement in silicon nanowire arrays with a large lattice constant for photovoltaic applications. *Opt. Express* **17**, 19371–19381 (2009)
6. Garnett, E.C., Yang, P.: Light trapping in silicon nanowire solar cells. *Nano Lett.* **10**, 1082–1087 (2010)

7. Sturmberg, B.C., Dossou, K.B., Botten, L.C., Asatryan, A.A., Poulton, C.G., de Sterke, C.M., McPhedran, R.C.: Modal analysis of enhanced absorption in silicon nanowire arrays. *Opt. Express* **19**(S5), A1067–A1081 (2011)
8. Jihun, O., Yuan, H.-C., Branz, H.M.: An 18.2%-efficient black-silicon solar cell achieved through control of carrier recombination in nanostructures. *Nat. Nanotechnol.* **7**, 743–748 (2012)
9. Peng, K., Juejun, H., Yan, Y., Yin, W., Fang, H., Ying, X., Lee, S.T., Zhu, J.: Fabrication of single-crystalline silicon nanowires by scratching a silicon surface with catalytic metal particles. *Adv. Funct. Mater.* **16**, 387–394 (2006)
10. Chen, C., Jia, R., Yue, H., Li, H., Liu, X., Deqi, W., Ding, W., Ye, T., Kasai, S., Tamotsu, H., Chu, J., Wang, S.: Silicon nanowire-array-textured solar cells for photovoltaic application. *J. Appl. Phys.* **108**, 094318–5 (2010)
11. Srivastava, S.K., Kumar, D., Singh, P.K., Kar, M., Kumar, V., Husain, M.: Excellent antireflection properties of vertical silicon nanowire arrays. *Sol. Energy. Mat. Sol. Cells* **94**, 1506–1511 (2010)
12. Kerr M.J.: Surface, emitter and bulk recombination in silicon and development of silicon nitride passivated solar cells. Ph.D. Thesis, Australian National University (2002)
13. Hilali, M.M., Al-Jassim, M.M., To, B., Moutinho, H., Rohatgi, A., Asher, S.: Understanding the formation and temperature dependence of thick-film Ag contacts on high-sheet-resistance Si emitters for solar cells. *J. Electrochem. Soc.* **152**(10), G742–G749 (2005)
14. Wallentin, J., Anttu, N., Asoli, D., Huffman, D., Åberg, I., Magnusson, M.H., Siefert, G., Fuss-Kailuweit, P., Dimroth, F., Witzigmann, B., Xu, H.Q., Samuelson, L., Deppert, K., Borgström, M.T.: InP Nanowire array solar cells achieving 13.8% efficiency by exceeding the ray optics limit. *Science* **339**, 1057–1060 (2013)
15. Huang, N., Lin, C., Povinelli, M.L.: Limiting efficiencies of tandem solar cells consisting of III–V-nanowire arrays on silicon. *J. Appl. Phys.* **112**, 064321 (2012)
16. Gharghi, M.: On the design and applicability of nanowire solar cells using low-grade semiconductors. *J. Appl. Phys.* **111**, 03501–03507 (2012)
17. Yoon, H.P., Yuwen, Y.A., Shen, H., Podraza, N.J., Mallouk, T.E., Dickey, E.C., Redwing, J. A., Wronski, C.R., and Mayer, T.S.: Parametric Study of Micropillar Array Solar Cells. Proceedings of the 37th IEEE Photovoltaics Specialists Conference, 2011, pp. 000303–000306
18. Gharghi, M., Fathi, E., Kante, B., Sivothythaman, S., Zhang, X.: Heterojunction silicon microwire solar cells. *Nanoletters* **12**, 6278–6282 (2012)
19. Wagner, R.S., Ellis, W.C.: Vapor–liquid–solid mechanism of single crystal growth. *Appl. Phys. Lett.* **4**(5), 89–90 (1964)
20. Spurgeon, J.M., Plass, K.E., Kayes, B.M., Brunshwig, B.S., Atwater, H.A., Lewis, N.S.: Repeated epitaxial growth and transfer of arrays of patterned, vertically aligned, crystalline Si wires from a single Si (111) substrate. *Appl. Phys. Lett.* **93**, 032112–3 (2008)
21. Putnam, M.C., Boettcher, S.W., Kelzenberg, M.D., Turner-Evans, D.B., Spurgeon, J.M., Warren, E.L., Briggs, R.M., Lewis, N.S., Atwater, H.A.: Si micro-wire array solar cells. *Energ. Environ. Sci.* **3**(8), 1037–1041 (2010)
22. Fonash, S.J.: *Solar Cell Device Physics*, 2nd edn. Academic, Burlington, MA (2010)
23. Oosterhout, S.D., Wienk, M.M., van Bavel, S.S., Thiedmann, R., Koster, L.J., Gilot, J., Loos, J., Schmidt, V., Janssen, R.A.: The effect of three-dimensional morphology on the efficiency of hybrid polymer solar cells. *Nat. Mat.* **8**, 818–824 (2009)
24. Yu, G., Gao, J., Hummelen, J.C., Wudl, F., Heeger, A.J.: Polymer photovoltaic cells enhanced efficiencies via a network of internal donor-acceptor heterojunctions. *Science* **270**(5243), 1789–1791 (1995)
25. Greenham, N.C., Peng, X., Alivisatos, A.P.: Charge separation and transport in conjugated-polymer/semiconductor-nanocrystal composites studied by photoluminescence quenching and photoconductivity. *Phy. Rev. B* **54**(24), 17628–17637 (1996)
26. Weickert, J., Dunbar, R.B., Hesse, H.C., Wiedemann, W., Schmidt-Mende, L.: Nanostructured organic and hybrid solar cells. *Adv. Mater.* **23**, 1810–1828 (2011)

27. Kuo, C.Y., Tang, W.C., Gao, C., Guo, T.F., Jeng, D.Z.: Ordered bulk heterojunction solar cells with vertically aligned TiO₂ nanorods embedded in a conjugated polymer. *Appl. Phys. Lett.* **93**, 033307–3 (2008)
28. Syu, H.-J., Shiu, S.-C., Lin, C.-F.: Silicon nanowire/organic hybrid solar cell with efficiency of 8.40 %. *Sol. Energ. Mat. Sol. Cells* **98**, 267–272 (2012)
29. Syu, H.-J., Shiu, S.-C., Lin, C.-F.: Effect of Nanowire Length to Silicon Nanowire/PEDOT:PSS Solar Cells. Proceedings of the 37th IEEE Photovoltaics Specialists Conference, Seattle, June, 2011, pp. 002490–002491
30. Alet, P.J.: Hybrid thin-film solar cells based on nan-structured silicon and semiconducting polymer. Ph.D. thesis, École Polytechnique (2008)
31. Hegedus, S.: Thin film solar modules: the low cost, high throughput and versatile alternative to Si wafers. *Prog. Photovol. Res. Appl.* **14**, 393–411 (2006)
32. Romeo, N., Bosio, A., Canevari, V., Podesta, A.: Recent progress on CdTe/CdS thin film solar cells. *Sol. Energy* **77**, 795–801 (2004)
33. Devaney, W.E., Chen, W.S., Stewart, J.M., Mickelsen, R.A.: Structure and properties of high efficiency ZnO/CdZnS/CuInGaSe₂ solar cells. *IEEE Trans. Electron. Dev.* **37**(2), 428–433 (1990)
34. Kolodziej, A.: Staebler-Wronski effect in amorphous silicon and its alloys. *Opto-Electron-Rev* **12**(1), 21–32 (2004)
35. Redfield, D.: Multi-pass thin film silicon solar cell. *App. Phys. Lett.* **25**, 647–648 (1974)
36. Yablonovitch, E.: Statistical ray optics. *J. Opt. Soc. Am.* **72**, 899–907 (1982)
37. Yablonovitch, E., Cody, G.D.: Intensity enhancement for textured optical sheets for solar cells. *IEEE Trans. Electron. Dev.* **ED-29**(2), 300–305 (1982)
38. Deckman, H.W., Roxlo, C.B., Yablonovitch, E.: Maximum statistical increase of optical absorption in textured semiconductor films. *Opt. Lett.* **8**(9), 491–493 (1983)
39. Rybczynski, J., Kempa, K., Herczynski, A., Wang, Y., Naughton, M.J., Ren, Z.F., Huang, Z.P., Cai, D., Giersig, M.: Subwavelength waveguide for visible light. *Appl. Phys. Lett.* **90**, 021104–1 (2007)
40. Naughton, M.J., Kempa, K., Ren, Z.F., Gao, Y., Rybczynski, J., Argenti, N., Gao, W., Wang, Y., Peng, Y., Naughton, J.R., McMahon, G., Paudel, T., Lan, Y.C., Burns, M.J., Shepard, A., Clary, M., Ballif, C., Haug, F.-J., Söderström, T., Cubero, O., Eminian, C.: Efficient nanocoax-based solar cells. *Physics. Status. Solidi. Rapid. Res. Lett.* **4**(7), 181–183 (2010)
41. Paudel, T., Rybczynski, J., Gao, Y.T., Lan, Y.C., Peng, Y., Kempa, K., Naughton, M.J., Ren, Z.F.: Nanocoax solar cells based on aligned multiwalled carbon nanotube arrays. *Phys. Status Solidi A* **208**, 924–927 (2011)
42. Hilali, M.M., Yang, S., Miller, M., Xu, F., Banerjee, S., Sreenivasan, S.V.: Enhanced photo-current in thin-film amorphous silicon solar cells Via shape controlled three-dimensional nanostructures. *Nanotechnology* **23**(40), 405203–405209 (2012)
43. Vanecek, M., Babchenko, O., Purkrt, A., Holovsky, J., Neykova, N., Poruba, A., Remes, Z., Meier, J., Kroll, U.: Nanostructured three-dimensional thin film silicon solar cells with very high efficiency potential. *Appl. Phys. Lett.* **98**, 163503–3 (2011)
44. Shir, D., Yoon, J., Chanda, D., Ryu, J.-H., Rogers, J.A.: Performance of ultrathin silicon solar microcells with nanostructures of relief formed by soft imprint lithography for broad band absorption enhancement. *Nano Lett.* **10**, 3041–3046 (2010)
45. Zhu, J., Yu, Z., Burkhard, G.F., Hsu, C., Connor, S.T., Xu, Y., Wang, Q., McGehee, M., Fan, S., Cui, Y.: Optical absorption enhancement in amorphous silicon nanowire and nanocone arrays. *Nano Lett.* **9**(1), 279–282 (2009)
46. Li, J.S., Yu, Y., Wong, S.M., Zhang, G., Lo, G.Q., Kwong, D.L.: Surface nanostructure optimization for solar energy harvesting in Si thin film based solar cells. *IEEE Tech. Digest-Int. Electron Devices Meeting*, 2009, pp. 547–550
47. Taflove, A., Hagness, S.C.: *Computational Electrodynamics: The Finite-Difference Time-Domain Method*, 3rd edn. Artech House, Boston, MA (2005)

48. Moharam, M.G., Gaylord, T.K.: Rigorous coupled-wave analysis of metallic surface-relief Gratings. *J. Opt. Soc. Am. A* **3**, 1780–1787 (2008)
49. Sergeant, N.P., Agarwal, M., Peumans, P.: High performance solar-selective absorbers using coated sub-wavelength gratings. *Opt. Express* **18**, 5525–5540 (2010)
50. Singh, J.: *Quantum Mechanics: Fundamentals and Applications to Technology*. Wiley, New York, NY (1997)
51. Lin, C.H., Leung, K.M., Tamir, T.: Modal transmission-line theory of three-dimensional periodic structures with arbitrary lattice configurations. *J. Opt. Soc. Am. A* **19**, 2005–2017 (2002)
52. Goldberg, D.E.: *Genetic Algorithms in Search, Optimization, and Machine Learning*. Addison Wesley, Upper Saddle River, NJ (1989)
53. Söderström, T., Haug, F.-J., Terrazoni-Daudrix, V., Niquille, X., Python, M., Ballif, C.: N/I buffer layer for substrate microcrystalline thin film silicon solar cell. *J. Appl. Phys.* **104**(10), 104505–104508 (2008)
54. Wei, E.I., Wallace, S., Choy, C.H., Chew, W.C.: A comprehensive study for the plasmonic thin-film solar cell with periodic structure. *Opt. Express* **18**(6), 5993–6007 (2010)
55. Bohren, C.F., Huffman, D.R.: *Absorption and Scattering of Light by Small Particles*. Wiley-Interscience, New York, NY (1983)
56. Bohren, C.F.: How can a particle absorb more than the light incident on it? *Am. J. Phys.* **51**(4), 323–327 (1983)
57. Pillai, S., Green, M.A.: Plasmonics for photovoltaic applications. *Sol. Energ. Mat. Sol. Cells* **94**, 1481–1486 (2010)
58. Catchpole, K.R., Polman, A.: Design principles for particle plasmon enhanced solar cells. *Appl. Phys. Lett.* **93**(19), 191113–3 (2008)
59. Pillai, S., Catchpole, K.R., Trupke, T., Green, M.A.: Surface Plasmon enhanced silicon solar cells. *J. Appl. Phys.* **101**, 093105–093108 (2007)
60. Catchpole, K.R., Polman, A.: Plasmonic solar cells. *Opt. Express* **16**(26), 217793–221800 (2008)
61. Atwater, H.A., Polman, A.: Plasmonics for improved photovoltaics. *Nat. Mater.* **9**, 206–213 (2010)
62. Kirkengen, M., Bergli, J., Galperin, Y.M.: Direct generation of charge carriers in c-Si solar cells due to embedded nanoparticles. *J. Appl. Phys.* **102**, 093713–093715 (2007)
63. Ashcroft, N.W., Mermin, N.D.: *Solid-State Physics*, 1st edn, pp. 1–20. Harcourt College Publisher, Philadelphia, PA (1976)
64. Xu, G., Tazawa, M., Jin, P., Nakao, S., Yoshimura, K.: Wavelength tuning of surface plasmon resonance using dielectric layers on silver island films. *Appl. Phys. Lett.* **82**, 3811–3813 (2003)
65. Gong, Y.: *Silicon-based photonic, plasmonic, and optomechanic devices*. Ph.D. Thesis, Stanford University (2010)
66. Mertens, H., Verhoeven, J., Polman, A., Tichelaar, F.D.: Infrared surface plasmons in two-dimensional silver nanoparticle arrays in silicon. *Appl. Phys. Lett.* **85**, 1317–1319 (2004)
67. Tu, W.-C., Chang, Y.-T., Yang, C.-H., Yeh, D.-J., Ho, C.-I., Hsueh, C.-Y., Lee, S.-C.: Hydrogenated amorphous silicon solar cell on glass substrate patterned by hexagonal nanocylinder array. *Appl. Phys. Lett.* **97**(19), 93109–3 (2010)
68. Schaadt, D.M., Feng, B., Yu, E.T.: Enhanced semiconductor optical absorption via surface plasmon excitation in metal nanoparticles. *Appl. Phys. Lett.* **86**, 063106–3 (2005)
69. Raether, H.: *Surface Plasmons on Smooth and Rough Surfaces and on Gratings*. Springer Tracts in Modern Physics, (Springer-Verlag: New York), **111**, (1988)
70. Maier, S.: *Plasmonics: Fundamentals and Applications*, 1st edn. Springer, New York, NY (2007)
71. Henzie, J., Lee, J., Lee, M.H., Hasan, W., Odom, T.W.: Nanofabrication of plasmonic structures. *Annu. Rev. Phys. Chem.* **60**, 147–165 (2009)

72. Ferry, V., Verschuuren, M.A., Li, H.B., Verhagen, E., Walters, R.J., Schropp, R.E., Atwater, H.A., Polman, A.: Light trapping in ultrathin plasmonic solar cells. *Opt. Express* **18**(2), A237–A245 (2010)
73. Haug, F.-J., Söderström, T., Cubero, O., Terrazoni-Daudrix, V., Ballif, C.: Plasmonic absorption in textured silver back reflectors of thin film solar cells. *J. Appl. Phys.* **104**, 064509–7 (2008)
74. Trevino, J., Forestiere, D., Di Martino, G., Yerci, S., Priolo, F., Dal Negro, L.: Plasmonic-photonics arrays with aperiodic spiral order for ultra-thin film solar cells. *Opt. Express* **20**(10), A418–A430 (2012)
75. Cho, E.-C., Park, S., Hao, X., Song, D., Conibeer, G., Park, S.C., Green, M.A.: Silicon quantum dot/crystalline silicon solar cells. *Nanotechnology* **19**(24), 245201 (2008)
76. Conibeer, G., Green, M.A., Cho, E.C., König, D., Cho, Y.H., Fangsuwannarak, T., Scardera, G., Pink, E., Huang, Y., Puzzer, T., Huang, S., Song, D., Flynn, C., Park, S., Hao, X., Mansfield, D.: Silicon quantum dot nanostructures for tandem photovoltaic cells. *Thin Solid Films* **516**, 6748–6756 (2008)
77. Conibeer, G., Perez-Wurfl, I., Hao, X., Di, D., Lin, D.: Si solid-state quantum dot-based materials for tandem solar cells. *Nanoscale Res. Lett.* **7**(193), 1–6 (2012)
78. Perez-Wurfl, I., Ma, L., Lin, D., Hao, X., Green, M.A., Conibeer, G.: Silicon nanocrystals in an oxide matrix for thin film solar cells with 492 mV open circuit voltage. *Sol. Energ. Mat. Sol. Cells* **100**, 65–68 (2012)
79. Hao, X.J., Cho, E.-C., Scardera, G., Shen, Y.S., Bellet-Amalric, E., Bellet, D., Conibeer, G., Green, M.A.: Phosphorus-doped silicon quantum dots for all-silicon quantum dot tandem solar cells. *Sol. Energ. Mat. Sol. Cells* **93**(9), 1524–1530 (2009)
80. Kolodinski, S., Werner, J.H., Wittchen, T., Queisser, H.J.: Quantum efficiencies exceeding unity due to impact ionization in silicon solar cells. *Appl. Phys. Lett.* **63**(17), 2405–2407 (1993)
81. Badescu, V., Landsberg, P.T., De Vos, A., Desoete, B.: Statistical thermodynamic foundation for photovoltaic and photothermal conversion. IIV. Solar cells with larger-than-unity quantum efficiency revisited. *J. Appl. Phys.* **89**, 2482–2490 (2001)
82. Werner, J.H., Kolodinski, S., Queisser, H.J.: Novel optimization principles and efficiency limits of semiconductor solar cell. *Phys. Rev. Lett.* **72**(24), 3851–3854 (1994)
83. De Vos, A., Desoete, B.: On the ideal performance of solar cells with larger-than-unity quantum efficiency. *Sol. Energ. Mat. Sol. Cells* **51**(3–4), 413–424 (1998)
84. Beard, M.C., Midgett, A.G., Law, M., Semonin, O.E., Ellingson, R.J., Nozik, A.J.: Variations in quantum efficiency of multiple exciton generation for a series of chemically treated PbSe nanocrystal films. *Nano Lett.* **9**(2), 836–845 (2009)
85. Luther, J.M., Gao, J., Lloyd, M.T., Semonin, O.E., Beard, M.C., Nozik, A.J.: Stability assessment on a 3% bilayer PbS/ZnO quantum Dot heterojunction solar cell. *Adv. Mater.* **22**, 3704–3707 (2010)
86. Jean, J., Chang, S., Brown, P.R., Cheng, J.J., Rekemeyer, P.H., Bawendi, M.G., Gradec, S., Bulović, V.: ZnO nanowire arrays for enhanced photocurrent in PbS quantum dot solar cells. *Adv. Mater.* **25**(20), 2790–2796 (2013)
87. Jacobs, S., Levy, M.Y., Marchena, E., Honsberg, C.B.: Silicon multiple exciton generation/pn junction hybrid solar cell. Proceedings of the 33rd IEEE Photovoltaic Specialists Conference, San Diego, May, 2008, pp. 1–5
88. Franceschetti, A., An, J.M., Zunger, A.: Impact ionization can explain carrier multiplication in PbSe quantum dots. *Nanoletters* **6**(10), 2191–2195 (2006)
89. Htoon, H., Hollingsworth, J.A., Dickerson, R., Klimov, V.: Effect of zero- to one-dimensional transformation on multiparticle Auger recombination in semiconductor quantum rods. *Phys. Rev. Lett.* **91**(22), 227401–227402 (2003)
90. El-Atwani, O., Ortoleva, S., Cimaroli, A., Allain, J.P.: Formation of silicon nanodots via ion beam sputtering of ultrathin gold thin film coatings on Si. *Nanoscale Res. Lett.* **6**(1), 403 (2011)

Chapter 6

High-Bandgap Silicon Nanocrystal Solar Cells: Device Fabrication, Characterization, and Modeling

Philipp Löper, Mariaconcetta Canino, Manuel Schnabel,
Caterina Summonte, Stefan Janz, and Margit Zacharias

Abstract Silicon nanocrystals (Si NCs) embedded in Si-based dielectrics provide a Si-based high-bandgap material (1.7 eV) and enable the construction of crystalline Si tandem solar cells. This chapter focusses on Si NC embedded in silicon carbide, because silicon carbide offers electrical conduction through the matrix material. The material development is reviewed, and optical modeling is introduced as a powerful method to monitor the four material components, amorphous and crystalline silicon as well as amorphous and crystalline silicon carbide. In the second part of this chapter, recent device developments for the photovoltaic characterization of Si NCs are examined. The controlled growth of Si NCs involves high-temperature annealing which deteriorates the properties of any previously established selective contacts. A membrane-based device is presented to overcome these limitations. In this approach, the formation of both selective contacts is carried out after high-temperature annealing and is therefore not affected by the latter. We examine p-i-n solar cells with an intrinsic region made of Si NCs embedded in silicon carbide. Device failure due to damaged insulation layers is analyzed by light beam-induced current measurements. An optical model of the device is presented for improving the cell current. A characterization scheme for Si NC p-i-n solar cells is presented which aims at determining the fundamental transport and recombination properties, i.e., the effective mobility lifetime product,

P. Löper (✉) • M. Schnabel • S. Janz
Fraunhofer ISE, Heidenhofstr. 2, 79110 Freiburg, Germany
e-mail: philipp.loeper@ise.fraunhofer.de; manuel.schnabel@ise.fraunhofer.de;
stefan.janz@ise.fraunhofer.de

M. Canino • C. Summonte
CNR-IMM, Via Piero Gobetti 101, 40129 Bologna, Italy
e-mail: canino@bo.imm.cnr.it; summonte@bo.imm.cnr.it

M. Zacharias
IMTEK, University Freiburg, Georges-Koehler-Allee 103, 79110 Freiburg, Germany
e-mail: zacharias@imtek.uni-freiburg.de

of the nanocrystal layer at device level. For this means, an illumination-dependent analysis of Si NC p-i-n solar cells is carried out within the framework of the constant field approximation. The analysis builds on an optical device model, which is used to assess the photogenerated current in each of the device layers. Illumination-dependent current–voltage curves are modelled with a voltage-dependent current collection function with only two free parameters, and excellent agreement is found between theory and experiment. An effective mobility lifetime product of $10^{-10} \text{ cm}^2/\text{V}$ is derived and confirmed independently from an alternative method. The procedure discussed in this chapter is proposed as a characterization scheme for further material development, providing an optimization parameter (the effective mobility lifetime product) relevant for the photovoltaic performance of Si NC films.

1 Crystalline Si Tandem Solar Cells

The impressive success in reaching very high conversion efficiencies with c-Si [1] has triggered the search for novel concepts overcoming the fundamental efficiency limits. Module costs have been reduced significantly due to upscaled production, but an ongoing long-term cost reduction cannot be achieved only with upscaled production and ever more sophisticated equipment. Rather, new solar cell concepts are required that permit overcoming the physical limitations of today's technologies. Figure 6.1 depicts the AM1.5G solar spectrum and illustrates the energy that can theoretically be converted by a silicon solar cell.

The theoretical efficiency limit arises from two loss mechanisms. Photons with energy less than the bandgap energy are not absorbed by the solar cell (red and rightmost arrow in Fig. 6.1), giving rise to transmission losses. High-energy photons, on the other hand, create a high-energy electron–hole pair in the solar

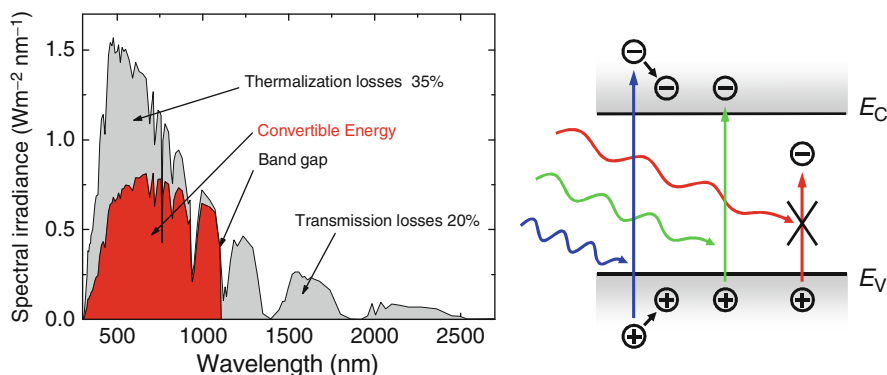


Fig. 6.1 (Left) The AM1.5G solar spectrum and the maximum energy convertible to electricity by a silicon solar cell. The fundamental efficiency limit arises from the loss mechanisms shown on right. The figure was taken from [2]

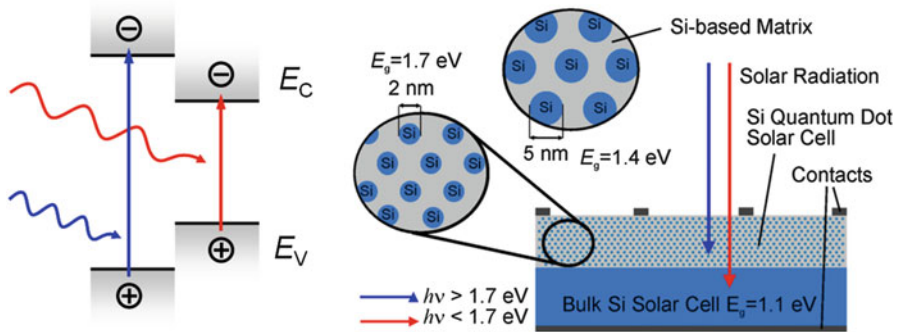


Fig. 6.2 (Left) Principle of stacked absorbers, each of which is matched to one wavelength. (Right) Scheme of an all-crystalline silicon tandem solar cell. The top solar cell consists of Si nanocrystal quantum dots that absorb only the high-energy photons. The bandgap of the Si nanocrystal quantum dots can be tuned by controlling the crystal size. The figure was taken from [2]

cell (blue and leftmost arrow in Fig. 6.1). The excess energy is dissipated to the crystal lattice (thermalization), and only a fraction of the incident solar radiation energy is converted to electricity. Ideal energy conversion is possible only for photons whose energy just matches the bandgap energy, indicated by the green arrows in Fig. 6.1.

The conversion of electromagnetic radiation to electrical energy can be optimized by matching the solar cell to the incident spectrum. This can be achieved by stacking multiple solar cells, each of which is adapted to a certain spectral region. Figure 6.2 (left) depicts the principle of such a multijunction or tandem solar cell. Each sub-cell absorbs only a certain spectral region and is optimized to minimize the thermalization upon illumination with this part of the solar spectrum. Tandem solar cells are already commercially available, and efficiencies of 37.7 % have been reached with III–V materials [3]. However, III–V solar cells are only of limited use for large-area power generation as several of the elements involved are toxic, rare, and expensive. The strong motivation to stick to silicon (Si) arises from the fact that it is the second most abundant element in the earth's crust [2], that it is not toxic, that it is quite strong mechanically, and that solar cell manufacturers can build on the highly developed Si microelectronics technology. Therefore, advanced solar cell concepts are desirable that are based on Si materials and compatible with Si technology. Tandem solar cells have been realized with amorphous and microcrystalline Si with a record efficiency of 13.4 %. However, amorphous and microcrystalline Si solar cells suffer from the so-called Staebler–Wronski effect [4], which reduces the efficiency by up to 30 % during operation.

A material which consists of crystalline Si and features a high bandgap is provided by silicon nanocrystals (Si NCs) embedded in a Si-based matrix material.

Since the first observation of visible photoluminescence from anodically etched Si [5], nanostructured Si has received a lot of attention due to the promise of a

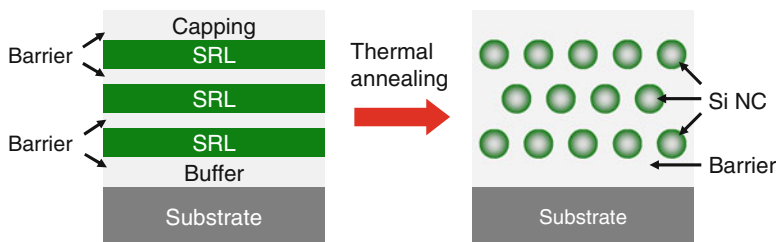


Fig. 6.3 Scheme for the fabrication of a Si nanocrystal superlattice by the multilayer approach [6]. Silicon-rich layers (SRL) are sandwiched between stoichiometric layers (barrier). The barrier layers restrict the Si NC growth and thereby enable a narrow size distribution. Si NC formation is induced by thermal annealing at high temperatures, usually around 1,100 °C. The figure was taken from [2]

high-bandgap material compatible with Si technology. In this context, a “high bandgap” refers to a bandgap value higher than in the extended Si crystal (bulk).

The bandgap has since been shown to be well controllable by tuning the NC size and thus the quantum confinement. The principle of a crystalline Si tandem solar cell is sketched in Fig. 6.2 (right). The high-energy photons (blue arrow) are absorbed in the Si NC top solar cell, while photons with less energy are transmitted by the latter and absorbed in the bottom solar cell. The bottom solar cell is made of bulk Si, e.g., a Si wafer or a thin film crystalline Si.

For large-area fabrication of size-controlled Si NCs, amorphous multilayer precursors are deposited and then thermally annealed to form the Si NCs [6]. The multilayer consists of a stack of alternating Si-rich (SRL) and stoichiometric (barrier) layers of a Si compound as shown in Fig. 6.3. Upon annealing, the Si excess in the Si-rich layers precipitates and clusters. Subsequently, the clusters are solid phase crystallized at temperatures around 1,100 °C. The stoichiometric layers act as barriers towards crystallite growth and thus limit the Si NC size.

2 Membrane-Based p-i-n Device for Substrate-Free Characterization

The necessity of using temperatures of around 1,100 °C for the fabrication of the Si NC layer imposes severe requirements on the thermal stability and the expansion coefficient of the substrate. Device fabrication is further complicated because the substrate hinders the access to the rear side of the Si NC layer. The simplest method is to use a conductive substrate as a back contact, e.g., a Si wafer. However, this complicates device analysis because both the Si NC layer as well as the Si wafer substrate, which even on its own would make a good solar cell, can contribute to the measured current–voltage (*IV*) curve. The Si NC layer contribution to the *IV* curve can theoretically be distinguished from that of the wafer using monochromatic light with a penetration depth below the Si NC layer thickness. The penetration depth $1/\alpha$

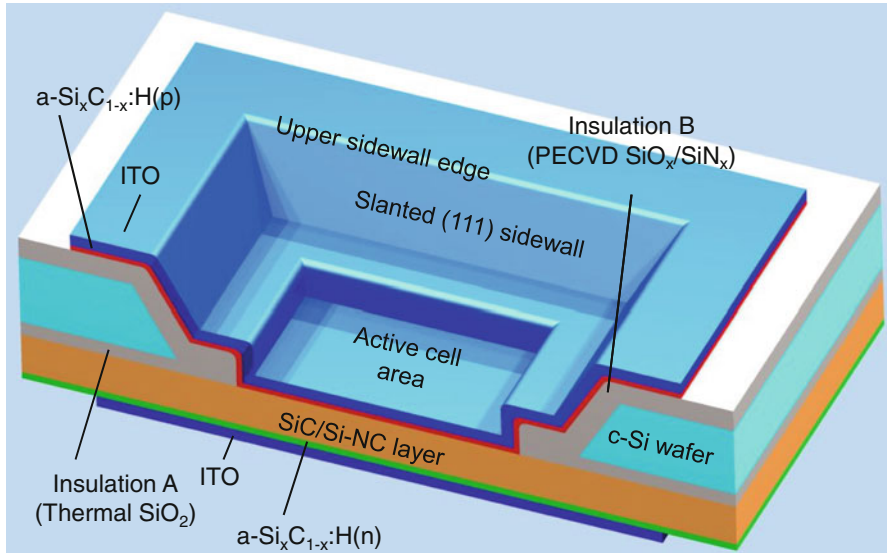


Fig. 6.4 Sketch of the membrane-based device. Reprinted with permission from [7]

for Si NCs in SiO_2 is about $10\ \mu\text{m}$ at 3 eV photon energy and $1\ \mu\text{m}$ at 4 eV photon energy [5]. Technologically viable Si NC layers are usually thinner than 300 nm. As the vast majority of the solar spectrum comprises photons with energies below 4 eV a large fraction of the incident light is thus transmitted through the Si NC film and generates charge carriers in the substrate wafer. This impedes the distinction between the Si NC contribution and that of the substrate wafer to the measured I/V curve. A solution could be the choice of a substrate wafer with an optical bandgap higher than that of the Si NC film, e.g., a silicon carbide wafer or an epitaxial gallium nitride on a silicon carbide or a sapphire wafer. However, the substrate wafer is also required to have a suitable work function and electron affinity to work as an electron or a hole collector. The terms “electron collector” and “hole collector” are used hereinafter according to [6] to describe the part of the solar cell that collects (contacts) the respective charge carrier type. They are frequently also called “emitters,” “back surface field,” or “selective contacts” in the literature.

In all concepts that involve a substrate which is also used as the back contact, the physical properties of the electrical back contact cannot be tuned independently from the solid-phase crystallization process of the Si NC layer. Any change of the thermal annealing step will also affect the properties of the electrical contact. A detailed review of Si NC devices that have been realized so far can be found in [7].

To enable an unequivocal photovoltaic characterization of Si NC films without the flaws discussed above, a membrane-based device was developed as shown in Fig. 6.4 [8]. Its key feature is the local removal and then encapsulation of the substrate after solid-phase crystallization of the Si NCs. After encapsulation of the

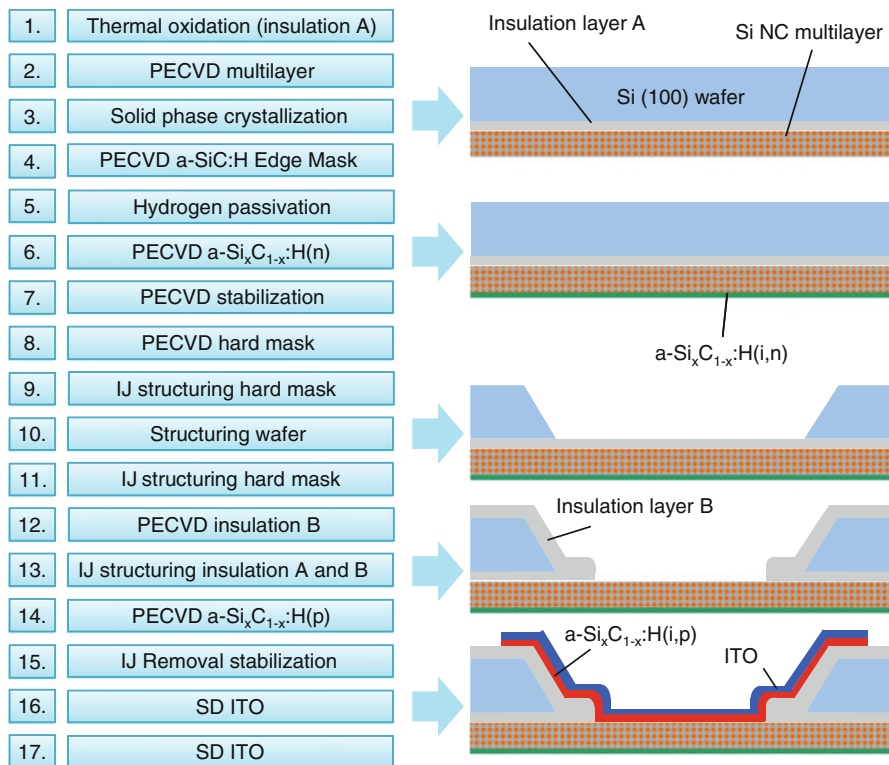


Fig. 6.5 (Left) Flow chart of the cell process for membrane-based p-i-n devices with a SiC-based absorber and doped $\text{Si}_x\text{C}_{1-x}:\text{H}$ as electron and hole collectors. Plasma-enhanced chemical vapor deposition (PECVD), sputter deposition (SD), inkjet printing (IJ), and wet chemical etching are used for deposition and structuring. (Right) The resulting structure is indicated after specific process steps. The front side is facing down in this sketch. The figure was taken from [2]

substrate to insulate it electrically and the subsequent local opening of the encapsulation at the Si NC layer, the Si NC layer can be accessed freely from both sides. A Si wafer is used as a substrate, and insulation and structuring are realized with Si-based dielectric layers deposited by PECVD. The membrane-based device structure shown in Fig. 6.4 permits a free choice of the selective contact material and the interface pretreatment. All electrically active materials can be chosen to have a bandgap comparable to or higher than the Si NC film. This permits an unambiguous characterization of the Si NC material. The structure can be realized as a p-i-n diode using an intrinsic and thin Si NC absorber. Photocurrent collection is thus enhanced by the electrical field between the hole collector (p) and the electron collector (n). Furthermore, device fabrication is compatible with standard Si process technology.

The fabrication sequence for a membrane device with an absorber that consists of Si NCs embedded in SiC is shown in Fig 6.5. The $\text{SiC}/\text{Si}_x\text{C}_{1-x}$ multilayer is deposited on a thermally oxidized wafer and then annealed at temperatures up to

1,100 °C to form the Si NCs [9]. The wafer is removed locally and insulated from the Si NC film by means of dielectric layers. After structuring the insulation layers, electron and hole collectors are formed by n-type and p-type $a\text{-Si}_x\text{C}_{1-x}\text{:H}$, respectively, and indium tin oxide (ITO) is deposited as a transparent contact on both sides. Details on the fabrication process can be found in [8] and [9]. All structuring steps except the local removal of the substrate are performed by inkjet printing of a hotmelt wax and etching in hydrofluoric acid (HF).

As the electron and hole collectors are established after the formation of the Si NCs by solid-phase crystallization, their electronic properties are not affected by the latter. The membrane-based device is thus a viable test device for the characterization of the physical properties of Si NC films prepared by high-temperature thermal annealing.

3 Silicon Nanocrystals in SiC by Solid-Phase Crystallization

Si NCs embedded in a SiC matrix are manufactured by depositing alternating Si-rich carbide (SRC) and SiC layers according to the multilayer approach described in Sect. 1. This method has the advantage of allowing the desired Si NC size and density in the plane to be tuned independently via the SRL thickness and the Si excess in the SRL, respectively. The structure resulting from this method can be considered as a Si NC superlattice. The method proved to be effective for producing Si NC superlattices in SiO_2 [10]. In analogy to the case of SiO_2 , the manufacturing of Si NCs in SiC requires the calibration of the processing conditions as a function of the desired Si NC density in the plane. This section gives an overview of the manufacturing technology and related issues as well as of the structural and light absorption properties of the resulting material.

3.1 Deposition by PECVD

The SiC and SRC layers can be deposited by sputtering [11] or by plasma-based techniques, such as inductively coupled plasma (ICP) [12] and PECVD [13–15].

The material described in the following is produced by PECVD. This technique involves dissociating the molecules of the Si, C, and H containing gas precursors by a glow discharge to produce a plasma. Generally the employed gases are SiH_4 , CH_4 , and if necessary H_2 [14] or Ar [13] for dilution. Monomethylsilane (MMS) has also been used as a Si and C precursor; the combination of MMS and SiH_4 allows for the control of the Si and C contents [15]. Since the dissociation is assisted by a physical mechanism, the deposition on the substrate is achieved at much lower temperatures than by chemical vapor deposition (CVD). In order to achieve sufficiently low

growth rates to produce SRC and SiC layers only a few nm thick, the plasma power density that can be used is limited. This in turn means that not all precursor molecules are fully dissociated by the plasma. Many are incorporated into the film as molecular radicals, and as all precursor gas molecules contain hydrogen, this implies a high incorporation of H. The substrate temperature being lower in PECVD than in CVD, the in situ H effusion is limited, which results in a large H content in PECVD layers. The large hydrogen content is the main feature that characterizes PECVD material also with respect to sputtered films. The Si content in the SRC as the parameter that determines the Si NC density in the SRC layer [10] is tuned by varying the SiH_4 and CH_4 flow rates.

In device manufacturing, the knowledge of the volume fractions can be used both as a check of the phase separation achieved [16] and as a tool to vary the optical properties of the solar cell absorber, because in composite materials the optical properties are directly related to the volume fraction of the components.

The design of a Si NC device also requires the knowledge of the material transformations in response to the thermal treatments. Upon annealing the materials crystallize and lose hydrogen, eventually reaching the density of bulk Si or SiC. This implies that the deposited layers undergo a shrinkage that has to be taken into account in device design [17].

Equations (6.1) and (6.2) describe the relationships between the atomic composition in as-deposited materials and the volumes of the components after annealing [17].

The volume of the Si excess in a multilayer is calculated by weighting the Si-rich carbide volume by the volume of the Si excess in the Si-rich carbide:

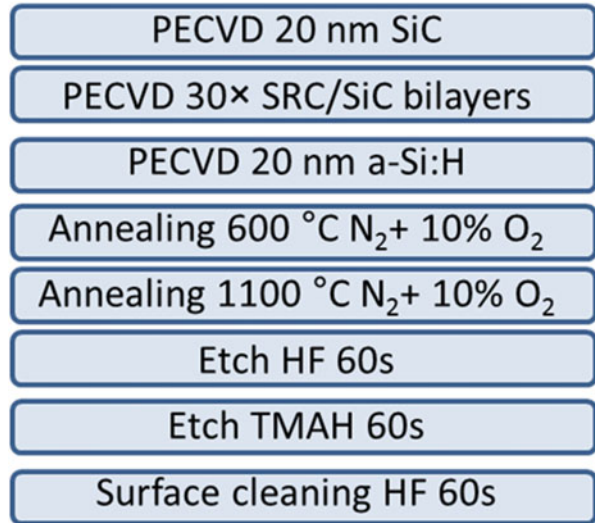
$$V_{\text{Si}} = V_{\text{Si,SRC}} \cdot \frac{d_{\text{SRC}}}{d_{\text{SRC}} + d_{\text{SiC}}} \quad (6.1)$$

V_{Si} is the volume of the Si excess in the multilayer, d_{SiC} and d_{SRC} the thicknesses of the annealed SiC and the SRC, respectively, and $V_{\text{Si,SRC}}$ the volume of the Si excess in the annealed SRC.

The volume of the Si excess in an SRC layer after phase separation, $V_{\text{Si,SRC}}$, depends on the Si fraction x according to a general formula for silicon alloys, such as Si-rich oxide, SRC, and Si-rich nitride. In the case of an SRC the volume fractions occupied by the Si and SiC phases under the hypothesis of complete separation are

$$\begin{aligned} V_{\text{Si}} &= \frac{(2x - 1) \cdot m_{\text{Si}} \cdot \rho_{\text{SiC}}}{(1 - x) \cdot (m_{\text{Si}} + m_{\text{C}}) \cdot \rho_{\text{Si}} + (2x - 1) \cdot m_{\text{Si}} \cdot \rho_{\text{SiC}}} \\ V_{\text{SiC}} &= \frac{(1 - x) \cdot (m_{\text{Si}} + m_{\text{C}}) \cdot \rho_{\text{Si}}}{(1 - x) \cdot (m_{\text{Si}} + m_{\text{C}}) \cdot \rho_{\text{Si}} + (2x - 1) \cdot m_{\text{Si}} \cdot \rho_{\text{SiC}}} \end{aligned} \quad (6.2)$$

Fig. 6.6 Sequence of the fabrication steps optimized to produce Si NCs in SiC



x is the Si content in the SRC, which means that $(2x - 1)$ is the excess of Si atoms and $(1 - x)$ the C content, m_{Si} and m_{C} are the atomic weights of the Si and C atoms, respectively, and ρ_{Si} and ρ_{SiC} are the densities of the Si and SiC components after annealing.

Furthermore, appropriate design of a multilayer requires the insertion of a crystallization barrier between the Si substrate and the multilayer in order to prevent the Si substrate from acting as crystallization seed during the subsequent annealing. Such a layer can reasonably be amorphous SiC or SiO₂.

In the case of a SiC matrix, an encapsulation is needed to prevent SiC reacting with oxygen during annealing, as this would lead to an undesired surface oxidation [18, 19]. Amorphous silicon has been found to be a suitable encapsulation layer as it can be deposited in the same PECVD chamber from similar gas precursors as the multilayer and oxidizes instead of the multilayer on annealing. Addition of 10 % O₂ to the nitrogen normally used as an annealing ambient helps to make the oxidation of the encapsulation more reproducible. The resulting SiO₂ and the residual $\mu\text{-Si}$ encapsulation are removed by wet etching. The process sequence is summarized in Fig. 6.6. This procedure results in a SiC-rich surface [19].

In the following sections, the multilayers will be labeled with a sequence of three numbers, representing the as-deposited multilayer layout: the first number represents the Si content x in the SRC multiplied by 100, the second the as-deposited SRC thickness in nm, and the third the integer part of the as-deposited SiC thickness in nm. For example, 65-3-5 is a multilayer in which the Si fraction in the SRC layer is 0.65, and the thickness of the SRC and the SiC is 3 and 5 nm, respectively. The number of bilayers is 30 in all cases.

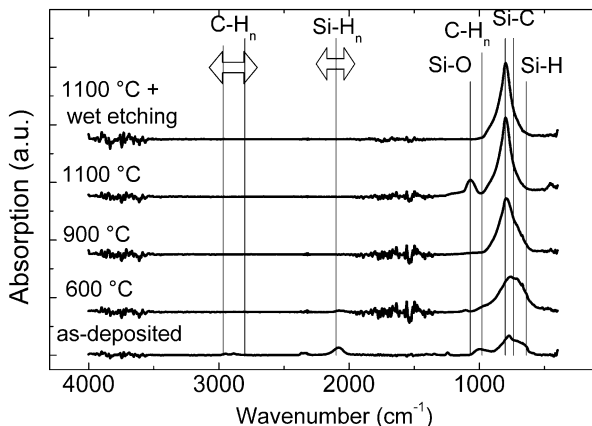


Fig. 6.7 Mid infrared absorption spectra of 65-3-3 after different fabrication steps: as-deposited, after annealing at 600 °C for 2 h, 900 °C for 1 h and 1,100 °C for 10 min, and after wet chemical etching in hydrofluoric acid. The *vertical lines* represent the absorption bands corresponding to vibrations commonly observed in Si–C–H alloys: from *right to left*, Si–H wagging, Si–C stretching, C–H_n wagging, Si–O stretching, Si–H_n stretching, and C–H_n stretching [21, 22]

3.2 Thermal Annealing

The formation of Si NCs starting from plasma-deposited SRC needs a high-temperature treatment in which the following phenomena take place: H evolution, phase separation of Si and SiC, SiC crystallization, and Si crystallization. These material transformations, except the Si crystallization, can be followed by Fourier transform infrared (FTIR) spectroscopy in the absorption modes. FTIR gives information on the atoms that compose the film as well as on the short- or medium-range order in a structure, being sensitive to the characteristic vibrations of atomic bonds. The absorption signal due to the homopolar Si–Si bonds is weak, because it results from a two-phonon process [20]. As a consequence, the contribution of the Si NCs to the absorption spectrum is negligible with respect to the one of the c-Si wafer substrates. Si–C bonds on the other hand exhibit a strong IR absorption which is readily monitored.

Figure 6.7 shows the mid infrared absorption spectra of 65-3-3 deposited on a 20 nm SiC crystallization barrier, as-deposited, after a series of thermal treatments (600, 900, and 1,100 °C) and after wet chemical etching. The spectra are corrected for substrate absorption, and a baseline is subtracted.

The spectrum of the as-deposited multilayer features broad absorption bands, indicating the structural disorder in the layer. The main peak at 773 cm⁻¹ is due to the stretching of the Si–C bonds in disordered structures [21]. The other peaks give evidence of the high H content that is typical in PECVD prepared layers: the broad peak around 640 cm⁻¹, which appears as a shoulder of the main 770 cm⁻¹ peak, is attributed to the wagging mode of the Si–H bond; the peak at 990 cm⁻¹ is attributed

to vibrations of the C–H₂ wagging mode within SiCH₂ complexes; the signals at 2,080 cm⁻¹ and around 2,800–3,000 cm⁻¹ are corresponding to the Si–H_n and the C–H_n stretching bands, respectively [21, 22].

The spectrum of the film annealed at 600 °C presents sharper features. The Si–C peak is more pronounced as a consequence of the phase separation, and the H-related peaks have almost disappeared due to H effusion, with the exception of some residual signal at 640 and 2,070 cm⁻¹ (Si–H bands) and 965 cm⁻¹ (C–H_n band).

Complete H effusion is observed at 900 °C. Complete H effusion is detected at 900 °C. We also observe a wavelength shift of the Si–C stretching mode from 773 to 800 cm⁻¹, accompanied by a change in peak shape from Gaussian to Lorentzian. Both effects are due to crystallization of the SiC phase. When a material crystallizes, the bonds become stronger, leading to peak shift to higher wavenumbers, and the distribution of bond lengths and angles is no longer random but exhibits a preferred configuration due to the ordering in the crystalline lattice. The spectrum of the 1,100 °C annealed layer also presents this Lorentzian Si–C peak as well as an additional signal centered around 1,070 cm⁻¹, indicating the presence of a Si–O bonds. This signal is related to surface oxidation and is eliminated by etching the sample in diluted hydrofluoric acid [19], see Fig. 6.6.

3.3 Si Crystallization

The vibrational modes of the Si–Si bonds, that are almost inactive in the IR, are Raman active according to the “rule of mutual exclusion” which holds for centrosymmetric crystals like Si. Thus, Si crystallization can be investigated by Raman scattering. Amorphous and crystalline Si exhibit Raman peaks at 520 and 470 cm⁻¹, respectively, and deconvolving the two peaks allows for a quantification of the fraction of Si that has crystallized with respect to the total. Diffraction techniques, such as X-ray diffraction (XRD) and bright field transmission electron microscopy (TEM), can be used to get complementary information. XRD gives a spectrum with distinct peaks that can be attributed to Si and SiC using the Bragg equation. The height of the peaks represents the crystallized fraction, while the full width at half maximum can be used to determine the mean size of the Si and SiC nanocrystalline domains, using the Scherrer equation for the full width at half maximum of the (111) diffraction peak [23]. The diffraction pattern exhibited by the SiC component also allows for the identification of the SiC polytype resulting from SiC crystallization, which is the cubic polytype 3C-SiC [24, 25] for annealing temperatures up to 1,100 °C. TEM allows for direct imaging of the actual Si NC superlattice structure, i.e., the SiC barrier thickness, the distance between the nanodots, and the mean nanodot size. By TEM non-ideal features, such as nanocrystal outgrowth beyond the SRC layer, Si and C interdiffusion between adjacent layers and continuous Si crystallization in the SRC can also be detected.

Nanodot formation and crystallization in silicon carbide fabricated using the multilayer approach to control the nanodot size proceed in a different way than in the SiO_2 matrix. In the Si/SiO_2 case, the nanodot diameter is effectively controlled by the thickness of the silicon-rich oxide layer and is independent of the annealing duration [26]. Phase separation readily occurs [16], and no residual amorphous fraction is observed, provided that sufficiently high annealing temperature is used.

In contrast, in the Si/SiC case the nanodot size is not easily controlled. Random nanocrystal distribution and outgrowth of Si NCs over the SRC/SiC bilayer thickness are observed if improper conditions are used, as this leads to Si and C interdiffusion between adjacent layers [27]. Even a high residual amorphous silicon fraction is detected by Raman, depending on the design (x , d_{SRC} , and d_{SiC}) [13, 24, 28]. This observation was recently proposed [29] to show strong similarities with the case of Ge NC nucleation in SiO_2 [30].

For the Ge/SiO_2 case [30], it has been demonstrated that the high interface energy between c-Ge and SiO_2 leads to the development of an amorphous shell around the Ge NCs. The formation of the a-Ge shell creates an effective interface that lowers the overall energy [30, 31]. The same phenomenon is likely to occur in the Si/SiC system due to the remarkably high energy of the c-Si/SiC interface, which stems from the 19 % lattice mismatch.

For thick SRC layers continuous crystallization is favored with respect to NC formation due to the low distance between the crystal nuclei, which implies that too low an amount of Si atoms is remaining to form the shell needed for the stability of isolated nanocrystals [29, 30]. This observation is in contrast with the description for the formation of Si NCs in SiO_2 matrix (see Fig. 6.3), in which the thickness of the SRL determines the nanodot size. As a consequence, only a limited range of nanodot sizes is achievable in the Si/SiC system by the multilayer method.

Figure 6.8 shows energy-filtered (EF) TEM micrographs of two annealed multilayers, 75-3-3 (a) and 95-3-3 (b). The electron energy loss spectra are filtered around the 17 eV Si plasmon energy. The Si-rich regions appear brighter, while the SiC shows a darker contrast. The two materials differ by the SRC composition. After annealing only the multilayer with the higher x shows a multilayer structure. In [29] a lower limit of 2.5–3 nm and $x > 0.75$ are proposed for a control of the multilayer structure. This image highlights the importance of understanding the material evolution upon annealing for a proper multilayer design.

4 Optical Modeling

This section aims at describing a particular approach for thin-film structural characterization, based on the fitting of optical reflectance and transmittance (R&T) spectra. UV–vis spectroscopy generally supplies information on the optical absorption of a composite material as a whole. In this section it will be shown that fitting of the R&T spectra allows for the extraction of the relative volumes of the

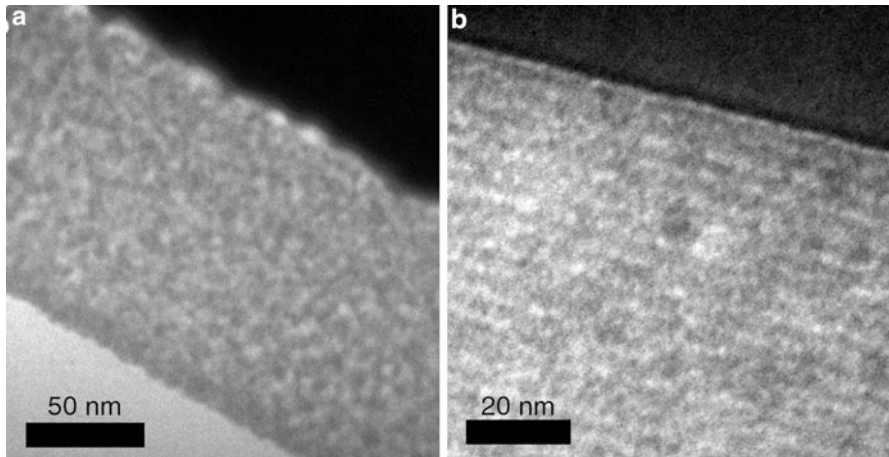


Fig. 6.8 EF-TEM micrographs of 75-3-3 (a) and 95-3-3 (b) after annealing at 1,100 °C. The Si-rich regions appear bright. The surface is on the *top right side* of the pictures

material subcomponents, SiC and Si, and for the amorphous and crystalline Si fractions of the total Si volume. This information can be used to extract the optical absorption of the sole Si component in the case of an absorbing matrix like SiC.

4.1 Introduction to the Method

The computer code Optical [32] calculates the R&T spectra of multilayer structures using a scattering matrix formalism for the light propagation. The interface matrix between two adjacent layers is defined using the Fresnel coefficient approach. The optical spectral functions for the wave propagation through a layer can take into account mixed-phase layers through the Bruggeman effective medium approximation (EMA). If the optical spectral functions of all the components are known, the software allows for the calculation of each layer composition and thickness using a χ^2 minimization.

However, proper spectral functions of the subcomponents of the multilayers at the different stages of the production process cannot be readily identified in the literature due to the high impact of the processing conditions on the optical properties of the material. This is especially true for SiC-based materials, i.e., the as-deposited a-Si_xC_{1-x}:H, the dehydrogenated amorphous SiC (a-SiC), and the crystallized SiC (μ c-SiC) [14]. In order to extract unknown (n,k) functions, reference single layers of the involved materials were produced, and their R&T spectra were fitted using the computer program MinitFit [33] that is based on a modified Tauc-Lorentz model [34]. It has to be noted, however, that this procedure assumes the equality of the optical properties of nanocrystals and of continuous nanocrystalline materials, which is not confirmed.

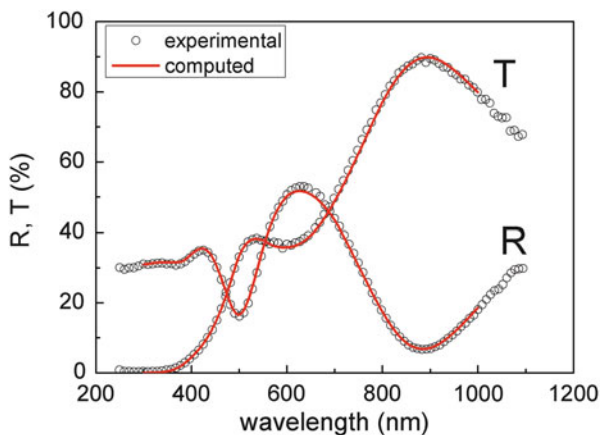


Fig. 6.9 Experimental and simulated R&T spectra of 65-3-5 after 1,100 °C annealing. The *symbols* are the measured spectra, and the *lines* are the computed spectra

The spectral data of the Si phases are drawn from [35] and [36]. The spectral data for SiO₂ are drawn from [37].

4.2 Modeling of SiC/Si NC Multilayers

The simulation of the annealed SiC/Si NC material is obtained by considering a stack of four layers: a low-density surface layer as residual from the wet etching sequence described in Sect. 3; the SiC/Si NC layer; the SiC crystallization barrier; and the substrate. The fitting procedure allows for the extraction of the thickness of each layer and the composition of the SiC/Si NC layer. The latter can be considered as an effective medium made up of $\mu\text{c-SiC}$, $\mu\text{c-Si}$, and a-Si . Based on the TEM diffraction patterns as well as the Lorentzian shape of the Si–C stretching band after thermal annealing at 1,100 °C the SiC sub-component is approximated as being completely microcrystalline. The assumption that the optical spectral functions of the Si NCs are the same as the ones of continuous nanocrystalline domains is made for simplicity but has an impact on the crystalline silicon fraction extracted by fitting of the R&T spectra.

Figure 6.9 shows as an example the R&T spectra measured on 65-3-5 deposited on a 20 nm SiC buffer layer and treated according to the sequence described in Fig. 6.6. The calculated spectra that best fit the experimental data are obtained for the following structure: 5 nm SiC surface, 133 nm SiC/Si NC, and 10 nm SiC crystallization barrier. The different structural features result in different signatures in the R&T spectrum: the fringe contrast in the region of transparency ($A = 0$ and $R + T \equiv 1$), that for the film in Fig. 6.9 lies between 700 and 1,000 nm, depends on the bulk refractive index and is therefore almost univocally related to the Si/SiC volume ratio. For a given Si/SiC ratio, the fringe period is univocally determined by

the thickness. The c-Si/a-Si ratio determines the onset and rise of transmittance, i.e., in particular the T maximum in the medium absorption wavelength range (500–700 nm in Fig. 6.9), in which the absorptivities of a-Si and μ c-Si show considerable difference. The Si NC layer shown in Fig. 6.9 is composed by 70 % SiC, 22 % a-Si, and 8 % μ c-Si.

The crystallized Si fraction, X_C , is given by the volume fraction of the crystallized Si divided by the total Si volume fraction:

$$X_C = \frac{V_{\mu\text{c-Si}}}{V_{\mu\text{c-Si}} + V_{\text{a-Si}}}. \quad (6.3)$$

According to (6.3) 23 % of the Si component crystallized during annealing in the sample of Fig. 6.9. The X_C extracted from optical simulation can be compared to structural characterization obtained by Raman spectroscopy. [28, 29] provide a comparison between the crystallized Si fraction obtained by the fitting of R&T spectra and by Raman spectroscopy. The results obtained by the two techniques are in good qualitative agreement. The absolute values of the Si crystallized fraction depend on the choice for the Si NC optical functions.

In conclusion, UV–vis R&T spectra provide a wide range of structural information about Si NC films when complemented with an optical simulation and can be used to determine the absorption properties in view of PV application.

4.3 Optical Properties of Nanocrystals

Following the scenario illustrated in Sect. 1, the ideal optical properties of Si NCs used as absorber material in the top device of a tandem solar cell should show a complete transparency for $E < E_g$ and a high absorption for $E > E_g$. The actual absorption spectrum of nanocrystals is still a matter of debate for a number of reasons. First, as it is correlated to the quantum confinement-related energy-level splitting, it depends on diameter, with related consequences for non-spherical nanocrystals. Secondly, as it is affected by the bonding configuration of atoms at the nanocrystal surface, it is sensitive to the environment [38]. Third, the application in solar cell devices implies attention to the absorption region just above gap, since ideal energy conversion can be obtained only in this energy range, see Fig. 6.1. The absorption of photons whose energy lies in this region is limited by the density of states and can be characterized with only moderate accuracy by a standard optical technique like ellipsometry. Several references exist on the topic, see for example [39–42], mostly focusing on the high-absorption region. In the medium-absorption region the most informative is probably [39]. An optical model for the medium-absorption region was recently proposed by Allegrezza et al. [43]. In the framework of the SiC/Si NC system, the precise determination of the absorption spectrum is complicated by the non-negligible band tail and the defect absorption in SiC [14].

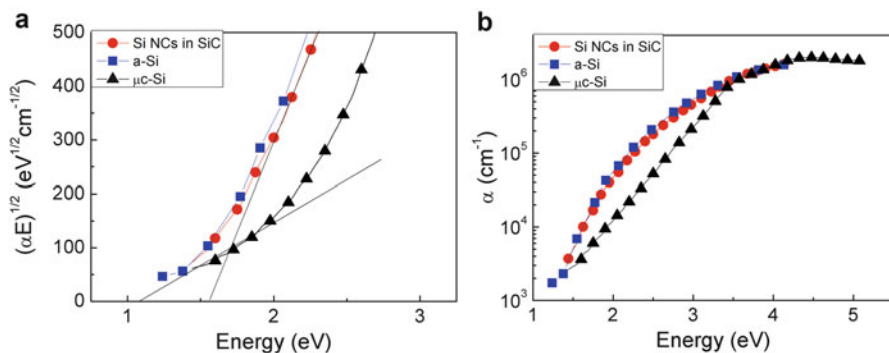


Fig. 6.10 (a) Tauc plot and (b) absorption spectra of the Si nanodot component in the SiC/Si NCs film of Fig. 6.9 and of a-Si [36] and $\mu\text{c-Si}$ [35]

Figure 6.10a reports the Tauc plot for the sole Si component obtained from the simulation of the R&T spectrum in Fig. 6.9. The Tauc plot of a-Si [36] and $\mu\text{c-Si}$ [35] are also reported for comparison. The Si nanodot component in the multilayer shows $E_g = 1.5$ eV that represents a blue shift with respect to the microcrystalline value. However, the absorption spectrum appears to be dominated by the amorphous component also detected by Raman. Figure 6.10b shows the absorption coefficient for the same materials. For energies above the bandgap, the Si nanodots exhibit an increased absorption with respect to microcrystalline silicon. This has a positive impact for solar cell devices, as it allows for the lowering of the absorber layer thickness provided that carrier lifetime is not severely limited by recombination in the amorphous phase.

5 Device Characterization

The concept of characterizing the Si NC film without any wafer influence using the membrane device structure introduced in Sect. 2 depends critically on the electrical insulation properties of the insulation layers. To ensure reliable characterization of the Si NC p-i-n diode it must first be proven electrically that for each structure the photovoltage and the photocurrent stem only from the “membrane diode” itself and not from the wafer. Only then further characterization can be carried out.

A potential contribution of the wafer to the photovoltaic properties of the overall device can be thought of as an additional “wafer diode” in parallel to the “membrane diode.” In order to separate the membrane diode characteristics from the “wafer diode,” the different device parts were illuminated separately and the overall IV curve was measured. In principle the device can be illuminated from either side. In order to demonstrate the device functionality, however, the structured and therefore critical side was illuminated to more readily detect a possible contribution of the wafer.

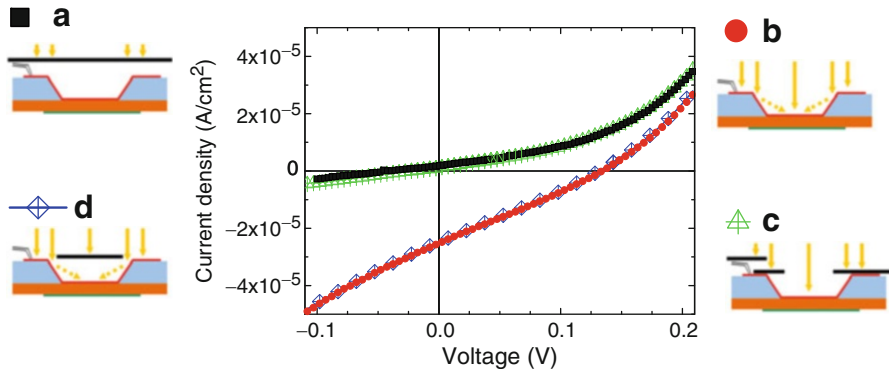


Fig. 6.11 Current–voltage curves of a malfunctioning membrane cell in dark (a), under full area illumination (b), and under illumination with shadow masks (c, d). The figure was taken from [2]

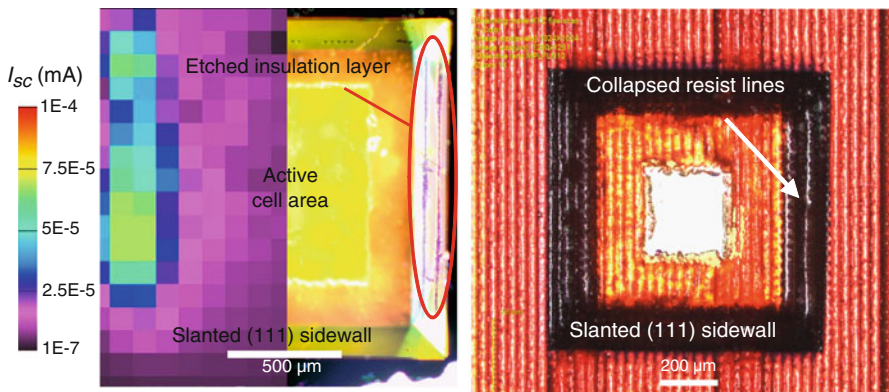


Fig. 6.12 (Left) Light beam-induced current (LBIC) map combined with the dark field micrograph of a malfunctioning membrane-based p-i-n solar cell. The LBIC map is mirrored along the vertical center line. The area of maximum current corresponds to the etched insulation layer. (Right) Optical micrograph of an inkjet printed membrane before structuring of insulation layer B (process step 13, cf. Fig. 6.5). The figure was taken from [2]

Figure 6.11 shows IV curves of one membrane cell in the dark (A), under illumination of the entire wafer (B), and under illumination with shadow masks (C, D). Mask C leaves only the membrane illuminated but shadows the surrounding wafer and contacts. Under mask D, only the “wafer diode” is illuminated and light can reach the membrane cell only by reflection at the slanted sidewalls. For the cell shown here, the IV curve with mask D reproduces the IV curve under full area illumination. This hints at a damaged insulation layer and a large wafer contribution to the overall IV curve.

A powerful tool to investigate the spatially resolved charge carrier collection properties and local shunting is light beam-induced current (LBIC) mapping. Figure 6.12 (left) shows an LBIC map along with the (mirrored) dark field optical

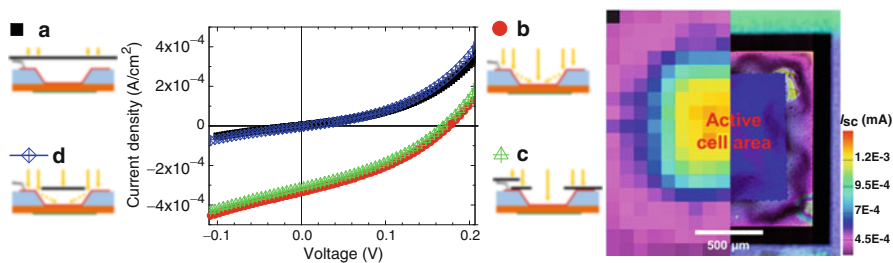


Fig. 6.13 (Left) Current–voltage curves of a correctly functioning membrane cell in dark (a), under full area illumination (b), and under illumination with shadow masks (c, d). (Right) Light beam-induced current map of the corresponding cell combined with an optical micrograph (mirrored). The figure was taken from [2]

micrograph of the same cell whose IV curves were shown in Fig. 6.11. A photocurrent from the slanted sidewalls can be seen in the LBIC image. In exactly this area the dark field image reveals two line-shaped etch-damaged regions. The insulation layer B is damaged here, giving rise to photocurrent collection from the wafer substrate in this area. Figure 6.12 (right) depicts an optical micrograph of an identically processed structure in step 13 of the fabrication process. The inkjet resist is printed in lines from a print head that moves in one direction over the sample. The typical line pattern of the inkjet resist can be seen in Fig. 6.12 (right) on the wafer surface, the membrane, and the slanted sidewalls. However, the line pattern exhibits a different period on the slanted sidewall on the right-hand side. Several ink lines merged here because the inkjet resist droplets rolled down the steep (54.7°) sidewalls. Hence, it can be concluded from the line pattern in Fig. 6.12 (left) that the insulation layer damage seen was caused by a collapse of the inkjet resist lines on the slanted sidewalls as seen in Fig. 6.12 (right). The line-shaped etch damage can thus be attributed to failure of the inkjet resist during wet chemical etching in step 13 or 15 (flow chart in Fig. 7.4).

The systematic study of all structures with light microscopy and LBIC supplemented by electron beam-induced current studies for selected structures as reported in [7] allows a clear identification of correctly functioning devices. After selection of those devices that appeared to be free of defects in the light microscope, a clear correlation was established between the results of IV and LBIC measurements. When an IV curve was attributed to the membrane but not the wafer based on the shadow mask procedure, LBIC measurements confirmed this behavior. An example of this behavior is shown in Fig. 6.13. The IV curve with shadow mask D resembles the dark IV curve very well, and the application of mask C demonstrates that the IV curve is due to the active cell area on the membrane only. The LBIC map (Fig. 6.13 right) finally confirms this behavior.

Based on these experiments, the following procedure was established: in a first step, all devices are analyzed by optical microscopy with special emphasis on the upper sidewall rims. Then, the insulation layer on the slanted sidewalls is checked

with dark field microscopy. If the structure appears to be free of defects, IV curves in dark, under full area illumination, and with shadow masks C and D are measured. If the IV curves demonstrate that the wafer does not influence the measurement, the structure is qualified as “good” and selected for further characterization.

EBIC and LBIC are current-sensitive methods and do not provide information on the magnitude of the photovoltage. The latter is provided by IV measurements employing shadow masks as shown in Figs. 6.11 and 6.13. However, the shadow mask method does not allow the identification of a potential contribution from the slanted sidewalls. Therefore, the IV characteristics of the entire structure were simulated for different cases of failing insulation layers. The simulation demonstrates that the photocurrent of the IV curve is indeed sensitive to an insulation layer failure. As the photovoltage was shown to be much less sensitive to insulation layer failure, current-sensitive methods such as LBIC or EBIC are viable tools to prove the origin of both the photocurrent and the photovoltage. Differently put, the simulations showed that if the photocurrent can be shown to originate from the membrane only, then the same can be assumed for the photovoltage.

6 Solar Cell Modeling

The optical absorption properties of the SiC/Si NC material extracted by UV–vis spectroscopy can be used to analyze the results obtained on membrane solar cell devices. Possible variations to the actual device structure are examined, with the aim of maximizing the fraction of light absorbed by the NCs.

6.1 Light Absorption in Individual Layers

As shown in Fig 6.4, the solar cell is schematically represented as a multilayer where the SiC/Si NC layer is embedded between two 10 nm thick SiC layers that account for the SiC crystallization barrier and the surface layer. The structure is completed on both sides by an a-Si_{0.95}C_{0.05} doped layer (20 and 25 nm on the top and on the back side, respectively) and an ITO layer (70 nm).

The upper limit for the short-circuit current, J_{gen} , of the device is determined by the overlap integral of the calculated absorptance of the membrane with the AM1.5G solar spectrum, under the assumption of a complete collection of electron/hole pairs generated in the SiC/Si NC absorber. The light absorbed in the doped layers should not contribute to the photocurrent due to the short minority carrier lifetime in highly doped materials.

The absorption spectrum of individual layers and the resulting global absorption of the membrane are shown in Fig. 6.14a.

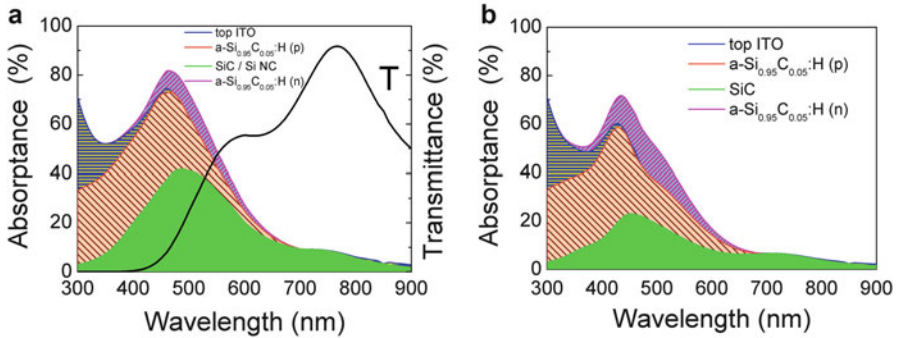


Fig. 6.14 (a) Computed transmittance spectrum (*black line*) of the membrane solar cell characterized in Sect. 5 and computed absorption spectrum of the entire device as the sum of the absorption in individual layers. (b) Computed absorption spectrum of a device with a SiC absorber (without Si NCs)

The calculated J_{gen} for this structure is 5.97 mA/cm^2 , represented by the green area in Fig 6.14a. The discrepancy between the theoretical and the experimental value is discussed in Sect. 7.

For comparison, the same calculation, yet having removed the Si NCs from the SiC layer, is reported in Fig. 6.14b. In this case, J_{gen} is 3.1 mA/cm^2 . It can be seen that the spectral shapes of the two cases (with and without NCs, panels a and b, respectively) are similar. However, the presence of Si NCs clearly enhances the absorption of light in the absorber layer and the overall structure.

6.2 Optimization of the Optical Properties

The identification of the contributions of each single layer to the overall absorption is the basis for the optimization of the device structure for future developments. It is apparent from Fig. 6.14a that a significant fraction of the incident light is lost in the top doped layer. Moreover, a significant fraction of light is transmitted through the device without generating any current. Popular solutions in the world of thin-film solar cells are the use of a window layer as front doped layer as well as a back stack based on a metal reflector [44].

A window layer is a high-bandgap doped material, typically p-doped $\text{a-Si}_x\text{C}_{1-x}$. The high-bandgap guarantees better transparency, yet with the drawback of less effective doping for increasing carbon content. A trade-off is therefore needed for the composition. Reducing the thickness also contributes to enhancing transparency. However, the window layer should not be thinner than the depletion region to avoid deterioration of the open-circuit voltage [45]. Within this context and taking advantage of preliminary optical characterization of $\text{a-Si}_x\text{C}_{1-x}$ materials, we used optical simulation to compute the impact of composition and thickness of the window layer on J_{gen} . The results are reported in Fig. 6.15a.

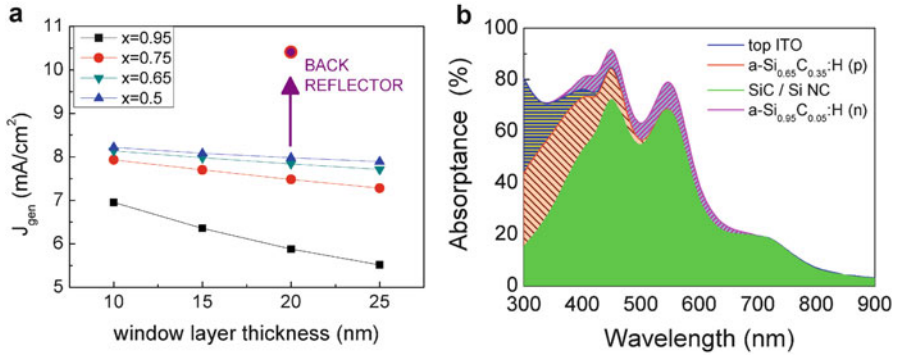


Fig. 6.15 (a) Computed J_{gen} for different top layer compositions and thicknesses. The further enhancement of J_{gen} when adding a back reflector is shown by a *circle*. (b) Computed absorption in the SiC/Si NC layer within the optimized solar cell structure including the back reflector (indicated by an *arrow* in (a))

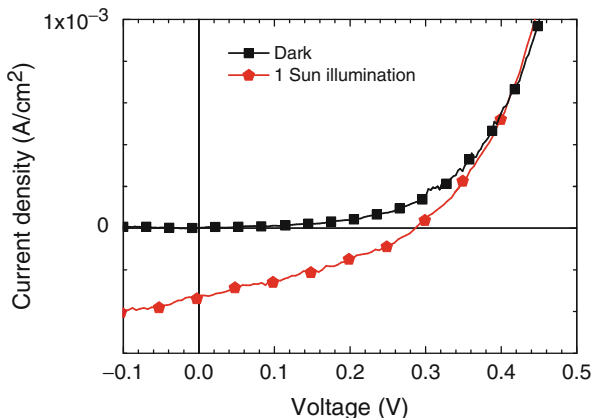
The figure shows that a slightly higher carbon content in the top a-Si_xC_{1-x}:H (p) layer (the hole collector) is already effective in increasing J_{gen} . The effect saturates with higher x . Moreover, J_{gen} shows little dependence on thickness, indicating that the larger thicknesses needed to guarantee higher built-in voltages will be only negligibly detrimental to the device. A reduction of transmission losses is predicted by introduction of a 30 nm silver back reflector that results in an increase of absorption in the SiC/Si NC layer by 30 %.

Figure 6.15b shows the computed absorption in the NC layer for the optimized structure including the back reflector. The fraction of light absorbed by the NC layer with respect to the total is higher due to the combined action of the wider bandgap of the window layer and of the back side mirror, indicating a possible improvement in the design of the device. The computed J_{gen} for this structure is 10.4 mA/cm².

7 Recombination and Transport Properties of Silicon Nanocrystals in SiC

Typical IV curves in dark and under illumination (light IV curve) of a membrane p-i-n solar cell are shown in Fig. 6.16. The membrane p-i-n solar cell was designed as depicted in Figs. 6.4 and 6.5 with the resulting optical properties presented in Fig. 6.14a. The measurements were taken at a sample temperature of 25 °C, and the illumination was set to 1,000 W/m² unless otherwise specified. The open-circuit voltage V_{OC} of the cell shown in Fig. 6.16 is 282 mV, and the short-circuit current density J_{SC} is 0.339 mA/cm². The fill factor (FF) is 36.2 %. The light IV curve in Fig. 6.16 exhibits a pronounced slope at 0 V, i.e., a short-circuit conductance, which is not present in the dark curve. The dark and light curves are also seen to cross over

Fig. 6.16 Representative dark and light IV curves. Reprinted with permission from [9]. Copyright 2013, American Institute of Physics



at a voltage of 400 mV. The crossover is a common feature for Si and chalcopyrite thin-film solar cells [46] and can be explained with a photo shunt or a voltage-dependent current collection function. The experimental J_{SC} value is only $0.06 \times J_{gen}$, indicating highly recombinative defects in the Si NC layer. The characteristics of the IV curves shown in Fig. 6.16 (shunt under illumination, crossover of light and dark IV curves, fill factor, J_{SC} and V_{OC} values) are typical for all membrane cell devices investigated.

The peculiar IV characteristics (shunting, high series resistance, low fill factor) do not permit an unequivocal fit of the one-diode model to the data as it is usually done for c-Si solar cells. Therefore, a detailed IV curve analysis must be undertaken. First, the dark curve is analyzed to determine the series resistance, parallel resistance, and ideality factor. In a second step, the dark diode parameters are used to fit the light IV curve according to the uniform field approximation assuming validity of the superposition principle [ref to theory].

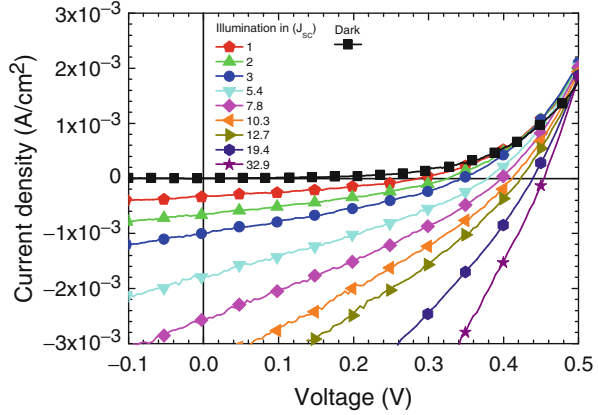
The dark parallel resistance $R_P = 11,808 \Omega \text{ cm}^2$ is calculated from the slope of the dark IV curve around 0 V (short-circuit resistance). The series resistance and diode ideality factor are then extracted using the small conductance method after Werner [47].

Having these parameters fixed, illumination-dependent IV measurements are employed with the objective to determine the effective mobility lifetime product $(\mu\tau)_{eff}$, which is a fundamental transport and recombination property of the material.

IV curves at illumination levels between 1 and 20 suns are shown in Fig. 6.17. The illumination level was adjusted with a Fresnel lens with variable distance to the sample.

All light IV curves in Fig. 6.17 exhibit a pronounced photo shunt indicating strong recombination in the Si NC layer. The following analysis is governed by the idea of a thin, undoped, and recombinative absorber within the electrical field between the highly doped regions. This case can be described with reasonable

Fig. 6.17 Illumination-dependent current–voltage curves. The cell was illuminated with a sun simulator and a Fresnel lens from the wafer side. Reprinted with permission from [9]. Copyright 2013, American Institute of Physics



simplifications using the uniform field approximation introduced by Crandall [48], which leads to a voltage-dependent photocurrent collection function $\chi(V)$, given by

$$\chi(V) = \frac{L_D}{d} \left(1 - \exp\left(-\frac{d}{L_D}\right) \right), \tag{6.4}$$

where d is the absorber thickness. The voltage dependency of the photocurrent collection function is “hidden” in the effective drift length L_D ,

$$L_D = (\mu\tau)_{\text{eff}}(V_{\text{FB}} - V)/d, \tag{6.5}$$

which describes the mean distance that a charge carrier will travel by drift in the electric field in the solar cell absorber before recombination. At flat band conditions (when the external voltage V equals the flat band voltage V_{FB}) the electric field is zero, drift does not occur, charge carriers do not reach the contacts anymore, and the photocurrent is zero. Hence, the dark current equals the light current J_{light} at that voltage, or differently put, V_{FB} is the voltage where the light and dark IV curves cross over.

The IV curve is defined by the collection function $\chi(V)$ as well as the parameters of the common one-diode model, which are the saturation current density J_0 , the ideality factor n , the series resistance R_S , the parallel resistance R_P , and the Boltzmann constant k_B :

$$J_{\text{light}}(V) = J_0 \left(\exp\left(\frac{qV}{k_B T}\right) - 1 \right) + \frac{V}{R_P} - J_{\text{gen}}\chi(V). \tag{6.6}$$

The advantage of the uniform field approximation is that it permits the analytical description of the entire light IV curve between short-circuit and open-circuit or crossover conditions. The light IV curve after (6.6) involves eight parameters (J_{gen} , J_0 , n , R_S , R_P , V_{FB} , $(\mu\tau)_{\text{eff}}$, d). As mentioned before, R_S , R_P , and n were determined

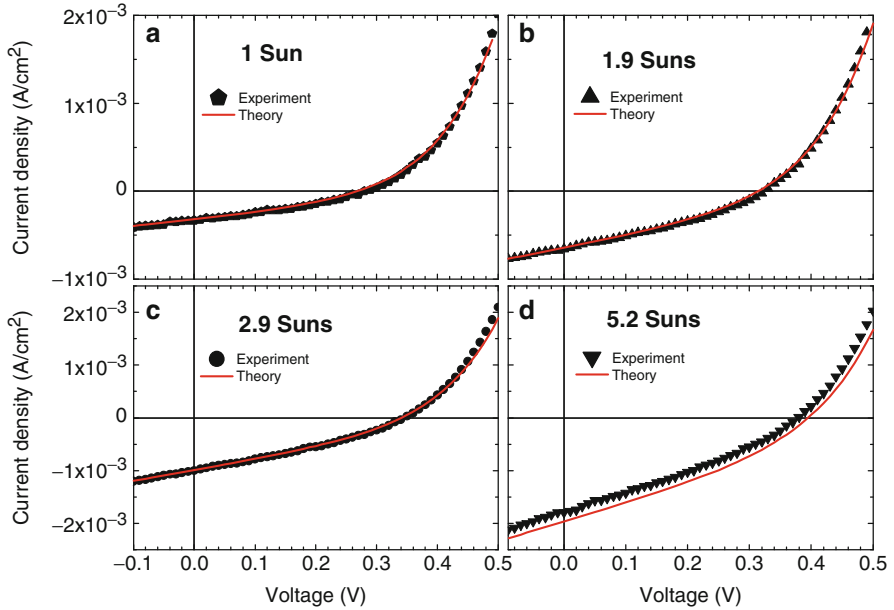


Fig. 6.18 Current–voltage curves of membrane-based p-i-n devices and the respective fits of the one-diode model with a voltage-dependent current collection function in the uniform field approximation [(6.6) with the collection function of (6.4)] to the data. Series resistance, parallel resistance, and ideality factor were fixed to the dark values. Reprinted with permission from [9]. Copyright 2013, American Institute of Physics

from the dark IV curve with the analysis after Werner [47], and V_{FB} was obtained from the crossover voltage. The absorber layer thickness and the maximum short-circuit current were obtained from the optical simulation discussed above. This procedure means that only J_0 and $(\mu\tau)_{\text{eff}}$ need to be fitted to the light IV curve (6.6). For an unequivocal determination of these two parameters, illumination-dependent current–voltage measurements were carried out and fitted simultaneously with the same set of parameters according to (6.6) (Fig. 6.18).

The illumination was set to $C \times J_{\text{gen}}$, where C is the light concentration calculated from the ratio of the respective short-circuit current and that under 1 sun illumination. The optical limit (5.97 mA/cm^2 , see Sect. 6) was used for J_{gen} at 1 sun illumination. The flat-band voltage was set to $1.2 \times V_{CO}$ for the best fit, where V_{CO} refers to the crossover voltage determined from Fig. 6.17. An excellent fit is obtained for a wide range of illumination intensities with $(\mu\tau)_{\text{eff}} = 2.6 \times 10^{-11} \text{ cm}^2/\text{V}$ and $J_0 = 5.2 \times 10^{-6} \text{ A/cm}^2$. The only parameter that is not confirmed independently is the dark saturation current. However, Hegedus [46] analyzed data from a large variety of thin-film solar cells and demonstrated that within a regime in which V_{OC} is linearly correlated with V_{FB} , the dark saturation current does not influence V_{OC} . As the IV curves presented here exhibit a linear dependence of V_{OC} on V_{FB} (not shown explicitly), it was concluded that J_0 only has a minor impact on V_{OC} .

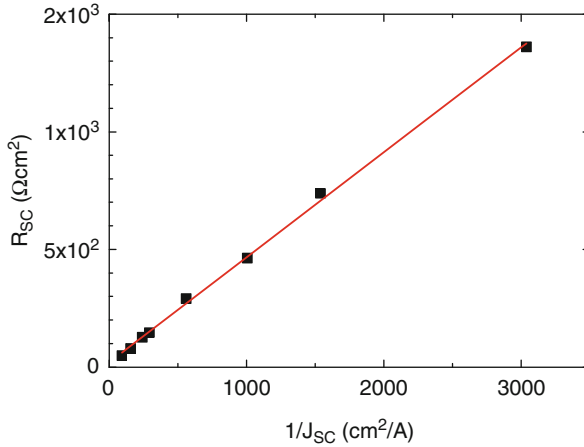


Fig. 6.19 Illumination dependence of the short-circuit resistance (*points*), and fit of (6.7) to the data. The slope of the linear regression is 0.3932 V. This corresponds to $(\mu\tau)_{\text{eff}} = 5.75 \times 10^{-10} \text{ cm}^2/\text{V}$ and an effective drift length of 150 nm with $V_{\text{FB}} = 0.4 \text{ V}$ at zero applied bias. Reprinted with permission from [9]. Copyright 2013, American Institute of Physics

The good agreement between the experimental data and the theory over a wide range of illumination densities (Fig. 6.18) strongly supports the validity of the presented analysis.

Complementary to the application of the uniform field approximation after Crandall, the analysis after Merten et al. [49] was applied. The latter is restricted to zero bias and results in the following expression for the short-circuit resistance R_{SC} :

$$R_{\text{SC}} = \left(\frac{dJ}{dV} \right)^{-1} \Bigg|_{V=0V} = \frac{1}{J_{\text{SC}}} \frac{(\mu\tau)_{\text{eff}} V_{\text{FB}}^2}{d^2} = \frac{L_{\text{D}}(V=0V)V_{\text{FB}}}{J_{\text{SC}}d}. \quad (6.7)$$

The effective drift length L_{D} is defined as in (6.5). As this analysis utilizes only directly accessible IV curve parameters, no IV curve fit is necessary. Equation (6.7) illustrates that the recombination appears in the IV curve as an illumination-dependent short-circuit resistance. The method can be used to extract the drift length from the slope of a plot of R_{SC} over $1/J_{\text{SC}}$. The illumination dependence of R_{SC} is depicted in Fig. 6.19. The experimental data obey (6.7) very well, and a linear regression yields a slope of 0.3932 V. This corresponds to an effective drift length of 150 nm and an effective mobility lifetime product of $(\mu\tau)_{\text{eff}} = 5.75 \times 10^{-10} \text{ cm}^2/\text{V}$ at short-circuit conditions and with V_{FB} set to equal the crossover voltage (0.4 V).

Furthermore, the mobility lifetime product agrees within one order of magnitude with the value of $(\mu\tau)_{\text{eff}} = 2.6 \times 10^{-11} \text{ cm}^2/\text{V}$ derived with the method after Crandall (cf. Fig. 6.18). The method after Merten et al. does not require knowledge of J_{gen} but utilizes only the directly accessible J_{SC} . On the other hand, the optical limit was assumed for J_{gen} for the IV curve fitting. As the optical limit is the ideal

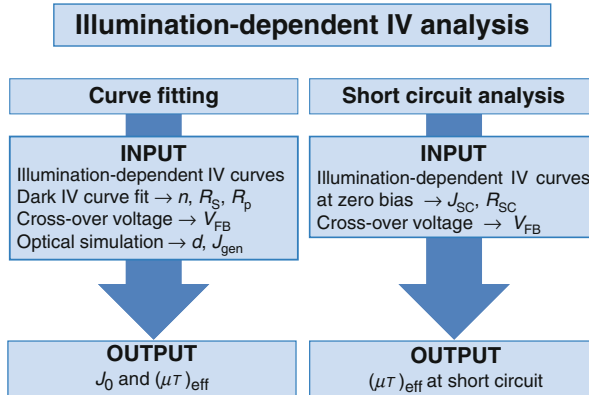


Fig. 6.20 Procedures for the illumination-dependent IV curve analysis. Simultaneous IV curve fits at various illumination levels yield the effective mobility lifetime product and the saturation current density. An analysis of the dark IV curve and an optical simulation are the prerequisites of this approach. A simplified procedure, whose validity is restricted to zero bias, is possible by analyzing the illumination dependence of the short-circuit parameters R_{SC} and J_{SC}

case it overestimates J_{gen} , and the procedure thus underestimates $(\mu\tau)_{eff}$ for a given short-circuit current. Thus, the analysis after Crandall is expected to yield a lower $(\mu\tau)_{eff}$ value than the method after Merten. Given the very limited foreknowledge about the Si NC material, both theories are in excellent agreement.

Figure 6.20 compares the required input parameters and the validity of the two procedures. The detailed curve fitting (Fig. 6.18) requires an analysis of the dark IV curve as well as an optical simulation of the entire device. The short circuit analysis on the other hand constitutes a simplified approach whose validity is restricted to zero bias. It makes use of the illumination dependence of R_{SC} and J_{SC} , which are both readily accessible IV curve parameters.

Both methods employed here ascribe any recombination in the entire device to the effective mobility lifetime product. As losses can also occur in the other device parts apart the Si NC absorber, e.g., by interface recombination or transport barriers, the value of $(\mu\tau)_{eff} \approx 10^{-10} \text{ cm}^2/\text{V}$ has to be seen as a lower limit to the electronic quality of the Si NC film itself.

8 Conclusion

The implementation of Si NCs as the top solar cell absorber is a promising solution to realize a crystalline silicon tandem solar cell. Especially attractive is the fabrication of Si NCs in a Si-based matrix as this approach is compatible with Si technology and photovoltaic production equipment.

In this chapter, the fabrication of Si NCs in a SiC matrix and its characterization as a solar cell absorber have been discussed. Different formation mechanisms

have been identified with respect to the case of a SiO_2 matrix. The ordered growth that takes place in SiO_2/SRO multilayers appears to be perturbed by the high c-Si/SiC interface energy, so size control in SiC/SRC multilayers is achieved only for particular conditions. From the optical point of view, Si NCs have demonstrated better absorption properties with respect to bulk silicon. However, the high volume fraction of residual amorphous phases detected by optical spectroscopy stresses the importance of further optimizing the crystallization process in order to avoid possible degradation of the electronic properties by the defect-rich dehydrogenated a-Si.

Furthermore, a membrane-based test device has been presented that enables the characterization of Si NC films on device level free of any substrate influence.

The membrane-based test device decouples the high-temperature annealing step from the formation of electron and hole collectors (doped regions) and thus enables for the first time a substrate-free photovoltaic characterization of Si NC films.

A detailed photovoltaic characterization was carried out with the aim to characterize the mobility lifetime product on device level. For this means, illumination-dependent IV measurements were analyzed in the framework of the uniform field approximation. An optical characterization and simulation were employed to extract the absorption of the Si NCs and of the SiC matrix and thus to derive an upper limit for the photogenerated current in the membrane p-i-n solar cell. The upper limit of the photogenerated current was used for the analysis of the illumination-dependent IV curves, and excellent agreement between experimental data and theory was found over a wide range of illumination intensities. The photovoltaic performance was found to be limited by charge carrier recombination. A lower limit of the effective mobility lifetime product in the order of $10^{-10} \text{ cm}^2/\text{V}$ was derived.

The procedure presented here, the illumination-dependent analysis of membrane-based Si NC p-i-n solar cells in conjunction with an elaborated optical device model, presents a powerful characterization scheme for Si NC solar cells. Si NC materials have so far been developed based on an optimization of their structural properties. The next step is to apply the characterization scheme discussed in this chapter to various Si NC materials for a comprehensive material development on the electrooptical level with the target of implementing Si NCs to the crystalline Si tandem solar cell.

Acknowledgement Funding from the European Community's Seventh Framework Programme (FP7/2007-2013) under grant agreement no. 245977 is gratefully acknowledged.

References

1. Glunz, S.W., Preu, R., Biro, D.: Crystalline silicon solar cells: state-of-the-art and future developments. In: Sayigh, A. (ed.) *Comprehensive Renewable Energy*, vol. 1, pp. 353–387. Elsevier, Oxford (2012)

2. Löper, P.: Silicon nanostructures for photovoltaics. Dissertation in submission, Universität Freiburg, Freiburg, Germany (2013)
3. Green, M.A., Emery, K., Hishikawa, Y., Warta, W., Dunlop, E.D.: Solar cell efficiency tables (version 41). *Prog. Photovolt. Res. Appl.* **21**(1), 1–11 (2013)
4. Staebler, D.L., Wronski, C.R.: Reversible conductivity changes in discharge-produced amorphous Si. *Appl. Phys. Lett.* **31**(4), 292–294 (1977)
5. Lee, B.G., Hiller, D., Luo, J.-W., Semonin, O.E., Beard, M.C., Zacharias, M., Stradins, P.: Strained interface defects in silicon nanocrystals. *Adv. Funct. Mater.* **22**(15), 3223–3232 (2012)
6. Cuevas, A.: Misconceptions and misnomers in solar cells. In: Proceedings of the 26th European Photovoltaic Solar Energy Conference, Frankfurt, Germany, 2012
7. Löper, P., Canino, M., Lopez-Vidrier, J., Schnabel, M., Schindler, F., Heinz, F., Witzky, A., Bellettato, M., Allegranza, M., Hiller, D., Hartel, A., Gutsch, S., Hernandez, S., Guerra, R., Ossicini, S., Garrido, B., Janz, S., Zacharias, M.: Silicon nanocrystals from high-temperature annealing: characterization on device level. *Phys. Status. Solidi.* **A210**, 669–675 (2013)
8. Löper, P., Stüwe, D., Künle, M., Bivour, M., Reichel, C., Neubauer, R., Schnabel, M., Hermle, M., Eibl, O., Janz, S., Zacharias, M., Glunz, S.W.: A membrane device for substrate-free photovoltaic characterization of quantum dot based p-i-n solar cells. *Adv. Mater.* **24**, 3124–3129 (2012)
9. Löper, P., Canino, M., Qazzazie, D., Schnabel, M., Allegranza, M., Summonte, C., Glunz, S. W., Janz, S., Zacharias, M.: Silicon nanocrystals embedded in silicon carbide: investigation of charge carrier transport and recombination. *Appl. Phys. Lett.* **102**(033507), 1–4 (2013)
10. Zacharias, M., Heitmann, J., Scholz, R., Kahler, U., Schmidt, M., Bläsing, J.: Size-controlled highly luminescent silicon nanocrystals: a SiO/SiO₂ superlattice approach. *Appl. Phys. Lett.* **80**(4), 661–663 (2002)
11. Song, D., Cho, E.-C., Conibeer, G., Cho, Y.-H., Huang, Y.: Fabrication and characterization of Si nanocrystals in SiC matrix produced by magnetron cosputtering. *J. Vac. Sci. Tech. B* **25**(4), 1327–1335 (2007)
12. Cheng, Q., Tam, E., Xu, S., Ostrikov, K.K.: Si quantum dots embedded in an amorphous SiC matrix: nanophase control by non-equilibrium plasma hydrogenation. *Nanoscale* **2**(4), 594–600 (2010)
13. Künle, M., Kaltenbach, T., Löper, P., Hartel, A., Janz, S., Eibl, O., Nickel, K.-G.: Si-rich a-SiC:H thin films: structural and optical transformations during thermal annealing. *Thin Solid Films* **519**(1), 151–157 (2010)
14. Summonte, C., Canino, M., Allegranza, M., Bellettato, M., Desalvo, A., Mirabella, S., Terrasi, A. Systematic characterization of silicon nanodot absorption for third generation photovoltaics. In: Proceedings of the 26th European Photovoltaic Solar Energy Conference, Hamburg, Germany, 21–25 Sept 2011, pp. 361–6
15. Kurokawa, Y., Miyajima, S., Yamada, A., Konagai, M.: Preparation of nanocrystalline silicon in amorphous silicon carbide matrix. *Jpn. J. Appl. Phys.* **45**(40), 1064–1066 (2006)
16. Summonte, C., Desalvo, A., Canino, M., Allegranza, M., Rosa, M., Ferri, M., Centurioni, E., Terrasi, A., Mirabella, S. Optical properties of silicon nanodots in SiC matrix, In: 25th European Photovoltaic Solar Energy Conference and Exhibition, Valencia, Spain, 2010
17. Shukla, R., Summonte, C., Canino, M., Allegranza, M., Bellettato, M., Desalvo, A., Nobili, D., Mirabella, S., Sharma, N., Jangir, M., Jain, I.P.: Optical and electrical properties of Si nanocrystals embedded in SiC matrix. *Adv. Mater. Lett.* **3**(4), 297–304 (2012)
18. Schnabel, M., Löper, P., Gutsch, S., Wilshaw, P.R., Janz, S.: Thermal oxidation and encapsulation of silicon-carbon nanolayers. *Thin Solid Films* **527**, 193–199 (2013)
19. Canino, M., Summonte, C., Allegranza, M., Shukla, R., Jain, I.P., Bellettato, M., Desalvo, A., Mancarella, F., Sanmartin, M., Terrasi, A., Löper, P., Schnabel, M., Janz, S.: Identification and tackling of a parasitic surface compound in SiC and Si-rich carbide films. *Mater. Sci. Eng. B* **178**, 623–629 (2013)
20. Johnson, F.A.: Lattice absorption bands in silicon. *Proc. Phys. Soc.* **73**, 265 (1959)

21. Kaneko, T., Nemoto, D., Horiguchi, A., Miyakawa, N.: FTIR analysis of a-SiC:H films grown by plasma enhanced CVD. *J. Cryst. Growth* **275**(1–2), e1097–e1101 (2005)
22. Summonte, C., Rizzoli, R., Bianconi, M., Desalvo, A., Iencinella, D., Giorgis, F.: Wide band-gap silicon-carbon alloys deposited by very high frequency plasma enhanced chemical vapor deposition. *J. Appl. Phys.* **96**(7), 3987–3997 (2004)
23. Scherrer, P.: *Göttinger Nachrichten Gesellschaft* **2**, 98 (1918)
24. Song, D., Cho, E.-C., Cho, Y.-H., Conibeer, G., Huang, Y., Huang, S., Green, M.A.: Evolution of Si (and SiC) nanocrystal precipitation in SiC matrix. *Thin Solid Films* **516**, 3824–3830 (2008)
25. Summonte, C., Canino, M., Allegrezza, M., Bellettato, M., Desalvo, A., Shukla, R., Jain, I.P., Crupi, I., Milita, S., Ortolani, L., López-Conesa, L., Estradé, S., Peiró, F., Garrido, B.: Boron doping of silicon rich carbides: electrical properties. *Mater. Sci. Eng. B* **178**, 551–558 (2013)
26. Hiller, D., Goetze, S., Zacharias, M.: Rapid thermal annealing of size-controlled Si nanocrystals: dependence of interface defect density on thermal budget. *J. Appl. Phys.* **109**(5), 054308–054308-5 (2011)
27. Künle, M.T.: Silicon carbide single and multilayer thin films for photovoltaic applications. Dissertation, Universität Tübingen, Tübingen, Germany (2011)
28. López-Vidrier, J., Hernández, S., Samà, J., Canino, M., Allegrezza, M., Bellettato, M., Shukla, R., Schnabel, M., Löper, P., López-Conesa, L., Estradé, S., Peiró, F., Janz, S., Garrido, B.: Structural, optical and electrical properties of silicon nanocrystals embedded in SixC1 – x/ SiC multilayer systems for photovoltaic applications. *Mater. Sci. Eng. B* **178**, 639–644 (2013)
29. Hernandez, S., Summonte, C., Allegrezza, M., Bellettato, M., Liscio, F., Canino, M., Desalvo, A. Space of formation of silicon nanocrystals in silicon carbide, In: *Proceedings of the E-MRS Spring Meeting, Strasbourg, France* (2013)
30. Peibst, R., Dürkop, T., Bugiel, E., Fissel, A., Costina, I., Hofmann, K.R.: Driving mechanisms for the formation of nanocrystals by annealing of ultrathin Ge layers in SiO₂. *Phys. Rev. B* **79**, 195316 (2009)
31. Zacharias, M., Streitenberger, P.: Crystallization of amorphous superlattices in the limit of ultrathin films with oxide interfaces. *Phys. Rev. B* **62**(12), 8391–8396 (2000)
32. Centurioni, E.: Generalized matrix method for calculation of internal light energy flux in mixed coherent and incoherent multilayers. *Appl. Opt.* **44**(35), 7532–7539 (2005), <http://www.bo.imm.cnr.it/users/centurioni/optical.html>
33. Allegrezza, M.: Minuitfit. <http://www.bo.imm.cnr.it/users/allegrezza/minuit/minuitfit.html>
34. Jellison Jr., G.E., Modine, F.A.: Parameterization of the optical functions of amorphous materials in the interband region. *Appl. Phys. Lett.* **69**(3), 371–373 (1996). Erratum, *ibid.* **69**:2137
35. Jellison, G.E., Chisholm, M.F., Gorbatskin, S.M.: Optical functions of chemical vapor deposited thin-film silicon determined by spectroscopic ellipsometry. *Appl. Phys. Lett.* **62**(25), 3348–3350 (1993)
36. Aspnes, D.E., Studna, A.A.: Dielectric functions and optical parameters of Si, Ge, GaP, GaAs, GaSb, InP, InAs, and InSb from 1.5 to 6.0 eV. *Phys. Rev. B* **27**(2), 985–1009 (1983)
37. Palik, E.D.: *Handbook of Optical Constants of Solids*. Academic, New York, NY (1991)
38. Guerra, R., Degoli, E., Ossicini, S.: Size, oxidation, and strain in small Si/SiO₂ nanocrystals. *Phys. Rev. B* **80**(155332), 1–5 (2009)
39. Alonso, M.I., Marcus, I.C., Garriga, M., Goñi, A.R., Jedrzejewski, J., Balberg, I.: Evidence of quantum confinement effects on interband optical transitions in Si nanocrystals. *Phys. Rev. B* **82**(4), 045302 (2010)
40. Moreno, J.A., Garrido, B., Pellegrino, P., Garcia, C., Arbiol, J., Morante, J.R., Marie, P., Goubilleau, F., Rizk, R.: Size dependence of refractive index of Si nanoclusters embedded in SiO₂. *J. Appl. Phys.* **98**(1), 013523–013523-4 (2005)
41. Losurdo, M., Giangregorio, M.M., Capezzuto, P., Bruno, G., Cerqueira, M.F., Alves, E., Stepihova, M.: Dielectric function of nanocrystalline silicon with few nanometers (<3 nm) grain size. *Appl. Phys. Lett.* **82**(18), 2993–2995 (2003)

42. Ding, L., Chen, T.P., Liu, Y., Ng, C.Y., Fung, S.: Optical properties of silicon nanocrystals embedded in a SiO₂ matrix. *Phys. Rev. B* **72**, 125419 (2005)
43. Allegranza, M., Hiller, D., Löper, P., Summonte, C.: Optical function and absorption edge of silicon nanocrystals, In: Proceedings of the E-MRS Spring Meeting, Strasbourg, France (2013)
44. Demontis, V., Sanna, C., Melskens, J., Santbergen, R., Smets, A.H.M., Damiano, A., Zeman, M.: The role of oxide interlayers in back reflector configurations for amorphous silicon solar cells. *J. Appl. Phys.* **113**(6), 064508–064508-9 (2013)
45. Dutta, U., Chatterjee, P.: The open circuit voltage in amorphous silicon p-i-n solar cells and its relationship to material, device and dark diode parameters. *J. Appl. Phys.* **96**(4), 2261–2271 (2004)
46. Hegedus, S.S.: Current–voltage analysis of a-Si and a-SiGe solar cells including voltage-dependent photocurrent collection. *Prog. Photovolt. Res. Appl.* **5**(3), 151–168 (1997)
47. Werner, J.H.: Schottky barrier and pn-junction I/V plots - small signal evaluation. *Appl. Phys. A* **47**, 291–300 (1988)
48. Crandall, R.S.: Modeling of thin film solar cells: uniform field approximation. *J. Appl. Phys.* **54**(12), 7176–7186 (1983)
49. Merten, J., Asensi, J.M., Voz, C., Shah, A.V., Platz, R., Andreu, J.: Improved equivalent circuit and analytical model for amorphous silicon solar cells and modules. *IEEE Trans. Electron Dev.* **45**(2), 423–429 (1998)

Chapter 7

Thiophene-Based Copolymers Synthesized by Electropolymerization for Application as Hole Transport Layer in Organic Photovoltaics Cells

Spyridon Soulis and Despina Triantou

Abstract The hole transport layer (HTL) is used in organic photovoltaics as an additional layer interposed between the active layer and the anode, with the intention of facilitating the conductance of the positively charged holes (formed in the active layer by the dissociation of the excitons) from the active layer towards the anode. The need for HTL is due to the inherent difficulties in the transportation of holes, which are not point defects, but actually they are rather more bulky polarons. There are several requirements that a material has to cover in order to be considered as an efficient HTL. The current state of the art in HTLs is the poly(3,4 ethylenedioxy thiophene):poly(styrene sulfonic acid) polymer blend. However, it has a series of drawbacks (especially in the long-term stability of the device) that limit its applicability. In this work, the use of electropolymerization for synthesizing copolymer films based on thiophene as alternative HTLs is presented. These films have the additional advantage that they can be tailor-made (i.e., they can be synthesized having specific thickness and band structure) so that they can best fit the needs of any possible active layer.

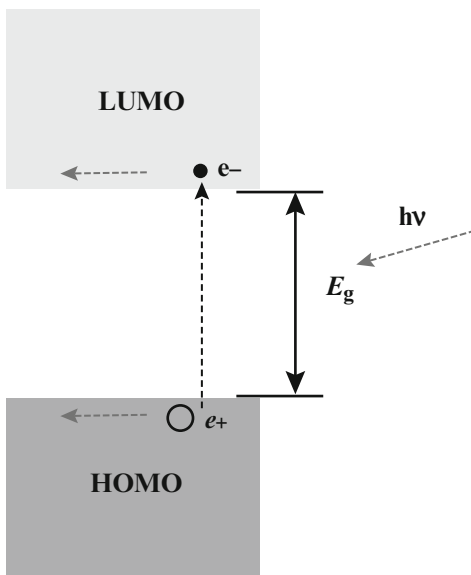
1 Introduction

Solar cells or photovoltaics (PVs) are devices that transform the optical energy (specifically, the solar light) into electrical one (i.e., current). Their function is based on the principle of the photoelectric effect, i.e., the interaction of radiation with electrons. In the photoelectric effect the incident radiation causes electron emission from the material; in the photovoltaic effect, the charge carriers formed

S. Soulis (✉) • D. Triantou

Laboratory Unit “Composite and Advanced Materials”, Department III “Materials Science and Engineering”, School of Chemical Engineering, National Technical University of Athens, 9-Heroon Polytec hniou str., Zografou Campus, 157 73 Athens, Greece
e-mail: sksoulis@central.ntua.gr; dstrian@gmail.com

Fig. 7.1 Schematic representation of the operating principle for photocurrent



by the incident radiation remain inside the material. Specifically, when the energy of the photons that consist the radiation is adequate, it is possible to excite the electrons of a material from their ground state into higher energy bands. Even though the details of the mechanism are more complicated, it can be considered that in the case of PVs, the electrons absorb sufficient energy so that they are driven into the lowest unoccupied molecular orbit (LUMO) of the material. There, they can move more or less freely, acting as carriers of the electric current. This is possible only for the electrons of the higher energy level of the material, i.e., those of the highest occupied molecular level (HOMO). The hole that remains in the HOMO after the excitation of the electron is positively charged (e^+) and also acts as current carrier. The flow of electrons in the LUMO and of the holes in the HOMO gives rise to what is called photocurrent. The difference between the energy of the HOMO and LUMO levels is termed “energy gap” (usually symbolized E_g) [1].

Theoretically, when a photon with an energy equal to (or slightly higher than) the E_g is absorbed by the material, it can produce photocurrent. Given that the solar radiation of interest is in the region of the optical spectrum (roughly 400–900 nm, or 1.5–3.3 eV), the E_g of the material should be in that order of magnitude (as schematically presented in Fig. 7.1). This energy gap corresponds to electric semiconductors. Thus, again theoretically, by selecting semiconductors with the proper HOMO–LUMO levels (absorbing photons in the region of solar light), a PV device might be constructed that will produce current from the sun ad infinitum. However, the reality is much more complex (and harsh).

All PVs are multilayer structures. From the point of view of electric circuits, PVs are equivalent to EMF elements (in the sense that they produce current for the circuit), so their contacts are named according to the EMF terminology convention. Thus, anode is the positive and cathode is the negative contact. In every case, there is at least one active layer, i.e., the layer which absorbs light and where the charged species that act as photocurrent carriers are formed. Even though there are several ways to classify the PVs, the most common way is by the materials used as the active layer. Generally speaking, there are two large categories, the inorganic and the organic PVs. The current commercial solar cell technology is based on inorganic PVs and particularly on silicon; it has grown fast enough due to the extensive use of silicon in the microelectronics industry, which led to economies of scale. However, it is understood that the technology of inorganic PVs has severe drawbacks: the manufacturing processes are energy consuming and not particularly cost effective, they are not good for lightweight applications, and the price of silicon (especially that of the pure and higher quality which is usually preferred) tends to increase. Moreover, in terms of durability and environmental stability silicon PVs leave much to be desired [1–4].

The second category is the organic PVs (OPVs). There are several low-molecular-weight organic molecules (mostly originating from organic dyestuffs, e.g., phthalocyanines) that behave reasonably well as active layers and have been proposed for OPVs, but there are some problems in their manufacturing and a large (yet unresolved) question about their stability in environmental conditions. Polymers, on the other hand, are considered much more stable (for example, it is more difficult for a polymer to melt flow when heated than a small organic molecule). Moreover, their manufacturing technologies could be easily scaled up to reach the industrial production level. Even though the general belief is that OPVs will someday outphase silicon-based PVs (due to their many advantages over their silicon-based counterparts), they have not yet achieved the necessary maturity to challenge the latter in commercial level. This is mainly due to the complexity of these devices that leaves many yet unsolved subjects [3, 5, 6].

In this chapter, we present one of these subjects, namely, the quest for proper hole transport layer (HTL). In the literature, the combination of poly(3,4 ethylenedioxy thiophene):poly(styrene sulfonic acid) (PEDOT:PSS) is generally accepted as the current “golden rule” for HTL. This is used in the form of water dispersion, synthesized by chemical polymerization. We present the use of electropolymerization as an efficient method for synthesizing thiophene-based copolymers with proper properties that can be considered as possible HTL alternatives. The use of electropolymerization permits the control of their electronic structure and their properties. Even though HTLs are used in various PV architectures, we focus in bulk heterojunction (BHJ) solar cells, because they seem to give the most promising results in terms of the quantum efficiency.

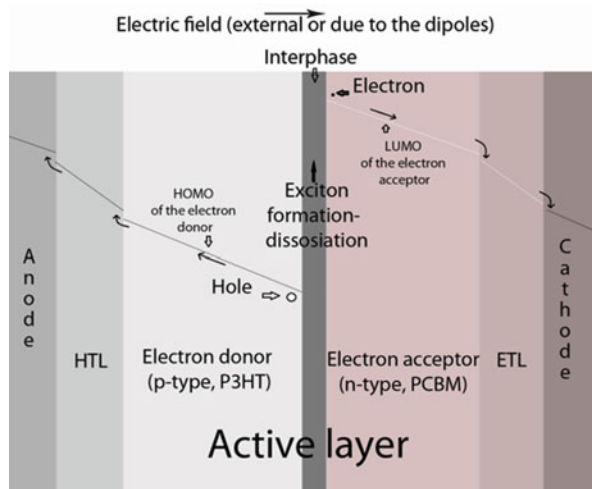
2 What Is the Necessity of the Hole Transport Layer

In the case of OPVs, the incident light does not directly excite electrons to the LUMO band, and the exact mechanism, through which OPVs transform light into current, is rather complicated [7–9], but it can be roughly described as a three-step process. Firstly, the incident light is absorbed by a chromophore material, leading to the formation of an exciton. Excitons are metastable excited states of molecules constituted by a pair of an electron with a positively charged hole; in materials that are not dielectric conductors (i.e., they do not contain static dipoles), the binding energy of the pair is considerable [8, 10]. Then, the exciton dissociates into positive (i.e., hole) and negative (i.e., electron) charge carriers by electron transfer from the electron donor (p-type material) to the electron acceptor (n-type material). Finally, the charged carriers are transported with various ways (e.g., by diffusion, by hopping) to the respective electrodes, giving rise to photocurrent. The total efficiency of an OPV to transform light into current depends on the efficiency of every one of these steps; in order to manufacture a good OPV, the efficiency of exciton formation, exciton dissociation, and transport of the charged species should be as high as possible [3, 11].

The first OPVs proposed were single-layer devices: this is the simplest architecture and can be easily manufactured. However, their efficiencies were so small that they were useful only as a proof of concept to the idea that organic molecules (either small ones or macromolecules) can produce photocurrent. Soon it was acknowledged that a bilayer architecture having separate electron donor and electron acceptor layers would be more efficient, a structure called flat heterojunction (FHJ). In the process it was also discovered that the FHJ architecture in polymer OPVs could provide only small efficiencies. This was attributed to the small interface between the two layers: in FHJ lay-up, for geometrical reasons the area of the interface is as much as the external surface of the cell itself. In such a case, only those excitons generated in an extremely thin layer near to the interface of the donor and acceptor will be able to dissociate prior to dissipative recombination. This could be avoided by using devices with very thin layers; unfortunately, the exciton diffusion length is generally much less than the optical absorption length, meaning that the quantum efficiency of such devices cannot increase. Nowadays, FHJ architecture is still applied only in OPVs of small organic molecules, where the deposition of the layers by sublimation of the substances dictates this kind of structure [1, 5, 12].

Since the excitons are produced in that same interface, the increase of the interface-to-volume ratio of the two layers was a prerequisite for achieving higher efficiencies. This could be accomplished by the concept of interpenetrating networks, and the BHJ architecture was applied, where the electron donor and electron acceptor layers are mixed together forming the bi-continuous active layer. Using this configuration, the probability of effective exciton dissociation (i.e., the accumulative probability of the exciton formation, its subsequent dissociation, and

Fig. 7.2 Idealized sketch of the way the BHJ OPVs work



the successful diffusion of the charged species to the corresponding electrodes) increases considerably [3, 4, 11, 13].

The first BHJ cells were demonstrated in 1995 but had a power conversion only around 1 % [13]. Even though the basic design remains the same, the improvements in many aspects of the fabrication process (particularly in controlling the blend morphology of the active layer) led to considerable increase of the efficiency, approaching the “psychological” limit of 10 % [3].

During the transition from the FHJ to the BHJ architecture, the concept of the HTL came forward. What was the reason to complicate the architecture by inserting a new layer? One graphical way to describe the function of the OPV is to imagine the electronic structure of the OPV as a “viscous liquid” and that the exciton dissociation creates two kinds of “particles” inside this “liquid”: the electrons that behave like “balls” and the holes that behave like “bubbles.” Thus, the former tend to go “down,” in the sense that they prefer to “drop” from the higher LUMO level to the lower, and the latter tend to go “up,” in the sense that they prefer to “climb” from the lower HOMO level to the higher. The energy level of every material in the device is not their respective absolute HOMO or LUMO energy values, but there is actually a gradient (or slope) of the energy level due to the presence of the electric field (external or due to the static dipoles in the device). Schematically, this is presented in Fig. 7.2. This figure is also valid from the physical point of view: holes are positive charge carriers that do not contain any mass (they actually are the result of electron extraction from the lattice), and electrons are negative charge carriers that do have mass. Someone would expect that the mass-less holes would diffuse more easily than electrons; however, they do have a volume (as the bubbles have, too)! The holes exist in the form of positively charged polarons. The polarons are not point charges (as in the case of the inorganic p-semiconductors) but a pair of a charge and an electron; this pair is not stable when its two elements are next to each

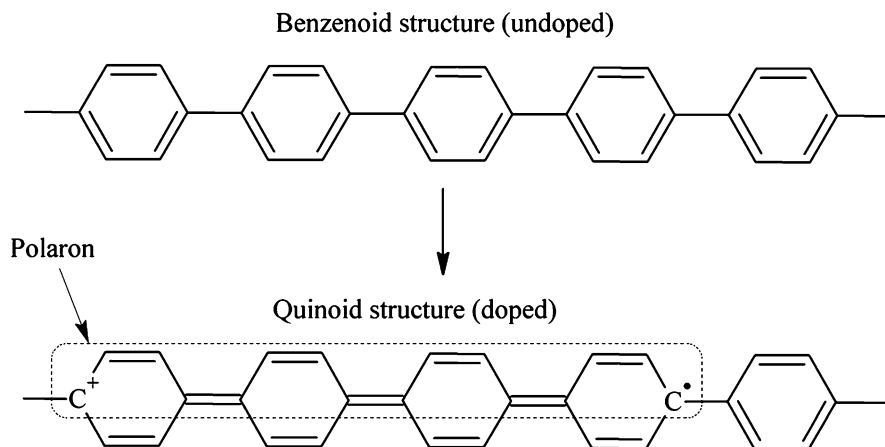


Fig. 7.3 Formation of polarons in poly(para-phenylene), PPP

other, but they are stabilized by changing the conformation of the polymer chain in a sequence of structural units. For example, the polaron in poly(para-phenylene) is stabilized by splitting the positive charge–electron pair in a sequence of three up to five aryl rings, leading to the related conformational change from the benzenoid to the quinoid structure (Fig. 7.3) [7, 14, 15]. Thus, the holes actually occupy a relatively large volume, and consequently their mobility is not so high [16]. Using the model of “liquid” electronic structure, it is like the “drag” (or “friction”) that the “bubble” has to overcome from the surrounding “viscous liquid.”

It was found that the HOMO level of the electron donors used does not match well with that of the anode (usually made of the transparent conductor indium tin oxide, ITO). Specifically, the difference between them is quite large. This led to entrapment of the holes in the electron donor–ITO interface (creating static charges), and it did not permit the efficient transport of the holes in the anode. In the “liquid” electronic structure model, this is equivalent to two “viscous liquids” with considerably different “levels”: the bubbles cannot easily climb from the low to the higher level and thus they tend to remain in the interface. Using a liquid with “intermediate” level (i.e., a HOMO between that of the electron donor and of ITO), it is much easier for the bubbles to pass. Thus, HTL can be imagined as a “liquid” with “lower viscosity” (actually, higher hole mobility) and proper “level” (i.e., HOMO band) that facilitates the transition of the “bubbles” through its mass.

HTLs have also been termed hole extraction layer (HEL) or (sometimes) electron-blocking layer (EBL), even though the latter can be also a separate layer. In all probabilities, the term HTL was firstly used in organic light-emitting diodes (OLEDs) and it was loaned from them [17, 18]. For achieving high-efficiency OLEDs the dual-injection architecture is used, a multilayer structure with discrete hole injection layers (HILs) and/or HTLs, light-emitting layers (EMLs), and

electron transport layers (ETLs). To avoid quenching of luminescence by these doped layers, a neutral HTL (with thickness of ca. 10 nm) is often deposited as a spacer between the p-doped HTL and the EML, whereas an electron-transporting spacer (again with a thickness of ca. 10 nm) is deposited between the ETL and EML [19].

3 Current State of the Art in HTLs and Its Limitations

In order for the HTL to be efficient and justify its use in the OPVs, it has to function in more than one way. An ideal HTL should cover a series of requirements, namely:

1. Its valence band (HOMO) should be higher but near that of the electron donor layer and lower than that of the ITO (or, more generally, that of the anode material).
2. The hole mobility should be as high as possible. This usually means that HTL has to be p-doped, but the use of undoped materials is not excluded as far as their hole mobility is large enough.
3. The HTL should be as transparent in the visible region as possible. This precondition has led to propose the use of extremely thin layers of materials, as low as a few nanometers.
4. The LUMO level should be well above that of the electron acceptor material. That is the reason why HTL is sometimes called EBL, but (as already mentioned) in some cases specific EBL layers have also been proposed.
5. In order for the layer to be more effective, the thickness of the layer should be optimal. The optimization derives from the combination of the material resistance and its absorption of the incident light.
6. The HTL should also act as a good interface between the active layer and the anode, ameliorating the problem of the different surfacial energies. Typically, the polymers (such as P3HT) are hydrophobic and conducting oxides (such as ITO) are hydrophilic, indicating that it would be difficult to achieve even films of the active layer over the electrode surface [9]. The HTL should act as intermediate that will permit the uniform spread of the active layer in the OPV device. If possible, the application of the HTL should decrease the surface roughness of the anode: the latter is directly related to the entrapment of charges and the formation of static charges in the interface.
7. The material should contain as low concentration of non-active charge carriers as possible. During the doping of the polymers, apart from the formation of charge carriers, an increase in the nonconducting charge carries also inadvertently happens, mainly through the formation of static dipoles. The nonconducting charge carriers give rise to the dielectric (i.e., imaginary) part of the conductivity and act as hole entrapments [6].
8. HTL should not have any detrimental effect on the device long-term stability and performance, or even better it should have a positive effect on both of them.

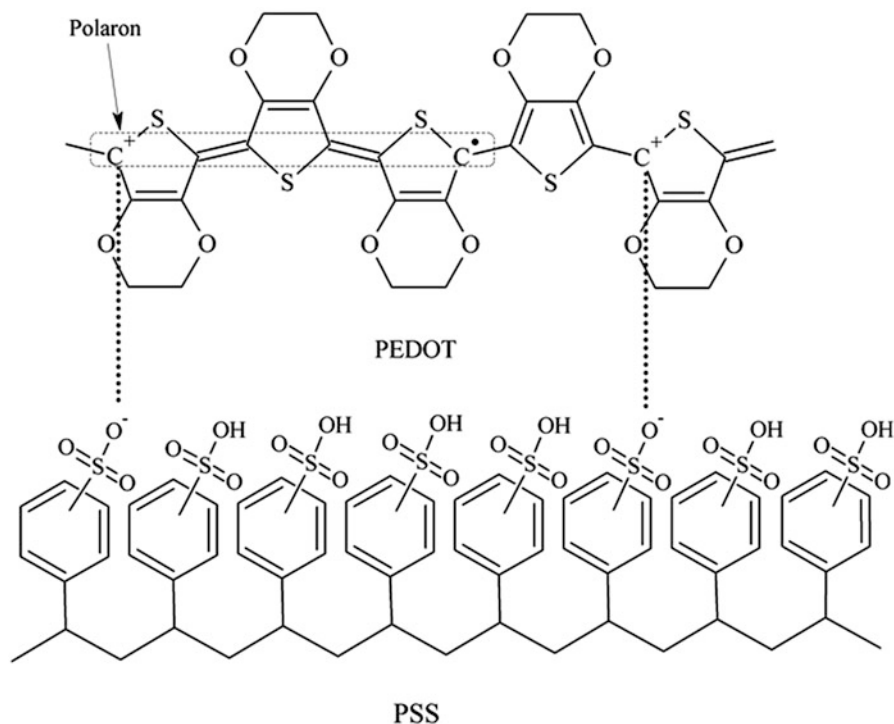


Fig. 7.4 Sketch of the doped PEDOT:PSS chemical structure

The current BHJ lay-up considered that the “golden rule” of the OPVs consists of an active layer with poly(3-hexyl thiophene) (P3HT)/phenyl-C61-butyric acid methyl ester (PCBM) blend. The former is the electron donor and the latter the electron acceptor. Theoretically, the chromophore material (i.e., the material responsible for the absorption of the light) in an OPV could be either the electron donor or the electron acceptor; however, PCBM (or, more generally, fullerene derivatives) absorbs very weakly in the optical range. Thus, in principle the chromophore is the electron acceptor material (again in most cases P3HT). The HTL consists of PEDOT:PSS (Fig. 7.4) [20]. The latter is actually a polymer blend, where PSS chains act as the counterbalancing anions when PEDOT is positively charged. It is accepted that the blend consists of alternating PSS–PEDOT macromolecules and that the PSS chains lie in parallel to (and sitting almost perpendicular to) the PEDOT chain level, a structure supported from density functional theory calculations [21, 22]. The most usual methods for the synthesis of PEDOT:PSS are direct reactions, such as the BAYTRON P method. According to the latter, EDOT is polymerized in a dispersion in water. In order to achieve this dispersion, PSS is used as the polyelectrolyte; Na₂S₂O₈ is used as initiator, and the polymerization is achieved at room temperature; similar reactions can be used to produce pure PEDOT. Today, there are several PEDOT:PSS solutions commercially available, each one combining different properties [2, 21, 23].

PEDOT:PSS has many advantages as HTL. First of all, it is actually transparent in the doped state (when undoped it has blue color). Moreover, values between -4.8 and -5.2 eV for its HOMO and between -4.3 and -3.0 eV for its LUMO have been reported; for the ITO, the corresponding HOMO values are between 5.0 and -4.7 eV, and for the P3HT the corresponding HOMO value is -5.2 eV [2, 11, 19, 20, 24]. Additionally, studies have shown that the deposition of the PEDOT:PSS layer onto ITO electrode decreases the surficial roughness of the latter [25]. Most of the times, PEDOT:PSS is applied as a water “solution” (more correctly, suspension or dispersion) [2]; even though not exactly “hydrophilic” material, the presence of a large concentration of sulfonic acid groups ensures that it is at least dispersible in aqueous media. In the typical BHJ construction, the PEDOT:PSS water solution is spin coated into an ITO-coated glass substrate (the OPV anode), then the film is heated (to evaporate residual water and to anneal it), afterwards the active layer is coated onto them (either with spin coating or printing or some other method; there are many variations in this step), and finally the metal cathode (usually Ag, Ca, or Al) is placed by vacuum deposition. To date, BHJs have efficiencies approaching 6–7 %, and even an efficiency value of 7.9 % has been reported [3, 11].

Even though PEDOT:PSS is the current paradigm, its performance as HTL is far from flawless. The main disadvantages are its acidic nature and its hydrophilicity [25–28]. The presence of the sulfonic acid groups means that the material is actually acidic in nature and values of pH between 1 and 2 have been measured. Even though the research on the degradation mechanisms in OPVs has only recently started, there are strong indications that the main degradation mechanism involves the acidic etching of the ITO from the PEDOT:PSS, leading to the migration of In or Sn cations towards the active layer [4, 15, 28, 29]. Additionally, it has been proposed that ITO etching could be the result of water absorbed by PEDOT:PSS; its subsequent dissociation forms proton cations that accelerate the procedure. This phenomenon has been related to the drop of the OPV performance and to the decrease of the device lifetime [26, 27]. As a matter of fact, the same acidic nature of PEDOT:PSS prohibits its use with other low-cost, transparent conducting oxides that are more easily etched by acids [4]. Moreover, it is suspected that the absorption of humidity by PEDOT:PSS from the environment leads to the formation of an insulating layer in the PEDOT:PSS-active layer interface, which could also lead to device failure [30]. Generally, water may act in more than one way (e.g., it can cause oxidation reactions or it can create short circuits); thus, the absorption of water by one of the layers could severely shorten the device lifetime [28].

It has been postulated that humidity induces formation of an insulating layer at the PEDOT:PSS/blend interface leading to device failure. For example, the replacement of PEDOT:PSS by MoO_3 considerably enhanced air stability of similar devices with an Al cathode, suggesting that PEDOT:PSS might accelerate the degradation. These limitations have led to investigations of other materials as effective replacements of PEDOT:PSS as the HTL in OPV devices; the alternatives suggested are mainly thin films of inorganic oxides (e.g., MoO_3). Finally, using

alternative to PEDOT:PSS active layers may not always work also as effectively as an HTL: if the LUMO of the active layer is not high enough, the possibility of electron diffusion inside the HTL (and their subsequent recombination with holes) increases considerably. This could also lead to a decrease of the device performance [12, 19, 22, 24, 27, 30–32].

4 Electropolymerization for Producing Thiophene Copolymers

Electropolymerization is a facile method for direct synthesis of polymer films [33–35]. One of the advantages is that the electronic structure and the thickness of the films can be easily controlled to fit certain needs (tailor-made band structure). As an example, in Table 7.1 the electronic structures of several polymers synthesized by electropolymerization are summarized [36, 37]. By varying the electropolymerization conditions, it is possible to produce materials with quite different electronic structure, even using the same basic chemical structure: for example, using thiophene as monomer, it was possible to synthesize thiophenes with HOMO between -4.90 and -5.19 eV, LUMO between -3.42 and -3.56 eV, and E_g between 1.43 and 1.63 eV. Electropolymerization also has the advantage that different structural units can be combined, producing copolymers with completely different physical properties than the corresponding homopolymers. Moreover, since the polymer grows directly on the surface of the electrode, the properties of the interface between these two layers can be almost ideal (for example, it is very difficult to scrap or to wash away with solvent the films formed onto the surface of an electrode); in some cases, the selection of a suitable substrate (containing proper active groups) may lead to grafting of the polymer onto the surface. Finally, the method could be modified for constructing multilayer structures. The main disadvantage of electropolymerization seems to be its complexity: in order to achieve the requested result there are many parameters of the process that need to be controlled; sometimes, minute changes in the parameters can lead to widely different final results [34]. This, combined with the inherent difficulties in designing a continuous electrochemical process, makes it seemingly difficult to scale up electropolymerization for high-throughput production lines. Even though it has been used in the fabrication of many other electronic devices (e.g., ECDs), electropolymerization has not been extensively used in OPVs (at least, up to now).

Electropolymerization can be carried out using either potentiostatic or potentiodynamic conditions, and in Table 7.1 the films are produced with either one of the methods. Apart from fluorinated (or, generally, halogenated) monomers, most of the substances reported in the literature are electropolymerized using anodic conditions (i.e., positive potential). What is important is the control of the voltage (otherwise the overpotential grows very fast and the films formed are

Table 7.1 Electronic band structures of homopolymer and copolymer films synthesized by electropolymerization

Materials	Code of polymers	E_{HOMO} (eV)	E_{LUMO} (eV)	E_{g} (eV)
Polyphenylenes	PP _{1.80/30}	-4.95	-3.42	1.53
	PP _{1.82/30}	-4.98	-3.43	1.55
	PP _{1.84/30}	-5.02	-3.53	1.49
	PP _{2a}	-5.01	-3.51	1.50
	PP _{2b}	-5.00	-3.52	1.48
Polythiophenes	PTh _{1.71/30}	-4.90	-3.45	1.45
	PTh _{1.73/30}	-4.90	-3.45	1.45
	PTh _{1.75/30}	-4.90	-3.42	1.48
	PTh _{2a}	-4.93	-3.50	1.43
	PTh _{2b}	-4.94	-3.45	1.49
Poly(3-methyl-thiophenes)	3MPTh _{1.55/30}	-4.70	-3.50	1.20
	3MPTh _{1.55/5}	-4.72	-3.50	1.22
	3MPTh _{1.57/30}	-4.70	-3.45	1.25
Thiophene/phenylene copolymers	(PP-PTh) _{1.80/30}	-5.11	-3.92	1.19
	(PP-PTh) _{1.82/30}	-5.20	-3.99	1.21
	(PP-PTh) _{1.88/30}	-5.08	-3.40	1.68
	(PP-PTh) _{1.90/30}	-4.91	-3.20	1.71
	(PP-PTh) _{2a}	-4.90	-3.47	1.43
	(PP-PTh) _{2b}	-5.00	-3.49	1.51
3-Methyl-thiophene/phenylene copolymers	(PP-3MPTh) _{1.55/30}	-4.80	-3.60	1.20
	(PP-3MPTh) _{1.55/5}	-4.72	-3.45	1.27
	(PP-3MPTh) _{1.55/2}	-4.80	-3.40	1.40
	(PP-3MPTh) _{1.57/2}	-5.05	-3.35	1.70

Explanation of the codes (indicative):

PTh_{1.71/30}: Polythiophene synthesized potentiostatically at 1.71 V (vs SCE) for 30 min

PTh_{2a} or PTh_{2b}: Polythiophene synthesized by cyclic voltammetry by scanning between +1 and +2 V (vs. SCE) for 40 or 80 sweeps (scan rate: 100 mV/s)

oxidized very fast); typically, this is achieved by using a three-electrode setup. The three electrodes are named working, counter, and reference. The working electrode is where the reactions happen, the counter electrode is used for measuring the current passing through the cell (i.e., not any electrochemical phenomena take place in it), and the reference electrode is used for keeping the potential of the working electrode to a defined (or desired) value. The counter electrode consists of an electrochemically inert material such as Pt and is separated from the solution by a porous ceramic frit. The reference electrode (such as the saturated calomel electrode/SCE) has very large resistance and stable potential for a large range of conditions; it is separated too from the solution, using a setup such as the Luggin capillary [35, 38]. The easier method for film synthesis is by using potentiostatic conditions, where the potential has a constant value and the film grows by the time of the experiment [39]. Figure 7.5 presents some characteristic cases of potentiostatic electropolymerizations. The film formation follows one of the several possible nucleation and growth mechanisms: for example, the nucleation can be

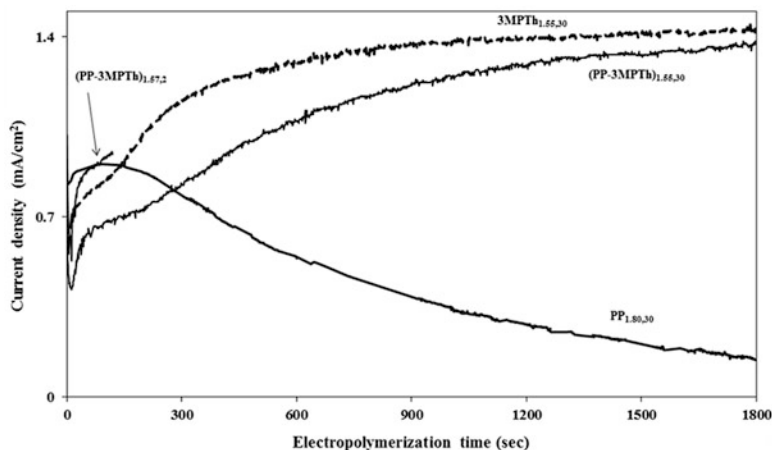


Fig. 7.5 Typical current–time curves for electropolymerization of thiophene copolymers

one, two, or three dimensional and could be controlled either by the charge transfer or by the diffusion; the mechanism of the film formation can be analyzed using the current–time curve. The most common mechanism involves 2-D growth of the nuclei, resulting in generally compact films [36].

Even though potentiostatic conditions are easier to be controlled, in the literature there is a consensus that the best results (in terms of film stability, homogeneity, and conductivity) are obtained using potentiodynamic conditions [34, 37, 40]. Some of the most widely studied conditions involve triangular-shaped pulses of voltage, better known as cyclic voltammetry (CV). In such a case, there is a sweep of the potential, starting from an initial value, reaching a final, and then returning back to the initial potential, using a defined potential scan rate [38]. In electropolymerizations, the scan of the potential starts from a low voltage value and increases to a high value (and is called the anodic sweep or scan) and then returns from the high value to the low (and is called the cathodic sweep or scan). Typically, the results are presented using the voltage–current graph, which forms a closed curve and is called cyclic voltammogram. Figure 7.6 shows some typical cyclic voltammograms for the electropolymerization of various polymers and copolymers. The shape of the CV depends on the monomer(s) used. The thickness of the films synthesized depends mainly on the electrochemical activity of the working electrode, but normally a single CV sweep produces very thin films, around 200 nm; films with such a small thickness are usually transparent or semitransparent. In order to produce thicker films, repetitive scans are used. When the monomer is electroactive enough (as, for example, in the case of thiophene), by repetitive scanning of the solution two oxidation and one reduction peaks can be distinguished in the CVs: the oxidation peak at higher potential is usually attributed to the electropolymerization of the film (or, more correctly, the electrodeposition of the polymer onto the surface of the electrode), the oxidation peak at lower potential is attributed to

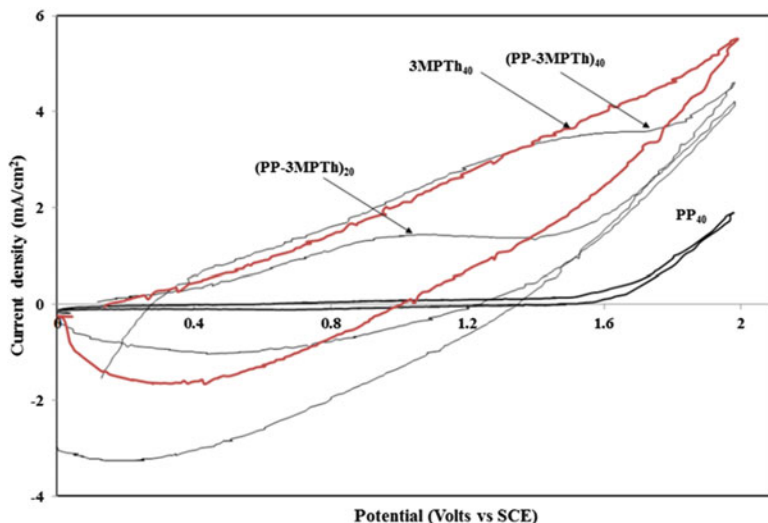
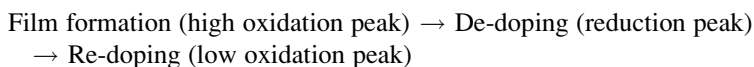


Fig. 7.6 Typical cyclic voltammograms for the electropolymerization of thiophene copolymers

the doping of the film, and the reduction peak is attributed to the de-doping of the polymer. Thus, the typical scheme for an electropolymerization CV is as follows:



This behavior is considered as a proof that the doping of the polymer is much easier than the electropolymerization; thus the films produced are directly in the doped state. The reduction can be either total or partial; the change of the oxidation state of the film is usually accompanied by a change in the color of the film. In some cases, the CVs do not present any peaks (or other features), which can be due to several reasons. For example, in the case of pyrrole the polymer is formed so easy and so fast that in its CVs no peaks appear. If the potential becomes anodic enough it is even possible for the film to be dissolved, but this is due to electrochemical decomposition reactions and not due to dissolving or polymer desorption from the electrode surface.

The CVs can be used in order to control the doping level of the film synthesized. The thickness of a film can be estimated from the total charge passed through the cell; moreover, the doping level of the film is determined by the ratio of oxidation charge (Q_{ox}) to reduction charge (Q_{red}) during the cycle. For example, in the case of the copolymerization of 3-methylthiophene (3MTh) with biphenyl, it was found that by repetitive scanning in the potential range from 0 up to +2 V, the ratio ($Q_{\text{ox}}/Q_{\text{red}}$) decreased after several repetitions to a saturation value below 1.0, indicating that the film formed was in the reduced state (which was also proven by its pink color). Using the same system of comonomers and repetitive scanning in the potential region from +1 up to +2 V, the ratio ($Q_{\text{ox}}/Q_{\text{red}}$) again decreased to a saturation value

which this time was around 5.0, indicating that the film formed was in the oxidized state (which was also proven by the blue to dark red color of the latter film). After 80 consequent repetitive scans, the first potential region afforded a reduced film with thickness of 8.6 μm and the second region an oxidized film with thickness of 9.6 μm [36, 37].

The combination of thiophene with other comonomers and their electropolymerization can lead to the synthesis of films that may replace PEDOT:PSS as active layer in OPVs for a number of reasons. Firstly, the films are hydrophobic and not acidic, minimizing the possibility of water affecting the device performance and lifetime and the acid etching of the anode. Secondly, the possibility of controlling the electronic structure of the films permits their application in OPVs with active layers that do not match well with the electronic structure of PEDOT:PSS (which is difficult to change). Thirdly, the interfaces in the electropolymerized films can be minimized (or, by using appropriate electrodes, even eliminated), reducing the need for annealing processes. Fourthly, the possibility of grafting the polymer onto the electrode surface means that the transport of the charges from the film to the electrode material will be almost totally unimpeded. For the OPVs, this means that there will be minimal losses between the HTL and the anode, accounting to the actual removal of one of the obstacles in the charge transport mechanism. This could lead to further increase of the total device efficiency of the OPVs. Finally the monomers used for the synthesis of the copolymer films are more inexpensive than PEDOT:PSS, indicating that their OPVs could be more cost effective.

5 Structure and Properties of Thiophene Copolymers Synthesized by Electropolymerization for Use as HTLs

5.1 Morphology

The potential conditions used for the electropolymerization influence strongly the structure of the films. The morphology of very thin films is not easy to be studied, but it is possible in films with thickness of several μm (Fig. 7.7). Copolymers of thiophene and biphenyl that had been synthesized with CV in the potential region from 0 up to +2 V have fibrillar structure with many round-shaped pores (Fig. 7.7a, b). The size of pores increases with increasing the number of sweeps, i.e., the film synthesized with 40 sweeps is more compact than that synthesized with 80 sweeps. Similar copolymers synthesized with CV in the potential region from +1 up to +2 V have also fibrillar structure with small pores but are more compact (Fig. 7.7c, d). Similarly, the copolymer of 3MTh with biphenyl synthesized with CV in the potential region from 0 up to +2 V has fibrillar structure with many round-shaped pores (Fig. 7.7e) and that synthesized with CV in the potential region from +1 up to +2 V has a spongelike structure with aggregates from 2 up to 7 μm (Fig. 7.7f). The latter morphology is more compact.

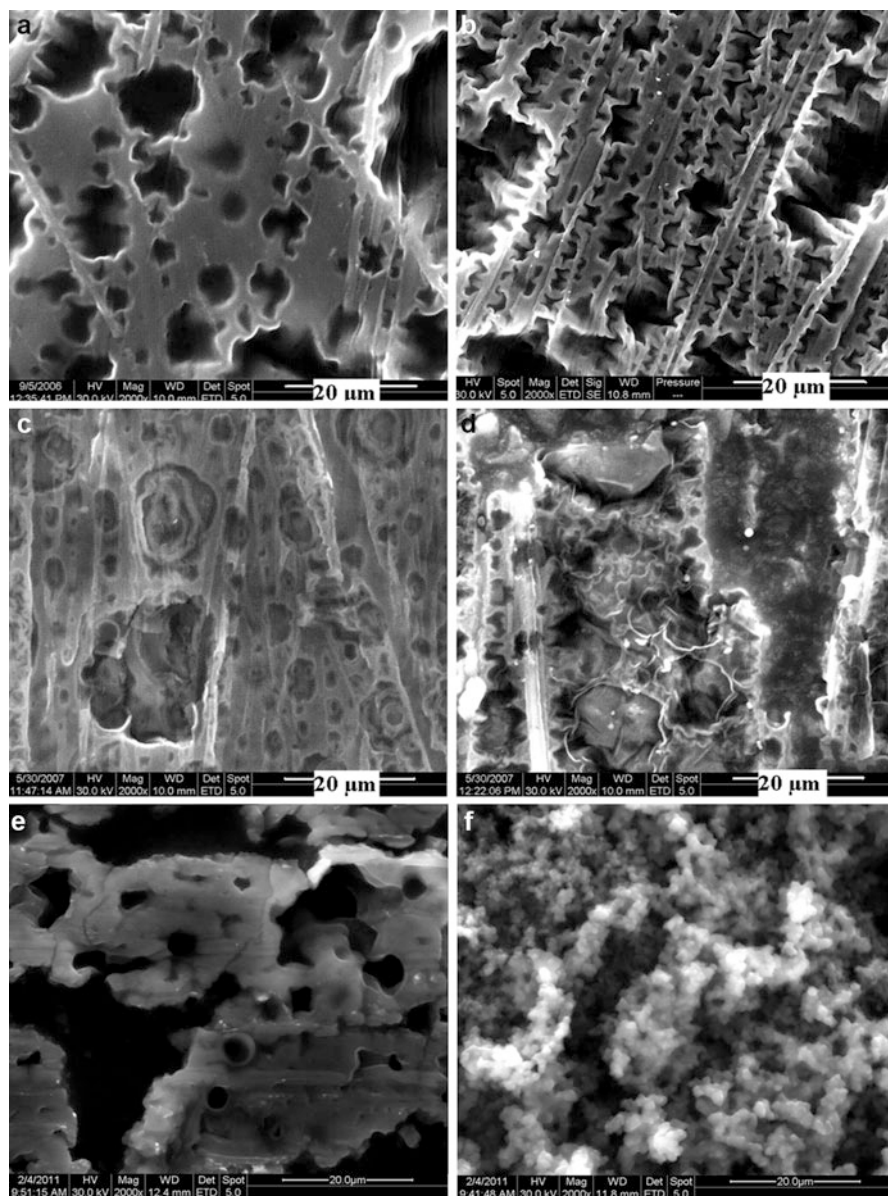


Fig. 7.7 SEM micrographs of thiophene-based copolymer films synthesized by CV (magnification $\times 2,000$): (a) PP-PTh, 0 up to +2 V, 40 sweeps; (b) PP-PTh, 0 up to +2 V, 80 sweeps; (c) PP-PTh, +1 up to +2 V, 40 sweeps; (d) PP-PTh, +1 up to +2 V, 80 sweeps; (e) PP-3MPTh, 0 up to +2 V, 80 sweeps; (f) PP-3MPTh, +1 up to +2 V, 80 sweeps

The different morphology of the copolymers confirms that the potential range and the number of sweeps have a strong influence on the film structure.

5.2 FTIR

The FTIR spectra of the thiophene-based copolymers synthesized by electropolymerization present only aromatic structures, with the main absorption peaks at 1,600, 1,570, 1,480, 1,400, 1,375, 1,240, 1,165, 980, and 943 cm^{-1} [5, 34, 36]. When 3MTh is used as comonomer, the aliphatic C–H peaks also appear [37]. The absorption peaks attributed to the sulfur in the thiophene ring (due to C–S–C and C–S bond deformations) are at 680 and 600 cm^{-1} . Generally, one of the problems with characterizing the aromatic-based polymers (and copolymers) with FTIR is that the different groups absorb in roughly the same wavenumbers, so it is very difficult to attribute a certain peak to a certain structure. What the FTIR spectra can give us is an indirect measure of the materials' doping level, using the ratio of the peaks for the quinoid (A_{1570}) and the benzenoid (A_{1480}) absorption bands; this has proven that it is directly correlated with the logarithm of electrical conductivity ($\log\sigma$) of the polymer [36, 37].

5.3 Electrochemical Stability of the Synthesized Films

The electrochemical stability of the films is measured by cyclic voltammetry in blank solution (i.e., a solution containing only solvent and electrolyte), with repetitive scans in various potential regions. The position of the reduction/oxidation (i.e., de-doping/re-doping) peaks and the total charge per cycle are determined, and the stability is estimated using the CV of the first cycle as reference. In the case of the thiophene copolymers synthesized by electropolymerization, the stability was determined in the regions from -2 up to $+2$ V and from 0 up to $+2$ V. Even though the stability depends on the potential region of the measurements, the copolymers exhibited remarkable stability, with at least one case of a film being electrochemically stable even after more than 250 consecutive scans. By comparison, in thiophene homopolymers (which are also considered quite stable electrochemical materials) the electrochemical stability of the films did not surpass 35 consecutive potential scans [36, 37]. In the literature, there are not many investigations of the electrochemical stability of similar materials; however, the stability of copolymer films synthesized by electropolymerization of 3MTh with 3-octylthiophene onto ITO electrodes using potentiostatic conditions has been reported and it is considerably smaller [39]. Even though they are not directly related, the electrochemical stability and the stability under operational conditions of a film (i.e., inside an OPV) are indirectly connected. Due to the solar trajectory, OPV function resembles more or less a cycle (going from no photocurrent during night to peaked photocurrent during day and back again). These operational characteristics bear a strong

resemblance to the cycling of the potential during the electrochemical stability measurements. Thus, it seems that the thiophene copolymer films synthesized by electropolymerization might be expected to be quite stable as an HTL layer inside an OPV.

5.4 Thermal Stability

The thermal stability of the copolymers was investigated with thermogravimetric analysis (TGA). The copolymers synthesized by electropolymerization start to decompose at about 100 °C and have about 50 % total weight loss when pyrolyzed up to 1,000 °C. Their weight loss behavior is similar to that of polythiophene homopolymers. The onset of the weight loss at 100 °C can be probably attributed to the decomposition of the BF_4^- counterions; the polymer backbone per se is almost certainly more stable, since it contains a fully aromatic structure, and that can be justified from the relatively high char residue at 1,000 °C. Using the results of the thermal stability analysis it was derived that the copolymers have a macromolecular structure containing distributed monomeric units of biphenyl and thiophene [36].

5.5 Application of the Thiophene Electropolymerized Copolymers as HTL in BHJ Solar Cells

One of the biggest advantages of the electropolymerized copolymer films based on thiophene derivatives is their exceptional stability in ambient conditions: indeed, they did not seem to be affected by the oxygen in the atmosphere even after prolonged storage time, and their conductivity did not drop. Even though the study for the application of the electropolymerized copolymers has only recently started, the first results of their OPVs are quite encouraging. Up to now, only a few films deposited onto ITO electrodes have been used in OPVs, using P3HT:PCBM as an active layer. Films were deposited by repetitive scans in the potential region from +1 up to +2 V. These films had pale blue color and exhibit improved transmittance at higher wavelengths, making them potentially interesting candidates for use with low-bandgap polymers [41]. The first film had a thickness of only 1.2 μm , which was not enough to work as an HTL (the cell was partially short-circuited). The second film, with a thickness of 2.5 μm , afforded a workable OPV, even though the performance was low. However, the performance of the OPVs should be improved; this can be achieved by optimizing the properties of the electropolymerized films and especially their thickness, conductivity, and transmittance. Nevertheless, their high stability indicates that their OPVs will also be very stable [37, 40].

6 Conclusions

The HTL used in multilayer OPVs, either FHJ or BHJ architectures, is one of the crucial components for improving the efficiency of the device. In order for a material to be applied as HTL, it has to cover a strict set of requirements. The current material of choice is the PEDOT:PSS which has many advantages but also some important shortcomings. Electropolymerization as a method can afford films with designed properties (e.g., specific electronic structure). The films synthesized by copolymerization of thiophene by cyclic voltammetry could be a good alternative HTL; however a lot of work is necessary in order to achieve the conditions that will afford the optimum results.

References

1. Nelson, J.: *The Physics of Solar Cells*. Imperial College Press, London (2003)
2. Po, R., Carbonera, C., Bernardi, A., Tinti, F., Camaioni, N.: Polymer- and carbon-based electrodes for polymer solar cells: toward low-cost, continuous fabrication over large area. *Sol. Energ. Mater. Sol. Cell.* **100**, 97–114 (2012)
3. von Hauff, E.: The role of molecular structure and conformation in polymer electronics. *Semiconduct. Semimet.* **85**, 231–260 (2011)
4. Olson, D.C., Ginley, D.S.: Nanostructured TCOs (ZnO, TiO₂, and beyond). In: Ginley, D.S. (ed.) *Handbook of Transparent Conductors*. Springer, New York, NY (2010)
5. Li, C., Liu, M., Pschirer, N.G., Baumgarten, M., Muellen, K.: Polyphenylene-based materials for organic photovoltaics. *Chem. Rev.* **110**, 6817–6855 (2010)
6. Kymissis, I.: *Organic Field Effect Transistors Theory, Fabrication and Characterization*. Springer, New York, NY (2009)
7. Moliton, A., Hiorns, R.C.: Review of electronic and optical properties of semiconducting π -conjugated polymers: applications in optoelectronics. *Polymer. Int.* **53**, 1397–1412 (2004)
8. Snedden, E.W., Monkman, A.P., Dias, F.B.: Photophysics of charge generation in organic photovoltaic materials: kinetic studies of geminate and free polarons in a model donor/acceptor system. *J. Phys. Chem. C* **116**, 86–97 (2012)
9. Bredas, J.L., Norton, J.E., Cornil, J., Coropceanu, V.: Molecular understanding of organic solar cells: the challenges. *Acc. Chem. Res.* **42**, 1691–1699 (2009)
10. Hardin, B.E., Hoke, E.T., Armstrong, P.B., Yum, J.-H., Comte, P., Torres, T., Frechet, J.M.J., Nazeeruddin, M.K., Gratzel, M., McGehee, M.D.: Increased light harvesting in dye-sensitized solar cells with energy relay dyes. *Nat. Photon.* **3**, 406–411 (2009)
11. Facchetti, A.: π -Conjugated polymers for organic electronics and photovoltaic cell applications. *Chem. Mater.* **23**, 733–758 (2011)
12. Tress, W., Leo, K., Riede, M.: Influence of hole-transport layers and donor materials on open-circuit voltage and shape of I–V curves of organic solar cells. *Adv. Funct. Mater.* **21**, 2140–2149 (2011)
13. Yu, G., Gao, J., Hummelen, J.C., Wudl, F., Heeger, A.J.: Polymer photovoltaic cells: enhanced efficiencies via a network of internal donor–acceptor heterojunctions. *Science* **270**, 1789–1791 (1995)
14. Simitzis, J., Triantou, D., Soulis, S.: Synthesis and characterization of electrically conducting copolymers based on benzene and biphenyl. *J. Appl. Polym. Sci.* **110**, 356–367 (2008)
15. Simitzis, J., Soulis, S., Triantou, D.: Benzene as a precursor for conducting polymers. In: Tranfo, G. (ed.) *Benzene and Its Derivatives*. Nova, New York, NY (2012)

16. Kymakis, E., Stylianakis, M.M., Spyropoulos, G.D., Stratakis, E., Koudoumas, E., Fotakis, C.: Spin coated carbon nanotubes as the hole transport layer in organic photovoltaics. *Sol. Energ. Mater. Sol. Cell.* **96**, 298–301 (2012)
17. Tang, H., Zhou, Z., Zhong, Y., Liao, H., Zhu, L.: Electropolymerization of 3-methylthiophene in the presence of a small amount of bithiophene and its usage as hole transport layer in organic light emitting diodes. *Thin Solid Films* **515**, 2447–2451 (2006)
18. Mutaguchi, D., Okumoto, K., Ohsedo, Y., Moriwaki, K., Shirota, Y.: Development of a new class of hole-transporting and emitting vinyl polymers and their application in organic electroluminescent devices. *Org. Electron.* **4**, 49–59 (2003)
19. Park, J.H., Lee, T.W., Chin, B.D., Wang, D.H., Park, O.O.: Roles of interlayers in efficient organic photovoltaic devices. *Macromol. Rapid Comm.* **31**, 2095–2108 (2010)
20. Niu, Y.H., Liu, M.S., Ka, J.W., Bardeker, J., Zin, M.T., Schofield, R., Chi, Y., Jen, A.K.Y.: Crosslinkable hole-transport layer on conducting polymer for high-efficiency white polymer light-emitting diodes. *Adv. Mater.* **19**, 300–304 (2007)
21. Groenendaal, L.B., Jonas, F., Freitag, D., Pielartzik, H., Reynolds, J.R.: Poly(3,4-ethylenedioxythiophene) and its derivatives: past, present, and future. *Adv. Mater.* **12**, 481–494 (2000)
22. Lenz, A., Kariis, H., Pohl, A., Persson, P., Ojamäe, L.: The electronic structure and reflectivity of PEDOT:PSS from density functional theory. *Chem. Phys.* **384**, 44–51 (2011)
23. Saito, Y., Kitamura, T., Wada, Y., Yanagida, S.: Poly(3,4-ethylenedioxythiophene) as a hole conductor in solid state dye sensitized solar cells. *Synth. Met.* **131**, 185–187 (2002)
24. Kettle, J., Waters, H., Horie, M., Chang, S.W.: Effect of hole transporting layers on the performance of PCPDTBT:PCBM organic solar cells. *J. Phys. D Appl. Phys.* **45**, 125102 (2012)
25. Bailo, D., Generosi, A., Rossi Albertini, V., Caminiti, R., De Bettignies, R., Paci, B.: Time-resolved morphological study of 'PEDOT:PSS' hole transporting layer for polymer solar cells. *Synth. Met.* **162**, 808–812 (2012)
26. Ecker, B., Nolasco, J.C., Pallarés, J., Marsal, L.F., Posdorfer, J., Parisi, J., von Hauff, E.: Degradation effects related to the hole transport layer in organic solar cells. *Adv. Funct. Mater.* **21**, 2705–2711 (2011)
27. Voroshazi, E., Verreet, B., Buri, A., Müller, R., Di Nuzzo, D., Heremans, P.: Influence of cathode oxidation via the hole extraction layer in polymer:fullerene solar cells. *Org. Electron.* **12**, 736–744 (2011)
28. Jørgensen, M., Norrman, K., Krebs, F.C.: Stability/degradation of polymer solar cells. *Sol. Energ. Mater. Sol. Cell.* **92**, 686–714 (2008)
29. Lee, S.T., Gao, Z.Q., Hung, L.S.: Metal diffusion from electrodes in organic light-emitting diodes. *Appl. Phys. Lett.* **75**, 1404–1406 (1999)
30. Steirer, K.X., Chesin, J.P., Widjonarko, N.E., Berry, J.J., Miedaner, A., Ginley, D.S., Olson, D. C.: Solution deposited NiO thin-films as hole transport layers in organic photovoltaics. *Org. Electron.* **11**, 1414–1418 (2010)
31. Olson, D.C., Piris, J., Collins, R.T., Shaheen, S.E., Ginley, D.S.: Hybrid photovoltaic devices of polymer and ZnO nanofiber composites. *Thin Solid Films* **496**, 26–29 (2006)
32. Chen, Z., Fang, J., Gao, F., Brenner, T.J.K., Banger, K.K., Wang, X., Huck, W.T.S., Sirringhaus, H.: Enhanced charge transport by incorporating additional thiophene units in the poly(fluorene-thienyl-benzothiadiazole) polymer. *Org. Electron.* **12**, 461–471 (2011)
33. Grimsdale, A.C., Müllen, K.: Polyphenylene-type emissive materials: poly(para-phenylene)s, polyfluorenes, and ladder polymers. *Adv. Polymer Sci.* **199**, 1–82 (2006)
34. Roncali, J.: Conjugated poly(thiophenes): synthesis, functionalization, and applications. *Chem. Rev.* **92**, 711–738 (1992)
35. Inzelt, G.: *Conducting Polymers*. Springer, Berlin (2008)
36. Simitzis, J., Triantou, D., Soulis, S.: Synthesis and characterization of electrically conducting copolymers based on biphenyl and thiophene. *J. Appl. Polym. Sci.* **118**, 1494–1506 (2010)

37. Triantou, D., Soulis, S., Koureli, S., De Sio, A., von Hauff, E.: Thiophene-based copolymers synthesized by electropolymerization for application as hole transport layer in organic solar cells. *J. Appl. Polym. Sci.* **127**, 585–592 (2013)
38. Marken, F., Neudeck, A., Bond, A.M.: Cyclic voltammetry. In: Scholz, F. (ed.) *Electroanalytical Methods*, 2nd edn. Springer, Berlin (2010)
39. Lemma, T., Yohannes, T.: Poly(3-methylthiophene-co-3-octylthiophene) based solid-state photoelectrochemical device. *J. Braz. Chem. Soc.* **18**, 818–823 (2007)
40. Triantou, D., Soulis, S., De Sio, A., von Hauff, E.: Polymer:fullerene solar cells prepared with electropolymerised doped copolymers, 4th International Symposium on Flexible Organic Electronics, ISFOE 2011, 10–13 July 2011, Thessaloniki, Greece, P51.
41. Zhu, Z., Waller, D., Gaudiana, R., Morana, M., Muehlbacher, D., Scharber, M., Brabec, C.: Panchromatic conjugated polymers containing alternating donor/acceptor units for photovoltaic applications. *Macromolecules* **40**, 1981–1986 (2007)

Chapter 8

Molecular Engineering of Efficient Dyes for p-Type Semiconductor Sensitization

Fabrice Odobel, Yann Pellegrin, Frédéric B. Anne, and Denis Jacquemin

Abstract Dye-sensitized solar cells (DSCs) based on p-type semiconductors such as nickel oxide have attracted considerable attention during the past 5 years. In this chapter, we focus on the progress related to improving p-DSC efficiency with the sensitizer. First, we summarize the specificities of p-DSC relative to conventional Grätzel cells, and then we establish the requirements for an efficient sensitizer. Second, we review all the results on published dyes and discuss the strategy for improvements. The molecular design principles of the dyes are also presented in order to pave the way and stimulate new directions.

1 Introduction

Inspired by the famous French philosopher André Malraux, one can be tempted to say that the twenty-first century will be solar, or it will not be. The mindless consumption of fossil or nuclear-based fuels has dragged the world into pollution, while exhaustion of the carbon-based resources would hurl the world economy into an unprecedented energy crisis. Solar-based energy appears as a providential candidate for the replacement of the carbon economy, being a clean, virtually inexhaustible on the scale of mankind, abundant, and rather uniformly distributed

F. Odobel (✉) • Y. Pellegrin • F.B. Anne
CEISAM, CNRS, UMR 6230, Université de Nantes, 2 rue de la Houssinière,
44322 Nantes Cedex 3, France
e-mail: Fabrice.Odobel@univ-nantes.fr; Yann.Pellegrin@univ-nantes.fr;
Frederic.Anne@univ-nantes.fr

D. Jacquemin
CEISAM, CNRS, UMR 6230, Université de Nantes, 2 rue de la Houssinière,
44322 Nantes Cedex 3, France

Institut Universitaire de France, 103 blvd St Michel, 75005, Paris Cedex 5, France
e-mail: Denis.Jacquemin@univ-nantes.fr

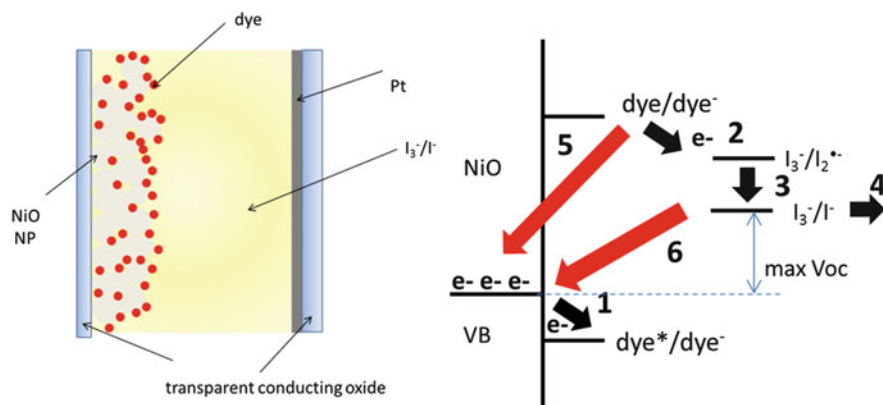


Fig. 8.1 Schematic representation of a p-DSC (*left*) and its operation principle (*right*). The *red arrows* indicate the recombination reactions

source of energy [1, 2]. In this context, dye-sensitized solar cells (DSCs) are cheap photovoltaic devices, which are capable of transforming solar light into electrical work. While photoelectrochemical devices based on the sensitization of n-type semiconductors (n-SCs), commonly referred as Grätzel cells [3, 4], have long dominated the world of DSCs, considerable attention is now given to alternative and complementary systems, which are based on the sensitization of wide-bandgap p-type semiconductors (p-SCs) [5, 6]. The operation principle of the latter is grounded in the light-triggered hole injection from a chemisorbed dye into the valence band of a wide-bandgap semiconductor, most often nickel oxide (NiO) (Fig. 8.1). This is precisely the opposite operation mechanism of conventional Grätzel cells. These new photoelectrodes represent valuable systems for solar energy conversion as they can be used first as an intrinsic solar cell technology, like Grätzel cells. Second, they can be associated with a TiO₂-based photoanode to build a tandem DSC, whose photoconversion efficiency (PCE) can go much beyond 15 % [7–10]. Indeed, tandem DSCs are probably the most potent opportunity to make DSCs an even greater attractive technology because they may offer high PCE while still remaining cheap to manufacture. In DSC tandem cell, the delicate recombination layer is not needed, which is often a cornerstone of many tandem cell optimization. Second, the fabrication of the whole system obeys the same low-cost manufacturing process as a conventional n-DSC because the photocathode (sensitized p-SC) relies exactly on the same procedure and the entire process is compatible with roll-to-roll manufacturing technology. Another possible utilization of a sensitized p-SC concerns the field of artificial photosynthesis, because the photocathode is a source of reducing equivalents, which can be subsequently used to activate small molecules, such as water or carbon dioxide, into energy-rich substances such as hydrogen or organic molecules. There have been two recent successful applications of photocathodes for the fabrication of dye-sensitized photoelectrosynthetic cell for water splitting [11, 12]. Although the performances

are still low, they give a real proof of concept of the feasibility of such endeavor. The first report on p-DSC appeared in 1999 by Lindquist and co-workers [13], another paper was then published by the same team next year [7], and there remains an induction period of about 5 years before the groups of Odobel in France and Hammarström in Sweden got involved in this burgeoning field [14, 15]. At that time, the exact operation principle was not fully demonstrated while it was claimed that the sensitizer excited state may be first oxidatively quenched by triiodide before injecting a hole in the SC [13, 16]. Today, the well-accepted mechanism of positive charge carrier photogeneration in p-DSCs is the following: upon photoexcitation of the sensitizer, its electronic excited state injects a hole in the valence band of the p-SC leading to the reduced sensitizer (reaction 1, Fig. 8.1) [6]. The hole diffuses into the network of sintered nanoparticles until it reaches the transparent conducting substrate and is collected into the external electrical circuit. Meanwhile, the sensitizer can be regenerated into its electronic ground state by reduction of the redox mediator, which is, most of the time, the triiodide/iodide shuttle (reaction 2, Fig. 8.1). Triiodide is reduced into iodine radical anion ($e^- + I_3^- \rightarrow I_2^{\cdot-} + I^-$) and dismutates into iodide ($I_2^{\cdot-} + e^- \rightarrow 2I^-$) before transporting the charges to the counter electrode to which it is oxidized back to triiodide, completing thus the circuit [17–19]. At this stage, it is important to note that this two-step reduction mechanism with triiodide/iodide redox shuttle entails a significant drop of the V_{oc} as the redox potential of $I_3^-/I_2^{\cdot-}$ is about 360 mV more negative than that of I_3^-/I^- (see below). Accordingly, there is a major dye regeneration energy loss, meaning that this electrolyte is far from being optimized as electron-transporting system for p-DSCs. In p-DSCs, there are two major sources of losses which are the recombination of the injected hole with the reduced sensitizer (reaction 5, Fig. 8.1) and with the electrolyte (reaction 6, Fig. 8.1) [5].

The sensitizer is responsible for light harvesting and charge generation at the photocathode; therefore it is a fundamental component of the cell efficiency. Because the field has not been yet explored by many teams to date, few sensitizers were investigated in NiO-based DSCs implying that there is a lot of room for new and exciting discoveries. In this chapter we review all the progresses made for the development of sensitizers for p-SCs and discuss the strategies for improving the performances of p-DSCs.

2 Specificities of p-DSCs

There are some obvious similarities between n-DSCs and p-DSCs, but there are also some fundamental differences making this vein of research a specific field by itself. Among the similarities, we can mention that the dye must exhibit the largest possible spectral overlap with the sun spectrum in order to harvest the maximum of the incoming solar energy. In other words, a good sensitizer must be panchromatic. The photostability is also an important requirement to sustain a long cell lifespan as it should support billions of photoexcitations without degradation for

10-year-long utilization. The chemical stability of the reduced dye is another criterion to guarantee a slow ageing of the cell upon light soaking as the dye will make many cycles between $S + h\nu \rightarrow S^* \rightarrow S^- \rightarrow S$. Avoiding dye aggregation and subsequent excited-state quenching is also essential to limit energy losses. Each peculiar aspect of p-DSCs is presented below, and we discuss how it affects the dye designing. The specific features of p-DSC dyes are as follows: (1) the excited state of the sensitizer needs to exhibit an oxidizing power to inject a hole into the valence band of the p-SC; conversely, sensitizers for TiO_2 are strong reducers in the excited state to donate an electron into the conduction band of the n-SC; (2) to diminish the unusually fast geminate charge recombination between the reduced dye and the injected hole in p-SC [14, 15, 18, 20, 21]; (3) to prevent the large interfacial current losses by recombination of the reduced form of the electrolyte and the holes in the p-SC nanoparticles [22]; (4) be functionalized by specific anchoring groups optimized to establish a strong linkage and a large electronic coupling with the p-SC [23]. All these discrepancies force the chemist to think differently when he or she aims at designing sensitizers for p-SCs. The general ideas exposed above are illustrated with examples in the second section of this chapter dealing with the sensitizers.

2.1 Thermodynamic Considerations for an Efficient p-DSC Dye

The hole injection and dye regeneration driving forces represent essential primary considerations for the choice of the sensitizer. Indeed, if the Gibbs free energy of these two reactions is lower than 0.2–0.3 eV, the probability of charge transfer between the semiconductor and the sensitizer is relatively modest, compromising thus a high PCE. Based on the redox potential, essentially the reduction potential of the dye ($E_{\text{Red}}(S/S^-)$), the adiabatic energy of the excited state ($E_{00}(S^*)$), and the position of the valence band edge of the p-SC ($E_{\text{VB}}(\text{p-SC})$), it is quite straightforward to determine the thermodynamic feasibility of these two reactions. The hole injection (ΔG_{inj}) and dye regeneration (ΔG_{reg}) Gibbs free energies can be estimated from the equations below:

$$\Delta G_{\text{inj}} = e[E_{\text{VB}}(\text{p-SC}) - (E_{00}(S^*) + E(S/S^-))] \quad (8.1)$$

$$\Delta G_{\text{reg}} = e[E(M/M^-) - E(S/S^-)] \quad (8.2)$$

where e is the elementary charge. Please note that these equations are only approximations as the Coulombic interactions between the charges are neglected. This electrostatic term depends on the distance between the interacting charges and on the solvent polarity. Finally, the semiconductor permittivity can also play an important role as it controls the degree of the electrostatic interaction between the hole and the electron on the sensitizer. For example, the permittivity of NiO is

relatively low ($\epsilon_r = 9.7$) [22], and therefore the ion pair is certainly significantly bound and needs extra energy to be dissociated as observed in organic photovoltaic cells. For NiO, which is the most used semiconductor in p-DSC, the valence band edge lies at 0.54 V [13] vs. normal hydrogen electrode (NHE), meaning that this material is a potentially good electron donor to many dyes. Accordingly, the criterion of significant Gibbs free energy for hole injection is easy to be met with a great collection of sensitizers. Conversely, the reduction of triiodide, which is the most commonly used redox shuttle, can represent a rate-determining process. It is well known that the triiodide/iodide couple displays a complex electrochemistry involving the exchange of several electrons [17]. As stated above, a close look at this regeneration reaction shows that the oxidation of the reduced sensitizer involves the couple $I_3^-/I_2^{\cdot-}$ and not I_3^-/I^- . The consequence is severe as $I_3^-/I_2^{\cdot-}$ exhibits a more negative potential ($E^\circ(I_3^-/I_2^{\cdot-}) = -0.08$ V vs. NHE) than I_3^-/I^- ($E^\circ(I_3^-/I^-) = 0.354$ V vs. NHE) indicating that the sensitizer must feature a much more negative reduction potential than what could be expected by considering I_3^-/I^- instead of $I_3^-/I_2^{\cdot-}$ ($\Delta E \approx 360$ mV in CH_3CN) [19].

2.2 The Low Photovoltage in Most p-DSCs

Another important difference between conventional Grätzel cells and p-DSCs is the generally low V_{oc} generated by the latter [5, 6]. From the thermodynamic point of view, the maximum open-circuit voltage ($V_{OC,max}$) delivered by a p-DSC cell is given by

$$V_{OC,max} = E(M/M^-) - E_{VB}(p-SC) \quad (8.3)$$

Using NiO as p-SC and the triiodide/iodide redox couple, the maximum achievable V_{oc} is around 150 mV. This represents a real handicap to reach high PCE. Although the V_{oc} is weakly dependent on the nature of the sensitizer, one can envision that the most efficient p-SCs will not rely on NiO but new p-SCs exhibiting deeper valence band potentials, and therefore will require sensitizers exhibiting higher oxidizing potential in the excited state than those required with NiO.

2.3 Anchoring Groups Specific to p-SCs

To efficiently inject charges in the semiconductor the dye must be firmly linked to the nanoparticle surface. As a result, the presence of an anchoring group on the sensitizer is mandatory. However, the optimal anchoring group for p-DSC may not be the same as that for TiO_2 . First because p-SCs are usually oxides based on soft metals such as Cu(I) and Ni(II). According to the Pearson acid–base concept, soft Lewis bases will be more favorable to establish strong bonds with soft Lewis acids. Even more important, it should be noted that a fast hole injection rate depends

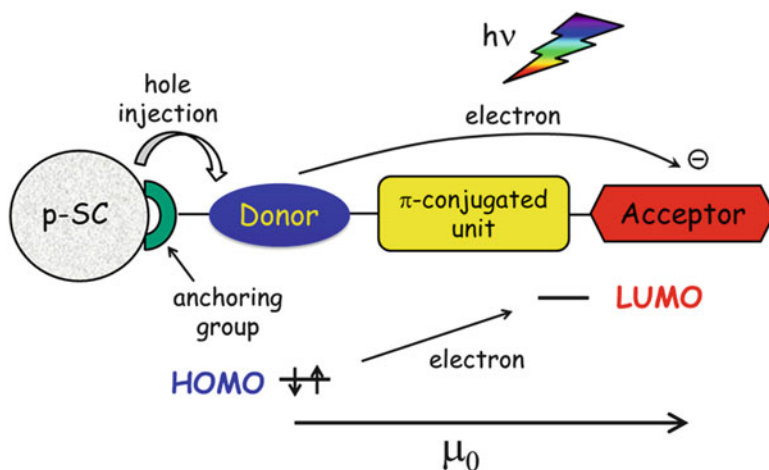


Fig. 8.2 Schematic structure of an optimized push-pull sensitizer for p-type semiconductor

on the electronic coupling of the dye to the metal oxide valence band states. Most studies on interfacial electron transfer with TiO_2 have shown that electron injection directly proceeds through the anchoring group [4]. The magnitude of this coupling is primarily determined by the spatial overlap between the HOMO orbital of the dye excited state and the donor valence band orbitals on the p-SC. Carboxylic acid, which is rather an electron-withdrawing group, favors electron injection in TiO_2 because it ensures that the LUMO orbital of the dye is partly localized upon the unit closest to the metal oxide surface, thereby promoting the electronic interactions with the conduction band. With a p-type SC the largest electronic coupling will be therefore obtained with electron-rich anchoring groups carrying a significant density of the HOMO orbital that will mix with the valence band wave function. Moreover, in the case of push-pull dyes, which represent a particularly efficient class of sensitizers [24], the charge transfer excited state must be vectorialized in the right direction, that is, the electron density should shift from the anchoring group to the other end of the molecule upon photon absorption (Fig. 8.2). Also the dipole moment of the dye should ideally be oriented in the direction opposite to the surface in order to bend the VB away from the vacuum level and enhance the V_{oc} . This is exactly the reverse molecular design from the one sought for TiO_2 sensitizers.

2.4 The Geminate Charge Recombination in p-DSC

A striking difference of p-type-sensitized semiconductor with classical n-type counterparts (TiO_2 or ZnO) is the extraordinary fast charge recombination between the injected hole and the reduced sensitizer. There have been several convincing

demonstrations of this quite general behavior with different classes of sensitizers on NiO-based photocathodes [14, 15, 18, 20, 21]. In p-DSCs, the dyes which lead to a slow geminate charge recombination are rather exceptions than generality. The reason for this peculiar behavior is not fully understood yet, but some explanations were put forward. First, charge recombination was shown to be located in the normal Marcus region owing to the participation of intra-bandgap states [25]. These states decrease the charge recombination Gibbs free energy and mediate the charge transfer. Second, as already mentioned above, the low permittivity of NiO makes the ion pair strongly bound preventing its dissociation, which is necessary for the charges to be collected into the external electrical circuit. One effective strategy to retard geminate recombination is to increase the separation distance between the electron (on the sensitizer) and the hole (in NiO) owing to the exponential decrease of the charge recombination rate with the distance [26, 27]. Therefore, by placing an electron-withdrawing group or a secondary electron acceptor at the extremity of the dye, the electron density can be shifted far away from the NiO surface which slows down the rate of the charge recombination. This is in line with the optimal molecular design illustrated in Fig. 8.2 and also promotes hole injection. The fast geminate recombination represents an important specificity of p-DSC which requires an appropriate molecular engineering to develop efficient dyes. Compared to TiO₂, the best performing sensitizers of NiO are usually more complex structures because they require more demanding and careful optimization.

2.5 Charge Recombination Between the Electrolyte and the Holes in the p-SC Nanoparticles

The important interfacial charge recombination between the photoinjected holes into NiO and the redox couple in the electrolyte is one of the major hurdles that need to be taken into account when designing dyes for p-DSC. These recombination reactions can be decreased by the interposition of an intermediate Al₂O₃ layer on the surface of the p-SC that passivates the latter [28, 29]. Another strategy is to introduce long alkyl chains on the sensitizer that will spread on the p-SC surface and create a barrier to prevent the approach of the redox shuttle close to the p-SC surface [10]. Sensitizers forming a closely packed monolayer on the p-SC surface can also physically block the access of the redox shuttle. Subtle molecular designs, which are sometimes difficult to anticipate, can induce such favorable organizations that have a deep impact on the overall photovoltaic performances of the dye.

3 Sensitizers Tested on NiO-Based DSCs

In this section, all the sensitizers tested so far (to the best of our knowledge) in p-DSCs are reviewed. This part is organized as follows. First the intrinsic sensitizers, namely, extended π -conjugated systems, are presented, and then push-pull organic dyes exhibiting charge transfer bands will be reviewed. The famous ruthenium polypyridine derivatives were naturally also investigated in p-DSCs, and some yield rather promising results. This section will logically end with the most efficient systems based on dyad-type dyes consisting of a dye linked to an electron acceptor, which is generally a naphthalene diimide (NDI) or perylene monoimide (PMI) moiety. The promising recent results obtained with p-SC sensitized with quantum dots will be surveyed, and finally the photovoltaic performances of all the dyes are summarized in Table 8.1.

3.1 Porphyrine and Erythrosine Sensitizers

To the best of our knowledge, the very first example of DSC with nanocrystalline NiO electrode dates back from 1999 and was given by He et al. [13]. They coated a NiO electrode with **Erythrosin** or tetrakis(4-carboxyphenyl)porphyrin (**TPPC**, see Fig. 8.3). With the former (latter) compound they measured a V_{oc} of 98.5 (82.7) mV and a J_{sc} of 0.079 (0.232) mA/cm². These values correspond to very small conversion efficiencies (<0.01 %, see Table 8.1), but this work stands as the proof of concept of p-DSC. Already in that seminal study, the authors pointed out the crucial need of optimizing the redox couple to improve the energetic performances of these cells. The **Erythrosin** photocathode was used the following year to build a tandem cell [7]. In 2005, two groups revived the interest in NiO-based p-SC: on the one hand, Hammarström, Odobel, and co-workers evaluated the performances of a phosphorous porphyrin, **PhosPorph** [14], and, on the other hand, Dalchiele's group compared the performances of **Eosin** and **Erythrosin** [30]. In the first work, a V_{oc} smaller than 100 mV was measured with a maximal IPCE of 2.5 % obtained at 446 nm that is at the position of the intense Soret absorption band of the **PhosPorph**. These limited performances, despite a large LHE in the Soret region, were rationalized for the first time by the rapid recombination between the electron located on the reduced dye and the hole in the surface. Indeed, in [14], the authors reported that, whilst the hole injection is extremely fast (2–20 ps), 80 % of the reactants are regenerated by recombination after 1 ns [14]. This difference between p-DSCs and n-DSCs was therefore demonstrated relatively early. The second investigation was mostly focused on morphological and optical characterizations of the photocathodes, but the authors demonstrated that the sensitization with **Eosin** and **Erythrosin**, respectively, increased the photocurrent by 60 and 200 % with respect to the bare NiO electrode [30]. The same two dyes were further tested by Bach and co-workers in 2008, who also investigated two rhodamines [31].

Table 8.1 Photovoltaic performances of all the sensitizers tested on p-type semiconductor and recorded under simulated AM 1.5 (1,000 W/m²)

Dyes	Electrolyte	J_{sc} (mA/cm ²)	V_{oc} (mV)	ff (%)	η (%)	Max. IPCE (%)	References
Erythrosin B	I ₃ ⁻ /I ⁻	0.23	83	27	0.0076	n.r.	[13]
TPPC	^a I ₃ ⁻ /I ⁻	0.08	99	29	0.0033	n.r.	[13]
PhosPorph	I ₃ ⁻ /I ⁻	n.r.	<100	n.r.	n.r.	2.5	[14]
Erythrosin J	I ₃ ⁻ /I ⁻	0.0008	n.r.	n.r.	n.r.	n.r.	[30]
Erythrosin J	I ₃ ⁻ /I ⁻	0.36	122	26	0.011		[31]
Eosin B	I ₃ ⁻ /I ⁻	0.0004	n.r.	n.r.	n.r.	n.r.	[30]
Eosin B	I ₃ ⁻ /I ⁻	0.14	77	29	0.0032		[31]
Rhodamine 101	I ₃ ⁻ /I ⁻	0.12	69	21	0.0022		[31]
Rhodamine 110	I ₃ ⁻ /I ⁻	0.15	80	25	0.0031		[31]
PI6	^a I ₃ ⁻ /I ⁻	0.94	70	33	0.02	5	[32]
PI3	^a I ₃ ⁻ /I ⁻	1.07	80	33	0.03	5	[32]
PI12	^a I ₃ ⁻ /I ⁻	1.41	85	30	0.04	14	[32]
PI7	^a I ₃ ⁻ /I ⁻	0.54	75	33	0.01	3	[32]
PI18	^a I ₃ ⁻ /I ⁻	1.41	70	33	0.03	23	[32]
PI19	^a I ₃ ⁻ /I ⁻	1.42	85	34	0.04	22	[32]
PDI1	I ₃ ⁻ /I ⁻	0.607	73	34	0.0153	n.r.	[35]
PDI2	I ₃ ⁻ /I ⁻	0.587	73	35	0.0147	n.r.	[35]
WS PDI	I ₃ ⁻ /I ⁻	0.025	77	24	0.00047	n.r.	[36]
NK-2684	I ₃ ⁻ /I ⁻	1.00	93	30	0.027	n.r.	[8]
NK-2684	I ₃ ⁻ /I ⁻	1.30	123	34	0.055	n.r.	[38]
NK-2612	I ₃ ⁻ /I ⁻	0.45	73	40	0.013	n.r.	[38]
NK-2612	I ₃ ⁻ /I ⁻	0.43	77	34	0.011	n.r.	[38]
FCF	I ₃ ⁻ /I ⁻	1.44	93	43	0.043	n.r.	[38]
C343	I ₃ ⁻ /I ⁻	0.55	98	29	0.016	n.r.	[31]
C343	I ₃ ⁻ /I ⁻	0.86	101	36	0.031	n.r.	[38]
C343	I ₃ ⁻ /I ⁻	1.89	71	39	0.05	n.r.	[40]
NKX-2311	I ₃ ⁻ /I ⁻	0.66	100	34	0.022	n.r.	[38]
P1	I ₃ ⁻ /I ⁻	5.48	84	33	0.15	63	[21]
P1	I ₃ ⁻ /I ⁻	2.51	110	29	0.08	35	[41]
P1	I ₃ ⁻ /I ⁻	3.01	106	37	0.12	38	[15]
P1	I ₃ ⁻ /I ⁻	5.48	84	34	0.15	64	[15, 21]
P1	I ₃ ⁻ /I ⁻	1.52	110	31	0.05	18	[42]
P1	I ₃ ⁻ /I ⁻	2.64	104	27	0.075	29	[43]
P1	I ₃ ⁻ /I ⁻	2.31	132	33	0.101	~23	[44]
P1	I ₃ ⁻ /I ⁻	2.88	140	33	0.133	~36	[47]
P2	I ₃ ⁻ /I ⁻	3.37	63	31	0.07	32	[21]
P3	I ₃ ⁻ /I ⁻	1.36	55	34	0.03	6	[21]
P4	I ₃ ⁻ /I ⁻	2.48	100	26	0.09	44	[41]
P7	I ₃ ⁻ /I ⁻	3.37	80	35	0.09	26	[21]
T1	I ₃ ⁻ /I ⁻	3.27	122	28	0.113	32	[43]
T2	I ₃ ⁻ /I ⁻	2.53	94	27	0.065	21	[43]
S1	I ₃ ⁻ /I ⁻	105	1.59	36	0.060	n.r.	[44]
S2	I ₃ ⁻ /I ⁻	115	1.39	36	0.058	n.r.	[44]
S3	I ₃ ⁻ /I ⁻	113	1.38	34	0.053	n.r.	[44]
S4	I ₃ ⁻ /I ⁻	125	2.25	33	0.093	28	[44]

(continued)

Table 8.1 (continued)

Dyes	Electrolyte	J_{sc} (mA/cm ²)	V_{oc} (mV)	ff (%)	η (%)	Max. IPCE (%)	References
S4	I ₃ ⁻ /I ⁻	94	1.43	37	0.050	12	[59]
S5	I ₃ ⁻ /I ⁻	122	2.18	35	0.092	n.r.	[44, 45]
S6	I ₃ ⁻ /I ⁻	131	2.05	32	0.087	n.r.	[44, 45]
O6	I ₃ ⁻ /I ⁻	97	1.04	37	0.037	14	[59]
O7	I ₃ ⁻ /I ⁻	90	1.74	38	0.060	18	[59]
p-SQ1	I ₃ ⁻ /I ⁻	117	1.22	37	0.053	~33	[47]
P-SQ2	I ₃ ⁻ /I ⁻	140	1.92	42	0.113	~18	[47]
N719	I ₃ ⁻ /I ⁻	0.008	4	0.5	~0	n.r.	[31]
Ru1	I ₃ ⁻ /I ⁻	0.25	75	34	0.0065	n.r.	[23]
Ru2	I ₃ ⁻ /I ⁻	0.78	95	34	0.025	n.r.	[23]
Ru3	I ₃ ⁻ /I ⁻	0.65	85	32	0.018	n.r.	[23]
Ru4	I ₃ ⁻ /I ⁻	0.63	85	34	0.019	n.r.	[23]
Ru5	I ₃ ⁻ /I ⁻	0.09	110	43	0.004	n.r.	[23]
Ru5	^b Co ^{III} /Co ^{II}	0.04	15	21	Ca. 0	n.r.	
O8	I ₃ ⁻ /I ⁻	0.44	63	36	0.009	2.02	[49]
O11	I ₃ ⁻ /I ⁻	1.16	79	36	0.033	5.49	[49]
O12	I ₃ ⁻ /I ⁻	1.84	82	34	0.051	9.08	[49]
Ru-NMI	I ₃ ⁻ /I ⁻	0.16	95	36	0.006	n.r.	[48]
Ru-NMI	^b Co ^{III} /Co ^{II}	0.28	195	34	0.020	n.r.	[48]
PMI-NDI	I ₃ ⁻ /I ⁻	1.76	120	34.5	0.073	32	[33]
PMI-NDI	^b Co ^{III} /Co ^{II}	1.2	285	41	0.141	28	[33]
PMI-PhNDI	I ₃ ⁻ /I ⁻	1.64	130	34.6	0.074	31	[33]
PMI-PhNDI	^b Co ^{III} /Co ^{II}	0.78	210	29.3	0.048	15	[33]
PMI-PhC60	I ₃ ⁻ /I ⁻	1.88	95	32.4	0.058	43	[33]
PMI-PhC60	^b Co ^{III} /Co ^{II}	0.58	180	38.8	0.040	23	[33]
PI18	I ₃ ⁻ /I ⁻	1.42	100	30.3	0.043	26	[33]
PI19	I ₃ ⁻ /I ⁻	1.32	110	31.6	0.046	26	[33]
Thioph2-PMI	I ₃ ⁻ /I ⁻	2.06	153	29	0.09	n.r.	[10]
Thioph2-PMI	I ₃ ⁻ /I ⁻	1.77	146	30	0.08	n.r.	[54]
Thioph'2-PMI	I ₃ ⁻ /I ⁻	1.06	122	29	0.04	n.r.	[54]
e-Thioph2-PMI	I ₃ ⁻ /I ⁻	2.24	147	30	0.10	n.r.	[54]
e-Thioph'2-PMI	I ₃ ⁻ /I ⁻	1.23	136	28	0.05	n.r.	[54]
Thioph4-PMI	I ₃ ⁻ /I ⁻	3.40	176	32	0.19	n.r.	[10]
Thioph6-PMI	I ₃ ⁻ /I ⁻	5.35	218	35	0.41	62	[10]
Thioph6-PMI	I ₃ ⁻ /I ⁻	1.32	305	34	0.14	12	[53]
Thioph6-PMI	I ₃ ⁻ /I ⁻	3.30	292	41	0.40	n.r.	[56]
Thioph6-PMI	I ₃ ⁻ /I ⁻	5.11	294	41	0.61	~50	[55]
Thioph6-PMI	^c Co ^{III} /Co ^{II}	4.44	709	42	1.30	n.r.	[57]

^aIn CH₃CN. n.r. = not reported

^bCo^{III}/Co^{II} corresponds to tris(4,4'-di-*tert*-butyl-2,2'-dipyridyl) cobalt complex with the ratio Co^{III}/Co^{II} = 0.1 M/0.1 M

^cCo^{III}/Co^{II} corresponds to tris(ethylenediamine) cobalt complex with the ratio Co^{III}/Co^{II} = 0.07 M/0.3 M

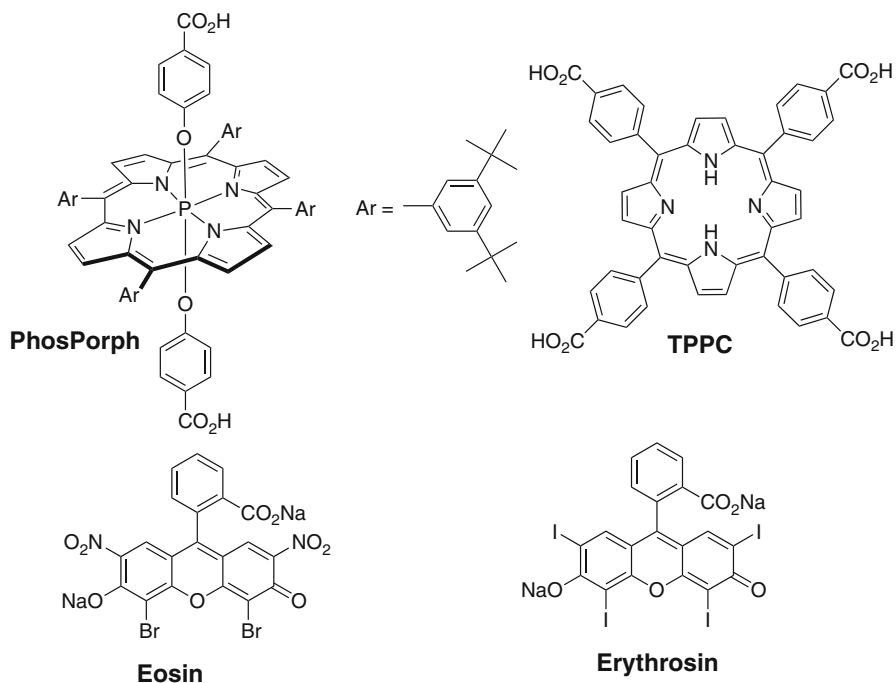


Fig. 8.3 Representation of the first (historical) intrinsic sensitizers used in p-SC [7, 13, 14, 30]

The performances of **Rhodamine-101** and **Rhodamine-110** are relatively alike (V_{oc} of 69 and 80 mV, respectively, J_{sc} of 0.12 and 0.15 mA/cm², and overall efficiencies not exceeding the one of **Eosin**). We underline that the absorption bands of all these dyes correspond to valence transitions of moderate intensities that do not imply any significant charge transfer nor strong variation of the dipole moment. Therefore, besides the abovementioned typical limitations of p-DSCs, the performances of these *classical* sensitizers are expected to be rather weak.

3.2 Perylene Imide Sensitizers

Perylene imide derivatives are famous dyes known for their strong absorptivity and extraordinary high photostability. Moreover, the bisimide electron-withdrawing units render this class of dyes a good electron acceptor and therefore a strong oxidant in the excited state. These two properties make them particularly well suited for being used as sensitizers in p-DSCs. Another advantage of perylene imide dyes is the characteristic spectroscopic signature of the reduced dye which cannot be confused with the singlet or the triplet excited state [34]. This feature enabled the group of Hammarström to evidence without any ambiguity the ultrafast

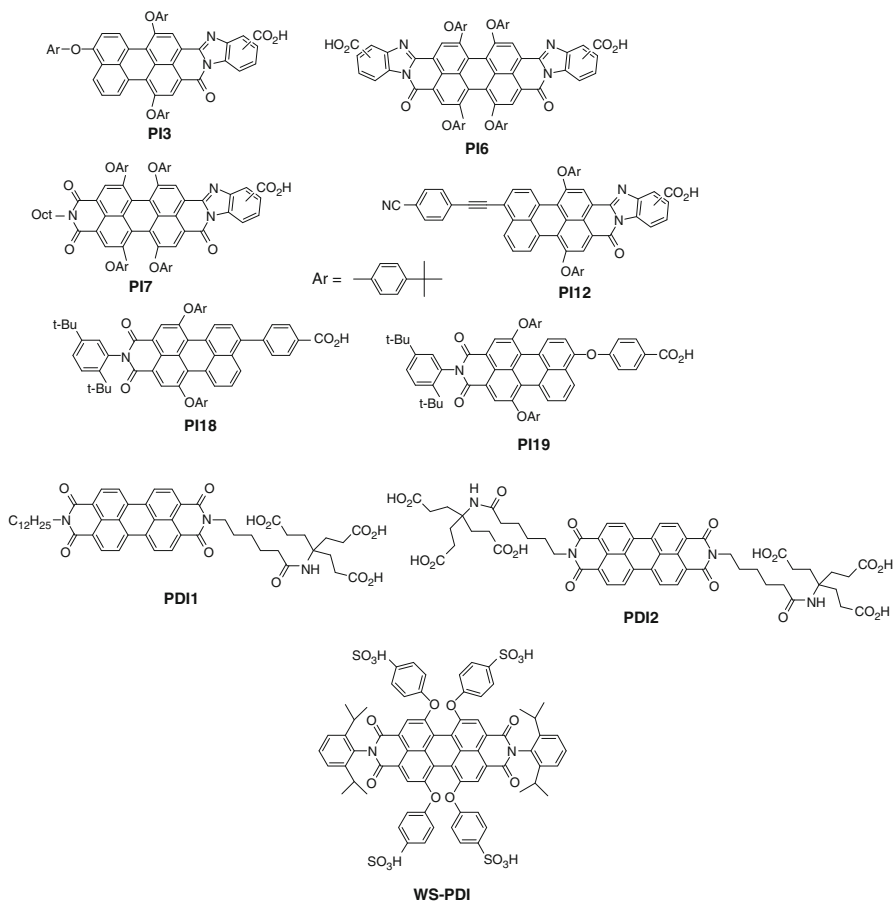


Fig. 8.4 Perylene imide sensitizers and related dyes [25, 32, 33]

formation of the reduced perylene imide **PI19⁻** and to prove that hole photo-injection is the main pathway for electricity production with this type of system (Fig. 8.4) [20]. The group of Odobel synthesized a series of differently substituted perylene imides, which essentially differ by both their reduction potentials and the position of their main absorption band (Fig. 8.4) [25, 32]. In this series of **PI3–PI19** dyes, the reduction potential of the dye ($E_{\text{REd}}(S/S^-)$) becomes more positive as the energy gap decreases meaning that the LUMO level is lowered with the bandgap. As a consequence, the reducing power of the reduced dye becomes weaker as the maximum absorbance wavelength is red-shifted. For all the dyes, a photophysical study by transient absorption spectroscopy showed that all the dyes inject holes with high rates (time constant less than 5 ps) but the charge recombination is fast as well (sub ns). The fluorescence lifetime of all these dyes being in the range of 4–5 ns, the injection quantum yield is therefore close to unity for all dyes. However,

the photovoltaic performances significantly differ within this series and they are strongly correlated with the reduction potential of the dye. The more negative the reduction potentials, the higher the PCE and the IPCE are. Accordingly, it was shown that the PCE is controlled by the Gibbs free enthalpy of the regeneration reaction. Indeed, as stated above, the reoxidation of the reduced dye involves the redox couple $I_3^-/I_2^{\cdot-}$ that presents a more negative redox potential than that of I_3^-/I^- . With perylene imides **PI6** and **PI7** the driving force is insufficient to insure a fast regeneration rate. This is all the more blatant that the recombination reaction is a very fast process that outcompetes the regeneration reaction. Within this series of dyes the maximum photovoltaic performances were measured with dyes **PI12** and **PI17–PI18**, which give PCE around 0.03–0.04 % (Table 8.1). One important lesson from this study is that when iodide/triiodide electrolyte is used, it is essential that the reduction potential of the dye must be sufficiently negative ($E_{\text{Red}}(S/S^-) < -1$ V vs. SCE) to promote an effective charge regeneration quantum yield. However, this limitation can be certainly circumvented with alternative electrolytes such as one-electron outer sphere redox couples. Another important finding of this study is that the triiodide anion actively participates in electricity production in the 380–400 nm region owing to its photodecomposition into $I_2^{\cdot-}$ which is a strong oxidant and can pull an electron from NiO valence band and form I^- . Moreover, the efficiency of this side reaction is dependent on the solvent because the potential of the $I_2^{\cdot-}/I^-$ couple decreases with the solvent polarity. For instance, whilst the photoactivity of $I_2^{\cdot-}$ towards electricity production is significant in acetonitrile (IPCE max around 25 %), it is decreased in propylene carbonate (IPCE max around 10 %).

More recently, Guldi and co-workers [35] investigated dendronized perylene diimide (**PDI1** and **PDI2** in Fig. 8.4). These two dyes are anchored on NiO via fully electronically decoupled multi-carboxylic acid arms suggesting weak electronic coupling with the semiconductor. The authors clearly detected the formation of aggregates both in solution and on NiO surface, which is the consequence of the strong tendency of these planar aromatic systems to form π – π interactions. The photovoltaic performances are quite similar and relatively modest for both dyes (PCE around 0.015 %) because they are certainly limited by the aggregation which induces excited-state quenching and competes with hole injection. Majima and co-workers [36] investigated the interfacial charge transfer dynamic of a water-soluble perylene diimide sensitizer (**WS-PDI**) bearing four sulfonic acid anchors by single-molecule fluorescence and transient absorption spectroscopy on bare NiO nanoparticle film and NiO coated with an overlayer of Al_2O_3 of a few angstroms. It was clearly observed that the Al_2O_3 overlayer improves both V_{oc} and J_{sc} because it diminishes charge recombination reactions. However, if the Al_2O_3 layer is too thick, the hole injection becomes sluggish and the photovoltaic performances decrease. The photovoltaic properties of **WS-PDI** were not the main focus of this study but they were nevertheless measured. They proved to be quite feeble, most certainly because of the very thin thickness of NiO film (60 nm), which precludes to achieve high absorbance of the photocathode and therefore limits the photocurrent. Overall, these studies showed that perylene imide dyes are attractive sensitizers for

p-SC because they already yield interesting performances. However, the published systems are probably not optimized yet, and new structures with higher performances are to come soon.

3.3 Cyanine Sensitizers

Cyanines are one of the most important classes of organic dyes, as they are stable organic structures presenting an extremely intense hallmark absorption whose position is principally controlled by the number of carbon atoms of the conjugation path [39]. Both the HOMO and LUMO are typically fully delocalized on the entire molecule, and cyanines are therefore not undergoing charge-transfer transitions. Several cyanine derivatives have been tested in p-DSC mainly by Suzuki's group (Fig. 8.5) [8, 37, 38]. In 2005, they reported the preparation of a tandem cell with high open-circuit voltage ($V_{oc} = 918$ mV) [8]. In that device, **NK-2684** was used to coat the photocathode. For the photocathode alone (i.e., without its n-DSC counterpart), they measured an open-circuit voltage of 93 mV and a short-circuit current of 1.00 mA/cm², the largest values at that time. In the tandem cell, built with this photocathode, they were able to increase the V_{oc} with respect to the n-type cell though this feat was at the price of a smaller current. In 2008, the same group synthesized via a polymer templating method p-DSC relying on the same **NK-2684 dye** [37]. They used this cyanine as a reference to examine cell properties obtained with various concentrations of tribloc copolymers (PEO-PPO-PEO). They reported value of IPCE in the 25–50 % range depending on the selected macromolecule, the best features being obtained with large PEO/PPO ratio [37]. A few months later, the same group performed a complementary investigation where three cyanines and one carbonium dye have been selected to fabricate p-type DSCs [38]: **NK-2684**, **NK-3628**, **NK-2612**, as well as **FCF** (Fig. 8.5). They have, respectively, obtained V_{oc} of 123, 77, 73, and 93 mV and J_{sc} of 1.30, 0.43, 0.45, and 1.44 mA/cm², corresponding to PCE of 0.055, 0.011, 0.013, and 0.043 % (Table 8.1). The two cyanines with the smallest efficiencies, **NK-3628** and **NK-2612**, present quite extended π delocalization paths and absorb light at very large wavelengths (752 and 786 nm, respectively), which implies relatively high (low) HOMO (LUMO) levels. Therefore, the driving force is probably too small to allow efficient hole injection. As I^- can act as an acceptor for the injected holes and obviously reduce the J_{sc} , the performance of **FCF**-based p-DSC was investigated using a large panel of I_2 and I^- concentrations by Mori and co-workers [38] (see also coumarins below). By increasing the amount of I_3^- in the electrolyte composition, significant improvements of the IPCE were, as expected, monitored in the iodine absorption region (350–450 nm), whereas smaller variations have been found in the region of the dye (ca. 600 nm), further confirming that the hole injection is an extremely fast process [38].

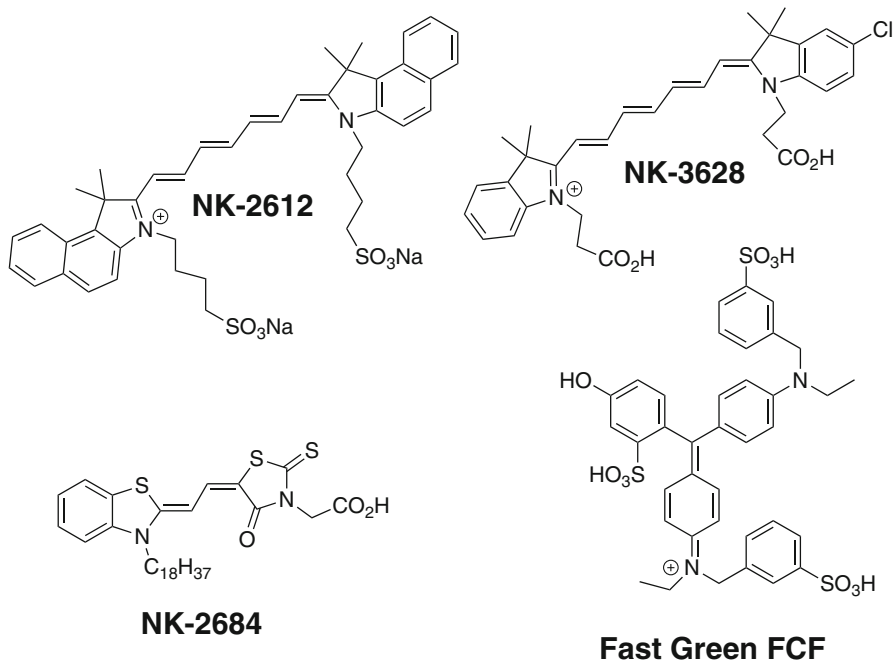
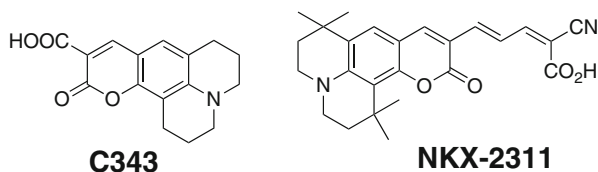


Fig. 8.5 Cyanine-like sensitizers [8, 37, 38]

Fig. 8.6 Coumarins used in p-DSC [15, 31, 38]



3.4 Coumarin Sensitizers

The first push-pull dyes used in p-DSCs were the coumarins with the 2008 studies of Bach and co-workers for **C343** [31] and of Mori et al. for both **C343** and **NKX-2311** (Fig. 8.6) [38], although photocathode sensitized with **C343** was studied previously [15]. **C343** is a well-known reference dye for Grätzel DSSC as it implies a significant intramolecular charge transfer. However, **C343** is not optimized for p-DSCs as theoretical calculations have demonstrated that the LUMO is located on the carboxylic group close to the surface whereas the HOMO is delocalized on the entire molecular skeleton [38]. Nevertheless, both groups of researchers reported non-trifling open-circuit voltage (ca. 100 mV) and current (0.86 mA/cm² in [8]) yielding rather important efficiencies, up to 0.031 % (see Table 8.1), a result that can even be further improved (see below) [40]. This was interpreted as the result

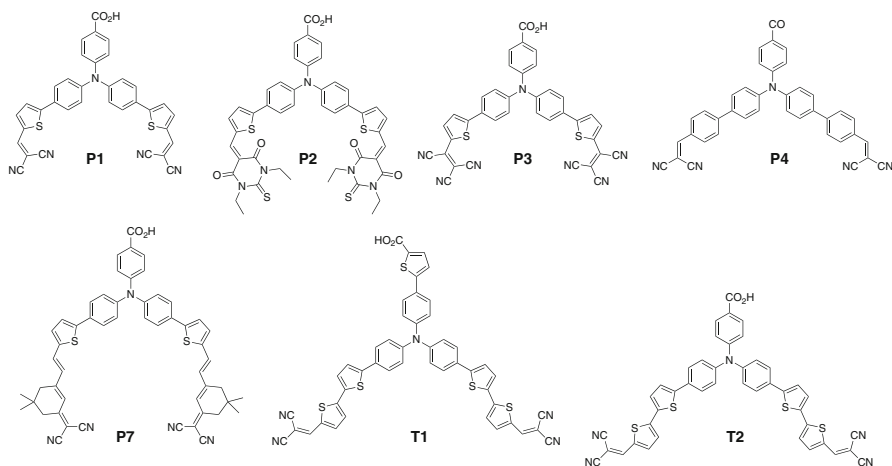


Fig. 8.7 Trisphenylamine-based dyes presenting two electron-withdrawing arms [21, 40–42]

of, on the one hand, the large oxidizing driving force of **C343** (its HOMO lies downhill to the valence band of NiO) and, on the other hand, the fact that the HOMO is fully delocalized on the dye, allowing a partial mixing with the bands of the surface despite the inadequate charge-transfer vectorialization. It is also noticeable that the injection of the holes into the semiconductor is the main deactivation path (ca. 200 fs) of **C343** [15]. For **C343**, an investigation of the impact of the composition of the electrolyte was performed as well. Keeping constant the concentration of I^- (0.5 M in the form of LiI), three concentrations of I_2 have been used: 0.05, 0.5, and 2 M [31]. This strongly impacted the measured photovoltaic data: the V_{oc} decreased steadily with increasing concentration (98, 65, and 37 mV for the three concentrations, respectively), whereas concomitantly the obtained J_{sc} strongly increased (0.55, 1.11, and 2.13 mA/cm^2 , respectively) [31]. Overall, these two variations nearly compensate each other, and the measured light-to-electricity conversion efficiency remained rather constant, peaking for the 0.5 M I_2 concentration. Interestingly, for **NKX-2311** that presents a larger CT, the performances are smaller (0.022 %) than for **C343** [38], but of course, in that case, the driving force is also smaller than for **C343**.

3.5 Trisphenylamine Push–Pull-Based Sensitizers

In 2008, Sun, Hagfeldt, and co-workers proposed the first organic push–pull dye with a charge-transfer direction specially designed to maximize the photovoltaic performances in p-DSC (**P1** in Fig. 8.7) [42]. In this compound, the donor moiety, a triphenylamine bearing a carboxylic anchoring group on one arm is located close to the surface, whereas the four strongly accepting cyano groups are located at the

opposite sides, allowing the captured electron to be held far from the NiO surface. The adequacy of this molecular design was confirmed by time-dependent density functional theory (TD-DFT) calculations relying on the B3LYP hybrid exchange correlation functional that demonstrated that the intense visible absorption (at 468 nm) implies an electronic promotion from the HOMO (delocalized on the full molecule including the anchoring moiety) to the LUMO mainly centered on the electron acceptors and vicinal conjugated rings [42]. In addition, measurements allowed to confirm that the HOMO lies significantly below (ca. 0.8 eV) the top valence band of NiO, while the LUMO is significantly above (ca. 1.2 eV) the potential of the iodine redox couple, allowing to have a large driving force for all charge-transfer processes. The first measured IPCE of **P1** was 18 % [42], amongst the best of that time (2008). **P1** gave a large V_{oc} of 110 mV in the line with the one obtained with traditional push-pull dyes such as **C343** (see above) but a much larger short-circuit current which resulted in an overall efficiency of 0.05 %, a significant success for a *simple* (non-dyadic) dye. When the quality of the mesoporous NiO film was improved, the performances were steadily increased both in 2009 [41] and 2010 [21, 40]. Indeed, in their first work, Sun and co-workers used a NiO layer thickness of only 0.6 μm , but they expected that thicker films would improve the efficiency of the cell [42]. In 2009, they roughly doubled the thickness of the film and optimized the composition of electrolyte as well. Indeed, they increased the concentration of the I^- from 0.5 to 1 M (so they used a 1 M LiI/0.1 M I_2 mixture) and replaced propylene carbonate by acetonitrile, which allowed to take advantage of the larger diffusion coefficient of iodine in the latter and hence to promote a more effective dye regeneration. With these modifications, the IPCE of **P1** was doubled (35 %) [41] and the V_{oc} remained constant (that is 110 mV), but the photocurrent was increased by almost a factor of two (to reach $J_{sc} = 2.51 \text{ mA/cm}^2$), yielding an impressive 0.08 % PCE. In the same study [41], they also synthesized and characterized the new dye **P4**. In this latter push-pull compound, the two thiophene rings have been replaced by phenyl groups. Unsurprisingly, TD-DFT calculations indicated that **P4** undergoes an intramolecular charge-transfer transition upon photon absorption with relatively similar absorption wavelength as that of **P1**. For **P4**, Sun and co-workers obtained an IPCE of 44 % exceeding the one of **P1**. Two hypotheses were proposed to explain this outcome: a larger inter-ring twisting between the phenyl rings or a stronger preassociation with iodine allowed a slower recombination with the holes injected in the semiconductor. In this 2009 study, **P4** consequently slightly outperformed **P1** due to an improved fill factor of 36 % instead of 29 %. Indeed the V_{oc} of 100 mV and J_{sc} of 2.48 mA/cm^2 of **P4** are comparable to those of **P1**. The performances of **P1** were further optimized in 2010 by engineering the photocathode that was assembled in two steps [21, 40]. This yielded, for **P1** (**P4** was not tested), a 64 % IPCE and a very large short-circuit current of 5.48 mA/cm^2 [21, 40]. This improvement of a factor of three with respect to their seminal investigation highlights that large conversion efficiencies are not only dye dependent but are also strongly related to the fabrication process of the solar cell. Indeed, with their latest developments, Sun and co-workers obtained a conversion of 0.05 % with the non-optimal **C343** dye, a

rather competitive value despite the inadequate CT direction in that coumarin [40]. In their latter study [21], Sun and co-workers compared the performances of four dyes differing by their accepting groups (**P1**, **P2**, **P3**, and **P7**, Fig. 8.7). The V_{oc} ranked **P1** > **P7** > **P2** > **P3** (84 > 80 > 63 > 55 mV), whereas the J_{sc} were ordered **P1** > **P7** = **P2** > **P3** (5.48 > 3.37 mA/cm² = 3.37 > 1.36 mA/cm²), and the best efficiency was reached with **P1** (0.15 %) whereas the worse was reached with **P3** (0.03 %, see Table 8.1 for more details). Femtosecond transient absorption spectroscopy revealed an extremely fast and efficient hole injection in NiO for both **P1** and **P3**. Indeed, while the excited state of these dyes possesses a rather short lifetime (ca. 30 ps), the injection was even faster. The poor solar cell performances of the latter dye were therefore correlated with the aggregation of the dye in the NiO film and the too weak driving forces for injection and regeneration reactions. Indeed the LUMO of **P3** was found to be too stabilized (−0.46 V vs. NHE compared to −0.93 V for **P1**) and hence closer to the potential of the I_3^-/I_2^- redox couple. On the contrary, they demonstrated that the fast regeneration of **P1** could be understood by a preassociation of I_3^- with the dye. In summary, these investigations of **Px** and **Tx** demonstrated that designing specific push–pull dyes for p-DSC provided much better performances but that a fine balance should be found between the intensities of the charge-transfer bands and the regeneration driving forces [21].

In 2012, Zhu et al. proposed further modifications of Sun's dyes by (1) introducing an additional thienyl moiety on the anchoring side (**T1** in Fig. 8.6) and (2) replacing the thiophene bearing the dicyanovinyl moieties of **P1** by bithiophene (**T2** in Fig. 8.7) [43]. The absorptions of **T1** (488 nm) and **T2** (485 nm) present a small bathochromic shift compared to **P1** (464 nm) but are significantly more intense. Concomitantly, the LUMO level of **T1** and **T2** are therefore slightly stabilized compared to **P1**, but the effect is much smaller than with **P3**, therefore not significantly impeding the regeneration process. Additionally, the excited-state lifetime of the two new dyes (3.17 ns for **T1** and 2.91 ns for **T2**) is larger than for the **P1** counterpart (2.66 ns). For **T1**, the authors reported an IPCE of 32 % at 480 nm, exceeding both the corresponding values for **T2** (21 %) and **P1** (29 %). Consistently, **T1** presented the largest V_{oc} (122 mV) and J_{sc} (of 3.27 mA/cm²) which can be compared to 94 mV and 2.53 mA/cm² for **T2** and 104 mV and 2.53 mA/cm² for **P1**. Therefore **T1** gave the best conversion efficiency (0.113 %, improving the **P1** result by ca. 50 % in the experimental setup of [43]). Using impedance measurements Zhu et al. demonstrated that this performance can be partly ascribed, not only to the long lifetimes of the excited state but also to the larger energetic barrier for recombinations between the holes in the valence band and the I^- in **T1** than in other dyes. The authors logically concluded that increasing the conjugation length between the anchoring group and the donor is beneficial, whereas longer donor/acceptor separations are detrimental.

An obvious complement to the “double-acceptors” discussed above are trisphenylamines where only one of the two arms bears an electron-withdrawing group. These structures, proposed by Lin and co-workers [44, 45] and Wu and co-workers [46], are shown in Fig. 8.8 and can present one or two anchoring groups.

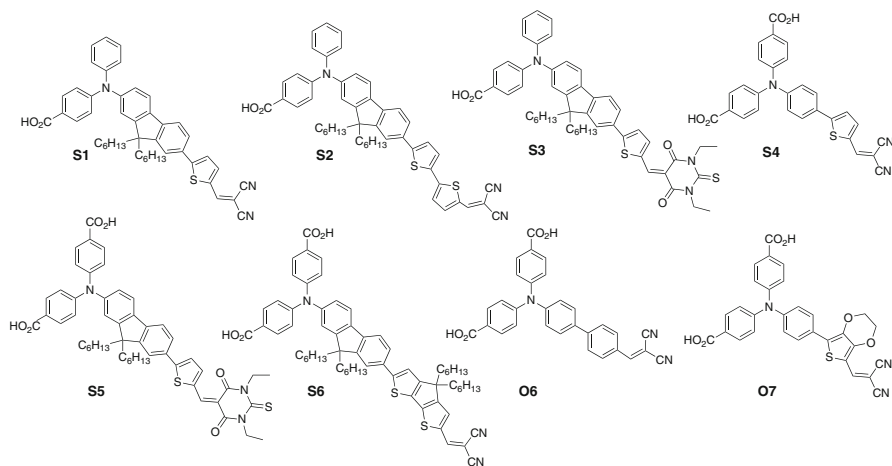


Fig. 8.8 Triphenylamine-based dyes with a single electron-accepting arm [44–46]

The most important finding of these studies is probably that the performances are significantly enhanced for the dyes presenting two carboxylic anchors. Indeed **S4–S6** outclass **S1–S3** (see Table 8.1). This is because the NiO surface is apparently more passivated by the former compounds, which in turn enhances the hole lifetime in the semiconductor by impeding the possible recombination with the electron of the electrolyte. Indeed, the ranking of both the V_{oc} and J_{sc} of these six dyes cannot be understood from their spectral properties (almost independent of the presence of one or two carboxylic groups) nor from the oxidation potentials (**S4** has the largest and **S6** the smallest) nor the dye loading on the surface. In their subsequent 2012 investigation, they used dyes **S5** and **S6** [45]. In the latter contribution, they have studied the influence of both the preparation conditions and the particle size of the precursor of NiO. Using smaller particles, they could obtain a more compact film, allowing an improved hole mobility due to better connections between the particles. This allowed increasing the short-circuit current by ca. 2 mA/cm^2 , underlining that a careful preparation of the photocathodes is mandatory to obtain efficient p-DSCs [45].

In a latter investigation, Ju et al. compared **S4** to two new dyes for which only the linker has been modified (**O6** and **O7**) [46]. They found that the EDOT structure, **O7**, was the most effective (see Table 8.1). Interestingly the LHE of **O7** and **S4** are very similar, the excited-state lifetimes are the smallest for **O7**, and the surface coverage is actually the largest with **S4**. The unexpected performances of **O7** can therefore be partly ascribed to a larger regeneration driving force, the LUMO of **O7** lying 0.06 eV (0.22 eV) above the one of **S4** (**O6**) and to the significantly improved IPCE.

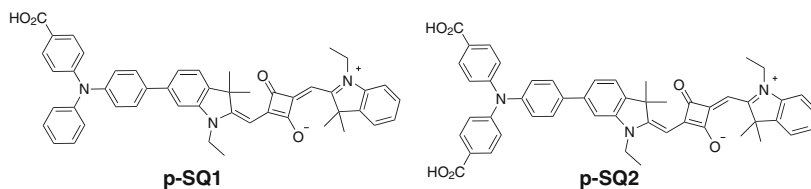


Fig. 8.9 Squaraine-arylamine dyes of Lin and co-workers [47]

In summary, these investigations of **Pn** and **Tn** demonstrated that designing specific push–pull dyes for p-DSC provided much better performances but that a fine balance should be found between the intensities of the charge-transfer bands and regeneration driving forces.

3.6 Squaraine Sensitizers

In 2012, Lin et al. have synthesized two other dyes presenting a triphenylamine donor bearing one or two anchoring groups but where the traditional acceptor has been replaced by squaraine: **p-SQ1** and **p-SQ2** (Fig. 8.9) [47]. Squaraines are very photostable dyes that present excited-state properties similar to those of the cyanines that display a very intense and tight near-IR absorption band and a low-lying LUMO. Nevertheless, the LUMO of both **p-SQ1** and **p-SQ2** remained significantly above the one of the iodine redox couple here, so they do not suffer a significant lack of driving force, as in **P3** (see above). With the dyes **p-SQ1** and **p-SQ2**, Lin and co-workers obtained a V_{oc} similar to the **P1** reference but a smaller photocurrent, leading to efficiencies of 0.053 and 0.113 % for **p-SQ1** and **p-SQ2**, respectively. The better performances of the structure presenting two anchoring groups were explained by, on the one hand, the larger dye loading on the surface (almost twice for the second dye) and, on the other hand, the suppression of the dark current. This clearly parallels the conclusions obtained for the dyes in Fig. 8.8 (see above). Because **p-SQ2** and **P1** have complementary absorption bands, Lin et al. co-sensitized photocathodes with a mixture of these two dyes at different ratios. This strategy did not lead to any significant improvement compared to **P1** in terms of efficiency despite the expected improvement of the IPCE. The most effective ratio seems to be a 4/6: **P1/p-SQ2**.

3.7 Ruthenium Complexes

Ruthenium complexes are particularly well suited for almost any kind of light-triggered electron transfer-based device [50, 51]. This is due to several built-in relevant features. First, they exhibit a broad, intense absorption in the visible part

of the solar spectrum. Second, the corresponding electronic transition is a metal-to-ligand charge transfer, i.e., an electron is formally transferred from the ruthenium-centered d orbitals towards vacant ligand-centered π^* orbitals upon photoexcitation. The corresponding relaxed excited state is a triplet, endowed with a long lifetime (ca. μs). Third, these complexes are synthetically versatile: an impressive collection of ruthenium–polypyridine complexes can be found in the literature and most importantly with a broad range of physical and chemical properties tunable *via* rational chemical engineering. Additionally, ruthenium complexes present the rare ability to behave as both good photo-reductants and good photo-oxidants. For all these reasons, it is no surprise if these molecular systems are closely associated to the birth of high-efficiency Grätzel-type DSCs in the early 1990s [3]. Part of this success relies on the remarkable photochemical properties of the interface TiO_2/Ru –polypyridine complexes.

Historically, the first ever ruthenium complex to have been tested in a p-DSC is the famous **N719** dye [31]. Intensely colored NiO photocathodes were obtained, but extremely weak performances were measured. As a matter of fact, a “blocking effect” was experienced, i.e., the p-DSC performed better when the p-SC was bare (the photovoltaic device is operated by direct bandgap excitation) rather than dyed with **N719** [31]. The latter has been specially designed for n-DSC and favors as such electron injection into the conduction band of an n-type semiconductor, thanks to electron vectorialization. In other words, **N719** is inadequate for hole injection (see Table 8.1), and in order to design efficient ruthenium-based sensitizers for pDSC, it is therefore mandatory to pay special attention to *hole vectorialization*, supporting *hole injection* into the valence band of a p-SC. This issue was addressed in two different ways with ruthenium complexes: (1) by analyzing the nature of the anchoring group allowing the chemisorption of the dye onto the semiconducting material and the tuning of the electronic communication between them and (2) by adjusting the energy levels of the anchoring ligand. In all cases, mesoporous NiO electrodes were used as photocathodes in the p-DSC setup.

In the first place, a series of ruthenium complexes, **Ru1**, **Ru2**, **Ru3**, and **Ru4**, bearing various anchoring groups has been designed (Fig. 8.10) [23]. The aim was to fish out suitable anchoring functions, which would support interfacial photoinduced hole transfer. Each functional group was chosen with a view to enrich the electron density near the anchor and subsequently to delocalize the HOMO of the dye onto the latter to favor hole injection. Moreover, the LUMO would be delocalized on ancillary ligands, away from the surface of the p-SC. Three main targets were focused on, namely, carbodithioic acid (**Ru1**), methylenephosphonic acid (**Ru2**), and styryl-catechol (**Ru3**), and results were compared to the dicarboxylic acid bearing benchmark **Ru4**. Rather weak performances were obtained with the corresponding photocathodes, mainly because of a poor light harvesting efficiency. Nevertheless, an interesting trend in the anchor adequacy has been highlighted, thanks to a combination of surface coverage analyses and TD-DFT calculations. The latter revealed indeed that the HOMO was essentially metal centered for all complexes but **Ru3**. Combined to a rather high association constant

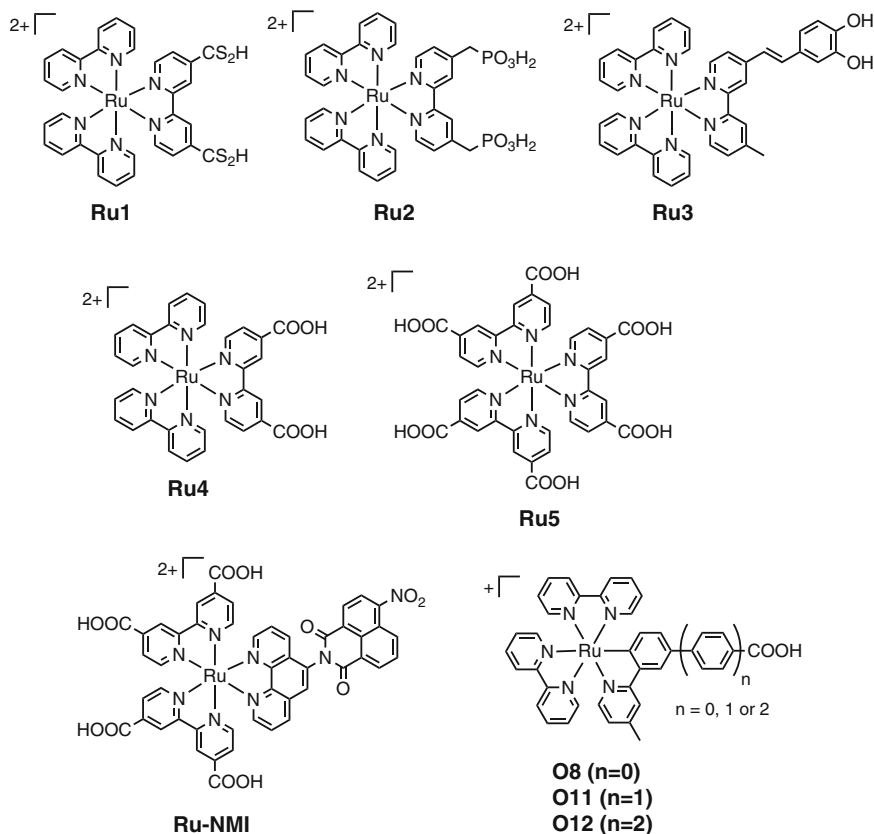


Fig. 8.10 Structures of the ruthenium complexes investigated in p-DSCs [23, 48, 49]

($4.9 \times 10^3 \text{ M}^{-1}$), the catechol function appeared as a relevant and promising anchor. However, the LUMO happened to be developed on the anchoring bpy ligand, thus favoring geminate charge recombination and leading to a weak overall photo-conversion efficiency. The same scenario is observed for **Ru1** and **Ru4** because of the strong π accepting nature of CO_2H and CS_2H . **Ru1** additionally displayed a weak affinity for the NiO surface entailing a really poor PCE. Finally, **Ru2** and **Ru4** feature a very high association constant with NiO (1.7×10^4 and $1.8 \times 10^5 \text{ M}^{-1}$, respectively), with subsequently high dye loading. This is the likely reason why **Ru4**, despite a non-optimal frontier orbital scheme, performed better than catechol-based **Ru3**. Finally, phosphonate linkers are well known to provide a very stable anchorage to the surface of oxide materials. In addition, the methylene spacer breaks the electronic communication between the phosphonic acid group PO_3H_2 and the bpy ligand, hence discouraging geminate charge recombination. This is probably why **Ru2** turned out to be the best dye among this series, thanks to a higher J_{sc} .

Further works to force the HOMO on the anchoring ligand of a ruthenium complex made use of carbometallated complexes with phenylpyridine ligands [49]. Indeed, it is reported that the HOMO of these organometallic entities is mostly delocalized over the metal center with very significant contribution from the carbanionic phenylpyridine ligands (**O8**, **O11**, and **O12** in Fig. 8.10). Moreover, the strong electron donating power of the latter entails a sizeable red shift of the absorption onset, and a better LHE is therefore provided. Additionally, **Ru5** bears a +1 charge, where all other complexes are 2+ cations; less inter dye Coulombic repulsion is expected for these systems, leading to a potentially higher surface coverage. Transient absorption spectroscopy revealed a ultrafast hole injection from the photoexcited chromophore into the valence band of NiO for **O8**, **O11**, and even **O12** despite the increasing distance between the Ru-bpy core and the semiconductor's surface [49]. However, geminate charge recombination proved to occur on a short time scale, below the diffusion time constant for redox mediators solubilized in the electrolyte and thus threatening the efficiency of dye regeneration. Interestingly though, as the size of the oligophenylene spacer increases (from zero to two phenyl groups), the lifetime of the interfacial charge-separated state clearly rises from a ps to a ns time scale, because the distance between the photogenerated charges is larger. As a result, the short-circuit current density steadily increased from **O8** to **O12**, reaching almost 2 mA/cm² with the latter, with a concomitant rise of the open circuit potential. The value of the latter remains low because of the inadequacy of the I₃⁻/I⁻-based electrolyte used in that work. However, the latter redox couple has one important advantage: it is believed to preassociate with the chemisorbed dye, therefore allowing the regeneration kinetics to compete with ultrafast geminate charge recombination.

Interestingly, ruthenium complexes behave in a very different manner on NiO than on TiO₂: although their excited state is in nature a charge-separated state, the exciton is unusually short lived, even if the hole transfer is properly vectorialized. A third approach was then investigated to increase the lifetime of the interfacial charge-separated state, with the ruthenium complex **Ru-NMI**: a Ru(dcbpyH₂)₂ core is covalently linked to a phen-nitronaphtalenemonoimide (phen-nitroNMI) moiety (Fig. 8.10) [48]. Although this system is not properly vectorialized, an ultrafast hole transfer from the Ru-bpy chromophore to the valence band of NiO is monitored, followed by a secondary electron shift from the photoreduced ruthenium-bpy core to the nitroNMI moiety. Overall the final charge-separated state features a huge lifetime of more than 10 μs, which is million times longer than any other interfacial charge-separated state ever measured for a ruthenium complex sensitizer (and most of the organic dyes studied so far). With the photogenerated electron driven farther away from the surface of NiO, the geminate charge recombination is efficiently suppressed. This entailed an improved PCE for **Ru-NMI** compared to model **Ru5**, especially when the Co^{III}/Co^{II} redox mediator was used instead of I₃⁻/I⁻. In the former case, preassociation of the cobalt complex with the anchored dyes is precluded because of the high steric hindrance. The regeneration reaction is therefore exclusively diffusion limited, and the charge recombination kinetics must be at least equal to k_{diff} . This condition is fulfilled with **Ru-NMI**,

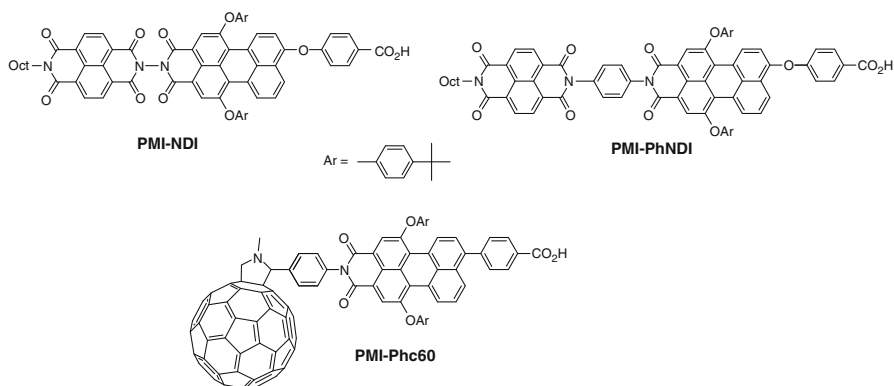


Fig. 8.11 Dyad systems developed by Odobel and co-workers [9, 20, 33]

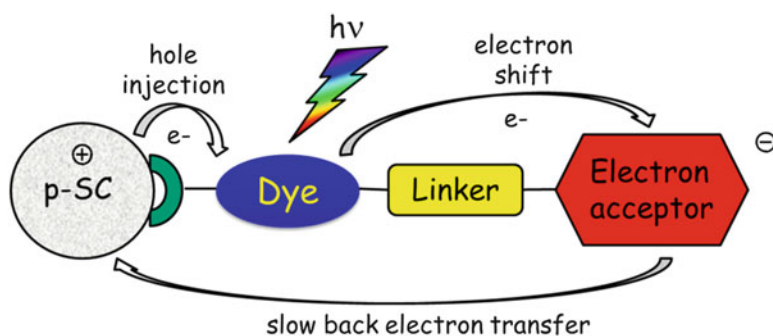


Fig. 8.12 Schematic structure of a sensitizer-donor system to attain a long-lived charge-separated state on p-SC

leading to decent PCE, thanks to a much enhanced output photo-potential of almost 200 mV. The reasons for such an improvement are grounded in the efficient suppression of dark current by using the bulky and slow $\text{Co}^{\text{III}}/\text{Co}^{\text{II}}$ electrolyte, and this will be more detailed below.

Ru5 is a puzzler, since it displays a very long interfacial charge-separated state lifetime, but does not work with a cobalt-based electrolyte. Coulombic repulsion between the redox mediator and the chemisorbed complex might be invoked to explain this experimental fact.

3.8 Dyads

As stated above, geminate charge recombination is one of the main deleterious processes which limit J_{sc} and V_{oc} in most p-DSCs (Fig. 8.11). To circumvent this fast recombination reaction, the group of Odobel proposed to design dyads composed of an effective sensitizer but connected to a secondary electron acceptor,

whose role is to pull away the electron far from the semiconductor surface (Figs. 8.11 and 8.12). This concept was tested with dyads such as **PMI-NDI**, **PMI-PhNDI**, and **PMI-PhC60**, and it proved to be particularly efficient as the charge-separated state lifetime was increased by a factor of 10^5 compared to the single-sensitizer PMI such as **PI18** or **PI19** (Fig. 8.4) [9, 20, 33]. As a result, the charge-separated state lifetime in these dyads lies in the microsecond time scale, which is the average value found in many simple sensitizers in TiO_2 -based DSCs.

It is important to underline that for a proper operation of these dyad systems, it is imperative that the electron shift reaction (from the reduced sensitizer to the electron acceptor) is very fast to compete with the recombination reaction (from the reduced sensitizer to the hole in NiO), which is generally very fast too in p-DSCs. This implies that the rate of this electron shift is finely optimized, and this can be done with a suitable linker having the optimal length, because the electronic coupling is a key parameter to control the rate of electron transfer [26]. This supplementary electron transfer step leads to a larger spatial separation of the electron and hole, which in turn yields a dramatic increase of the lifetime but at the expense of reducing power stored in the final charge-separated state. With the iodide/triiodide electrolyte, this can represent a drawback since this redox shuttle requires a particularly high reducing power to reduce I_3^- into I_2^- . This was confirmed with the dyads **PMI-NDI**, **PMI-PhNDI**, and **PMI-PhC60** which give just a slightly higher PCE as compared with the references **PI18** or **PI19** (Fig. 8.11) [33]. This is rationalized by the fact that the reduced sensitizer is not sufficiently reductive to significantly increase the regeneration quantum yield in spite of its much longer lifetime. C_{60} is more reducing than the NDI units ($\Delta E \approx 100$ mV), explaining thus why **PMI-PhC60** gives more photocurrent than the other dyads with the iodide/triiodide electrolyte (Table 8.1). However, a long-lived charge-separated state becomes particularly worthwhile with the cobalt electrolyte because Co^{III} polypyridine complexes are slow electron acceptors owing to the large reorganization energy accompanying the large spin change upon reduction into Co^{II} [9, 33, 52]. The cobalt electrolyte is indeed only compatible with long-lived charge-separated state as the regeneration reaction rate falls in the μs time scale, but it is a monoelectronic acceptor with a lower redox potential that makes it compatible with much weaker reduced sensitizer [52]. Furthermore and very importantly, the cobalt electrolyte leads to a much higher V_{oc} because the interfacial recombination between Co^{II} complexes and the injected holes is slowed down in comparison with that of I_3^- [52].

Since 2010, Bach, Bauerle, and co-workers have developed a series of dyads presenting a trisphenylamine donor possessing two anchoring groups, an oligothiophene linker and a PMI electron acceptor that have been demonstrated to be very effective to limit the recombination (see above) [10, 54]. As can be seen in Fig. 8.13, they proposed several modifications on the linker, while they kept constant the nature of the two extremities. In their initial investigation, the **Thioph2-PMI**, **Thioph4-PMI**, and **Thioph6-PMI** series were considered, and semiempirical simulations demonstrated that the LUMO is systematically centered on the PMI whereas the HOMO is localized on the donor and bridge for the shortest

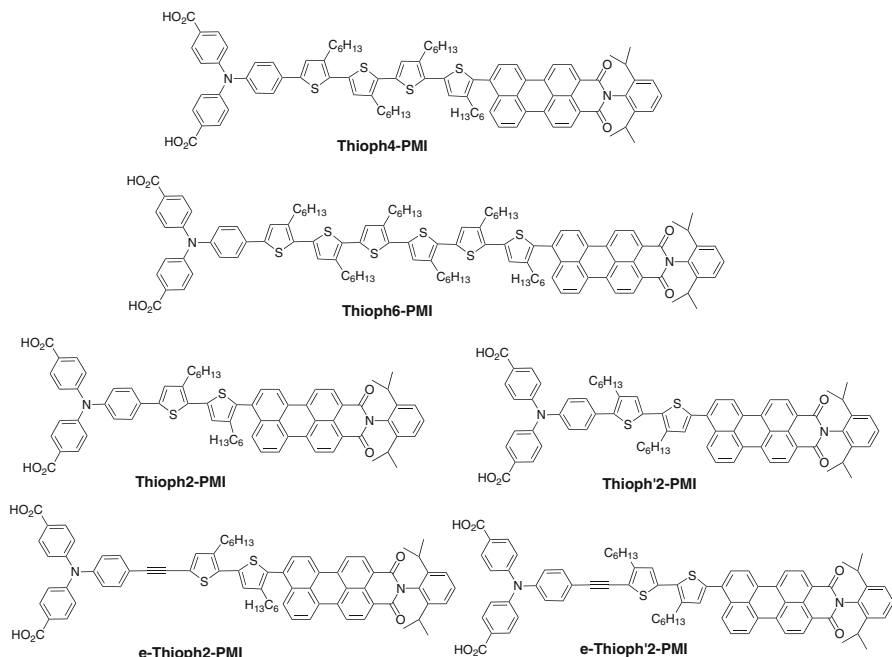
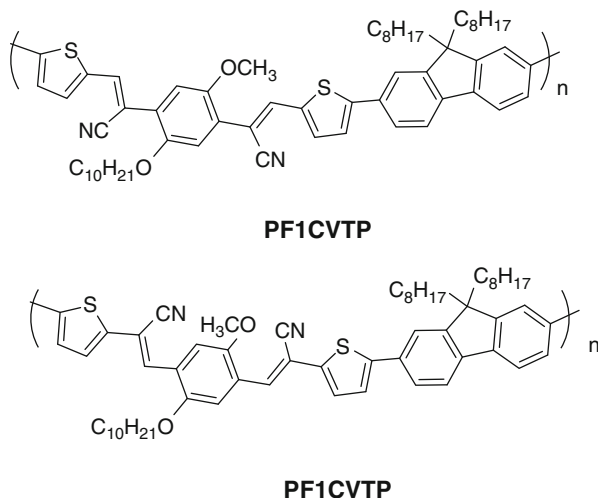


Fig. 8.13 Bach's oligothiophene-PMI dyads [10, 53–57]

system and on the hexathiophene moiety for the most extended compounds. Consequently, the reduction potential (LUMO energy) was almost unaffected by the size of the linker and the driving force for regeneration remained constant (and sizeable) for the full series, whereas the electron–hole separation increased with the length of the linker. Therefore, all major parameters steadily improve with increasing oligothiophene size (see Table 8.1), and **Thioph6-PMI** provided a conversion efficiency of 0.41 %, one of the largest ever recorded in p-DSC [10]. The major advance of this seminal work was to demonstrate that hole injection can take place at a nearly perfect yield. Using a **N719**-dyed photoanode, the authors were able to build an effective tandem cell that did not require extensive engineering. They later extended their works in three major directions: optimizing the fabrication of the NiO film [53, 55, 56], changing the redox shuttle [57], and making structural modification from the set of **Thioph2-PMI**, **Thioph4-PMI**, and **Thioph6-PMI** dyes [54]. Firstly, in 2011, the same authors produced large amounts of stable highly crystalline octahedral NiO particles that when coated with **Thioph6-PMI** allowed to reach an open-circuit voltage of 350 mV, a very large value for an iodine-based p-DSC [53]. They also built NiO nanorods, which allowed to use thicker films (1.7 μm) and subsequently to increase the overall efficiency thanks to enhanced fill factors and V_{oc} [54]. A few months later, by tuning again the crystallinity of the semiconductor using a high-temperature posttreatment, they improved the hole lifetime and reached a 0.61 % efficiency for the cell (Table 8.1)

Fig. 8.14 Two polyfluorene polyphenylene copolymers synthesized by Chavhan and co-workers [58]



[55]. Secondly, for the same **Thioph6-PMI** dye, they used the $[\text{Co}(\text{en})_3]^{2+/3+}$ redox couple (en = ethylene diamine) [57]. This allowed to reach a V_{oc} of 709 mV while keeping a large current, leading to a PCE of 1.3 %, the current world record in p-DSC. These advantages are related to the very large hole–electron separation and hence a very long hole lifetime (66 μs) in the NiO bulk, comparable to that of electron lifetime recorded in conventional n-DSCs. Surprisingly, the authors note that these hole lifetimes are rather independent of the electrolyte [57]. Thirdly, they compared the performances of **Thioph2-PMI**, **Thioph'2-PMI**, **e-Thioph2-PMI**, and **e-Thioph'2-PMI** [54] that either are regioisomers or differ only by the addition of an ethynyl linker. Changing the location of the alkyl chain (**Thioph'2-PMI** and **e-Thioph'2-PMI**) induces a small redshift and a broadening of the lowest energy band, related to a smaller torsion between the different components of the dyes. However, this leads to degraded photovoltaic performances: a better coupling between the donor and the acceptor is not systematically beneficial. On the contrary, the use of an ethynyl linker allowed to slightly increase the J_{sc} and efficiency compared to their original counterparts (see Table 8.1) [54].

3.9 Polymers

In 2010, Chavhan et al. reported the sensitization of a NiO photocathode by two n-type conjugated polymers **PF1CVTP** and **PF2CVTP** (poly(fluorene-bis(1-cyanovinyl)nethienylene)phenylene) and poly(fluorene-bis(2-cyanovinyl)nethienylene)phenylene), respectively, see Fig. 8.14 [58]. The authors noted that the NiO has to be prepared in the presence of oxygen to allow the formation of Ni^{3+} cations that allow the formation of intraband states and, subsequently, charge

transport. Measurements confirmed hole transfer from the polymer to NiO. The exciton formed in the polymer diffuses on extended distances (25 nm for PF1CVTP and 17 nm for **PF2CVTP**), but, as in other NiO-based devices, the charge recombination at the NiO interface is extremely fast. The authors concluded that only the exciton of the bulk of the polymer films could be collected. In terms of photovoltaic performances **PF2CVTP**-based device emerges as a more effective system layer because of its larger photoconductance: a V_{oc} of 198 mV, a J_{sc} of 0.023 mA/cm², and a ff of 33 %. For **PF2CVTP**, the IPCE was 1.5 % at 380 nm (absorbance of NiO) but only 0.5 % at 580 nm (polymer). The authors proposed that the lack of heterojunction in the device is a part of the explanation for the low V_{oc} .

3.10 Quantum Dots

Semiconductor nanocrystals or quantum dots (QDs) can also be used instead of molecular dyes to sensitize NiO. QDs are not properly speaking molecular dyes, and therefore they are beyond the scope of this chapter, but they have been increasingly studied in the field of DSCs legitimating some comments. Their main advantages reside on their high extinction coefficients, which is a particularly well-suited feature to overcome the generally ultrathin layers of p-SC; their photo- and electrochemical stabilities constitute real advantages to warrant the long life-span of the cell; the possibilities to generate multiple electron-hole pairs per photon to escape from the Shockley-Queisser limit is an additional boon, and the tunability of their bandgaps by controlling the particle size enables to prepare QDs with a wide range of colors. The typical semiconductors that are used for this application are chalcogenides such as CdS or CdSe in the form of quantum dots, and they already gave promising results [60–64]. That is why they will certainly attract increasing attention in the field of p-DSCs. Today, the highest photovoltaic performances with quantum dot-sensitized solar cells in NiO-based devices were obtained with a mixture of CdS/CdSe as sensitizers which led to a maximum IPCE of 30 % around 400 nm and $V_{oc} = 86$ mV, $J_{sc} = 0.87$ mA/cm², and ff = 32 % giving $\eta = 0.024$ % [61]. The deposition of a layer of CdSe QDs over CdS is important to limit the losses by charge recombination with the electrolyte. However, the best-performing QDSC employed CoO nanowires as p-SC and CdS as sensitizer and performed a $V_{oc} = 110$ mV, $J_{sc} = 4.42$ mA/cm², and ff = 22 % giving $\eta = 0.107$ % [62].

4 Conclusions and Perspectives

The optimization of the photovoltaic properties of p-DSC remains an important challenge due to the specific properties of this new type of solar cell. Today, the solar-to-electricity conversion efficiencies of photocathodes remain much lower than their photoanode counterparts used in n-DSC. The sensitizer is a core

component of the cell efficiency; therefore there is a lot to be gained with the development of new dyes. During the past 5 years, thanks to the continuous improvements of the dyes (smartly vectorialized charge-transfer dyes and/or dyads allowing to reduce the recombination rates), of the surfaces (better processed NiO allowing an increased hole mobility between the nanoparticles), and of the redox shuttle (more adequate to p-DSC than the triiodide/iodide couple) a lot of progresses were made since the PCE of p-DSCs has passed from less than 0.1 % to over 1 % with only a limited number of teams working on this area. However, some advances are really needed to push further the PCE much above 5 %. Towards this goal, synthesizing and testing new families of dyes certainly represent a real opportunity to develop better performing cells, and this will also bring a deeper knowledge regarding the structure/efficiency relationship. Organic push-pull dyes are certainly promising candidates, provided that the electron acceptor is introduced at the opposite extremity of the anchoring group. Push-pull systems also offer the tremendous opportunities to tune the redox potentials and the absorption bands upon modification of the electron-donating or -releasing strength of the substituents and of the nature and the length of the π -conjugated spacer. Currently, the major limitation in p-DSC is caused by the major charge recombination reactions which are still challenging to control. The sensitizer can be an essential component to retard the usually fast geminate recombination, especially by geographically and electronically decoupling the electron density far away from the p-SC surface upon hole injection. A close packing of the sensitizers on the surface of the p-SC could also prevent the approach of the redox mediator and thereby block the interfacial charge recombination with the electrolyte. Another important breakthrough would concern the discovery of efficient sensitizers with simple structures relying on readily accessible synthetic procedures while yielding long-lived charge-separated state. Indeed, so far the only very efficient sensitizers are bicomponent systems which require time-consuming multi-step synthesis.

Developing sensitizers performing well in IR and near-IR region is challenging but particularly important to exploit a wider part of the incident sunlight energy especially in view of tandem cell fabrication. However, it must be kept in mind that a DSC is a complex system and therefore a multiparameter device which must be optimized according to a comprehensive approach taking into account several components at the same time rather than optimizing one element after the other. The optimal choice of the sensitizer will be certainly strongly bound to the electrolyte and the nature of the p-SC, knowing that the replacement of NiO by a better suited p-SC has initiated important research activity in the past 2 years [65–67]. Overall, it is clear that p-DSC is a fast-moving research area which gives rise to more and more scientific interest and will probably stimulate new ideas.

Acknowledgements The authors thank the “Région Pays de la Loire” for the program PERLE1&2 and NiOPhotoCat and the ANR-Progelec agency (program POSITIF n° ANR-12-PRGE-0016-01). F.B.A. is indebted to the *Région des Pays de la Loire* for his PhD grant. D.J. acknowledges both the European Research Council (ERC) and the *Région des Pays de la Loire* for financial support in the framework of a Starting Grant (Marches—278845) and a *recrutement sur poste stratégique*, respectively.

References

1. Lewis, N.S., Nocera, D.G.: Powering the planet: chemical challenges in solar energy utilization. *Proc. Natl. Acad. Sci. U. S. A.* **103**, 15729–15735 (2007)
2. Balzani, V., Credi, A., et al.: Photochemical conversion of solar energy. *ChemSusChem* **1**, 26–58 (2008)
3. O'Regan, B., Grätzel, M.: A low-cost, high-efficiency solar cell based on dye-sensitized colloidal titanium dioxide films. *Nature* **353**, 737–740 (1991)
4. Hagfeldt, A., Boschloo, G., et al.: Dye-sensitized solar cells. *Chem. Rev.* **110**, 6595–6663 (2010)
5. Odobel, F., Pellegrin, Y., et al.: Recent advances and future directions to optimize the performances of p-type dye-sensitized solar cells. *Coord. Chem. Rev.* **256**, 2414–2423 (2012)
6. Odobel, F., Le Pleux, L., et al.: New photovoltaic devices based on the sensitization of p-type semiconductors: challenges and opportunities. *Acc. Chem. Res.* **43**, 1063–1071 (2010)
7. He, J., Lindström, H., et al.: Dye-sensitized nanostructured tandem cell—first demonstrated cell with a dye-sensitized photocathode. *Sol. Energy Mater. Sol. Cells* **62**, 265–273 (2000)
8. Nakasa, A., Usami, H., et al.: A high voltage dye-sensitized solar cell using a nanoporous NiO photocathode. *Chem. Lett.* **34**, 500–501 (2005)
9. Gibson, E.A., Smeigh, A.L., et al.: A p-type NiO-based dye-sensitized solar cell with a Voc of 0.35 V. *Angew. Chem. Int. Ed.* **48**, 4402–4405 (2009)
10. Nattestad, A., Mozer, A.J., et al.: Highly efficient photocathodes for dye-sensitized tandem solar cells. *Nat. Mater.* **9**, 31–35 (2010)
11. Li, L., Duan, L., et al.: Visible light driven hydrogen production from a photo-active cathode based on a molecular catalyst and organic dye-sensitized p-type nanostructured NiO. *Chem. Commun.* **48**, 988–990 (2012)
12. Tong, L., Iwase, A., et al.: Sustained solar hydrogen generation using a dye-sensitized NiO photocathode/BiVO₄ tandem photo-electrochemical device. *Energy Environ. Sci.* **5**, 9472–9475 (2012)
13. He, J., Lindström, H., et al.: Dye-sensitized nanostructured p-type nickel oxide film as a photocathode for a solar cell. *J. Phys. Chem. B* **103**, 8940–8943 (1999)
14. Borgström, M., Blart, E., et al.: Sensitized hole injection of phosphorus porphyrin into NiO: toward new photovoltaic devices. *J. Phys. Chem. B* **109**, 22928–22934 (2005)
15. Morandiera, A., Boschloo, G., et al.: Photoinduced ultrafast dynamics of coumarin 343 sensitized p-type-nanostructured NiO films. *J. Phys. Chem. B* **109**, 19403–19410 (2005)
16. Splan, K.E., Massari, A.M., et al.: A porous multilayer dye-based photoelectrochemical cell that unexpectedly runs in reverse. *J. Phys. Chem. B* **108**, 4111–4115 (2004)
17. Boschloo, G., Hagfeldt, A.: Characteristics of the iodide/triiodide redox mediator in dye-sensitized solar cells. *Acc. Chem. Res.* **42**, 1819–1826 (2009)
18. Morandiera, A., Boschloo, G., et al.: Coumarin 343-NiO films as nanostructured photocathodes in dye-sensitized solar cells: ultrafast electron transfer, effect of the I³⁻/I⁻ redox couple and mechanism of photocurrent generation. *J. Phys. Chem. C* **112**, 9530–9537 (2008)
19. Boschloo, G., Gibson, E.A., et al.: Photomodulated voltammetry of iodide/triiodide redox electrolytes and its relevance to dye-sensitized solar cells. *J. Phys. Chem. Lett.* **2**, 3016–3020 (2011)
20. Morandiera, A., Fortage, J., et al.: Improved photon-to-current conversion efficiency with a nanoporous p-type NiO electrode by the use of a sensitizer-acceptor dyad. *J. Phys. Chem. C* **112**, 1721–1728 (2008)
21. Qin, P., Wiberg, J., et al.: Synthesis and mechanistic studies of organic chromophores with different energy levels for p-type dye-sensitized solar cells. *J. Phys. Chem. C* **114**, 4738–4748 (2010)
22. Huang, Z., Natu, G., et al.: Probing the low fill factor of NiO p-type dye-sensitized solar cells. *J. Phys. Chem. C* **116**, 26239–26246 (2012)

23. Pellegrin, Y., Le Pleux, L., et al.: Ruthenium polypyridine complexes as sensitizers in NiO based p-type dye-sensitized solar cells: effects of the anchoring groups. *J. Photochem. Photobiol. A* **219**, 235–242 (2011)
24. Mishra, A., Fischer, M.K.R., et al.: Metal-Free organic dyes for dye-sensitized solar cells: from structure: Property relationships to design rules. *Angew. Chem. Int. Ed.* **48**, 2474–2499 (2009)
25. Smeigh, A.L., Pleux, L.L., et al.: Ultrafast recombination for NiO sensitized with a series of perylene imide sensitizers exhibiting Marcus normal behaviour. *Chem. Commun.* **48**, 678–680 (2012)
26. Jortner, J., Ratner, M.: *Molecular Electronics*. Blackwell Science, London (1997)
27. Bonhôte, P., Moser, J.-E., et al.: Long-lived photoinduced charge separation and redox-type photochromism on mesoporous oxide films sensitized by molecular dyads. *J. Am. Chem. Soc.* **121**, 1324–1336 (1999)
28. Uehara, S., Sumikura, S., et al.: Retardation of electron injection at NiO/dye/electrolyte interface by aluminium alkoxide treatment. *Energy Environ. Sci.* **3**, 641–644 (2010)
29. Natu, G., Huang, Z., et al.: The effect of an atomically deposited layer of alumina on NiO in P-type dye-sensitized solar cells. *Langmuir* **28**, 950–956 (2011)
30. Vera, F., Schrebler, R., et al.: Preparation and characterization of Eosin B- and Erythrosin J-sensitized nanostructured NiO thin film photocathodes. *Thin Solid Films* **490**, 182–188 (2005)
31. Nattestad, A., Ferguson, M., et al.: Dye-sensitized nickel(II)oxide photocathodes for tandem solar cell applications. *Nanotechnology* **19**, 295304/295301–295304/295309 (2008)
32. Gibson, E.A., Le-Pleux, L., et al.: The role of the triiodide/iodide redox couple in dye regeneration in p-type dye-sensitized solar cells. *Langmuir* **28**(15), 6485–6493 (2012)
33. Le Pleux, L., Smeigh, A.L., et al.: Synthesis, photophysical and photovoltaic investigations of acceptor-functionalized perylene monoimide dyes for nickel oxide p-type dye-sensitized solar cells. *Energy Environ. Sci.* **4**, 2075–2084 (2011)
34. Gosztola, D., Niemczyk, M.P., et al.: Excited doublet states of electrochemically generated aromatic imide and diimide radical anions. *J. Phys. Chem. A* **104**, 6545–6551 (2000)
35. Feihl, S., Costa, R.D., et al.: Nickel oxide nanostructured electrodes towards perylenediimide-based dye-sensitized solar cells. *RSC Adv.* **2**, 11495–11503 (2012)
36. Bian, Z., Tachikawa, T., et al.: Single-molecule charge transfer dynamics in dye-sensitized p-type NiO solar cells: influences of insulating Al₂O₃ layers. *Chem. Sci.* **3**, 370–379 (2012)
37. Sumikura, S., Mori, S., et al.: Photoelectrochemical characteristics of cells with dyed and undyed nanoporous p-type semiconductor CuO electrodes. *J. Photochem. Photobiol. A* **194**, 143–147 (2008)
38. Mori, S., Fukuda, S., et al.: Charge-transfer processes in dye-sensitized NiO solar cells. *J. Phys. Chem. C* **112**, 16134–16139 (2008)
39. Mishra, A., Behera, R.K., et al.: Cyanines during the 1990s: a review. *Chem. Rev.* **100**, 1973–2012 (2000)
40. Li, L., Gibson, E.A., et al.: Double-layered NiO photocathodes for p-type DSSCs with record IPCE. *Adv. Mater.* **22**, 1759–1762 (2010)
41. Qin, P., Linder, M., et al.: High incident photon-to-current conversion efficiency of p-type dye-sensitized solar cells based on NiO and organic chromophores. *Adv. Mater.* **21**, 2993–2996 (2009)
42. Qin, P., Zhu, H., et al.: Design of an organic chromophore for p-type dye-sensitized solar cells. *J. Am. Chem. Soc.* **130**, 8570–8571 (2008)
43. Zhu, L., Yang, H., et al.: Modified triphenylamine-dicyanovinyl-based donor–acceptor dyes with enhanced power conversion efficiency of p-type dye-sensitized solar cells. *Chem. Asian J.* **7**, 2791–2795 (2012)
44. Yen, Y.-S., Chen, W.-T., et al.: Arylamine-based dyes for p-type dye-sensitized solar cells. *Org. Lett.* **13**, 4930–4933 (2011)

45. Hsu, C.-Y., Chen, W.-T., et al.: Charge transporting enhancement of NiO photocathodes for p-type dye-sensitized solar cells. *Electrochim. Acta* **66**, 210–215 (2012)
46. Natu, G., Hasin, P., et al.: Valence band-edge engineering of nickel oxide nanoparticles via cobalt doping for application in p-type dye-sensitized solar cells. *ACS Appl. Mater. Interfaces* **4**(11), 5922–5929 (2012)
47. Chang, C.-H., Chen, Y.-C., et al.: Squaraine-arylamine sensitizers for highly efficient p-type dye-sensitized solar cells. *Org. Lett.* **14**, 4726–4729 (2012)
48. Freys, J.C., Gardner, J.M., et al.: Ru-based donor-acceptor photosensitizer that retards charge recombination in a p-type dye-sensitized solar cell. *Dalton Trans.* **41**, 13105–13111 (2012)
49. Ji, Z., Natu, G., et al.: Synthesis, photophysics, and photovoltaic studies of ruthenium cyclometalated complexes as sensitizers for p-type NiO dye-sensitized solar cells. *J. Phys. Chem. C* **116**, 16854–16863 (2012)
50. Balzani, V., Juris, A., et al.: Luminescent and redox-active polynuclear transition metal complexes. *Chem. Rev.* **96**, 759–834 (1996)
51. Campagna, S., Puntoriero, F., et al.: Photochemistry and photophysics of coordination compounds: ruthenium. In: Balzani, V., Campagna, S. (eds.) *Photochemistry and Photophysics of Coordination Compounds I*, vol. 280, pp. 117–214. Springer, Berlin (2007)
52. Gibson, E.A., Smeigh, A.L., et al.: Cobalt polypyridyl-based electrolytes for p-type dye-sensitized solar cells. *J. Phys. Chem. C* **115**, 9772–9779 (2011)
53. Zhang, X.L., Huang, F., et al.: Enhanced open-circuit voltage of p-type DSC with highly crystalline NiO nanoparticles. *Chem. Commun.* **47**, 4808–4810 (2011)
54. Weideler, M., Mishra, A., et al.: Synthesis and characterization of perylene-bithiophene-triphenylamine triads: studies on the effect of alkyl-substitution in p-type NiO based photocathodes. *J. Mater. Chem.* **22**, 7366–7379 (2012)
55. Zhang, X.L., Zhang, Z., et al.: Sensitization of nickel oxide: improved carrier lifetime and charge collection by tuning nanoscale crystallinity. *Chem. Commun.* **48**, 9885–9887 (2012)
56. Zhang, X.L., Zhang, Z., et al.: Charge transport in photocathodes based on the sensitization of NiO nanorods. *J. Mater. Chem.* **22**, 7005–7009 (2012)
57. Powar, S., Daeneke, T., et al.: Highly efficient p-type dye-sensitized solar cells based on tris (1,2-diaminoethane)cobalt(II)/(III) electrolytes. *Angew. Chem. Int. Ed.* **125**, 630–633 (2013)
58. Chavhan, S.D., Abellon, R.D., et al.: Sensitization of p-type NiO using n-type conducting polymers. *J. Phys. Chem. C* **114**, 19496–19502 (2010)
59. Ji, Z., Natu, G., et al.: Linker effect in organic donor-acceptor dyes for p-type NiO dye sensitized solar cells. *Energy Environ. Sci.* **4**, 2818–2821 (2011)
60. Chan, X.-H., Jennings, J.R., et al.: Characteristics of p-NiO thin films prepared by spray photocathodes pyrolysis and their application in CdS-sensitized. *J. Electrochem. Soc.* **158**, H733–H740 (2011)
61. Safari-Alamuti, F., Jennings, J.R., et al.: Conformal growth of nanocrystalline CdX (X = S, Se) on mesoscopic NiO and their photoelectrochemical properties. *Phys. Chem. Chem. Phys.* **15**, 4767–4774 (2013)
62. Mao, Y.-Q., Zhou, Z.-J., et al.: P-type CoO nanowire arrays and their application in quantum dot-sensitized solar cells. *RSC Adv.* **3**, 1217–1221 (2013)
63. Kang, S.H., Zhu, K., et al.: Hole transport in sensitized CdS-NiO nanoparticle photocathodes. *Chem. Commun.* **47**, 10419–10421 (2011)
64. Wu, X., Yeow, E.K.L.: Charge-transfer processes in single CdSe/ZnS quantum dots with p-type NiO nanoparticles. *Chem. Commun.* **46**, 4390–4392 (2010)
65. Renaud, A., Chavillon, B., et al.: CuGaO₂: a promising alternative for NiO in p-type dye solar cells. *J. Mater. Chem.* **22**, 14353–14356 (2012)
66. Yu, M., Natu, G., et al.: p-type dye-sensitized solar cells based on delafossite CuGaO₂ nanoplates with saturation photovoltages exceeding 460 mV. *J. Phys. Chem. Lett.* **3**, 1074–1078 (2012)
67. Xiong, D., Xu, Z., et al.: Hydrothermal synthesis of ultrasmall CuCrO₂ nanocrystal alternatives to NiO nanoparticles in efficient p-type dye-sensitized solar cells. *J. Mater. Chem.* **22**, 24760–24768 (2012)

Chapter 9

Dye-Doped Polysiloxane Rubbers for Luminescent Solar Concentrator Systems

Marta Buffa and Michael G. Debije

Abstract After introducing the argument for the use of luminescent solar concentration in PV energy generation we will describe in some detail production and characterisation of luminescent solar collector (LSC) devices based on the dye Lumogen Red 305 dispersed in a matrix (polysiloxane) that, unlike the more common polycarbonate and (poly)methyl methacrylate hosts, is flexible. The feasibility of flexible LSC devices is discussed.

1 Introduction

The intensity of solar radiation on Earth's surface is about $1,353 \text{ kW/m}^2$ (solar constant). This radiation is characterised by a black-body spectrum corresponding to a temperature of around 6,000 K when it reaches the solar photosphere; when it traverses the atmosphere, it is attenuated by multiple interactions with air molecules, aerosols, and dust and by absorption by oxygen, ozone, water vapour, and carbon dioxide. The spectrum measured on the surface of the planet is shown in Fig. 9.1. The reference spectrum of solar radiation on Earth's surface can be found in IEC 60904-3, air mass AM = 1.5. Other factors influencing the intensity and wavelength distribution of solar radiation on Earth's surface are latitude, altitude, season, and atmospheric conditions; for example, the radiation incident on a horizontal surface is on average $700\text{--}1,000 \text{ kW h/m}^2$ in northern Europe,

M. Buffa (✉)

Dipartimento di Ingegneria dei Materiali e Tecnologie Industriali, Università di Trento,
via Mesiano 77, 38123 Povo (Tn), Italy
e-mail: marta.buffa@ing.unitn.it

M.G. Debije

Chemical Engineering & Chemistry, Eindhoven University of Technology, Den Dolech 2,
5600 Eindhoven, The Netherlands

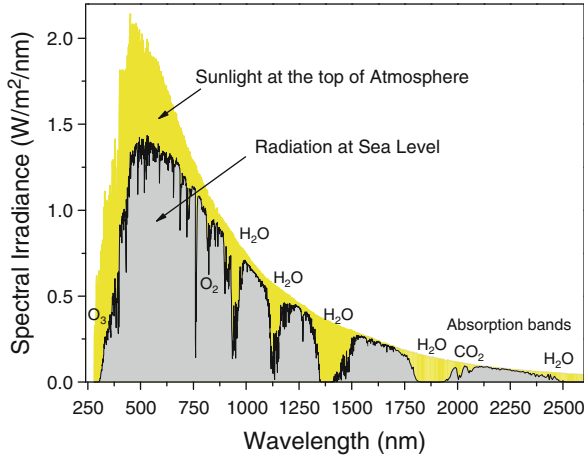


Fig. 9.1 Sunlight spectrum at the top of atmosphere and at ground level, compared to that of a black body at 5,250 °C. The gaps in the spectrum are due to absorption by chemical species in the atmosphere [1]

900–1,300 kW h/m² in central Europe, 1,300–1,800 kW h/m² in southern Europe, and 1,800–2,300 kW h/m² at the equator.

There are a few limiting factors that preclude the possibility that all Earth's energy generation challenges may be solved solely through photovoltaic generation:

- The extended surface area necessary
- The discontinuity in power production and the problems related to network managing
- The high cost of the semiconductors necessary to produce solar cells

PV generation, however, can assist the daily economy of single or isolated buildings. For all these reasons it is desirable to develop simple and low-cost PV systems that may be integrated in the urban setting.

2 Optical Solar Concentrators

Due to the high cost of PV materials, it is desirable to concentrate light collected over large areas to devices of smaller area. Optical solar concentrators can be divided into imaging and non-imaging.

Imaging concentrators [2] focus incident parallel sun rays to a spot or a line via mirrors or lenses. Since only direct sunlight can be focused, this type of concentrator requires a tracking system. Fresnel lenses, a common lens type in these systems, present problems of non-uniform illumination at the PV cell, which reduces

performance and creates “hot spots,” and a cooling system is required for the mirrors due to the considerable heat production, adding both complexity and cost.

Non-imaging concentrators [3] instead focus sun rays to the PV cell, but no image of the sun is produced. They use direct and diffuse light, so it is not necessary to employ a tracking system. An example is the compound parabolic concentrator which consists of two reflective parabolic surfaces having their focal points at opposite ends of the PV cell. Rays entering the system inside the acceptance angle are focused onto the PV cell area.

Another example of a non-imaging device is the luminescent solar collector (LSC), first proposed in the 1970s [4, 5]. Initially proposed for greenhouse glazing, the development of the LSC has been hindered by a number of practical limitations.

3 LSCs

An LSC consists of a flat plate of glass, plastic, or liquid cell doped with a luminescent dye [6, 7]. All the edges of the collector may be covered by solar cells, or specific edge(s) may host the PV cell with reflective mirrors placed on the other edges.

The functionality of an LSC is illustrated in Fig. 9.2. Sunlight incident on the LSC (1) is absorbed by the dye molecules (2). Light is subsequently re-emitted at a longer wavelength (3), and a fraction of this emitted light is transported to the edges via total internal reflection (TIR) (4). Light is finally absorbed by the solar cell (5). Some loss mechanisms are front surface reflection (6), transparency to high wavelengths (7), and losses from the escape cone for light emitted at the Brewster angle (8). In addition, luminescence may be reabsorbed by the dye molecules if they have overlapping absorption and emission spectra (9), which may either result in

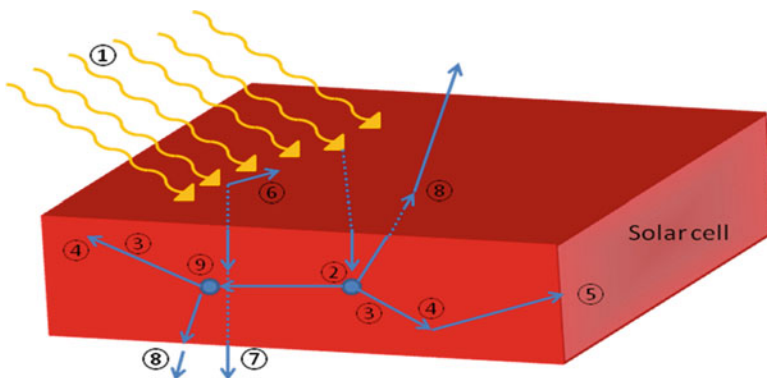


Fig. 9.2 Possible light interactions with the LSC, from [8]. See text for details

loss of luminescence (if the fluorescent quantum yield of the luminophore is less than unity) or emitted luminescence, with the same potential loss mechanisms just described.

Incident solar radiation enters the device through the exposed surface; selected wavelengths are absorbed by the luminescent dye and re-emitted [9, 10]. TIR occurs at the interface between a medium with higher refractive index (n) (e.g., glass, plastics) and one with lower index (e.g., air). If light hits the interface between plastic and air at a larger angle than the critical angle, it remains trapped within the plate; otherwise, it is lost through the surface. The amount of emitted light that will be totally internally reflected (L) is determined by the index n of the matrix material by

$$L = \frac{(n^2 - 1)^{1/2}}{n}$$

The critical angle θ_c is determined by

$$\theta_c = \sin^{-1}\left(\frac{1}{n}\right)$$

The advantages of LSC are as follows

- Both direct and diffused light are absorbed, so no tracking system is required, reducing installation costs. These systems are suitable for locations where high-intensity illumination cannot be achieved on a regular basis and where diffused radiation makes up 60 % or more of the radiation incident on a flat surface [11].
- The emission band of the luminescent species can be matched to the maximum spectral response of the PV cell; thus the possibility arises to break down the solar spectrum into segments and concentrate them simultaneously, stacking plates containing dyes with different absorption characteristics and matching them with different solar cells.
- As photons whose energy is below the bandgap are not converted into electricity but heat and as a general rule the performance of solar cells deteriorates with increasing temperature, it is desirable to prevent sub-bandgap radiation from reaching the cell. In LSC devices radiation from energy losses and infrared light is dispersed throughout the front plate avoiding efficiency losses in the PV cell, which remains cooler than a standard PV [12]. LSCs could be well suited for building integrated photovoltaics (BIPV) as shading devices or active building facades.

The disadvantages of LSCs are as follows

- Some luminescent dyes suffer from reduced photostability [13].
- Reabsorption may result in considerable light loss, a result of the limited Stokes shifts (i.e., the difference in wavelength between the absorption and the emission peak).

- The absorption range of the dyes is often limited, restricting the fraction of the solar spectrum that can be exploited by the PV cell.

4 Equipment for Our Experiment

In this section all the elements used for the electrical characterisation of the samples are presented.

Three types of solar cells were tested:

- Si photodiode
- InGaP solar cells
- GaAs solar cells

These three types of photovoltaics have different external quantum efficiencies (EQEs) as shown in Fig. 9.3:

The efficiencies of InGaP solar cells, GaAs solar cells, and Si photodiodes peak between 450 and 550 nm, between 600 and 850 nm, and around 950 nm, respectively. These calibration spectra were obtained using a spectrophotometer, measuring the power output of the cells and normalising the output power to a UV-enhanced, photodiode-calibrated round photodetector (New Focus Model 2032) that had a diameter of 5.8 mm and a response range of 190–1,100 nm. Results were normalised to power per unit area.

The experimental apparatus is presented in Fig. 9.4. The solar cells were connected with a rheostat with range from 0.1 to 100,000 Ω . A voltmeter and an ammeter were connected in parallel and in series, respectively.

In order to perform repeatable measurements, a 300 W solar simulator was used. Although the device can simulate up to two “suns,” all our measurements were carried out with a one-sun setting.

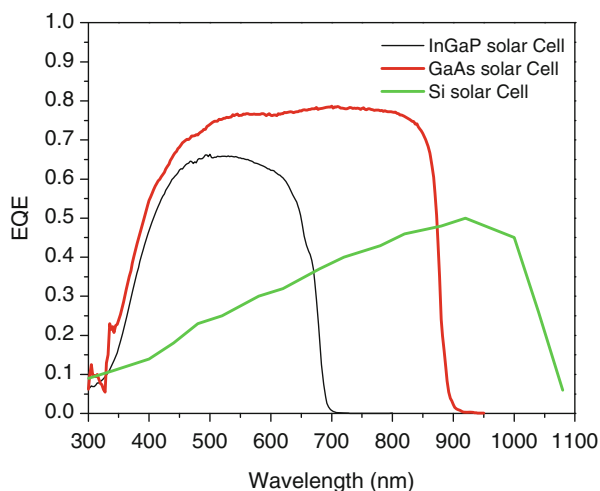
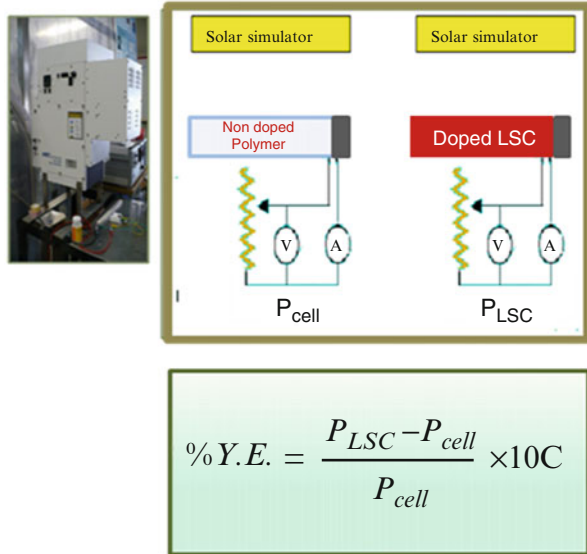


Fig. 9.3 EQE of the three types of solar cells: InGaP, Si, and GaAs [14]

Fig. 9.4 Schematic representation of the experimental apparatus and the formula used to calculate the yield enhancement (%Y.E.) [14]

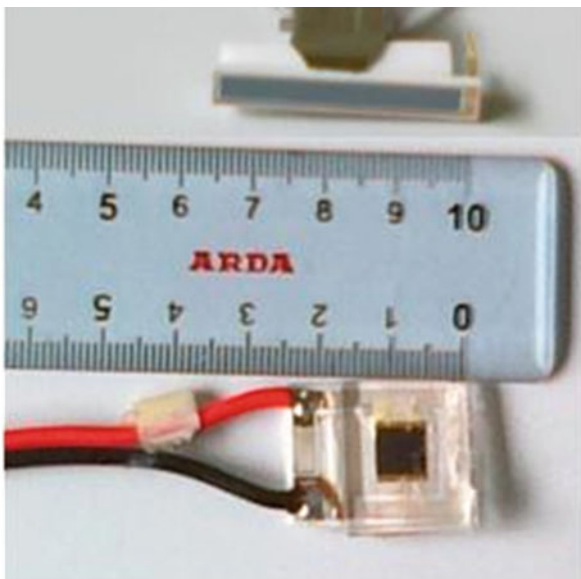


Some measurements were also performed in open air; in order to collate various measurements, we determined only the open-circuit current, which is proportional to the power incident on the cell. We did so because we wanted to minimise the error deriving from the variability of the solar power: every measurement of the complete I–V graph took about 10 min to complete, and in that time sun lighting conditions can vary and strongly affect the results. Measuring only the short circuit current was faster, and the results remained comparable.

The Si photodiode was purchased from Hamamatsu (type: S3588-03 2a) with an active area of $3 \times 35 \text{ mm}^2$. The InGaP and GaAs solar cells were bought from CESI and their active areas were $5 \times 5 \text{ mm}^2$. These cells were contacted by AUREL and did not have any protective coating. They were used as received in the WLS experiment, while in the LSC experiment the two solar cells were coated in 2 mm of clear polysiloxane (Fig. 9.5). The need to encapsulate cells for LSC application derives from the architecture of the cells themselves; the gold contacts that transport the current from the surface to the external contacts are arches suspended on a slot that works as charge carrier of the opposite sign, so the Au arches collapsing into the slot would cause a short circuit which would badly damage the cell. For this reason, it was important to fold the arches into a matrix; the second purpose of this procedure was to protect the surface of the cell, which is very sensitive to scratches and impurities. An ideal LSC could be directly cast to the front of the cell, but we preferred encapsulation to casting in order to be able to re-utilise the cells in the future.

Throughout the experiment, performance of the PV cells was measured before and after every step of preparation.

Fig. 9.5 Comparison between Si and GaAs solar cells (the InGaP solar cell has the same appearance as the GaAs) [14]



Edge emissions were directly measured with an SLMS 1050 integrating sphere (Labsphere) equipped with a diode array detector (RPS900, International Light). The LSC samples were placed in a custom-made sample holder with a black background with one edge incident to the opening of the sphere and exposed to a collimated light source from a 300 W solar simulator with filters to approximate the 1.5 AM (global) solar spectrum (Lot-Oriel), located at a distance of about 15 cm. Light output spectra and intensity from the emission edge of the sample were recorded. Total output was determined by integrating the recorded spectra over the range of 350–750 nm.

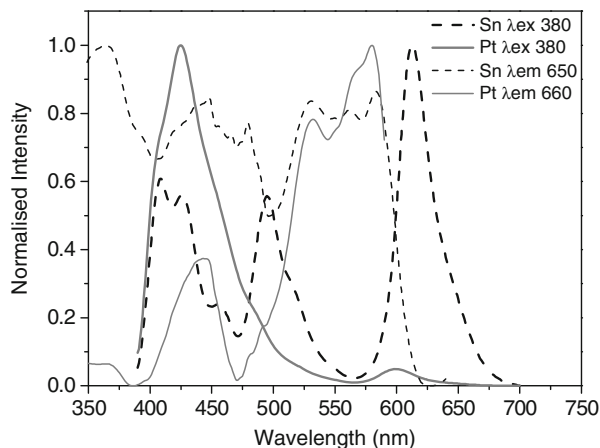
5 Polysiloxane Doped with Lumogen

Polysiloxane catalyst can interact with organic dyes as demonstrated in a previous paper using polysiloxane and 3-hydroxyflavone (3HF) [15]. This reaction also proceeds for the perylene-based Lumogen dyes used in this work; spectra collected immediately after the production of the samples and 1 year later displayed shifted peaks, suggesting interactions between the catalyst and the dye. A gradual change in the colour of the dye, influencing the fluorescent emission, was already noticeable during polymerisation.

Lumogen[®] F Red 305 (LR305) is one of the most promising molecules for optical solar concentrators and has been used in the past in poly(methylmethacrylate) (PMMA), poly(carbonate) (PC), and other studies as a doping molecule for luminescent concentrators [7, 16–19].

Two samples were produced with a combination of the three dyes: Lumogen violet, Lumogen Yellow 083, and Lumogen Red 305 in Pt-catalysed polysiloxane

Fig. 9.6 Fluorescence spectra of a mixture of Lumogen Violet 570, Lumogen Yellow 083, and Lumogen Red 305 in Pt- and Sn-catalysed polysiloxane [14]



and in Sn-catalysed polysiloxane. As shown in Fig. 9.6, the emission from the dyes in the Sn-catalysed siloxane was in good agreement with literature data, while the peaks in the Pt-catalysed polysiloxane spectrum are either weaker than expected (Lumogen Yellow 083) or shifted, as in the case of LR305 that emits under 600 nm rather than 610 nm, as in Sn-catalysed polysiloxane.

The efficiency of LR305 is relatively high [15] with photostability higher than that of other BASF Lumogen dyes [20].

Tanaka et al. [17] studied the properties of LR305 and Orange 240 and their photo-oxidation and photo-reduction. Equilibrium exists between the two forms; the photo-reduced dye has a lower fluorescence than the photo-oxidised (type II photo-oxidation). Photodegradation takes place when the two phenomena become irreversible.

5.1 Lumogen Red in Polysiloxane-Based LSCs

The absorbance spectra of the doped samples are characterised by a peak at 565 nm, with an amplitude increase with concentration. The qualitative comparison of fluorescence emission intensity in Fig. 9.7 shows that the light yield tends to increase with concentration up to 0.01 % and then decreases.

A deeper understanding of the effects of concentration on the fluorescence features of the dyes can be obtained comparing the shapes of the spectra in Fig. 9.8, where the excitation and emission spectra are shown of (poly)siloxane (PS) sheets doped with low and high concentrations of LR305, normalised to the maximum peak intensity. As can be observed, in samples with lower dye concentrations the excitation and emission peaks are located around 560 and 590 nm, respectively. By increasing the amount of LR305 by three orders of magnitude, these peaks shift to about 555 and 594 nm. It is worth noting that the

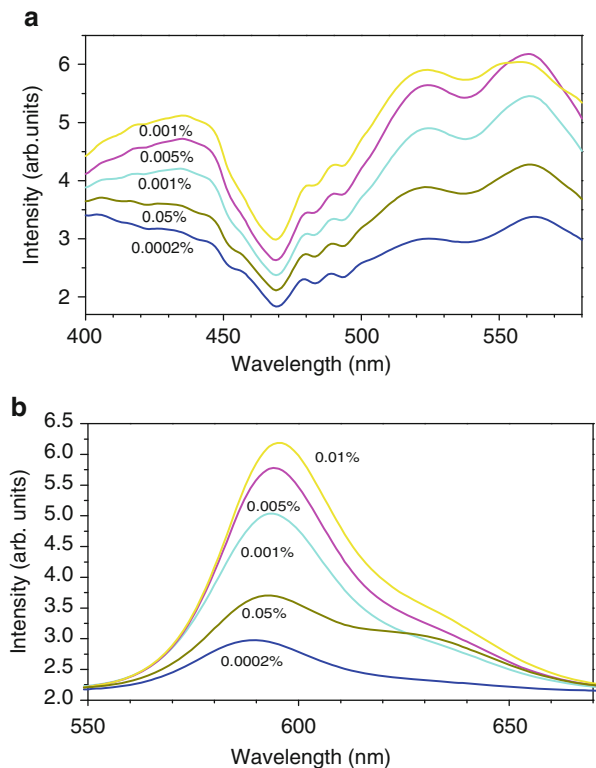


Fig. 9.7 Excitation (a) and emission (b) spectra of PS waveguides with 0.0002, 0.001, 0.005, 0.01, and 0.05 wt% of LR305 in a polysiloxane matrix. Excitation and emission wavelengths were 520 and 620 nm, respectively [13]

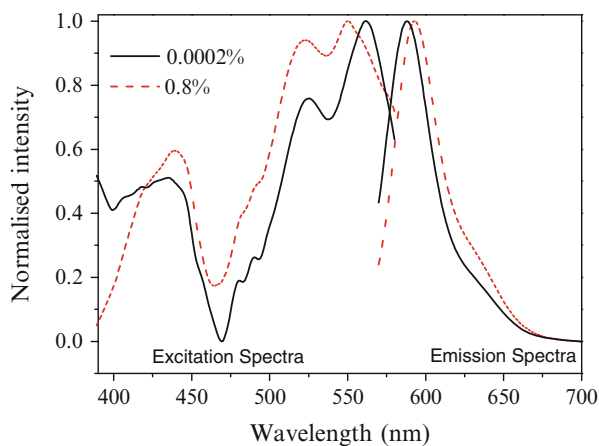


Fig. 9.8 Normalised excitation and emission spectra of PS sheets with 0.0002 wt% (black line) and 0.08 wt% (red line) of LR305. Excitation and emission wavelengths were 560 and 590 nm, respectively [13]

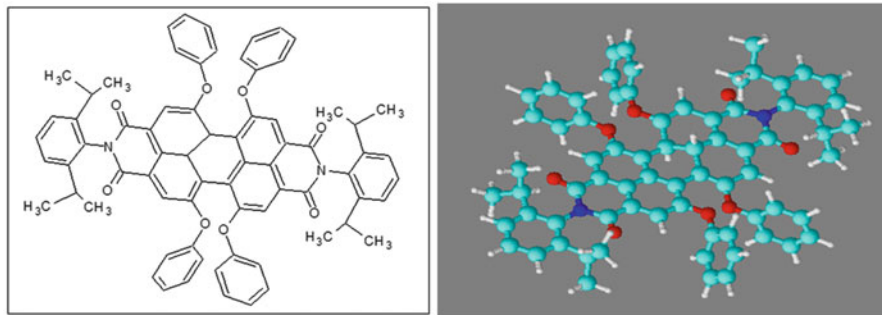


Fig. 9.9 Chemical structure of LR305 in 2D and 3D view produced with ChemsSketch (ACD Labs) [13]

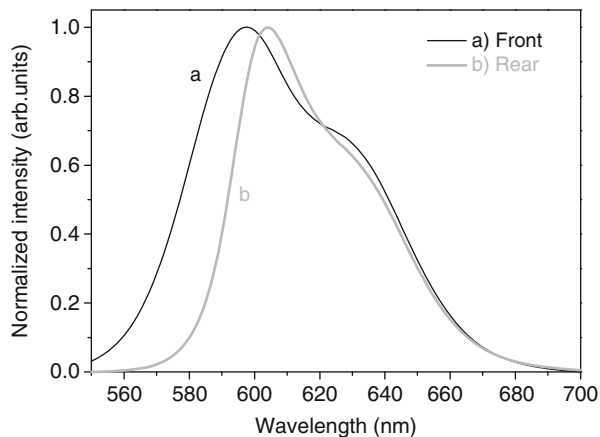
datasheet provided by BASF locates the absorption and emission maxima in ethanol, respectively, at 578 and 613 nm. In contrast, in PC the peaks were located at 573 and 597 nm [20].

The discrepancy between spectra measured in different environments is related to the chemical structure of LR305, reported in [21] and depicted in Fig. 9.9. The perylenediimide molecule presents several hydrogen-bonding acceptor functional groups (carbonyl oxygen, ether bridges, imide nitrogen). Thus, in ethanol the absorption/emission features are affected by specific interactions with the hydroxyl groups of the solvent, which can induce significant red shifts of the spectra with respect to the unperturbed molecule [22]. These interactions cannot occur between the dye and the hydroxyl-free polysiloxane matrix used in this work. Comparing the case of PC, where strongly polar carbonyl groups are present along the macromolecule, and the almost non-polar, alkyl shielded Si–O–Si bonds in polysiloxanes, it can be envisaged that a blue shift in both absorption and emission peaks in the case of a non-polar matrix is expected, as a result of less efficient solvent relaxation mechanism.

As for concentration effects, LR305 was found to be resistant to aggregation-induced fluorescence quenching in the case of solid matrices up to concentrations of 100 mM [22]. Keeping in mind that the maximum concentration of LR305 in PS reached in this work is about 30 mM (assuming the density of PS to be about 1 g/cm³), one may have therefore expected an absence of quenching and aggregation in the present case as well, where the appearance of the shoulder at 635 nm in highly concentrated samples, accompanied by a small blue shift of the main excitation component and enhanced intensity of the secondary excitation peak at about 525 nm, was indeed observed in the case of high load of LR305 in PMMA matrices [21, 23, 24]. The intrinsically different chemical nature of PMMA and PS as solid matrices should be considered. The strongly polar acrylate side groups in PMMA differ strongly from the almost apolar nature of the alkyl-shielded siloxane macromolecule, so concentration quenching effects in PS-derived samples cannot be ruled out.

Some samples were produced as films of polysiloxane with LR305 deposited on top of a non-doped polysiloxane slab. Films generally had a high concentration in

Fig. 9.10 Emission from the front and rear surface of a sample, exciting at 530 nm. See text for details [14]



order to convert the highest possible number of incoming photons, but this was prevented by the nature of the polysiloxane matrix, as a solubility limit was reached. Moreover, over the time span of 1 month samples with a film of LR305 in polysiloxane over an empty silicone rubber tend to change significantly as the dye in the polysiloxane diffuses through the empty silicone and the samples become red. In addition, diffused LR305 has different optical properties. In Fig. 9.10 the emission spectrum upon excitation at 530 nm of the same sample taken from (a) the front surface (the one with the deposited film) and (b) the rear surface, which is the one where the dye had been diffused, is shown. The emission is shifted by 10 nm (the maximum being located at 595 nm in the front surface case and 605 nm in the rear surface case).

This indicates that LR305 does not interact with the lattice and is free to move into the polysiloxane, which probably makes for a different arrangement of the molecule inside the lattice, presumably creating some preferential orientation that modifies the spectra as shown in Fig. 9.10.

Gold nanoparticles play the role of promoting the absorption peak at 530 nm and making the transmission of energy more efficient. Samples with embedded gold nanoparticles present an enhancement of the absorption peak at 530 nm only for higher concentrations as shown in Fig. 9.11; for lower concentrations the difference is not appreciable; in fact the absorption bands of the two molecules (dyes and gold nanoparticles) overlap. Exciting on the red band the emission is always less intense than in the sample without the Au nanoparticles.

Gold nanoparticles (Au NPs) are able to enhance the emission efficiency of dye molecules, acting as nano-antennae. In this case, through the resonance energy transfer process, the dye absorption is improved and, in turn, emission is enhanced. However, the realisation of such a system is not trivial and requires a close proximity of the dye molecule to the gold cluster, to the extent that the boundary gold atoms can be seen as “grafted” to the organic molecule. This molecular architecture was successfully obtained through Au NPs and rhodamine molecule, exploiting the electrostatic attraction between the cationic form of the dye and the

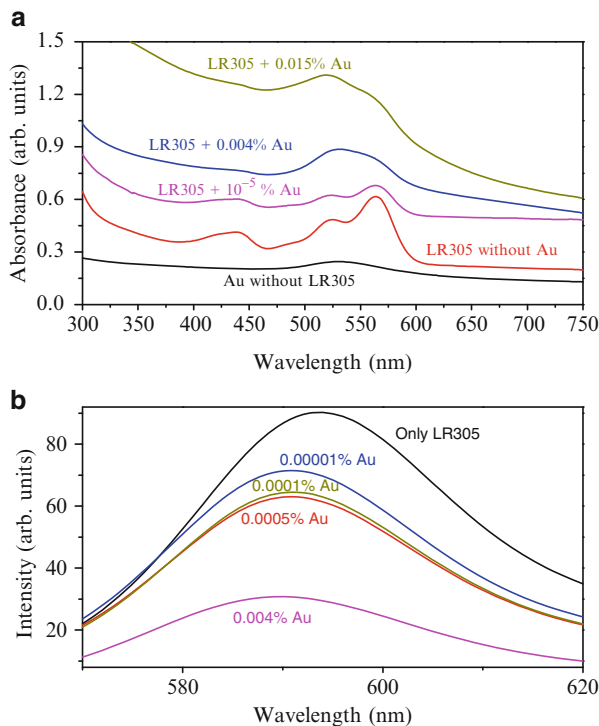


Fig. 9.11 (a) Absorption spectra of a polysiloxane film doped solely with gold and polysiloxane waveguides doped with 0.001 wt% LR305 and with different concentrations of gold. (b) Emission spectra ($\lambda_{\text{ex}} = 540$ nm) of 0.001 wt% LR305-doped samples with different gold concentrations [13]

negative charge lying on the surface of the nanoparticles [25]. In this work, which is to some extent a preliminary step on the path towards Au NP/dye complexes, the interaction between growing NP and dye is negligible, though carbonyl moieties on the diimide portion of LR305 were expected to establish coordination with gold atoms. Unfortunately, the lack of any appreciable benefit to emission intensity in bulk samples seems to indicate that this effect did not take place.

6 LSCs

The Lumogen series dyes were tested as LSCs in order to evaluate their performance inside matrices.

For application as an LSC, the Lumogen series was studied and the most promising dye was identified. The results are presented in Fig. 9.12; some dyes as Lumogen Blue 650 and Yellow 170 have worse results than plain polysiloxane,

Fig. 9.12 Performance comparison within the Lumogen series. Concentrations are 0.1 wt% [14]

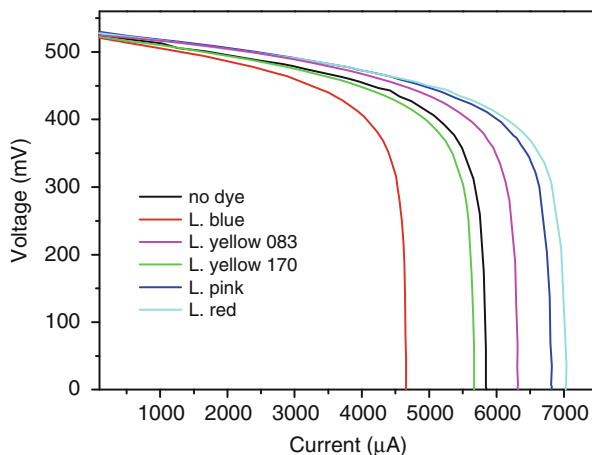
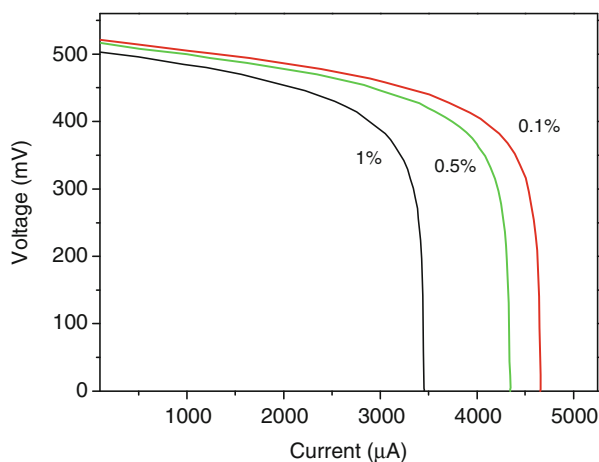


Fig. 9.13 Current–tension curves from samples with three concentrations (1, 0.5, and 0.1 wt%) of Lumogen Blue650 [14]



while Lumogen Red 305 and Pink 285 perform fairly well, aided by broader absorption spectra.

Dyes that have smaller Stokes shifts, such as Lumogen Blue 650 and Yellow 170, caused a decrease in power output when tested with a silicon photodiode whose efficiency peaks at 1,100 nm. Comparison of different concentrations of the same dye demonstrated the influence of reabsorption: lower dye concentrations gave better responses in power output (see Fig. 9.13).

Having established that Lumogen Red 305 is the best option available to us for LSC purposes, we began the production and testing of larger samples in earnest.

Both bulk and thin-film samples were produced; all samples had their top surface exposed to light from a solar simulator, and the emissions from the four edges measured with an integrating sphere and the average single edge output were evaluated integrating the emission between 400 and 800 nm. The efficiency of

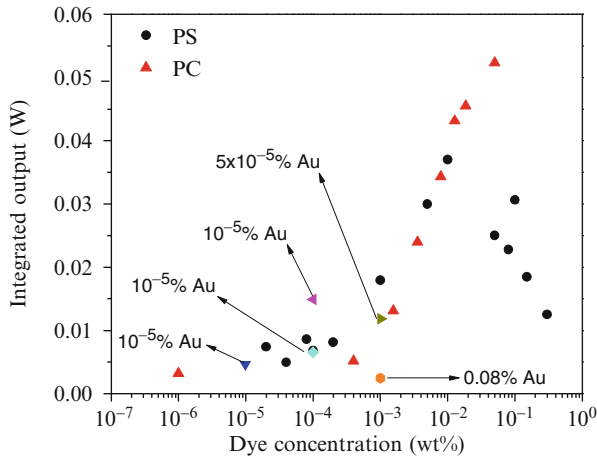


Fig. 9.14 Measurements of output power from the samples with an integrating sphere. A comparison between polysiloxane samples at different doping concentrations is presented and compared to data from dye-filled (poly)carbonate (PC) waveguides [13]

the samples was compared with that of a few PC samples doped with the same dye molecule [26]—see Fig. 9.14. Polysiloxane displays a comparable behaviour to PC samples at low dye concentrations (up to a value of 0.01 wt% of LR305), after which there is a pronounced decrease in output power from the polysiloxane samples while the PC samples continue to show increased output all the way to ~ 0.1 wt%. The addition of gold nanoparticles to the polysiloxane matrices did not have a significant impact on the edge emission results. This suggests that the dye molecule behaves differently in different matrices, in agreement with the fluorescence spectra of LR305 in polysiloxane (as previously reported) and polycarbonate [17–29]. The emission decrease in polysiloxane-derived samples for high dye concentrations can be ascribed to a decrease in the solubility of the dye within the matrix and to aggregation phenomena, giving rise to fluorescence quenching, through reabsorption or activation of non-radiative decay paths. As previously discussed, though no clear evidence of the formation of excimers or aggregates comes from the excitation and emission spectra of the samples, the different chemical environment experienced by LR305 molecules dispersed in a strongly polar environment (as in the case of PMMA or PC) or in an almost non-polar medium (as in the case of polysiloxane) may influence the properties of the sample.

Studying the samples under a solar simulator with three different types of cells we obtained similar responses as those obtained with the integrating sphere. For all three types of cells used (GaAs, InGaP, and Si photodiode) the best performance observed corresponded to a 0.01 % concentration of LR305, though for the GaAs solar cells the response of the sample with 0.005 % LR305 was comparable.

From the results reported in Table 9.1 below it is possible to compare the power output produced by some significant samples.

Table 9.1 Results obtained with selected samples and solar cells

Sample	Power Si (mW)		Power InGaP (mW)		Power GaAs (mW)	
Non-filled PS	0.75		0.33		2.42	
0.001 % LR PS	1.19	59 %	0.59	79 %	2.80	16 %
0.005 % LR PS	1.52	103 %	0.62	88 %	2.99	24 %
0.01 % LR PS	1.67	123 %	0.75	127 %	2.85	18 %

A clear trend in performance can be derived from the results in Table 9.1. The efficiency of the InGaP cells peaks around 500–600 nm. GaAs solar cells do not benefit much from application to the edges of LSCs, as their efficiency curve is almost flat in the wavelength range where the dye collects and re-emits light (their efficiency peaks around 800 nm). The efficiency of the Si photodiode is very poor in the range 400–590 nm; hence the collection of light at lower wavelength and re-emission at higher wavelength can make for a considerable improvement, as can be deduced from the EQE.

The optical matching between the solar cells and LSCs was quite different: the Si photodiode was used as received (this comprised the polymeric window in front of the cell surface), the GaAs solar cell was embedded in a thick layer of polysiloxane of the same type as that of the LSC, while a thin polyester film protected the InGaP cell from the sample and a dielectric thin strip prevented the Au contacts from collapsing into the slot. The presence of two thin films on the Si Ph and InGaP solar cells favours the transmission of light, while the thick polysiloxane on GaAs seems to work as a dispersive media.

An intriguing observation was made when, because of the solidification of a bubble, a sample was left with a large (about 1 cm in diameter) depression in the middle of the light-facing surface. When the power output of this deformed sample was compared to that of “normal” samples with the same dye concentration (10^{-4} % LR305) it was noticed that the former actually performed better than the latter: the silicon photodiode, respectively, yielded 1.12 and 0.97 mW. The power output of the deformed sample was found to be higher than that exhibited by smooth, higher concentration (10^{-3} wt%) samples even with the GaAs cell. This suggests that a perfectly flat light-facing surface may not be required for good LSC performance.

In Table 9.2 a comparison between samples of different lengths is reported. The maximum power is higher for shorter samples. For example, with the 5 cm sample with 0.001 % LR the maximum power was 0.59 mW, while a 12 cm sample with the same dye concentration displayed a power output of only 0.49 mW; at the concentration of 0.01 % LR, the maximum powers of the shorter and longer samples, respectively, were 0.74 and 0.68 mW.

Another intriguing observation was made comparing the performance of two adjacent shorter (5 cm) samples, one of which fully lit, to a non-uniformly lit longer (12 cm) sample (see Fig. 9.15). Not only was the power output higher in the former set-up than with the latter (see Table 9.2), but also the power output of the longer sample was smaller than the power output of *one* shorter sample. Note that the

Table 9.2 Results with selected samples of different length, collected with the InGaP solar cell under a solar simulator

Sample concentrations	InGaP maximum power (mW)
Empty	0.34
0.001 % LR	0.59
0.001 % LR long	0.49
0.01 % LR	0.74
0.01 % LR long	0.68

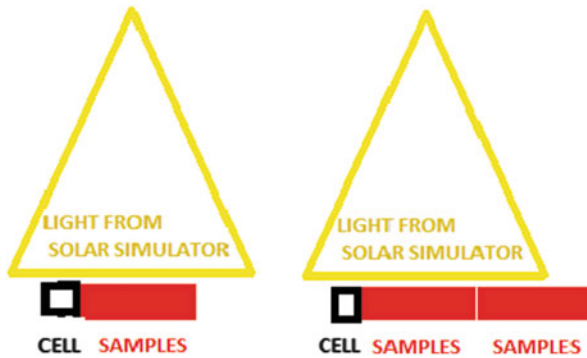


Fig. 9.15 Schematic representation of the experimental set-up for comparing the performance of one shorter sample with that of two adjacent shorter samples or one longer sample. The solar simulator could not uniformly light the second shorter sample or the longer one [14]

position of the cell relative to the light source remained constant so as to make results fully comparable.

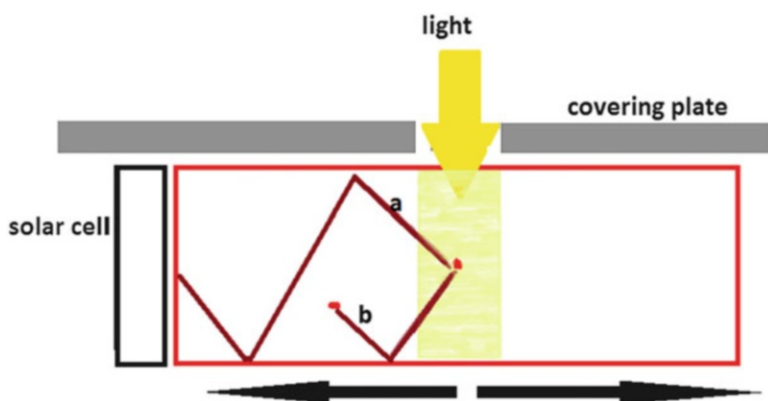
Interestingly, this result was reversed when the measurements were repeated in actual sunlight, the longer sample now performing better than one or two shorter samples. As a complete set of measurements obviously required some time, in order to obtain fully comparable results (characterised by common illumination conditions) only the short circuit current was measured. The open-circuit voltage depends on many factors but mainly on the cell itself and its temperature. For this reason, all the measurements were carried out with the same cell, and only the short circuit current (that under our experimental conditions was a fair representation of power) was collected. All the measurements were collected over as short a time as possible, and the empty cell was measured both at the beginning and at the end of the session to guarantee that lighting conditions had not changed (Table 9.3).

With all three cell types, the longer samples outperformed the shorter devices. The best performance was achieved by a sample with a concentration of 0.01 % LR305, in agreement with the results obtained with the integrating sphere.

In order to investigate the discrepancy between the results obtained with the solar simulator and those obtained with actual sunlight, the samples were retested

Table 9.3 Short circuit current measurements performed in open air

Sample concentrations	InGaP I_{sc} (mA)	GaAs I_{sc} (mA)	Silicon I_{sc} (mA)
Empty	0.50	3.31	4.08
0.001 % LR	0.89	3.95	6.42
0.001 % LR long	1.27	4.50	8.28
0.005 % LR	1.15	4.40	5.96
0.005 % LR long	1.23	4.70	6.88
0.01 % LR	1.22	4.51	6.05
0.01 % LR long	1.80	5.37	9.18

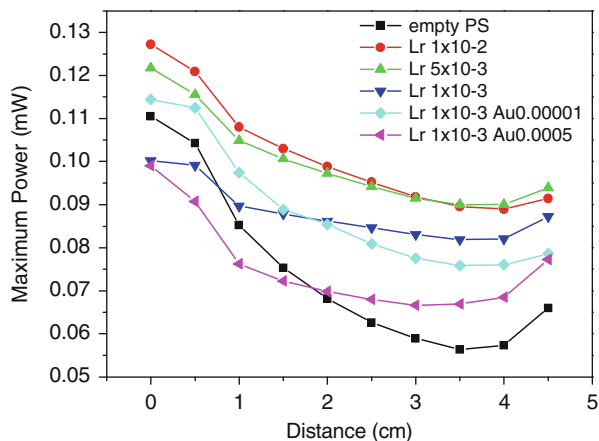
**Fig. 9.16** Only a slice is lit in the LSC device. A photon re-emitted by a dye molecule may be eventually absorbed by the cell (a) or by another dye molecule (b) [14]

(collecting, as always, the maximum power at the edge) illuminating only one “slice” at a time, as shown in Fig. 9.16.

The power corresponding to the first point in Fig. 9.17 is particularly high due to scattering of an amount of light directly from the solar simulator. The last two points, to which a higher power output corresponds than that displayed by the preceding points, are on the other hand affected by edge reflection effects [30, 31]. Neglecting the first and last points an exponential-like behaviour is apparent, in accordance with Batchelder’s work [32].

The results indicate that the power collected when the non-doped polysiloxane sample is completely illuminated equals the sum of the powers collected illuminating the single slices (see Fig. 9.17); the sum of the single-slice powers is nevertheless systematically less than the whole-sample power when a doped sample is considered. In fact, while the sum of the single-slice powers with the empty polysiloxane sample is 0.74 mW and the whole-sample power is 0.75 mW, in the case of a 0.01 % LR305 sample the sum of the single-slice powers is 1.01 mW and the whole-sample power is 1.68 mW; when the concentration of LR305 is 0.005 %

Fig. 9.17 Maximum power of selected samples as a function of the distance between the illuminated portion of the sample and the Si cell surface. The width of the illumination window was 5 mm [14]



the figures are 0.99 and 1.53 mW, and when the concentration is 0.001 % they are 0.88 and 1.19 mW.

Although complete investigation of this phenomenon is outside the scope of the present project, reabsorption is the likely reason [33–35]. A high dye concentration, while beneficial in the portions of the sample that are thoroughly lit, may be altogether detrimental in portions that are not. Concentrators may thus be envisaged with gradients in dye content so as to accommodate fixed gradients in illumination due to the proximity of shadowing or reflecting elements.

7 Conclusions

LSCs are promising for the manufacturing of small-size PV devices. In particular, the development of flexible polysiloxane-based LSCs may make possible the exploiting of ambient light. A further advantage of polysiloxane is its ease of use: it is possible to produce LSCs that can be stuck onto virtually any surface or easily replaced when their service life expires. Polysiloxanes with Lumogen Red 305 dye have demonstrated a good efficiency.

The use of optical and direct measurements with solar cells improves our comprehension of the phenomena that take place inside LSCs, providing experimental figures against which present theoretical predictions of LSC behaviour may be validated.

References

1. <http://rredc.nrel.gov/solar/spectra/am1.5/>. Retrieved 14 Feb 2013
2. Kaiyan, H., Hongfei, Z., Yixin, L., Ziqian, C.: An imaging compounding parabolic concentrator. Proceedings of ISES World Congress 2007, vols. I–V, pp. 589–592 (2009)
3. Winston, R.: Principles of solar concentrators of a novel design. Sol. Energy **16**, 89–95 (1974)

4. Goetzberg, A., Greubel, W.: Solar energy conversion with fluorescent concentrators. *Appl. Phys.* **14**, 123–139 (1977)
5. Weber, W.H., Lambe, J.: Luminescent greenhouse collector for solar radiation. *Appl. Optics* **15**, 2299–2300 (1976)
6. Mansour, A.F.: Outdoor testing of luminescent solar concentrators in a liquid polymer bulk plate of PMMA. *Polym. Test.* **17**, 153–162 (1998)
7. Debije, M.G., Verbunt, P.P.C.: Thirty years of luminescent solar concentrator research: solar energy for the built environment. *Appl. Energy Mater.* **2**, 12–35 (2012)
8. <http://siser.eps.hw.ac.uk/research/conversion.html>. Retrieved 10 Oct 2011
9. Farrel, D.J., Yoshida, M.: Operating regimes for second generation luminescent solar concentrators. *Prog. Photovolt. Res. Appl.* **20**, 93–99 (2012)
10. Verbunt, P.C.P., Kaiser, A., Hermans, K., Bastiaansen, C.W.M., Broer, D.J., Debije, M.G.: Controlling light emission in luminescent solar concentrators through the use of dye molecules aligned in a planar manner by liquid crystals. *Adv. Funct. Mater.* **19**, 2714–2719 (2009)
11. Goetzber, A.: Florescent solar energy collector: operating conditions with diffused light. *Appl. Phys.* **16**, 399–404 (1978)
12. Richards, B.S., Shalav, A., Corkish, R.P.: A low escape cone loss luminescent solar concentrators. 19th E.C. Photovoltaic Solar Energy Conference, Paris, France, 7–11 June 2004, pp. 113–116
13. Hermann, A.M.: Luminescent solar concentrators a review. *Sol. Energy* **29**, 323–329 (1982)
14. Buffa, M.: Coating for energetic and sensing applications. PhD Thesis, Trento (2012)
15. Young, M.: *Optics and Lasers: Including Fibers and Optical Waveguides*. Springer, Germany (2000)
16. Slooff, L.H., Bende, E.E., Burgers, A.R., Budel, T., Pravettoni, M., Kenny, R.P., Dunlop, E.D., Büchtemann, A.: A luminescent solar concentrator with 7.1% power conversion efficiency. *Phys. Status Solidi RRL* **2**, 257–259 (2008)
17. Tanaka, N., Barashkov, N., Heath, J., Sisk, W.N.: Photodegradation of polymer-dispersed perylene di-imide dyes. *Appl. Optics* **45**, 3846–3851 (2006)
18. Kinderman, R., Sloof, L.H., Burgers, A.R., Bakker, N.J., Buchtemann, A., Danz, R., van Roosmalen, J.A.M.: I-V Performance and stability of dyes for luminescent plate concentrators. *J. Sol. Energy Eng.* **129**, 277–283 (2007)
19. Sloof, L.H., Kinderman, R., Burgers, A.R., Bakker, N.J., van Roosmalen, J.A.M., Buchtemann, A., Danz, R., Schleusener, M.: Efficiency enhancement of solar cells by application of a polymer coating containing a luminescent dye. *J. Sol. Energy. Eng.* **129**, 272–276 (2007)
20. <http://www2.basf.us/additives/pdfs/p3201e.pdf>. Retrieved 30 Jan 2012
21. Colby, K.A., Burdett, J.J., Frisbee, F.F., Zhu, L., Dillon, R.J., Bardeen, C.J.: Electronic energy migration on different time scales: concentration dependence of the time-resolved anisotropy and fluorescence quenching of Lumogen Red in Poly(methyl) methacrylate. *J. Phys. Chem. A* **114**, 3471–3482 (2010)
22. Al-Kaysi, R.O., Ahn, T.S., Muller, A.M., Bardeen, C.J.: The photophysical properties of chromophores at high (100 mM and above) concentrations in polymers and as neat solids. *Phys. Chem. Chem. Phys.* **8**, 3453–3459 (2006)
23. Fara, V.L., Grigorescu, R., Dimofte, C.: Optimum efficiency of fluorescent solar concentrators. In: *Optical Materials Technology for Energy Efficiency and Solar Energy Conversion XI: Selective Materials, Concentrators and Reflectors, Transparent Insulation and Superwindows*, pp. 306–312. SPIE, Toulouse-Labege, France (1992)
24. Wilson, L.R.: Luminescent solar concentrators: a study of optical properties, re-absorption and device optimization. Ph.D. Thesis, Edinburgh (2010)
25. Iosin, M., Baldeck, P., Astilean, S.: Plasmon-enhanced fluorescence of dye molecules. *Nucl. Instrum. Methods Phys. Res. B* **267**, 403–405 (2009)
26. Debije, M.G., Verbunt, P.P.C., Rowan, B.C., Richards, B.S., Hoeks, T.L.: Measured surface loss from luminescent solar concentrator waveguides. *Appl. Optics* **47**, 6763–6768 (2008)

27. Mansour, A.F., et al.: Laser dyes doped with poly(ST-Co-MMA) as fluorescent solar collectors and their field performance. *Polym. Test.* **24**, 519–525 (2005)
28. Seybold, G., Wagenblast, G.: New perylene and violanthrone dyestuffs for fluorescent collectors. *Dyes Pigments* **11**, 303–317 (1989)
29. Slooff, L.H., Kinderman, R., Burgers, A.R., Büchtemann, A., Danz, R., Meyer, T.B., Chatten, A.J., Farrell, D., Barnham, K.W.J., Van Roosmalen, J.A.M.: The luminescent concentrator illuminated. *Proc. SPIE* **6197**, 1–8 (2006)
30. Peters, M., Goldschmidt, J.C., Löper, P., Bläsi, B., Gombert, A.: The effect of photonic structures on the light guiding efficiency of fluorescent concentrators. *J. Appl. Phys.* **105**, 0149010–0149013 (2009)
31. Chatten, A.J., Barnham, K.W.J., Buxton, B.F., Ekins-Daukes, N.J.: A new approach to modelling quantum dot concentrators. *Sol. Energy Mater. Sol. Cells* **75**, 363–371 (2003)
32. Batchelder, J.S., Zewail, A.H., Cole, T.: Luminescent solar concentrators. 1: Theory of operation and techniques for performance evaluation. *Appl. Optics* **18**, 3090–3110 (1979)
33. Sholin, V., Olson, J.D., Carter, S.A.: Semiconducting polymers and quantum dots in luminescent solar concentrators for solar energy harvesting. *J. Appl. Phys.* **101**, 123114-1–123114-9 (2007)
34. Earp, A.A., Smith, G.B., Franklin, J.B., Swift, P.D.: Optimisation of a three-colour luminescent solar concentrator daylighting system. *Sol. Energy Mater. Sol. Cells* **84**, 411–426 (2004)
35. Rowan, B.C., Wilson, R., Richards, B.S.: Advanced material concepts for luminescent solar concentrators. *IEEE J. Sel. Top. Quantum Electron.* **14**, 1312–1321 (2008)

Chapter 10

Engineering FRET-Based Solar Cells: Manipulation of Energy and Electron Transfer Processes in a Light Harvesting Assembly

Soumik Sarkar, Samim Sardar, Abhinandan Makhal, Joydeep Dutta, and Samir Kumar Pal

Abstract From the prevalent interest in the advancement of renewable energy sources, dye-sensitized solar cells (DSSCs) have emerged as one of the front running prospects due mainly to a constructive balance between cost and efficiency. In this chapter, we will review our works on the utility of using Förster resonance energy transfer (FRET) in the light harvesting dynamics of zinc oxide (ZnO)-based nanomaterials, which has recently shown promise for significant improvement in various aspects of photoelectrochemical cells. Firstly, we have used ZnO nanoparticles (NPs) and Oxazine 1 as model donor and acceptor, respectively, to investigate the key ultrafast process of FRET in the NP–dye system. The consequence of the energy transfer on the performance of a model ZnO NP-based DSSC has also been explored by using well-known Ruthenium-based sensitizers N719 attached to ZnO NPs offering as an intrinsic co-sensitizer. By using a picosecond-resolved FRET technique, we have also demonstrated the role of the gold layer in promoting photoinduced charge transfer from ZnO–Au nanocomposite to a model contaminant methylene blue (MB). Due to the formation of the Schottky barrier at the ZnO–Au interface and the higher optical absorptions of the ZnO–Au photoelectrodes arising from the surface plasmon absorption of the Au NPs, enhanced power-conversion efficiency was achieved compared to bare ZnO-based DSSCs. Finally, potential co-sensitization of extrinsic sensitizer CdTe quantum dots (QDs) in ZnO nanorod (NR)-based DSSCs has been established where we have shown two major pathways by which CdTe QDs may contribute to the net photocurrent in a DSSC: (1) a direct injection of charge carriers from QDs

S. Sarkar • S. Sardar • A. Makhal • S.K. Pal (✉)

Department of Chemical, Biological and Macromolecular Sciences, S.N. Bose National Centre for Basic Sciences, Block JD, Sector III, Salt Lake, Kolkata 700 098, India
e-mail: skpal@bose.res.in

J. Dutta

Water Research Center, Sultan Qaboos University, PO Box 17, 123 Al-Khoudh, Sultanate of Oman

to ZnO semiconductor via photoinduced electron transfer (PET) and (2) an indirect excitation of the sensitizing dye N719 molecules by funneling harvested light via FRET. Based on these advantages, the short-circuit current density and the photoconductivity of the QD-assembled DSSCs with distinct architectures are found to be much higher than DSSCs fabricated with N719 sensitizer only. As demonstrated, the multipath enhancement offered in this device architecture results in an increased and extended photo-response with respect to the individual materials employed. Further engineering of suitable donor acceptor pairs and optimization of charge separation in conjugated molecular blends has the potential to become a continuing avenue toward enhancing hybrid DSSC efficiencies.

1 Introduction

The promising dye-sensitized solar cell (DSSC) is a relatively new class of low-cost solar cells suitable for renewable electricity generation [1, 2]. It is based on the process of conversion of solar energy to electrical energy by employing sensitizers adsorbed on the surface of wide band gap n-type semiconductor metal oxide nanoparticles (NPs), typically TiO_2 [3], ZnO [4], SnO_2 [5], Nb_2O_5 [6], etc. During the operation, photons intercepted by sensitizers create electron-hole pairs that are rapidly separated at the NP surface; followed by electrons injected into the semiconductor NPs and holes leaving to the opposite side of the device by means of redox species (usually I^-/I_3^-) in an electrolyte in liquid [7] or solid state [8]. State-of-the-art TiO_2 -based DSSCs using Ruthenium sensitizers, which primarily absorbs light in the region of 350–700 nm, offer power-conversion efficiency of only 11 % [9] and it has been recognized that the key improvement of the efficiency of DSSCs is to increase their spectral absorption range. In a recent study, it has been estimated that a DSSC with power-conversion efficiency of 15 % using I^-/I_3^- redox couple must absorb ~ 80 % of the solar spectrum from 350 to 900 nm [10]. Light absorption in DSSCs is determined by the molar extinction coefficient of the sensitizers, the surface coverage of the dye (dye molecules nm^{-2}), and the total surface area of the oxide film [11]. The sensitizers have traditionally been made from ruthenium-based complexes (for example, N719, Z907) [9, 12] that have fairly broad absorption spectra ($\Delta\lambda \approx 350$ nm) but low molar extinction coefficients ($5,000\text{--}20,000 \text{ M}^{-1} \text{ cm}^{-1}$). Organic dyes have recently been developed with substantially higher molar extinction coefficients ($50,000\text{--}200,000 \text{ M}^{-1} \text{ cm}^{-1}$), but they have very narrow spectral bandwidths ($\Delta\lambda \approx 250$ nm) [13]. Dye cocktails lead to a broader absorption spectra [14], but because of the absence of dyes that absorb efficiently in the red part of the spectrum, generally a lower efficiency is achieved. As dyes with strong absorptivity do not typically exhibit broad absorption overlapping the solar spectra, this is one of the major pitfalls of using dyes as photosensitizers in solar cells [15]. In an attempt to achieve enhanced light absorption and to broaden the spectral response, co-sensitization of the semiconductor NPs (titania) by dyes with complementary absorption spectra, has recently been

demonstrated [16]. However, the limitations of available sites at the surface of semiconductor NPs for the co-sensitizing dyes constrain the total light absorbed in the solar cells.

To improve the possibility of enhanced light absorption, the use of Förster resonance energy transfer (FRET), also known as electronic energy transfer, has recently experienced widespread research interest of several groups [17–22] including ours [23–27]. The mechanism of FRET involves a donor in an excited electronic state, which may transfer its excitation energy to a nearby acceptor in a non-radiative fashion through a long-range dipole–dipole interaction [28]. The theory is based on the concept of treating an excited donor as an oscillating dipole that can undergo energy exchange with a second dipole having similar resonance frequency. In principle, if the fluorescence emission spectrum of the donor molecule overlaps the absorption spectrum of an acceptor molecule, and the two are within a minimal distance (1–10 nm) from one another, the donor can directly transfer its excitation energy to the acceptor via exchange of a virtual photon. It is evident from the recent literatures that FRET serves as a popular signal transduction mechanism to develop bio-sensing systems and bioassays for proteins, peptides, nucleic acids, and small molecules [29–33]. FRET-based quantum dot (QD) pH sensors have been made [34], and electrical control of FRET in QDs has been demonstrated [35]. FRET in organic molecules has been used to study conformational changes in DNA [36] and to detect DNA with high sensitivity [37]. It has also been used in solar concentrators [38] and to improve quantum yields in organic light-emitting devices [39, 40]. Most importantly, FRET shows promise toward efficient solar energy conversion by using inexpensive and engineered fabrication processes in both QD-sensitized solar cells (QDSSCs) and DSSCs. In QDSSCs, the use of QDs as light harvesters has stimulated a lot of interests because of its higher extinction coefficient compared to conventional dyes [41] for efficient light energy conversion [42–45]. Because of the size quantization property, the optical and electronic properties of the semiconductor QDs can be engineered to further tune the response of QDSSCs [46–48]. In addition, QDs open up new possibilities for the utilization of hot electrons [49] or multiple charge carrier generation with a single photon [50]. Multiple-carrier generation in PbSe nanocrystals has shown that two or more excitons can be generated with a single photon of energy greater than the band gap [51]. The performance of a QDSSC is currently limited by several factors, including a limited choice of electrolytes with which QDs are chemically compatible, insufficient passivation of recombination channels (usually attributed to surface traps), and limited QD-loading capacities [52]. Recent studies have shown that it is possible to stabilize CdS QD-based DSSCs by coating the QD-sensitized nanoporous electrodes with a thin amorphous TiO₂ layer, which enables the use of various QD sensitizers in the presence of iodine-based electrolytes [53]. Utilizing two sensitizing layers of sensitizers N719 and CdS QDs separated by an amorphous TiO₂ layer, a significant increase in cell efficiency compared to a QD monolayer cell has been reported [54]. In a more recent study, Etgar et al. have used a cobalt complex (Co²⁺/Co³⁺) as an electrolyte in the solar cells, which permits direct

contact between the QDs and the electrolyte [17]. Choi et al. have recently demonstrated the coupling of semiconductor nanocrystal and a red-NIR organic dye with complementary spectral absorption in the visible region [55]. Alternatively, the employment of FRET from covalently linked energy donor molecules to the semiconductor (titania) surface-attached sensitizers has been demonstrated in the literature [56], where higher excitation transfer efficiency (>89 %) between attached dye molecules followed by a subsequent improvement in the device external quantum efficiency of 5–10 % between 400 and 500 nm spectral range has been reported. The overall enhancement of power conversion efficiency of the DSSC was still low (<9 %), which was argued to arise because of an increase in the open-circuit voltage (V_{OC}) rather than because of an increase in the short-circuit photocurrent density (J_{SC}). Recently, it has been demonstrated that unattached, highly-luminescent chromophores inside a liquid electrolyte can absorb high-energy photons and can efficiently transfer the energy to the anchored near-infrared sensitizer leading to an increase in optical absorption efficiency [15]. In another work, enhancement in photovoltaic device performance has been reported using long-range resonant energy transfer from a dissolved luminescent dopant confined in the interwire spaces of a nanowire array electrode to an acceptor species confined at the surface of the nanowires [20].

Although most of the reported works on DSSCs are based on TiO_2 porous thin films, various nanostructures of ZnO have also been used for DSSC fabrication [8, 57, 58]. The advantages of using ZnO over TiO_2 are its direct wide band gap (3.37 eV), higher exciton binding energy (60 meV) compared to TiO_2 (4 meV) [59, 60], and higher electron mobility ($200 \text{ cm}^2 \text{ V}^{-1} \text{ s}^{-1}$) over TiO_2 ($30 \text{ cm}^2 \text{ V}^{-1} \text{ s}^{-1}$), while the conduction band edges of both materials are located at approximately the same level [61]. This unique combination of properties opens, in principle, wide possibilities of using ZnO in DSSC fabrication. An irreversible electron injection from organic molecules into the conduction band of ZnO semiconductor was first experimentally evidenced by H. Tributsch and M. Calvin [62]. Nowadays, this efficient electron transporting material shows promises in various technologies similar to DSSCs, such as inverted polymer solar cells [63, 64], QDSSCs [65, 66], and hybrid light emitting diodes [67]. Another advantage of using ZnO over TiO_2 is different morphologies such as nanoparticles [68, 69], hierarchical aggregates [70, 71], porous films [72], nanosheets [73], nanowires [8, 74], tetrapods [75], hollow tubes [76] can be prepared with relative ease. A large range of fabrication procedures is available for ZnO nanostructures, such as sol-gel processes [77, 78], chemical bath deposition, including hydrothermal [74], electrodeposition [72], spray pyrolysis [71], polyol hydrolysis [79], chemical vapor deposition [80], etc. However, the efficiency of DSSCs based on ZnO nanostructures is still very low (7.5 %) [71]. One of the possibilities to enhance the efficiency of ZnO-based DSSC is the enhancement of the light absorbing ability of the DSSC. It has to be noted that ZnO can absorb high-energy photons (>3.37 eV) and offers photoluminescence (PL) in the visible region (2.25 eV) [27, 81]. Careful use of the defect mediated ZnO PL for the excitation of the surface

adsorbed sensitizer, in order to enhance the overall efficiency of the ZnO-based DSSC will be discussed. We also approached to fabricate the composite nanocluster-based DSSCs where Au NPs have been employed to facilitate efficient charge separation, thus serving as a Schottky-barrier for reducing the rate of electron-hole recombination. In another study, we have demonstrated that size tunable CdTe QDs capped with 3-mercaptopropionic acid (MPA), assembled in an N719-sensitized solar cell, can absorb visible-light in the gaps, where sensitizer N719 has lower absorption or does not absorb any light. In this design, QDs serve as a co-sensitizer that can directly transfer electrons to ZnO NRs. Moreover, the QDs, those are not in a direct attachment to the ZnO NR surface, funnel the absorbed energy to nearby dye molecules via FRET rather than contributing directly as sensitizers. By using steady-state and picosecond-resolved fluorescence spectroscopy, we have demonstrated that PL from QDs can be useful to excite the sensitizer molecules for an enhanced light absorption. The consequence of QD-mediated electron and energy-harvesting processes on the overall performance of a model QD-assembled DSSC will also be discussed in the following sections.

2 Materials and Methods

2.1 Preparation of ZnO Nanoparticles (NPs) and ZnO–Au Nanocomposites (NCs)

In order to synthesize colloidal solution of ZnO NPs, zinc acetate dihydrate, Zn(CH₃COO)₂·2H₂O (Merck) was used as starting material. ZnO NP colloidal solution in ethanol was synthesized by following our earlier reports [81–83]. Briefly, A 20 ml 4 mM zinc acetate solution was prepared in ethanol (Merck) followed by a dilution up to 50 % by adding another 20 ml fresh ethanol to the solution. Then 20 ml of 4 mM NaOH solution in ethanol was added to it under constant stirring. The reaction beaker was then kept in a preheated water bath at 60 °C for 2 h to hydrolyze, after which a transparent ZnO NP colloid was obtained. Next, ZnO–Au NC colloid was prepared by in situ synthesis of Au NPs on the surface of the ZnO NPs. 5 ml of 1 mM chloroauric acid, H₂AuCl₄·H₂O (Sigma) ethanolic solution was slowly added to as-synthesized ZnO NP colloid under constant stirring at 25 °C. The stirring was continued for 15 min. Then 7 ml of 5 mM sodium borohydride, NaBH₄ (Sigma), in ethanol solution was added drop-wise to the solution in order to reduce gold chloride to Au NPs. Immediately after adding NaBH₄, the solution became red from pale yellow indicating the formation of the Au NPs in the ZnO NP colloid. The weight ratio between ZnO and Au after the preparation process was found to be 1.3:1. The colloidal solutions of ZnO NPs and ZnO–Au NCs were used to perform all the spectroscopic studies.

2.2 Preparation of ZnO Nanorods (NRs)

The most widely used fabrication method to obtain vertically-aligned ZnO nanostructures is the hydrothermal method [84]. First, FTO substrates were cleaned ultrasonically with soap water, acetone, ethanol, and deionized (DI) water. 15 mM of zinc acetate dihydrate was dissolved in 10 mL of DI water, which was sprayed on top of the clean FTO substrates (from a distance of 25 cm) at a rate of 1 mL min^{-1} . The substrates were preheated to $420 \text{ }^\circ\text{C}$ on a hot-plate before spraying. After spraying 10 mL completely, the substrates were allowed to cool to room temperature followed by annealing in air at $300 \text{ }^\circ\text{C}$ for 5 h. The ZnO NPs seeded FTO substrates were then placed in a sealed chemical bath containing equimolar concentration of zinc nitrate hexahydrate and hexamethylenetetramine (20 mM) at $95 \text{ }^\circ\text{C}$ for 20 h. This leads to the growth of ZnO NRs of length ca. 3–4 μm , diameter 100–200 nm. The ZnO NRs coated substrates were then retracted from the chemical bath, were rinsed several times with DI water, and were annealed at $350 \text{ }^\circ\text{C}$ for 60 min to remove any organic impurities prior to further use.

2.3 Preparation of 3-MPA Capped CdTe QDs

Several synthetic routes to CdTe QDs have been reported [85–90]. In this study, 0.12 mol of CdCl_2 was dissolved in deionized (DI) water. To this solution 0.024 mol of tri-sodium citrate dihydrate, 0.03 mol of Na_2TeO_3 , 0.011 mol of 3-MPA, and 0.086 mol of NaBH_4 were added successively and were stirred to make the stock solution for CdTe QD synthesis. This stock solution was refluxed for 7, 20, and 30 min in a commercial Panasonic microwave oven (low-power mode) to synthesize 440, 500, and 550 nm absorption peak QDs, respectively. The QDs with 610 nm absorption peak were synthesized by refluxing the stock solution in a commercial oven at $106 \text{ }^\circ\text{C}$ for 9 h. As-prepared QDs, without any further purification, were used in the fabrication of QD decorated ZnO NR-based DSSCs.

2.4 Fabrication of ZnO-Based DSSCs

The ZnO NP-based photoelectrodes were prepared by in situ synthesis of ZnO NPs on commercial fluorinated tin oxide (FTO) glass substrates (Asahi, Japan) using a simple hydrothermal process [84]. CdTe QD-decorated photoelectrodes (PEs) were fabricated by dipping the ZnO NR coated FTO (as discussed in Sect. 2.2) into CdTe colloid at $60 \text{ }^\circ\text{C}$ for 3 h. The photoelectrodes were removed, were washed with ethanol, and were annealed at $165 \text{ }^\circ\text{C}$ for 1 h. This cycle was repeated three times to obtain a uniform layer of CdTe particles on the ZnO surface. For co-sensitizing the photoelectrodes with N719 dye, the as-prepared CdTe QD coated PEs were dipped

into a 0.5 mM dye N719 in ethanol solution for 24 h in dark at room temperature. After 24 h, the substrates were withdrawn from the dye solution and were rinsed with ethanol several times in order to remove the excess dye on the film surface. We define this geometry of the sample as ZnO–QD–N719. In another architecture, we have dipped the ZnO NR with N719 first, and then PEs were coated with CdTe QDs (ZnO–N719–QD architecture). The same procedures were followed to prepare the substrates for the time-resolved measurements, only by replacing FTO plates with quartz. The photoelectrodes sensitized with N719 only (control) were fabricated by dipping ZnO photoelectrodes directly into 0.5 mM dye solution for 24 h following a similar procedure as described above. The photoelectrodes were then dried in dark at room temperature in a controlled humidity chamber (40 % humidity) for 2 h. A thin layer of platinum (Pt) catalyst deposited on the FTO substrates was used as a counter electrode to assemble the DSSC. The counter electrodes were prepared by dropping 10 μL of 5 mM chloroplatinic acid ($\text{H}_2\text{PtCl}_6\cdot\text{H}_2\text{O}$) solution in isopropanol on FTO substrates followed by the thermal decomposition of the $\text{H}_2\text{PtCl}_6\cdot\text{H}_2\text{O}$ to Pt NPs at 385 $^\circ\text{C}$ for 30 min. A single layer of Surlyn 1702 (50 μm thickness) from Dupont was placed between the two electrodes, and the device was sealed. The liquid electrolyte composed of the 0.5 M LiI, 0.05 M I_2 , and 0.5 M 4-*tert*-butylpyridine (TBP) in acetonitrile (ACN) was then filled in the cell using capillary force through small holes drilled on the counter electrode. Finally, the holes in the counter electrode were sealed to prevent the electrolyte from leaking. It is to be noted that, QDs are relatively less stable in iodine-based electrolyte [91], and in the technological applications of QD-decorated solar cells selection of other iodine-free electrolytes would be more appreciated. The characteristics of the solar cells reported here were recorded immediately after filling in the electrolytes in the sandwich structure in order to minimize losses due to corrosion of the CdTe QDs [48].

2.5 Characterization Methods

High-resolution transmission electron microscopy (HRTEM) experiments are performed by FEI (Technai S-twin) instrument operated at 200 kV. Scanning electron microscopy (SEM) images were taken using a JEOL JSM-6301F operated at 20 kV. Steady-state absorption and emission spectra were measured with a Shimadzu UV-2450 spectrophotometer and Jobin Yvon Fluoromax-3 fluorimeter, respectively. All the photoluminescence transients were taken using the picoseconds-resolved time-correlated single photon counting (TCSPC) technique. We used a commercially available picosecond diode laser-pumped (LifeSpec-ps) time-resolved fluorescence spectrophotometer from Edinburgh Instruments, UK. The picosecond excitation pulse from the picoquant diode laser was used at 375 and 633 nm with instrument response function (IRF) of 80 ps. A microchannel-plate-photomultiplier tube (MCP-PMT, Hammamatsu) was used to detect the photoluminescence from the sample after dispersion through a monochromator. For all transients the polarizer on the emission side was adjusted to be at 55 $^\circ$ (magic angle) with respect to the

polarization axis of the excitation beam. The observed fluorescence transients were fitted by using a nonlinear least square fitting procedure to a function $(X(t) = \int_0^t E(t') R(t - t') dt')$ comprising convolution of the IRF $(E(t))$ with a sum of exponentials $\left(R(t) = A + \sum_{i=1}^N B_i e^{-t/\tau_i}\right)$ with pre-exponential factors (B_i) , characteristic lifetimes (τ_i) , and a background (A) . Relative concentration in a multi-exponential decay is finally expressed as, $c_n = \frac{B_n}{\sum_{i=1}^N B_i} \times 100$. The average lifetime (amplitude-weighted) of a multi-

exponential decay [28] is expressed as as, $\tau_{av} = \sum_{i=1}^N c_i \tau_i$.

In order to estimate FRET efficiency of the donor (ZnO) and hence to determine distance of donor–acceptor pairs, we followed the methodology described in [28]. The Förster distance (R_0) is given by,

$$R_0 = 0.211 \times [\kappa^2 n^{-4} Q_D J]^{\frac{1}{6}} \text{ (in \AA)} \quad (10.1)$$

where, κ^2 is a factor describing the relative orientation in space of the transition dipoles of the donor and acceptor. For donor and acceptors that randomize by rotational diffusion prior to energy transfer, the magnitude of κ^2 is assumed to be $2/3$. The refractive index (n) of the medium is assumed to be 1.4. Q_D , the integrated quantum yield of the donor in the absence of acceptor are measured with respect to a reference dye. For example, the Q_D value for the colloidal ZnO NPs was measured to be 3.8×10^{-3} by using Coumarin 500 as a reference. J , the overlap integral, which expresses the degree of spectral overlap between the donor emission and the acceptor absorption, is given by,

$$J = \frac{\int_0^\infty F_D(\lambda) \varepsilon_A(\lambda) \lambda^4 d\lambda}{\int_0^\infty F_D(\lambda) d\lambda} \quad (10.2)$$

where, $F_D(\lambda)$ is the fluorescence intensity of the donor in the wavelength range of λ to $\lambda + d\lambda$ and is dimensionless; $\varepsilon_A(\lambda)$ is the extinction coefficient (in $M^{-1} \text{ cm}^{-1}$) of the acceptor at λ . If λ is in nm, then J is in units of $M^{-1} \text{ cm}^{-1} \text{ nm}^4$. Once the value of R_0 is known, the donor–acceptor distance (r_{DA}) can be easily calculated using the formula,

$$r_{DA}^6 = \frac{[R_0^6(1 - E)]}{E} \quad (10.3)$$

Here E is the efficiency of energy transfer. The energy transfer efficiency is measured using the relative fluorescence lifetime of the donor, in absence (τ_D) and presence (τ_{DA}) of the acceptor.

$$E = 1 - \frac{\tau_{DA}}{\tau_D} \quad (10.4)$$

We are also interested to obtain the thickness of the surface layer emitting visible light by using a simple model [92]. In order to obtain the below band gap (BBG) (550 nm, i.e., 2.25 eV) and near band edge (NBE) (365 nm, i.e., 3.39 eV) emission of the ZnO NPs, we have excited the sample with 320 nm (3.87 eV) light. The luminescence peak intensity ratio of the NBE to BBG emission for spherical particles of radius r and with a surface recombination layer of thickness t , is given by [93],

$$\frac{I_{NBE}}{I_{BBG}} = C \left(\frac{r^3}{3rt(r-t) + t^3} - 1 \right) \quad (10.5)$$

The constant C , along with other quantities, contains the oscillator strengths, which in turn depend on the particle morphology. In order to calculate t from the above equation, we have taken the magnitude of C as 3.89 for small spherical particles [93] with radius $r \approx 3$ nm. In our system I_{NBE} (365 nm)/ I_{BBG} (550 nm) ≈ 0.853 . Putting the values in (10.5), the thickness of the surface layer, t , was found to be 1.30 nm. It represents an effective distance from the surface (effective diffusion length), within which the excited carriers recombine at the surface.

We have studied the complexation between ZnO NP with different concentrations of N719 dye. The ratio of the fluorescence intensity of the ZnO NP in the absence (I_0) and presence (I) of the quencher N719 was plotted in Fig. 10.5c, d by using Stern–Volmer equation [28].

$$\frac{I_0}{I} \text{ or } \frac{\tau_0}{\tau} = 1 + K_{SV}[Q] \quad (10.6)$$

where, I_0/I is the relative steady-state emission intensity, τ_0/τ is the relative excited state lifetime and K_{SV} is the Stern–Volmer constant.

In order to measure device performance, the incident photon-to-current conversion efficiency (IPCE) and photocurrent–voltage (J – V) characteristics were determined. The J – V characteristic measurements of the DSSCs were performed under AM1.5G sun irradiation (100 mW cm^{-2}) using 150 W small beam simulator (Sciencetech, model SF150). The IPCE, defined as the number of electrons collected per incident photon, was evaluated from short-circuit photocurrent (J_{SC}) measurements at different wavelengths (λ), and the IPCE was calculated using (10.7),

$$\text{IPCE \%} = [1,240 \times J_{SC}(\text{A/cm}^2)] / [\lambda(\text{nm}) \times P(\text{W/cm}^2)] \times 100 \% \quad (10.7)$$

where, P is the incident light power. The fill factor (FF) and power conversion efficiency (η) of the solar cells can be determined from (10.8) and (10.9),

$$FF = V_M J_M / V_{OC} J_{SC} \quad (10.8)$$

$$\eta = \frac{V_{OC} J_{SC} FF}{P_{in}} \quad (10.9)$$

where, V_M and J_M are the voltage and current density at the maximum power output, J_{SC} and V_{OC} are the short-circuit current and open-circuit voltage, respectively [94, 95].

At a fixed bias voltage of 5 V, the photoconductivity across the thickness of the thin films was measured by using FTO as one of the electrodes and a small (4 mm diameter) drop of mercury (Hg) on top of the film as a counter electrode. The light source (intensity 25 mW cm^{-2}) was turned ON and OFF every 20 s, and the obtained current values were continuously recorded using a programmable multimeter (Gwinstek GDM-396).

3 Results and Discussion

3.1 Dynamics of Light Harvesting in ZnO NPs [23]

In order to understand the key ultrafast processes associated to the dynamics of light-harvesting, we demonstrate our studies on the ultrafast energy transfer dynamics from ZnO NP to a well-known biological marker, Oxazine 1 (OX1). The cationic OX1 dye is supposed to bind at the surface of the n-type ZnO NP. The absorption and emission spectra of ZnO (energy donor) and OX1 (energy acceptor) are shown in Fig. 10.1. The broad emission peak of ZnO NPs centered at 550 nm is attributed to come from defect states at the surface [93, 96].

A. van Dijken et al. [97] proposed that the visible emission is due to the recombination of an electron from the conduction band with a deep electron trapping center of V_O^{++} , which is considered as oxygen vacancy center. Alternatively, K. Vanheusden et al. [98] suggested that the recombinations of isolated V_O^+ centers with photoexcited holes are responsible for the green emission. Because of the large surface-to-volume ratio of the ZnO NPs, efficient and fast trapping of photogenerated holes at surface sites are well speculated. However, the broad emission band can be decomposed into two components. The predominant emission energy is concentrated around the $\lambda = 550 \text{ nm}$ (2.25 eV) line while a smaller emission band occurs at around $\lambda = 495 \text{ nm}$ (2.50 eV). It has been reported that the emission center around 550 nm occurs from defect states near the surface layer (within a shell of t) while the shorter wavelength 495 nm emission occurs from defects near the bulk of the NPs [92, 93], which is located inside at a distance $>t$ from the surface. As the size of the NP is increased, the relative contribution of the 495 nm emission increases. The absorption and emission spectra of the acceptor OX1 at the surface are also consistent with that reported in the literature [99].

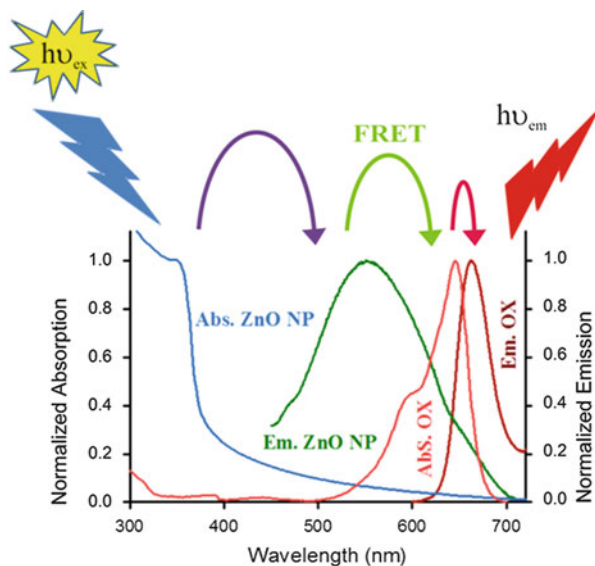


Fig. 10.1 Normalized absorption (*blue*) and emission (*green*) spectra of ZnO NP with diameter of ~6 nm. Cascade harvesting of blue photon to red photon in the ZnO NP–OX1 complex is shown. The normalized absorption and emission of OX1 are shown (Reproduced by permission of the IOP Publishing)

The consistency of the spectral pattern of the acceptor OX1 with the other studies clearly rules out the possibility of any damage of the OX1 molecule at the ZnO surface. The spectral overlap of the ZnO emission spectrum with that of the OX1 absorption spectrum is shown in Fig. 10.2a. The estimated value of the overlap integral is 3.79×10^{15} . The faster excited state lifetime of the ZnO–OX1 adduct with respect to that of the free ZnO NPs is clearly noticeable from Fig. 10.2b. The baseline upliftment comes from the long lifetime component, which is not ending in our experimental time window.

The detailed spectroscopic and fitting parameters of the fluorescence decays are represented in Table 10.1. From the average lifetime calculation for the ZnO–OX1 complex, we obtain the effective distance between the donor and the acceptor, $r_{DA} \approx 1.58$ nm, using (10.3) and (10.4). It is noted that r_{DA} is much smaller than the radius of the NP (~3 nm; inset Fig. 10.2b) and is comparable to the thickness t of the surface layer of the NPs, i.e., $r > r_{DA} \approx t$. In the case of organic acceptor molecules at the surface of a semiconductor QD (CdSe) donor, the overall donor–acceptor distance is reported to be nearly equal (or larger) to the radius of the donor quantum dot [100]. The relatively shorter donor–acceptor distance in the case of ZnO–OX1 system compared to other systems [100] can be rationalized from the fact that the origin of the PL peaking at 550 nm is essentially from the surface layer of approximate thickness 1.3 nm of the ZnO NPs.

In order to compare the FRET efficiency from other emission centers (Scheme 10.1) of ZnO NPs, we have also studied the energy transfer dynamics at $\lambda_{em} = 495$ nm. The relative dynamical quenching of the ZnO–OX1 system with

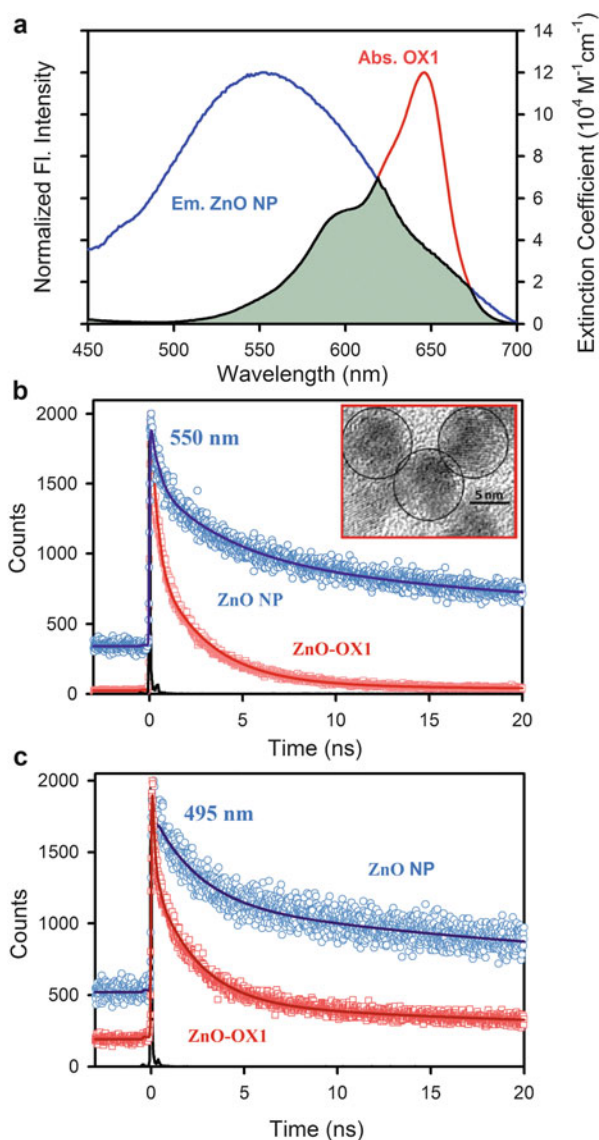
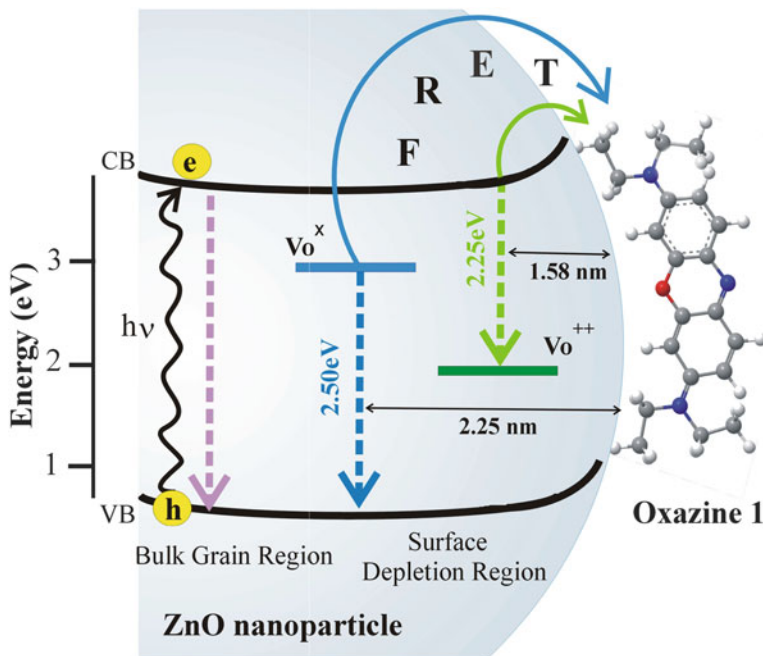


Fig. 10.2 (a) Steady-state absorption spectra of OX1 (red) and emission spectra of ZnO NP (blue) are shown. An overlapping zone between emission of ZnO NP and absorption of acceptor OX1 is indicated as a *green shaded zone*. The picosecond-resolved fluorescence transients of ZnO NP, in absence (blue) and in presence of acceptor OX1 (red) (excitation at 375 nm) collected at (b) 550 nm and (c) 495 nm, are shown. *Inset* of the figure (b) shows the HRTEM image of ZnO NPs (Reproduced by permission of the IOP Publishing)

Table 10.1 Picosecond-resolved luminescence transients of various samples

Sample	τ_1 (ns)	τ_2 (ns)	τ_3 (ns)	τ_{av} (ns)
ZnO NP (550 nm)	47.6 ± 0.8 (40 %)	3.79 ± 0.19 (23 %)	0.281 ± 0.003 (37 %)	20.32
ZnO NP-OX1 (550 nm)	19.0 ± 0.7 (1.4 %)	2.80 ± 0.02 (33.3 %)	0.259 ± 0.005 (65.3 %)	1.37
ZnO NP (495 nm)	35.1 ± 0.9 (30 %)	2.48 ± 0.15 (30 %)	0.089 ± 0.009 (40 %)	11.29
ZnO NP-OX1 (495 nm)	32.5 ± 0.4 (10 %)	2.32 ± 0.02 (36 %)	0.148 ± 0.006 (54 %)	4.17
ZnO NR (495 nm)	10.4 ± 0.1 (6.3 %)	2.44 ± 0.02 (28.2 %)	0.159 ± 0.004 (65.5 %)	1.45
ZnO rod-OX1 (495 nm)	8.454 ± 0.06 (5.1 %)	1.52 ± 0.01 (21.0 %)	0.087 ± 0.003 (73.9 %)	0.82
OX1 in EtOH (665 nm)	0.693 ± 0.001 (100 %)	–	–	0.69
ZnO NP-OX1 (665 nm)	0.867 ± 0.002 (100 %)	–	–	0.87

The emission from ZnO NPs (emission at 495 and 550 nm) was detected with 375 nm excitation. The emission of the acceptor OX1 in ethanol and at ZnO surface (emission at 665 nm) was detected with 633 nm laser excitation. *Numbers in the parentheses indicate relative weightage*

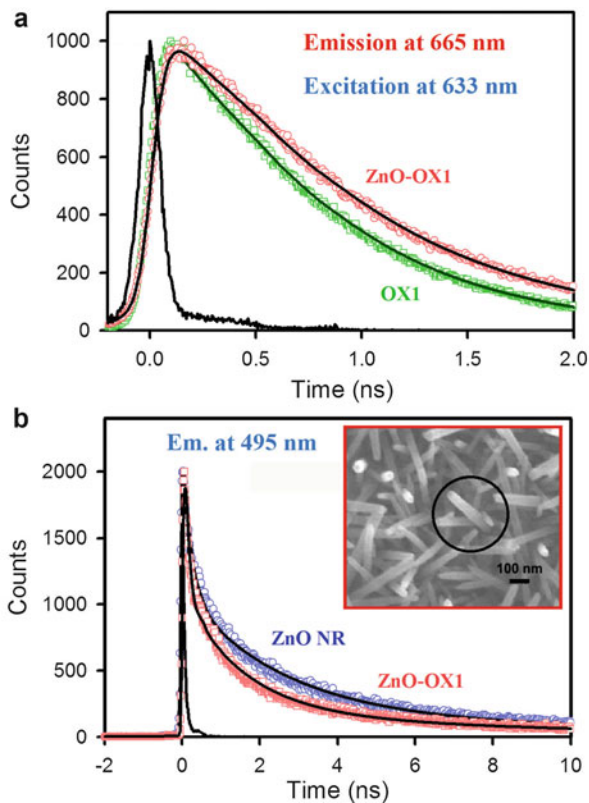


Scheme 10.1 Schematic diagram of ZnO NPs–OX1 nanocomposite depicting the FRET dynamics from different oxygen vacancy centers (V_{O}^{++}/V_{O}^{+} , V_{O}^{+}/V_{O}^{\times}) of ZnO NPs to OX1 molecules. Singly charged oxygen vacancy center (V_{O}^{+}), present in the surface depletion region, captures a hole to generate V_{O}^{++} center, leading to an emission in with a peak in the vicinity of 2.25 eV (550 nm). In absence of depletion region V_{O}^{+} becomes neutral center (V_{O}^{\times}) by capturing one electron from the conduction band, which is responsible for an emission at 2.50 eV (495 nm). Typical FRET distances from different energy states of ZnO NPs to surface adsorbed OX1 are also shown. The band gap excitation (3.87 eV, i.e., 320 nm) is shown by *curved arrows* (Reproduced by permission of the IOP Publishing)

respect to free ZnO at 495 nm is shown in Fig. 10.2c. The relevant data are also given in Table 10.1. From the average lifetime data and using (10.3) and (10.4) we obtain for the 495 nm emission $r_{DA} = 2.25$ nm, which is much larger than that observed at 550 nm. In this case $r \approx r_{DA} > t$ clearly indicating that the emission at 495 is from defect sites located within the bulk of the NPs. The efficiency of the FRET (E) as obtained from (10.4) is found to be the highest for 550 nm line (93 %) and much smaller (63 %) for the 495 nm line.

We have extended our studies on the attachment of the OX1 molecules at the surface of the ZnO NRs. The NRs are very important components for the state-of-the-art ZnO-based DSSCs [101]. The morphology of ZnO NR was characterized by SEM. A typical SEM image of ZnO NR (Figure 10.3b inset) shows 400 nm long and 40 nm wide NR growths. The NRs are found to offer photoluminescence peaking at 495 nm. The spectral characteristic is consistent with the fact that the emission is dominated by the bulk state of the semiconductor [93, 102]. As shown in Fig. 10.3b, the fluorescence quenching of the ZnO NR-OX1 adduct offers insignificantly small quenching with efficiency 44 % compared to that of the free

Fig. 10.3 (a) The picoseconds-resolved fluorescence transients of acceptor OX1 (green) and OX1 in presence of ZnO NP (red), (excitation at 633 nm) collected at 665 nm. (b) Time resolved quenching spectrum of ZnO NRs in presence (red) and absence (blue) of OX1 (excitation at 375 nm) collected at 495 nm. *Inset* of the figure shows the SEM image of ZnO NRs (Reproduced by permission of the IOP Publishing)



NRs in the bulk ethanol. No attempt has been made to estimate donor–acceptor distance in the case of NR-OX1 adduct because of the inadequate quantum yield of the ZnO NRs. We also considered the possibility of electron transfer from the ZnO surface to a well-known electron acceptor OX1 [99]. It has been demonstrated that the molecule offers an ultrafast fluorescence decay following an electron transfer reaction [103]. However, from Fig. 10.3a it is evident that the fluorescence decay of OX1 at the ZnO surface is slightly longer than that in the bulk ethanol.

The observation clearly rules out the possibility of any kind of electron transfer reaction in the quenching process of the ZnO NPs. Furthermore, a slight lengthening of the excited state lifetime of the acceptor molecule OX1 confirms its proximity to ZnO surface, which makes OX1 molecule more restricted. The overall picture that evolved from our studies is summarized in Scheme 10.1.

3.2 Role of Resonance Energy Transfer in Light Harvesting of Zinc Oxide-Based Dye Sensitized Solar Cells [24]

After a detailed understanding of the defect states in ZnO NPs, the effect of defect-mediated light harvesting process on the overall efficiency of a model DSSC has been demonstrated. We have explored the FRET dynamics from ZnO

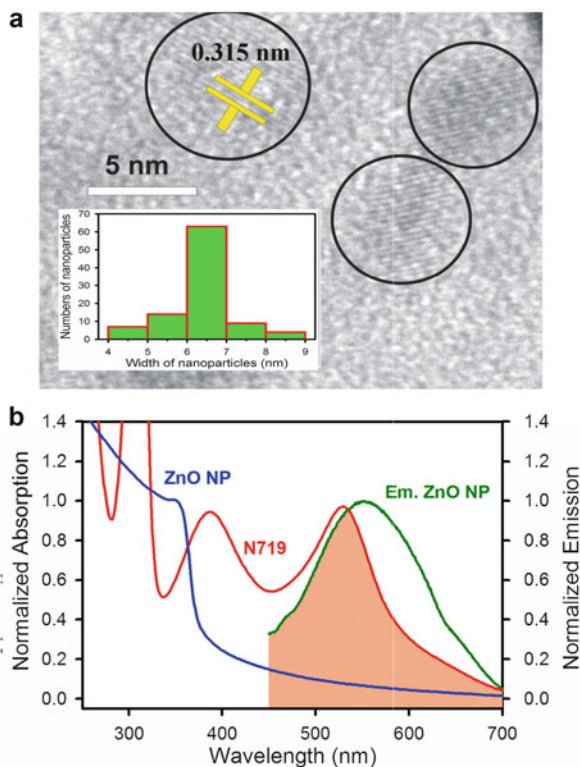


Fig. 10.4 (a) HRTEM image showing ZnO NPs with ~ 3 nm radius. *Inset* shows the size distribution of the ZnO NPs. (b) Steady-state absorption spectra of ZnO NP (blue), N719 (red) and emission spectra of ZnO NP (green) are shown. An overlapping zone between emission of ZnO NP and absorption of acceptor N719 is indicated as a red shaded zone. Reprinted with permission from J. Phys. Chem. C 116, 14248–14256 (2012). Copyright 2013 American Chemical Society

semiconductor NPs to surface adsorbed N719 sensitizers. By using steady-state and picosecond-resolved fluorescence spectroscopy, we have demonstrated that PL from ZnO NPs can be used to excite the sensitizer molecules for the enhancement of light absorption possibility. The study also reveals that physical migration of the photoinduced charge from the ZnO NPs to the sensitizers is insignificantly small in the de-excitation of the semiconductor NPs. The effect of the ZnO-mediated light harvesting process on the overall efficiency of a model DSSC has also been demonstrated.

The HRTEM image of the ZnO NPs is shown in Fig. 10.4a and a predominance of NPs with diameters of 6–7 nm were found in the synthesized colloids (inset of Fig. 10.4a). Figure 10.4b shows the UV–Vis absorption spectra of ZnO NP and dye N719. The PL spectrum of the ZnO NPs upon excitation with 375 nm is also shown in the figure. Significant spectral overlap of the ZnO PL spectrum with that of the absorption of N719 justifies the possibility of energy transfer from ZnO to the N719

dye molecules. In order to investigate the complexation of ZnO NPs with the sensitizer N719, we have studied the steady-state PL of the ZnO NPs in the presence of various concentrations of N719 as shown in Fig. 10.5a.

We have studied the PL transients at 550 nm (excitation at 375 nm) (Table 10.2) in the absence and presence of N719 dyes, as shown in Fig. 10.5b. The PL quenching, as evident from the steady-state and time-resolved PL studies, shows the affinity of the N719 dyes with the ZnO NPs. Detailed Stern–Volmer (S–V) analysis on the quenching of the ZnO PL (as shown in Fig. 10.5a, c) reveals the S–V constants to be K_{SV} (steady state) = $1.14 \times 10^7 \text{ M}^{-1} \text{ S}^{-1}$ and K_{SV} (time resolved) = $0.87 \times 10^7 \text{ M}^{-1} \text{ S}^{-1}$, respectively. The similarity of K_{SV} constants from steady-state and time-resolved measurements indicate the ZnO PL quenching to be dynamic in nature. In other words, the possibility of formation of non-fluorescent ZnO–N719 complex in the ground state is found to be negligibly small.

The dynamic nature of the PL quenching of ZnO NPs upon complexation with N719 is further justified from the FRET from donor ZnO to the surface adsorbed sensitizer N719. The overall FRET efficiency is found to be 74 %. In this case the spectral overlap integral, J (10.2) and the Förster distance (R_0) are found to be 6.597×10^{14} and 1.84 nm, respectively. From FRET dynamics, it has to be noted that the effective distance (r_{DA}) between the donor (ZnO NP) and the acceptor (N719) is 1.54 nm, which is much lower than that of the average radii of the NPs (~3 nm). In a FRET study [104] on cadmium selenide (CdSe) QD (donor) and a surface adsorbed organic dye (ethidium bromide; acceptor), the donor–acceptor distance was found to be close to the radius of the quantum dot. The relatively shorter donor–acceptor distance compared to the radius of the ZnO nanocrystallites in the present study, can be rationalized from the fact that the origin of the PL peaking at 550 nm essentially arises from the crystallites exposed in the surface of ZnO NPs. It is important to note that the thickness of the surface layer (t) obtained from calculation (10.5) is found to be 1.30 nm, which is comparable to the effective distance between the donor and acceptor calculated from FRET study. The observation is consistent with the fact that there is a surface region from where the defect related emission occurs.

In order to investigate the effect of light harvesting of high energy photons by the host ZnO semiconductor in a model DSSC, we have studied the photocurrent–voltage (J – V) characteristics as shown in Fig. 10.6a. The J – V characteristics of the solar cells were measured in two different experimental conditions. Firstly, we have excited the cells with whole solar spectrum (circle-line presentation in Fig. 10.6). Secondly, we used a yellow filter to block the solar spectra below 400 nm (high energy photons) as shown in a square-line presentation in Fig. 10.6a. The total light power in both the cases was very carefully maintained at 100 mW cm^{-2} . The open circuit voltage (V_{OC}) and short-circuit current density (J_{SC}) values are found to be much higher when the device performance was measured under whole solar spectrum. Upon the use of the optical filter, a sharp decrease in current from 1,190 to 668 $\mu\text{A cm}^{-2}$ was observed. In retrospect, compared to 44 % change in the short circuit current, V_{OC} reduced marginally by 6.7 % while fill factor (FF) reduced only by around 11.8 % (Table 10.3). As shown in Fig. 10.4b the sensitizer N719 absorbs very little in the UV region (below 400 nm) of the solar spectrum. Thus it is expected that the efficiency of the solar cell will not be

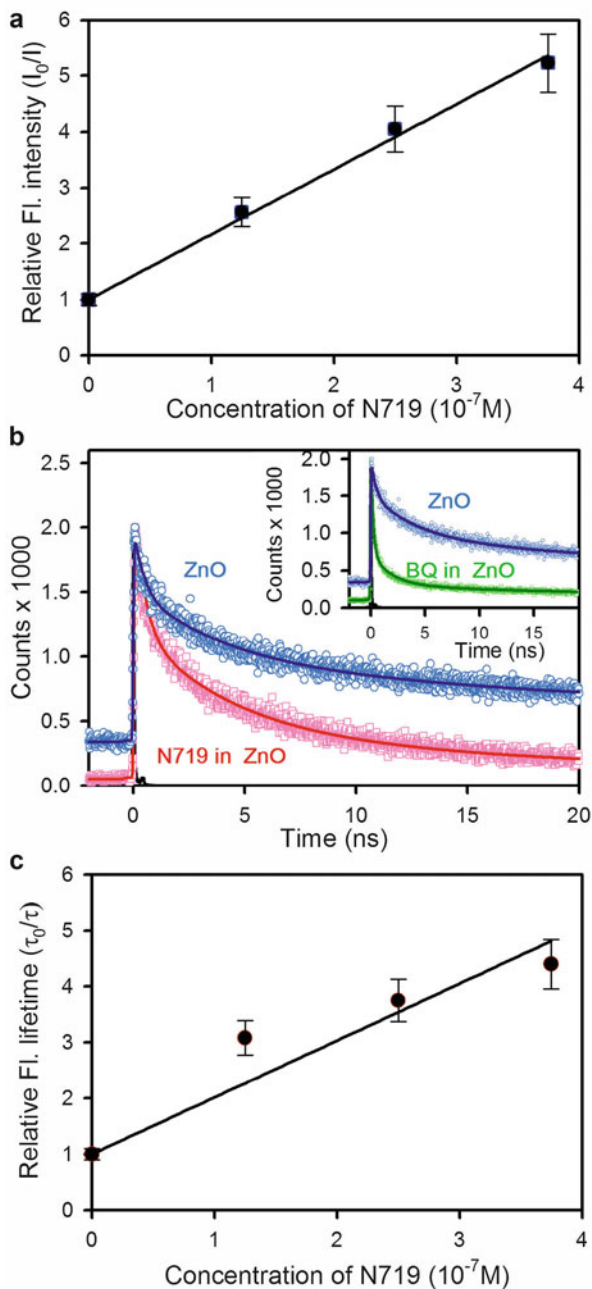


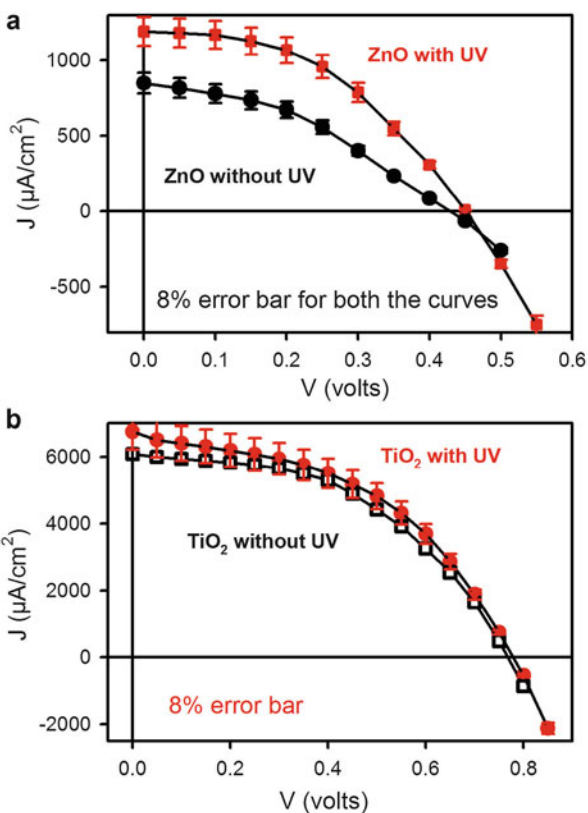
Fig. 10.5 (a) Steady-state emission intensity of ZnO NPs (excitation at 375 nm) in presence of increasing concentration of N719 dye relative to that of ZnO emission without N719. (b) The picoseconds-resolved fluorescence transients of ZnO NP, in absence (blue) and in presence of acceptor N719 (red) (excitation at 375 nm) collected at 550 nm. *Inset* show the faster PL decay of ZnO in the presence of BQ. (c) Excited state lifetime of the PL emission of ZnO NPs (excitation at 375 nm) in the presence of increasing concentration of N719 dye relative to that of ZnO emission without N719 is shown. Reprinted with permission from J. Phys. Chem. C 116, 14248–14256 (2012). Copyright 2013 American Chemical Society

Table 10.2 Picosecond-resolved luminescence transients of ZnO NPs in the presence and absence of N719

Sample	τ_1 (ns)	τ_2 (ns)	τ_3 (ns)	τ_{avg} (ns)
ZnO NP (bare)	47.6 (41 %)	3.78 (23 %)	0.280 (36 %)	20.32
ZnO NP + N719	29.1 (12 %)	3.86 (38 %)	0.344 (50 %)	5.25
ZnO NP + BQ	30.2 (6 %)	1.93 (18 %)	0.187 (76 %)	2.20

The emission from ZnO NPs (at 550 nm) was detected with 375 nm laser excitation. Numbers in the parentheses indicate relative weightage

Fig. 10.6 J - V curves of (a) ZnO NP and (b) TiO_2 NP-based DSSCs in the presence and absence of UV. Reprinted with permission from *J. Phys. Chem. C* 116, 14248–14256 (2012). Copyright 2013 American Chemical Society



affected much on the presence of high energy photons due to the absence of noticeable optical absorption in the dye at lower wavelengths (below 400 nm). This observation clearly demonstrates that ZnO DSSCs can harvest high energy photons as well. High energy photons were found to have a minimum effect on the solar cell performance of TiO_2 -based solar cells fabricated with the same sensitizer (Fig. 10.6b). These observations (Fig. 10.6, Table 10.3) reveal that the efficiency of ZnO-based DSSC increases by 118 % if the UV portion of the AM1.5 spectra is employed, which was compared to a marginal 9 % increase in efficiency in the case of TiO_2 -based DSSCs.

Table 10.3 Device performance^a of the DSSCs with ZnO and TiO₂ NPs

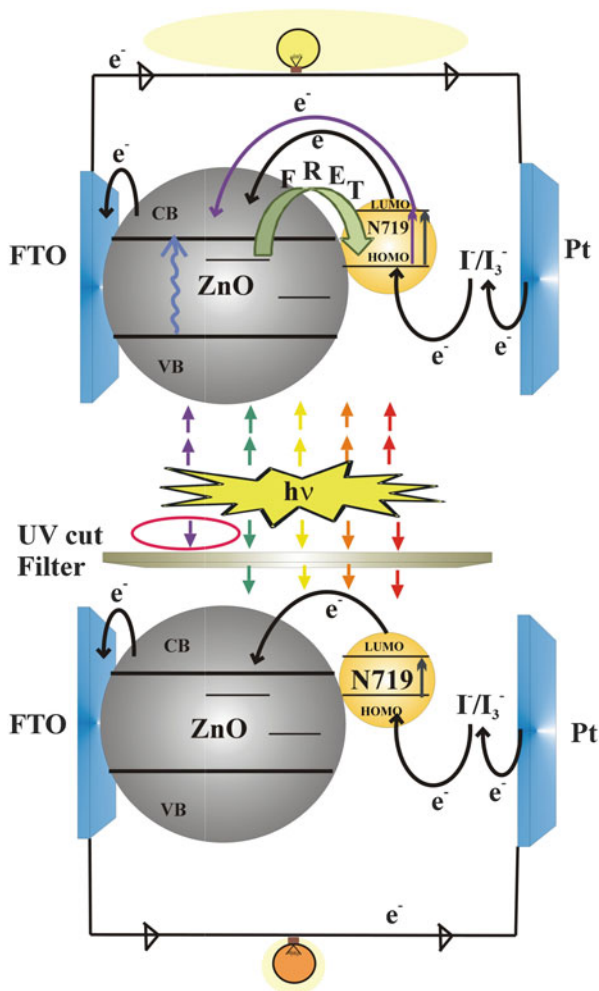
Device with N719	V_{OC} (V)	J_{SC} ($\mu\text{A cm}^{-2}$)	FF (%)	η (%)
ZnO NP (with UV)	0.45	1190.00	44.66	0.24
ZnO NP (without UV)	0.42	668.00	39.39	0.11
TiO ₂ NP (with UV)	0.77	6760.00	46.30	2.41
TiO ₂ NP (without UV)	0.77	6086.67	47.15	2.21

^aShort circuit photocurrent densities (J_{SC}), open-circuit voltage (V_{OC}), fill factor (FF), and efficiency (η) (see (10.8) and (10.9))

It is clear that harvesting of high energy photons in the case of TiO₂-based DSSCs does not contribute appreciably to the enhancement of the device efficiency. It is worth noting that the efficiency obtained from the model DSSC using NPs is lower compared to the maximum efficiency reported where NR has been taken in order to provide higher surface area and better charge transport.

It has to be noted that N719 is a redox active organic dye [20]. In this regard the PL quenching of the ZnO NPs upon adsorption of the dye may be associated with excited state electron transfer from ZnO to the N719 dye molecule. In order to investigate the electron transfer dynamics from the ZnO NPs upon excitation, we have studied the complexation of the NPs with an organic molecule, benzoquinone (BQ), which is well known as an electron acceptor [105] and efficiently accepts excited electrons from the surface of semiconductor quantum dots [106].

From our studies the quenching of the PL intensity of ZnO NPs upon complexation with BQ is evident. As shown in the inset of Fig. 10.5b, a very sharp decay in fluorescence at 550 nm in the presence of the electron acceptor is indicative of the fast transfer of excited electrons from the conduction band of the ZnO NPs into the LUMO of BQ molecules. The ZnO–BQ system exhibited a faster initial decay with a time period of 0.187 ns with a majority (76 %) of the excited electrons following this path (Table 10.2). The faster decay in presence of BQ as compared to N719 at the same excitation of 375 nm may be indicative of energy transfer from the ZnO donor NPs to the N719 acceptor molecules rather than transfer of electrons. In the case of pure ZnO in ethanol (Fig. 10.5b), the excited state lifetime ($k_{nr} = 0$) of ZnO NPs is 20.32 ns, which yields a radiative rate constant of $4.92 \times 10^7 \text{ s}^{-1}$. Upon the addition of N719 and BQ in separate ZnO NP solution, the average lifetimes were found to reduce to 5.25 and 2.20 ns, with rate constants of 1.90×10^8 and $4.55 \times 10^8 \text{ s}^{-1}$, respectively. We have calculated electron transfer rate, which is directly reflected in the non-radiative rate constants (k_{nr}). The calculated k_{nr} values were found to be 1.41×10^8 and $4.06 \times 10^8 \text{ s}^{-1}$ for the ZnO–N719 and ZnO–BQ systems, respectively. From the above k_{nr} values, we can conclude that the electron transfer rate, in case of ZnO–BQ composite, is threefold higher compared to the energy transfer in ZnO–N719 system. In the case of electron transfer from excited state ZnO NPs to N719, the short-circuit current of the ZnO NP-based DSSC is expected to be reduced. However, as shown in Fig. 10.6, the efficiency of the DSSCs in the presence of UV light (i.e., when the ZnO NPs were excited) is increased. Charge conservation clearly rules out any possibility of back electron transfer from ZnO NPs to the sensitizer N719. The overall picture that is evident from our studies is represented in Scheme 10.2.



Scheme 10.2 It represents a model DSSC based on the ZnO NPs, which contain sufficient defect states, namely, oxygen vacancy centers near surface depletion region. The system consists of a fluorinated tin oxide (FTO) on which semiconductor ZnO NP (gray big circle) is fabricated. The sensitizer dye N719 (small yellow circle) is bound to ZnO NP by surface adsorption. The entire structure is immersed in a liquid redox electrolyte (I^-/I_3^-). In regular DSSC, light is directly absorbed by the sensitizer, exciting an electron from HOMO to LUMO level. In the proposed configuration that contains a semiconductor having appreciable amount of defect states, an additional “indirect excitation” of N719 is introduced by using the sensitivity of FRET. In the FRET-based cell, the semiconductor NP is found to be excited in the presence of UV light, by which, an electron is promoted from the valance band to the conduction band, followed by energy transfer from excited states of semiconductor to N719 molecules via FRET. Thereafter, charge separation occurs exactly as it does in regular DSSCs and electron is injected from the excited state of the dye into the conduction band of the semiconductor electrode and the electron is thus transported to the charge collector. In presence of a UV cut-filter the FRET-based cell performs like a regular DSSC as no energy transfer from ZnO NP to N719 takes place due to the absence of UV light. Reprinted with permission from J. Phys. Chem. C 114, 10390–10395 (2010). Copyright 2013 American Chemical Society

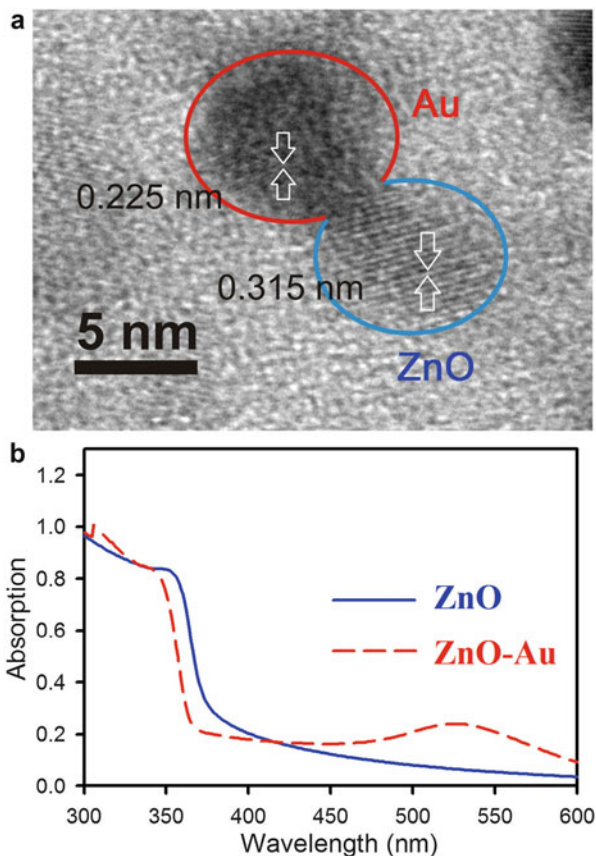
3.3 *Photoselective Excited State Dynamics in ZnO–Au Nanocomposites and Their Implications in Photocatalysis and Dye-Sensitized Solar Cells [25]*

In this section, we aimed to elucidate the mechanism of pronounced intrinsic emission from colloidal ZnO and ZnO–Au NCs upon above band-edge and below band-gap excitation. To probe the correlation between dynamics of photo-generated carrier trapping at the defect sites and kinetics of charge migration from ZnO and ZnO–Au semiconductors, methylene blue (MB) degradation was examined using UV light and optical filters. Photostability and luminescence studies from a ZnO–Au NC colloidal dispersion reveal FRET dynamics from donor semiconductor to gold acceptor. Finally, we have designed a model DSSC-based on ZnO NPs, which leads to an increase in short-circuit photo-current (J_{SC}) and improved overall efficiency (η) in the presence of Au NPs. The reason behind the giant improvement in efficiency is also clarified by photoconductivity measurements of the ZnO NP and ZnO–Au NC thin films.

The structure, crystalline phase, size, and morphology of ZnO NPs and ZnO–Au NCs were determined (with TEM). Representative HRTEM images of the ZnO–Au NCs are illustrated in Fig. 10.7a, where the measured average diameters are 6 nm and 8 nm for ZnO and Au NPs, respectively. From TEM observation it was found that, the ZnO–Au NCs are fairly monodisperse and their shapes are different from that of the spherical ZnO NPs due to the incorporation of Au components. The higher contrast of Au observed in the TEM image is due to the higher electron density of metallic Au compared to semiconducting ZnO. The relevant TEM images are shown in Fig. 10.8a–c. After the synthesis of ZnO–Au NCs, the Zn–Au weight ratio was calculated by using a field emission-type scanning electron microscope (FEI-SEM; Quanta 200). From EDAX analysis it was found to be 1.3:1 as shown in the table below.

The visible absorption spectrum of gold grown onto the ZnO NPs was clearly characterized by the plasmon resonance peak of Au NPs. Figure 10.7b shows the absorption spectra of the ZnO–Au NCs and pure ZnO NPs. It is generally believed that the band-edge absorption of semiconductor in the quantum-confined size regime (≤ 7 nm) is dependent on the particle size [107]. There is no distinct variation in absorption characteristics in the range 300–420 nm, which implies that no apparent growth of ZnO NPs occurred during the formation of Au on ZnO NPs. An SP band, resulting from Au in the ZnO–Au NCs, centered at ~ 525 nm can also be observed in the NC (Fig. 10.7b). In Fig. 10.9a we have plotted the excitation spectra of bare ZnO NPs and ZnO–Au NCs monitored at the emission peaks (368 nm and 550 nm, respectively). The room temperature PL spectra of both the bare ZnO NPs and ZnO–Au NCs (Fig. 10.9b) are composed of one broad emission band upon excitation below the band-gap ($\lambda_{ex} = 375$ nm) and two emission bands upon excitation above the band-edge ($\lambda_{ex} = 320$ nm). The narrow UV band centered at 368 nm is due to exciton recombination. Analysis of the broad emission observed in our sample in the blue-green region shows that it is composed of two

Fig. 10.7 (a) HRTEM image of *dumbbell-like* ZnO–Au NCs with Au attached to the ZnO surface. (b) Steady state absorption spectra of bare ZnO NPs (blue) and ZnO–Au NCs (red) showing the SP band at 520 nm (Reproduced by permission of the PCCP Owner Societies)



emission bands (shown as dotted lines in Fig. 10.9b (inset)), which are marked as P1 and P2 [96]. The characteristics of each emission band depend upon whether it arises from a doubly charged vacancy center V_{O}^{++} (P2) or a singly charged vacancy center V_{O}^{+} (P1). The V_{O}^{++} center, created by capture of a hole by the V_{O}^{+} center in a depletion region, leads to the P2 emission line. The singly charged center (V_{O}^{+}) in the absence of a depletion region turns into a neutral center (V_{O}^{\times}) upon the capture of an electron (n-type ZnO) from the conduction band, which then recombines with a hole in the valence band giving rise to the P1 emission [93]. The spectral content of the blue-green band is determined by the relative weight of the two overlapping emission peaks.

As shown in Fig. 10.9b, when excitation below the band-gap ($\lambda_{ex} = 375$ nm) was used, the defect-related emission is suppressed in the presence of Au NPs. Herein, we propose FRET from donor ZnO NP to Au acceptor, which is responsible for the observed suppression of emission bands.

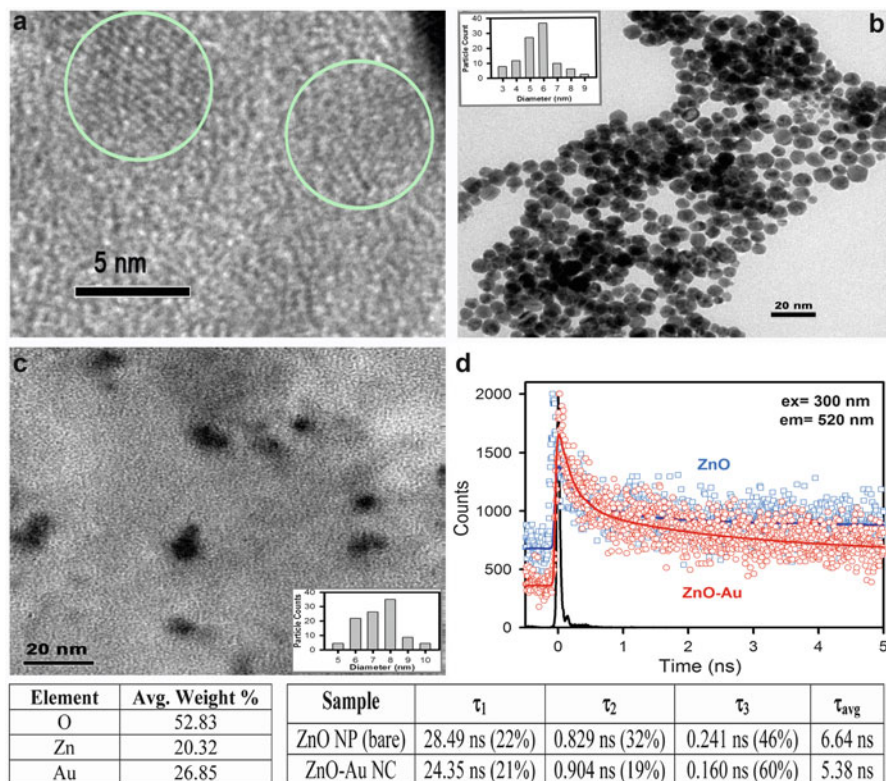


Fig. 10.8 (a) HRTEM image of bare ZnO NPs. (b) TEM image of bare ZnO NPs (*inset* shows particle size distribution of ZnO NPs). (c) TEM image of ZnO–Au NCs (*inset* shows particle size distribution of Au NPs attached to ZnO NPs). Table (*left*) shows EDAX analysis of ZnO–Au NCs by using a field emission-type SEM. Table (*right*) shows picosecond-resolved luminescence transients of ZnO NPs in the presence and absence of Au NPs. The *numbers* in the *parentheses* indicate relative weightage. (d) The emissions from ZnO NPs and ZnO–Au NCs (probing at 520 nm) were detected with a 300 nm laser excitation (Reproduced by permission of the PCCP Owner Societies)

The spectral overlap of the ZnO emission spectrum with that of the Au absorption spectrum is shown in Fig. 10.10a. The faster excited state lifetime of the ZnO–Au NC with respect to that of the free ZnO NP is clearly noticeable from Fig. 10.10b. Details of the spectroscopic parameters and the fitting parameters of the fluorescence decays are tabulated in Table 10.4. In order to estimate FRET efficiency of the donor (ZnO) and hence to determine distances of donor–acceptor pairs, we followed the methodology described in chapter 13 of reference [28]. In this case the spectral overlap integral, J (10.2) is found to be 2.82×10^{16} .

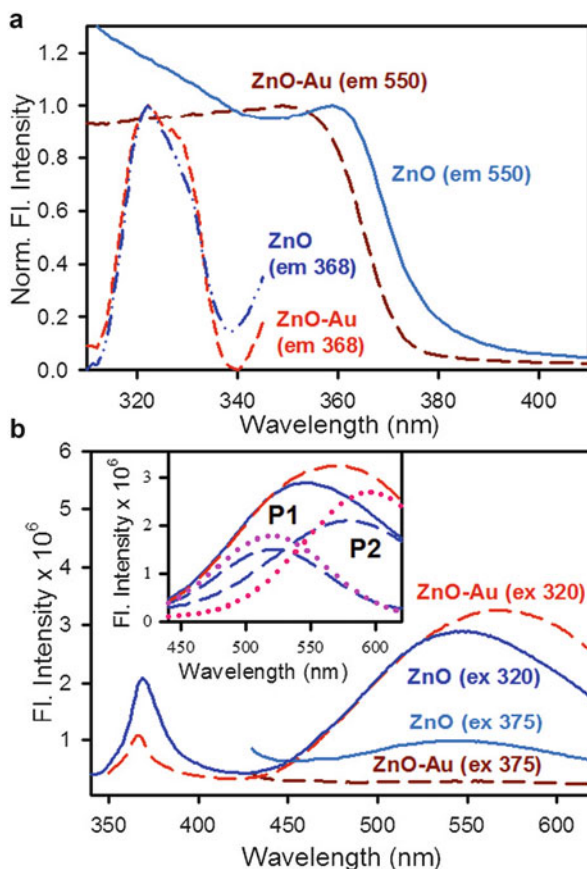


Fig. 10.9 (a) Excitation spectra of ZnO NPs (blue) and ZnO–Au NCs (red) monitored at 368 and 550 nm. (b) Steady-state emission spectra of ZnO NPs (blue) and ZnO–Au NCs (red) are shown (excitation at 320 and 375 nm). The *inset* shows that the defect related green emission is composed of two bands, P1 and P2 (Reproduced by permission of the PCCP Owner Societies)

From the average lifetime calculation for the ZnO–Au NC, we obtain the effective distance between the donor and the acceptor, $r_{DA} \approx 2.55$ nm, using (10.3) and (10.4). It is to be noted that the smaller value of r_{DA} compared to the radius of the ZnO NPs (~ 3 nm; Fig. 10.7a) can be rationalized from the fact that the origin of the PL peaking at 550 nm arises essentially from surface defects in the ZnO NPs [23]. Moreover, comparing the PL spectra of bare ZnO NPs and ZnO–Au NCs upon excitation above the band-edge, it was observed that the emission due to excitonic recombination is suppressed, while the defect-related emission is red shifted in the presence of Au NPs. In this respect, we have shown that the energy is transferred from the Vo^+ center to Au NPs, which leads to a reduction in the PL intensity at 520 nm. The energy transfer efficiency (E) is found to be $\sim 19\%$ (Fig. 10.8d), which is much lower value compared to that of below band-gap

Fig. 10.10 (a) SP band of Au NPs and emission spectra of ZnO NPs are shown. An overlapping zone between emission of ZnO NPs and absorption of acceptor Au is indicated as a *gray shaded zone*. (b) The picosecond-resolved fluorescence transients of ZnO NPs, in the absence (*blue*) and presence of acceptor Au (*red*) (excitation at 375 nm) collected at 550 nm (Reproduced by permission of the PCCP Owner Societies)

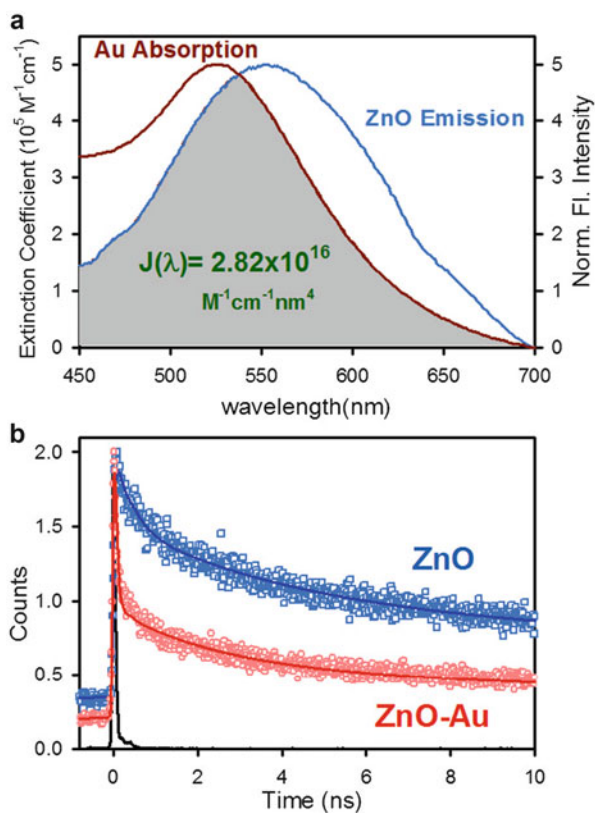


Table 10.4 Dynamics of picosecond-resolved luminescence transients of ZnO NPs in the presence and absence of Au NPs^a and the kinetics parameters^b for the photoselective degradation of methylene blue in the presence of ZnO and ZnO–Au nanocolloids

Dynamics study				
Samples	τ_1 (ns)	τ_2 (ns)	τ_3 (ns)	τ_{avg} (ns)
ZnO NP (bare)	47.58 (41 %)	3.78 (23 %)	0.280 (36 %)	20.48
ZnO–Au NC	33.34 (8 %)	2.60 (10 %)	0.051 (82 %)	2.97
Kinetics study [$y = A \exp(-kt) + y_0$]				
Samples and filters	k (sec^{-1})	A (%)	R^2	
ZnO (420 HP)	1.055×10^{-3}	2.66	0.96	
ZnO–Au (420 HP)	1.388×10^{-3}	2.78	0.93	
ZnO (460 LP)	2.203×10^{-3}	11.68	0.97	
ZnO–Au (460 LP)	2.528×10^{-3}	29.31	0.99	
ZnO (320 HP-460 LP)	2.340×10^{-3}	23.55	0.99	
ZnO–Au (320 HP-460 LP)	2.287×10^{-3}	19.65	0.99	

^aThe emissions from ZnO NPs and ZnO–Au NCs (probing at 550 nm) were detected with a 375 nm laser excitation. *Numbers in the parentheses* indicate relative weightage

^bKinetic constants (k), regression coefficients (R^2), and the percentages of photoselective degradation (A). *Parentheses* indicate the optical filters used in the study

excitation ($E = \sim 85\%$). In retrospect, excited electrons are preferentially trapped by V_{O}^{++} center, which is originated by V_{O}^{+} center by capturing a hole. The formation of V_{O}^{++} centers is more favorable upon band-edge excitation since the photogenerated holes have enough time to migrate during thermalization of highly excited electrons. This leads to more facile recombination of excited electrons via V_{O}^{++} centers, and this recombination pathway is supported by the appreciable red shift observed in ZnO–Au NCs upon above band-edge excitation. However, the decrease in band-edge emission intensity in the presence of Au NPs is well understood, whereby, Au acts as a sink that can store and shuttle photogenerated electrons [108, 109]. As per our understanding, the optical activity of surface defect states in the overall emission of the semiconductor solely depends on the excitation wavelength.

It was reported by several researchers that in the presence of metal NPs in close proximity to semiconductor NPs, enhanced photocatalytic degradation of test solutions was observed. Thus we compared the role of a Au layer in promoting photogenerated charges in ZnO–Au and ZnO colloids by carrying out photo-reduction of a test contaminant [MB, purchased from Carlo Erba]; MB is known to be an excellent probe for the study of interfacial electron transfer in colloidal semiconductor systems [81]. In general, the higher the charge migration from the surface of the ZnO semiconductor, the faster will be the degradation of the surface-attached MB. We have used a fiber-optic-based system for the measurement of light-induced chemical processes with spectroscopic precision. To demonstrate the sensitivity and usefulness of our designed system, we previously conducted a detailed study of the photodeterioration of vitamin B2 (riboflavin) in aqueous phase [110]. In order to obtain different excitations we have used three different types of filters placed on a homemade UV bath (60 W; normally used for water purification). The optical filters, namely, 420 high pass (HP), 460 low pass (LP), and 320 high pass (HP), were chosen in order to achieve controlled and preferential excitation. The characteristics of the optical filters are shown in Fig. 10.11a, which clearly depicts that 420 HP (passes light above 420 nm) is only used for the SP excitation of Au NPs, 460 LP (passes light below 460 nm) is used for the above band-edge excitation of ZnO, and the combined use of 320 HP and 460 LP (passes light above 320 nm and below 460 nm) leads to preferential excitation of below band-gap excitation of ZnO. In Fig. 10.11b, the relative concentration (C_t/C_0) of MB in solution is plotted with respect to UV irradiation time, the results of which indicate the photodegradation of MB upon continued UV irradiation. It is to be noted that there was no obvious change in the concentration of MB stored in the dark for several hours (data are not shown here). Under selective UV radiation we have recorded the absorption peak of MB (at 655 nm) at 5 s intervals, using SPECTRA SUITE software supplied by Ocean Optics, and plotted it against the time of photoirradiation. All the photodegradation curves were found to follow a first-order exponential equation, and the kinetic parameters are represented in Table 10.4. The decrease in the absorbance at 655 nm implies the generation of the colorless photoproduct leuco-methylene blue (LMB). Note that in the present study we are interested in exploring the long-time photodegradation of MB (for several minutes). To compare the photodegradation of

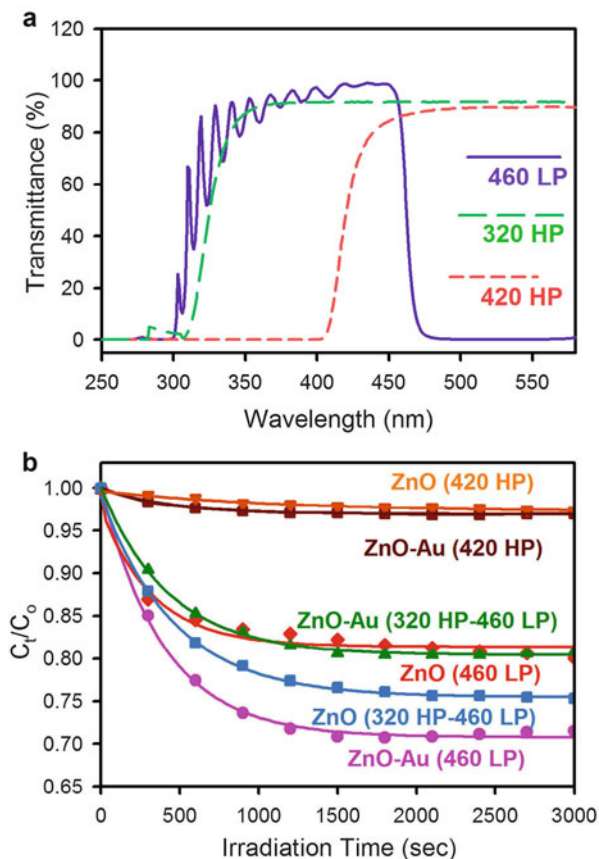


Fig. 10.11 (a) The transmittance spectra of 320 high pass (green), 420 high pass (red), and 460 low pass (violet) optical filters are shown. (b) Plot of relative concentration (C_t/C_0) vs. time for the degradation of MB (monitored at 655 nm) is shown. The degradation is performed in the presence of colloidal solutions of ZnO NPs and ZnO–Au NCs under different excitation conditions (parentheses indicate the optical filters used for the desired excitation) (Reproduced by permission of the PCCP Owner Societies)

MB in the presence of ZnO NPs and ZnO–Au NCs with a 420 HP filter, it is clearly shown that no considerable change in absorbance peak at 655 nm takes place upon Au SP excitation. The photodegradation rates are found to be 1.055×10^{-3} and $1.388 \times 10^{-3} \text{ s}^{-1}$, and the percentages of total photodegradation (i.e., the value of A in the first-order kinetic equation shown in Table 10.4) are 2.66 and 2.78 for ZnO and ZnO–Au NCs, respectively. It reveals that electron transfer from Au NPs to MB is not allowed upon direct excitation of Au. Upon, replacing the 420 HP filter with a 460 LP filter, we observed an increase in the photodegradation rates in the presence of Au NPs ($k_{\text{ZnO}} = 2.203 \times 10^{-3} \text{ s}^{-1}$, $k_{\text{ZnO–Au}} = 2.258 \times 10^{-3} \text{ s}^{-1}$), and the percentage of photodegradation also improved from $A_{\text{ZnO}} = 11.68$ to $A_{\text{ZnO–Au}}$

= 29.31. This is attributed to improved charge separation in the presence of Au NPs, which also can store and shuttle excited electrons, thereby suppressing recombination. Such Au NP-stabilized ZnO NPs behave as more efficient electron accumulators (at the conduction band) than the bare oxide [111]. In retrospect, the photodegradation rate of MB was observed to decrease ($k_{\text{ZnO}} = 2.340 \times 10^{-3} \text{ s}^{-1}$, $k_{\text{ZnO-Au}} = 2.287 \times 10^{-3} \text{ s}^{-1}$), and the percentage of total photodegradation was found to be much lower ($A_{\text{ZnO}} = 23.55$, $A_{\text{ZnO-Au}} = 19.65$) in the presence of Au NPs when we used combined optical filters of 320 HP and 460 LP. This happens because excited electrons of ZnO can easily occupy the defect centers and resonantly transfer their energy to Au NPs via non-radiative processes (FRET, as previously discussed). As a consequence, in presence of Au, excited electrons are unable to migrate from the ZnO surface to perform the reduction of MB. Thus, it is important to note that the differences in rate constants are not significant, whereas considerable differences in the magnitude of total photodegradation are observed during above band-edge and below band-gap excitation of ZnO and ZnO–Au NCs. This is due to the fact that the total number of active electrons available for carrying out MB degradation is different for ZnO and ZnO–Au NCs for any particular excitation. Our study clearly demonstrates that the role of incorporated metal on semiconductor for facilitating redox reactions is solely dependent on the excitation of the semiconductor.

The efficient charge migration in metal-semiconductor NCs is expected to lead to improved DSSC performance of ZnO–Au NCs compared to bare ZnO [112]. Thus, we measured and directly compared the IPCE (using (10.7)) of ZnO and ZnO–Au-based DSSCs. Each of the two examined ZnO and ZnO–Au-based cells contained the same sensitizer dye N719 and I^-/I_3^- electrolyte, to allow for a fair comparison. The IPCE curves of the two cells are presented in Fig. 10.12a, which shows a broad spectral response in the range 440–600 nm. Significant enhancement in photocurrent generation is seen upon deposition of Au NPs on the ZnO electrodes. The enhancement in the photocurrent generation efficiency is indicative of the fact that the Au NPs assist in the charge separation within the nanostructured ZnO film as well as improve the interfacial charge transfer processes. Figure 10.12b shows the photocurrent–voltage (J – V) characteristics for solar cells, constructed using the bare ZnO NPs and ZnO–Au NCs. The short-circuit current density (J_{SC}) and the open-circuit voltage (V_{OC}) of the ZnO–Au NC-based DSSC were $261.87 \mu\text{A cm}^{-2}$ and 0.605 V, respectively, which are much higher than that of the bare ZnO-based DSSC ($J_{\text{SC}} = 7.5 \mu\text{A cm}^{-2}$, $V_{\text{OC}} = 0.394$ V). The calculated values of FF and the overall power conversion efficiency of the ZnO-based DSSC were 30 % and 0.012 %, respectively, which are substantially improved in the presence of gold (FF = 53 % and $\eta = 0.8$ %). Table 10.5 summarizes the measured and calculated values obtained from each J – V curve.

We have also extended the photovoltaic measurements with ZnO NR and ZnO–Au NC solar cells with dye N719 [112] and their J – V characteristics were measured under AM 1.5 illuminations, as shown in Table 10.6. In Fig. 10.13a, the best J – V characteristics obtained for both bare ZnO NR and ZnO–Au NC DSSCs

Fig. 10.12 (a) Dependence of the incident photon conversion efficiency on the incident wavelength for ZnO NP (blue) and ZnO–Au NC (red) films cast on an FTO plate. (b) Photocurrent–voltage (J – V) characteristics of ZnO–Au NC and ZnO NP (inset) based DSSC (with 10.5 klux illumination intensity at the area of 0.16 cm² from a 90 W xenon lamp) (Reproduced by permission of the PCCP Owner Societies)

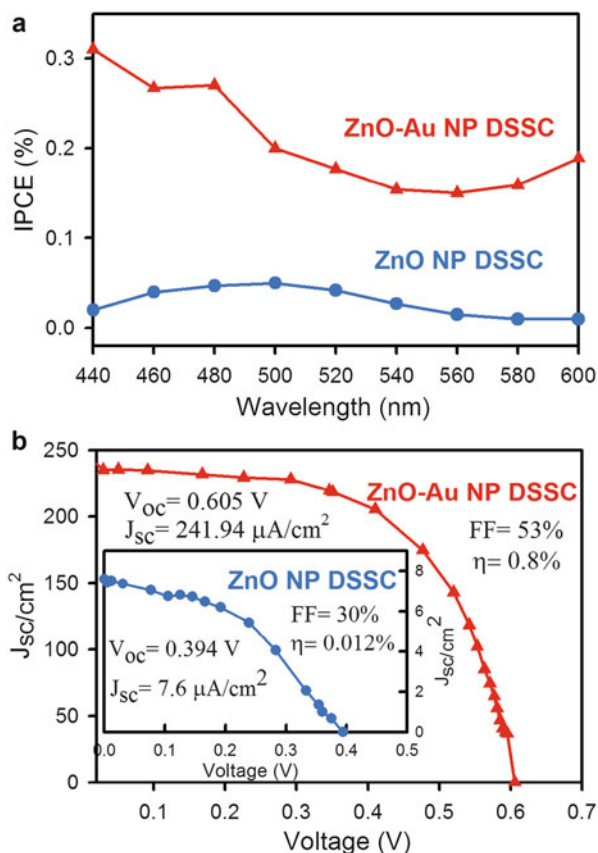


Table 10.5 Device performance^a of the DSSCs with ZnO NP and ZnO–Au NC

Device with N719	V_{oc} (V)	J_{sc} ($\mu\text{A cm}^{-2}$)	FF (%)	η (%)
ZnO NP	0.394	7.5	44	0.012
ZnO–Au NC	0.605	261.87	53	0.8

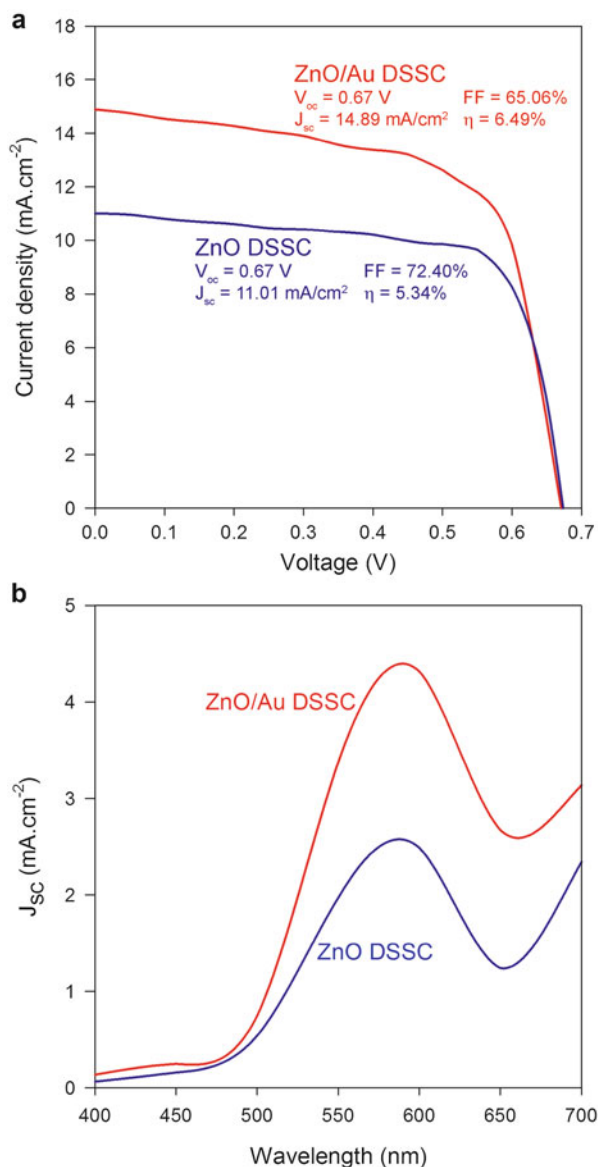
^aShort circuit photocurrent densities (J_{sc}/cm^2), open-circuit voltage (V_{oc}), fill factor (FF), and efficiency (η) (see (10.8) and (10.9))

Table 10.6 J – V characteristics of the bare ZnO NR and ZnO–Au NC DSSCs, measured at 1 sun illumination (100 mW cm⁻²)^a

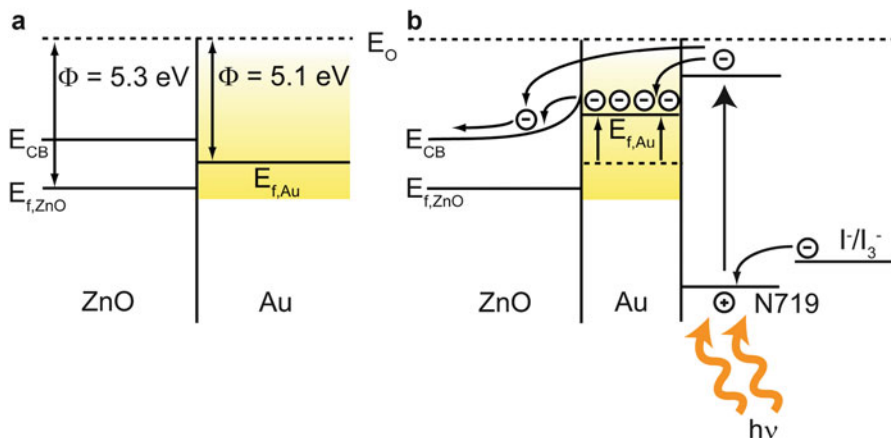
J – V parameters	Bare ZnO NR DSSC			ZnO–Au NC DSSC		
	Cell I	Cell II	Cell III	Cell I	Cell II	Cell III
V_{oc} (V)	0.67	0.67	0.67	0.67	0.65	0.66
J_{sc} (mA cm ⁻²)	10.98	11.01	10.84	14.89	14.28	14.45
FF (%)	71.55	72.40	70.31	65.06	63.00	65.78
η (%)	5.27	5.34	5.11	6.49	5.85	6.28

^aThe active area of all the DSSCs was maintained at 0.1 cm² during these experiments

Fig. 10.13 (a) J - V characteristics of the bare ZnO NR and ZnO-Au NC DSSC, measured at 1 sun (AM 1.5 G) illumination and (b) short circuit photocurrent density of the bare ZnO NR and ZnO-Au NC DSSCs measured at different incident wavelengths. The active area of all the DSSCs was maintained at 0.1 cm^2



are shown. It was found that the photocurrent of the ZnO NR DSSC improved upon the incorporation of Au NPs in the ZnO NR photoelectrode. For the ZnO-Au NC DSSC, $\sim 35\%$ improvement in J_{sc} (14.89 mA cm^{-2}) was obtained compared to the bare ZnO NR DSSC (11.01 mA cm^{-2}) and the overall power conversion efficiency improved from 5.34 to 6.49%. In Fig. 10.13b, the photocurrent response of bare ZnO NR and ZnO-Au NC-based DSSC measured at different incident wavelengths



Scheme 10.3 (a) Energy band positions and formation of the Schottky barrier in the ZnO–Au NC system and (b) possible electron transfer path in the ZnO–Au NC DSSC, where the *dashed line* (in Au) represents the position of the Fermi level of Au before electron injection from dye N719. E_O represents the vacuum energy level

are shown. Due to the surface plasmon absorption of Au NPs, an improved photocurrent response was observed above 500 nm illumination in case of the ZnO–Au NC DSSC compared to the bare ZnO NR DSSC. The improved device performance observed in case of the ZnO–Au NC DSSC can also be attributed to the presence of the Schottky barrier at the ZnO–Au interface, which would block the back electron transfer from the CB of ZnO to the I^-/I_3^- redox electrolyte. In ZnO–Au NC system, due to the higher work function of ZnO ($\Phi \sim 5.3$ eV) compared to Au ($\Phi \sim 5.1$ eV), a Schottky barrier forms at the ZnO–Au interface. Upon light irradiation, the electrons from excited dye molecules are injected to the Au NPs embedded on the surface of ZnO NRs resulting in an electron accumulation in the Au NP. As a result, the Fermi energy level of the Au NPs is pushed closer to the CB of the ZnO and transfer of electrons from Au NPs to the CB of ZnO could occur to establish charge equilibrium in the system. Some of the electrons from dye can also directly injected to the CB of the ZnO. The formation of the Schottky barrier at the ZnO–Au NC system and the possible electron transfer path in ZnO–Au DSSC is schematically represented in Scheme 10.3 [112].

The photoconductivity measurement [113, 114] of the ZnO NP and ZnO–Au NC thin films were necessary in order to further understand the electron mobility (i.e., performance of the semiconductor) and charge transfer mechanism. Figure 10.14 shows the photocurrent response for the ZnO NP and ZnO–Au NC thin films, where an improved photocurrent was observed for the ZnO–Au NC thin film (~ 70 μA) under illuminated condition compared to the ZnO NP thin film (~ 1.5 μA).

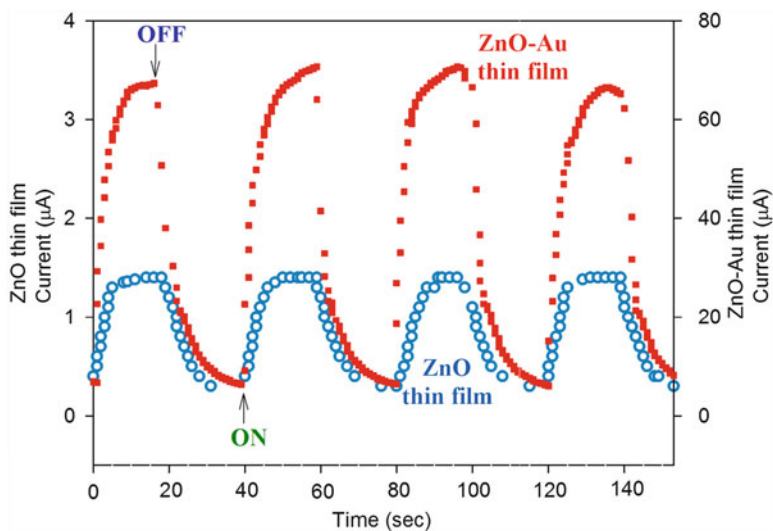
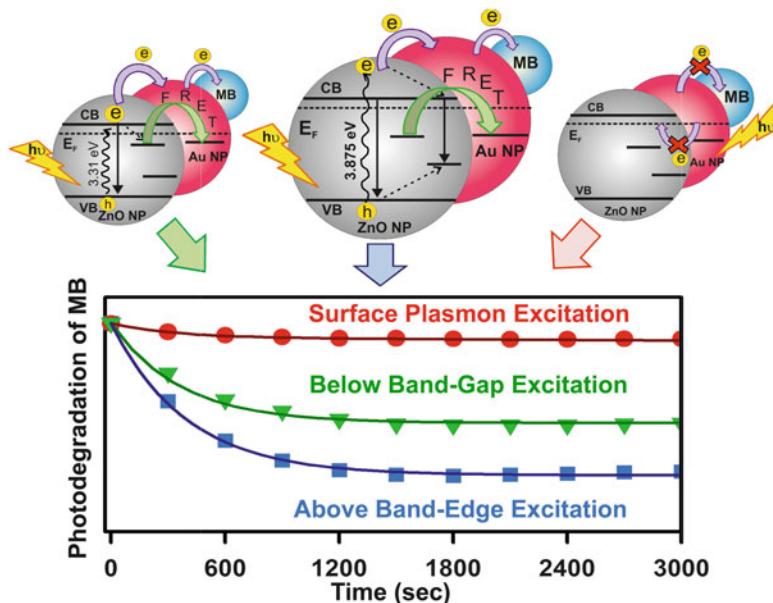


Fig. 10.14 Photocurrent responses of ZnO NP and ZnO–Au NC thin films under bias voltage of 5 V. The photocurrent was measured across the thickness of the films with 25 mW cm^{-2} incident power from a halogen light source (Reproduced by permission of the PCCP Owner Societies)

This shows that the photogenerated electrons in ZnO NPs (from visible light absorption by the intermediate Vo^+ center) are transferred to Au NPs, as mentioned earlier contributing in enhanced photocurrent of the ZnO–Au NC thin films compared to the ZnO NP. In case of the model DSSC shown here, a similar mechanism is responsible for the enhanced photocurrent observed (Fig. 10.12b) in the presence of Au NPs along with the ZnO NPs. Some of the injected electrons from the excited N719 dye to the CB of ZnO are captured by the intermediate defect sites of ZnO (Vo^+) resulting in poor photocurrent and fill factor of DSSC. However, in the presence of Au NPs in the ZnO thin film, we have observed higher photocurrent ($J_{\text{SC}} = 261.87 \text{ } \mu\text{A cm}^{-2}$) and fill factor ($\text{FF} = 53 \%$) compared to the ZnO NP DSSC ($J_{\text{SC}} = 7.5 \text{ } \mu\text{A cm}^{-2}$ and $\text{FF} = 44 \%$). Thus, it is noted that the ratios of improved photocurrent response (70:1.5) and short circuit current (261.9:7.5) for ZnO and ZnO–Au semiconductors are comparable. The improvement observed in the overall device performance is mainly due to increased conductivity by transferring the trapped electrons in Vo^+ centers of ZnO to Au NPs, which then contribute to the photocurrent as well as the fill factor of the DSSC. It is worth noting that the efficiency obtained from the model DSSC with the use of NPs is lower than the maximum efficiency reported [115] with NRs, which were employed to provide higher surface area and better charge transport. The overall mechanistic explanation for the excitation-dependent recombination processes and the catalytic activity of Au NPs in the ZnO–Au NCs, as schematically shown in Scheme 10.4.



Scheme 10.4 Schematic representation of the metal–semiconductor system: The system consists of a semiconductor ZnO NP (gray big ball) containing appreciable amounts of defect states on which a Au NP (red big ball) is fabricated. MB (small blue ball) is bound to the ZnO–Au NC by surface adsorption. The dynamics of charge separation and interparticle charge/energy migration of the entire structure is shown. Thereafter, photodegradation of MB under different excitation conditions is also shown by a graph, which reveals the mediating role of Au NP in photocatalysis (Reproduced by permission of the PCCP Owner Societies)

3.4 Dual-Sensitization via Electron and Energy Harvesting in CdTe QDs Decorated ZnO NR-Based DSSCs [26]

In this section, we will demonstrate the utilization of two sensitizers (one acting as energy donor while the other as an acceptor) by using the novel approach of FRET that can be very useful in order to achieve both broadening of optical absorption region in DSSCs as well as increasing the absolute loading of absorbing media on the semiconductor. We have explored that size tunable CdTe QDs capped with 3-mercaptopropionic acid (MPA), assembled in an N719-sensitized solar cell, can absorb visible light in the gaps where N719 has lower absorption or does not absorb any light. In this design, QDs serve as a co-sensitizer, which can directly transfer electrons to ZnO NRs. Moreover, the QDs that are not in a direct attachment to the ZnO NR surfaces harvest the absorbed energy to nearby dye molecules via FRET rather than contribute directly as sensitizers. By using steady-state and picosecond-resolved fluorescence spectroscopy, we have demonstrated that PL from QDs can be useful to excite the sensitizer dye molecule for an enhanced light absorption. The consequence of QD mediated electron and light-harvesting processes on the overall performance of a model QD-assembled DSSC has also been demonstrated.

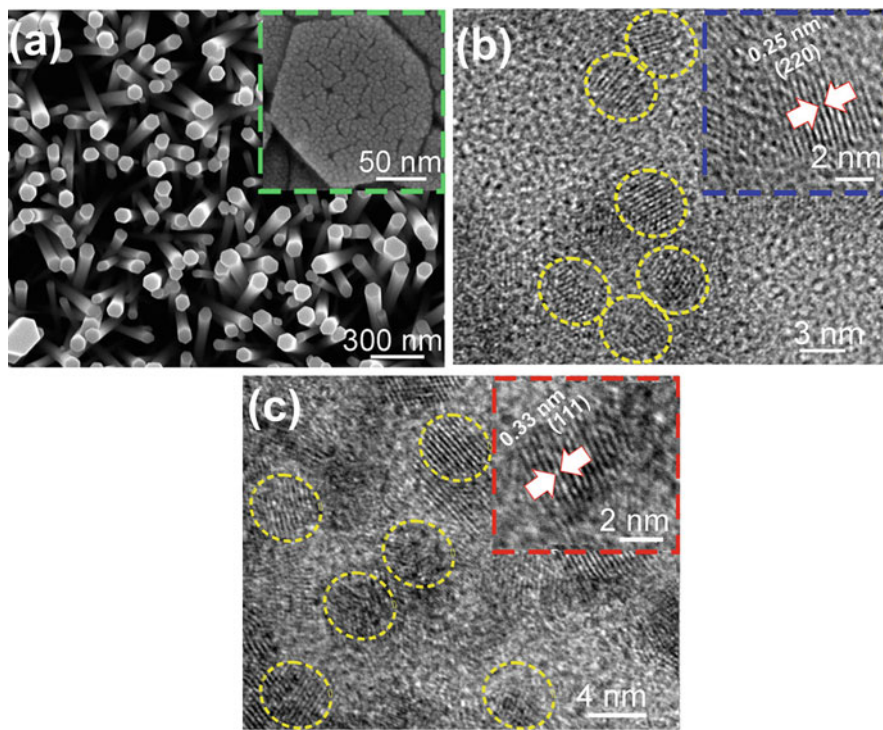


Fig. 10.15 (a) Top-view SEM image of vertically aligned ZnO NRs decorated on an FTO plate; the *inset* shows a closer view of hexagonal ZnO NR on which CdTe QDs are attached. TEM images of (b) QD1 and (c) QD2 (two representative QDs) are shown; the *insets* show their corresponding HRTEM image. Reprinted with permission from J. Phys. Chem. C 116, 14248–14256 (2012). Copyright 2013 American Chemical Society

The morphological characterization by SEM (Fig. 10.15a) indicates the formation of arrays of ZnO NRs with a preferential growth direction along the polar facets in the [0002] direction of the ZnO hexagonal wurtzite crystal. The NRs growing perpendicular to the substrate are nearly uniform in length ($\sim 3 \mu\text{m}$) and possess a characteristic hexagonal cross section with diameter in the range of $\sim 180 \text{ nm}$. Inset shows the magnified top-view of a typical single NR decorated with CdTe QDs. Figure 10.15b–c show the TEM images of two distinctly different sizes of CdTe QDs (QD1 and QD2), which are found to be $\sim 4 \pm 0.2$ and $\sim 5 \pm 0.4 \text{ nm}$ in diameter. As shown in the insets of Fig. 10.15b–c, HRTEM image reveals the fringes of CdTe with a lattice spacing of 0.33 and 0.25 nm corresponding to (111) and (220) planes of cubic CdTe crystal, which are in good agreement with previous reports [116]. Both the absorption and PL spectra of CdTe QDs exhibit “quantum size effect,” as shown in Fig. 10.16. The tunable absorption bands of CdTe QDs can be so adjusted that they preferentially cover the ‘gaps’ of sensitizer N719 absorption, i.e., where sensitizer has none or very low extinction coefficient (Fig. 10.16a).

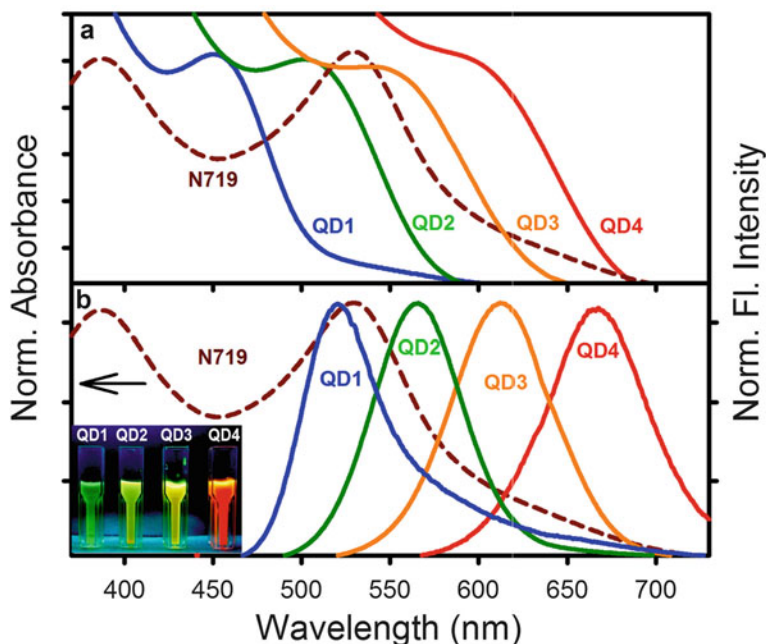


Fig. 10.16 (a) Normalized absorption spectra of the sensitizing dye N719 and 3-MPA-capped CdTe QDs with average diameters of 4 nm (QD1), 5 nm (QD2), 7 nm (QD3), and 9 nm (QD4). (b) Significant overlap between absorption spectra of N719 and photoluminescence (PL) spectra of four different-sized CdTe QDs is shown. Reprinted with permission from J. Phys. Chem. C 116, 14248–14256 (2012). Copyright 2013 American Chemical Society

As can be observed in Fig. 10.16b, there are significant overlaps between the optical absorption of sensitizer N719 and the emission bands of CdTe QDs, which is one of the foremost criteria for FRET dynamics. As shown in Fig. 10.17, upon 375 nm laser excitation, strong emissions of CdTe QDs (deposited on a quartz plate) were suppressed in the presence of sensitizer N719. Herein, we propose FRET from donor CdTe QDs to N719 acceptor [117], which is responsible for the observed suppression of the emission bands. The donor thus decays to the ground state while the acceptor is still excited. It results in the excitation of the acceptor from an indirect process, i.e., the acceptor effectively captures photons that are not directly absorbed by it. The faster excited state lifetime of the CdTe-N719 composite with respect to that of the free QDs is clearly noticeable in Fig. 10.18. Details of the spectroscopic parameters and the fitting parameters of the fluorescence decays are tabulated in Table 10.7.

The quantum yields (Q_D) of the donors in the absence of acceptor are measured with respect to a reference dye Rhodamine 123 ($Q_D = 0.9$) and presented in Table 10.8. From the average lifetime calculation for the CdTe-N719 adduct, we obtain the effective distance (using (10.3) and (10.4)) between the donor and the acceptor, r_{DA} to be 3.72 ± 0.03 , 4.14 ± 0.06 , 4.38 ± 0.08 and 4.22 ± 0.04 nm for

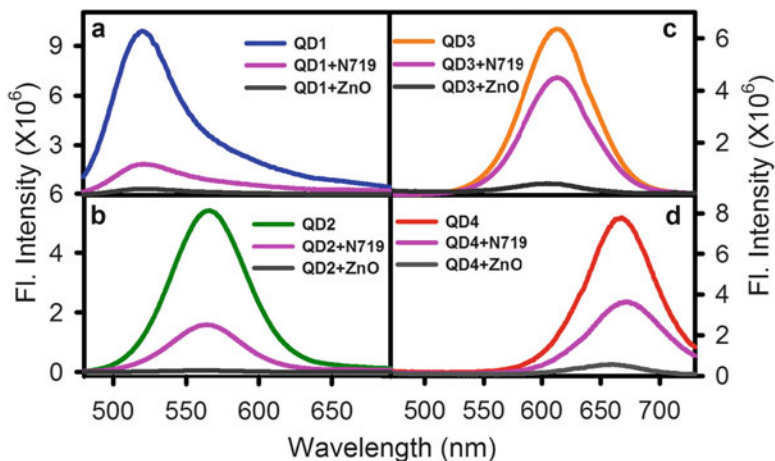


Fig. 10.17 Steady-state emission quenching of different-sized CdTe QDs (a, QD1; b, QD2; c, QD3; d, QD4) in the presence of sensitizing dye N719 and ZnO NRs. Excitation was at 375 nm. Reprinted with permission from J. Phys. Chem. C 116, 14248–14256 (2012). Copyright 2013 American Chemical Society

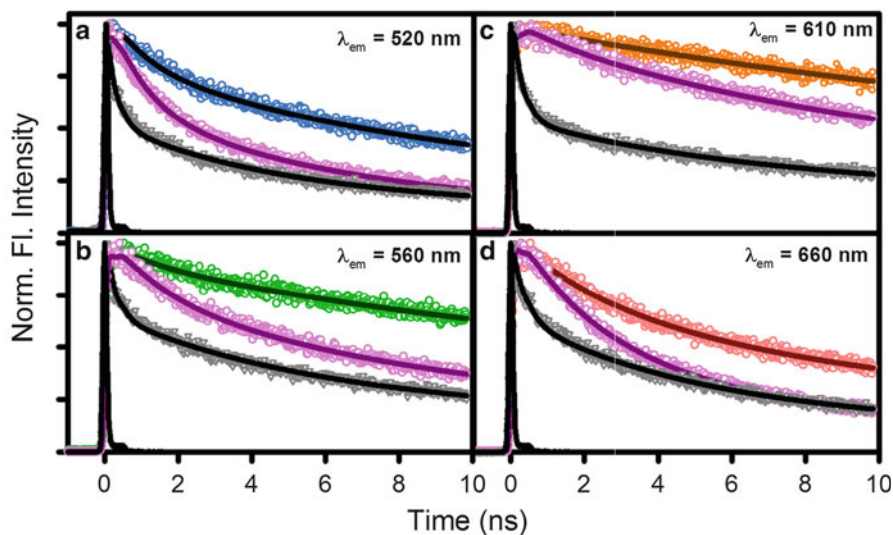


Fig. 10.18 The picosecond-resolved fluorescence transients of four different-sized CdTe QDs (a, QD1; b, QD2; c, QD3; d, QD4) in the absence and presence of sensitizing dye N719 (pink) and ZnO NRs (gray). The excitation wavelength was at 375 nm. Reprinted with permission from J. Phys. Chem. C 116, 14248–14256 (2012). Copyright 2013 American Chemical Society

QD1 to QD4, respectively. It is to be noted that the insignificant variations in donor–acceptor distances compared to the radii of the QDs (measured from TEM image) can be rationalized from the fact that the origin of the PL arises essentially from surface states in the CdTe QDs [48]. Both the degree of overlap and distance

Table 10.7 Dynamics of picosecond-resolved luminescence transients of CdTe QDs (QD1–QD4) in the presence and absence of sensitizer N719 and ZnO NRs^{a,t}

Sample	Observed wavelength (nm)	τ_1 (ns)	τ_2 (ns)	τ_3 (ns)	τ_{avg} (ns)	$k_{\text{nr}} \times 10^7$ (s ⁻¹)
QD1 (abs 445 nm)	520	0.93 ± 0.03 (30 %)	6.80 ± 0.15 (38 %)	35.80 ± 0.45 (32 %)	14.30 ± 0.21	–
QD1 + N719	520	0.90 ± 0.03 (40 %)	4.80 ± 0.12 (38 %)	23.40 ± 0.38 (22 %)	7.30 ± 0.14	$k_{\text{FRET}} = 6.70 \pm 0.16$
QD1 + ZnO	520	0.21 ± 0.02 (61 %)	4.20 ± 0.05 (25 %)	21.30 ± 0.23 (14 %)	4.20 ± 0.05	$k_{\text{PET}} = 17.00 \pm 0.40$
QD2 (abs 500 nm)	560	1.10 ± 0.15 (15 %)	9.90 ± 0.78 (33 %)	40.20 ± 0.95 (52 %)	24.30 ± 0.77	–
QD2 + N719	560	1.20 ± 0.08 (25 %)	7.50 ± 0.20 (43 %)	34.90 ± 0.50 (32 %)	14.70 ± 0.27	$k_{\text{FRET}} = 2.60 \pm 0.10$
QD2 + ZnO	560	0.21 ± 0.02 (52 %)	4.70 ± 0.07 (25 %)	26.20 ± 0.16 (23 %)	7.30 ± 0.06	$k_{\text{PET}} = 10.00 \pm 0.40$
QD3 (abs 550 nm)	610	0.84 ± 0.05 (3 %)	16.20 ± 0.88 (45 %)	43.60 ± 0.9 (52 %)	29.90 ± 0.87	–
QD3 + N719	610	0.80 ± 0.08 (7 %)	8.80 ± 0.27 (32 %)	28.30 ± 0.68 (61 %)	20.10 ± 0.51	$k_{\text{FRET}} = 1.60 \pm 0.03$
QD3 + ZnO	610	0.22 ± 0.07 (61 %)	4.30 ± 0.12 (13 %)	27.40 ± 0.14 (26 %)	7.80 ± 0.02	$k_{\text{PET}} = 9.50 \pm 0.06$
QD4 (abs 610 nm)	660	2.35 ± 0.17 (27 %)	8.10 ± 0.94 (36 %)	31.80 ± 1.40 (37 %)	15.30 ± 0.90	–
QD4 + N719	660	2.18 ± 0.06 (36 %)	7.10 ± 0.30 (36 %)	27.30 ± 1.00 (28 %)	10.90 ± 0.41	$k_{\text{FRET}} = 2.60 \pm 0.07$
QD4 + ZnO	660	0.27 ± 0.02 (49 %)	4.30 ± 0.50 (31 %)	21.70 ± 0.13 (20 %)	5.80 ± 0.19	$k_{\text{PET}} = 10.70 \pm 0.20$

^aThe emission from CdTe QDs (emission at 520 nm, 560 nm, 610 nm, and 660 nm, respectively) was detected with 375 nm laser excitation. k_{nr} represents non-radiative (FRET/PET) rate constant. *Numbers in the parentheses* indicate relative weightages

Table 10.8 Various FRET parameters^a obtained for different sized CdTe QDs and N719 dye molecules

FRET pairs	$J(\lambda) \times 10^{14}$ ($M^{-1} \text{ cm}^{-1} \text{ nm}^4$)	Q_D	R_0 (nm)	E_{TR} (%)	r_{DA} (nm) from FRET	r (nm) from TEM
QD1 + N719	9.2 ± 0.2	0.18 ± 0.01	3.69 ± 0.05	0.490 ± 0.003	3.72 ± 0.03	2.00 ± 0.11
QD2 + N719	7.5 ± 0.3	0.29 ± 0.02	3.86 ± 0.07	0.400 ± 0.008	4.14 ± 0.06	2.50 ± 0.20
QD3 + N719	5.1 ± 0.2	0.45 ± 0.03	3.90 ± 0.07	0.330 ± 0.002	4.38 ± 0.08	3.50 ± 0.14
QD4 + N719	3.6 ± 0.1	0.40 ± 0.02	3.61 ± 0.04	0.290 ± 0.012	4.22 ± 0.04	4.50 ± 0.25

^aOverlap integral ($J(\lambda)$), quantum yield (Q_D) in the absence of acceptor, Förster distance (R_0), FRET efficiency calculated from time-resolved study (E_{TR}), and donor-acceptor distance (r_{DA}) between the FRET pairs and radii (r) of QDs measured from TEM images

between donor and acceptor have been accounted simultaneously for FRET efficiency estimation. The energy transfer efficiency from QD to N719 is observed to decrease with a subsequent decrease in overlap integral, which is consistent with previous studies [118, 119]. The calculated FRET parameters are also presented in Table 10.8.

Although FRET is an interesting phenomenon that requires neither physical contact nor charge exchange, however, direct attachment of the CdTe QDs with the ZnO NRs leads to photo-induced electron transfer (PET) from QDs to the conduction band of ZnO. Similar PET studies have been reported in the literature, which is a fundamental process of QDSSC that ultimately pilots a direct sensitization of the solar cell performance [48, 120, 121]. The rate of charge recombination, energy transfer, and charge injection processes (reactions i, ii, and iii, respectively) dictate the emission decay of CdTe QDs.

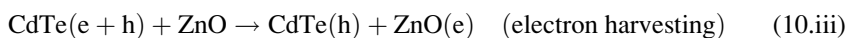
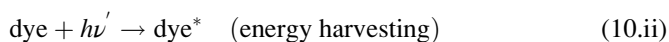
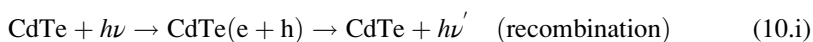
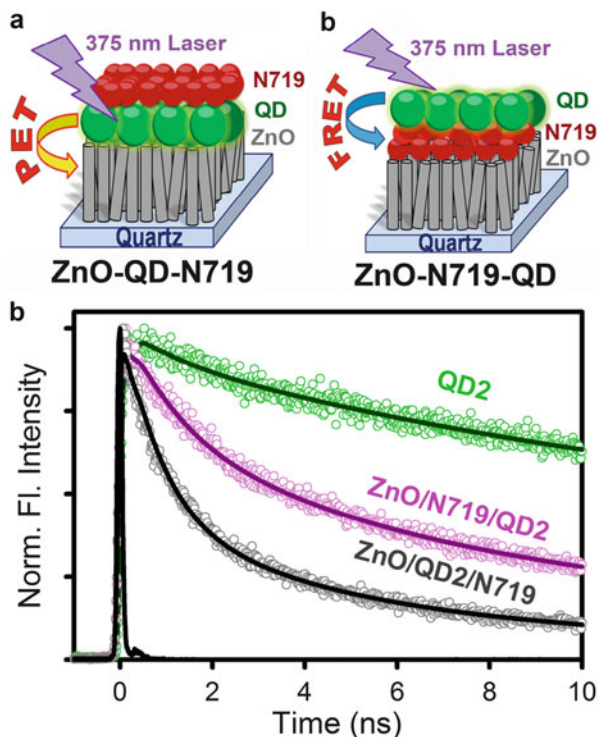


Figure 10.18 shows the emission decay of CdTe QDs anchored to ZnO NR films on a quartz plate, recorded with 375 nm diode laser excitation. As observed in the previous studies, both heterogeneity of samples and varying degree of surface defects introduce multi-exponential decay behavior to the charge recombination process [47, 48]. A significant decrease in QD lifetime, however, was observed in the presence of ZnO NRs. In particular, the fast component, which contributes nearly 61 % of the decay, shows a major decrease in lifetime from 0.93 ± 0.03 to 0.21 ± 0.02 ns in the smallest QD-ZnO composite. The apparent rate constants, k_{nr} , were determined for the non-radiative processes by comparing the lifetimes of CdTe in absence (τ_0) and in presence (τ) of N719 and ZnO NRs, using (10.10).

$$k_{\text{nr}} = \frac{1}{\langle\tau\rangle} - \frac{1}{\langle\tau_0\rangle} \quad (10.10)$$

For the smallest QD (i.e., QD1), the apparent rate constant for charge injection into ZnO NRs was estimated to be $1.7 \times 10^8 \text{ s}^{-1}$, whereas the rate of energy transfer from QD1 to N719 is $6.7 \times 10^7 \text{ s}^{-1}$. Therefore, it is evident that the charge injection from the excited CdTe to the ZnO NRs occurs with a rate constant that is an order of magnitude higher than that of energy transfer between CdTe to N719. It should be noted that the above estimation of average lifetimes takes into account both short and long-lived components. A major population of the charge injection process occurs with a greater rate constant (as high as 10^9 s^{-1}) if we compare only the fast component of the emission transients. For example, ~61 % of the emission decay of CdTe QDs on ZnO surface occurs with a lifetime of 0.21 ± 0.02 ns, indicating the major fraction of the charge injection event occurs on an ultrafast time scale.

Fig. 10.19 Two different architectures of CdTe QD decorated dye-sensitized ZnO NR substrates, namely, (a) ZnO–QD–N719 and (b) ZnO–N719–QD. (c) The picosecond-resolved fluorescence transients of CdTe QD2 showing PET and FRET in two different architectures. The excitation wavelength was 375 nm and the emission was monitored at 560 nm. Reprinted with permission from J. Phys. Chem. C 116, 14248–14256 (2012). Copyright 2013 American Chemical Society



In order to investigate the mechanism of co-sensitization of CdTe QDs in the layered architectures (Fig. 10.19a, b) related to DSSC fabrication, picosecond-resolved fluorescence study was performed (Fig. 10.19c). The fluorescence transient of the bare QDs not in the vicinity of N719 and/or ZnO is shown in the figure as a reference. In the ZnO–QD–N719 architecture (Fig. 10.19a), QDs are sandwiched between ZnO NRs and N719. In these conditions, QDs can either directly transfer electrons to the conduction band (CB) of ZnO NRs or can non-radiatively transfer energy to sensitizer N719. The fluorescence decay parameters, as shown in Table 10.9, are comparable to the distinct lifetimes of an electron transfer process (Table 10.7). Therefore, the picosecond-resolved fluorescence transient of CdTe QDs in the ZnO–QD–N719 architecture reveals a “direct injection” of charge carriers from QDs to ZnO NRs via PET. It is to note that the role of the capping ligands of the colloidal QDs has been demonstrated to have paramount importance on the efficient charge separation at the QD–polymer interface [122]. In this respect, the electron transfer pathway is found to prevail over the FRET process with short chain 3-MPA ligands associated to CdTe QDs. In the other architecture, ZnO–N719–QD (Fig. 10.19b), the QDs are separated by a layer of N719 molecules from the ZnO NRs whereby light harvesting could only occur through FRET from QDs to N719. It is being conventional that the N719 dye binds the ZnO by using its carboxylic groups [123], as a result the residual chains of N719

Table 10.9 Dynamics of picosecond-resolved luminescence transients of CdTe QDs (QD1–QD4) in the presence and absence of sensitizer N719 and ZnO NRs^a

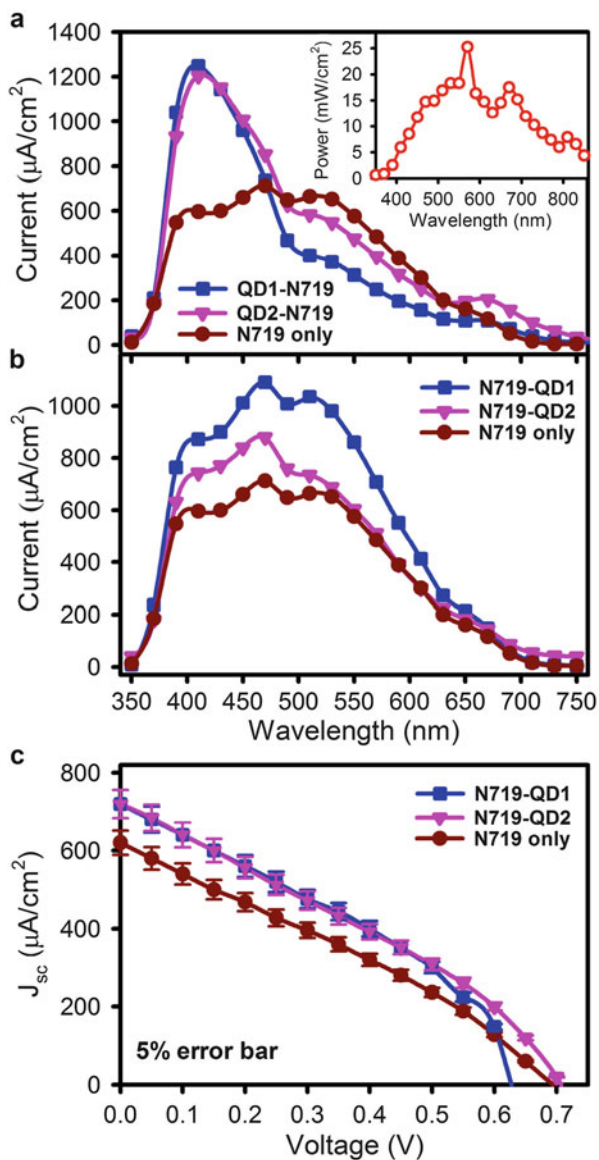
Sample	Observed wavelength (nm)	τ_1 (ns)	τ_2 (ns)	τ_3 (ns)	τ_{avg} (ns)	$k_{\text{nr}} \times 10^7$ (s ⁻¹)
QD2 (abs 500 nm)	560	1.10 ± 0.15 (15 %)	9.90 ± 0.78 (33 %)	40.20 ± 0.95 (52 %)	24.30 ± 0.77	–
ZnO-N719-QD2	560	1.20 ± 0.18 (33 %)	7.00 ± 0.65 (45 %)	32.00 ± 0.86 (22 %)	10.60 ± 0.54	5.30 ± 0.31
ZnO-QD2-N719	560	0.72 ± 0.09 (59 %)	4.50 ± 0.45 (33 %)	22.80 ± 0.82 (8 %)	7.30 ± 0.27	9.60 ± 0.38

^aThe emission from CdTe QD (emission at 560 nm) was detected with 375 nm laser excitation. Numbers in the parentheses indicate relative weightages

are free and away from the ZnO, which allows them to interlace with the 3-MPA ligands of the QDs via efficient hydrophilic interactions. This sort of an association results in an average distance between the donor and the acceptor, which lies within the Förster radius and allows an efficient energy transfer. The assorted lifetimes (Table 10.9) of the QDs in this particular configuration are comparable to the decay parameters of the energy transfer route (as shown in Table 10.7), which reveals that an additional “indirect-excitation” of N719 can be introduced by using the sensitivity of FRET and this type of engineered solar cells should contribute to higher photocurrents. The non-radiative rate constants (k_{nr}) in these two architectures, as presented in Table 10.9, are almost analogous to the k_{nr} values of the individual systems that lead to either energy or electron transfer pathways (Table 10.7).

The effectiveness of QD decoration in solar cell performance was evaluated by employing them in a photoelectrochemical cell with the two different architectures (Fig. 10.19a, b) as discussed before. The use of CdTe QDs as a sensitizer in photoelectrochemical cells have been investigated by several research groups [19, 48, 124, 125]. DSSC devices fabricated with N719 dye as sensitizer in the presence and the absence of CdTe QDs (QD1 and QD2) were characterized by wavelength-dependent photocurrent spectroscopy (Fig. 10.20a, b) and photocurrent–voltage (J – V) measurements (Fig. 10.20c); the resulting photovoltaic parameters are summarized in Table 10.10. The wavelength-dependent photocurrent is the number of electrons collected under known photon intensity that was evaluated from the short-circuit photocurrent (J_{SC}) measured for different incident wavelengths (λ). The inset of Fig. 10.20a shows the wavelength-dependent incident power of the monochromator. The photocurrent vs. wavelength plot of the ZnO–QD–N719 architecture is presented in Fig. 10.20a, which shows a spectral response in the range of 350–750 nm. In devices without any modification of the dye sensitizer with QDs, the broad photocurrent spectrum is attributed to the photo-generated charge carrier in sensitizer N719 [20]. As shown in the figure, the presence of QD1 ($\lambda_{abs} = 440$ nm) and QD2 ($\lambda_{abs} = 500$ nm) into the sensitization process lead to a dramatic increase in the photocurrent in the spectral region of blue photons indicating the occurrence of a direct injection of electrons from QDs to ZnO NRs, similar to the observations made by the picosecond-resolved fluorescence studies (Fig. 10.19c). In this case, it is to be noted that dye (N719) loading was lower in ZnO–QD–N719 architecture compared to that of ZnO–N719 assembly due to prior attachment of QD to the ZnO NRs. Therefore, at 530 nm (maximum optical absorption in N719) the photocurrent was found to be lower in ZnO–QD–N719 compared to ZnO–N719 system. Hence, a fair comparison of wavelength-dependent photocurrent and overall device performance of these architectures is not likely when the amounts of dye present in different architectures are not similar. For a better assessment, we engineered devices with similar dye loading in ZnO–N719–QD and ZnO–N719 solar cells. The ZnO–N719–QD architecture shows increased photocurrent (Fig. 10.20b) compared to ZnO–N719 system throughout the spectral region as additional photo-generated charge carriers from N719 dye (via FRET) adds up to the net photocurrent. Figure 10.20c shows the J – V characteristics of solar cells with ZnO–N719–QD architecture as compared to solar

Fig. 10.20 Photocurrent vs. wavelength spectra for DSSCs comprising (a) ZnO–QD–N719 and (b) ZnO–N719–QD architectures, respectively. The *inset* shows incident power vs. wavelength plot. (c) Photocurrent–voltage (J – V) characteristics for ZnO–N719–QD architecture. Reprinted with permission from J. Phys. Chem. C 116, 14248–14256 (2012). Copyright 2013 American Chemical Society



cells sensitized with dye only. As shown in Table 10.10, the calculated values of FF and the overall power conversion efficiencies of ZnO–N719-based DSSCs are found to improve in the presence of QD assembly. Overall, the analysis of photo-device data in the measured ZnO–N719–QD configuration reflects similarly the co-sensitization of CdTe QDs tagged with the sensitivity of FRET as observed by the picosecond-resolved fluorescence study (Fig. 10.19c).

Table 10.10 Device performance^a of the DSSCs made of two different architecture of QD loading

Device with N719	V_{OC} (V)	J_{SC} ($\mu\text{A cm}^{-2}$)	FF (%)	η (%)
ZnO–N719–QD1	0.63 ± 0.04	720 ± 36	35.27 ± 2.70	0.16 ± 0.01
ZnO–N719–QD2	0.71 ± 0.03	720 ± 29	30.99 ± 1.31	0.16 ± 0.01
ZnO–N719	0.69 ± 0.05	620 ± 33	29.92 ± 0.50	0.13 ± 0.01

^aShort circuit photocurrent densities (J_{SC}/cm^2), open-circuit voltage (V_{OC}), fill factor (FF), and efficiency (η)

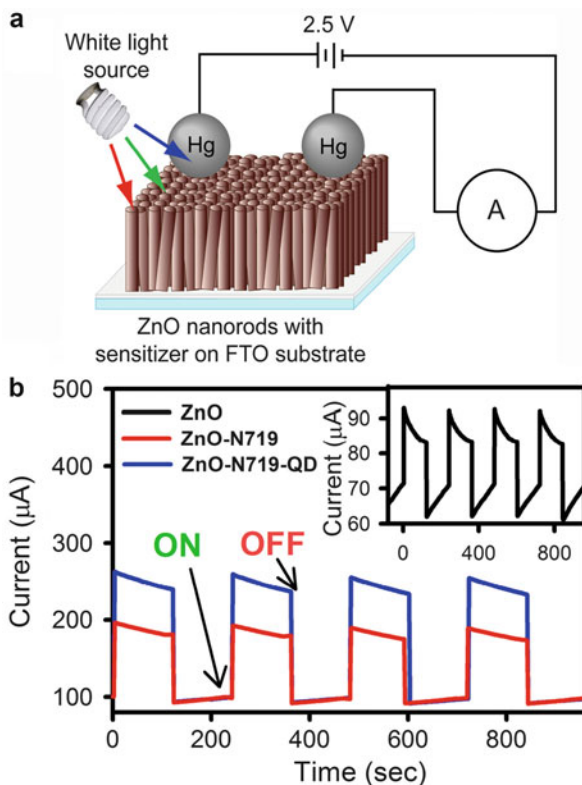
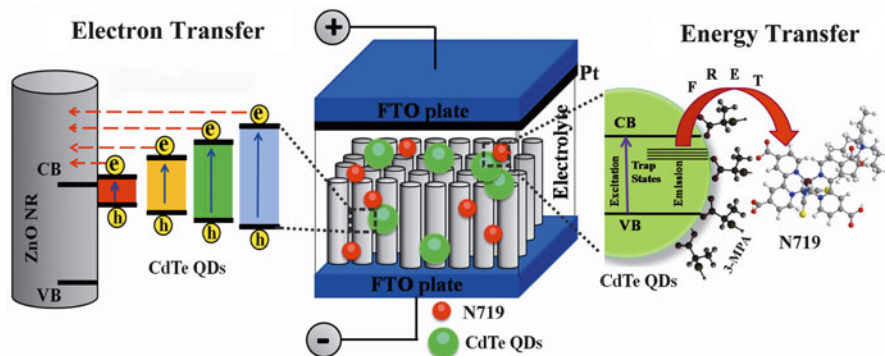


Fig. 10.21 (a) Schematic representation of photoconductivity measurement setup by using FTO as one of the electrodes and a small (4 mm diameter) drop of mercury (Hg) on top of the film as a counter electrode. (b) Photocurrent responses of ZnO NRs (inset), ZnO–N719, and ZnO–N719–QD2 arrays under bias voltage of 2.5 V. The photocurrent was measured across the thickness of the films with 25 mW cm^{-2} incident power from a halogen light source. Reprinted with permission from J. Phys. Chem. C 116, 14248–14256 (2012). Copyright 2013 American Chemical Society

The photoconductivity measurement [25] of the ZnO NR, ZnO–N719 and ZnO–N719–QD thin films were carried out in order to better understand the contribution of QDs via FRET to the net photocurrent in the devices. Figure 10.21b shows the photocurrent response for the ZnO NR (inset), ZnO–N719, and



Scheme 10.5 Dual-sensitization in QD-decorated DSSCs: The system consists of a fluorinated tin oxide (FTO) on which semiconductor ZnO NR (gray cylinder) is fabricated. The sensitizer dye N719 (small red circle) and 3-MPA-capped CdTe QDs (big green circle) are bound to ZnO NR by surface adsorption. The directly attached QDs lead to sensitization via efficient charge injection from excited semiconductor nanocrystal, CdTe into ZnO NR. Moreover, the QDs that are within the close proximity of sensitizing dye N719 introduce an additional indirect excitation of N719 by using the sensitivity of FRET. The upshot of the above dual-sensitization mode is found to be reflected in the overall solar cell performance. Reprinted with permission from J. Phys. Chem. C 116, 14248–14256 (2012). Copyright 2013 American Chemical Society

ZnO–N719–QD2 thin films. An improved photocurrent was observed for the ZnO–N719–QD2 thin film ($\sim 260 \mu\text{A}$) under illuminated conditions compared to the ZnO–N719 thin film ($\sim 190 \mu\text{A}$). This shows that an additional “indirect excitation” of N719 can be obtained by decorating the dye molecules with CdTe QDs. For the model DSSCs prepared with the same arrangement of ZnO–N719–QD, we observed a similar enhancement of photocurrent (Fig. 10.20c) in the presence of CdTe QDs, which further confirms the contribution of FRET towards the improvement of efficient energy harvesting in dual-sensitized solar cells.

4 Conclusion

In summary, we have characterized the defect centers, in particular, the oxygen vacancy centers in ZnO NPs and also explored the dynamics of light harvesting in near-infrared region by using OX1 chromophore. By studying picosecond-resolved fluorescence transients at 550 nm, we have shown that efficient FRET ($\sim 93\%$) occurs from doubly-charged oxygen vacancy centers (V_{O}^{++}) to the acceptor OX1 in the ZnO–OX1 adduct. Comparatively, a less efficient (63%) light harvesting dynamics was found by monitoring the emission peak at 495 nm, which arises from singly charged oxygen vacancy centers (V_{O}^+). The overall picture that evolved from our studies is summarized in Scheme 10.1. It is to be noted that the FRET distance (r_{DA}) is dependent on the emission wavelength of ZnO NPs whether

it arises from surface or near bulk states. Therefore, r_{DA} can be interpreted as a parameter that signifies the distance between the probe (OX1) and the different vacancy states of ZnO NPs. Our experimental observations may find relevance in the light harvesting devices using ZnO NPs.

Subsequently, time-correlated single photon counting spectroscopy was carried out to understand the resonance energy transfer phenomenon in a ZnO–N719 system, which is extensively used in DSSCs, as illustrated in Scheme 10.2. The semiconductor ZnO NPs were found to transfer their excited state energy to N719 sensitizers at the surface of the NPs. The observed energy transfer process in the presence of high-energy photons leads to a significant increase in J_{SC} (~78 %) in ZnO-based DSSCs leading to more than ~118 % increased energy conversion efficiency (η), whereas TiO₂-based solar cells showed marginal increase in J_{SC} and a slight efficiency improvement (~9 %). It has been found that the energy transfer process does not involve any physical migration of electron from photoexcited ZnO to the sensitizing dyes. Our study may find relevance in the enhancement of high-energy photon harvesting, which utilizes semiconductor defect centers without any further accumulation of external co-sensitizers. The observed FRET processes in the light harvesting dynamics open a novel way toward the utilization of new materials containing appreciable amount of defect states. These findings provide the importance of the various semiconductors containing inherent optical defect centers and how the defect centers can be beneficially utilized for light harvesting/sensitization.

We also provided a mechanistic explanation for the excitation-dependent recombination processes and the catalytic activity of Au NPs in the ZnO–Au NCs, as schematically shown in Scheme 10.4. A better understanding of the charge-transfer processes at the semiconductor–metal interface is crucial for optimizing the performance of such materials in photocatalysis and DSSCs. Our results demonstrate that the excited ZnO NPs resonantly transfer visible optical radiation to the Au NPs upon below band-gap excitation of the semiconductor. A singly charged vacancy center of the ZnO semiconductor is demonstrated to be responsible for the visible optical radiation transfer from ZnO NPs to Au NPs, whereas a combination of the energy transfer between surface defects and surface plasmon of Au NPs, as well as thermalization of photogenerated electron–hole pair and their recombination in the ZnO NPs is believed to take place simultaneously upon above band-edge excitation. We observe that the prepared ZnO–Au NCs are stable and efficient enough for the environmental purification of organic pollutants. As a low-cost photovoltaic cell, the incident photon-to-current conversion efficiency and short-circuit current is significantly improved in presence of Au NPs, which is attributed to the better electron mobility of the ZnO–Au NCs. This approach may give rise to a new class of multifunctional materials with possible applications in energy-conversion devices.

Finally, we have demonstrated the utilization of dual-sensitization in DSSCs as schematically represented in Scheme 10.5. The steady-state and the time-resolved luminescence measurements on 3-MPA-capped CdTe QDs reveal the size-dependent charge injection characteristics of ZnO photoelectrodes. The QDs that

are not in a direct contact with the semiconductor can harvest visible light, which is resonantly transferred to sensitizer N719 dyes, thereby offering an indirect excitation of the dye molecules. To investigate the improvement of light-harvesting because of QD decoration in a DSSC, wavelength-dependent photocurrent, photocurrent–voltage (J – V) characteristics, and photoconductivity measurements were performed for both the QD-assembled and reference (only sensitizing dye) devices. The co-sensitization in the presence of CdTe QDs leads to a significant increment in photocurrent throughout the visible spectral region and also enhances the short-circuit current density as additional photogenerated charge carriers from N719 dye (via FRET) adds up to the net photocurrent. As we continue to modify, study, and improve such FRET pair sensitizers, the realization of truly inexpensive, stable, and efficient DSSCs grows nearer.

Acknowledgements S.S. thanks UGC (India) and A.M. thanks CSIR (India) for fellowships. We thank DST (India) for financial grants DST/TM/SERI/2k11/103. We thank Tanujjal Bora (Asian Institute of Technology, Bangkok), Sunandan Baruah (Assam Don Bosco University, Guwahati), Karthik Lakshman, Htet H. Kyaw (Sultan Qaboos University, Sultanate of Oman), and Prof. A. K. Raychaudhuri (S. N. Bose National Centre) for the collaboration work.

References

1. O'Regan, B., Grätzel, M.: *Nature* **353**, 737–740 (1991)
2. Grätzel, M.: *Nature* **414**, 338–344 (2001)
3. Bai, Y., Cao, Y., Zhang, J., Wang, M., Li, R., Wang, P., Zakeeruddin, S.M., Grätzel, M.: *Nat. Mater.* **7**, 26–630 (2008)
4. Anta, J.A., Guillen, E., Tena-Zaera, R.J.: *Phys. Chem. C* **116**, 11413–11425 (2012)
5. Ferrere, S., Zaban, A., Gregg, B.A.J.: *Phys. Chem. B* **101**, 4490–4493 (1997)
6. Sayama, K., Sugihara, H., Arakawa, H.: *Chem. Mater.* **12**, 3825–3832 (1998)
7. Kruger, J., Plass, R., Grätzel, M., Cameron, P.J., Peter, L.M.J.: *Phys. Chem. B* **107**, 7536–7539 (2003)
8. Law, M., Greene, L.E., Johnson, J.C., Saykally, R., Yang, P.: *Nat. Mater.* **4**, 455–459 (2005)
9. Nazeeruddin, M.K., Angelis, F.D., Fantacci, S., Selloni, A., Viscardi, G., Liska, P., Ito, S., Takeru, B., Grätzel, M.J.: *Am. Chem. Soc.* **127**, 16835–16847 (2005)
10. Hamman, T.W., Jensen, R.A., Martinson, A.B.F., Ryswyk, H.V., Hupp, J.T.: *Energy Environ. Sci.* **1**, 66–78 (2008)
11. Grätzel, M.J.: *Photochem. Photobiol. A* **164**, 3–14 (2004)
12. Wang, P., Zakeeruddin, S.M., Moser, J.E., Nazeeruddin, M.K., Sekiguchi, T., Grätzel, M.: *Nat. Mater.* **2**, 402–407 (2003)
13. Yum, J.H., Walter, P., Huber, S., Rentsch, D., Geiger, T., Nüesch, F., Angelis, F.D., Grätzel, M., Nazeeruddin, M.K.J.: *Am. Chem. Soc.* **129**, 10320–10321 (2007)
14. Fan, S.Q., Cao, R.J., Xi, Y.X., Gao, M., Wang, M.D., Kim, D.H., Kim, C.W., Ko, J.J.: *Optoelectron. Adv. Mater.* **3**, 1027–1033 (2009)
15. Hardin, B.E., Hoke, E.T., Armstrong, P.B., Yum, J.H., Comte, P., Torres, T., Frechet, J.M.J., Nazeeruddin, M.K., Grätzel, M., McGehee, M.D.: *Nat. Photonics* **3**, 406–411 (2009)
16. Cid, J.J., Yum, J.H., Jang, S.R., Nazeeruddin, M.K., Martinez-Ferrero, E., Palomares, E., Ko, J., Grätzel, M., Torres, T.: *Angew. Chem. Int. Ed.* **119**, 8510–8514 (2007)
17. Etgar, L., Park, J., Barolo, C., Lesnyak, V., Panda, S.K., Quagliotto, P., Hickey, S.G., Nazeeruddin, M.K., Eychmuller, A., Viscardi, G., et al.: *RSC Adv.* **2**, 2748–2752 (2012)

18. Giménez, S., Rogach, A.L., Lutich, A.A., Gross, D., Poeschl, A., Susha, A.S., Mora-Seró, I., Lana-Villarreal, T., Bisquert, J.: *J. Appl. Phys.* **110**, 014314 (2011)
19. Ruland, A., Schulz-Drost, C., Sgobba, V., Guldi, D.M.: *Adv. Mater.* **23**, 4573–4577 (2011)
20. Shankar, K., Feng, X., Grimes, C.A.: *ACS Nano* **3**, 788–794 (2009)
21. Buhbut, S., Itzhakov, S., Tauber, E., Shalom, M., Hod, I., Geiger, T., Garini, Y., Oron, D., Zaban, A.: *ACS Nano* **4**, 1293–1298 (2010)
22. Buhbut, S., Itzhakov, S., Oron, D., Zaban, A.J.: *Phys. Chem. Lett.* **2**, 1917–1924 (2011)
23. Makhal, A., Sarkar, S., Bora, T., Baruah, S., Dutta, J., Raychaudhuri, A.K., Pal, S.K.: *Nanotechnology* **21**, 265703 (2010)
24. Makhal, A., Sarkar, S., Bora, T., Baruah, S., Dutta, J., Raychaudhuri, A.K., Pal, S.K.: *J. Phys. Chem. C* **114**, 10390–10395 (2010)
25. Sarkar, S., Makhal, A., Bora, T., Baruah, S., Dutta, J., Pal, S.K.: *Phys. Chem. Chem. Phys.* **13**, 12488–12496 (2011)
26. Sarkar, S., Makhal, A., Lakshman, K., Bora, T., Dutta, J., Pal, S.K.: *J. Phys. Chem. C* **116**, 14248–14256 (2012)
27. Sarkar, S., Makhal, A., Baruah, S., Mahmood, M.A., Dutta, J., Pal, S.K.: *J. Phys. Chem. C* **116**, 9608–9615 (2012)
28. Lakowicz, J.R.: *Principles of fluorescence spectroscopy*, 2nd edn. Kluwer Academic, New York (1999)
29. Scheller, F.W., Wollenberger, U., Warsinke, A., Lisdat, F.: *Curr. Opin. Biotechnol.* **12**, 35–40 (2001)
30. Iqbal, S.S., Mayo, M.W., Bruno, J.G., Bronk, B.V., Batt, C.A., Chambers, J.P.: *Biosens. Bioelectron.* **15**, 549–578 (2000)
31. Whitcombe, D., Theaker, J., Guy, S.P., Brown, T., Little, S.: *Nat. Biotechnol.* **17**, 804–807 (1999)
32. Cardullo, R.A., Agrawal, S., Flores, C., Zamecnik, P.C., Wolf, D.E.: *Proc. Natl. Acad. Sci. U. S. A.* **85**, 8785–8789 (1988)
33. Ha, T., Enderle, T., Ogletree, D.F., Chemla, D.S., Selvin, P.R., Weiss, S.: *Proc. Natl. Acad. Sci. U. S. A.* **93**, 6264–6268 (1996)
34. Snee, P.T., Somers, R.C., Nair, G., Zimmer, J.P., Bawendi, M.G., Nocera, D.G.J.: *Am. Chem. Soc.* **128**, 13320–13321 (2006)
35. Becker, K., Lupton, J.M., Muller, J., Rogach, A.L., Talapin, D.V., Weller, H., Feldmann, J.: *Nat. Mater.* **5**, 777–781 (2006)
36. Clegg, R.M., Murchie, A.I.H., Zechel, A., Lilley, D.M.: *Proc. Natl. Acad. Sci. U. S. A.* **90**, 2994–2998 (1993)
37. Zhang, C.Y., Yeh, H.C., Kuroki, M.T., Wang, T.H.: *Nat. Mater.* **4**, 826–831 (2005)
38. Currie, M.J., Mapel, J.K., Heidel, T.D., Goffri, S., Baldo, M.A.: *Science* **321**, 226–228 (2008)
39. Baldo, M.A., O'Brien, D.F., You, Y., Shoustikov, A., Sibley, S., Thompson, M.E., Forrest, S.R.: *Nature* **395**, 151–154 (1998)
40. Chin, P.T.K., Hikmet, R.A.M., Janssen, R.A.J.: *J. Appl. Phys.* **104**, 013108 (2008)
41. Yu, W.W., Qu, L., Guo, W., Peng, X.: *Chem. Mater.* **15**, 2854–2860 (2003)
42. Kamat, P.V.J.: *Phys. Chem. C* **111**, 2834–2860 (2007)
43. Zhang, Q., Guo, X., Huang, X., Huang, S., Li, D., Luo, Y., Shen, Q., Toyoda, T., Meng, Q.: *Phys. Chem. Chem. Phys.* **13**, 4659–4667 (2011)
44. Ruhle, S., Shalom, M., Zaban, A.: *Chem. Phys. Chem.* **11**, 2290–2304 (2010)
45. Shalom, M., Ruhle, S., Hod, I., Yahav, S., Zaban, A.J.: *Am. Chem. Soc.* **131**, 9876–9877 (2009)
46. Kamat, P.V.J.: *Phys. Chem. C* **112**, 18737–18753 (2008)
47. Kongkanand, A., Tvrđy, K., Takechi, K., Kuno, M., Kamat, P.V.J.: *Am. Chem. Soc.* **130**, 4007–4015 (2008)
48. Bang, J.H., Kamat, P.V.: *ACS Nano* **3**, 1467–1476 (2009)
49. Ross, R.T., Nozik, A.J.: *J. Appl. Phys.* **53**, 3813–3818 (1982)
50. Schaller, R.D., Agranovich, V.M., Klimov, V.I.: *Nat. Phys.* **1**, 189–194 (2005)

51. Schaller, R.D., Klimov, V.I.: *Phys. Rev. Lett.* **92**, 186601 (2004)
52. Kamat, P.V., Tvrđy, K., Baker, D.R., Radich, J.G.: *Chem. Rev.* **110**, 6664–6688 (2010)
53. Shalom, M., Dor, S., Ruhle, S., Grinis, L., Zaban, A.J.: *Phys. Chem. C* **113**, 3895–3898 (2009)
54. Shalom, M., Albero, J., Tachan, Z., Martínez-Ferrero, E., Zaban, A., Palomares, E.J.: *Phys. Chem. Lett.* **1**, 1134–1138 (2010)
55. Choi, H., Nicolaescu, R., Paek, S., Ko, J., Kamat, P.V.: *ACS Nano* **5**, 9238–9245 (2011)
56. Siegers, C., Hohl-Ebinger, J., Zimmermann, B., Würfel, U., Mülhaupt, R., Hinsch, A., Haag, R.: *Chem. Phys. Chem.* **8**, 1548–1556 (2007)
57. Keis, K., Bauer, C., Boschloo, G., Hagfeldt, A., Westermark, K., Rensmo, H., Siegbahn, H.J.: *Photochem. Photobiol. A Chem.* **148**, 57–64 (2002)
58. Suh, D.I., Lee, S.Y., Kim, T.H., Chun, J.M., Suh, E.K., Yang, O.B., Lee, S.K.: *Chem. Phys. Lett.* **442**, 348–353 (2007)
59. Yang, P., Yan, H., Mao, S., Russo, R., Johnson, J., Saykally, R., Morris, N., Pham, J., He, R., Choi, H.: *Adv. Funct. Mater.* **12**, 323–331 (2002)
60. Xia, J.B., Zhang, X.W.: *Eur. Phys. J. B* **49**, 415–420 (2006)
61. Quintana, M., Edvinsson, T., Hagfeldt, A., Boschloo, G.J.: *Phys. Chem. C* **111**, 1035–1041 (2007)
62. Tributsch, H., Calvin, M.: *Photochem. Photobiol.* **14**, 95–112 (1971)
63. Krebs, F.C., Nielsen, T.D., Fyenbo, J., Wadstrøm, M., Pedersen, M.S.: *Energy Environ. Sci.* **3**, 512–525 (2010)
64. Ajuria, J., Etxebarria, I., Cambarau, W., Munecas, U., Tena-Zaera, R., Jimeno, J.C., Pacios, R.: *Energy Environ. Sci.* **4**, 453–458 (2010)
65. Kramer, I.J., Sargent, E.H.: *ACS Nano* **5**, 8506–8514 (2011)
66. Semonin, O.E., Luther, J.M., Choi, S., Chen, H.-Y., Gao, J., Nozik, A.J., Beard, M.C.: *Science* **334**, 1530–1533 (2011)
67. Sessolo, M., Bolink, H.J.: *Adv. Mater.* **23**, 1829–1845 (2011)
68. Saito, M., Fujihara, S.: *Energy Environ. Sci.* **1**, 280–283 (2008)
69. Ambade, S.B., Mane, R.S., Han, S.-H., Lee, S.-H., Sung, M.-M., Joo, O.-S.J.: *Photochem. Photobiol. A* **222**, 366–369 (2011)
70. Zhang, Q.F., Chou, T.R., Russo, B., Jenekhe, S.A., Cao, G.Z.: *Angew. Chem. Int. Ed.* **47**, 2402–2406 (2008)
71. Memarian, N., Concina, I., Braga, A., Rozati, S.M., Vomiero, A., Sberveglieri, G.: *Angew. Chem. Int. Ed.* **50**, 12321–12325 (2011)
72. Yoshida, T., Zhang, J.B., Komatsu, D., Sawatani, S., Minoura, H., Pauporte, T., Lincot, D., Oekermann, T., Schlettwein, D., Tada, H., et al.: *Adv. Funct. Mater.* **19**, 17–43 (2009)
73. Lin, C.-Y., Lai, Y.-H., Chen, H.-W., Chen, J.-G., Kung, C.-W., Vittal, R., Ho, K.-C.: *Energy Environ. Sci.* **4**, 3448–3455 (2011)
74. Xu, C., Wu, J., Desai, U.V., Gao, D.J.: *Am. Chem. Soc.* **133**, 8122–8125 (2011)
75. Chen, W., Qiu, Y., Zhong, Y., Wong, K.S., Yang, S.J.: *Phys. Chem. A* **114**, 3127–3138 (2010)
76. Vayssieres, L., Keis, K., Hagfeldt, A., Lindquist, S.E.: *Chem. Mater.* **13**, 4395–4398 (2001)
77. Redmond, G., Fitzmaurice, D., Graetzel, M.: *Chem. Mater.* **6**, 686–691 (1994)
78. Hoyer, P., Weller, H.J.: *Phys. Chem.* **99**, 14096–14100 (1995)
79. Zhang, J., Xu, Q., Feng, Z., Li, M., Li, C.: *Angew. Chem. Int. Ed.* **47**, 1766–1769 (2008)
80. Galoppini, E., Rochford, J., Chen, H.H., Saraf, G., Lu, Y.C., Hagfeldt, A., Boschloo, G.J.: *Phys. Chem. B* **110**, 16159–16161 (2006)
81. Baruah, S., Sinha, S.S., Ghosh, B., Pal, S.K., Raychaudhuri, A.K., Dutta, J.: *J. Appl. Phys.* **105**, 074308 (2009)
82. Baruah, S., Thanachayanont, C., Dutta, J.: *Sci. Technol. Adv. Mater.* **9**, 025009 (2008)
83. Sugunan, A., Warad, H.C., Boman, M., Dutta, J.J.: *Sol-Gel Sci. Technol.* **39**, 49–56 (2006)
84. Baruah, S., Dutta, J.: *Sci. Technol. Adv. Mater.* **10**, 013001 (2009)

85. Rogach, A.L., Franzl, T., Klar, T.A., Feldmann, J., Gaponik, N., Lesnyak, V., Shavel, A., Eychmuller, A., Rakovich, Y.P., Donegan, J.F.J.: *Phys. Chem. C* **111**, 14628–14637 (2007)
86. Gaponik, N., Talapin, D.V., Rogach, A.L., Hoppe, K., Shevchenko, E.V., Kornowski, A., Eychmuller, A., Weller, H.J.: *Phys. Chem. B* **106**, 7177–7185 (2002)
87. Wuister, S.F., Swart, I., Driel, F.V., Hickey, S.G., Donegaa, C.D.M.: *Nano Lett.* **3**, 503–507 (2003)
88. Brennan, J.G., Siegrist, T., Carroll, P.J., Stuczynski, S.M., Reynders, P., Brus, L.E., Steigerwald, M.L.: *Chem. Mater.* **2**, 403–409 (1990)
89. Murray, C.B., Norris, D.J., Bawendi, M.G.J.: *Am. Chem. Soc.* **115**, 8706–8715 (1993)
90. Aldeek, F., Balan, L., Medjahdi, G., Roques-Carnes, T., Malval, J.P., Mustin, C., Ghanbaja, J., Schneider, R.J.: *Phys. Chem. C* **113**, 19458–19467 (2009)
91. Li, L., Yang, X., Gao, J., Tian, H., Zhao, J., Hagfeldt, A., Sun, L.J.: *Am. Chem. Soc.* **133**, 8458–8460 (2011)
92. Shalish, I., Temkin, H., Narayanmurti, V.: *Phys. Rev. B* **69**, 245401 (2004)
93. Ghosh, M., Raychaudhuri, A.K.: *Nanotechnology* **19**, 445704 (2008)
94. Tang, Y.B., Chen, Z.H., Song, H.S., Lee, C.S., Cong, H.T., Cheng, H.M., Zhang, W.J., Bello, I., Lee, S.T.: *Nano Lett.* **8**, 4191–4195 (2008)
95. Beek, W.J.E., Wienk, M.M., Janssen, R.A.J.: *Adv. Funct. Mater.* **16**, 1112–1116 (2006)
96. Ye, J.D., Gu, S.L., Qin, F., Zhu, S.M., Liu, S.M., Zhou, X., Liu, W., Hu, L.Q., Zhang, R., Shi, Y., et al.: *Appl. Phys. A* **81**, 759–762 (2005)
97. Dijken, A.V., Meulenkamp, E.A., Vanmaekelbergh, D., Meijerink, A.: *J. Lumin.* **87–89**, 454–456 (2000)
98. Vanheusden, K., Warren, W.L., Seager, C.H., Tallant, D.R., Voigt, J.A.: *J. Appl. Phys.* **79**, 7983 (1996)
99. Pal, S.K., Mandal, D., Sukul, D., Bhattacharyya, K.: *Chem. Phys.* **249**, 63–71 (1999)
100. Narayanan, S.S., Sinha, S.S., Pal, S.K.J.: *Phys. Chem. C* **112**, 12716–12720 (2008)
101. Jiang, C.Y., Sun, X.W., Lo, G.Q., Kwong, D.L.: *Appl. Phys. Lett.* **90**, 263501 (2007)
102. Zheng, Y., Chen, C., Zhan, Y., Lin, X., Zheng, Q., Wei, K., Zhu, J., Zhu, Y.: *Inorg. Chem.* **46**, 6675–6682 (2007)
103. Shirota, H., Pal, H., Tominaga, K., Yoshihara, K.: *Chem. Phys.* **236**, 355–364 (1998)
104. Narayanan, S.S., Sinha, S.S., Verma, P.K., Pal, S.K.: *Chem. Phys. Lett.* **463**, 160–165 (2008)
105. Burda, C., Green, T.C., Link, S., El-Sayed, M.A.J.: *Phys. Chem. B* **103**, 1783–1788 (1999)
106. Makhall, A., Yan, H., Lemmens, P., Pal, S.K.J.: *Phys. Chem. C* **114**, 627–632 (2010)
107. Haase, M., Weller, H., Henglein, A.J.: *Phys. Chem.* **92**, 482–487 (1988)
108. Subramanian, V., Wolf, E.E., Kamat, P.V.J.: *Phys. Chem. B* **107**, 7479–7485 (2003)
109. Subramanian, V., Wolf, E.E., Kamat, P.V.J.: *Am. Chem. Soc.* **126**, 4943–4950 (2004)
110. Sinha, S.S., Verma, P.K., Makhall, A., Pal, S.K.: *Rev. Sci. Instrum.* **80**, 053109 (2009)
111. Cozzoli, P.D., Curri, M.L., Agostiano A. *Chem. Commun.* 3186–3188 (2005)
112. Bora, T., Kyaw, H.H., Sarkar, S., Pal, S.K., Dutta, J.: *Beilstein J. Nanotechnol.* **2**, 681–690 (2011)
113. Hu, L., Yan, J., Liao, M., Wu, L., Fang, X.: *Small* **7**, 1012–1017 (2011)
114. Fang, X., Bando, Y., Liao, M., Gautam, U.K., Zhi, C., Dierre, B., Liu, B., Zhai, T., Sekiguchi, T., Koide, Y., et al.: *Adv. Mater.* **21**, 2034–2039 (2009)
115. Keis, K., Magnusson, E., Lindstrom, H., Lindquist, S.E., Hagfeldt, A.: *Sol. Energy Mater. Sol. Cells* **73**, 51–58 (2002)
116. Pehnt, M., Schulz, D.L., Curtis, C.J., Jones, K.M., Ginley, D.S.: *Appl. Phys. Lett.* **67**, 2176–2178 (1995)
117. Mora-Sero, I., Gross, D., Mittereder, T., Lutich, A.A., Susha, A.S., Dittrich, T., Belaidi, A., Caballero, R., Langa, F., Bisquert, J., et al.: *Small* **6**, 221–225 (2010)
118. Li, M., Cushing, S.K., Wang, Q., Shi, X., Hornak, L.A., Hong, Z., Wu, N.J.: *Phys. Chem. Lett.* **2**, 2125–2129 (2011)
119. Batabyal, S., Makhall, A., Das, K., Raychaudhuri, A.K., Pal, S.K.: *Nanotechnology* **22**, 195704 (2011)

120. Robel, I., Kuno, M., Kamat, P.V.J.: *Am. Chem. Soc.* **129**, 4136–4137 (2007)
121. Mora-Sero, I., Bisquert, J., Ditttrich, T., Belaidi, A., Susha, A.S., Rogach, A.L.J.: *Phys. Chem. C* **111**, 14889–14892 (2007)
122. Martínez-Ferrero, E., Albero, J., Palomares, E.J.: *Phys. Chem. Lett.* **1**, 3039–3045 (2010)
123. Ruankham, P., Macaraig, L., Sagawa, T., Nakazumi, H., Yoshikawa, S.J.: *Phys. Chem. C* **115**, 23809–23816 (2011)
124. Aga, R.S. Jr., Jowhar, D., Ueda, A., Pan, Z., Collins, W.E., Mu, R., Singer, K.D., Shen, J.: *Appl. Phys. Lett.* **91**, 232108 (2007)
125. Cao, X., Chen, P., Guo, Y.J.: *Phys. Chem. C* **112**, 20560–20566 (2008)

Chapter 11

Chlorophyll-Derived, Cyclic Tetrapyrrole-Based Purpurins as Efficient Near-Infrared-Absorption Donor Materials for Dye-Sensitized and Organic Solar Cells

Taojun Zhuang, Yuwei Wang, and Xiao-Feng Wang

Abstract Near-infrared-absorbing chlorophyll derivatives, namely purpurin-18 methyl esters, with (c-H₂P and c-ZnP) and without (H₂P and ZnP) carboxyl group at the C3 position of chlorin macrocycle have been studied in either dye-sensitized solar cells (DSSCs) or organic-heterojunction solar cells (OSCs). The presence of carboxyl groups gives negligible effect to either the energy levels or the electronic distribution of the purpurin molecules. These purpurins readily form aggregation not only on semiconductor surface through self-assembled adsorption but also on solid surface through strong π - π interaction during spin-casting. In carboxyl purpurin-based DSSCs, the energy gap between the lowest unoccupied molecular orbital (LUMO) level of purpurin and conduction band edge of TiO₂ is insufficient for the charge separation, and results in low photocurrent generation, except for a case that using both c-ZnP as sensitizer and 4-*tert*-butylpyridine-free electrolyte gives the best solar power conversion efficiency (η) of up to 5.1 %. The replacement of TiO₂ by SnO₂ with a deeper conduction band edge increases the photocurrent, but reduces the photovoltage, and as the results, gives negligible improvement at η values. In purpurin-based OSCs, in contrast, the energy gap between the LUMO levels of purpurin molecules and fullerene acceptors is sufficient for efficient charge separation. In C₇₀-based planar heterojunction solar cells, a thin active layer of 5 nm gave the best η values of up to 1.3 % and 1.7 % for H₂P and ZnP, respectively. To improve the photovoltaic performance, bulk heterojunction (BHJ) solar cells with the purpurin: PC₇₀BM blends were fabricated. The optimal blend ratio was 1:4 for both purpurins, due to

T. Zhuang • X.-F. Wang (✉)

Research Center for Organic Electronics (ROEL), Graduate School of Engineering,
Yamagata University, 4-3-16 Jonan, Yonezawa, Yamagata 992-8510, Japan
e-mail: tjzhuang@yz.yamagata-u.ac.jp; xf-wang@yz.yamagata-u.ac.jp

Y. Wang

Department of Chemistry, Renmin University of China, Beijing 100872,
People's Republic of China
e-mail: kfwangyuwei@ruc.edu.cn

the most efficiently balanced charge transport toward both electrodes. ZnO as the exciton blocking layer improved both the photocurrent and voltage for the ZnP-based BHJ solar cells but not for the H₂P-based BHJ solar cells. This difference has been attributed to an inefficient charge separation at the H₂P/ZnO interface that competes with the normal charge separation at the H₂P/PC₇₀BM interface. The best η value of up to 2 % has been achieved for ZnP-based BHJ solar cells at the elevated temperature.

1 Introduction

The fast consumption of limited fossil fuels nowadays and resulting energy and environmental crisis make it more urgent than ever to find a clean and renewable energy source. Solar energy is expected to play a crucial role in the world's energy consumption in the future. Since the first practical silicon solar cells was fabricated at Bell Laboratories in 1954, numbers of efficient solar cells with varied materials and structures have been developed and most of them are based on inorganic materials, such as single and multicrystalline silicon, GaAs, Cu(In,Ga)Se₂, and CdTe. Although high power conversion efficiency (η) can be obtained by these inorganic devices, many problems such as high cost, toxic or complex process still hinder the extensive application. In last two decades, solar cells based on organic absorbing materials, i.e., dye-sensitized solar cells (DSSCs) and organic solar cells (OSCs), have attracted considerable attention as promising energy sources due to their advantages of light weight, low cost, easy fabrication, and abundant and varied material sources [1–13]. Significant efforts have been devoted in recent years to improving the efficiency, and the peak efficiency of the DSSCs and OSCs are over 12 % and 10 % to date, respectively [14, 15]. On the other hand, both DSSCs and OSCs have certain advantages and drawbacks of their own, and the feature of one system may help in overcoming the weakness of the other. As an example, the problem of electrolyte leakage in DSSCs has been overcome with a solid-state hole transport material, i.e., spiro-OMeTAD, developed in OSCs [16]. Still, these two types of organic-based solar cells were always regarded as completely independent photovoltaic systems with little overlaps, because no comprehensive studies have been carried out so far on both systems. In view of this, we, however, are trying to correlate both systems of DSSCs and OSCs with the same type of electron donor material, i.e., purpurin molecules in the present chapter.

1.1 Working Principle of Dye-Sensitized Solar Cells

Figure 11.1 shows the device structure and energy level diagram of a typical DSSC. In such a device, the generation of photocurrent from incident light contains several steps: (1) the dye sensitizers on the surface of semiconductor nanocrystalline (such

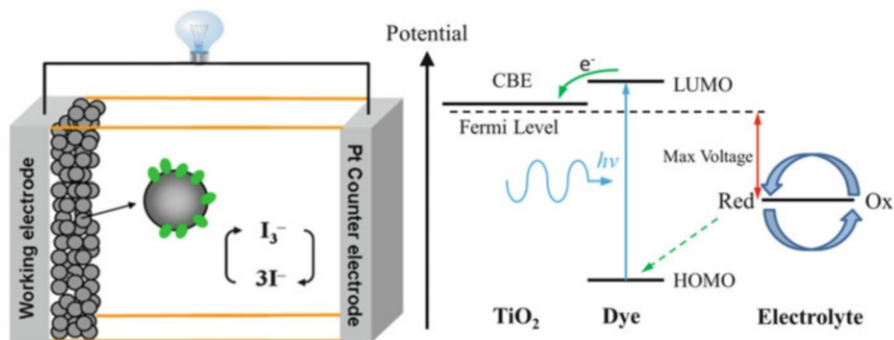


Fig. 11.1 Schematic presentation of a typical dye-sensitizer solar cell and its energy level diagram

as TiO_2 or SnO_2) films absorb light to generate excited state dye sensitizers; (2) dye sensitizers at the excited state inject electrons into the broad conduction band (CB) of the semiconductor oxide and then electrons transport through the semiconductor film to flow to external circuit; (3) the radical cation of dye sensitizer is reduced by electron donation from the electrolyte (I^-/I_3^- redox couple is most frequently used in the electrolyte) that is infiltrated into the porous semiconductor film; (4) the electrons inflowing from the external circuit restore the redox couple in the electrolyte at the counter-electrode. Thus, the incident photon-to-current conversion efficiency (IPCE) of a DSSC can be described as the following equation:

$$\text{IPCE}(\lambda) = \text{APCE} \times \text{LHE}(\lambda) = \Phi_{\text{inj}} \times \eta_{\text{col}} \times \text{LHE}(\lambda), \quad (11.1)$$

where APCE is absorbed photon-to-current conversion efficiency that should be divided into two terms, i.e., the overall electron injection efficiency (Φ_{inj}) between dye sensitizer and semiconductor electrode and the overall charge collective efficiency over solar cell (η_{col}); $\text{LHE}(\lambda)$ is the light-harvesting efficiency and λ is the wavelength of incident light. The photocurrent of a DSSC is affected by the processes of light-harvesting, electron injection, and charge collection, and the maximum voltage under illumination is decided by the difference between the quasi Fermi level of the semiconductor oxide and the redox couple in the electrolyte [3].

As same as other photovoltaics, the overall power conversion efficiency of DSSCs is determined by the current density measured at short circuit (J_{sc}), the open-circuit voltage (V_{oc}), the fill factor (FF), and the intensity of the incident light (P_0).

$$\eta = J_{\text{sc}} V_{\text{oc}} \text{FF} / P_0 \quad (11.2)$$

FF can assume values between 0 and 1 and is defined by the ratio of the maximum power (P_{max}) of the solar cell divided by V_{oc} and J_{sc} ,

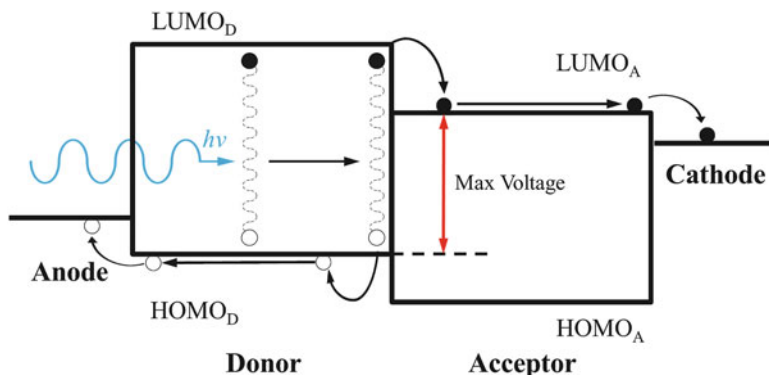


Fig. 11.2 Energy level diagram of an organic solar cell with a donor–acceptor interface

$$FF = P_{\max}/(V_{oc}J_{sc}) \quad (11.3)$$

P_{\max} is the product of the current density and voltage where the power output of the cell reach maximum. Increasing the shunt resistance (R_{sh}) and decreasing the series resistance (R_s) as well as reducing the overvoltage for diffusion and electron transfer will lead to higher FFs.

1.2 Working Principle of Organic Solar Cells

Compared to DSSCs, OSCs without the electrolyte have more intrinsic advantages of organic materials and are easier to be fabricated. Besides, some merits such as flexible and roll to roll production are based on the assumption that OSCs were prepared by wet processes requiring electron donor and acceptor materials with sufficient solubility in organic solvents. With this viewpoint, all of OSCs studied in following parts were fabricated through solution process.

In a typical OSC shown in Fig. 11.2, the basic structure is donor–acceptor (D–A) heterojunction comprising of p-type and n-type organic semiconductors and with such a structure, four subsequent processes to generate photocurrent: (1) organic layers absorb incident photons to generate electron–hole pairs (excitons); (2) excitons diffuse towards the donor–acceptor interface; (3) excitons dissociate by charge transfer at D–A interface; (4) holes and electrons transport in donor and acceptor layers, and are collected at the electrodes. Thus, the IPCE here can be described with the following equation:

$$IPCE(\lambda) = \eta_A(\lambda)\eta_{ED}\eta_{CT}\eta_{CC}, \quad (11.4)$$

where $\eta_A(\lambda)$ is absorption efficiency; η_{ED} is exciton diffusion efficiency which is mainly determined by exciton diffusion length (L_D) as well as the morphology of

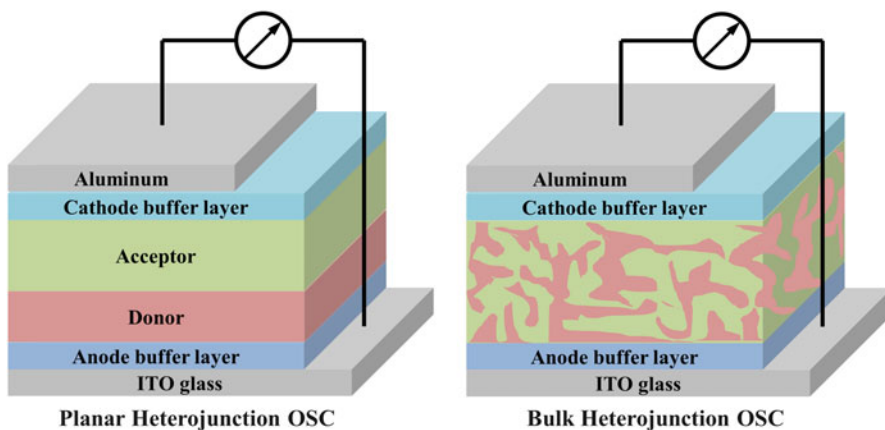


Fig. 11.3 Schematic of organic solar cells with planar and bulk heterojunction structures

the D–A interface; η_{CT} is charge transfer efficiency at the interface; η_{CC} is charge collection efficiency. Besides, the V_{oc} of OSCs is governed by the difference between the highest occupied molecular orbital (HOMO) of the donor and the lowest unoccupied molecular orbital (LUMO) of the acceptor [7].

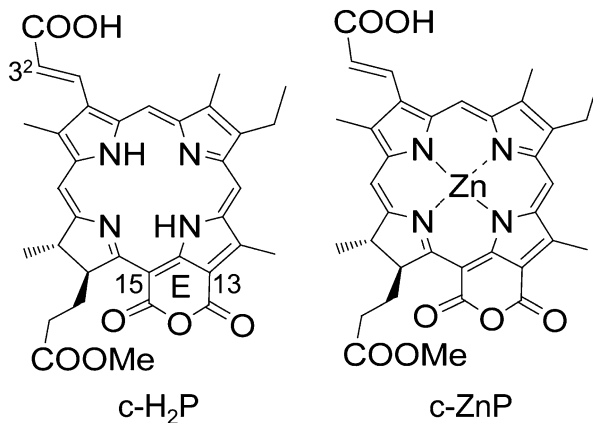
Similar to DSSCs, both R_s and R_{sh} influence FF of OSCs. Moreover, the relatively low carrier mobility of organic semiconductor limits the FF of OSCs since charges need transport through the organic film in OSCs rather than through the semiconductor oxide in DSSCs.

As shown in Fig. 11.3, planar and bulk heterojunction structures are most commonly used architectures in OSCs and both have their own advantages. In a planar heterojunction device, homogeneous films of donor and acceptor are in favor of hole and electron transport, respectively, but charge generation is limited around the vicinity of D–A interface due to the short L_D (~ 10 nm), resulting in a relatively low photocurrent. The bulk heterojunction devices can provide a larger interface throughout the whole active layer to obtain better J_{sc} but interpenetrating network of donor and acceptor can hinder the carrier transport and increase the recombination in OSCs, leading to a reduced FF.

1.3 The Electron Donor: Purpurin Molecules

Since organic absorber plays a key role in efficient photovoltaic performance of the DSSCs, many efforts have been paid to develop efficient dye sensitizers, which are expected to absorb sunlight over the wide range from visible to near-infrared regions, to transfer electrons to a semiconductor electrode with high quantum yield, and to align on the semiconductor surface with suitable morphology to avoid the reversed electron transfer from semiconductor to electrolyte [17, 18].

Fig. 11.4 Chemical structures of carboxyl purpurin molecules used in Sect. 2



Among the dye sensitizers tested in DSSCs, cyclic tetrapyrrole-based molecules, especially porphyrins, chlorins, bacteriochlorins, and phthalocyanines, became most promising in recent studies, due to their unique molecular structures allowing molecular engineering for suitable photochemical and photophysical properties [19–21]. To get the cyclic tetrapyrrole-type dyes absorbing a near-infrared region, some strategies, which may include π -extension of the cyclic tetrapyrrole rings, have already been proposed [22, 23]. From this viewpoint, progress in developing chlorin- and bacteriochlorin-based sensitizers is impressive, and the best solar energy to electricity conversion efficiency has reached to be 8 % [24–27].

Extensive usage of solar energy through the visible to the near-infrared regions is an efficient way not only for DSSCs but also for OSCs to promote the photocurrent generation [28–30]. Therefore, some cyclic tetrapyrrole-based molecules with intense absorption in the near-infrared region, such as porphyrins and phthalocyanines, have also been developed for solution processed OSCs [31, 32].

Purpurins are a set of major derivatives of natural chlorophyll molecules, in which the two carbonyl groups were situated at the 13- and 15-positions (see Fig. 11.4), prepared through basic and oxidative cleavage of C13¹–C13² bond on the E-ring of the parent chlorophylls. Since the absorption capability and the structural stability of purpurin molecules are much superior to that of the corresponding chlorin molecules possessing the original E-ring, the feasibility of purpurin molecules in photovoltaic applications can be expected.

In Sect. 2, a pair of purpurin sensitizers (*trans*-3²-carboxy-purpurin-18 methyl ester) with and without zinc at the central position, *c*-ZnP and *c*-H₂P, have been used in DSSCs. These dye sensitizers have been found in aggregate morphology on a semiconductor surface. In order to optimize the electron injection and charge collection efficiencies at the dye-semiconductor interfaces, different semiconductor electrodes including TiO₂ and SnO₂ and electrolytes with and without 4-*tert*-butylpyridine (TBP) have been compared. Multiple electron injection pathways at the purpurin-semiconductor interface have been elucidated. Finally, the kinetics of

exciton annihilation of dye sensitizer upon different surrounding electrolyte conditions has been studied with sub-picosecond time-resolved absorption spectroscopy.

In Sect. 3, another pair of carboxyl-free purpurin dyes with and without zinc, ZnP, and H₂P, have been used as the electron donor in solution processed planar and bulk heterojunction OSCs. For the planar heterojunction (PHJ) OSCs, the thickness of the purpurin/C₇₀ active layer was optimized, whereas for the bulk heterojunction (BHJ) OSCs, the purpurin/PC₇₀BM blending ratios ranging from 1:1 to 1:6 were examined, and the electron and hole mobilities of blend films were measured by the method of space charge limited current (SCLC) [33]. The different behaviors of purpurin dyes in OSCs and DSSCs were discussed.

2 DSSCs Based on Carboxyl Purpurins

2.1 Aggregation Formation of Purpurin Molecules on Semiconductor TiO₂ Surface Through Self-Adsorption

Figure 11.4 shows the molecular structures of the pair of dye sensitizers, c-H₂P and c-ZnP. A major difference between the synthetic two purpurin sensitizers and their natural chlorin analogues possessing an exo-five-membered ring with an oxo moiety is the electron density of the E-ring at the ground state, which provides an additional force to cause the π - π stacking between adjacent purpurin molecules, especially when they are tightly adsorbed on semiconductor surface on semiconductor surface. The dye aggregate, both the H- and J-types, usually causes changes in the absorption spectra. Figure 11.5a shows the absorption spectra of dye sensitizers dissolved in ethanol, and Fig. 11.5b shows the absorption spectra of dye sensitizers deposited on TiO₂ nanocrystalline thin films. Compared to the two dye sensitizers in ethanol solution, absorption spectra of the dyes on TiO₂ films exhibited three distinguishable characteristics: (1) their Q_x and Q_y bands shift to longer wavelength region; (2) ratios of the intensity of Q_y peak to that of Q_x peak decrease; and (3) most importantly, both Q_x and Q_y bands broaden. These changes in the absorption spectra can be attributed to the aggregation of dye molecules on TiO₂ surface, being similar to what we observed in our previous investigation on oxo-bacteriochlorin sensitizers [22]. On the other hand, we have never observed such clear aggregate formation for their chlorin analogues on TiO₂ surface, supporting our predication that the large π system in purpurin structure is the origin to cause strong π - π stacking. The aggregation of dye molecules on the semiconductor surface can cause both exciton delocalization and annihilation and result in worse electron injection and charge collection to give reduced IPCE and η values.

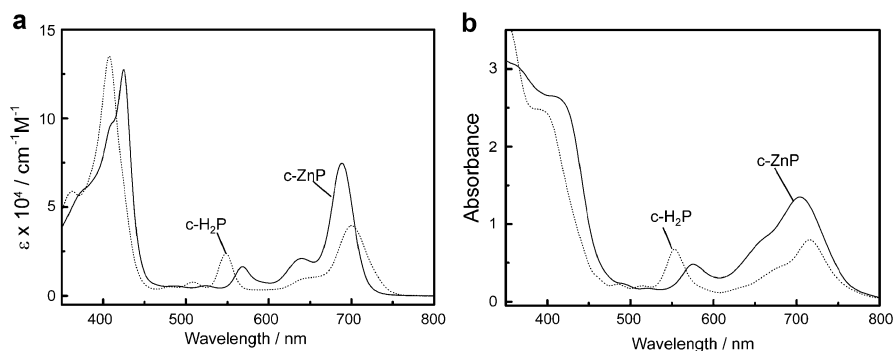


Fig. 11.5 Electronic absorption spectra of dye sensitizers dissolved in ethanol (a) and deposited on TiO₂ thin films (b)

2.2 TiO₂-Based DSSCs Using Purpurins as Sensitizers

In previous studies, it has been concluded that zinc as the central metal of cyclic tetrapyrroles enhanced the performance of porphyrin-based solar cells but reduced the performance of chlorin-based solar cells [20]. This is because, for these chlorin analogues, the shift of HOMO orbital to a higher energy level reduces the rate of electron transfer from I^-/I_3^- redox couple to the radical cation of dye, while the energy levels of LUMO orbital are sufficiently high for efficient electron injection to the conduction band of TiO₂ [20]. In the case of purpurin sensitizers, the fact that their LUMO energy levels shift to lower energy level may make the story completely different. Here we will first theoretically evaluate the effect of the central zinc on the performance of solar cells using purpurin sensitizers. In Fig. 11.6, we calculated the frontier molecular orbitals of both sensitizers, c-ZnP and c-H₂P. The electronic localization in their four orbitals, HOMO-1, HOMO, LUMO, and LUMO+1, for both sensitizers is similar, indicating equal excitonic coupling between these purpurin sensitizers and TiO₂. On the other hand, we also calculated the energy levels of these four molecular orbitals in ethanol together with HOMO and LUMO energy levels that experimentally measured by the ultraviolet photoelectron spectroscopy and absorption spectra of dyes on TiO₂ (Fig. 11.5b), respectively, and compared them with the conduction band of TiO₂ ($E_{\text{CB}} = 3.3 \text{ eV}$), as depicted in Fig. 11.7. For each sensitizer, the observed and calculated HOMO levels were more or less similar, while the observed LUMO energy levels were lower than the corresponding calculated LUMO energy levels. The band energy levels of all the four molecular orbitals for c-ZnP shift to positive sides from the corresponding values of c-H₂P, even though the energy gaps between molecular orbitals in each sensitizer are almost equal. Most importantly, the energy level of the LUMO orbital of c-H₂P is at the lower side of that of the conduction band edge (CBE) of TiO₂. Thus, the electron injection toward TiO₂ from the LUMO of c-H₂P should be inactive.

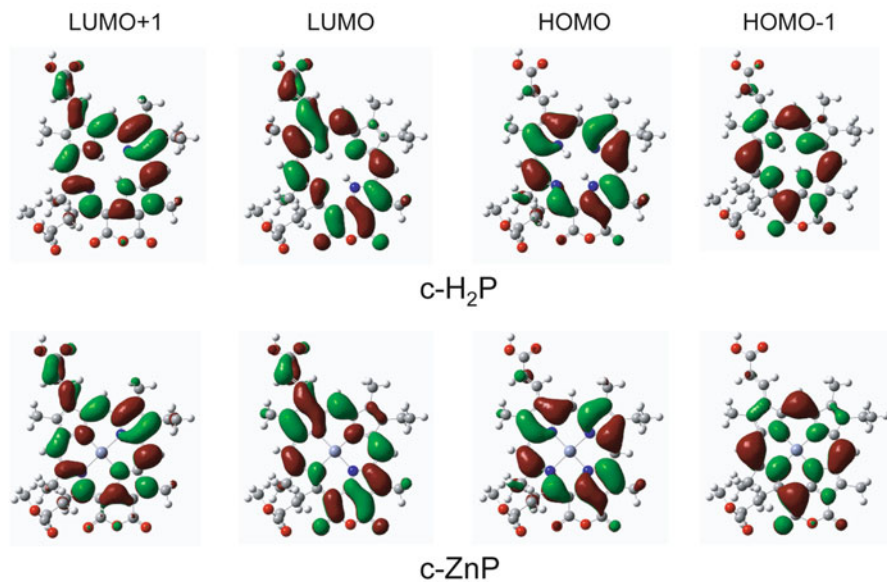


Fig. 11.6 Frontier molecular orbitals of the two sensitizers based on DFT/B3LYP/DGDZVP calculations with CPCM (ethanol)

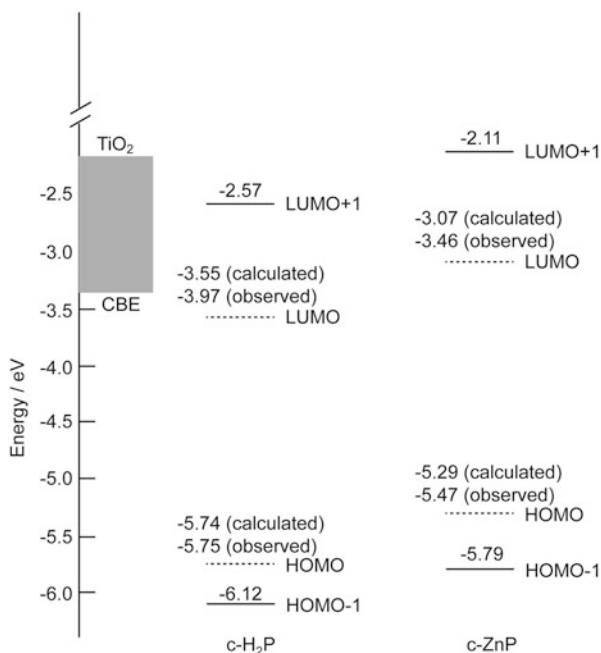


Fig. 11.7 Comparison of energy levels of the HOMO-1, HOMO, LUMO, LUMO+1 molecular orbitals of the dye sensitizers to that of the CBE of TiO₂. The observed HOMO levels were obtained experimentally with the UV photoelectron spectroscopy, and the observed LUMO level were estimated with the Q_y absorption peaks of the dye sensitizers on TiO₂

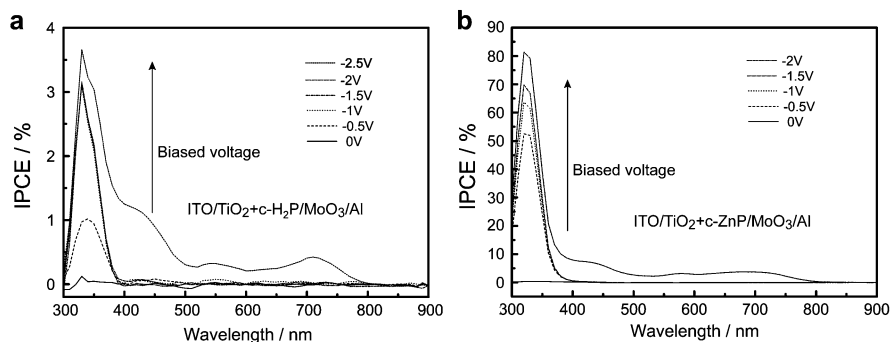


Fig. 11.8 IPCE profiles of the photovoltaic diodes based on the dye-sensitized TiO_2 thin films and measured under different biased voltages

To visualize the electron transfer process at the dye-semiconductor interface, a solid-state photovoltaic diode would be very useful, since we can exclude some complicated events in solution-based DSSCs. In each photovoltaic diode, a configuration containing FTO, compact TiO_2 , dye-sensitized TiO_2 , MoO_3 , and Al was commonly used. Indeed, the purpurin sensitizers are suitable p-type materials for this purpose because they can form dye aggregates on TiO_2 surface which allow charge carriers diffuse in the dye layer. (Actually, typical Ru-complex dye N719 has also been tried to fabricate such a solid-state photodiode, and only ohmic character of such device can be observed.) Figure 11.8 shows the IPCE profiles of photovoltaic diodes based on these two sensitizers, measured at different biased voltages. With such outside building potential on the device, the photoelectron generation in the absorption region of TiO_2 increased with an increase of voltage in both cases. The larger IPCE value in the case of c-ZnP to that of c-H₂P can be attributed to a better hole mobility of the former than the latter sensitizer. This suggests that solar cells based on c-ZnP may give higher photovoltaic performance than that based on c-H₂P, when a liquid-state electrolyte was applied. Furthermore, the photoelectrical response in the dye absorption region can be observed at biased voltages of -2.5 V and -2.0 V for c-H₂P and c-ZnP, respectively, and the difference of 0.5 V is somehow coincident with the difference between the calculated energy levels of LUMO orbitals of the sensitizers (0.48 eV), although the definitions of volt and electron volt are completely different. Thus, c-ZnP is a relatively better dye sensitizer than c-H₂P because it provides relatively higher carrier mobility for forward electron transfer and allows electron injection to take place possibly from the LUMO orbital to the CBE of TiO_2 , especially when their energy levels are comparable.

Figure 11.9 shows the IPCE profiles and current density–voltage (I – V) curves of TiO_2 -based DSSCs using these two dye sensitizers under the standard AM1.5 illumination (100 mW cm^{-2}). Table 11.1 shows the relevant parameters that obtained from the I – V curves. When the electrolyte A, i.e., 0.1 M LiI, 0.05 M I_2 , and 0.6 M 1-propyl-3-methylimidazolium iodide in a mixture of acetonitrile and

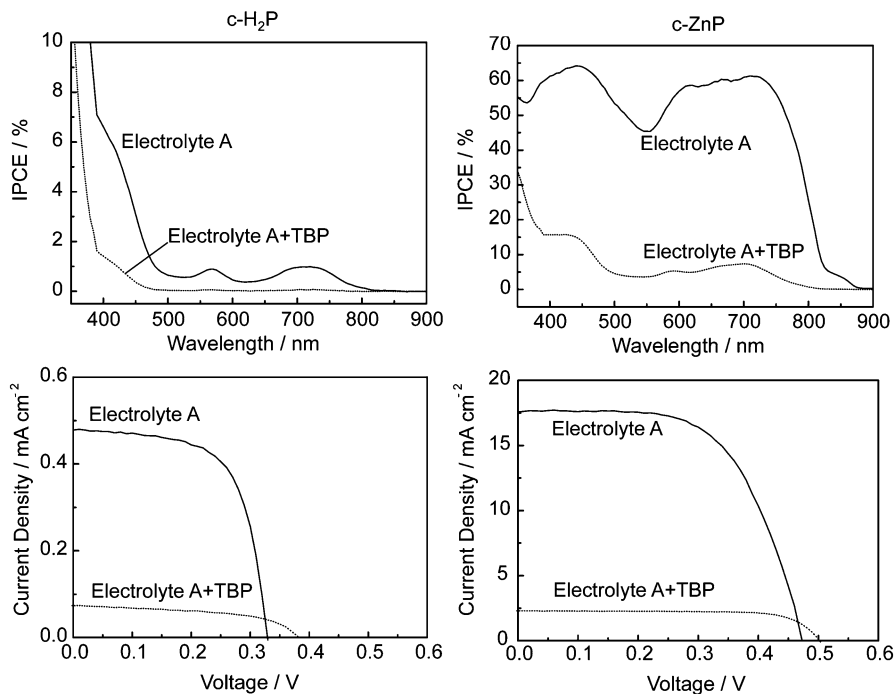


Fig. 11.9 IPCE profiles and I - V curves of DSSCs based on c -H₂P- and c -ZnP-sensitized TiO₂ electrodes. Electrolytes with and without TBP were examined

Table 11.1 Photovoltaic performance of DSSCs using c -H₂P and c -ZnP as sensitizers and TiO₂ as semiconductor electrode

Purpurin	Electrolyte	J_{sc} (mA cm ⁻²)	V_{oc} (V)	FF	η (% at $P_0 = 1$ sun)
c -H ₂ P	A	0.48	0.33	0.65	0.10
	A+0.5M TBP	0.07	0.38	0.53	0.01
c -ZnP	A	17.6	0.48	0.60	5.1
	A+0.5M TBP	2.3	0.50	0.75	0.86

valeronitrile (1:1, v/v), which consists of Li⁺ and I⁻/I₃⁻ redox couple, was employed, the energy levels of LUMO orbital of both the sensitizers should be close to the calculated values. In such circumstance, efficient electron injection can take place not from the LUMO orbital of c -H₂P, but from that of c -ZnP, and hence, high photocurrent generation can be observed in a solar cell based not on the former sensitizer, but on the latter. J_{sc} of DSSC based on c -ZnP is much larger than that based on c -H₂P, which is in good agreement with the prediction with LUMO energy levels. Importantly, photocurrent can be generated in a substantially broad wavelength range from 350 to 900 nm in c -ZnP to give a very high J_{sc} value of up to 17.6 mA cm⁻².

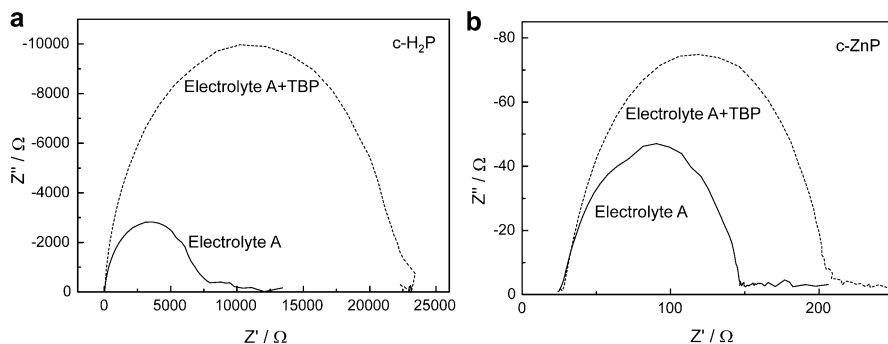


Fig. 11.10 EIS Nyquist plots for DSSCs based on c-H₂P (a) and c-ZnP (b) sensitizers under AM1.5 illumination

In our previous investigation on oxo-bacteriochlorin sensitizers [22], the effect of TBP has been elucidated to shift the CBE of TiO₂ to a higher energy level to reduce the photocurrent and, at the same time, increase the photovoltage. Here, TBP was again added into the electrolyte to study the effect of band shift on the performance of solar cells based on these purpurin sensitizers. Sure enough is that TBP does shifted the energy level of CBE over the LUMO level of c-ZnP, since the photocurrent of solar cell suddenly dropped to 2.3 mA cm⁻², which is only 13 % of the original value, the V_{oc} value was not improved by a similar degree, so that the η value was reduced from 5.1 to 0.86 %. Similarly, upon addition of TBP in electrolyte, J_{sc} and η of c-H₂P-based solar cells decrease from 0.48 to 0.07 mA cm⁻² and from 0.1 % to 0.01 %, respectively. The decrease of photocurrent and photovoltaic performance in c-ZnP-based solar cells upon addition of TBP in electrolyte can be explained by the change in the electron injection rate between the LUMO orbital of the dye and the TiO₂ electrode. Most probably, an inefficient electron injection took place from the LUMO orbital with a lower energy level to TiO₂, when TBP was used, since the density of state (DOS) of TiO₂ nanocrystalline is broad, and a potential acceptor state of TiO₂ called intrinsic acceptor level may exist [34]. Furthermore, each exciton of the dye sensitizer functions not only as a particle but also as an electromagnetic wave, which allows exciton to cross a certain energetic barrier to reach the TiO₂ CBE. In contrast, the energy level of the LUMO orbital of c-H₂P is below the CBE of TiO₂ even without adding TBP into the electrolyte. Pushing the CBE of TiO₂ further down with TBP will cause very unfavorable electron injection from LUMO orbital. The tiny photocurrent response in the TBP-based c-H₂P solar cell as shown in the IPCE profile is most likely contributed from the LUMO+1 orbital rather than the LUMO orbital. Thus, the decrease of photocurrent of c-H₂P-based solar cell upon additional TBP in electrolyte can be explained by the change of electron donor state of the dye sensitizer.

The difference in the electron injection process upon addition of TBP in these solar cells based on two sensitizers can be also proved with electronic impedance spectroscopy at the dye-semiconductor interface. Figure 11.10 shows the Nyquist

plots of electronic impedance spectra (EIS) for DSSCs based on these sensitizers under the standard AM1.5 illumination (100 mW cm^{-2}). In ordinary Nyquist plots, two semicircles that correspond to electron transfer in the electrolyte and at the Pt electrode should appear at low and high frequency region, respectively. In the present case using purpurin sensitizers, the extremely large charge transfer impedance (R_{ct}) at the TiO_2 -dye-electrolyte interface causes the other semicircles invisible. The impedance values of the *c*-H₂P-based solar cells are substantially larger than that of *c*-ZnP-based solar cells, which is in good agreement with our prediction based on the DFT calculations and the J_{sc} values in I - V curves of corresponding solar cells, supporting our conclusion that the difference of photocurrent was originated from the difference in the electron transfer at the semiconductor-dye interface. Moreover, additional TBP increases the R_{ct} value and thus caused the decreased photocurrent, especially in *c*-H₂P-based solar cells. This is a clear indication that electron injection donor state changes from LUMO to LUMO+1.

2.3 *SnO₂-Based DSSCs Using Purpurins as Sensitizers*

As discussed above, the CBE energy level of TiO_2 is not suitable for electron injection taking place from the LUMO orbital of purpurin sensitizers, especially when TBP was used in the electrolyte. This observation suggests the replacement of TiO_2 by alternative wide band gap semiconductor that has the CBE energy level below the LUMO level of the dye sensitizers. Among such materials, SnO_2 is obviously one of the best candidates due to its suitable CBE energy level that was 0.4 eV below the CBE level of TiO_2 . Besides the energy levels, the electronic coupling of the dye with both semiconductor materials might also be different. Figure 11.11 shows the extended DFT calculation results for the two sensitizers connected to TiO_2 and SnO_2 molecules through bidentate chelating mode. The electron distribution over the cyclic tetrapyrrole rings in each dye sensitizer on both semiconductors is almost equal, except for the LUMO+1 orbital, at which the electronic coupling of dye with SnO_2 seems to be slightly stronger than that with TiO_2 . Thus, it is predicted that purpurin solar cells based on SnO_2 electrode should give higher photocurrent than that based on TiO_2 due to the easiness of electron injection taking place from the LUMO of dye to CBE of semiconductor.

In fact, the aggregation of purpurin sensitizers would slightly shift the energy level of the LUMO orbitals of the dye to either higher (H-type) or lower (J-type) sides. However, these changes cannot be reflected in our calculations due to the limitation of the TD-DFT method. Since the real case could be extremely complicated and out of our capability, we simply skipped further discussions on these issues.

Interestingly, changes in the absorption spectrum of dye on SnO_2 films were observed upon addition of different electrolytes. At the top of Fig. 11.12, the absorption spectra of both sensitizers on SnO_2 films have been measured upon addition of electrolytes in which the TBP was absent or present. In these dye

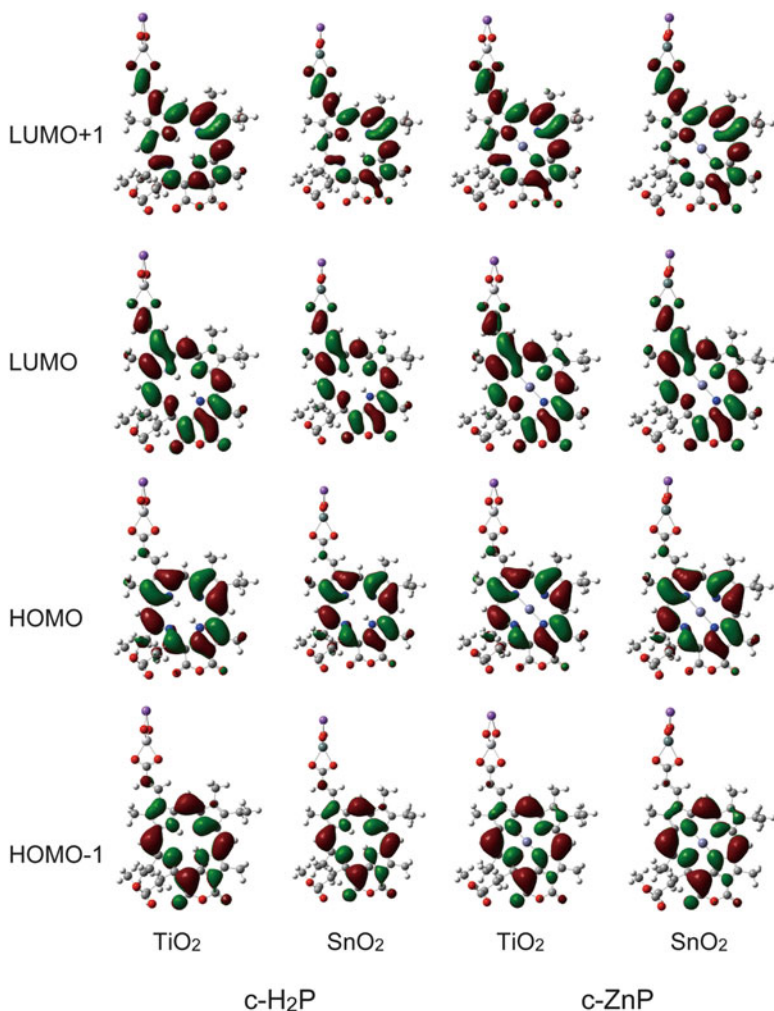


Fig. 11.11 Frontier orbitals of c-H₂P and c-ZnP carboxylate anions with TiO₂Na⁺ and SnO₂Na⁺ based on DFT/B3LYP/DGDZVP with CPCM (ethanol)

absorption spectra on SnO₂, more monomer characters can be observed in TBP-containing electrolyte, based on a comparison with the absorption spectra of dyes in solution (Fig. 11.5a), while more aggregate characters can be observed in TBP-free electrolyte. It is very likely that TBP can function as a kind of blocking agent to remove the weakly bound dye molecules. Therefore, purpurin sensitizers on SnO₂ are in both monomer and aggregate morphologies in TBP-enriched and TBP-free electrolytes, respectively. Such difference in morphology attracts a great interest at the photovoltaic performance of solar cells using above conditions, since the photovoltaic properties of dye aggregates remain unclear in relevant literatures [22, 35].

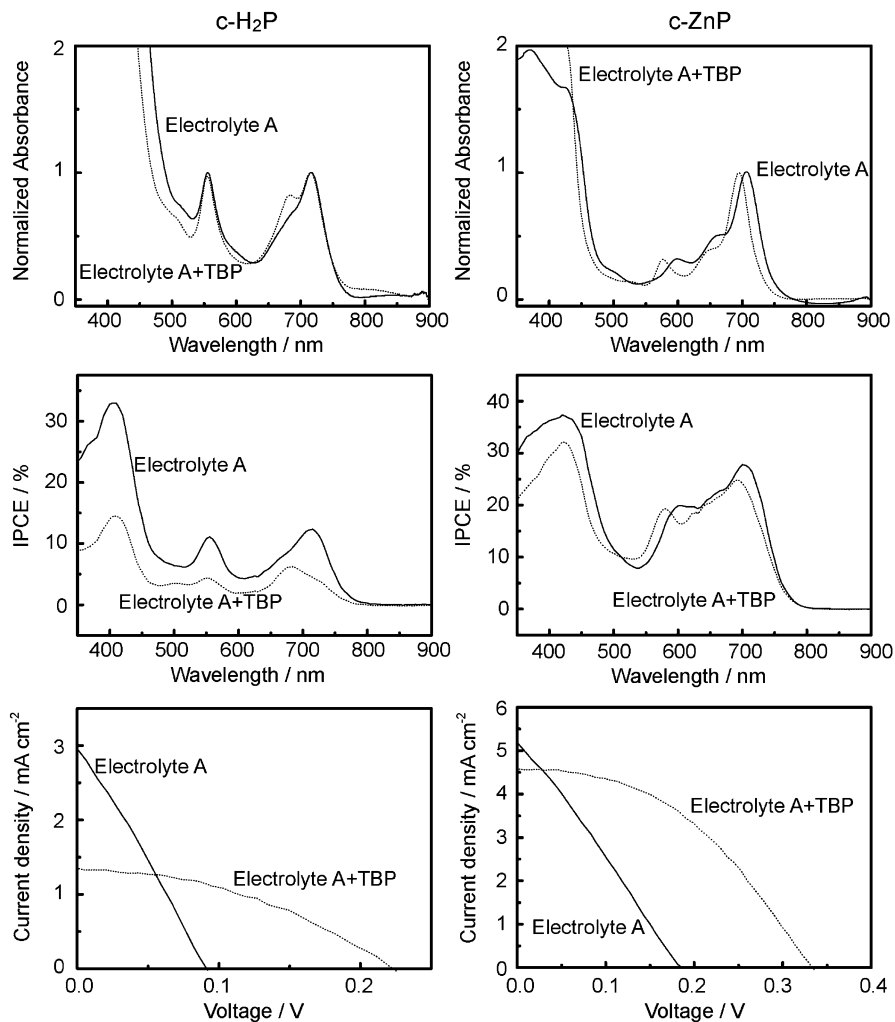


Fig. 11.12 Electronic absorption spectra of dye-sensitized SnO₂ thin films with different electrolytes. IPCE profiles and I - V curves of DSSCs based on c-H₂P- and c-ZnP-sensitized SnO₂ electrodes. Electrolytes with and without TBP were compared

The middle and bottom of Fig. 11.12 show the IPCE profiles and I - V curves of SnO₂-based solar cells using these two sensitizers, respectively, and Table 11.2 lists the relevant parameters obtained from the I - V curves. For each sensitizer, electrolytes with and without TBP have been compared. Again, solar cells based on c-ZnP give rise to higher photovoltaic performance than that based on c-H₂P, indicating electron injection efficiency from c-ZnP to semiconductor electrode is

Table 11.2 Photovoltaic performance of DSSCs using c-H₂P and c-ZnP as sensitizers and SnO₂ as semiconductor electrode

Purpurin	Electrolyte	J_{sc} (mA cm ⁻²)	V_{oc} (V)	FF	η (% at $P_0 = 1$ sun)
c-H ₂ P	A	2.96	0.098	0.25	0.07
	A+0.5M TBP	1.35	0.25	0.35	0.12
c-ZnP	A	5.1	0.18	0.27	0.26
	A+0.5M TBP	4.6	0.33	0.43	0.66

higher than that from c-H₂P, which is predictable with energy gap law. On the other hand, TBP significantly reduces the η value in TiO₂-based solar cells but increases this value in SnO₂-based solar cells for both dye sensitizers. As detailed in Table 11.2, when TBP was used in SnO₂-based solar cells, the changes of parameters are negligible in J_{sc} but significant in V_{oc} and FF. When TBP was used, the improvement in J_{sc} value in SnO₂ solar cells to that in TiO₂ solar cells is mainly due to a favorable electron injection taking place from LUMO orbital of dye to CBE of semiconductor, although the light-harvesting capability by SnO₂ films was less effective than that by TiO₂ films due to the absence of scattering layer. Moreover, the shapes of IPCE profiles nicely resemble their absorption spectra, suggesting not only monomers but also aggregates of dye sensitizers can contribute to the photocurrent generation. Since aggregates of dye sensitizers are weakly deposited on the semiconductor surface through π - π stacking, the generated charges of these weakly bound sensitizers migrate through those covalently bound sensitizers to the semiconductor surface. Thus, we can safely conceive that our finding is a strong evidence to prove a kind of remote electron injection mechanism in DSSCs, in which people have a relief that only covalently deposited dye sensitizers can contribute to the final photocurrent generation. The relatively small V_{oc} values of SnO₂ solar cells to that of TiO₂ solar cells is mainly originated from the smaller energy gap between the quasi Fermi level of SnO₂ and the I⁻/I₃⁻ redox couple. Very importantly, the enhancement of the photocurrent of the c-H₂P-based solar cells upon the replacement of semiconductor electrode suggests that the performance of near-infrared absorptive dye-based DSSCs might be improved in a similar way.

In previous investigations, the exciton annihilation caused by dye aggregate formation has been found to be a major parameter to determine the photovoltaic performance in DSSCs [27]. The present research allows a more quantitative evaluation on the effect of the dye aggregation on the excited state dynamics. Figure 11.13 shows the time-resolved absorption spectra (TAS) of c-ZnP in ethanol solution, recorded both for visible and near-infrared regions. Here, the TAS study focuses only on c-ZnP because this dye gives relatively higher photovoltaic performance. The TAS spectra in visible region consists a typical bleaching signal at \sim 700 nm that has been also observed for chlorophyll derivatives in previous study [27]. An exponential fitting result on the TAS spectra suggests that the bleaching signal consists of a decay process with the time constant of up to 5 ns, corresponding to the excited state lifetime of the dye molecules. In the near-infrared region, a peak generated at 1,000 nm with the lifetime of up to 3.4 ns could be assigned to the absorption of electrons.

Fig. 11.13 Sub-ps time-resolved absorption spectra of c-ZnP in ethanol solution

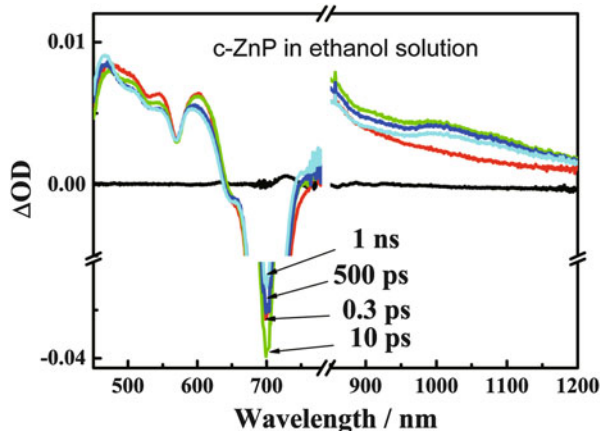


Table 11.3 Time constants τ s in exponential fitting results of TAS measurements on c-ZnP-modified SnO₂ films

Wavelength (nm)	Electrolyte	τ_1 (ps)	τ_2 (ps)	τ_3 (ps)
700	–	1.1	17	1,800
	A	1.0	7.6	5,244
	A+0.5M TBP	2.2	46	3,433
1,000	–	0.4	4.2	4.2
	A	0.03	3.0	36
	A+0.5M TBP	0.1	3.8	72

Figure 11.11 shows the TAS results for c-ZnP deposited on SnO₂ and to which different electrolytes were introduced. In our previous study [27], the recovery dynamics of the bleaching signal at 700 nm was directly related to three processes, including the recombination of injected free charges, the annihilation of excited state excitons, and the relaxation of the excited state electrons. Similarly, the TAS results at 700 nm of the present c-ZnP on SnO₂ could be also exponentially fitted with three components. Table 11.3 lists the three time constants of the fitting results. Since the time constant τ_3 in each fitting result is extremely large, it can be safely assigned to the excited state relaxation. Compared to the bare SnO₂ film, when electrolyte A is used, the constant τ_1 has negligible change, while the constant τ_2 becomes smaller. It has been found that Li⁺ in electrolyte usually push down the energy level of the CBE to more positive, and this can help the electron injection from the dye to SnO₂ to give a shorter time constant [36]. On the other hand, the presence of electrolyte A has little influence at the dye aggregate, and this will give similar time constant for exciton annihilation. Therefore, τ_1 is more relevant to the dynamics of exciton annihilation, while τ_2 is relevant to the charge recombination process. The presence of TBP significantly reduced the formation of dye aggregates, and as a result, τ_1 is doubled. Apparently, the larger τ_2 is due to the shift of CBE energy level to negative side, as discussed in the previous section.

The TAS spectrum at 1,000 nm has been referred to the absorption of electrons. When the dye sensitizer was excited, ultrafast electron injection will take place

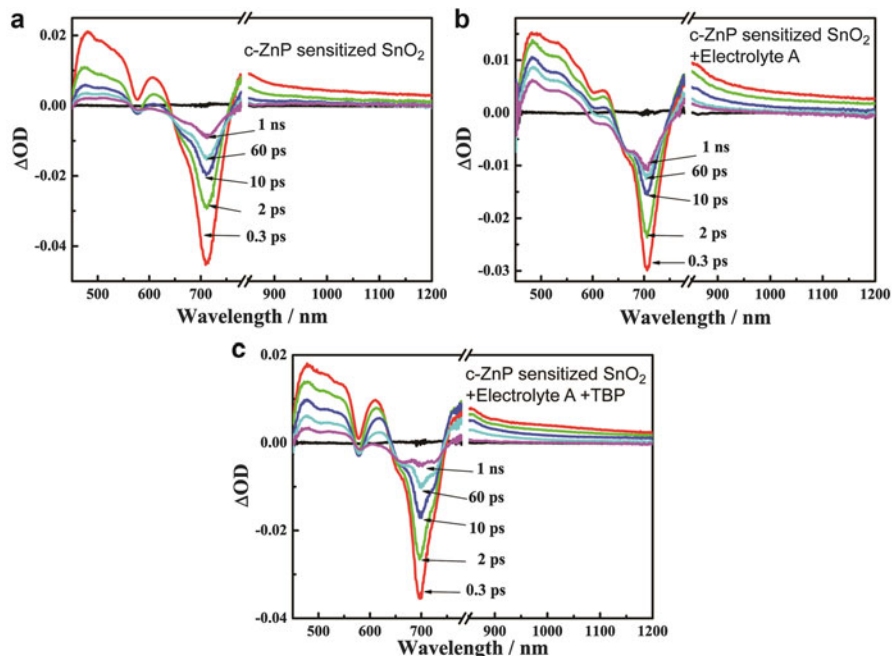


Fig. 11.14 Sub-ps time-resolved absorption spectra of c-ZnP-sensitized SnO_2 electrodes. The effect of different electrolytes was compared

from the dye to SnO_2 . The decay of this signal in Fig. 11.14 is therefore assigned to the electron injection dynamics. In Table 11.3, the TAS signals at 1,000 nm could be exponentially fitted with three time constants. To the present system, the constant τ_1 is most important because more than half of electrons were injected at this early stage. It is quite reasonable that the use of electrolyte A enhances the electron injection rate ($0.4 \rightarrow 0.03$ ps), while the present of TBP in electrolyte A will slightly reduce the electron injection rate ($0.03 \rightarrow 0.1$ ps) because the CBE of SnO_2 shifts with these Li^+ and TBP additives.

Finally, we have to critically evaluate the purpurin sensitizers as a potential candidate for future photovoltaic application. The present maximum overall power conversion efficiency of 5.1 % for c-ZnP-based solar cell is still less than that of 8.0 % for the previous chlorin-based solar cell [27]. The three parameters to determine η value were $J_{\text{sc}} = 17.6 \text{ mA cm}^{-2}$, $V_{\text{oc}} = 0.48 \text{ V}$, and $\text{FF} = 0.60$ for c-ZnP and $J_{\text{sc}} = 17.4 \text{ mA cm}^{-2}$, $V_{\text{oc}} = 0.64 \text{ V}$, and $\text{FF} = 0.72$ for chlorin sensitizer. Although c-ZnP has larger light-harvesting efficiency, i.e., larger extinction coefficient and threshold absorption wavelength, than the chlorin sensitizer, the photocurrent generated by c-ZnP is comparable to that generated by the chlorin sensitizer, owing to slightly worse charge collection efficiency in solar cell based on c-ZnP to that based on the chlorin, as supported by the electrical impedance spectra. Therefore, the lower η value of c-ZnP to that of the chlorin sensitizer can be attributed to a lower V_{oc} and FF values. The V_{oc} value in a DSSC is mainly

determined by the difference between the energy levels of quasi Fermi level of TiO_2 and redox potential of I^-/I_3^- [37]. Additive like TBP can enhance the V_{oc} value by pushing the quasi Fermi level to upper energy level significantly. However, as discussed above, this strategy is not suitable for the present purpurin sensitizers with the LUMO level very close to the CBE of TiO_2 . Also, TBP can improve the FF value of DSSCs by avoiding the aggregate of dye sensitizer on the TiO_2 surface to reduce series resistance. Recent progress on cobalt complexes as alternatives of I^-/I_3^- for DSSCs has provided a way to improve the relatively low V_{oc} value of purpurin-based solar cells [38]. Furthermore, there is still room left to improve the photovoltaic performance of purpurin-based solar cells by shifting the LUMO orbital of the purpurin sensitizer further to a higher energy level while keeping the narrow band gap of the sensitizer unchanged upon molecular engineering.

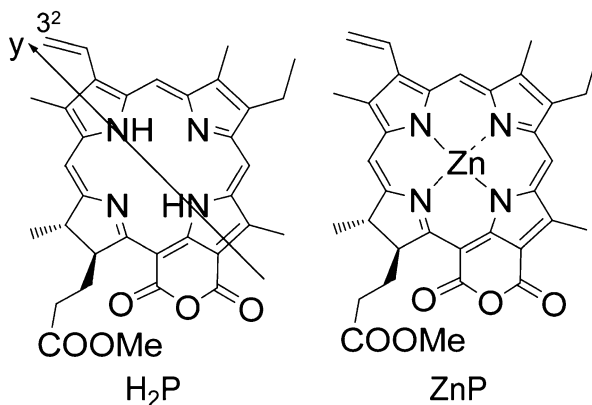
3 OSCs Based on Purpurins

3.1 *Optical and Physical Properties of Purpurins as Thin Solid Films*

Purpurin molecules are cyclic tetrapyrroles that have strong absorption peaks in the near-infrared region. Compared to some chlorin and porphyrin analogs derived simply from natural chlorophylls, purpurin molecules have a six-membered E-ring with an anhydride moiety that makes the molecule very stable against the air and high temperature. In Sect. 2, a pair of purpurins with carboxyl group have been used as dye sensitizers for efficient DSSCs [39]. It has been found that the electron injection from purpurins to TiO_2 nanocrystalline films is energetically unfavorable, and a low photocurrent was observed especially in metal-free purpurin-based DSSCs. Replacing TiO_2 by SnO_2 , its deep conduction band level improved the electron transfer and thus the photocurrent of purpurin-based DSSCs but reduced the photovoltage, because the voltage of DSSCs was mainly determined by the difference of the quasi Fermi level of the semiconductor electrode and the redox potential of the electrolyte [37], and the quasi Fermi level of SnO_2 is much lower than that of TiO_2 . Thus, the problems of energy mismatch and low voltage substantially limit the further application of this material in DSSCs.

Similar to DSSCs, the photocurrent of OSCs is also partially determined by a charge separation process between the donor and acceptor materials, although the acceptor molecules are not inorganic semiconductors but organic semiconductors such as fullerenes with a suitable LUMO: the LUMO level of fullerene C_{60} , for example, is equal to -4.3 eV, which is deep enough for electrons to be transferred from purpurin molecules. The V_{oc} of OSCs is, however, mainly determined by the difference between the LUMO energy level of the acceptor and HOMO energy level of the donor [40–42]. Therefore, it is considered that these purpurin dyes with a low LUMO energy level may be very suitable as the system of OSCs rather than DSSCs, because both photocurrent and photovoltage generations are more

Fig. 11.15 Chemical structures of purpurin molecules used in Sect. 3



favorable in the former device than in the latter. Furthermore, in the previous study on DSSCs [39], the Zn-based purpurin sensitizer exhibits better charge carrier mobility than the corresponding metal-free purpurin sensitizer in the electrolyte free solid-state device, indicating that Zn-based purpurin must have a larger potential than metal-free purpurin, when they were employed as the p-type donors in OSCs.

Figure 11.15 shows the chemical structures of a pair of purpurin dyes used in this study of OSCs. The absorption capability and the structural stability of purpurin molecules bearing a six-membered E-ring with an anhydride moiety are much superior to those of the corresponding chlorin molecules possessing the original five-membered E-ring. In Sect. 2 on purpurin-based DSSCs [39], a 2-carboxyethenyl group ($-\text{CH}=\text{CH}-\text{COOH}$) at the C3 position was used to bind with inorganic semiconductors for facilitating interfacial electron injection. Here, the unnecessary carboxyl group ($-\text{COOH}$) at the C3² position of the purpurin molecules was replaced by a hydrogen atom, because a carboxyl moiety can cause strong intermolecular hydrogen bonding between adjacent purpurin molecules to reduce the solubility of the dye in hydrophobic solvents. However, it is a concern of whether this change at the chemical structure may alter the optical property of the purpurin dyes, especially when they are used as a thin solid film. Otherwise this change will partially affect the comparability of the present study to the previous study [39]. After comparing the absorption spectra of the pair of purpurin dyes with their analogs used in DSSCs, we found that the presence of the electron withdrawing carboxyl group slightly changed the peak width of the *Q*-band and the density of the Soret band. However, these small differences do not affect the present investigation. Figure 11.16 compares the absorption spectra of the purpurin dyes both in chloroform solutions and thin films prepared by spin-coating a chloroform solution of the dyes (1 mg mL^{-1}) on a MoO_3 -modified ITO substrate. Interestingly, compared to the dyes in the solution, the spin-coating films moved the absorption peaks to a longer wavelength region together with a substantially broadened bandwidth. These phenomena are partially attributable to the formation of dye aggregates. In fact, the carboxyl purpurin sensitizers have been

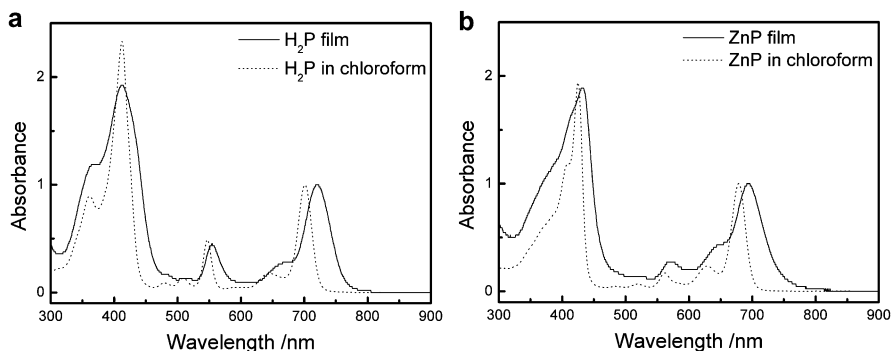


Fig. 11.16 Absorption spectra of H₂P (a) and ZnP (b) dissolved in the CHCl₃ and deposited as thin solid films. The spectra were normalized at the longest wavelength (λ_y) absorption maxima

found to form aggregates on the TiO₂ semiconductor surface [39], because they are closely packed side by side on the surface of TiO₂ through the rigid carboxylate linkage. In the present study, the formation of aggregates may merely originate from the solvent evaporation during the spin-coating process to cause the strong π - π stacking between purpurin molecules. Thus, the similarity of molecular arrangement for purpurin dyes both self-assembled on the inorganic semiconductor surface and as spin-coated on the ITO surface must give a rise to similar carrier mobility. That means, if the molecular arrangement is a factor to determine the carrier mobility, ZnP molecules should give a better hole mobility than H₂P molecules, because the former shows better charge transport capability in the dye-sensitized solid-state diode [39].

Besides the molecular arrangement of purpurins in thin films that regulates the intermolecular charge transfer, the electron distribution at the HOMO and LUMO orbitals of each purpurin molecule will partially determine the interfacial charge separation and carrier mobility. In Fig. 11.17, we calculated the frontier molecular orbitals including HOMO-1, HOMO, LUMO, and LUMO+1 for both purpurin dyes. Similar to their carboxyl-functionalized analogs [39], the electrons of the purpurins are delocalized over the cyclic tetrapyrrole ring at the HOMO level and aligned along the y-axis at the LUMO level, and the presence of central metal Zn does not affect the electron distribution. The coincidence of chemical and physical properties of the purpurin dyes used in this study on organic heterojunction solar cells with those of their analogs used in the previous investigation on DSSCs is capable of comparing the two different organic photovoltaics at the same level, and such a comparison can provide some information for further development of these kinds of functional materials.

As earlier pointed out by many research groups, the morphology of electron donor thin films plays an important role in determining the photovoltaic performance of OSCs [11, 43]. In the present study, the fact that both purpurin dyes form aggregates strongly requires measurements of the morphologies of H₂P and ZnP films. Figure 11.18 shows the height and 3D images of H₂P and ZnP thin films spin-coated on MoO₃-modified ITO substrates from a 1 mg mL⁻¹ chloroform

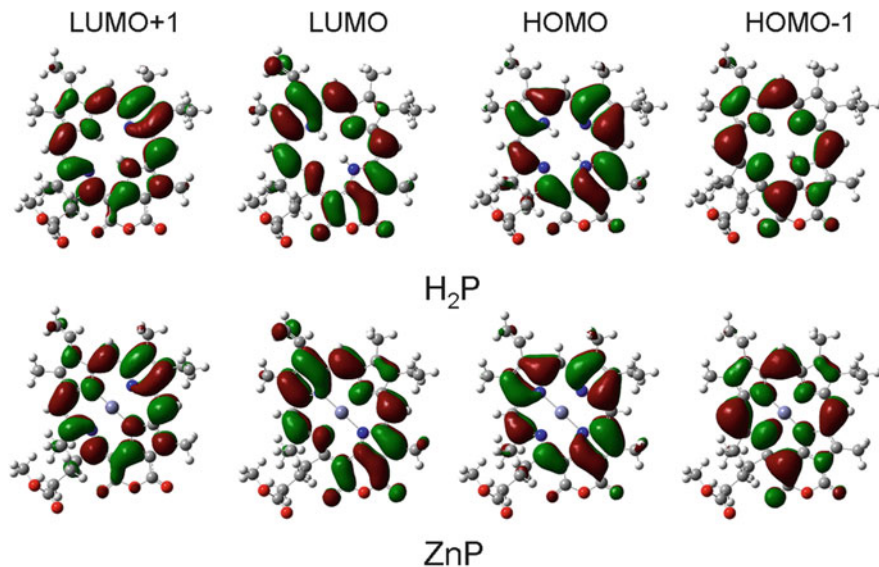


Fig. 11.17 Frontier molecular orbitals of H₂P and ZnP based on DFT/B3LYP/DGDZVP calculation with CPCM (chloroform)

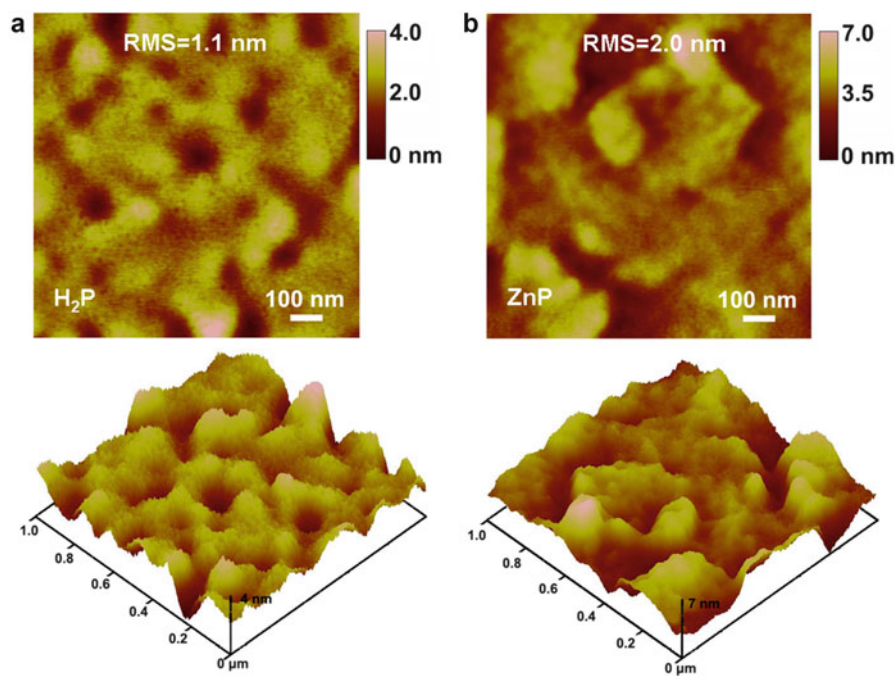


Fig. 11.18 AFM height and 3D images of H₂P (a) and ZnP (b) thin films on the MoO₃-modified ITO substrate

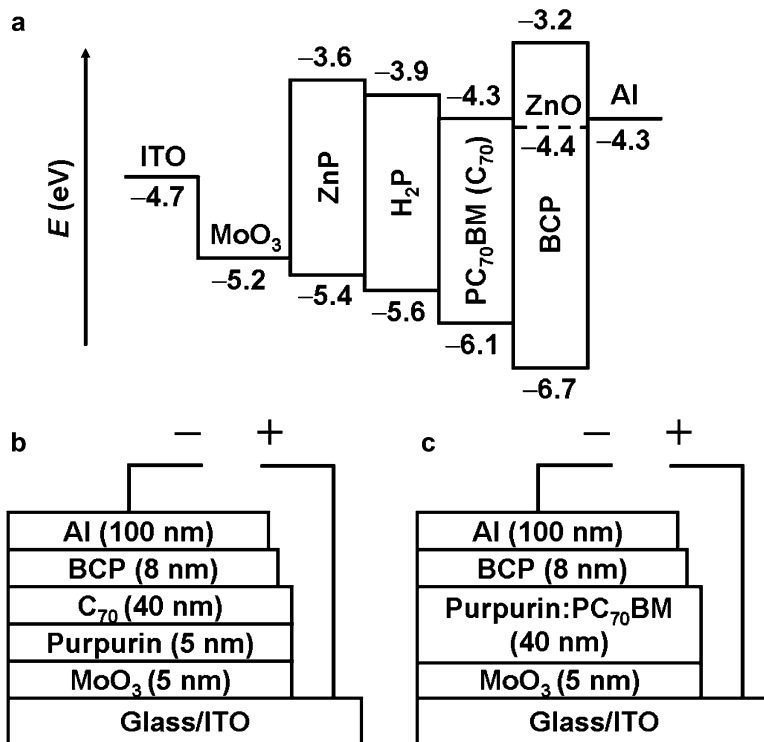


Fig. 11.19 Energy alignment of each layer (a) and configurations for PHJ (b) and BHJ OSC devices (c)

solution. The root-mean-square (rms), a factor to determine the film roughness obtained by computational analysis, was inserted on the film images. It can be clearly seen in the AFM images that both purpurin dyes gave a certain level of roughness in the vertical direction, and the rms values for H_2P and ZnP thin films were 1.1 nm and 2.0 nm, respectively. The larger roughness of the ZnP film than that of the H_2P film can be attributed to a higher level of aggregation in the former through the $\text{Zn} \cdots \text{O}$ bond as observed in artificial photosynthetic systems [44]. This observation also suggests that the ZnP film should give a higher carrier mobility than the H_2P film [45, 46], and OSCs based on the former material should give a better photovoltaic performance than that based on the latter material, if the LUMO orbitals of both purpurin dyes are aligned above the fullerene acceptors.

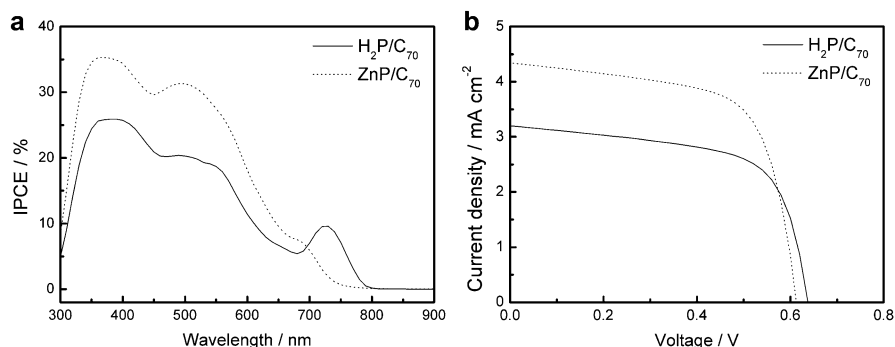


Fig. 11.20 IPCE profiles (a) and I - V curves (b) for purpurin-based PHJ devices

Table 11.4 Photovoltaic performance of purpurin/ C_{70} planar heterojunction solar cells

Purpurin	J_{sc} (mA cm^{-2})	V_{oc} (V)	FF	η (% at $P_0 = 1$ sun)
H_2P	3.20	0.64	0.64	1.31
ZnP	4.34	0.60	0.66	1.74

3.2 Planar Heterojunction OSCs Using Purpurins as the Electron Donor

Figure 11.19a depicts the energy alignment of materials used in each layer, and Fig. 11.19b shows the device configuration of the PHJ solar cells using the pair of purpurin dyes. The HOMO and LUMO energy levels are -5.6 and -3.9 eV and -5.4 and -3.6 eV for H_2P and ZnP, respectively. The LUMO levels of both purpurin dyes are sufficiently high, so that electrons can be transferred to the acceptor molecule C_{70} , which has the LUMO level at -4.3 eV. At the anode side, a 5 nm thick MoO_3 buffer layer has been used to modify the bare ITO substrate. The work function of MoO_3 is -5.2 eV, which is wonderfully located in between the work function of ITO (-4.7 eV) and the HOMO levels of purpurin dyes, allowing holes to be transferred to the anode side. Moreover, a buffer layer of BCP was used as the exciton blocking layer in between of the C_{70} layer and aluminum electrode. Importantly, the purpurin layers could be prepared by spin coating from a 1 mg mL^{-1} chloroform solution, because both purpurin dyes have an excellent solubility in chloroform.

Figure 11.20 shows the IPCE profiles (a) and I - V curves (b) of PHJ solar cells based on the purpurin dyes. Table 11.4 lists the relevant parameters extracted from the I - V curves. The four parameters related to the photovoltaic performance including J_{sc} , V_{oc} , FF, and η for PHJ solar cells were 4.34 mA cm^{-2} , 0.60 V,

0.66, and 1.74 % based on ZnP and 3.20 mA cm^{-2} , 0.64 V, 0.64, and 1.31 % based on H₂P. In spite of the discrepancy in the photovoltaic performances of PHJ solar cells based on both purpurin dyes, significant variation was not observed as in previous investigations on purpurin based DSSCs [39], indicating that the charge separation is valid in the purpurin-fullerene interface, due to the relatively low energy level of the LUMO orbital of fullerene. It was also noted that the J_{sc} values obtained by integration of IPCE spectra in the whole absorption region are quite low compared to the state-of-the-art OSCs [47, 48]. There are many factors to determine the J_{sc} in OSCs including, though may not limited to, the light-harvesting capability, the charge separation, and the charge carrier collection efficiencies. By fabricating PHJ devices with varied thicknesses of purpurin films, the optimized thickness of purpurin layers was obtained and it was only 5 nm. This thickness of purpurin layer provides very limited absorption capability of the corresponding PHJ solar cells. Further expansion of the purpurin film thickness always reduces the J_{sc} and η values, most probably due to the limited carrier mobility of purpurin molecules (see Table 11.6 for the details), since these purpurin films are amorphous.

On the other hand, the V_{oc} of the purpurin-based PHJ solar cells seems rather complicated. Generally speaking, the V_{oc} value of OSCs is mainly determined by the difference between the LUMO energy level of the acceptor molecule and the HOMO energy level of the donor molecule. Moreover, the real value will be limited by the energy of the bound charge transfer (CT) state of the donor-acceptor pairs. In the present system, the fact that the two purpurin dyes have a difference of 0.2 eV in the HOMO energy level but give a difference of only 0.04 V in the V_{oc} value does not fall into the above situation. This is most likely due to the difference of the recombination dynamics at the purpurin-fullerene interface. Actually, according to the previous report [49], the V_{oc} value of a PHJ solar cell using small dye molecules-based donor materials should obey the following equation:

$$V_{oc} = \frac{nkT}{q} \ln \left(\frac{J_{sc}}{J_{so}} \right) + \frac{\Delta E_{DA}}{2q} \quad (11.5)$$

where J_{so} is determined by a number of materials properties that determine the carrier generation/recombination rate, independent of the energy barrier of the donor and acceptor molecules, ΔE_{DA} . Here, the hole mobilities (μ_h) measured by SCLC method for H₂P and ZnP were 6.08×10^{-7} and $1.21 \times 10^{-5} \text{ cm}^2/(\text{V s})$, respectively. Compared to the electron mobility (μ_e) of C₇₀ at $4.21 \times 10^{-3} \text{ cm}^2/(\text{V s})$, purpurin molecules with low hole mobility may play a major role in determining the charge carrier recombination rate at the donor-acceptor interface, since the processes of carrier transport and recombination are always competing after the vanishment of charge separation. Moreover, the higher FF in the PHJ solar cell with ZnP than that with H₂P is simply attributable to the larger hole mobility in the former than that in the latter [50].

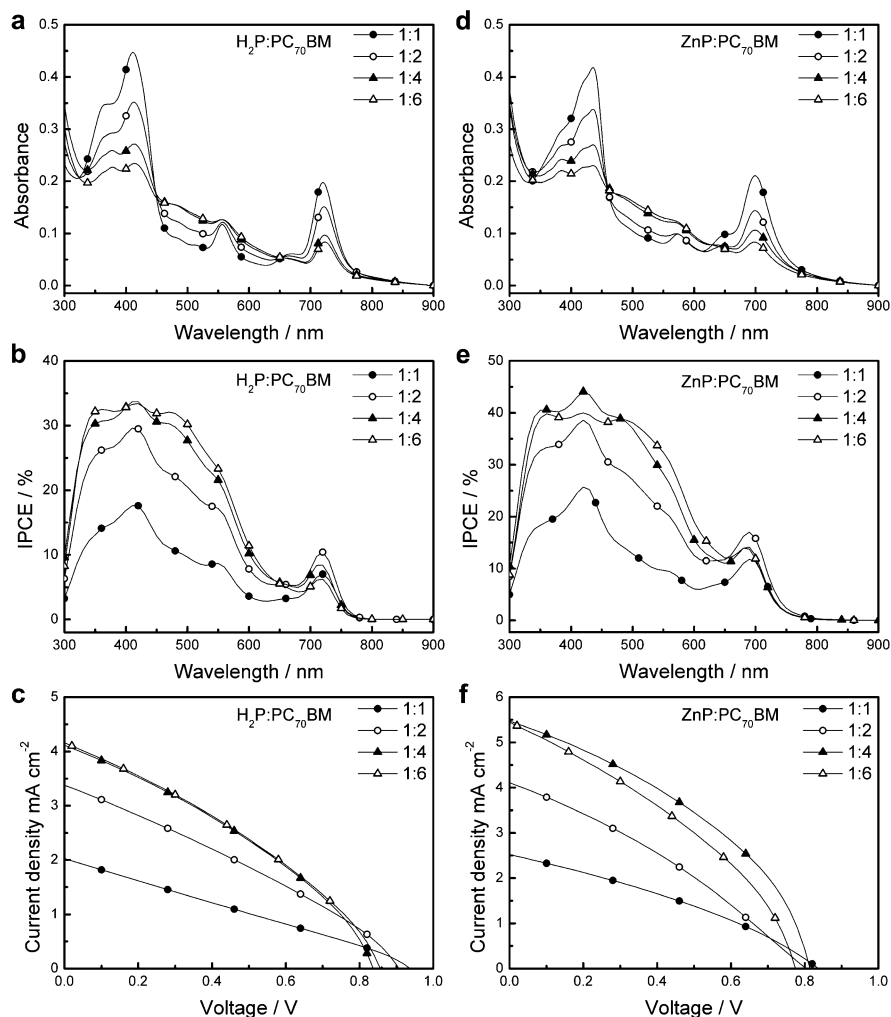


Fig. 11.21 Absorption spectra of purpurin:PC₇₀BM films with different blending ratios for H₂P (a) and ZnP (d), the corresponding IPCE profiles (b) and (e), *I*-*V* curves of BHJ devices (c) and (f) based on these films with H₂P and ZnP

Thus, the limited absorption from purpurin molecules and the imbalanced charge transport toward both cathode and anode may be the key parameters to limit the photovoltaic performance of purpurin-based PHJ solar cells. These problems motivate us to fabricate BHJ solar cells with purpurin/PC₇₀BM blends, since this kind of solar cell configuration can improve both light-harvesting and charge separation

Table 11.5 Photovoltaic performance of purpurinPC₇₀BM BHJ solar cells with various blending ratios

Purpurin	Blend ratio	J_{sc} (mA cm ⁻²)	V_{oc} (V)	FF	η (% at $P_0 = 1$ sun)
H ₂ P	1:1	1.98	0.90	0.27	0.48
	1:2	3.32	0.88	0.31	0.90
	1:4	4.12	0.84	0.34	1.18
	1:6	4.18	0.83	0.33	1.15
ZnP	1:1	2.37	0.83	0.31	0.62
	1:2	4.06	0.81	0.31	1.00
	1:4	5.40	0.80	0.39	1.69
	1:6	5.43	0.76	0.36	1.48

and minimize the imbalanced charge transport through optimizing the donor/acceptor blend ratio. Furthermore, such BHJ solar cells can be easily prepared by the spin-casting method, endowing it with better cost performance than the PHJ solar cells.

3.3 Bulk Heterojunction OSCs Using Purpurins as the Electron Donor

Figure 11.21a, d show the absorption spectra of the purpurin/PC₇₀BM blend films with different blend weight ratio from 1:1 to 1:6. For both H₂P and ZnP, the absorption peaks from the purpurin molecules decrease with a decrease of the purpurin content ratio, whereas the change of absorption from the PC₇₀BM part is opposite. It is also noteworthy that the amount of purpurin molecules in the blend film does not affect the peak position, indicating that the purpurin molecules are not homogeneously dispersed in the film, but forms the small islands in the film. The BHJ solar cells based on these blend films have been fabricated with a device configuration as shown in Fig. 11.19c. Figure 11.21 also shows the IPCE profiles and the I - V curves of the purpurin-based BHJ solar cells, and Table 11.5 lists the relevant parameters obtained from these I - V curves. The shape of each IPCE profile was similar to the corresponding absorption spectrum but with changed intensities at the purpurin and PC₇₀BM parts. For both purpurin molecules, the blend ratio at 1:1 gives intense absorption peaks, but the corresponding IPCE values at the peak positions were lower than those in the other blend ratios. Obviously, the absorption capability is not a major determining factor for the photocurrent in such solar cells. In the I - V curves of both the purpurin-based BHJ solar cells, J_{sc} reaches the highest value at the blend ratio of 1:4 and then saturates or decreases toward both larger and smaller blend ratios, whereas the V_{oc} values decrease with a decrease of the blend ratio. As a result of these changes in both photocurrent and photovoltage with

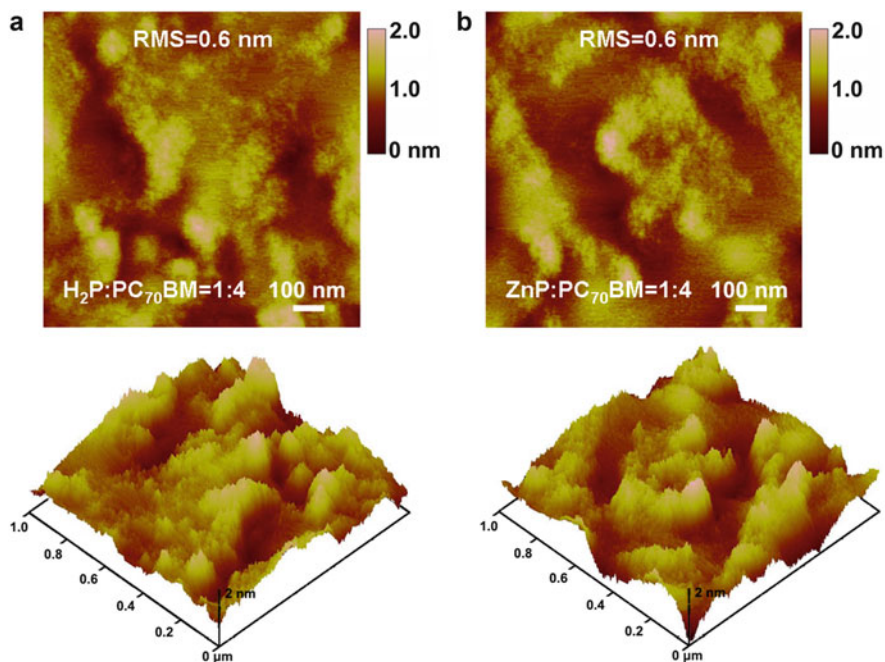


Fig. 11.22 AFM height and 3D images of H₂P:PC₇₀BM (a) and ZnP: PC₇₀BM films (b) with 1:4 blending ratio on MoO₃ modified ITO substrate

changed blend ratio, the highest η values were 1.18 % and 1.69 %, obtained for BHJ solar cells with H₂P and ZnP, respectively, at the blend ratio of 1:4.

Figure 11.22 shows the AFM images of the films with the blend ratio of purpurin/PC₇₀BM = 1:4, because these films give the best photovoltaic performance in BHJ solar cells. The rms roughness factors for these blend films were much smaller than those for the bare purpurin films in Fig. 11.18. The decreased roughness of the film originates from the reduced aggregation of the purpurin dyes in the blend film. The amorphous nature of such blend films raises a concern that the hole mobility of the blend film may be substantially reduced.

In order to explain the variation at the photocurrent upon different blend ratio of donor/acceptor molecules, both hole and electron mobilities of the blend films were determined by SCLC method. In Table 11.6, the hole mobility of the H₂P-based blend films increases from 3.06×10^{-8} to 4.79×10^{-7} cm²/(V s) with a decrease of H₂P/PC₇₀BM blend ratio from 1:1 to 1:4 and then decreases to 2.84×10^{-7} cm²/(V s) with further decreasing the blend ratio to 1:6, whereas the electron mobility increases with decreasing the blend ratio. In contrast, the hole mobility of the ZnP-based blend films decreases from 4.87×10^{-6} to 3.88×10^{-7} cm²/(V s) throughout decreasing the ZnP/PC₇₀BM blend ratio from 1:1 to 1:6, although the change of electron mobility was similar to that of the

Table 11.6 Carrier mobility data derived from single carrier devices using space charge limited current method

Carrier mobility	Purpurin	Blend ratio			PC ₇₀ BM
		1:1	1:2	1:4	
μ_h (cm ² /V s)	H ₂ P	3.06×10^{-8}	1.15×10^{-7}	4.79×10^{-7}	2.84×10^{-7}
μ_e (cm ² /V s)		8.75×10^{-5}	1.40×10^{-4}	2.14×10^{-4}	2.41×10^{-4}
μ_h (cm ² /V s)	ZnP	1:1	1:2	1:4	1:6
μ_e (cm ² /V s)		4.87×10^{-6}	2.64×10^{-6}	1.06×10^{-6}	3.88×10^{-7}
μ_e (cm ² /V s)		1.02×10^{-4}	1.70×10^{-4}	2.80×10^{-4}	4.58×10^{-4}
					8.14×10^{-4}

H₂P-based blend films. In the ideal principle, the hole mobility of the blend films is determined by that of the p-type purpurins, and more purpurin molecules mixed in the film, much larger hole mobility should be obtained, and vice versa. The observed hole mobility results of ZnP/PC₇₀BM BHJ films fall nicely into this case. However, this principle hardly explains the results of the hole mobility for the case of H₂P/PC₇₀BM BHJ films. The only explanation is that the holes generated in the blend film may be dissipated through the n-type material PC₇₀BM, since PC₇₀BM itself also has certain hole mobility, which can be a counterpart to the low hole mobility from H₂P molecule. The final hole mobility of the blend film is a sum of the hole mobility from both the donor and acceptor molecules. In fact, similar phenomena have been also observed for polymer and subphthalocyanine-based BHJ solar cells [51–55]. A solid proof to support the above hypothesis is that the PCBM cation radical could be detected in the polymer/PCBM blend films in a recent ultrafast absorption spectroscopic study [56]. Despite the difference in the hole mobility, the charge transport reaches a balanced situation for both the purpurin molecules when the blend ratio of purpurin/PC₇₀BM is 1:4, which is in good agreement with the observed photovoltaic performance for the BHJ solar cells.

The phenomenon that V_{oc} values decrease with decreasing the blend ratio for both the purpurin molecules is also hardly understood, because the V_{oc} values of the monolayer device based on PC₇₀BM mixed with low concentration donor were mainly dominated by the Schottky junction between the PC₇₀BM and MoO₃ [57]. In Fig. 11.23, the performance parameters of J_{sc} , V_{oc} , FF, and η were plotted as the function of the light illumination intensity for both H₂P-based (a–d) and ZnP-based BHJ solar cells (e–h) with different blend ratios. For both purpurin molecules with different purpurin/PC₇₀BM blend ratios, the change of the J_{sc} versus light power intensity has very similar trend, indicating that exciton annihilation is not a big issue in the present system [22, 27]. However, the trend of the V_{oc} values upon the lowering of power intensity varies for different blend ratios. As suggested by (11.5) in the previous part, the V_{oc} value is proportional to the J_{sc} and affected by the recombination rate between the acceptor and donor molecules. The slope of the curves for the V_{oc} value becomes small with decreasing the blend ratio, when the high power intensity was applied. The low V_{oc} value at reduced blend ratio can therefore be attributed to the serious charge recombination at larger PC₇₀BM content.

Furthermore, the FF value of OSCs usually increases with lowering power intensity, because a reduced amount of charge carriers can be easily transferred to both electrodes. The BHJ solar cells with purpurins also follow the above rule. As a result of these changes of J_{sc} , V_{oc} , and FF upon different power intensities, the η values for these purpurin-based BHJ solar cells increase with reduced power intensity, and the best η of up to 2.6 % has been achieved for the ZnP-based BHJ solar cell (1:4) at 1 mW cm⁻² illumination intensity.

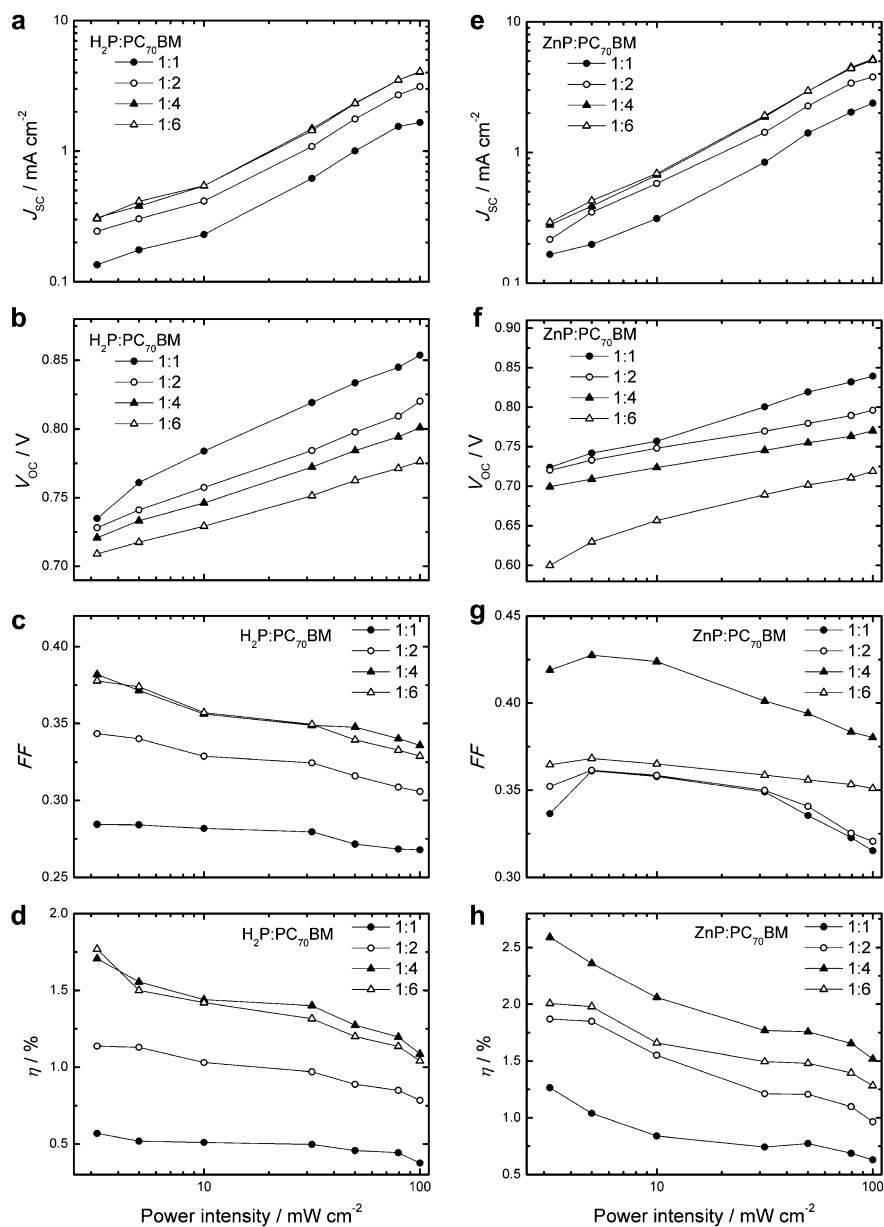


Fig. 11.23 Plots of four key parameters including J_{sc} , V_{oc} , FF, and η , as the function of incident light intensity, for H₂P (a–d) and ZnP (e–h)

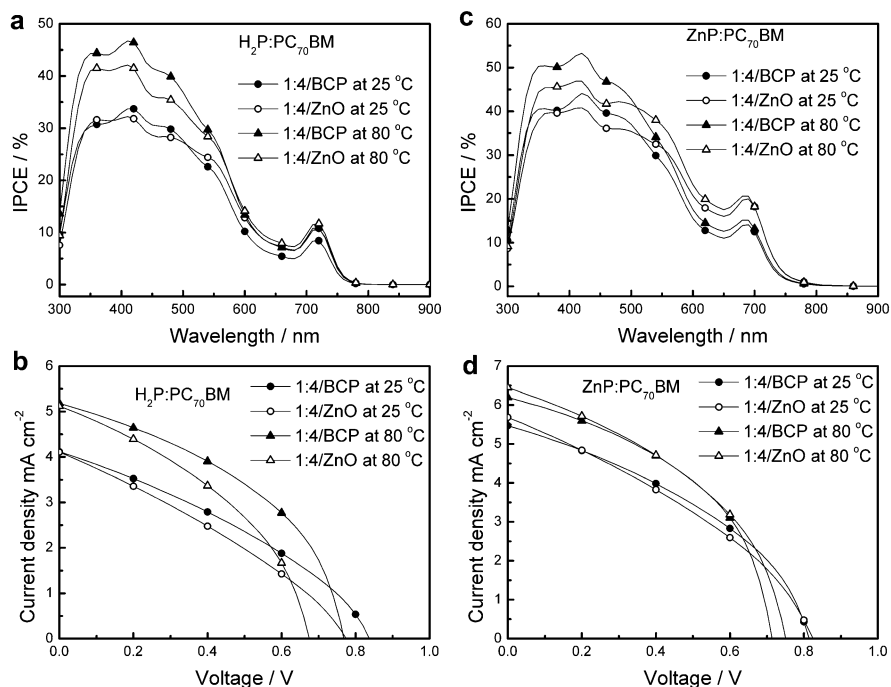


Fig. 11.24 IPCE profiles (a and c) and I - V curves (b and d) for BHJ solar cells with different exciton blocking layers at 25 and 80 °C for H₂P (a and d) and ZnP (c and d)

Table 11.7 Effects of exciton blocking layer and examined temperature on photovoltaic performance of BHJ solar cells with the blend ratio of purpurin:PC₇₀BM = 1:4

Purpurin	Layer	Temperature (°C)	J_{sc} (mA cm ⁻²)	V_{oc} (V)	FF	η (% at $P_0 = 1$ sun)
H ₂ P	BCP	25	4.12	0.84	0.34	1.18
	ZnO	25	4.07	0.77	0.31	1.00
	BCP	80	5.18	0.77	0.43	1.71
	ZnO	80	5.12	0.68	0.40	1.37
ZnP	BCP	25	5.40	0.80	0.39	1.69
	ZnO	25	5.67	0.81	0.35	1.64
	BCP	80	6.20	0.72	0.46	2.03
	ZnO	80	6.45	0.75	0.42	2.02

3.4 BHJ Solar Cells Based on Purpurin/PC₇₀BM Films with 1:4 Blend Ratio: Effect of Exciton Blocking Layer and Elevated Temperature

In the last part, the optimal blend ratio of 1:4 gives the highest photovoltaic performance for BHJ solar cells based on both H₂P and ZnP. Follow-up

experiments were carried out to further improve their photovoltaic performance by replacing the exciton blocking layer with ZnO. Compared to BCP as the exciton blocking layer used above, ZnO as a wide band gap inorganic semiconductor could be more promising, because ZnO has better stability and carrier mobility and can be processed from the solution. Figure 11.24 compares the IPCE profiles and the I - V curves of BHJ solar cells using both purpurin molecules with either BCP or ZnO as the exciton blocking layer. Table 11.7 lists the relevant parameters obtained from the I - V curves. Interestingly, the use of ZnO gives a different effect on a pair of the purpurins. Compared to the BHJ solar cells using BCP, the IPCE data at the Q_y absorption region was almost equal for H₂P but was about 30 % enhanced for ZnP. As the result of the change in IPCE, the J_{sc} value of H₂P-based solar cells was practically similar, but that of ZnP-based solar cells slightly improved from 5.40 to 5.67 mA cm⁻², upon the replacement of BCP with ZnO. Moreover, the use of ZnO caused the V_{oc} value decreased from 0.84 to 0.77 V for H₂P but increased slightly from 0.80 to 0.81 V for ZnP. The above different changes at the J_{sc} and V_{oc} values upon the replacement of the exciton blocking layer may originate from the electron transfer between the purpurin molecules and the ZnO layer, because ZnO is a good n-type semiconductor. Through fabricating the fullerene-free monolayer devices with purpurins and ZnO, we found that certain photocurrents and photovoltages can only be generated with H₂P not with ZnP. When ZnO was used in the H₂P-based BHJ devices, competitive charge separation occurs both at the H₂P/PC₇₀BM and H₂P/ZnO interfaces, and the charge separation efficiency of the former interface is much higher than that of the latter interface, so that a reduced photocurrent was observed. Also, the competitive charge transport will also reduce the photovoltage of such a device, due to mixing effect of potentials built in the H₂P/PC₇₀BM and the H₂P/ZnO interfaces. In contrast, there is no photoresponse observed for the ZnP/ZnO monolayer device, the charge separation at this interface must be inactive, and slightly enhanced photocurrent of the ZnP-based BHJ solar cell should come from the scattering effect of ZnO nanoparticles.

Finally, we tried to evaluate the thermal stability of such BHJ solar cells by heating the solar cells to 80 °C to measure the photovoltaic performance. The IPCE profiles and the I - V curves of such heated devices were also shown in Fig. 11.24. Compared to the room temperature measurement, each solar cell gives better J_{sc} and FF but worse V_{oc} at 80 °C. At high temperature, the improved J_{sc} and FF can be attributed to the increased carrier mobility of the materials, and the reduced V_{oc} can be attributed to much more serious charge recombination kinetics at the donor-acceptor interface; both must follow the rule of traditional thermal dynamics. The best η values of up to 2 % were recorded for the ZnP-based BHJ solar cells at such high temperature. Importantly, the device performance returned to the original values when the device was cooled to the room temperature, indicating these purpurin dyes in the device have excellent thermal stability.

4 Conclusions

In this chapter, DSSCs and OSCs based on the same type of near-infrared-absorbing purpurins have been studied in detail. When using a pair of carboxyl purpurins, c-H₂P and c-ZnP, as sensitizers in DSSCs, the dye sensitizers have been found to form aggregation on semiconductor surface through self-assembly. With TiO₂ as semiconductor electrode, the electron injection is taking place from LUMO orbital in c-ZnP but from LUMO+1 orbital in c-H₂P. The presence of TBP substantially suppressed the electron injection between dye and TiO₂. The use of SnO₂ improves the photocurrent generation in both sensitizers, especially when TBP was present in electrolyte. The excitons generated in aggregate of dyes can contribute to the photocurrent generation through exciton diffusion toward the SnO₂ electrode. TBP can also reduce the aggregate formation on semiconductor surface, and this will reduce the exciton annihilation, as revealed by the study of the sub-picosecond time-resolved absorption spectroscopies.

On the other hand, the suitable LUMO levels of fullerene-based acceptors to that of purpurin molecules suggest fabricating OSCs with these molecules to facilitate electron transfer at the donor–acceptor interface. Purpurin dyes without carboxyl, H₂P, and ZnP, can also form aggregate through simple spin-coating process, though the morphology of films is still amorphous. The charge separation can occur at the purpurin/C₇₀ interface, which proves that organic semiconductors are better electron acceptor for small molecule dyes with low LUMO levels. It has been found that a very thin layer of up to 5 nm of purpurin film gives the highest photovoltaic performance for the purpurin-based PHJ cells. In order to improve the charge separation, BHJ cells have been also fabricated with active layers with different purpurin/PC₇₀BM blend ratios. When the blend ratio of purpurin/PC₇₀BM reaches 1:4, the solar cell gives rise to the highest photovoltaic performance, which is due to the balanced charge carrier transport toward both electrodes as supported by the electron and hole mobility results. Replacement of the exciton blocking layer BCP by ZnO reduces the J_{sc} and V_{oc} values of H₂P-based BHJ solar cell but enhances these values of the ZnP-based BHJ solar cell. This different effect of ZnO was attributed to the fact that the competitive charge separation at either the H₂P/PC₇₀BM or H₂P/ZnO interface can only occur, but no evidence of the charge separation was observed at the ZnP/ZnO interface.

In summary, the present study combining both DSSCs and OSCs with same type electron donor materials not only deepen our knowledge about these different organic photovoltaic systems but also lead to considerations of using near-infrared-absorbing materials for highly efficient solar cells.

Acknowledgements The authors thank Prof. Hitoshi Tamiaki and Dr. Shin-ichi Sasaki for preparing the purpurin materials, Dr. Osamu Kitao for carrying out DFT and TD-DFT calculation, and Prof. Junji Kido, Prof. Tsukasa Yoshida, Dr. Ziruo Hong, Prof. Jian-Ping Zhang, and Dr. Takeshi Sano for stimulated discussions. This work was partially supported by Grants-in-Aid for Young Scientists (A) (23686138) (to X.-F.W) from the Japan Society for the Promotion of Science (JSPS), and by Japan Regional Innovation Strategy program by the Excellence (J-RISE) from Japan Science and Technology Agency (JST).

References

1. O'Regan, B., Grätzel, M.: A low-cost, high-efficiency solar cell based on dye-sensitized colloidal TiO₂ films. *Nature* **353**, 737–740 (1991)
2. Chiba, Y., Islam, A., Watanabe, Y., Komiyama, R., Koide, N., Han, L.: Dye-sensitized solar cells with conversion efficiency of 11.1%. *Jpn. J. Appl. Phys.* **45**, L638–L640 (2006)
3. Grätzel, M.: Recent advances in sensitized mesoscopic solar cells. *Acc. Chem. Res.* **42**, 1788–1798 (2009)
4. Tang, C.W.: Two-layer organic photovoltaic cell. *Appl. Phys. Lett.* **48**, 183 (1986)
5. Ma, W., Yang, C., Gong, X., Lee, K., Heeger, A.J.: Thermally stable, efficient polymer solar cells with nanoscale control of the interpenetrating network morphology. *Adv. Funct. Mater.* **15**, 1617–1622 (2005)
6. Li, G., Shrotriya, V., Huang, J., Yao, Y., Moriarty, T., Emery, K., Yang, Y.: High-efficiency solution processable polymer photovoltaic cells by self-organization of polymer blends. *Nat. Mater.* **4**, 864–868 (2005)
7. Günes, S., Neugebauer, H., Sariciftci, N.S.: Conjugated polymer-based organic solar cells. *Chem. Rev.* **107**, 1324–1338 (2007)
8. Liang, Y., Wu, Y., Feng, D., Tsai, S.-T., Son, H.-J., Li, G., Yu, L.: Development of new semiconducting polymers for high performance solar cells. *J. Am. Chem. Soc.* **131**, 56–57 (2009)
9. Chen, H.-Y., Hou, J., Zhang, S., Liang, Y., Yang, G., Yang, Y., Yu, L., Wu, Y., Li, G.: Polymer solar cells with enhanced open-circuit voltage and efficiency. *Nat. Photon.* **3**, 649–653 (2009)
10. Li, Y., Guo, Q., Li, Z., Pei, J., Tian, W.: Solution processable D-A small molecules for bulk-heterojunction solar cells. *Energy Environ. Sci.* **3**, 1427–1436 (2010)
11. Walker, B., Kim, C., Nguyen, T.-Q.: Small molecule solution-processed bulk heterojunction solar cells. *Chem. Mater.* **23**, 470–482 (2011)
12. Mishra, A., Bäuerle, P.: Small molecule organic semiconductors on the move: promises for future solar energy technology. *Angew. Chem. Int. Ed.* **51**, 2020–2067 (2012)
13. Wang, X.-F., Wang, L., Wang, Z., Wang, Y., Tamai, N., Hong, Z., Kido, J.: Natural photosynthetic carotenoids for solution-processed organic bulk-heterojunction solar cells. *J. Phys. Chem. C* **117**, 804–811 (2013)
14. Yella, A., Lee, H.W., Tsao, H.N., Yi, C., Chandiran, A.K., Nazeeruddin, M.K., Diao, E.W.-G., Yeh, C.-Y., Zakeeruddin, S.M., Grätzel, M.: Porphyrin-sensitized solar cells with cobalt (II/III)-based redox electrolyte exceed 12 percent efficiency. *Science* **6056**, 629–634 (2011)
15. You, J., Dou, L., Yoshimura, K., Kato, T., Ohya, K., Moriarty, T., Emery, K., Chen, C.-C., Gao, J., Li, G., Yang, Y.: A polymer tandem solar cell with 10.6% power conversion efficiency. *Nat. Commun.* **4**, 1446 (2013)
16. Fabregat-Santiago, F., Bisquert, J., Cevey, L., Chen, P., Wang, M., Zakeeruddin, S.M., Grätzel, M.: Electron transport and recombination in solid-state dye solar cell with spiro-OMeTAD as hole conductor. *J. Am. Chem. Soc.* **131**, 558–562 (2009)
17. Robertson, N.: Optimizing dyes for dye-sensitized solar cells. *Angew. Chem. Int. Ed.* **45**, 2338–2345 (2006)
18. Ooyama, Y., Harima, Y.: Molecular designs and syntheses of organic dyes for dye-sensitized solar cells. *Eur. J. Org. Chem.* **18**, 2903–2934 (2009)
19. Imahori, H., Umeyama, T., Ito, S.: Large π -aromatic molecules as potential sensitizers for highly efficient dye-sensitized solar cells. *Acc. Chem. Res.* **42**, 1809–1818 (2009)
20. Wang, X.-F., Tamiaki, H.: Cyclic tetrapyrrole based molecules for dye-sensitized solar cells. *Energy Environ. Sci.* **3**, 94–106 (2010)
21. Walter, M.G., Rudine, A.B., Wamser, C.C.: Porphyrins and phthalocyanines in solar photovoltaic cells. *J. Porphyrins Phthalocyanines* **14**, 759–792 (2010)
22. Wang, X.-F., Kitao, O., Zhou, H., Tamiaki, H., Sasaki, S.: Efficient dye-sensitized solar cell based on oxo-bacteriochlorin sensitizers with broadband absorption capability. *J. Phys. Chem. C* **113**, 7954–7961 (2009)

23. Lo, C.-F., Hsu, S.-J., Wang, C.-L., Cheng, Y.-H., Lu, H.-P., Diau, E.W.-G., Lin, C.-Y.: Tuning spectral and electrochemical properties of porphyrin-sensitized solar cells. *J. Phys. Chem. C* **114**, 12018 (2010)
24. Wang, X.-F., Arihiro, M., Koyama, Y., Nagae, H., Sasaki, S., Tamiaki, H., Wada, Y.: Effects of plant carotenoid spacers on the performance of a dye-sensitized solar cell using a chlorophyll derivative: enhancement of photocurrent determined by one electron-oxidation potential of each carotenoid. *Chem. Phys. Lett.* **423**, 470–475 (2006)
25. Wang, X.-F., Koyama, Y., Nagae, H., Wada, Y., Sasaki, S., Tamiaki, H.: Dependence of photocurrent and conversion efficiency of titania-based solar cell on the Q_y absorption and one electron-oxidation potential of pheophorbide sensitizer. *J. Phys. Chem. C* **112**, 4418–4426 (2008)
26. Wang, X.-F., Kitao, O., Zhou, H., Tamiaki, H., Sasaki, S.: Extension of π -conjugation length along the Q_y axis of a chlorophyll a derivative for efficient dye-sensitized solar cells. *Chem. Commun.* 1523–1525 (2009)
27. Wang, X.-F., Tamiaki, H., Wang, L., Tamai, N., Kitao, O., Zhou, H., Sasaki, S.-I.: Chlorophyll-a derivatives with various hydrocarbon ester groups for efficient dye-sensitized solar cells: static and ultrafast evaluations on electron injection and charge collection processes. *Langmuir* **26**, 6320–6327 (2010)
28. Brabec, C.J., Gowrisanker, S., Halls, J.J.M., Laird, D., Jia, S., Williams, S.P.: Polymer–fullerene bulk-heterojunction solar cells. *Adv. Mater.* **22**, 3839–3856 (2010)
29. Li, G., Zhu, R., Yang, Y.: Polymer solar cells. *Nat. Photon.* **6**, 153–161 (2012)
30. Li, Y.: Molecular design of photovoltaic materials for polymer solar cells: toward suitable electronic energy levels and broad absorption. *Acc. Chem. Res.* **45**, 723–733 (2012)
31. Matsuo, Y., Sato, Y., Niinomi, T., Soga, I., Tanaka, H., Nakamura, E.: Columnar structure in bulk heterojunction in solution-processable three-layered p-i-n organic photovoltaic devices using tetrabenzoporphyrin precursor and silylmethyl[60]fullerene. *J. Am. Chem. Soc.* **131**, 16048–16050 (2009)
32. Hori, T., Miyake, Y., Yamasaki, N., Yoshida, H., Fujii, A., Shimizu, Y., Ozaki, M.: Solution processable organic solar cell based on bulk heterojunction utilizing phthalocyanine derivative. *Appl. Phys. Expr.* **3**, 101602 (2010)
33. Blom, P.W.M., Mihailetchi, V.D., Koster, L.J.A., Markov, D.E.: Device physics of polymer: fullerene bulk heterojunction solar cells. *Adv. Mater.* **19**, 1551–1566 (2007)
34. Kitao, O.: Photoinduced electron transfer in dye-sensitized solar cells: modified Sakata–Hashimoto–Hiramoto model (MSHH). *J. Phys. Chem. C* **111**, 15889–15902 (2007)
35. Hiriuch, T., Miura, H., Uchida, S.: Highly efficient metal-free organic dyes for dye-sensitized solar cells. *J. Photochem. Photobiol. A Chem.* **164**, 29–32 (2004)
36. Haque, S.A., Palomares, E., Cho, B.M., Green, A.N.M., Hirata, N., Klug, D.R., Durrant, J.R.: Charge separation versus recombination in dye-sensitized nanocrystalline solar cells: the minimization of kinetic redundancy. *J. Am. Chem. Soc.* **127**, 3456–3462 (2005)
37. Cahen, D., Hodes, G., Grätzel, M., Guillemoles, J.F., Riess, I.: Nature of photovoltaic action in dye-sensitized solar cells. *J. Phys. Chem. B* **104**, 2053–2059 (2000)
38. Feldt, S.M., Gibson, E.A., Gabrielsson, E., Sun, L., Boschloo, G., Hagfeldt, A.: Design of organic dyes and cobalt polypyridine redox mediators for high-efficiency dye-sensitized solar cells. *J. Am. Chem. Soc.* **132**, 16714–16724 (2010)
39. Wang, X.-F., Wang, L., Tamai, N., Kitao, O., Tamiaki, H., Sasaki, S.: Development of solar cells based on synthetic near-infrared absorbing purpurins: observation of multiple electron injection pathways at cyclic tetrapyrrole–semiconductor interface. *J. Phys. Chem. C* **115**, 24394–24402 (2011)
40. Scharber, M.C., Mühlbacher, D., Koppe, M., Denk, P., Waldsuf, C., Heeger, A.J., Brabec, C.J.: Design rules for donors in bulk-heterojunction solar cells—towards 10 % energy-conversion efficiency. *Adv. Mater.* **18**, 789–794 (2006)
41. Maurano, A., Hamilton, R., Shuttle, C.G., Ballantyne, A.M., Nelson, J., O'Regan, B., Zhang, W., McCulloch, I., Azimi, H., Morana, M., Brabec, C.J., Durrant, J.R.: Recombination

- dynamics as a key determinant of open circuit voltage in organic bulk heterojunction solar cells: a comparison of four different donor polymers. *Adv. Mater.* **22**, 4987–4992 (2010)
42. Yamamoto, S., Orimo, A., Ohkita, H., Benten, H., Ito, S.: Molecular understanding of the open-circuit voltage of polymer:fullerene solar cells. *Adv. Energy Mater.* **2**, 229–237 (2012)
 43. Beaujuge, P.M., Fréchet, J.M.J.: Molecular design and ordering effects in π -functional materials for transistor and solar cell applications. *J. Am. Chem. Soc.* **133**, 20009–20029 (2011)
 44. Saga, Y., Shibata, Y., Tamiaki, H.: Spectral properties of single light-harvesting complexes in bacterial photosynthesis. *J. Photochem. Photobiol. C Photochem. Rev.* **11**, 15–24 (2010)
 45. Shepherd, W.E.B., Platt, A.D., Hofer, D., Ostroverkhova, O., Loth, M., Anthony, J.E.: Aggregate formation and its effect on (opto)electronic properties of guest-host organic semiconductors. *Appl. Phys. Lett.* **97**, 163303 (2010)
 46. Kaafarani, B.R.: Discotic liquid crystals for opto-electronic applications. *Chem. Mater.* **23**, 378–396 (2011)
 47. Wei, G., Wang, S., Sun, K., Thompson, M.E., Forrest, S.R.: Solvent-annealed crystalline squaraine: PC₇₀ BM (1:6) solar cells. *Adv. Energy Mater.* **1**, 184–187 (2011)
 48. Zhou, J., Wan, X., Liu, Y., Long, G., Wang, F., Li, Z., Zuo, Y., Li, C., Chen, Y.: A planar small molecule with dithienosilole core for high efficiency solution-processed organic photovoltaic cells. *Chem. Mater.* **23**, 4666–4668 (2011)
 49. Perez, M.D., Borek, C., Forrest, S.R., Thompson, M.E.: Molecular and morphological influences on the open circuit voltages of organic photovoltaic devices. *J. Am. Chem. Soc.* **131**, 9281–9286 (2009)
 50. Kageyama, H., Ohishi, H., Tanaka, M., Ohmori, Y., Shirota, Y.: High performance organic photovoltaic devices using amorphous molecular materials with high charge-carrier drift mobilities. *Appl. Phys. Lett.* **94**, 063304 (2009)
 51. Melzer, C., Koop, E.J., Mihaiilechi, V.D., Blom, P.W.M.: Hole transport in poly(phenylene vinylene)/methanofullerene bulk-heterojunction solar cells. *Adv. Funct. Mater.* **14**, 865 (2004)
 52. Mihaiilechi, V.D., Koster, L.J.A., Blom, P.W.M., Melzer, C., de Bore, B., van Duren, J.K.J., Janssen, R.A.J.: Compositional dependence of the performance of poly(p-phenylene vinylene):methanofullerene bulk-heterojunction solar cells. *Adv. Funct. Mater.* **15**, 795–801 (2005)
 53. Tuladhar, S.M., Poplavskyy, D., Choulis, S.A., Durrant, J.R., Bradley, D.D.C., Nelson, J.: Ambipolar charge transport in films of methanofullerene and poly(phenylenevinylene)/methanofullerene blends. *Adv. Funct. Mater.* **15**, 1171–1182 (2005)
 54. Zhang, F., Mammo, W., Andersson, L.M., Admassie, S., Andersson, M.R., Inganäs, O.: Low-bandgap alternating fluorene copolymer/methanofullerene heterojunctions in efficient near-infrared polymer solar cells. *Adv. Mater.* **18**, 2169–2173 (2006)
 55. Pandey, R., Gunawan, A.A., Mkhoyan, K.A., Holmes, R.J.: Efficient organic photovoltaic cells based on nanocrystalline mixtures of boron subphthalocyanine chloride and C₆₀. *Adv. Funct. Mater.* **22**, 617–624 (2012)
 56. Yamamoto, S., Guo, J., Ohkita, H., Ito, S.: Formation of methanofullerene cation in bulk heterojunction polymer solar cells studied by transient absorption spectroscopy. *Adv. Funct. Mater.* **18**, 2555–2562 (2008)
 57. Zhang, M., Wang, H., Tian, H., Geng, Y., Tang, C.W.: Bulk heterojunction photovoltaic cells with low donor concentration. *Adv. Mater.* **23**, 4960–4964 (2011)

Chapter 12

Hybrid Solar Cells: Materials, Interfaces, and Devices

Giacomo Mariani, Yue Wang, Richard B. Kaner, and Diana L. Huffaker

Abstract Photovoltaic technologies could play a pivotal role in tackling future fossil fuel energy shortages, while significantly reducing our carbon dioxide footprint. Crystalline silicon is pervasively used in single junction solar cells, taking up ~80 % of the photovoltaic market. Semiconductor-based inorganic solar cells deliver relatively high conversion efficiencies at the price of high material and manufacturing costs. A great amount of research has been conducted to develop low-cost photovoltaic solutions by incorporating organic materials. Organic semiconductors are conjugated hydrocarbon-based materials that are advantageous because of their low material and processing costs and a nearly unlimited supply. Their mechanical flexibility and tunable electronic properties are among other attractions that their inorganic counterparts lack. Recently, collaborations in nanotechnology research have combined inorganic with organic semiconductors in a “hybrid” effort to provide high conversion efficiencies at low cost. Successful integration of these two classes of materials requires a profound understanding of the material properties and an exquisite control of the morphology, surface properties, ligands, and passivation techniques to ensure an optimal charge carrier generation across the hybrid device. In this chapter, we provide background information of this novel, emerging field, detailing the various approaches for obtaining inorganic nanostructures and organic polymers, introducing a multitude of methods

G. Mariani (✉) • D.L. Huffaker

Department of Electrical Engineering, University of California, Los Angeles,
420 Westwood Plaza, Los Angeles, CA 90095, USA
e-mail: giacomomariani@ucla.edu; huffaker@ee.ucla.edu

Y. Wang • R.B. Kaner

Department of Chemistry and Biochemistry, University of California, Los Angeles,
607 Charles E. Young Drive East, Box 951569, Los Angeles, CA 90095, USA
e-mail: yuewang@chem.ucla.edu; kaner@chem.ucla.edu

for combining the two components to achieve the desired morphologies, and emphasizing the importance of surface manipulation. We highlight several studies that have fueled new directions for hybrid solar cell research, including approaches for maximizing efficiencies by controlling the morphologies of the inorganic component, and in situ molecular engineering via electrochemical polymerization of a polymer directly onto the inorganic nanowire surfaces. In the end, we provide some possible future directions for advancing the field, with a focus on flexible, lightweight, semitransparent, and low-cost photovoltaics.

1 Introduction

The advancements in the design and fabrication of photovoltaics can be categorized into three different generations of solar cells. The first generation of solar cells includes large-area, silicon-based modules estimated to account for 86 % of the total photovoltaic market. However, mainly due to high manufacturing costs, a second generation of cells, thin-film solar cells, has been introduced to address low costs and high flexibility that permit integration on roof tops, solar shingles, etc. The most cutting-edge technology is represented by the third generation of solar cells that completely replaces the standard paradigm of a two-dimensional (2-D) planar p–n junction with new materials and novel three-dimensional (3-D) design approaches. Polymer-based, nanostructure-based, or dye-sensitized solar cells represent some of the innovative alternatives for which research teams are investing a considerable amount of time. Crystalline silicon solar cells have recently achieved laboratory efficiencies of 25 % [1], requiring a honeycomb texturing along with a rear local diffusion of dopants. The adjective “crystalline” refers to the crystal growth phase during the preparation of the cylindrical semiconductor ingots.

After oxygen, silicon (Si) is the most abundant element on earth. Generally, silicon is obtained by the reduction of silicon dioxide with carbon in an electric furnace from 1,500 to 2,000 °C. The silicon used in the semiconductor industry for the fabrication of devices is then further purified to bring impurity levels below the parts-per-billion level. In order to fabricate a silicon solar cell, a large, doped ingot is first sectioned into smaller ingots of proper size. Subsequently, each ingot is sliced and cleaned to yield a series of wafers. Phosphorus is then diffused into the semiconductor to constitute the second side of the photojunction. Lastly, metal grid contacts are realized by screen-printing techniques. The process chain is depicted schematically in Fig. 12.1.

The nonoptimized material usage and the multi-stepped fabrication involved are hindering the achievement of a solar grid parity. A situation of grid parity occurs when a source of alternative power (e.g. solar) becomes cost competitive with standard sources (e.g. fossil fuel-based). In order to minimize the material usage and reduce the overall costs, new radical strategies to further slice the silicon wafers into thin films of semiconductors are being explored. An alternative solution to lower the cost of solar cells is represented by the development of organic

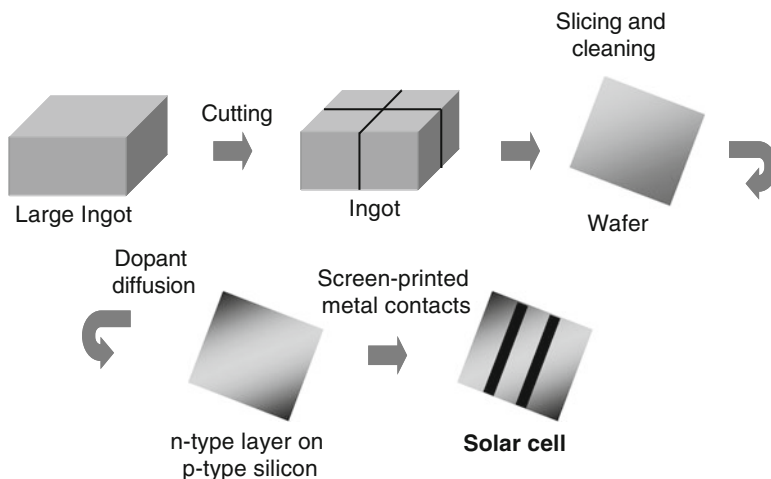


Fig. 12.1 Sequence of fabrication process for a silicon semiconductor solar cell

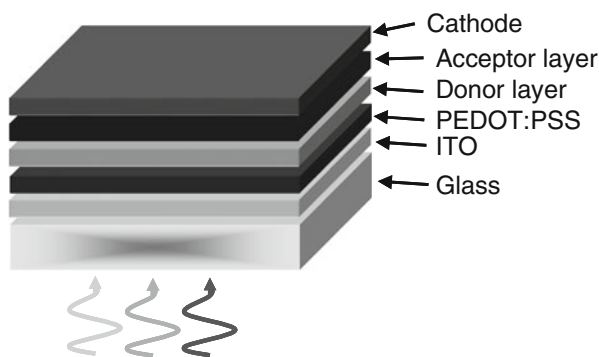


Fig. 12.2 Schematic of a single-junction organic solar cell with back illumination. PEDOT:PSS is the abbreviation for poly(3,4-ethylenedioxythiophene):poly(styrenesulfonate), and ITO for indium tin oxide

photovoltaic devices. One of the most important milestones was the introduction of a C_{60} fullerene derivative to replace the conventional n-type polymers in organic solar cells [2]. In a typical organic device, donor and acceptor interfaces are intimately mixed together to constitute a bulk heterojunction (Fig. 12.2). Such blends constitute the active absorber, able to harvest the photons and generate free charge carriers that can be collected at the electrodes. The mixture is in liquid form and can be promptly spin-coated on arbitrary substrates. To date, the highest efficiency for this class of solar cells amounts to 10.6%. Building efficient devices requires a systematic analysis of three different areas: materials design,

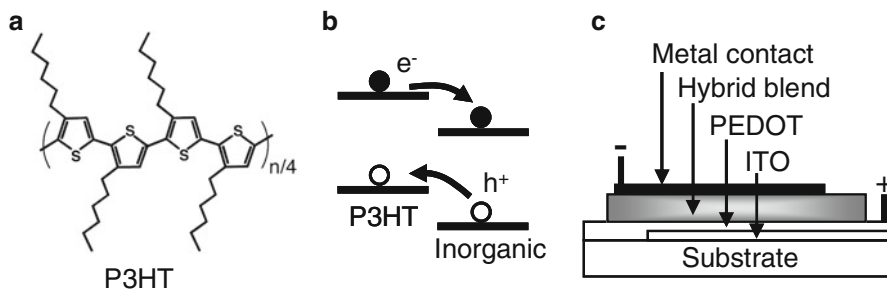


Fig. 12.3 (a) Chemical structure of regioregular P3HT: poly(3-hexylthiophene), a commonly used hole-conducting conjugated polymer. (b) Electron and hole transport in the hybrid composite band structure. (c) A typical single-junction hybrid solar cell on an arbitrary substrate

morphology, and interface engineering. The total thickness for the light-harvesting active layer in solution-processed photovoltaics is only a few hundred nanometers. This allows for low cost and flexible architectures, with processes compatible with roll-to-roll manufacturing for high-volume production. To date, one of the main challenges is to unravel the complex selection of degradation phenomena that occurs in this type of optoelectronic device. Photolytic and photochemical reactions are activated under illumination directly from the polymer, degrading the conversion efficiency over time in ambient atmosphere [3].

In order to provide the highest efficiency at reasonable prices, hybrid photovoltaic technologies emerged to combine the benefits of organic and inorganic materials. The photovoltaic layer is typically constituted of semiconducting polymers (e.g. P3HT, Fig. 12.3a) intimately mixed with inorganic nanocrystals or other nanostructures. The classical inorganic solar cells mentioned earlier have a higher carrier mobility; whereas organic solar cells benefit from considerably higher optical absorption coefficients. The charge transfer in this new class of photojunctions can be studied in composites of p-type conjugated polymers with n-type inorganic semiconductors, or vice versa [4] (Fig. 12.3b, c).

2 Background on Hybrid Photovoltaics

Organic/inorganic hybrid solar cells are attracting growing attention and becoming a vibrant field of research. All inorganic solar cells have higher efficiencies due to their excellent carrier mobility, but are generally expensive.

The low-cost polymer solar cells, on the other hand, often lacks air stability and satisfactory performance due to inferior transport properties. Combining these two types of materials offers a potential solution to create the next-generation of low-cost, efficient solar cells. Numerous hybrid devices have been demonstrated. However, common processing techniques for polymers, including spin-coating, inkjet printing, or doctor blading (only applicable to planar substrates) result in nonconformal coatings or thickness gradients when applied to three-dimensional

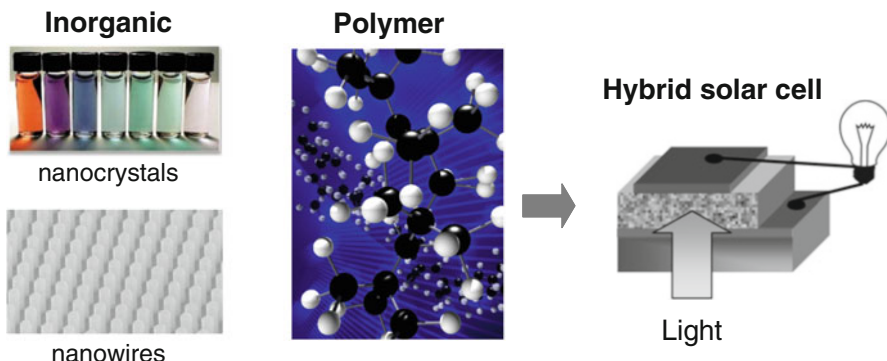


Fig. 12.4 The combination of organic and inorganic materials enables hybrid solar cells

structures. Hence, the reported hybrid solar cells are usually fabricated by either intimately mixing n-type inorganic nanostructures such as silicon nanocrystals, cadmium selenide, zinc oxide, lead sulfide, or titanium dioxide into the polymer prior to spin-coating, or infiltrate the polymer solution/dispersion into the 3-D inorganic arrays to form an interdigitated block-like film (Fig. 12.4). Both approaches diminish the purpose of having well-oriented, high mobility, 3-D structured inorganic arrays that possess the unique advantage of directional charge transport and light trapping. Typical power conversion efficiencies for these devices ranges from ~ 0.04 to 3.2% [5], demanding further improvement. Aside from the device structure, the flexibly tunable physical properties of the polymeric conductors by modern synthetic chemistry enable the optimization of the energy level alignment for organic and hybrid solar cells. Unfortunately, such desirable properties come at the price of extensive molecular engineering and intensive ad hoc synthesis, and the resulting polymers are often air-sensitive and need to be processed in glove-boxes. These structural and property limitations constitute as the major hurdle in building a practical, highly efficient hybrid solar cell that can be potentially commercialized. Furthermore, coating a well-defined 3-D inorganic semiconductor pattern, such as oriented nanowires, with an organic conductor allows for a high interface area and 3-D features for the overall device, which is difficult to achieve with the all organic counterparts due to the lack of effective patterning techniques. As a result, materials development leading to inorganic and organic semiconductor/conductors with desired properties that can offer optimized morphology for charge transport and light harvesting is crucial and has become an expanding field of investigation.

3 Materials Development

Materials development refers to a research field aimed at prototyping engineered materials with innovative functionalities. Some representative examples include light-weight, resilient carbon-fiber-based fabrics, porous structures for enhanced

battery capacity, ultraviolet-resistant coatings based on nanocrystals, and many others. Sun-driven energy generation requires efficient materials that combine ultra-high photon absorption with a carrier generation/extraction close to unity. To do so, inorganic and organic chemists are intensively investigating novel approaches to tailor artificial materials in such a way that the power conversion efficiency is maximized. Inorganic materials developments concentrate on nanostructures (i.e. nanowires, colloidal quantum dots, etc.) that could bring in novel capabilities at the materials level in terms of optimized photon management or carrier transport. Organic materials developments are aimed at engineering polymers with more planar backbones, lower bandgaps, and good solubilities in order to increase their carrier mobility, stability, and solution processability.

3.1 Inorganic Nanomaterials: Top-Down vs. Bottom-Up Approach

Semiconductor nanomaterials represent the main thrust of nanotechnology and nanoscience. Their unique size-scaling properties are of interest to charge transport, energy conversion, fracture strength, and many other fields. Generally, nanomaterials can comprise both classical and quantum behaviors suggesting approaches like “materials-by-design” [6]. The ratio of surface area-to-volume for nanomaterials is much greater than their bulk counterparts; therefore, a majority of the atoms are close to the surface, rendering them more weakly bonded and more reactive. Quantum mechanical effects become important when the structure size is on the same scale as the electron wavelength, and quantum confinement occurs resulting in changes in electronic and optical properties. Currently, semiconductor nanomaterials are still at the research level, holding promise in many applications such as photovoltaics and hydrogen production (renewable energies), nanoscaled transistors, light-emitting diodes, bio-chemical sensors (e.g. track and destroy cancer cells), energy storage (e.g. batteries). Nanosized materials can, in principle, be made using both top-down and bottom-up techniques. The former can be imagined as sculpting from a block of stone. The starting material is gradually modified in shape until the desired structure is achieved. Nanolithography can be considered the most representative example of a top-down fabrication approach for nanomaterials. Semiconductor materials are first patterned by a mask where the exposed portion is etched away. Based on the level of resolution, the etching step can be carried out chemically (etchants), mechanically, or through X-rays or focused ion beams. The limitations of top-down fabrication are related to diffraction effects where the practical limit for deep ultraviolet optical lithography is around 100 nm. To define sub-100 nm features, electron beams can be used down to 15 nm features. The drawback is the very low throughput. On the other hand, bottom-up techniques can be visualized as building a brick house where the single brick is represented by atoms or molecules, placed one by one to constitute the targeted structure. These processes

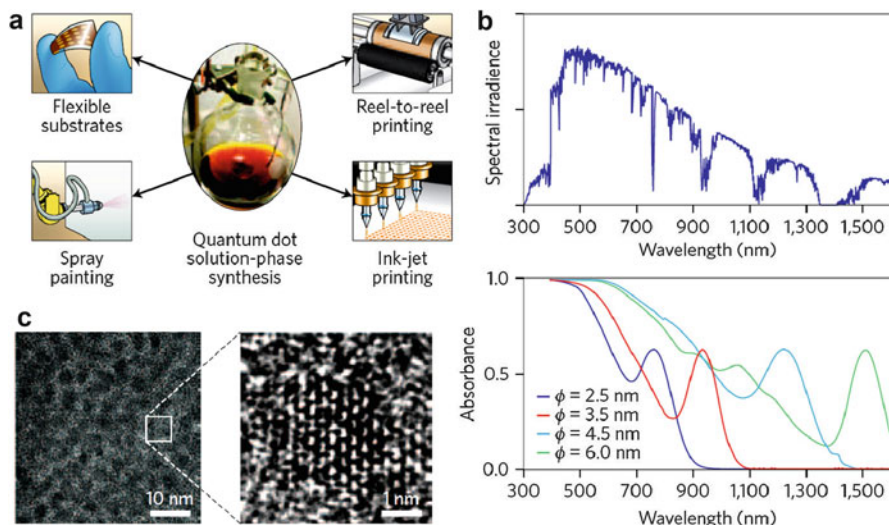


Fig. 12.5 (a) After synthesis, the colloidal quantum dots can be deposited onto flexible substrates by spray-coating, reel-to-reel printing, or ink-jet printing. (b) The quantum dot absorption can be tuned as a function of diameter size to better match the solar spectrum energy distribution. (c) A transmission electron microscopy image of a sphere-shaped single-crystalline colloidal quantum dot

are time-inefficient so self-assembly techniques are employed where atoms arrange themselves as required. Part of the challenge is to be able to fabricate robust structures along with complicated patterns.

3.1.1 Nanocrystals: A Colloidal Synthesis

Monodispersed, nanometer-scale crystals (known as nanocrystals) give rise to novel optical, electronic, magnetic, and structural features by exploiting size-dependent effects. In order to map out size-dependent properties, it is necessary to achieve a uniform synthesis in terms of shape, size, and composition [7] (Fig. 12.5a). When the diameter of such particles is reduced below the carrier wavefunction, the absorption spectrum becomes widely tunable as well as the corresponding bandgap (Fig. 12.5b). The synthesis of colloidal nanocrystals is an elegant interplay between molecular inorganic chemistry and solid-state semiconductor materials chemistry. The adoption of solution-processable synthetic chemistry to engineer small inorganic colloids represents a powerful tool to tune size, shape, and composition in a bottom-up approach [8]. Colloidal nanocrystals can be grown in the form of nanorods, faceted prisms, and spheres (Fig. 12.5c) and composed of metals, oxides, or semiconductors. Alternatively, hydrothermal techniques represent a promising synthetic method because of the low-temperature process and ease of controllability of the particle size. Furthermore, the growth is

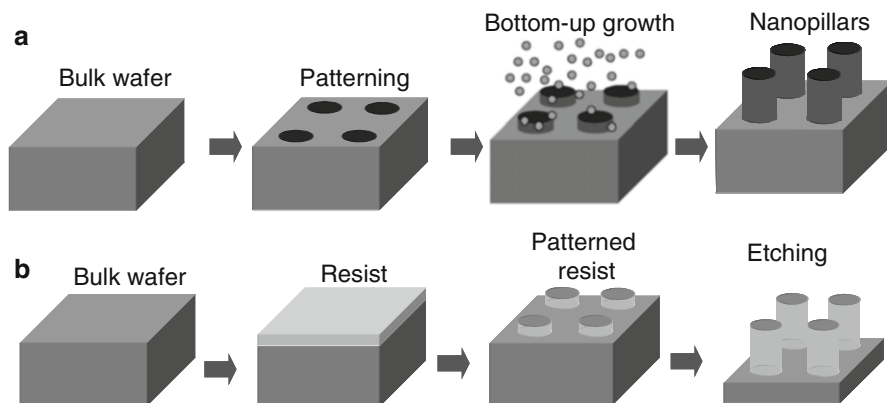


Fig. 12.6 (a) Bottom-up growth of nanowires. The bulk wafer is first patterned (silicon dioxide mask or metal catalyst). Subsequently, gases are flown into a reactor and the growth of nanowires initiates. The final nanowire length can be tuned according to the growth time. (b) Top-down fabrication of nanowires. The bulk wafer is first covered by resist, which is patterned by a lithographic technique (e.g. nanoimprint, electron-beam lithography, and self-assembled beads). The pattern constitutes a hard mask. The wafer is then dry- (or wet-) etched and the nanostructures formed

catalyst-free, environmentally benign, and only requires the use of simple equipment. At the research level, the conversion efficiency record for colloidal quantum dot solar cells is 6 % [9]. In order to surpass efficiencies of 10 %, it is necessary for the hole and electron mobilities to exceed $10^{-1} \text{ cm}^2 \text{ V}^{-1} \text{ s}^{-1}$, with a bandgap as trap-free as possible [9].

Recently, the first tandem nanocrystal-based solar cell has been reported [10] exploiting the size-effect tuning of a single material (lead sulfide). The tandem configuration boosts the open-circuit voltage of the solar cell to above one volt with an overall power conversion efficiency of up to 4.2 %.

3.1.2 Nanowires: Epitaxy vs. Etching

Nanowires can be defined as structures that have a constrained lateral size from a few to several tens of nanometers, longitudinally unconstrained. Epitaxial synthesis of nanowires from gaseous sources was first developed by Wagner and collaborators [11], where crystalline nanowires were grown epitaxially from the surface of catalytic metal clusters. This approach opened up a route to heterogeneous, radial, or super-lattice structures [12] (Fig. 12.6a). Furthermore, the opportunity of incorporating dopants during growth allows for the design of advanced optoelectronic devices including solar cells, light-emitting diodes, and transistors. Controlling the density and position of each nanowire for practical fabrication can be difficult. Patterning the metal catalyst is a method to precisely define dimensions, spacings, and aspect ratios: the corresponding vertical growth will directly stem from the patterned metal catalyst (i.e. Au or Cu). The growth direction

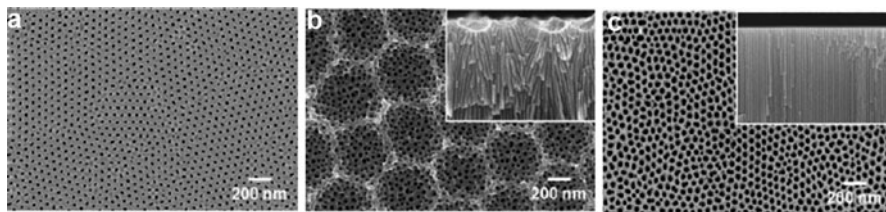


Fig. 12.7 (a) Scanning electron microscope image of porous alumina prepared by two-step anodization. (b) First and (c) second step anodization

can be guided by adopting different crystallographic directions (e.g. $\langle 110 \rangle$ vs. $\langle 100 \rangle$) of the substrate. Top-down nanowires combine wafer-scale semiconductor growth with advanced lithographic processing. Photolithography, electron-beam lithography, nanoimprint lithography have been exploited as patterning methods to define a mask for either wet or dry etching. Subsequently, the unmasked constituent material is isotropically or anisotropically etched to realize the targeted structure. The roughness of the sidewalls limits the selectivity of the process. The etching approach only allows for engineering the design along the longitudinal direction, without accessing radial components (Fig. 12.6b). Despite that, the exact knowledge of doping levels (from the planar growth) represents a powerful tool with respect to bottom-up techniques.

3.1.3 Nanoporous Structures

Nanoporous structures have received increasing attention due to their unique applications in catalysis reactions, DNA translocation, hybrid solar cells, and as templates for nanostructure self-assembly [13]. Nanoporous structures are comprised of a multitude of nanopores, nanocavities, or nanochannel arrays where the pore size and porosity can be tuned at will at the nanoscale. Anodic aluminum oxide constitutes a prime example of a self-ordered nanopore membrane (Fig. 12.7), exhibiting tunable diameters with high aspect ratio as well as superior thermal and chemical stabilities [14].

Nanoporous TiO_2 electrodes have been actively investigated in dye-sensitized hybrid solar cells where each nanopore represents a storage site for the electrolyte solution [15]. High power conversion efficiencies (10–11 %) have been reported with promising solutions to overcome charge recombination, and increase light scattering properties of the film while improving the interfacial energetics between the electrolyte and the nanoporous material. The science of infiltration of a polymer or electrolyte into such porous matrices is still under investigation. Recently, polymers with different molecular weights have been shown to modify the degree of infiltration, suggesting a direct relationship with the size of the polymer. Benzene-based solutions can infiltrate down the network up to several micrometers where the major constraint is the average chain length that needs to be smaller with respect to the diameter of the nanopore [16].

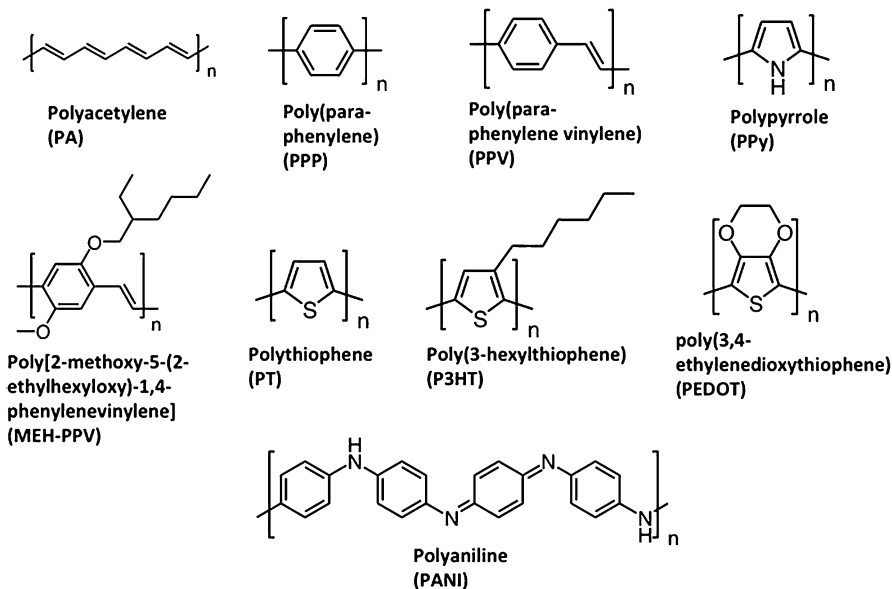
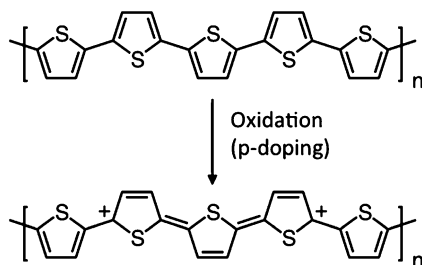


Fig. 12.8 Chemical structures of some representative synthetic metals and semiconductors

3.2 Organic Polymers: Properties, Doping, Design, and Synthesis

Compared with inorganic materials, the field of organic semiconductors/conductors is nascent. Nevertheless, ever since the discovery of polyacetylene in the 1970s, conducting polymers have garnered tremendous amount of interest in both fundamental science and novel applications, leading to the Nobel Prize in Chemistry awarded to Alan Heeger, Alan MacDiarmid, and Hideki Shirakawa in 2000 for the discovery and development of synthetic metals and semiconductors [17]. Through rigorous research over the past few decades, the chemical and physical properties of conducting polymers are now fairly understood. Their unique aspects of combining the electrical properties of metals and semiconductors coupled with their mechanical flexibility and solution processability has enabled a vibrant field of research that led to the development of flexible supercapacitors, artificial mussels/actuators, sensors, organic field-effect transistors (OFET), organic light emitting diodes (OLED), organic photovoltaic devices (OPV), among many other applications [18]. Common examples of conducting polymers are listed in Fig. 12.8, featuring the chemical structure of polyacetylene (PA), polyparaphenylene (PPP), polyparaphenylene vinylene (PPV), polypyrrole (PPy), poly(2,5-dialkoxy)paraphenylene vinylene (MEH-PPV), polythiophene (PT), poly(3-alkyl)thiophene (P3AT), poly(ethylenedioxythiophene) (PEDOT), and polyaniline (PANI).

Fig. 12.9 Scheme for chemical doping of a conducting polymer: polythiophene



3.2.1 Charge Transfer and Doping

In order to understand the conducting polymers' role in photovoltaic research, it is necessary to have a basic knowledge of their charge transport and doping mechanism. The conjugated backbones of these polymers allow the delocalization of electrons in π -bonds formed by the overlapping p_z -orbitals. The electronic structure of a neutral conjugated polymer typically consists of a completely filled valence band, more commonly known as the π -band or the HOMO to chemists, and an empty conduction band (the π^* -band or the LUMO). The energy difference between the π and the π^* bands is the bandgap of the material, typically ranging from 1 to 2.5 eV, reminiscent of those of semiconductors. In order to induce carrier transport and thus electrical conductivity, a doping process to either inject electrons into the π^* band or remove electrons from the π band is necessary, analogous to the doping concept in inorganic materials [19, 20].

There are four general ways to dope a conducting polymer:

1. Chemical doping
2. Electrochemical doping
3. Interfacial doping
4. Photo-excitation doping

Chemical Doping

Chemical doping can be achieved by exploring the charge-transfer redox chemistry of the material or its acid-base chemistry if applicable. The polymer can be oxidized into a positively charged moiety, balanced out by the negative charges of the oxidizing agent, creating hole mobility in the conjugated backbone and thus rendering the material p-type. Similarly, reducing the polymer backbone causes it to become negatively charged with electron mobility, thus n-type. A common example is shown in Fig. 12.9. Most conducting polymers are more readily p-type doped. When the doping level is sufficiently high, the polymer becomes metallic.

Polyaniline represents an interesting case of chemical doping [21]. Simply oxidizing it into its conjugated emeraldine base oxidation state does not lead to

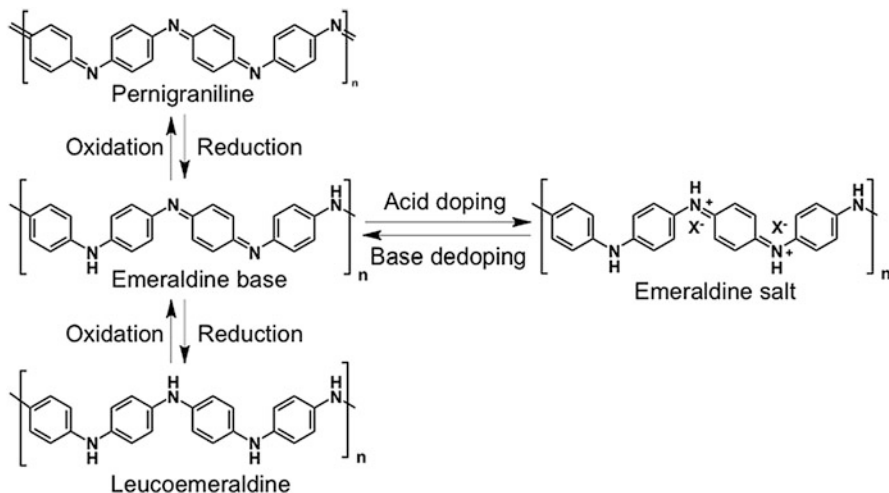


Fig. 12.10 The various oxidation states and the unique acid/base doping/dedoping chemistry of polyaniline

electrical conductivity as the polymer remains neutral in charge. An acid has to be used to protonate the imine nitrogens in order to induce hole mobility. This process is highly reversible as the acid dopants can be readily removed by neutralizing with a base (dedoping), rendering the polymer poorly conductive again (Fig. 12.10).

Electrochemical Doping

Chemical doping is an excellent method to realize metallic behavior by fully doping the backbone. However, intermediate doping levels are difficult to control as partial doping often leads to regions of completely doped polymer, while other regions remain undoped. Electrochemical doping shares a similar underlying mechanism as chemical doping, but offers much better control of doping levels. In a typical setup, three electrodes are immersed in an electrolyte solution: (1) the working electrode in general is a conducting substrate with the polymer of interest attached; (2) the counter electrode, typically a metal wire, coil, sheet, or mesh, balances the charge with that from the working electrode; and (3) the reference electrode, such as a saturated calomel electrode (SCE) or Ag/AgCl electrode, defines 0 V reference voltage in the electrochemical cell. A certain doping level can be readily achieved by applying a fixed voltage in order for the conducting polymer on the working electrode to reach electrochemical equilibrium, allowing homogeneous doping throughout the entire film.

Fig. 12.11 Schematic of a typical top contact, bottom gate organic field effect transistor

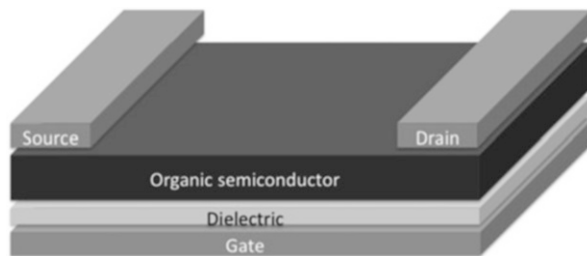


Photo-excitation Doping

Semiconducting polymers can also be doped by photo-excitation, which is of great importance for photovoltaic applications. Most of these polymers have high absorption efficiency. Upon light illumination, bound electron-hole pairs, also known as excitons, are generated. In an organic solar cell where a p-n junction interface occurs, excitons diffuse to such an interface and split into electrons and holes due to the potential difference (a minimum of 0.3 V is required). The electrons and holes are then extracted to the cathode and anode of the device, respectively, and are collected [22].

Interfacial Doping

Semiconducting polymers can be doped by charge injection at a metal-semiconductor interface as well [23]. Holes can be injected into the filled π -band from the metal electrodes, leading to hole mobility. Similarly, electron mobility can be created by the injection of electrons into the empty π^* band. The most widely used application for this type of doping is field-effect transistors (FET). Figure 12.11 shows a typical organic thin-film FET structure.

For instance, in order to achieve hole mobility, a negative gate voltage needs to be applied to cause electron accumulation at the dielectric surface, thus creating holes at the semiconducting polymer/dielectric interface. At the same time, a negative drain voltage is necessary for the movement of the holes across the source and drain electrodes through this interface, leading to hole mobility.

Among the four general types of doping mechanisms, it is necessary to make the distinction that the chemical and electrochemical doping in a sense are permanent, since the dopants are integrated as part of the material and will remain until removed via chemical or electrochemical methods. On the other hand, doping by photo-excitation or charge injection are temporary, as a continuous photon or charge source is needed, and the mobility in the material will vanish once the source is removed.

3.2.2 Molecular Design and Engineering

With the different methods to induce doping and thus carrier mobility, organic conductors pose as interesting alternatives in many applications to their inorganic counterparts that have traditionally dominated the market. In particular, the conducting polymers are attractive because of their high absorption efficiency, flexibility, tunable chemical and electronic structures, and solution processability. In order to tailor these polymers for specific applications, a tremendous amount of effort has been devoted to the design and synthesis of sophisticated polymers with optimized solubility, energy levels, and solid-state packing. These parameters are crucial in the realm of solar cells. The different methods for achieving these properties are discussed below.

Methods for Inducing Solubility

It is a priority to make conducting polymers soluble or solution dispersible because this allows the polymers to be processed by methods such as spin-coating, spray coating, roll-to-roll processing, in order to significantly lower the manufacturing cost, and render conducting polymers an attractive alternative to their inorganic counterparts despite the inferior electrical properties. One approach to induce solubility of an otherwise insoluble polymer is by using a chemical dopant that can be dissolved in organic solvents [24]. For example, camphorsulfonic acid, a bulky organic acid, can be used to chemically dope polyaniline (PANI) into the metallic form and induce solubility in many organic solvents. Poly(3,4-ethylenedioxythiophene):poly(styrenesulfonate) (PEDOT:PSS) is another benchmark material that takes advantage of counter-ion induced solubility, as PSS functions as the dopant, but also assists the dispersion of PEDOT in water [25].

Forming colloidal dispersions is another method for rendering polymers processable [26]. This method has become especially popular since the advent of nanotechnology in the 1990s. Typically, uniformly shaped small particles, such as nanofibers or nanospheres, are produced by either a template-guided or a template-free method, and can often form stable dispersions due to their small size and the inter-particle repulsion, arising from the surface charges.

Within the realm of organic solar cell research, probably the most important and commonly used method for inducing solubility is by covalently attaching solubilizing functional groups to the polymer backbone using organic chemistry. Semiconducting polymers used in p-n junction solar cells typically cannot contain chemical dopants as they need to be doped via photo-excitation when illuminated with light, which eliminates the possibility of counter-ion doping induced solubility. Hence, synthesizing polymers that can be readily dissolved in common organic solvents becomes crucial for the solar cell industry. The most noticeable example is the functionalization of polythiophene, which is insoluble in virtually all organic or aqueous solvents. However, the attachment of an alkyl chain such as hexyl at the C3

position allows the polymer to become soluble in common organic solvents such as chloroform or dichlorobenzene. Hydrocarbon side chains with different lengths or containing polar groups have also been exploited.

Energy Level Engineering

Tuning the energy gaps for semiconducting polymers have probably been one of the most significant factors that have propelled polymer solar cells to efficiencies that are promising for commercialization [27].

The efficiency of a solar cell is defined by (12.1)

$$\eta = (J_{sc} \times V_{oc} \times FF) / (P_{in}) \quad (12.1)$$

where J_{sc} , V_{oc} , FF, and P_{in} are the short circuit current density, open circuit voltage, fill factor, and power of the incident light ($AM\ 1.5G\ 1000\ W/m^2$), respectively. Since J_{sc} is heavily influenced by the amount of light absorption, it is also important to tune the bandgap of the materials in order to achieve a broader solar spectrum absorption range, which can enhance the photocurrent. A powerful method for achieving such a goal is to include alternating electron donor/acceptor (also known as electron push/pull) units in the polymer backbone [28]. Such architecture increases the effective resonance length of the π electrons, facilitating π electron delocalization, and hence resulting in a polymer with extended absorption beyond the visible spectrum. For example, one of the most successful push/pull polymers is PBDTTT, where a strong pull unit, thieno[3,4-b]thiophene (TT) is copolymerized with a push unit, benzo[1,2-b:4,5-b']dithiophene (BDT). Its chemical structure along with some of the other efficient molecular engineered polymers are illustrated in Fig. 12.12. Many of these polymers also provide further enhancement to the J_{sc} by offering a more crystalline microstructure due to the planar units in the polymer backbone, which leads to higher mobility and more efficient charge transport.

Improving the V_{oc} is also important for optimizing the solar cell efficiency. V_{oc} is largely determined by the energy level difference between the HOMO level of the donor and the LUMO of the acceptor; therefore, one way to increase the solar cell efficiency is to design a donor polymer with a lower HOMO level. However, improvement of the J_{sc} by narrowing the band gap often leads to a rise in the HOMO level as well, which deteriorates the V_{oc} . Recently, elegant molecular engineering has paved the way for lowering the HOMO level while maintaining the low bandgap. For example, for PBDTTT, a strongly electron withdrawing atom such as fluorine can be attached to the electron pull TT unit, leading to lowering of the HOMO and LUMO levels simultaneously, while maintaining the bandgap [29].

Although such sophisticatedly engineered molecules have led to great success in organic solar cells, they are yet to be tested for hybrid solar cells. Since the charge transferring and separation mechanism at the organic/inorganic interfaces are still debatable for hybrid solar cells, coupled with the ad hoc synthesis and the high cost

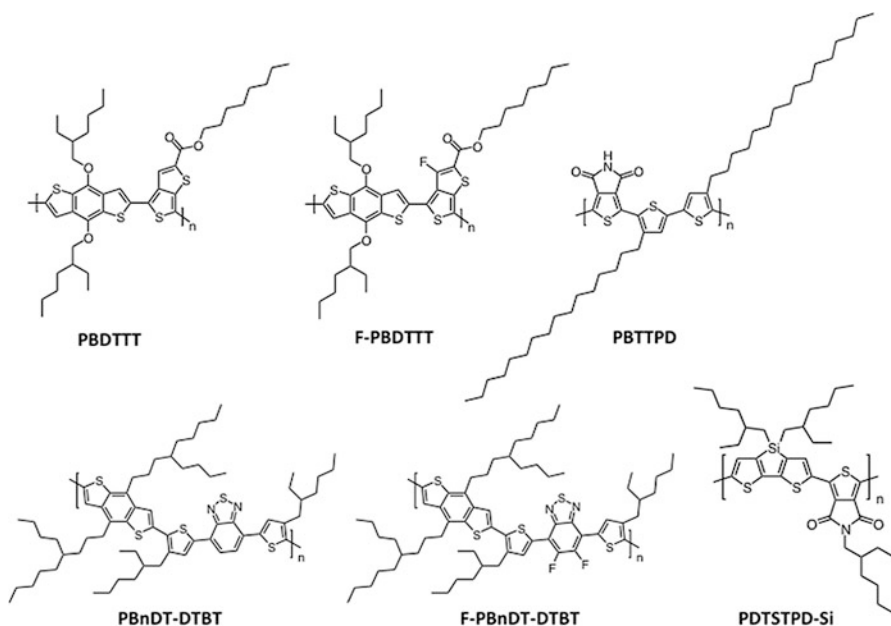


Fig. 12.12 A new generation of highly molecularly engineered polymers with lower bandgap and optimizing HOMO/LUMO levels for photovoltaic applications

of these new polymers, benchmark materials such as P3HT or PEDOT are typically used, with P3HT for p–n junction hybrid photovoltaic devices, and PEDOT for their Schottky counterparts.

3.2.3 Synthesis of Benchmark Polymers

Since P3HT and PEDOT have both been well developed, most hybrid solar cell studies involving these polymers have utilized their commercially available forms, which can be purchased from Sigma-Aldrich® or Clevios™, among many other specialized chemical companies. The polymer typically is marketed in the forms of a solid, dispersion, or solution, which can be spin-coated onto the inorganic layer or other planar substrates. However, for studies with more controlled processes or more complex structures, it is necessary to generate the polymers in situ. A few general synthetic approaches are discussed below.

Chemical Synthesis

Conducting or semiconducting polymers can be synthesized via chemical or electrochemical routes. P3HT can be made in the regiorandom or regioregular form

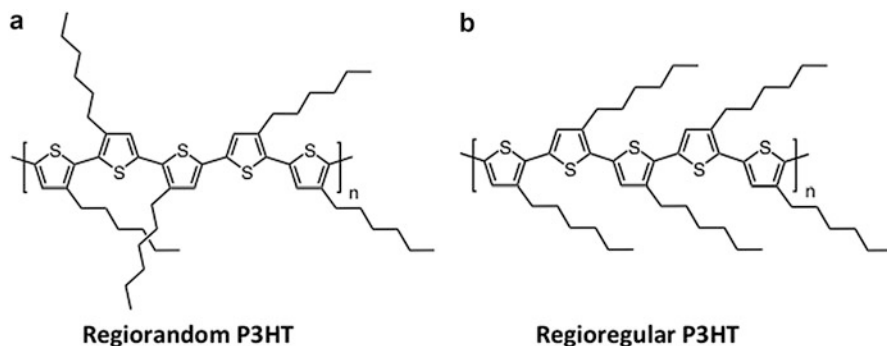


Fig. 12.13 Chemical structures illustrating the difference between (a) regiorandom versus (b) regioregular P3HT

(Fig. 12.13). Regioregular P3HT is desired and typically used for solar cell purposes because the regularity of the hexyl attachment position not only leads to less torsion angles in the polymer backbone, providing a longer conjugated pathway for π electrons to travel, but also allows for more ordered intermolecular packing that increases the mobility of the material. Regioregular P3HT can be synthesized via a Grignard metathesis reaction, or by Reike zinc reactions [30, 31].

PEDOT can be produced chemically in organic solvents using an oxidant such as FeCl_3 or $\text{Fe}(\text{OT}_s)_3$, where OTs stands for tosylate. The resulting product, however, is a black, insoluble, and infusible solid that is difficult to characterize and process. A more practical approach towards high-quality PEDOT is to polymerize the monomer in an aqueous polyelectrolyte, often poly(styrenesulfonate) (PSS) with $\text{Na}_2\text{S}_2\text{O}_8$ as the oxidizing agent. The resulting PEDOT is chemically doped with PSS, which also induces dispersibility of PEDOT in water. The aqueous dispersion is dark blue in color and can be readily processed into uniform thin films. The commercially available PEDOT:PSS dispersions are produced largely based on this synthesis [25].

PEDOT can also be polymerized in the solid state [32]. When 2,5-dibromo-3,4-ethylenedioxythiophene (DBEDOT), a white, crystalline solid, is stored at room temperature over a prolonged period (i.e. 2 years), the crystals turn dark blue/black in color, while maintaining the morphology of the starting monomer. Characterization indicates that the dark product is PEDOT doped with bromine, and possesses a rather high conductivity (80 S cm^{-1}). Such solid-state polymerization can be greatly accelerated and completed in 24 h by heating to 60°C . The conductivity of the resulting PEDOT, however, drops to 33 S cm^{-1} , since a prolonged process at lower temperature typically leads to more ordered intermolecular packing.

Electrochemical Synthesis

Another powerful approach towards the synthesis of conducting polymers is electropolymerization. Using a setup similar to that for electrochemical doping

discussed earlier, the monomer is oxidized on the anode, typically a metal or other conductive surface. Polymers can be formed under potentiodynamic (by scanning cyclic voltammetry passing its oxidation potential), potentiostatic (constant voltage), or galvanostatic (constant current) approaches. For example, EDOT can be readily polymerized into a sky-blue, conductive PEDOT film on the working electrode, in either organic or aqueous electrolyte solutions [25]. Electropolymerization only requires a small amount of monomer, and can yield films with controlled thicknesses. However, the polymer can only be generated on a conductive substrate, which limits the application range of polymers produced via this method.

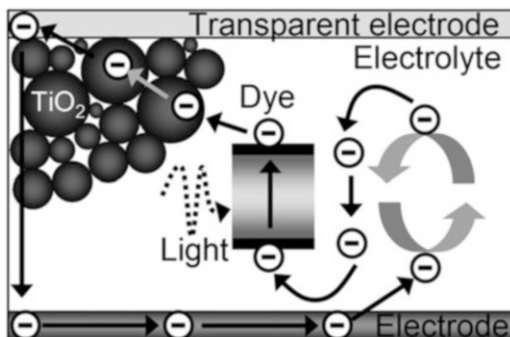
4 Morphology

Hybrid organic–inorganic solar cells constitute a viable route to convert solar power into electricity at low manufacturing costs. The hybrid composite resulting from combining organic conjugated polymers with inorganic semiconductor nanostructures is highly dependent on the morphology of the individual constituents. One-dimensional structures can provide directional carrier transport, but are often difficult to achieve for hybrid composites. Optimum layer thickness is also important due to the short exciton diffusion length of organic materials (5–20 nm). However, the organic films optimized for exciton diffusion and charge separation are often way too thin for abundant light absorption, which requires a ~100–200 nm layer. Furthermore, it is desirable for both constituents to be single crystalline for efficient charge transport, which is readily achievable for inorganic materials, but extremely challenging for their organic counterparts. Inducing a certain level of crystallinity, however, is possible for polymers, and therefore also needs to be taken into consideration. The overall dimensionality of the device is important as well. For instance, with the same junction interfacial area, a solar cell with a 3-D structure has the dual function of light trapping, hence increasing the efficiency. From the hybrid solar cell literature, the most intensively studied devices in general can be categorized based on their morphologies/device architectures, as discussed below.

4.1 *Types of Hybrid Solar Cells*

Several types of hybrid solar cells have been developed based on the different methods for combining the two materials. One approach is to incorporate a photoactive semiconductor working electrode and counter electrode, both immersed in an electrolyte containing suitable redox couples, known as a dye-sensitized solar cell (DSSC). A second method is by depositing a layer of polymer film on top of an inorganic film or wafer resulting in a bilayer structure. A third approach is to form a bulk heterojunction that can be fabricated from blends of an electron-donor polymer

Fig. 12.14 Schematic of photon absorption (dye), carrier generation/transport (electrolyte and TiO_2 particles), extraction (electrodes) in dye-sensitized solar cells



and electron-acceptor nanocrystals, with the advantage of being solution processable and possessing an efficient, continuous charge transport pathway. The fourth method is to constitute an interpenetrating network by infiltrating or coating an organic material on an ordered inorganic semiconductor nanostructure array, where the order and the small feature size can dramatically enhance the exciton separation and transport to the respective electrodes.

4.1.1 Dye Sensitized Solar Cell (DSSC)

Dye-sensitized solar cells are attractive since the constituents are low-cost materials that can be printed in large volumes. The uniqueness of these devices relies on the fact that light absorption and electron and hole transport are each handled by separate materials [33]. Typically, the dye is attached to a wide-bandgap semiconductor (e.g. ZnO or TiO_2) and when it absorbs photons, photoexcited electrons travel to the conduction band of the semiconductor, carrying the electron to one of the electrodes. A redox couple reduces the oxidized dye back to neutral and hauls the positive charge to the counter-electrode. In such a way, electric current can flow under light to an external load (Fig. 12.14).

4.1.2 Bilayer Structure

Bilayer structure is the most primitive solar cell structure. The active layer material, whether for p-n or Schottky junction, are two thin films sandwiched between the anode and cathode electrodes [34]. A typical structure is shown in Fig. 12.15, as a polymer layer is deposited by spin-coating on top of an inorganic film or wafer. Such structure is not practical for hybrid solar cells as the interfacial area is very small—only the lateral dimension of the device, and hence yields very low short-circuit currents. Furthermore, due to the delicate balance between needing a thin organic film in order to match its low exciton diffusion length and the requirement of a thick film so that an adequate amount of light can be

Fig. 12.15 Device structure of a bilayer hybrid solar cell

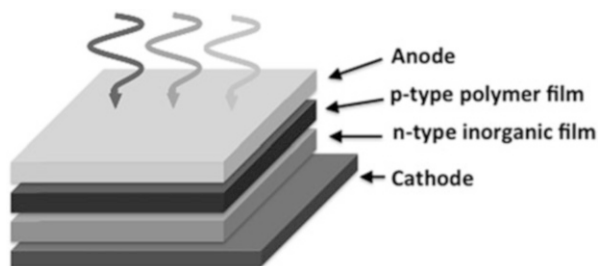
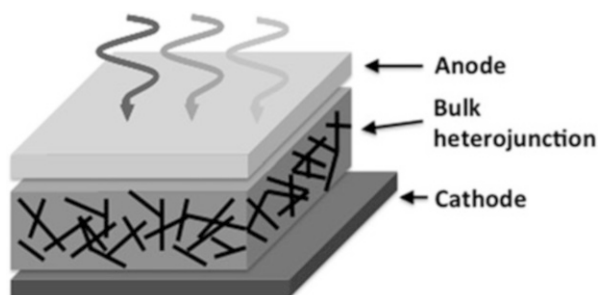


Fig. 12.16 Device structure of a bulk heterojunction hybrid solar cell



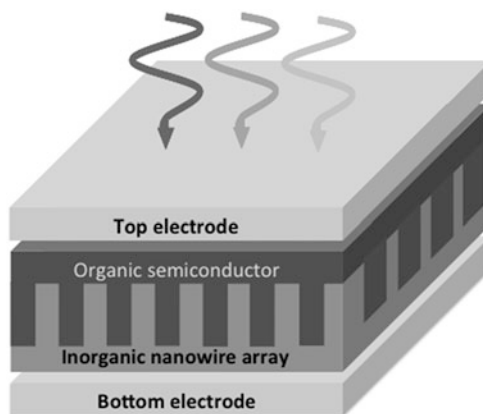
absorbed, the thickness of the organic layer is difficult to optimize and hence, poses as another factor leading to low efficiency. However, the simplicity of the bilayer structure allows for fundamental studies of figures of merit for solar cells at the interface of the two materials, which can serve as control experiments or tools for trouble shooting more complicated structures (e.g. bulk heterojunctions or interdigitated architectures) so that the exact factors leading to higher efficiencies can be deciphered.

4.1.3 Bulk Heterojunction Solar Cells

Bulk heterojunctions (BHJs) have been adopted in polymer and colloidal nanoparticle solar cells to improve energy conversion efficiency [35]. Generally, nanowires or nanocrystals are mixed with conjugated polymers or fullerenes in the form of a solution-based blend, then spin-coated onto a substrate. A typical device structure is illustrated in Fig. 12.16. Most common blends use n-type inorganic nanostructures with p-type polymers. One of the earliest hybrid solar cells is based on such an active layer morphology, with CdSe nanorods as the acceptor blended into the P3HT donor solution, leading to a 1.7 % efficiency. Many follow up studies have been performed including GaAs/P3HT BHJ devices [36].

Despite the success of such structures in all organic solar cells, they are not as desirable for hybrid solar cells partly because of the high loading necessary for inorganic materials, especially 0-D structures, to create a continuous pathway

Fig. 12.17 An ordered, interdigitated heterojunction solar cell showing the interpenetrating network formed by a combination of organic/inorganic layers



for charge transport and collection. Also, unlike all organic blends, the phase segregation for organic/inorganic blends is difficult to control, which is crucial for this type of solar cell. Furthermore, the morphological stability of the blend film needs to remain intact over the device lifetime, which could be problematic for hybrid blends due to nanowire/particle migration over time as a result of the huge density difference between the organic and inorganic components.

4.1.4 Interdigitated/Ordered Structures

The adoption of ordered, interdigitated heterojunctions as illustrated in Fig. 12.17 has been explored as a means to improve the charge extraction before undesired recombination processes become predominant. Recent advancements in nanofabrication made sub-100 nm patterning routinely available. Vertical inorganic nanostructures (e.g. nanopillars or nanorods) that are perpendicular with respect to the substrates are advantageous because (1) the density and point-to-point distance between nanostructures can be tuned in an ordered fashion without incurring concentration gradients or inhomogeneity once reduced to a practical device, (2) the uni-directionality of all the 1-D inorganic nanostructures, which are also typically single crystalline, provides directional and rapid carrier transport for the solar cells, and (3) it unfolds an enormous opportunity for creating ordered, high interfacial area structures with organic materials, as it is difficult to create interdigitated or core/shell structures out of polymers alone due to their molecular flexibility. These architectures are advantageous compared to their planar counterparts because the active junction area is greatly enhanced, which also increases the probability of photogenerated carriers to be extracted before recombination can occur. This aspect relaxes the requirement of having ultra-high purity materials necessary for planar solar cells. Therefore, we direct our focus in the next

section to these type of structures because of their vast potential for achieving high efficiencies and other unique properties.

4.2 Efficient Hybrid Photovoltaics Based on Ordered Structures

Due to the significant advantages of having an ordered structure as discussed in previous sections, photovoltaic devices based on patterned 1-D nanostructure arrays will be the focus of this section.

One significant benefit of having a 1-D nanostructure array is that the amount of active absorber can be reduced without compromising the overall optical absorption due to their light trapping effects. Nanoscale texturing stemming from ensembles of nanowires, nanodomains, or nanocones considerably improves the light absorption over a broad range of wavelengths. In standard planar solar cells, the p–n junction is formed by dopant diffusion into the crystal. This ion implantation process requires extremely high temperatures (~1,000 °C). Significant efforts have been reported to form a photoactive heterojunction at lower temperatures. Recently, a hybrid radial-junction design that combines silicon microwires with amorphous silicon shells achieved efficiencies of up to 12.2 % [37]. A nanowire-based hybrid structure exploits the enhancement in light absorption from the sub-wavelength texturing, while the conductive polymer represents the other side of the junction. In a radial geometry, the constituting material for the shell is not required to be of high-grade quality since the carriers will be collected through the thin shell along the radial direction.

A multitude of methods can be used to achieve such attractive architectures for hybrid solar cells, including infiltration of a polymer into the inorganic nanowire arrays, controlled spin-coating of a polymer solution to form a coating on nanowires, self-assembly of end-functionalized polymers onto the inorganic constituent surface, and direct electropolymerization with in situ materials engineering to create a tunable core/shell hybrid structure.

4.2.1 Infiltration

Infiltration/percolation of conjugated polymers into nanoporous materials or a nanorod array (e.g. TiO₂) have been exploited for many of the earlier studies aiming to achieve ordered/semi-ordered active layer structures. The main hurdle in this concept using nanoporous materials is the difficulty in filling the pores efficiently. Infiltration effectiveness can be improved by using a proper surface modifier. Filling ordered, controlled morphologies of n-type inorganic semiconductor with p-type organic polymers can be easier compared to a randomly porous structure and be more effective in charge transport.

Another efficient device is achieved with crystalline perovskites [38], which combines a transparent p-type hole conductor (e.g. spiro-OMeTAD) and mesoporous alumina (Al_2O_3), delivering up to 10.9 % power conversion efficiency. This class of solar cells shows open-circuit photovoltages in excess of 1.1 V, despite the narrow bandgap of 1.55 eV. The engineered structure takes advantage of mesoporous alumina that forces the electrons to be transported through the perovskite. The strength of hybrid photovoltaics resides especially in the fact that the fabrication is solution-processable, allowing reel-to-reel, flexible manufacturing integrations.

Vertically grown nanorods short in length are also appealing inorganic candidates [39]. A polymer solution can be spin-coated or drop-cast onto the nanorod array so that the polymer fills all the gaps in-between the rods, forming an interdigitated structure reminiscent of that shown in Fig. 12.17. The height of the nanorods, thus the final active layer thickness, should be kept at around 200 nm—the optimal thickness for organic solar cells absorption. However, due to the approximately equal amount of organic and inorganic materials used in this structure and the significantly higher mobility of the inorganic material, there is likely to be a build up of charges for carriers that the polymer transfers, thus leading to low efficiency. Therefore, a core/shell-like architecture is desirable for realizing efficient hybrid solar cells.

4.2.2 Controlled Spin-Coating

Perhaps the most widespread method adopted to form organic-inorganic heterojunctions is controlled spin-coating. This process involves depositing a small quantity of conjugated polymer onto the center of the sample and then spinning it at high speed. The centripetal torque will force the polymer to spread out to the edges of the sample. The resulting thickness will depend on the properties of the polymer solution (e.g. viscosity and surface tension) and the parameters of the spin process (e.g. ramp, speed, and time). One limitation of this method is that it works well for planar and low aspect-ratio surfaces (e.g. cones), but not the more demanding high aspect ratio nanowires. This is due to the fact that the centripetal force while spinning will restrict the polymer to predominantly flow horizontally, limiting the chance of pore infilling or coverage of high-aspect ratio nanostructures (e.g. nanowires). For instance, hybrid solar cells can be created by coating poly (3-hexylthiophene) (P3HT) on GaAs nanowires by carefully tuning the spin-coating conditions [40]. A standard fabrication process is presented in Fig. 12.18. The n-type GaAs nanopillars are grown in the form of ordered arrays and low-cost spin-coating is adopted to realize the p-type coating of P3HT. To complete the device, indium tin oxide is sputtered as a transparent top contact. However, the conversion efficiency greatly depends on the treatment that the GaAs surface undergoes prior to the polymer deposition.

Modifying the inorganic 1-D morphologies presents another route for achieving well controlled core/shell structures. For instance, a vertically asymmetrical architecture of the inorganic constituent, such as nanocones or nanodomes, can facilitate

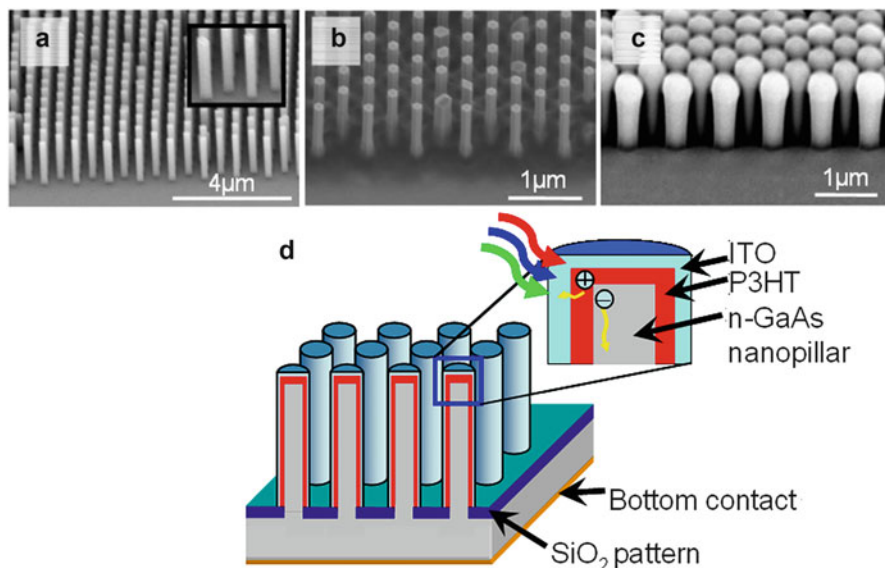


Fig. 12.18 (a) A semiconductor nanopillar array after epitaxial growth. (b) An inorganic/organic matrix after P3HT spin-coating. (c) Top transparent contact deposition. (d) Schematic of the final device with several layers involved

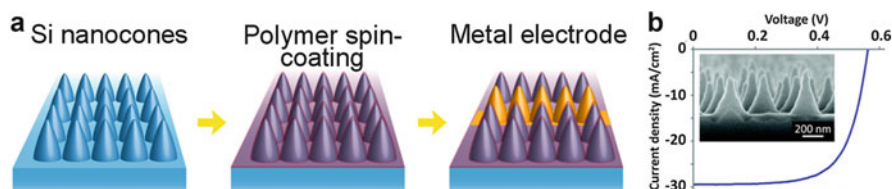


Fig. 12.19 (a) Schematic of the fabrication sequence for silicon/polymer hybrid solar cells. (b) Current density–voltage characteristic under light of the corresponding solar cells

uniform coating via spin-coating. Since the polymer solution tends to settle near the bottom with such processing method, the significantly larger bottom of the nanocones allow for the spreading and thus a more uniform coating of the polymer (Fig. 12.19). Schottky hybrid cells comprising conformal coatings of PEDOT on periodic n-Si nanocones recently exhibited efficiencies of up to 9.6 % [41].

4.2.3 Self-assembly

Polymeric semiconductors can be self-assembled onto the surface of inorganic nanowires. A P3HT/ZnO hybrid nanowire photovoltaic device is used as an example here [42].

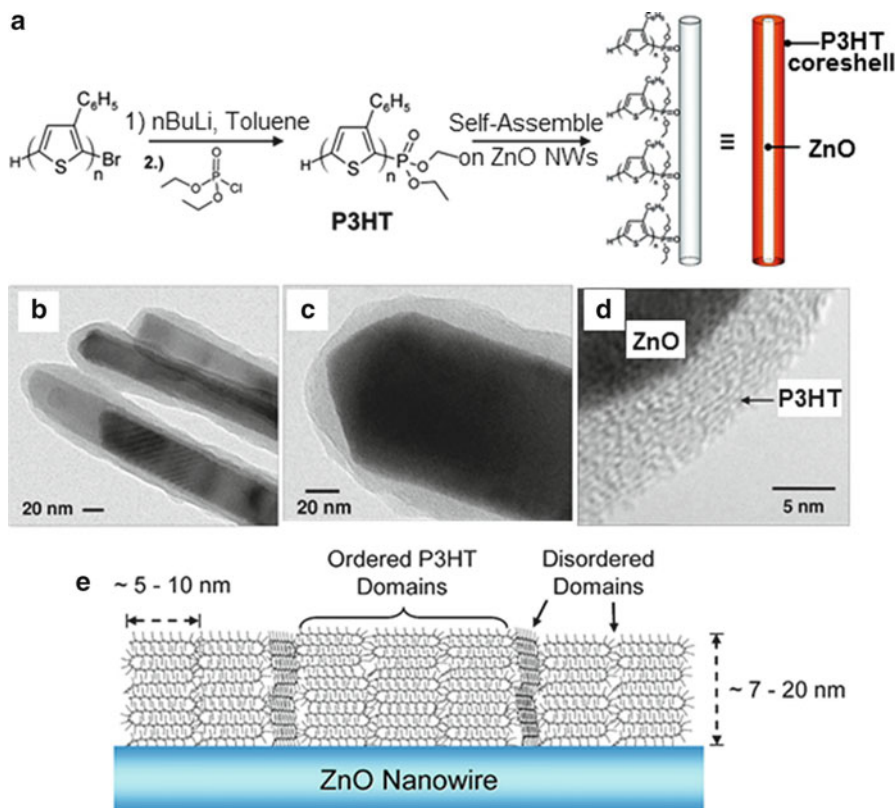


Fig. 12.20 A single nanowire P3HT/ZnO hybrid solar cell achieved by self-assembling the end-functionalized polymer onto the nanowire surface: (a) Synthetic scheme of the phosphonic acid-terminated P3HT and its assembly onto ZnO nanowires. (b–d) TEM analysis showing the core/shell structure and the lamellar packing of the P3HT chains on the ZnO surface. A proposed packing model is shown in (e)

Very little interactions exist between the donor P3HT and the acceptor ZnO, meaning that either the ZnO surface or the P3HT needs to be functionalized in order for self-assembly to occur. Bromine-terminated regioregular P3HT was reacted with butyllithium then diethylchlorophosphate to yield a phosphonic ester-end group for the P3HT molecules (Fig. 12.20a). The phosphonic ester group has high affinity for ZnO, thus leading the P3HT chains to form ordered lamellae on the ZnO nanowire surfaces (Fig. 12.20b–d). The thickness of the polymer coating is about 7–20 nm, which is close to the exciton diffusion length in organic materials. A single nanowire solar cell was fabricated with Al in contact with the P3HT as the anode, and Au as the cathode for the ZnO end. A low device efficiency of 0.036 % was obtained. However, it is mostly due to the fact that little light can be absorbed by a single nanowire, leading to a J_{sc} of only ~ 0.32 mA cm $^{-2}$. A large area array

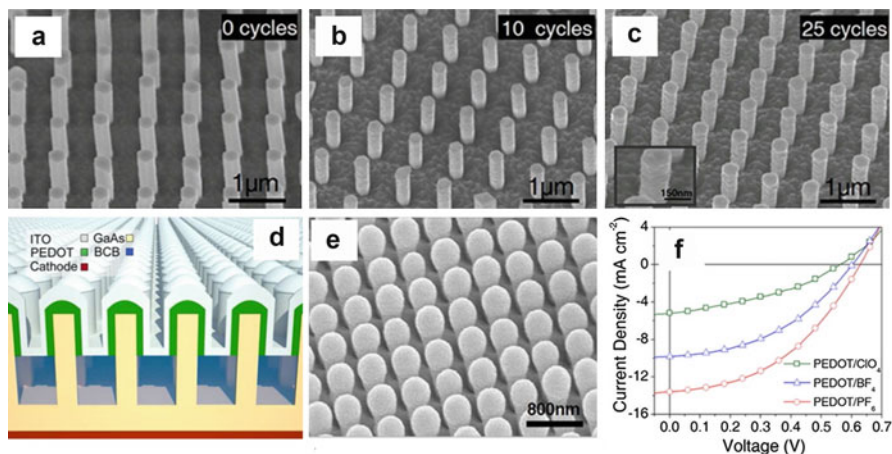


Fig. 12.21 Three-dimensional core/shell hybrid solar cells and device performance tuning achieved by in situ materials engineering via direct electropolymerization of an organic material onto an inorganic nanopillar arrays. (a–c) Illustrate the polymer shell thickness control using different numbers of scan cycles. (d and e) Shows the schematic of the solar cell and the SEM of the actual completed device with ITO top electrodes, respectively. The J – V characteristics of the solar cell with PEDOT doped with different dopants are presented in (f)

containing thousands of such hybrid nanowires can lead to a much higher short circuit current density and thus improved conversion efficiency.

4.2.4 Direct Electrochemical Polymerization

All the methods discussed above share the common ground that they are based on combining the synthesized organic and inorganic components via different approaches. However, the organic conductor/semiconductor can also be directly polymerized onto ordered inorganic nanowire arrays by direct electrochemical polymerization. A one-compartment three-electrode setup similar to that for electrochemical doping discussed in Sect. 3.2.1.2 is also suitable for this purpose. A Schottky junction GaAs/PEDOT core/shell nanowire solar cell serves as an example here [43]. A highly doped n-GaAs wafer with vertically oriented nanowire arrays was used as the working electrode, while a Ag/AgCl reference electrode and a Pt sheet counter electrode complete the setup. Anodic polymerization under potentiodynamic conditions achieved by scanning cyclic voltammetry (CV) passing the oxidation potential of the EDOT monomer dissolved in an electrolyte solution led to a uniform PEDOT film on the GaAs nanowire surfaces (Fig. 12.21b, c). The film thickness was found to have a direct relationship with the number of CV cycles, offering a simple method for controlling the polymer thickness. Furthermore, by taking advantage of the in situ electrochemical doping of the PEDOT with the counterions from the electrolyte solution, the properties of

the PEDOT shell can be readily tuned simply by incorporating different electrolytes. Five counteranions that can dope PEDOT were tested: poly(styrenesulfonate) (PSS^-), dodecyl sulfate (DS^-), perchlorate (ClO_4^-), tetrafluoroborate (BF_4^-), and hexafluorophosphate (PF_6^-). Each dopant led to a different conductivity value for the final PEDOT film, with PEDOT/ ClO_4 , PEDOT/ BF_4 , and PEDOT/ PF_6 possessing the highest three conductivities of 68, 90, and 116 S cm^{-1} , respectively. Slightly different HOMO energy levels results from these three films as well. The higher conductivities and the deeper HOMO level for PEDOT lead to direct improvement in all figures of merit for the solar cells, resulting in PCEs of 1.07, 2.71, and 4.11 % for n-GaAs nanowires with PEDOT/ ClO_4 , PEDOT/ BF_4 , and PEDOT/ PF_6 shells, respectively (Fig. 12.21f). This method opens up new opportunities to (1) achieve conformal coating of organic material on ordered inorganic nanowire arrays, which preserves the 3-D morphology of the final cell, (2) in situ material engineering of the organic component in terms of feature size, energy level, and electrical properties, and (3) the combination of all these factors that provides us the ability to rationally design and tune the performance of a hybrid solar cell.

5 Interface Manipulation

Functionalization and surface treatment of nanostructures is an area of crucial importance in the nanotechnology field. Controlling the surface properties and tuning its interactions at the nanometer scale represent critical issue for high-performance devices. Engineering the interactions between such diverse organic and inorganic classes of materials represents an essential step towards understanding the corresponding interface properties upon the solar cell behavior.

5.1 Surface Functionalization

The study presented in Sect. 4.2.3 provides an excellent example for illustrating the importance of surface functionalization. Inorganic surfaces often do not provide a high enough affinity for the desired polymers to bond. Therefore, either the surface of the inorganic material needs to be modified, or the polymer has to be functionalized, either at the end of the chain or on the backbone. For example, in order to form a P3HT/CdSe quantum dot hybrid, the surface of the CdSe was capped with (4-bromophenyl)methyl dioctylphosphine oxide (DOPO-Br), so that the vinyl-terminated P3HT can be readily grafted onto the quantum dot [44]. Alternatively, for the study presented in Sect. 4.2.3, no surface modification was performed for ZnO, but the P3HT chain terminal needs to be converted to a phosphonic ester in order for bonding to occur. Its oxygenated

groups interact with the oxygen from the ZnO surface, thus leading to grafting and self-assembly.

5.2 *Surface Passivation*

At the nanometer scale, surface properties become more relevant since the surface-to-volume ratio increases. The surfaces of nanostructures can be affected by electronically active surface states due to unterminated atomic chains or dangling bonds. Surface passivation aims to rebond these dangling bonds with certain passivating agents while maintaining charge neutrality after the passivation [45]. For instance, one recent study of hybrid solar cells based on poly(3-hexylthiophene) and GaAs nanopillars [40] shows that the surface passivation is crucial to alleviate the surface states on the nanopillar facets, leading to a much enhanced efficiency. Nonetheless, only simple inorganic molecules were adopted (e.g. $(\text{NH}_4)_2\text{S}$). Organo-thiol-based molecules can form self-assembled monolayers on semiconductor surfaces, which not only passivate, but also offer well-defined and tunable properties. Organic surface modifiers are currently being investigated since they promote infiltration of polymers along high-aspect ratio configurations. Surface passivation can be extended also to fully inorganic solar cells where nanostructures are exploited [46].

6 **Future Directions in Hybrid Photovoltaics**

Current state-of-the-art hybrid solar cells based on nanowires and pyramids are able to achieve up to 10 % power conversion efficiencies [47]. On the other side, recent advances in nanowire-based InP photovoltaics demonstrated efficiencies up to 13.8 % [48]. These numbers raise the bar for nanostructured solar cells and reduce the skepticism gap with respect to mature, mass-produced planar solar cells. Another important aspect for nanotechnology applied to photovoltaics is the reuse of substrates [49]. Considering that the active area is represented by the sole nanostructures (not the substrate as in conventional solar cells), the primary function of the mother substrate is to support a lattice-matched growth. In fact, subsequent to growth, the nanowires can be detached from their platform enabling the fabrication of vertically aligned electronic devices with metal electrodes on arbitrary supporting substrates (e.g. Kapton film, aluminum foils, and flexible plastic) [50]. Such a process eliminates any manufacturing cost related to the substrate, which can be reused consecutively. Thin-film photovoltaics are often included into flexible designs. However, a highly efficient nanowire solar cell necessitates only ~12 % of an active semiconductor material, further reducing material-associated expenses. For the organic component, aside from the benchmark materials such as P3HT and PEDOT, very few newer and molecularly

engineered polymers, such as those outlined in Fig. 12.12 that have led to highly efficient organic solar cells, have been tested for hybrid photovoltaics. As the synthetic approaches become more mature and with extensive interdisciplinary collaborations, these sophisticated polymers are likely to help enhance the hybrid solar cell efficiencies as well. In fact, a new class of polymers specifically designed and produced to align with the energy levels and physical properties of the inorganic components could emerge and lead to a new altitude for photovoltaic research. Furthermore, the bendability of the 3-D structures arising from the inorganic nanowire arrays coupled with the flexibility of the organic coatings could potentially lead to low cost, flexible, possibly wearable photovoltaics. The colloidal dispersibility or solution solubility of the organic materials also allows for ink-jet printing or spray coating of polymers onto the inorganic nanowire arrays, providing golden opportunities for roll-to-roll manufacturing of hybrid solar cells.

References

1. Green, M.A., Emery, K., Hishikawa, Y., Warta, W., Dunlop, E.D.: Solar cell efficiency table (version 41). *Prog. Photovolt. Res.* **21**, 1–11 (2013)
2. Li, G., Zhu, R., Yang, Y.: Polymer solar cells. *Nat. Photon.* **6**, 153–161 (2012)
3. Jorgesen, M., Norrman, K., Gevorgyan, S.A., Tromholt, T., Andreasen, B., Krebs, F.C.: Stability of polymer solar cells. *Adv. Mater.* **24**, 580–612 (2012)
4. Arici, E., Sariciftci, N., Serdar, N., Dieter, M.: *Encyclopedia of Nanoscience and Nanotechnology*, vol. 3, pp. 99–944. (2004)
5. Gunes, S., Sariciftci, N.S.: Hybrid solar cells. *Inorg. Chim. Acta* **361**, 581–588 (2008)
6. Whitesides, G.M., Kriebel, J.K., Mayers, B.T.: *Nanostructure Science and Technology*. Springer Publisher (2005)
7. Murray, C.B., Sun, S., Gaschler, W., Doyle, H., Betley, T.A., Kagan, C.R.: *IBM J. Res. Dev.* **45**, 47–56 (2001)
8. Allen, P.M.: *Semiconductor nanocrystals: synthesis, mechanism of formation, and applications in biology*. PhD Dissertation, MIT (2010)
9. Sargent, E.H.: Colloidal quantum dot solar cells. *Nat. Photon.* **6**, 133–135 (2012)
10. Wang, X., Koleilat, G.I., Tang, J., Liu, H., Kramer, I.J., Debnath, R., Brzozowski, L., Barkhouse, D.A.R., Levina, L., Hoogland, S., Sargent, E.H.: Tandem colloidal quantum dot solar cells employing a graded recombination layer. *Nat. Photon.* **5**, 480–484 (2011)
11. Wagner, R.S., Ellis, W.C.: Vapor-liquid solid mechanism of single crystal growth. *Appl. Phys. Lett.* **4**, 89 (1964)
12. Kim, D.-H., Lu, N., Ghaffari, R., Rogers, J.A.: Inorganic semiconductor nanomaterials for flexible and stretchable bio-integrated electronics. *NPG Asia Mater.* **4**, 1–9 (2012)
13. Ouyang, G., Yang, G., Sun, C., Zhu, W.: *Small* **4**, 1359–1362 (2008)
14. Lee, J., Ju, H., Yi, Y., Lee, J., Uhm, S., Lee, J.K., Lee, H.J.: *J. Phys. Chem. C* **4**, 2915–2918 (2012)
15. Gebeyehu, D., Brabec, C.J., Sariciftci, N.S., Vangeneugden, D., Kiebooms, R., Vanderzande, D., Kienderger, F., Schindler, H.: Hybrid solar cells based on dye-sensitized nanoporous TiO₂ electrodes and conjugated polymers as hole transport materials. *Synth. Met.* **125**, 279–287 (2002)

16. Johansson, E.M.J., Pradhan, S., Wang, E., Unger, E.L., Hagfeldt, A., Andersson, M.R.: Efficient infiltration of low molecular weight polymer in nanoporous TiO₂. *Chem. Phys. Lett.* **502**, 225–230 (2011)
17. MacDiarmid, A.G.: “Synthetic metals”: a novel role for organic polymers (Nobel lecture). *Angew. Chem. Int. Ed.* **40**(14), 2581–2590 (2001)
18. Zhou, Y., Geng, J., Li, G., Zhou, E., Chen, L., Zhang, W.: *J. Polym. Sci. B Polym. Phys.* **44**, 764–769 (2006)
19. Bredas, J.L., Street, G.B.: Polarons, bipolarons, and solitons in conducting polymers. *Acc. Chem. Res.* **18**(10), 309–315 (1985)
20. McGehee, M.D., Miller, E.K., Moses, D., Heeger, A.J.: Advances in Synthetic Metals, 1st ed. Chap. 2, pp. 98–205. In: Bernier, P., Lefrant, S., Bidan, G. (eds.) Elsevier, Switzerland (1999)
21. Tran, H.D., Li, D., Kaner, R.B.: One-dimensional conducting polymer nanostructures: bulk synthesis and applications. *Adv. Mater.* **21**(14–15), 1487–1499 (2009)
22. Mayer, A.C., Scully, S.R., Hardin, B.E., Rowell, M.W., McGehee, M.D.: Polymer-based solar cells. *Mater. Today* **10**(11), 28–33 (2007)
23. Reese, C., Bao, Z.: Organic single-crystal field-effect transistors. *Mater. Today* **10**(3), 20–27 (2007)
24. Reghu, M., Cao, Y., Moses, D., Heeger, A.J.: Counterion-induced processibility of polyaniline—transport at the metal-insulator boundary. *Phys. Rev. B* **47**(4), 1758–1764 (1993)
25. Groenendaal, B.L., Jonas, F., Freitag, D., Pielartzik, H., Reynolds, J.R.: Poly(3,4-ethylenedioxythiophene) and its derivatives: past, present, and future. *Adv. Mater.* **12**(7), 481–494 (2000)
26. Li, D., Kaner, R.B.: How nucleation affects the aggregation of nanoparticles. *J. Mater. Chem.* **17**(22), 2279–2282 (2007)
27. Liang, Y.Y., Yu, L.P.: A new class of semiconducting polymers for bulk heterojunction solar cells with exceptionally high performance. *Acc. Chem. Res.* **43**(9), 1227–1236 (2010)
28. Su, Y.-W., Lan, S.-C., Wei, K.-H.: Organic photovoltaics. *Mater. Today* **15**(12), 554–562 (2012)
29. Chen, H.Y., Hou, J., Zhang, S., Liang, Y., Yang, G., Yang, Y., Yu, L., Wu, Y., Li, G.: Polymer solar cells with enhanced open-circuit voltage and efficiency. *Nat. Photon.* **3**(11), 649–653 (2009)
30. Chen, T.-A., Rieke, R.D.: The first regioregular head-to-tail poly(3-hexylthiophene-2,5-diyl) and a regiorandom isopolymer: Ni vs Pd catalysis of 2(5)-bromo-5(2)-(bromozincio)-3-hexylthiophene polymerization. *J. Am. Chem. Soc.* **114**, 10087–10088 (1992)
31. Mao, H., Xu, B., Holdcroft, S.: Synthesis and structure-property relationships of regioirregular poly(3-hexylthiophenes). *Macromolecules* **26**, 1163–1169 (1993)
32. Meng, H., Perepichka, D.F., Wudl, F.: Facile solid-state synthesis of highly conducting poly(ethylenedioxythiophene). *Angew. Chem. Int. Ed.* **115**(6), 682–685 (2003)
33. Hardin, B.E., Snaith, H.J., McGehee, M.D.: The renaissance of dye-sensitized solar cells. *Nat. Photon.* **6**, 162–169 (2012)
34. Ayllon, J.A., Lira-Cantu, M.: Application of MEH-PPV/SnO₂ bilayer as hybrid solar cell. *Appl. Phys. A Mater. Sci. Proc.* **95**(1), 249–255 (2009)
35. Huynh, W.U., Dittmer, J.J., Alivisatos, A.P.: Hybrid nanorod-polymer solar cells. *Science* **295**(5564), 2425–2427 (2002)
36. Ren, S., Zhao, N., Crawford, S.C., Tambe, M., Bulovic, V., Gradecak, S.: Heterojunction photovoltaics using GaAs nanowires and conjugated polymers. *Nano Lett.* **11**(2), 408–413 (2011)
37. Gharghi, M., Fathi, E., Kante, B., Sivonthaman, S., Zhang, X.: Heterojunction silicon microwire solar cells. *Nano Lett.* **12**, 6278–6282 (2012)
38. Lee, M.M., Teuscher, J., Miyasaka, T., Murakami, T.N., Snaith, H.J.: Efficient hybrid solar cells based on meso-superstructured organometal halide perovskites. *Science* **338**, 643–647 (2012)

39. Kuo, C.Y., Tang, W.C., Gau, C., Guo, T.F., Jeng, D.Z.: Ordered bulk heterojunction solar cells with vertically aligned TiO₂(2) nanorods embedded in a conjugated polymer. *Appl. Phys. Lett.* **93**(3), 033307 (2008)
40. Mariani, G., Laghumavarapu, R.B., Tremolet de Villers, B., Shapiro, J., Senanayake, P., Lin, A., Schwartz, B.J., Huffaker, D.L.: Hybrid conjugated polymer solar cells using patterned GaAs nanopillars. *Appl. Phys. Lett.* **97**, 013107 (2010)
41. Jeong, S., Garnett, E.C., Wang, S., Yu, S., Fan, S., Brongersma, M.L., McGehee, M.D., Cui, Y.: Hybrid silicon nanocone-polymer solar cells. *Nano Lett.* **12**, 2971–2976 (2012)
42. Briseno, A.L., Holcombe, T.W., Boukai, A.I., Garnett, E.C., Shelton, S.W., Frechet, J.J., Yang, P.: Oligo- and polythiophene/ZnO hybrid nanowire solar cells. *Nano Lett.* **10**(1), 334–340 (2010)
43. Mariani, G., Wang, Y., Wong, P.S., Lech, A., Hung, C.H., Shapiro, J., Prikhodko, S., El-Kady, M., Kaner, R.B., Huffaker, D.L.: Three-dimensional core-shell hybrid solar cells via controlled in situ materials engineering. *Nano Lett.* **12**(7), 3581–3586 (2012)
44. Xu, J., Wang, J., Mitchell, M., Mukherjee, P., Jeffries-EL, M., Petrich, J.W., Lin, Z.Q.: Organic-inorganic nanocomposites via directly grafting conjugated polymers onto quantum dots. *J. Am. Chem. Soc.* **129**(42), 12828–12833 (2007)
45. Huang, X., Lindgren, E., Chelikowsky, J.R.: Surface passivation method for semiconductor nanostructures. *Phys. Rev. B* **71**, 165328 (2005)
46. Mariani, G., Wong, P.-S., Katzenmeyer, A.M., Leonard, F., Shapiro, J., Huffaker, D.L.: Patterned radial GaAs nanopillar solar cells. *Nano Lett.* **11**, 2490–2494 (2011)
47. He, L., Lai, D., Wang, H., Jiang, C., Rusli: High-efficiency Si/polymer hybrid solar cells based on synergistic surface texturing of Si nanowires on pyramids. *Small* **8**, 1664–1668 (2012)
48. Wallentin, J., Anttu, N., Asoli, N., Huffman, M., Aberg, I., Magnusson, M.H., Siefer, G., Fuss-Kailuweit, P., Dimroth, F., Witzigmann, B., Xu, H.Q., Samuelson, L., Deppert, K., Borgstrom, M.T.: InP nanowire array solar cells achieving 13.8% efficiency by exceeding the ray optics limit. *Science* (2013). doi: [10.1126/science.1230969](https://doi.org/10.1126/science.1230969)
49. Spurgeon, J.M., Plass, K.E., Kayes, B.M., Brunshwig, B.S., Atwater, H.A., Lewis, N.S.: Repeated epitaxial growth and transfer of arrays of patterned, vertically aligned, crystalline Si wires from a single Si(111) substrate. *Appl. Phys. Lett.* **93**, 032112 (2008)
50. Weisse, J.M., Lee, C.H., Kim, D.R., Zheng, X.: Fabrication of flexible and vertical silicon nanowire electronics. *Nano Lett.* **12**, 3339–3343 (2012)

Chapter 13

Implication of Porous TiO₂ Nanoparticles in PEDOT:PSS Photovoltaic Devices

Yahia Djaoued, Jacques Robichaud, Srinivasan Priya, Balaji Subramanian, E. Gondek, M. Pokladko-Kowar, P. Karasinski, and I.V. Kityk

Abstract Recent developments in the synthesis of mesoporous nanocrystalline titanium oxide (TiO₂) have opened up several new opportunities in the construction of efficient photovoltaic (PV) cells. In this chapter, we describe principles involved in the construction of organic photovoltaic cell and the influence of the main parameters for the case of PEDOT:PSS polymers. At the outset different architectures of the PEDOT:PSS photovoltaics are described and later incorporation of the TiO₂ nanoparticles in their architectures is carefully considered. A special attention is given to the technique of photovoltaic cell preparation and the basic principles of their functionality. A significant emphasis has been devoted to the current–voltage characteristics of photovoltaic cells, thus constructed with and without nanocrystalline TiO₂, as well as to the ways it can be further improved. We also describe the synthesis of mesoporous TiO₂ nanoparticles using titanium alkoxides as precursor and polyethylene glycol (PEG) of different molecular mass as templating agent to induce mesoporosity. The interaction of PEG with titanium alkoxides in polar and nonpolar solvents was studied in detail by macro-Raman spectroscopy, solid-state NMR and MALDI-TOF-MS. The removal of PEG as well as the crystallization process was obtained by hot water treatment at low

Y. Djaoued • J. Robichaud • S. Priya • B. Subramanian

Laboratoire de Recherche en Matériaux et Micro-spectroscopies Raman et FTIR, Université de Moncton, Campus de Shippagan 218, boul. J.-D. Gauthier, Shippagan, NB, Canada E8S 1P6

E. Gondek • M. Pokladko-Kowar

Institute of Physics, Cracow University of Technology, ul.Podchorążych 1, Kraków 30-084, Poland

P. Karasinski

Department of Optoelectronics, Silesian University of Technology, 44-100, ul. B. Krzywoustego 2, Gliwice, Poland

I.V. Kityk (✉)

Electrical Engineering Department, Czestochowa University of Technology, Czestochowa, Poland

e-mail: iwank74@gmail.com

temperature (90 °C). The mesoporosity was retained after further calcination up to 500 °C. Porosity, morphology, and microstructures of the resultant products were characterized by SEM, nitrogen adsorption–desorption measurements, micro-Raman spectroscopy and XRD. The mesostructure of the TiO₂ particles facilitates enhanced transport of electrons, resulting in improved photovoltaic efficiency. Influence of TiO₂ nanoparticles on the photovoltaic efficiency of the ITO/PEDOT: PSS/fluorine copolymers/polythiophene:TiO₂/Al architecture is analyzed. Influence of TiO₂ NP on the principal parameters of different PV architecture is discussed. The analysis of the efficiency is performed using both experimental and theoretical quantum chemical approach.

1 Introduction to Photovoltaic Cells

1.1 Architecture of Photovoltaic Cells

In this section principles of organic photovoltaic cell devices will be briefly presented. Organic PV cells have been considered as a good alternative to traditional Silicon-based PV devices, owing to relative simplicity of their production, their mechanical flexibility, and low production costs [1–5]. Generally there are four types of photovoltaic cells (see Fig. 13.1). The first type is a single layered + architecture embedded between the ITO electrode and Al electrode (Fig. 13.1a).

The second architecture contains two active layers, donor layer (D) deposited on ITO electrode and acceptor layer (A) with deposited Al electrode (Fig. 13.1b) [6]. There is also an architecture in which the active layer is formed by a mixture of donor (D) and acceptor (A) materials (Fig. 13.1c). This mixture is embedded between the particular electrodes (ITO and Al). More complicated is the fourth type, which is multilayered. On the ITO there is deposited a donor layer, afterwards the mixture of donor–acceptor material and finally the Al electrode (Fig. 13.1d) [7]. The technology based on the mixture of donor and acceptor is basic for the so-called bulk heterojunction [8, 9] (Fig. 13.2).

1.2 Photovoltaic Cells of Bulk Heterojunction Type

Actually the conception of bulk heterojunction for organic photovoltaic cells is very promising with respect to other types of photovoltaic cells [10–13]. Among the different materials, recently an enhanced interest is emerging to use conjugated polymers and low-molecular chromophore in photovoltaics due to possible the coexistence of excellent mechanical features with optoelectronic ones for conventional semiconductors [14].

In Fig. 13.3a, b, two examples of bulk heterojunction photodiodes are presented. In the first structure the organic layer is deposited on the glass ITO substrate (which

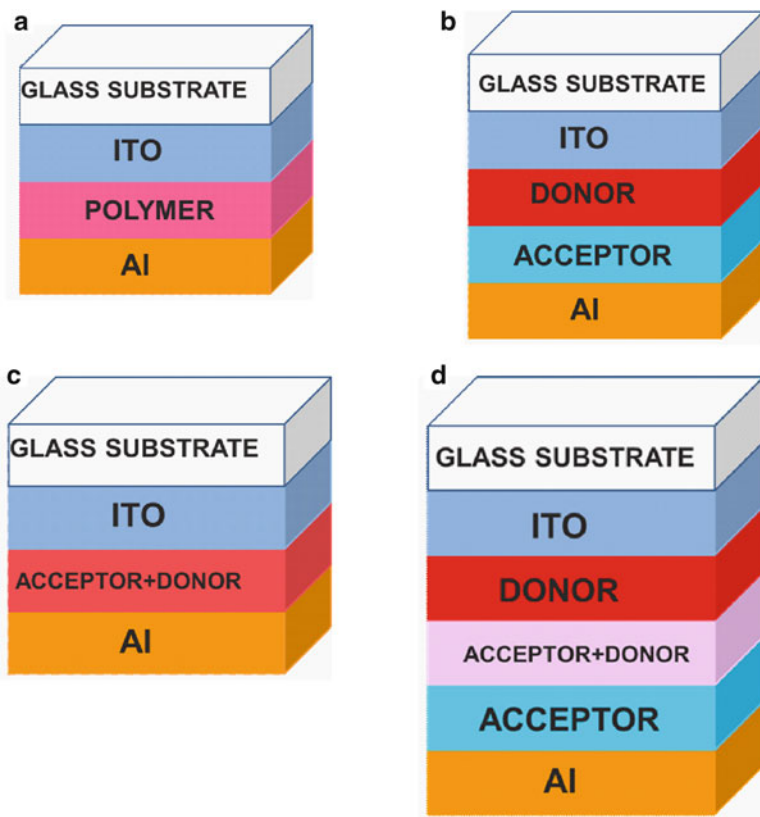


Fig. 13.1 Principal types of photovoltaic cells (a) single layered, (b) two-layered, (c) mixture, (d) multilayered

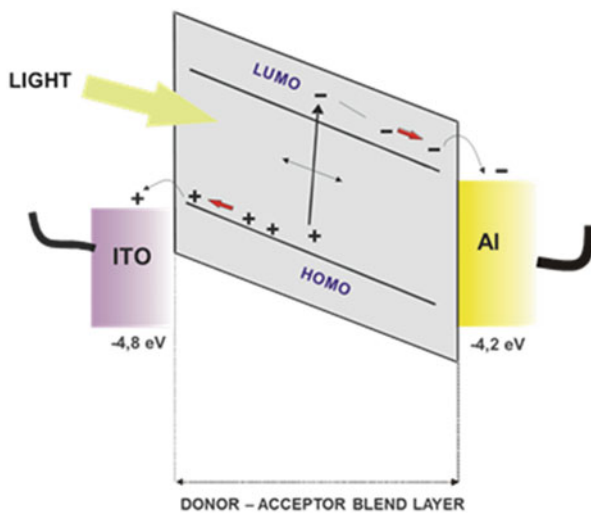


Fig. 13.2 Photovoltaic cells possessing bulk heterojunction

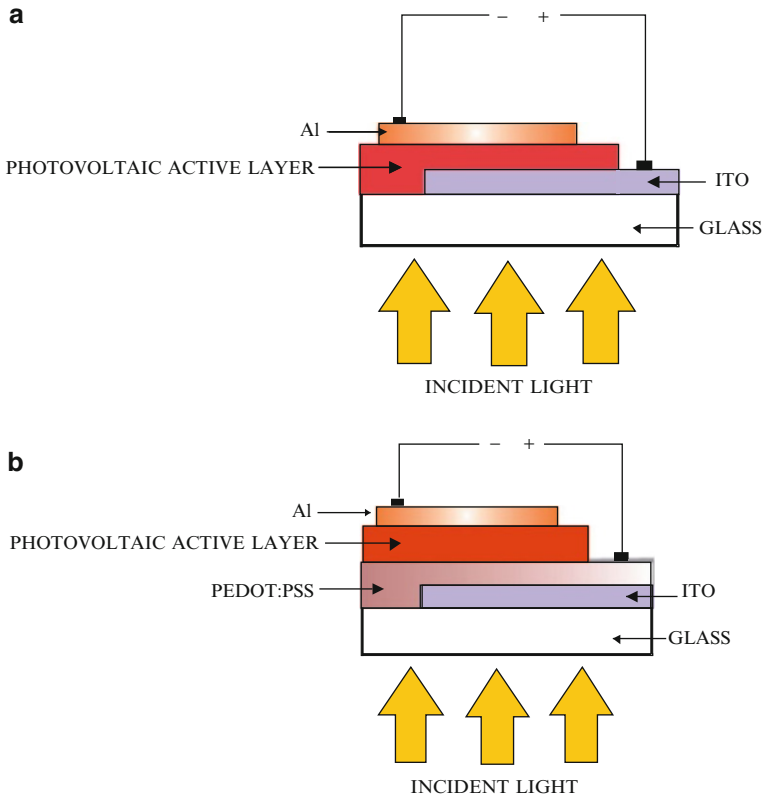


Fig. 13.3 (a) “Bulk heterojunction” type photodiode with structure ITO/active layer of Al. (b) Photodiodes of bulk heterojunction type with architecture ITO/PEDOT:PSS/active layer/Al

serves as anode) and for the second structure the mixture of PEDOT:PSS is deposited on the glass ITO layer [15]. The PEDOT:PSS mixture is a conjugated conduction polymer dissolved in water. Additionally, such deposition improve the roughness of the ITO surface and favors hole transport to the ITO electrode. The working output voltage for ITO is equal to -4.8 eV, and for the PEDOT:PSS mixture this value is equal to -5.2 eV [16, 17].

1.3 Principal Mechanisms in the Photovoltaic Devices

The whole photovoltaic effect is caused by several factors: photon absorption, creation of excitons, exciton diffusion, charge separation, carrier transport, gathering of the charge by the electrodes, and transport of the charge to the circuit [18].

1.3.1 Stage I: Photon Absorption. Creation of Excitons

Sunlight is absorbed by the photovoltaic cell. The organic-based cells may absorb only part of the external light. This is a consequence of the relatively large energy gap value of organic materials (conjugated polymers and low-molecular compounds). Hence, the real absorption for most of the known conjugated polymers is equal to about 30 % for an energy band gap exceeding 2.0 eV.

An enhancement of absorption may be achieved by a decrease of the energy gap; however, it may impart undesirable influence on the open circuit voltage V_{OC} . Absorption at a level of 80 % would require an energy gap value varying between 1 and 1.2 eV. An overlap of the absorption spectrum of the organic active layer with the emission spectrum of the sun enhances the efficiency of the photon absorption [16].

Layer thicknesses play the principal role in the absorption of sunlight. Normally the thickness of these layers about 100 nm. An increase in the active layer thickness improves the ability to absorb photons using organic materials. Unfortunately, this factor simultaneously hinders the carrier transport features.

Additional losses may be caused by photon reflection from the active layer or transmission of photons through active materials. The investigation of such kind of losses is still in the process of exploration. Generally, photon absorption leads to the creation of electron–hole pairs coupled by Columbic forces (excitons). Their behavior in the PV cell leads to undesirable exciton recombination.

1.3.2 Stage II: Exciton Diffusion

The creation of electron–hole pair (exciton) occurs at specific point on the active layer. Such a point may be located anywhere in the active layer. The diffusion path length should be commensurable with the thickness of the active layer. During the diffusion, recombination may also occur, in which case we do not have charge carriers.

Traditionally the diffusion length in polymers is equal to about 10 nm.

1.3.3 Stage III: Charge Separation

Charge separation may occur on the metal/organic active layer junction as well as on the different impurities or carrier trapping levels. For the case of bulk heterojunction devices, which have a mixture of donor and acceptor material, the corresponding separation may appear on the donor–acceptor interfaces. One advantage for such kind of photovoltaic cells is their relatively large effective surfaces for donors and acceptors, which is distributed in the whole bulk active layer. In such case not all the excitons may be separated and they can partially be recombined.

1.3.4 Stage IV: Charge Transport

The separated carriers (as described above) should move to the corresponding electrodes. An interaction with other charge trapping levels or with atoms (ions)

partially restrains the carrier transport processes. Generally the carrier transport is more complicated because here, the active layer plays a role of simultaneous transport for electrons and holes, which may stimulate undesirable recombination.

1.3.5 Stage V: Gathering of Charges on Electrodes

The separated carriers transported near the electrodes should exceed the barrier potential on the organic materials, and ITO and Al junctions. Near the electrodes, there is a high probability of recombination processes. After overcoming the barrier potential near the electrodes, the charge carriers are gathered on electrodes and after they are transported to the circuit.

1.4 Processes on the Heterojunction Metal/Semiconductor

Field emission and thermoelectronic emission are the basic mechanisms describing the transport of charge carriers through the barrier, which occurs at the metal/semiconductor junction. The field emission current through potential barrier, at low temperature, is described by the equation [19]

$$J = \frac{A^*T^2}{\Phi} \left(\frac{eE}{akT} \right)^2 \exp \left[-\frac{2a\Phi^{3/2}}{3qE} \right], \quad (13.1)$$

where A^* is the effective Rydberg constant; $a = \frac{4\pi(2m^*)^{1/2}}{h}$, m^* is effective mass of an electron, T is the absolute temperature, e is the electron charge, and E is the electric field strength. The field emission caused by tunneling through the triangle barrier Φ is observed at high fields and low temperatures.

For the case of the Schottky barrier the current density is dependent on the applied DC electric field as well as on the barrier potential value. It is expressed by the equation:

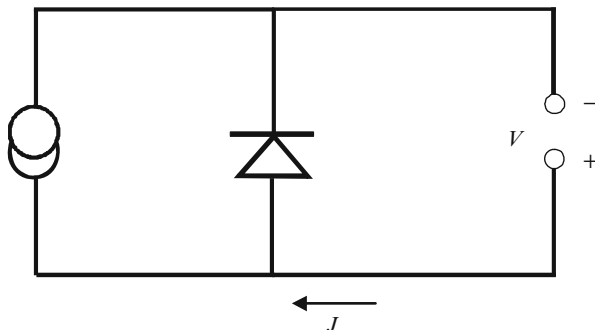
$$J = A^*T^2 \left(\frac{b}{kT} \right)^2 \frac{(\Phi + qU)}{\Phi} \exp \left[-\frac{2\Phi^{3/2}}{3b(\Phi + eU)^{1/2}} \right], \quad (13.2)$$

where b is a constant depending on the material, and U is the applied voltage. The current density may also be expressed as,

$$J = S \exp \left(\frac{eU}{nkT} \right), \quad (13.3)$$

where S is a constant, and $n = 1$ at high temperature [20].

Fig. 13.4 The equivalent circuit for a photovoltaic cell



Another possible mechanism describing the current at the junction is the thermoelectronic emission expressed by:

$$J = A^*T^2 \exp\left[-\frac{\Phi}{kT}\right]. \quad (13.4)$$

The barrier height decreases after the application of an external electric field E , and this dependence may be described by the equation:

$$\Delta\Phi = \sqrt{\frac{e^3 E}{4\pi\epsilon_0}}, \quad (13.5)$$

where ϵ_0 is the dielectric constant in vacuum.

1.5 Some Typical Models of Photovoltaic Cell

The function of photovoltaic devices may be represented by equivalent electric circuits (Fig. 13.4). The circuit is formed of a perfect diode and current source. The current–voltage features for a perfect photovoltaic cell may be described as the sum of the current density for a non-illuminated diode and a simultaneous current source [2].

The current density for a non-illuminated diode may be expressed by the equation:

$$J = J_{BS} \left[\exp\left(\frac{eV}{nkT}\right) - 1 \right], \quad (13.6)$$

where J_{BS} is the current density of saturation at inverted polarization.

For the real organic photovoltaic cells, this description should be slightly modified. The modification consists in an extension of the electric circuit using an additional shunt resistance R_{Sh} and some successor serial resistance R_S (Fig. 13.5).

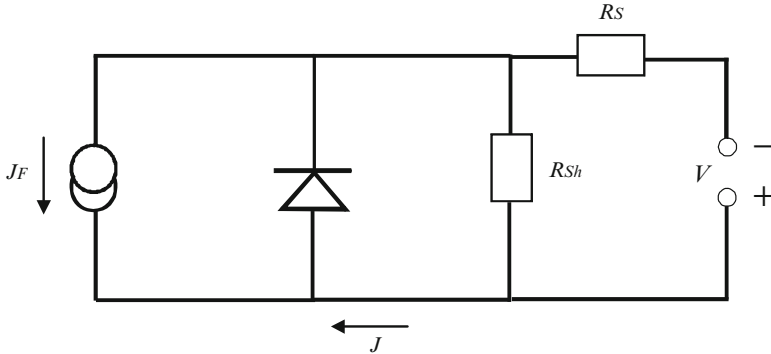


Fig. 13.5 Equilibrium circuit for the real photovoltaic cell modified by shunt and serial resistances

These two resistances disturb substantially the shape of the current–voltage characteristics. An extension of the equivalence electric circuit, Fig. 13.5, allows the definition of the total current density for the real photovoltaic cell [21]. The total current density is a sum of three components, i.e., current density originating from the diode, current density through the shunt resistance, and the short circuit current, such that

$$J = J_{BS} \left[\exp\left(\frac{e}{nkT}(V - JR_S) - 1\right) \right] + \frac{V - JR_S}{R_{sh}} - J_F, \tag{13.7}$$

where J_F is the photocurrent density in the photovoltaic device under the influence of external light [22].

The serial resistance R_S is described by the following equation:

$$\frac{\partial V}{\partial J} \Big|_{J=0} = R_S + \frac{R_{Sh}}{1 + \frac{J_{BS}R_{Sh}}{V_{(T)}} \exp\left(\frac{V_{OC}}{V_{(T)}}\right)} \approx R_S. \tag{13.8}$$

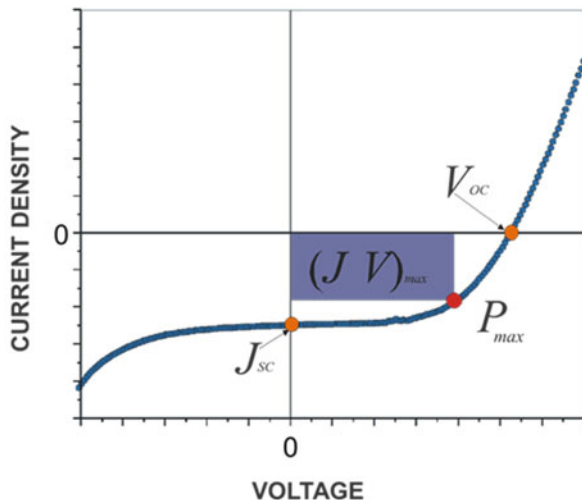
Assuming that $V \gg V_{OC}$, where V_{OC} is the open circuit voltage, the shunt resistance can be obtained from the equation:

$$\frac{\partial V}{\partial J} \Big|_{V=0} = R_S + \frac{R_{Sh}}{1 + \frac{J_{BS}R_{Sh}}{V_{(T)}} \exp\left(-\frac{J_{SC}R_S}{V_{(T)}}\right)} \approx R_S + R_{Sh} \approx R_{Sh}, \tag{13.9}$$

where V is the applied voltage and T is the temperature.

The key parameter defining the photovoltaic effect is the efficiency of power conversion [16]. More simply, this parameter may be presented as the efficiency of conversion of light energy into electrical energy. This parameter is described by the equation:

Fig. 13.6 Typical current–voltage features of a photo-galvanic cell



$$\eta = \frac{J_{sc}V_{oc}FF}{P_L}, \quad (13.10)$$

where FF is a filling factor. The FF coefficient is described by the equation:

$$FF = \frac{(JV)_{max}}{J_{sc}V_{oc}}, \quad (13.11)$$

where J_{sc} is the short circuit current density and V_{oc} is the open circuit voltage (Fig. 13.6).

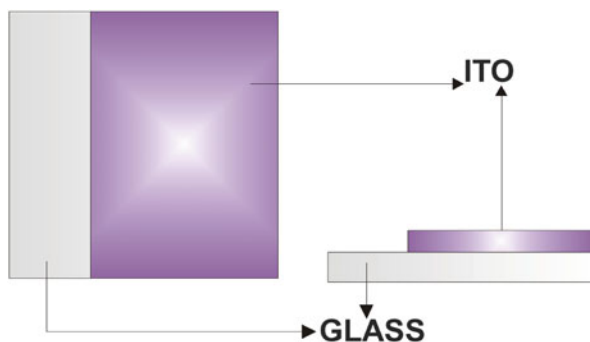
For the present consideration we have chosen the light power density to be a fixed value P_L , equal to 1.26 mW cm^{-2} . The maximum values of current density, J_{max} , and voltage, V_{max} , are obtained by following I - V curves (the quadrics of the current–voltage dependences ($I(V)$)) for the given photovoltaic cell (Fig. 13.6). The corresponding current–voltage dependence allows defining the point corresponding to the maximal power of the studied diode, P_{max} . P_{max} is a point at which the product of current density and voltage is a maximum and it is described by the expression:

$$P_{max} = (JV)_{max} = J_{sc}V_{oc}FF. \quad (13.12)$$

Both the shunt, and serial resistances, have an influence on the filling factor FF. Moreover, for this coefficient, some role is played by trapping levels, recombination, as well as carrier diffusion [23, 24].

Some decrease of the filling factor may be caused by huge serial resistance. The filling factor described by (13.11) defines the photodiode quality and defines the principle features for these devices.

Fig. 13.7 Glass plate partially deposited with ITO layer



The next crucial parameter is J_{SC} . This parameter is determined by carrier mobility of electrons and holes as well as their life time. Another important parameter defining the photovoltaic cell is the open circuit voltage, V_{OC} . The energy gap of organic active material limits the voltage in the open circuit. V_{OC} is defined by a distance between the donor HOMO level and the acceptor LUMO level for such kind of heterojunction. Additional layer of PEDOT:PSS in such photovoltaic cell which are deposited on the glass has an influence on the open circuit voltage. For the considered case, the dependence of the voltage in the open circuit is related to the working output function in the open circuit [21, 23].

1.6 Some Principles of Construction and Technology of “Bulk Heterojunction” Photovoltaic Cells Production

Below, we shortly consider some technological aspects of photovoltaic cells of bulk heterojunction for the architecture ITO/organic active layer/Al, and ITO/PEDOT:PSS/organic layer/Al. The entire technological process has several stages. During the first stage, glass substrates deposited with thin transparent ITO layer were fabricated. Their sizes were 15 mm × 15 mm. The thin ITO layer was covered by an additional protective layer. Using the etching method ¼ part of ITO was removed. For etching 40 % bromic acid (HBr) was used. After the etching, ¼ of the ITO protective surface was removed using tetrahydrofuran (THF), acetone, as well as alcohol in the ultrasound washing system. To eliminate organic pollutions the substrate was annealed during 24 h at temperatures of 70–100 °C. After this procedure, a substrate is ready for deposition of thin organic layers (Fig. 13.7). It should be emphasized that the ITO layer serves as a positive electrode (anode).

On the second stage a solution of conjugated conducting polymers and low-molecular chromophores were prepared. The organic compounds were dissolved in organic solvents. Afterwards using these solvents the mixtures of conjugated polymers and low-molecular chromophores were prepared. The organic layers were deposited using the spin-coating method (Fig. 13.8). The rotation speed

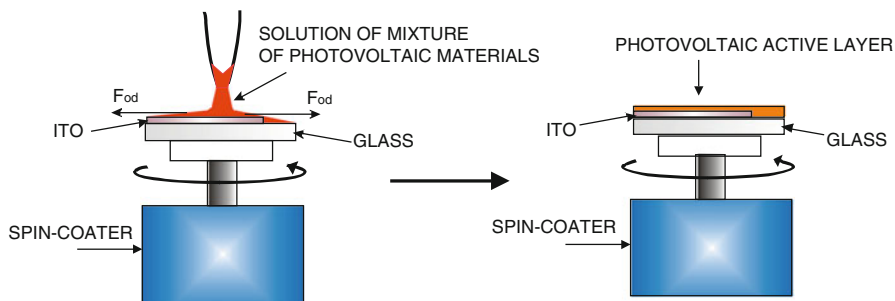


Fig. 13.8 Principal scheme of spin-coating film's preparation

which is necessary to fabricate the thin film is about 1,000 rotation per minute, due to the centrifugal force resistance of the corresponding solvent. After deposition of the thin film we increase the rotation speed up to 2,000 rotation per min in order to dry the previously deposited layer. Usually the thickness of the organic layer is about 100 nm.

At the beginning the thin film of PEDOT:PSS mixture was deposited. As a second step, the deposition of the organic active layer with architecture ITO/PEDOT:PSS/active organic layer/Al was done. The deposition of such film was performed using a spin-coating method similar to the preparation of organic materials. The rotation speed was equal to about 3,000 rotation per minute. Afterwards, the glass substrate with ITO, together with PEDOT:PSS was thermo annealed at temperature of 70–200 °C in order to eliminate water. An organic active layer is deposited on the substrate. The last stage of the photovoltaic cell preparation is the thermal evaporation of the Al layer. The deposited Al film forms the negative electrode (cathode). The evaporation of the Al thin film is performed in a Pfeiffer 160 PLS vacuum evaporator in vacuum at 10^{-6} Torr. The Al film thickness is equal to about 100 nm. After these different stages of preparation we obtain organic photovoltaic architecture with structure ITO/organic active layer/Al (Fig. 13.9a) and the structure with additional PEDOT:PSS layer (Fig. 13.9b).

1.7 Methods of Current–Voltage Monitoring on Photovoltaic Cell

The determination of the photovoltaic effect requires measurements of current–voltage dependences for the studied photovoltaic cells (Fig. 13.10).

The external voltage is applied using a KEITHLEY—2400 current source and using a pico-ammeter to measure the current. All the setup is operated using an external PC. At the beginning, the cell is put in the dark where the measurements of

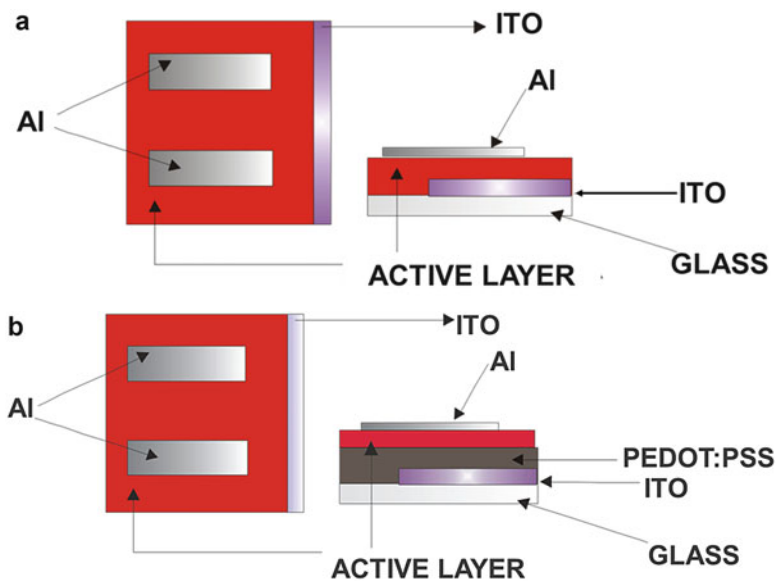


Fig. 13.9 (a) Principal structure of photovoltaic cell with architecture ITO/active organic layer/Al. (b) The structure of photovoltaic cell with architecture ITO/PEDOT:PSS/active layer/Al

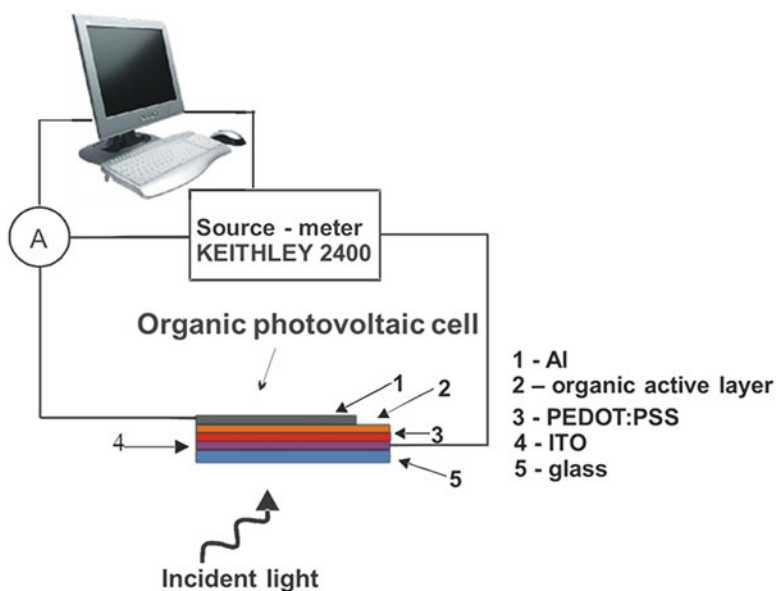


Fig. 13.10 Setup for current-voltage measurements of photovoltaic cells

voltage and current through the photovoltaic devices are performed. In the second step the specified photovoltaic cell is illuminated with a lamp of a fixed power density of 1.26 mW cm⁻² and the current–voltage features are measured.

2 Organic Chromophores

2.1 1*H*-Pyrazole-[3,4-*b*]-quinolin Derivatives

In 1928 T. Tomasik and Niemientorski from Lvov Polytechnique have first synthesized heterocyclic compounds belonging to the 1*H*-pyrazole [3,4-*b*] quinolin class. These materials belong to the wide class of nitrogen heterocyclic compounds possessing aromatic structures where besides the carbon atoms lie the nitrogen atom [25]. Some of these materials are used as electroluminescent cell, luminophore, and transport carrier materials. Wolfrum has published an article about the light indicators in 1962 [26].

Different chemical groups may be connected to the backbone of pyrazole-quinoline. Usually the chemical groups may be attached to the site positions indicated as 1, 3, 4, 6, 7 (Fig. 13.11). In the present section the main derivatives of 1*H*-pyrazole [3,4-*b*] quinolin group will be presented, to which, to the principal backbone, side chemical groups in the positions 1, 3, 4 are attached. The corresponding substituent will be indicated as R1, R3, and R4. Modification of 1*H*-pyrazole [3,4-*b*] quinolin, due to the attachment of different chemical groups, influences the electro-optical properties of the molecules and favors a spectral shifts of the emission and absorption spectra. During the last 15 year the Department of Polymers at the Technical University of Krakow has conducted complex studies of chromophores possessing azo-heterocyclic groups [6, 28–31].

Below the chemical formulae of these chromophores are presented in Table 13.1 and in Figs. 13.12–13.15.

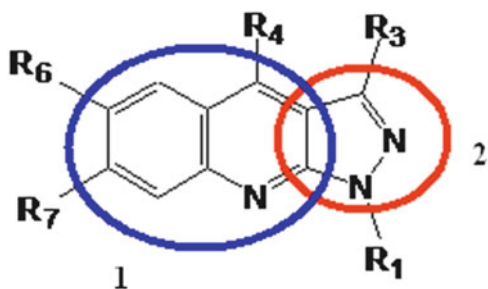
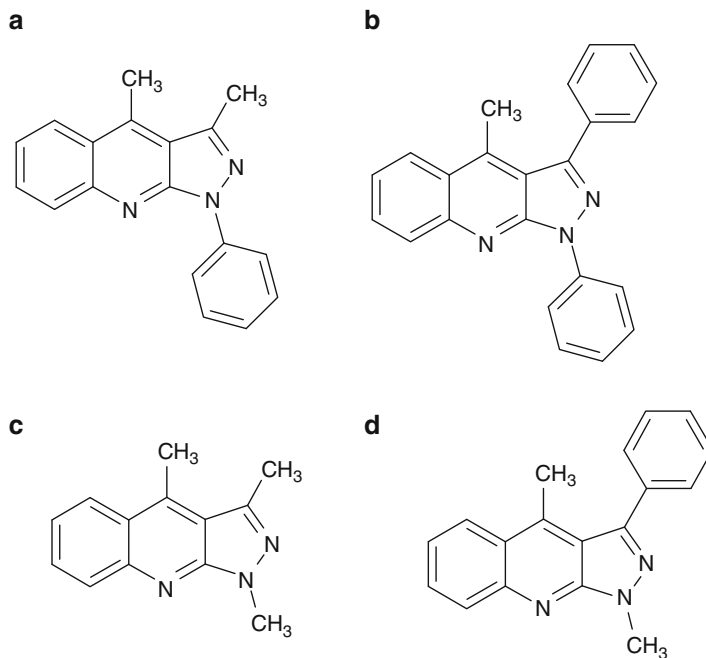


Fig. 13.11 General formulae of 1*H*-pyrazole [3,4-*b*]quinolin: 1-quinolin; 2-pyrazole

Table 13.1 Chemical notations, chemical substituent, and indications for the studied low-molecular chromophores, where the phenyl group is indicated as Ph and methyl as Me

Chemical notations	R1	R3	R4	Molecular identification
1-Phenyl-3,4-dimethyl-1 <i>H</i> -pyrazole-[3,4- <i>b</i>]quinolin	Ph	Me	Me	PAQ1
1,3-Diphenyl-4-methyl-1 <i>H</i> -pyrazole-[3,4- <i>b</i>]quinolin	Ph	Ph	Me	PAQ2
1,3,4-Trimethyl-1 <i>H</i> -pyrazole [3,4- <i>b</i>]-quinolin	Me	Me	Me	PAQ3
3-Phenyl-1,4-dimethyl-1 <i>H</i> -pyrazole [3,4- <i>b</i>]-quinolin	Me	Ph	Me	PAQ4
4-Chlor-1-phenyl-3-methy;-1 <i>H</i> -perazole[3,4- <i>b</i>]quinolin	Ph	Me	Cl	Mol1
4-(1-Nafthyloxy)-1-phenyl-3-methyl-1 <i>H</i> -pirazole [3,4- <i>b</i>]quinolin	Ph	Me	1-Nafthyloxy	Mol2
4-(4-Biphenyloxy)-1-phenyl-3-methyl-1 <i>H</i> -pyrazole [3,4- <i>b</i>]quinolin	Ph	Me	4-Biphenyloxy	Mol3
4-(2- <i>tert</i> -Butylofenoksy)-1-phenyl-3-methyl-1 <i>H</i> -pyrazole [3,4- <i>b</i>]quinolin	Ph	Me	2- <i>tert</i> -Butyl-phenoxy	Mol4
4-(2-Biphenyloxy)-1-phenyl-3-methyl-1 <i>H</i> -pyrazole [3,4- <i>b</i>]quinolin	Ph	Me	2-Biphenyloxy	Mol5

**Fig. 13.12** Chemical formulae for the low-molecular chromophores: (a) PAQ1, (b) PAQ2, (c) PAQ3, (d) PAQ4

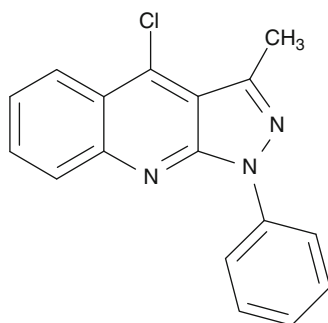


Fig. 13.13 Chemical formula for chromophore Mol1

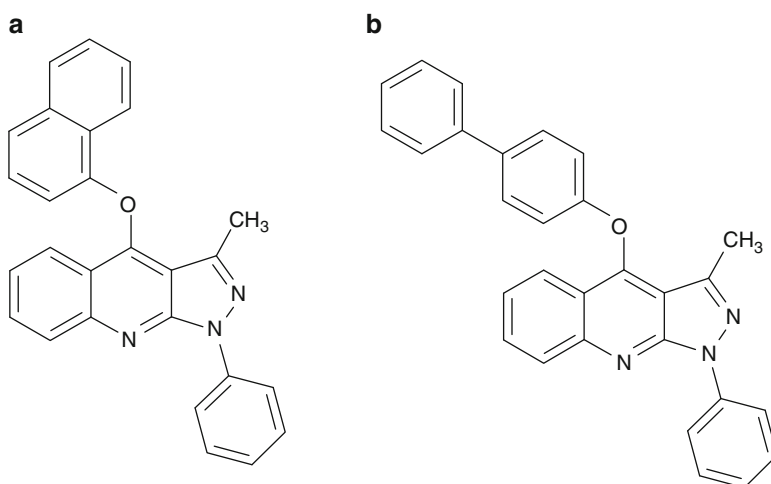


Fig. 13.14 Chemical structure of low-molecular chemical chromophores (a) Mol2, (b) Mol3

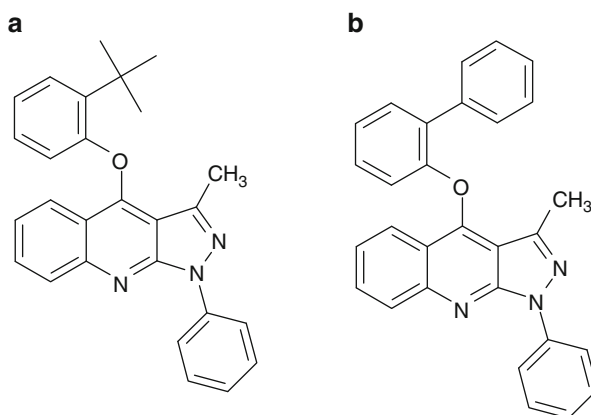


Fig. 13.15 Chemical formulae for the used chromophore: (a) Mol4, (b) Mol5

Fig. 13.16 Chemical structure of poly (3-decylthiophene) (PDT)

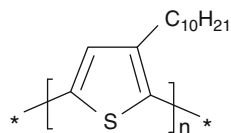


Fig. 13.17 Chemical structure of poly (3-octylthiophene) (P3OT)

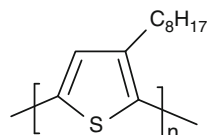
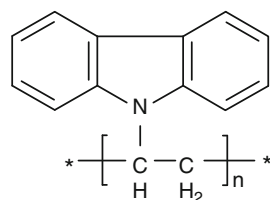


Fig. 13.18 Chemical formulae of poly (*N*-vinyl carbazole) (PVC)



2.2 Used Polymers

Polythiophene and their derivatives are electrically conducting π -conjugated polymers. Application of polythiophenes and their derivatives allows to enhance the efficiency of the PV devices [32–36]. Here we briefly describe the PV devices based on the polythiophene derivatives such as poly(3-decylthiophene) (PDT) (Fig. 13.16), poly(3-octylthiophene) (P3OT) (Fig. 13.17), and PEDOT:PSS (Fig. 13.20).

Similarly, for the PV cell a conducting polymer such as poly(*N*-vinyl-carbazole) (PVC) (Fig. 13.18) was used. PVC was first synthesized in 1934 by Reppe and coworkers. Photoconductivity was discovered by Hoegle and this has stimulated the use of these conducting polymer materials. This material is characterized by a high degree of crystallinity, a high thermal stability, and a glass transition temperature of ~ 200 °C. Its promising photoconductivity allows its use in the development of electronics, electrophotography, as well as in optoelectronics [7, 37–40]. We have applied PVC to the fabrication of thin organic films, which were part of the architecture of organic photovoltaics (PV). The active layer is composed of PVC doped with chromophores which were derivatives of 1*H*-pyrazolo-[3,4-*b*]chinolin and 4-aryloxy-1*H*-pyrazolo[3,4-*b*]chinolin.

In addition to PVC, electron-acceptor dopants favor the creation of PVC complexes for this material and an enhancement of its photoconducting and photo-sensitive features.

Fig. 13.19 Chemical formula of tetracyanoethylene (TCNE)

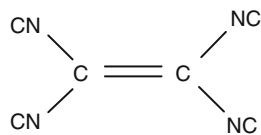
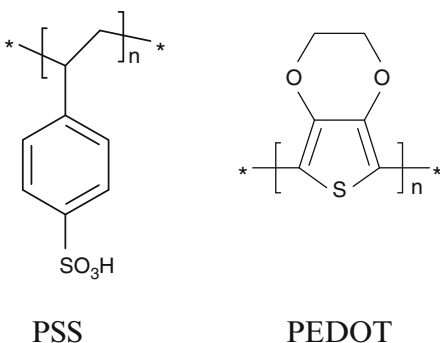


Fig. 13.20 Chemical molecule PSS and PEDOT



PVC doped by tetracyanoethylen (TCNE) (Fig. 13.19) forms a complex PVC:TCNE.

One of the benefits of complex PVC:TCNE is a coexistence of photoconductive and photosensitive features with chemical stability, thermal stability, and chemical flexibility.

Finally as conducting polymer, a mixture of PEDOT:PSS was used, which serves as a film possessing hole conductivity. The mixture of PEDOT:PSS (Fig. 13.20) presents a conjugated polymer dissolved in water. The output work for ITO is varied within the -4.7 to -4.9 eV, and at the same time, the output work for the mixture PEDOT:PSS is equal to -5.2 eV [16, 17]. Their common feature is their transparency within the spectral range 350 nm up to 900 nm [41].

3 Interfaces Formed by Active Organic Layers/Electrode. HOMO and LUMO Levels

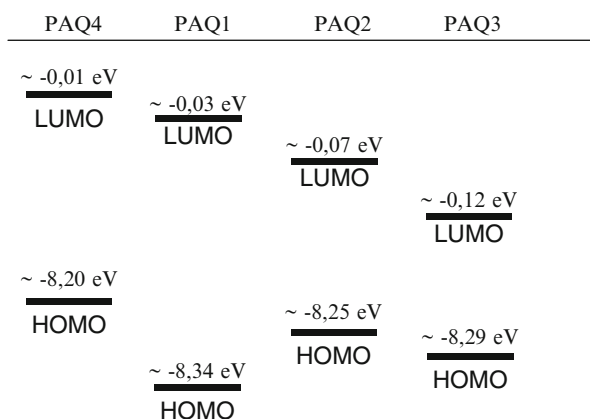
Theoretical calculations for the highest occupied molecular orbital (HOMO) and lowest unoccupied molecular orbital (LUMO) levels in the case of 1*H*-pyrazole-[3,4-*b*] quinolin were evaluated using quantum chemical package HyperChem 7.5 [42]. The AM1 semiempirical method takes into account three types of interactions: inter-electronic, correlation (two-center two-electron, two-center one-electron, and one-center one-electron). The data presented in Tables 13.2 and 13.3 for HOMO and LUMO levels were evaluated for the isolated molecule, and the influence of neighbors and solvents were neglected.

Table 13.2 HOMO and LUMO levels for chromophore PAQX

Chromophore	HOMO (eV)	LUMO (eV)
PAQ1	-8.34	-0.03
PAQ2	-8.25	-0.07
PAQ3	-8.29	-0.12
PAQ4	-8.20	-0.01

Table 13.3 HOMO and LUMO levels for molecule Molx

Molecule	HOMO (eV)	LUMO (eV)
Mol1	-9.00	-0.27
Mol2	-8.15	-0.57
Mol3	-8.40	-0.25
Mol4	-8.51	-0.16
Mol5	-8.45	-0.30

Fig. 13.21 HOMO and LUMO levels for the molecules of the PAQX family

Comparison of HOMO and LUMO levels for PAQX (Fig. 13.21) is possible only for the isolated molecule.

A similar comparison of the HOMO and LUMO levels for the Molx molecules (Fig. 13.22) is necessary to understand their behavior in the active layer.

In this chapter we consider organic materials which are promising for applications in organic photovoltaic cells. We have chosen two types of low-molecular chromophore compounds: 1*H*-pirazolo[3,4-*b*]quinoline (PAQX) derivatives and 4-aryloxy-1*H*-pyrazol-[3,4-*b*]quinoline—(Molx) derivatives, which were embedded into the polymer matrices. We explore several groups of organic photovoltaic cells with bulk heterojunction using modification of the organic active layer as well as the architecture of the cell by incorporating an additional PEDOT:PSS layer. Further, we present some results of measurements for the short circuit current J_{SC} as well as of the open circuit voltage V_{OC} .

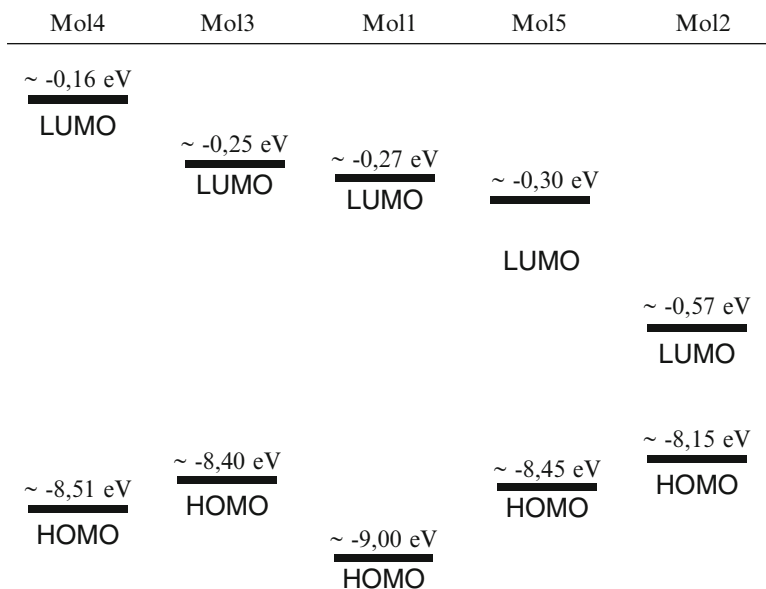


Fig. 13.22 HOMO and LUMO levels for molecules from the Molx family

3.1 Photovoltaic Cells with Architecture ITO/PAQX + PDT/Al and ITO/PEDOT:PSS/PAQX + PDT/Al

The first type of photovoltaic cells that we explore has ITO/PAQX + PDT/Al and ITO/PEDOT:PSS/PAQX + PDT/Al structures. Poly(3-decyloctiofen) (PDT) was used as a donor, and the derivative of 1*H*-pyrazol[3,4-*b*] quinolin (PAQX) was used as an acceptor.

The LUMO energy level (-0.03 eV) for PAQ1 chromophore is situated between those of for PAQ4 chromophore (-0.01 eV) and for PAQ2 chromophore (-0.07 eV). The LUMO level (-0.12 eV) is the lowest for the PAQ3 molecule (Fig. 13.21). The HOMO and LUMO energy levels for the poly(3-decyloctiofenu) molecule with respect to the HOMO and LUMO levels of the studied pyrazole-quinoline define the charge carrier transport between the donor and acceptor, and the energy level differences among them play a crucial role for the charge carrier transport. The potential gradient which occurs between the LUMO levels of donor (PDT) and of acceptor (PAQX) stimulates the charge carrier transport.

The typical dependences are presented in Figs. 13.23–13.26 and the corresponding parameters are given in Tables 13.4 and 13.5. The highest conversion efficiency η equal to 0.45 % (Table 13.5) was obtained for the PV cell with architecture ITO/PEDOT:PSS/PAQ1 + PDT/Al—(NPV1). The organic active layer was formed by mixture 1-phenyl-3,4-dimethyl-1*H*-pyrazolo-[3,4-*b*] quinolin

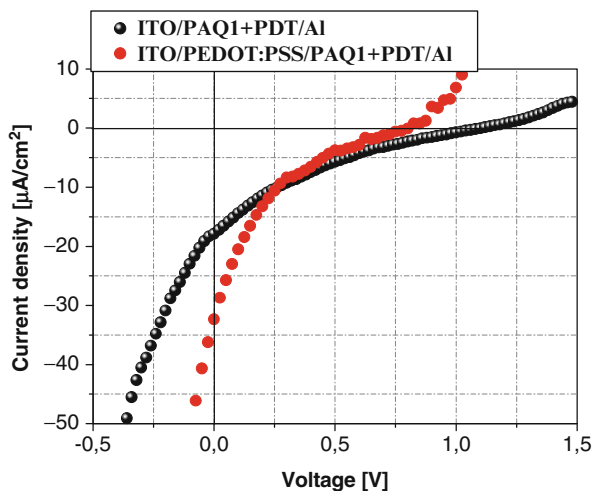


Fig. 13.23 Current–voltage characteristics during the illumination for photovoltaic devices with ITO/PAQ1 + PDT/Al (PV1) and ITO/PEDOT:PSS/PAQ1 + PDT/Al (NPV1) structures

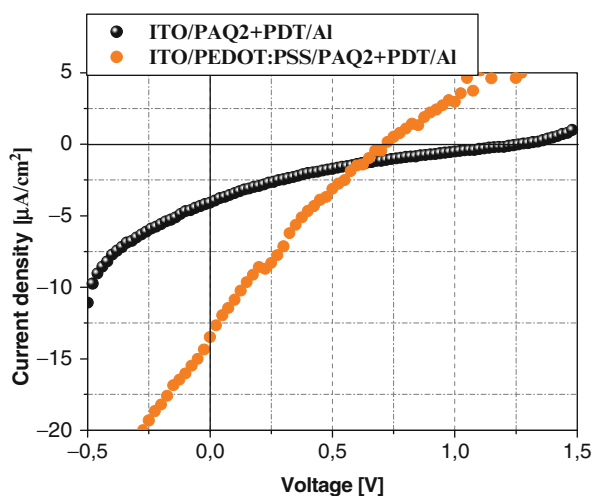


Fig. 13.24 Current–voltage characteristics during illumination for photovoltaic devices with ITO/PAQ2 + PDT/Al (PV2) and ITO/PEDOT:PSS/PAQ2 + PDT/Al (NPV2) structures

in matrix poly(3-decylothiophene). The measured short circuit current density J_{SC} for NPV1 was $\sim 32 \mu\text{A cm}^{-2}$, at the open circuit voltage equal to about 0.9 V. The photocell with the same organic active layer without the PEDOT:PSS (ITO/PAQ1 + PDT/Al—(PV1)), possessed a conversion efficiency equal to about 0.26 %.

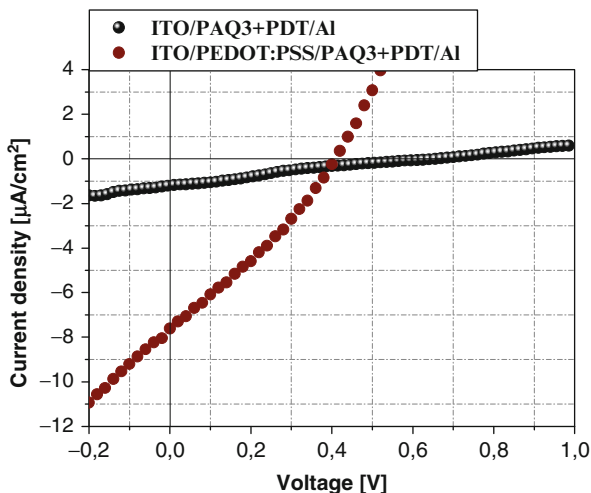


Fig. 13.25 Current–voltage characteristics during illumination for photovoltaic devices with ITO/PAQ3 + PDT/Al (PV3) and ITO/PEDOT:PSS/PAQ3 + PDT/Al (NPV3) structures

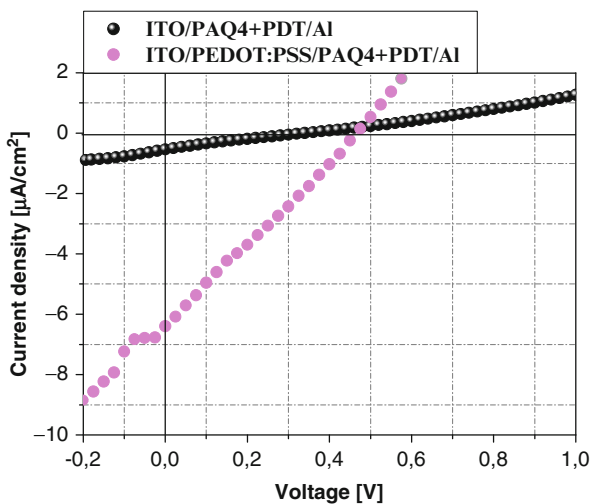


Fig. 13.26 Current–voltage characteristics during illumination of photovoltaic devices with ITO/PAQ4 + PDT/Al (PV4) and ITO/PEDOT:PSS/PAQ4 + PDT/Al (NPV4) structures

Incorporation of an additional PEDOT:PSS layer to the photovoltaic cell favors carrier transport to electrodes. For photovoltaic cells with PEDOT:PSS additional layers an enhancement of the conversion efficiency was observed with respect to the photocells without PEDOT:PSS. In the photocells with PEDOT:PSS, the short circuit current density J_{SC} was also enhanced with respect to the cells without this

Table 13.4 Shunt and serial resistances for studied photovoltaic cells

Architecture of photovoltaic cell	Notation	Serial resistance, R_S (M Ω)	Shunt resistance, R_{Sh} (M Ω)
ITO/PAQ1 + PDT/Al	PV1	0.04	0.03
ITO/PEDOT:PSS/PAQ1 + PDT/Al	NPV1	0.005	0.007
ITO/PAQ2 + PDT/Al	PV2	0.15	0.20
ITO/PEDOT:PSS/PAQ2 + PDT/Al	NPV2	0.04	0.03
ITO/PAQ3 + PDT/Al	PV3	0.81	0.45
ITO/PEDOT:PSS/PAQ3 + PDT/Al	NPV3	0.01	0.10
ITO/PAQ4 + PDT/Al	PV4	0.36	0.45
ITO/PEDOT:PSS/PAQ4 + PDT/Al	NPV4	0.01	0.13

Table 13.5 Principal parameters defining the photovoltaic features [43]

Photovoltaic architecture	Short circuit current density, J_{SC} ($\mu\text{A cm}^{-2}$)	Open current voltage, V_{OC} (V)	Filling factor, FF	Conversion efficiency, η (%)
ITO/PAQ1 + PDT/Al	17.84	1.08	0.17	0.26
ITO/PEDOT:PSS/PAQ1 + PDT/Al	32.15	0.92	0.19	0.45
ITO/PAQ2 + PDT/Al	4.09	1.23	0.18	0.07
ITO/PEDOT:PSS/PAQ2 + PDT/Al	13.50	0.72	0.21	0.18
ITO/PAQ3 + PDT/Al	1.19	0.65	0.21	0.013
ITO/PEDOT:PSS/PAQ3 + PDT/Al	7.65	0.41	0.30	0.07
ITO/PAQ4 + PDT/Al	0.86	0.32	0.36	0.008
ITO/PEDOT:PSS/PAQ4 + PDT/Al	6.21	0.46	0.27	0.06

layer. Moreover, an additional PEDOT:PSS layer favored a decrease of serial resistance R_S and shunt resistance R_{Sh} with respect to the same photocells without PEDOT:PSS (Table 13.4).

For the NPV3 and NPV4 cells, the shunt resistance is at least one order higher with respect to the serial resistance. This means that the recombination may occur in the places which are very far from the charge separation. It is necessary to emphasize that the filling factor FF for NPV3 and NPV4 was higher with respect to the NPV1 and NPV2 cells (Table 13.5). For the NPV1 and NPV2 cells, the serial resistance and shunt resistance were almost of the same order. For the photovoltaic cell NPV3 (ITO/PEDOT:PSS/PAQ3 + PDT/Al) the active organic layers were formed by a mixture of 1,3,4-Trimethyl-1*H*-pyrazole [3,4-*b*]quinoline and PDT, while in the NPV4 cell (ITO/PEDOT:PSS/PAQ4 + PDT/Al), the active organic layer was formed by a mixture of 3-phenyl-1,4-dimethyl-1*H*-pyrazolo-[3,4-*b*]quinoline and PDT.

In Fig. 13.27 the current–voltage features are presented for four photovoltaic cells, PV1, PV2, PV3, and PV4, possessing the ITO/PAQX + PDT/Al structure during illumination, and $I(V)$ for PV1 put in the dark. The analogous comparison for $I(V)$ is performed for NPV1–NPV4 possessing an ITO/PEDOT:PSS/PAQX + PDT/Al architecture (Fig. 13.28). The $I(V)$ features are given during illumination and the latter are compared with the dark $I(V)$ features for NPV3.

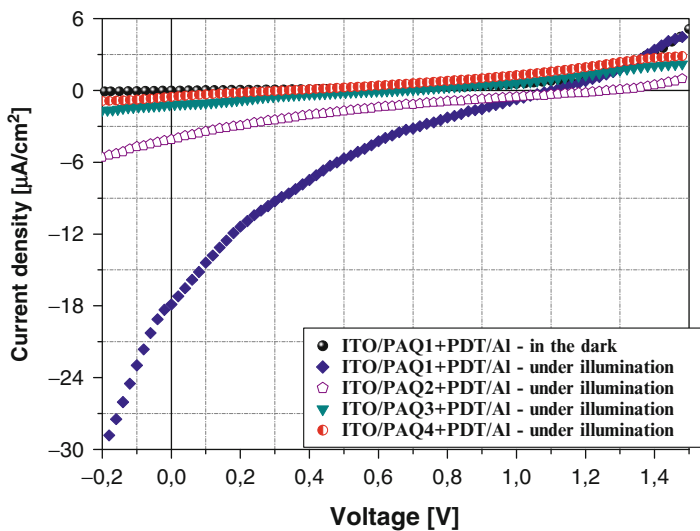


Fig. 13.27 Comparison of current–voltage for photocells with ITO/PAQX + PDT/Al architecture during illumination and without the illumination [43]

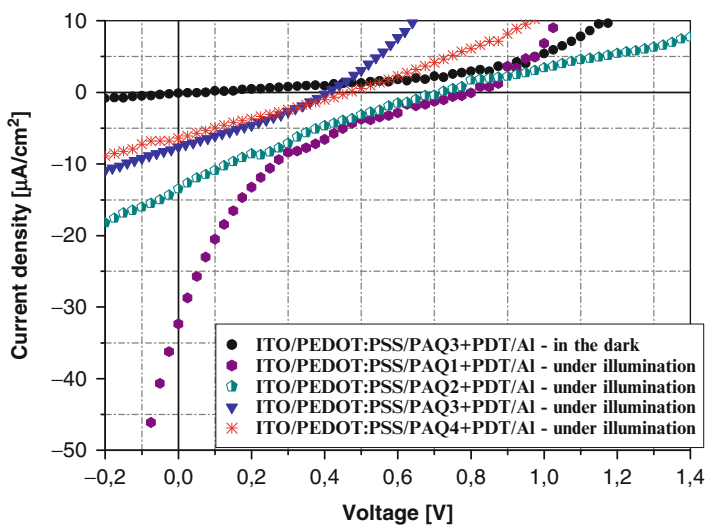


Fig. 13.28 Comparison of current–voltage characteristics of photocells with ITO/PEDOT:PSS/PAQX + PDT/Al structure during illumination and without the illumination

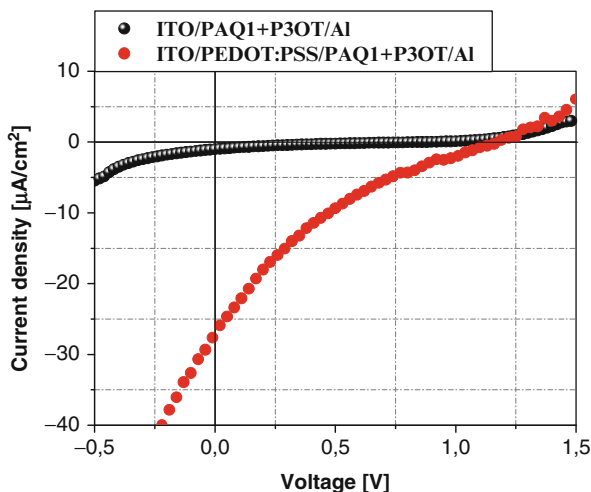


Fig. 13.29 Current–voltage characteristics for the photocell with ITO/PAQ1 + P3OT/Al (PV5) and ITO/PEDOT:PSS/PAQ1 + P3OT/Al (NPV5) architectures

3.2 Photovoltaic Cells with ITO/PAQX + P3OT/Al and ITO/PEDOT:PSS/PAQX + P3OT/Al Architectures

The next studied group of PV cells possessed ITO/PAQX + P3OT/Al [44] and ITO/PEDOT:PSS/PAQX + P3OT/Al architectures. These photocells are different from those presented before owing to the polymer matrix. The active organic layer was a mixture of group 1*H*-pirazolo-[3,4-*b*]quinoline (PAQX) and poly(3-octyl-thiophene) (P3OT).

The principal results are given in Figs. 13.29–13.32. Similar to the former group, the highest power efficiency η was achieved for PV cell with a PEDOT:PSS layer, in which pyrazoloquinoline derivative PAQ1 was used as an acceptor; however, poly(3-octyl-thiophen) was used as a donor. The theoretical value of LUMO level for PAQ1 was equal to -0.03 eV (Table 13.2). This cell has an ITO/PEDOT:PSS/PAQ1 + P3OT/Al (NPV5) structure.

In Tables 13.6 and 13.7 the parameters describing the PV cells are presented which have the ITO/PAQX + P3OT/Al and ITO/PEDOT:PSS/PAQX + P3OT/Al architectures. The conversion efficiency for NPV5 at short circuit current densities J_{SC} is equal to $27 \mu\text{A cm}^{-2}$, and the open circuit voltage V_{OC} is 1.16 V, which gives an efficiency of 0.37 % (Table 13.7). The PV5 cell with the same active layer PAQ1 + P3OT, but without PEDOT:PSS layer possessed a conversion efficiency of $\eta = 0.01$ % (at short circuit, J_{SC} equals to about $1 \mu\text{A cm}^{-2}$) (Table 13.7).

The results unambiguously show that an additional layer of PEDOT:PSS enhances the conversion efficiency as well as the current density with respect to the cells without this layer (Table 13.7). Incorporation of an additional layer of

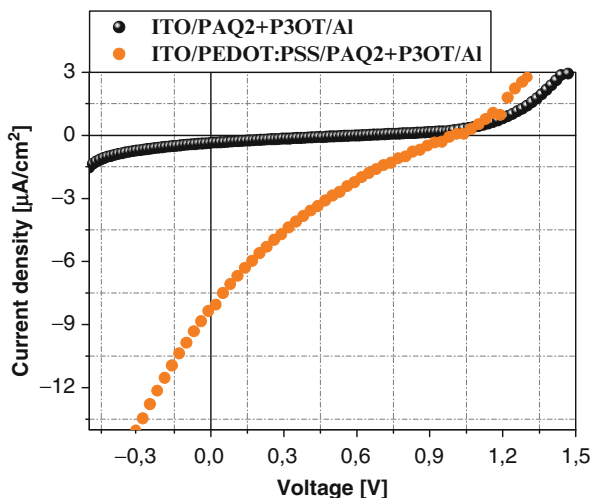


Fig. 13.30 Current–voltage dependence during the illumination of PV cell with ITO/PAQ2 + P3OT/Al (PV6) and ITO/PEDOT:PSS/PAQ2 + P3OT/Al (NPV6) architectures

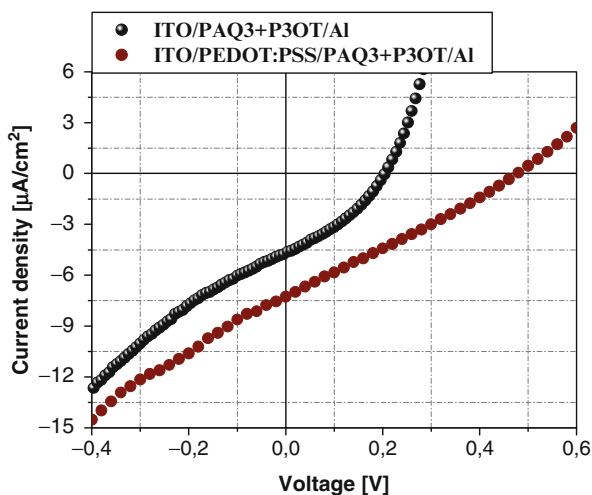


Fig. 13.31 Current–voltage dependence for the PV cells with ITO/PAQ3 + P3OT/Al (PV7) and ITO/PEDOT:PSS/PAQ3 + P3OT/Al (NPV7) architectures

PEDOT:PSS between the ITO electrode and the organic layers has changed the value of serial resistance R_S and shunt resistance R_{Sh} favoring enhanced hole transport to the ITO electrode.

In the PV cells with the same active layer and additional layer of PEDOT:PSS, serial, resistance and shunt resistance were decreased with respect to the same photocells without the PEDOT:PSS (Table 13.6). For the PV cells with an ITO/PEDOT:PSS/PAQX + P3OT/Al structure, the shunt resistance was at least

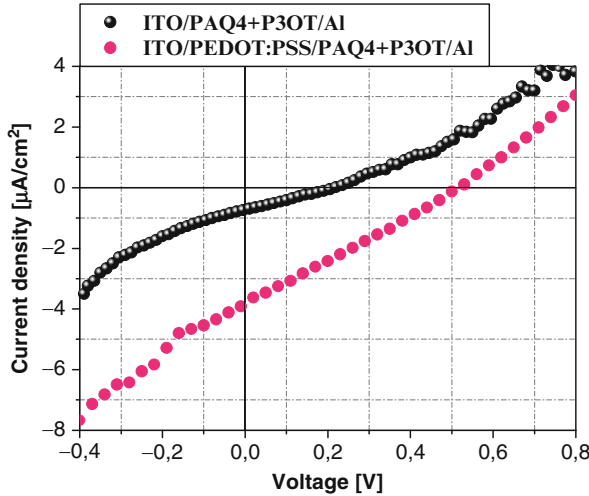


Fig. 13.32 Current–voltage characteristics for the PV cells with ITO/PAQ4 + P3OT/Al (PV8) and ITO/PEDOT:PSS/PAQ4 + P3OT/Al (NV8) architectures

Table 13.6 Serial and shunt resistances for the studied PV cells

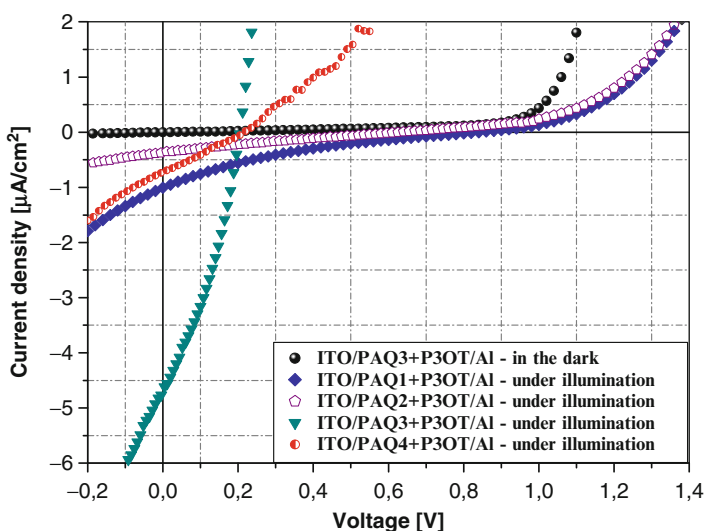
PV architecture	Indication	Serial resistance, R_S (M Ω)	Shunt resistance, R_{Sh} (M Ω)
ITO/PAQ1 + P3OT/Al	PV5	0.10	0.34
ITO/PEDOT:PSS/PAQ1 + P3OT/Al	NPV5	0.004	0.01
ITO/PAQ2 + P3OT/Al	PV6	0.17	0.09
ITO/PEDOT:PSS/PAQ2 + P3OT/Al	NPV6	0.008	0.07
ITO/PAQ3 + P3OT/Al	PV7	0.01	0.08
ITO/PEDOT:PSS/PAQ3 + P3OT/Al	NPV7	0.009	0.13
ITO/PAQ4 + P3OT/Al	PV8	0.08	0.32
ITO/PEDOT:PSS/PAQ4 + P3OT/Al	NPV8	0.009	0.12

one order higher with respect to the serial resistance. For such photocells, the carrier recombination may appear in places far from the places corresponding to charge carrier separation. For the NPV5–NPV8 the FF coefficient was increased with an increase of the difference between the serial and shunt resistances. For an excess of the shunt resistance with respect to the serial resistance, the corresponding FF was higher (Table 13.6). Such dependence was not observed for the PV cells with an ITO/PAQX + P3OT/Al architecture.

In Fig. 13.33 the current–voltage characteristics are presented for four photovoltaic cells, PV5–PV8, an ITO/PAQX + P3OT/Al/architecture. The analogous comparison was done for the $I(V)$ features for NPV5–NPV8 with an ITO/PEDOT:PSS/PAQX + P3OT/Al structure (Fig. 13.34). The $I(V)$ features were also done during the illumination with the dark $I(V)$ features for NPV6.

Table 13.7 Principal parameters obtained for the fabricated PV cells

Photovoltaic architecture	Short circuit current density, J_{SC} ($\mu\text{A cm}^{-2}$)	Open voltage, V_{OC} (V)	Filling factor, FF	Conversion efficiency, η (%)
ITO/PAQ1 + P3OT/Al	1.00	0.82	0.17	0.01
ITO/PEDOT:PSS/PAQ1 + P3OT/Al	27	1.16	0.15	0.37
ITO/PAQ2 + P3OT/Al	0.36	0.63	0.21	0.004
TO/PEDOT:PSS/PAQ2 + P3OT/Al	8	0.92	0.22	0.13
ITO/PAQ3 + P3OT/Al	4.67	0.20	0.53	0.04
ITO/PEDOT:PSS/PAQ3 + P3OT/Al	7.23	0.47	0.27	0.074
ITO/PAQ4 + P3OT/Al	0.72	0.22	0.15	0.006
ITO/PEDOT:PSS/PAQ4 + P3OT/Al	3.84	0.51	0.27	0.042

**Fig. 13.33** Comparison of C - V characteristics for the PV architecture ITO/PAQX + P3OT/Al during illumination and without the illuminations [3.3]

3.3 PV Cells with ITO/PAQX + PVK:TCNE/Al and ITO/PEDOT:PSS/PAQX + PVK:TCNE/Al Architectures

The next group of PV cells possess an ITO/PAQX + PVK:TCNE/Al architecture. The organic active layer is a mixture of 1*H*-pirazolo[3,4-*b*]quinoline (PAQX) (acceptor) embedded into the matrix PVC-TCNE (donor). The PAQX is used as an acceptor and PVK:TCNE as a donor. Comparing with the former studies, in this case the donor chromophore is changed. This caused a shift of energy positions for the HOMO and LUMO levels for donors and acceptors, respectively.

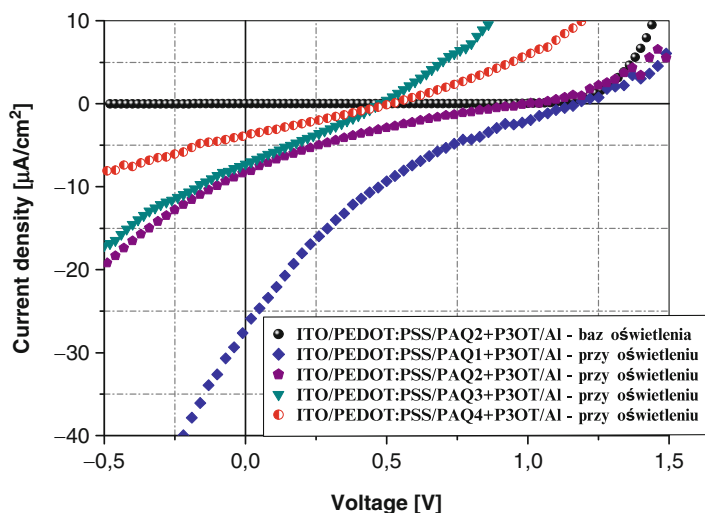


Fig. 13.34 Comparison of $C-V$ characteristics for the PV architecture ITO/PEDOT:PSS/PAQX + P3OT/Al during illumination and without the illumination

The LUMO level (-0.03 eV) for chromophore PAQ1 is situated between the LUMO level for PAQ4 (-0.01 eV) and LUMO level for PAQ2 (-0.07 eV). The lowest energy positions with respect to the mentioned molecule has the lowest LUMO energy (-0.12 eV) for PAQ3 chromophore (Table 13.2 and Fig. 13.21). Relative positions of the PAQX LUMO levels with respect to LUMO levels for the polymer matrix influence the junction between the donor and acceptor and the related exciton dissociation related to charge carrier transport. The principal results are given in Figs. 13.35–13.38.

The PV cell with an ITO/PEDOT:PSS/PAQ4 + PVK:TCNE/Al architecture (NPV12) is characterized by the highest conversion power efficiency η (for such class of PV cells) which is equal to 0.44 %. The short circuit current density J_{SC} was $18.8 \mu\text{A cm}^{-2}$ [45], at an open circuit voltage of 0.96 V (Table 13.9). The organic active layer (OAL) was formed by a mixture of PAQ4 (3-phenyl-1,4-dimethyl-1*H*-pyrazolo[3,4-*b*]quinoline) in a PVK:TCNE matrix. For comparison the same PV cell without the additional PEDOT:PSS layer, possessed a power efficiency conversion $\eta = 0.15$ %. The short circuit current density J_{SC} for PV12 was $3 \mu\text{A cm}^{-2}$, at an open circuit voltage V_{OC} of 1.3 V (Table 13.9).

Tables 13.8 and 13.9 show the principal parameters for the PV cells with ITO/PAQX + PVK:TCNE/Al and ITO/PEDOT:PSS/PAQX + PVK:TCNE/Al architectures. The additional layer of PEDOT:PSS for PV cell ITO/PAQX + PVK:TCNE/Al favors an enhancement of J_{SC} .

For PV9, R_S was higher than R_{Sh} of the remaining PV cell from this series (PV10–PV12 and NPV9–NPV12). The serial resistance was at least one order higher with respect to the shunt resistance (Table 13.8). For such kind of PV cell the FF factors are given in Table 13.9. The highest FF filling factor was observed for PV12, for which the difference between the shunt and serial resistances was very huge: $R_{Sh} \gg R_S$.

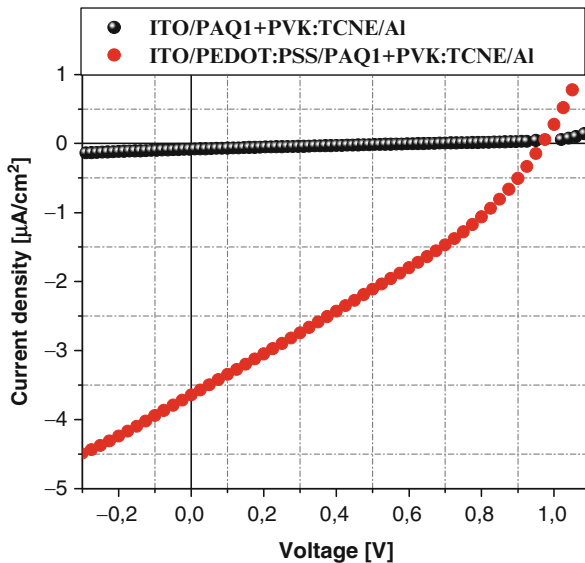


Fig. 13.35 *I-V* characteristics for PV cell with architecture ITO/PAQ1 + PVK:TCNE/AI (PV9) and ITO/PEDOT:PSS/PAQ1 + PVK:TCNE/AI (NPV9)

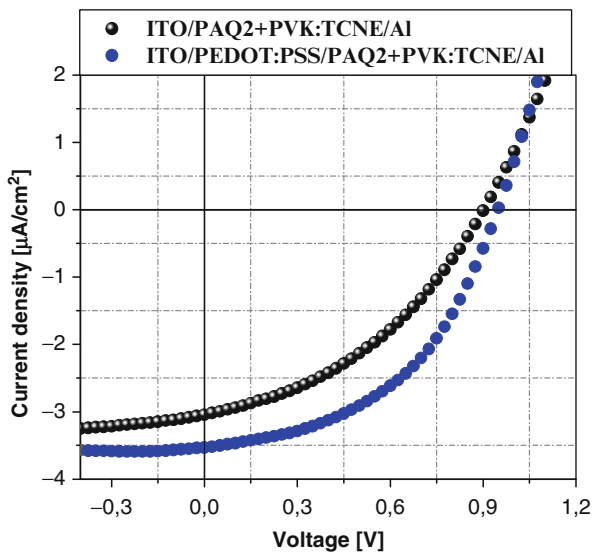


Fig. 13.36 *I-V* characteristics for PV cell with ITO/PAQ2 + PVK:TCNE/AI (PV10) and ITO/PEDOT:PSS/PAQ2 + PVK:TCNE/AI (NPV10) architecture

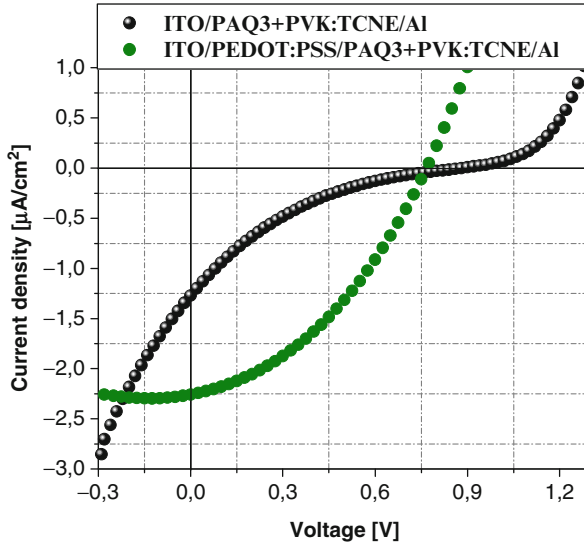


Fig. 13.37 I - V characteristics for PV cell with architecture ITO/PAQ3 + PVK:TCNE/Al (PV11) and ITO/PEDOT:PSS/PAQ3 + PVK:TCNE/Al (NPV11)

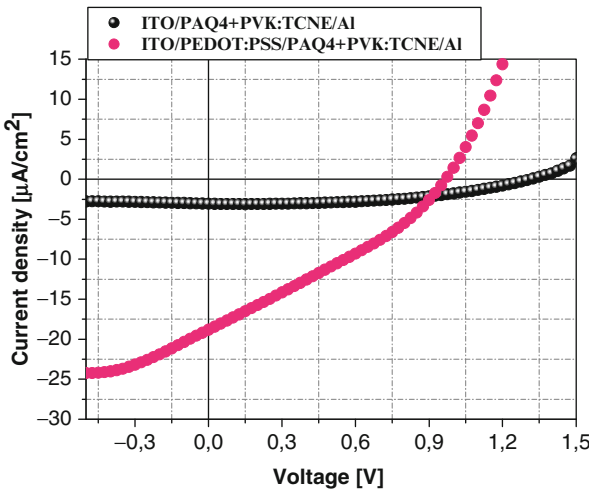


Fig. 13.38 I - V characteristics during the illumination for the PV cell with architecture: ITO/PAQ4 + PVK:TCNE/Al (PV12) and ITO/PEDOT:PSS/PAQ4 + PVK:TCNE/Al (NPV12) [45]

Figure 13.39 compares the dark $I(V)$ feature for ITO/PAQ4 + PVK:TCNE/Al with the $I(V)$ features for ITO/PAQX + PVK:TCNE/Al after illumination. The analogous couple of PV cell features for the cells with architecture ITO/PEDOT:PSS/PAQX + PVK:TCNE/Al is given in Fig. 13.40.

Table 13.8 Resistance parameters for the studied PV cells

Architecture of the PV cell	Notation	Serial resistance, R_S (M Ω)	Shunt resistance, R_{Sh} (M Ω)
ITO/PAQ1 + PVK:TCNE/Al	PV9	8.30	6.6
ITO/PEDOT:PSS/PAQ1 + PVK:TCNE/Al	NPV9	0.08	0.34
ITO/PAQ2 + PVK:TCNE/Al (PV10)	PV10	0.06	1.1
ITO/PEDOT:PSS/PAQ2 + PVK:TCNE/Al	NPV10	0.04	2.22
ITO/PAQ3 + PVK:TCNE/Al	PV11	0.05	0.28
ITO/PEDOT:PSS/PAQ3 + PVK:TCNE/Al	NPV11	0.06	1.12
ITO/PAQ4 + PVK:TCNE/Al	PV12	0.80	12.5
ITO/PEDOT:PSS/PAQ4 + PVK:TCNE/Al	NPV12	0.01	0.1

Table 13.9 Principal parameter of the studied PV cells

PV cell architecture	Short circuit current density, J_{SC} ($\mu\text{A cm}^{-2}$)	Open voltage circuit, V_{OC} (V)	Filling factor, FF	Power conversion efficiency, η (%)
ITO/PAQ1 + PVK:TCNE/Al	0.08	0.65	0.22	0.0009
ITO/PEDOT:PSS/PAQ1 + PVK: TCNE/Al	3.64	0.95	0.31	0.085
ITO/PAQ2 + PVK:TCNE/Al	3.00	0.89	0.39	0.084
ITO/PEDOT:PSS/PAQ2 + PVK: TCNE/Al	3.54	0.93	0.45	0.12
ITO/PAQ3 + PVK:TCNE/Al	1.30	0.86	0.16	0.014
ITO/PEDOT:PSS/PAQ3 + PVK: TCNE/Al	2.24	0.76	0.39	0.053
ITO/PAQ4 + PVK:TCNE/Al	3.10	1.30	0.50	0.15
ITO/PEDOT:PSS/PAQ4 + PVK: TCNE/Al	18.80	0.96	0.31	0.44

3.4 Photovoltaic Cells with Architecture ITO/Molx + P3OT/Al and ITO/PEDOT:PSS/Molx + P3OT/Al

The last group of the PV cells has ITO/Molx + P3OT/Al and ITO/PEDOT:PSS/Molx + P3OT/Al architectures. The PV architecture was formed by a mixture of 4-aryloksy-1H-pirazolo[3,4-b]chinolin derivative (acceptor) and (Molx) poly (3-oktylotiofenu) (P3OT) (donor) (Molx). The theoretical quantum chemical simulations of HOMO and LUMO energy positions for Molx are presented in Table 13.3. The energy positions for HOMO and LUMO levels for poly (3-decylothiophene) with respect to energy positions of the HOMO levels for the given pyrazolochinoline influence the separation of excitons on the carrier charge transport between the donor and acceptor.

The LUMO level for Mol1chromohore is equal to -0.27 eV and is situated between the Mol3 LUMO level (-0.25 eV) and the Mol5 LUMO level (-0.30 eV). Above the Mol3 LUMO level there is Mol4 LUMO level (-0.16 eV). The lowest

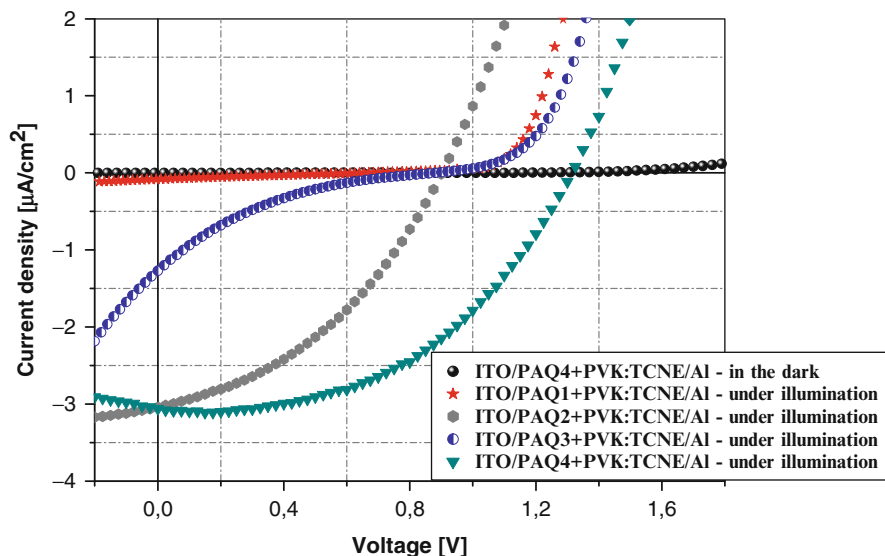


Fig. 13.39 Comparison of the I - V dependences for the PV ITO/PAQX + PVK:TCNE/Al cells during and without the illumination

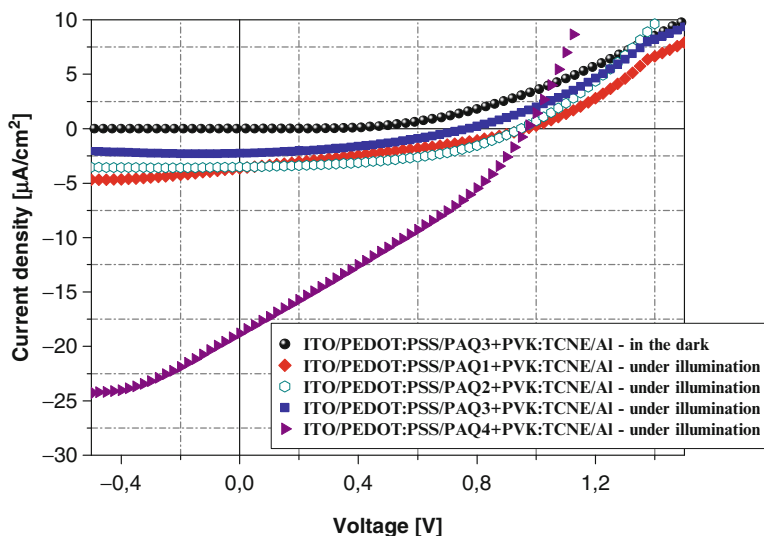


Fig. 13.40 Comparison of the I - V dependences for the PV ITO/PEDOT:PSS/PAQX + PVK:TCNE/Al during and without the illumination

energy position exists for Mol2 (-0.57 eV) (Table 13.3 and Fig. 13.22). The corresponding results with the addition of the PEDOT:PSS layer are given in Fig. 13.41, 13.42, 13.43, 13.44, and 13.45. A better power conversion efficiency (up to 0.42 %) was achieved for PV cell with an ITO/PEDOT:PSS/Mol2 + P3OT/Al

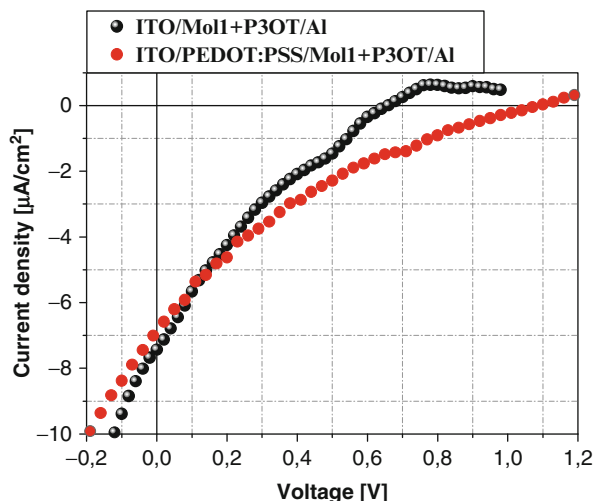


Fig. 13.41 Illuminated I - V dependence for the PV architecture ITO/Mol1 + P3OT/Al (PV13) and ITO/PEDOT:PSS/ Mol1 + P3OT/Al (NPV13)

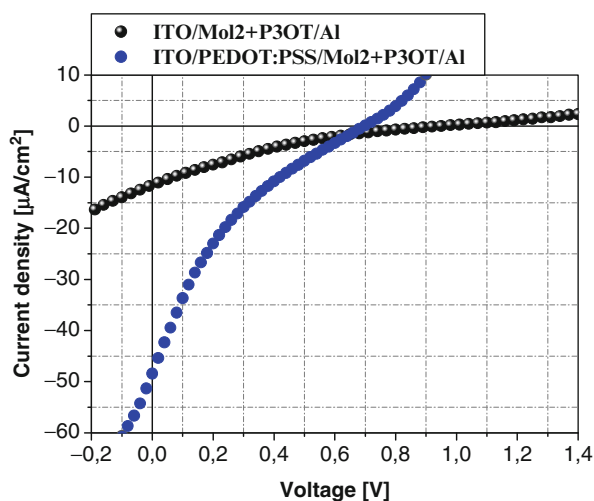


Fig. 13.42 I - V characteristics during illumination of the PV cell with an architecture ITO/Mol2 + P3OT/Al (PV14) and ITO/PEDOT:PSS/ Mol2 + P3OT/Al (NPV14)

architecture (NPV14). The current density J_{SC} for NPV14 was equal to $47 \mu\text{A cm}^{-2}$, at an open circuit voltage equal to 0.7 V (Table 13.11). The active layer was formed by a mixture of 4-(1-Naftyloksy)-1-phenyl-3-mehyl-1*H*-pyrazolo-[3,4-*b*]chonoline (Mol2) in P3OT matrix. For the PV cell with the same PV14 active layer but without the PEDOT:PSS layer situated between the ITO and a mixture of Mol2 + P3OT, the

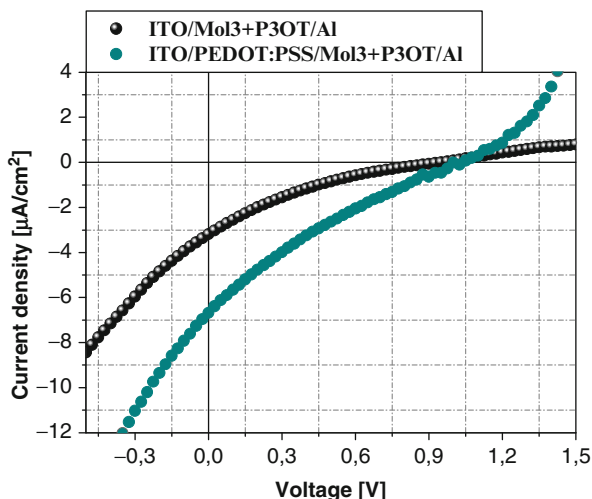


Fig. 13.43 I - V characteristics during the illumination of the PV cell with an architecture ITO/Mol3 + P3OT/Al (PV15) and ITO/PEDOT:PSS/ Mol3 + P3OT/Al (NV15)

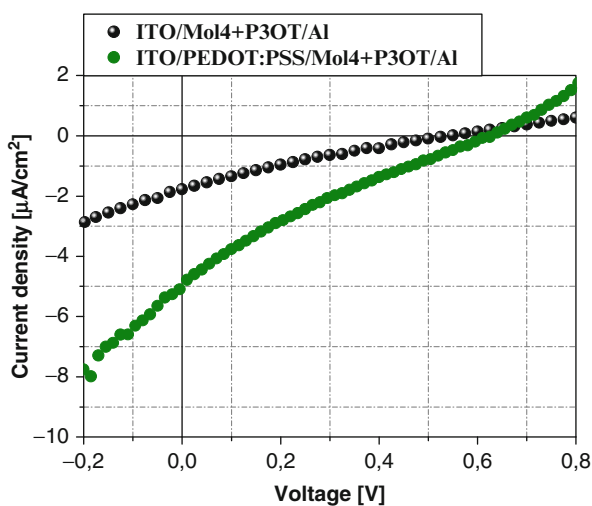


Fig. 13.44 I - V features for the PV cell with architecture ITO/Mol4 + P3OT/Al (PV16) and ITO/PEDOT:PSS/ Mol4 + P3OT/Al (NPV16)

power conversion efficiency was equal to about 0.14 %. For PV14 (ITO/Mol2 + P3OT/Al) the short circuit current density J_{SC} was equal to $11.5 \mu\text{A cm}^{-2}$, at an open circuit voltage of 0.89 V (Table 13.11). For the ITO/PEDOT:PSS/Mol4 + P3OT/Al architecture (NPV16), the obtained conversion efficiency η was 0.30 % at a short circuit current density of $17.5 \mu\text{A cm}^{-2}$. The active organic layer was formed by a

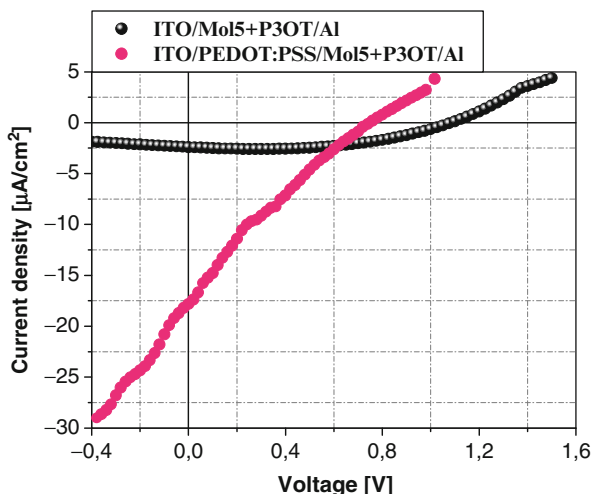


Fig. 13.45 Current–voltage characteristics during the illumination of the PV cell with architecture ITO/Mol5 + P3OT/Al (PV17) and ITO/PEDOT:PSS/ Mol5 + P3OT/Al (NPV17)

Table 13.10 Serial and shunt resistances of PV cells with different architecture

PV architecture	Indication	Serial resistance, R_S (M Ω)	Shunt resistance, R_{Sh} (M Ω)
ITO/Mol1 + P3OT/Al (PV13)	PV13	2.27	0.07
ITO/PEDOT:PSS/Mol1 + P3OT/Al (NPV13)	NPV13	0.07	0.07
ITO/Mol2 + P3OT/Al (PV14)	PV14	0.08	0.04
ITO/PEDOT:PSS/Mol2 + P3OT/Al (NPV14)	NPV14	0.002	0.01
ITO/Mol3 + P3OT/Al (PV15)	PV15	1.10	0.14
ITO/PEDOT:PSS/ Mol3 + P3OT/Al (NPV15)	NPV15	0.07	0.05
ITO/Mol4 + P3OT/Al (PV16)	PV16	0.13	0.24
ITO/PEDOT:PSS/ Mol4 + P3OT/Al (NPV16)	NPV16	0.03	0.06
ITO/Mol5 + P3OT/Al (PV17)	PV17	0.13	0.90
ITO/PEDOT:PSS/ Mol5 + P3OT/Al (NPV17)	NPV17	0.048	0.10

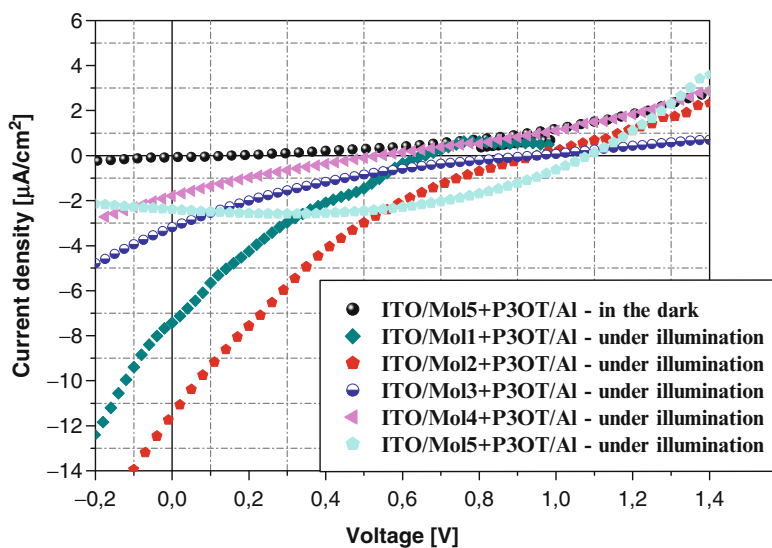
mixture of 4-(2-*tert*-Butylphenoksy)-1-phenyl-3-methyl-1*H*-pyrazolo[3,4-*b*] chinolina (Mol4) and P3OT. PV cell, PV16, with the same active layer, however without the additional PEDOT:PSS layer, had an efficiency η equal to 0.11 % (Table 13.11).

All the parameters characterizing the PV cells with the ITO/Mol x + P3OT/Al and ITO/PEDOT:PSS/Mol x + P3OT/Al architecture are presented in Tables 13.10 and 13.11.

Mol x has the lowest LUMO energy level of the chromophores (Fig. 13.22). The PV cell which is based on the Mol2 has the highest power efficiency for this group. The efficiency for the PV cell based on Mol5 is comparable to that of Mol2. We have established that with the increase of the energy positions of the LUMO level

Table 13.11 Principal parameters describing the PV effects for the different PV architecture of cells [46]

PV architecture	Short current density, J_{SC} ($\mu\text{A cm}^{-2}$)	Open circuit voltage, V_{OC} (V)	Filling factor, FF (%)	Power conversion efficiency, η (%)
ITO/Mol1 + P3OT/Al	7.34	0.67	0.19	0.07
ITO/PEDOT:PSS/Mol1 + P3OT/Al	7.0	1.00	0.18	0.10
ITO/Mol2 + P3OT/Al	11.5	0.89	0.17	0.14
ITO/PEDOT:PSS/Mol2 + P3OT/Al	47	0.7	0.16	0.42
ITO/Mol3 + P3OT/Al	3.15	0.84	0.20	0.04
ITO/PEDOT:PSS/Mol3 + P3OT/Al	6.7	1.00	0.17	0.10
ITO/Mol4 + P3OT/Al	1.7	0.54	0.24	0.02
ITO/PEDOT:PSS/Mol4 + P3OT/Al	5.0	0.62	0.21	0.053
ITO/Mol5 + P3OT/Al	2.4	1.07	0.54	0.11
ITO/PEDOT:PSS/Mol5 + P3OT/Al	17.5	0.75	0.21	0.30

**Fig. 13.46** Comparison of the I - V for the PV cell with architecture ITO/Molx + P3OT/Al with and without the illumination [46]

(Mol1, Mol3, and Mol4), the output PV efficiency should decrease (Fig. 13.22). It may be caused by an existence of the UMO level for P3OT compared to the pyrazolochinoline defining the exciton dissociation and carrier transport.

The incorporation of additional layer of PEDOT:PSS to ITO/Molx + P3OT/Al have caused an enhancement of the conversion efficiency and on the short circuit current density (see Table 13.11) (Figs. 13.46 and 13.47).

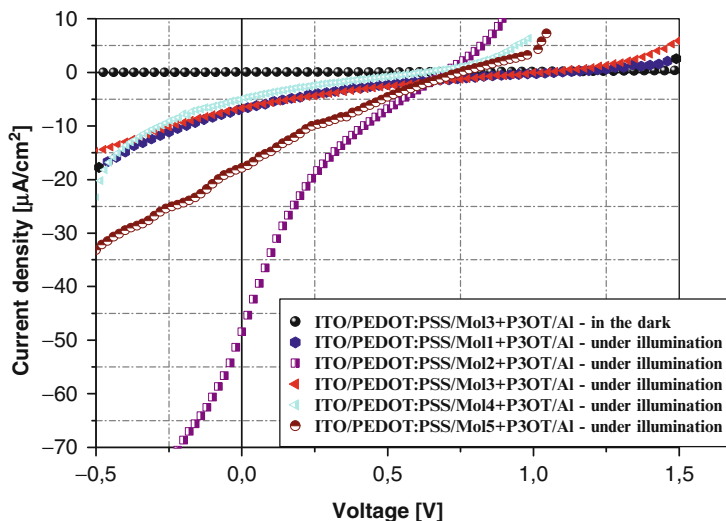


Fig. 13.47 Comparison of the I - V for the PV cell with architecture ITO/PEDOT:PSS/Mol x + P3OT/Al during and without the illumination

From the quantum chemical calculations performed (Table 13.3) one can conclude that the PV cells possessing the Mol2 should have the better conversion efficiency with respect to power conversion. It is a consequence of relative energy positions for the LUMO Mol x levels (Fig. 13.22) and working output energy for aluminum—Al (-4.3 eV). From the LUMO level for chromophore Mol2 (-0.57 eV), the charge carriers are transferred to the Al layer and afterwards they flow to the external electric circuit. For chromophores Mol5 (-0.30 eV), Mol1 (-0.27 eV), and Mol3 (-0.25 eV), where the LUMO levels are very close to each other, the carrier transport to Al is commensurable. The Mol4 LUMO level (-0.16 eV) is situated above the LUMO levels of the remaining chromophores (Mol1, Mol2, Mol3, Mol5). The charge transfer from the Mol4LUMO level to Al should be more complicated with respect to the rest of molecules. This is in agreement with the results from the theoretical simulations. A better experimental efficiency with respect to light power was achieved for the PV cell-containing Mol1 (Table 13.11).

4 TiO₂ Nanoporous Materials for Photovoltaics

4.1 TiO₂ in Solar Cells

After the pioneering works of Gratzel and coworkers [47, 48], there were a lot of reports devoted to the use of TiO₂ as a host for dye sensitization [49]. Such kind of dye-sensitized PV cells allow efficiencies of $\sim 10\%$ and nanocrystalline TiO₂ plays a crucial role in attaining such an efficiency. TiO₂ is a wide band gap semiconductor

and it should be sensitized by organic chromophore (dye) possessing a relatively high absorption in the wavelengths of the visible range in EM spectra. Chromophores normally only absorb a small part of the incident sunlight (about 1 %). With TiO_2 , an increase in light absorption is brought about because of an injection of photoexcited electrons into the band gap with the simultaneous formation of oxidized dye molecules on the TiO_2 surface. One way to enhance the output of PV devices is to restrain the quick recombination after photoexcitation. Here the main efforts were devoted to the exploration of the recombination mechanism for TiO_2 NP.

One of the principal roles is played here by electron transfer process at the transparent tin oxide substrate–electrolyte interfaces. During the recombination process, photoinjected electrons are transported to the semiconductor surfaces and may be transferred to empty electrolyte levels through intermediate trapping levels.

In this case, great attention should be paid to the nanoparticle surface states from the so-called quasi-Fermi level surface [50]. It was shown that electronic states with different kinetic features do not achieve a quasi-Fermi equilibrium level with the carriers inside the nanoparticles. Such Fermi levels allow kinetic trapping and de-trapping processes in the studied nanoparticles. Finally these processes define the recombination kinetics of the photocarriers and first of all their recombination efficiency.

Usually the experimental confirmation of the dominating role of the process of the radiation recombination dynamics in size-controlled TiO_2 requires sophisticated studies of fluorescence spectra [51]. To obtain the necessary confirmation, usually picosecond time-resolved experiments, as a function of the excitation density and the nanoparticle size, are necessary. The recombination dynamics is defined by two main processes related to the direct excitation of the trapping levels and kinetics of the de-trapping processes due to non-radiative surface states.

Another possibility to control the surface NP trapping levels in the TiO_2 is based on the photocurrent transient measurements applying low power pulsed laser under continuous illumination of bias light [52]. The values of recombination times are evaluated by intensity-modulated photovoltage method. Following such studies it was established that donor–acceptor path length increases and time τ decreases with the increase of the NP particle sizes up to 32 nm. The origin of such increase is assumed to be a consequence of decreasing film surface area, where exist the charged trapping states related to the features of grain boundaries. Additionally the existence of surface trapping levels was detected by photoluminescence [53].

Following the time-integrated photoluminescence spectra and picosecond time-resolved experiments as a function of the nanoparticle size, excitation density, and temperature, it was found that photoluminescence is caused both by a bulk and a surface radiative recombination, together with distinct spectral shifts. Moreover, the intrinsic defect nature of the emission is shown, providing a quantitative evaluation of volume and surface contributions.

Due to the discovered features of the interface trapping levels for the TiO_2 dye-sensitized solar cell (DSSC), it has attracted wide attention for the potential

application of converting sunlight into electricity. Organic dyes blended with TiO₂ nanoparticles (NPs) may be considered as important photocell materials, especially in the visible spectral range. The functional materials are organized as a sandwiched type to undergo photon-induced current process. Following photoexcitation, the embedded organic dye molecules may favor electron transfer (ET) to the TiO₂ conduction band. The injected electrons are moved through the semiconductor material and the external load to the counter electrode. At this electrode, the corresponding dye is reduced by electron donors and then the circuit is complete. The electron motion kinetics for typical dye/TiO₂ composites is varied from femtosecond to several hundred picoseconds. The injected electrons are situated in either sub-band or the surface trapping states of the TiO₂ semiconductor. A portion of the electrons, thermally de-trapped from the reduced semiconductor, may possibly undergo some recombination with corresponding dyes.

4.1.1 Technology of TiO₂ Films

Worldwide industrial development, along with its benefits, has resulted in tremendously increased consumption of nonrenewable energy resources, and in the generation and accumulation of waste by-products at a devastating rate. In order to reduce fossil fuel consumption, limit atmospheric pollution, and avoid catastrophic global climate changes in the near future, countries around the world are looking to tap into solar energy which is a principal renewable energy resource. One promising and widely studied technology that directly harnesses the energy of the sun is based on photovoltaic devices. Although silicon-based photovoltaic technology yield high efficiency, recent development of DSSCs (Dye-Sensitized Solar Cells) opened up applications of solar energy for small electronic devices. DSSCs are usually based on nanocrystalline (NC) anatase TiO₂. Since then various modifications have been carried out to construct an energy efficient photovoltaic device (PV). In this chapter, we emphasize on the application of NC TiO₂ as an active component in the construction of doped organic solar cells. In general, applications of TiO₂ are numerous, including photocatalytic, photovoltaic, electrochromic, photochromic, electroluminescence devices and sensors. In 1964, Kato et al. [54] published their work on the photocatalytic oxidation of tetralin (1,2,3,4 tetrahydronaphthalene) by a TiO₂ suspension, which was followed by McLintock et al. [55] investigating the photocatalytic oxidation of ethylene and propylene in the presence of oxygen adsorbed on TiO₂. However, the most important discovery that extensively promoted the field of photocatalysis was the "Honda-Fujishima Effect" first described by Fujishima and Honda in 1972 [56]. This well-known chemical phenomenon involves electrolysis of water, which is related to photocatalysis. Photoirradiation of a TiO₂ (rutile) single crystal electrode immersed in an aqueous electrolyte solution induced the evolution of oxygen from the TiO₂ electrode and the evolution of hydrogen from a platinum counter electrode when an anodic bias was applied to the TiO₂ working electrode. The photocatalytic properties of TiO₂ inspired several other applications which utilize the

photoresponse of TiO_2 . In 1991, O'Regan and Grätzel [57–59] reported an efficient solar cell-containing nanosized TiO_2 particles coated with organic chromophore groups (dyes) active under visible light termed as DSSCs. Since then, dye-sensitized TiO_2 has received much attention in photovoltaic applications. The high refractive index of TiO_2 results in efficient diffuse scattering of the light inside the porous photoelectrode, which significantly enhances light absorption [57–59] and the photovoltaic response. The invention of DSSCs led to the development of photoelectrochromic device, in which the photovoltaic property of dye-sensitized TiO_2 was merged with the inorganic electrochromic device [60, 61]. These applications were made possible due to the crystalline nature, crystallite size, and optical properties of TiO_2 . Next section briefly describes the crystal structures of TiO_2 and their electronic properties, which eventually govern their photovoltaic properties.



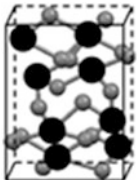
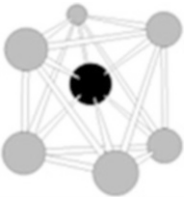
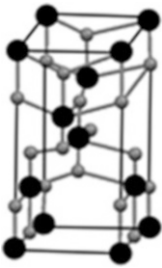
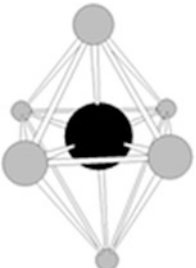
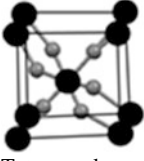

4.2 Crystal Structures of TiO_2 and Their Electronic Properties

TiO_2 belongs to the family of transition metal oxides and it is known to exist in various polymorphs. Vegard reported the original structural studies on anatase and rutile polymorphs in 1916 [62]. During the same year, Pauling et al. reported the first structural studies on brookite polymorphs [63]. There are four commonly known polymorphs of TiO_2 found in nature: anatase (tetragonal), brookite (orthorhombic), rutile (tetragonal), and TiO_2 (B) (monoclinic) [64]. Besides these polymorphs, two additional high-pressure forms have been synthesized from the rutile phase. These are TiO_2 (II) [65] with a PbO_2 structure and TiO_2 (H) [66] with a hollandite structure. In this chapter, only the crystal structures and properties of the rutile, anatase, and brookite polymorphs are considered (Table 13.12) [67–69].

Several reports have appeared providing detailed and accurate structural parameters of these three important polymorphs of TiO_2 [67, 70–72]. In general, the structure of brookite was found to be orthorhombic, and that of anatase, and rutile, was identified as tetragonal. Although, they belong to different space groups, the structure of these polymorphs can be described by a fundamental representative octahedron composed of oxygen ions in the vertices, and a titanium atom near the center [73]. Table 13.12 presents the unit cell parameters, space group, unit cell structure and the representative octahedron of three TiO_2 polymorphs.

Brookite: Brookite TiO_2 belongs to the orthorhombic crystal system (Table 13.12). Its unit cell is constituted by octahedra, in which the titanium atom is located near the center, with oxygen atoms on the vertices. The Ti–O and O–O bond lengths in the octahedron are all different, which leads to a distorted octahedron. The Ti–O bond length varies from 0.183 to 0.230 nm. Two of these bonds have shortest distances of 0.183 and 0.187 nm, which represent strong interactions. The brookite crystal structure is formed when the octahedra share three edges [73]. It has tunnels

Table 13.12 Space group, lattice parameters, and density of three TiO₂ polymorphs (brookite, anatase, and rutile) along with their common unit cell and octahedron representation (adapted from Bokhimi et al. [18])

Titania polymorph	Space group and lattice parameters (a, b, c in Å)	Unit cell	Octahedron Representation of local order
			
Brookite Density 3.99 g cm ⁻¹	Pbca $a = 9.184$ $b = 5.447$ $c = 5.154$	 Orthorhombic	
Anatase Density 3.79 g cm ⁻¹	I4 ₁ /amd $a = b = 3.784$ $c = 9.515$	 Tetragonal	
Rutile Density 4.13 g cm ⁻¹	P4 ₂ /mnm $a = b = 4.5936$ $c = 2.9587$	 Tetragonal	

along the c axis, which can incorporate, small cations like hydrogen and lithium. Although such a structure is interesting, very few reports exist which present the availability or synthesis of pure brookite [73].

Anatase: It is one of the most widely studied polymorphs of TiO₂. Table 13.12 shows the structural parameters, unit cell structures, and representative octahedron of this polymorph. It has a tetragonal structure, but the distortion of the TiO₆ octahedron is slightly larger when compared to the rutile phase [69, 71]. Muscat et al. [72] found that the anatase phase is more stable than the rutile at 0 K, but the energy difference between these two phases is small ($\sim 2\text{--}10$ kJ mol⁻¹). When compared with brookite, anatase has higher unit cell symmetry since there are only five different bond lengths in its representative octahedron. The bond lengths between oxygen atoms in the equatorial plane are the same, and the shortest among the O–O bonds is 0.280 nm. These bonds form four edges that are shared

with other octahedra, and this sharing defines the crystal structure of anatase. Also, the equatorial Ti–O bonds are of the same length (0.194 nm). This clearly shows the higher symmetry in anatase and leads to tunnels not only along the c direction as in brookite but also along the $[0\ 1\ 0]$ and $[1\ 0\ 0]$ directions. This makes the anatase crystal structure extremely porous and facilitates the trapping of host of ions and molecules, such as Li, Ru(bi pyridine), etc. [73].

Rutile: Among the polymorphs of TiO_2 presented in Table 13.12, the highest symmetric structure is possessed by Rutile. It has a tetragonal structure and contains six atoms per unit cell with the TiO_6 octahedron slightly distorted [70, 74, 75]. Unlike brookite and anatase, the crystal structure of rutile is defined by the sharing of two edges and two vertices of the octahedron. This leads to a higher symmetry of the crystal structure. Although a tunnel with square cross section is formed, incorporation of foreign atoms can only occur when the rutile is to be formed. If foreign atoms occupy the available sites in the tunnel during the first stage of the synthesis, the probability for the formation of anatase or brookite is high [73]. The rutile phase is stable at most temperatures and pressures up to 60 kbar, where TiO_2 (II) becomes the thermodynamically favored phase [76]. Zhang et al. [77] found that anatase and brookite structures transformed to the rutile phase after reaching a certain particle size, with the rutile phase becoming more stable than anatase for particle sizes greater than 14 nm. Once the rutile phase formed, it grew much faster than anatase.

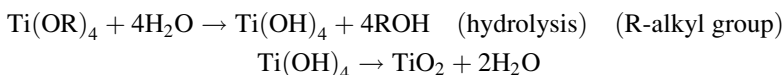
TiO_2 is a large band semiconductor, with band gaps of 3.2, 3.02, and 2.96 eV for the anatase, rutile, and brookite, respectively [78]. The valence band of TiO_2 is composed of the 2p orbitals of oxygen hybridized with the 3d orbitals of titanium, while the conduction band is only the 3d orbitals of titanium [79]. When TiO_2 is exposed to light, electrons in the valence band are excited to the conduction band leaving behind holes (h^+). The excited electrons (\bar{e}) in the conduction band are now in a purely 3d state and because of dissimilar parity, the transition probability of \bar{e} to the valence band decreases, leading to a reduction in the probability of \bar{e}/h^+ recombination. The anatase structure is preferred over other polymorphs for solar cell applications because of its higher electron mobility, low dielectric constant, and lower density [64, 78, 79].

4.3 Background on the Synthesis of Nanocrystalline TiO_2 Powder

A variety of techniques have been used for the preparation of TiO_2 nanoparticles, such as sol–gel, hydrothermal, solvothermal, and direct oxidation [74]. Among those, sol–gel remains a preferred method as it is a low temperature, cost effective process, which allows the application of structure directing agents to synthesize porous TiO_2 products.

Usually the process involves the use of molecular precursors, mainly titanium alkoxides. In general, titanium tetra-etoxyde ($\text{Ti}(\text{OEt})_4$), titanium tetra-isopropoxide

(Ti(OiPr)₄), or titanium tetra-*n*-butoxide (Ti(OnBu)₄) are used as starting precursor materials and are dissolved in alcohols. The subsequent steps involve hydrolysis of a titanium precursor, which normally proceeds via an acid-catalyzed hydrolysis of titanium (IV) alkoxide followed by condensation [80–84].



The development of Ti–O–Ti chains is favored with low content of water, low hydrolysis rates, and excess titanium alkoxide in the reaction mixture. The formation of Ti(OH)₄ is favored with high hydrolysis rates for a medium amount of water. The presence of a large quantity of Ti–OH and insufficient development of three-dimensional polymeric skeletons lead to loosely packed first-order particles. Polymeric Ti–O–Ti chains are developed in the presence of an excess of water. Closely packed first-order particles are yielded via a three-dimensionally developed gel skeleton [85]. The most common way to impart crystallinity of thus formed polymeric gel is calcination at temperatures above 400 °C. An obvious disadvantage of this high temperature treatment is that the prepared TiO₂ particles have reduced surface hydroxyl groups, increased particle size, and decreased surface area. From this point of view, a low temperature synthetic route towards NC-TiO₂ is of high demand. In this chapter, we describe a template mediated sol–gel method, developed in our laboratory, to synthesize NC TiO₂ at low temperature and its subsequent annealing at high temperatures [86, 87]. A sol was prepared from Ti(O^{*n*}Bu)₄ in ethanol in the presence of polyethylene glycol (PEG) as a templating agent yielding NC anatase TiO₂ films when treated in hot water at temperatures below 90 °C, under atmospheric pressure for 1 h [86, 87]. It needs to be noted that PEG had been used by several researchers, for the formation of mesoporous TiO₂. For example, Kajihara et al. and Bu et al. investigated the macroscopic morphology and mechanism of macroscopic domain formation in TiO₂ films from the system containing PEG [88–90]. Stathatos et al. found that size of TiO₂ nanoparticles, film thickness, roughness, and fractality of the film surface can be controlled by choosing the length of the PEG chain [91]. Further, in these reports, the crystallization of the TiO₂ films required a postdeposition thermal treatment at relatively high temperatures (400 °C or above) and PEG has been envisaged only as a templating agent in forming porous films.

In this context, our template mediated sol–gel methodology mentioned earlier, gains significance which prompted us to investigate: (i) the chemical reactivity of the PEG templating agent with the precursor Ti(O^{*n*}Bu)₄; (ii) the isolation and characterization of the titanium-PEG hybrid materials resulting from reaction i; and (iii) the mechanistic aspects involved in the formation of anatase NC-TiO₂ by subjecting titanium-PEG hybrid materials to hot water (~90 °C) under atmospheric pressure. Our detailed investigation on the role of PEG has been published elsewhere [86]. In the subsequent sections, we present a summary of the important results of our investigation in obtaining porous NC TiO₂ powders for application in PV devices.

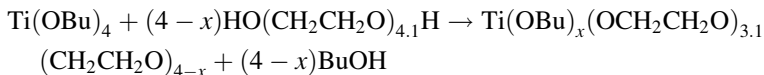
4.4 Templated Sol–Gel Process: Interaction of Reactants

In our sol–gel process, along with the titanium alkoxide precursor, ethanol was used as a solvent, and PEG 200 was the templating agent. We followed the interactions of the reactants and the main results are presented below. Although we are presenting the case for titanium butoxide, these processes have been tested and proved by us for other titanium alkoxides such as titanium ethoxide and titanium isopropoxide.

The interaction of $Ti(O^nBu)_4$ with ethanol: As mentioned earlier, any sol–gel process involves the interaction of precursors and the solvents. For example, we have shown that if $Ti(O^nBu)_4$ was used as the precursor in ethanol, an exchange reaction takes place between them. This was observed by a systematic precursor–solvent concentration controlled reaction and followed by Raman spectroscopy. This is a *trans* esterification reaction, in which the butoxy groups of $Ti(O^nBu)_4$ undergoes exchange with ethoxy group of EtOH.



The interaction of $Ti(O^nBu)_4$ with PEG200: In our sol–gel process, we used PEG 200 as a templating agent. The interaction of PEG 200 with $Ti(O^nBu)_4$ results in the formation of *n*-butanol, which suggests that a nucleophilic substitution reaction takes place between $Ti(O^nBu)_4$ and PEG 200. The hydroxyls of PEG 200 chains coordinate titanium with the subsequent elimination of *n*-butanol as shown in the following equation.



Though both ethanol and PEG 200 react with butoxy groups of $Ti(O^nBu)_4$, both bridging and terminal butoxy groups are exchanged with ethanol, whereas with PEG 200, the reaction takes place systematically first at terminal butoxy positions up to 1:3 molar ratio of $Ti(O^nBu)_4$ and PEG 200 and then with the bridging butoxy groups. In the sol, ethanol and PEG 200 are present along with $Ti(O^nBu)_4$, hence we anticipate that at a given moment, there is a competition between ethanol and PEG 200 to react with $Ti(O^nBu)_4$ to substitute the butoxy groups.

When $Ti(O^nBu)_4$ was reacted with an equimolar quantity of PEG 200 in EtOH, a hybrid material was obtained and it was found to be insoluble in most organic solvents. The Raman spectra of titanium-PEG 200 hybrid material implies that oxygen atoms of polyether chain in PEG 200 interact with the titanium center in the titanium-PEG 200 hybrid materials. Further support for this observation comes from the NMR data. Figure 13.48 shows the solid-state 1H MAS NMR spectra of titanium-PEG 200 hybrid material. In Fig. 13.48, the butoxy ligands of the titanium-PEG 200 hybrid material exhibit a singlet around 0.85 ppm for CH_3 protons, the CH_2 protons resonate around 1.29 and 1.42 ppm, whereas the OCH_2 protons are

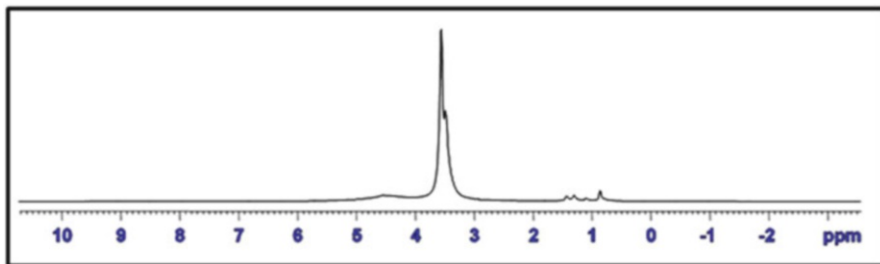


Fig. 13.48 ¹H NMR spectra and structures of Ti-PEG 200 hybrid material

deshielded and appear as a broad singlet around 4.55 ppm. Along with the butoxy ligands, the titanium-PEG 200 hybrid material has ethoxy ligands as is evidenced from NMR. The CH₃ protons of the ethoxy ligands appear as a singlet at 1.09 ppm, whereas its OCH₂ protons appear along with those of the butoxy ligands at 4.54 ppm. The OCH₂ protons of the ethoxy and butoxy ligands in the titanium-PEG 200 hybrid material are deshielded compared to those in pure ethanol and butanol due to the binding of the oxygen of the OCH₂ moieties with titanium centers. It is interesting to note that the ¹H MAS NMR spectrum exhibits two more broad peaks at 3.55 and 3.48 ppm for the OCH₂ protons of the polyether chain of PEG 200. This could be due to the interaction of PEG 200 with the titanium centers in the compound as described in our earlier report [90]. When the hydroxyl (OH) groups of PEG 200 undergo nucleophilic substitution reaction with pure Ti(OⁿBu)₄, the two terminal OCH₂ moieties of the polyether chain of PEG 200 are bound to titanium centers in such a way that, one terminal OCH₂ moiety binds with titanium center covalently and the other one bridges two titanium centers. The rest of the OCH₂ moieties of the polyether chain of PEG 200 are present in between the terminal OCH₂ moieties. Comparison of the spectrum of titanium-PEG 200 hybrid material with the spectrum of pure PEG 200 shows that all three have bands that are similar to those of the polyether chain of PEG 200. This suggests that the conformation of polyether chains in titanium-PEG 200 hybrid material is similar to that in pure PEG 200.

The molecular weight of titanium-PEG 200 hybrid material was determined by MALDI-TOF mass spectrometry as shown in Fig. 13.49. Polymeric pattern were observed for titanium-PEG 200 hybrid material, with the molecular weights in the range of 600–1,700 Da with the repeat mass of 143 in the matrix TIA (*trans*-3-indole acrylic acid). Thus the titanium-PEG 200 hybrid material is found to be a polymer. In hybrid material, the Ti centers are bridged by PEG 200. Also, the spectrum shows the possibility of having a mixture of polymers as more than one fragmentation pattern is seen. This is in good agreement with the NMR spectral data. Thus Raman, IR, NMR, and MALDI-TOF studies show that the hybrid material has covalently bound PEG with titanium center of Ti(OⁿBu)₄ evidencing the chemical interaction of PEG with Ti(OⁿBu)₄.

The synthesis and X-ray structure of titanium ethylene glycolate complex was reported by Wang et al. The staggered arrangement of Ti–O skeleton in ethylene

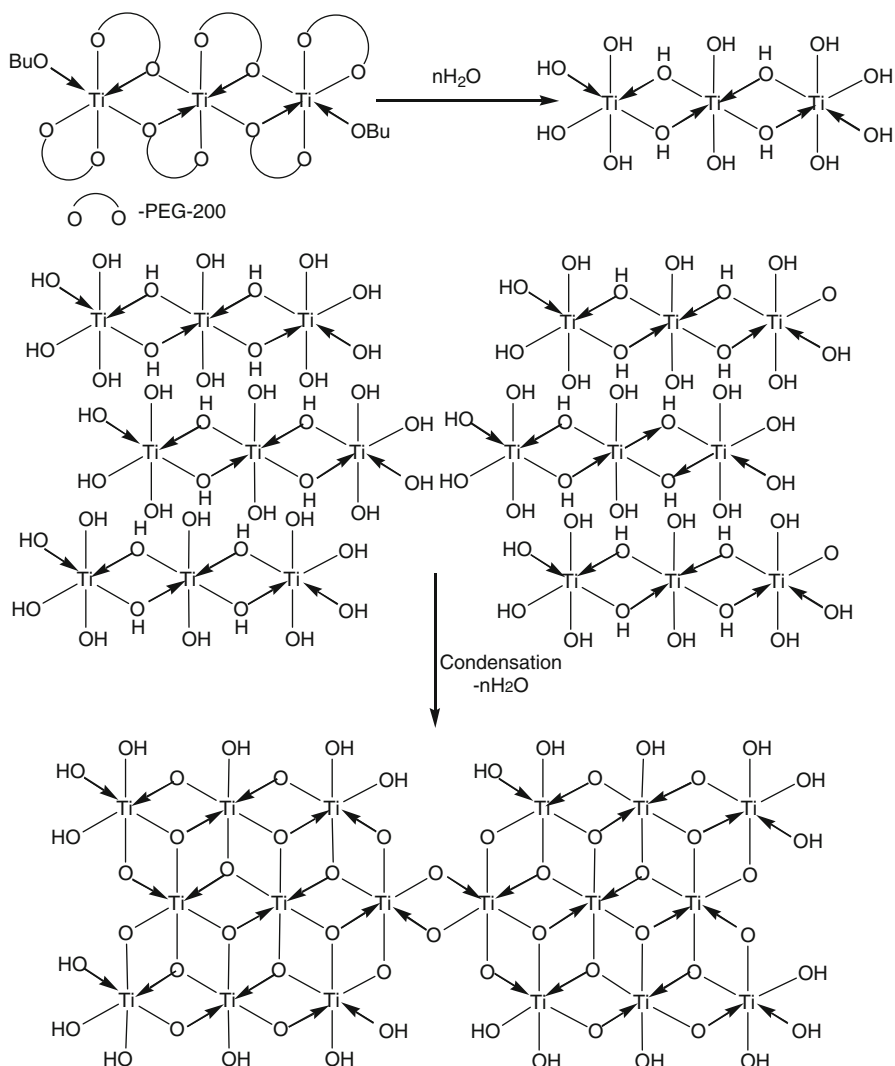
PEG 200. Thus upon hot water treatment of the polymer obtained from PEG 200 with Ti(O^{*n*}Bu)₄, PEG 200 leaches out, leaving behind anatase NC-TiO₂.

The X-ray structure of one-dimensional titanium glycolate single crystal [Ti(OCH₂CH₂O)₂] synthesized by the reaction of Ti(O^{*n*}Bu)₄ with ethylene glycol in the presence of *n*-butylamine under hydrothermal conditions at 160–170 °C for 5 days, was reported by Wang et al. [92]. Upon calcination at 500 °C, Ti(OCH₂CH₂O)₂ transformed into anatase. Although the composition of the anatase TiO₂ is different from the Ti(OCH₂CH₂O)₂ crystal, both of them have the same shape. Wang et al. established that the staggered sequence of edge-sharing in the TiO₆ chain along the *c*-axis of Ti(OCH₂CH₂O)₂ is very similar to that seen in the anatase structure. In this present work, the bonding of PEG 200 with titanium in the hybrid material (polymer) is similar to that of ethylene glycol observed in the Ti(OCH₂CH₂O)₂ crystal.

Upon hot water treatment, the titanium-PEG 200 hybrid material undergoes hydrolysis to give Ti–OH bond with the expulsion of PEG-200 and ROH (R = Et, ^{*n*}Bu). Though, the hydrolysis reaction takes place, Ti–O skeleton in the titanium-PEG 200 hybrid material remains intact. The Ti–OH bonds undergo condensation with neighboring Ti–OH forming Ti–O–Ti three-dimensional networks leading to anatase TiO₂ formation. The whole process of forming TiO₂ network is shown in Scheme 13.1. Gröhn et al. reported that the polymers, such as PEG dispersed in dendrimers, were used as a template-matrix for the formation of inorganic nanoclusters [93]. The nanoclusters formed inside the polymer–dendrimer network are stabilized by the polymer–dendrimer matrix. In titanium-PEG 200 hybrid material, the Ti–O backbone is stabilized by the polymeric network-containing PEG molecules. The polymer chain-containing Ti–O in the backbone results in clusters of nanometer size and forms TiO₂ nanoparticles. Thus the structure of the polymer, that binds PEG with titanium, and the orientation of Ti–O bonds are in such a way that, when the polymer undergoes hydrolysis with hot water, PEG leaches out leaving behind TiO₂ anatase nanocrystallites. These types of reactions are universal among Titanium alkoxides. We have shown such low temperature processes can be effective for Titanium ethoxide and Titanium isopropoxide.

4.6 Synthesis of NC TiO₂ Used in the PV Studies

Titanium tetra-isopropoxide (Ti(OiPr)₄) is used as the starting material in the preparation of a TiO₂ sol. Ti(OiPr)₄ is first mixed with a small amount of ethanol and stirred for 1 h. A mixture of water containing 3 wt.% HCl and ethanol is then poured under stirring into the transparent solution to promote hydrolysis; the molar ratio of H₂O to Ti(OiPr)₄ used is 1:1. Finally, polyethylene glycol of molecular weight 200, 400, or 600 is added slowly to this solution and stirred for one hour. The concentration of Ti(OiPr)₄ in the solution is 0.5 mol L⁻¹. The solution is then aged overnight, and placed under low heat on a heating jacket to evaporate the ethanol and water. The following day, a clear gel is obtained which is further dried in an



Scheme 13.1 Mechanism of low temperature formation of NC anatase TiO_2 upon hot water treatment

oven at $100\text{ }^\circ\text{C}$ for 1 day. The powder obtained from the drying is treated in distilled/deionized hot water (at $90\text{ }^\circ\text{C}$) for 1 h. The obtained powder was found to be crystalline. In this work, the powder was further heat treated at 400 and $500\text{ }^\circ\text{C}$. In our previous work we have shown that heating to $400\text{ }^\circ\text{C}$ does not increase the crystallite sizes, and hence the quality of obtained crystallites at low temperature is not compromised [94]. In order to bring out the role of crystallite sizes, samples were annealed at $500\text{ }^\circ\text{C}$, as it is known that, the crystallite sizes of

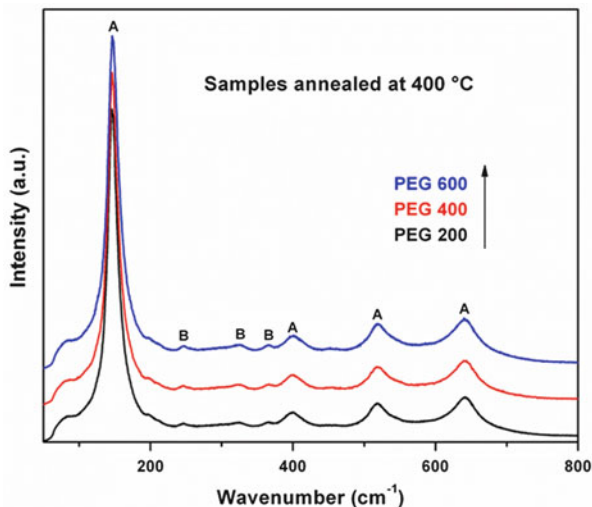


Fig. 13.50 Raman spectra of TiO₂ sample synthesized from PEG 200, 400, and 600, crystallized in hot water at 90 °C, and further annealed at 400 °C

anatase TiO₂ increase when heat treated at 500 °C. Hence after decantation and filtration the powder is annealed in air at temperatures of 400 and 500 °C for 2 h.

The samples were studied by Raman spectroscopy and by XRD technique to identify the TiO₂ polymorphs that were formed. Figure 13.50 shows the Raman spectra of NC TiO₂ samples prepared using PEG 200, 400, and 600, which were boiled and subsequently calcined at 400 °C. Raman spectra show high intensity modes at 146.0, 146.3, and 146.4 cm⁻¹ for the samples prepared using PEG 200, 400, and 600, respectively. Also, Raman lines with peak position of 403, 515, and 638 cm⁻¹ were also observed. These modes belong to the anatase polymorph of TiO₂. In addition to these bands very low intensity bands at 125, 152, 194, 246, 324, 412, 492, 545, and 640 cm⁻¹, which belong to brookite polymorphs of TiO₂, indicating the presence of brookite in the samples synthesized. Thus Raman spectroscopic studies establish the presence of two polymorphs in samples synthesized at 400 °C. Figure 13.51 shows the Raman spectra of TiO₂ samples prepared by using PEG 200, 400, and 600, which were boiled and subsequently calcined at 500 °C. The high intensity Raman line is observed at 144.6, 144.0, and 144.0 cm⁻¹ for the NC TiO₂ samples prepared using PEG 200, 400, and 600, respectively. Further, the modes seen at 403, 515, and 638 cm⁻¹, indicate that these samples are rich in anatase polymorph of TiO₂. In addition to the bands of anatase, Raman spectra show the presence of brookite, as the low intensity modes corresponding the brookite are observed in these samples.

X-Ray diffraction studies on the NC TiO₂ samples prepared at 400 and 500 °C were performed and they are shown in Figs. 13.52 and 13.53, respectively. The XRD line patterns of brookite, anatase, and rutile are also shown in the figure.

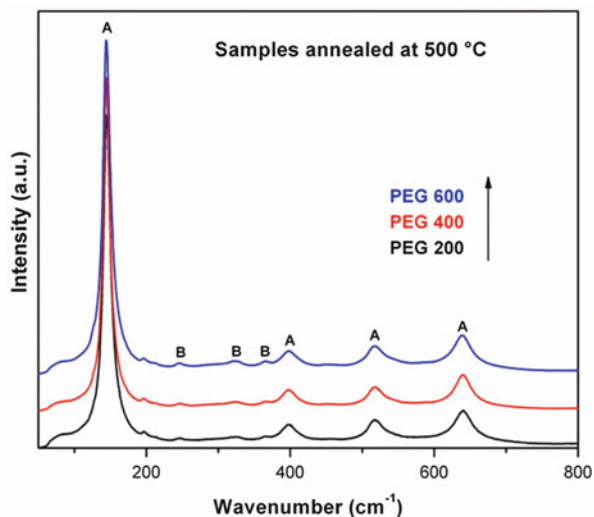


Fig. 13.51 Raman spectra of TiO₂ sample synthesized from PEG 200, 400, and 600, crystallized in hot water at 90 °C, and further annealed at 500 °C

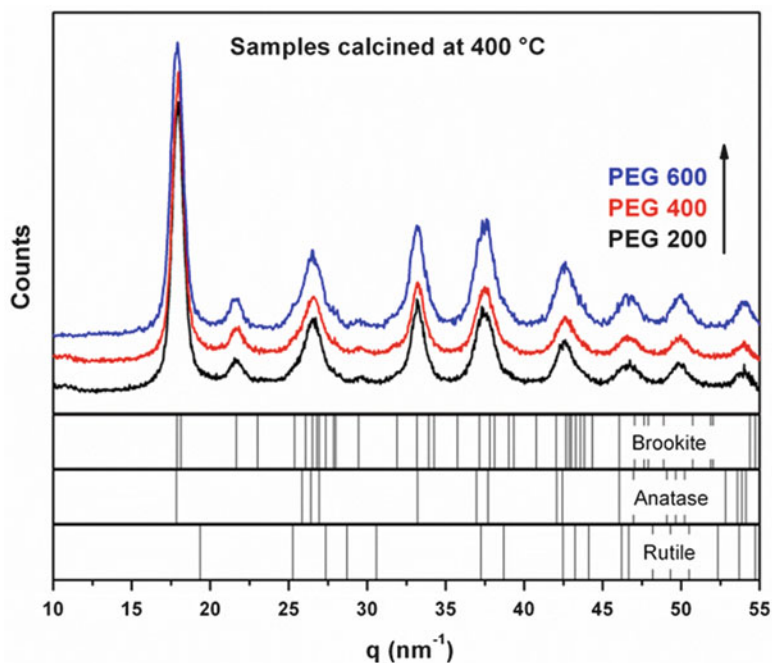


Fig. 13.52 XRD pattern of TiO₂ sample synthesized from PEG 200, 400, and 600, crystallized in hot water at 90 °C, and further annealed at 400 °C

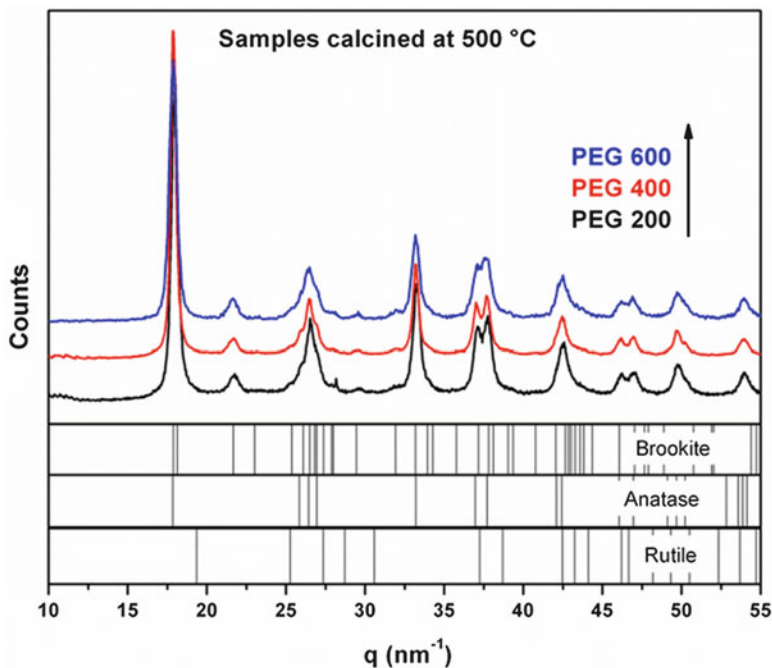


Fig. 13.53 XRD pattern of TiO₂ sample synthesized from PEG 200, 400, and 600, crystallized in hot water at 90 °C, and further annealed at 500 °C

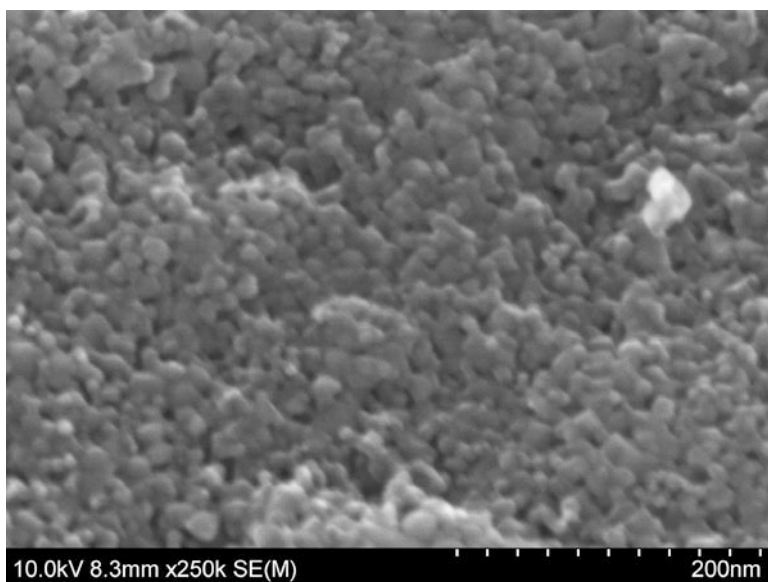
Table 13.13 Phase content of TiO₂ samples prepared with PEG 200, 400, and 500, and annealed at 400 and 500 °C after treatment in hot water at 90 °C

PEG used	Phase content of TiO ₂ sample			
	Brookite (%)		Anatase (%)	
	Heated at 400 °C	Heated at 500 °C	Heated at 400 °C	Heated at 500 °C
200	27	18	73	82
400	31	19	69	81
500	38	28	62	72

An examination of diffraction patterns indicate that, NC TiO₂ samples prepared at 400 °C as well as 500 °C, consist principally of anatase polymorphs with brookite. This observation is in agreement with the above-described Raman results. The ratios of anatase and brookite polymorphs in these samples were calculated from the XRD data and are listed in Table 13.13. The crystallite sizes of NC TiO₂ samples prepared using PEG 200, 400, and 600, show marginal increase in sizes from 5.8 to 7.7 nm when calcined at 400 °C, whereas a marginal increase from 10 to 12 nm was seen when the crystals are calcined at 500 °C. Thus XRD studies demonstrate the nanocrystallinity of the synthesized NC TiO₂ samples.

Table 13.14 BET surface area and adsorption average pore width of the mesoporous TiO₂ samples

Sample prepared with	Sample calcined at		Sample calcined at	
	400 °C	500 °C	400 °C	500 °C
	BET surface area (m ² g ⁻¹)		Adsorption average pore width by BET (nm)	
PEG 200	140.4	76.38	5.72	6.62
PEG 400	135.6	71.4	5.22	6.33
PEG 600	119.8	69.3	5.45	7.46

**Fig. 13.54** FESEM image of TiO₂ powder synthesized from PEG 400, crystallized in hot water at 90 °C, and further annealed at 500 °C

Nitrogen adsorption–desorption: Nitrogen adsorption–desorption measurements were performed on the TiO₂ samples prepared with PEG 200, 400, and 600. The isotherms are of type IV, which, according to IUPAC's classification is an indication of mesoporosity. The BET method was applied to determine the surface area and adsorption average pore width. The results are presented in Table 13.14.

Microstructure: Microstructural morphology NC-TiO₂ samples treated in hot water at 90 °C and further annealed at 400 and 500 °C for 1 h in air were studied by FESEM. Figure 13.54 shows the typical FESEM image of the TiO₂ sample obtained from the solution prepared with PEG 400, crystallized in hot water at 90 °C, and further annealed at 500 °C. The image shows crystallites of ~14 nm, which is in agreement with crystallite size of ~12 nm obtained from XRD measurements. Also, the sample exhibits porous features with pores of 5–10 nm sizes indicating the

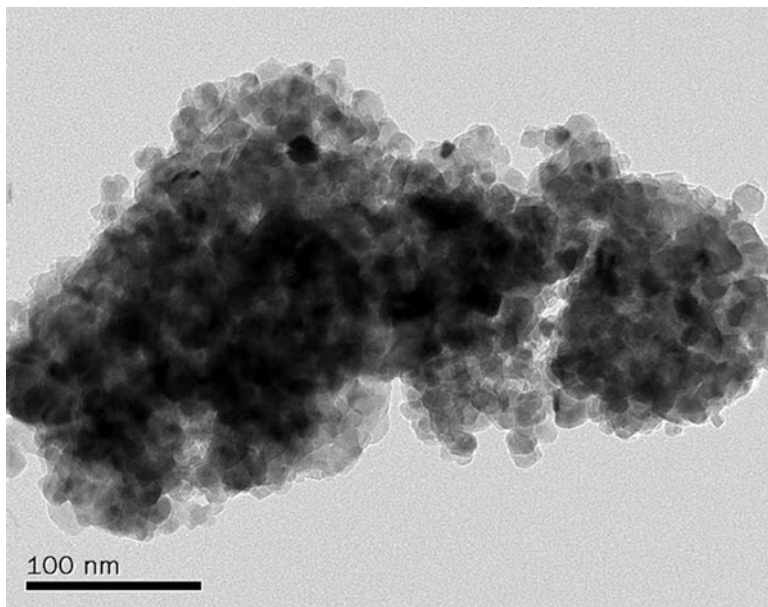


Fig. 13.55 TEM image of TiO₂ powder synthesized from PEG 600, crystallized in hot water at 90 °C, and further annealed at 500 °C

mesoporosity. The samples synthesized with PEG 200, and 600 show a similar microstructure at 250k magnification.

TEM: Figure 13.55 shows the TEM image of a TiO₂ sample prepared with PEG 600, treated in hot water at 90 °C, and further annealed at 500 °C for 1 h. The particle size is estimated to be around 18 nm. This image also shows the porous nature of the sample.

4.7 Manifestation of the TiO₂ NP in the PV Cells

For the studies we have considered active layers with a thickness of approximately 300 nm. The absence of aggregates was monitored by an optical microscope with a resolving power of 1.5 μm . To show the influence of the TiO₂ we have chosen two TiO₂ NP annealed at different temperatures.

The current–voltage dependences are presented in Fig. 13.56. One can see two principal ranges. The first one corresponds to low voltage of polarization, where the current is prevalingly determined by local losses in the active material layer. In the second, the current increases exponentially versus the voltage, and here the dominant mechanism is diffusion-like. The following photovoltaic parameters were defined, i.e., short current density I_{sc} , and open circuit voltage U_{oc} . From the curves

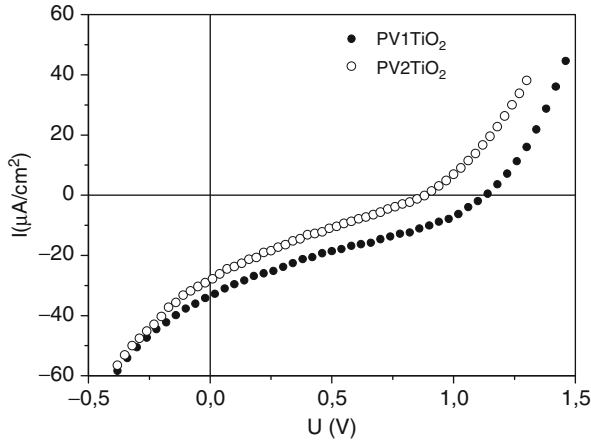


Fig. 13.56 I-U curves of PV1TiO₂ (filled dots) and PV2 TiO₂ (empty dots) devices used to calculate the fill factor (FF)

in Fig. 13.56, we calculated the fill factor FF for each photovoltaic device using $FF = P_{\max}/(U_{oc}I_{sc}) = (U_{mp}I_{mp})/(U_{oc}I_{sc})$, where U_{mp} and I_{mp} are the voltage and current at point of maximum power output of the device.

We found that a low content of TiO₂ has some influence on the formation of the isolated islands in the active layer, and only a small influence on the improvement of carrier transport. It also leads to a reduction of the recombination probability for separated carriers leading to reduced photocell efficiency. One can assume that better photovoltaic efficiency for PV2 as compared to PV0 is a consequence of additional light scattering on the TiO₂ and higher light absorption. For the particles with sizes below $\lambda/20$, the corresponding scattering is isotropic [79]. In the active layers PV1 and PV2 there the same mass amount of TiO₂ (wt. 30 %), which in turn are distinguished by particle sizes. The photovoltaic cells possessed the following architecture: ITO/PEDOT:PSS/PDT(poly-3-decylothiophene) as donor + fluorene copolymer (as indicated below +30 % of TiO₂)/Al. The typical thickness of the organic active layers was equal to about 300 nm (value obtained following the spectroscopic ellipsometry—Wollam Inc. model VASE) and lateral dimensions 5×5 mm. Careful monitoring in polarizing optical microscope (resolving power 1.5 μm) didn't show any visible signs of aggregation. The such fabricated devices (PV1 and PV2) were used for photovoltaic experiments.

In structure PV1 the nanocrystallite sizes are lower, and it leads to higher efficiency of the scattering. However, such large differences the NP content is not the sole reason of such differences. The observed higher short current density I_{sc} , as well as open circuit voltage V_{oc} , may also be a consequence of different electrical features for these materials. Generally following the obtained data, one can conclude that for device PV1, possessing the TiO₂ NP with the higher energy gap, the U_{oc} is substantially higher than that for device PV2 (see Table 13.15 and Figs. 13.57 and 13.58).

Table 13.15 Principal data for the TiO₂ containing PV cell

Active layer composition	U_{OC} (V)	I_{SC} ($\mu A\ cm^{-2}$)	FF	QE (%)
PV 0	0.81	27.58	0.156	0.27
PV 1	1.13	33.49	0.275	0.80
PV 2	0.88	28.20	0.225	0.43

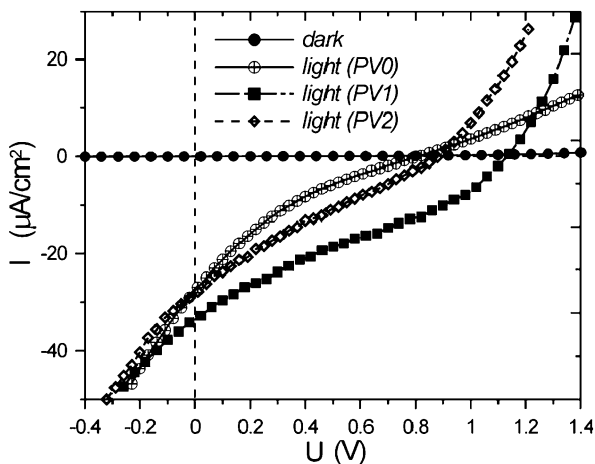


Fig. 13.57 Linear $C-V$ feature for the studied TiO₂ doped PV cells in the fourth quadrant under $1.3\ mW\ cm^{-2}$ illumination

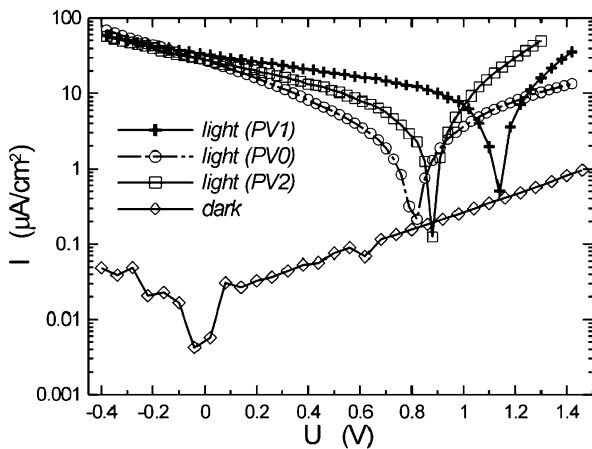


Fig. 13.58 Semilogarithmic $C-V$ dependences under the same illumination conditions

5 Conclusion

We present the basic principles of functioning of the photovoltaic cells. We presented above some aspects of the photovoltaic organic cells with and without the TiO₂ nanoparticles. The principal parameters defining the photovoltaic efficiencies are discussed. Their improvement during the technological processes is discussed. We have shown the possibility to improve the PV efficiencies by appropriately changing both the organic chromophores and the TiO₂ NP. The principal conclusion consists in a fact that for the PV architecture with lower nanocrystallite sizes there is a higher efficiency of the scattering. However, such large differences of the NP content are not the only reason of such differences. The observed higher short current density I_{sc} , as well as open circuit voltage V_{OC} may also be a consequence of different electrical features for these materials. Additionally for device PV, possessing the TiO₂ NP with the higher energy gap, the U_{OC} is substantially higher than that for device with the lower energy gap. All the obtained data show that final PV response is a consequence of the influence of different factors indicated above.

References

1. Castro, F.A., Faes, A., Geiger, T., Graeff, C.F.O., Nagel, M., Nüesch, F., Hany, R.: *Synth. Met.* **156**, 973–978 (2006)
2. Brabec, C., Dyakonov, V., Parisi, J., Sariciftci, N.S.: *Organic Photovoltaics Concepts and Realization*. Springer Verlag, Berlin (2003)
3. Ibrahim, M.A., Roth, H.K., Schroedner, M., Konkin, A., Zhokhavets, U., Gobsch, G., Scharff, P., Sensfuss, S.: *Org. Electron.* **6**, 65–77 (2005)
4. Suresh, P., Balaraju, P., Sharma, S.K., Roy, M.S., Sharma, G.D.: *Sol. Energy Mater. Sol. Cells* **92**, 900–908 (2008)
5. Yoo, S., Potscavage Jr., W.J., Domercq, B., Han, S.-H., Li, T.-D., Jones, S.C., Szoszkiewicz, R., Levi, D., Riedo, E., Marder, S.R., Kippelen, B.: *Solid-State Electron.* **51**, 1367–1375 (2007)
6. Pokladko, M., Bogdał, D., Matras, K., Gondek, E., Sanetra, J.: *Modern Polymeric Materials for Environmental Applications*, 2 International Seminar Kraków, 2 (2006) pp. 25–30
7. Sanetra J.: *Fizyczne właściwości układów polimerowych zawierających grupę karbazolową w aspekcie zastosowania ich w diodach elektroluminescencyjnych*. Zeszyty Naukowe, Podstawowe Nauki Techniczne nr 23, Kraków (2001)
8. Barltrop, J.A., Coyle, J.C.: *The principles of Photochemistry*. Warsaw (1987)
9. Hoppe, H., Sariciftci, N.S.: *J. Mater. Res.* **19**, 312–367 (2004)
10. Nelson, J.: *Curr. Opin. Solid State Mater. Sci.* **6**, 87–95 (2002)
11. Lochab, B., Burn, P.L., Barkhouse, A., Kirov, K.R., Assender, H.E., Keeble, D.J., Thomsen, E. A., Lewis, A.J., Samuel, I.D.W.: *Org. Electron.* **8**, 801–812 (2007)
12. Goris, L., Loi, M.A., Cravino, A., Neugebauer, H., Sariciftci, N.S., Polec, I., Lutsen, L., Andries, E., Manca, J., DeSchepper, L.: *D. Vanderzande. Synth. Met.* **138**, 249–253 (2003)
13. Pradhan, B., Pal, A.J.: *Synth. Met.* **155**, 555–559 (2005)
14. Luszczynska, B., Dobruchowska, E., Glowacki, I., Ulanski, J., Jaiser, F., Yang, X., Neher, D., Danel, A.: *J. Appl. Phys.* **99**, 024505 (2006)
15. Kymakis, E., Stratakis, E., Koudoumas, E.: *Thin Solid Films* **515**, 8598–8600 (2007)

16. Winder, C., Sariciftci, N.S.: *J. Mater. Chem.* **14**, 1077–1086 (2004)
17. Shirakawa, H., MacDiarmid, A.G., Heeger, A.J.: *Chem. Commun.* **1** (2003)
18. Goris, L., Loi, M.A., Cravino, A., Neugebauer, H., Sariciftci, N.S., Polec, I., Lutsen, L., Andries, E., Manca, J., De Schepper, L., Vanderzande, D.: *Synth. Met.* **138**, 249–253 (2003)
19. Greenham, N.C., Friend, R.H.: *Semiconductor devices physics of conjugated polymers. Solid State Phys.* **49**, 1–148 (1996)
20. Kao, K.C., Hwang, W.: *Electrical Transport in Solids*. Pergamon Press, Oxford (1981)
21. Seanor, D.A. (ed.): *Electrical Properties of Polymers*. Academic Press, New York (1982)
22. Hoppe, H., Sariciftci, N.S.: *J. Mater. Res.* **19**(7), 1924 (2004)
23. Valaski, R., Muchenski, F., Mello, R.M.Q., Micaroni, L., Roman, L.S., Hümmelgen, I.A.: *J. Solid State Electrochem* **10**, 24–27 (2006)
24. Sato, Y., Yamagishi, K., Yamashita, M.: *Opt. Rev.* **12**(4), 324–327 (2005)
25. He, Z., Danel, A., Milburn, G.H.W.: *J. Lumin.* **122–123**, 605–609 (2007)
26. Wolfrum, G., Pütter, R., Menzel, K.: *Angew. Chem.* **21**, 839 (1962)
27. Gondek, E., Kityk, I.V., Danel, A., Wisła, A., Pokladko, M., Sanetra, J., Sahraoui, B.: *Mater. Lett.* **60**, 3301–3306 (2006)
28. Pokladko, M., Gondek, E., Sanetra, J., Danel, A.: *Sci. Bull. Phys. Łódź* **26**, 81–86 (2006)
29. Pokladko, M., Sanetra, J., Gondek, E., Nizioł, J., Pokrop, R., Jaglarz J.: *e-Polymers* (2006) <http://www.e-polymers.org>. ISSN1618-7229
30. Całus, S., Gondek, E., Danel, A., Jarosz, B., Pokladko, M., Kityk, A.V.: *Mater. Lett.* **61**, 3292–3295 (2007)
31. Danel, K., Gondek, E., Pokladko, M., Kityk, I.V.: *J. Mater. Sci. Mater. Electron.* **20**, 171–176 (2009)
32. Reyes-Reyes, M., López-Sandoval, R., Liu, J., Carroll, D.L.: *Sol. Energy Mater. Sol. Cells* **91**, 1478–1482 (2007)
33. Lee, J.H., Seoul, C., Park, J.K., Youk, J.H.: *Synth. Met.* **145**, 11–14 (2004)
34. Cutler, C.A., Burrell, A.K., Collis, G.E., Dastoor, P.C., Officer, D.L., Too, C.O., Wallace, G.G.: *Synth. Met.* **123**, 225–237 (2001)
35. De Bettignies, R., Leroy, J., Firon, M., Sentein, C.: *Synth. Met.* **156**, 510–513 (2006)
36. Tsekouras, G., Too, C.O., Wallace, G.G.: *Synth. Met.* **157**, 441–447 (2007)
37. Gondek E.: “Badanie wybranych polimerów jako materiałów elektroluminescencyjnych i fotowoltaicznych.” Kraków (2005) – rozprawa doktorska
38. Jan Pielichowski, Andrzej Puszyński: “Chemia polimerów”, TEZA Wydawnictwo Naukowo – Techniczne, Kraków (2004)
39. Pearson, J.M., Stolka, M.: *Poly(N-vinylcarbazole)*. Gordon and Breach Science Publishers, New York (1981)
40. Grazulevicius, J.V., Stroehriegl, P., Pielichowski, J., Pielichowski, K.: *Prog. Polym. Sci.* **28**, 1297–1353 (2003)
41. Chasteen, S.V.: “Exciton dynamics in conjugated polymer photovoltaics: steady-state and time resolved optical spectroscopy,” University of California, Santa Cruz, Dec. 2005
42. Gondek, E.: “Studies of some polymers as electro-luminescent and photovoltaic materials.” PhD Thesis, Krakow (2005)
43. Pokladko, M., Gondek, E., Sanetra, J., Danel, A.: A comparison between a donor - Acceptor blend layer photovoltaic cell and a double layer photovoltaic cell devices. *Sci. Bull. Phys. Politechnika Łódzka, Łódź* **26**, 81–86 (2006)
44. Pokladko, M., Gondek, E., Sanetra, J., Danel, A.: Ogniwa fotowoltaiczne typu “hetetozłącze objętościowe”. XVI Ogólnopolska Konferencja Krtształy Molekularne 2008, 8–12 września 2008. Poznań – Białejewko P-50-[poster]
45. Pokladko, M., Gondek, E., Danel, A., izioł, J., Armatus, P., Sanetra, J.: “Zastosowanie materiałów organicznych w fotowoltaice”. XVII Ogólnopolska Konferencja “Kryształy Molekularne” 13–17 września 2010r. Instytut Chemii Fizycznej i Teoretycznej Pol. Wrocławskiej, Polanica Zdrój, P-42-[poster]

46. Pokladko, M., Gondek, E., Danel A.: "Ogniwa fotowoltaiczne na bazie organicznych materiałów". *Czasopismo Techniczne*-NP/2011 (2011) pp. 77–83. Politechnika Krakowska
47. Regan, B.O., Grätzel, M.: *Nature* **153**, 737 (1991)
48. Nazeruddin, M.K., Kay, A., Rodicio, I., Humphry-Baker, R., Muller, E., Liska, P., Vlachopoulos, N., Grätzel, M.: *J. Am. Chem. Soc.* **115**, 6382 (1993)
49. Kalyanasundram, K., Grätzel, M.: *Coord. Chem. Rev.* **77**, 347 (1998)
50. Mora-Sero, I., Bisquert, J.: *Nano Lett.* **3**, 945–949 (2003)
51. Cavigli, L., Bogani, F., Vinattieri, A., Cortese, L., Colocci, M., Faso, V., Baldi, G.: *Solid State Sci.* **12**(11), 1877–1880 (2010)
52. Nakade, S., Saito, Y., Kubo, W., Kitamura, T., Wada, Y., Yanagida, S.: *J. Phys. Chem. B* **107** (33), 8607–8611 (2003)
53. Cavigli, L., Bogani, F., Vinattieri, A., Faso, V., Baldi, G.: *J. Appl. Phys.* **106**, 053516 (2009)
54. Kato, S., Masuo, F.: Titanium dioxide-photocatalyzed oxidation I. *Kogyo Kagaku Zasshi* **67**, 42–50 (1964)
55. McLintock, S., Ritchie, M.: *Trans. Faraday Soc.* **61**, 1007–1016 (1965)
56. Fujishima, A., Honda, K.: *Nature* **238**, 37–38 (1972)
57. Regan, O., Grätzel, M.: *Nature* **353**, 737–740 (1991)
58. Kay, A., Grätzel, M.: *Sol. Energy Mater. Sol. Cells* **44**, 99–117 (1996)
59. Grätzel, M.: *J. Photochem. Photobiol. C: Photochem. Rev.* **4**, 145–153 (2003)
60. Balaji, S., Djaoued, Y., Albert, A.-S., Bruning, R., Beaudoin, N., Robichaud, J.: *J. Mater. Chem.* **21**, 3940 (2011)
61. Djaoued, Y., Badilescu, S., Ashrit, P.V., Bersani, D., Lottici, P.P., Robichaud, J.: *J. Sol-Gel Sci. Technol.* **24**, 255 (2002)
62. Vegard, L.: Results of crystal analysis. *Philos. Mag.* **32**(191), 505–518 (1916)
63. Pauling, L., Sturdivant, J.H.: *Z. Kristallograph.* **68**, 239–256 (1916)
64. Carp, O., Huisman, C.L., Reller, A.: *Prog. Solid State Chem.* **32**, 33–117 (2004)
65. Simons, P.Y., Dacheille, F.: *Acta Crystallogr.* **23**, 334–336 (1967)
66. Latroche, M., Brohan, L., Marchand, R.: K0.06TiO2. *J. Solid State Chem.* **81**, 78–82 (1989)
67. Cromer, D.T., Herrington, K.: *J. Am. Chem. Soc.* **77**, 4708–4709 (1955)
68. Baur, V.W.H.: *Acta Crystallogr.* **14**, 214–216 (1961)
69. Mo, S., Ching, W.: *Phys. Rev. B* **51**, 13023–13032 (1995)
70. Thompson, T.L., Yates Jr., J.T.: *Chem. Rev.* **106**, 4428–4453 (2006)
71. Linsebigler, A.L., Lu, G., Yates, J.T.: *Chem. Rev.* **95**, 735–758 (1995)
72. Muscat, J., Swamy, V., Harrison, N.M.: *Phys. Rev. B* **65**, 1–15 (2002)
73. Bokhimi, X., Morales, A., Aguilar, M., Toledo-Antonio, J.A., Pedraza, F.: *Int. J. Hydrogen Energy* **26**, 1279–1287 (2001)
74. Chen, X., Mao, S.S.: *Chem. Rev.* **107**, 2891–2959 (2007)
75. Diebold, U.: *Surf. Sci. Rep.* **48**, 53–229 (2003)
76. Norotsky, A., Jamieson, J.C., Kleppa, O.J.: *Science* **158**, 338–389 (1967)
77. Zhang, Q., Gao, L., Guo, J.: *Appl. Catal. B Environ.* **26**, 207–215 (2000)
78. Wunderlich, W., Oekermann, T., Miao, L., et al.: *J. Ceram. Process. Res.* **5**, 343–354 (2004)
79. Paxton, A.T., Thiên-Nga, L.: *Phys. Rev. B* **57**, 1579–1584 (1998)
80. Bessekhoud, Y., Robert, D., Weber, J.V.: *J. Photochem. Photobiol. A* **157**, 47 (2003)
81. Anderson, M.A., Gieselmann, M.J., Xu, Q.: *J. Membr. Sci.* **39**, 243 (1988)
82. Barbe, C.J., Arendse, F., Comte, P., Jirousek, M., Lenzmann, F., Shklover, V., Grätzel, M.: *J. Am. Ceram. Soc.* **80**, 3157 (1997)
83. Barringer, E.A., Bowen, H.K.: *Langmuir* **1**, 414 (1985)
84. Oskam, G., Nellore, A., Penn, R.L., Searson, P.C.: *J. Phys. Chem. B* **107**, 1734 (2003)
85. Sugimoto, T.: *Adv. Colloid Interface Sci.* **28**, 65 (1987)
86. Djaoued, Y., Badilescu, S., Ashrit, P.V., Bersani, D., Lottici, P.P., Bruning, R.: *J. Sol-Gel Sci. Technol.* **24**, 247 (2002)
87. Priya, S., Balaji, S., Djaoued, Y., Robichaud, J.: *J. Raman Spectrosc.* **40**, 1885–1894 (2009)
88. Kajihara, K., Yao, T.: *J. Sol-Gel Sci. Technol.* **16**, 257 (1999)

89. Kajihara, K., Yao, T.: *J. Sol-Gel Sci. Technol.* **12**, 193 (1998)
90. Bu, S., Jin, Z., Liu, X., Du, H., Cheng, Z.: *J. Sol-Gel Sci. Technol.* **30**, 239 (2004)
91. Stathatos, E., Lianos, P., Falaras, P.: *Prog. Colloid Polym. Sci.* **118**, 96 (2001)
92. Wang, D., Yu, R., Kumada, N., Kinomura, N.: *Chem. Mater.* **11**, 2008 (1999)
93. Gröhn, F., Bauer, B.J., Kim, G., Amis, E.: *Hydrophobically Macromol.* **34**, 6701 (2001)
94. Balaji, S., Djaoued, Y., Robichaud, J.: *J. Raman Spectrosc.* **37**, 1416–1422 (2006)

Chapter 14

Light Trapping for Solar Cells

Hsin-Hung Cheng, Shih-Wen Chen, Jen-You Chu, Ding-Zheng Lin,
Tsung-Dar Cheng, Yi-Ping Chen, Ying-Yu Chang, Hung-Ying Yang,
Yung-Ming Yeh, Yu-Sheng Wang, and Jia-Han Li

Abstract The textured microstructures and the photonic nanostructures for light trapping structures are discussed. The inverted pyramidal microstructures with and without the tips were fabricated, and their light trapping performances were measured by the reflectance spectroscopy and simulated by ray tracing method. It is found that there are more chances of light reflecting between the surfaces of the tips and the inverted pyramids. Four kinds of nanophotonic light trapping structures are simulated by the finite-difference time-domain method, and their optical transmissions and light trapping performances are calculated. The results show that mixing the dielectric and metallic nanoparticles or materials can have superior light trapping performances as comparing to using dielectric nanoparticles only or using metallic nanoparticles only. The other kinds of light trapping structures and their outlooks are also given.

1 Introduction

Although it still has several decades before running out of fossil fuels on earth and it has abundant coal mines which can be used for more than 200 years according to current industry development, we are facing fast climate change which is generally thought as the consequences of using fossil fuels and burning the coals to power most of our daily lives since industry revolution a century ago. Thus, how to use the

H.-H. Cheng • S.-W. Chen • Y.-Y. Chang • H.-Y. Yang • Y.-M. Yeh
Y.-S. Wang • J.-H. Li (✉)

Department of Engineering Science and Ocean Engineering, National Taiwan University,
No. 1, Sec. 4, Roosevelt Road, Taipei 10617, Taiwan
e-mail: jjahan@ntu.edu.tw

J.-Y. Chu • D.-Z. Lin • T.-D. Cheng • Y.-P. Chen
Material and Chemical Research Laboratories, Industrial Technology Research Institute,
No. 195, Sec. 4, Chung Hsing Road, Chutung, Hsinchu 31040, Taiwan

green energy efficiently and economically becomes an important issue in twenty-first century. Solar energy, which is one of the green energy, comes from the sunlight directly and surrounds us globally. It is no doubt that solar energy is one of the most important renewable energy resources in long-term view. However, the solar cell industry has been impacted by financial crisis and economic instability during these years. To keep the rapid growth momentum of using solar energy, it relies on the policies from different country governments but it is also important to keep the research on the novel method to transfer solar energy to electricity with higher efficiency and lower cost. This paves the road for the developments and applications of solar energy [1, 2]. Many different methods have been studied and proposed to increase the solar cell efficiency. One obvious solution to enhance the solar cell absorption is using different materials, such as crystalline silicon (c-Si) [3], amorphous silicon (a-Si) [4, 5], gallium arsenide (GaAs) [6], cadmium telluride (CdTe) [7], GaSb/GaAs quantum rings [8], organic material [9], and tandem solar cells by combining several materials [10]. The c-Si material is widely used commercially because it is cheap and abundant as comparing to other materials; however, its absorption is poor and the thick c-Si material is required to absorb the solar energy. The bandgap of silicon is 1.12 eV which is not at the optimized bandgap for solar spectrum, and it limits the efficiency to absorb the solar energy. The a-Si has stronger absorption and it is used for thin film solar cell materials; however, the efficiency is not as high as c-Si solar cells. The GaAs has high conversion efficiency up to more than 30 % because its bandgap is close to the optimized bandgap for single absorbed material; however, it is high cost. The Cadmium Telluride (CdTe) also has good conversion efficiency, and the cost can be decreased as the development of technology on this material. Due to the fact that Cd is a highly polluted material, it has many limitations. Recently, combining different materials to absorb different spectrum of solar energy has been developed and the efficiency can be very high [11, 12]. These techniques require complicated fabrication techniques and expensive manufacturing processes. Thus, the multiple junction solar cells are not easy to be commercialized in the near future. One of the most other important techniques to increase the solar cell efficiency is using the light trapping structures to increase the light absorption into the solar cell materials. The purpose of light trapping structures is to increase the light or photons trapped in the solar cell materials which can generate the electron-hole pair under light. The light trapping structures can reduce the cost by using inexpensive substrate and lower price solar cell materials to achieve better absorption properties. Thus, developing better light trapping structures is important for thin film solar cells. The light trapping structures can increase the optical path length, and thus reduce the material usage in solar cells. Also, the minority carrier diffusion length should be long enough to generate the electron-hole pairs in solar cell materials. It results the need for high absorption coefficient or good light trapping structures.

For crystalline silicon-based solar cells, the antireflection layers can be used to increase the light transmission efficiency [13, 14]. The refractive index of antireflection layer material should be chosen between the refraction indices

of material and air. The most-often-used antireflection materials include SiO_2 , SiN_x , TiO_2 , Al_2O_3 , CeO_2 , etc. [15]. It can be used to combine the textured structures for better light trapping enhancements. The textured silicon surface structures can be etched by various etchants, such as NaOH [16], TMAH [17, 18], and KOH [19]. Different textured structures have been reported, including the pyramidal textured surfaces [20], inverted pyramidal [21, 22], honeycomb [23], nanowire [24], gratings [25], V-grooved [26], and other kinds of structures [27–29]. Most of these structures are too large and not suitable for thin film solar cells with micrometer or sub-micrometer ranges [30]. The thin film solar cells become more important because the material usage and cost are reduced. The plasmonic solar cells get a lot of attention recently because it can be used for light trapping and not hard to merge the plasmonic nanoparticles or structures into thin film solar cell fabrications [31, 32]. The plasmonic nanoparticles are pivotal to trap light in thin film solar cells. Three light trapping techniques are recommended in recent report [32]. One method is to provide a systematic approach to trap light by scattering from the surface metal nanoparticles into solar cell [33, 34]. The other two methods are embedding metal nanoparticles in solar cell and corrugating the back metal surface [35] individually. As the sizes of the metal nanoparticles are smaller than the light wavelength, the resonance of the nanoparticles behaves as the dipole sources. The dipole sources placed on a semiconductor substrate scatter the light into the substrate due to that the light prefers to flux into the high refractive index material [31]. The enhancement of absorption by surface plasmonic effect is significant in previous report [36]. Metallic nanoparticles embedded in dielectric material can be treated as gradient refractive index structure to decrease the reflection [37]. The allocations of silver nanoparticles at the front of active layer and at the backend of active layer give divergent effects of absorption via the period of nanoparticles [38]. The direct contact of metallic particles and semiconductor induce undesired damping of surface plasmon resonances. A space layer can avoid this situation [39]. To enhance the absorption, the combination of silver nanoparticles and the silica layer were used [40–42] and distributing silver and silica nanoparticles on the solar cells were applied [43, 44]. They also form as core-shell structure which improves enormous absorption in solid-state dye-sensitized solar cells [45–47].

The brief introduction and literature review of light trapping structures for solar cells are given in Sect. 1 in our best understanding. The limit of light trapping enhancements is described in Sect. 2. The evaluation of light trapping enhancements is discussed in Sect. 3. To be more specific, the textured structures for enhancing light trapping are discussed, and a novel inverted pyramidal structure with tips is discussed in Sect. 4. Also, the nanophotonic structures using metallic or dielectric nanoparticles are discussed in Sect. 5. Four specific nanophotonic structures with mixing metallic and dielectric materials for thin film light trapping structures are discussed in Sect. 6. The possible directions to design light trapping structures for high efficiency solar cells and the conclusions of this chapter are given in Sect. 7.

2 Limit of Light Trapping Enhancements

Using the ray optics theory, the light trapping structure has the maximum absorption limit in the solar cell material slab which is often called as Lambertian limit or Yablonsvitch limit [48, 49]. The Lambertian limit is often referred to an ideal rough surface which can scatter the light randomly into the solar cell material, and the optical path length can be increased by a factor of $4n^2$, where n is the refractive index of the solar cell slab. The limit can be $4n^2/\sin^2\theta$ in consideration of using some devices to collect light within an angle 2θ [50]. Thus, obtaining a light trapping structure to the Lambertian limit can reduce the solar cell slab thickness a lot in a factor of $4n^2/\sin^2\theta$. The random scattering structure or randomly textured surface is in Lambertian limit which has been researched for a long time. Recently, several light trapping methods to overcome the Lambertian limit has been proposed and studied. The fundamental limit of light trapping enhancements in grating structures and nanophotonic structures has been studied by the statistical temporal coupled-mode theory recently [51, 52], and it shows that the light trapping enhancement beyond the Lambertian limit is achievable as the optical modes exhibit deep-subwavelength-scale field confinement with angular dependency. The light trapping beyond the ray optic limit is studied, and design rules of an elevated local density of optical states are described for the solar cell material absorber [53]. With better light trapping structure, not only the light optical path can increase in the solar cell materials but also give better photon-generated charge carriers collection due to the thin film thickness between the electrodes. For thin film or ultra-thin film solar cells, the light trapping structures become more important because the light has to be captured in the thin materials before it reflects back to the air region. There are many nanophotonic light trapping methods for thin film solar cells [54], for example, the nanowire [55–57], plasmonic structures [32], and nanoparticles [33, 58].

3 Evaluation of Light Trapping Enhancements

The purpose of light trapping structures is to increase the light or photons trapped in the solar cell materials which can generate the electron–hole pair under light illuminations. The light trapping structures do not only affect the optical trapping properties but also affect the electron–hole generation or recombination efficiencies. Instead of considering the electric properties in the materials, the optical trapping properties of the light trapping structures are evaluated in most situations. The evaluation of current or voltage generated by solar cells combined with light trapping structures can be also used to understand the optical trapping properties. To evaluate the optical properties of light trapping structures, the light absorptions for the solar cells with light trapping structures are often compared with a standard sample without the light trapping structures. This is often called

enhancement factor. It can be also calculated by the photocurrent at specific wavelength divided by the photocurrent for a standard sample. The other way to evaluate the light trapping performances is to calculate or to measure the short circuit current densities for testing structures and they are compared with the standard samples. Sometimes, it is also similar as the representations of quantum efficiency as a function of wavelength.

4 Light Trapping of the Textured Surfaces: Taking the Inverted Pyramidal Structures Without and with the Tips as the Examples

There are different methods to fabricate the textured surfaces, and one of the most useful methods is using the etching process to fabricate the desired patterns. Recently, the inverted pyramid structures with the tips have been proposed to enhance the light trapping properties [59], and it is found that it has better antireflection performances as comparing to the inverted pyramid structures without the tips, which is often called passivated emitter, rear locally diffused (PERL) structures [22]. In this section, we present the study of light trapping performances for the inverted pyramidal structures with the tips and without the tips on crystalline silicon wafers. The textured structures are fabricated in crystalline silicon and their optical reflections are measured in comparison with the inverted pyramids without the tips. The reflection properties of these structures are also studied by the ray tracing method.

The photolithography process, which is a pattern-transfer process that transfers the design of mask to the photoresist on the silicon wafer surface, is used to control the precise patterns after etching processes. The inverted pyramidal structures without and with the tips was fabricated by photolithography processes. The schematic diagram of process steps for fabricating inverted pyramidal with the tips structures is shown in Fig. 14.1. The 4-in. p-type $\langle 100 \rangle$ crystalline silicon wafers with the thickness 525 μm are used to demonstrate the fabrication processes. First, the silicon wafers are cleaned in the ultrasonic vibrator using piranha solution ($\text{H}_2\text{SO}_4:\text{H}_2\text{O} = 3:1$ by volume). Then, the 1.8 μm -thick silicon nitride (Si_3N_4) buffer layer was evaporated on silicon wafer by using plasma-enhanced chemical vapor deposition (PECVD) as hard mask. Next, the photoresist was coated on the whole silicon wafer by using spinner. To print the photomask design on the photoresist, the photolithography (EVG 620 top side mask aligner, EVGroup) was adopted in this step. Using the photoresist pattern on the silicon wafer, the silicon nitride etching window was formed by the reactive ion etching (RIE; RIE-10N, Samco, Inc.). Then, the photoresist at the substrate surface were all removed. The 10 wt% tetramethyl ammonium hydroxide (TMAH) was unitized as the wet etching solution for silicon. The temperature of wet etching was actively controlled during the measurements at 90 ± 1 $^\circ\text{C}$. For wet etching parameters, the

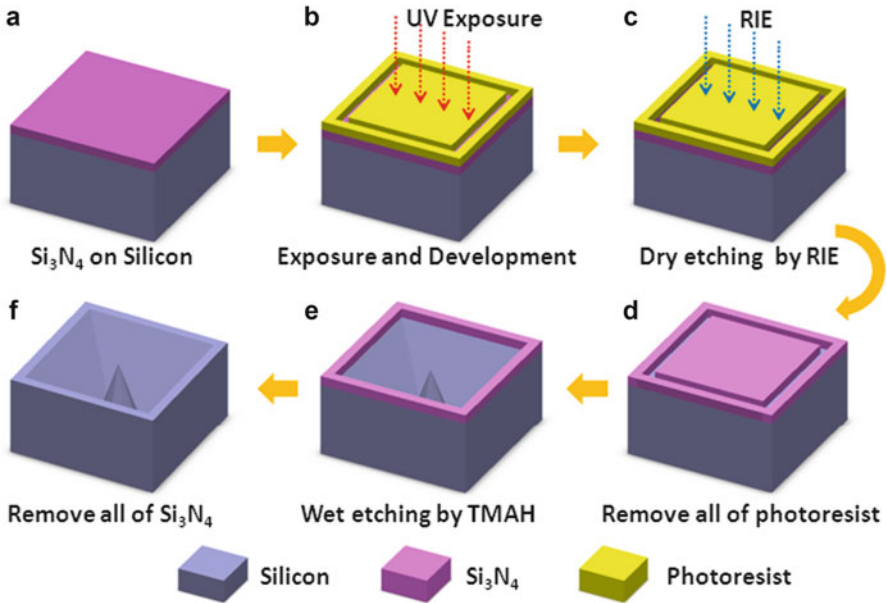


Fig. 14.1 Schematic diagram of process steps for fabrication of inverted pyramidal with the tips, where (a) is silicon nitride layer deposit on silicon wafer, (b) is the UV exposure to transfer the photomask pattern on the photoresist and development of the photoresist, (c) is the dry etching of silicon nitride by RIE, (d) is to remove the photoresist, (e) is the wet etching of silicon wafer by TMAH, and (f) is to remove the remaining silicon nitride

wet etching time was varied to achieve a desirable etching profile of inverted pyramidal with the tips for antireflective characteristics. The areas of these structures are $1\text{ cm} \times 1\text{ cm}$ with $10\text{ }\mu\text{m}$ unit structure. Finally, the silicon nitride on the structures was removed by using phosphoric acid (H_3PO_4). It is worthy to mention that different structures with various tip depth and tip size can be obtained by controlling the wet etching process and mask patterns before using phosphoric acid to clear the whole silicon nitride.

By using the anisotropic crystalline etching simulation software, the structures after fabrication processes are simulated and shown in Fig. 14.2. These simulations can not only provide the illustration of fabricated structures but also give the fabrication parameters under ideal conditions, such as etching time and etching concentration. To understand the morphology of the fabricated samples, the scanning electron microscopy (SEM; Nova NanoSEM 450, FEI Europe) and the atomic force microscope (AFM; Digital Instrument Dimension 3100) were used. Figure 14.3 shows the AFM images of the fabricated inverted pyramidal structures without and with the tips, and the inset figures are their corresponding SEM photos. In SEM images, it is observed that the inverted pyramidal structures with and without the tips can be fabricated. The length of unit structures is $12\text{ }\mu\text{m}$ with $0.5\text{ }\mu\text{m}$ flat surface after removing all silicon nitride materials. From the SEM image

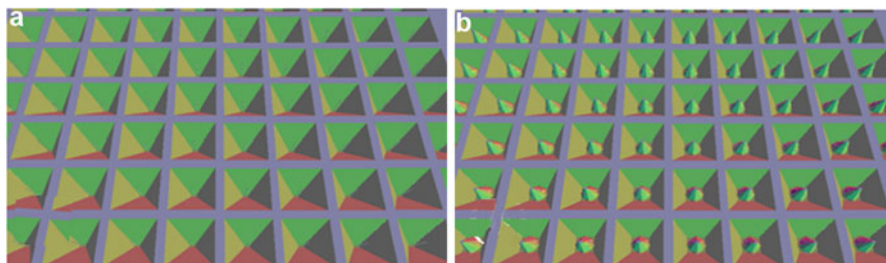


Fig. 14.2 Anisotropic crystalline etching simulations of inverted pyramidal structures, where (a) shows the structure without the tips and (b) shows the structure with the tips

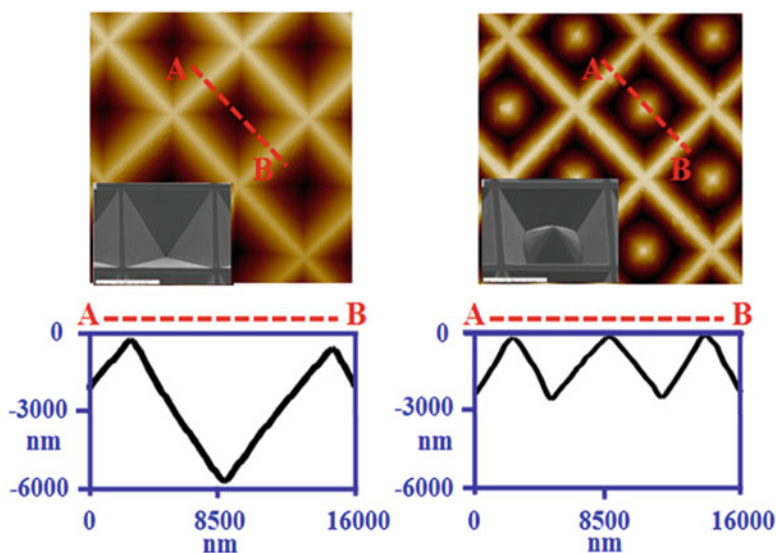


Fig. 14.3 AFM images of the inverted pyramidal structures without and with the tips, where *inset figures* are the SEM image with tilt angle. The *bottom figures* are the cross-section profiles along the AB lines (16 μm) in the *top figures* measured by means of AFM

results, the facets of our fabricated structures are smooth with few defects. The AFM photos in Fig. 14.3 show the 3D profiles of fabricated structures. The angle and depth of the tip measured by AFM can be used for the structure parameters in further simulation study. The 3D profile can be used for the cross-section results to identify its angle structure relationship. From the cross-section image of the structure without the tips in Fig. 14.3, the inverted pyramidal structure has the angle of 54.74° on the dip of inverted pyramidal, the unit structure is about $12 \mu\text{m}$ with a depth of $5.8 \mu\text{m}$. From the cross-section image of the structure with the tips in Fig. 14.3, the inverted pyramidal structure with the tips has the tip depth of $2.1 \mu\text{m}$ under the region unit structure of $12 \mu\text{m}$, and the fabricated tip structures show a base tilt angle of 45° .

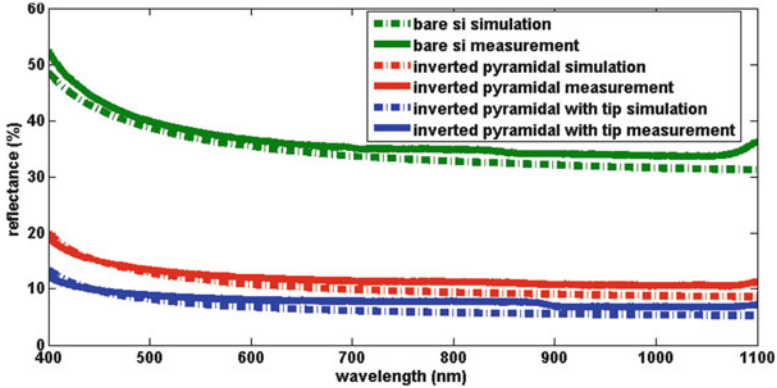


Fig. 14.4 The measured reflectances (*solid lines*) and simulated reflectances (*dashed lines*) verse wavelength for the cases of bare Si, inverted pyramidal structures without the tips, and inverted pyramidal structures with the tips. The flat surfaces surrounding the unit structure are not considered in the simulation results

In order to certify the effect of the inverted pyramidal structures with and without the tips, the reflectances were analyzed by UV–VIS–NIR spectrophotometer (V-570, Jasco, Inc.) with integrating sphere for wavelengths ranging from 400 to 1,100 nm. The smaller incident light angle is $\sim 8^\circ$ which is near normal incidence. At the same time, we simulate the reflections of these structures based on the measured structure parameters by the ray tracing software Tracepro [60]. The area of the simulation structure is $10 \mu\text{m} \times 10 \mu\text{m}$ and the thickness is $200 \mu\text{m}$. The simulation source is assumed plane wave which wavelength range is from 400 to 1,100 nm. There are total 10,000 light rays irradiated from the top surface down to the whole structure, and the incidence lights power is set as 1 W. Figure 14.4 shows the measurement and simulation results of the inverted pyramidal structure without and with the tips. The difference between inverted pyramidal structures without the tips and with the tips was compared. From the experiment and simulation results, the reflection is smaller for the pyramidal structures with the tips. Compared to the inverted pyramidal structures without the tips, its reflection reduces to 3–4 %.

According to the above results, the inverted pyramidal structures with the tips have smaller reflections as comparing to the inverted pyramidal without the tips. On the other hand, the time of reflection of light incident on these two structures can be analyzed by the ray tracing simulations. For the inverted pyramidal structures without the tips, the percentages of the areas have two times of reflections 59.26 % and three times of reflections 40.74 %, but no more than four times of reflections. For the inverted pyramidal structures with the tips, the percentages of the areas have two times of reflections 22.71 %, three times of reflections 55.26 %, four times of reflections 21.89 %, and five times or more of reflections 0.14 %. The results indicate that the structure we proposed can reach more times of reflection

and it can absorb more light. The relations between current and voltage of the solar cells with our designed antireflection structures in ideal situation can be calculated by the detail balance theory [61] and the reflections obtained by the ray tracing method. Considering the silicon bandgap and AM 1.5 solar spectra [62] and assuming the quantum efficiency as one, the short circuit current density of inverted pyramidal structures without the tips can be calculated as 38.24 mA/cm^2 and the inverted pyramidal structures without the tips is 39.56 mA/cm^2 . Although it is not reality, it can give the evaluation of the electronic performances after sunlight illuminations. The short circuit current density can be enhanced about 3.45 % as if these antireflection structures are integrated with electrodes for electric power throughput.

5 Light Trapping of the Nanophotonic Structures with Metallic or Dielectric Nanoparticles

Recently, using nanophotonic, subwavelength, or deep-subwavelength structures for enhancing the light trapping properties in thin film or ultra-thin film solar cells get a lot of attention. The silicon material is considered as the solar cell substrates for the simulation cases in this section. The thickness of the silicon materials is not considered to avoid complexities. Although this consideration is not valid for the solar cells with finite thin film thickness, the simulation results demonstrated in this section can give the physical understanding and the light trapping mechanism can be easier to capture under the simplified assumptions. In this section, usage of the metallic nanoparticles or dielectric nanoparticles for light trapping structures is demonstrated, and their performances are discussed. Because of the structures are comparable of light wavelength, the geometrical optics is not valid, and the rigorous electromagnetic simulations are taken for the study of these nanophotonic structures.

Figure 14.5a shows the cross-sectional view and the top view of the simulation scheme for the periodic metallic nanoparticles on the silicon substrate. The normal incident light is set to propagate to the structures with x -polarization for the wavelength from 400 to 1,100 nm. The periodic boundary conditions are set on the x - y boundaries to form the square nanoparticle array. The perfectly matched layers are set at the top and bottom in z -axis. Because the structures are symmetric, the results for x -polarization are same as y -polarization. Thus, the results for x -polarization can represent the results for unpolarized light, such as sun light. If the structures are not symmetric or the angle dependence has to be considered, the simulations for s -polarization and p -polarization should be simulated separately and then average of these results is for simulating unpolarized sun light conditions. The simulations are done by the Lumerical FDTD Solutions Software [63], which is based on the finite-different time-domain method. Figure 14.5b shows the

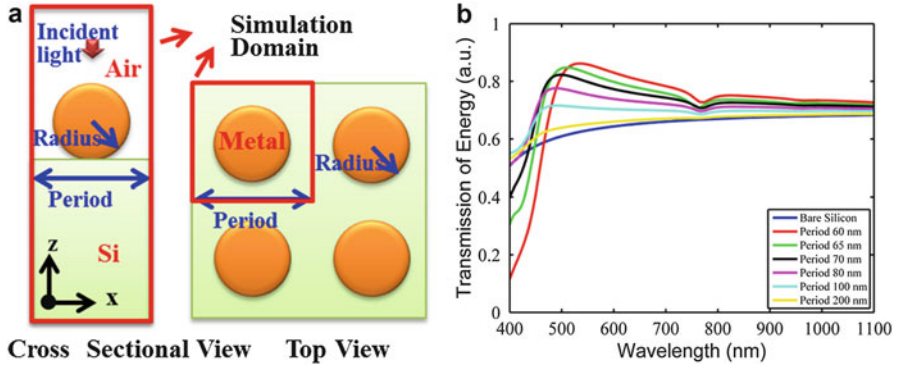


Fig. 14.5 (a) The cross-sectional view and top view of the simulation scheme, and (b) transmission curves of silver nanoparticles with radius 25 nm but different periods

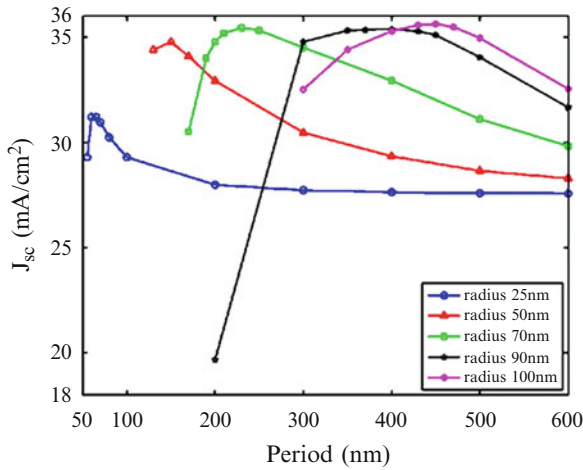
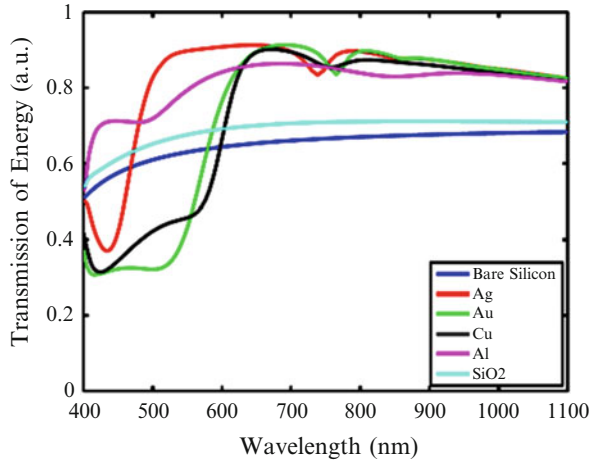


Fig. 14.6 The calculated short circuit current of varied radii of nanoparticles via the period of the nanoparticle array

transmission energy into silicon with various periods for the silver nanoparticles which radiuses are fixed at 25 nm. It is found that the peak value of transmission decreases, and the curve is close to the result for bare silicon without nanoparticles when the array period becomes larger.

To be easier to evaluate and to compare the light trapping performances for the nanoparticle distributions with different period, size, and material, the short circuit current densities are calculated by the transmissions from FDTD simulations and the detail balance theory is used in consideration of AM 1.5 solar spectra [61, 62]. As shown in previous section, to be easier, the quantum efficiency is assumed as one although it is not reality but it can give the evaluation of the electronic performances after sunlight illuminations. Figure 14.6 shows the

Fig. 14.7 The transmission energy into the silicon substrate for the nanoparticles with different materials. The period and radius of the nanoparticles are 400 nm and 90 nm, respectively



calculations for the periodic silver nanoparticles with different period and size. It is found that the maximum short circuit current appears at longer period as the nanoparticle size is larger. It should be also noticed that the short circuit current densities are not large as the nanoparticle radius is only 25 nm.

Considering the material effect, Fig. 14.7 shows the metallic nanoparticles with period 400 nm and radius 90 nm but different metallic material. It is found that the copper and gold nanoparticles have similar transmission simulation results because their optical properties are similar in the spectrum we consider. The silver nanoparticles perform better due to the low loss of silver material in most spectrum regions.

Figure 14.8 represents the short circuit current densities which are calculated from transmission energy via period with 25, 50, 70, 90, and 100 nm radii, respectively, for silver, aluminum, gold, copper, and silicon dioxide nanoparticles. Silver and aluminum have better performances in these figures as comparing to the other materials. From the results of silicon dioxide nanoparticles, it is found that the maximum of short circuit current densities happens for the close-packed form, i.e., the period is same as the diameter of the nanoparticles. This can be also used to explain why the performance of silica nanoparticle distribution in Fig. 14.7 is not good because it is not close-packed form in Fig. 14.7. It is different for metallic nanoparticle cases, which needs the gaps between metallic nanoparticles to allow better light trapping performances.

To understand the period effect for metallic nanoparticles, the transmissions for the silver nanoparticles array with radius 100 nm and period 250, 450, and 600 nm are shown in Fig. 14.9a. The radiation patterns of different periodic silver nanoparticles with 100 nm radii are represented in Fig. 14.9b–d at wavelength 836 nm, and the maximum short circuit current appears at 450 nm period. The periods of the particle are 250, 450, and 600 nm. If the space of two particles is close for the case with period 250 nm, the strong field enhancement concentrates

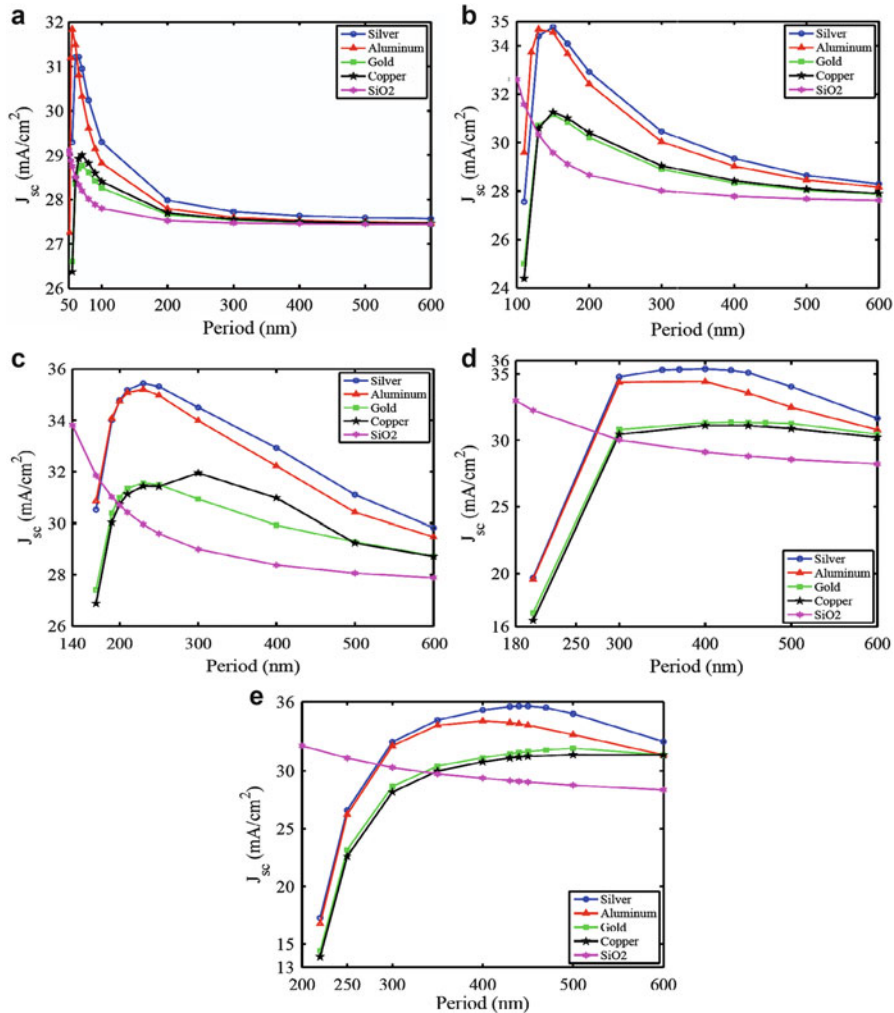


Fig. 14.8 The short circuit current densities verse period for the nanoparticles with radii of (a) 25 nm, (b) 50 nm, (c) 70 nm, (d) 90 nm, and (e) 100 nm, respectively

between particles. If the space of two particles is too far for the case with period 600 nm, some regions of silicon material does not have good light transmissions because the silver nanoparticles can only radiate the light energy into the silicon material in finite regions. The suitable space between two silver nanoparticles should be chosen, such as the case with period 450 nm, to have better transmission energy into silicon materials.

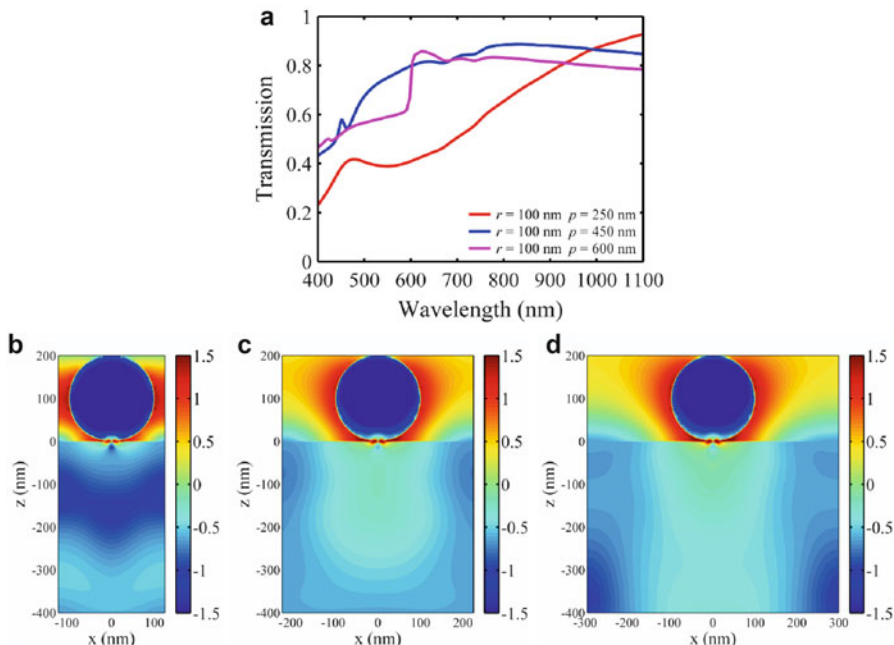


Fig. 14.9 (a) The transmission of 100 nm silver nanoparticle array with period 250, 450, and 600 nm. The electric field intensity distributions of the cases with period (b) 250 nm, (c) 450 nm, and (d) 600 nm at wavelength 836 nm

6 Light Trapping for the Nanophotonic Structures with Mixing Metallic and Dielectric Nanoparticles or Materials

In previous section, the metallic nanoparticles and dielectric nanoparticles distributed atop the silicon substrate are discussed. From these simulation results, the good light trapping properties with suitable material, period, and size of nanoparticles can be chosen for silicon solar cell materials. During these years, there are some debates to use metallic nanoparticles or dielectric nanoparticles for better light trapping performances [44, 64]. We propose to use mixing of dielectric material and metallic nanoparticles atop the silicon substrate to get better light trapping performances as comparing to using metallic nanoparticles only or dielectric nanoparticles only [33, 34]. A systematic approach to analyze the silver nanoparticles and silica material combinations for four different kinds of structures are provided here.

Figure 14.10 shows the structure which has the silver nanoparticles wrapped inside the silica nanoparticles atop the silicon substrate. The structures with various radii of silver and silica nanoparticles are simulated by FDTD method. The light transmissions for the structures with different radii of silica and silver particles are

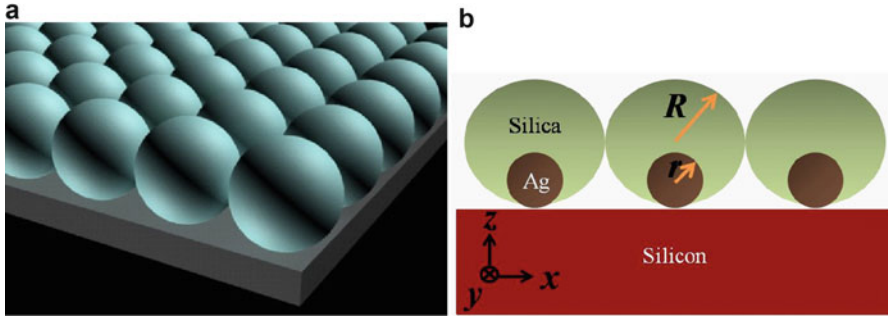


Fig. 14.10 (a) Top view of the structure A, with mixing metallic and dielectric materials and (b) the cross-sectional view of structure, where R is the radius of the silica particle and r is the radius of the silver particle

shown in Fig. 14.11. It is found that the optical transmission increases as the radius of silica increases for most cases. The optical transmission is stronger at longer wavelength but weaker at shorter wavelength. It is because of the silver nanoparticles have strong absorptions at short wavelength. It is also found that there is red-shift for optical transmission as the radii of silver nanoparticles increase. It is found that the optical transmission decreases as the radius of silver nanoparticles is close to the radius of silica nanoparticles. If the ratio of radius of silver and silica nanoparticles is more than 0.5, the absorption is obviously small in short wavelength range. According to the simulated transmission results in Fig. 14.11, the total transmitted photon numbers for each different structure can be calculated based on AM 1.5 solar spectra and the results are shown in Fig. 14.12. It is found that more photons can transmit into the silicon substrate as the ratio $r/R \sim 0.5$. To show how the light goes into the silicon material, the electric field intensities for the cases in Fig. 14.11c at wavelength 674 nm are plotted in Fig. 14.13. It is found that the higher electric field concentrates at the region between silica particles and the silicon material for the case with small silver nanoparticle, i.e., $r = 20$ nm. For the case with the ratio $r/R \sim 0.5$, i.e., $r = 40$ nm and $R = 80$ nm, there is more light going into the silicon material. If the silver nanoparticle is large, the strong field enhancement couples between silver and silica particles and only few light energy penetrates into silicon. Thus, the suitable ratio of r and R can be designed to get the better photon transmissions.

The second structure with mixing metallic and dielectric nanoparticles is shown in Fig. 14.14, where the silica particles are stacked upon the silver particles atop the silicon substrate. The structures with various radii of silver and silica nanoparticles are simulated by FDTD method. The light transmissions of structure B with different parameters are shown in Fig. 14.15. Similar as the simulation results of structure A, the simulation results of structure B has the stronger optical transmission at longer wavelength but weaker at shorter wavelength. Also, the optical transmission decreases sharply as the radius of silver nanoparticles is close to the radius of silica nanoparticles, and it is even worse than base silicon substrate case.

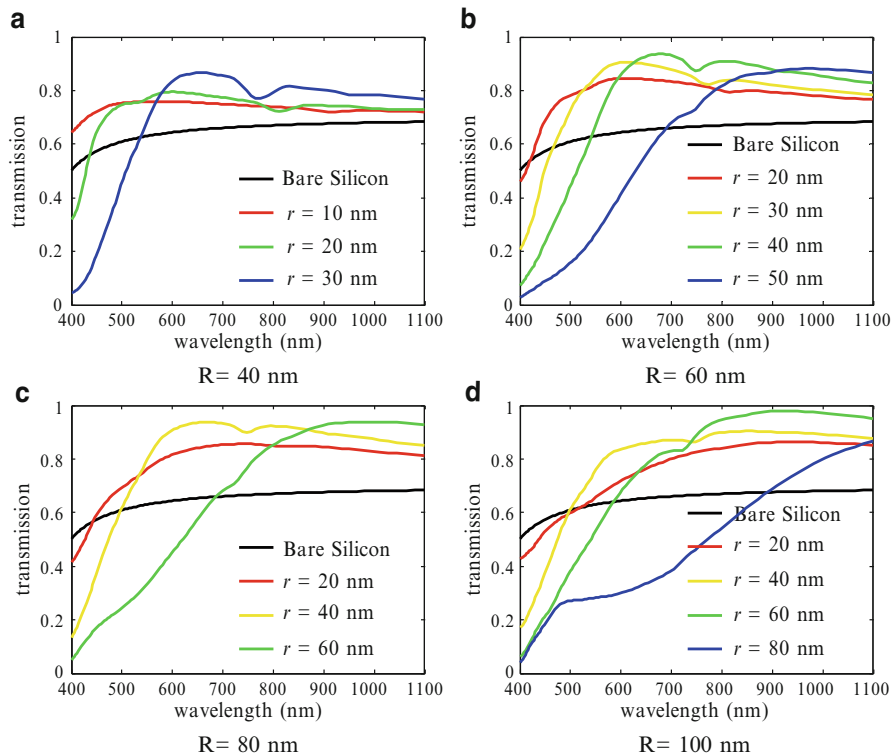


Fig. 14.11 The optical transmission of the structure A with the close-packed form, where the radius of silica nanoparticles is (a) 40 nm, (b) 60 nm, (c) 80 nm, and (d) 100 nm, and the radii of the silver nanoparticles are varied for each sub-figures

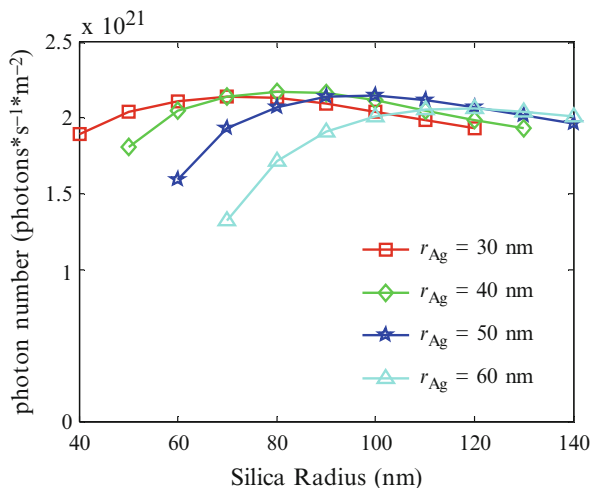


Fig 14.12 The total photon number transmitting into the silicon material per second and per unit area in consideration of the AM 1.5 solar spectra for the structure A with different sizes of silica and silver nanoparticles

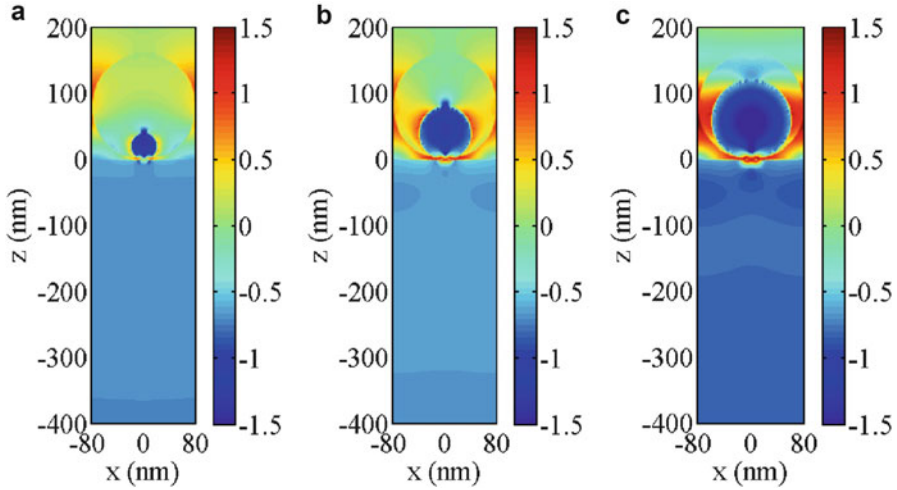


Fig. 14.13 The electric field intensity distributions normalized by the incident waves in x - z planes for the incident light with wavelength 674 nm in the structure A, where the radius of silver nanoparticles is 20 nm for (a), 40 nm for (b), and 60 nm for (c). The radius of silica nanoparticles is 80 nm in all cases. The scale bar is in logarithmic scale

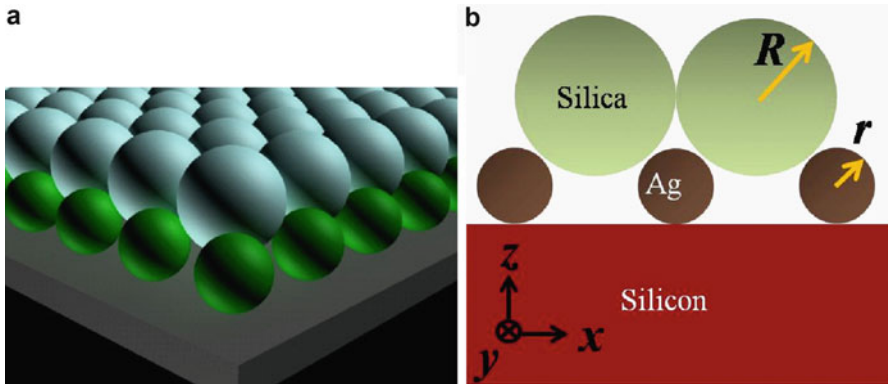


Fig. 14.14 (a) The top view and (b) the cross-sectional view of structure B

This is because the whole structure is dominated by the almost close-packed form of silver nanoparticles. From the calculated photon number in Fig. 14.16, the photon number decreases sharply as the radius of silver and silica have the same values. Figure 14.17 is the electric field distribution for the cases with $R = 60$ nm at wavelength 747 nm where the maximum photon number appears at $r = 40$ nm and $R = 60$ nm in Fig. 14.16. If the silver particles are too small, the electric field scatters to free space. If silver particles are very close to each other, the transmission energy is limited into the silicon material. It is found that structure A can

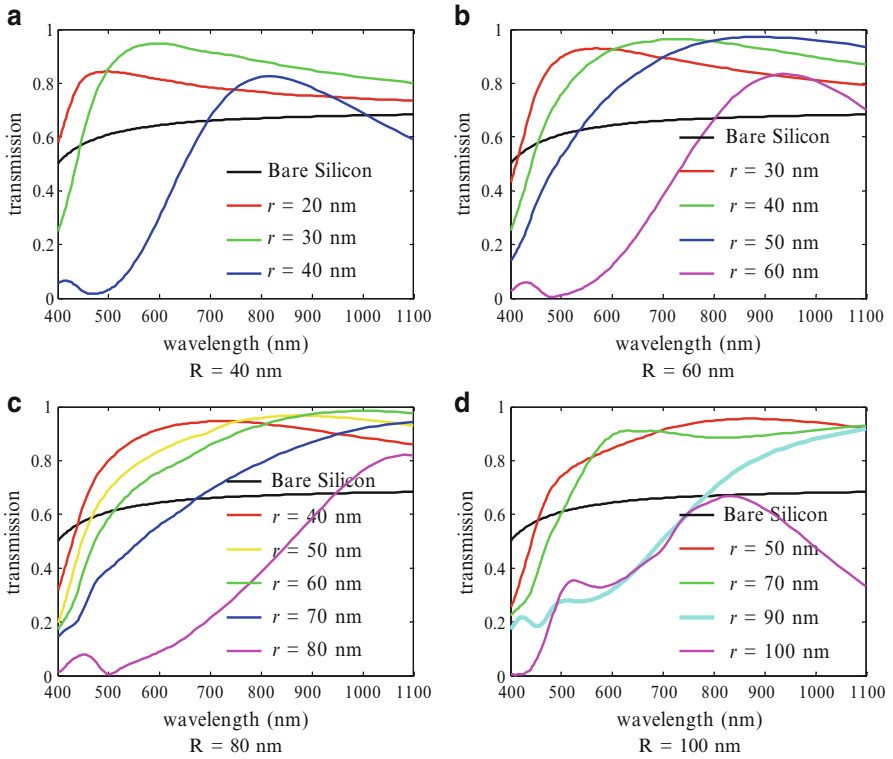


Fig. 14.15 The optical transmission of structure B with the close-packed form, where the radius of silica nanoparticles is fixed at (a) 40 nm, (b) 60 nm, (c) 80 nm, and (d) 100 nm. The radii of the silver nanoparticles are varied

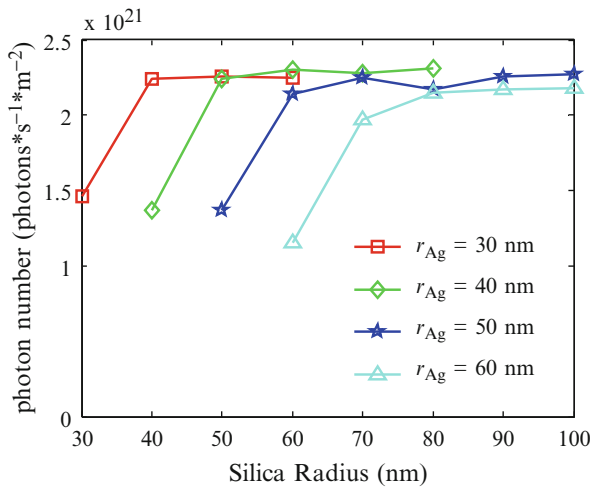


Fig. 14.16 The total photon number transmitting into the silicon material per second and per unit area in consideration of the AM 1.5 solar spectra for structure B with different sizes of silica and silver nanoparticles

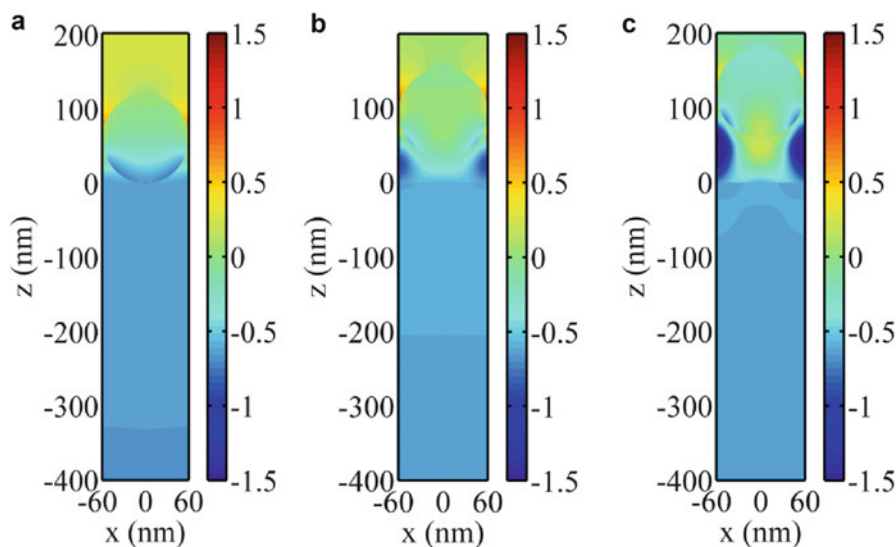


Fig. 14.17 The electric field intensity distributions normalized by the incident waves in x - z planes for the incident light with wavelength 747 nm in the structure B, where the silica nanoparticles in radius 60 nm and the silver nanoparticles in radius 30 nm for (a), 40 nm for (b), and 50 nm for (c). The scale bar is in logarithmic scale

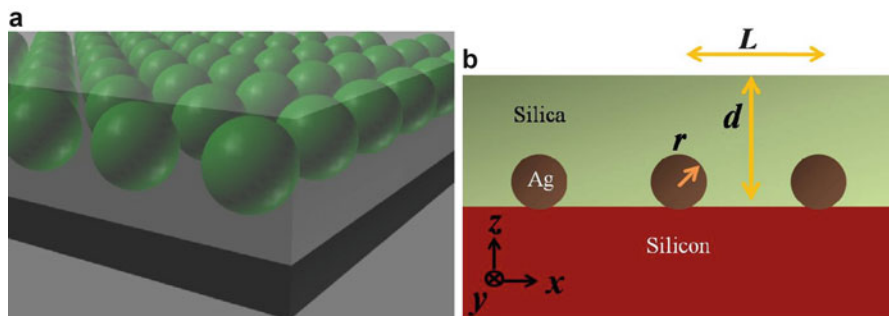


Fig. 14.18 (a) Top view and (b) the cross-sectional view of structure C

generate stronger field at the interface of silicon and silver particles, but structure B can bring more energy into silicon.

The third structure is the periodic silver particle array is embedded in a silica layer atop the silicon substrate as shown in Fig. 14.18. Figure 14.18a is the top view and Fig. 14.18b is the cross-sectional view of structure C, where r is the radius of the silver particle, d is the thickness of the silica layer, and L is the period of the array. Various cases with different d , L , and r are simulated and the results are shown in Fig. 14.19a. The maximum photon generation appears at the case with $r = 70$ nm, $d = 120$ nm, and $L = 460$ nm in Fig. 14.19a. If the radius of silver is

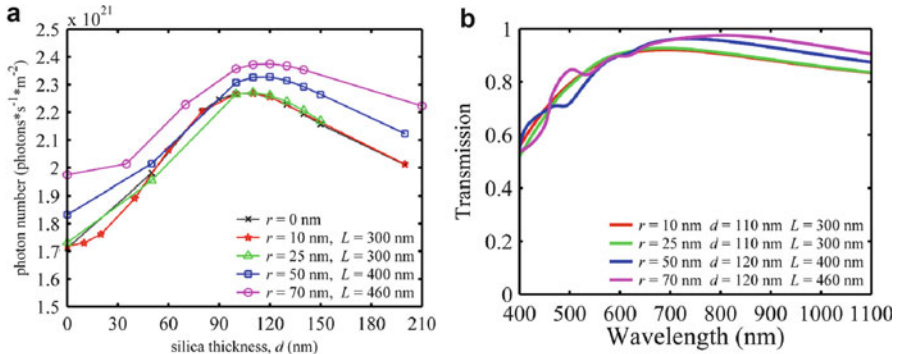


Fig. 14.19 (a) The photon number verse different silica thicknesses with various radii and periods and (b) the transmission curves for the optimized cases of each curve in (a)

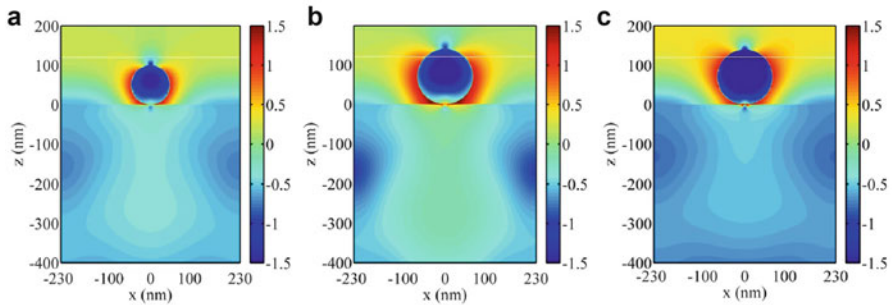


Fig. 14.20 The electric field intensity distributions normalized by the incident waves in $x-z$ planes for the incident light with wavelength 804 nm in the structure C, where silica thin film is 120 nm and the radiuses of the silver nanoparticles is 50 nm for (a), 70 nm for (b), and without silica layer for (c). The period for all cases is 460 nm. The white line stands for the surface of silica thin film. The scale bar is in logarithmic scale

small as 25 nm, the photon number generation is similar as no silver particles. The effect of d is more than the effect of L when the radius of silver is small and L is larger than the radius. The transmission curves for the optimized cases each curve in Fig. 14.19a are shown in Fig. 14.19b. The electric field intensities for the cases with silica thin film 120 nm and the radiuses of the silver nanoparticles 50 nm and 70 nm are shown in Fig. 14.20a and b, respectively. It shows that the strong field enhancements and more light guiding into the silicon material. To be compared, Fig. 14.20c shows the electric field intensities for the same nanoparticle structure but without the silica thin film in Fig. 14.20b. It is obvious that some light are scattered back to the air regions by the silver nanoparticles, and it results smaller photon number transmissions as shown in Fig. 14.19a.

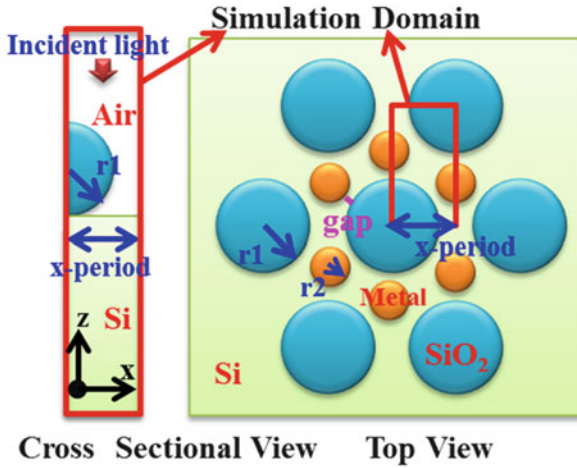


Fig. 14.21 Cross-sectional view and top view of the simulation scheme for structure D, where r_1 and r_2 indicate the radius of silica nanoparticles and metallic nanoparticles, respectively

The fourth nanophotonic structure D with mixing the dielectric and metallic nanoparticles is shown in Fig. 14.21, where the smaller nanoparticles are metallic and the larger nanoparticles are dielectric. With systematic study [34], it is found that light trapping structure with mixing dielectric and metallic nanoparticles can be superior than the structure with dielectric nanoparticles only or metallic nanoparticles only. This is because that the metallic nanoparticles can provide the plasmonic antenna effects and the dielectric nanoparticles provide the effective refractive index benefits. With careful chosen nanoparticle parameters, the optimized optical transmissions for AM 1.5 solar spectra can be obtained. Figure 14.22 shows the transmission energy for different size of silver nanoparticles with silica nanoparticles. It is found that the good transmission happens for the radius ratio 0.5 in Fig. 14.22a, and the red shift happens as the particle sizes get larger with fixed radius ratio in Fig. 14.22b. The electric field intensities for three cases with radius ratio 0.1, 0.5, and 0.9, under wavelength 774 nm are shown in Fig. 14.23. For smaller ratio, the silver nanoparticles are too small and cannot radiate light energy well into the silicon materials. For larger ratio, strong electric field intensities happen at the regions between silver and silica nanoparticles but little light energy can transmit into silicon material. With the ratio 0.5, it can be seen that the light can transmit into the silicon material well. These findings can be useful for guidelines to design nanophotonic light trapping structures by mixing dielectric and metallic nanoparticle distributions.

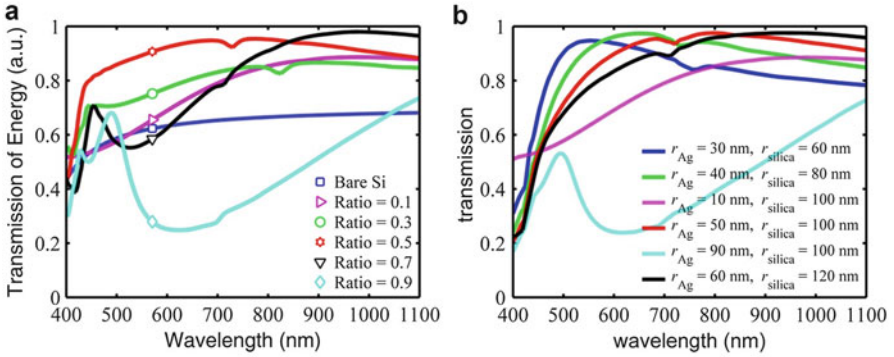


Fig. 14.22 (a) The energy transmission of small silver nanoparticles in radius 10, 30, 50, 70, and 90 nm with large silica nanoparticles in radius 100 nm which have the form of close-packed structure upon silicon substrate. (b) The transmission of silica nanoparticles in radii 60, 80, 100, and 120 nm at Ratio = 0, where Ratio indicates the radius of metal particle divide the radius of silica nanoparticles. The maximum photon number occurs in the case $r_{silica} = 100$ nm and $r_{Ag} = 50$ nm

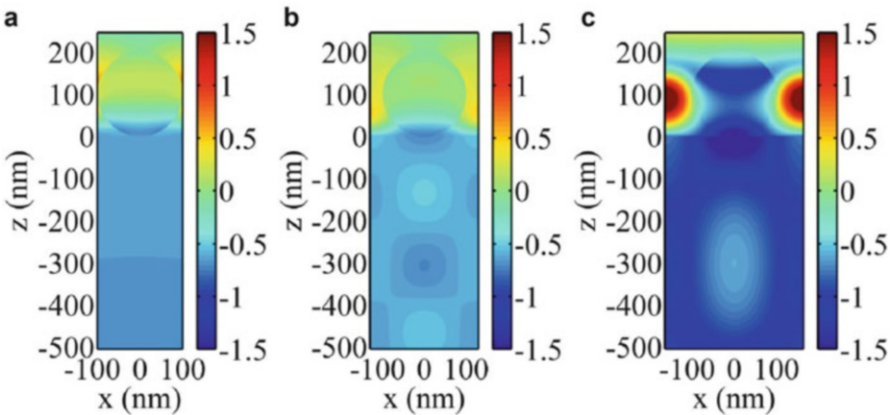


Fig. 14.23 The electric field intensity distribution in x - z plane and incident light at wavelength 774 nm where the radius of large silica nanoparticles is 100 nm with small silver nanoparticles in radius (a) 10 nm, (b) 50 nm, and (c) 90 nm. The scale bar is in logarithmic scale

7 Conclusions and Outlook

In this chapter, the micrometer-scale textured structures and nanometer-scale photonic structures for using as the light trapping structures in solar cells applications have been studied. For the micrometer-scale textured structures, the reflectivities of the tips inside the inverted pyramidal structures are studied numerically and experimentally. The results show that the structures with the suitable tips

can increase the antireflection efficiency, and it shows that the light can have multiple reflections between different surfaces of the textured structures and the tips. Thus, more light energies are trapped and absorbed by the silicon materials. Four different nanophotonic light trapping structures are presented and their optical performances are studied numerically by rigorous electromagnetic simulations. The results show that combinations of metallic and dielectric nanoparticles or materials can have better light trapping performances than using one single material. The presented structures and the described physical explanations can be useful for the designs of light trapping structures for the solar cells, light emissions, or other antireflection applications.

The two-dimensional disordered nanophotonic media has been studied to enhance the light trapping with broaden illumination incident angles and wavelengths [65, 66]. It is expected that the study of the random patterns on the light trapping performances will give more attentions [67]. Besides the disordered or random structures, the multiscale light trapping structures can be important in current solar cell manufacturing. For example, one can distribute the nanoparticles or nanophotonic structures on the microscale inverted pyramidal nanostructures with the tips. This can give immediate light trapping improvements and it should be not hard to integrate into the current fabrication processes. The photosynthesis happens in plant every day, and we think that there will be more research to use the design from the grana in chloroplast of plant for design better engineered light trapping structures with good quantum efficiency [68].

During recent year, there are more and more scientific studies on the fundamental theory of the light trapping structures for high efficiency solar cells. This gives the scientists and engineers having more understandings of high-performance light trapping structures. Although this may be not an easy task, more elegant engineering designs of light trapping structures in consideration of different type solar cells and merging into manufacturing processes will be developed in the coming years.

Acknowledgments This work was supported by the Seed Project of NTU-ITRI Nano Center, National Science Council of Taiwan (NSC-96-2221-E-002-133-MY3, NSC-98-2120-M-002-004, NSC-100-2221-E-002-155), NTU Career Development Project (10R70816, 101R7816), and Tzong Jwo Jang Educational Foundation (97-S-A10).

References

1. Wolf, M.: Historical development of solar cell. In: Backus, C.E. (ed.) *Solar Cells*. IEEE Press, New York (1976)
2. Green, M.A., Emery, K., Hishikawa, Y., Warta, W., Dunlop, E.D.: Solar cell efficiency tables (version 41). *Prog. Photovolt. Res. Appl.* **21**(1), 1–11 (2013)
3. Powell, D.M., Winkler, M.T., Choi, H.J., Simmons, C.B., Berney Needleman, D., Buonassisi, T.: Crystalline silicon photovoltaics: a cost analysis framework for determining technology pathways to reach baseload electricity costs. *Energy Environ. Sci.* **5**, 5874–5883 (2012)

4. Daif, O.E., Drouard, E., Gomard, G., Kamiski, A., Fave, A., Lemiti, M., Ahn, S., Kim, S., Cabarrocas, P.R.I., Jeon, H., Seassal, C.: Absorbing one-dimensional planar photonic crystal for amorphous silicon solar cell. *Opt. Express* **18**, A293–A299 (2010)
5. Deckman, H.W., Wronski, C.R., Witzke, H., Yablonovitch, E.: Optically enhanced amorphous silicon solar cells. *Appl. Phys. Lett.* **42**, 968–970 (1983)
6. Grandidier, J., Callahan, D.M., Munday, J.N., Atwater, H.A.: Gallium arsenide solar cell absorption enhancement using whispering gallery modes of dielectric nanospheres. *IEEE J. Photovolt.* **2**(2), 123–128 (2012)
7. Li, B., Liu, J., Xu, G., Lu, R., Feng, L., Wu, J.: Development of pulsed laser deposition for CdS/CdTe thin film solar cells. *Appl. Phys. Lett.* **101**, 153903 (2012)
8. Carrington, P.J., Wagener, M.C., Botha, J.R., Sanchez, A.M., Krier, A.: Enhanced infrared photo-response from GaSb/GaAs quantum ring solar cells. *Appl. Phys. Lett.* **101**, 231101 (2012)
9. Cao, J., Zhan, Z., Hou, L., Long, Y., Liu, P., Mai, W.: Optical modeling of organic solar cells based on rubrene and C₇₀. *Appl. Opt.* **51**, 5718–5723 (2012)
10. Shahrjerdi, D., Bedell, S.W., Ebert, C., Bayram, C., Hekmatshoar, B., Fogel, K., Lauro, P., Gaynes, M., Gokmen, T., Ott, J.A., Sadana, D.K.: High-efficiency thin-film InGaP/InGaAs/Ge tandem solar cells enabled by controlled spalling technology. *Appl. Phys. Lett.* **100**, 053901 (2012)
11. Imenes, A.G., Mills, D.R.: Spectral beam splitting technology for increased conversion efficiency in solar concentrating systems: a review. *Sol. Energy Mater. Sol. Cells* **84**, 19–69 (2004)
12. Polmanand, A., Atwater, H.A.: Photonic design principles for ultrahigh-efficiency photovoltaics. *Nat. Mater.* **11**, 174–177 (2012)
13. Chiao, S.C., Zhou, J.L., Macleod, H.A.: Optimized design of an antireflection coating for textured silicon solar cells. *Appl. Opt.* **32**, 5557–5560 (1993)
14. Dobrowolski, J.A., Poitras, D., Ma, P., Vakil, H., Acree, M.: Toward perfect antireflection coatings: numerical investigation. *Appl. Opt.* **41**, 3075–3083 (2002)
15. Singh, P., Sharma, S.N., Ravindra, N.M.: Applications of porous silicon thin films in solar cells and biosensors. *JOM* **62**(6), 15–24 (2010)
16. Xi, Z., Yang, D., Que, D.: Texturization of monocrystalline silicon with tribasic sodium phosphate. *Sol. Energy Mater. Sol. Cells* **77**(3), 255–263 (2003)
17. Iencinella, D., Centurioni, E., Rizzoli, R., Zignani, F.: An optimized texturing process for silicon solar cell substrates using TMAH. *Sol. Energy Mater. Sol. Cells* **87**(1–4), 725–732 (2005)
18. Papet, P., Nichiporuk, O., Kaminski, A., Rozier, Y., Kraiem, J., Lelievre, J.F., Chaumartin, A., Fave, A., Lemiti, M.: Pyramidal texturing of silicon solar cell with TMAH chemical anisotropic etching. *Sol. Energy Mater. Sol. Cells* **90**(15), 2319–2328 (2006)
19. Hayashi, S., Minemoto, T., Takakura, H., Hamakawa, Y.: Influence of texture feature size on spherical silicon solar cells. *Rare Metal* **25**(6), 115–120 (2006)
20. Campbell, P., Green, M.A.: Light trapping properties of pyramidally textured surfaces. *J. Appl. Phys.* **62**(1), 243–249 (1987)
21. Baker-Finch, S.C., McIntosh, K.R.: Reflection of normally incident light from silicon solar cells with pyramidal texture. *Prog. Photovolt. Res. Appl.* **19**(4), 406–416 (2011)
22. Zhao, J., Wang, A., Altermatt, P.P., Wenham, S.R., Green, M.A.: 24% efficient per l silicon solar cell: recent improvements in high efficiency silicon cell research. *Sol. Energy Mater. Sol. Cells* **41/42**, 87–99 (1996)
23. Zhao, J., Wang, A., Green, M.A., Ferrazza, F.: 19.8% efficient ‘honeycomb’ textured multicrystalline and 24.4% monocrystalline silicon solar cells. *Appl. Phys. Lett.* **73**, 1991–1993 (1998)
24. Tsakalagos, L., Balch, J., Fronheiser, J., Korevaar, B.A., Sulima, O., Rand, J.: Silicon nanowire solar cells. *Appl. Phys. Lett.* **91**, 233117–233120 (2007)

25. Lee, Y.C., Huang, C.F., Chang, J.Y., Wu, M.L.: Enhanced light trapping based on guided mode resonance effect for thin-film silicon solar cells with two filling-factor gratings. *Opt. Express* **16**(11), 7969–7975 (2008)
26. Nakaya, H., Nishida, M., Takeda, Y., Moriuchi, S., Tonegawa, T., Machida, T., Nunoi, T.: Polycrystalline silicon solar cells with V-grooved surface. *Sol. Energy Mater. Sol. Cells* **34** (1–4), 219–225 (1994)
27. Wang, X.D., Graugnard, E., King, J.S., Wang, Z.L., Summers, C.J.: Large-scale fabrication of ordered nanobowl arrays. *Nano Lett.* **4**(11), 2223–2226 (2004)
28. Leem, J.W., Joo, D.H., Yu, J.S.: Biomimetic parabola-shaped AZO subwavelength grating structures for efficient antireflection of Si-based solar cells. *Sol. Energy Mater. Sol. Cells* **95** (8), 2221–2227 (2011)
29. Leem, J.W., Yu, J.S., Song, Y.M., Lee, Y.T.: Antireflective characteristics of disordered GaAs subwavelength structures by thermally dewetted Au nanoparticles. *Sol. Energy Mater. Sol. Cells* **95**(2), 669–676 (2011)
30. Hamakawa, Y. (ed.): *Thin-Film Solar Cells: Next Generation Photovoltaics and Its Applications*. Springer, Berlin (2004)
31. Catchpole, K.R., Polman, A.: Plasmonic solar cells. *Opt. Express* **16**(26), 21793–21800 (2008)
32. Atwater, H.A., Polman, A.: Plasmonics for improved photovoltaic devices. *Nat. Mater.* **9**(3), 205–213 (2010)
33. Yeh, Y.-M., Wang, Y.-S., Li, J.-H.: Enhancement of the optical transmission by mixing the metallic and dielectric nanoparticles atop the silicon substrate. *Opt. Express* **19**(S2), A80–A94 (2011)
34. Yang, H.-Y., Chen, S.-W., Lin, I.-B., Li, J.-H.: Enhanced light trapping for the silver nanoparticles embedded in the silica layer atop the silicon substrate. *Appl. Phys. A* **112**(3), 525–532 (2013)
35. Dewan, R., Knipp, D.: Light trapping in thin-film silicon solar cells with integrated diffraction grating. *J. Appl. Phys.* **106**(7), 074901–074907 (2009)
36. Duche, D., Torchio, P., Escoubas, L., Monestier, F., Simon, J.J., Flory, F., Mathian, G.: Improving light absorption inorganic solar cells by plasmonic contribution. *Sol. Energy Mater. Sol. Cells* **93**, 1377–1382 (2009)
37. Yang, L., Xuan, Y., Tan, J.: Efficient optical absorption in thin-film solar cells. *Opt. Express* **19** (S5), A1165–A1174 (2011)
38. Vedraïne, S., Torchio, P., Duche, D., Flory, F., Simon, J.J., LeRouzo, J., Escoubas, L.: Intrinsic absorption of plasmonic structures for organic solar cells. *Sol. Energy Mater. Sol. Cells* **95**, S57–S64 (2011)
39. Pala, R.A., White, J., Barnard, E., Liu, J., Brongersma, M.L.: Design of plasmonic thin-film solar cells with broadband absorption enhancements. *Adv. Mater.* **21**(34), 3504–3509 (2009)
40. Yang, Y., Pillai, S., Mehrvarz, H., Kampwerth, H., Ho-Baillie, A., Green, M.A.: Enhanced light trapping for high efficiency crystalline solar cells by the application of rear surface plasmons. *Sol. Energy Mater. Sol. Cells* **101**, 217–226 (2012)
41. Pillai, S., Beck, F.J., Catchpole, K.R., Ouyang, Z., Green, M.A.: The effect of dielectric spacer thickness on surface plasmon enhanced solar cells for front and rear side depositions. *J. Appl. Phys.* **109**(7), 073105 (2011)
42. Xu, R., Wang, X., Liu, W., Song, L., Xu, X., Ji, A., Yang, F., Li, J.: Optimization of the dielectric layer thickness for surface-plasmon-induced light absorption for silicon solar cells. *Jpn. J. Appl. Phys.* **51**(4), 042301 (2012)
43. Huang, C.K., Lin, H.H., Chen, J.Y., Sun, K.W., Chang, W.-L.: Efficiency enhancement of the poly-silicon solar cell using self-assembled dielectric nanoparticles. *Sol. Energy Mater. Sol. Cells* **95**(8), 2540–2544 (2011)
44. Matheu, P., Lim, S.H., Derkacs, D., McPheeters, C., Yu, E.T.: Metal and dielectric nanoparticle scattering for improved optical absorption in photovoltaic devices. *Appl. Phys. Lett.* **93** (11), 113108 (2008)

45. Qu, D., Liu, F., Yu, J., Xie, W., Xu, Q., Li, X., Huang, Y.: Plasmonic core-shell gold nanoparticle enhanced optical absorption in photovoltaic devices. *Appl. Phys. Lett.* **98**(11), 113119 (2011)
46. Akimov, Y.A., Koh, W.S.: Design of plasmonic nanoparticles for efficient subwavelength light trapping in thin-film solar cells. *Plasmonics* **6**(1), 155–161 (2011)
47. Brown, M.D., Suteewong, T., Kumar, R.S.S., D’Innocenzo, V., Petrozza, A., Lee, M.M., Wiesner, U., Snaith, H.J.: Plasmonic dye-sensitized solar cells using core-shell metal-insulator nanoparticles. *Nano Lett.* **11**(2), 438–445 (2011)
48. Yablonoitch, E.: Statistical ray optics. *J. Opt. Soc. Am.* **72**(7), 899–907 (1982)
49. Green, M.: Lambertian light trapping in textured solar cells and light-emitting diodes: analytical solutions. *Prog. Photovolt. Res. Appl.* **10**(4), 235–241 (2002)
50. Campbell, P., Green, M.A.: The limiting efficiency of silicon solar cells under concentrated sunlight. *IEEE Trans. Electron Dev.* **ED-33**(2), 234–239 (1986)
51. Yu, Z., Raman, A., Fan, S.: Fundamental limit of light trapping in grating structures. *Opt. Express* **18**(S3), A366–A380 (2010)
52. Yu, Z., Raman, A., Fan, S.: Fundamental limit of nanophotonic light trapping in solar cells. *Proc. Natl Acad. Sci. U.S.A.* **107**(41), 17491–17496 (2010)
53. Callahan, D.M., Munday, J.N., Atwater, H.A.: Solar cell light trapping beyond the ray optic limit. *Nano Lett.* **12**, 214–218 (2012)
54. Mokkapati, S., Catchpole, K.R.: Nanophotonic light trapping in solar cells. *J. Appl. Phys.* **112**, 101101 (2012)
55. Garnett, E., Yang, P.: Light trapping in silicon nanowire solar cells. *Nano Lett.* **10**(3), 1082–1087 (2010)
56. Law, M., Greene, L.E., Johnson, J.C., Saykally, R., Yang, P.: Nanowire dye-sensitized solar cells. *Nat. Mater.* **4**, 455–459 (2005)
57. Kayes, B.M., Atwater, H.A., Lewis, N.S.: Comparison of the device physics principles of planar and radial p-n junction nanorod solar cells. *J. Appl. Phys.* **97**, 114302 (2005)
58. Chen, M.-C., Yang, Y.-L., Chen, S.-W., Li, J.-H., Aklilu, M., Tai, Y.: Self-assembled monolayer immobilized gold nanoparticles for plasmonic effects in small molecule organic photovoltaic. *ACS Appl. Mater. Interfaces* **5**(3), 511–517 (2013)
59. Cheng, H.-H., Chang, Y.-Y., Chu, J.-Y., Lin, D.-Z., Chen, Y.-P., Li, J.-H.: Light trapping enhancements of inverted pyramidal structures with the tips for silicon solar cells. *Appl. Phys. Lett.* **101**, 141113 (2012)
60. Lambda Research Corporation: <http://lambdare.com/>.
61. Nelson, J.: *The Physics of Solar Cells*. Imperial College Press, London (2003)
62. Reference solar spectral irradiance: Air Mass 1.5. <http://redec.nrel.gov/solar/spectra/am1.5/>.
63. Lumerical FDTD Solution: <http://www.lumerical.com/>.
64. Akimov, Y.A., Koh, W.S., Sian, S.Y., Ren, S.: Nanoparticle-enhanced thin film solar cells: metallic or dielectric nanoparticles? *Appl. Phys. Lett.* **96**(7), 073111 (2010)
65. Vynck, K., Burresti, M., Riboli, F., Wiersma, D.S.: Photon management in two-dimensional disordered media. *Nat. Mater.* **11**, 1017–1022 (2012)
66. Burresti, M., Pratesi, F., Vynck, K., Prasciolu, M., Tormen, M., Wiersma, D.S.: Two-dimensional disorder for broadband, omnidirectional and polarization-insensitive absorption. *Opt. Express* **21**(S2), A268–A275 (2013)
67. Li, J.-H., Chen S.-W., Wang, Y.-S., Yeh Y.-M.: Effect of nanoparticle distribution on light transmission through the silicon substrate. *Proceeding of IQEC/CLEO Pacific Rim*, pp. 2153–2154, Sydney, Australia, 28 August–1 September 2011.
68. Li, J.-H., Wang, S.-J., Chang, S.-P., Chang, Y.-M., Chen, S.-J.: Numerical and experimental study of optical properties of grana under different wavelength light. *Plant Biol.* 2010, Abstract # P14018, Montréal, Canada, 31 July–4 August, 2010.

Chapter 15

Anti-reflective Silicon Oxide p-Layer for Thin-Film Silicon Solar Cells

Konrad Schwanitz and Stefan Klein

Abstract A novel kind of microcrystalline silicon oxide ($\mu\text{c-SiO}_x(\text{p})\text{:H}$) based p-layer has been developed at Applied Materials, Inc. over the last few years. This boron doped p-layer serves as a window and anti-reflective layer in micromorph (a-Si:H/ $\mu\text{c-Si:H}$) tandem solar cells on ZnO substrates. Adjusting the refractive index in the range of 2–3.5 of the p-layer enables the use as a refractive index matching layer between ZnO ($n \sim 2$) and silicon ($n \sim 4$). This results in a significant decrease of reflection up to 3 %. As a consequence the short circuit current increases significantly in the silicon thin film solar cell device. In this chapter we show that the material properties of this new kind of p-layer are closely connected to the performance of the solar cells and even reduces the light-induced degradation (LID) of a-Si/ $\mu\text{c-Si}$ tandem junction cells.

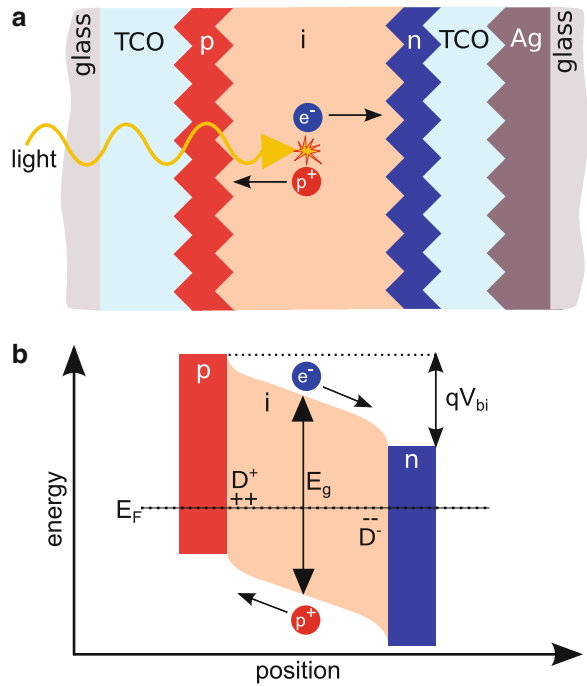
1 Introduction

Silicon thin film solar cells unite several advantages like low toxicity of its components, high availability of its materials, the monolithic integration and the scalability of producing large area modules. Unlike crystalline and polycrystalline silicon, thin film silicon of amorphous structure feature a direct bandgap of 1.7 eV [3]. Thus having a higher absorption coefficient makes it possible to use only thin films as absorber layers $< 1 \mu\text{m}$ in contrast to crystalline and polycrystalline silicon solar wafers, that have to have a thickness of several hundred micrometers.

Despite of these advantageous features, the amorphous silicon suffers from an unwanted effect leading to degradation of the material, well known as the Staebler–Wronski effect [4]. Due to UV light exposure, silicon–hydrogen bonds

K. Schwanitz (✉) • S. Klein
Applied Materials GmbH & Co. KG, Thin Film Solar Cells, Solar Business Group,
Siemensstraße 100, 63755 Alzenau, Germany
e-mail: koni.schwanitz@gmx.de

Fig. 15.1 (a) Schematic picture of the p–i–n solar cell and (b) simplified energy diagram of a p–i–n solar cell under short circuit condition. The built-in potential qV_{bi} determines the maximum amount of photo voltage. Defect states D^+ and D^- cause a band bending at the pi- and in-interfaces (adapted from [6], not drawn to scale)



are cracked and defect states are created by silicon dangling bonds. This defect states can lead to trapping and recombination of charge carriers, hence decreases the cell current. This detrimental effect, which affects the solar cell efficiency over time, is minimized by a sufficiently slow deposition and incorporation of a sufficient amount of hydrogen in the amorphous layers.

The IMT Neuchatel introduced in 1994 the microcrystalline silicon as an intrinsic absorber layer in a solar cell [5], which shows, if at all, this LID to a very small extent. Although this material has with 1.1 eV a lower bandgap than amorphous silicon, its absorption coefficient in the visible light region is lower, thus the deposition of thicker layers for sufficient absorption is required. In order to exploit the different bandgaps of amorphous and microcrystalline silicon, tandem junction cells were developed. Amorphous silicon is used in the top cell absorbing light of shorter wavelength, whereas the bottom cell comprises of the microcrystalline material, which absorbs light in the longer wavelength region.

Photons, that enter the intrinsic silicon absorber layer of the solar cell and have sufficient energy E_g , create an electron–hole pair in the absorber layer (Fig. 15.1). In a p–i–n solar cell device like the thin film silicon solar cell, electrons and holes are separated from each other by an electric field, which is build up by the p- and the n-layer. This electric field is applied to the charge carriers, thus electrons e^- and holes p^+ have a potential energy which is at most the built-in potential qV_{bi} . The electric field over the intrinsic silicon absorber layer is not only determined by

the bandgap of the p-, i- and n-layer, but also by the doping level of the p- and n-layer and the thickness and defect concentration of the i-layer. The positively charged D^+ defects close to the p-i-interface and at the negatively charged D^- defects at the i-n-interface cause a band bending of the ideally linear band structure. This makes the charge movement within the bulk of the intrinsic absorber layer towards the p- and n-electrode more difficult due to a lowered drift force. By moving apart from each other, electrons and holes generate a photo voltage across the intrinsic absorber layer and contribute towards the photo current of the solar cell.

Since the mobility of holes in silicon is lower compared to electrons, the light enters the solar cell through the p-layer. The main part of the light is absorbed in the i-layer close to the p-layer, therefore the travel distance for the holes is much shorter than for electrons. Thus allowing more photons to reach the intrinsic absorber layer and reducing trapping or recombination of charge carriers by defects close to the doped p- and n-layer, the efficiency of the solar cell is improved by an increase in cell current. In terms of optimizing the optical and electrical properties of the p-layer, the four main objectives are

1. reduction of the reflection loss at the interfaces of TCO / p-layer / i-layer,
2. reduction of the absorption loss of the p-layer,
3. formation of a good electrical contact of the p-layer with the front electrode, and
4. building up the electric field for the p-i-n device.

These requirements appear to be contradictory, so it is one of the key challenges for the development of high-efficiency silicon solar cells to address all four points. Several approaches are discussed in literature. Most common are either to introduce an intermediate layer between the TCO and the p-layer or using a low absorbing p-layer like $\mu\text{c-SiC}$ [7].

Often sputtered TiO_2 is used as an index matching layer [8, 9] that refractive index lies in between TCO and p-layer in order to minimize reflection losses. Because of the wide bandgap of around 3.0 eV TiO_2 [10], absorption is not critical. But due to its low conductivity, integrating such a TiO_2 layer results in a higher series resistance of the solar cell device. In particular, using sputter-etched ZnO [5] requires an additional sputter process. This is a big disadvantage because of the difficulty and the costs for the implementation of this additional process step in a production line.

Another approach in terms of minimizing absorption losses is implementing a wide bandgap $\mu\text{c-SiC}$ layer [7] as a part of the p-layer is a common approach to enhance cell currents. Very high cell current densities of $<29 \text{ mA/cm}^2$ have been reported with $\mu\text{c-SiC}$ single junction cells [11]. For the deposition of device quality $\mu\text{c-SiC}$ layers usually HWCVD is employed. The big disadvantage of this deposition method is the difficulty of the production of large area modules. However, like for the TiO_2 layer the deposition of the $\mu\text{c-SiC}$ layer requires an additional process step, which causes addition costs in production of solar cells.

In order to avoid the disadvantages of these approaches we have developed a new p-layer stack based on $\mu\text{c-SiO}_x\text{:H(p)}$, which can help to fulfill the four main

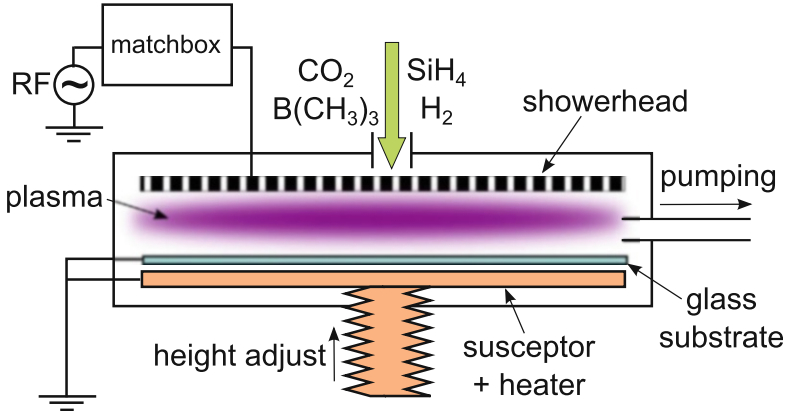


Fig. 15.2 A schematic drawing of the capacitively coupled PECVD reactor

objectives mentioned above [1, 2]. Also other groups reported promising results of a similar p-layer with micro- or nanocrystalline morphology [12–17]. The refractive index can be adjusted in the range between 2 and 3.5 (at a wavelength of 500 nm). Compared to TiO_2 the $\mu\text{c-SiO}_x\text{:H(p)}$ layers have higher conductivity and significantly lower absorption than a-SiC layers. Regarding the production of $\mu\text{c-SiO}_x\text{:H(p)}$ the process is very similar to the $\mu\text{c-Si(p):H}$ -layers and can be deposited in a standard PECVD equipment for large area solar cell production.

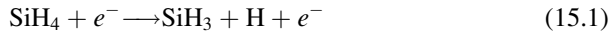
2 Deposition Process

Large area silicon thin-film modules ($1.1 \times 1.3 \text{ m}^2$) can be produced on both commercial substrates like $\text{SnO}_2\text{:F}$ as well as in-house produced ZnO. In the case of $\text{SnO}_2\text{:F}$, only the deposition of an amorphous p-layer is allowed. The reason is, that the $\text{SnO}_2\text{:F}$ is reduced by the plasma for a microcrystalline p-layer, which has higher power and hydrogen dilution.

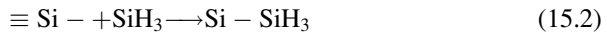
In this present work the triple p-layer stack has been deposited only on in-house produced ZnO:Al substrate. The ZnO is produced in a horizontal coater with a DC sputter process [18, 19]. Subsequently the ZnO substrate is etched anisotropically with HCl in order to texture the surface of the ZnO. By the roughness of the ZnO:Al surface the light in-coupling is increased due to the so called “light trapping”, which is described in literature [20, 21].

The silicon layers are deposited in a multi-chamber CVD cluster tool using standard 13.56 MHz PECVD processes in capacitively coupled reactors (Fig. 15.2). The alternating electrical field enhances the excitation of the atoms of the used process gases. Consequently an effective deposition process takes place already at quite low temperatures around 200 °C. Regarding the decomposition of silane (SiH_4)

in the PECVD reactor, SiH_3 and SiH_2 are the most common species. Unlike the SiH_2 radicals, the SiH_3 radicals are mainly responsible for the film growth, because of its high reaction probability with hydrogen forming silane or its polymers [22–26]. Besides a multitude of possible chemical reactions, the first reaction step towards film growth is the formation of SiH_3 :

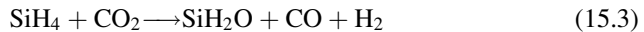


The bonding of the SiH_3 molecules from the gas phase occurs only on dangling bonds of silicon as [26]



The intrinsic top cell absorber layer (a-Si:H) has been produced with a deposition rate of about 3 Å/s. This rather slow deposition rate is necessary in order to have sufficient hydrogen concentration (10–20 at.%) and therefore less defects. On the other hand the bottom cell $\mu\text{c-Si:H}$ layer has to be deposited faster (~ 5 Å/s) with a high-pressure and high-power process for a profitable production of solar cells, because the bottom cell is about five times thicker (> 1 μm).

But now we want to focus on the silicon oxide p-layer. The SiO_x -layers were made by adding CO_2 to the process gas. The main reaction path can be summarized as [27]



As a dopant gas for the p-doped layers trimethylboron ($\text{B}(\text{CH}_3)_3$; TMB) diluted in hydrogen has been used. Another commonly used dopant gas is diborane (B_2H_6). The deposition rate of the silicon oxide p-layer is with ~ 1.2 Å/s even lower than in the case of undoped amorphous silicon. But this does not affect the productivity significantly, because of the small thickness of the p-layer (30–50 s deposition time for the $\mu\text{c-SiO}_x\text{:H(p)}$ layer only). Quite the contrary, the slow deposition rate allows us to adjust the thickness of the silicon oxide p-layer more accurately.

Boron has a high diffusivity in a-Si:H, which is even higher than in crystalline silicon [28]. Thus attention has to be taken on the deposition temperature of the p- and i-layer: Choosing a significantly higher temperature for the intrinsic silicon absorber compared to the doped p-layer leads to boron diffusion from the p- to the i-layer. This is due to the movement of the boron atoms in the p-layer over dangling bonds, which are higher in number in material with an unrelaxed matrix, i.e. deposited at lower temperatures [29]. A higher temperature subsequently used for the i-layer promotes diffusion from the p- to the i-layer. Boron is contaminating the i-layer, because it creates defect states, where recombination occurs. Also oxygen as a contaminant in the intrinsic absorber layers acts as a donor, thus plays a detrimental role in the device as well [30].

The n-layers were doped with hydrogen-diluted phosphine. As back contact a sputtered ZnO/Ag stack was used. The same equipment is also used to make small test cells (1 cm^2), defined by laser scribing.

3 The p-Layer Components

We implemented the silicon oxide p-layer stack in single and tandem junction thin-film silicon solar cells on ZnO and replaced the conventionally used $\mu\text{c-Si(p):H}$ / a-Si(p):H double layer (Fig. 15.3). The p-layer stack consists of

- A microcrystalline $\mu\text{c-Si(p):H}$ layer with a thickness of about 5 nm. The microcrystalline p-layer is needed in order to provide a good contact to the crystalline and textured ZnO:Al. On the other hand due to its high refractive index ($n \sim 3.8$) one seeks for depositing the $\mu\text{c-Si(p):H}$ layer as thin as possible, since it is an optical barrier. However, being deposited prior to the oxygen p-layers, it might be the case that the $\mu\text{c-Si(p):H}$ layer is oxidized by the subsequent deposition process of the $\mu\text{c-SiO}_x(\text{p):H}$ layer.
- A microcrystalline silicon oxide p-layer ($\mu\text{c-SiO}_x(\text{p):H}$) with a thickness of about 5–10 nm, thus a little bit thicker than the $\mu\text{c-Si(p):H}$ layer. The refractive index is with $n \sim 2.7$ in between the refractive index of the front contact (ZnO:Al) and the a-Si:H absorber. Due to this better refractive index matching it has the function of an anti-reflection layer.

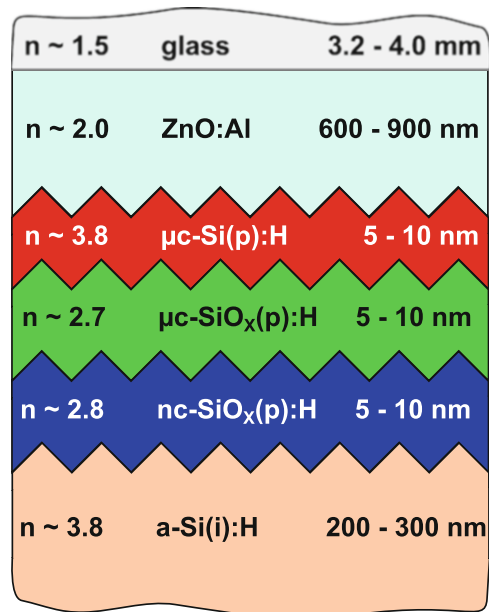


Fig. 15.3 The p-layer stack used in single and tandem junction devices with the adjacent ZnO:Al on glass (*top*) and the a-Si:H absorber (*bottom*)

- A silicon oxide p-layer with low crystallinity (nc-SiO_x(p):H) and a similar thickness as the μc-Si(p):H layer. The deposition process of this nc-SiO_x(p):H layer is based upon the μc-SiO_x(p):H layer, only the TMB flow is much higher to decrease the crystallinity. Moreover a high TMB flow enables us to build up the electric field due to the high dopant concentration. In order to have a good contact to the both adjacent layers like the a-Si(i):H layer and the μc-SiO_x(p):H layer, the crystallinity is low, but the nc-SiO_x(p):H is not fully amorphous. Furthermore the refractive index lies in between the one of the μc-SiO_x(p):H and of the a-Si(i):H layer.

Resulting from the configuration of this triple p-layer stack a graded crystallinity is provided over the ZnO / p-layer / a-Si(i):H interface. Moreover refractive index matching is given from the glass to the silicon absorber layer except a very thin μc-SiO_x(p):H layer with unmatched refractive index.

4 Single-Layer Properties of μc-SiO_x(p):H

In this section, the most important optical,¹ electrical and morphological properties of the μc-SiO_x(p):H layer are investigated. The absorption, refractive index, optical bandgap, electrical conductivity and crystalline fraction have been measured on a single layer (Figs. 15.4 and 15.5). Moreover the thickness uniformity and deposition rate are determined (Fig. 15.7). The most important parameter for tuning these material properties mentioned above of the μc-SiO_x(p):H layer is the CO₂ gas flow.

4.1 Optical Properties

Since the silicon oxide p-layer acts like a window layer, a low absorption is crucial for allowing more photons to reach the absorber layer. By measuring the reflection and transmission, the absorption coefficient $\alpha(\lambda)$ of the μc-Si(p):H and μc-SiO_x(p):H layer has been determined according to Hishikawa [31]

$$\alpha(\lambda) = -\frac{1}{d} \cdot \ln\left(\frac{T}{1-R}\right) \quad (15.4)$$

¹The reflection as an optical property is not treated here as a single layer property, since it depends on adjacent layers. Thus it is included in Sect. 5.1.

Fig. 15.4 The absorption coefficient α as a function of the energy of incident light for $\mu\text{c-Si(p):H}$ (without oxygen) and for the $\mu\text{c-SiO}_x(\text{p}):H$ layer (116 sccm CO_2 gas flow)

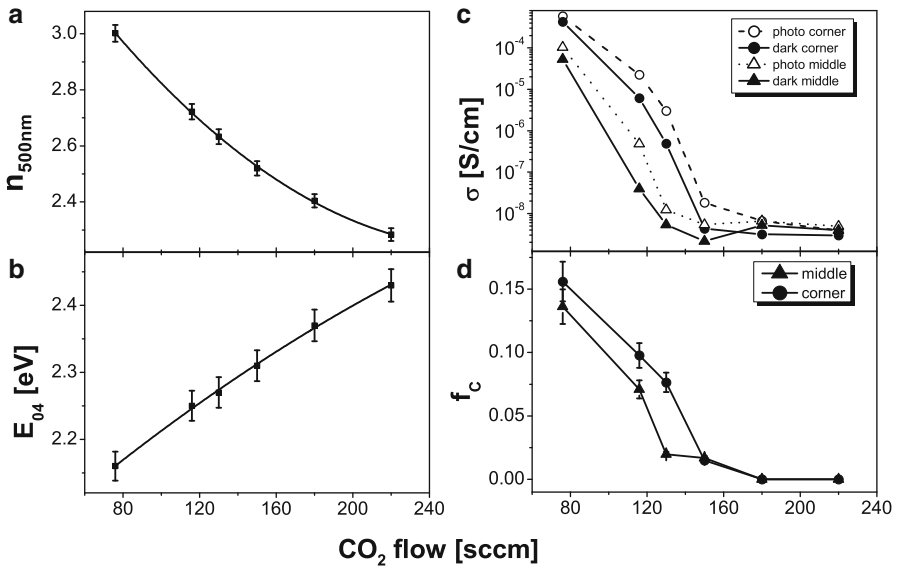
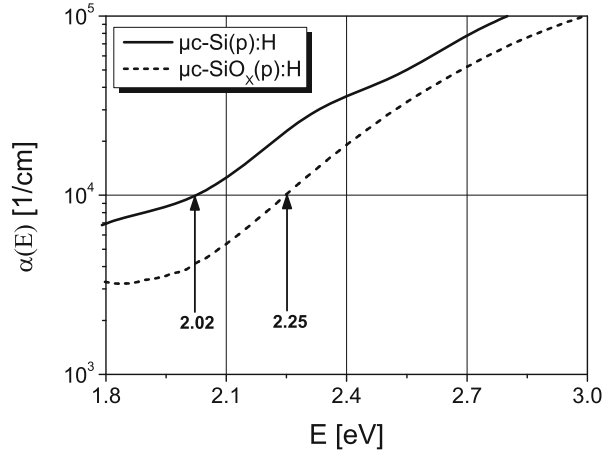


Fig. 15.5 Single-layer properties like refractive index in (a), bandgap E_{04} (b), conductivity σ (c) and crystalline fraction f_c (d) of the $\mu\text{c-SiO}_x(\text{p}):H$ as a function of CO_2 gas flow

where d is the thickness, T the transmission and R the reflection of the layer. An absorption diagram containing the $\mu\text{c-Si(p):H}$ and $\mu\text{c-SiO}_x(\text{p}):H$ layer is shown in Fig. 15.4.

The determination of the next important quantity of the silicon oxide p-layer, the optical bandgap E_{04} , can be illustrated by means of the absorption diagram (Fig. 15.4). Where the absorption curve has an absorption coefficient of

10^4 cm^{-1} , one can read at the x -axis the respective energy value, e.g. 2.25 eV for the $\mu\text{c-SiO}_x(\text{p})\text{:H}$ and 2.02 eV for the $\mu\text{c-Si}(\text{p})\text{:H}$ layer.

The refractive n index of the single layers has been determined by applying an iterative fitting algorithm procedure to the measured reflection and transmission spectra of the substrates (Fig. 15.5a). It is the critical quantity for tuning the anti-reflective properties.

Closely related to the absorption coefficient is the optical bandgap. The higher the bandgap, the lower the absorption coefficient. As one can see, the absorption coefficient α is, depending on the energy of incident light, up to a factor of 2 lower for the $\mu\text{c-SiO}_x(\text{p})\text{:H}$ layer at a used CO_2 gas flow of 116 sccm than for the $\mu\text{c-Si}(\text{p})\text{:H}$ -layer (Fig. 15.4). The bandgap for the less absorbing $\mu\text{c-SiO}_x(\text{p})\text{:H}$ layer with 2.25 eV is higher than for the $\mu\text{c-Si}(\text{p})\text{:H}$ layer without oxygen (2.02 eV). For layers containing more oxygen by using higher CO_2 gas flows one can see from Fig. 15.5b, that the bandgap E_{04} increases up to 2.43 eV at 220 sccm CO_2 . For sure the CO_2 gas flow is a strong parameter for tuning the absorption and bandgap of the $\mu\text{c-SiO}_x(\text{p})\text{:H}$ layer. But also for adjusting the refractive index the oxygen content in the layer is the main driver. By increasing the CO_2 gas flow from 76 to 220 sccm, the refractive index can be reduced significantly from 3.0 to below 2.3. In conjunction with the refractive index of the adjacent layers, the reflectance is defined as explained below (Sect. 5.1).

4.2 Electrical and Morphological Properties

The electrical conductivity σ is defined as the proportional factor of the current density \mathbf{j} and the electrical field \mathbf{E} . Since σ is the reciprocal value of the specific resistivity ρ and with $\rho = R \cdot \frac{A}{l}$ it is

$$\sigma = \frac{\mathbf{j}}{\mathbf{E}} = \frac{l}{R \cdot A} \quad (15.5)$$

with l as the length and A as the cross-section area of the conductor. The electrical conductivity in the p-layer is critical for the charge carrier transport and has to be sufficiently high in order to avoid cell current loss by recombination of charge carriers. In-plane conductivity of the $\mu\text{c-SiO}_x(\text{p})\text{:H}$ layer was measured with a Keithley source measurement unit on sputtered coplanar Al contacts in the dark and under illumination (Fig. 15.5c). Besides the doping concentration in the silicon oxide p-layer, the electrical conductivity σ is closely related to the crystalline fraction f_C of the silicon oxide p-layer. The electrical conductivity in microcrystalline material is several orders of magnitude higher than in amorphous material due to less scattering of charge carriers.

The crystallinity of the $\mu\text{c-SiO}_x(\text{p})\text{:H}$ layer has been determined by Raman spectroscopy, which relies on the inelastic scattering of electromagnetic radiation by a material. In order to calculate the crystal fraction f_C from the Raman spectra, each spectrum has been fitted by five components representing the different phonon modes described in [32]

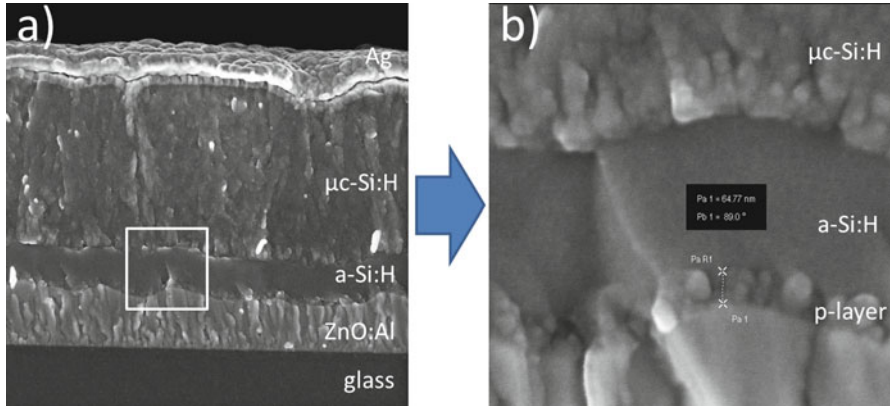


Fig. 15.6 SEM micrograph of (a) the tandem junction silicon solar cell and (b) the silicon oxide p-layer stack with a thickness of about 65 nm (thicker than the 30 nm used in the device). In contrast to the appearance of the a-Si:H layer the p-layer-stack shows small crystal grains

$$f_c = \frac{I_{510} + I_{520}}{I_{330} + I_{440} + I_{480} + I_{510} + I_{520}} \quad (15.6)$$

with I_{520} as the line intensity of microcrystalline silicon, I_{510} for the grain boundaries and I_{480} for the amorphous phase. The lines at 330 and 440 cm^{-1} are from the LA and LO modes. A blue laser with 473 nm excitation wavelength has been used in order to have a short penetration depth ($\sim 200 \text{ nm}$ for $\mu\text{c-SiO}_x(\text{p})\text{:H}$), which allows to measure thin layers (Fig. 15.5d).²

Evidently, the trend for the electrical conductivity and crystalline fraction (Fig. 15.5c, d) looks congruent with each other. Above a certain CO_2 flow (here 150 sccm) the $\mu\text{c-SiO}_x(\text{p})\text{:H}$ gets fully amorphous, which causes a drastic conductivity drop of five orders of magnitude down to 10^{-8} S/cm . We observe a big difference of conductivity values especially at 116 and 130 sccm between corner cells (10^{-4} to 10^{-5} S/cm) and middle cells (10^{-7} to 10^{-8} S/cm). In contrast the cell data of middle cells do not differ from corner cells. This implies, that we have a much higher transversal conductivity than the measured lateral conductivity for our silicon oxide p-layers, which is consistent with results published by Cuony et al. [14]. This is most likely due to the columnar growth of the microcrystals of the $\mu\text{c-SiO}_x(\text{p})\text{:H}$ layer.

A smaller difference than from middle to corner coupons we observe between the dark and photo conductivity. This means, that charge carriers are generated in the p-layer. Because of the higher recombination probability inside the p-layer due to its higher defect level, this effect is unwanted.

² Nevertheless even with the 473 nm laser the layer have to be at least 100 nm thick, which is about three times thicker than the thickness of the p-layer being used in the solar cell device.

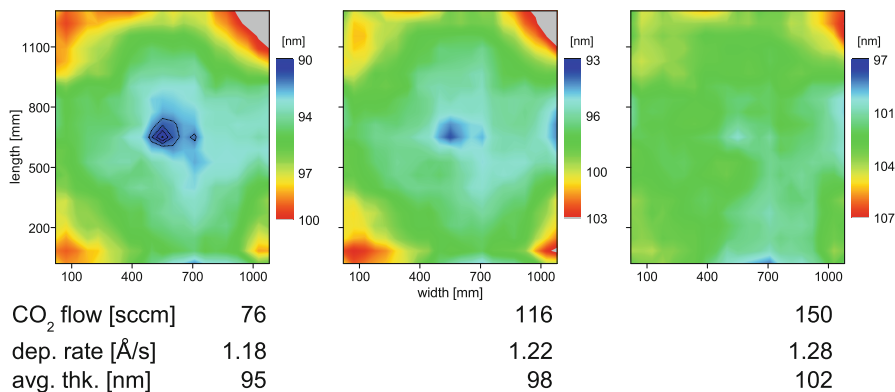


Fig. 15.7 Thickness uniformity data of the $\mu\text{c-SiO}_x(\text{p})\text{:H}$ layer on $1.1 \times 1.3 \text{ m}^2$ glass substrates. Increasing the CO_2 flow improves the thickness uniformity and slightly increases the deposition rate. The thickness mappings have been scaled $\pm 5\%$ around average thickness

Compared to the crystalline fraction of $f_C \sim 0.4$ for $\mu\text{c-Si}(\text{p})\text{:H}$ even the highest f_C value for the silicon oxide layer ($\mu\text{c-SiO}_x(\text{p})\text{:H}$) displayed in Fig. 15.5d ($f_C \sim 0.15$) is rather low.

Scanning electron microscopy (SEM) has been employed to picture a cross-section of a micromorph tandem junction cell (Fig. 15.6). One may notice, that the p-layer appears to be crystalline in contrast to the smooth amorphous a-Si:H layer on top of the p-layer stack. It appears to be contradictory, that there have been determined rather low crystal fraction values (f_C) of the $\mu\text{c-Si}(\text{p})\text{:H}$ layer by Raman spectroscopy (Fig. 15.5). It is reported in literature, that the crystal fraction of the p-layer increases with its thickness [33]. But for the Raman measurements even a higher thickness has been used of $\sim 100 \text{ nm}$ on a glass sheet compared to the thickness of $\sim 65 \text{ nm}$ on crystalline ZnO in the SEM micrograph (Fig. 15.6). Thus the only reason of this deviation can be that glass has been used as a substrate for the Raman measurements for the crystal fraction determination, whereas in the device the p-layer is deposited on top of highly crystalline ZnO. This explains the low crystallinity values of the $\mu\text{c-SiO}_x(\text{p})\text{:H}$ layer measured with Raman. Despite this offset of the absolute numbers, the trend of crystallinity as a function of CO_2 gas flow is still valid, but the real numbers for the crystalline fraction of the $\mu\text{c-SiO}_x(\text{p})\text{:H}$ layer is assumed to be much higher in the cell device.

Besides its impact on the optical, electrical and morphological properties, the CO_2 gas flow has a significant influence on the thickness homogeneity across the $1.1 \times 1.3 \text{ m}^2$ glass sheet, shown in Fig. 15.7. Apparently a higher gas flow helps to improve the homogeneity. In addition, it increases slightly the deposition rate, which has been reported in literature as well [27] (Fig. 15.7).³

³The $\mu\text{c-SiO}_x(\text{p})\text{:H}$ single layers have been deposited with a thickness of $\sim 100 \text{ nm}$ in order to be able to measure them by reflection and transmission mapping measurement equipment.

5 The Silicon Oxide p-Layer Stack in the Solar Cell

Beyond the development of the material properties of the silicon oxide p-layer of single layers, improving its interplay in terms of solar cell device performance is crucial. Because of this complex interplay of the silicon oxide p-layer stack within the cell, implementing a beneficial p-layer stack in terms of reducing optical losses while keeping sufficient electrical and morphological properties requires diligence. Following the four objectives mentioned in Sect. 1 minimizing the absorption and reflection losses is improving the quantum efficiency. This leads to higher cell currents, represented in the IV curve by the short circuit current I_{SC} . The doping level and a sufficient thickness of the p-layer stack is critical for building up an electrical field, thus for the open circuit voltage V_{OC} . The contact behavior is responsible for the fill factor (FF) of the solar cell. All these features of the IV curve determine the overall cell efficiency (CE).

5.1 Reflection

The benefit of anti-reflective coatings depend on the principle of cancellation of light waves by destructive interference reflected from the top and the bottom of the coating. Destructive interference occurs at a phase shift of π (180°) of light waves. Due to the fact, that the light waves have to pass the coating two times because of the reflection at the interface, the ideal thickness d of the anti-reflective coating is determined to a quarter wavelength of the incident light in conjunction with the refractive index n to

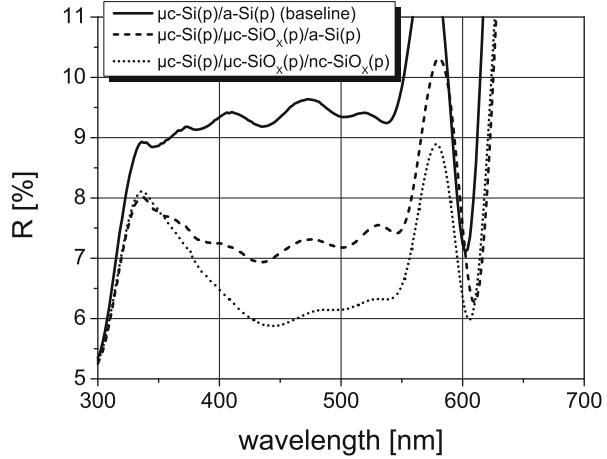
$$d = \frac{\lambda}{4 \cdot n_1} \quad (15.7)$$

In terms of minimizing reflection losses at interfaces, the ratios of the refractive indexes of the layer on top n_0 , of the anti-reflection layer n_1 and the substrate n_2 should be equal in order to have the same intensity of the two light beams. Thus the ideal refractive index of the anti-reflection layer n_1 is determined by the geometric mean of both the refractive index of the layer on top n_0 and below n_2 [34]:

$$\frac{n_0}{n_1} = \frac{n_1}{n_2} \implies n_1 = \sqrt{n_0 \cdot n_2} \quad (15.8)$$

Deduced from Fresnel's law, in the case of normal incidence of light and neglecting the absorption, one can estimate the reflectivity R at the wavelength of the reflection minimum λ to

Fig. 15.8 The reflectivity in the tandem junction cell device has been reduced 3 % at 500 nm wavelength by deposition of $\mu\text{c-SiO}_x(\text{p})$:H and $\text{nc-SiO}_x(\text{p})$:H compared to the baseline process (*solid line*)



$$R = \frac{I_r}{I_i} = \left(\frac{n_0 n_2 - n_1^2}{n_0 n_2 + n_1^2} \right)^2 \quad (15.9)$$

Following this simple model,⁴ having no index matching layer in between TCO ($n \sim 2.0$) and a-Si:H absorber layer ($n \sim 3.8$), one calculates the reflectance of the light passing through the glass and TCO to $R \sim 8.2\%$ at the wavelength of minimum reflectance (compare Fig. 15.8. But for almost zero reflectance, the anti-reflective layer needs to have a refractive index $n = 2.82$, where our used $\mu\text{c-SiO}_x(\text{p})$:H layer is not too far away (Fig. 15.3). The $\mu\text{c-Si}(\text{p})$ layer is neglected in this consideration, since it is just 5 nm thick and might not cover the rough ZnO-p-layer interface.

Our experimental result in Fig. 15.8 shows a clear trend of reduction of reflectivity by implementation of the $\mu\text{c-SiO}_x(\text{p})$:H layer of 2 % and finally by substitution of the a-Si(p):H layer with the $\text{nc-SiO}_x(\text{p})$:H layer of 3 % compared to the baseline (at 500 nm wavelength). At higher wavelength above ~ 700 nm the reflectivity of tandem junction with and without silicon oxide p-layer is about the same.

A deposition time series has been conducted between 0 and 400 s of $\mu\text{c-SiO}_x(\text{p})$:H in the tandem junction solar cell device (Fig. 15.9). Here it is illustrated that even by bare eye one can observe a change of the optical properties of the cell. Due to interference effects, which vary with the thickness of the $\mu\text{c-SiO}_x(\text{p})$:H layer, each coupon has a different color. Compared to the baseline process without $\mu\text{c-SiO}_x(\text{p})$:H layer, the coupons at 50–150 s deposition time appear much darker. At higher deposition times the coupons get brighter again, thus having a higher reflectivity. Therefore it has a lower reflectivity in the visible spectral range.

⁴This is only a rough estimation, since we have, due to the textured surface, no normal incidence and have a p-layer stack consisting of three different layers.

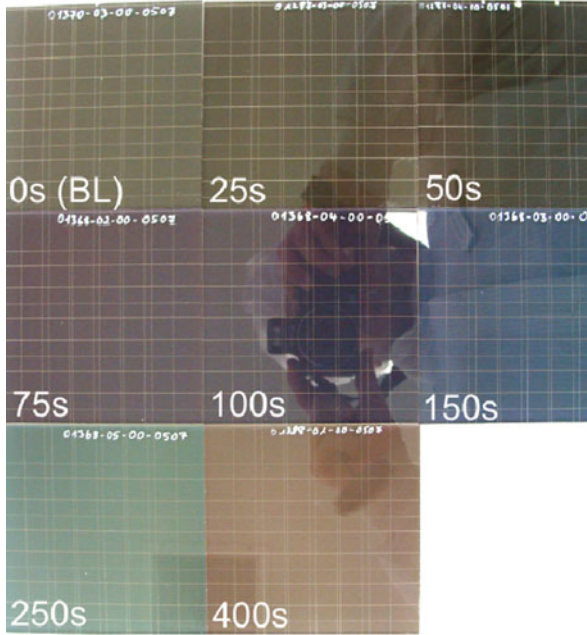


Fig. 15.9 Color change of the laser coupons with deposition time of $\mu\text{c-SiO}_x(\text{p})\text{:H}$ layer indicates interference effects. Compared to the baseline (0 s), already at 50 s deposition time the silicon absorber appears much darker. All coupons shown have been made with a CO_2 gas flow of 58 sccm

5.2 Quantum Efficiency

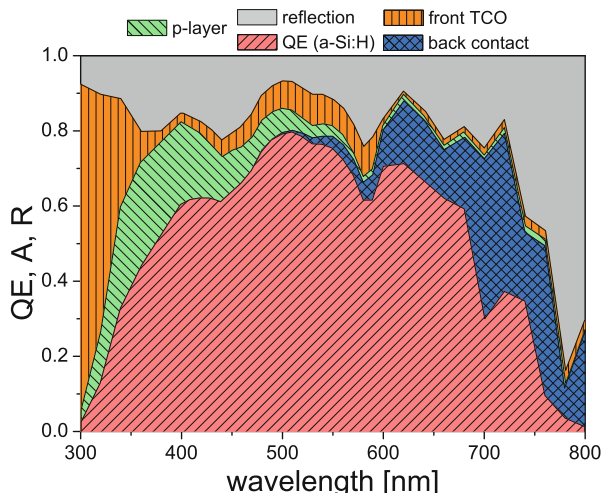
The quantum efficiency (QE) is defined as the efficiency of converting incident photons into electrons. It is distinguished into external and internal quantum efficiency (EQE and IQE, respectively). EQE is the ratio of the number of photons hitting the solar cell n_ν to the number of collected electrons in the solar cell n_e , whereas the IQE takes only the number of photons being absorbed in the intrinsic absorber layer into account. In this work we consider the EQE, since we are interested in the absorption and reflection loss of the p-layer. According to Kirchartz et al. [35], the EQE can be written as

$$\text{EQE}(\lambda) = \frac{n_e}{n_\nu} = \frac{1}{q} \cdot \frac{dJ_{\text{SC}}(\lambda)}{d\Phi(\lambda)} \quad (15.10)$$

with q for the elementary electric charge, $d\Phi(\lambda)$ for the incident photon flux and $dJ_{\text{SC}}(\lambda)$ for the current density within the photon wavelength interval $d\lambda$.

In an ideal case, the quantum efficiency is 1, i.e. per one incident photon one hole and electron is generated and collected at the respective electrode. But in reality this

Fig. 15.10 Simulated quantum efficiencies, absorption losses and reflection loss in the a-Si:H single junction solar cell with a conventional p-layer (redrawn from [36])



not achievable due to several loss mechanisms. In Fig. 15.10 the amounts of absorption losses are attributed to the layers used in a thin-film silicon solar cell. As one can see, the p-layer causes in the blue wavelength region from about 350 to 450 nm the biggest fraction of absorption loss, ranging from 10 to 20 %. As already mentioned above (Sect. 4) the absorption loss by the conventional p-layer can be reduced up to 60 % by implementing the silicon oxide p-layer (Fig. 15.4).

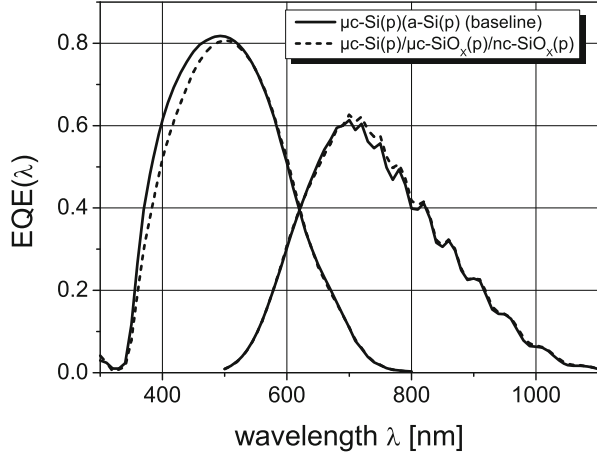
In this simulation the reflection loss is not distinguished between each layer, thus the absolute amount of reflection loss caused by the p-layer is unknown. But it can be estimated by a measurements of tandem junction solar cells with and without the silicon oxide p-layer (Fig. 15.8). So the reflection loss by the conventional p-layer amounts at least 3 % in the wavelength region of 450–550 nm, since this is the difference between conventional and the silicon oxide p-layer.

Regarding the measured quantum efficiency of the solar cell devices shown by Fig. 15.11, the silicon oxide p-layer enhances the current response in the top cell up to 0.3 mA/cm^2 , whereas the bottom cell current decreases slightly ($\sim 0.2 \text{ mA/cm}^2$). The gain in top cell current can be attributed to the reduction of reflectivity and absorption for visible light by the silicon oxide p-layer stack. The deposition time of the silicon oxide p-layer is limited by a strong I_{SC} decrease due to higher absorption in the short wavelength region ($< 500 \text{ nm}$) by depositing a too thick $\mu\text{c-SiO}_x(\text{p})$:H layer.

5.3 Solar Cell Performance Data

We just want to briefly define the key parameters in terms of performance of the solar cell. For more details further textbook reading is recommended [37–39]. Basically the performance and behavior of a solar cell is described by its characteristic IV curve. Four characteristic quantities like the conversion efficiency (CE) (or η),

Fig. 15.11 Due to the lower absorption of the silicon oxide p-layer the blue response in the top cell increases, but bottom cell current decreases slightly



the fill factor (FF), the open circuit voltage V_{OC} and the short circuit current I_{SC} can be derived by means of the IV curve.

The conversion efficiency as the most important quantity of a solar cell is defined as the ratio of the output power P_{max} at the maximum power point to the power of incident light at equal area (P_{in}) as

$$CE = \frac{P_{max}}{P_{in}} = \frac{I_{SC} \cdot V_{OC} \cdot FF}{P_{in}} \tag{15.11}$$

This very basic expression of the conversion efficiency unites all four mentioned quantities in one equation by using the definition of the fill factor:

$$FF = \frac{P_{max}}{I_{SC} \cdot V_{OC}} \tag{15.12}$$

In principle, the solar cell works like a diode, thus the dark IV curve can be derived from the Shockley-equation [40]

$$I(V) = I_0 \cdot \left[\exp\left(\frac{qV}{nkT}\right) - 1 \right] \tag{15.13}$$

with an ideality factor for the diode n , which amounts between 1 and 2, depending on where charge carrier recombinations take place. If the recombination occurs in areas free from the electrical field n approaches 1, and n goes against 2 for recombination processes within the field of the space charge layer, i.e. close to the p-layer. Thus the ideality factor could be an indicator for the quality of the pi interface. In order to account for the resistivity of the conducting materials and the leakage current in a solar cell, a serial R_S and parallel resistance R_P is included in

the equation. In the case of illumination, the equation can be extended by addition of the photo current $I_{ph}(V)$ to the dark current under the assumption of the superposition principle. For the photo current $I_{ph}(V)$ we can derive from (15.13) to

$$I_B(V) = I_0 \cdot \left[\exp\left(\frac{q(V - I_B(V) \cdot R_S)}{nkT}\right) - 1 \right] + \frac{V - I_B(V) \cdot R_S}{R_P} - I_{ph}(V) \quad (15.14)$$

For the ideal case of an infinite R_P and evanescent R_S the photo current $I_{ph}(V)$ equals the amount of short circuit current I_{SC} at no external voltage applied: $I_{ph}(V = 0) = I_{SC}$. Therefore the second term in (15.14) becomes zero and we can approximate the open circuit voltage V_{OC} to

$$V_{OC} \simeq \frac{nkT}{q} \cdot \ln\left(\frac{I_{ph}(V_{OC})}{I_0} + 1\right). \quad (15.15)$$

For the determination of CE, FF, V_{OC} and I_{SC} an IV curve has been measured with a large area flasher by HALM according to the IEC class A requirements. Each single layer for either the small $1 \times 1 \text{ cm}^2$ cell coupons or the complete $1.1 \times 1.3 \text{ m}^2$ modules were deposited on large-area glass substrates.

The IV data of $1 \times 1 \text{ cm}^2$ coupons has been measured at different places of a $1.1 \times 1.3 \text{ m}^2$ substrate and is displayed in Fig. 15.12. We observe an increased short circuit current (I_{SC}) and fill factor (FF) and higher cell efficiency (CE), but a lower open circuit voltage (V_{OC}) with $\mu\text{c-SiO}_x(\text{p})\text{:H}$ layer. The best solar cell efficiency results have been achieved with thinner $\mu\text{c-Si}(\text{p})\text{:H}$ and $\mu\text{c-SiO}_x(\text{p})\text{:H}$ layers and a thicker $\text{nc-SiO}_x(\text{p})\text{:H}$. By increasing the $\text{nc-SiO}_x(\text{p})\text{:H}$ layer, we gain a higher V_{OC} and FF, which overcompensates the slightly lower I_{SC} . Due to the higher p-doping level by a much higher TMB flow during deposition the $\text{nc-SiO}_x(\text{p})\text{:H}$ keeps up the electric field between n- and p-layer across the i-layer resulting in a higher cell voltage. Making the $\mu\text{c-Si}(\text{p})\text{:H}$ too thick decreases the V_{OC} due to the lower bandgap of the $\mu\text{c-Si}(\text{p})\text{:H}$ in conjunction with the band alignment with the $\mu\text{c-SiO}_x(\text{p})\text{:H}$ and $\text{nc-SiO}_x(\text{p})\text{:H}$ layer. In addition the gain in FF is most pronounced at a thinner $\mu\text{c-Si}(\text{p})\text{:H}$ layer, but the FF breaks down dramatically, if it is absent or too thin. Therefore the $\mu\text{c-Si}(\text{p})\text{:H}$ layer is still needed as a contact layer between the silicon oxide p-layer and ZnO. Compared to the baseline process without $\mu\text{c-SiO}_x(\text{p})\text{:H}$ layer we observed a slight gain in absolute initial efficiency by $\sim 0.1 \%$, which is due to the higher current and higher fill factor.

5.4 Light-Induced Degradation

As already mentioned above (Sect. 1), the Staebler–Wronski effect is based on the cracking of Si–H bondings due to UV light exposure over time. As a consequence defect states are created, which are a source of recombination of charge carriers,

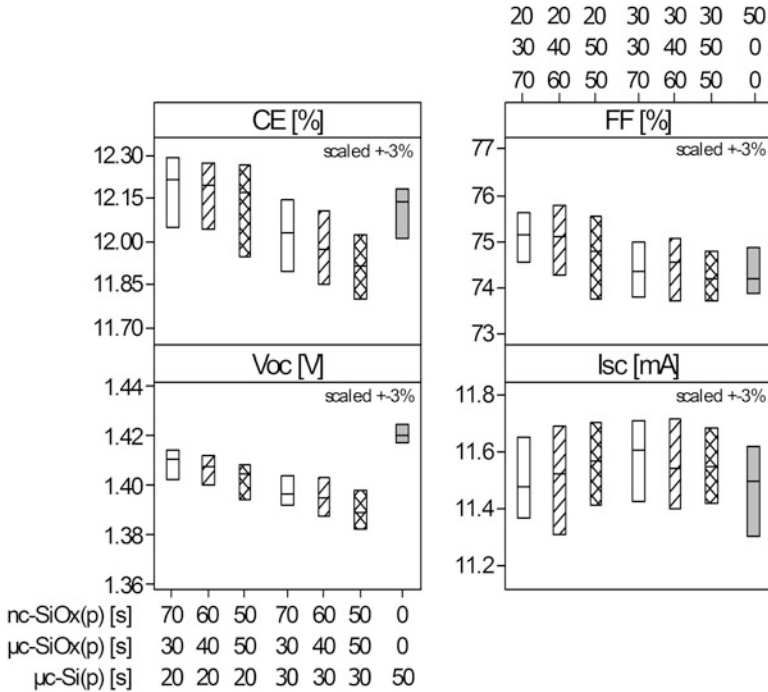


Fig. 15.12 Box plot of IV-data of thickness series of all three p-layers, the $\mu\text{c-Si(p):H}$, $\mu\text{c-SiO}_x(\text{p):H}$ and $\text{nc-SiO}_x(\text{p):H}$ compared to baseline data (*gray box*). The data was measured on $1 \times 1 \text{ cm}^2$ laser coupon solar cells (each data box contains IV-data of 90 solar cells). On the X-axis the deposition time in seconds of each p-layer component is given

thus affecting the cell efficiency by a decreasing cell current and the fill factor. Therefore in terms of efficiencies of thin film silicon solar cells and modules, one has to distinguish between initial and stabilized efficiency, referring to the efficiencies before and after UV light exposure for a certain time.

In order to determine the efficiency of stabilized solar cells, light soaking was accomplished at $50 \pm 5 \text{ }^\circ\text{C}$ with a class C AM 1.5 light source under open circuit conditions. Three different samples with the newly developed p-layer stack ($\mu\text{c-Si(p):H}$, $\mu\text{c-SiO}_x(\text{p):H}$ and $\text{nc-SiO}_x(\text{p):H}$ layer) and one baseline sample as a reference have been measured at the begin without light soaking and then in 50 h steps up to 300 h UV light exposure.

Unlike the comparably small gain in absolute initial cell efficiency of 0.1 % (Sect. 5.3), after 300 h of UV light exposure the great benefit of applying an silicon oxide p-layer becomes evident. The cell efficiency average of $1 \times 1 \text{ cm}^2$ laser coupons of tandem junction cells with $\mu\text{c-SiO}_x(\text{p):H}$ and $\text{nc-SiO}_x(\text{p):H}$ layer is around 11.1 % (Fig. 15.13). The CE of cells with the conventional p-layer without oxygen is significantly lower at $\sim 10.7 \%$, which is mostly due to a decrease in top cell current. Based upon the initial CE the relative efficiency loss for the tandem

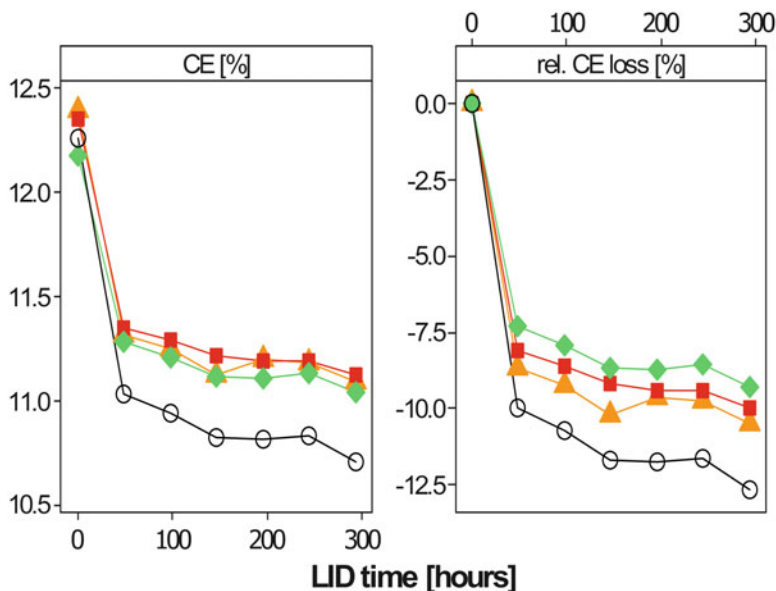


Fig. 15.13 Box plot of IV-data of thickness series of all three p-layers, the $\mu\text{c-Si(p):H}$, $\mu\text{c-SiO}_x(\text{p):H}$ and $\text{nc-SiO}_x(\text{p):H}$ (orange triangle, red square, green diamond) compared to baseline data (open circle). The data was measured on $1 \times 1 \text{ cm}^2$ laser coupons. On the X-axis the deposition time in seconds of each p-layer is given

junction cells with the new $\mu\text{c-SiO}_x$ based p-layers amounts 9.1–10.5 %. With the conventional p-layer the relative loss in CE is significantly higher with 12.5 %. Overall we achieved stabilized module efficiencies of 10.1 % after 1,000 h of light soaking on $1.1 \times 1.3 \text{ m}^2$ [2].

6 Conclusions

From the $\mu\text{c-SiO}_x(\text{p):H}$ single layer results we observed, that the optical on the one hand and the electrical and morphological properties on the other hand counteract each other. Getting a low absorbing material with low refractive index requires the addition of higher amounts of oxygen, whereas the conductivity same as the crystalline fraction limits the addition of oxygen. Therefore as the best balance between refractive index and E_{04} bandgap (Sect. 4.1) on the one hand and conductivity and crystallinity on the other hand, the CO_2 gas flow has been adjusted to 116 sccm for both silicon oxide layers in the solar cell ($\mu\text{c-SiO}_x(\text{p):H}$ and $\text{nc-SiO}_x(\text{p):H}$).

Regarding the implementation of the complete silicon oxide p-layer stack in the solar cell device, a significant reduction of the reflection, especially in the blue wavelength region (350–450 nm) compared to the conventional p-layer without

oxygen, has been achieved. The silicon oxide p-layer increases the top cell current up to 0.3 mA/cm^2 . This enables us to use thinner top cell a-Si(i):H-layers, which helps to reduce LID. In conjunction with a LID we achieve an absolute 0.4 % gain of stable cell efficiency after 300 h of light soaking. These improvements enable thinner cells, which saves deposition time and as a consequence drives down the cost of thin film silicon solar cell production significantly.

Recalling the four main objectives stated in Sect. 1, we conclude:

1. We could reduce the reflection loss at the interfaces of TCO/p-layer/i-layer by 3 % (see Sect. 5.1).
2. A reduction of the absorption loss of the p-layer has been achieved successfully. Depending on the wavelength of incident light, the $\mu\text{c-SiO}_x(\text{p}):\text{H}$ layer has up to a factor of 2 lower absorption compared to the $\mu\text{c-Si}(\text{p})::\text{H}$ layer (see Sect. 4.1).
3. We formed a good electrical contact of the silicon oxide p-layer with the front electrode, which has been proven by an even higher fill factor of cells containing the new p-layer compared to cells with the conventional p-layer (see Sect. 5.3).
4. The electric field for the p–i–n device could be built up also with the silicon oxide p-layer, and the V_{OC} of solar cells with the silicon oxide p-layer is almost as high as for the cells with the conventional p-layer (see Sect. 5.3).

Acknowledgements The authors are much obliged especially to their former colleagues Tobias Stolley, Susanne Buschbaum, Martin Rohde, Christian Stömmer, Philipp Obermeyer, Inge Vermeir, Elisabeth Sommer, Daniel Severin, Niels Kuhr, Markus Kreß, Sonja Noll-Baumann, Tobias Repmann, Stephan Wieder and all other former members of the R&D solar group at Applied Materials Alzenau for their valuable contribution. The authors gratefully acknowledge the support by the members of the Analytics Department of Applied Materials in Alzenau, Jürgen Schröder and Karin Witting. The authors would like to thank the Bundesministerium für Umwelt, Naturschutz und Reaktorsicherheit, which partially funded this work under contract no. 0327568A. Last, but not least the author gratefully thanks the Alzenau SFTC-team for producing the solar modules.

References

1. Schwanitz, K., Klein, S., Stolley, T., Rohde, M., Severin, D., Trassl, R.: Anti-reflective microcrystalline silicon oxide p-layer for thin-film silicon solar cells on ZnO. *Sol. Energy Mater. Sol. Cells* **105**, 187–191 (2012)
2. Klein, S., Wieder, S., Buschbaum, S., Rohde, M., Schwanitz, K., Stolley, T., Stömmer, C., Severin, D., Straub, A., Schmidt, U.I., Ahmed, K.: Large area thin film silicon modules with 10% efficiency for production. *Phys. Status Solidi C* **8**, 2978–2981 (2011)
3. Cody, G.D.: The optical absorption edge of a-Si:H. In: Pankove, J.I. (ed.) *Hydrogenated Amorphous Silicon, Part B: Optical Properties*, pp. 11–82. Academic, Orlando (1984)
4. Staebler, D.L., Wronski, C.R.: Reversible conductivity changes in discharge-produced amorphous Si. *Appl. Phys. Lett.* **31**, 292–294 (1977)
5. Meier, J., Fluckiger, R., Keppner, H., Shah, A.: Complete microcrystalline p–i–n solar cell—crystalline or amorphous cell behavior? *Appl. Phys. Lett.* **65**, 860–862 (1994)
6. Repmann, T.: Stapelsolarzellen aus amorphem und mikrokristallinem Silizium. *Berichte des Forschungszentrums Jülich, Aachen* (2003)

7. Lim, K.S., Konagai, M., Takahashi, K.: A novel structure high conversion efficiency pSiC/graded pSiC/iSi/nSi/metal and substrate type amorphous silicon solar cell. *J. Appl. Phys.* **56**, 538–542 (1984)
8. Southwell, W.H.: Gradient-index antireflection coatings. *Opt. Lett.* **8**, 584–586 (1983)
9. Das, C., Lambertz, J., Huepkes, J., Reetz, W., Finger, F.: A constructive combination of antireflection and intermediate-reflector layers for a-Si/mc-Si thin film solar cells. *Appl. Phys. Lett.* **92**, 053509/1–053509/3 (2008)
10. Pascual, J., Camassel, J., Mathieu, H.: Fine structure in the intrinsic absorption edge of TiO₂. *Phys. Rev. B* **18**, 5606–5614 (1978)
11. Chen, T., Huang, Y., Dasgupta, A., Luysberg, M., Houben, L., Yang, D., Carius, R., Finger, F.: Microcrystalline silicon carbide window layers in thin film silicon solar cells. *Sol. Energy Mater. Sol. Cells* **98**, 370–378 (2012)
12. Sihanugrist, P., Yoshida, T., Ichikawa, Y., Sakai, H.: Amorphous silicon oxide with microcrystalline Si phase. *J. Non Cryst. Solids* **164–166**, 1081–1084 (1993)
13. Sihanugrist, P., Sasaki, T., Asano, A., Ichikawa, Y., Sakai, H.: Amorphous silicon oxide and its application to metal/n-i-p/ITO type a-Si solar cells. *Sol. Energy Mater. Sol. Cells* **34**, 415–422 (1994)
14. Cuony, P., Marending, M., Alexander, D.T.L., Boccard, M., Bugnon, G., Despeisse, M., Ballif, C.: Mixed phase p-type silicon oxide containing silicon nanocrystals and its role in thin-film silicon solar cells. *Appl. Phys. Lett.* **97**, 213502/1–213502/3 (2010)
15. Lambertz, A., Finger, F., Hollaender, B., Rath, J.K., Schropp, R.E.I.: Boron-doped hydrogenated microcrystalline silicon oxide (mc-SiOx:H) for application in thin-film silicon solar cells. *J. Non Cryst. Solids* **17**, 1962–1965 (2012)
16. Krajangsang, T., Kasashima, S., Hongsingthong, A., Sihanugrist, P., Konagai, M.: Effect of p- $\mu\text{c Si}_1 - x\text{O}_x\text{:H}$ layer on performance of hetero-junction microcrystalline silicon solar cells under light concentration. *Curr. Appl. Phys.* **12**, 515–520 (2012)
17. Despeisse, M., Battaglia, C., Boccard, M., Bugnon, G., Charrière, M., Cuony, P., Haenni, S., Loeffgren, L., Meillaud, F., Parascandolo, G., Soederstroem, T., Ballif, C.: Optimization of thin film silicon solar cells on highly textured substrates. *Phys. Status Solidi A* **208**, 1863–1868 (2011)
18. Obermeyer, P., Repmann, T., Severin, D., Vermeir, I., Schmidt, U.I., Witting, K., Schröder, J., Müller, J., Kuhr, N., Kress, M., Schwanitz, K., Klein, S., Wieder, S.: Large area thin film silicon solar cells and modules on textured ZnO:Al front contacts. In: Proceedings of the 24th European PVSEC, vol. 21–25, pp. 2313–2316. EUPVSEC, Hamburg (2009)
19. Daube, C., Schmidt, U.I., Severin, D., Kürthen, C., Görgens, C., Ahmed, K., Vermeir, I., Kuhr, N., Klein, S., Straub, A., Wieder, S., Forster, D., Zilbauer, T., Rembeck, A., Schubert, R., Rohde, M., Stömmmer, C., Deppisch, T.: Advanced large area TCO production line for economic manufacturing of high efficiency a-Si/mc-Si based thin film modules. In: Proceedings of the 25th European PVSEC, vol. 6–10, pp. 2771–2774. EUPVSEC, Valencia (2010)
20. Kluth, O., Löffl, A., Wieder, S., Beneking, C., Appenzeller, W., Houben, L., Rech, B., Wagner, H., Hoffmann, S., Waser, R., Anna Selvan, J.A., Keppner, H.: Texture etched Al-doped ZnO: a new material for enhanced light trapping in thin film solar cells. In: Proceedings of the 26th IEEE Photovoltaic Specialists Conference, pp. 715–718. IEEE, Piscataway (1997)
21. Kluth, O., Rech, B., Houben, L., Wieder, S., Schöpe, G., Beneking, C., Wagner, H., Löffl, A., Schock, W.: Texture etched ZnO:Al coated glass substrates for silicon based thin film solar cells. *Thin Solid Films* **351**, 247–253 (1999)
22. von Keudell, A., Abeson, J.: Direct insertion of SiH₃ radicals into strained Si–Si surface bonds during plasma deposition of hydrogenated amorphous silicon films. *Phys. Rev. B* **59**, 5791–5798 (1999)
23. Street, R.A.: *Hydrogenated Amorphous Silicon*. Cambridge University Press, Cambridge (1992)
24. Gallagher, A.: Neutral radical deposition from silane discharges. *J. Appl. Phys.* **63**, 2406–2413 (1988)

25. Ganguly, G., Matsuda, A.: Defect formation during growth of hydrogenated amorphous silicon. *Phys. Rev. B* **47**, 3661–3670 (1992)
26. Tanaka, K., Maruyama, E., Shimada, T., Okamoto, H.: *Amorphous Silicon*. Wiley, New York (1999)
27. Samanta, A., Das, D.: Studies on the structural properties of SiO:H films prepared from (SiH₄+CO₂+He) plasma in RF-PECVD. *Sol. Energy Mater. Sol. Cells* **93**, 588–596 (2009)
28. Matsumara, H., Sakai, K., Maeda, M., Furukawa, S., Horiuchi, K.: Measurement of boron diffusivity in hydrogenated amorphous silicon by using nuclear reaction ¹⁰B(n,α)⁷Li. *J. Appl. Phys.* **54**, 3106–3110 (1983)
29. De Salvador, D., Napolitani, E., Mirabella, S., Bruno, E., Impellizzeri, G., Bisognin, G., Pecora, E.F., Priolo, F., Carnera, A.: Experimental investigations of boron diffusion mechanisms in crystalline and amorphous silicon. *Mater. Sci. Eng. B* **154–155**, 240–246 (2008)
30. Torres, P., Meier, J., Fluckiger, R., Kroll, U., Anna Selvan, J.A., Keppner, H., Shah, A., Littlewood, S.D., Kelly, I.E., Giannoulas, P.: Device grade microcrystalline silicon owing to reduced oxygen contamination. *Appl. Phys. Lett.* **69**, 1373–1375 (1996)
31. Hishikawa, Y., Nakamura, N., Tsuda, S., Nakano, S., Kishi, Y., Kuwano, Y.: Interference-free determination of the optical absorption coefficient and the optical gap of amorphous silicon thin films. *Jpn. J. Appl. Phys.* **30**, 1008–1014 (1991)
32. Smit, C., van Swaaij, R.A.C.M.M., Donker, H., Petit, A.M.H.N., Kessels, W.M.M., van de Sanden, M.C.M.: Determining the material structure of microcrystalline silicon from Raman spectra. *J. Appl. Phys.* **94**, 3582–3588 (2003)
33. Adhikary, K., Ray, S.: Characteristics of p-type nanocrystalline silicon thin films developed for window layer of solar cells. *J. Non Cryst. Solids* **353**, 2289–2294 (2007)
34. Macleod, H.A.: *Thin-Film Optical Filters*. CRC Press, Boca Raton (2010)
35. Kirchartz, T., Ding, K., Rau, U.: Fundamental electrical characterization of thin-film solar cells. In: Abou-Ras, D., Kirchartz, T., Rau, U. (eds.) *Advanced Characterization Techniques for Thin Film Solar Cells*, pp. 35–61. Wiley VCH, Weinheim (2011)
36. Palanchoke, U., Jovanov, V., Kurz, H., Obermeyer, P., Stiebig, H., Knipp, D.: Plasmonic effects in amorphous silicon thin film solar cells with metal back contacts. *Opt. Express* **20**, 6340–6347 (2012)
37. Nelson, J.: *The Physics of Solar Cells*. Imperial College Press, London (2003)
38. Würfel, P.: *Physics of Solar Cells—From Basic Principles to Advanced Concepts*. Wiley VCH, Weinheim (2009)
39. Markvart, T., Castaner, L.: *Practical Handbook of Photovoltaics—Fundamentals and Applications*. Elsevier, Oxford (2003)
40. Sze, S.M., Ng, K.K.: *Physics of Semiconductor Devices*. Wiley, New York (2006)

Chapter 16

Design Guidelines for High Efficiency Plasmonics Silicon Solar Cells

Pushpa Raj Pudasaini and Arturo A. Ayon

Abstract We report a novel solar cell design concept, for high optical absorption in the thin active layer of photovoltaic devices due to localized surface plasmon effects arising on the employed metallic nanoparticle arrays. The proposed solar cell geometry consists of sub-wavelength nanotextured surface in combination with plasmonics metal nanoparticles. The detailed balance analysis is carried out for the limiting efficiency of an optimized nanotextured surface in combination with the gold (Au) nanoparticle arrays described herein. The ultimate efficiency of the optimized nanostructured silicon surface decorated by the Au nanoparticle arrays is 39.67 %, which compares favorably with the ultimate efficiency of 31.11 % for an optimized nanotextured surface without Au nanoparticles. For the proposed geometry of the solar cell, the maximum short circuit current density (J_{SC}) and the power conversion efficiency (PCE) of 31.57 mA/cm² and 25.42 %, respectively, are achieved on a single-crystal silicon layer of thickness 2.8 μm, compared to the predicted J_{SC} and PCE values of 25.45 mA/cm² and 20.87 %, respectively, for an optimized structure of the same thickness without Au plasmonics effects. The influence of a silicon dioxide/silicon nitride (SiO₂/Si₃N₄) stack as a dielectric spacer layer, which could also serve as a surface passivation for nanotextured surface, on the optical absorption performance of plasmonics Au nanoparticle is also presented.

1 Introduction

Single junction solar cells made from single-crystal silicon are still the preferred market choice due to their relatively high efficiency, and for the same reason they represent more than 80 % of the current photovoltaic market. However, silicon is an

P.R. Pudasaini (✉) • A.A. Ayon
MEMS Research Laboratory, Department of Physics and Astronomy, University of Texas
at San Antonio, One UTSA Circle, San Antonio, TX 78249, USA
e-mail: pbz620@my.utsa.edu

indirect band gap material having relatively poor absorption performance. The thickness of the silicon film required to absorb the most part of the solar spectrum should be larger than the inverse of the absorption coefficient for the wavelength corresponding to near band-edge ($\alpha_{\text{bandedge}} \sim 1,050 \text{ nm}$). On the basis of this simple fact, for a single pass of light, the thickness of silicon film required to absorb the usable part of the solar spectrum should be almost a millimeter. Such a silicon film thickness is not desirable for the commercial production of solar cell due to numerous reasons, for instance, (1) the onerous cost of the material being used in the solar cell device, (2) the collection efficiency of the photogenerated carrier in the device, etc. Specifically, currently marketed solar cells use a crystalline silicon active layer of thickness 180–300 μm , which account for almost 40 % of the total module cost. Additionally, it is rather difficult to have a minority carrier diffusion length comparable to such a silicon film thickness. Thus, there is great interest in reducing the thickness of the silicon substrate employed in solar cell devices. On the other hand, light trapping in solar cells has played an important role in improving absorption performance of the devices by allowing weakly absorbed light to go through multiple reflections within the cell. It also provides some significant advantages including the reduction of cell thickness, reduced processing time and cost, and improved cell efficiency. The idea of light trapping inside a semiconductor by total internal reflection was first reported by John in 1965 [1]. In 1982, Yablonovitch and Cody [2] reported that the local light intensity in a randomly textured film can be enhanced by the factor $4n^2$, where “ n ” is the index of refraction of the textured medium. Since then, various light trapping structures including randomly or periodically textured surfaces [3–12], plasmonic metal nanoparticles [13–24], and numerous other plasmonic and photonic structures [25–29] have been intensively studied. In the last few years, sub-wavelength surface nanotexturing have attracted considerable attention due to their unique optical and electrical properties. Excellent light absorption and hence better power conversion efficiency (PCE) of silicon nanostructured topographies, such as, silicon nanowires (SiNW), silicon nanopillars (SiNP), silicon nanoholes (SiNH), and silicon nanocones (SiNC) have been demonstrated both theoretically and experimentally [3, 4, 8, 10, 12, 30–33]. The advanced light trapping effect of silicon nanostructured devices is mainly due to the presence of a large numbers of photonic bands and relatively small group velocities, which implies a higher density of states of photons and hence, larger optical absorption compared to homogeneous silicon thin film. The sub-wavelength nanostructured surface of the thin active layer of a solar cell is also promising for suppressing light reflections, and thus enhancing light trapping due to the gradual change in the index of refraction. Furthermore, metallic nanostructures supporting surface plasmons have been proposed as an alternative method to achieve light trapping in thin film solar cells. Metal nanoparticles like gold (Au), silver (Ag) interact strongly with visible and infrared photons due to the excitation of localized surface plasmons (LSPs). LSPs are the collective oscillation of free electron in the metallic nanoparticles that allow light to be manipulated at the nanoscale. This approach

has the potential to reduce the physical thickness of solar cells while maintaining the optical thickness constant, due to the two basic reasons, namely, (1) the metallic nanoparticles can be used as sub-wavelength scattering elements to couple and trap freely propagating light wave into the substrate, and (2) the metallic nanoparticles can be used as sub-wavelength antennas in which the plasmonics near field is coupled to the substrate, increasing its effective cross-section area. A major benefit of a plasmonic light trapping lies in the fact that the metallic nanoparticles can be deposited at the final stage of the device fabrication process without the need to change any processing conditions and compromise the material or the surface quality. Moreover, the optical properties of the surface plasmon can be decoupled from the electrical properties of the solar cell, and hence it can be optimized independently. The ability of the plasmons to guide and confine light on sub-wavelength scales is opening up new design possibilities for solar cells. In this chapter, we report a novel solar cell design concept having the possibility of enhanced light absorption and hence greater efficiency of operation. The proposed solar cell consists of sub-wavelength textured surface decorated by plasmonics metal nanoparticles.

2 Light Scattering by Metal Nanoparticles

Metal nanoparticles interact strongly with visible and infrared photons due to the excitation of LSPs. LSPs are the collective oscillation of free electron in the metal nanoparticles. The strongest optical interaction occurs at a resonance, with the resonance condition being a function of nanoparticles size, shape, and type of metal, as well as the local dielectric environment. Upon excitation the LSPs can decay radiatively, resulting in scattering, or non-radiatively, resulting in absorption. The sum of the absorption and scattering is known as extinction, and the extinction peak occurs at the resonance wavelength of the LSPs. The extinction resonance peak can be tuned by changing the effective dielectric medium of the metallic nanoparticles. According to the Mie scattering theory, for sufficiently small particles (comparable with the wavelength of the incident light λ) with a dielectric permittivity ϵ_p , the absorption and scattering cross-sections are given by [34].

$$C_{\text{abs}} = \frac{2\pi}{\lambda} \text{Im}[\alpha] \quad (16.1)$$

$$C_{\text{sca}} = \frac{1}{6\pi} \left(\frac{2\pi}{\lambda} \right)^4 |\alpha|^2 \quad (16.2)$$

$$\text{where, } \alpha = 3V \left[\frac{\epsilon_p - \epsilon_m}{\epsilon_p + 2\epsilon_m} \right] \quad (16.3)$$

is the polarizability of the particle, V is the volume of particle, and ϵ_m is the dielectric function of the surrounding medium. Ostensibly, when $\epsilon_p = -2\epsilon_m$,

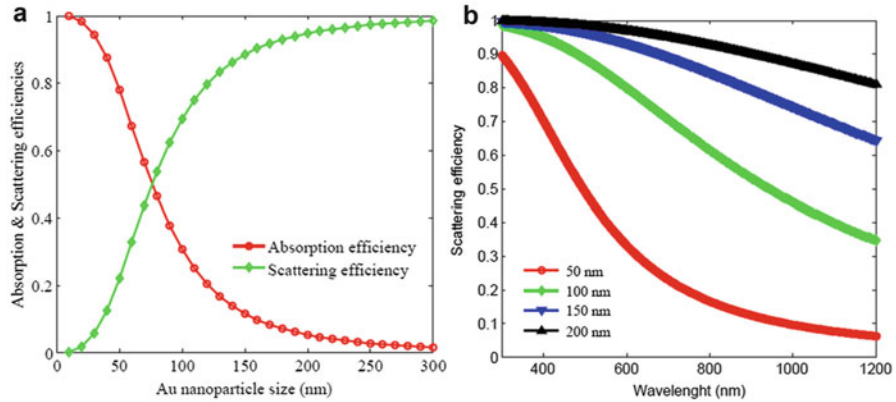


Fig. 16.1 (a) Absorption and scattering efficiencies versus sizes of Au nanoparticle at 550 nm, (b) scattering efficiency as a function of wavelength for different Au nanoparticles sizes

the particle polarizability will become relatively large. This is known as the surface plasmon resonance. At the surface plasmon resonance, the scattering and absorption cross-sections can exceed the geometrical cross-section of the particles. For light trapping purposes in thin film solar cells, the light scattering by the plasmonics nanoparticles should be greater than the parasitic absorption of the particle itself. To measure the scattering and absorption performances of the particles, we defined the scattering and absorption efficiencies by:

$$Q_{\text{abs}} = \frac{C_{\text{abs}}}{C_{\text{abs}} + C_{\text{sca}}} \quad (16.4)$$

$$Q_{\text{sca}} = \frac{C_{\text{sca}}}{C_{\text{abs}} + C_{\text{sca}}} \quad (16.5)$$

The scattering efficiency of the plasmonics nanoparticle depends on the particle size, shape, and type of the particle as well as its surrounding medium. The absorption and scattering efficiencies of the gold (Au) nanoparticle of various sizes are plotted in Fig. 16.1.

Figure 16.1a depicts the variation of the absorption and scattering efficiencies as a function of the size of the Au nanoparticle for an incident radiation of wavelength 550 nm. Ostensibly, scattering dominates over the absorption for particle diameters greater than 100 nm. Although not shown here, for even larger particles the scattering efficiency is again dominated by the absorption. This is because of increased retardation effects and higher order multipole excitations, which decrease the scattering efficiency of the particle. The variation of scattering efficiency with the wavelength of incident radiation for different particle sizes is shown in Fig. 16.1b. It depicts that there is a noticeable increase in the scattering efficiency as the particle size increases from 50 to 200 nm, and this effect extends to those wavelengths where silicon has poor absorption performance. The surrounding

dielectric medium along with the shape and size of the particles has a significant role to tune the resonance scattering peak which is important in order to optimize the light coupling into the substrate for photovoltaic application.

3 Review of Plasmonics Light Trapping for Photovoltaic Application

The optical properties of metallic nanoparticles have been studied since early in the eighteenth century. In more recent years, it has been extensively studied, in particular due to the discovery that Raman scattering can be increased by an order of magnitude through the use of metallic nanostructures [35]. Since then, there has been a profusion of work in both the fundamental properties and the applications of plasmonic resonance, especially in integrated optics and bio-sensing [36, 37]. Resonance scattering due to plasmon resonances in the metallic nanoparticles leads to a reduced reflection over the broad spectral range. Different groups have studied this antireflection effect of random and periodic arrays of metallic nanoparticles for photovoltaic applications both theoretically and experimentally [13, 14, 24, 38–40]. The pioneering work in the area of plasmonic enhancement of light sensitive devices was done by Stuart and Hall. They reported that an enhancement in the photocurrent of a factor of 18 could be achieved for a 165 nm thick silicon-on-insulator photodetector at the wavelength of 800 nm using silver (Ag) nanoparticles on the surface of the devices [41]. Schaadt et al. have reported an 80 % enhancement on photocurrent at the wavelength of 500 nm on highly doped wafer-based solar cells by depositing gold nanoparticles on its surface [39]. Derkacs et al. have reported an 8 % improvement in the overall PCE of thin film amorphous silicon solar cells by using Au nanoparticles [40]. Pillai et al. reported an overall photocurrent enhancement of 33 % and 19 %, on 1.25 μm thick silicon-on-insulator and wafer-based solar cells, respectively, by depositing Ag nanoparticles on the surface of the solar cells [13]. Ouyang et al. demonstrated a short circuit current density enhancement of 27 % on thin film silicon solar cell employing self-assembled Ag nanoparticles on the rear surface of the cell [19]. Beck et al. reported a relative increase in photocurrent of 10 % for 22 μm thick silicon cell by incorporating the self-assembled Ag nanoparticles on the rear surface of the device [18]. Recently, Tan et al. have reported a net gain of 2 mA/cm^2 in short circuit current density without deterioration of an open circuit voltage and a fill factor of the device, by using silver nanoparticle as a plasmonic back reflector [15].

Solar cell performance improvement due to the plasmonic effect of metallic nanoparticles have also been reported for other types of solar cells, like dye sensitized solar cells and organic solar cells [42–48]. Ding et al. have reported for the first time the use of plasmonic effects to increase the light absorption, and hence efficiency of dye sensitized solar cells [43]. They reported the PCE of 5.9 % for Ag plasmonic back reflector dye sensitized solar cell. Häggglund et al. have reported the enhanced carrier generation in dye sensitized TiO_2 film using Au nanodisc [49]. Rand et al. have reported enhanced efficiencies for ultrathin film organic solar cells

due to the presence of very small silver nanoparticles [47]. Morfa et al. have reported an increase in efficiency by a factor of 1.7 for organic bulk heterojunction solar cells [48]. Chen et al. have reported enhanced PCE of organic solar cells after blending the Au nanoparticles into the anodic buffer layer [50].

4 Light Trapping Performance of the Proposed Nanostructured Plasmonics Silicon Solar Cells

Figure 16.2 depicts the schematic of the proposed silicon nanostructures such as silicon nanopillars (a), and silicon nanoholes (b), incorporating the plasmonic Au nanoparticles on the top of the nanopillars and on the surface as well as bottom-of-a-trench of the nanoholes. Figure 16.2c depicts the two-dimensional unit cell structure of silicon nanoholes arrays textured surface with the periodicity P , diameter D , and nanohole depth H .

The plasmonic metal nanoparticles can be incorporated in nanostructured silicon thin film by thermal dewetting of thin metallic film deposited selectively on its surface [51–53]. Figure 16.3 depicts the ordered gold nanoparticle arrays fabricated on planar and silicon nanopillars arrays textured surface by annealing 35 nm gold film at 850 °C for 30 min. To evaluate the optical absorption performance of the solar cells, we calculate the ultimate efficiency η , which is defined as the efficiency of the photovoltaic cell as the temperature approaches 0 K, when each photon with energy greater than the band gap energy produces one electron hole pair [54].

$$\eta = \frac{\int_0^{\lambda_g} I(\lambda) A(\lambda) \frac{\lambda}{\lambda_g} d\lambda}{\int_0^{\infty} I(\lambda) d\lambda} \quad (16.6)$$

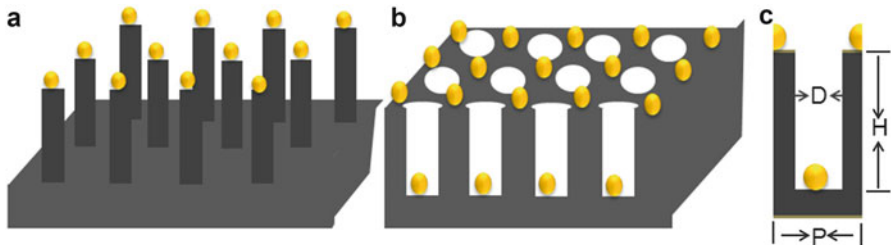


Fig. 16.2 Schematic of silicon nanopillars (a), and silicon nanoholes (b), arrays surface textured thin film in combination with Au nanoparticles on the top of the nanopillars, and on the surface as well as bottom-of-a-trench of the nanoholes, respectively. The two-dimensional unit cell structure of proposed silicon nanoholes arrays surface textured solar cells (c)

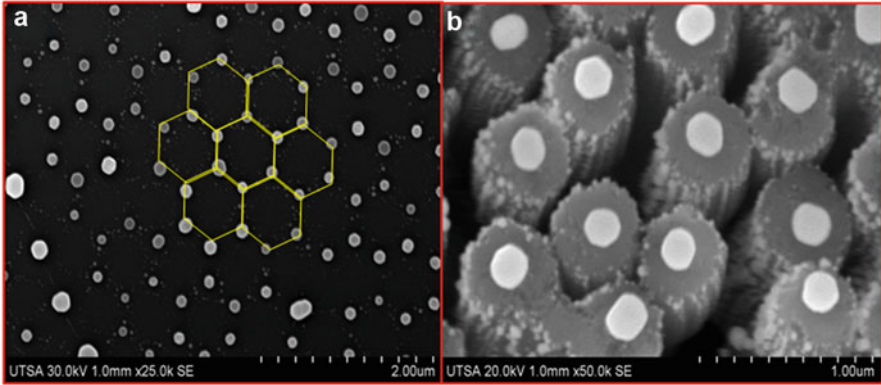


Fig. 16.3 SEM micrographs of ordered Au nanoparticle arrays in (a) planar silicon surface, (b) SiNP arrays textured surface, fabricated by annealing the selectively deposited thin Au films at 850 °C for 30 min

where $I(\lambda)$ is the solar intensity per wavelength interval corresponding to an air mass of 1.5 directly normal and a circumsolar spectrum [55], $A(\lambda)$ is the absorbance, λ is the wavelength, and λ_g is the wavelength corresponding to the band gap energy (E_g).

The optical simulation of the proposed geometry of the solar cell was carried out by using the commercially available COMSOL multiphysics software. The plane electromagnetic wave polarized in the x -direction was assumed to be normally incident on the sample. The energy range of incident wave varies from 1 to 4 eV, which corresponds to the wavelength range of 1,240 to 310 nm. As the SiNP/SiNH arrays are infinite in x -direction, the model is set up for one unit cell of the SiNP/SiNH structure, flanked by Floquet boundary conditions describing the periodicity. The solution in one side of the unit cell equals the solution on the other side multiplied by the complex valued phase factor. The phase shift between the boundaries is evaluated by the perpendicular component of the wave vector. Perfectly matched layers are used in both $+y$ and $-y$ directions for simulating the infinitely extended air medium.

The structural parameters of the SiNP/SiNH arrays play an important role in determining the light absorption performance of the device. Hence, the SiNP/SiNH arrays were optimized for the higher optical absorption in terms of nanopillar height H , periodicity P , and silicon filling fraction F . We defined the filling fraction F as the area occupied by the silicon in one unit cell of the sample. The total thickness of the sample is taken as 2.8 μm , with underlying silicon thin film of thickness 0.8 μm , which is a comparable value observed in thin film silicon solar cell technology. The values of the dielectric constant used in this work can be found elsewhere [56]. The electric field variation in a unit cell structure of SiNP arrays texture surface with and without Au particles are shown in Fig. 16.4a, for an incident radiation of wavelength 500 nm.

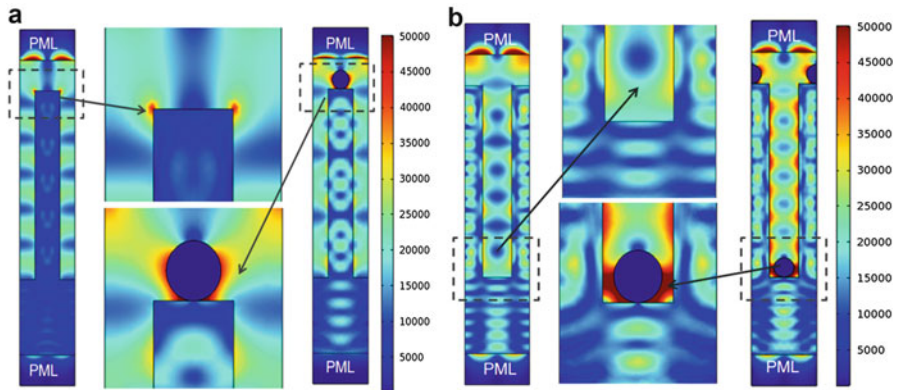


Fig. 16.4 Electric field distribution on the unit cell structure of SiNP arrays textured surface (a), and SiNH arrays textured surface (b) with and without Au nanoparticles

Ostensibly, the incident radiation is effectively scattered by the nanopillars. Furthermore, the presence of Au nanoparticle on the surface of the SiNP arrays seems more effective to confine and guide the incident radiation towards the underlying silicon substrate. This is due to the near field enhancement around the Au nanoparticles due to the presence of LSPs and also a far enhancement due to the wide angular scattering of the incident radiation by the metallic nanoparticles. Figure 16.4b shows the electric field distribution on a unit cell structure of SiNH arrays textured surface with and without Au nanoparticles. Noticeably, strong LSPs were developed on the Au nanoparticles at the bottom of the nanohole compared to the nanoparticles on the top of the surface due to the difference in effective dielectric of the surrounding medium. The optical absorption performance of the SiNP and SiNH arrays textured surface are measured in terms of the ultimate efficiency of the solar cell. Figure 16.5a depicts the variation of ultimate efficiency as a function of silicon filling fraction for various periodicities of SiNP arrays textured surface. Ostensibly, the ultimate efficiency improves with both the increase in silicon filling fraction and the SiNP arrays periodicity. The reason for the higher optical absorption, and hence the higher ultimate efficiency is because of the antireflection effect due to the gradual change of index of refraction with filling fraction and, the light trapping properties including the excitation of guided resonance mode. However, as the silicon filling fraction increase beyond 0.5 the ultimate efficiency was observed to decrease for higher values of SiNP array periodicities due to increases in specular reflection of the short wavelength radiation. The maximum value of ultimate efficiency of 26.88 % was calculated for the SiNP array textured solar cell for the array periodicity of 650 nm and a silicon filling fraction of 0.6.

The variations of ultimate efficiency with silicon filling fraction for various SiNH arrays periodicities are shown in Fig. 16.5b. The ultimate efficiency increases with the increase in both silicon filling fraction and SiNH arrays periodicity as in

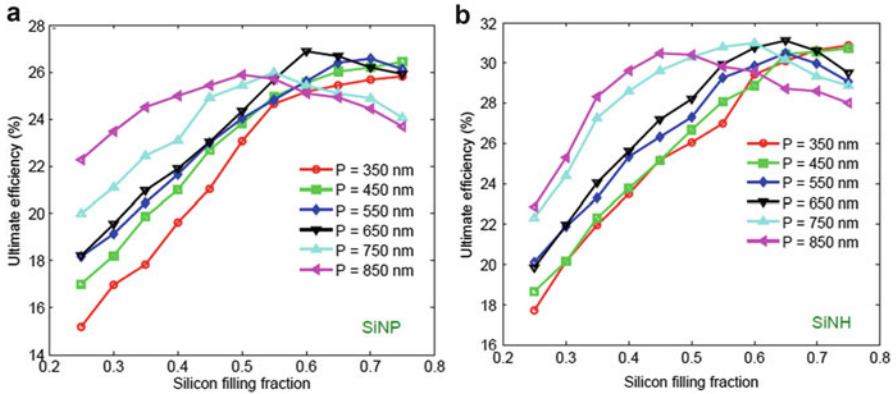


Fig. 16.5 Ultimate efficiency versus silicon filling fraction for different periodicities of SiNP arrays textured surface (a), SiNH arrays textured surface (b)

SiNP arrays textured solar cells. It reaches a maximum of 31.11 % for an array periodicity of 650 nm and a silicon filling fraction of 0.65, which is almost 16 % higher compared to its counterpart SiNP array textured surface with the same periodicity and almost the same silicon filling fraction. The SiNH array textured surface performs better than SiNP array textured surface for enhanced light trapping purpose for all the values of array periodicities and silicon filling fractions studied, which is in good agreement with results reported elsewhere [3, 32].

This is due to the presence of guided resonance of higher order diffraction modes. The effects of the presence of plasmonic Au nanoparticles on the SiNP/SiNH arrays textured surface on optical absorption performance of the devices describe herein are shown in Fig. 16.6a. The green line with open circles corresponds to the optimized SiNP arrays (with array periodicity and silicon filling fraction of 650 nm and 0.6, respectively) textured surface without Au plasmonic effect, and the blue line with open squares corresponds to the SiNP arrays textured surface with Au plasmonic effect. Ostensibly, the ultimate efficiency of SiNP arrays textured surface with Au plasmonic effect is higher compared to its counterpart without plasmonic effect for the any silicon filling fraction. The magenta line with open triangles corresponds to the optimized SiNH array textured surface with Au plasmonic effect, reaches a maximum ultimate efficiency of 38.58 %, which is 24.01 % greater than its counterpart SiNH array textured surface without Au nanoparticles (31.11 %, back line with open squares). The forward scattering of incident radiation towards the higher index silicon substrate due to the LSPs arising on Au nanoparticles were responsible for the higher optical absorption, and hence the higher ultimate efficiency of Au decorated nanotextured devices.

To obtain a photogenerated carrier profile (G), the photogenerated carriers are integrated to the continuity equation. It is defined as the divergence of the pointing vector S , which can be expressed as:

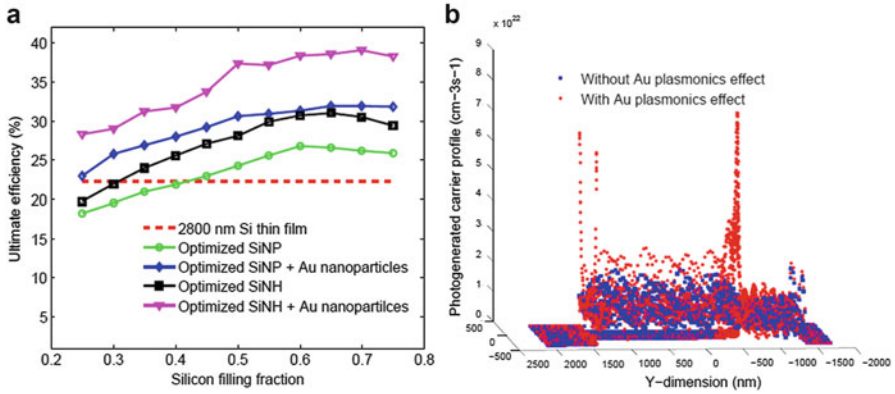


Fig. 16.6 Variation of ultimate efficiency as a function of silicon filling fraction in an optimized SiNP/SiNH arrays textured surface with and without Au nanoparticles (a), photogenerated carrier profile in the unit cell structure of the SiNH arrays with and without Au plasmonics effect (b)

$$G = n_{\text{quan}} \frac{\pi(-\varepsilon''_r)|E|^2}{h}, \quad (16.7)$$

where E is the electric field obtained from the optical simulation, ε''_r is the imaginary part of the semiconductor material's permittivity, and n_{quan} is the quantum efficiency, which is given by:

$$n_{\text{quan}} = \text{step}\left(\frac{h\nu}{E_g}\right) \begin{cases} 0, & (h\nu < E_g) \\ 1, & (h\nu > E_g) \end{cases} \quad (16.8)$$

where E_g is the energy band gap of the semiconductor and $h\nu$ is the photon energy. The photogenerated carrier profile on the unit cell structure of SiNH array textured surface with and without Au plasmonic effect is shown in Fig. 16.6b. The near field enhancement due to the LSP arising on the Au nanoparticles is responsible for the spike in the carrier generation in the vicinity of the particle. While the far field enhancement due to the scattering of the incident radiation due to the presence of LSPs is responsible for the increased carrier generation throughout the unit cell structure of SiNH arrays textured surface.

5 Detailed Balanced Limits for Performance Parameters of the Proposed Solar Cell Geometry

The detailed balanced analysis was carried out to obtain the ultimate limit of the performance parameters, like short circuit current density, open circuit voltage, and PCE of the proposed solar cells device. The short circuit current density (J_{SC}) is

proportional to the number of photons above the band gap; it is assumed that all such photons are absorbed to generate the electron hole pairs and every photo-generated carrier can reach the electrodes which contribute to the photocurrent. In this case, the ultimate limit for the short circuit current density is given by:

$$J_{sc} = \int_0^{\lambda_g} I(\lambda)A(\lambda) \frac{e\lambda}{hc} d\lambda \quad (16.9)$$

The J - V characteristic of an ideal diode to describe the electrical properties of the solar cells is written as:

$$V(J) = \frac{k_B T}{q} \ln \left[\left(\frac{J_{sc} - J}{J_0 \gamma} \right) + 1 \right] \quad (16.10)$$

where $\gamma = \frac{A_{junc}}{A_{illu}}$, J is the current density of the solar cell, V is the voltage between the terminals of the cell, J_0 is the reverse saturation current density. A_{illu} and A_{junc} are the illumination area and junction area of the solar cell geometry, respectively. Evidently, γ depends upon the specific geometry of the solar cells. For the axial p-n junction, where p and n regions are vertically stacked, the value of γ is approximated by the filling fraction of the silicon nanostructured arrays textured surface. The reverse saturation current J_0 is given by

$$J_0 = \frac{2\pi q}{h^3 c^2} (n_T^2 + n_B^2) k_B T (2k_B^2 T^2 + 2k_B T E_g + E_g^2) \times \exp\left(-\frac{E_g}{k_B T}\right) \quad (16.11)$$

where n_T and n_B are the refractive indices of the superstrate and substrate of the solar cells, respectively, k_B is Boltzmann's constant. For crystalline silicon with the band gap energy (E_g) of 1.1 eV at $T = 300$ K, the value of J_0 is 5.4×10^{-13} mA/cm². Assuming $J_{sc} \gg J_0$, and setting $J = 0$, we obtain the open circuit voltage, which is given by:

$$V_{oc} = \frac{k_B T}{q} \ln \left(\frac{J_{sc}}{J_0} \right) - \frac{k_B T}{q} \ln \gamma \quad (16.12)$$

Furthermore, the PCE of the solar cell is defined by:

$$PCE = \frac{V_{oc} J_{sc} FF}{I_{in}} \quad (16.13)$$

where I_{in} is incident solar power density and is equal to 900.14 W/m² for the ASTM AM1.5 direct and circumsolar spectrum, and FF is the fill factor defined by:

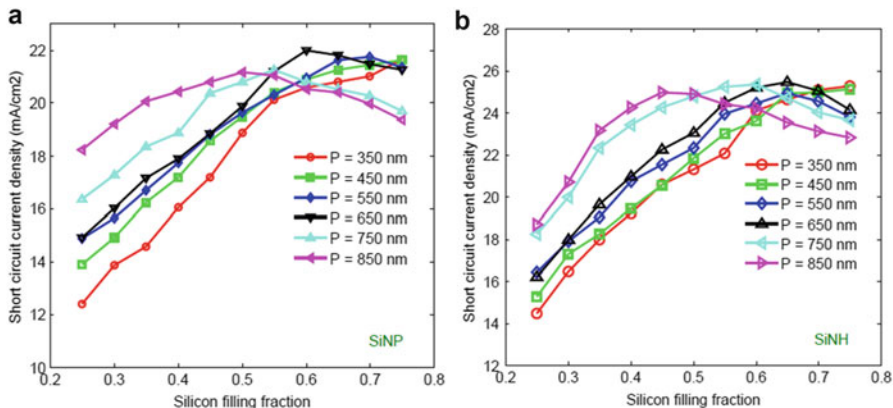


Fig. 16.7 Short circuit current density versus silicon filling fraction for different periodicities of SiNP arrays textured surface (a), SiNH arrays textured surface (b)

$$FF = \frac{V_{mpp} J_{mpp}}{V_{oc} J_{sc}} \quad (16.14)$$

with V_{mpp} and J_{mpp} are voltage and current density at maximum power point, respectively.

The ultimate limit of short current density (J_{SC}) for SiNP arrays textured surface is shown in Fig. 16.7a. The maximum J_{SC} value of 21.99 mA/cm² was achieved for the SiNP array textured solar cells with the arrays periodicity of 650 nm and silicon filling fraction of 0.6. The short circuit current density improves with the increase in both the filling fraction and the periodicity of the SiNP array textured surface due to the enhanced light absorption performance of the device. However, the J_{SC} values saturate and start to roll off as the filling fraction exceed 0.6, especially for higher periodicities. Figure 16.7b depicts the calculated values of J_{SC} for the SiNH arrays textured solar cells for different SiNH array periodicities. The maximum value of J_{SC} of 25.45 mA/cm² was calculated for SiNH array textured solar cells for the optimized structure of array periodicity of 650 nm and silicon filling fraction of 0.65, which is ~16 % higher than the J_{SC} value of the optimized SiNP array textured solar cells. The Au plasmonics effect on the ultimate limit of short circuit current density (J_{SC}) and the open circuit voltage (V_{OC}) for SiNP/SiNH arrays textured surface are shown in Fig. 16.8.

The blue line with open squares and the magenta line with open triangles in Fig. 16.8a correspond to the SiNP and SiNH array textured surfaces in combination with Au nanoparticle arrays, respectively, reaches the maximum values of J_{SC} of 26.17 mA/cm² and 31.57 mA/cm², respectively, which compare favorably well with 21.99 mA/cm² and 25.45 mA/cm² for SiNP and SiNH textured surface without Au plasmonics effect, respectively. The dashed red line corresponds to J_{SC} value for a 2.8 μ m thin film silicon layer with an optimized silicon nitride (Si₃N₄) antireflection coating (ARC) layer of thickness 45 nm is also plotted for comparison.

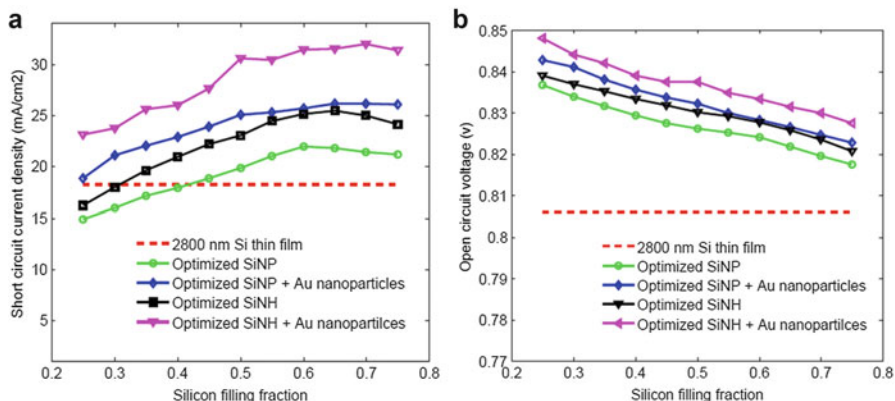


Fig. 16.8 Short circuit current density (a), open circuit voltage (b) versus Si filling fraction in SiNP/SiNH arrays textured surface with and without Au nanoparticles

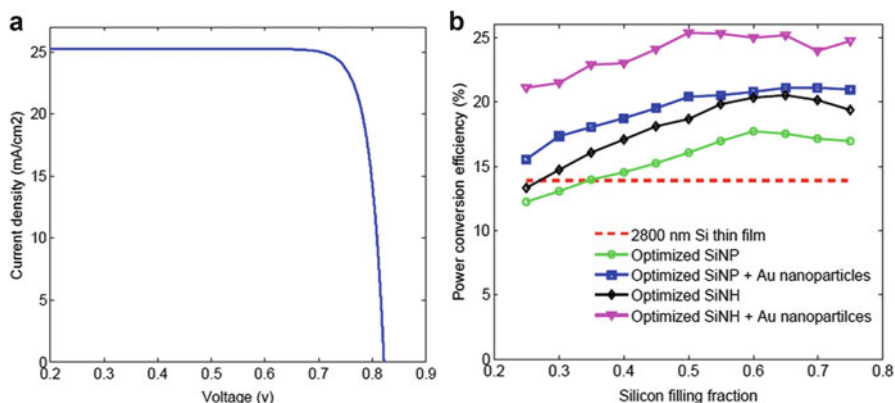
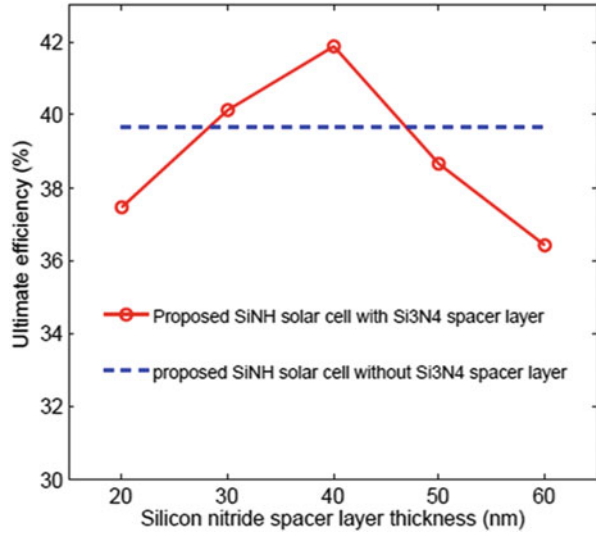


Fig. 16.9 Current density–voltage ($J-V$) characteristics for the optimized SiNH arrays textured solar cells with nanohole periodicity of 650 nm and silicon filling factor of 0.65 (a). The power conversion efficiency versus silicon filling fraction for SiNP/SiNH arrays textured solar cells with and without Au nanoparticles (b)

The dependence of V_{OC} on silicon filling fraction for the proposed solar cell geometry is shown in Fig. 16.8b. Ostensibly, V_{OC} decreases with increases in the filling fraction. The variation of V_{OC} over the entire range of parameters studied is less than 3 %. Higher V_{OC} values were obtained throughout the entire range of Si filling fractions with the utilization of Au plasmonic effects. This is because of increased values of J_{SC} for almost the same values of γ .

The current–voltage ($J-V$) characteristic of the optimized SiNH array textured solar cells is plotted in Fig. 16.9a. The fill factor (FF) for the optimized geometry is found to be 88 %. Figure 16.9b depicts the comparison of power conversion

Fig. 16.10 Ultimate efficiencies as a function of silicon nitride spacer layer thickness for the proposed geometry of SiNH arrays textured plasmonic solar cells. The ultimate efficiency of the proposed solar cell without Si₃N₄ dielectric spacer layer is also plotted for comparison



efficiencies (PCE) of the SiNP/SiNH arrays textured surface with and without Au plasmonic effects. The blue line with open squares corresponds to SiNP array textured surface in combination with Au plasmonic effects, which gives the maximum PCE of 21.12 % compared to 17.72 % (green line with open circles) for the SiNP array textured surface without Au nanoparticles. Furthermore, SiNH array textured surface with Au plasmonic effects (magenta line with open triangles) reaches a maximum PCE of 25.42 %, which is 21.8 % greater than its counterpart without plasmonics effect.

The sub-wavelength nanotextured thin film solar cells has a higher surface area compared to planar thin film solar cells and traditional micro-pyramid textured wafer-based solar cells, which brings out more surface defects, dangling bonds, and an increased number of minority carrier trapping centers. Furthermore, the presence of gold nanoparticles directly on the nanotextured surface of the solar cells serves as a carrier recombination center. Hence, a thin dielectric spacer layer which could also work as a passivation layer for the nanotextured surface is inevitable. However, the dielectric spacer layer thickness has a large influence on the light coupling efficiency of the plasmonic metal nanoparticles. Pillai et al. have reported that a thin dielectric layer is desirable to enhance the scattering from the metallic nanoparticles [20]. Hydrogen-rich silicon nitride (SiN_x:H), silicon dioxide (SiO₂), and aluminum oxide (Al₂O₃) are widely used dielectric passivation layers in thin film solar cells technology [57–60]. We used an SiO₂/Si₃N₄ passivation stack, with SiO₂ as an intermediate layer for the conformal coating on nanotextured surface. We optimized the thickness of Si₃N₄ layer on top of the 10 nm thick SiO₂ for higher optical absorption. Figure 16.10 depicts the ultimate efficiency of the proposed geometry of SiNH array textured solar cell as a function of the thickness of the Si₃N₄ passivation layer (graph with red line). The ultimate efficiency improves with

the increase in thickness of the dielectric Si_3N_4 spacer layer; this could be due to the antireflection effect of the coated layer on the silicon surface. It starts to decrease as the thickness exceeds 40 nm. This is due to the reduced coupling efficiency of the LSPs to the underlying silicon substrate. The ultimate efficiency for the proposed geometry without passivation layer (graph with blue dotted line) is also plotted for comparison.

6 Conclusions

The plasmonics effect of Au nanoparticles for optical absorption enhancement in nanostructured surfaces is studied via simulation for thin film solar cell application. We studied the detailed balanced limit for the limiting values of short circuit current density (J_{SC}), open circuit voltage (V_{OC}), and PCE for different solar cell geometries. The proposed geometry of SiNH array in combination with Au nanoparticle arrays on its surface as well as at the bottom-of-a-trench is promising to achieve higher photon absorption and hence higher PCE. The computed PCE of 25.42 % for the proposed geometry discussed in this letter is almost 21 % greater than its counterpart without Au nanoparticles. The optimized $\text{SiO}_2/\text{Si}_3\text{N}_4$ passivation stack is also proposed with less optical reflection. Therefore, the proposed geometry of the solar cell with just 2.8 μm of silicon could be very crucial to abate the cost of solar energy in the future.

Acknowledgement We thank Dr. Mike Gerhold, Technical Manager of the U.S. Army Research Office, for the financial support provided for this project (ARO grant number W911NF-13-1-0110).

References

1. John, A.: US Patent No 3,487,223 (1965)
2. Yablonovitch, E., Cody, G.: Intensity enhancement in textured optical sheets for solar cells. *IEEE Trans. Electron Devices* **29**, 300–305 (1982)
3. Han, S., Chen, G.: Optical absorption enhancement in silicon nanohole arrays for solar photovoltaics. *Nano Lett.* **10**, 1012–1015 (2010)
4. Li, J., Yu, H.Y., Wong, S.M., Zhang, G., Sun, X., Lo, P.G.-Q., Kwong, D.: Si nanopillar array optimization on Si thin films for solar energy harvesting. *Appl. Phys. Lett.* **95**, 033102 (2009)
5. Peng, K.-Q., Wang, X., Wu, X., Lee, S.T.: Fabrication and photovoltaic property of ordered macroporous silicon. *Appl. Phys. Lett.* **95**, 143119 (2009)
6. Christesen, J.D., Zhang, X., Pinion, C.W., Celano, T.A., Flynn, C.J., Cahoon, J.F.: Design principles for photovoltaic devices based on Si nanowires with axial or radial p–n junctions. *Nano Lett.* **12**, 6024–6029 (2012)
7. Srivastava, S.K., Kumar, D., Vandana, Sharma, M., Kumar, R., Singh, P.K.: Silver catalyzed nano-texturing of silicon surfaces for solar cell applications. *Sol. Energy Mater. Sol. Cells* **100**, 33–38 (2012)

8. Yang, T.C., Huang, T., Lee, H., Lin, T., Yen, T.: Applying silicon nanoholes with excellent antireflection for enhancing photovoltaic performance. *J. Electrochem. Soc.* **159**, B104–B108 (2012)
9. Chen, T.G., Yu, P., Chen, S.W., Chang, F.Y., Huang, B.Y., Cheng, Y.C., Hsiao, J.C., Li, C.K., Wu, Y.R.: Characteristics of large-scale nanohole arrays for thin-silicon photovoltaics. *Prog. Photovolt.* (2012). doi:[10.1002/ppp.2291](https://doi.org/10.1002/ppp.2291)
10. Tian, B., Zheng, X., Kempa, T.J., Fang, Y., Yu, N., Yu, G., Huang, J., Lieber, C.M.: Coaxial silicon nanowires as solar cells and nanoelectronic power sources. *Nature* **449**, 885–889 (2007)
11. Hu, L., Chen, G.: Analysis of optical absorption in silicon nanowire arrays for photovoltaic applications. *Nano Lett.* **7**, 3249–3252 (2007)
12. Stelzner, T., Pietsch, M., Andrä, G., Falk, F., Ose, E., Christiansen, S.: Silicon nanowire-based solar cells. *Nanotechnology* **19**, 295203 (2008)
13. Pillai, S., Catchpole, R.K., Trupke, T., Green, M.A.: Surface plasmon enhanced silicon solar cells. *J. Appl. Phys.* **101**, 093105 (2007)
14. Nakayama, K., Tanabe, K., Atwater, H.A.: Plasmonic nanoparticle enhanced light absorption in GaAs solar cells. *Appl. Phys. Lett.* **93**, 121904 (2008)
15. Tan, H., Santbergen, R., Smets, A., Zeman, M.: Plasmonic light trapping in thin-film silicon solar cells with improved self-assembled silver nanoparticles. *Nano Lett.* **12**, 4070–4076 (2012)
16. Atwater, H.A., Polman, A.: Plasmonics for improved photovoltaic devices. *Nat. Mater.* **9**, 205–213 (2010)
17. Akimov, Y.A., Ostrikov, K., Li, E.P.: Surface plasmon enhancement of optical absorption in thin-film silicon solar cells. *Plasmonics* **4**, 107–113 (2009)
18. Beck, F.J., Mokkapatil, S., Catchpole, K.R.: Plasmonic light-trapping for Si solar cells using self-assembled Ag nanoparticles. *Prog. Photovolt.* **18**, 500–504 (2010)
19. Ouyang, Z., Zhao, X., Varlamov, S., Tao, Y., Wong, J., Pillai, S.: Nanoparticle-enhanced light trapping in thin-film silicon solar cells. *Prog. Photovolt.* **19**, 917–926 (2011)
20. Pillai, S., Beck, F.J., Catchpole, K.R., Ouyang, Z., Green, M.A.: The effect of dielectric spacer thickness on surface plasmon enhanced solar cells for front and rear side depositions. *J. Appl. Phys.* **109**, 073105 (2011)
21. Daif, O.E., Tong, L., Figeys, B., Nieuwenhuysen, K.V., Dmitriev, A., Dorpe, P.V., Gordon, I., Dross, F.: Front side plasmonic effect on thin silicon epitaxial solar cells. *Sol. Energy Mater. Sol. Cells* **104**, 58–63 (2012)
22. Pudasaini, P.R., Ayon, A.A.: High efficiency nanotextured silicon solar cells. *Opt. Commun.* **285**, 4211–4214 (2012)
23. Spinelli, P., Ferry, V.E., Groep, J., Lare, M., Verschuuren, M.A., Schropp, R.E., Atwater, H. A., Polman, A.: Plasmonic light trapping in thin-film Si solar cells. *J. Opt.* **14**, 024002 (2012)
24. Spinelli, P., Hebbink, M., Waele, R., Black, L., Lenzmann, F., Polman, A.: Optical impedance matching using coupled plasmonic nanoparticle arrays. *Nano Lett.* **11**, 1760–1765 (2011)
25. Bermel, P., Luo, C., Zeng, L., Kimerling, L.C., Joannopoulos, J.D.: Improving thin-film crystalline silicon solar cell efficiencies with photonic crystals. *Opt. Express* **15**, 16986–17000 (2007)
26. Spinelli, P., Verschuuren, M.A., Polman, A.: Broadband omnidirectional antireflection coating based on subwavelength surface Mie resonators. *Nat. Commun.* **3**, 692 (2012)
27. Catchpole, K.R., Mokkapatil, S., Beck, F., Wang, E.-C., McKinley, A., Basch, A., Lee, J.: Plasmonics and nanophotonics for photovoltaics. *MRS Bull.* **36**, 461–467 (2011)
28. Polman, A., Atwater, H.A.: Photonic design principles for ultrahigh-efficiency photovoltaics. *Nat. Mater.* **11**, 174–177 (2012)
29. Munday, J.N., Atwater, H.A.: Large integrated absorption enhancement in plasmonic solar cells by combining metallic gratings and antireflection coatings. *Nano Lett.* **11**, 2195–2201 (2011)
30. Garnett, E., Yang, P.: Light trapping in silicon nanowire solar cells. *Nano Lett.* **10**, 1082–1087 (2010)

31. Li, J., Yu, H.Y., Li, Y., Wang, F., Yang, M., Wong, S.M.: Low aspect-ratio hemispherical nanopit surface texturing for enhancing light absorption in crystalline Si thin film-based solar cells. *Appl. Phys. Lett.* **98**, 021905 (2011)
32. Wang, F., Yu, H., Li, J., Wong, S., Sun, X.W., Wang, X., Zheng, H.: Design guideline of high efficiency crystalline Si thin film solar cell with nanohole array textured surface. *J. Appl. Phys.* **109**, 084306 (2011)
33. Pudasaini, P.R., Ayon, A.A.: Nanostructured thin film silicon solar cells efficiency improvement using gold nanoparticles. *Phys. Stat. Sol. A* **209**, 1475–1480 (2012)
34. Huffman, D., Bohren, C.: *Absorption and Scattering of Light by Small Particles*. Wiley, New York (1998)
35. Nie, S.: Probing single molecules and single nanoparticles by surface-enhanced Raman scattering. *Science* **275**, 1102–1106 (1997)
36. Maier, S.A., Brongersma, M.L., Kik, P.G., Meltzer, S., Requicha, A.G., Atwater, H.A.: Plasmonics a route to nanoscale optical devices. *Adv. Mater.* **13**, 1501–1505 (2001)
37. Hoa, X.D., Kirk, A.G., Tabrizian, M.: Towards integrated and sensitive surface plasmon resonance biosensors: a review of recent progress. *Biosens. Bioelectron.* **23**, 151–160 (2007)
38. Stuart, H.R., Hall, D.G.: Absorption enhancement in silicon-on-insulator waveguides using metal island films. *Appl. Phys. Lett.* **69**, 2327 (1996)
39. Schaadt, D.M., Feng, B., Yu, E.T.: Enhanced semiconductor optical absorption via surface plasmon excitation in metal nanoparticles. *Appl. Phys. Lett.* **86**, 063106 (2005)
40. Derkacs, D., Lim, S.H., Matheu, P., Mar, W., Yu, E.T.: Improved performance of amorphous silicon solar cells via scattering from surface plasmon polaritons in nearby metallic nanoparticles. *Appl. Phys. Lett.* **89**, 093103 (2006)
41. Stuart, H.R., Hall, D.G.: Island size effects in nanoparticle-enhanced photodetectors. *Appl. Phys. Lett.* **73**, 3815 (1998)
42. Brown, M.D., Suteewong, T., Kumar, R.S., D’Innocenzo, V., Petrozza, A., Lee, M.M., Wiesner, U., Snaith, H.J.: Plasmonic dye-sensitized solar cells using core–shell metal–insulator nanoparticles. *Nano Lett.* **11**, 438–445 (2011)
43. Ding, I.K., Zhu, J., Cai, W., Moon, S.J., Cai, N., Wang, P., Zakeeruddin, S.M., Grätzel, M., Brongersma, M.L., Cui, Y., McGehee, M.D.: Plasmonic dye-sensitized solar cells. *Adv. Energy Mater.* **1**, 52–57 (2011)
44. Sheehan, S.W., Noh, H., Brudvig, G.W., Cao, H., Schmuttenmaer, C.A.: Plasmonic enhancement of dye-sensitized solar cells using core–shell–shell nanostructures. *J. Phys. Chem. C* **117**, 927–934 (2013)
45. Lu, L., Luo, Z., Xu, T., Yu, L.: Cooperative plasmonic effect of Ag and Au nanoparticles on enhancing performance of polymer solar cells. *Nano Lett.* **13**, 59–64 (2013)
46. Kulkarni, A.P., Noone, K.M., Munechika, K., Guyer, S.R., Ginger, D.S.: Plasmon-enhanced charge carrier generation in organic photovoltaic films using silver nanoprisms. *Nano Lett.* **10**, 1501–1505 (2010)
47. Rand, B.P., Peumans, P., Forrest, S.R.: Long-range absorption enhancement in organic tandem thin-film solar cells containing silver nanoclusters. *J. Appl. Phys.* **96**, 7519 (2004)
48. Morfa, A.J., Rowlen, K.L., Reilly III, T.H., Romero, M.J., Lagemaat, J.: Plasmon-enhanced solar energy conversion in organic bulk heterojunction photovoltaics. *Appl. Phys. Lett.* **92**, 013504 (2008)
49. Hägglund, C., Zäch, M., Kasemo, B.: Enhanced charge carrier generation in dye sensitized solar cells by nanoparticle plasmons. *Appl. Phys. Lett.* **92**, 013113 (2008)
50. Chen, F.-C., Wu, J.-L., Lee, C.-L., Hong, Y., Kuo, C.-H., Huang, M.H.: Plasmonic-enhanced polymer photovoltaic devices incorporating solution-processable metal nanoparticles. *Appl. Phys. Lett.* **95**, 013305 (2009)
51. Wang, D., Ji, R., Schaaf, P.: Formation of precise 2D Au particle arrays via thermally induced dewetting on pre-patterned substrates. *Beilstein J. Nanotechnol.* **2**, 318–326 (2011)

52. Wang, D., Schaaf, P.: Two-dimensional nanoparticle arrays formed by dewetting of thin gold films deposited on pre-patterned substrates. *J. Mater. Sci. Mater. Electron.* **22**, 1067–1070 (2010)
53. Wang, D., Ji, R., Albrecht, A., Schaaf, P.: Ordered arrays of nanoporous gold nanoparticles. *Beilstein J. Nanotechnol.* **3**, 651–657 (2012)
54. Shockely, W., Queisser, H.J.: Detailed balance limit of efficiency of p-n junction solar cells. *J. Appl. Phys.* **32**, 510 (1961)
55. Air mass 1.5 Spectra, American Society for Testing and Materials. Available <http://redc.nrel.gov/solar/spectra/am1.5/>
56. Pallik, E.D.: *Handbooks of Optical Constants of Solids*. Academic, New York (1998)
57. Dingemans, G., Kessels, W.M.: Status and prospects of Al₂O₃-based surface passivation schemes for silicon solar cells. *J. Vac. Sci. Technol. A* **30**, 040802 (2012)
58. Miyajima, S., Irikawa, J., Yamada, A., Konagai, M.: High quality aluminum oxide passivation layer for crystalline silicon solar cells deposited by parallel-plate plasma-enhanced chemical vapor deposition. *Appl. Phys. Express* **3**, 012301 (2010)
59. Soppe, W., Rieffe, H., Weeber, A.: Bulk and surface passivation of silicon solar cells accomplished by silicon nitride deposited on industrial scale by microwave PECVD. *Prog. Photovolt.* **13**, 551–569 (2005)
60. Lee, Y., Oh, W., Dao, V.A., QamarHussain, S., Yi, J.: Ultrathin oxide passivation layer by rapid thermal oxidation for the silicon heterojunction solar cell applications. *Int. J. Photoenergy* **2012**, 1–5 (2012)

Chapter 17

Plasmon-Enhanced Excitonic Solar Cells

Shuai Chang, Lawrence Tien Lin Lee, and Tao Chen

Abstract The exciton dissociation in excitonic solar cells (XSCs) is controlled by interface, where the generated electrons on one side and holes produced on the other side. In this device configuration, the interfacial characteristics are crucial for the operation, while the bulk property is less critical. Due to the unique characteristics of materials and operation mechanism, the fabrication of XSCs allows low-cost, large-scale solution processing, and the utilization of various printing techniques, instead of high-cost vacuum deposition and purification process applied in the fabrication of conventional p–n junction solar cells. To date, power conversion efficiencies exceeding 10 % have been achieved in some XSCs at lab scale. For the practical applications, the energy conversion efficiencies are required to be further improved, especially at module scale. In this chapter, we pay special attention to the recent development in the application of metal (e.g., Au and Ag) nanoparticles to increase the light utilization in XSCs for high photovoltaic conversion efficiency. This type of light trapping, on the ground of localized surface plasmon resonance and propagating surface plasmon polariton, provides an alternative approach to the development of new light absorbing materials to span the strong spectral response over broader ranges. The methodologies and enhancement mechanisms regarding a series of typical device architectures will be discussed.

S. Chang • L.T.L. Lee • T. Chen (✉)
Department of Physics, The Chinese University of Hong Kong, Shatin,
N.T., Hong Kong, China
e-mail: taochen@phy.cuhk.edu.hk

1 Introduction

Solar cells can be classified into two categories according to the distinct operation principles: conventional solar cells, such as silicon p–n junction solar cells, and excitonic solar cells (XSCs), including dye-sensitized solar cells (DSSCs, Fig. 17.1a), molecular semiconducting bilayered solar cells (Fig. 17.1b), bulk-heterojunction (BHJ) semiconducting polymer solar cells (Fig. 17.1c) as well as quantum dot-sensitized solar cells. A crucial distinction between the two categories is that the operation of the former device generates electron–hole pair normally in the bulk of p-type semiconducting absorbers, while in the illuminated XSCs the generation of charge carrier is concurrent with the initial charge separation at the interface [1, 2]. This characteristic of XSCs renders the requirement on the purity of materials in XSCs being not as strict as that in silicon-based solar cells, which enables the device fabrication avoiding high-cost and high-technology vacuum deposition apparatus and allows large-area screen-printing and continues roll-to-roll processing. Therefore, XSCs are recognized as promising low-cost alternative photovoltaic (PV) devices to conventional p–n junction thin film solar cells. During the past decades, a great deal of efforts has been put into the development of XSCs [3–20], especially on the DSSCs and BHJ polymer solar cells. Bilayered organic solar cells, on the other hand, are less studied due to

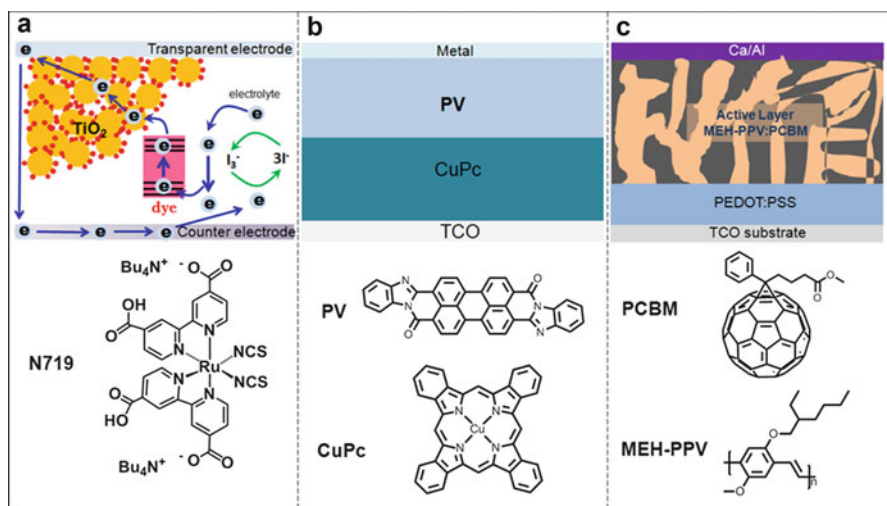


Fig. 17.1 Schematic diagrams of typical excitonic solar cells: (a) DSSCs, (b) planar-junction bilayer organic solar cells, and (c) 3D bulk-heterojunction polymer solar cells. *N719 dye* *cis*-bis(isothiocyanato)bis(2,2'-bipyridyl)-4,4'-dicarboxylato-ruthenium(II)-bis-tetrabutylammonium, *PV* perylene tetracarboxylic derivative, *CuPc* copper phthalocyanine, *PCBM* [6,6]-phenyl C₇₁-butyric acid methyl ester, *MEH-PPV* poly[2-methoxy-5-(2-ethylhexyloxy)-1,4-phenylenevinylene]

the intrinsically small interfacial area that generates relatively low efficiency. Previous efforts have led to power conversion efficiencies (PCEs) of “hero” devices (DSSCs and BHJ polymer solar cells) exceeding 10 % [20–22]. Obviously, to reduce the cost for the practical applications, further efforts are necessary to be made to improve the PCEs both at lab scale and, particularly, at module scale [18, 23–26].

In this context, we focus on the improvement of PCEs in XSCs by plasmonic metal nanoparticles (NPs). This chapter starts from the introduction of key characteristics of different kinds of XSCs, followed by the basic principles of plasmon-enhanced XSCs and some practical examples on how to apply metal NPs to improve the energy conversion efficiency.

DSSC, also known as the Grätzel cell, was firstly demonstrated by O’Regan and Grätzel in 1991 [16]. In this device structure, sunlight enters the cell through the transparent-conductive electrode, striking the dye on the surface of the TiO₂ NP mesoporous film (Fig. 17.1a). Photons striking the dye with enough energy to be absorbed create an excited state of the dye, from which an electron can be “injected” directly into the conduction band of the TiO₂. From there it moves by diffusion to the anode (also called collecting electrode) [27, 28]. Meanwhile, the dye molecule that has lost an electron strips one from I⁻ in electrolyte, oxidizing it into I₃⁻. The I₃⁻ then recovers its missing electron by mechanically diffusing to the counter electrode, thus reintroducing the electrons after flowing through the external circuit.

Several important parameters are used to characterize the quality of DSSCs. The overall efficiency (i.e., PCE) is the total amount of electrical power produced for a given amount of solar power shining on the cell:

$$\text{PCE} = \frac{J_{\text{sc}} V_{\text{oc}} \text{FF}}{P_{\text{in}}} \quad (17.1)$$

where J_{sc} is the short-circuit photocurrent density, V_{oc} represents the open-circuit photovoltage, FF is the fill factor, and P_{in} is the intensity of the incident light. In principle, the V_{oc} is dependent on the energy level difference between the quasi-Fermi level of TiO₂ and the chemical potential of the redox couples.

Incident photon-to-electron conversion efficiency (IPCE) characterizes the wavelength-dependent photocurrent generation. It is the product of light-harvesting efficiency (LHE), electron injection efficiency (ϕ_{inj}), and charge collection efficiency (ϕ_{col}) at certain wavelength:

$$\text{IPCE} = \text{LHE}(\lambda) \times \phi_{\text{inj}} \times \phi_{\text{col}} = \text{LHE}(\lambda) \times \text{APCE} \quad (17.2)$$

where APCE is the absorbed photon to current conversion efficiency and shows how efficient the numbers of absorbed photons are converted into current. Obviously, APCE can be obtained by dividing the IPCE by the LHE (0–100 %).

To date, most of the efficient ($>10\%$) DSSCs are based on the ruthenium polypyridyl complex N3, the closely related (N719), black dye (N749) or a few organic molecules [20, 27]. For optimized DSSCs employing ruthenium-based complex, IPCE is near to 80% for wavelengths <650 nm, then tails off at longer wavelengths (750 nm) due to minimal (10%) light-harvesting efficiency.

Planar heterojunction-based organic solar cell is the simplest device architecture that achieve exciton dissociation (Fig. 17.1b). This type of PV device was initially developed by Tang in 1980s [29]. The charge pair is formed after the dissociation of excitons by internal electric field. Thereafter, the charges and holes percolate to collection electrode under built-in electric field. In this device structure, the current that reaches the contacts in the absence of applied field is defined as J_{sc} . The maximum potential generated by the device is defined as V_{oc} . Similarly, the quality of the device can be expressed by FF, which is the ratio between the maximum power generated (P_{max}) and the product of J_{sc} and V_{oc} .

A fact is that most of the organic semiconductors possess exciton diffusion length of in 3–10 nm range, which significantly limits the efficiency of bilayered (planar) heterojunction devices. In other words, excitons generated at a site with larger distance from the heterojunction than the exciton diffusion length will most probably be recombined rather than finally harvested as effective carrier for the device efficiency. Therefore, the thickness of the active layer must be very thin in order to transport carriers quickly to electrode before recombination. Obviously, the inadequate absorber materials seriously limit the sunlight harvesting efficiency of the devices.

To harvest more sunlight using thick absorber layer, most of the researches extend the bilayered structures to 3D nanostructured internal architectures in which the domain size of the polymer is on the order of twice of the diffusion length (Fig. 17.1c) [30]. This device configuration enables efficient exciton generation (near a heterojunction) and dissociation as well as final charge transport for high energy conversion efficiency. The highest PCE of BHJ polymer solar cell has reached $\sim 10\%$ [21, 24]. Current investigations focus more on the BHJ solar cells, rather than bilayered organic solar cells, since BHJ solar cells are more promising when it comes to high PCE.

The approaches for the PCE improvement are distinct regarding different XSC structures. Every components in each of the device structure play synergistically roles in determining the final PCE. However, sufficient sunlight harvesting is the first priority for boosting the PCE to higher or close to theoretical values. A basic method to expand the strong spectral response of XSCs to broader ranges, i.e., from visible to near-infrared (NIR) region, is the development of red/NIR light absorbing materials. However, it is usually difficult to synthesize new dye molecules and semiconductor molecules and polymers that simultaneously meet with requirements of narrow bandgap, suitable energy levels, and high extinction coefficient and mobility. Therefore, to make full use of the most efficient existing light absorbing materials should be an effective and convenient way to achieve highly efficient XSCs.

2 Plasmonics for Photovoltaics

Metal nanoparticles exhibit powerful and fascinating optical properties, such as the enhancement of Raman scattering signal, photothermal therapy and strong light scattering and extinction [31–36]. These properties rely on the induced electric field upon the electromagnetic wave irradiation. When metal NPs, especially Au and Ag, under the external electromagnetic wave, it will cause the collective oscillation of surface electrons. This type of collective oscillation is defined as localized surface plasmon resonance (LSPR), the frequency is dependent on the band structure of the metallic materials, the shape and size of the metal nanoparticles [37, 38], which provides unique platforms for achieving desired plasmon frequency. Basically, the scattering and absorption cross-sections are described as [39]:

$$C_{\text{abs}} = \frac{2\pi}{\lambda} \text{Im}[\alpha] \quad (17.3)$$

$$C_{\text{sca}} = \frac{1}{6\pi} \left(\frac{2\pi}{\lambda} \right)^4 |\alpha|^2 \quad (17.4)$$

where α is the polarizability of the particle, given by

$$\alpha = 3V \left[\frac{\varepsilon/\varepsilon_m - 1}{\varepsilon/\varepsilon_m + 2} \right] \quad (17.5)$$

in which V is the volume of the particle, ε the permittivity of the metal, and ε_m the permittivity of the surrounding medium. The scattering efficiency Q_{sca} is given by:

$$Q_{\text{sca}} = C_{\text{sca}} / (C_{\text{sca}} + C_{\text{abs}}) \quad (17.6)$$

A striking feature of SPR is that the optical cross-sections of the metal NPs are usually much larger than their geometric cross-section [40]. For example, the optical cross-section of 100 nm AgNP can be ten times more than the geometric cross-section at the plasmon frequency. On the other hand, the cross-section of Au or Ag is normally 10^5 times of dye molecules. Therefore, the proper use of plasmonic effects will be a promising pathway to increase light absorption in the solar cells. It has been demonstrated in various solar cells such as amorphous silicon-based solar cells [41, 42], gallium arsenide solar cells [43], organic solar cells [44–46], and DSSCs [47–49]. Generally, there are three mechanisms for the improvement of light utility in XSCs (Fig. 17.2) [50].

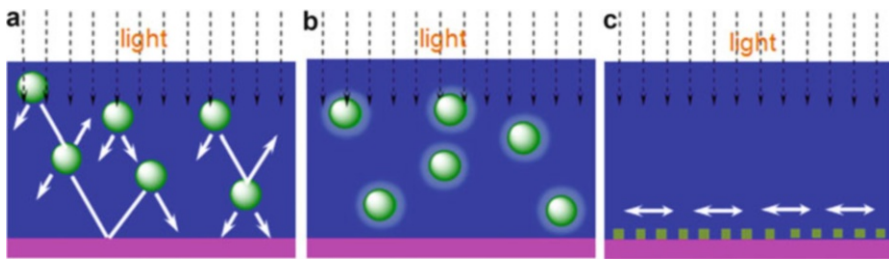


Fig. 17.2 Plasmonic light-trapping mechanisms for solar cells. (a) Light trapping by scattering from metal nanoparticles in the solar cell, causing an increase in the effective optical path length in the cell. (b) Light trapping by the excitation of localized surface plasmons in metal nanoparticles embedded in the active layer, which increase the optical density around the metal nanoparticles. (c) Light trapping by the excitation of surface plasmon polaritons at the electrode, in which a patterned metal nanoparticle structure couples light to surface plasmon polariton or photonic modes that propagates electromagnetic wave to different directions [50]

2.1 Scattering of Light by Metallic Nanoparticles to Increase the Effective Optical Path Length

In this approach, metal NPs usually embedded in the absorber layer of DSSC and BHJ polymer solar cells, in which light can acquire an angular spread and thus lead to increased optical path length (Fig. 17.2a).

2.2 Excitation of Localized Surface Plasmon Resonances of Metallic Nanoparticles

Due to the strong field enhancement of metal NPs, the use of metal NPs can significantly increase the light absorption when dye molecules or semiconducting polymer absorbing materials residing in the vicinity of the metal NPs. In this perspective, the metal NPs serve as “antenna” for the incident light and thus “concentrates” the incident energy in LSPR mode. This type of light trapping is in a manner of increasing the optical density of the solar cells. The generated electric field can be described as following:

$$E_{\text{out}}(r) = E_0 \hat{z} - \left[\frac{\epsilon_{\text{in}} - \epsilon_{\text{out}}}{\epsilon_{\text{in}} + 2\epsilon_{\text{out}}} \right] \alpha^3 E_0 \left[\frac{\hat{z}}{r^3} - \frac{3z}{r^5} r \right] \quad (17.7)$$

where E_0 and E_{out} are the electric field of incident light and the electric field outside the metal nanoparticles, ϵ_{in} and ϵ_{out} are the dielectric constant of the metal NPs and that of the external environment, and α is the radius of the metal NP [51]. It can be

seen that the surface plasmon-induced electric field decreases quickly with increasing distance from the NPs. Therefore, this type of light trapping usually requires the absorber materials locating in the close proximity of the metal NPs.

2.3 Coupling to Propagating Surface Plasmon Polariton Modes

In the third type of plasmonic light trapping, patterned periodic metal NPs on the electrodes are usually applied to convert light into surface plasmon polariton (SPP) (Fig. 17.2c), which enables the electromagnetic wave penetrating into or reflecting back into the solar cells, depending on the 3D geometric parameters [52]. The generation of SPPs at the electrode can efficiently trap and guide light in the absorber (active) layer of the solar cells, which thus increase the light utilization of XSCs. It should be noted that the generation of plasmon resonance depends on the size, shape, and dielectric environment of the metal NPs, and the field enhancements are quite sensitive to the distance and only produced in very close proximity to the NPs. However, the efficiency of propagating SPP waves is determined by periodic grating structures of the metal NPs. In this type of light trapping, the patterned structures render free space light waves to gain sufficient in-plane momentum in order to couple to the SPP waves with shorter wavelength (higher propagation constant). Notably, SPP can produce a large penetration depth (100 nm–1 μ m) into the absorber layer adjacent to the metal, which allows the absorption enhancements in thicker active layers in a solar cell [50].

3 Plasmon-Enhanced Dye-Sensitized Solar Cells

So far there is no a dye possessing high extinction coefficient in the range from full visible to NIR, the use of plasmonic effect for light trapping can be an efficient way to make full use of the dyes and explore the new possibilities of achievable efficiency. In this section, we analyze the three mechanisms for plasmon-enhanced DSSCs.

3.1 Improvement of Sunlight Utility in DSSCs Using Bare Metal Nanoparticles

Incorporation of “bare (without additional surface coating layer)” metal NPs into TiO₂ network has demonstrated plasmon-enhanced charge carrier generation and reduced reflection. This method is straightforward; the preparation is usually carried

by incorporation of metal NPs into TiO₂ NPs. For example, Nahm et al. blended AuNPs (diameter at ~100 nm) with commercial P25 NPs as photoanode in DSSCs for the enhancement of light utility [53]. It is found that the incorporation of AuNPs significantly improves the absorption from 70.1 to 82.6 % (Fig. 17.3a). As a result of the increased light absorption, the PCE shows an increasing trend at the initial stage, i.e., the mass ratio of AuNPs/TiO₂ increased from 0 of AuNPs to 0.01, 0.03, and 0.05. When the concentration reaches 0.07, the PCE dropped (Fig. 17.3b). The PCE increment is firstly ascribed to the significantly improved J_{sc} , which is evidenced by the IPCE spectra (Fig. 17.3c). Optical characterizations on the dye-adsorbed film show greater extinction and absorption over the whole wavelength, but the reflectance did not show much change (Fig. 17.3d, e). Particularly, the absorption enhancement is stronger at longer wavelengths. The changes in absorption spectra are consistent with the IPCE alternations, indicating the plasmon-enhanced light utility in DSSCs. Due to the absorption of AuNPs throughout the visible ranges with strong peak near to the plasmon absorption, the IPCEs show increases in the whole visible range.

In the incorporation of the metal NPs into the anode of DSSCs, appropriate concentration is vital for the performance improvement. In this case, the mass ratio of 0.05 in the Au/TiO₂ film shows strong extinction and weak reflectance and thus higher absorption at the plasmon band, indicating that stronger extinction as a result of the LSPR generated field enhancement prevails over the prolonged optical path lengths from light scattering. The final PCE is increased from 2.7 to 3.3 % through the incorporation of AuNPs with diameter at 100 nm at mass ratio of 0.05.

The position of metal NPs in the DSSCs is also an important parameter for plasmon-enhanced light harvesting. Generally, in the use of LSPR and scattering effect of metal NPs, the metal NPs can be located onto the surface of anode or inside the 3D network. A comparison was performed by embedding AuNPs into anode and on the top of TiO₂ anode film and on top of dye molecules [54]. It is observed that the embedded AuNPs in anode can significantly improve photocurrent generation at 500–600 nm, which is corresponding with the plasmon band of spherical AuNPs. The optical absorption spectra of the anode with regard to AuNPs also show significantly improved light absorption when AuNPs located inside the anode, while those on top of the anode show less improved light absorption. Obviously, once AuNPs located on the top of anode film, only very small amount of dye molecules can utilize the LSPR-increased optical density, while larger amount of dye can absorb more light when AuNPs were distributed inside the anodes. This is especially useful in guiding the design of plasmon-enhanced solar cells. Owing to the thin anode films, the PCE of conventional DSSCs is 0.94 %, while it was remarkably improved to 2.28 % with Au NPs incorporation, indicating the efficiency of plasmon-enhanced device performance.

A potential problem of using metal NPs for the enhancement of DSSCs is that the metal NPs can serve as electron traps, which can increase the recombination rate of generated electrons, which competes with the electron flow to the collection

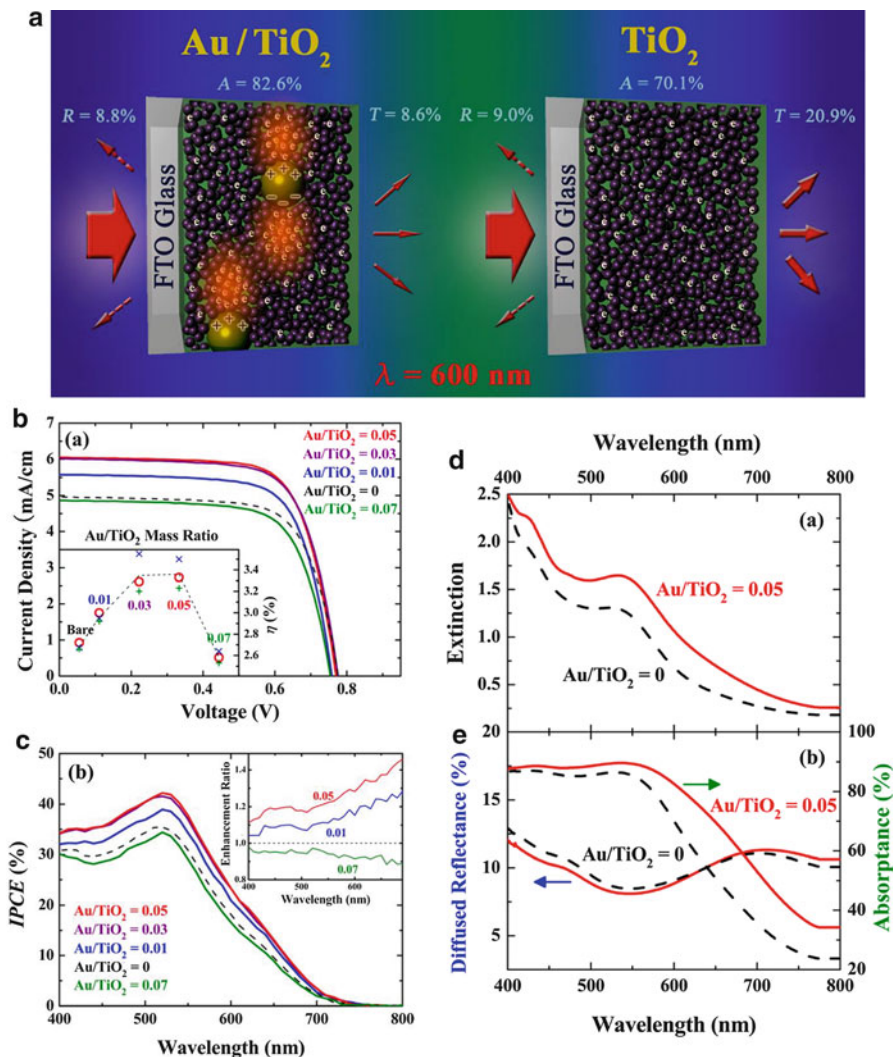


Fig. 17.3 (a) Schematic diagram illustrating the light trapping enhancement of Au nanoparticle-incorporated DSSC. Field enhancement near the Au nanoparticles is depicted as *light grey (orange-color online)* regions. (b) Photocurrent density–voltage characteristics of DSSCs at various Au/TiO₂ mass ratios. The *inset* shows the power conversion efficiency of DSSCs with respect to the Au/TiO₂ mass ratio. (c) IPCE spectra of DSSCs at various Au/TiO₂ mass ratios. The IPCE-enhancement ratios are also shown compared with the bare DSSC (Au/TiO₂) in the *inset*. (d) Extinction of Au/TiO₂ film (*solid red line*) and TiO₂ film (*dashed black line*) after dye adsorption. (e) Diffused reflectance (*left blue arrows*) and absorbance (*right green arrows*) of films after dye adsorption. Reproduced with permission from *Appl. Phys. Lett.* 99, 253107 (2011). Copyright 2011 American Institute of Physics

electrode through metal-TiO₂ layer [55]. In this regards, sandwiched structure composed of TiO₂/AgNPs/TiO₂ for DSSCs has been demonstrated to suppress the recombination induced by AgNPs to some extent [56]. It should be noted that AgNPs also possess excellent plasmonic properties, the plasmon band of spherical AgNPs located at round 430 nm [37]. The design of sandwiched structure is because the in-plane SPR of AgNPs is perpendicular to the direction of electron transport which can reduce the fluctuation of TiO₂ and electron trapping. Obviously, the incorporation of AgNPs can also be anticipated to increase the light utility. It is found that, upon the addition of AgNPs, the light absorption of the dye-adsorbed film is greatly enhanced while the reflectance is significantly reduced, which generate more sunlight for harvesting. This leads to a 23 % enhancement in the photocurrent density. A detailed investigation shows that the sandwiched structure is the most efficient one when compared with the incorporation of the Ag on the top of TiO₂ NPs or the anode with only TiO₂/TiO₂ in bilayer structure.

The direct incorporation of colloidal metal NPs in TiO₂ anode can probably lead to the aggregation, which will cause LSPR band shift. In addition, the aggregation could reduce the plasmon-enhanced light utility due to the reduction in “plasmon loci”. In other words, this results in less dye molecules having the chance to absorb the plasmon-induced light trapping. Therefore, the use of a supporter to distribute the metal NPs would, to a certain extent, reduce the aggregation especially at the high concentration of metal NPs. In this regard, AgNP-decorated SiO₂ nanospheres (diameter at around 400 nm) have been applied in DSSCs [57]. Due to the large size silica nanospheres in the anode, less dye molecules are adsorbed, while it still leads to device efficiency improvement through the plasmon-enhanced light utilization. When compared the UV-Vis absorption spectra of TiO₂ with TiO₂/core-shell particle films, the results show that, with the incorporation of AgNPs, the absorption spectrum exhibited two small humps with peaks of 480 and 610 nm, respectively. The increased absorption indicated that the core-shell particles enable dye molecules absorbing more photons due to the light scattering and focusing effect. This improvement is important owing to optical cross-section is not uniform in the visible range of the conventional ruthenium dye molecules as well as some organic molecules like porphyrin-based dyes [58].

In the application of naked metal NPs in the anodes, due to the electrical conductivity of metal NPs, they can trap both electrons and holes and thus act as recombination sites. To reduce this negative effect and enable charge carriers quickly transporting to the collecting electrode, anode films are usually fabricated to be relatively thin (no more than 4 μm) in comparison to the typical thickness of DSSC anodes (ca. 12 μm or even thicker), thus only small amounts of dye molecules allow to be adsorbed, which serious limited the overall performance. The other potential threat of employing bare metal NPs is that the NPs may suffer from the corrosion of I⁻/I₃⁻ liquid electrolyte. Therefore, appropriate protections are required. This topic will be discussed in the following section.

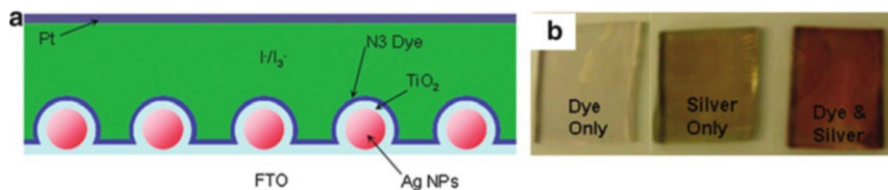


Fig. 17.4 (a) Scheme of solar cells composed of AgNPs, ALD deposited TiO_2 layer and dye, and (b) photos of dye on transparent conducting glass substrate, AgNPs on transparent conducting glass substrate and dye adsorbed on amorphous TiO_2 with 2.0 nm in thickness. Reproduced with permission from *J. Am. Chem. Soc.* 131, 8407–8409 (2009). Copyright 2009 American Chemical Society

3.2 Semiconductor- or Insulator-Encapsulated Metal Nanoparticles in DSSCs

In the development of coating materials to prevent the corrosion of metal NPs by I^-/I_3^- -based electrolyte and suppress the metal surface-induced recombination, metal oxide (e.g., TiO_2 and SiO_2) are usually applied as coating materials to protect the surface of metal NPs. To achieve high efficiency, embedding the core-shell NPs into the TiO_2 anode layer of the devices has been demonstrated to be an effective route to maximize the light trapping by LSPR and light scattering. In this case, the shell thickness is an important parameter since the intensity of LSPR-generated electric field is sensitively dependent on the distance from the metal cores (17.7); the use of thin shell would generate large field intensity for high optical density. On the other hands, the scattering effect of metal NPs should not be significantly influenced by the shell thickness provided that the shell possesses good transparency.

To systematically investigate the shell thickness-dependent light harvesting, the Hupp group used atomic layer deposition (ALD) of TiO_2 onto transparent-conductive oxide (TCO) supported silver NPs to finely control the thickness of TiO_2 layer and thus the distance between dye molecules and Ag cores (~36 nm) [49]. It is observed that with the thickness increase, the light extinction of dye molecules become weaker and weaker. Two factors contribute to this change: (1) the increase of TiO_2 thickness would cause the plasmon band shift due to the increased dielectric constant, which results in less efficient coupling between the absorption of dye molecules (N3) and the plasmon band. (2) The increase of the TiO_2 thickness also lead to the drastically decreased field intensity since it is exponentially dependent on the distance between dye and AgNPs (17.7).

The comparison on the IPCE among the dye only cell, silver only, and dye and silver and TiO_2 cell (Fig. 17.4b) was made and found that the dye- and silver-based DSSCs show greatly enhanced IPCEs. At an optimized distance, the IPCE is increased from 0.2 to 1.4 % in a prototype DSSC. In the other set of investigation,

upon the increase of TiO₂ thickness, the IPCE gradually decreased. To quantify the enhancement, the plasmon enhancement factor can be calculated based on the following equation:

$$\text{Enhanced Factor} = \frac{J_{\text{sc(Dye+Silver)}}}{(J_{\text{sc(Dye)}} \times 1.4) + J_{\text{sc(Silver)}}} \quad (17.8)$$

The estimation show that the photocurrent generation in plasmon-enhanced DSSC is six times of the plasmon-free DSSCs.

As stated, the surface protection with metal oxide can reduce the etching process of the metal cores. Obviously, thicker metal oxide shell can effectively reduce the etching, while a negative effect is that it decreases plasmon coupling between dye molecules and plasmonic metal NPs. Therefore, a critical thickness is require for achieving both high efficiency of light harvesting and improved stability. This issue is rarely demonstrated in the use of core-shell metal oxide plasmon enhancers. The ALD approach provides a unique opportunity to study this effect. In this work, they exposed the resulting assemblies to corrosive I⁻/I₃⁻ electrolyte and concluded that in prevention of the AgNPs from corrosion, ca. 7.7 nm (300 cycles of ALD) crystalline TiO₂ layer must be deposited. Furthermore, due to the deposition of 0.2 nm (two cycles) of an Al₂O₃ adhesion layer, the required TiO₂ thickness was reduced to 5.8 nm (211 cycles). This provides a convenient route to take full advantage of plasmon-enhanced light harvesting in DSSCs.

While the ALD approach provides an excellent platform for studying the distance-dependent plasmon-enhanced DSSCs, for 3D anodes of DSSCs, this method is not applicable. Therefore, a colloidal synthesis of core-shell structures and then incorporating into TiO₂ NPs for anode is more feasible. Qi et al. manifested the synthesis of core-shell Ag-TiO₂ NPs for the application in enhancing light harvesting in DSSCs [47]. It is reported that a very thin shell of TiO₂ (ca. 2 nm) was coated on the Ag core through a colloidal synthesis. This thin shell allows maximizing the effect of LSPRs and maintaining the stability of metal NPs to some extent in the work. Due to the high extinction coefficient of AgNPs, the addition of AgNPs can reduce the thickness of the anode in that the optical density is increased in the device (Fig. 17.5a, b). In addition to the increased optical density and the optical path length, the decreased film thickness can also reduce the recombination probability due to the decreased electron transport path length (Fig. 17.5c, d). The other advantage of using TiO₂ as coating material is that it is compatible with TiO₂ anode and serves as medium for the charge transport (Fig. 17.5e, f).

In solution phase, naked AgNPs (in the absence of TiO₂ encapsulation) can increase the light absorption of the dye molecules (Fig. 17.5g1-g3). In the Ag-TiO₂ nanoparticles and dye solution, similarly, the Ag-TiO₂ can also increase the light absorption. Remarkably, after 16 h incubation, the light absorption is further improved to a great extend (Fig. 17.5h1-h3), indicating the incubation allows the dye anchoring on Ag-TiO₂ surface and thus absorbing more light due to LSPR in

the vicinity of Ag core being stronger. Finally, on the thin film, the dye-adsorbed Ag-TiO₂ anode shows more efficient light absorption (Fig. 17.5i1–i3).

The Tang group used a simple hydrothermal method to produce Au-TiO₂ hollow submicrospheres with tunable shell for plasmon enhancers [48]. In this method, the AuNPs were firstly synthesized; they were then distributed in the growth solution of TiO₂ spheres. After hydrolysis and condensation, the hollow structures formed, with multiple or single AuNPs cores inside the spheres (Fig. 17.6a). Herein the TiO₂ sphere can also serve as a media for charge transport (Fig. 17.6b). In this investigation, once the TiO₂ hollow submicrospheres were used as anode materials, the PCE is 7.06 %, which is significantly higher than that made of P25 electrode with a PCE of 6.25 %. Furthermore, the PCE was improved to 8.13 % when Au-TiO₂ hollow submicrospheres are used as the working electrode. It is believed that besides the enhanced light absorption due to strong surface plasmon resonances of AuNS cores, a Schottky barrier was also formed at the metal Au and the semiconductor TiO₂ interface [48], thus reducing the possibility of electrons going from the semiconductor back to either the dye or the electrolyte.

In addition to TiO₂, SiO₂ can also be an efficient coating material. Snaith and coworkers encapsulated AuNPs with a layer of SiO₂ to overcome the major problems (surface corrosion and surface-induced recombination). In this work, I⁻/I₃⁻ electrolyte-based DSSCs and N719 ruthenium as sensitizer were used for the DSSCs. The devices incorporating Au-SiO₂ NPs into the TiO₂ anode show desirable FF (0.73) and high V_{oc} (0.76 V). This study also confirmed that the thickness 3 nm of silica shell is suitable for preventing significant electron or hole tunneling onto the metal core. Similarly, the use of Au-SiO₂-TiO₂ core-multiple shell structures can also improve the device efficiency by incorporating them into the TiO₂ anode network [59].

From the above discussion, both SiO₂ and TiO₂ are good coating materials for preventing the corrosion of metal NPs and demonstrating the effectiveness LSPR. Obviously, the electrical conductivity of SiO₂ and TiO₂ are clearly different; SiO₂ is insulator while TiO₂ is wide band gap semiconductor. How the electrical properties influence the device performance is a significant problem that needs to be resolved for rational application of plasmon effect in solar cells. Mostly recently, the Kamat group performed a comparative study in the use of Au-TiO₂ and Au-SiO₂ for DSSCs [60]. Herein, several important findings are highlighted. Firstly, due to the charging effect of AuNPs and the excitation of TiO₂ under UV irradiation, the plasmon band of Au-TiO₂ shift from 530 to 516 nm, the increased electron density in the Au core is ascribed to the shift. Since the conduction band of TiO₂ ($E_{CB} = -0.5$ V versus NHE) is more positive than the Fermi level of Au ($E_F = 0.45$ V versus NHE), the charge transport from TiO₂ to Au is allowed (Fig. 17.7a). However, in Au-SiO₂ solution, there is no such phenomenon observed.

The working schemes of electron transport in the two cases are different. In a traditional DSSC, the charge was injected from the excited dye into TiO₂

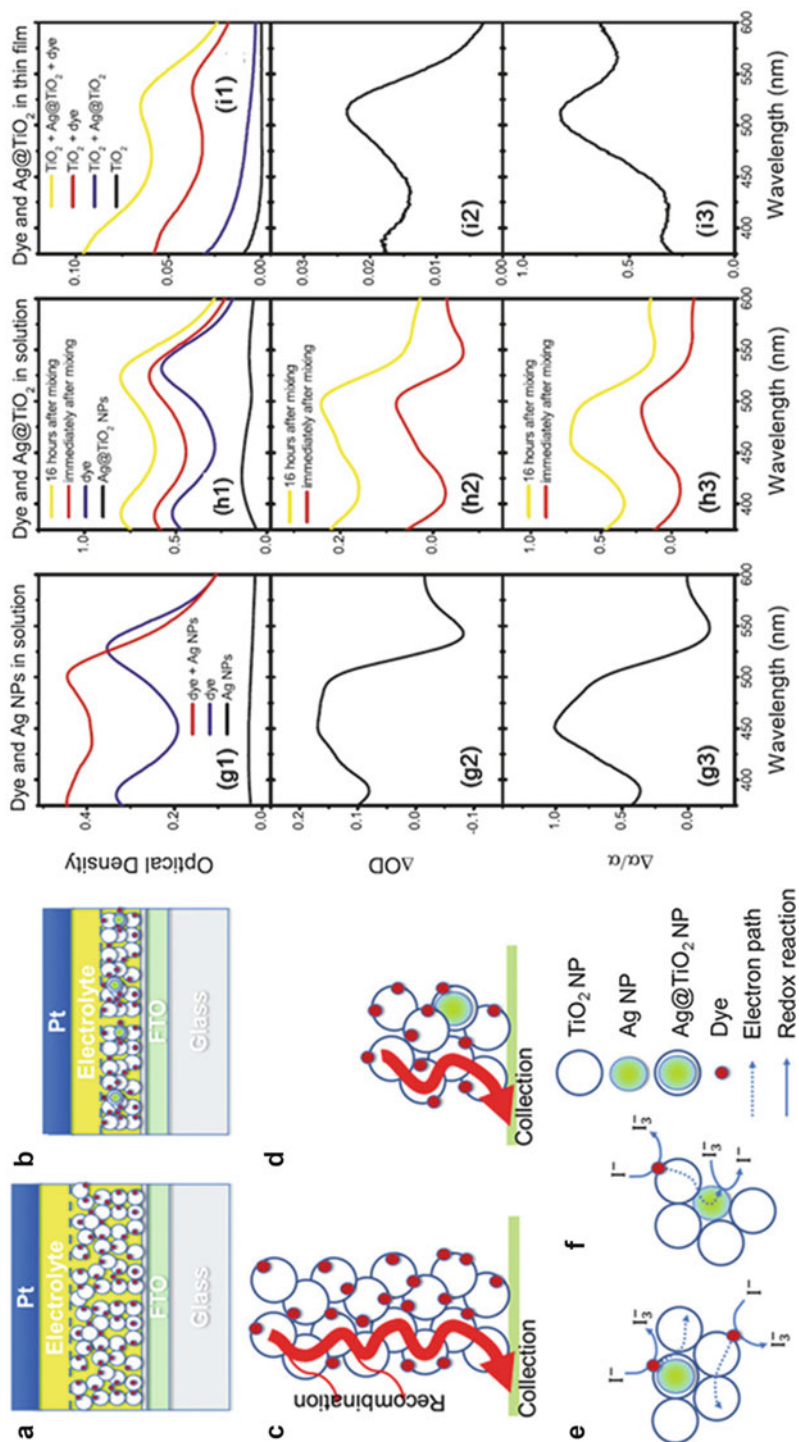


Fig. 17.5 Device structures of conventional DSSCs (**a**) and plasmon-enhanced DSSCs (**b**), in which plasmon-enhanced DSSCs require thinner film and less material to achieve the same PCE. Illustration of photogenerated electron collection in conventional DSSCs (**c**) and plasmon-enhanced DSSCs (**d**). Mechanisms of plasmon-enhanced DSSCs using Ag-TiO₂ NPs (**e**) and Ag NPs (**f**). (**g1**) Optical absorption spectra of AgNPs, ruthenium dye molecules, and their mixture in ethanol solution. (**g2**) Net changes of dye absorption due to the presence of AgNPs in solution. (**g3**) Relative changes of effective extinction coefficient of dye due to the presence of AgNPs in solution. (**h1**) Optical absorption spectra of Ag-TiO₂ NPs, ruthenium dye molecules, and their mixtures (immediately after mixing and 16 h after mixing) in ethanol solution. (**h2**) Net changes of dye absorption due to the presence of Ag-TiO₂ NPs in solution. (**h3**) Relative changes of effective extinction coefficient of dye due to the presence of Ag-TiO₂ NPs in solution. (**i1**) Optical absorption spectra of Ag-TiO₂ NPs, ruthenium dye molecules, and their mixtures in the matrix of TiO₂ thin film. (**i2**) Net changes of dye absorption due to the presence of Ag-TiO₂ NPs in thin film. (**i3**) Relative changes of effective extinction coefficient of dye due to the presence of Ag-TiO₂ NPs in thin film. Reproduced with permission from *ACS Nano* 5 (9), 7108–7116 (2011). Copyright 2011 American Chemical Society

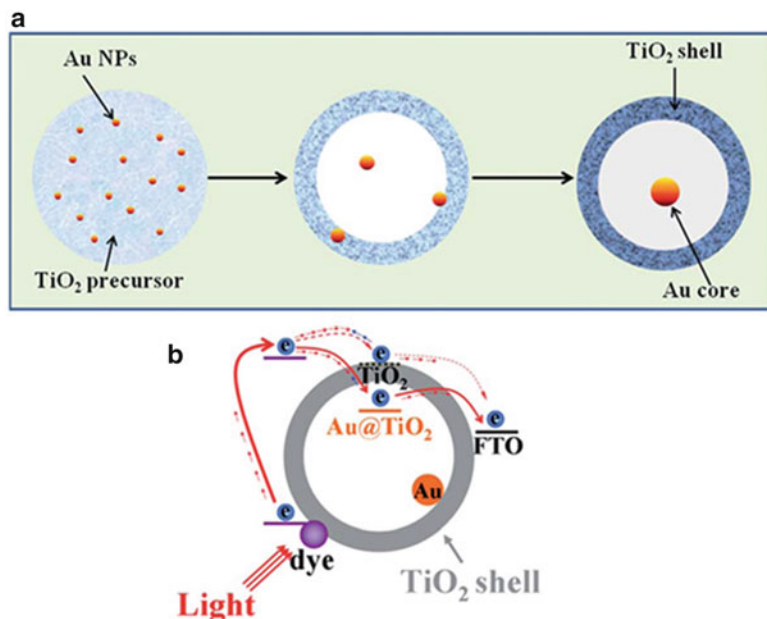


Fig. 17.6 Illustrations of (a) formation process of Au-TiO₂ hollow submicrospheres and (b) the charge separation process in the DSSCs with the photoanode of Au-TiO₂ hollow submicrospheres. Reproduced with permission from *Energy Environ Sci* 5 (5), 6914–6918 (2012). Copyright 2012 Royal Society of Chemistry

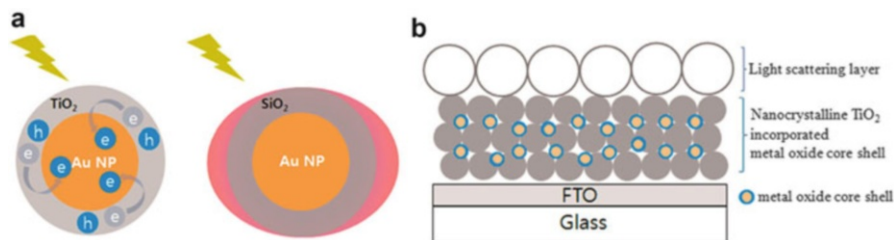


Fig. 17.7 (a) Charging effect (Au-TiO₂) versus plasmonic effect (Au-SiO₂) of metal core oxide shell particles. (b) Schematic drawing depicting the layered structure of a mesoscopic TiO₂ film incorporating core-shell particles typically employed for high-efficiency DSSC. Reproduced with permission from *ACS Nano* 6 (5), 4418–4427 (2012). Copyright 2012 American Chemical Society

nanoparticles followed by the transport of electrons to the collecting electrode surface. However, once Au-SiO₂ NPs present in the network (Fig. 17.7b), the influence was primarily limited to LSPR, resulting in better charge separation. The apparent Fermi level of the composite film was not affected by such LSPR effect. While Au-SiO₂ is different, herein Au is capable of accepting electrons from the neighboring TiO₂/dye particles due to the conducting properties of TiO₂.

This further results in Fermi level equilibration and causes the shift of the apparent Fermi level to more negative potential, which thus leads to the increase in the open-circuit voltage of the DSSC.

To date, most of the studies focus on the utilization of spherical Au and Ag NPs for the improvement of light harvesting in DSSCs. The plasmon bands of them concentrate on 530 and 430 nm, respectively, which are overlapping with (or close to) the absorption peak of conventional efficient dye molecules. In standard device structures, nearly all the light at this absorption band of the molecules can be harvested [61]. Therefore, the use of plasmon effect for the improvement of the light utility is limited in standard devices. However, there is plenty of room at the longer wavelengths, most of the Ru-based dye molecules show significantly reduced absorption coefficient over the longer wavelength (Fig. 17.8a). Notably, it is estimated that to achieve PCE over 15 % DSSC has to increase sunlight at longer wavelength near to about 900 nm. Therefore, the use of plasmonic effect to increase the longer wavelength sunlight is more preferable. Our group has performed the investigation of using Au nanorods (NRs) to increase the low photon energy sunlight harvesting in DSSCs (Fig. 17.8b) [4].

Different from the conventional synthesis of spherical Au and Ag NPs, AuNRs are synthesized using cetyltrimethylammonium bromide (CTAB) as morphological controlling surfactant. Owing to the long aliphatic tail of CTAB, it is difficult to encapsulate AuNR surface with a thin and dense layer of TiO_2 or SiO_2 to introduce AuNRs into DSSCs. We developed a simple method to coat AuNR surface with Ag_2S to introduce plasmonic AuNRs into DSSCs. Herein the Au– Ag_2S is just as “insulator” due to high conduction band of Ag_2S (Fig. 17.8c). For the synthesis, AuNR surface was deposited with a layer of Ag by reducing AgNO_3 with ascorbic acid. Ag is then transformed to Ag_2S by reacting with Na_2S (Fig. 17.8d) [62]. After the encapsulation of Ag_2S on AuNR surface, they were introduced into anode by mixing AuNR– Ag_2S nanocrystals with TiO_2 NPs. The thicknesses of Ag_2S were controlled to be 2 nm (Fig. 17.8d) to 6 nm.

UV–vis absorption spectra of the anode films revealed that the enhanced light absorption is proportional to the incorporating concentration of AuNR– Ag_2S . On the other hand, transmittance spectra presented a reducing trend at 600–750 nm upon the addition of AuNR– Ag_2S . Both of them indicate the plasmon-enhanced light absorption and reduced light transmittance. In the plasmon-enhanced solar cells, the photocurrent generation is more relevant to the metal NPs enhanced dye or other absorber materials light absorption for device performance improvement. To make a detailed comparison, we integrated the IPCE at 600–720 nm and the whole IPCE spectra for the DSSCs with various concentrations of AuNR– Ag_2S (with shell thickness of 2 nm). The value of IPCE (600–720 nm)/IPCE represents the contribution from the 600–720 nm regions to the overall IPCE. As a result, the values were improved from 8.5 % to 9.2 and 11.7 % with the increase of AuNR– Ag_2S , clearly demonstrating the improved conversion of low energy sunlight into photocurrent. In addition, the Ag– Ag_2S selectively enhances photocurrent generation at around 430 nm, which is absorption band of Ag– Ag_2S (Fig. 17.8a). Finally, the AuNRs enhanced light trapping effect leads to the PCE increasing from 4.3 to 5.6 % when

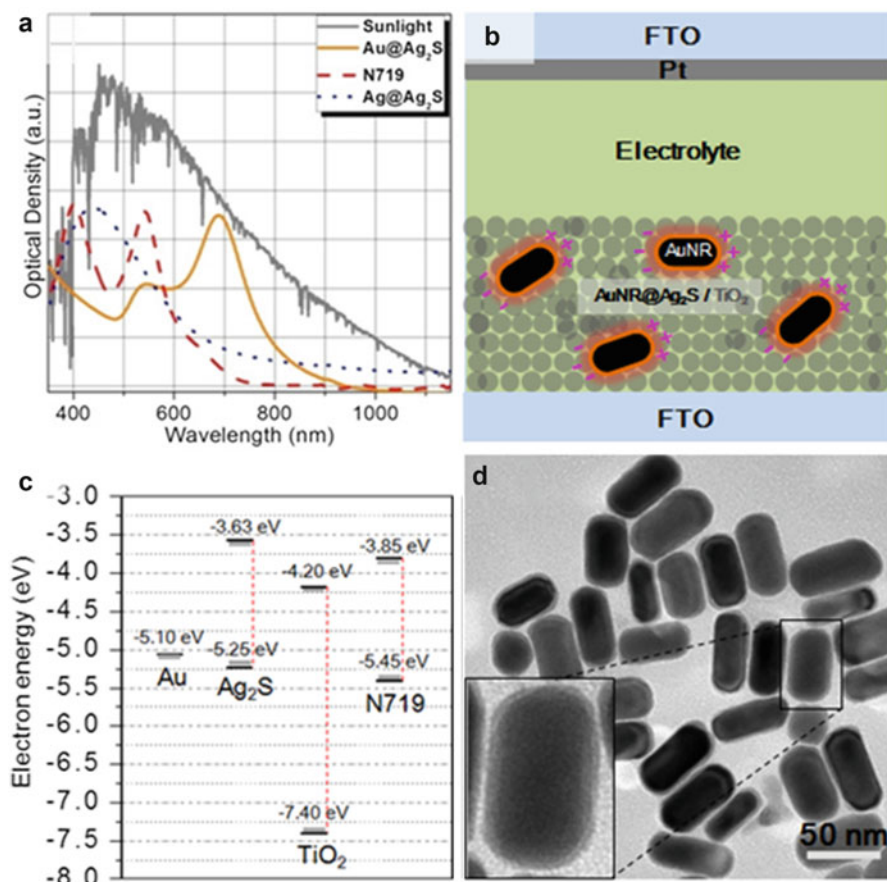


Fig. 17.8 Solar irradiance spectrum, absorption of AuNR-Ag₂S (2 nm in shell thickness) and N719 dye solution in acetonitrile and *t*-butanol and Ag₂S-encapsulated Ag nanoparticles, AgNP-Ag₂S (a), device configuration of the plasmon-enhanced DSSCs, in which dye molecules were not included for clearness (b), energy level alignment of the perspective materials in the DSSCs (c), TEM image of AuNR-Ag₂S with Ag₂S thickness of 2 nm (d)

the anode film is 6 μm . Further, the PCE is improved from 5.8 to 7.1 % when the film is 11 μm .

Other approaches to keep the metal NPs from direct contact with dye and electrolyte include in situ synthesis of metal-semiconductor nanocomposite from the precursors of metal and semiconductor. Muduli et al. fabricated TiO₂ NPs coated with Au using high purity titanium tetraisopropoxide and HAuCl₄ as precursors [63]. Analyzed by electrochemical impedance spectroscopy, the electron transfer resistance at TiO₂-dye-electrolyte interface was considerably decreased in the case of TiO₂-Au. In addition, a posttreatment method to coat the “naked” metal NPs with isolating materials after their incorporation into the photoanode is an

alternative method. In one report, the as-prepared AgNP/TiO₂ photoanodes were immersed in titanium(IV) isopropoxide solution in refluxing isopropyl alcohol for a period of time, removed and rinsed, and then calcined at elevated temperature, resulting in a Ag_xTiO₃ shell on the AgNPs. On the ground of photoelectrochemical characterizations, this protocol is proved to be sufficient for preventing silver from corrosion [64].

3.3 Coupling to Propagating Surface Plasmon Polariton Modes to Enhance Light Utilization in DSSCs

The use of SPP in DSSCs is usually carried out by preparing patterned metal NP arrays on the conducting electrodes, either anode or cathode. In a fundamental study, a simplified model of DSSC was used to investigate the energy transfer from LSPR to the active layer of the cell [65]. Patterned, elliptical gold disk arrays which were lithographed by electron beam on a thin, compact TiO₂ layer. The TiO₂ layer was sensitized by a monolayer of dye molecules. For the patterned samples, light polarization was in parallel either to the major disk axes or to the minor disk axes, giving rise to two well-distinguished resonance peaks, this is in agreement with the observation of strong polarization dependence. Photoconductance measurements are efficient ways to study the influence of the AuNPs on the electron injection rate. Comparison of the photoconductance of only Au and only dye-sensitized TiO₂ layers showed that the main contribution to the visible light photoconductivity is electron injection from the dye into the TiO₂ conduction band, while the measurements carried out on two tantamount but 90° rotated samples exhibited polarization induced photoconductivity peaks around 660 nm which is independent of the array orientation, indicating an enhanced dye charge carrier generation rate driven by the polarization of LSPR.

A practical application of the SPP effect has been implemented in solid-state DSSCs (ssDSSCs). Through a nanoimprint lithography assisted approach, 2D arrays of silver nanodomes were fabricated on the transparent conducting oxide glass as plasmonic back reflector for DSSCs (Fig. 17.9a, b–d) [66]. Firstly, the simulation based on finite-element method shows that the dome structure can produce an absorption enhancement over a planar metallic mirror.

By tuning the space density of the metal nanocrystal arrays, the light utilization was greatly improved. For a device made with dye Z907, the short-circuit current was enhanced by 16 % for ssDSSC with patterned back reflector and the PCE increased from 3.15 to 3.87 %. From the IPCE spectra of Z907 sensitized ssDSSCs (Fig. 17.9e), an increment over the whole wavelength range was observed and the enhancement was more pronounced between 550 and 750 nm where the absorption coefficient of Z907 is relatively small, which may be attributed to the effect of SPP. Furthermore, the C220 sensitized ssDSSC shows considerable improvement over broad range once the dome-structured plasmonic back reflector was applied.

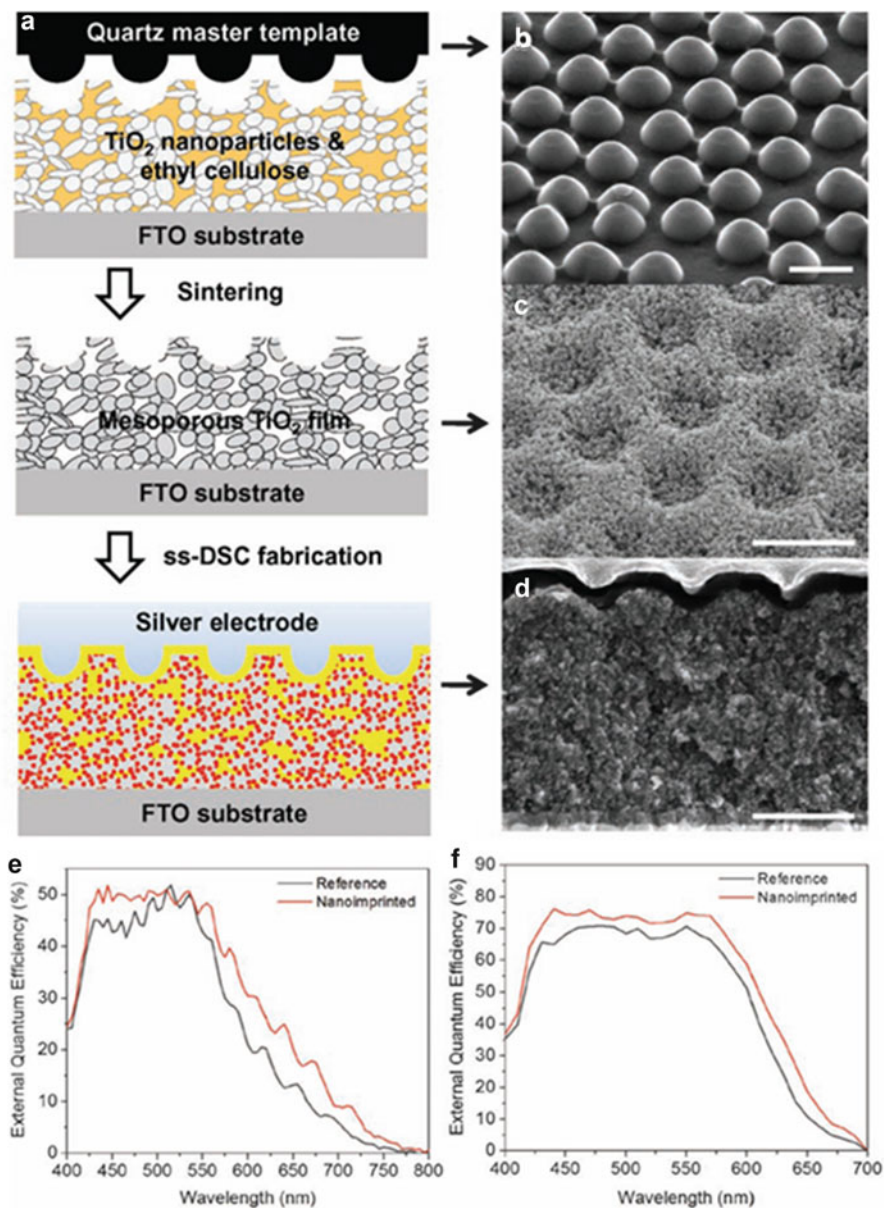


Fig. 17.9 (a) Schematic illustration of the plasmonic ss-DSSC fabrication process. The sintering step is carried out in air to remove the polymer binder in TiO₂ paste film. The ss-DSSC fabrication procedures include the following steps: TiO₂ film is treated with TiCl₄ aqueous solution, sensitized with dye molecules (*dots*), infiltrated with spiro-OMeTAD (*yellow*), and silver electrode is evaporated on top. (b) 45°-tilt SEM image of the nanodome quartz template. (c) 45°-tilt SEM image of imprinted mesoporous TiO₂ film after sintering. (d) Cross-sectional SEM image of plasmonic ss-DSSC, with 2D array of silver nanodomains in the back contact. Scale bars in (b–d) are 1 μm. External quantum efficiency (EQE) spectra of ss-DSSCs made with Z907 dye (e) and C220 dye (f). Reproduced with permission from *Adv Energy Mater* 1 (1), 52–57 (2011). Copyright © 2011 WILEY-VCH Verlag GmbH & Co. KGaA, Weinheim

4 Plasmon-Enhanced Polymer Solar Cell

Despite the advantages of polymer solar cell such as mechanical flexibility, low-cost, low temperature processing, light weight and semi-transparency, due to the generally short exciton diffusion length in the polymer solar cell [23, 67], the thickness of the BHJ active layer (such as those formed by interjunction of donor polymer, e.g., poly(3-hexylthiophene) (P3HT) and acceptor polymer, e.g., [6,6]-phenyl C₇₁-butyric acid methyl ester (PCBM)) is always limited to about 100–200 nm in order to avoid severe recombination, but this reduces the absorption of light at the same time [23]. Therefore different measures had been explored to increase the absorption of light without increasing the thickness of the active layer in polymer solar cell. Development of new semiconducting materials with high extinction coefficient, low lowest unoccupied molecular orbital (LUMO), and high highest occupied molecular orbital (HOMO) is a basic way to achieve more efficient sunlight harvesting. However, due to the synthetic barriers, it is usually difficult to develop new polymers. As shown above, metal NPs with tunable plasmon band which can be simply achieved by changing the morphologies, such as aspect ratio. The use of plasmon effect to improve the light utilization is an alternative route. The concept of plasmon-enhanced polymer solar cell is generally similar to that in DSSCs. There are generally two approaches to incorporate metal NPs into polymer solar cells. (1) Incorporating metal NPs in the buffer layer (Fig. 17.10a), usually poly(3,4-ethylenedioxythiophene): poly(styrene sulfonate) (PEDOT:PSS). (2) Incorporating metal NPs in the active layer (Fig. 17.10b).

We firstly introduce the incorporation of AuNPs into the anodic buffer layer PEDOT:PSS (with P3HT:PCBM as the active layer spin-coated on ITO) to utilize the LSPR effect [68]. The resonance peak of the AuNPs (ca. 550 nm) is near to the absorption peak of the P3HT/PCBM composite, thus the NPs can provide the device with enhanced light absorption efficiency. This was shown in the increased

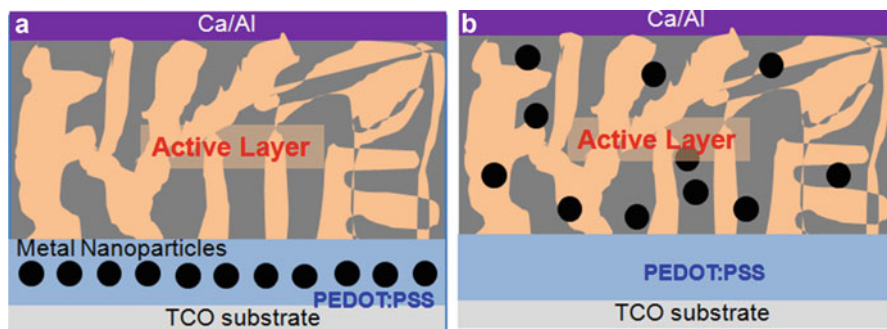


Fig. 17.10 Schematic illustration of the plasmon-enhanced bulk-heterojunction polymer solar cells, in which the metal nanoparticles embedded in the buffer layer (a) or in the active layer of the polymer solar cells (b)

PCE of the plasmonic device of 4.24 % (c.f. 3.57 % for the reference device, same in brackets below), which was mainly contributed by the increased short-circuit current of 10.22 mA cm^{-2} (c.f. 9.16 mA cm^{-2}) and fill factors of 70.32 % (c.f. 66.06 %), but keeping the open-circuit voltage (0.59 V) the same on the other hand. Such enhancement could be explained by the forward scattering effect and the local electromagnetic field enhancement effect. For the forward scattering effect, light is trapped by multiple and high-angle scattering by the AuNPs, thus increasing the optical path for better light utilization. Local enhancement (as strong as 100 times) of the electromagnetic field boosts the creation of exciton in the active layer, since the number of exciton produced is proportional to the intensity of the electromagnetic field.

Dual plasmon enhancement by AgNPs and AuNPs can also be achieved by incorporating both of them in the anodic layer of PEDOT [69]. Herein, polythieno [3,4-b]-thiophene/benzodithiophene:[6,6]-phenyl C_{71} -butyric acid methyl ester (PTB7:PC₇₁BM) was used as the absorber layer spin-coated on ITO. In this system, the spectrum of absorption enhancement due to LSPR can be broadened from the addition of the second type of NPs, in addition to the other LPR enhancements in the single-type NP case. The control device in the absence of metal NPs shows a PCE of 7.25 %, those with Ag and Au incorporations reach 8.01 % and 8.16 %, respectively. It was finally increased to the 8.67 % in the dual plasmonic NPs enhanced solar cells, the corresponding J - V is depicted in Fig. 17.11a. It can be found that the PCE improvement is mainly originated from the enhanced short-circuit current with the open-circuit voltage while fill factor kept similar. External quantum efficiency (EQE) characterization is an effective method to study the plasmon-enhanced photocurrent generation (Fig. 17.11b). The EQE of AgNP incorporated solar cell shows enhancement especially in the region of 420 to 600 nm, while the AuNPs incorporated solar cell show pronounce EQE from 520 to 750 nm, which is in consistent with the UV-vis absorption spectra (Fig. 17.11c) and demonstrates clearly the plasmon-enhanced photocurrent generation. As expected, by using Ag and Au NPs incorporated solar cells, the enhancement in photocurrent generation is in a broad range of 400–750 nm.

The correlation between photocurrent density (J_{ph}) and effective voltage (V_{eff}) (Fig. 17.11d) gives rise to the information about the maximum exciton generation rate (G_{max}) and exciton dissociation probabilities of the device. The values of G_{max} of the control device and dual plasmon-enhance device are $8.53 \times 10^{27} \text{ m}^{-3} \text{ s}^{-1}$ and $9.54 \times 10^{27} \text{ m}^{-3} \text{ s}^{-1}$. G_{max} is related to the maximum absorption of incident photons [70]; the enhanced G_{max} indicates the increased light absorption as a result of dual metal NPs incorporation. It is also found that LSPR can facilitate the dissociation of the excitons into free carriers.

Besides the buffer layer, metallic NPs can also be incorporated into the active layer or even all the polymer layers to improve the optical absorption by plasmonic effect [44], but one should be cautious to the size of the NPs since the device would be short circuited if they were too large and improperly incorporated. On the other hand, when incorporating the NPs into the active layer of polymer solar cells, the ligands used on the NPs can also cause some negative effect. Liu et al. had found

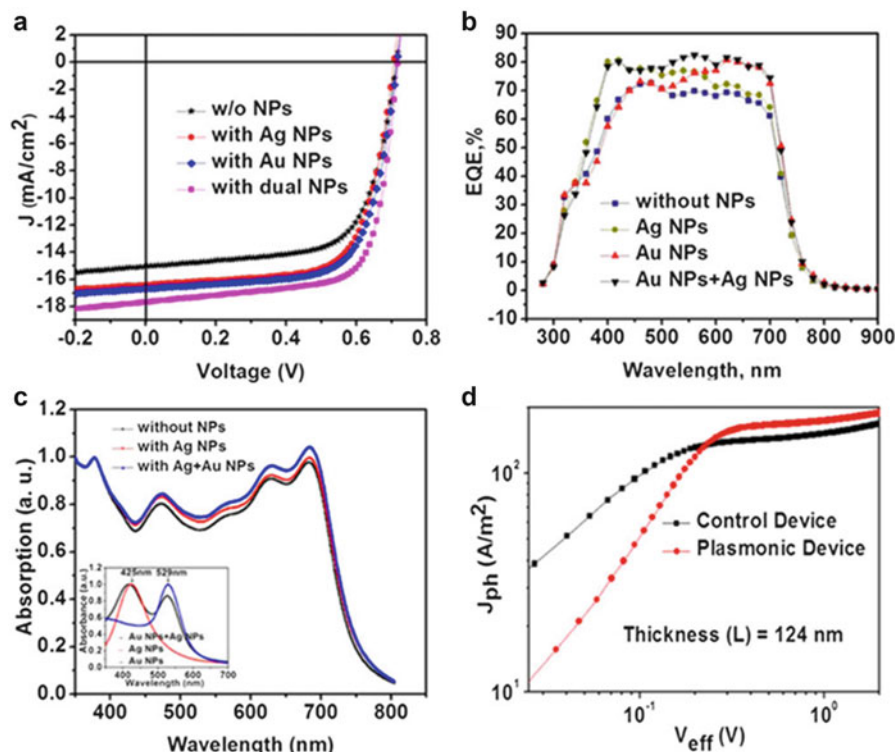


Fig. 17.11 (a) Current–voltage characteristics of solar cells with and without metal NPs. (b) External quantum efficiency of PTB7/PC70BM-based devices with and without NPs. (c) UV–vis absorption spectra of PTB7/PC70BM without NPs, with Ag NPs and with dual NPs. *Inset:* UV–vis absorption spectrum of NPs in water. (d) Photocurrent density (J_{ph}) versus effective voltage (V_{eff}) characteristics of the control and dual NPs devices. Reproduced with permission from *Nano Lett* 13 (1), 59–64 (2012). Copyright 2012 American Chemical Society

that the commonly used hexadecyl amine (HDA) greatly reduced the solar cell performance if such ligand-capped AuNPs were incorporated in the PEDOT:PSS/P3HT:PCBM interface, while the other commonly used ligand dodecanethiol (DTT) would have only very small or even no deteriorating effect on the device performance [71]. Bare Au NPs (i.e., without capping ligands) might not be favorable. In the electrical model, bare AuNPs might become hole hopping sites, carrier recombination centers or electron scattering centers [72], due to which the charge carriers transport and collection in the device would be hindered, which is similar to the above-mentioned issue that the inappropriate incorporation of metal NPs may cause short circuit in the device.

In addition to LPR generated by distributed metal NPs, some other metallic periodic structures can bring SPR effects to the device. Li et al. had combined the utilization of the LSPR and SPR in one device by embedding AuNPs

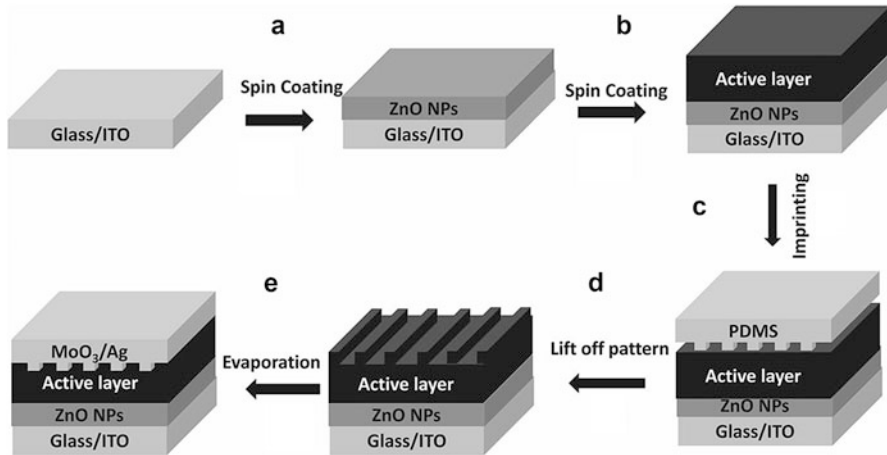


Fig. 17.12 The scheme of patterned polymer solar cells, (a) spin coating ZnO nanoparticles on ITO substrate, (b) spin coating active layer on ZnO nanoparticles, (c) imprinting PDMS pattern on active layer, (d) Lift off PDMS pattern, and (e) deposited MoO₃ (8 nm)/Ag (100 nm) on active layer to form metal grating. Reproduced with permission from *Adv Mater*, 3046–3052 (2012). Copyright © 2012 WILEY-VCH Verlag GmbH & Co. KGaA, Weinheim

(50 nm diameter) in the active layer made of PBDTTT-C-T:PC₇₁BM and employing Ag grating (periodicity 750 nm) in the back electrode [44]. The device fabrication process is illustrated in Fig. 17.12. The PCE of the device benefited from both two kinds of plasmonic resonance was advanced from 7.59 % (without grating and metal NPs) to 8.79 %, which was originated from the improved J_{sc} and FF while V_{oc} remained constant. In addition to the optical enhancement mentioned before (scattering and strengthened near metallic surface electromagnetic field), the better J_{sc} and FF were also regarded to be coming from field enhancement. For instance, the larger interface area from the grating pattern, improved balance of the electron and hole mobilities by the Au NPs, and the lower series resistance contributing from both the NPs and the grating.

Furthermore, grating pattern (700 nm period and 40 nm height) on the silver back electrodes of the device was also fabricated for such purpose [73]. The device fabrication is similar to that presented in Fig. 17.12. The device with patterned Ag had about 10 % increases in the short-circuit current, which lead to the PCE improvement from 7.20 to 7.73 %. While other two parameters (V_{oc} and FF) are similar, compared with the reference device (without grating). The better J_{sc} stemmed from the absorption enhancement by the grating's scattering effect and SPR, which was confirmed by the coincidence of the wavelength with maximum absorption enhancement and the wavelength of the simulated SPR at the metal grating back electrode.

In a theoretical study of the plasmonic effect by the AuNPs embedded in the P3HT:PCBM active layer [72], Zhu et al. showed from their model under low volume ratio limit (<2 %) of NPs. Device structure and the energy level alignment

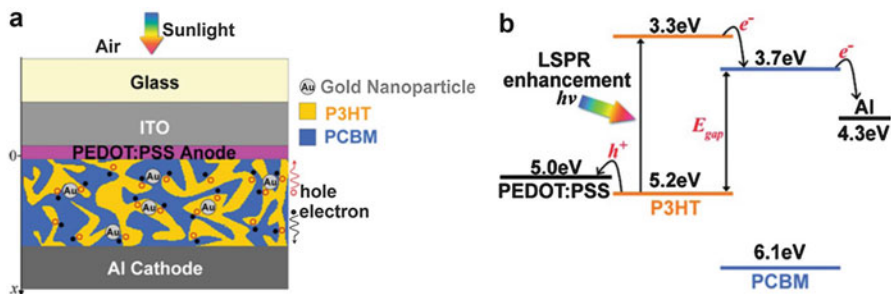


Fig. 17.13 (a) Illustration of polymer bulk-heterojunction solar cells with Au nanoparticles embedded in active layers. (b) Schematic of the energy levels of the bulk-heterojunction solar cells. The electron and hole are transported through the respective materials and collected by the electrodes. The difference between the HOMO of P3HT and the LUMO of PCBM is E_{gap} . Reproduced with permission from *Nanoscale* 4 (6), 1978–1981 (2012). Copyright 2012 Royal Society of Chemistry

are shown in Fig. 17.13. The absorption band edge can extend to longer wavelength (650–750 nm) when the NP volume ratio increases from 0 to 2 %, in addition to the significant absorption enhancement at around 650 nm. Such effect is the result of near field light concentration by LSPR, and the band edge extension is owing to the shorter average distance between the NPs when the incorporated NPs' volume ratio rises. However, only the enhanced portion below 650 nm could be utilized since there is no absorption by P3HT:PCBM above 650 nm, while the remaining portion above 650 nm at last should be mostly dissipated into the plasmon damping loss of the metallic NPs. Therefore, some small band gap donor polymers were introduced in recent researches [44, 73].

On the other hand, there is a larger increase of local photon absorption rate near the hole transport layer. This is essential to polymer solar cell where holes in the active layer usually have a lower mobility than the electrons. If plasmon enhancement produces more holes close to the hole transport layer for easier extraction, the number of holes that are lost during carrier transport due to reduced bimolecular recombination, thus raising the photocurrent. To some extent, such theoretical result could elucidate the better holes extraction (thus balanced the hole and electron mobilities disparity) and reduced charge recombination found in devices incorporating optimized volume ratio of metallic NPs in their active layers.

In addition to the methods of embedding metal NPs in buffer layer and active layer, the direct distribution of metal NPs onto transparent conducting oxide glass (e.g., ITO) substrate also demonstrates improved light harvesting for the devices. This approach is usually carried out by functionalizing the surface of ITO with a self-assembled monolayer, which enables the controllable deposition of metal NPs on the ITO surface [74]. A basic investigation shows that Ag nanoprisms can increase the charge generation by three times when compared with the plasmon-free polymer solar cells based on P3HT:PCBM. It is observed that the polariton

generation increases linearly with the sample extinction, promising for practical increase in photocurrent generation in organic solar cells [75].

At last, the use of plasmonic metal NPs to enhance light utility in bilayered organic solar cells is rarely seen, probably because of the intrinsically low efficiency when compared with BHJ polymer solar cells and the technical problem since the active layer is too thin to well-embed metal NPs. A possible approach is to incorporate metal NPs on the ITO surface [76] and to improve the light absorption for photocurrent generation. This type of device structure can alter the electrical field in the active layer and thus lead to the increase of z component of electrical field, which in turn facilitates exciton dissociation [76].

5 Conclusions

The use of metal nanoparticles to enhance light harvesting has been demonstrated as an effective route to enhance the light harvesting efficiency. This type of light trapping provides an alternative approach to the development of absorber materials such as new dye molecules and semiconducting polymers. There are generally three mechanisms for the enhancement: increasing optical density through “light focusing” by metal nanoparticles, extending the effective optical path length and propagating surface plasmon polariton. The synthesis and properties of metal nanoparticles have been well developed. The plasmon band can be conveniently and finely tuned from visible to NIR region. On the other hand, previous efforts have obtained absorber materials (both dye molecules and semiconducting polymers) possessing strong spectral response in some specific regions, with very small absorption coefficient beside these regions. Therefore, the efficient coupling between the light harvesting materials with plasmonic nanoparticles will lead to significant photovoltaic conversion improvement of excitonic solar cells.

Acknowledgements This authors acknowledge the financial support from CUHK Focused Scheme B Grant “Center for Solar Energy Research” and CUHK University Grant-Direct Allocation (Project Code: 2060437).

References

1. Gregg, B.A.: Excitonic solar cells. *J. Phys. Chem. B* **107**(20), 4688–4698 (2003)
2. Gregg, B.A.: The photoconversion mechanism of excitonic solar cells. *MRS Bull.* **30**(1), 20–22 (2005)
3. Chen, T., Hu, W., Song, J., Guai, G.H., Li, C.M.: Interface functionalization of photoelectrodes with graphene for high performance dye-sensitized solar cells. *Adv. Funct. Mater.* **22**(22), 5245–5250 (2012)

4. Chang, S., Li, Q., Xiao, X., Wong, K.Y., Chen, T.: Enhancement of low energy sunlight harvesting in dye-sensitized solar cells using plasmonic gold nanorods. *Energy Environ. Sci.* **5**, 9444–9448 (2012)
5. Chen, T., Guai, G.H., Gong, C., Hu, W.H., Zhu, J.X., Yang, H.B., Yan, Q.Y., Li, C.M.: Thermoelectric Bi₂Te₃-improved charge collection for high-performance dye-sensitized solar cells. *Energy Environ. Sci.* **5**(4), 6294–6298 (2012)
6. Guai, G.H., Song, Q.L., Guo, C.X., Lu, Z.S., Chen, T., Ng, C.M., Li, C.M.: Graphene-counter electrode to significantly reduce Pt loading and enhance charge transfer for high performance dye-sensitized solar cell. *Sol. Energy* **86**(7), 2041–2048 (2012)
7. Yang, L., Leung, W.W.-F.: Application of a bilayer TiO₂ nanofiber photoanode for optimization of dye-sensitized solar cells. *Adv. Mater.* **23**(39), 4559–4562 (2011)
8. Feng, X., Shankar, K., Varghese, O.K., Paulose, M., Latempa, T.J., Grimes, C.A.: Vertically aligned single crystal TiO₂ nanowire arrays grown directly on transparent conducting oxide coated glass: synthesis details and applications. *Nano Lett.* **8**(11), 3781–3786 (2008)
9. Ghadiri, E., Taghavinia, N., Zakeeruddin, S.M., Grätzel, M., Moser, J.-E.: Enhanced electron collection efficiency in dye-sensitized solar cells based on nanostructured TiO₂ hollow fibers. *Nano Lett.* **10**(5), 1632–1638 (2010)
10. Bessho, T., Zakeeruddin, S.M., Yeh, C.Y., Diau, E.W.G., Grätzel, M.: Highly efficient mesoscopic dye-sensitized solar cells based on donor-acceptor-substituted porphyrins. *Angew. Chem. Int. Ed. Engl.* **49**(37), 6646–6649 (2010)
11. Kimura, M., Nomoto, H., Masaki, N., Mori, S.: Dye molecules for simple co-sensitization process: fabrication of mixed-dye-sensitized solar cells. *Angew. Chem. Int. Ed. Engl.* **51**(18), 4371–4374 (2012)
12. Clifford, J.N., Martinez-Ferrero, E., Viterisi, A., Palomares, E.: Sensitizer molecular structure-device efficiency relationship in dye sensitized solar cells. *Chem. Soc. Rev.* **40**(3), 1635–1646 (2011)
13. Vougioukalakis, G.C., Philippopoulos, A.I., Stergiopoulos, T., Falaras, P.: Contributions to the development of ruthenium-based sensitizers for dye-sensitized solar cells. *Coord. Chem. Rev.* **255**(21–22), 2602–2621 (2011)
14. Grätzel, M.: Recent advances in sensitized mesoscopic solar cells. *Acc. Chem. Res.* **42**(11), 1788–1798 (2009)
15. Bach, U., Lupo, D., Comte, P., Moser, J.E., Weissortel, F., Salbeck, J., Spreitzer, H., Grätzel, M.: Solid-state dye-sensitized mesoporous TiO₂ solar cells with high photon-to-electron conversion efficiencies. *Nature* **395**(6702), 583–585 (1998)
16. Oregan, B., Grätzel, M.: A low-cost, high-efficiency solar-cell based on dye-sensitized colloidal TiO₂ films. *Nature* **353**(6346), 737–740 (1991)
17. Law, M., Greene, L.E., Johnson, J.C., Saykally, R., Yang, P.D.: Nanowire dye-sensitized solar cells. *Nat. Mater.* **4**(6), 455–459 (2005)
18. Li, G., Shrotriya, V., Huang, J., Yao, Y., Moriarty, T., Emery, K., Yang, Y.: High-efficiency solution processable polymer photovoltaic cells by self-organization of polymer blends. *Nat. Mater.* **4**(11), 864–868 (2005)
19. Hardin, B.E., Hoke, E.T., Armstrong, P.B., Yum, J.-H., Comte, P., Torres, T., Frechet, J.M.J., Nazeeruddin, M.K., Grätzel, M., McGehee, M.D.: Increased light harvesting in dye-sensitized solar cells with energy relay dyes. *Nat. Photon* **3**(7), 406–411 (2009)
20. Yella, A., Lee, H.W., Tsao, H.N., Yi, C.Y., Chandiran, A.K., Nazeeruddin, M.K., Diau, E.W.G., Yeh, C.Y., Zakeeruddin, S.M., Grätzel, M.: Porphyrin-sensitized solar cells with cobalt (II/III)-based redox electrolyte exceed 12 percent efficiency. *Science* **334**(6056), 629–634 (2011)
21. You, J., Dou, L., Yoshimura, K., Kato, T., Ohya, K., Moriarty, T., Emery, K., Chen, C.-C., Gao, J., Li, G., Yang, Y.: A polymer tandem solar cell with 10.6% power conversion efficiency. *Nat. Commun.* **4**, 1446 (2013)

22. Ito, S., Murakami, T.N., Comte, P., Liska, P., Gratzel, C., Nazeeruddin, M.K., Gratzel, M.: Fabrication of thin film dye sensitized solar cells with solar to electric power conversion efficiency over 10%. *Thin Solid Films* **516**(14), 4613–4619 (2008)
23. Thompson, B.C., Frechet, J.M.J.: Organic photovoltaics—polymer-fullerene composite solar cells. *Angew. Chem. Int. Ed. Engl.* **47**(1), 58–77 (2008)
24. Son, H.J., Carsten, B., Jung, I.H., Yu, L.: Overcoming efficiency challenges in organic solar cells: rational development of conjugated polymers. *Energy Environ. Sci.* **5**(8), 8158–8170 (2012)
25. Jorgensen, M., Norrman, K., Krebs, F.C.: Stability/degradation of polymer solar cells. *Sol. Energy Mater. Sol. Cells* **92**(7), 686–714 (2008)
26. Zhao, D.W., Tan, S.T., Ke, L., Liu, P., Kyaw, A.K.K., Sun, X.W., Lo, G.Q., Kwong, D.L.: Optimization of an inverted organic solar cell. *Sol. Energy Mater. Sol. Cell* **94**(6), 985–991 (2010)
27. Hagfeldt, A., Boschloo, G., Sun, L., Kloo, L., Pettersson, H.: Dye-sensitized solar cells. *Chem. Rev.* **110**(11), 6595–6663 (2010)
28. Frank, A.J., Kopidakis, N., van de Lagemaat, J.: Electrons in nanostructured TiO₂ solar cells: transport, recombination and photovoltaic properties. *Coord. Chem. Rev.* **248**(13–14), 1165–1179 (2004)
29. Tang, C.W.: Two-layer organic photovoltaic cell. *Appl. Phys. Lett.* **48**(2), 183–185 (1986)
30. Yu, G., Gao, J., Hummelen, J.C., Wudl, F., Heeger, A.J.: Polymer photovoltaic cells—enhanced efficiencies via network of internal donor-acceptor heterojunctions. *Science* **270**(5243), 1789–1791 (1995)
31. Jiang, R., Chen, H., Shao, L., Li, Q., Wang, J.: Unraveling the evolution and nature of the plasmons in (Au Core)–(Ag Shell) nanorods. *Adv. Mater.* **24**(35), OP200–OP207 (2012)
32. Ni, W.H., Chen, H.J., Su, J., Sun, Z.H., Wang, J.F., Wu, H.K.: Effects of dyes, gold nanocrystals, pH, and metal ions on plasmonic and molecular resonance coupling. *J. Am. Chem. Soc.* **132**(13), 4806–4814 (2010)
33. Chen, H.J., Kou, X.S., Yang, Z., Ni, W.H., Wang, J.F.: Shape- and size-dependent refractive index sensitivity of gold nanoparticles. *Langmuir* **24**(10), 5233–5237 (2008)
34. Kneipp, K., Kneipp, H., Kneipp, J.: Surface-enhanced Raman scattering in local optical fields of silver and gold nanoaggregates—from single-molecule Raman spectroscopy to ultrasensitive probing in live cells. *Acc. Chem. Res.* **39**(7), 443–450 (2006)
35. Campion, A., Kambhampati, P.: Surface-enhanced Raman scattering. *Chem. Soc. Rev.* **27**(4), 241–250 (1998)
36. Tian, Z.Q., Ren, B., Wu, D.Y.: Surface-enhanced Raman scattering: from noble to transition metals and from rough surfaces to ordered nanostructures. *J. Phys. Chem. B* **106**(37), 9463–9483 (2002)
37. Wiley, B., Sun, Y., Xia, Y.: Synthesis of silver nanostructures with controlled shapes and properties. *Acc. Chem. Res.* **40**(10), 1067–1076 (2007)
38. Wu, D., Xu, X., Liu, X.: Influence of dielectric core, embedding medium and size on the optical properties of gold nanoshells. *Solid State Commun.* **146**(1–2), 7–11 (2008)
39. Pillai, S., Green, M.A.: Plasmonics for photovoltaic applications. *Sol. Energy Mater. Sol. Cells* **94**(9), 1481–1486 (2010)
40. Bohren, C.F.: How can a particle absorb more than the light incident on it? *Am. J. Phys.* **51**(4), 323–327 (1983)
41. Mühlischlegel, P., Eisler, H.-J., Martin, O.J.F., Hecht, B., Pohl, D.W.: Resonant optical antennas. *Science* **308**(5728), 1607–1609 (2005)
42. Ditlbacher, H., Krenn, J.R., Schider, G., Leitner, A., Aussenegg, F.R.: Two-dimensional optics with surface plasmon polaritons. *Appl. Phys. Lett.* **81**(10), 1762–1764 (2002)
43. Bozhevolnyi, S.I., Volkov, V.S., Devaux, E., Laluet, J.-Y., Ebbesen, T.W.: Channel plasmon subwavelength waveguide components including interferometers and ring resonators. *Nature* **440**(7083), 508–511 (2006)

44. Li, X.H., Choy, W.C.H., Huo, L.J., Xie, F.X., Sha, W.E.I., Ding, B.F., Guo, X., Li, Y.F., Hou, J.H., You, J.B., Yang, Y.: Dual plasmonic nanostructures for high performance inverted organic solar cells. *Adv. Mater.* **24**(22), 3046–3052 (2012)
45. Chen, F.-C., Wu, J.-L., Lee, C.-L., Hong, Y., Kuo, C.-H., Huang, M.H.: Plasmonic-enhanced polymer photovoltaic devices incorporating solution-processable metal nanoparticles. *Appl. Phys. Lett.* **95**(1), 013305 (2009)
46. Morfa, A.J., Rowlen, K.L., Reilly III, T.H., Romero, M.J., van de Lagemaat, J.: Plasmon-enhanced solar energy conversion in organic bulk heterojunction photovoltaics. *Appl. Phys. Lett.* **92**(1), 013504-1–013504-3 (2008)
47. Qi, J., Dang, X., Hammond, P.T., Belcher, A.M.: Highly efficient plasmon-enhanced dye-sensitized solar cells through metal@oxide core-shell nanostructure. *ACS Nano* **5**(9), 7108–7116 (2011)
48. Du, J., Qi, J., Wang, D., Tang, Z.: Facile synthesis of Au@TiO₂ core-shell hollow spheres for dye-sensitized solar cells with remarkably improved efficiency. *Energy Environ. Sci.* **5**(5), 6914–6918 (2012)
49. Standridge, S.D., Schatz, G.C., Hupp, J.T.: Distance dependence of plasmon-enhanced photocurrent in dye-sensitized solar cells. *J. Am. Chem. Soc.* **131**(24), 8407 (2009)
50. Atwater, H.A., Polman, A.: A plasmonics for improved photovoltaic devices. *Nat. Mater.* **9**(3), 205–213 (2010)
51. Willets, K.A., Van Duyne, R.P.: Localized surface plasmon resonance spectroscopy and sensing. *Annu. Rev. Phys. Chem.* **58**(1), 267–297 (2007)
52. Ferry, V.E., Sweatlock, L.A., Pacifici, D., Atwater, H.A.: Plasmonic nanostructure design for efficient light coupling into solar cells. *Nano Lett.* **8**(12), 4391–4397 (2008)
53. Nahm, C., Choi, H., Kim, J., Jung, D.R., Kim, C., Moon, J., Lee, B., Park, B.: The effects of 100 nm-diameter Au nanoparticles on dye-sensitized solar cells. *Appl. Phys. Lett.* **99**(25), 253107 (2011)
54. Hou, W.B., Pavaskar, P., Liu, Z.W., Theiss, J., Aykol, M., Cronin, S.B.: Plasmon resonant enhancement of dye sensitized solar cells. *Energy Environ. Sci.* **4**(11), 4650–4655 (2011)
55. Zhao, G., Kozuka, H., Yoko, T.: Effects of the incorporation of silver and gold nanoparticles on the photoanodic properties of rose bengal sensitized TiO₂ film electrodes prepared by sol-gel method. *Sol. Energy Mater. Sol. Cell* **46**(3), 219–231 (1997)
56. Lin, S.J., Lee, K.C., Wu, J.L., Wu, J.Y.: Enhanced performance of dye-sensitized solar cells via plasmonic sandwiched structure. *Appl. Phys. Lett.* **99**(4), 043306 (2011)
57. Ding, B., Lee, B.J., Yang, M., Jung, H.S., Lee, J.-K.: Surface-plasmon assisted energy conversion in dye-sensitized solar cells. *Adv. Energy Mater.* **1**(3), 415–421 (2011)
58. Wang, C.L., Lan, C.M., Hong, S.H., Wang, Y.F., Pan, T.Y., Chang, C.W., Kuo, H.H., Kuo, M.Y., Diao, E.W.G., Lin, C.Y.: Enveloping porphyrins for efficient dye-sensitized solar cells. *Energy Environ. Sci.* **5**(5), 6933–6940 (2012)
59. Sheehan, S.W., Noh, H., Brudvig, G.W., Cao, H., Schmittenmaer, C.A.: Plasmonic enhancement of dye-sensitized solar cells using core-shell-shell nanostructures. *J. Phys. Chem. C* **117**(2), 927–934 (2013)
60. Choi, H., Chen, W.T., Kamat, P.V.: Know thy nano neighbor. Plasmonic versus electron charging effects of metal nanoparticles in dye-sensitized solar cells. *ACS Nano* **6**(5), 4418–4427 (2012)
61. Hamann, T.W., Jensen, R.A., Martinson, A.B.F., Van Ryswyk, H., Hupp, J.T.: Advancing beyond current generation dye-sensitized solar cells. *Energy Environ. Sci.* **1**(1), 66–78 (2008)
62. Liu, M.Z., Guyot-Sionnest, P.: Preparation and optical properties of silver chalcogenide coated gold nanorods. *J. Mater. Chem.* **16**(40), 3942–3945 (2006)
63. Muduli, S., Game, O., Dhas, V., Vijayamohan, K., Bogle, K.A., Valanoor, N., Ogale, S.B.: TiO₂-Au plasmonic nanocomposite for enhanced dye-sensitized solar cell (DSSC) performance. *Sol. Energy* **86**(5), 1428–1434 (2012)

64. Jeong, N.C., Prasittichai, C., Hupp, J.T.: Photocurrent enhancement by surface plasmon resonance of silver nanoparticles in highly porous dye-sensitized solar cells. *Langmuir* **27**(23), 14609–14614 (2011)
65. Hagglund, C., Zach, M., Kasemo, B.: Enhanced charge carrier generation in dye sensitized solar cells by nanoparticle plasmons. *Appl. Phys. Lett.* **92**(1), 013113 (2008)
66. Ding, I.K., Zhu, J., Cai, W.S., Moon, S.J., Cai, N., Wang, P., Zakeeruddin, S.M., Gratzel, M., Brongersma, M.L., Cui, Y., McGehee, M.D.: Plasmonic dye-sensitized solar cells. *Adv. Energy Mater.* **1**(1), 52–57 (2011)
67. Erb, T., Zhokhavets, U., Gobsch, G., Raleva, S., Stuhn, B., Schilinsky, P., Waldauf, C., Brabec, C.J.: Correlation between structural and optical properties of composite polymer/fullerene films for organic solar cells. *Adv. Funct. Mater.* **15**(7), 1193–1196 (2005)
68. Wu, J.-L., Chen, F.-C., Hsiao, Y.-S., Chien, F.-C., Chen, P., Kuo, C.-H., Huang, M.H., Hsu, C.-S.: Surface plasmonic effects of metallic nanoparticles on the performance of polymer bulk heterojunction solar cells. *ACS Nano* **5**(2), 959–967 (2011)
69. Lu, L., Luo, Z., Xu, T., Yu, L.: Cooperative plasmonic effect of Ag and Au nanoparticles on enhancing performance of polymer solar cells. *Nano Lett.* **13**(1), 59–64 (2012)
70. Mihailtchi, V.D., Koster, L.J.A., Hummelen, J.C., Blom, P.W.M.: Photocurrent generation in polymer-fullerene bulk heterojunctions. *Phys. Rev. Lett.* **93**(21), 216601 (2004)
71. Liu, H.J., Goh, W.P., Leung, M.Y., Li, Y.N., Norsten, T.B.: Effect of nanoparticle stabilizing ligands and ligand-capped gold nanoparticles in polymer solar cells. *Sol. Energy Mater. Sol. Cell* **96**(1), 302–306 (2012)
72. Zhu, J.F., Xue, M., Hoekstra, R., Xiu, F.X., Zeng, B.Q., Wang, K.L.: Light concentration and redistribution in polymer solar cells by plasmonic nanoparticles. *Nanoscale* **4**(6), 1978–1981 (2012)
73. You, J.B., Li, X.H., Xie, F.X., Sha, W.E.I., Kwong, J.H.W., Li, G., Choy, W.C.H., Yang, Y.: Surface plasmon and scattering-enhanced low-bandgap polymer solar cell by a metal grating back electrode. *Adv. Energy Mater.* **2**(10), 1203–1207 (2012)
74. Shahin, S., Gangopadhyay, P., Norwood, R.A.: Ultrathin organic bulk heterojunction solar cells: plasmon enhanced performance using Au nanoparticles. *Appl. Phys. Lett.* **101**(5), 053109 (2012)
75. Kulkarni, A.P., Noone, K.M., Munchika, K., Guyer, S.R., Ginger, D.S.: Plasmon-enhanced charge carrier generation in organic photovoltaic films using silver nanoprisms. *Nano Lett.* **10**(4), 1501–1505 (2010)
76. Chen, M.-C., Yang, Y.-L., Chen, S.-W., Li, J.-H., Aklilu, M., Tai, Y.: Self-assembled monolayer immobilized gold nanoparticles for plasmonic effects in small molecule organic photovoltaic. *ACS Appl. Mater. Interfaces* **5**(3), 511–517 (2013)

Chapter 18

Interfaces in III–V High Efficiency Solar Cells

Alexander S. Gudovskikh, Nikolay A. Kalyuzhnyy, Sergey A. Mintairov,
and Vladimir M. Lantratov

Abstract The III–V multijunction solar cells consist of numerous layers with a transition between semiconductors of different composition—hetero-interfaces, which can impair the quality and performance of the cells. The properties of the hetero-interfaces and their impact to GaInP/GaAs/Ge solar cells performance are explored in this chapter. It was demonstrated that among all interface-related factors (like recombination at the interface states) the undesired potential barriers at the isotype hetero-interfaces have the most significant influence on cell performance at high sun concentration. In particular, a significant valence band offset at the hetero-interfaces between III-arsenides (GaAs, AlGaAs) and III-phosphides (GaInP, AlInP) leads to undesired potential barriers for majority carriers at the p–p isotype heterojunction interfaces that results in significant losses. A set of the experimental techniques was successfully applied for the interface characterization. The presence of the potential barrier and its effective height at the mentioned above interfaces were experimentally determined. Another phenomenon at the III-V/IV heterojunction interfaces is described on example of GaInP/Ge interface. An unexpected “parasitic” potential barrier was observed at this interface, which is related to inter-diffusion process.

A.S. Gudovskikh (✉)

Renewable Energy laboratory, St. Petersburg Academic University-Nanotechnology Research and Education Centre of the Russian Academy of Sciences, Hlopina str. 8/3, 194021 Saint-Petersburg, Russia
e-mail: gudovskikh@edu.ioffe.ru

N.A. Kalyuzhnyy • S.A. Mintairov • V.M. Lantratov

Photovoltaics Lab, IOFFE Physical-Technical Institute, 26 Polytekhnicheskaya str., 194021 Saint-Petersburg, Russia
e-mail: Nickk@mail.ioffe.ru; mintairov@scell.ioffe.ru; Lantr@scell.ioffe.ru

1 Introduction

III–V multijunction solar cells demonstrate the highest efficiency (more than 40 % under concentration) being one of the most successful paths of photovoltaic development [1]. Stacking several junctions with different band gap allows one to significantly reduce the losses due to charge carriers thermalization. However, the appropriate materials choose for the photoactive junctions (subcells) require on the one hand an optimal value of the band gap and on the other hand the best lattice match is also required. From the dependence of the band gap, E_g , on lattice constant for III–V and IV semiconductors one can select the most optimal material combination of $\text{Ga}_{0.52}\text{In}_{0.48}\text{P}$ ($E_g = 1.9$ eV), Ga(In)As ($E_g = 1.42$ eV), and Ge ($E_g = 0.66$ eV) [2]. Although in terms of band gap this combination does not give the maximum theoretical efficiency for triple-junction cells, the fact that they are lattice matched allows to produce GaInP/Ga(In)As/Ge heterostructure solar cells with a perfect crystalline quality in a single process. Thus GaInP/Ga(In)As/Ge triple-junction cells are currently the main part of the mass production of high efficiency multijunction solar cells. They are widely used in space and terrestrial concentrated photovoltaic due to high efficiency under concentrated sunlight and high radiation resistance.

Usually p–n homojunctions are used as photoactive junction in III–V multijunction solar cells. The subcells are connected by tunnel junctions. While isotype heterojunctions are formed on the both sides of p–n junction in order to avoid the recombination at the interfaces. As demonstrated in Fig. 18.1 the potential barriers for the minority carriers reflect them avoiding the recombination at the contacts and tunnel junctions. On the other hand the barrier layers should not limit the transport of the majority carriers. The front potential barrier is called as wide-band-gap windows and the bottom barrier is called as back surface field (BSF).

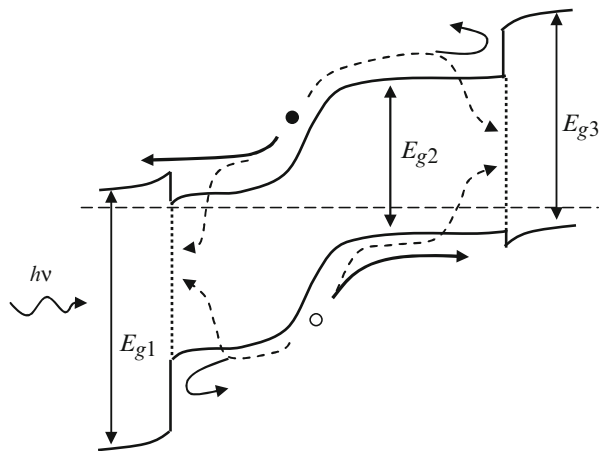
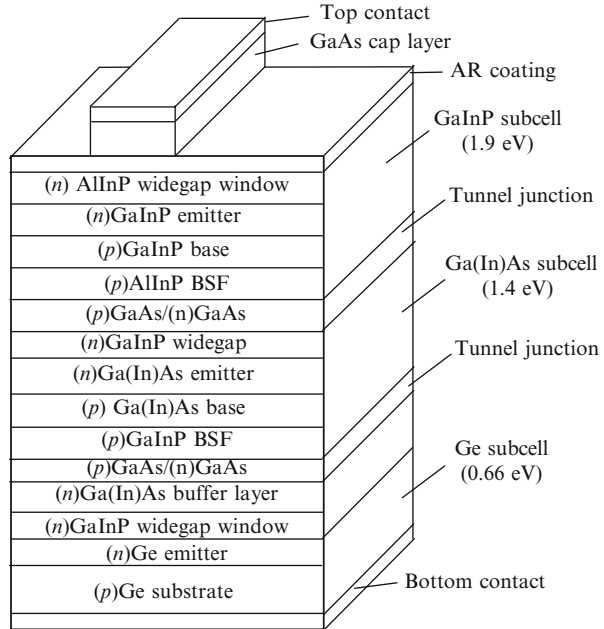


Fig. 18.1 Schematic band diagram of the p–n homojunction subcell with isotype heterojunction barrier layers

Fig. 18.2 Example of GaInP/GaInAs/Ge solar cell design



An example of GaInP/Ga(In)As/Ge triple-junction solar cell design is illustrated in Fig. 18.2. Such solar cells consist of a large number of different layers (up to 20 or more) with a different composition and certainly with a significant amount of different interfaces. Interface properties are a very important issue for any heterojunction devices. In case of multijunction solar cells they may play a key role for operation of such devices. The problem is complicated by the fact that real interfaces could be far from ideal case.

There are different reasons way it is not always possible to reach an ideal heterointerface. At high growth temperatures the inter-diffusion of semiconductor materials components is possible. The interface states may cause energy levels associated with the imperfection of the structure, due to mismatch of crystal lattices of materials forming the heterojunction. The states at the interface may occur due to the presence of impurities and defects introduced during growth. In addition, the states may be formed as a result of the stress caused, in particular, the difference in the thermal expansion coefficients.

Among III–V semiconductors the properties of heterojunctions between GaAs and $\text{Al}_x\text{Ga}_{1-x}\text{As}$ alloys are the most studied. There are many reports denoted to GaAs/AlGaAs-based heterojunctions [3]. The success of GaAs solar cells, where AlGaAs is used as wide gap window and BSF layers [4], is mainly due to favorable combination between those materials. The increase of Al content in alloys leads to significant rise of E_g , but lattice constant has very small variation. This increase of E_g is mainly caused by increase of the conduction band offset as demonstrated in Fig. 18.3a [5].

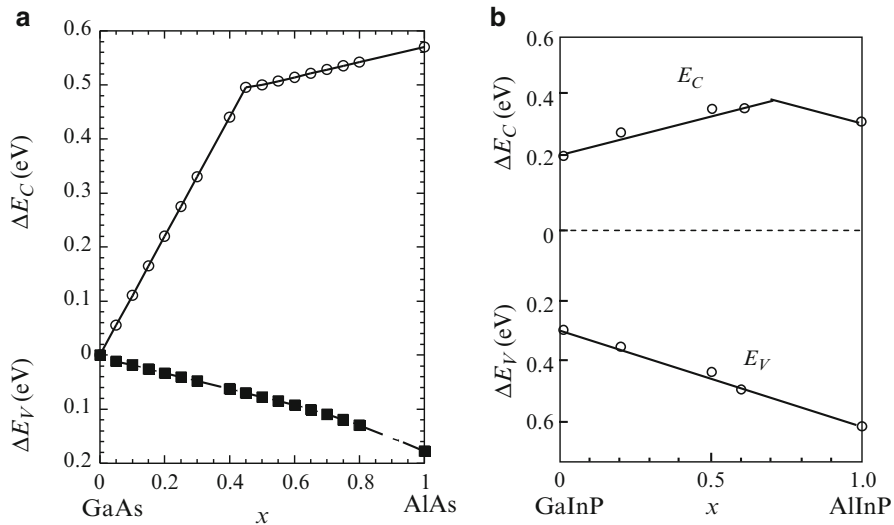


Fig. 18.3 Dependence on Al content of band gap offsets for GaAs/Al_xGa_{1-x}As [5] (a), and GaAs/(Al_xGa_{1-x})_{0.51}In_{0.49}P [6] (b) interfaces

However, despite to all advantage of AlGaAs/GaAs heterointerfaces the main problem of AlGaAs is its sensitivity to oxygen. Oxygen leads to deep levels in AlGaAs, which are very effective nonradiative recombination centers. Therefore the heterojunction between GaAs and lattice-matched Ga_{0.52}In_{0.48}P alloy has attracted a lot of attention. This GaInP alloy without Al is less sensitive to the oxygen content in the reactor. The extremely low values of the surface recombination velocity ($S_{it} < 1.5$ cm/s) were reached at the GaAs/Ga_{0.52}In_{0.48}P interface [7]. This fact leads to intensive use of GaInP layers in the design of GaAs-based solar cells.

The heterojunctions between III-arsenides and III-phosphides are widely used in multijunction solar cells (see Fig. 18.2). The band gap in quaternary alloys (Al_xGa_{1-x})_{0.51}In_{0.49}P lattice matched to GaAs (or Ge) may be similarly varied with Al content. But in contrary to GaAs/AlGaAs interfaces the increase of Al concentration leads to rise of valence band offset at the GaAs/AlGaInP interface (Fig. 18.3b) [6]. As discussed in this chapter, this difference in band discontinuity behavior for III-arsenides and III-phosphides interfaces is very important issue for the solar cell development.

In this chapter the properties of the heterojunction interfaces between epitaxial layers grown under conditions of maximum lattice matching are reviewed. The structures were grown by metal organic vapor phase epitaxy (MOVPE)—the main industrial method used to produce multijunction solar cells. The structural properties of the grown layers were studied by X-ray diffraction, photoluminescence, and scanning electron microscopy, which demonstrated the high structural quality.

2 GaInP-Based Solar Cells

As mentioned above ternary and quaternary alloys of III-phosphides matched to GaAs ($\text{Ga}_{0.52}\text{In}_{0.48}\text{P}$, $\text{Al}_{0.53}\text{In}_{0.47}\text{P}$ and $(\text{Al}_x\text{Ga}_{1-x})_{0.51}\text{In}_{0.49}\text{P}$) are the most suitable material combination for fabrication of top subcell in multijunction (GaInP/Ga(In)As/Ge) solar cells. Photoactive p-n homojunction is formed in GaInP ($E_g = 1.9$ eV), while AlInP ($E_g = 2.26$ eV) and AlGaInP are used for barrier layers.

However, interface properties for AlInP/GaInP solar cells are one of the key factors [8]. It was experimentally demonstrated that solar cells with n-type emitter and p-type base, like (n)AlInP/(n)GaInP/(p)GaInP/(p)AlGaInP (hereafter, n-p structures) exhibit higher efficiency compared to inverse structure (p)AlInP/(p)GaInP/(n)GaInP/(n)AlGaInP (hereafter, p-n structures). The main feature of the p-n structures is a knee in I - V curves near to open circuit voltage (V_{OC}), which leads to decrease of fill factor (FF) and, therefore, efficiency [8, 9].

In [10] it was shown that origin of this knee is related to the interface properties of (p)GaAs/(p)AlInP/(p)GaInP heterojunction. Different GaInP solar cells were grown by MOVPE on n- and p-type GaAs substrates to study the influence of the interface properties to performance [11]. The both types of n-p and p-n structures were grown with 30 nm AlInP window layer, which was capped by GaAs contact layer of n- and p-type, respectively. Typical experimental I - V curves measured at 1 sun (AM1.5D) illumination for the both types of fabricated cells are presented in Fig. 18.4 and their parameters are given in Table 18.1. The best performance was reached for the n-p structure with (n)AlInP window. The p-n structure has lower values of short circuit current (J_{SC}) and V_{OC} , but its main feature is a well-pronounced knee in I - V curve, which leads to a significant reduction of FF and, therefore, of efficiency.

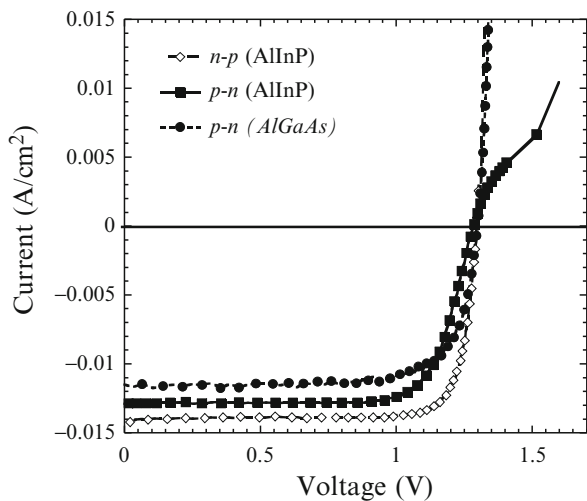
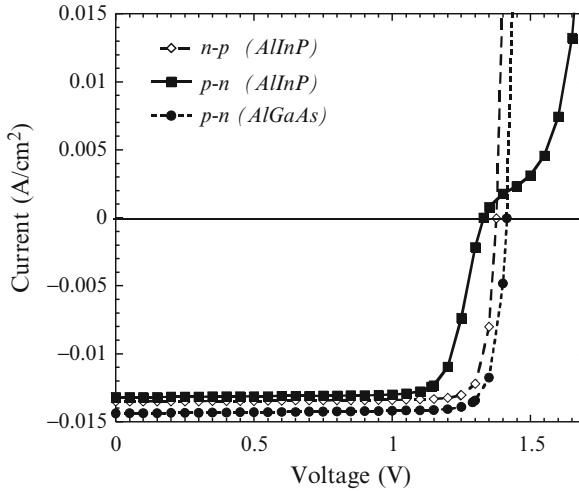


Fig. 18.4 Typical experimental I - V curves measured at AM1.5D (1 sun) illumination for: n-p and p-n structures with AlInP window, p-n structure with $\text{Al}_{0.8}\text{Ga}_{0.2}\text{As}$ window

Table 18.1 Experimental/calculated parameters of I - V curves at AM1.5D (1 sun) illumination for three different GaInP solar cells

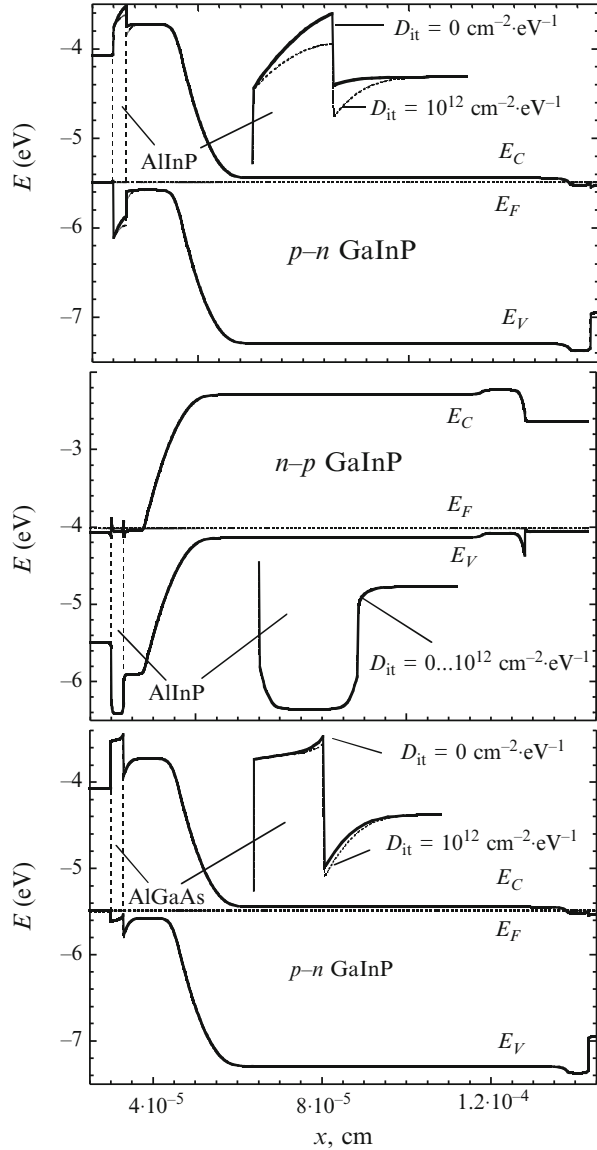
Parameter	n-p (AlInP)	p-n (AlInP)	p-n (AlGaAs)
J_{SC} (mA cm ⁻²)	13.6/13.5	12.5/13.2	11.96/14.4
V_{OC} (V)	1.3/1.38	1.28/1.33	1.3/1.41
FF (%)	81/87.5	75/80.9	76/86.1
η (%)	14.3/16.3	11.6/14.2	11.8/17.5

**Fig. 18.5** Calculated I - V curves under AM1.5D (100 mW cm^{-2}) illumination for: n-p and p-n structures with AlInP window, p-n structure with $\text{Al}_{0.8}\text{Ga}_{0.2}\text{As}$ window

To explain this behavior of the I - V curves they were calculated by numerical simulations using AFORS-HET software [12]. One dimension structures GaAs cap layer/wide gap window/GaInP homojunction/GaAs contact layer with ohmic top and bottom contacts were considered [13]. The I - V curves calculated without interface states under AM1.5D (100 mW cm^{-2}) illumination are presented in Fig. 18.5. The calculated curves reproduce well the experimental results and the calculated parameters, which are presented in Table 18.1, correspond to the experimental data. The n-p structure has normal I - V curve behavior and better performance, while p-n structure exhibits the knee in I - V curve similar one in experimental curves leading to lower efficiency. The I - V curve of the p-n structure with (p) $\text{Al}_{0.8}\text{Ga}_{0.2}\text{As}$ window layer was also calculated (Fig. 18.5). In this case I - V curve has no knee. Moreover, this structure has the better values of J_{SC} , V_{OC} and efficiency compared to the n-p structure with (n)AlInP window.

The difference in behavior of I - V curves for n-p and p-n structures with AlInP window may be explained in terms of band diagram. The equilibrium band diagrams calculated for those structures are shown in Fig. 18.6. The band discontinuity at the interfaces is calculated according to Anderson's approach [14] from electron affinity. The values of the band gap and electron affinity used in the

Fig. 18.6 Calculated equilibrium band diagram for p-n structures with (p)AlInP window (a), n-p structures with (n)AlInP window (b), and p-n structure with (p)Al_{0.8}Ga_{0.2}As window (c). Simulation is performed for two values of D_{it} (0 and 10^{12} cm⁻² eV⁻¹)



simulations are presented in Table 18.2. A large value of the valence band offset (ΔE_V) at the GaAs/AlInP and AlInP/GaInP interfaces of p-n structure lead to appearance of a high potential barrier (about 0.6 eV) for majority carriers (holes) moved from emitter to front contact (Fig. 18.6a). This barrier limits hole transport and leads to a knee in I - V curves under light. Moreover, the band bending occurred in the (p)AlInP layer leads to an electric field which drives electrons generated in this layer toward the front metal contact where they recombine. In other words, the generation of electrons in the (p)AlInP layer results in recombination losses.

Table 18.2 Main material and interface parameters used in the simulations

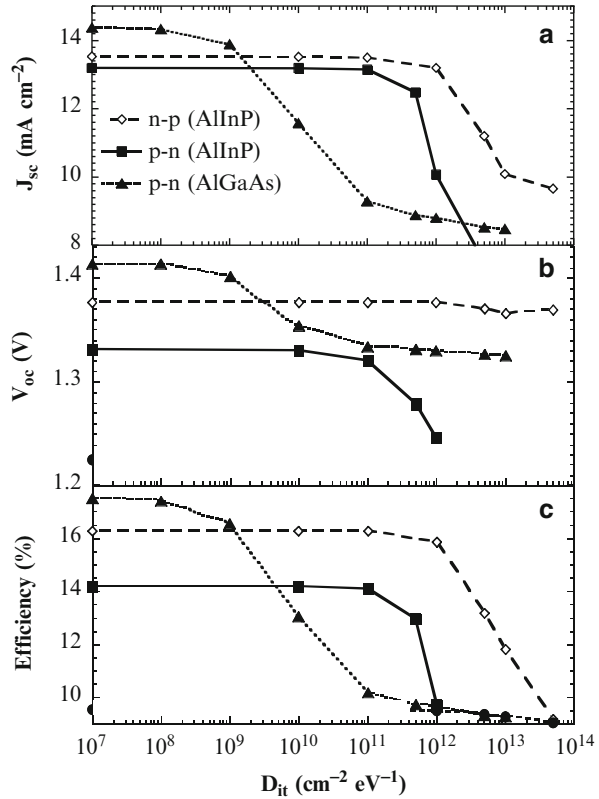
Material	E_g (eV)	χ (eV)
GaAs	1.42 [16]	4.07 [16]
$\text{Ga}_{0.52}\text{In}_{0.48}\text{P}$	1.85 [17]	4.01 [19]
$\text{Al}_{0.53}\text{In}_{0.47}\text{P}$	2.35 [18]	3.78 [19]
$\text{Al}_{0.8}\text{Ga}_{0.2}\text{As}$	2.09 [17]	3.53 [5]
$\text{Al}_{0.4}\text{Ga}_{0.6}\text{As}$	1.92 [17]	3.63 [5]
$(\text{Al}_{0.6}\text{Ga}_{0.4})_{0.51}\text{In}_{0.49}\text{P}$	2.26 [17]	3.83 [17]
$(\text{Al}_{0.3}\text{Ga}_{0.7})_{0.51}\text{In}_{0.49}\text{P}$	2.13 [17]	3.89 [17]
<i>Interface</i>	ΔE_C (eV)	ΔE_V (eV)
GaAs/ $\text{Al}_{0.53}\text{In}_{0.47}\text{P}$	0.3	0.63
$\text{Ga}_{0.52}\text{In}_{0.48}\text{P}/\text{Al}_{0.53}\text{In}_{0.47}\text{P}$	0.23	0.27
GaAs/ $\text{Al}_{0.8}\text{Ga}_{0.2}\text{As}$	0.54	0.13
$\text{Ga}_{0.52}\text{In}_{0.48}\text{P}/(\text{Al}_{0.3}\text{Ga}_{0.7})_{0.51}\text{In}_{0.49}\text{P}$	0.12	0.16
$\text{Al}_{0.8}\text{Ga}_{0.2}\text{As}/(\text{Al}_{0.3}\text{Ga}_{0.7})_{0.51}\text{In}_{0.49}\text{P}$	0.35	0.39

The simulations predict that reduction of (p)AlInP layer thickness (down to 15 nm) as well as increasing its doping level lead to disappearance of the knee in I - V curves under 1 sun illumination [10]. This results correspond well to experimental data reported in [8] where an improvement of the I - V curve shape was observed for increased doping concentration of the (p)AlInP layer and also are in good agreement with experimental data reported in [15] for the p-n structures with 15 nm thick (p)AlInP layer, which does not exhibit a knee under non-concentrated light. However, for concentrated light the experiment and the simulations for the both cases demonstrate appearance of the knee with a significant deterioration of solar cell performance [15].

In case of n-p structure the barriers for the majority carriers (electrons) crossing the window do not exceed 0.15 eV due to lower value of the conduction band offset (ΔE_C) and the barriers are much narrower because of higher doping concentration of the (n)AlInP layer. The electron transport through the window is not limited and, therefore, no knee in I - V curves is observed. Thus the knee in I - V curves for p-n structures with AlInP window is caused by parasitic potential barrier for majority carriers, which is formed due to large valence band offset at the GaAs/AlInP interface.

The calculated band diagram for p-n structure with (p) $\text{Al}_{0.8}\text{Ga}_{0.2}\text{As}$ window is shown in Fig. 18.6c. The (p) $\text{Al}_{0.8}\text{Ga}_{0.2}\text{As}$ layer forms high barrier for electrons, which limits the recombination at the front contact, while the barrier for holes at the $\text{Al}_{0.8}\text{Ga}_{0.2}\text{As}/\text{GaInP}$ interface is low and narrow enough for unlimited transport through this interface. The experimental and calculated I - V curves for this structure presented in Figs. 18.4 and 18.5, respectively, have the same behavior without any knee [15]. While the performance of the experimental p-n structures with (p) $\text{Al}_{0.8}\text{Ga}_{0.2}\text{As}$ window is significantly low compared to the simulations results. The both J_{SC} and V_{OC} values are reduced (see Table 18.1) resulting in dramatic drop of efficiency. As will be described below this difference is caused by recombination losses at the $\text{Al}_{0.8}\text{Ga}_{0.2}\text{As}/\text{GaInP}$ interface states.

Fig. 18.7 Calculated J_{SC} (a), V_{OC} (b), and efficiency (c) D_{it} for n-p and p-n structures with AlInP window and p-n structures with $Al_{0.8}Ga_{0.2}As$ window



When the density of interface states, D_{it} , is not negligible, an enhanced recombination and changes of the band diagram could appear at the interfaces. The influence of the states at the interface window/emitter to solar cell performance was also studied by the simulations [10]. The interface was described by introducing a very thin ($d = 1$ nm) defective GaInP layer (with a band gap, E_g , of 1.85 eV) between the emitter GaInP and window layers. The defect distribution, g_{it} , in this interface layer was taken as constant through the bandgap, assuming donor/acceptor-like defects in the lower/upper half of the bandgap. The electron and hole capture cross-sections were set at $10^{-14} cm^2$. The interface defect density, D_{it} , was defined as the product of $g_{it} \times d$.

The results of theoretical study of the effect of the interface states on solar cell characteristics such as J_{SC} , V_{OC} , and efficiency are presented in Fig. 18.7a, b, and c, respectively. The increase of D_{it} at the AlInP/GaInP interface from 0 to $10^{11} cm^{-2} eV^{-1}$ does not lead to significant changes in performance of n-p and p-n structures with a AlInP window. For $D_{it} > 10^{11} cm^{-2} eV^{-1}$ J_{SC} decreases with increasing D_{it} for both n-p and p-n structures. On the contrary, the p-n structure

with a p-Al_{0.8}Ga_{0.2}As window layer is very sensitive to D_{it} at the Al_{0.8}Ga_{0.2}As/GaInP interface. The drastic decrease of J_{SC} , V_{OC} , and efficiency begins at $D_{it} > 10^8$ cm⁻² eV⁻¹, while for $D_{it} > 10^{11}$ cm⁻² eV⁻¹ the decrease of those parameters becomes weaker.

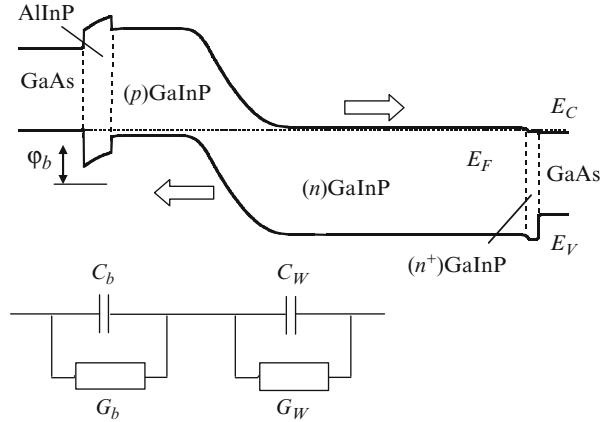
In case of a window/emitter isotype heterojunction the recombination rate is determined by the concentration of minority carriers at the interface [16]. Thus, the holes generated in the n-emitter and (n)AlInP layers of the n-p structure recombine at the AlInP/GaInP interface. But due to a favorable band diagram of this structure (see insert of Fig. 18.6b) holes move away from the interface by the electric field leading to a lower recombination rate and to a lower sensitivity to D_{it} . For p-n structures, the electron concentration at the interface should be considered. For $D_{it} < 10^{12}$ cm⁻² eV⁻¹, the band diagram of the p-n structure with a AlInP window has less advantages compared to the n-p structure (see insert of Fig. 18.6a), but still provides relatively low sensitivity of solar cell performance to D_{it} (Fig. 18.7). For the p-n structure with a (p)Al_{0.8}Ga_{0.2}As window, the high value of conduction band offset, ΔE_C , at the Al_{0.8}Ga_{0.2}As/GaInP interface leads to a band bending in the GaInP emitter (see insert of Fig. 18.6c) resulting in a significant electric field, which drives the electrons from the p-emitter to the Al_{0.8}Ga_{0.2}As/GaInP interface providing an enhanced recombination at this interface. This specific feature of the band diagram explains the high sensitivity to D_{it} of solar cell performance for p-n structure with a (p)Al_{0.8}Ga_{0.2}As window (Fig. 18.7c). High sensitivity to interface states may also explain the observed difference between experimental (Fig. 18.4) and calculated (Fig. 18.5) I - V curves. These results are in agreement with the high value of interface recombination velocity (10⁶ cm s⁻¹) at the (p)Al_{0.8}Ga_{0.2}As/(p)GaInP interface reported in [9].

Thus the importance of the band structure at the heterojunction interfaces for solar cell performance was demonstrated using theoretical simulations. In particular, an appearance of the parasitic potential barrier for majority carriers may significantly affect the efficiency. An experimental study of the interface band structure is required for further detailed analysis of the charge carrier transport.

2.1 Study of the Interface Band Structure by Admittance Spectroscopy

There is a wide range of techniques used for III-V interface characterization. The structural properties of the GaInP/GaAs interfaces were studied by XRD [20]. The values of the recombination velocity at the GaInP/GaAs interfaces were measured using time resolved photoluminescence [7]. A large number of techniques were used for the determination of such important interface parameters as values of the band offset: X-ray photoemission spectroscopy (GaInP/GaAs) [21], photoluminescence (PL) and PL excitation [22–26], and hydrostatic-pressure-dependent PL [27]. Also the values of the valence band offset (ΔE_V) and the

Fig. 18.8 Schematic band diagram and simplified equivalent circuit of admittance for p–n GaInP solar cell with (p)AlInP window



interface charge density at AlGaInP/GaAs interface were obtained by C-V profiling [6]. The above-mentioned techniques rely on a given number of assumptions, which may limit their applications. For example, there is still an open question about band offset values because of a wide spread of these values obtained by different authors using those techniques for GaInP/GaAs (ΔE_V : 0.32–0.46 eV) and AlInP/GaInP (ΔE_V : 0.17–0.36 eV) interfaces [17].

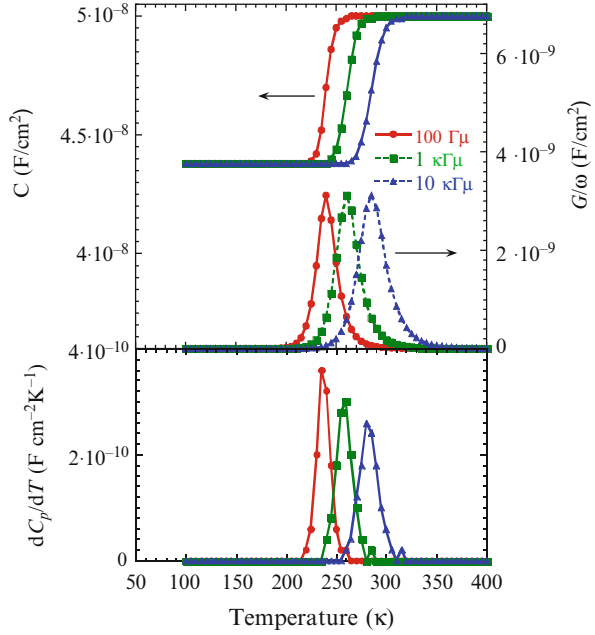
In this section the capability of admittance spectroscopy for study the interface properties of III-phosphides solar cells will be explored. In general, capture and emission of charge carriers at and from gap states lead to charge changes and, therefore, may result in a capacitance contribution. This fact allows one to use the admittance spectroscopy for defect characterization in space charge regions [28] and at heterointerfaces [29]. Here the admittance spectroscopy will be applied to deduce barrier heights at heterointerfaces, in particular between the window layer and the emitter layer of III-phosphides solar cells.

A schematic band diagram of p–n GaInP structure with (p)AlInP window is presented in Fig. 18.8. A high potential barrier for the holes is formed at the p–GaAs/p–AlInP interface due to the high valence band offset leading to the depletion of the whole p–AlInP window layer. The simplest analysis of the admittance spectra may be made in terms of the equivalent circuit [30], as described in Fig. 18.8. C_W and G_W are the capacitance and conductance of the depletion region of the p–n junction in GaInP. These are in series with C_b and G_b , being the parallel capacitance and conductance of the depletion region formed by the potential barriers at the “cap GaAs/window” and “window/GaInP emitter” interfaces.

Neglecting the conductance of the p–n junction G_W the equivalent parallel capacitance, C_p , and conductance, G_p , are equal to

$$C_p = \frac{C_W G_b^2 + \omega^2 C_W C_b (C_W + C_b)}{G_b^2 + \omega^2 (C_W + C_b)^2}, \quad (18.1)$$

Fig. 18.9 Calculated dependences of $C_p(T)$, G_p/ω (T) (a) and dC_p/dT (b)



$$G_p = \frac{\omega^2 C_W G_b}{G_b^2 + \omega^2 (C_W + C_b)^2}, \quad (18.2)$$

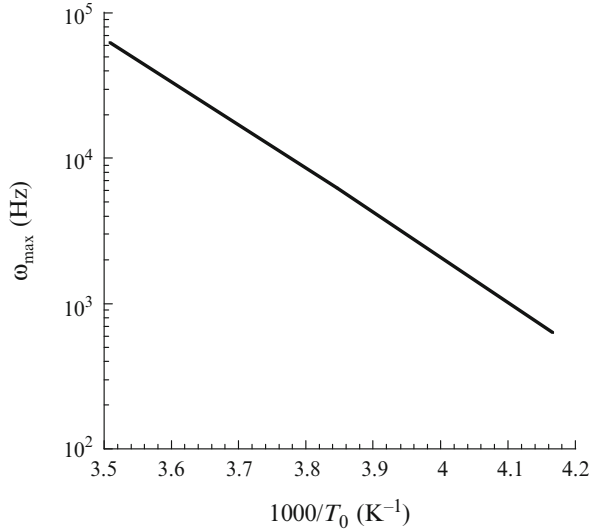
where ω is the angular frequency. Assuming that G_b is dominated by thermoionic emission over the potential barrier it may be expressed as:

$$G_b = G_0 \exp\left(\frac{-q\varphi_b}{kT}\right), \quad (18.3)$$

where G_0 is the temperature-dependent thermoionic emission pre-factor, q is the electron charge, φ_b is the effective height of the potential barrier, k is Boltzmann's constant, and T is the temperature.

The calculated temperature dependences of C_p and G_p/ω , using formulas (18.1), (18.2), and (18.3) with temperature independent values of C_W , C_b , and G_0 for different frequencies are presented in Fig. 18.9. Capacitance curves exhibit a step. At low temperatures (high frequencies) the transport of the majority carriers through potential barriers at the interfaces is limited, i.e., the conductance G_b is low and the total capacitance can be expressed as C_W in series to C_b . At higher temperatures (lower frequencies) the majority carriers can overpass the potential barriers at the interfaces, i.e., conductance G_b is large enough to shunt the capacitance C_b and the total capacitance is equal to the capacitance of the depletion region of the p-n junction, C_W .

Fig. 18.10 An Arrhenius plot of the frequency dependence obtained from the maximum in G_p/ω vs. T or inflection point in dC_p/dT vs. T curves

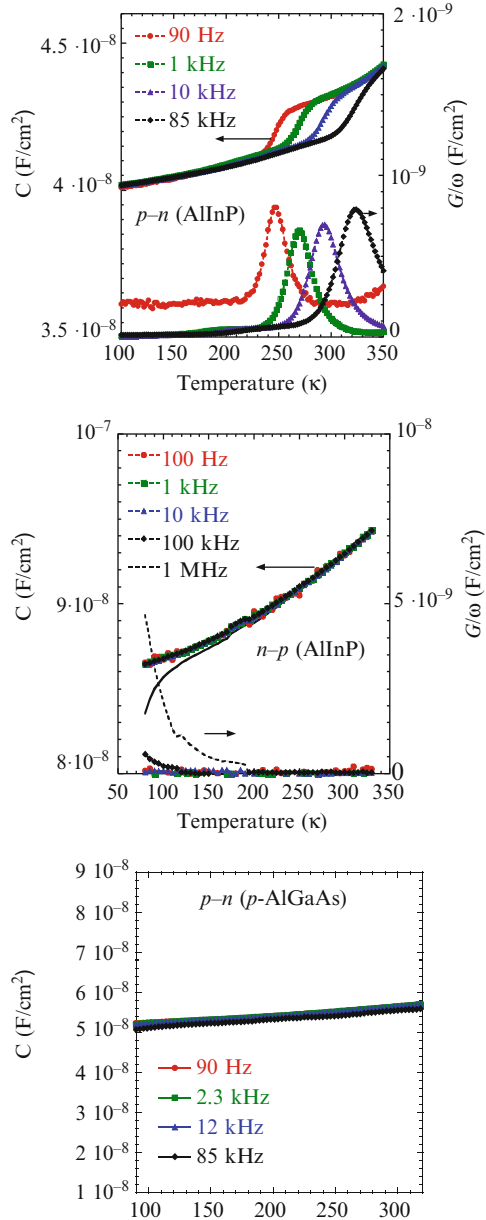


The step in capacitance curves is accompanied by a maximum in conductance. The conductance maximum in $G_p/\omega(T)$ curves corresponds to the inflection point in the $C_p(T)$ curves as demonstrated in Fig. 18.9b, where the derivative of the capacitance against temperature, dC_p/dT , is presented. The position of this feature is shifted to higher temperature when increasing the frequency. This shift in the temperature position versus frequency may be used to obtain the activation energy of the underlying process. An Arrhenius plot of the measurement frequency at the conductance maximum (or at the inflection point in the capacitance), shown in Fig. 18.10, gives an activation energy equal to the potential barrier height ϕ_b (0.6 eV) used in the calculations.

For a more detailed analysis in [30] the numerical simulations of the admittance spectra were performed for different GaInP structures. The simulation results correspond well to the described above simplified calculation. In other word, this simplified model demonstrates the way for a direct determination of the effective potential barrier height using admittance spectroscopy. It should be noted that the correlation between the activation energy of the C – T – ω curves and the value of the effective potential barrier is a very important issue, which can be used for the characterization of different isotype heterojunctions. Obviously, the determination of the barrier height from experimental data will be affected by the temperature dependence of parameters like the thermoionic emission pre-factor G_0 . However, these temperature dependences are weak compared to the activated barrier overcoming, and the related error on the determination of the potential barrier if one just neglects these temperature variations is of the order of a few kT s.

When experimental measurements of the admittance spectra performed on solar cells with front grid contact one should care about influence of the spreading [31]. If the emitter layer conductance strongly depends on temperature, for instance, in case of p-type GaInP doped by Zn or Mg, which have high ionization energy, the

Fig. 18.11 Experimental $C-T-\omega$ and $G/\omega-T-\omega$ curves for p-n structure with (p)AlInP window (a) and n-p structure with (n) AlInP (b) for p-n structure with (p)AlGaAs window ($V_{dc} = 0$)



activation energy could be determined with a significant error [30]. To avoid this problem the best way is to perform the measurements for the structures with full metal contact (not a grid).

The experimental $C-T-\omega$ and $G/\omega-T-\omega$ curves measured for different structures with full metal top contact are presented in Fig. 18.11. The p-n structure with (p)

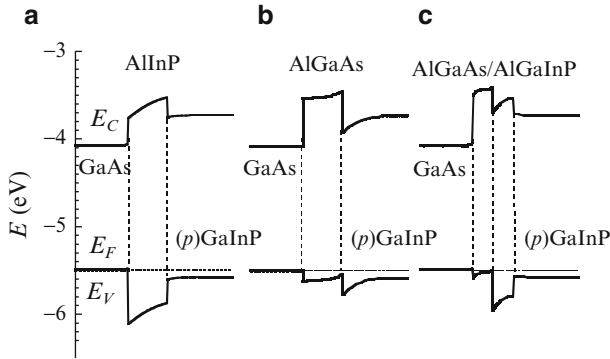


Fig. 18.12 Calculated band diagram at equilibrium for p–n structures with (p)AlInP (a), (p)Al_{0.8}Ga_{0.2}As (b), and Al_{0.8}Ga_{0.2}As/(Al_{0.6}Ga_{0.4})_{0.51}In_{0.49}P (c)

AlInP window exhibits a step in C – T – ω curves at 200–300 K, which is accompanied by maximum of conductance. This admittance behavior confirms the presence of a potential barrier for majority carriers. Activation energy deduced from the measured dependences is equal approximately to 0.6 eV, which corresponds to the value obtained from the simulations and it is in good agreement with the values of ΔE_V at GaAs/AlInP interface reported by other authors, 0.54–0.63 eV [6, 32]. The obtained value of E_a corresponds also to that of the effective barrier for the holes used in analysis of I – V curves under illumination [10].

For the n–p structure with (n)AlInP no step (peak) can be observed in the explored range of temperature and frequency (Fig. 18.11b). Only at the highest measured frequency (1 MHz) the $C(T)$ and $G/\omega(T)$ curves exhibit some feature at low temperature, which could be related to the existence of a step in capacitance and peak in conductance that could be revealed at lower temperature. The p–n structure with AlGaAs window also demonstrates no features in admittance spectra (Fig. 18.11c). For both cases one can assume no potential barriers, which can affect the transport properties.

Thus, it was experimentally demonstrated that the high potential barrier for majority carriers at the (p)GaAs/(p)AlInP interface leads to limitation of charge carrier transport. Therefore, to improve the performance of p–n GaInP solar cells another p-type window, which does not form a significant barrier for the holes, should be found.

2.2 Double layer Wide Gap Window for p–n Structures

As was mentioned above a significant valence band offset at the (p)GaAs/(p)AlInP interface (Fig. 18.12a) does not allow to use this heterojunction in solar cells operated under concentration. In case of (p)AlGaAs window the low value of ΔE_V at the (p)AlGaAs/(p)GaAs interface provides successful hole transport

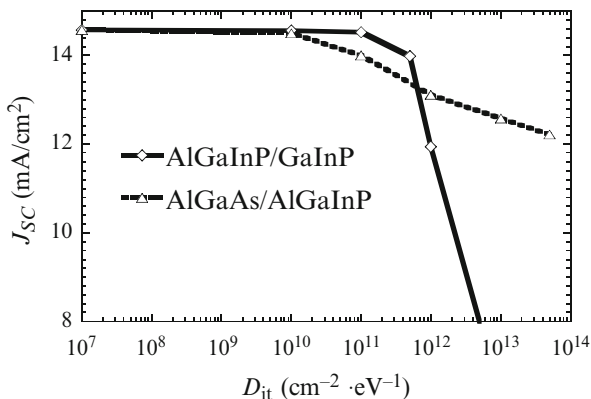


Fig. 18.13 Calculated dependences of J_{SC} on D_{it} at the $(\text{Al}_{0.6}\text{Ga})_{0.5}\text{In}_{0.49}\text{P}/\text{GaInP}$ and $\text{Al}_{0.8}\text{Ga}_{0.2}\text{As}/(\text{Al}_{0.6}\text{Ga}_{0.4})_{0.51}\text{In}_{0.49}\text{P}$ interfaces for p–n structure with double window $\text{Al}_{0.8}\text{Ga}_{0.2}\text{As}/(\text{Al}_{0.6}\text{Ga}_{0.4})_{0.51}\text{In}_{0.49}\text{P}$ (AM1.5D 100 mW cm^{-2})

through this heterojunction (Fig. 18.12b). But the band bending at the (p)AlGaAs/(p)GaInP interface leads to enhanced recombination at this interface resulting in a decrease of solar cell efficiency.

In [15] it was suggested to combine the advantages of (p)GaAs/(p)AlGaAs and (p)AlGaInP/(p)GaInP interfaces using double layer window (p)AlGaAs/(p)AlGaInP. The calculated band diagram of the top side of the junction with such double layer window is demonstrated in Fig. 18.12c. The top (p)AlGaAs layer in contact with (p)GaAs forms low barrier for holes and bottom (p)AlGaInP layer in contact with (p)AlGaInP has a lower band bending leading in lower recombination rate at the interface states. The barrier height for the holes (about 0.4 eV) is lower in this case compared to that with p-AlInP window (0.6 eV). According to the simulations of I – V curves under illumination this barrier height is low enough for normal hole transport at 300 K. No knee in I – V curves was also observed up to 1,000 sun illuminations. The influence of defect states at the (p)AlGaInP/(p)GaInP interface on solar cell performance (demonstrated in Fig. 18.13) is not significant up to values of the density of states of $10^{12} \text{ cm}^{-2} \text{ eV}^{-1}$. This is much better than for the (p)AlGaAs/(p)GaInP interface where a dramatic decrease was observed for values of the density of states higher than $10^9 \text{ cm}^{-2} \text{ eV}^{-1}$. The detailed analysis of the simulation results is presented elsewhere [15]. The best efficiency under 1,000 sun AM1.5D illumination was obtained for the cell with $\text{Al}_{0.8}\text{Ga}_{0.2}\text{As}/(\text{Al}_{0.6}\text{Ga}_{0.4})_{0.51}\text{In}_{0.49}\text{P}$ window.

According to the calculation results the experimental p–n GaInP heterostructures with (p)AlGaAs/(p)AlGaInP window were grown. The results of admittance measurements performed on such structure with full metal contact are shown in Fig. 18.14a [33]. In the temperature range of 120–220 K the capacitance has a step accompanied by a peak in conductance. The activation energy of this capacitance (conductance) step (peak) is in the range 0.23–0.27 eV. At lower temperature the capacitance and conductance seem to have another step and peak, respectively. The simulation of admittance spectra (Fig. 18.14b) predicts the presence of two

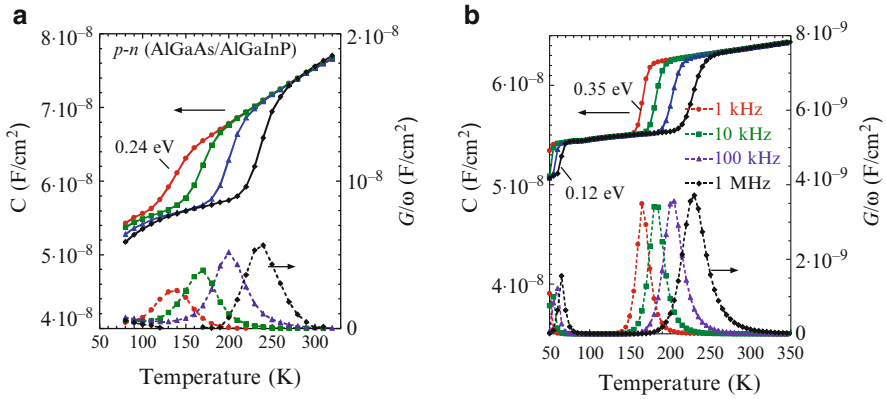


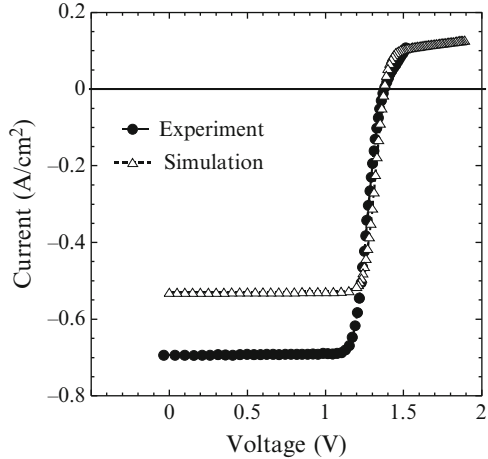
Fig. 18.14 Experimental (a) and calculated (b) C - T - ω and G/ω - T - ω curves for p-n GaInP structures with (p)AlGaAs/(p)AlGaInP window

steps (peaks). The step at low temperature corresponds to the transport over the barrier at the (p)GaAs/(p)AlGaAs interface with an activation energy of 0.12 eV related to this barrier height. The second step (peak) at higher temperature corresponds to the transport over the barrier at the (p)AlGaAs/(p)AlGaInP interface with the activation energy of 0.35 eV. Thus the activation energy obtained from admittance measurements corresponds to the effective barrier height of the AlGaAs/AlGaInP interface. The lower value of the activation energy obtained from the experiment compared to the simulation may be caused by tunneling through the spike in the valence band. Of greatest importance, the obtained experimental value of the effective barrier (0.25 ± 0.02 eV) is low enough to ensure good transport of the majority carriers. No knee was observed in experimental I - V curves up to 150 sun [33] demonstrating the experimental confirmation of the double layer window approach.

3 III-Phosphide/III-Arsenide Interfaces in Multijunction Solar Cells

The described particular problem of potential barrier for majority carriers in GaInP solar cells may be regarded in more general view. If one considers the band discontinuity between III-phosphides and III-arsenides (Fig. 18.3), in general case increase of Al content leads to rise of the valence band offset. A large value of ΔE_V is favorable for isotype n-n heterojunction but undesirable for charge carrier transport through isotype p-p heterojunction, while the both type of heterojunctions are necessary for effective surface recombination suppression. Taking into account the fact that in multijunction solar cells wide gap III-phosphides (AlGaInP) are

Fig. 18.15 Experimental and calculated I - V curve for GaAs/Ge solar junction with (p)AlGaInP layer under 40 suns AM1.5D illumination



widely used for barrier layers, in particular in GaAs subcells, the properties of p-type III-phosphides/III-arsenides interfaces require a special attention.

The influence of (p)AlGaInP/(p)AlGaAs interface properties to carrier transport was studied on dual-junction GaAs/Ge solar cell where (p)AlGaInP layer was used at the bottom side of GaAs subcell. The I - V curves for this solar cell under small concentration (20–40 sun) have a well-defined knee near to V_{OC} (Fig. 18.15), indicating a transport limitation by parasitic barrier.

To get independent experimental confirmation of this barrier the admittance spectroscopy was used. In the measured C - T - ω curves presented in Fig. 18.16a three capacitance steps may be selected with activation energies of $E_{a1} \approx 0.1$ eV, $E_{a2} \approx 0.5$ eV, $E_{a3} \approx 0.4$ eV. The calculated band diagram of the GaAs/Ge solar cell (Fig. 18.16b) has also few potential barriers at the interfaces of bottom (p-type) side of GaAs subcell, which effective heights may be correlated with obtained activation energies.

The I - V curves of the considered dual-junction GaAs/Ge solar cells were simulated taking into account the tunnel junction [34]. The behavior of the calculated I - V curve presented in Fig. 18.15 corresponds quite well to the experimental one. The simulations made only for top GaAs subcell taking into account the bottom p-type interfaces (Fig. 18.16b) also predicts an appearance of the knee in I - V curves under concentrated light. Thus, the presence of the potential barriers for majority carriers at the p-side of GaAs sub cell is obvious.

It was suggested to use AlGaAs barrier layer for BSF of GaAs subcell because of lower ΔE_V value at the AlGaAs/GaAs interface. The calculated band diagram of the p-type bottom side of GaAs subcell and tunnel junction for GaAs/Ge solar cell is presented in Fig. 18.17a. In contrast to case of III-phosphides (Fig. 18.16b) for (p) AlGaAs barrier layer there is no potential barriers for the holes. The calculated I - V curves presented in Fig. 18.17b for dual-junction GaAs/Ge solar cell with (p) AlGaAs BSF exhibits no knee.

Taking into account the obtained results two types of triple-junction GaInP/GaAs/Ge solar cells were fabricated, which contain GaAs subcell with (p)AlGaInP

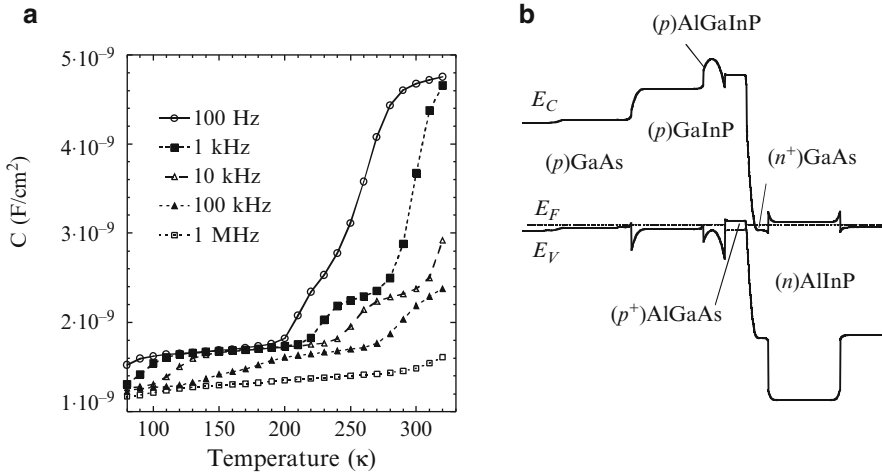


Fig. 18.16 Experimental C – T – ω curves for dual-junction GaAs/Ge solar cell (a). Calculated band diagram of bottom side of GaAs subcell and tunnel junction for GaAs/Ge solar cell (b)

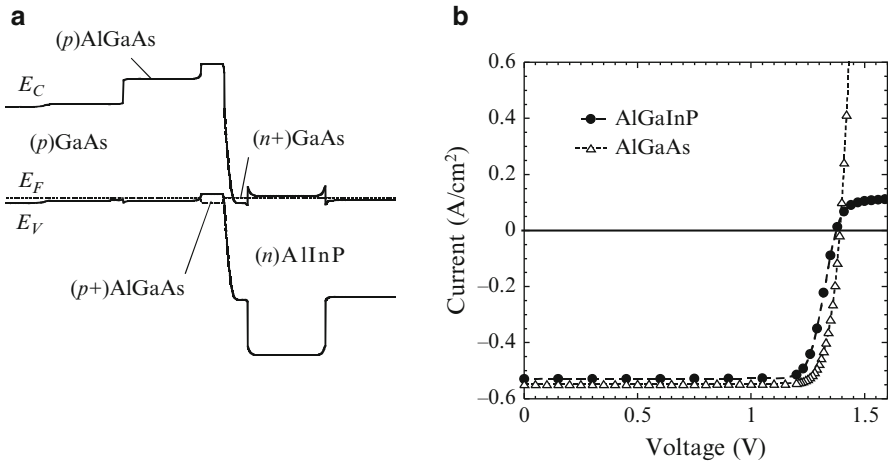


Fig. 18.17 Band diagram of dual-junction GaAs/Ge solar cell with AlGaAs (a). Calculated I – V curves for GaAs/Ge solar cell with AlGaInP and AlGaAs BSF layers (b)

and (p)AlGaAs BSF layers. Experimental I – V curves measured under concentrated light for these solar cells are presented in Fig. 18.18. Cell with (p)AlGaInP BSF layer has a knee (Fig. 18.18a) similar to described dual-junction GaAs/Ge with AlGaInP barrier layer (Fig. 18.15). This is expected because in multijunction cells all subcells are connected in series and charge carriers transport limitation in one of the subcells affects on the entire structure. On the other hand, the structure with (p)AlGaAs BSF layer does not exhibit any knee up to sun concentration of 1,000 (Fig. 18.18b) indicating low enough barrier height for effective majority carries transport.

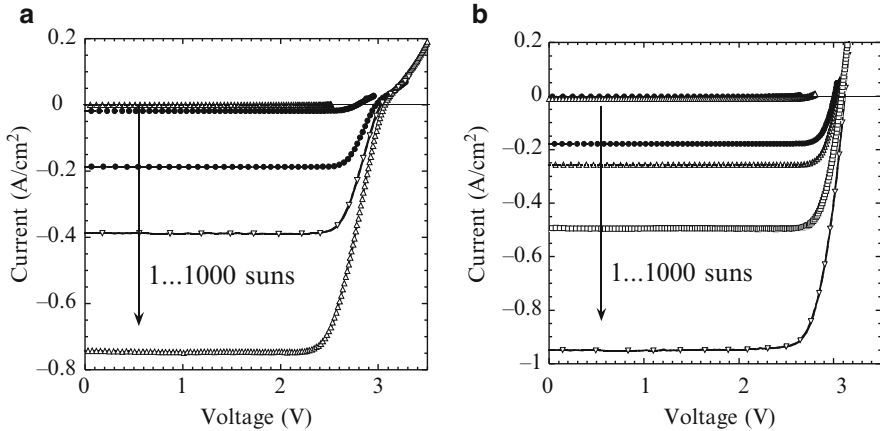


Fig. 18.18 Experimental I - V curves under concentrated light of different intensity for triple-junction GaInP/GaAs/Ge solar cells which contains GaAs subcell with (p)AlGaInP (a) and (p)AlGaAs (b) BSF layers

The described example demonstrates that parasitic potential barrier for majority carriers could appear at the interface between the III-phosphides and III- arsenides of p-type conductivity. This phenomenon must be considered in the design and analysis of multijunction solar cells based on III-V material.

4 III-Phosphide/Ge Interfaces in Multijunction Solar Cells

Ge-based structures are of great interest for high efficiency III-V multijunction solar cells due to several advantages described above. The Ge subcell contribution is at least 6 % of the absolute efficiency and up to 10 % in the theoretical estimations [35].

To form the bottom Ge subcell the epitaxial III-V layers grown on the Ge substrate (conventionally by the MOVPE) are used as a source for doping impurities to form Ge p-n junction and as a wide-band-gap window for the Ge subcell [4]. In case of p-type Ge substrate the V-group atoms diffuse into Ge during the growth process resulting in n-type heavy doped region—emitter. It was experimentally demonstrated that GaInP layer is preferred compare to GaAs [36]. The diffusion coefficient of As is significantly higher compared to P and, therefore, in case of GaAs n-emitter in Ge should be much thicker (approximately 1 μm for GaAs and 0.1 μm for GaInP). The thicker emitter means increased recombination losses due to high defect concentration in diffused layer that was observed in spectral response of Ge cells.

On the other hand the electrical properties of the III-V/IV interface have not been enough studied so far, especially when the diffusion processes are involved. The interface phenomena may affect the charge carrier transport of Ge subcells as

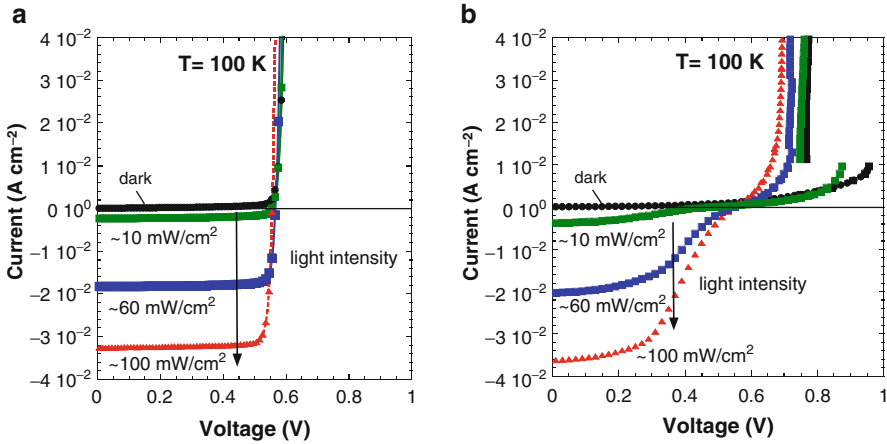


Fig. 18.19 I - V curves at 100 K in the dark and under different light intensity for “as grown” (a) and “subcells” (b) GaInP/Ge heterostructures

well as whole multijunction solar cells [37]. The band structure and charge carrier transport properties of the GaInP/Ge heterostructure solar cells were studied in [38]. Ge solar cells were fabricated by the MOVPE growth of a silicon-doped (n)GaInP layer on the p-Ge substrate doped with Ga. Because the properties of Ge subcell embedded in a multijunction cell are of the main interest the experimental simulation of the Ge subcell was performed by an additional thermal treatment of a single Ge cell. This treatment reproduces the Ge subcell in GaInP/GaInAs/Ge solar cells. These “subcell” structures are compared to the structures without any additional thermal treatment, which are referred “as grown.”

The I - V curves for GaInP/Ge “subcells” have similar behaviors to “as grown” structures at temperatures above 200 K, while at lower temperatures a strong difference was observed (Fig. 18.19). The dark I - V curves for “subcells” at 100 K (Fig. 18.19b) clearly demonstrate an S-shape behavior, which is somewhat similar to Shockley diode. The “set on” voltage of the S-shape increases with temperature decrease (from 0.78 V at 110 K to 0.9 V at 100 K).

The difference in I - V curves at low temperature was also observed under illumination (Fig. 18.19). The “as grown” sample demonstrates a normal behavior of I - V curves for photodiode structure (Fig. 18.19a). While the “subcell” structure has a knee in the I - V curves near the open circuit voltage (Fig. 18.19b). Another feature for the “subcell” structures is a reduction of the “set on” voltage value of the S-shape with increasing the light intensity. The S-shape disappeared when light intensity reaches approximately 0.1 W cm^{-2} .

It should be noted that at low temperature a similar S-shape behavior of the dark I - V curves as well as the both features of the light I - V curves: the knee and the dependence of the “set on” voltage on light intensity were also observed for triple-junction GaInP/GaAs/Ge solar cells fabricated by different manufactures.

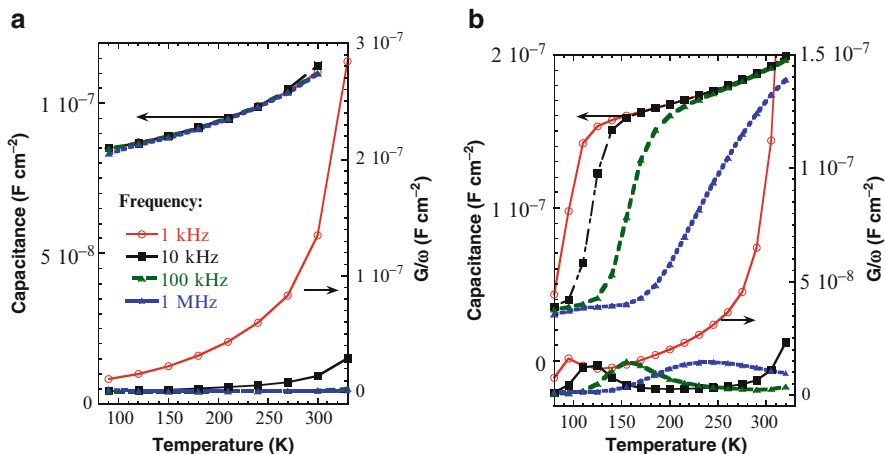


Fig. 18.20 C - T - ω and G/ω - T - ω curves for “as grown” (a) and “subcells” (b) GaInP/Ge heterostructures ($V_{DC} = 0$ V)

The admittance spectroscopy was applied for study of the GaInP/Ge heterostructures. The measured C - T - ω curves for “as grown” and “subcell” structures are presented in Fig. 18.20. For the “as grown” sample no specific features in the C - T - ω and G/ω - T - ω curves have been observed (Fig. 18.20a), which means that no potential barrier was detected. The “subcell” structure exhibits a characteristic step in the C - T - ω curves (Fig. 18.20b) accompanied by peaks in the G/ω - T - ω curves. The obtained value of the activation energy being in the range of 0.05–0.1 eV (for different samples) corresponds to the effective height of the potential barrier.

The experimental data of the light I - V curves (Fig. 18.19b) and the admittance spectroscopy (Fig. 18.20b) indicate a presence of the undesirable potential barrier for majority carriers in “subcell” heterostructures. The origin of this barrier formation could be related to the diffusion process at the GaInP/Ge interface. In fact, simultaneously with phosphorous (V-group atom) diffusion from GaInP to the Ge wafer, which forms the n-type region of the p-n junction in p-Ge, gallium, and indium diffusion to Ge also exists. As Ga and In are acceptor impurities for Ge, they could form a p-type region. The diffusion coefficient at growth temperature of phosphorous ($\sim 2.4 \times 10^{-11} \text{ cm}^2 \text{ s}^{-1}$) is much higher compared to that of gallium ($\sim 3.5 \times 10^{-13} \text{ cm}^2 \text{ s}^{-1}$) [39] that causes a deeper diffusion of phosphorous into the Ge wafer. However, the solubility limit of Ga in Ge ($4.5 \times 10^{20} \text{ cm}^{-3}$) is significantly higher than that of phosphorous ($5 \times 10^{19} \text{ cm}^{-3}$) [40, 41]. Therefore a local concentration of Ga atoms diffused to Ge at the GaInP/Ge interface could be significantly higher compared to that of P atoms leading to a narrow region with a p-type doping domination as schematically demonstrated in Fig. 18.21. The inversion of the conduction type in this region near the interface causes the potential barrier for electrons, which can affect the transport properties of a Ge solar cell.

Fig. 18.21 Schematic profile of P and Ga concentration in Ge substrate

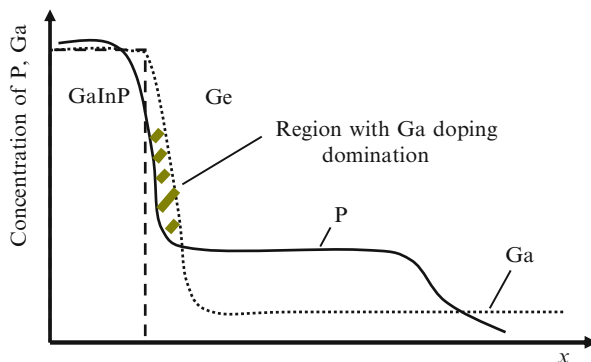
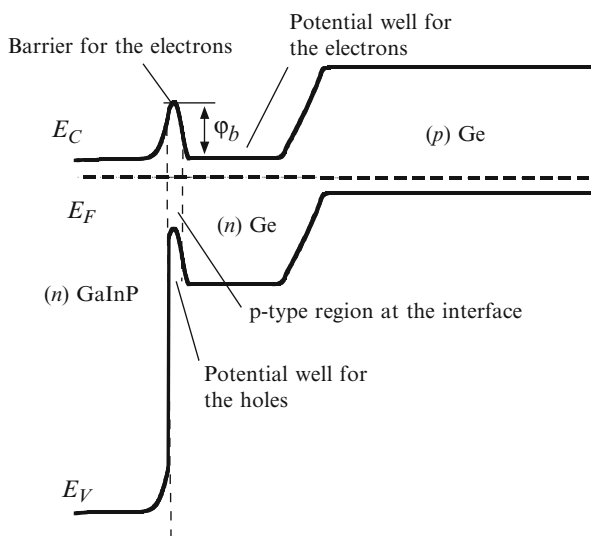


Fig. 18.22 Schematic band diagram proposed for “subcell” GaInP/Ge structures



The schematic band diagram with the potential barrier at the n-GaInP/n-Ge interface was proposed for “subcell” structures (Fig. 18.22). The behavior of the experimental I – V curves and admittance spectra was reproduced by the numerical simulations using the proposed model with a 60 nm thick p-type Ge ($3 \times 10^{17} \text{ cm}^{-3}$) layer introduced at the interface between the (n)GaInP and (n)Ge, which forms the potential barrier of about 0.1 eV [38]. The simulations have shown a good agreement with experimental data meaning that the presence of the potential barrier for electrons at the GaInP/Ge interface can explain the observed behavior at low temperatures for the “subcell” structures.

To confirm the presence of the potential barrier at the (n)GaInP/(n)Ge interface, the admittance spectroscopy and C – V profiling measurements were performed on specially fabricated Au/(n)GaInP/(n)Ge structures with a Schottky barrier on n-type

Ge wafers. The fabricated (n)GaInP/(n)Ge heterostructures were treated in the same conditions as “subcells.” The both admittance spectroscopy and C-V profiling measurements indicate the presence of the potential barrier at the (n)GaInP/(n)Ge interface [38]. The estimated values of the effective barrier height (0.12 eV) and width (55 nm) obtained with both methods are in good agreement and correspond well to the values estimated for “subcell” GaInP/Ge structures.

Thus, the undesirable potential barrier for majority carriers at the n-GaInP/n-Ge heterointerface was determined. The origin of this barrier layer can be attributed to the simultaneous diffusion of V (phosphorous) and III (gallium and indium) group atoms into the Ge substrate. This phenomenon seems to be a general problem of the III–V/IV heteroepitaxial interface, which should be considered.

5 Conclusion

The main loss mechanisms related to the interface properties in high efficiency III–V heterojunction solar cells were considered. It was shown that in case of epitaxial lattice matched solar cells their performance is mainly affected by band discontinuities leading undesirable potential barriers for major carriers. In particular, it was shown that a large valence band offset at the interface between III-phosphides and III-arsenides may result in parasitic potential barrier for the majority carriers in case of p-type isotype heterojunctions. Another discussed issues related to the properties of the interfaces between the III–V compounds and IV semiconductors. An example of GaInP/Ge heterojunction was considered. It has been shown that even in the case of perfect epitaxial interface, but in case of different groups of semiconductor compounds the inter-diffusion processes may affect the heterojunction properties.

References

1. King, R.R., Law, D.C., Edmondson, K.M., et al.: 40% efficient metamorphic GaInP/GaInAs/Ge multijunction solar cells. *Appl. Phys. Lett.* **90**, 183516 (2007)
2. Olson, J.M., Friedman, D.J., Kurtz, S.: High-Efficiency III-V Multijunction Solar Cells Handbook of Photovoltaic Science and Engineering. In: Luque, A., Hegedus, S. (eds.) John Wiley & Sons, Ltd, Chichester (2003)
3. Sharma, B.L., Purohit, R.K.: *Semiconductor Heterojunctions*. Pergamon, Elsevier Science & Technology (1974)
4. Andreev, V.M.: GaAs and high-efficiency space cells. In: Markvart, T., Castafier, L. (eds.) *Practical Handbook of Photovoltaics: Fundamentals and Applications*, pp. 433–2003. Elsevier Science, New York (417)
5. Adachi, S., GaAs, A.S.: AlAs, and $\text{Al}_x\text{Ga}_{1-x}\text{As}$: material parameters for use in research and device applications. *J. Appl. Phys.* **58**, R1–R29 (1985)
6. Watanabe, M.O., Ohba, Y.: Interface properties for GaAs/InGaAsP heterojunctions by the capacitance-voltage profiling technique. *Appl. Phys. Lett.* **50**, 906–908 (1987)

7. Olson, J.M., Ahrenkiel, R.K., Dunlavy, D.J., et al.: Ultralow recombination velocity at Ga_{0.5}In_{0.5}P/GaAs heterointerfaces. *Appl. Phys. Lett.* **55**, 1208 (1989)
8. Kurtz, S.R., Olson, J.M., Friedman, D.J., et al.: Passivation of interfaces in high-efficiency photovoltaic devices. In: Hasegawa, H., Hong, M., Lu, Z.H., Pearton S.J. (eds.) *Proc. of the Compound Semiconductor Surface Passivation and Novel Device Processing Symposium. Mat. Res. Soc. Symp. Proc.*, vol. 573. pp. 95–106. Warrendale, USA (1999)
9. Wojtczuk, S.J., Vernon, S.M., Sanfacion M.M.: Comparison of windows for *p*–on–*n* InGaP solar cells. *Proc. of the 23th IEEE Photovoltaic Specialists Conf.* pp. 655–658 (1993)
10. Gudovskikh, A.S., Kaluzhniy, N.A., Lantratov, V.M., et al.: Numerical modelling of GaInP solar cells with AlInP and AlGaAs windows. *Thin Solid Films* **516**, 6739–6743 (2008)
11. Lantratov, V.M., Kaluzhniy, N.A., Mintairov, S.A., Timoshina, N.K., Shvarts, M.Z., Andreev, V.M.: *Semiconductors* **41**, 727 (2007)
12. Stangl, R., Kriegl, M., Schmidt, M.: AFORS-HET, Version 2.2, a numerical computer simulation program for simulation of heterojunction solar cells and measurements. *Proc. of the IEEE 4th World Conf. on Photovolt. Energy Conv.* vol 2, pp. 1350–1353. Hawaii, USA (2006)
13. Yang, M.J., Yamaguchi, M., Takamoto, T., et al.: Photoluminescence analysis of InGaP top cells for high-efficiency multi-junction solar cells. *Sol. Energy Mater. Sol. Cells* **45**, 331–339 (1997)
14. Anderson, R.L.: Germanium-gallium arsenide heterojunction. *IBM J. Res. Dev.* **4**(3), 283 (1960)
15. Gudovskikh, A.S., Kalyuzhnyy, N.A., Lantratov, V.M., Mintairov, S.A., Shvarts, M.Z., Andreev, V.M.: Properties of interfaces in GaInP solar cells. *Semiconductors* **43**(10), 1363–1368 (2009)
16. Sze, S.M.: *Physics of Semiconductor Devices*, 2nd edn. John Wiley & Sons, New York (1981)
17. Vurgaftman, I., Meyer, J.R., Ram-Mohan, L.R.: Band parameters for III–V compound semiconductors and their alloys. *J. Appl. Phys.* **89**, 5815–5875 (2001)
18. Bour, D.P., Shealy, J.R., Wicks, G.W., Schaff, W.J.: Optical properties of Al_xIn_{1-x}P grown by organometallic vapor phase epitaxy. *Appl. Phys. Lett.* **50**, 615–617 (1987)
19. Jiang, C.-S., Friedman, D.J., Moutinho, H.R., Al-Jassim, M.M.: Profiling the built-in electrical potential in III–V multijunction solar cells. *Proc. of the 4th World Conf. on Photovolt. Energy Conv. (WCPEC-4)* pp. 853–856. Hawaii, USA (2006)
20. He, X., Razeghi, M.: *J. Appl. Phys.* **73**, 3284 (1993)
21. Dehaese, O., Wallart, X., Schuler, O., Mollot, F.: X-ray photoemission characterization of interface abruptness and band offset of Ga_{0.5}In_{0.5}P grown on GaAs. *J. Appl. Phys.* **84**, 2127–2132 (1998)
22. Liedenbaum, T.H.F., Valster, A., Severens, A.L.G.J., Hooft, G.W.: Determination of the GaInP/AlGaInP band offset C. *Appl. Phys. Lett.* **57**, 2698–2700 (1990)
23. Dawson, M.D., Duggan, G.: Exciton localization effects and heterojunction band offset in (Ga, In)P–(Al, Ga, In)P multiple quantum wells. *Phys. Rev. B* **47**, 12598–12604 (1993)
24. Dawson, M.D., Najda, S.P., Kean, A.H., et al.: Measurement of the direct energy gap of Al_{0.5}In_{0.5}P: implications for the band discontinuity at Ga_{1-x}In_xP/Al_yIn_{1-y}P. *Phys. Rev. B* **50**, 11190–11191 (1994)
25. Ishitani, Y., Minagawa, S., Kita, T., et al.: The optical processes in AlInP/GaInP/AlInP quantum wells. *J. Appl. Phys.* **80**, 4592–4598 (1996)
26. Vignaud, D., Mollot, F.: Conduction band offset in the Al_xGa_yIn_{1-x-y}P/Ga_{0.52}In_{0.48}P system as studied by luminescence spectroscopy. *J. Appl. Phys.* **93**, 384–389 (2003)
27. Patel, D., Hafich, M.J., Robinson, G.Y., Menoni, C.S.: Direct determination of the band discontinuities in In_xGa_{1-x}P/In_yAl_{1-y}P multiple quantum wells. *Phys. Rev. B* **48**, 18031–18036 (1993)
28. Lang, D.V., Cohen, J.D., Harbison, J.P.: Measurement of the density of gap states in hydrogenated amorphous silicon by space charge spectroscopy. *Phys. Rev. B* **25**, 5285–5320 (1982)

29. Gudovskikh, A.S., Kleider, J.P., Damon-Lacoste, J., et al.: Interface properties of a-Si:H/c-Si heterojunction solar cells from admittance spectroscopy. *Thin Solid Films* **511–512**, 385–389 (2006)
30. Gudovskikh, A.S., Kleider, J.P., Chouffot, R., et al.: III-phosphides heterojunction solar cell interface properties from admittance spectroscopy. *J. Phys. D: Appl. Phys.* **42**, 165307 (2009)
31. Fahrner, W.R., Goesse, R., Scherff, M., et al.: Admittance measurements on a-Si/c-Si heterojunction solar cells. *J. Electrochem. Soc.* **152**, G819–G823 (2005)
32. Kuo, H.C., Kuo, J.M., Wang, Y.C., et al.: Determination of the band offset of GaInP–GaAs and AlInP–GaAs quantum wells by optical spectroscopy. *J. Electron. Mater.* **26**, 944–948 (1997)
33. Gudovskikh, A.S., Kleider, J.P., Kalyuzhnyy, N.A., et al.: Band structure at heterojunction interfaces of GaInP solar cells. *Sol. Energy Mater. Sol. Cells* **94**, 1953–1958 (2010)
34. Gudovskikh, A.S., Zelentsov, K.S., Kalyuzhnyy, N.A., et al.: Interfaces in III-V multijunction solar cells: characterization and modelling. *Eur. Mater. Res. Soc. Conf. E-MRS 2011. Nice, France* (2011)
35. Friedman, D.J., Olson, J.M., Ward, S., et al.: Ge concentrator cells for III-V multijunction devices. *Proc. of the 28th IEEE Photovolt. Spec. Conf.* p. 965. Alaska, USA (2000)
36. Yamaguchi, M., Takamoto, M., Araki, K.: Super high-efficiency multi-junction and concentrator solar cells. *Sol. Energy Mater. Sol. Cells* **90**, 3068–3077 (2006)
37. Van Ruyven, L.J.: Phenomena at heterojunctions. *Annu. Rev. Mater. Sci.* **2**, 501–528 (1972)
38. Gudovskikh, A.S., Zelentsov, K.S., Kalyuzhnyy, N.A., et al.: Interface properties of GaInP/Ge heterostructure subcells of multijunction solar cells. *J. Phys. D: Appl. Phys.* **45**, 495305 (2012)
39. Hannay, N.B.: *Semiconductors*. Reinhold Publishing Corporation, New York (1959)
40. Zakharov, N.D., Rozhanskij, V.N., Korchazhkina, R.L.: Defects evolving from the decomposition of a solid solution of phosphorus in germanium. *Fiz. Tverd. Tela* **16**, 1444–1450 (1974) (in Russian)
41. Fistul, V.I., Yakovenko, A.G., Gvelesiani, A.A., Tsygankov, V.N., Korchazhkina, R.L.: Solubility and segregation of electrically active phosphorus in Ge. *Izv. Akad. Nauk SSSR Neorg. Mater.* **11**, 539–541 (1975)

Chapter 19

Broadband and Omnidirectional Anti-reflection Coating for III/V Multi-junction Solar Cells

Silke L. Diedenhofen, Gabriele Vecchi, Gerard Bauhuis,
and Jaime Gómez Rivas

Abstract Graded refractive index layers reduce the reflection and increase the coupling of light into a substrate by optical impedance matching at the interfaces. Due to the optical impedance matching, reflections at the interfaces are not possible for a broad wavelength range, rendering this type of anti-reflection coating a promising candidate for III/V multi-junction solar cells. Graded refractive index layers can be modeled using a transfer-matrix method for isotropic layered media. We derive the transfer-matrix method and we show calculations of the reflection from and the transmission into an AlInP layer coated with different anti-reflection coatings. We describe a new type of anti-reflection coating based on tapered semiconductor nanowires and we show reflection and transmission measurements of those kind of anti-reflection coatings on top of different substrates.

S.L. Diedenhofen (✉)

ICFO - The Institute of Photonic Sciences, Av. Carl Friedrich Gauss, 3, 08860 Castelldefels
(Barcelona), Spain
e-mail: silke.diedenhofen@icfo.es

G. Vecchi

FOM Institute AMOLF, c/o Philips Research Laboratories, High-Tech Campus 4,
5656 AE Eindhoven, The Netherlands
e-mail: gabrielevecchi@yahoo.it

G. Bauhuis

Institute for Molecules and Materials, Applied Materials Science, Radboud University
Nijmegen, Heyendaalseweg 135, 6525 AJ Nijmegen, The Netherlands
e-mail: G.Bauhuis@science.ru.nl

J.G. Rivas

FOM Institute AMOLF, c/o Philips Research, High-Tech Campus 4, 5656 AE Eindhoven,
The Netherlands

Applied Physics, Photonics & Semiconductor Nanophysics, Eindhoven University of
Technology, 5600 MB Eindhoven, The Netherlands
e-mail: rivas@amolf.nl

1 Introduction

Photovoltaic research has provided many solutions to increase the efficiency of solar cells [12]. Triple junction solar cells with efficiencies exceeding 40 % have already been demonstrated [13, 20]. These triple junction solar cells have a germanium cell at the bottom, a GaAs middle cell, and a InGaP cell at the top and because of their monolithic structure, the current of the solar cell is limited by the lowest current generated in one of the subcells. The bandgap energy of Ge is low and Ge absorbs light of a broad range of wavelengths, resulting in a current in this cell that exceeds the current in the GaAs and InGaP subcells, in which light in a narrower wavelength range is absorbed. Therefore, the anti-reflection coating for this type of solar cells has to be optimized for the wavelength range in which InGaP and GaAs are absorbing, i.e., 300–875 nm. For longer wavelengths, the reflection losses are less critical.

Nowadays, research is focusing on the realization of quadruple solar cells [30]. Quadruple solar cells have expected efficiencies exceeding 50 % [19]. A schematic of a possible quadruple solar cell is given in Fig. 19.1a. In this example, the solar cell consists of four different subcells, where the medium with the highest electronic bandgap energy forms the top subcell, for example, InGaP. Below the top subcell, GaAs, InGaAsP, and InGaAs subcells are fabricated, each absorbing the light of a spectral energy lower than the one above. The top-most layer of the solar cell is an AlInP window layer for passivation of the InGaP cell. In this example the quadruple cell consists of two mechanically stacked tandem cells. Both tandem cells are grown lattice matched, the first two subcells on GaAs and the last two subcells on InP [23].

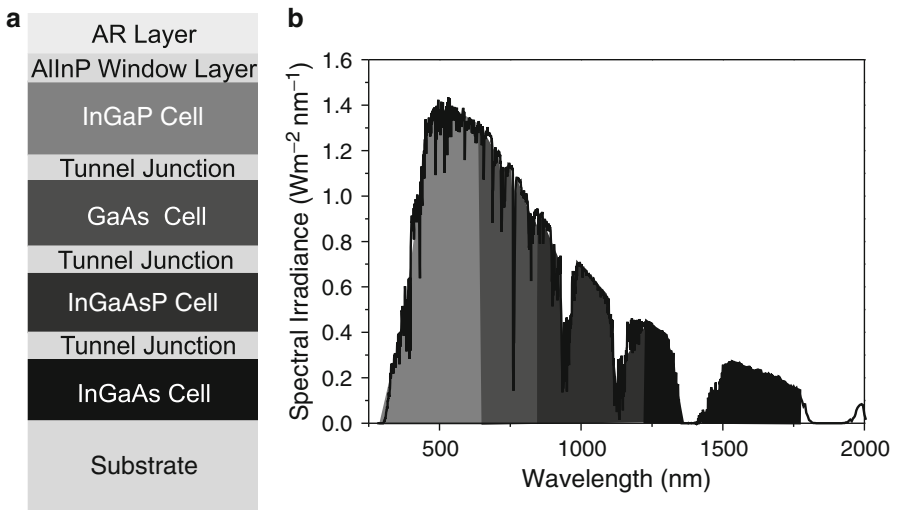
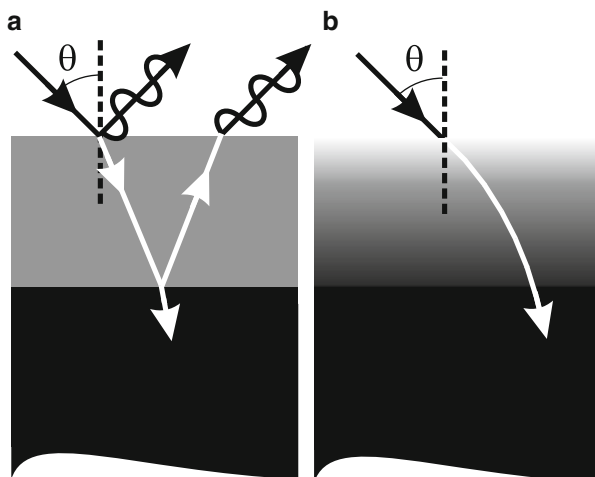


Fig. 19.1 (a) Schematic of a quadruple solar cell and (b) solar spectrum AM1.5D and absorption band of the individual junctions of the quadruple solar cell

Fig. 19.2 (a) Step index anti-reflection layers reduce the reflection due to destructive interference of light reflected at different interfaces. (b) Graded index coatings refract the light gradually into the substrate without allowing for reflections (figure reproduced from [6])



In these quadruple solar cells, each subcell absorbs nearly the same amount of photons. To show the wide spectral range that can be covered with multi-junction solar cells, Fig. 19.1b shows the solar irradiance standard AM1.5D, including the absorption bands of a quadruple-junction solar cell. Therefore, this type of solar cell requires an anti-reflection coating that covers a wavelength range from 300 to 1,700 nm [19]. The MgF_2/ZnS double-layer anti-reflection coatings that are used for III/V single junction solar cells are not sufficient for reducing the reflection over the broad wavelength range that is absorbed by the multiple junctions [9, 30]. Broadband anti-reflection layers are necessary to approach an optimal performance and the maximum efficiency that has been theoretically calculated. The spectral range of an anti-reflection coating is not the only factor limiting the efficiency of multi-junction solar cells. As these solar cells will be mainly installed in solar concentrator systems, the angular response has to be optimized as well.

Anti-reflective layers can be classified into two different types: (1) homogeneous layers or step-index layers and (2) inhomogeneous layers or graded index layers [8]. Step-index layers reduce the reflection due to destructive interference of light reflected at different interfaces [2]. The working principle of the step-index layers is illustrated in Fig. 19.2a. The fabrication of single anti-reflection layers is well known for decades [21], but the layer thickness and material have to be chosen carefully for each wavelength, angle, and substrate. The bandwidth of these coatings is lower than one octave, for example, 400–700 or 800–1,100 nm, and the angle of incidence is limited to 30° [15]. In contrast to step-index layers, graded refractive index layers reduce the reflection due to a gradually increasing refractive index from the top to the bottom. This gradual increase of the refractive index leads to optical impedance matching at the interfaces and does not allow for reflections (see Fig. 19.2b). Graded refractive index coatings have been extensively studied theoretically [8, 11, 27–29]. Southwell found that an optimum anti-reflection coating that reduces the reflection from glass should have a refractive index

distribution along its thickness that follows a quintic function, that is a polynomial with degree 5 [29]. Dobrowolski et al. provide an extensive comparison of different homogeneous and graded refractive index coatings and further investigate different types of quintic refractive index profiles [8, 27]. Theoretically, a drastic reduction of the reflection for angles up to 80° and for a wavelength range of one order of magnitude is possible, for example from 400 nm to 4 μm [27].

Since Bernhard reported in 1967 that the eyes of moths are covered with nanostructures that improve the light coupling [1], the effect of these nanostructures has been investigated intensely [4, 5, 10, 16–18, 22, 24, 25, 31, 32, 37, 38, 40–42]. Nanostructures improve the light coupling into the eyes of night-seeing moths by forming a layer with graded refractive index varying from a value close to 1 at the air–nanostructure interface to the refractive index of the eye. While it was known that graded refractive index coatings can reduce the reflection and therefore improve the coupling efficiency into high-index materials, fabrication of layers with a refractive index close to the refractive index of air remained challenging. Nowadays, nanostructuring techniques allow the fabrication of subwavelength structures which exhibit a very low effective refractive index when packed densely together. A complete review about nanostructured anti-reflection coatings is given in [3].

Recently, Xi et al. demonstrated a graded refractive index structure that was fabricated in a bottom-up process using SiO_2 and TiO_2 nanowires. These nanowires were fabricated by oblique-angle depositions on AlN [37]. The graded refractive index structure was achieved by varying the filling fraction of nanowires from one layer to the next, and by changing the material from a low refractive index material at the top (SiO_2) to a material with a higher refractive index at the bottom (TiO_2). Therefore, the evaporation of two materials is necessary for these coatings. Lee et al. employed a different bottom-up approach based on chemical vapor deposition. Using this technique, they have demonstrated anti-reflection coatings consisting of single materials [24]. These coatings are formed by ZnO nanowires grown on a Si substrate. Transmission measurements for visible wavelengths have not been possible because of the silicon substrates [24], and the effects of light scattering by the nanowires on the reduction of the reflection could not be determined. Further, the reflection from Si substrates has been reduced by etching different kinds of nanostructures into the substrate with top-down nanostructuring processes [16, 31, 32, 40]. With these etching techniques, very low values of the specular reflection have been reported. However, it has not been unambiguously demonstrated whether this reduced reflection occurs due to light scattering by the nanostructures, to an enhanced absorption in the anti-reflection layer, to refractive index matching to the substrate, or to a combination of these phenomena. An important limitation of etched silicon surfaces is that the anti-reflection layer is also absorbing. The fabrication of nonabsorbing anti-reflection layers on top of absorbing substrates is thus impossible by etching.

We describe in this chapter bottom-up grown tapered GaP nanowires forming a broadband and omni-directional anti-reflection coating [6, 7]. The bottom-up growth method used for fabricating nanowires allows hetero-epitaxial growth,

that is, the growth of different materials with different crystal structure on top of each other. Therefore, this technique provides the possibility for growing a passive anti-reflection layer on top of the active layer of the solar cell. Having a passive, non-absorbing anti-reflection layer is advantageous because of the following reasons. Surface carrier recombination can be dominant in active, absorbing nanostructured materials due to their large surface-to-volume-ratio. This effect is not relevant in the case of passive nanostructures, such as the proposed anti-reflection nanowire layers, since light is not absorbed in these structures. Carriers are generated only in the active multi-junction solar cell, beneath the nanowire coating, where they can be separated and extracted. While it has been proposed that a modified quintic refractive index profile can provide the largest reduction of the reflection, fabrication of modified index profiles using nanowires is not trivial. A quadratic index profile from conical nanowires is expected, since the refractive index is proportional to the nanowire filling fraction and the filling fraction scales with the area.

The aim of this chapter is to provide an introduction to graded-refractive index coatings that are based on tapered GaP nanowires. In Sect. 19.2 we introduce the transfer matrix method that is used to calculate the transmission through and reflection from multi-layer systems. We compare calculations of the photocurrent densities of III/V quadruple solar cells covered with different anti-reflection coatings. These calculations have revealed that a graded refractive index layer increases the photocurrent density of the solar cell with respect to a solar cell coated with a standard MgF_2/ZnS double-layer anti-reflection coating [7]. We describe in Sect. 19.3 the vapor–liquid–solid (VLS) growth of tapered GaP nanowires on GaP and AlInP/GaAs substrates. Further, we explain the anti-reflective behavior of GaP nanowires on top of a GaP substrate. We show transmittance and reflectance measurements that have unambiguously demonstrated that tapered GaP nanowires form an anti-reflection coating [6]. We end the chapter with a description of the anti-reflective behavior of tapered GaP nanowires on an AlInP/GaAs substrate [7]. The anti-reflective behavior of these nanowires constitute a proof-of-principle as they are the first experimental verification that tapered GaP nanowires could be used as an anti-reflection layer for III/V solar cells.

2 Transfer Matrix Method

The transfer matrix method can be used for modeling graded refractive index layers [39]. In this section, we shortly introduce this method. Let us consider a three-layer system as the one depicted in Fig. 19.3. The electric field amplitude of an electromagnetic plane wave of angular frequency ω propagating with the z-component of the wavevector k_z in the xz plane is given by

$$\mathbf{E} = \mathbf{E}(x)e^{i(\omega t - k_z z)}. \quad (19.1)$$

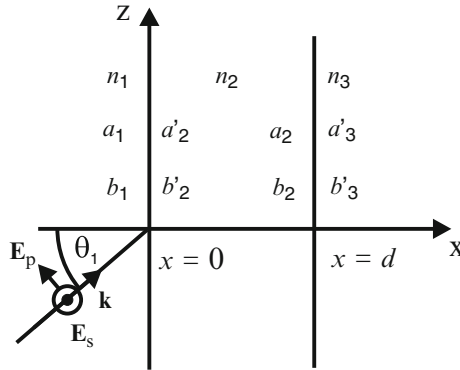


Fig. 19.3 A three-layer system consisting of three materials with refractive indices n_1 , n_2 , and n_3 , respectively. The field amplitudes at the interfaces are given by a_1, a'_2, a_2, a'_3 , for the right-traveling waves and b_1, b'_2, b_2, b'_3 for the left-traveling wave. The incident light beam with the wavevector \mathbf{k} and the angle of incidence θ_1 is defined in medium 1

Further, we assume that the light is linearly polarized, either s-polarized, i.e., $\mathbf{E} \parallel \mathbf{y}$ or $E_x = E_z = 0$, or p-polarized, i.e., $\mathbf{H} \parallel \mathbf{y}$ or $E_y = 0$. If we assume that light is only impinging on the three-layer system from medium 1, the electric field in layer 1 and 2 consists of a right- and left-traveling wave and can be written as

$$E(x) = ae^{-ik_x x} + be^{ik_x x} \equiv a(x) + b(x), \tag{19.2}$$

where $\pm k_x$ are the x-components of the wave vector given by $k_x = n_\alpha \frac{2\pi}{\lambda} \cos \theta_\alpha$ in medium α with refractive index n_α , angle inside the medium θ_α , and at vacuum wavelength λ . The field amplitudes a and b are constant in each homogeneous layer. The amplitude of the wave traveling to the right is represented by $a(x)$, while the left traveling component is described by $b(x)$. We define the various amplitudes at the interfaces between the different media as

$$\begin{aligned} a_1 &= a(0^-), \\ b_1 &= b(0^-), \\ a'_2 &= a(0^+), \\ b'_2 &= b(0^+), \\ a_2 &= a(d^-), \\ b_2 &= b(d^-), \\ a'_3 &= a(d^+), \\ b'_3 &= b(d^+) = 0, \end{aligned} \tag{19.3}$$

where 0^- represents the left side and 0^+ the right side of the interface at $x = 0$, and d^- and d^+ represent the left and right side of the interface at $x = d$ (see Fig. 19.3).

If we represent the left and right traveling components of the electric field as column vectors, the vectors at each side of the interface are related by

$$\begin{pmatrix} a_1 \\ b_1 \end{pmatrix} = \mathbf{D}_{1,2} \begin{pmatrix} a'_2 \\ b'_2 \end{pmatrix}, \quad (19.4)$$

$$\begin{pmatrix} a'_2 \\ b'_2 \end{pmatrix} = \mathbf{P}_2 \begin{pmatrix} a_2 \\ b_2 \end{pmatrix}, \quad (19.5)$$

$$\begin{pmatrix} a_2 \\ b_2 \end{pmatrix} = \mathbf{D}_{2,3} \begin{pmatrix} a'_3 \\ b'_3 \end{pmatrix} \quad (19.6)$$

where $\mathbf{D}_{1,2}$, and $\mathbf{D}_{2,3}$ are the so-called transmission matrices and \mathbf{P}_2 is the propagation matrix that accounts for the propagation in the layer. The matrices are defined for layer α as follows:

$$\mathbf{D}_{\alpha,\alpha+1} = \frac{1}{t_{\alpha,\alpha+1}} \begin{pmatrix} 1 & r_{\alpha,\alpha+1} \\ r_{\alpha,\alpha+1} & 1 \end{pmatrix} \quad (19.7)$$

and

$$\mathbf{P}_\alpha = \begin{pmatrix} e^{i\phi_\alpha} & 0 \\ 0 & e^{-i\phi_\alpha} \end{pmatrix}, \quad (19.8)$$

where $t_{\alpha,\alpha+1}$ and $r_{\alpha,\alpha+1}$ are the Fresnel amplitude transmission and reflection coefficients for the interface [2] and $\phi_\alpha = \frac{2\pi}{\lambda} n_\alpha \cos \theta_\alpha L$ is the phase change of light traveling through the layer, with L the thickness of the layer.

From (19.4) to (19.6), the amplitudes a_1 , b_1 , and a'_3 and b'_3 are related by the multiplication of the transmission matrix and the propagation matrix

$$\begin{aligned} \begin{pmatrix} a_1 \\ b_1 \end{pmatrix} &= \mathbf{D}_{1,2} \mathbf{P}_2 \mathbf{D}_{2,3} \begin{pmatrix} a'_3 \\ b'_3 \end{pmatrix} \\ &= \begin{pmatrix} M_{11} M_{12} \\ M_{21} M_{22} \end{pmatrix} \begin{pmatrix} a'_3 \\ b'_3 \end{pmatrix} \\ &= \mathbf{M} \begin{pmatrix} a'_3 \\ b'_3 \end{pmatrix}. \end{aligned} \quad (19.9)$$

The multiplication of the matrices can be represented by the transfer matrix \mathbf{M} consisting of the four elements M_{11} , M_{12} , M_{21} , and M_{22} .

The reflection and transmission of a plane wave through the three-layer structure for light coming from layer 1 are defined as

$$r = \left(\frac{b_1}{a_1} \right)_{b'_3=0}, \quad (19.10)$$

and

$$t = \left(\frac{a'_3}{a_1} \right)_{b'_3=0}, \quad (19.11)$$

respectively, where b'_3 is set to 0 as there is not a traveling wave from right to left in medium 3. Using (19.9), the amplitude reflection and transmission coefficients of the layered system are given by

$$r = \frac{M_{21}}{M_{11}} \quad (19.12)$$

and

$$t = \frac{1}{M_{11}}. \quad (19.13)$$

The reflectance R for the case that the medium of layer 1 is lossless is defined as

$$R = |r|^2 = \left| \frac{M_{21}}{M_{11}} \right|^2. \quad (19.14)$$

If the bounding layers, 1 and 3, are both dielectrics, with real n_1 and n_3 , the transmission T for a wave incident with an angle θ_1 is given by

$$T = \frac{n_3 \cos \theta_3}{n_1 \cos \theta_1} |t|^2 = \frac{n_3 \cos \theta_3}{n_1 \cos \theta_1} \left| \frac{1}{M_{11}} \right|^2, \quad (19.15)$$

with θ_3 the angle the light forms with the x axis in the third layer related to θ_1 by Snell's law.

While we have explained above the transfer-matrix method for three layers, the formalism for a multi-layer structure can be easily deduced by multiplying the transmission and propagation matrices for each layer involved. For modeling the graded refractive index of the nanowire layer, the nanowire layer is "sliced" into sublayers with a thickness much smaller than the wavelength and each having a slightly increased refractive index with respect to the preceding layer. This slicing of the layers is illustrated in Fig. 19.4. In this schematic, the gradient in color represents a change in refractive index.

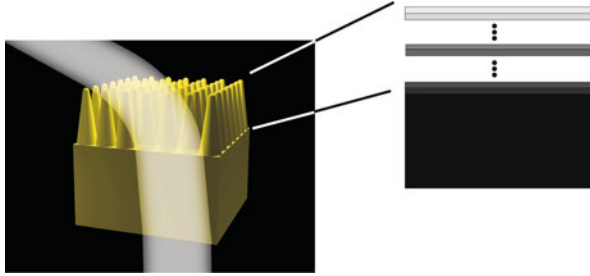


Fig. 19.4 The graded refractive index of conical nanowires is modeled by “slicing” the nanowire layer into sublayers, each having a slightly increased refractive index than the layer before, indicated by the gradient in *color*

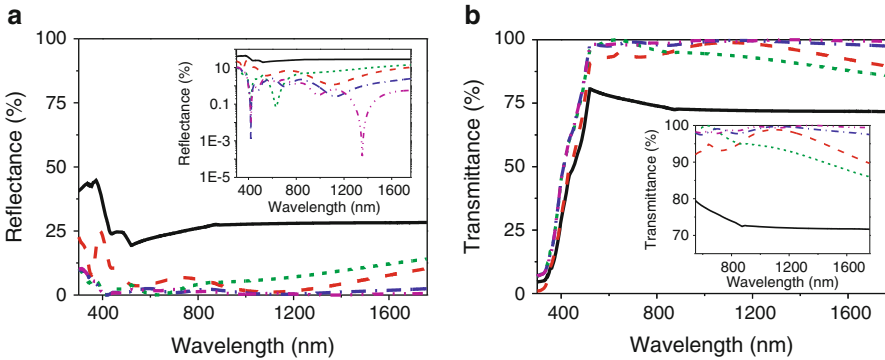


Fig. 19.5 (a) Calculation of the reflectance from and (b) transmittance through a 30 nm thin AlInP layer on top of an infinitely thick GaAs substrate coated with different anti-reflection layers in linear scale and logarithmic scale (inset of **a**). The *black solid curves* correspond to the reflectance and transmittance of a bare AlInP layer. The AlInP layer is coated with a MgF₂/ZnS anti-reflection coating with thicknesses of 89 nm (ZnS) and 105 nm (MgF₂) (*red dashed curves*), a parabolically increasing refractive index layer from 1.0 to 3.3 with a thickness of 250 nm (*olive short-dashed curves*), 500 nm (*blue dash-dotted curves*), and 1 μm (*magenta dash-dot-dotted curves*). The inset of (b) shows a zoom-in of the calculation of the transmittance (figures reproduced from [7])

2.1 Comparison of Different Anti-reflection Layers

It has been shown in [7] that graded refractive index anti-reflection coatings can increase the bandwidth of reduced reflection compared to double-layer antireflection coatings. Therefore, the reflection from and transmission through an AlInP window layer on top of an infinitely thick GaAs substrate coated with MgF₂/ZnS double-layer anti-reflection coating and graded refractive index anti-reflection coatings with different thicknesses have been calculated. Figure 19.5a displays the reflectance in a linear and logarithmic scale (inset), calculated using the transfer matrix

method from an AlInP layer with a thickness of 30 nm on top of an infinitely thick GaAs substrate coated with different anti-reflection layers. In these calculations, the refractive index of AlInP varies from 3.06–2.14i at 350 nm to 2.77 at 1,700 nm and the refractive index of GaAs from 3.28–2.06i at 350 nm to $3.36-5.32 \cdot 10^{-5}i$ at 1,700 nm. These values had been determined from ellipsometry measurements on the materials used in the experiments shown in the next section. The refractive indices of ZnS and MgF₂ vary between 2.8–0.13i and 2.27 and between 1.38 and 1.37, respectively, for wavelengths in the range 350–1,700 nm. The black solid curves in Fig. 19.5a show the calculated reflectance of the bare AlInP/GaAs layers without an anti-reflection coating. The reflectance from the AlInP/GaAs layers coated with a MgF₂/ZnS double-layer anti-reflection coating with thicknesses of 89 nm (ZnS) and 105 nm (MgF₂) is displayed by the red long-dashed curves in Fig. 19.5a. The calculated reflectance from the AlInP/GaAs layers coated with the MgF₂/ZnS anti-reflection coating is lower than 10 % for wavelengths between 450 and 1,700 nm. This anti-reflection coating reduces the reflection for a rather broad wavelength range, but the bandwidth is not optimal for reducing the reflectance over the wavelength range in which III/V multi-junction solar cells absorb light.

Further, Fig. 19.5a displays calculations of the reflectance from a 30 nm thin AlInP layer on top of an infinitely thick GaAs substrate that is coated with three lossless graded refractive index layers with different thicknesses. These calculations have been performed by “slicing” the graded refractive index layers into sublayers, according to Fig. 19.4. The refractive index of these layers is parabolically increasing from 1.0 to 3.3, and the thicknesses of the layers are 250, 500, and 1,000 nm, respectively. The anti-reflection layer has been implemented in the transfer-matrix calculation by considering sublayers with a thickness of 10 nm. These calculations are displayed in Fig. 19.5a by the olive short-dashed (250 nm), the blue dash-dotted (500 nm), and the magenta dashed-dot-dotted curves (1,000 nm), respectively. The graded refractive index layer with a thickness of 250 nm does not decrease the reflectance significantly for wavelengths longer than 850 nm, but the reflectance of the graded refractive index layers with a thickness of 500 and 1,000 nm are around 1 % or lower for a broad wavelength range. When a 1,000 nm thick graded refractive index anti-reflection coating is applied to the AlInP/GaAs layers, the reflection is the lowest. In this coating, the gradient of the refractive index between adjacent sublayers is the smallest.

Analogous to the reflectance calculations, calculations of the transmittance through a 30 nm thin AlInP layer on top of an infinitely thick GaAs substrate coated with the same anti-reflection layers as above have been performed. For these calculations, only the real part of the refractive index of GaAs has been considered. The calculated transmittance is shown in Fig. 19.5b in linear scale. The inset of Fig. 19.5b shows a zoom-in to highlight the differences of the coatings. The solar spectrum weighted transmittance (SSWT) has been determined from the calculated transmittance of the different layers by

$$\text{SSWT} = \frac{\int F(\lambda) \cdot T(\lambda) d\lambda}{\int F(\lambda) d\lambda}, \quad (19.16)$$

where $F(\lambda)$ and $T(\lambda)$ are the photon flux (AM1.5G, 1,000 W/m²) and the calculated transmittance, respectively. The integration has been performed in the wavelength range from 300 to 1,760 nm. The solar weighted transmittances of the five different samples are 69.2 % for a bare solar cell, 86.3 % for the MgF₂/ZnS anti-reflection coating, 89 % for the 250 nm thick graded refractive index layer, 91.5 % for the 500 nm thick graded refractive index layer, and 91.7 % for the 1 μm thick graded refractive index layer. Therefore, the solar weighted transmittance can be increased by 6.3 % when the 1 μm thick graded refractive index layer is used as an anti-reflection layer instead of the double layer MgF₂/ZnS coating.

Using the transfer matrix method, the reflectance from and transmittance through each individual layer of a III/V multi-junction solar cell have been calculated [14]. For these calculations the III/V solar cell consisted of InGaP, GaAs, InGaAsP, and InGaAs with electronic bandgaps that correspond to cut-off wavelengths of respectively 649, 873, 1,215, and 1,770 nm. From these values of transmittance and reflectance the absorption in each sublayer has been determined. Multiplying the absorption in each subcell by the photon flux results in the amount of photons absorbed in each subcell. The internal quantum efficiency (IQE) of each subcell was set to unity, meaning that every photon absorbed in one of the layers contributes to the photocurrent density of the cell. With this IQE the electron–hole pair generation was calculated, resulting in a subcell-specific photocurrent. With this method it is possible to calculate an unlimited amount of optical layers but it is limited by the difficulties in predicting the reflections between subcells. The model has been verified by comparing the calculated reflection of a single junction solar cell coated with different anti-reflection layers to the measured reflection [14].

The photocurrent densities in each subcell and the resulting photocurrent density of the quadruple solar cell are given in Table 19.1 for a solar cell coated with a perfect anti-reflection coating, without anti-reflection coating, with a MgF₂/ZnS double-layer anti-reflection coating, and with graded refractive index layers with parabolically increasing refractive index from 1.0 to 3.3 over a thickness of 250, 500, and 1,000 nm. The first column in Table 19.1 shows the maximum photocurrent densities and the maximum efficiency of the solar cell if a perfect anti-reflection layer is used, i.e., all incident light within the absorption band of the solar cell is transmitted into and absorbed in the solar cell. The maximum photocurrent density that can be achieved when all incident light is absorbed is 13.36 mA/cm². When applying a graded refractive index layer with a thickness of 1,000 nm and a parabolically increasing refractive index from 1 to 3.3 to the solar cell, a photocurrent density of 13.28 mA/cm² can be achieved. This photocurrent density is limited by the bottom cell. The calculated photocurrent density in the solar cell coated with the MgF₂/ZnS double-layer anti-reflection coating is 12.54 mA/cm² and is in all subcells lower than the photocurrent density in the solar cell coated with the thickest-graded refractive index layer. The photocurrent

Table 19.1 Calculated photocurrent densities of a III/V quadruple junction solar cell coated with a perfect anti-reflection layer (AM1.5G), different graded refractive index (GI) anti-reflection layers that have a parabolically increasing refractive index from 1.0 to 3.3 over the given thickness, a MgF₂/ZnS double-layer anti-reflection coating with thicknesses of 89 nm (ZnS) and 105 nm (MgF₂) (AR layer), and a bare cell without anti-reflection layer

	AM1.5G	1,000 nm GI layer	500 nm GI layer	250 nm GI layer	AR layer	Bare cell
Top cell current (mA/cm ²)	16.71	13.82	13.8	13.81	12.54	10.83
Second cell current (mA/cm ²)	15.4	15.08	15.09	14.88	14.4	11.45
Third cell current (mA/cm ²)	14.98	14.94	14.9	14.16	14.72	10.86
Bottom cell current (mA/cm ²)	13.36	13.28	13.13	11.91	12.54	9.57
Resulting current (mA/cm ²)	13.36	13.28	13.13	11.91	12.54	9.57

Table reproduced from [7]

density in the solar cell coated with this graded refractive index layer is increased by 5.9 % with respect to that of the cell with the double-layer anti-reflection coating.

3 GaP Nanowires as Anti-reflection Layers

We introduce in this section the growth of the tapered GaP nanowires on GaP and AlInP/GaAs substrates and we show the anti-reflective behavior of tapered nanowires on both substrates. We describe first the anti-reflection properties of GaP nanowires that are grown on top of a GaP substrate. As the electronic bandgap energy of GaP is 2.26 eV ($\lambda = 548$ nm) transmission and reflection measurements have been possible for wavelengths longer than 548 nm to unambiguously demonstrate that the tapered GaP nanowires form an anti-reflection layer. Further, we describe the growth of GaP nanowires on top of AlInP/GaAs substrates and we describe the reflection and transmission of these layers. Because of the electronic bandgap of GaAs being 1.43 eV ($\lambda = 873$ nm), transmission measurements have been only possible for wavelengths longer than 873 nm.

3.1 Growth of Tapered GaP Nanowires

GaP nanowires were fabricated using the VLS growth mechanism by metal-organic vapor phase epitaxy (MOVPE) [36]. For VLS growth, a metal catalyst particle is used to seed the growth of the nanowire underneath it. The VLS growth allows the hetero-epitaxial growth of nanowires, i.e., on a substrate of a different material than that of the nanowire. The nanowires have been grown on a double-side polished (111) GaP substrate with a thickness of 500 μm (Sample I) or on a 30 nm thick AlInP layer on top of a polished (100) n⁺⁺-doped GaAs wafer (Sample II). A schematic of Sample I is given in Fig. 19.6a and in Fig. 19.7a for Sample II.

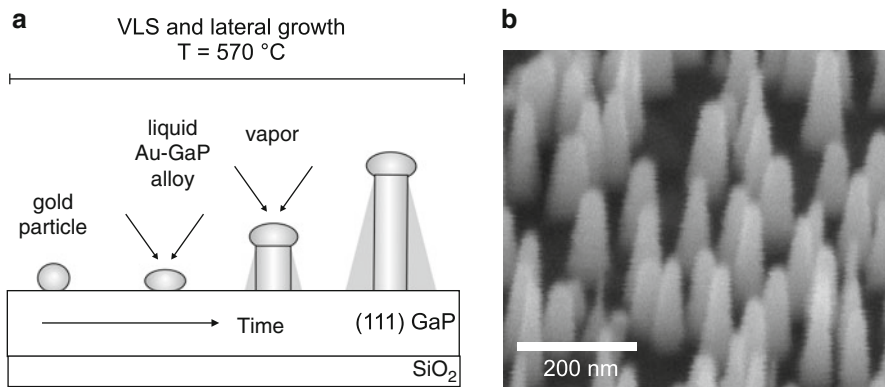


Fig. 19.6 (a) Schematic describing the growth of the nanowires on Sample I. At a temperature of 570 °C, both VLS and lateral growth occur simultaneously resulting in tapered or conical nanowires. (b) Scanning electron micrograph of Sample I

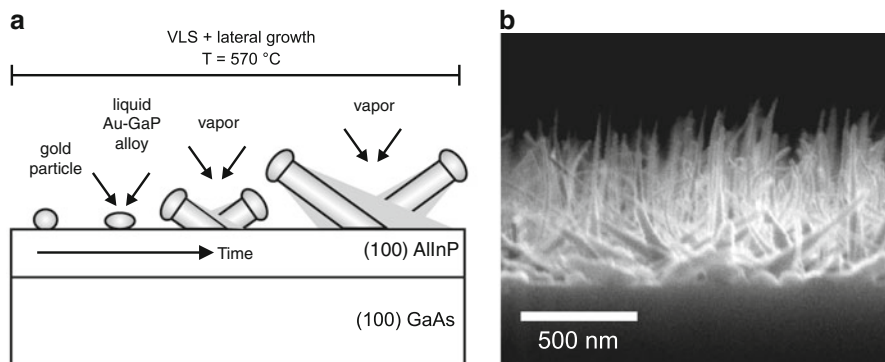


Fig. 19.7 (a) Schematic of the growth of the nanowires on Sample II. The nanowire growth is catalyzed by a gold particle deposited on a (100) semiconductor substrate. Tapered nanowires grow under an angle of 35° with respect to the substrate at a temperature of 570 °C and the length of the nanowires is defined by the growth time. (b) Cross-sectional SEM image of Sample II

For Sample I a film of SiO₂ with a thickness of 500 nm was deposited on the backside of the GaP substrate to avoid etching of this surface during a surface cleaning process before the growth.

The morphology of the nanowires depends on the growth conditions and the crystallographic direction of the substrate. Conically shaped nanowires can be grown by adjusting the temperature of the substrate such that VLS and lateral growth occur simultaneously. As nanowires grow preferentially into the [111] direction [35], the nanowire growth direction can be varied by choosing substrates with different crystallographic direction. Nanowire growth on (111) substrates results in vertically aligned nanowires, while nanowires grown on (100) substrate form an angle of 35° with the substrate. In the following, we describe the growth of

Table 19.2 Growth time and temperature of GaP nanowires on the given substrates

Sample	Substrate	Growth time (s)	Growth temperature (°C)	Length (nm)
I	GaP	600	570	178 ± 25
II	AlInP/GaAs	180	570	600 ± 100

Sample **I** is grown on top of a GaP substrate, Sample **II** on top of an AlInP layer on a GaAs substrate. The averaged layer thickness is also listed. This value was obtained from SEM images

nanowires on (111) GaP substrates and on (100) AlInP/GaAs substrates. The VLS growth of nanowires on (111) substrates is schematically described in Fig. 19.6a. Gold with an equivalent layer thickness of 0.3 nm has been evaporated on a GaP substrate. The gold-coated substrate is placed in a reactor, where it is heated in a phosphine (PH₃) atmosphere. The gold film forms small gold particles with random size distribution and position during annealing in the MOVPE reactor. The gold particles melt and form liquid droplets. When the desired growth temperature is reached, the trimethyl-gallium (TMG) is added into the reactor. The semiconductor crystal grows at the solid/liquid interface. After growth, the reactor is cooled down in a phosphine atmosphere. The initial diameter of the nanowires is determined by the size of gold particles, and thus determines the diameter at the top of the rod. When the growth temperature exceeds a critical value it is also possible to induce side-wall growth [34]. The side-wall growth of the nanowires is not catalyzed by the gold particle, therefore at low temperatures in the MOVPE reactor the sidewalls grow at a much slower rate than the VLS growth. For Samples I and II, the temperature was such that lateral growth is significant. The base of the nanowires is exposed to the side-wall growth for the longest time, therefore, the diameter is the largest at the base, and it gradually decreases toward the top of the rod. The apex angle of the conical shape can be adjusted, as the lateral growth is more pronounced with respect to the vertical growth at higher temperatures [34]. The growth parameters of both samples are given in Table 19.2. Figure 19.6b shows a scanning electron microscopy (SEM) image of Sample **I**. Due to tapering of the nanowires, the GaP filling fraction increases from the top to the bottom of the layer.

To investigate the feasibility of nanowire graded refractive index layers on top of multi-junction solar cells, layers of tapered GaP nanowires have been grown on top of AlInP. AlInP is commonly used as upper window layer in III/V solar cells [33]. For matching the growth conditions to that of a real solar cell device, 30 nm of AlInP have been grown on top of a polished (100) n⁺⁺-doped GaAs wafer. This AlInP layer has been protected by a 300 nm thick GaAs layer. Before nanowire growth, this GaAs layer has been removed by etching the substrate in 28 % NH₄OH:H₂O₂:H₂O (1:1:100). Immediately after this etching step, gold with an equivalent layer thickness of 0.3 nm has been evaporated and the gold-coated substrate has been placed in the MOVPE reactor.

Considering that nanowires grow preferentially into the [111] direction [35], the orientation of the nanowires with respect to the substrate can be varied by growing them on substrates with different crystallographic orientation. On a (100) substrate, the nanowires grow preferentially with an angle of 35° with respect to the substrate

surface according to the $\langle 111 \rangle$ direction. III/V solar cells are typically fabricated using (100) GaAs substrates. Figure 19.7a displays a schematic representation of the nanowire growth on a (100) substrate. The growth of nanowires on top of (100) substrates is catalyzed by a gold particle. The top diameter of the nanowires is defined by the size of this gold particle. According to the growth of Sample I, the temperature of the substrate during growth was chosen such that vertical and lateral growth occurs. Sample II is grown on an AlInP layer on top of a (100) GaAs substrate. Therefore, the nanowires on this sample grow preferentially with an angle of 35° with respect to the substrate surface. Figure 19.7b shows a SEM image of Sample II. The nanowires are grown epitaxially with preferential growth in the $\langle 111 \rangle$ direction, however, some nanowires also grow normal to the substrate. The thickness of the nanowire layer has been determined to be 600 ± 100 nm. The variation of the layer thickness can be attributed to nanowires growing into different crystallographic directions with different growth rates.

3.2 GaP Nanowires on Top of GaP Substrates

A graded refractive index layer can be achieved in ensembles of conically shaped nanowires, due to the variation of the filling fraction of GaP along the growth direction of the nanowires [6]. To determine the anti-reflection characteristics of conically shaped GaP nanowires, the broadband specular reflectance from and direct transmittance through Sample I has been measured. The reflectance has been measured at an angle of incidence of 6° with respect to the surface normal and the transmittance was measured at normal incidence. The resulting transmittance and reflectance spectra are displayed in Fig. 19.8a and c, respectively, with blue open circles for Sample I. For comparison, the black solid squares show the transmittance and reflectance measurements of a bare GaP substrate with a layer of 500 nm of SiO₂ at the backside (Reference I). The sharp absorption edge at 2.26 eV ($\lambda = 548$ nm) is visible for both samples that corresponds to the electronic band gap of GaP. The small dip in the transmittance and the maximum in the reflectance of the GaP substrate around 1.76 eV ($\lambda = 700$ nm) are due to a Fabry-Pérot resonance in the SiO₂ layer at the backside of the GaP substrate. From the sum of the reflectance and transmittance measurements, the scattering losses of the samples can be estimated (see Fig. 19.8e). The transmittance plus reflectance is 100 % for energies below 2.26 eV for Reference I (black solid squares). As expected, there are no losses in the substrate below the band gap energy of GaP. Interband absorption has a dominant influence at higher energies.

Figure 19.8a reveals that the transmittance through Sample I is not increased with respect to the transmittance through the bare GaP substrate from ~ 1.88 eV ($\lambda = 660$ nm) to 2.3 eV (550 nm). At these energies, Rayleigh scattering by the nanowires reduces the transmittance and cancels its enhancement due to the anti-reflection [26]. However, the transmittance increases for lower energies as scattering losses become negligible. The transmittance of Sample I at 1.38 eV ($\lambda = 900$ nm), is increased by

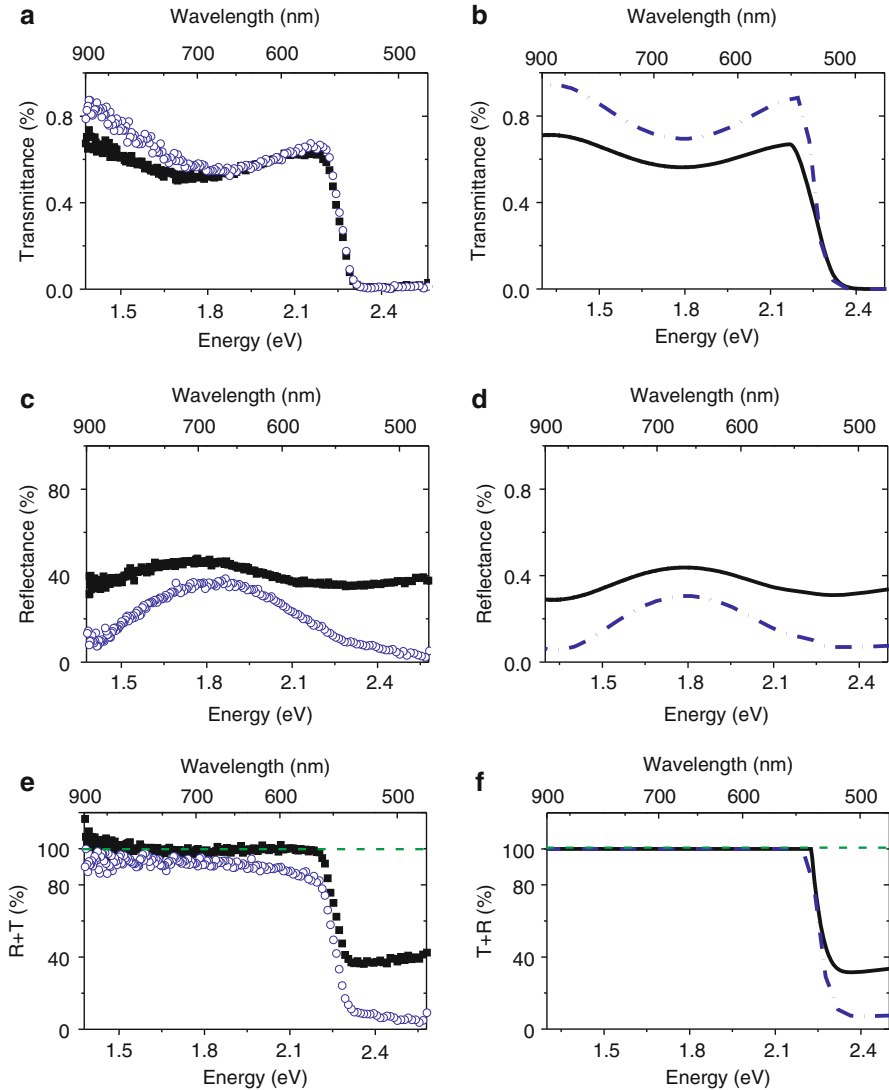


Fig. 19.8 (a) Measured transmittance and (b) calculated transmittance for normal incidence, (c) measured reflectance and (d) calculated reflectance at an angle of incidence of 6° , (e) the sum of measured reflectance and transmittance, and (f) the sum of calculated reflectance and transmittance. The measurements (calculations) for a bare GaP substrate with one side covered by a 500 nm (490 nm) layer of SiO_2 are shown as *black squares* (*black solid curve*). The *blue circles* (*blue dashed-dotted curve*) correspond to the measurements (calculations) of Sample I (figure reproduced from [6])

20 % compared to the substrate. The small shift of the dip in transmittance (see Fig. 19.8a) and the peak in reflectance (see Fig. 19.8c) at ~ 1.85 eV (670 nm), compared to the transmittance and reflectance of Reference I, is related to a Fabry–Pérot interference in the nanowire layer, which is superimposed to the reflection in the back SiO_2 layer.

The sum of reflectance and transmittance (Fig. 19.8e) of Sample I (blue open circles) increases from 85 % at 2.15 eV ($\lambda = 575$ nm) to ~ 95 % at 1.38 eV ($\lambda = 900$ nm). The small reduction of the sum of reflectance and transmittance when increasing the energy can be attributed to light scattering in the nanowire layer. The enhanced transmittance measurements of Fig. 19.8a demonstrate that the reduction in specular reflectance reported in Fig. 19.8c is not only due to surface roughness or scattering in the nanowire layer, but also to the refractive-index matching that the nanowire layer provides between air and GaP.

Figure 19.8b, d, f show calculations of the transmittance and reflectance, of Sample I (blue dashed-dotted curve) and a bare GaP substrate covered on one side with a SiO_2 layer with a thickness of 490 nm (black solid curve). These calculations have been performed with the transfer-matrix method described in Sect. 19.2. The calculated system consists of five layers: air, nanowire layer, GaP substrate, SiO_2 , and air. The nanowire layer is sliced into 50 horizontal sublayers, each of them having a thickness of 5 nm. For Sample I a quadratically increase of the refractive index per sublayer with the length of the nanowires has been assumed. This quadratic increase is based on the assumption that the filling fraction is proportional to the square of the diameter of the nanowires, and that the effective refractive index is proportional to the GaP filling fraction. From the calculations, a variation of the refractive index over the nanowire layer length from 1.1 up to 2.1 has been determined. The calculations (Fig. 19.8b, d, f) show the same trend as the measurements (Fig. 19.8a, c, e). The small discrepancies can be attributed to the aforementioned scattering, which is not included in the calculations. Both measurement and calculation show a reduction for the sum of transmittance and reflectance (Fig. 19.8e, f) with respect to the bare GaP substrate for energies higher than the electronic band gap of GaP. This reduction can be attributed to an enhanced absorption in GaP due to the anti-reflection coating.

To determine the effect of the anti-reflection layer independently from the reflections in the substrate, calculations of the reflectance from and transmittance through a nanowire layer on top of an infinitely thick GaP substrate (black solid curves, Fig. 19.9) have been performed. These calculations are compared in Fig. 19.9a, b to the reflectance from and transmittance through a similar nanowire layer on top of a 500 μm thick GaP substrate covered with 490 nm SiO_2 on the backside (red dashed curves). While there is a minor oscillation visible in the calculation assuming an infinite substrate, the calculations of the same anti-reflection layer on top of 500 μm GaP covered with 490 nm of SiO_2 on the backside show large variations in the transmittance and reflectance as a function of wavelength. Comparing both calculations, it can be concluded that the modulation of the transmittance and reflectance through Sample I are due to Fabry–Pérot resonances in the SiO_2 layer in the bottom of the wafer and on the nanowire film on top.

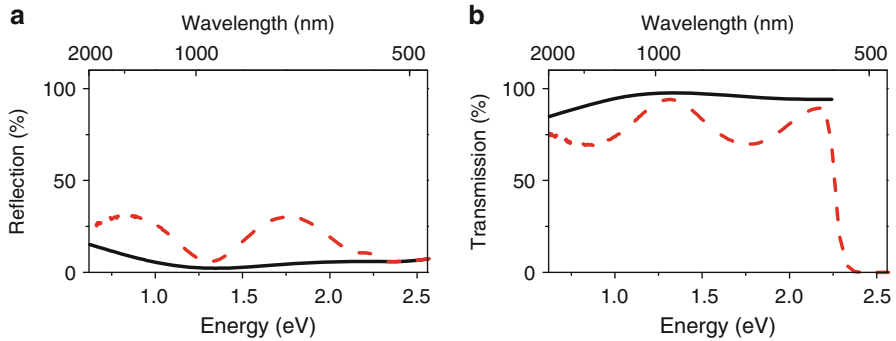


Fig. 19.9 (a) Calculated reflectance and (b) transmittance for a graded refractive index layer with a parabolically increasing refractive index on top of an infinite GaP substrate (*black solid curve*) and on a 500 μm thick GaP substrate with a 490 nm thick SiO₂ layer on the backside (*red dashed curve*). The graded index layer has a thickness of 250 nm and the refractive index is varied from 1.1 at the top to 2.1 at the bottom

The minor oscillations in the calculation of the anti-reflection layer on top of the infinitely thick GaP substrate, indicates that the nanowire layer acts both as a graded-refractive-index coating and a single-layer interference coating.

3.3 Tapered GaP Nanowires on AlInP/GaAs Substrates

We have shown in the previous section that tapered GaP nanowires form a graded refractive index layer that increases light coupling into a GaP substrate. Here, we show that GaP nanowires on top of an AlInP/GaAs substrate similarly reduce the reflection from and increase the transmission through an AlInP/GaAs substrate. While it has been possible to measure the transmission through the nanowire layer on top of a GaP substrate for wavelengths as low as 550 nm, the transmission can only be measured for wavelengths longer than 873 nm when the nanowires are on top of an AlInP/GaAs substrate. For wavelengths shorter than 873 nm, the incident light is fully absorbed in the GaAs substrate and no light is transmitted.

To demonstrate that GaP nanowires on top of an AlInP/GaAs substrate form a graded refractive index layer, measurements of the angle-integrated reflection from and transmission through the AlInP/GaAs substrate (Reference II) and the AlInP/GaAs substrate coated with tapered nanowires (Sample II) have been done. The total reflectance and transmittance has been measured for wavelengths between 350 and 2,000 nm using the integrating sphere PerkinElmer Lambda 950 commercial setup. The PerkinElmer Lambda 950 spectrometer consists of a tungsten-halogen and a deuterium lamp, in combination with an integrating sphere, a photomultiplier for visible, and a PbS detector for infrared light. The working principle of an integrating sphere is described in Fig. 19.10a in transmission and

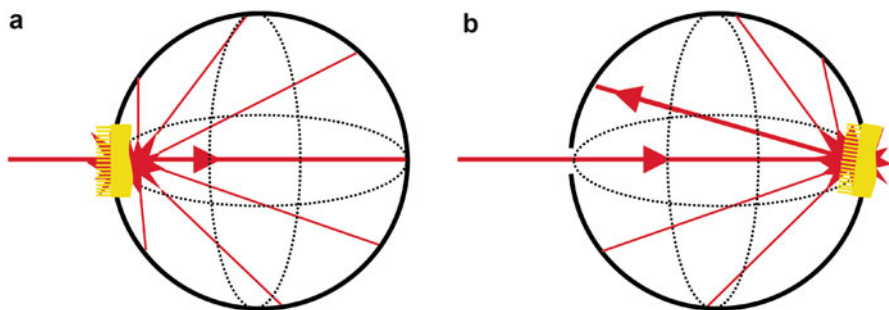


Fig. 19.10 Schematic of the integrating sphere used for (a) total transmittance measurements and (b) for total reflectance measurements. The direct transmitted or reflected beam and the diffuse transmitted or reflected beam can be measured simultaneously by using the integrating sphere. For the reflectance measurement, the sample is mounted with an angle of 8° with respect to the incident light so that the specularly reflected beam does not escape from the sphere

in Fig. 19.10b in reflection. For the transmittance measurements, the sample was mounted in front of the integrating sphere, so that all transmitted light was collected, that is the zeroth-order and diffusely transmitted light. For the reflectance measurements, the sample was mounted at the backside of the integrating sphere with its surface normal at an angle of 8° with respect to the incident light beam, so that all the reflected light from the sample could be collected and detected. The integrating sphere is coated at the inside with a diffusive coating. Specularly reflected or transmitted light and the diffusely reflected or transmitted light are randomized and the intensity is equally distributed over the sphere. Measuring the intensity on each point of the sphere will lead to the same result. The diffusely reflected light is measured by making a small opening in the integrating sphere in such a way that the specularly reflected light escapes from the sphere. The reflection measurements on the samples are normalized by the reflection of a white-standard to obtain the absolute reflectance of the sample. From the total reflectance, R , and the diffuse reflectance, R_{dif} , the specular reflectance, R_{spec} , can be determined by $R_{\text{spec}} = R - R_{\text{dif}}$. Measuring the reflection with an integrating sphere is a good technique for determining the characteristics of nanostructured anti-reflection coatings on top of absorbing substrates. As the specularly and diffusely reflected light can be determined independently, anti-reflective and scattering properties of the nanostructures can be determined independently.

The measured total reflectance (black squares), diffuse reflectance (red circles), and the resulting specular reflectance (blue triangles) from Reference II are displayed in Fig. 19.11a. At wavelengths below the electronic bandgap of GaAs (873 nm) the total and specular reflectance are similar (28 %) and the diffuse reflectance is negligible. This low diffuse reflectance is expected for a flat layer. For wavelengths longer than 873 nm, the reflectance increases to 36 %, as the reflectance of the backside of the substrate is contributing to the measurement. At these wavelengths, the diffuse reflectance is slightly increased, indicating that the backside of the sample is rougher than the front side. From these two

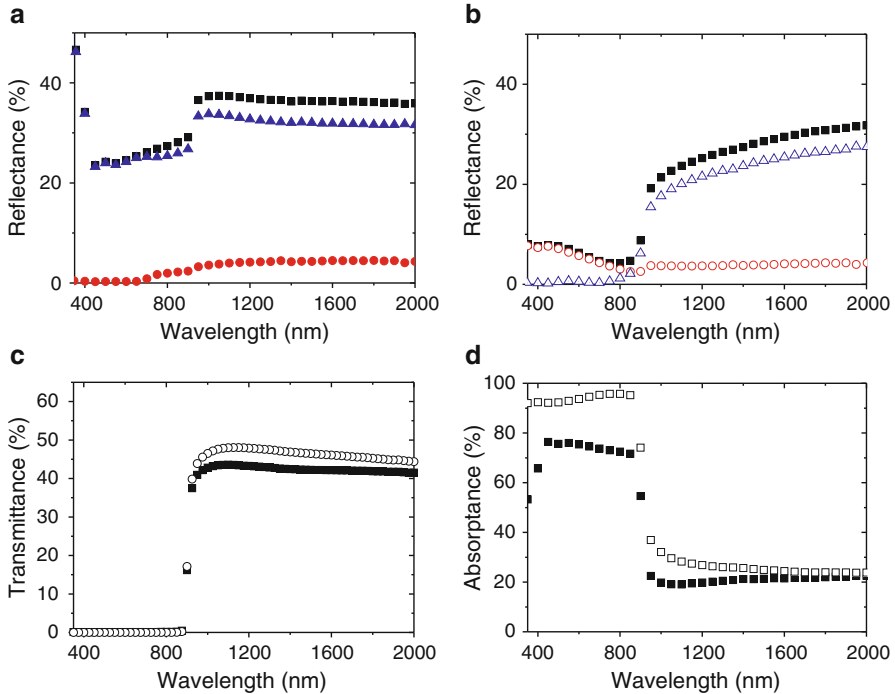


Fig. 19.11 (a) Measured reflectance from the AlInP/GaAs substrate and (b) measured reflectance from the AlInP/GaAs substrate coated with tapered nanowires. In both graphs the total reflectance (black squares), specular reflectance (blue triangles), and diffuse reflectance (red circles) are displayed. (c) Measured total transmittance through and (d) measured absorbance in the AlInP/GaAs substrate (solid circles) and the AlInP/GaAs substrate coated with tapered nanowires (open circles) (figure reproduced from [7])

measurements, the contribution to the reflection of the substrate backside and the AlInP front side of the sample can be understood.

Additionally, the total and diffuse reflectance from Sample II have been measured. These measurements are displayed in Fig. 19.11b. The total reflectance (black squares) is strongly reduced compared to the measurement of the AlInP/GaAs substrate. While the total reflectance is lower than 10 % at wavelengths below 873 nm, the total reflectance increases for wavelengths above the electronic bandgap of GaAs as in the case of the bare AlInP/GaAs substrate. This increased total reflectance can be attributed to the reflectance of the backside of the substrate. The diffuse reflectance (red circles) is dominating the total reflectance for wavelengths shorter than 873 nm. The increasing diffuse reflectance with decreasing wavelength is due to scattering of light from the thick bottom part of the nanowires [26]. For wavelengths longer than 865 nm, the diffuse reflectance is similar to that of the AlInP/GaAs substrate, indicating that scattering of light from the nanowires is negligible at these wavelengths.

Although these first measurements have demonstrated that the reflectance of the AlInP/GaAs substrate coated with tapered nanowires is significantly reduced with respect to the bare AlInP/GaAs substrate, the reflectance of the nanowire sample needs to be further decreased for a perfect anti-reflection coating. Therefore, a smaller gradient of the refractive index has to be realized. Further, the bottom diameter of the nanowires has to be decreased to reduce the diffuse reflection at short wavelengths and the density of nanowires has to be increased to achieve a high index of refraction at the interface with the AlInP.

To determine the enhancement of the coupling of light into the AlInP/GaAs substrate by the tapered nanowires, the total transmittance through Reference II (solid circles in Fig. 19.11c) and through Sample II (open circles) have been measured. For wavelengths below 873 nm, the transmission is negligible in both measurements, as the light is absorbed in the 360 μm thick GaAs substrate. For wavelengths above the electronic bandgap of GaAs ($\lambda = 873$ nm), the transmittance through the bare AlInP/GaAs substrate increases strongly, reaching 43 % for wavelengths longer than 950 nm. The transmittance through Sample II is 47 %. The transmittance through Sample II and Reference II are influenced by residual free-carrier absorption for wavelengths above the electronic bandgap of GaAs, which also causes the rather low increase of the transmittance through Reference II coated with nanowires with respect to the bare AlInP/GaAs substrate. This residual absorptance A can be determined by $A = 100 \% - R - T$, with R and T being the total reflectance and transmittance, respectively. The absorptance in Reference II and in Sample II are displayed in Fig. 19.11d. The absorption in the nanowire-coated sample (open squares) is increased with respect to the uncoated substrate (solid squares) for all wavelengths. For the wavelength range below 873 nm, the fact that less light is reflected is the main cause for the enhanced absorption (absorptance higher than 90 %) in the sample coated with nanowires. For the wavelength range above 873 nm, the increased absorption might be attributed to diffusely transmitted light due to the nanowires. The diffusely transmitted light travels through the GaAs with a longer optical path length, resulting in a higher absorption probability due to free-carrier absorption.

The desired anti-reflection coating should omnidirectionally reduce the reflection and increase the transmission into the solar cell because multi-junction solar cells are usually installed in concentrator systems. To determine the angle-dependence of the response of the anti-reflection layer, the zero-order transmission through Sample II and Reference II have been measured for angles of incidence from 0° to 55° using unpolarized light. Figure 19.12 displays the transmission through Sample II normalized to the transmission through Reference II. For all wavelengths and angles, the normalized transmission is above unity, meaning that for all wavelengths and angles, the transmission into the AlInP/GaAs layer is increased by the presence of the nanowire layer. The insets in Fig. 19.12 show cuts to the measurement at a wavelength of 1,300 nm as a function of angle of incidence, and at an angle of incidence of 25° as a function of wavelength. These cuts show that overall the transmission is increased by around

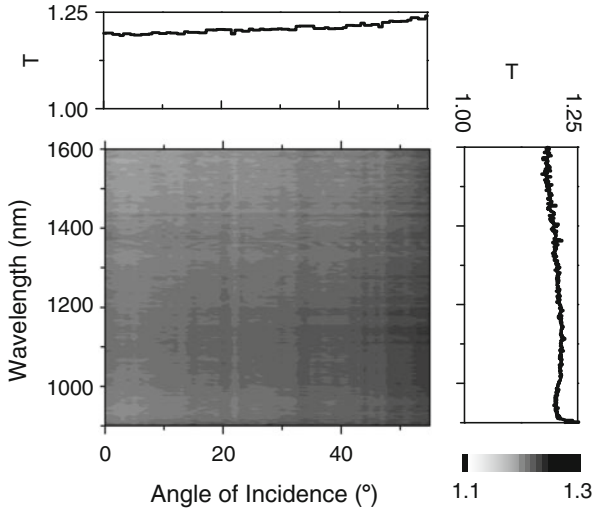


Fig. 19.12 Measured transmission through the AlInP/GaAs substrate coated with nanowires normalized to the transmission through an AlInP/GaAs substrate as a function of angle of incidence and wavelength. The *top inset* shows a cut to the measurement at 1,300 nm and the *right inset* shows a cut at an angle of incidence of 25° (figure reproduced from [7])

20 %. In a Fresnel lens-based concentrator system the light is typically incident over angles from 0° to 30° ; however, higher angles of incidence would allow thinner concentrator modules.

Solar cells that are installed in concentrator systems have to be robust to high irradiance levels. To determine if the nanowire layer is stable under concentrated sunlight, Sample II has been illuminated with 125 suns (AM1.5G) for 4 h. During the illumination, the sample was mounted on a Cu base for temperature control and the temperature of the sample was kept at 50°C . The reflection before and after illumination on five different positions of the sample has been measured, and no significant difference between the measurements has been found. From the reflection measurements before and after illumination with 125 suns, it has been concluded that the nanowire layer is stable under concentrated sunlight.

4 Conclusions

In conclusion, we have described the anti-reflective properties of layers of GaP nanowires. These anti-reflective properties have been determined by wavelength- and angle-dependent transmittance and reflectance measurements. The reflectance and transmittance of graded refractive index layers are described quantitatively using a transfer-matrix method for isotropic layered media. We have presented calculations showing that the photocurrent density of a III/V quadruple solar cell

can be increased when applying a graded refractive index coating to the solar cell instead of the standard MgF_2/ZnS double-layer anti-reflection coating.

GaP nanowires have been fabricated by metal organic vapor phase epitaxy using the VLS mechanism and we have shown that the enhanced transmittance and corresponding reduced reflectance of these layers is related to a graded refractive index in the nanowire layer. The enhanced direct transmittance show that scattering and absorption are weak in these layers.

For demonstrating the feasibility of graded refractive index layers on solar cells, layers of tapered GaP nanowires on AlInP/GaAs substrates have been grown and the transmission and reflection properties of these layers have been investigated. The reflection from AlInP/GaAs substrates can be reduced by coating the substrate with a graded refractive index layer. The described experiments reveal that the total reflection is indeed reduced over a broad spectral range when applying tapered GaP nanowires on top of an AlInP/GaAs substrate and that the transmission into the substrate is increased for a wide spectral and angular range. These results render tapered nanowires a promising candidate for increasing the efficiency of III/V multi-junction solar cells.

Acknowledgements SLD acknowledges funding from European Commission's Seventh Framework Programme for Research under contract PIEF-GA-2011-298596 and thanks Dr. Fiona Beck for useful discussions. This work is part of the research program of the "Stichting voor Fundamenteel Onderzoek der Materie (FOM)," which is financially supported by the "Nederlandse organisatie voor Wetenschappelijk Onderzoek (NWO)" and is part of an industrial partnership program between Philips and FOM.

References

1. Bernhard, C.G.: Structural and functional adaption in a visual system. *Endeavour* **26**, 79 (1967)
2. Born, M., Wolf, E.: *Principles of Optics*, 6th edn. Cambridge University Press, Cambridge (1997)
3. Chattopadhyay, S., Huang, Y.F., Jen, A.J., Ganguly, A., Chen, K.H., Chen, L.C.: Anti-reflecting and photonic nanostructures. *Mater. Sci. Eng.* **R 69**, 1–35 (2010)
4. Chiu, C.H., Yu, P., Kuo, H.C., Chen, C., Lu, T.C., Wang, S., Hsu, S.H., Cheng, Y.J., Chang, Y. C.: Broadband and omnidirectional antireflection employing disordered GaN nanopillars. *Opt. Express* **16**, 8748–8754 (2008)
5. Clapham, P.B., Hutley, M.C.: Reduction of lens reflexion by the "moth eye" principle. *Nature* **224**, 281–282 (1973)
6. Diedenhofen, S.L., Vecchi, G., Algra, R.E., Hartsuiker, A., Muskens, O.L., Immink, G., Bakkers, E.P.A.M., Vos, W.L., Gómez Rivas, J.: Broad-band and omnidirectional antireflection coatings based on semiconductor nanorods. *Adv. Mater.* **21**, 973–978 (2009)
7. Diedenhofen, S.L., Grzela, G., Haverkamp, E., Bauhuis, G., Schermer, J., Gómez Rivas, J.: Broadband and omnidirectional anti-reflection layer for III/V multi-junction solar cells. *Sol. Energy Mater. Sol. Cells* **101**, 308–314 (2012)
8. Dobrowolski, J.A., Poitras, D., Ma, P., Vakil, H., Acree, M.: Toward perfect antireflection coatings: numerical investigation. *Appl. Opt.* **41**(16), 3075–3083 (2002)
9. Friedman, D.: Progress and challenges for next-generation high-efficiency multijunction solar cells. *Curr. Opin. Solid State Mater. Sci.* **14**, 131–138 (2010)

10. Gombert, A., Glaubitt, W., Rose, K., Dreiholz, J., Bläsi, B., Heinzel, A., Sporn, D., Döll, W., Wittwer, V.: Subwavelength-structured antireflective surfaces on glass. *Thin Solid Films* **351**, 73–78 (1999)
11. Grann, E.B., Moharam, M.G., Pommet, D.A.: Optimal design for antireflective tapered two-dimensional subwavelength grating structures. *J. Opt. Soc. Am. A* **12**, 333–339 (1995)
12. Green, M.A., Emery, K., Hishikawa, Y., Warta, W., Dunlop, E.D.: Solar cell efficiency tables (version 41). *Prog. Photovolt.: Res. Appl.* **21**(1), 1–11 (2013)
13. Guter, W., Schöne, J., Philipps, S.P., Steiner, M., Siefert, G., Wekkeli, A., Welsler, E., Oliva, E., Bett, A.W., Dimroth, F.: Current-matched triple-junction solar cell reaching 41.1 % conversion efficiency under concentrated sunlight. *Appl. Phys. Lett.* **94**, 223504 (2009)
14. Haverkamp, E.J., Mulder, P., Bauhuis, G.J., Schermer, J.J., Voncken, M.M.A.J., van Deelen, J., van Niftrik, A.T.J., Larsen, P.K.: Spectrum and bandgap optimized antireflection coating by numerical simulations. In: 20th European Photovoltaic Solar Energy Conference, Barcelona, Spain, 6–10 June (2005)
15. Hobbs, D.S., MacLeod, B.D., Riccobono, J.R.: Update on the development of high performance anti-reflecting surface relief micro-structures. *Proc. SPIE* **6545**, 65450Y (2007)
16. Huang, Y.F., Chattopadhyay, S., Jen, Y.J., Peng, C.Y., Liu, T.A., Hsu, Y.K., Pang, C.L., Lo, H. C., Hsu, C.H., Chang, Y.H., Lee, C.S., Chen, K.H., Chen, L.C.: Improved broadband and quasi-omnidirectional anti-reflection properties with biomimetic silicon nanostructures. *Nat. Nanotechnol.* **2**, 770–774 (2007)
17. Kanamori, Y., Sasaki, M., Hane, K.: Broadband antireflection gratings fabricated upon silicon substrates. *Opt. Lett.* **24**, 1422–1424 (1999)
18. Kikuta, H., Toyota, H., Yu, W.: Optical elements with subwavelength structured surfaces. *Opt. Rev.* **10**, 63–73 (2003)
19. King, R.R., Law, D.C., Edmondson, K.M., Fetzer, C.M., Kinsey, G.S., Yoon, H., Krut, D.D., Ermer, J.H., Sherif, R.A., Karam, N.H.: Advances in high-efficiency III–V multijunction solar cells. *Adv. Optoelectron.* **2007**, 29523 (2007)
20. King, R.R., Law, D.C., Edmondson, K.M., Fetzer, C.M., Kinsey, G.S., Yoon, H., Sherif, R.A., Karam, N.H.: 40% efficient metamorphic GaInP/GaInAs/Ge multijunction solar cells. *Appl. Phys. Lett.* **90**, 183516 (2007)
21. Laff, R.A.: Silicon nitride as an antireflection coating for semiconductor optics. *Appl. Opt.* **10** (4), 968–969 (1971). <http://ao.osa.org/abstract.cfm?URI=ao-10-4-968>
22. Lalanne, P., Morris, G.M.: Antireflection behaviour of silicon subwavelength periodic structures for visible light. *Nanotechnology* **8**, 53–56 (1997)
23. Law, D.C., King, R., Yoon, H., Archer, M., Boca, A., Fetzer, C., Mesropian, S., Isshiki, T., Haddad, M., Edmondson, K., Bhusari, D., Yen, J., Sherif, R., Atwater, H., Karam, N.: Future technology pathways of terrestrial III–V multijunction solar cells for concentrator photovoltaic systems. *Sol. Energy Mater. Sol. Cells* **94**(8), 1314–1318 (2010)
24. Lee, Y.J., Ruby, D.S., Peters, D.W., McKenzie, B.B., Hsu, J.W.P.: ZnO nanostructures as efficient antireflection layers in solar cells. *Nano Lett.* **8**, 1501 (2008)
25. Lohmüller, T., Helgert, M., Sundermann, M., Brunner, R., Spatz, J.P.: Biomimetic interfaces for high-performance optics in the deep-UV light range. *Nano Lett.* **8**, 1429 (2008)
26. Muskens, O.L., Diedenhofen, S.L., van Weert, M.H.M., Borgström, M.T., Bakkens, E.P.A.M., Gómez Rivas, J.: Epitaxial growth of aligned semiconductor nanowire metamaterials for photonic applications. *Adv. Funct. Mater.* **18**, 1039 (2008)
27. Poitras, D., Dobrowolski, J.A.: Toward perfect antireflection coatings. 2. Theory. *Appl. Opt.* **43**(6), 1286–1295 (2004)
28. Rayleigh, L.: On reflection of vibrations at the confines of two media between which the transition is gradual. *Proc. Lond. Math. Soc.* **s1-11**(1), 51–56 (1879)
29. Southwell, W.H.: Gradient-index antireflection coatings. *Opt. Lett.* **8**(11), 584–586 (1983)
30. Stan, M., Aiken, D., Cho, B., Cornfeld, A., Ley, V., Patel, P., Sharps, P., Varghese, T.: High-efficiency quadruple junction solar cells using OMVPE with inverted metamorphic device structures. *J. Cryst. Growth* **312**, 1370–1374 (2010)

31. Sun, C.H., Min, W.L., Linn, N.C., Jiang, P.: Templated fabrication of large area subwavelength antireflection gratings on silicon. *Appl. Phys. Lett.* **91**, 231105 (2007)
32. Sun, C.H., Jiang, P., Jiang, B.: Broadband moth-eye antireflection coatings on silicon. *Appl. Phys. Lett.* **92**, 061112 (2008)
33. Tommila, J., Polojärvi, V., Aho, A., Tukiainen, A., Viheriälä, J., Salmi, J., Schramm, A., Kontio, J.M., Turtiainen, A., Niemi, T., Guina, M.: Nanostructured broadband antireflection coatings on AlInP fabricated by nanoimprint lithography. *Sol. Energy Mater. Sol. Cells* **94**, 1845–1848 (2010)
34. Verheijen, M.A., Immink, G., de Smet, T., Borgström, M.T., Bakkers, E.P.A.M.: Growth kinetics of heterostructured GaP-GaAs nanowires. *J. Am. Chem. Soc.* **128**, 1353–1359 (2006)
35. Wacaser, B.A., Dick, K.A., Johansson, J., Borgström, M.T., Deppert, K., Samuelson, L.: Preferential interface nucleation: an expansion of the VLS growth mechanism for nanowires. *Adv. Mater.* **21**, 153–165 (2009)
36. Wagner, R.S., Ellis, W.C.: Vapor–liquid–solid mechanism of single crystal growth. *Appl. Phys. Lett.* **4**, 89–90 (1964)
37. Xi, J.Q., Schubert, M.F., Kim, J.K., Schubert, E.F., Chen, M., Lin, S.Y., Liu, W., Smart, J.A.: Optical thin-film materials with low refractive index for broadband elimination of fresnel reflection. *Nat. Photonics* **1**, 176–179 (2007)
38. Yan, X., Poxson, D.J., Cho, J., Welsler, R.E., Sood, A.K., Kim, J.K., Schubert, E.F.: Enhanced omnidirectional photovoltaic performance of solar cells using multiple-discrete-layer tailored- and low-refractive index anti-reflection coatings. *Adv. Funct. Mater.* **23**, 583–590 (2013)
39. Yeh, P.: *Optical Waves in Layered Media*. Wiley, New York (1988)
40. Yu, Z., Gao, H., Ge, H., Chou, S.Y.: Fabrication of large area subwavelength antireflection structures on Si using trilayer resist nanoimprint lithography and liftoff. *J. Vac. Sci. Technol. B* **21**, 2874–2877 (2003)
41. Zhou, W., Tao, M., Chen, L., Yang, H.: Microstructured surface design for omnidirectional antireflection coatings on solar cells. *J. Appl. Phys.* **102**, 103105 (2007)
42. Zhu, J., Yu, Z., Burkhard, G.F., Hsu, C.M., Connor, S.T., Xu, Y., Wang, Q., McGehee, M., Fan, S., Cui, Y.: Optical absorption enhancement in amorphous silicon nanowire and nanocone arrays. *Nano Lett.* **9**, 279–282 (2009)

Chapter 20

Radiation Effects of Space Solar Cells

Xin Gao, Sheng-sheng Yang, and Zhan-zu Feng

Abstract Photovoltaic solar arrays are preferably used as primary power source for majority of spacecraft today. The space radiation environment causes gradual solar cells performance degradation, thus limiting the lifetime of the solar array. In planning a space mission, engineers need to know the expected cell degradation in the space radiation environment, so a degradation model is required to predict the behaviors of solar cells in space. In this chapter, the irradiation experimental results were presented about silicon, single-junction and triple-junction GaAs solar cells, and thin film solar cells to compare radiation effects of electrons and protons on these solar cells, and also to provide experimental data for predictions of the cell performances. An approach developed by the US Naval Research Laboratory (NRL), also usually referred to as displacement damage dose methodology, is presented to predict triple-junction GaAs solar cell degradation using a particular case of protons and electrons irradiation. Enough information was presented to enable readers to make their own predictions for other solar cells using the method that works the best in a specific case. Compared to the on-orbit data from several satellite solar arrays, a good match can be found between the on-orbit data and the predicted results by NRL methodology, indicating the NRL method can provide the valuable reference for solar array design. However, the performance prediction of a-Si solar cells in space cannot be readily predicted by the NRL approach, and is still under discussion.

X. Gao (✉) • S.-s. Yang
Science and Technology on Vacuum & Cryogenics Technology
and Physics Laboratory, Lanzhou Institute of Physics, China Academy
of Space Technology, Lanzhou 730000, China
e-mail: gaoxin510@hotmail.com

Z.-z. Feng
Science and Technology on Material Performance Evaluating in Space Environment
Laboratory, Lanzhou Institute of Physics, Lanzhou 730000, China

1 Introduction

Photovoltaics are, by far, the primary space power source for earth orbiting satellites and many interplanetary spacecrafts, due to a combination of factors, e.g. high reliability, proven manufacturing, good qualification heritage, scalability to the required power levels and affordable costs. To date, all satellite solar-powered systems have used solar cells made of single-crystal semiconductors, namely silicon, and single-junction, dual-junction and triple-junction GaAs-based technologies. However, maximum on-orbit power provided by current space power generation technologies is expected to reach the limitations of approximate 30 kW, due to inefficient stowage and low mass efficiency. Emerging thin film photovoltaics (TFPV) for space power offer major improvements in power per stowed volume and power per mass over current space power technology, which have the potentials to enable larger space power requirements to be met in the near future.

Solar cells used in space will face a totally different situation from that used as terrestrial power. The space environment is often characterized by a harsh radiation environment that consists of many different types of charged particles varying over a wide energy range. Exposure to these charged particles typically degrades the electrical performance of semiconductor devices, especially less-shielded space solar array, thus limiting the lifetime of the solar array. Therefore, to be used in space, understanding the radiation response of solar cell is extremely important for accurate predictions of the expected mission lifetime. However the radiation damage to solar cells is a complex function of cell material and doping, cover glass and backplane shielding, and the system orbit and lifetime. With the rapid development of new solar cell types, satellite designers and space cell manufacturers need to continually qualify new cell technologies or new generations of existing technologies for the use of these solar cells in space.

2 Space Radiation Environment

The space radiation environment consists of a variety of relativistic electrons, protons, and other heavier ions. These particles can cause both ionization and displacement damage effects in space systems. System exposure to the particles varies depending on location in space, the solar cycle, and the amount of shielding provided to the sensitive parts of the system. The most damaging particles on solar cells are the high-energy electrons and protons that can cause lattice displacement damage. For earth-orbiting and near-earth systems, the primary source of these particles is from the geomagnetically trapped particles in the Van Allen belts. Damaging protons can also be encountered during periods of high solar activity when solar coronal mass ejections occur. The electron energies, according to current models, range from a few eV to about 10 MeV. Trapped protons range in energy up to about 400 MeV and solar protons can reach 1 GeV. For missions to other planets

such as Jupiter, the proton energies are similar to those found for earth systems, but the electron energies can reach in the hundreds of MeVs. The radiation environments for most of earth orbiting spacecrafts are described in the following sections.

2.1 Geostationary Earth Orbit (GEO) Mission

The GEO spacecrafts are used primarily for commercial telecommunication applications and designed for longer lifetime. The main environmental concern on solar array is radiation damage of solar cells primarily from the trapped electrons. Trapped protons are lower in number compared with electrons in this orbit, although still significant. In addition, the flux of higher energy protons emitted during solar flares may be very damaging to the solar cell, because geomagnetic shielding is much weaker in GEO. Solar array performance degradation during a single solar flare activity may be equal or greater than that accumulated after a full year or lifetime of spacecraft exposure to the normal trapped radiation fluxes. It is very important to note that future communication spacecrafts are being planned for longer operational life times, the lifetime may vary in the range of 15–20 years. These longer lifetimes mean solar array is exposed to the higher level of radiation fluxes. The most important solar cell characteristics for these missions are high end-of-life (EOL) efficiency; a characteristic that can be achieved significantly by improved efficiency, resistance to radiation damage, and lightweight.

2.2 Low Earth Orbit (LEO) Mission

Low earth orbit is a roughly circular earth orbit at relatively low altitudes of 500–2,000 km. LEO has advantages of low cost from the point of view of launching and power requirements on board the spacecraft. The LEO low inclination orbits (those passing near the Equator regions) are characterized by low levels of radiation damage from the trapped electrons and protons. High inclination orbits (those passing near or over the Polar regions) suffer greater radiation damage because shielding by the earth's magnetic field is not as effective as it is near the equator. In addition, the South Atlantic Anomaly is more susceptible to higher radiation damage because the trapped radiation belts dip to lower altitudes. However, the radiation environment in these altitudes is less than the GEO orbits.

2.3 Medium Earth Orbit (MEO) Mission

A medium earth orbit (MEO) is the region of space around the earth above LEO and below GEO. The most common useful satellites in this region is for navigation, communication, and geodetic/space environment science. The most common

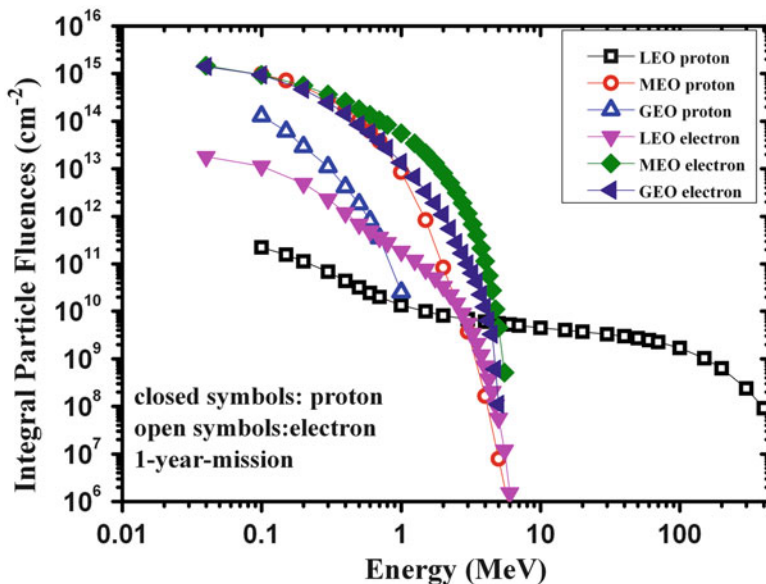


Fig. 20.1 Integral electron and proton spectra for a typical GEO, MEO, and LEO orbit using the traditional AP8 and AE8 radiation models

altitude is approximate 20,200 km, which yields an orbital period of 12 h, as used, for example, by the Global Positioning System (GPS), other satellites in MEO include Glonass (with an altitude of 19,100 km), Compass (with an altitude of 21,500 km) and Galileo (with an altitude of 23,222 km) constellations. Communications satellites that cover the North and South Pole are also put in MEO. The orbital periods of MEO satellites range from about 2 to nearly 24 h. The MEO orbits are attractive for both military and commercial applications, but MEO presents a harsh radiation environment. The MEO orbit contain high fluences ($>10^{13}/\text{cm}^2/\text{year}$) of protons with energies less than 1 MeV, and moderate fluences ($>10^{11}/\text{cm}^2/\text{year}$) of protons with energies greater than 1 MeV. The electron spectrum is similar to GEO, but a higher fluence over 1 MeV.

Figure 20.1 presents the integral electron and proton spectra of GEO (35,870 km, 0°), MEO (20,000 km, 42.5°), and LEO (800 km, 99°) orbits, using the traditional AP8 and AE8 radiation models and the JPL stormy solar flare model [1].

3 Space Solar Cells and Their Components

Space solar cells are now available in the production lots, except thin film solar cells. When a solar array is located in a spacecraft in orbit, the surfaces are exposed to an isotropic spectrum of radiation and the solar array is typically shielded. The front surface of a space solar cell is usually shielded against radiation

damage using specially attached coverglass, while the underside is typically shielded by the substrate and the panel material. The shielding material attenuates the incident particle spectrum so that surface of the solar cell actually experiences a slowed-down spectrum. Flexible thin film photovoltaic blanket (FTFPV) consists of low cost thin film solar cell network deposited on flexible polymer or stainless steel substrate and integrated monolithically. Among of numerous thin-film cell technologies, amorphous silicon (a-Si) and Cu(In,Ga)Se₂ (CIGS)-based thin-film solar cells have shown more appropriate performances for space use, which have superior radiation hardness compared to single crystalline solar cells and the self annealing effect that is highly temperature dependent and the radiation damage on thin-film solar cells can be partially reversed. Each solar cell technology is briefly discussed in the following sections.

3.1 Space Solar Cells

3.1.1 Silicon (Si) Solar Cell

Si solar cells were used extensively for majority of the space solar array applications in the past and also uses presently for low cost and low power space mission applications. The solar cell is basically made by using either 10 or 20 Ω m, p-type silicon wafer with back surface reflector (BSR) and front and rear weldable contacts, with an average production lot efficiency of ~13 % at 1 AMO solar constant.

3.1.2 Thin Silicon Solar

Thin silicon solar cell is an advanced solar cell device with higher efficiency and lighter in mass. This solar cell has the special features of front surface texturing, back surface field and reflector, front and rear surface passivation, dual layer antireflection coatings, front and rear surface weldable contacts. The main aim of reducing the thickness of the solar cell was to reduce the mass of the solar cell blanket and to improve the radiation resistance for the space radiation environment. These improvements have produced a significant performance gains over the conventional silicon solar cell, with an average production lot power conversion efficiency of ~16 % at 1 AMO solar constant for a 100 μ m thickness thin silicon solar cell.

3.1.3 Single-Junction (SJ) GaAs/Ge Solar Cell

Single junction gallium arsenide solar cell grown on Ge substrate of 140–150 μ m thick using metal-organic chemical vapor deposition (MOCVD) method. An epitaxially grown GaAs solar cell has AR coating and front and rear weldable contacts with an average power conversion efficiency of ~18 % at 1 AMO solar constant.

3.1.4 Multi-Junction (MJ) GaInP₂/GaAs/Ge Solar Cell

GaAs-based multijunction solar cell consists of two additional solar cell junctions of GaInP₂ and Ge on both sides of GaAs junction to make triple-junction (TJ) solar cell. Single crystalline Ge substrate generally is used as substrate. This solar cell consists of multilayer AR coating, front and rear electrical contacts with integrated shunt diode to protect from reverse bias degradation. The production lot TJ solar cell has an average power conversion efficiency of ~27 % at 1 AM0 solar constant.

3.1.5 A-Si Solar Cell (Thin Film)

The thin film a-Si solar cell shows the promise of power conversion efficiencies on flexible substrates. These solar cells are either deposited on metal foils or polymer composite substrates to meet the spacecraft lightweight solar array requirements. Currently amorphous silicon solar cells on flexible stainless steel and polymer substrates have shown conversion efficiencies of ~10 % at 1 AM0 solar constant for large area (500–1,000 cm²) solar cell modules.

3.1.6 Copper Indium Gallium Diselenide (CIGS) Solar Cell (Thin Film)

Thin film polycrystalline CIGS solar cells developed for terrestrial application on glass substrates are now available commercially with power conversion efficiency of more than 10 % at AM1.5. The solar cell comprising flexible thin film CIGS coating is deposited on either flexible polyimide or stainless steel substrate and window layer deposited on it using chemical deposition. Large area modules of CIGS solar cells deposited on flexible substrate with conversion efficiency of ~12 % at 1 AM0 solar constant space conditions are currently now produced in the pilot plants.

3.2 Cover Glasses

Cover glasses have been a necessary and integral part of space solar arrays since their inception. The main function of the cover glass is to protect the underlying solar cell from the harsh radiation environment of space. To decrease the degradation in solar cell power caused by the injecting charging particles, solar cell manufacturers bond cover glass to the solar cell. The glass both stops low energy charging particles and slows higher energy particles. These glasses are formed either from fused silica or specially formulated ceria doped glass types that are resistant to radiation damage, for example Pilkington's CMX, CMG, CMO [2].

The glass type and thickness determine the energy cutoff point for charging particles that reach the solar cell material. The energy spectrum in the mission environment determines the glass thickness chosen. For example, the proton

spectrum for a GEO mission falls off quickly for proton energies above 2 MeV. A 100- μm thick Ceria-doped cover glass is typically used for a GEO mission, as it stops protons up to ~ 3 MeV. LEO and MEO missions have more severe proton spectra, and therefore require thicker cover glass for the same environmental protection. If the cover glass material is sufficiently thick, lower energy protons will stop completely in the cover glass while the spectrum of higher energy protons is shifted to lower energies. However, the tradeoff of increased weight due to additional shielding must also be considered. No cover glass is assumed for flexible thin film solar cell modules because of their high radiation resistance.

3.3 *Space Solar Array Substrates*

There are four different classes of solar array configurations: rigid planar arrays, flexible planar arrays, flexible thin film arrays, and concentrator arrays.

The rigid solar panel substrates are made with ~ 18 mm thick aluminum honeycomb core, covered with a woven, carbon fiber face sheet with the solar cell side insulated with kapton. This configuration of solar panel with hold down points and hinges gives the areal mass density of ~ 1.4 kg/m². The flexible solar panel substrate consists of a graphite fiber reinforced plastic of ~ 0.13 mm thick composite, enveloped with two sheets of 0.05 mm thick Kapton on its outer surfaces. The flexible planar solar panel of this configuration gives the areal mass density of 0.65 kg/m². Thin flexible film solar cell modules are directly deposited on flexible, thin, lightweight composite substrates using standard automated thin film deposition techniques. Structure mass calculations for the flexible thin film planar array give an areal mass density of ~ 0.35 kg/m². Though there are different solar concentrator designs studied and developed, only few have seen the great maturity and used for operational spacecrafts.

For the present space applications, rigid planar arrays were used as substrate configurations for most of spacecraft solar arrays. Their areal mass densities are usually far greater than ~ 0.22 kg/m² areal density of cover glass. So the solar cell radiation damages are mainly determined by front side irradiation through the coverglass for rigid planar arrays, whereas the back shielding is assumed to be infinite. However in the cases of flexible planar arrays and flexible thin film planar arrays, radiation damages from the back substrates must be considered, due to a comparable areal density between the cover glass and the back substrate.

4 **Radiation Damage Mechanisms in Solar Cells**

Energetic incident particles lose their energy through ionizing and nonionizing processes as they travel through a given target material. The ionization produces electron-hole pairs that primarily impact insulating materials which may trap charges. From the point of view of photovoltaic operation, the primary effect of

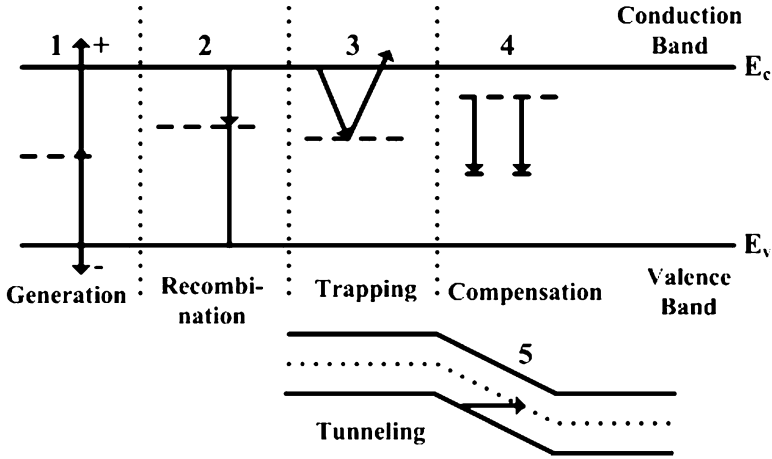


Fig. 20.2 This is a schematic representation of the effects that radiation-induced defect levels can have on current transport in a solar cell

particle irradiation of a solar cell is displacement damage where atoms in the semiconductor lattice are moved from their equilibrium position to form point defects like vacancies and interstitials or defect complexes like vacancy-impurity clusters. These defects can form energy levels within the forbidden gap of the semiconductor forming charge trapping centers, which give rise to recombination centers thereby degrading the minority carrier diffusion length [3–5]. The existence of these defect centers affects charge transport in essentially five basic ways as shown schematically in Fig. 20.2 [6].

Carrier generation (labeled #1 in Fig. 20.2) occurs when the existence of the defect energy level makes it statistically favorable for a charge carrier to move from a bound to a free energy level. The liberated charges are then swept away by the junction field, which produces a current. This causes the dark IV characteristic to increase, which degrades the photovoltage (i.e., V_{oc}). Recombination (labeled #2 in Fig. 20.2) occurs when it is statistically favorable for an electron–hole pair to recombine at the defect site. When this occurs, free charge carriers are lost resulting in degradation of the photocurrent (i.e. I_{sc}). Trapping (labeled #3 in Fig. 20.2) occurs when a defect level is able to capture and temporarily localize free charge carriers, which are then thermally reemitted. The fourth mechanism illustrated in Fig. 20.2 is referred to as compensation. Compensation occurs when a defect level permanently localizes a free charge carrier supplied by the dopant atoms. This reduces the majority charge carrier density and is referred to as carrier removal. The fifth mechanism is trap-assisted tunneling where the position of the defect level effectively lowers the tunneling potential.

The determination of solar cell degradation parameters is complicated because several different defects are usually created by irradiation and it is difficult to sort out those that act as nonradiative recombination centers and to measure their

associated minority carrier capture cross-section with correct accuracy. Other defects trap free carriers and therefore reduce the apparent doping levels in the base and the emitter. However, in space irradiation, they play a negligible role because their concentration is usually small compared with the doping concentration. For instance, an equivalent fluence of 10^{16} cm^{-2} 1 MeV electrons, which corresponds to a typical space condition, introduces a total of 10^{16} cm^{-3} defects in GaAs while the emitter and base of a cell are doped at a level of several 10^{17} cm^{-3} [7].

5 On-Ground Irradiation Experiments of Solar Cells

The use of a solar cell in space radiation environment requires knowledge of the degradation of current–voltage (I – V) characteristics under light illumination. Illuminated current–voltage (I – V) measurements of each sample were usually performed both before and after irradiation using an solar simulator under AM0 condition (air mass zero, 1 sun, 25 °C conditions). Air mass zero represents the solar irradiance observed in space. This degradation is typically characterized through the decrease of the maximum power (P_m), short-circuit current (J_{sc}), open-circuit voltage (V_{oc}), and fill factor (FF) induced by the interaction with energetic particles present in space.

To predict the degradation of a particular electrical parameter of a solar cell in a space radiation environment, it is necessary to know how the parameter responds to different electron and proton energies: i.e., the energy dependence of the damage coefficients (DCs). A damage coefficient can be generated for any measurable physical parameter of a device, such as carrier lifetime, carrier diffusion length, shifts in threshold current, LED light output, and many other parameters. The DCs can be obtained through irradiating solar cells from ground-based radiation facilities (e.g. electron and proton accelerators) using unidirectional, mono-energetic electrons or protons. The appropriate particle test energies and fluencies are determined through radiation environmental predictions of the flight orbit. Once the energy dependence of the DCs is known, predictions of the cell performance in space can be determined for a given radiation environment.

In this section, the irradiation experimental results were presented about silicon, single-junction and triple-junction GaAs solar cells, and thin film solar cells to compare radiation effects of electrons and protons on these solar cells, and also to provide experimental data for predictions of the cell performances.

Figure 20.3 shows the normalized values of short circuit current (I_{sc}), open circuit voltage (V_{oc}) and maximum power data, the ratio of the value after irradiation to the one before irradiation, measured on GaInP₂/GaAs/Ge triple-junction solar cells as a function of proton and electron fluences for different energies indicated by the open symbols and by the solid symbols, respectively [8].

For a given degradation level, the fluence level increases for decreasing electron energy indicating that the higher energy electrons do relatively more damage,

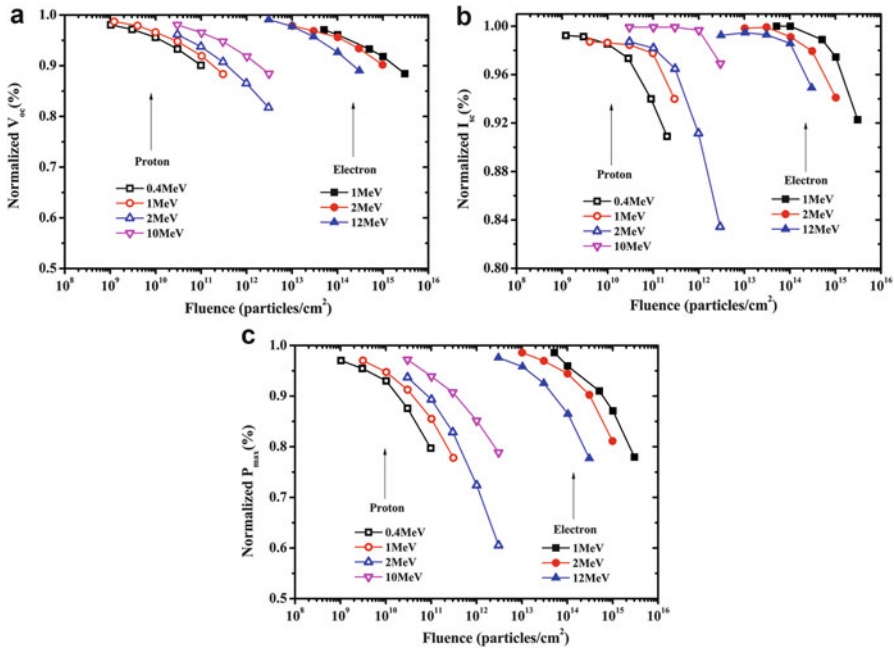


Fig. 20.3 Normalized values of open circuit voltage (a), short circuit current (b), and maximum output power (c) of TJ GaAs solar cells as a function of proton and electron fluence for various particle energies

whereas the opposite is true for proton irradiation. This is correlated with nonionizing energy loss (NIEL) of electron and proton in semiconductor materials. NIEL represents displacement damage energy transferred to the target lattice by an irradiating particle. The proton NIEL increases with decreasing energy, whereas electron NIEL shows a contrary trend. Thus, lower energy protons produce more displacement damage resulting in a more serious power degradations. Furthermore, as the proton slows down, its energy decreases further and the NIEL increases accordingly. This process continues until the proton eventually comes to rest. As a result, lower energy protons create more damage culminating in a peak in the defect concentration at the end of the proton track. However, as the injecting proton energy becomes too low to reach the active layer of solar cell, it may do smaller displacement damage than higher energy proton does [8, 9]. It can also be found that the fluence level was demanded higher for electron to give rise to the same degradation level than for proton, which can be attributed to the fact that NIEL of proton is far higher than that of electron at same energy.

An $\text{InGaP}_2/\text{GaAs}/\text{Ge}$ solar cell consists of three p-n junctions stacked on top of one another, where the thickness and bandgap of each subcell is specifically chosen to maximize absorption of the illumination source spectrum. The total device photovoltage is the sum of photovoltages from each subcell. The photocurrent of the TJ GaAs cell, however, is limited to the least value of the three subcells, which

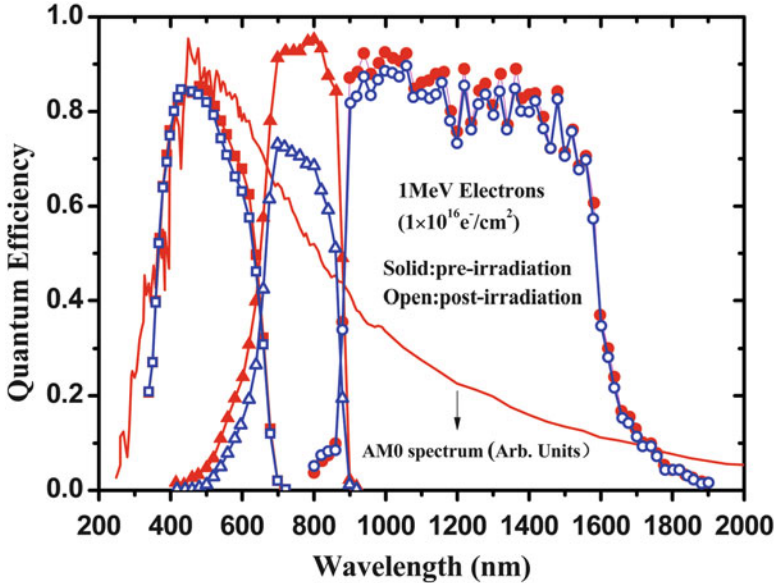


Fig. 20.4 Electron radiation-induced degradation of spectral response of a triple-junction GaInP₂/GaAs/Ge solar cell

is referred to as the “current limiter.” As a result, the radiation response of the TJ GaAs cell is primarily controlled by the most radiation sensitive subcell. To show this explicitly, a measurement of the quantum efficiency (a measure of how efficiently a solar cell converts individual wavelengths of light into electricity) of a InGaP₂/GaAs/Ge cell will show the effect of irradiation on the spectral response of each subcell overlapping the AM0 spectrum, which is shown in Fig. 20.4 for both before and after 1 MeV electron irradiation [10]. The integral of each of these curves with the incident spectrum yields the photocurrent. Given the wide absorption range of the Ge subcell, it produces significantly more photocurrent than the top two junctions, even after irradiation, so it does not limit the current. The photocurrents of the top two subcells, on the other hand, are quite closely matched in the as-grown device. However, under irradiation, the GaAs subcell degrades much faster than the InGaP₂ subcell so that it limits the current. The majority of the degradation occurs due to diffusion length degradation in the GaAs subcell, and in all cases, this subcell becomes the current-limiting junction after irradiation.

The structure of the TJ cell can be engineered to control the radiation resistance to some extent. The as-grown condition is referred to as beginning-of-life (BOL). The after irradiation condition is referred to as end-of-life (EOL). Indeed, current matching is the condition for maximum power output, and a TJ cell can be designed to achieve current matching at BOL or at EOL. Since the GaAs cell degrades more rapidly, a current matched cell at EOL will be top cell limited at BOL. This will sacrifice some of the BOL power but result in optimum EOL performance.

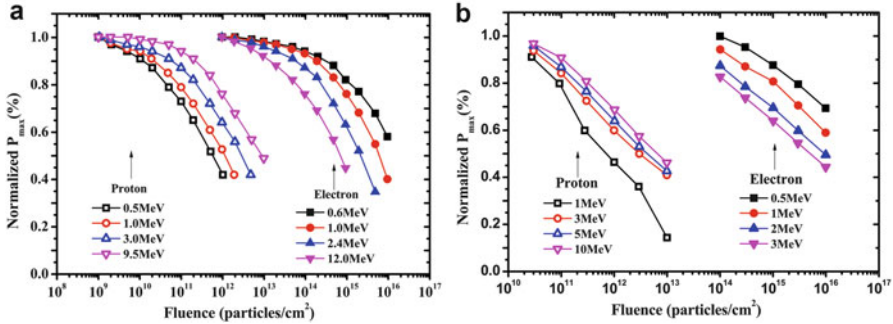


Fig. 20.5 Normalized maximum output power of SJ GaAs solar cells (a) and silicon solar cells (b) as a function of proton and electron fluence for various particle energies

Some ways of attaining a top-cell limited device include thinning the top cell, decreasing absorption in the interconnecting tunnel junction, and extending the GaAs subcell absorption range. When top-cell limited at BOL, the degradation of a MJ cell will be controlled by the more radiation resistant InGaP₂ top-cell until a specific irradiation level is reached where the photocurrent of the GaAs subcell is degraded to the level of the top-cell leaving the device current matched. The challenge, then, is to engineer the cell structure so that the radiation level corresponding to current matching coincides with the predicted radiation level of a specific space mission. Instead, it is the cell structure that more significantly controls the radiation-response, and it has been shown how the cell structure may be optimized for maximum BOL and EOL performance.

Figure 20.5 shows the normalized maximum power data, measured on single-junction GaAs/Ge solar cells and on single-crystal 50 μm thick n + p type BSR silicon solar cells as a function of proton and electron fluences for different energies indicated by the open symbols and by the solid symbols, respectively [11, 12]. The data of short circuit current (I_{sc}) and open circuit voltage (V_{oc}) are not shown here. It can be seen that irradiation with protons and electrons at different fluences and energies degrades the properties of single-junction GaAs and Si solar cells in the same manner as for the cases of TJ GaAs solar cells.

Thin film solar cells are a rapidly emerging technology for space applications. The two primary technologies under development are α -Si and CIGS solar cells. Figure 20.6 shows the response of the maximum power P_m parameter of a-Si solar cells to the irradiations [13]. In the case of proton irradiation, relatively little variation is seen among the three energies. In the electron irradiation case, the lower energy irradiation is seen to cause the most degradation. These results are not consistent with the values of electron NIEL. This can be attributed to the absence of thermally controlled condition during irradiations, which cannot remove accumulated heat in Si materials produced by ionizing energy loss of irradiating electrons, thereby resulting in a significant annealing of radiation damage.

To predict the performance degradation of solar cells in space, knowledge of the relaxation of radiation-induced defects might be equally important. Indeed, the α -Si

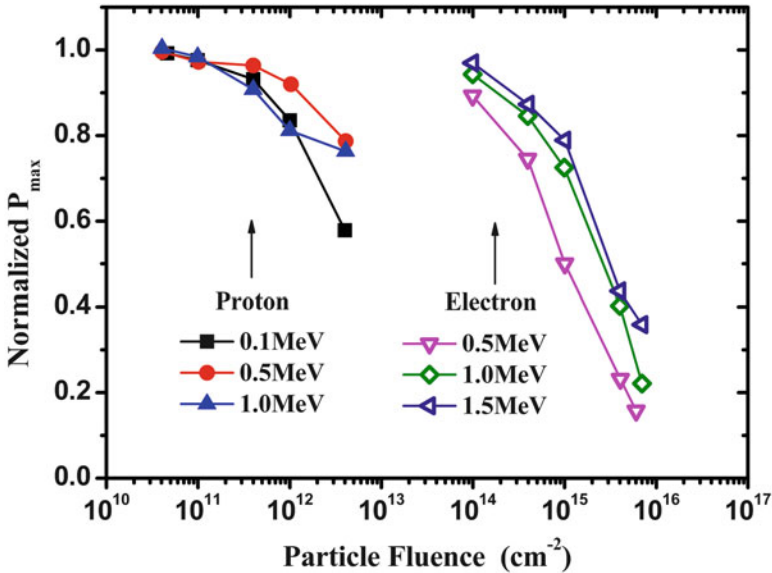


Fig. 20.6 Data depicting the response of P_{\max} in a-Si solar cells to proton and electron irradiation

solar cells can undergo significant annealing of radiation damage at temperatures as low as $60\text{ }^{\circ}\text{C}$, a typical solar array temperature in space. Both a-Si and CIGS TF-PV devices have demonstrated the ability to self repair (anneal) at a substantial rate when subjected to operating temperatures of $60\text{--}80\text{ }^{\circ}\text{C}$, whereas conventional crystalline Si and III–V compound cells do exhibit some annealing, but at much higher temperatures which is not typical for operational spacecraft.

To demonstrate this, one set of a-Si solar cells was subjected to a 24-h, $60\text{ }^{\circ}\text{C}$ thermal anneal after each irradiation fluence. The results measured after the 1 MeV electron irradiations are shown in Fig. 20.7 [13]. When the annealing is included, these cells display extreme radiation resistance.

Figure 20.8 shows the degradation behavior of hydrogenated a-Si (a-Si:H) solar cell as a function of 10 MeV proton fluence, and the sample temperatures were kept at $25\text{ }^{\circ}\text{C}$ (LT) and at $58\text{ }^{\circ}\text{C}$ (HT) during irradiations [14]. The remaining factor of P_{\max} at HT were normalized by the values at LT using the temperature coefficients. The results clearly showed that performance degradation was substantially affected by the sample temperature during irradiation. Figure 20.8 also displays the typical degradation behavior of crystalline Si (c-Si) space solar cells for comparison. The c-Si solar cell structure was optimized for space use and the radiation tolerance was enhanced. The comparison results clearly showed that the radiation tolerance of a-Si:H solar cells were much superior to that of c-Si solar cells. In particular, the a-Si:H cell kept 55 % of P_{\max} up to a fluence of $1.0 \times 10^{14}/\text{cm}^2$, whereas the c-Si cell completely lost its electric output by this fluence. Considering the thermal recovery occurring above room temperature, better EOL performance (better

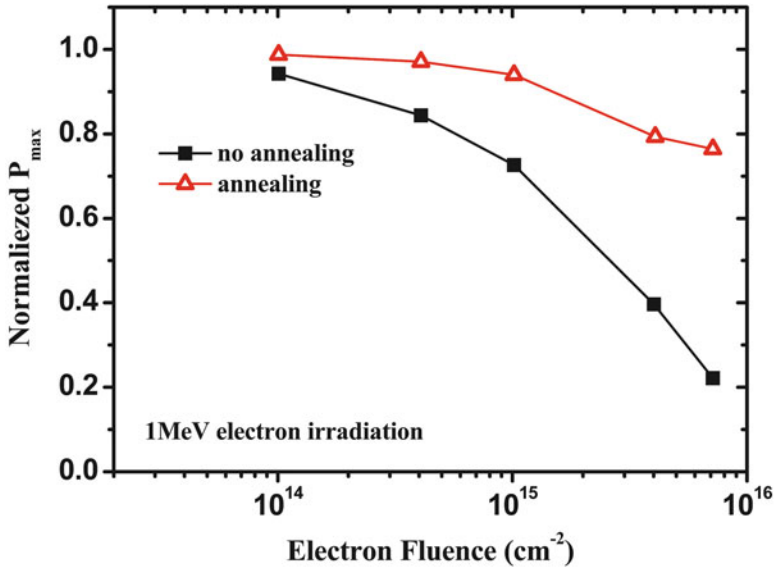


Fig. 20.7 1 MeV electron irradiation data for the a-Si solar cells where data that included a 24-h, 60 °C thermal anneal after each irradiation fluence are compared to data taken without an annealing step

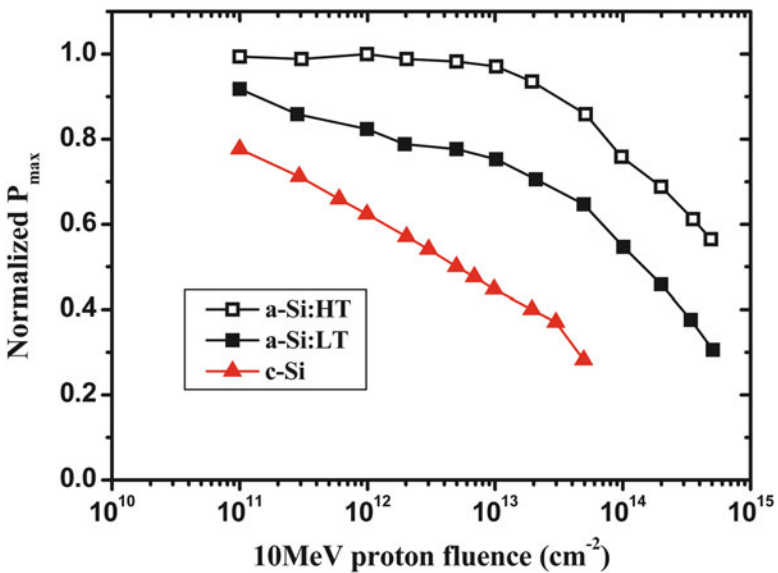


Fig. 20.8 Degradation curves of P_{max} of the a-Si thin film solar cells irradiated with 10 MeV protons. Results of crystalline silicon space solar cell are denoted by *triangle symbols in red* for comparison

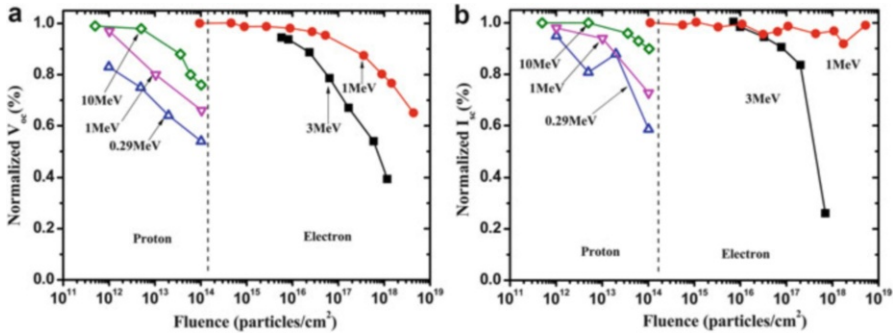


Fig. 20.9 (a) Normalized open circuit voltage and (b) normalized short circuit current of CIGS solar cells after irradiation with electron energies of 1.0 and 3.0 MeV, and proton energies of 0.29, 1, and 10 MeV

radiation tolerance) of a-Si:H solar cells is expected for the higher temperature condition, especially at slightly higher temperature than RT environments.

Figure 20.9 summarizes the results of irradiation experiments of CIGS solar cells with different electron and proton energies [15]. The consequences of 3 MeV electron irradiation on CIGS solar cells are different from that of the 1 MeV electron irradiations, especially I_{sc} heavily degraded. Reference [16] correlates this finding with the generation of a deeper defect detected by admittance spectroscopy. For 10 MeV protons the situation is similar to the 1 MeV electrons: with only little losses of I_{sc} , the loss of V_{oc} dominates the efficiency degradation. After 0.29 MeV proton irradiation, losses of V_{oc} and I_{sc} equally contribute to the efficiency degradation. Protons in MeV energy range and high-energy electrons basically cause displacement damage that is uniform through the depth of a 2 μ m thick CIGS absorber. In contrast, upon irradiation with protons of energies in the range $100 \text{ keV} < E < 500 \text{ keV}$, a highly localized displacement damage is expected [17, 18].

It should also be noted here that the CIGS cells also do display a relatively low annealing temperature, like the a-Si cells. Figure 20.10a depicts the thermal annealing of V_{oc} and I_{sc} of CIGS solar cells after 3 MeV electron irradiation [16]. The relaxation of I_{sc} starts just above room temperature and result in full recovery at 360 K. In contrast, the V_{oc} relaxation begins at 360 K, and the initial value of V_{oc} is no reestablished at a maximum temperature of 440 K. A result for 290 keV-proton-irradiated CIGS solar cells is shown in Fig. 20.10b [17]. With annealing time of 300 s, the relaxation of both V_{oc} and I_{sc} begins at annealing temperature of 360 K and peaks at 400–420 K. Similarly to the data in Fig. 20.10a, isochronal annealing after proton irradiation leads to full recovery of I_{sc} and to partial recovery of V_{oc} . The open circle symbols at 440 K represent an additional annealing step with annealing time of 30 min. Other study on thermal annealing of CIGS solar cells after proton irradiations yields results that are consistent with the data in Fig. 20.10b [19].

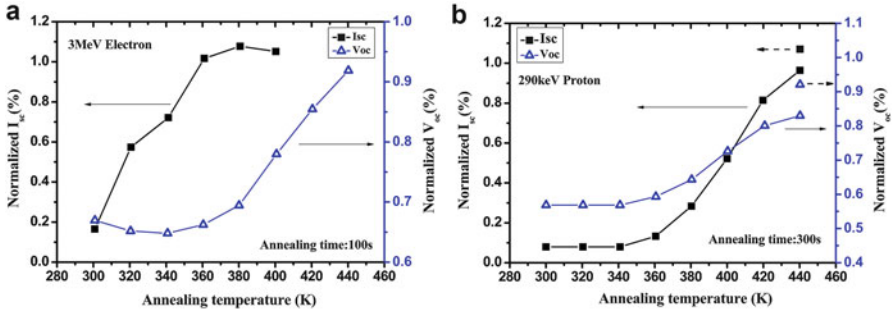


Fig. 20.10 Isochronal annealing of CIGS solar cells (a) after 3 MeV electron irradiation with a fluence of $8 \times 10^{17} \text{ cm}^{-2}$ and (b) after 290 keV proton irradiation with a fluence of $5 \times 10^{14} \text{ cm}^{-2}$. All measurements are performed at room temperature

6 Damage Models and Predictions

In planning a space mission, engineers need a method of predicting the expected cell degradation in the space radiation environment. This is not a simple calculation, however, because the rate of degradation for a given type of cell depends on the energies of the incident protons and electrons. In addition, the front surface of the cell is usually shielded by coverglass, and the back surface by the substrate material of the cell and the supporting array structure, so that the incident particle spectrum is slowed down before it impinges on the active regions of the cell. Finally, different kinds of cell technologies respond differently to irradiation depending on the materials used, the thickness of the active regions, and the types and concentrations of dopants employed.

There are several steps necessary in any method that is developed to predict solar cell response in a space radiation environment [20]. First, a way is needed to correlate the degradation caused by particles of different energies, i.e., the energy dependence of the cell damage coefficients must be determined. Second, the radiation environment needs to be accurately specified, including the effects of any shielding materials present. Finally, a method must be found to convolute the energy dependence of the damage coefficients with the radiation environment for the duration of the mission in a way that makes comparison with a ground test result possible. This last step is usually accomplished by means of a standard or characteristic degradation curve for a particular cell type.

There are currently two main approaches being used to model solar cell degradation in space. The first method was developed at the US Jet Propulsion Laboratory (JPL) more than 30 years ago and has been described in four extensive NASA publications [3, 4, 21, 22]. The goal of this approach is the determination of the normal-incidence 1 MeV electron fluence, which produces the same level of damage to the cell as a specified space radiation environment.

The second method was developed at the US Naval Research Laboratory (NRL) and has been described over the last 20 years in a series of publications and

conference proceedings [23–29]. The essence of the NRL method is the calculation of the displacement damage dose for a given mission using the energy dependence of the damage coefficients, and the proton and electron spectra incident on a bare cell. The relative damage coefficients are calculated from the nonionizing energy loss (NIEL) for protons and electrons traversing the cell material. The NRL approach is generally easier to implement than the JPL method, because it requires far fewer experimental measurements to specify the relative damage coefficients. In principle, the NRL approach requires ground measurements made at only one proton and two electron energies. Indeed, the NRL approach are utilized more extensively in predicting the degradation of space solar cells at present, especially when only limited experimental data are available, as is often the case with new and emerging cell technologies.

In this chapter, only the NRL approach, also usually referred to as displacement damage dose methodology, are presented using the particular case of protons and electrons incident on triple-junction GaAs cells as an example. Enough information will be presented to enable readers to make their own predictions using the method that works the best in a specific case.

In this case, the first step is to determine the energy dependence of the relative damage coefficients from a calculation of the nonionizing energy loss (NIEL) for electrons and protons incident on the material from which the cell is made. The calculations determine the energy transferred to the target atoms as a result of several possible interactions with incident protons or electrons. In order to perform the calculations, accurate values for the differential cross sections for Rutherford, nuclear elastic and nuclear inelastic interactions are needed [29, 30].

NIEL is defined as the part of the energy, lost per unit length by a particle moving in the material, through Coulomb (elastic), nuclear elastic, and nuclear inelastic interactions thereby producing the initial displacement damage and excited phonons. This displacement damage creates defect energy levels in semiconductors that can act as trapping and recombination centers. It is the introduction of these defect levels that degrade the photovoltaic response of a solar cell through a reduction in the minority carrier diffusion length. The units of NIEL are typically MeV/cm or MeV cm²/g. NIEL is a calculated quantity that takes into account the various interactions of an incident particle with a target atom/material. NIEL can be written as an integral over solid angle [30–32]. i.e.

$$\text{NIEL}(E) = \frac{N_A}{A} \int_{\theta_{\min}}^{\pi} \left[\frac{d\sigma(\theta, E)}{d\Omega} \right] T(\theta, E) L[T(\theta, E)] dT \quad (20.1)$$

where N_A is Avogadro's number, A is the atomic weight, and θ_{\min} is the scattering angle for which the recoil energy equals the threshold for atomic displacement. $d\sigma/d\Omega$ is the total differential cross section (elastic and inelastic) for atomic displacements. T is the recoil energy of the target atoms and $L(T)$ is the so called partition factor which partitions the energy into ionizing and nonionizing events.

The NIEL for protons and electrons incident upon the three materials of a InGaP₂/GaAs/Ge solar cell are shown in Fig. 20.11. The NIEL values are quite

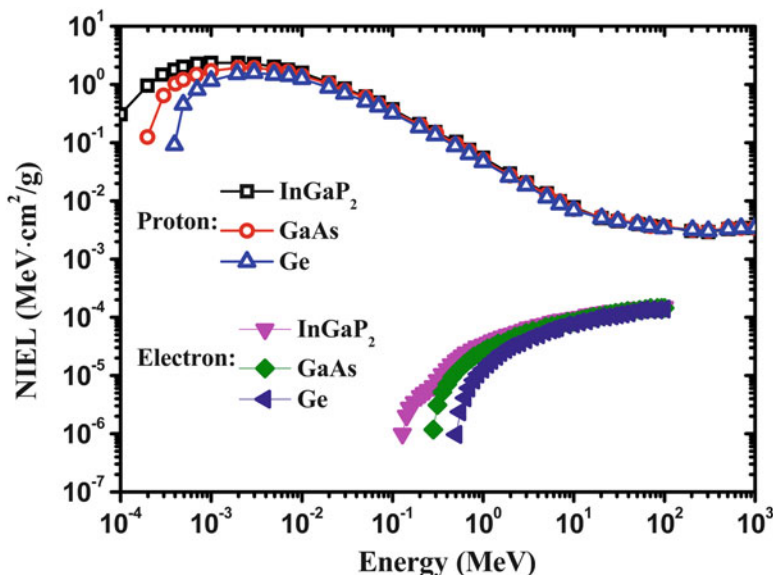


Fig. 20.11 NIEL calculated for electrons and protons incident upon InGaP₂, GaAs, and Ge

similar for the three materials since the interaction cross sections vary with the average atomic number of the material which are essentially equal amongst the three. It can be seen in Fig. 20.11 that the electron NIEL increases with energy, whereas the proton NIEL generally decreases with increasing energy except close to the threshold. This is qualitatively the behavior interpreted in data shown in Fig. 20.3. It is a notable feature of Fig. 20.3 that all the curves appear to have the same shape, with the curves for protons shifted to higher fluence and those for electrons shifted to lower fluence as the energy increases. This suggests that the performance degradations of the cell occur as a result of the introduction of a similar type of damage to the cell.

Since the NIEL is a calculation of the rate at which damage is transferred to the lattice, the discussion above suggests that the curves in Fig. 20.3 should collapse to a single curve if they are individually multiplied by the NIEL for the appropriate incident particle. This superposition certainly will only occur if there is a linear dependence between the damage coefficient and the NIEL. The amount of nonionizing radiation dose deposited by the irradiating particle is referred to as displacement damage dose [32], which is calculated by multiplying the particle fluence by the appropriate NIEL value for the given irradiating particle, energy and target material, as shown in (20.2)

$$D_d = \Phi(E)S(E) \left[\frac{S(E)}{S(E_{\text{ref}})} \right]^{(n-1)} \quad (20.2)$$

where $\Phi(E)$ is the fluence of particles with energy E and $S(E)$ the corresponding NIEL. $S(E_{\text{ref}})$ is the NIEL for reference energy, and D_d is the resulting effective displacement damage dose. The reference energy for electron is usually taken as 1 MeV. The quantity in square brackets accounts for a nonlinear dependence on NIEL. For any value of n other than unity, the D_d represents an effective D_d for the given particle and reference energy (E_{ref}). For solar cell analysis, this is only an issue for electron irradiation data. Proton irradiation data have been consistently shown to vary linearly with NIEL ($n = 1$). The available data suggests that when the active region is primarily composed of p-type material the electron DCs often follow a quadratic dependence on NIEL ($n = 2$), whereas that for n-type material follows a linear dependence ($n = 1$), and for the most part, the DCs follow a power law dependence on NIEL with an exponent varying between the value of 1 and 2 [33–35]. In the case of ionization the unit of dose is the rad, where 1 rad is equivalent to 100 ergs/g. In the displacement damage case, a unique dose unit has not been defined but it is convenient to use MeV/g.

Returning to the TJ GaAs cell data of Fig. 20.3, the data of the normalized maximum power correlated in terms of D_d are shown in Fig. 20.12. In order to cause the data to collapse to a single curve, a nonlinear least squares fitting of (20.2) is used to determine the best value of n . Since the triple-junction cells degradation are primarily controlled by the response of the GaAs subcell, the GaAs NIEL will be used to calculate D_d . With $E_{\text{ref}} = 1$ MeV, a value of $n = 1.8$ has been found to describe the data for P_{max} degradation well. The electron data are given in terms of 1 MeV electron equivalent D_d . The photocurrent and photovoltage were also seen to fall on a single curve, but not shown here.

The correlation of the data in terms of D_d is seen to reduce the full degradation data set to two curves, one for the electron and the other for the proton irradiation data. The solid curves shown in Fig. 20.12 represent fits of the data to the following semi empirical equation [4]:

$$\frac{P(D_d)}{P_0} = 1 - C \log \left(1 + \frac{D_d(E)}{D_x} \right) \quad (20.3)$$

where $P(D_d)/P_0$ represents the normalized parameter of interest, $D_d(E)$ is the effective dose given by (20.2), and C and D_x are fitting parameters to be determined. The solid line represents the characteristic curves generated using (20.3) for the cells. Typically, the fits can be performed with a common C parameter used to describe both the electron and proton data, while an individual D_x value is determined for each (designated by D_{xc} and D_{xp} for the electron and proton datasets, respectively). The fitting parameters are characteristic for this solar cell structure, and the best correlation is obtained with $C = 0.199$ and $D_{xc} = 1.2 \times 10^9$ MeV/g. The parameter R_{ep} is 0.17, defined as the ratio of D_{xc} and D_{xp} .

As is apparent in Fig. 20.12, the electron and proton data, when correlated in terms of D_d , do not necessarily fall on the same curve. Therefore, an electron to proton damage equivalency factor (R_{ep}) is required to collapse the electron data onto the proton curve. R_{ep} can be determined graphically from the separation of the

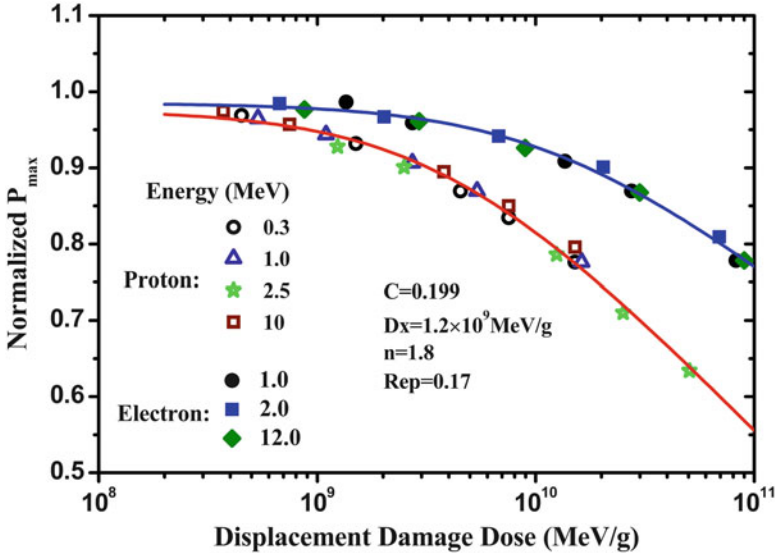


Fig. 20.12 Normalized maximum power of the TJ GaAs solar cell as a function of D_d

electron and proton curves along the D_d axis or as the value of D_{xe}/D_{xp} . Thus, in total, within the D_d method, five parameters are required to parameterize the radiation response of a specific solar cell technology: C , D_{xe} , D_{xp} , n , and R_{ep} . The characteristic curve can be used to predict the cell response to irradiation by any particle energy or by a particle spectrum, and it can be seen that only a few experimental data are required to determine the characteristic parameters of the curve.

Considering the space radiation environment analysis of the D_d methodology, the next step is to determine the particle spectra that emerge from the backside of the shielding materials and are, thus, directly incident upon the solar cell active region. Within the D_d methodology, these spectra are calculated based on knowledge of the incident spectra and the material properties of the shielding materials, and the spectra emerging from the shielding materials is referred to as the slowed-down spectra. The determination of the slowed-down spectra is described in detail in reference [26, 36–38].

The next step in the analysis of the space radiation environment is to reduce the slowed-down spectra to an equivalent value of D_d . This is accomplished by expanding (20.2) to an integral over energy. The integration is performed separately for the electron and proton spectra, and the results are summed using the R_{ep} factor as shown in (20.4).

$$D_d = \int \frac{d\Phi(E_p)}{dE_p} \cdot \text{NIEL}(E_p) dE_p + R_{ep} \int \frac{d\Phi(E_e)}{dE_e} \cdot \text{NIEL}(E_e) \left[\frac{\text{NIEL}(E_e)}{\text{NIEL}(1 \text{ MeV})} \right]^{n-1} dE_e \quad (20.4)$$

In (20.4), $d\Phi/dE$ refers to the differential particle spectrum, and the reference energy for the electron contribution has been set to 1 MeV. Because values of n and

Table 20.1 The calculated D_d deposited in GaAs material before and behind silica coverglass and predicted P_{\max} after a 5-year on-orbit flight

Orbit type	Coverglass thickness (μm)	Effective 1 MeV electron D_d (MeV/g)	Proton D_d (MeV/g)	Normalized P_{\max}
GEO	0	2.17×10^9	–	0.850
	100	1.50×10^9	–	0.865
MEO	0	4.11×10^9	3.44×10^{13}	0.0
	100	2.87×10^9	8.71×10^7	0.831
LEO	0	2.01×10^7	7.89×10^9	0.672
	100	1.15×10^7	2.74×10^7	0.904

R_{ep} are required in this calculation, a specific cell technology must be specified at this point in the analysis. This step is important when predictions are being made for degradation in a combined electron and proton environment. With the equivalent value of D_d determined from (20.4), one simply returns to the ground test data, expressed in terms of D_d , and reads the expected EOL degradation factor (Fig. 20.12), which completes the analysis.

As an example to demonstrate crystalline solar cell performance predictions, the predicted EOL of the TJ GaAs solar cell after a 5-year on-orbit flight, in typical LEO, MEO, and GEO radiation environments in Fig. 20.1, are presented in Table 20.1, using the parameters $C = 0.199$, $D_{\text{xc}} = 1.2 \times 10^9$ MeV/g, $n = 1.8$, and $R_{\text{ep}} = 0.17$.

It can be found that the D_d deposited by electron before shielding can be reduced no more than 50 % by using a 100 μm -thick coverglass. However in the case of proton, the D_d can be enormously lowered more than two orders of magnitude by the same coverglass. For the MEO radiation environment the D_d received by the unshielded solar cells will be mainly contributed by the proton radiation, whereas the electron radiation will dominate the D_d received by the shielded solar cells. The use of the coverglass is vital important for shielding the damages by low energy proton. A further reduction in the D_d can be achieved by increasing the coverglass thickness but would result in an increase of the overall weight of the solar array.

It has been shown that the D_d methodology can accurately predicts particle damage in single, dual, and triple-junction GaAs-based devices for all particle energies enough to reach the cell active region. The methodology has been validated through accurate prediction of measured on-orbit data from space flight experiments. The only technology where the current D_d approach does not offer simplification is for thick crystalline Si cells. In these cells, the active regions are significantly thicker than in III–V and thin film cells because of the low optical absorption coefficient of Si. Under these conditions there is not a well defined and constant particle spectrum over the whole active region. Of course this can also be solved through simulating particle transport in Si material to obtain the absorbed dose deposited in the active layer of Si cell. For thick Si cell technologies, therefore, the JPL experimental approach, although time consuming, is probably the more straightforward method.

Considering the performance prediction of a-Si solar cells in Fig. 20.6, it can be noted that in the electron irradiation case, the lower energy irradiation is seen to cause the most degradation. These results are not consistent with the displacement damage dose methodology. It appears that, in these amorphous materials, the amount of solar cell damage cannot be directly related to the amount of displacement damage calculated assuming a crystalline Si lattice structure. So it is not expected that the on-orbit performances of these cells can be readily predicted by the NRL approach.

There are a lot of the research works on evaluation and prediction of a-Si thin-film solar cells for space applications. Srour, et al. reported their irradiation experiments that radiation-induced degradation of a-Si can be scaled according to the ionizing radiation dosage [39]. The displacement damage contributes to radiation-induced degradation only when the ionization to displacement dose deposition ratio is low (low energy proton). Based on their finding, they developed a model that predicts a-Si degradation in space according to the ionization-to-displacement ratio. However some researchers from the Air Force Research Laboratory (AFRL), the Naval Research Laboratory (NRL), and SFA Inc. applied the NRL methodology to analyze irradiated thin-film a-Si solar cells [40]. In contrast to findings by Srour et al., they observed that the proton irradiation data correlate well with the displacement damage dosage. Granata et al. have initiated a new study on thin-film photovoltaics for applications in the harsh radiation environment of MEO, and tried to set up a model to predict performance degradation of a-Si thin film solar cell in MEO environment [41]. Further experiments are still underway to clarify the degradation mechanisms of a-Si thin film cells for accurately predicting the cell behaviors in space.

Data on CIGS solar cells in Fig. 20.9, there exists some scatter in these data. Nevertheless, the data do appear to fit the D_d methodology. However, the on-orbit EOL performance predictions of the CIGS cells must incorporate annealing effects into the D_d methodology, due to annealing effect arising at typical space solar array temperatures, heating by solar illumination.

The annealing rate of irradiated CIGS solar cells is expressed in the following equation [42]:

$$B = B_d \exp(-At) \quad (20.5)$$

where B is the degradation after annealing, B_d is the degradation before annealing, A is the annealing rate and t is annealing time. The annealing rates of solar cell parameters can be determined by annealing experiments. The on-orbit cell performance recovery of CIGS solar cells due to thermal annealing can be obtained by incorporating (20.3) and (20.5).

To validate the D_d methodology, predictions of on-orbit performance have been compared to space flight data obtained from several space experiments [28, 38, 42, 43]. These predictions were made using the D_d model. In all cases, the predicted data match the experimental data very well. The COMETS results are especially pleasing since that spacecraft underwent seven orbital corrections.

The Equator-S mission afforded the opportunity to validate the D_d model for thin-film, CuInSe_2 cells. The MDS-1 satellite validated the on-orbit thermal annealing effect of CIGS solar cell, indicating that radiation degradation and recovery of CIGS solar cells occur simultaneously in space.

7 Summary

In this chapter, the basic mechanisms governing the cell radiation response have been identified, and their impact on the cell electrical performance has been described. The NRL approach, a comprehensive analysis of the radiation response characteristics of III–V multijunction solar cells, has been presented. The NRL approach is easier to implement in most cases, especially for new and emerging cell technologies, because only a few ground measurements are needed to establish the necessary damage coefficients. However, for experimental databases that have already been established, the JPL method has a long history of successful implementation and is the only straightforward way to deal with thick crystalline Si cell technologies.

There needs to be more study of how to correctly model electron irradiation of shielded cells. The validity of the continuous slowing down approximation, which is often used for electron transport through coverglass materials, is uncertain under these conditions, even though agreement is sometimes found with predictions made for solar cell degradation in space electron environments. Radiation effects of low energy proton on solar cells need also to be investigated carefully to improve the accuracy of the predicted results analyzed in terms of displacement damage dose.

With the rapid development of new solar cell types, new cell technologies or new generations of existing technologies will probably step into applications in space power. However, for these new advanced technologies to operate efficiently in space, they must be resistant to the harsh space radiation environment. Experiment works must be campaigned to clarify the basic mechanisms of radiation damage in these solar cell materials, and show how these advanced devices respond to radiation exposure. So satellite designers and space cell manufacturers still need to continually qualify radiation responses of solar cells for the use in space.

References

1. Vette, J.I.: The NASA/National Space Science Data Center Trapped Radiation Environment Model Program (1964–1991). NASA-TM-107993 (1991)
2. Russell, J., Jones, G., Hall, J.: Development of a High Efficiency UVR/IRR Coverglass for Triple Junction Solar Cells, NASA/CP—2007-214494, 243–250 (2007)
3. Tada, H.Y., Carter, J.R., Anspaugh, B.E., Downing, R.G.: The Solar Cell Radiation Handbook, 3rd edn, pp. 69–82. JPL Publication, Pasadena, CA (1982)

4. Anspaugh, B.E.: GaAs Solar Cell Radiation Handbook, pp. 96–99. JPL Publication, Pasadena, CA (1996)
5. Weaver, B.D., Walters, R.J.: Displacement damage effects in electronic and optoelectronic devices. *Recent Res. Dev. Appl. Phys.* **6**, 747–776 (2003)
6. Srour, J.R.: Displacement damage effects in electronic materials, devices, and integrated circuits. Tutorial short course notes. In: IEEE Nuclear and Space Radiation Effects Conference, Portland, OR (1988)
7. Pons, D., Bourgoin, J.C.: Irradiation induced defects in GaAs. *J. Phys. C: Solid State Phys.* **18**, 3839–3871 (1985)
8. Sharps, P.R., Aiken, D.J., Stan, M.A., Thang, C.H., Fatemi, N.: Proton and electron radiation data and analysis of GaInP₂/GaAs/Ge solar cells. *Prog. Photovolt: Res. Appl.* **10**, 383–390 (2002)
9. Messenger, S.R., Burke, E.A., Morton, T.L., Summers, G.P., Walters, R.J., Warner, J.H.: Modelling low energy proton radiation effects on solar cells. In: 3rd World Conference on Photovoltaic Energy Conversion, 11–18 May Osaka, Japan 2003
10. Messenger, S.R., Burke, E.A., Walters, R.J., Warner, J.H., Summers, G.P., Lorentzen, J.R., Morton T. R., Taylor, S.J.: Quantifying Low Energy Proton Damage in Multijunction Solar Cells. NASA/CP—2007-214494, 8–17 (2007)
11. Anspaugh, B.E.: Proton and electron damage coefficients for GaAs/Ge solar cells. Proc. 22nd IEEE Photovoltaic Specialists Conference, Louisville, KY, 1593–1598 (1991)
12. Yamaguchi, M.: Displacement damage analysis of single crystal 50 μm thick silicon solar cells. In: Proc. 26th Photovoltaic Specialist Conf. (PVSC), Anaheim, CA, 987–990 (1997)
13. Walters, R.J., Morton, T.L., Messenger, S.R.: Displacement Damage Effects in Solar Cells—Mining Damage from the Microelectronics and Photonics Test Bed Space Experiment. NASA/TP—2004-213338 (2004)
14. Sato, S., Sai, H., Ohshima, T., Imaizumi, M., Shimazaki, K., Kondo, M.: Electron and Proton Irradiation Effects on Substrate-Type Amorphous Silicon Solar Cells. In: Proc. 37th Photovoltaic Specialist Conf. (PVSC), 001615–001619 (2011)
15. Jasenek, A., Rau, U., Weinert, K., Schock, H.W., Werner, J.H.: Radiation response of Cu(In, Ga)Se₂ Solar cells. In: Proc. 3rd World Conference on Photovoltaic Energy Conversion, Osaka, Japan, 596–598 (2003)
16. Weinert, K., Jasenek, A., Rau, U.: Consequence of 3-MeV electron irradiation on the photovoltaic output parameters of Cu(In, Ga)Se₂ solar cells. *Thin Solid Films* **431–432**, 453–456 (2003)
17. Weinert, K., Schwickert, M., Rau, U.: Irradiation of Cu(In,Ga)Se₂ thin film solar cells with 110-, and 290-keV protons. In: Proc. 3rd World Conference on Photovoltaic Energy Conversion, Osaka, Japan, 687–700 (2003)
18. Boden, A., Braunig, D., Klaer, J., Karg, F.H., Hosselbarth, B., La Roche, G.: Proton-irradiation of Cu(In, Ga)Se₂ and CuInS₂ thin film solar cells. In: Proc. 28th IEEE Photovolt. Spec. Conf., pp. 1038–1041. IEEE, Piscataway, NJ (2000)
19. Kawakita, S., Imaizumi, M., Yamaguchi, M., Kushiya, K., Ohshima, T., Itoh, H., Matsuda, S.: Annealing enhancement effect by light illumination on proton irradiated Cu(In, Ga)Se₂ thin film solar cells. *Jpn. J. Appl. Phys.* **41**, L797–L799 (2002)
20. Messenger, S.R., Summers, G.P., Burke, E.A., Walters, R.J., Xapsos, M.A.: Modeling solar cell degradation in space: a comparison of the NRL displacement damage dose and the JPL equivalent fluence approaches. *Prog. Photovolt: Res. Appl.* **9**, 103–121 (2001)
21. Anspaugh, B.E., Downing, R.G.: Radiation Effects in Silicon and Gallium Arsenide Solar Cells Using Isotropic and Normally Incident Radiation, pp. 61–84. JPL Publication, Pasadena, CA (1984)
22. Anspaugh, B.E.: The Solar Cell Radiation Handbook - Addendum 1: 1982–1988, pp. 69–82. JPL Publication, Pasadena, CA (1989)
23. Summers, G.P., Walters, R.J., Xapsos, M.A., Burke, E.A., Messenger, S.R., Shapiro, P., Statler, R.L.: A new approach to damage prediction for solar cells exposed to different

- radiations. In *IEEE Proc. 1st World Conference on Photovoltaic Energy Conversion, Waikoloa, Hawaii, 2068–2073* (1994)
24. Messenger, S.R., Burke, E.A., Xapsos, M.A., Summers, G.P., Walters, R.J., Jun, I., Jordan, T.: NIEL for heavy ions: an analytical approach. *IEEE Trans. Nucl. Sci.* **50**, 1919–1926 (2003)
 25. Summers, G.P., Messenger, S.R., Burke, E.A., Xapsos, M.A., Walters, R.J.: Contribution of low energy protons to the degradation of shielded GaAs solar cells in space. *Prog. Photovolt: Res. Appl.* **5**, 407–413 (1997)
 26. Summers, G.P., Messenger, S.R., Burke, E.A., Xapsos, M.A., Walters, R.J.: Low energy proton-induced displacement damage in shielded GaAs solar cells in space. *Appl. Phys. Lett.* **71**, 832–834 (1997)
 27. Messenger, S.R., Xapsos, M.A., Burke, E.A., Walters, R.J., Summers, G.P.: Proton displacement damage and ionizing dose for shielded devices in space. *IEEE Trans. Nucl. Sci.* **44**, 2169–2173 (1997)
 28. Morton, T.L., Chock, R., Long, K., Bailey, S., Messenger, S.R., Walters, R.J., Summers, G.P.: Use of displacement damage dose in an engineering model of GaAs solar cell radiation damage. In *Proc. of Tech. Digest 11th Intl. Photovoltaic Science and Engineering Conference, Hokkaido, Japan*, 815–816 (1999)
 29. Jun, I., Xapsos, M.A., Messenger, S.R., Burke, E.A., Walters, R.J., Summers, G.P., Jordan, T. M.: Proton nonionizing energy loss (NIEL) for device applications. *IEEE Trans. Nucl. Sci.* **50**, 1924–1928 (2003)
 30. Burke, E.A.: Energy dependence of proton-induced displacement damage in Silicon. *IEEE Trans. Nuc. Sci.* **33**, 1276–1281 (1986)
 31. Summers, G.P., Burke, E.A., Dale, C.J., Wolicki, E.A., Marshall, P.W., Gehlhausen, M.A.: Correlation of particle-induced displacement damage in Silicon. *IEEE Trans. Nuc. Sci.* **34**, 1133–1139 (1987)
 32. Burke, E.A., Dale, C.J., Summers, G.P., Stapor, W.J., Xapsos, M.A., Palmer, T., Zuleeg, R.: Energy dependence of proton-induced displacement damage in Gallium Arsenide. *IEEE Trans. Nuc. Sci.* **34**, 1220–1226 (1987)
 33. Messenger, S.R., Summers, G.P., Burke, E.A., Walters, R.J., Xapsos, M.A.: Modeling solar cell degradation in space: a comparison of the NRL displacement damage dose and the JPL equivalent fluence approaches. *Prog. Photovolt: Res. Appl.* **9**, 103–121 (2001)
 34. Yamaguchi, M., Takamoto, T., Taylor, S.J., Walters, R.J., Summers, G.P., Flood, D.J., Ohmori, M.: Correlation for damage in diffused-junction InP solar cells induced by electron and proton irradiation. *J. Appl. Phys.* **81**, 6013–6018 (1997)
 35. Warner, J.H., Messenger, S.R., Walters, R.J., Summers, G.P., Romero, M.J., Burke, E.A.: Displacement damage evolution in GaAs following electron, proton and silicon ion irradiation. *IEEE Trans. Nuc. Sci.* **53**, 1961–1968 (2007)
 36. Gao, X., Yang, S.S., Xue, Y.X., Li, K., Li, D.M., Wang, Y., Wang, Y.F., Feng, Z.Z.: Effects of electron radiation on shielded space triple-junction GaAs Solar cells. *Chin. Phys. B* **18**(11), 5015–5019 (2009)
 37. Yang, S.S., Gao, X., Wang, Y.F., Feng, Z.Z.: Displacement damage characterization of electron radiation in triple-junction GaAs solar cells. *J Spacecraft Rockets* **48**, 23–26 (2011)
 38. Gao, X., Yang, S.S., Feng, Z.Z., Zhang, L.: Evaluation and prediction of the degradation of space Si solar cells induced by low-earth-orbit radiation environment. *Chin. Phys. C* **36**, 900–904 (2012)
 39. Srour, J.R., Vendura Jr., G.J., Lo, D.H., Toporow, C.M.C., Dooley, M., Nakano, R.P., King, E. E.: Damage mechanisms in radiation-tolerant amorphous silicon solar cells. *IEEE Trans. Nucl. Sci.* **45**, 2624–2631 (1998)
 40. Tlomak, P., Reinhardt, K.C., Walters, R.J., Messenger, S.R.: Radiation hardness tests of flexible, thin-film photovoltaics for space applications. In: *Proc. SPRAT Conference, Cleveland, OH*, 10–14 (2001)

41. Granata, J.E., Sahlstrom, T.D., Hausgen, P., Messenger, S.R., Walters, R.J., Lorentzen, J.R.: Thin-film photovoltaic radiation testing and modeling for a MEO orbit. In: Proc. 31st IEEE PVSC, Lake Buena Vista, Florida (2005)
42. Kawakita, S., Imaizumi, M., Sumita, T., Kushiya, K., Ohshima, T., Yamaguchi, M., Matsuda, S., Yoda, S., Kamiva, T.: Super radiation tolerance of CIGS solar cells demonstrated in space by MDS-1satellite. In: 3rd World Conference on Photovoltaic Energy Conversion, Osaka Japan (2003)
43. Walters, R.J., Summers, G.P., Messenger, S.R.: Analysis and modeling of the radiation response of multijunction space solar cells. In: Proc. 28th IEEE Photovolt. Spec. Conf., pp. 1092–1097. IEEE, Piscataway, NJ (2000)

Chapter 21

Thin-Film III–V Solar Cells Using Epitaxial Lift-Off

G.J. Bauhuis, P. Mulder, and J.J. Schermer

Abstract Epitaxial lift-off is used to create thin-film III–V solar cells without sacrificing the GaAs wafer. It is based on selective etching of an AlAs release layer between the wafer and the cell structure using an HF solution. The wafer can be reused for subsequent deposition runs thereby reducing the cost of the cells. The thin-film cell can be transferred to any new carrier, e.g. glass, plastic, silicon, or metal foil. Although epitaxial lift-off was first demonstrated in 1978, it took until the 1990s to make significant progress in understanding the process and devising new ways to increase the etch rate. The first single-junction epitaxial lift-off cells were made in 1996. Thin-film cells offer new cell applications based on their flexibility, low weight, and possibility to deposit the cell structure in reverse order. Today the world record for single-junction cells is held by a thin-film GaAs cell, whose performance is partly based on the increased photon recycling factor in cells with a back contact acting as a mirror. Also state of the art tandem and inverted metamorphic thin-film cells have been demonstrated.

1 Introduction

III–V solar cells are usually not referred to as thin-film cells, because the cell structures are deposited on relatively thick GaAs or Ge wafers in order to obtain high quality single crystalline material. These materials are direct band gap semiconductors with high absorption coefficients, therefore a thickness of only a few micrometers is sufficient to absorb the light that the cell can convert into electricity. In the present wafer-based fabrication techniques, the cell structure and the wafer are processed together to a thick solar cell. The wafers are expensive

G.J. Bauhuis (✉) • P. Mulder • J.J. Schermer
Institute for Molecules and Materials, Radboud University Nijmegen,
Heyendaalseweg 135, 6525 AJ Nijmegen, The Netherlands
e-mail: g.bauhuis@science.ru.nl; p.mulder@science.ru.nl; j.schermer@science.ru.nl

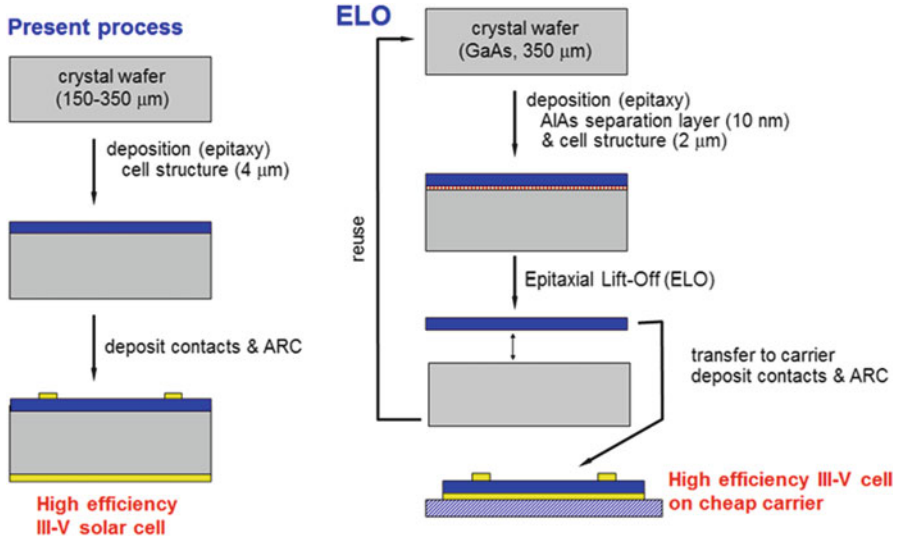


Fig. 21.1 Schematic representation of the production process for wafer-based III-V cells (*left*) and thin-film cells using epitaxial lift-off with the potential of substrate reuse (*right*)

(about \$100 for a 4 in. diameter GaAs wafer) and determine a significant part of the cost of III-V cells. Therefore it makes sense to separate the cell structure from the wafer. This leaves a thin-film structure, which can be transferred to a low cost foreign carrier, and the wafer which, after reconditioning, can be reused for the deposition of the next cell structure. Currently, the most mature technique to do this is Epitaxial Lift-off (ELO) where the separation is done by selective wet etching of a thin release layer between cell structure and wafer. ELO is based on the extremely high etching selectivity of $>10^6$ [1, 2] for an $\text{Al}_x\text{Ga}_{1-x}\text{As}$ ($x > 0.6$) release layer cladded between GaAs layers in an aqueous HF solution. In Fig. 21.1 schematic presentations of the wafer-based and thin-film production processes are shown.

Apart from the cost aspect, thin-film III-V cells have a number of benefits with respect to wafer-based cells, i.e. low weight, flexibility, different cell concepts as the inverted metamorphic cell [3] where the cell structure is deposited in inverse order. In the third paragraph of this chapter a more extensive overview of the thin-film cell properties will be given.

In 1978 the first attempts to separate devices from a GaAs substrate were described by Konagai et al. [4] using the so-called Peeled Film Technology. A wax layer was applied to support the circa 30 μm thick, LPE grown, fragile thin-film during the etching of a 5 μm thick release layer. After this first attempt, the method was abandoned for a long time because the lateral etch rate was too low to be of any practical use. Almost a decade later, it was noted that if the film structures have a thickness in the range of a few micrometers, the tension induced by the wax support layer causes the III-V film to curl up as it becomes undercut [5]. This was concluded to be beneficial for removal of the etch products during the

process. The release layer thickness was reduced to the 10–100 nm range. As a result the lateral etch rate of the now named Epitaxial Lift-off process was raised to about 0.3 mm/h [6]. Using this process many GaAs but also InP-based devices such as photodiodes [7, 8], LEDs [9, 10], lasers [11, 12], HEMTs [13] and FETs [14] transferred to silicon, sapphire, and glass plates were demonstrated. However, the process still suffered from some severe limitations. First of all the etch rate was fairly low. As a result the demonstrated devices were generally limited to several millimeters in size. ELO was typically performed by preparing the samples with wax and submerging them in the HF solution until the thin-films were found floating in the solution which could, depending on size, take up to several days. Secondly the tension induced by the wax could not be controlled well, which made it difficult to improve the process. For industrial utilization it was essential to obtain a better control over the technique so that the process could be optimized for the separation of large area devices at sufficiently high etch rates. With this goal in mind the work on ELO at the Radboud University Nijmegen was started in the mid 1990s. An ELO setup was developed to allow for a systematic investigation on the basic parameters that determine the etch rate [2, 15–19] and a model to describe the process was developed [20, 21]. By making some essential modifications to the original ELO method, like the use of a temporary flexible carrier and applying a controlled force to allow the etchant to reach the etch front, the etch rate increased by more than a factor of 100 to rates well above 30 mm/h [16, 19, 21]. The ELO method has evolved to a process capable of separating layer structures from entire wafers (Fig. 21.2). Conventional photolithography techniques and wet chemical etching can be used to process the thin-film into a cell, with no loss in material quality or efficiency.

2 The Epitaxial Lift-Off Process

The basis of the Epitaxial Lift-Off process is the application of a thin, typically 10 nm, $\text{Al}_x\text{Ga}_{1-x}\text{As}$ (with $x > 0.6$, mostly x is taken as 1) release layer deposited on the wafer before the actual III–V cell structure. Since AlGaAs has a lattice constant that is almost identical to GaAs, only a minimal additional lattice misfit strain is introduced and the perfect crystal structure of the wafer can be maintained. During the ELO process the release layer is removed by wet chemical etching in an HF solution, while keeping the cell structure free of damage. It is essential to force the crevice open to allow transport of reaction products to and from the etchfront. Using a wax support layer makes it difficult to control the parameters that determine the etch rate. At the Radboud University Nijmegen a weight-induced epitaxial lift-off (WI-ELO) process was developed to investigate the etch mechanism and study the process parameters. In the WI-ELO setup an HF resistant temporary carrier is mounted on top of the epilayer structure. This carrier, typically a plastic foil, provides continuous support and allows for manipulation of the thin film

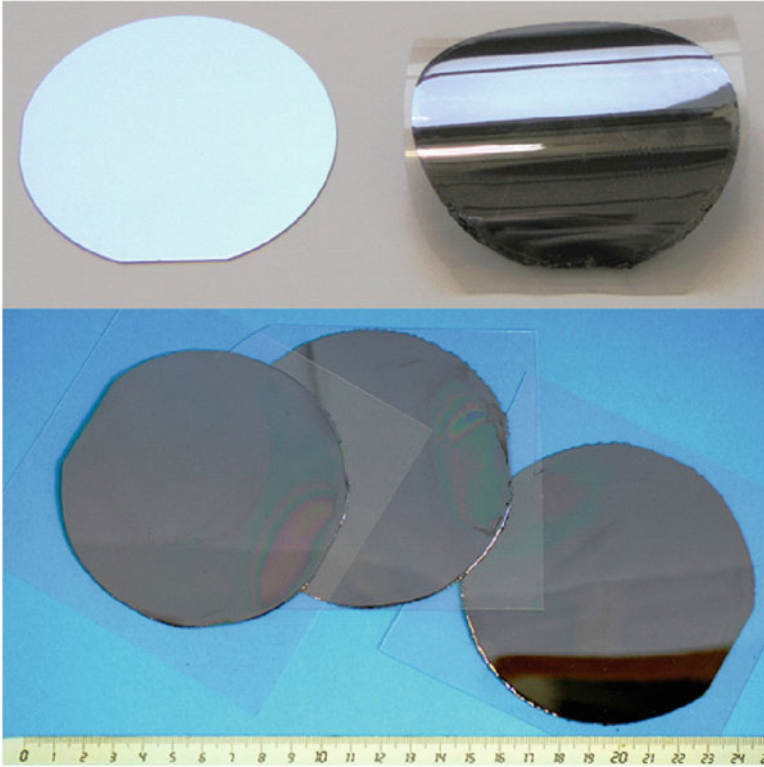


Fig. 21.2 Epitaxial lift-off of wafer sized thin-film structures. *Upper* picture a 2 in. GaAs wafer and thin-film structure on a flexible carrier after ELO. Picture *below* three thin-film structures retrieved from a single 4 in. Ge wafer

during and after the lift-off process. A weight attached to the foil is used as a controllable external force to the film to open the crevice with a radius of curvature R .

A process was developed in which the sample with the carrier is mounted upside down in a closed container (see Figs. 21.3 and 21.4a) [15, 16]. In the initial set-up, a saturated vapor is created by the HF solution in the container. Under these conditions one droplet of etch solution positioned on the plastic foil against the edge of the sample on the side of the weight is generally sufficient to separate the epitaxial film from its substrate. In a later stage, the setup was modified to supply fresh etchant to the etch front at all times by a continuous flow of HF solution in order to maintain a constant etch rate. A disadvantage of this setup is that if the lift-off proceeds, the foil easily bends too much. This frequently results in cracking of the epitaxial layer structure in the final part of the process. For this reason a setup was developed in which the slit is forced open with a constant radius of curvature by guiding the foil and the part of the film that is separated over a curved surface

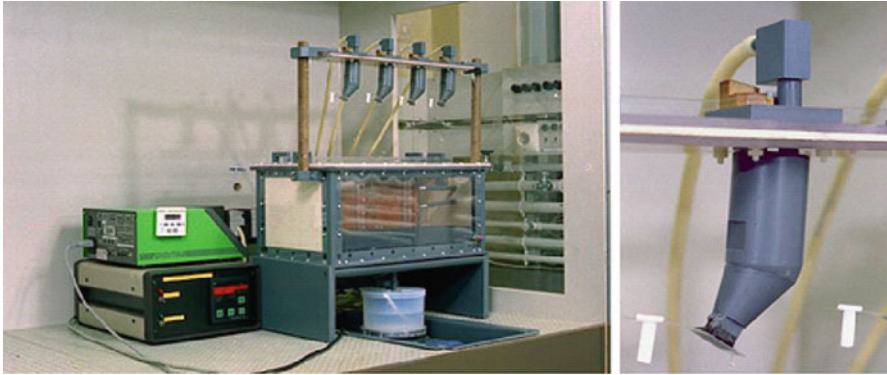


Fig. 21.3 Setup used for the weight-induced epitaxial lift-off process with plastic container, pump, and temperature controlled HF reservoir. This setup can be used for four samples in parallel. On the *right* a detail of a support rod with small area sample, foil, weight, and HF supply probe. The setup is shown with the samples in mounting position above the container. After mounting the four samples are simultaneously lowered in the container and the etch process is started

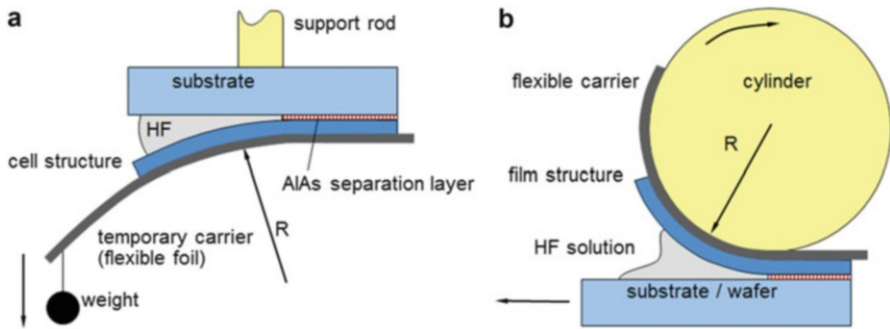


Fig. 21.4 Schematic representation of the ELO process: (a) WI-ELO setup with a weight attached to the foil, (b) wheel setup for a constant radius of curvature

(see Fig. 21.4b). The size of the curved surface can easily be scaled-up to adapt for different wafer diameters. The process was demonstrated for 2 and 4 in. wafers (see Fig. 21.2) but there is no fundamental limitation to scale-up the process towards larger wafers.

The reaction of AlAs with an aqueous HF solution is complex. In a systematic study the solid, aqueous, and gaseous reaction products of the etch process in the absence of transport limitations were examined by a number of techniques [20]. It was found that aluminum fluoride, both in solid form as well as in solution, and arsine gas are formed. Also oxygen-related species such as AsO^+ , AsOH^- , and AsO_2^+ were detected indicating that solid arsenic is oxidated as an intermediate

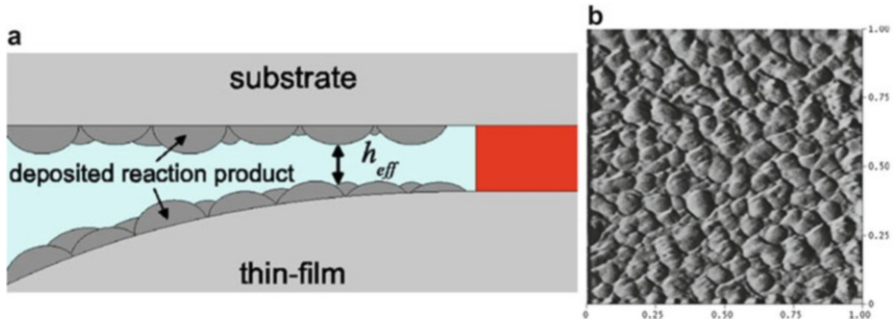
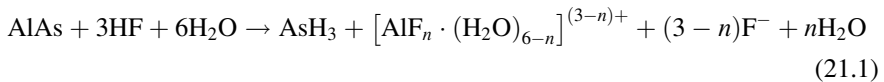


Fig. 21.5 (a) Schematic representation of the situation during the ELO process where reaction products are deposited on the thin-film and the substrate surfaces, (b) AFM image of the substrate surface side after lift-off. The scale is given in micrometers

step in the reaction. The etching chemistry can be described by a set of overall reactions given by:



with $n = 0, 1, 2, 3$. If the etch process takes place in the ELO geometry (i.e. through a narrow crevice) transport limitations have to be taken into account. The fact that the ELO process can be maintained with a constant high etch rate over a long period of time if the crevice is bended open, indicates that the reaction products with a relatively low solubility are at least removed a sufficient distance away from the etch front before they eventually are redeposited at the walls of the crevice (see Fig. 21.5a). AFM surface analysis of the substrate and thin-film after ELO confirm the redeposition of material during the process (see Fig. 21.5b) [21]. Initially the deposits were suspected to be mainly $\text{AlF}_3 \cdot \text{H}_2\text{O}$, but in a later stage SIMS analyses indicated that solid arsenic is a major compound in the redeposited material [56]. This explains the fact that we were never able to detect gaseous AsH_3 during ELO processing. Furthermore it is found that the presence of oxygen in the etching environment accelerates the etching process, while under the same conditions a total absence of oxygen resulted in the process coming to a halt [19]. This seems to indicate that without oxygen the redeposition of solid arsenic more easily results in total blocking of the etch front while oxygen by removing arsenic as As_2O_3 prevents or undoes this blocking mechanism allowing the ELO process to continue.

2.1 Key Process Parameters

For the application of ELO the process needs to have a sufficiently high etch rate. It is and always will be a relatively slow process. With an etch rate of less than 1 mm/h it initially took more than a day to lift-off a 2 in. diameter thin-film

structure. Therefore an important goal was to speed up the process to a time scale of hours for lifting of a 4 in. thin-film, which is in the same order as the deposition time of the solar cell layer structures by MOCVD. To understand the chemistry and how the relevant parameters influence the etch rate, a diffusion and reaction-related model (DR model) was developed based on the notion that the overall etch rate V_e is determined by both the diffusion of HF to the etch front and its subsequent reaction with the AlAs release layer [21]. According to this model V_e is given by:

$$V_e = \frac{[HF]}{R_d + R_r} \quad (21.2)$$

with $[HF]$ the HF concentration in the bulk of the solution and $R_d + R_r$ the resistance of the etch process related to diffusion and the reaction chemistry. The resistances can be expressed as:

$$R_d = \frac{\pi\sqrt{Rh}3[AlAs]}{\sqrt{2D_0}} e^{-\frac{E_{a,d}}{kT}} \quad (21.3)$$

and

$$R_r = \frac{1}{A} e^{-\frac{E_{a,r}}{kT}} \quad (21.4)$$

With h the release layer thickness, R the radius of curvature, $[AlAs]$ the molar concentration of solid AlAs, D_0 the diffusion coefficient, $E_{a,d}$ the activation energy for the diffusion of HF, T the temperature, A the Arrhenius constant, and $E_{a,r}$ the activation energy for the surface reaction. The WI-ELO setup was used to verify the model by determining the influence of some of the ELO process parameters on V_e . It was found that the DR model yields etch rates which are in quantitative agreement with those obtained experimentally.

The linear dependence of V_e on the HF concentration was found experimentally for $[HF] < 15$ mol/kg. For higher concentration V_e saturates, which indicates that the ELO process is limited in some way not accounted for by the DR model. The most likely explanation is that the exchange of molecules to the etch front is hindered by an insufficient effective opening of the slit.

The etch rate is reaction-rate related by the dependence on the composition of the release layer. Because the lattice constant of AlAs is slightly higher than that of GaAs, there is a small negative in-plane strain ε present on the release layer. By adding small amounts of phosphorus this strain can be varied. For 10 nm thick $AlAs_{1-y}P_y$ release layers, the etch rate was determined for y between 0 and 8 %. The results shown in Fig. 21.6 indicate a maximum V_e for $y = 2$ % at a small compressive strain, with a 30 % gain in etch rate with respect to AlAs ($y = 0$).

The release layer thickness influences the diffusion limited etch rate. At a fixed temperature and radius of curvature,

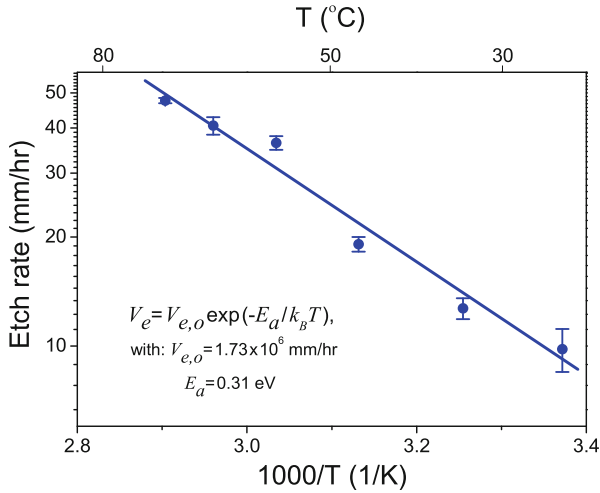


Fig. 21.6 Lateral etch rate as a function of the phosphorus fraction in the $\text{AlAs}_{1-y}\text{P}_y$ release layer

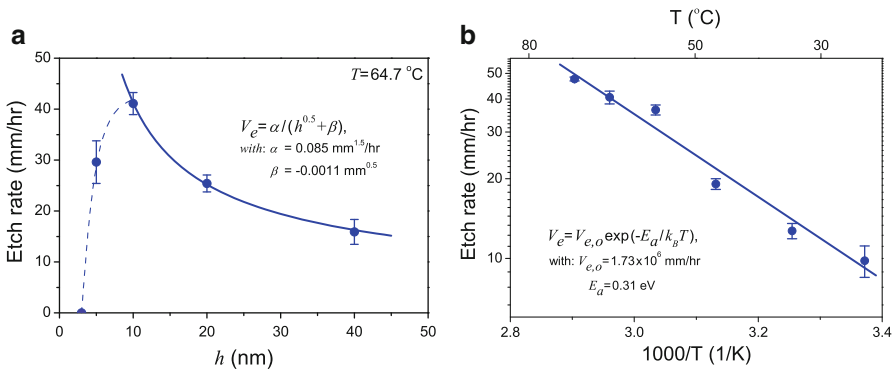


Fig. 21.7 Lateral etch rate in 20 % HF solution as a function of (a) layer thickness and (b) process temperature

$$V_e = \frac{\alpha}{\sqrt{h} + \beta} \tag{21.5}$$

With α and β being constants. As shown in Fig. 21.7a this relationship is valid if h is not too low. In the range between 5 and 10 nm the etch process slows down, if h is decreased further the etch process comes to a halt.

The radius of curvature R determines the opening angle of the crevice. R was varied by applying different weights to the carrier [16]. The dependence of the etch rate on R is described by the sum of a constant and a term with $V_e \sim R^{-0.5}$. V_e increases as R is reduced. However, an increased curvature involves a higher risk of

breaking the single crystal ELO films so care should be taken with the optimization of this parameter.

From the relationships (21.2), (21.3), and (21.4), it can be deduced that the etch rate increases exponentially with process temperature:

$$V_e = V_{e,0} e^{-\frac{E_a}{kT}} \quad (21.6)$$

For $h = 10$ nm, V_e is raised by a factor of 5 if the temperature is increased from room temperature to 70 °C (Fig. 21.7b). For practical reasons T is limited to 100 °C and might best be kept at a value between 50 and 60 °C.

Other parameters that have been investigated as strain applied to the wafer during the lift-off process [17], n- or p-type doping levels in the release layer [2], aluminum fraction x (must be >0.6) in the Al_xGaAs release layer [3], the addition of a surfactant or anti-foaming agent [22] do not influence the etch rate to the same extent.

In summary, it can be concluded that for optimized practically applicable settings an etch rate exceeding 30 mm/h is feasible, resulting in a lift-off time of around 3 h for a 4 in. wafer.

2.2 ELO Methods for Small Area Devices

Alternative approaches for ELO are directed to the production of microchips using a transfer-printing technique to peel and print a large number of small thin-film structures onto glass or plastic [23]. The layer stack for this method is identical to other ELO methods: a device structure that is grown over an AlAs release layer, only in this approach the AlAs layer is much thicker (1 μm) than generally applied for the full area lift-off. In this method not the entire wafer area is lifted off, but small area device structures. To do this, before lift-off the material is separated into square blocks by vertical etching through the device structure to enable exposure of the release layer to HF by immersion. Each individual device is then transfer printed one at a time, in a step and repeat fashion, onto the carrier.

An interesting feature of the transfer print method is that several device structures separated by release layers can be deposited in a single growth run and released one by one. This technique has been demonstrated for a trilayer assembly with single-junction GaAs solar cells. The cells show a slight decrease in performance from the top to the bottom cell, which is attributed to Zn diffusion. Yoon et al. [23] calculated a reduction in the cell's growth cost of about 50 % for a stack of ten cell structures. A serious drawback of this method is the small device area (<0.5 mm²). Such small cells can be applied for CPV, but are less suited for large area (space) panels.

Another small area lift-off approach developed by Horng et al. [24] is the use of cross-shaped pattern array to provide the etch path for the HF. After the cross-shaped holes are etched, a 50 μm thick nickel layer covering only the device areas is applied by electroplating. The nickel is attracted by a magnet to decrease the etch

time during etching in an HF bath and acts as the thin-film carrier after lift-off. In this way, an entire wafer-sized thin-film structure is lifted-off simultaneously. The individual devices can be separated afterwards. The lateral etch rate decreases with increasing cell area (between 1×1 and 5×5 mm), but is always below 1 mm/h.

3 Epitaxial Lift-Off Cells

Conventional triple junction cells grown on Ge have their limitations. They are inflexible, brittle, and relatively heavy. Therefore wafer-based cells require some kind of structural support to prevent damage. Thin-film III–V cells produced with the ELO technique offer new opportunities for device design, based on the fact that the thin-film carrier can be selected on its material properties rather than crystal growth demands. Figure 21.8 shows an example of flexible thin-film cells with a metal backing. Substrate reuse and thus lower cell cost has been the main driver for the development of ELO thin-film cells, but apart from this there are many interesting new concepts and applications which are not possible for wafer-based cells.

3.1 Thin-Film III–V Cell Development

The first good quality thin-film III–V cell, a 4 cm^2 GaAs cell with a 23.3 % efficiency, was made by Kopin in 1990 [25] at a time when the best wafer-based GaAs cell performance was 25.1 %. The thin-film was not lifted off chemically like in ELO but mechanically using the CLEFT (Cleavage of Lateral Epitaxial Films for Transfer) technique [26]. The cell was used in a mechanical tandem in combination with CIS bottom cell. The total efficiency was 25.8 % which made it the best mechanically stacked tandem cell at that time intended for use in space. No progress in CLEFT was reported after 1990.

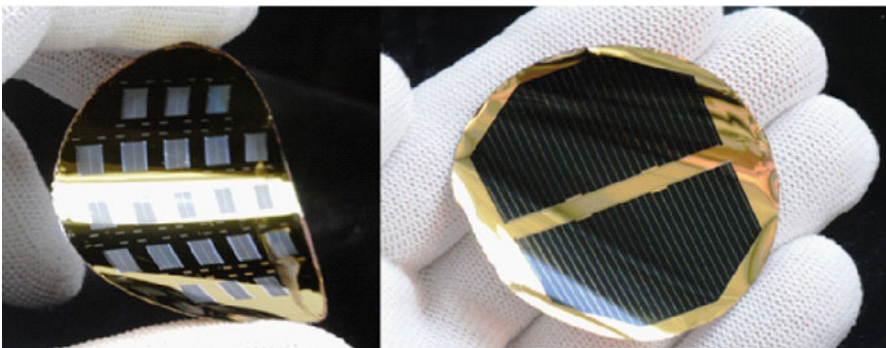


Fig. 21.8 Flexible ELO thin-film cells with a metal foil backing

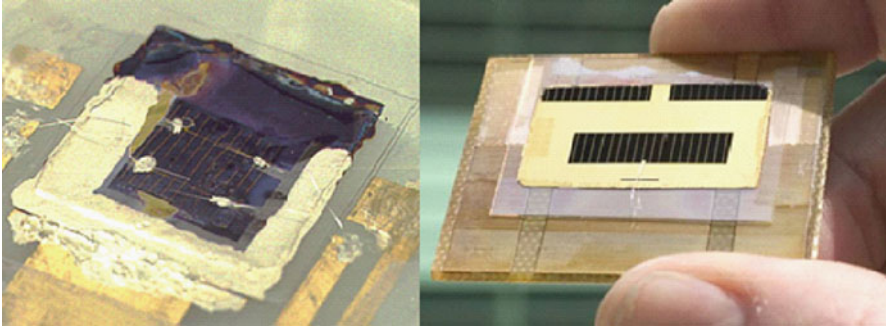


Fig. 21.9 One of the first operational ELO cells produced at Radboud University (*left*) and the first ELO cell reaching a thin-film cell record efficiency of 24.5 % in 2006 (*right*)

The first cell results for ELO GaAs cells were presented in 1996 [27, 28]. Lee et al. used the tension in the wax to produce small thin-film cells transferred to glass substrates after lift-off. Metallization and mesa etching were done prior to lift-off with both top and bottom contacts on the front side of the cell. The cell showed good open circuit voltage V_{oc} and short circuit current J_{sc} values, but a relatively low FF due to a high series resistance. In the same year, using the large area lift-off approach, research at Radboud University Nijmegen showed a thin-film cell that also had proper V_{oc} and J_{sc} values, but with an even lower FF [28, 29]. The efficiency was around 10 %, compared to 24 % for a wafer-based cell with a similar layer structure. Metallization for this thin-film cell was done after lift-off, with a full area back contact. Normally the cells undergo an anneal treatment at 450 °C to reduce the contact resistance between metal contact and semiconductor. This was not possible for the thin film on the new host substrate, because of the differences in expansion coefficient between III–V material and the carrier, resulting in the cell's low FF. Another problem was the choice for $Al_{0.85}$ GaAs as the window material in the cell structure. The window is then also attacked by the HF during the lift-off, which required protection layers on the side walls that had to be removed afterwards. Also, as can be seen in Fig. 21.9 wiring of the cell was not done by bonding but with a conductive paste. Notwithstanding these imperfections which indicated that new approaches were required for several steps in the cell processing, the quality of the lifted-off material proved to be excellent showing the potential of the method. Gradually solutions were found to improve processing of the thin-film cell on a foreign carrier up to the level of a record single-junction thin-film cell with an efficiency of 24.5 % in 2006 [45].

Figure 21.9 shows the visual improvements made from the first cell to this first record cell. Further tuning of the cell structure resulted in an equal 26.1 % record efficiency for a single junction GaAs cell in a regular wafer-based structure as well as in the thin-film configuration in 2009 [30]. This irrefutably demonstrates that the material quality is not affected by the ELO process. The thin-film cell used a back reflecting mirror and a reduced base thickness, but with a value of 1.045 V the potential raise in open-circuit voltage was not fully realized (see Sect. 3.3 of this chapter). Recently, Alta Devices demonstrated a thin-film GaAs cell with a V_{oc} of

1.122 V and an efficiency of 28.8 % [31–33], which is the highest single-junction cell efficiency up to now. ELO GaAs thin-film cells produced by several other groups confirm that there is no loss in material quality or cell efficiency after epitaxial lift-off [23, 34–37].

From a lift-off perspective, multi-junction cell structures only differ from single-junction GaAs cells in their higher thickness. This increased thickness can slow down the etch rate somewhat and thus increase the lift-off time, but this is normally not a problem. It was noticed that the InGaP etching behavior for thin-films is not the same as for material on the wafer [38]. Therefore in the processing of the thin-film cells other etchants than HCl are preferred. Excellent ELO multi-junction cells were produced by several groups including tandem cells [39, 40] and IMM cells [41].

3.2 Low Power to Weight Ratio/Flexibility

For space solar cells high efficiency, high radiation resistance, a low weight, and flexibility are the desired features. Because of their highest power output wafer-based III–V cells have been dominant over other cell types since the late 1990s. Wafer-based cells are mounted on a rigid honeycomb structure to prevent the wafers from breaking, resulting in relatively high weight. A thin-film cell on a flexible host substrate does not require a rigid panel assembly. This introduces new low weight options for panel design. In the past, other attempts were made for thin-film space cells which used a-Si or CIGS materials. In Japan, the experiences with these thin-films have already been used to develop light-weight solar panels containing III–V cell solar sheets from dual-junction solar cells [42]. A panel containing several sheets is unfolded using a pantographic structure. The power of the panel is 100 W/kg, compared to 50–70 W/kg for a typical rigid panel. Another example of thin-film solar cells in space applications, where PV modules can be folded and rolled is given by Farah [43].

The cells flexibility and low weight in combination with a high cell efficiency can also be used for terrestrial applications, especially if portable power is required. For example, a 10.25×15.5 in. panel with 30 single-junction GaAs thin-film cells was tested for application as battery charging device for the military [44]. The panels, with the cells laminated between two sheets of transparent fluoropolymer film, have an efficiency of 19.6 % which is considerably higher than the currently used 7.8 % CIGS panels.

3.3 New Device Designs

Wafer-based cells have a full area back contact. A thin-film cell allows access to the backside of the device. This makes it possible to apply a metal grid on front and back side. In this design the cell can be used as a bifacial cell [45] where illumination takes place from both top and bottom side using a relatively cheap mirror setup.

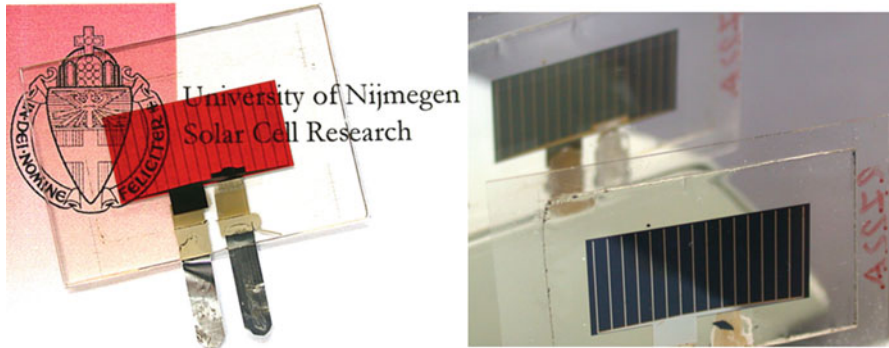


Fig. 21.10 Examples of thin-film cell designs: semitransparent InGaP cell (*left*) and bifacial GaAs cell (*right*)

Such a cell can also be applied as semitransparent cell for mechanical stacking on a lower bandgap cell. An example is a thin-film InGaP cell combined with a Si cell [46] or an InGaAsP/InGaAs tandem cell grown on InP combined with a GaAs cell [47]. In Fig. 21.10 an InGaP and GaAs semitransparent cell are shown. The InGaP cell is illuminated from the bottom, which is the reason for the red color coming from the transmitted photons with a wavelength above 650 nm.

In a thin-film cell with a full area back contact the metal (mostly gold or silver) also serves as a mirror for nonabsorbed photons. This doubles the optical thickness of the cell, so half of the wafer-based cell thickness is sufficient to absorb the light [48]. Using the reflectivity of the metal mirror, the thin-film cell can be designed to take advantage of the so-called photon recycling effect. This effect was already described in 1977 by Asbeck [49] and was experimentally confirmed by the very high photoluminescence lifetimes measured in GaAs layers cladded by AlGaAs [50]. Photons emitted through radiative recombination in the active layers are confined within the cell and likely to be reabsorbed. Effectively, the minority carrier lifetime is raised potentially by one order of magnitude [51]. The recycled photons are emitted isotropically, in order to be reabsorbed with a high yield they have to be reflected on the back side by the metal mirror and on the front side by the large difference in refractive index between the III–V material and air. Only $n^2/4$ (2 % for GaAs) of the recycled photons escapes on the front side [31], whereas the reflectivity of a gold or silver mirror on GaAs can be as high as 94–96 %. For optimal light trapping, loss mechanisms as interface recombination at the window/emitter or BSF/base interface, absorption in the contact layers and nonradiative recombination in the active layers and at the perimeter must be kept as low as possible. In good quality GaAs, bulk nonradiative recombination is much lower than the radiative recombination. Perimeter recombination (nonradiative) can become a significant fraction of the total recombination for small area cells.

The saturation current density J_0 of a thin-film cell is given by [51]:

$$J_0 = q \frac{n_i^2}{N_A} W \left[\frac{1}{\tau_{nr}} + \frac{1}{\phi \tau_r} + \frac{S}{W} \right] \quad (21.7)$$

where N_A is the base carrier concentration, W is the width of the base layer, ϕ is the photon recycling factor, τ is the (radiative or nonradiative) lifetime and S is the recombination velocity at the base-BSF heterointerface. Assuming $\tau_{nr} \gg \phi \tau_r$ and $\phi = 10$ a value of 2×10^{-21} A/cm² for J_0 is calculated for a GaAs cell. Using a realistic short circuit current of 29 mA/cm², an open circuit voltage of 1.15 V can be calculated from

$$V_{oc} = \frac{kT}{q} \left[\ln \left(\frac{J_{sc}}{J_0} + 1 \right) \right] \quad (21.8)$$

Calculations done by Miller et al. [31] based on the Shockley-Queisser limit also indicate that V_{oc} will be close to 1.15 V for a thin-film cell with a 100 % mirror reflectivity. For a wafer-based GaAs cell they calculated a maximum V_{oc} of 1.08 V. This difference between thin-film and wafer-based cells is confirmed by the experimentally obtained best V_{oc} values for GaAs cells: 1.122 V [32] and 1.038 V [30], respectively. The best single junction thin-film cell currently has an efficiency of 28.8 % [32] compared to 26.4 % for a cell on the wafer [52]. Therefore, by applying a high-quality mirror on the back of a thin-film cell, the GaAs single-junction cell efficiency can be increased by 9 % (relative) with respect to a wafer-based cell.

Current state of the art III–V cells are 3-junction cells consisting of the active materials InGaP, (In)GaAs and Ge (Fig. 21.11a). These cells are limited in efficiency by the Ge bottom cell, which, with 0.7 eV has a lower bandgap than desired. Future cells will likely feature 4, 5, or even 6 junctions in order to increase the efficiency to values above 45 % under concentration [53]. This is difficult with only lattice matched materials grown on GaAs or Ge. An example of a new multijunction approach initiated by NREL [3, 54] is the inverted metamorphic (IMM) cell where graded buffer layers are used to alter the lattice constant to accommodate the growth of InGaAs subcell material with a 1.0 eV bandgap. The InGaP and GaAs subcells with the lattice constant of the substrate are grown first. Then gradually the lattice constant is increased, as shown schematically in Fig. 21.11b, using a graded buffer. Finally, the InGaAs subcell is grown with the new lattice constant. The cell structure is grown in inverse order, and this implies that after growth the wafer and cell structure need to be separated to facilitate use of the cell in the “sunny side up” direction (Fig. 21.11b). The epitaxial lift-off process can be used for this separation. IMM cells have been demonstrated with efficiencies of 40.8 % (AM1.5, 326 suns concentration) for 3-junction [28] and 32.0 % (AM0, 1 sun) for 4-junction cells [55] and have the potential for further increase in number of junctions and efficiency.

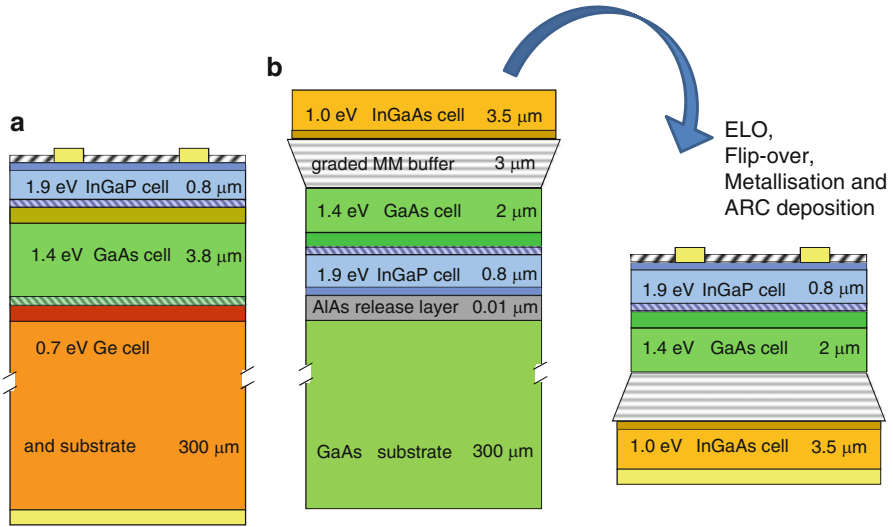


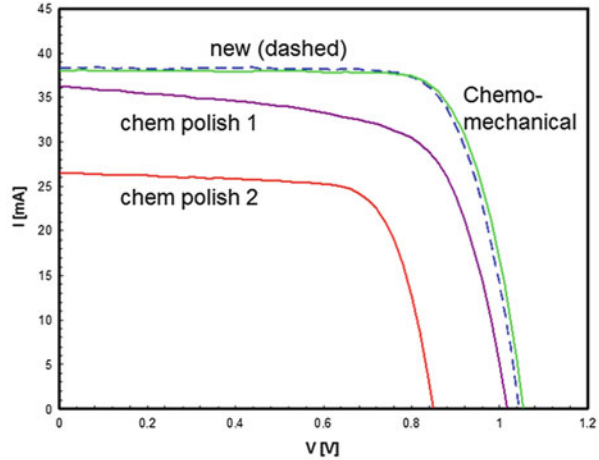
Fig. 21.11 Schematics of (a) conventional 3-junction cell on wafer and (b) 3-junction IMM cell where epitaxial lift-off is used to separate the cell structure from the wafer. The high bandgap subcells (InGaP and GaAs) are deposited lattice matched followed by the metamorphic InGaAs subcell

4 Substrate Reuse

One of the aims of ELO is to allow multiple reuse of the wafer after lift-off to reduce cell cost. Ideally, a minimum of wafer re-preparation between consecutive lift-offs is required. However, exposure to the HF solution increases the surface roughness of the wafer on a nanometer scale. The roughness is about 0.3 nm for new so-called epi-ready wafers and between 2 and 4 nm for wafers that have been subjected to a 20 % HF solution for 21 h. In addition during ELO reaction residues are left on the surface [56], mainly elemental arsenic. During storage of the etched wafer under ambient conditions, from this arsenic As_2O_3 particles are formed. As a consequence of surface roughening and contamination, a re-preparation of the surface is necessary before the wafer is again suited for growth of a cell structure.

The easiest method of preparation is the application of a polishing etch solution to reduce the surface roughness of the wafer after ELO. The smoothest surface is obtained using an ammonia-peroxide solution. A wafer subjected to 21 h in HF appears clean and smooth to the naked eye after exposure to the polishing etchant and the roughness is reduced to 0.4 nm [57]. Is this sufficient for wafer reuse for solar cells? In Fig. 21.12 the IV-curves of two GaAs cells from the same reused wafer are shown together with the curve from a thin-film cell grown a new wafer. Clearly, chemical polishing with only ammonia-peroxide results in a serious deterioration of the cell performance and a nonuniformity over the wafer. The conclusion can only be that this procedure does not sufficiently remove all surface contamination that is left after ELO.

Fig. 21.12 IV-curves of thin-film GaAs solar cells lifted-off from new and reused substrates. The wafers that have been treated with a polishing etchant show a clear degradation in performance, whereas the chemo-mechanically treated wafers show identical performance to cells from new wafers



A second reclaim method is to subject the wafers to a procedure that includes a mechanical polishing step which is also used in the fabrication of epi-ready GaAs wafers as purchased from a commercial wafer vendor. In this process first any surface contamination is removed, followed by a chemo-mechanical planarization process to polish the surface. The minimum thickness loss of the GaAs wafer is about 10 μm , so multiple reuse of a wafer is viable. This reclaim process is commercially available at a price which is typically in the order of 15–20 % of the regular price for new GaAs wafers. It has been demonstrated [57] that with chemo-mechanical polishing of the wafers a series of consecutive thin-film solar cells without any reduction in cell performance can be produced (see Fig. 21.12).

A third option is the use of protection layers deposited on the wafer before the release layer in order to avoid direct contact between the HF etchant and the wafer surface. After lift-off the protection layers can be selectively removed by wet chemical etching before the wafer is loaded into the reactor chamber. Lee et al. [58] have subjected a wafer with protection layers on top to an HF solution for 48 h to simulate the ELO process. They found a similar roughness for the surface after etching of the protection layers as for a new wafer. Cells grown on these two types of wafers showed an identical performance. Horng et al. [24] produced single-junction wafer-based GaAs cells on recycled wafers that were used for ELO up to four times. After each ELO step the protection layers were chemically etched and a new ELO structure consisting of protection layers, release layer and a 3 μm thick GaAs layer, was grown. The performance of the cells decreased to below 90 % of the initial performance when the substrate was reused more than twice. This is attributed to an increase in the diode saturation current I_0 caused by a lower material quality of the grown crystal. Both these papers show results of wafer-based cells on reused wafers. Up to now, good quality ELO thin-film cells grown on reused wafers with protection layers have not been demonstrated.

5 Future Perspectives

With today's record efficiency of 44.0 % under a concentration of 942 suns [38] III–V solar cells have not reached their full potential. The multi-junction concept has the perspective of obtaining efficiencies above 45 % and maybe even 50 % under concentration. New designs for cells with more than three junctions require the use of thin-film cells in some form [27, 59, 60] either as a free standing thin-film cell or in combination with cells grown on different wafer materials through a layer transfer process.

A basic method for obtaining a thin-film cell by etching/polishing of the wafer after growth is widely used [1, 28, 29], but this is an expensive method because the wafer, which has a large contribution in the total cell cost, is lost. Epitaxial lift-off offers the possibility of wafer reuse and is more and more maturing after being under investigation for more than 20 years, resulting in good quality cells and a stable process. Other options, i.e. the controlled spalling technology [61, 62], are still in its infancy.

In the last 5 years, companies such as Alta Devices [63] and Microlink Devices [26, 50, 52, 54] have developed a wafer-scale, epitaxial lift-off manufacturing process and are currently in pilot production. Activities in Europe are also initiated (tf2 devices). The transfer printing technique is adopted by Semprius to produce cells for CPV [64]. These commercial activities show the potential of ELO as a production method for III–V thin-film cells. The application of thin-film cells offers new opportunities. In space cells the flexibility and low weight can lead to different design of the panels of which the first concepts have already been developed [24, 25]. For terrestrial purposes these high-efficiency cells are initially used for mobile systems where the thin-film properties such as low weight, nonbrittleness, and flexibility can be exploited. Examples are unmanned aerial vehicles (UAVs), military applications as charging tents and backpacks, and consumer electrics (mobile phones). In a later stage wide scale application in CPV or flat panel PV can be expected.

References

1. Wu, X.S., Coldren, L.A., Merz, J.L.: Selective etching characteristics of HF for Al_xGa_{1-x}As/GaAs. *Electron. Lett.* **21**, 558–559 (1985)
2. Voncken, M.M.A.J., Schermer, J.J., Bauhuis, G.J., Mulder, P., Larsen, P.K.: Multiple release layer study of the intrinsic lateral etch rate of the epitaxial lift-off process. *Appl. Phys. A* **79**, 1801–1807 (2004)
3. Geisz, J.F., Kurtz, S., Wanlass, M.W., Ward, J.S., Duda, A., Friedman, D.J., McMahon, W.E., Moriarty, T.E., Kiehl, J.T.: High-efficiency GaInP/GaAs/InGaAs triple-junction solar cells grown inverted with a metamorphic bottom junction. *Appl. Phys. Lett.* **91**, 023502 (2007)
4. Konagai, M., Sugimoto, M., Takahashi, K.: High efficiency GaAs thin film solar cells by peeled film technology. *J. Cryst. Growth* **45**, 277–280 (1978)
5. Yablonovitch, E., Gmitter, T., Harbison, J.P., Bhat, R.: Extreme selectivity in the lift-off of epitaxial GaAs films. *Appl. Phys. Lett.* **51**, 2222–2224 (1987)

6. Yablonoitch, E., Hwang, D.M., Gmitter, T.J., Florez, L.T., Harbison, J.P.: Van der Waals bonding of epitaxial liftoff films onto arbitrary substrates. *Appl. Phys. Lett.* **56**, 2419–2421 (1990)
7. Schumacher, H., Gmitter, T.J., LeBlanc, H.P., Bhat, R., Yablonoitch, E., Koza, M.A.: High-speed InP/GaInAs photodiode on sapphire substrate. *Electron. Lett.* **25**, 1653–1654 (1989)
8. Kobayashi, F., Sekiguchi, Y.: GaAsSchottky photodiode fabricated on glass substrate using epitaxial lift-off technique. *Jpn. J. Appl. Phys.* **31**, L850–L852 (1992)
9. Schnitzer, I., Yablonoitch, E., Caneau, C., Gmitter, T.J., Scherer, A.: 30% external quantum efficiency from surface textured thin-film, light emitting diodes. *Appl. Phys. Lett.* **63**, 2174–2176 (1993)
10. Sasaki, Y., Katayama, K., Koishi, T., Shibahara, K., Yokoyama, S., Miyazaki, S., Hirose, M.: High speed GaAs epitaxial lift-off and bonding with high alignment accuracy using a sapphire plate. *J. Electrochem. Soc.* **146**, 710–712 (1999)
11. Yablonoitch, E., Kapon, E., Gmitter, T.J., Yun, C.P., Bhat, R.: Double heterostructure GaAs/AlGaAs thin film diode lasers on glass substrates. *IEEE Photon. Technol. Lett.* **1**, 41–42 (1989)
12. Pollentier, I., Buydens, L., Van Daele, P., Demeester, P.: Fabrication of a GaAs-AlGaAs GRIN-SCH SQW laser diode on silicon by epitaxial lift-off. *IEEE Photon. Technol. Lett.* **3**, 115–117 (1991)
13. Shah, D.M., Chan, W.K., Caneau, C., Gmitter, T.J., Song, J.-I., Hong, B.P., Micelli, P.F., De Rosa, F.: Epitaxial lift-off GaAs HEMT's. *IEEE Trans. Electron Dev.* **42**, 1877–1881 (1995)
14. Morf, T., Biber, C., Bächtold, W.: Effects of epitaxial lift-off on the DC, RF and thermal properties of MESFET's on various host materials. *IEEE Trans. Electron Dev.* **45**, 1407–1413 (1998)
15. Schermer, J.J., Bauhuis, G.J., Mulder, P., Meulemeesters, W.J., Haverkamp, E., Voncken, M. M.A.J., Larsen, P.K.: High rate epitaxial lift-off of InGaP films from GaAs substrates. *Appl. Phys. Lett.* **76**, 2131–2133 (2000)
16. Voncken, M.M.A.J., Schermer, J.J., Maduro, G., Bauhuis, G.J., Mulder, P., Larsen, P.K.: Influence of radius of curvature on the lateral etch rate of the weight induced epitaxial lift-off process. *Mat. Sci. Eng. B* **95**, 242–248 (2002)
17. Voncken, M.M.A.J., Schermer, J.J., Bauhuis, G.J., Van Niftrik, A.T.J., Larsen, P.K.: Strain-accelerated etching of AlAs for epitaxial lift-off. *J. Phys. Condens. Matter* **16**, 3585–3596 (2004)
18. Van Niftrik, A.T.J., Schermer, J.J., Bauhuis, G.J., Van Deelen, J., Mulder, P., Larsen, P.K.: The influence of $\text{In}_x\text{Ga}_{1-x}\text{As}$ and $\text{GaAs}_{1-y}\text{Py}$ layers surrounding the AlAs release layer in the epitaxial lift-off process. *Crystal Growth & Design* **7**, 2472–2480 (2007)
19. Van Niftrik, A.T.J., Schermer, J.J., Bauhuis, G.J., Mulder, P., Larsen, P.K., Van Setten, M.J., Attema, J.J., Tan, N.C.G., Kelly, J.J.: The role of HF species and dissolved oxygen on the epitaxial lift-off process of GaAs using AlAsP release layers. *J. Electrochem. Soc.* **155**, D35–D39 (2008)
20. Voncken, M.M.A.J., Schermer, J.J., Van Niftrik, A.T.J., Bauhuis, G.J., Mulder, P., Larsen, P. K., Peters, T.P.J., De Bruin, B., Klaassen, A., Kelly, J.J.: Etching AlAs with HF for epitaxial lift-off applications. *J. Electrochem. Soc.* **151**, G346–G351 (2004)
21. Van Niftrik, A.T.J., Schermer, J.J., Bauhuis, G.J., Mulder, P., Larsen, P.K., Kelly, J.J.: A diffusion and reaction related model of the epitaxial lift-off process. *J. Electrochem. Soc.* **154**, D629–D635 (2007)
22. Maeda, J., Sasaki, Y., Dietz, N., Shibahara, K., Yokoyama, S., Miyazaka, S., Hirose, M.: High-rate GaAs epitaxial lift-off technique for optoelectronic integrated circuits. *Jpn. J. Appl. Phys.* **36**, 1554–1557 (1997)
23. Yoon, J., Sungjin, J., Chun, I.S., Jung, I., Kim, H.-S., Meitl, M., Menard, E., Li, X., Coleman, J. J., Paik, U., Rogers, J.A.: GaAs photovoltaics and optoelectronics using releasable multilayer epitaxial assemblies. *Nature* **465**, 329–334 (2010)
24. Horng, R.H., Tseng, M.C., Wu, F.L., Li, C.H., Wu, C.H., Yang, M.D.: Thin film solar cells fabricated using cross-shaped pattern epilayer lift-off technology for substrate recycling applications. *IEEE Trans. Electron Dev.* **59**, 666–672 (2012)

25. Gale, R.P., McClelland, R.W., King, B.D., Gormley, J.V.: High-efficiency thin-film AlGaAs-GaAs double heterostructure solar cells. In: Proceedings of 20th IEEE Photovoltaic Specialists Conference, Las Vegas, Nevada, pp. 446–450 (1988)
26. McClelland, R.W., Bozler, C.O., Fan, J.C.C.: A technique for producing epitaxial films on reusable substrates. *Appl. Phys. Lett.* **37**, 560–562 (1980)
27. Lee, X.Y., Verma, A.K., Wu, C.Q., Goertemiller, M., Yablonovitch, E.: Thin film GaAs solar cells on glass substrates by epitaxial liftoff. In: Proceedings of 25th IEEE Photovoltaic Specialists Conference, Washington, DC, pp. 53–55 (1996)
28. Hageman, P.R., Bauhuis, G.J., Van Geelen, A., Van Rijsingen, P.C., Schermer, J.J., Giling, L. J.: Large area, thin film epitaxial lift off III/V solar cells. In: Proceedings of 25th IEEE Photovoltaic Specialists Conference, Washington, DC, pp. 57–60 (1996)
29. Van Geelen, A., Hageman, P.R., Bauhuis, G.J., Van Rijsingen, P.C., Schmidt, P., Giling, L.J.: Epitaxial lift-off GaAs solar cell from a reusable GaAs substrate. *Mat. Sci. Eng. B* **45**, 162–171 (1997)
30. Bauhuis, G.J., Mulder, P., Haverkamp, E.J., Huijben, J.C.C.M., Schermer, J.J.: 26.1% thin-film GaAs solar cell using epitaxial lift-off. *Sol. Energ. Mat. Sol. Cell.* **93**, 1488–1491 (2009)
31. Miller, O.D., Yablonovitch, E., Kurtz, S.R.: Strong internal and external luminescence as solar cells approach the Shockley-Queisser limit. *IEEE J. Photovolt.* **2**, 303–311 (2012)
32. Green, M.A., Emery, K., Hishikawa, Y., Warta, W., Dunlop, E.D.: Solar cell efficiency tables (version 41). *Progr. Photovolt.* **21**, 1–11 (2013)
33. Kayes, B.M., Nie, H., Twist, R., Spruytte, S.G., Reinhardt, F., Kizilyalli, I.C., Hgashi, G.S.: 27.6% conversion efficiency, a new record for single-junction solar cells under 1 sun illumination. In: Proceedings of 36th IEEE Photovoltaic Specialists Conference, Seattle, WA, pp. 4–8 (2011)
34. Taguschi, H., Soga, T., Jimbo, T.: Epitaxial lift-off process for GaAs solar cell on Si substrate. *Sol. Energ. Mat. Sol. Cell.* **85**, 85–89 (2005)
35. Tseng, M.-C., Horng, R.-H., Wu, F.-L., Wu, C.-H., Yang, M.-D.: Performance of GaAs/Mirror/Cu-substrate thin-film solar cells. *IEEE Trans. Electron Dev.* **58**, 3898–3904 (2011)
36. Omnes, F., Guillaume, J.C., Nataf, G., Jäger-Waldau, G., Vennegues, P., Gibart, P.: Substrate free GaAs photovoltaic cells on Pd-coated silicon with a 20% AM1.5 efficiency. *IEEE Trans. Electron Dev.* **43**, 1806–1811 (1996)
37. Tatavarti, R., Dzankovic, A., Martin, G., Tuminello, F., Navaratnarajah, R., Du, G., Vu, D.P., Pan, N.: Lightweight, low cost GaAs solar cells on 4" epitaxial liftoff (ELO) wafers. In: Proceedings of 33th IEEE Photovoltaic Specialists Conference, San Diego, CA, pp. 1–4 (2008)
38. Van Deelen, J., Mulder, P., Bauhuis, G.J., Van Niftrik, A.T.J., Haverkamp, E.J., Schermer, J.J., Larsen, P.K.: Study of wet chemical etching of $\text{Al}_x\text{Ga}_{1-x}\text{InP}_2$ films using hydrochloric acid. *J. Electrochem. Soc.* **153**, C442–C448 (2006)
39. Tatavarti, R., Hillier, G., Martin, G., Wibowo, A., Navaratnarajah, R., Tuminello, F., Hertkorn, D., Disabb, M., Youtsey, C., McCallum, D., Pan, N.: Lightweight, low cost InGaP/GaAs dual-junction solar cells on 100 mm epitaxial liftoff (ELO) wafers. In: Proceedings of 34th IEEE Photovoltaic Specialists Conference, Philadelphia, PA, pp. 2065–2067 (2009)
40. Bauhuis, G.J., Mulder, P., Haverkamp, E.J., Schermer, J.J., Nash, L.J., Fulgoni, D.J.F., Ballard, I.M., Duggan, G.: Inverted thin film InGaP/GaAs tandem solar cells for CPV applications using epitaxial lift off. In: Proceedings of 35th IEEE Photovoltaic Specialists Conference, Honolulu, Hawaii, pp. 1243–1247 (2010)
41. Tatavarti, R., Wibowo, A., Elarde, F., Tuminello, F., Pastor, R., Giannopoulos, T., Osowski, M., Chan, C., Youtsey, C., Hillier, G., Pan, N.: Large area, epitaxial lift-off, inverted metamorphic solar cells. In: Proceedings of 36th IEEE Photovoltaic Specialists Conference, Seattle, WA, pp. 1941–1944 (2011)
42. Shimazaki, K., Kobayashi, Y., Takahashi, M., Imaizumi, M., Takamoto, T., Ito, T., Nozaki, Y.: Progress in development of ultra-lightweight solar panel using space solar sheet. In: Proceedings of 35th IEEE Photovoltaic Specialists Conference, Honolulu, Hawaii, pp. 725–730 (2010)

43. Farah, J.: Dry-epitaxial lift-off, integration, interconnect and encapsulation of foldable/rollable high efficiency solar cell modules. In: Proceedings of 37th IEEE Photovoltaic Specialists Conference, Seattle, WA, 2012
44. Trautz, K.M., Jenkins, P.P., Walters, R.J., Scheiman, D., Hoheisel, R., Tatavarti, R., Chan, R., Miyamoto, H., Adams, J.G.J., Elarde, V.C., Grimsley, J.: Mobile solar power. *IEEE J. Photovolt.* **3**, 535–541 (2013)
45. Schermer, J.J., Bauhuis, G.J., Mulder, P., Haverkamp, E.J., Van Deelen, J., Van Niftrik, A.T.J., Larsen, P.K.: Photon confinement in high-efficiency, thin-film III-V solar cells obtained by epitaxial lift-off. *Thin Solid Films* **511–512**, 645–653 (2006)
46. Schermer, J.J., Mulder, P., Bauhuis, G.J., Voncken, M.M.A.J., Van Deelen, J., Haverkamp, E., Larsen, P.K.: Epitaxial lift-off for large area thin film III/V devices. *Phys. Stat. Sol. A* **202**, 501–508 (2005)
47. Hanappel, T., Sagol, B.E., Seidel, U., Szabo, N., Schwarzburg, K., Bauhuis, G.J., Mulder, P.: Measurement of an InGaAsP/InGaAs tandem solar cell under GaAs. In: Proceedings of 33th IEEE Photovoltaic Specialists Conference, San Diego, CA, pp. 1–3 (2008)
48. Bauhuis, G.J., Schermer, J.J., Mulder, P., Voncken, M.M.A.J., Larsen, P.K.: Thin film GaAs solar cells with increased quantum efficiency due to light reflection. *Sol. Energ. Mat. Sol. Cell.* **83**, 81–90 (2004)
49. Asbeck, P.: Self-absorption effects on the radiative lifetime in GaAs-AlGaAs double heterostructures. *J. Appl. Phys.* **48**, 820–822 (1977)
50. Ahrenkiel, R.K., Dunlavy, D.J., Keyes, B., Vernon, S.M., Dixon, T.M., Tobin, S.P., Miller, K. L., Hayes, R.E.: Ultralong minority-carrier lifetime epitaxial GaAs by photon recycling. *Appl. Phys. Lett.* **55**, 1088–1090 (1989)
51. Lush, G., Lundstrom, M.: Thin film approaches for high-efficiency III-V cells. *Sol. Cell.* **30**, 337–344 (1991)
52. Green, M.A., Emery, K., Hishikawa, Y., Warta, W., Dunlop, E.D.: Solar cell efficiency tables (version 36). *Progr. Photovolt.* **16**, 346–352 (2010)
53. Law, D.C., King, R.R., Yoon, H., Archer, M.J., Boca, A., Fetzer, C.M., Mesropian, S., Isshiki, T., Haddad, M., Edmondson, K.M., Bhusari, D., Yen, J., Sherif, R.A., Atwater, H.A., Karam, N.H.: Future technology pathways of terrestrial III-V multijunction solar cells for concentrator photovoltaic systems. *Sol. Energ. Mat. Sol. Cell.* **94**, 1314–1318 (2010)
54. Geisz, J.F., Friedman, D.J., Ward, J.S., Duda, A., Olavarria, W.J., Moriarty, T.E., Kiehl, J.T., Romero, M.J., Norman, A.G., Jones, K.M.: 40.8% efficient inverted triple-junction solar cell with two independently metamorphic junctions. *Appl. Phys. Lett.* **93**, 123505 (2008)
55. Stan, M., Aiken, D., Cho, B., Cornfeld, A., Diaz, J., Ley, V., Korostyshevsky, A., Patel, P., Sharps, P., Varghese, T.: Very high efficiency triple junction solar cells grown by MOVPE. *J. Cryst. Growth* **310**, 5204–5208 (2008)
56. Smeenk, N.J., Engel, J., Mulder, P., Bauhuis, G.J., Bissels, G.M.M.W., Schermer, J.J., Vlieg, E., Kelly, J.J.: Arsenic formation on GaAs during etching in HF solutions: relevance for the epitaxial lift-off process. *ECS J. Solid State Sci. Technol.* **2**, P58–P65 (2013)
57. Bauhuis, G.J., Mulder, P., Haverkamp, E.J., Schermer, J.J., Bongers, E., Oomen, G., Köstler, W., Strobl, G.: Wafer reuse for repeated growth of III-V solar cells. *Prog. Photovolt.* **18**, 155–159 (2010)
58. Lee, K., Zimmerman, J.D., Xiao, X., Sun, K., Forrest, S.R.: Reuse of GaAs substrates for epitaxial lift-off by employing protection layers. *J. Appl. Phys.* **111**, 033527 (2012)
59. Cornfeld, A.B., Patel, P., Spann, J., Aiken, D., McCarthy, J.: Evolution of a 2.05 eV AlGaInP top sub-cell for 5 and 6J-IMM applications. In: Proceedings of 38th IEEE Photovoltaic Specialists Conference, Austin, TX, 2012
60. Patel, P., Aiken, D., Chumney, D., Cornfeld, A., Lin, Y., Mackos, C., McCarthy, J., Miller, N., Sharps, P., Stan, M.: Initial results of the monolithically grown six-junction inverted metamorphic multi-junction solar cell. In: Proceedings of 38th IEEE Photovoltaic Specialists Conference, Austin, TX, 2012

61. Bedell, S.W., Shahrjerdi, D., Hekmatshoar, B., Fogel, K., Lauro, P.A., Ott, J.A., Sosa, N., Sadana, D.: Kerf-less removal of Si, Ge, and III-V layers by controlled spalling to enable low-cost PV technologies. *IEEE J. Photovolt.* **2**, 141–147 (2012)
62. Shahrjerdi, D., Bedell, S.W., Ebert, C., Bayram, C., Hekmatshoar, B., Fogel, K., Lauro, P., Gaynes, M., Gokmen, T., Ott, J.A., Sadana, D.K.: High-efficiency thin-film InGaP/InGaAs/Ge tandem solar cells enabled by controlled spalling technology. *Appl. Phys. Lett.* **100**, 053901 (2012)
63. Mattos, L.S., Scully, S.R., Syfu, M., Olson, E., Yang, L., Ling, C., Kayes, B.M., He, G.: New module efficiency record: 23.5% under 1-sun illumination using thin-film single-junction GaAs solar cells. In: *Proceedings of 37th IEEE Photovoltaic Specialists Conference*, Seattle, WA, pp. 3187–3190 (2011)
64. Furman, B., Menard, E., Gray, A., Meitl, M., Bonafede, S., Kneeburg, D., Ghosal, K., Bukovnik, R., Wagner, W., Gabriel, J., Seel, S., Burroughs, S.: A high concentration photovoltaic module utilizing micro-transfer printing and surface mount technology. In: *Proceedings of 37th IEEE Photovoltaic Specialists Conference*, Seattle, WA, pp. 475–480 (2011)

Index

A

- Al-back-surface-field (Al-BSF), 17
- Aluminium oxide (Al_2O_3)
 - Al-BSF, 17
 - atomic layer deposition, 18–19
 - boron-doped emitter, 20
 - chemical passivation, 20–21
 - field-effect passivation, 17
 - p-SC nanoparticles, 221
 - TMA molecules, 18
- Amorphous silicon (a-Si), 475–476
 - Au nanoparticles, 501
 - 3D nanostructures, 140–147
- Amorphous silicon nitride (SiN_x)
 - antireflection coating, 28
 - antireflection materials, 451
 - antireflective properties, 15
 - fabrication process, 24
 - IBC cells, 34
 - MIS structures, 16
 - plasma gas dissociation, 15
 - surface passivation effect, 16
- Atomic force microscope (AFM), 340, 346, 454, 455, 628
- Atomic layer deposition (ALD), 18–21, 525–526

B

- Back surface field (BSF), 3, 4, 12, 33, 38, 546, 547, 562–564
- Black silicon solar cells, 133
- Bulk heterojunction (BHJ)
 - hole transport layer, 198–199
 - hybrid solar cells, 359
 - OSCs, purpurins
 - absorption spectra, 344, 345
 - AFM images, 346

- blend ratios, 345–346
- elevated temperature, 350–351
- exciton blocking layer, 350–351
- FF value, 348
- IPCE profiles, 345, 346
- PC_{70}BM , 348
- performance parameters of, 348, 349
- SCLC method, 346, 347
- PEDOT:PSS photovoltaic devices
 - photodiodes, 390, 392
 - spin-coating method, 398–399
- and planar, 323

C

- CdTe QD decorated ZnO nanorod DSSC
 - dual-sensitization
 - absorption and PL spectra, 301–302
 - device performance, 310–311
 - different architectures, 307–309
 - effectiveness, 309
 - excited state lifetime, 302, 303, 306
 - fluorescence decays, 302, 304
 - light absorption, 300
 - morphological characterization, 301
 - photoconductivity measurement, 311–312
 - photocurrent vs. wavelength spectra, 309–310
 - photo-induced electron transfer, 306
 - quantum yields and FRET parameters, 302, 305, 306
 - schematics, 312
 - steady-state emission quenching, 302, 303
 - fabrication, 272–273
 - QD and nanorod preparation, 272

Chalcopyrites

- quantum dots
 - colloidal nanoparticles, 123
 - cost-effective method, 123
 - dry deposition methods, 123
 - scanning electron microscopy, 123–124
 - scanning tunneling microscopy, 124
 - tetrahedral quantum dots, 125–126
- quantum wells
 - Cu-poor off-stoichiometries, 120
 - EDX, 120–121
 - hydrogen atmosphere, 119
 - III-V semiconductors, 120
 - MBE/MOVPE, 119
 - metal-organic compounds, 119
 - multilayer stack, 121–122
 - quantum confinement, 122–123
 - SIMS measurements, 120
 - TEM, 120

Cleavage of lateral epitaxial films for transfer (CLEFT) technique, 632–634

Coumarins, 229–230

Cyanines, 228

Czochralski (Cz) method, 4–5

D

- Dye-sensitized solar cell (DSSC), 427–428
- absorption spectra, 268–269
 - bare metal nanoparticles, sunlight utility anode, 522
 - direct incorporation, 524
 - electrical conductivity, 524
 - IPCE spectra, 522–523
 - light trapping, 522–523
 - mass ratio, 522
 - optical characterization, 522–523
 - potential problem, 522, 524
- C345, 229
- carboxyl purpurins (*see* Purpurins molecules)
- CdTe QD based ZnO nanorods (*see* CdTe QD decorated ZnO nanorod DSSC)
- c-H₂P and c-ZnP, 325
- device structure and energy level, 320–321
- electrolyte leakage, 320
- electron donor, 323–325
- energy transfer efficiency, 274–275
- fill factor, 275–276, 321–322
- hybrid solar cells, 375
- IPCE, 275, 321
- luminescence intensity ratio, 275
- nanostructured metal oxide, 138
- N719 dye, 309
- NiO-based DSCs

coumarin sensitizers, 229–230

cyanine sensitizers, 228

dyads, 238–241

perylene imide sensitizers, 225–228

polymers, 241–242

porphyrine and erythrosine sensitizers, 222–225

quantum dots, 242

ruthenium complexes, 234–238

squaraine sensitizers, 234

trisphenylamine push-pull-based sensitizers, 230–234

organic absorbing materials, 320

p-DSC

anchoring group, 219–220

electrolyte and photoinjected holes, 221

geminate charge recombination, 220–221

low photovoltage, 219

thermodynamic considerations, 218–219

photoconductivity, 276

photocurrent of, 321

photoluminescence transients, 273–274

power conversion efficiency, 275–276, 321

Ruthenium sensitizers, 268

semiconductor/insulator

ALD, 525, 526

conventional synthesis, 531

corrosion prevention, 527

electron transport, 527, 530

Γ/I_3 -electrolyte, 527

IPCE, 525–526

light harvesting, improvement of, 531

metal cores, 525, 530

N719 ruthenium, 527

posttreatment method, 532–533

in situ synthesis, 532

structure of, 526–529

surface protection, 526

Tang group, 527, 530

UV-vis absorption spectra, 531–532

solid-state hole transport material, 320

SPP, 533–534

surface plasmon polariton, 533–534

TiO₂ nanoporous materials, 427–428

ZnO semiconductor, 283

E

Electroluminescence (EL), 80

EL intensity decay, 73–74

LED, 73–74

TO phonon, 71

radiative recombination, 71

- Shockley–Read–Hall mechanism, 73
- wavelength distribution, 72
- Electronic energy transfer. *See* Förster
- resonance energy transfer (FRET)
- Electronic impedance spectra (EIS), 330, 331
- Electropolymerization, 197
 - direct electrochemical polymerization, 382–383
 - monomer, 374
 - polymers, 373–374
 - thiophene copolymers
 - advantages, 204
 - BHJ solar cells, 211
 - copolymerization of 3-methylthiophene, 207
 - counter electrode, 205
 - current–time curve, 206
 - cyclic voltammetry, 206
 - disadvantages, 204
 - electrochemical stability, 210–211
 - FTIR spectra, 210
 - homopolymer and copolymer films, 204–205
 - morphology, 208–210
 - potentiostatic/potentiodynamic
 - conditions, 204, 205
 - thermal stability, 211
 - three-electrode setup, 205
 - typical cyclic voltammograms, 206, 207
- Emitter-wrap-through (EWT) solar cell
 - advantages, 35
 - external and internal quantum efficiencies, 37–38
 - fill factors, 38–39
 - physical vapour deposition, 35
 - process sequence, 36
 - RISE-EWT, 38
- Energy dispersive X-ray spectroscopy (EDX), 120, 121
- Epitaxial lift-off (ELO)
 - flexible thin-film cells
 - bifacial cell, 634
 - CLEFT technique, 632–634
 - conventional 3-junction cell, 636–637
 - IMM cell, 636–637
 - InGaP/GaAs semitransparent cell, 635
 - low power to weight ratio/flexibility, 634
 - optimal light trapping, 635
 - photons, 635
 - reflectivity, 635
 - saturation current density, 636
 - Shockley-Queisser limit, 636
 - future aspects, 639
 - peeled film technology, 624–625
 - process parameters
 - AFM, 628
 - AlA reaction, 627–628
 - etch rate, 628–630
 - HF solution, 626–627
 - lift-off process, 631
 - radius of curvature, 630–631
 - small area devices, 631–632
 - temperature, 631
 - wet chemical etching, 625
 - WI-ELO setup, 625–626
 - substrate reuse, 637–638
 - wafer cells, 623–624
- Erythrosine, 222–225
- Excitonic solar cells (XSCs)
 - characteristics, 516
 - DSSC (*see* Dye-sensitized solar cell (DSSC))
 - photovoltaics
 - absorption cross-sections, 519
 - LSPR, 520–521
 - plasmonic light-trapping mechanisms, 520
 - polarizability, 519
 - scattering efficiency, 519
 - SPP, 520–521
 - polymer solar cell
 - advantages, 535
 - buffer/active layer, 535–536
 - current-voltage characteristics, 536–537
 - disadvantages, 535
 - dual plasmon enhancement, 536
 - electrical field, 540
 - external quantum efficiency, 536–537
 - fabrication process, 537–538
 - grating pattern, 538
 - hexadecyl amine, 536–537
 - HOMO, 535
 - LUMO, 535
 - photocurrent density *vs.* effective voltage, 536–537
 - photocurrent generation, 539–540
 - plasmonic effect, 538–539
 - transport layer, 539
 - UV-vis absorption spectra, 536–537
 - power conversion efficiency
 - cost, 517
 - electric field, 518
 - IPCE, 517–518
 - mesoporous film, 516–517
 - parameters, 517
 - plasmonic metal nanoparticles, 517
 - structure of, 518
- External quantum efficiency (EQE), 488

F

- Finite-difference time domain (FDTD)
 - method, 142
- Förster resonance energy transfer (FRET)
 - CdTe QD based ZnO nanorods (see CdTe QD decorated ZnO nanorods DSSC)
 - mechanism, 269
 - organic molecules, 269
 - quantum dot, 269–270
 - ZnO-based DSSC (see ZnO-based DSSC)

G

- GaAs-based multijunction solar cell, 602
- GaN solar cells
 - admittance spectroscopy
 - Arrhenius plot, 557
 - capacitance/conductance, 555–557
 - n–p structure, 558–559
 - photoluminescence, 554
 - p–n structure, 555, 558–559
 - properties, 555
 - simulation results, 557
 - techniques, 554–555
 - temperature dependences, 556
 - thermoionic emission, 556
 - double layer wide gap window, p–n structures, 559–561
 - I*–*V* curves
 - AFORS-HET software, 550
 - AlInP window layer, 549–551
 - equilibrium band diagram, 550–551
 - fill factor, 549
 - interface defect density, 553
 - J_{SC} , V_{OC} , and efficiency, 553–554
 - n–p structure, 551–552
 - parameters, 549–550
 - p–n structure, 551–552
 - simulations, 551–552
 - window/emitter isotype heterojunction, 550–554
 - n-type/p-type emitter, 549
 - photoactive p–n homojunction, 549
- GaN nanowires
 - AlInP/GaAs substrates
 - absorptance, 590–591
 - angle-integrated reflection, 588
 - concentrator systems, 592
 - PerkinElmer Lambda, 950
 - spectrometer, 588–589
 - reflectance, 589–590
 - refractive index, 591
 - top/right inset, 591–592
 - transmittance, 591
 - GaP substrates, 585–588

VLS growth

- AlInP layer, 582–585
- GaP substrate, 582–584
- gold-coated substrate, 584
- SEM image, 583–584
- Geostationary earth orbit (GEO)
 - mission, 599

H

- Heterojunction with intrinsic thin-layer (HIT)
 - solar cell, 1, 3, 12, 22
 - AMPS/AFORS-HET software, 43
 - junction formation process, 41
 - n-type CZ-Si substrates, 41
 - p-type HIT solar cells, 42–43
 - SHJ solar cells, 39
 - TCO layers and metal electrodes, 40
 - transparent and anti-reflection layer, 40
- High-efficiency solar cells
 - Auger recombination, 88–89
 - electron–hole pairs, 87
 - minority carrier lifetime, 88–89
 - open-circuit voltage (*see* Open-circuit voltage (V_{OC}))
 - radiative recombination and photon recycling
 - chemical potential, 93
 - PR factor, 94
 - radiative lifetime, 94
 - reabsorption and reemission processes, 93
 - transport device, 95
 - radiative recombination lifetime, 88
 - Shockley–Read lifetime, 88
 - silicon-based solar cells (*see* Silicon-based solar cells)
- Highest occupied molecular orbital (HOMO), 326, 339, 342–343, 371–372, 535
 - chromophore PAQX, 406
 - ITO/Molx + P3OT/Al, 419–425
 - ITO/PAQX + PDT/Al, 406–411
 - ITO/PAQX + P3OT/Al, 412–416
 - ITO/PAQX + PVK:TCNE/Al architecture, 415–419
 - ITO/PEDOT:PSS/Molx + P3OT/Al architecture, 419–425
 - ITO/PEDOT:PSS/PAQX + PDT/Al structures, 406–411
 - ITO/PEDOT:PSS/PAQX + PVK:TCNE/Al, 415–419
 - Molx molecule, 406
 - XSC, 535
- Hole transport layer (HTL)
 - bulk heterojunction, 198–199

- electropolymerization, thiophene
 - copolymers
 - advantages, 204
 - BHJ solar cells, 211
 - copolymerization of 3-methylthiophene, 207
 - counter electrode, 205
 - current–time curve, 206
 - cyclic voltammetry, 206
 - disadvantages, 204
 - electrochemical stability, 210–211
 - FTIR spectra, 210
 - homopolymer and copolymer films, 204–205
 - morphology, 208–210
 - potentiostatic/potentiodynamic conditions, 204, 205
 - thermal stability, 211
 - three-electrode setup, 205
 - typical cyclic voltammograms, 206, 207
 - excitons, 198
 - flat heterojunction, 198
 - function, 201
 - HOMO level, 200
 - organic light-emitting diodes, 200
 - PEDOT:PSS, 202–204
 - poly(para-phenylene), 200
 - Honda-Fujishima effect, 427
 - Hybrid solar cells
 - bulk heterojunction, 359
 - inorganic materials, 361, 362
 - inorganic nanomaterials
 - epitaxy vs. etching nanowires, 364–365
 - materials-by-design, 360
 - nanocrystals, 365–364
 - nanolithography, 362
 - nanoporous structures, 365
 - quantum mechanical effects, 362
 - interface manipulation
 - surface functionalization, 383–384
 - surface passivation, 384
 - morphology
 - BHJs, 376–377
 - bilayer structure, 375–376
 - controlled spin-coating, 379–380
 - direct electrochemical polymerization, 382–383
 - DSSC, 375
 - interdigitated/ordered structures, 377–378
 - infiltration/percolation, 378–379
 - polymeric semiconductors, 380–382
 - organic materials developments, 360–362
 - organic polymers
 - chemical doping, 367–368
 - chemical structures, 366
 - chemical synthesis, 372–373
 - electrochemical doping, 368
 - electrochemical synthesis, 373–374
 - energy level engineering, 371–372
 - inducing solubility method, 370–371
 - interfacial doping, 369
 - photo-excitation doping, 369
 - photovoltaics, 358
 - P3HT chemical structure, 360
 - polymer–silicon hybrid solar cell, 138
 - prototyping engineered, 361
 - screen-printing techniques, 358
 - solar grid parity, 358
 - sun-driven energy generation, 362
 - Hydrogenated amorphous silicon (a-Si:H)
 - chemical passivation, 22
 - conventional PECVD, 22
 - degradation behavior, 609, 610
 - ICP system, 23
 - mechanism, 21
 - p–n junction, 10
 - polymer and n-type a-Si:H film, 139
 - Si thin-film solar cells, 21
- I**
- Incident photon-to-current conversion efficiency (IPCE), 275, 295, 296
 - BHJ solar cells, 345, 351
 - DSSC, 321, 523
 - LUMO+1 orbital, 330
 - organic solar cells, 322–323
 - PHJ solar cells, 342
 - photovoltaic diode, 328
 - SnO₂-based solar cells, 334
 - Incident photon-to-electron conversion efficiency (IPCE)
 - DSSC, 522–523
 - PCE, 517–518
 - Interdigitated back-contact (IBC) cells
 - advantages, 32–33
 - cost-effective processing approaches, 34–35
 - emitter and BSF dopings, 32
 - emitter fractions, 33
 - front surface field, 33
 - maximum cell efficiencies, 33–34
 - Internal quantum efficiency (IQE), 25–26, 488, 581
 - Inverted metamorphic (IMM) cell, 636–637

L

Light beam-induced current (LBIC)
 mapping, 181–183

Light trapping structures
 cadmium telluride (CdTe), 450
 crystalline silicon (c-Si) material, 450
 electron-hole pair, 450
 evaluation of, 452–453
 gallium arsenide (GaAs), 450
 inverted pyramidal structures
 AFM images of, 454–455
 anisotropic crystalline etching
 simulation, 453, 454
 antireflective characteristics, 452
 crystalline silicon wafers, 451
 fabrication of, 451, 452
 measured reflectances, 456
 PERL, 451
 photolithography processes, 451
 ray tracing simulations, 456, 457
 simulated reflectances, 456
 textured structures, 451

Lambertian limit/Yablonvitch limit, 452
 literature review of, 451
 nanophotonic structures (*see* Nanophotonic
 light trapping structures)
 plasmonic nanoparticles, 451
 plasmonic solar cells, 451
 ray optics theory, 452
 silicon-based solar cells, 450
 solar energy, 450
 textured silicon surface structures, 451

Localized surface plasmon resonances (LSPR),
 519–521, 526–527, 530, 533,
 535–537

Localized surface plasmons (LSPs), 498, 506

Low earth orbit (LEO) mission, 599, 600, 603

Lowest unoccupied molecular orbital (LUMO)
 chromophore PAQX, 406
 ITO/Molx +P3OT/Al, 419–425
 ITO/PAQX + PDT/Al, 406–411
 ITO/PAQX + P3OT/Al, 412–416
 ITO/PAQX + PVK:TCNE/Al architecture,
 415–419
 ITO/PEDOT:PSS/Molx + P3OT/Al
 architecture, 419–425
 ITO/PEDOT:PSS/PAQX + PDT/Al
 structures, 406–411
 ITO/PEDOT:PSS/PAQX + PVK:TCNE/
 Al, 415–419
 LUMO+1 orbital, 330
 Molx molecule, 406
 planar heterojunction, 342

polymer solar cell, 535
 purpurins molecules, 326, 327
 XSC, 535

LSC. *See* Luminescent solar concentrator
 (LSC) systems

Luminescent solar concentrator (LSC) systems
 advantages, 250
 disadvantages, 250–251
 external quantum efficiencies, 251
 GaAs solar cells, 251, 253, 261
 incident solar radiation, 250
 InGaP solar cells, 251, 261–262
 light interactions, 249
 lumogen series, 258–259
 optical solar concentrators, 248–249
 photovoltaic generation, 248
 polysiloxane, 260
 gold nanoparticles, 257
 lumogen red, 254–258
 polysiloxane film, 258
 Si photodiode, 251–253, 261, 264

LUMO. *See* Lowest unoccupied molecular
 orbital (LUMO)

M

Magnetically grown Czochralski (Mcz)
 silicon, 6

Medium earth orbit (MEO) mission, 599–600

Metal organic vapor phase epitaxy (MOVPE),
 117, 119–120, 124
 GaInP solar cells, 549
 III-phosphide/Ge interfaces, 564–565

Metal-oxide-semiconductor (MIS), 16

Mie scattering theory, 499

III-V Multi-junction solar cells
 band discontinuity behavior, 548
 band gap offsets, 547–548
 bottom-up growth method, 574–575
 GaInP/Ga(In)As/Ge solar cell design, 547
 GaInP solar cells (*see* GaInP solar cells)
 GaP nanowires (*see* GaP nanowires)
 heterointerface, 547
 homogeneous/step-index layers, 573–574
 inhomogeneous/graded index layers, 574
 MOVPE, 548
 nanostructures, 574
 oxygen, 548
 III-phosphide/Ge interfaces
 admittance spectroscopy, 566
 charge carrier transport, 564–565
 C–T– ω and G/ ω –T– ω curves, 566
 diffusion process, 566–567

- doping impurities, 564
 - electrical properties, 564
 - I - V curves, 565–566
 - p-type substrate, 564
 - Schottky barrier, 567–568
 - subcell structures, 567–568
 - III-phosphide/III-arsenide interfaces
 - AlGaAs BSF layers, 562–564
 - band discontinuity, 548, 561
 - C-T- ω curves, 562–563
 - I - V curves, 562
 - potential barriers, 546
 - quadruple solar cell, 572–573
 - SiO₂ and TiO₂ nanowires, 574
 - surface carrier recombination, 575
 - thermolization, 546
 - transfer matrix method (*see* Transfer matrix method)
 - Multiple exciton generation (MEG), 157–159
- N**
- Nanophotonic light trapping structures
 - metallic/dielectric nanoparticles
 - Lumerical FDTD Solutions Software, 457
 - period and radius, 458
 - periodic silver nanoparticles, 457, 458
 - short circuit current densities, 458, 459
 - silicon material, 457
 - silver nanoparticle array, 459, 461
 - transmission energy, 459
 - mixing metallic and dielectric nanoparticles/materials
 - electric field intensity distributions, 462, 464, 467–469
 - energy transmission, 468, 469
 - nanophotonic structure D, 468
 - optical transmission, 462, 463
 - photon number, 462–467
 - silicon substrate, 466
 - silver nanoparticles, 461, 462
 - Nanostructured silicon solar cells
 - hybrid organic solar cells, 137–139
 - micro-wire solar cells
 - CVD growth techniques, 136
 - electronic disadvantage, 135
 - filling ratio, 135
 - heterojunction Si micro-wire solar cell, 136
 - industrial feasibility, 136–137
 - surface-to-volume ratio, 135
 - thin-film solar cells (*see* Thin-film solar cells (TFSCs))
 - third-generation solar cells
 - multiple exciton generation, 157–159
 - tandem quantum dot structures, 155–156
 - wafer-based c-Si solar cells
 - Auger recombination, 134
 - black silicon surface, 133
 - broadband antireflection, 132
 - Fabry-Perot resonances, 133
 - low doping, 133–134
 - nano-sphere lithography, 132
 - photolithography techniques, 134
 - SiNW array, 132
 - SRV dependence, 134
 - Nonionizing energy loss (NIEL)
 - a-Si solar cells, 609, 617–618
 - CIGS solar cells, 611, 618–619
 - definition, 613
 - InGaP₂/GaAs/Ge solar cell, 613, 614
 - integral over solid angle, 613
 - irradiating particle, energy and target material, 606, 614–615
 - nuclear elastic/inelastic interactions, 613
 - on-ground irradiation experiments, 605–606
 - TJ GaAs cell data, D_a methodology
 - coverglass, 617
 - normalized maximum power, 615–616
 - on-orbit data, 617
 - parameters, 617
 - particle spectra, 616
 - R_{ep} factor, 616–617
 - semi empirical equation, 615
- O**
- Open-circuit voltage (V_{oc})
 - band-to-band current, 92–93
 - dark current reduction, 90
 - g-r current density, 91
 - narrow-gap devices, 92
 - p-DSC cell, 219
 - silicon filling fraction, 509
 - solar spectrum, 283
 - trap-assisted tunneling currents, 92–93
 - Organic chromophores
 - 1*H*-pyrazole-[3,4-*b*]-quinolin derivatives, 401–403
 - polythiophene derivatives, 404–405
 - Organic photovoltaics (PV) cells. *See* Hole transport layer (HTL)
 - Organic polymers, 139
 - chemical doping, 367–368

- Organic polymers (*cont.*)
 chemical structures, 366
 chemical synthesis, 372–373
 electrochemical doping, 368
 electrochemical synthesis, 373–374
 energy level engineering, 371–372
 inducing solubility method, 370–371
 interfacial doping, 369
 photo-excitation doping, 369
- Organic solar cells (OSCs)
 charge transfer efficiency, 323
 electron donor and acceptor materials, 322
 exciton diffusion efficiency, 322
 IPCE, 322
 organic absorbing materials, 320
 planar and bulk heterojunction structures, 323
 purpurin molecules (*see* Purpurin molecules)
 spiro-OMeTAD, 320
- OSCs. *See* Organic solar cells (OSCs)
- P**
- Passivated emitter and rear cell (PERC),
 3, 4, 12, 37
 alkaline texturing process, 25
 fabrication process, 24
 phosphorus diffusion, 24
 phosphorus silicate glass, 25
 physical vapour deposition, 26
 reflectance and internal quantum efficiency, 25–26
 thermal degradation, 27
- Passivated emitter and rear locally diffused (PERL) cells, 3, 4, 14, 453
 elective emitter SE design, 28
 external quantum efficiency, 28
 light boron layer, 29
 multi-Si and Fz-Si materials, 28
 Pluto-PERC and Pluto-PERL cells, 31–32
 p-p⁺ high-low junction, 28
 wavelength dependent reflection, 28
- Passivated emitter and rear totally diffused (PERT) cells, 3, 4, 30
- Peeled film technology, 624–625
- PerkinElmer Lambda 950 spectrometer, 588–589
- PHJ. *See* Planar heterojunction (PHJ)
- Phosphorus silicate glass (PSG), 25
- Photoluminescence (PL), 59, 167, 270, 273, 280, 302, 426, 548, 554, 635
 free electrons, 81
 laser radiation, 76
 nonradiative recombination rate, 79–80
 quasi-steady-state current, 76–78
 SCR, 78
- Photovoltaic (PV) nanomaterials
 solar energy conversion
 absorbed energy flux, 98
 Carnot limit, 95
 entropy generation, 96
 irreversible process, 98
 Landsberg limit, 97
 non-equilibrium EHPs, 97
 Onsager relations, 98
 photochemical and photosynthesis process, 98
 photovoltaic engine, 96
 SQ approach, 97
 SQ limit (*see* Shockley–Queisser (SQ) limit)
- Physical vapour deposition (PVD), 26, 35, 38
- Planar heterojunction (PHJ), 325
 energy alignment, 341, 342
 HOMO and LUMO energy levels, 342
 IPCE profiles, 342–343
 molecules-based donor materials, 343
 photovoltaic performances, 343–345
- Plasma-enhanced chemical vapor deposition (PECVD), 10, 14–15, 139, 174, 478
 chemical vapor deposition, 171–172
 monomethylsilane, 171
- Plasmonics metal nanoparticles
 Ag nanoparticles, 501
 detailed balanced analysis
 Boltzmann's constant, 507
 current–voltage (J–V) characteristic, 509
 PCE, 507
 reverse saturation current, 507
 short circuit current density, 506–509
 silicon filling fraction, 508, 509
 ultimate efficiency, 510
- DSSC, 501
 light scattering, 499–501
 LSPs, 498, 499
- nanostuctured silicon
 Au nanoparticle, 504
 Au nanoparticle arrays, 502, 503
 COMSOL multiphysics software, 503
 electric field distribution, 504
 Floquet boundary conditions, 503
 nanopillars, 504
 optical absorption performance, 504
 photogenerated carrier profile, 505, 506
 quantum efficiency, 506

- silicon nanoholes, 502
 - structural parameters, 503
 - ultimate efficiency vs. silicon filling fraction, 504–506
 - optical thickness constant, 499
 - OSC, 501–502
 - Raman scattering, 501
 - resonance scattering, 501
 - silicon film thickness, 498
 - Polymers, 241–242
 - Poly (3,4 ethylenedioxy thiophene):poly (styrene sulfonic acid) (PEDOT:PSS) photovoltaic devices
 - architecture of, 390, 391
 - bulk heterojunction (*see* Bulk heterojunction (BHJ))
 - current density, non-illuminated diode, 395
 - current-voltage features, 397
 - current-voltage monitoring, 399–401
 - equivalent electric circuits, 395–396
 - heterojunction metal/semiconductor processes, 394–395
 - HOMO (*see* Highest occupied molecular orbital (HOMO))
 - LUMO (*see* Lowest unoccupied molecular orbital (LUMO))
 - organic chromophores
 - 1H-pyrazole-[3,4-b]-quinolin derivatives, 401–403
 - polythiophene derivatives, 404–405
 - principal mechanisms
 - charge separation, 393
 - charge transport, 393–394
 - electron-hole pair, 393
 - gathering, charges on electrodes, 394
 - photon absorption, 393
 - serial resistance R_s , 396
 - TiO₂ nanoporous materials
 - brookite polymorphs, 439
 - crystal structures and electronic properties, 428–430
 - current-voltage dependences, 441, 442
 - DSSCs, 427–428
 - Honda-Fujishima effect, 427
 - microstructure, 440–441
 - molecular precursors, 430
 - NC Anatase, 434–435
 - nitrogen adsorption-desorption, 440
 - PEG chain, 431
 - principal data, 442, 443
 - Raman spectra, 437
 - semilogarithmic, 442, 443
 - sol-gel process, 430, 432–434
 - TEM image, 441
 - Ti(OiPr)₄, 435
 - TiO₂ polymorphs, 437
 - Ti-O-Ti chains, 431
 - X-Ray diffraction, 437, 438
 - Porphyrine, 222–225
 - Purpurin molecules
 - OSCs
 - absorption spectra, 338, 339
 - BHJ (*see* Bulk heterojunction (BHJ))
 - BHJ solar cells, 350–351
 - Chemical structures, 337, 338
 - electron donor, 323–325
 - H₂P and ZnP thin films, 339–340
 - molecular arrangement, 339
 - PHJ (*see* Planar heterojunction (PHJ))
 - photocurrent of, 337
 - Zn-based purpurin sensitizer, 338
 - SnO₂-based DSSCs, sensitizers
 - absorption spectra, 331–333
 - CBE energy level, 331
 - c-ZnP, 336
 - electron injection dynamics, 336
 - IPCE profiles, 333
 - TAS, 334–336
 - TBP, 337
 - TD-DFT method, 331
 - TiO₂-based DSSCs
 - c-ZnP and c-H₂P sensitizers, 326, 327
 - EIS Nyquist plots, 330–331
 - HOMO-1, HOMO, LUMO+1 molecular energy levels, 326, 327
 - IPCE profiles, 328, 329
 - LUMO orbital, 326, 327
 - oxo-bacteriochlorin sensitizers, 330
 - self-adsorption spectra, 325, 326
 - TBP, 330
 - TiO₂ nanocrystalline thin films, 325
- Q**
- Quantum dots (QD)
 - chalcopyrites (*see* Chalcopyrites)
 - doping structure, 107
 - electron extraction, hot electron, 105
 - IR, 103–105, 109
 - NiO-based DSCs, 242
 - photoelectron capture and recombination, 106–107
 - Q-BIC technology, 108
- R**
- Rigorous coupled wave analysis (RCWA), 142
 - Ruthenium
 - carbanionic phenylpyridine ligands, 237
 - electronic transition, 235

- Ruthenium (*cont.*)
 photo-oxidants, 235
 Ru5, 237, 238
 Ru-NMI, 237
 Ru1, Ru2, Ru3, and Ru4, 235–236
- S**
- Scanning electron microscopy (SEM), 454, 583–584
 Au nanoparticle arrays, 503
 CuGaSe₂, 124
 3D nano-pyramidal structures, 141
 morphological characterization, 301
 nano-coaxial a-Si solar cells, 140
 quantum dot, 126
 “Swiss cheese” 3D nano-pattern., 141
 tandem junction silicon solar cell, 484, 485
 thiophene-based copolymer films, 209
 ZnO NR, 280, 301
- Secondary ion mass spectrometry (SIMS), 120, 628
- Shockley–Queisser (SQ) limit
 electron levels, 101–102
 photocarrier kinetics, 102–103
 photon management, 100–101
- Silicon-based solar cells
 emitter materials
 deposited emitter, 10
 diffused emitter, 9
 EWT and MWT cells, 35–39
 functional materials, 23–24
 high-efficiency technologies, 3
 HIT cell, 39–43
 IBC cells, 32–35
 low-cost technologies, 3
 mono-Si material
 acid texturing, 9
 cost, 6, 7
 Cz method, 4–5
 etching mask, 8
 loaf zone technique, 5–6
 Mcz silicon, 6
 multiwire sawing, 6
 point defect, 5
 polycrystalline, 5
 wet chemical treatment, 8
 multi-Si material
 block casting, 7
 unidirectional growth technique, 7
 passivated emitter and rear cell (*see* Passivated emitter and rear cell (PERC))
- passivation materials
 aluminium oxide, 17–20
 amorphous silicon, 21–23
 amorphous silicon nitride, 15–17
 back surface field, 12
 chemical passivation, 11
 dielectric films, 11
 field effect passivation, 10, 11
 SiO₂ and SiO_x, 13–15
 PERL and PERT Cells, 27–30
 p-n junction, 3
 PV market, 2
- Silicon nanocrystals (Si NCs), 498
 crystalline silicon tandem solar cell
 AM1.5G solar spectrum, 166
 amorphous and micro crystalline solar cells, 167
 bandgap, 168
 fabrication, 168
 III-V solar cells, 167
 device characterization, 181–183
 membrane p-i-n solar cells, 168–171
 optical modeling
 optical spectral functions, 177
 properties, 179–180
 SiC/Si NC multilayers, 178–179
 UV-vis spectroscopy, 176
 recombination and transport properties
 current-voltage curves, 188
 dark and light *IV* curves, 186–187
 diode ideality factor, 186
 fill factor, 185
 illumination-dependent *IV* curve analysis, 190
 p-i-n solar cell, 185
 series resistance, 186
 short-circuit resistance, 189
- Si-rich carbide
 crystallization, 175–176
 PECVD, 171–173
 thermal annealing, 174–175
- solar cell modeling
 light absorption, 183–184
 optical properties, 184–185
- Silicon oxide (SiO₂) nanowires
 bottom-up approach, 574
 GaP substrates, 585–588
 VLS growth, 583
- Silicon thin film solar cells
 advantages, 475
 amorphous and microcrystalline silicon, 475–476
 deposition process, 478–480

- $\mu\text{c-SiO}_x(\text{p})\text{:H}$ single layer
 - CO₂ gas flow, 485
 - electrical and morphological properties, 483–485
 - optical properties, 481–483
 - production of, 478
 - p–i–n solar cell, 476–477
 - silicon oxide p-layer stack
 - components of, 480–481
 - implementation of, 493–494
 - light-induced degradation, 491–493
 - quantum efficiency, 488–489
 - reflection, 486–488
 - in single and tandem junction devices, 480
 - solar cell performance data, 489–491
 - Staebler–Wronski effect, 475
 - TiO₂ layer, 477
 - Single-crystal silicon (c-Si)
 - Auger recombination, 63
 - design and fabrication technology, 63
 - edge electroluminescence (*see* Electroluminescence (EL))
 - edge luminescence, 59–60, 64
 - EL intensity, 70
 - factors, 66
 - free carrier absorbance, 68
 - SiGe alloys, 66
 - transverse optical phonons, 64–65
 - edge photoluminescence (*see* Photoluminescence (PL))
 - laser radiation, 62
 - light trapping structures, 450
 - radiative recombination, 60–61
 - wafer-based c-Si solar cells
 - Auger recombination, 134
 - black silicon surface, 133
 - broadband antireflection, 132
 - Fabry-Perot resonances, 133
 - low doping, 133–134
 - nano-sphere lithography, 132
 - photolithography techniques, 134
 - SiNW array, 132
 - SRV dependence, 134
 - Single junction (SJ) gallium arsenide (GaAs/Ge) solar cell, 601
 - Solar spectrum weighted transmittance (SSWT), 580–581
 - Space charge limited current method (SCLC) method, 325, 346, 347
 - Space solar cells
 - coverglass, 602–603
 - damage models
 - degradation rate, 612–613
 - NRL/JPL approach (*see* Nonionizing energy loss (NIEL))
 - solar cell response, 612
 - GaAs-based multijunction solar cell, 602
 - irradiation experiments
 - air mass zero, 605
 - α -Si solar cells, 608–611
 - beginning-of-life, 607–608
 - CIGS solar cells, 611–612
 - damage coefficients, 605
 - degradation curves, 609–611
 - end-of-life, 607–608
 - InGaP₂/GaAs/Ge solar cell, 606–607
 - isochronal annealing, 611–612
 - NIEL, 605–606
 - normalized maximum power data, 608
 - open circuit voltage, normalized values of, 605–606
 - radiation damage mechanisms, 603–605
 - single junction gallium arsenide solar cell, 601
 - Si solar cells, 601
 - space radiation environment
 - GEO, 599
 - LEO, 599
 - MEO, 599–600
 - space solar array substrates, 603
 - thin film a-Si solar cell, 602
 - thin film polycrystalline CIGS solar cell, 602
 - thin silicon solar, 601
 - Squaraines, 234
 - Staebler–Wronski effect (SWE), 139, 475, 491
 - Surface plasmon polariton (SPP), 147, 152–155, 521, 533
 - DSSC, 533–534
 - photovoltaics, 520–521
 - Surface recombination velocity (SRV), 134, 135
- T**
- Thin-film (TF)
 - a-Si solar cell, 139, 141, 142, 145, 159, 602, 610, 618
 - bifacial cell, 634
 - chalcopyrite structures
 - CdTe, 116
 - homogeneity, 116–117
 - nanostructuring approach, 117–119
 - Shockley-Queisser limit, 117

- Thin-film (TF) (*cont.*)
- CLEFT technique, 632–634
 - conventional 3-junction cell, 636–637
 - IMM cell, 636–637
 - InGaP/GaAs semitransparent cell, 635
 - low power to weight ratio/flexibility, 634
 - optimal light trapping, 635
 - photons, 635
 - polycrystalline CIGS solar cells, 602
 - reflectivity, 635
 - saturation current density, 636
 - Shockley-Queisser limit, 636
 - III–V solar cells (*See* Epitaxial lift-off (ELO))
- Thin-film solar cells (TFSCs)
- 3D nanostructures
 - Asahi texture glass a-Si cell, 145
 - current-voltage measurements, 146
 - FDTD method, 142, 144
 - genetic algorithm, 143–144
 - high-aspect-ratio pyramids, 143
 - imprint lithography, 141
 - Monte Carlo optical simulations, 145
 - nano-pillar/nano-coax a-Si solar cells, 140, 141
 - optical modeling, 142
 - photo-absorption, 140
 - RCWA algorithm, 142
 - "Swiss cheese" nano-pattern, 141
 - V-shaped morphologies, 147
 - plasmonics
 - light scattering, 148–150
 - optical antennas, 149–152
 - surface-plasmon polaritons, 152–155
- Time-resolved absorption spectra (TAS), 334, 335
- Titanium tetra-isopropoxide (Ti(OiPr)₄), 431, 435
- Transfer matrix method
- conical nanowires, 578–579
 - electric field amplitude, 575–576
 - Fresnel amplitude transmission, 577
 - MgF₂/ZnS double layer anti-reflection coating
 - internal quantum efficiency (IQE), 581
 - photocurrent density, 581–562
 - reflectance, 579–580
 - refractive indices, 579–580
 - SSWT, 580–581
 - propagation matrix, 577
 - reflectance, 578
 - reflection coefficients, 577–578
 - right/left-traveling wave, 576
 - transmission matrices, 577–578
- Transmission electron microscope (TEM), 120, 121, 175, 176, 288, 290, 291, 303, 441, 532
- Trimethyl aluminium (TMA) molecules, 18
- V**
- Vapor–liquid–solid (VLS) growth, 136
- AlInP layer, 582–585
 - GaP substrate, 582–584
 - gold-coated substrate, 584
 - SEM image, 583–584
- W**
- Weight-induced epitaxial lift-off (WI-ELO), 625–626, 629
- Z**
- ZnO-based DSSC
- hydrothermal process, 272
 - nanoparticle and nanocomposite preparation, 271
 - resonance energy transfer
 - device performance, 285–286
 - J-V curves, 283, 285
 - PL transients, 283–285
 - schematics, 286–287
 - ZnO-N719 spectral overlap, 282–283
- ZnO-Au nanocomposites
- device performance, 295, 296
 - excitation and emission spectra, 288, 289, 291
 - fluorescence decays, 290, 292
 - HRTEM images, 288, 289
 - interfacial electron transfer, 293–295
 - IPCE, 295, 296
 - J-V characteristics, 295–297
 - photocurrent response, 297–299
 - preparation, 271
 - schematics, 299–300
 - spectral overlap, 290, 292
 - TEM images, 288, 290
 - vs. ZnO NPs, 291
- ZnO-OX1 system
- absorption and emission spectra, 276–277
 - energy transfer dynamics, 277, 280
 - NR-OX1 adduct, fluorescence quenching, 280–281
 - spectral pattern, 277, 278
 - spectroscopic and fitting parameters, 277, 279
- ZnO vs. TiO₂, 270